PACIFIC SYMPOSIUM ON

BIOCOMPUTING 2026

PACIFIC SYMPOSIUM ON BIOCOMPUTING 2026

Kohala Coast, Hawaii, USA,
3 – 7 January 2026

Edited by

Russ B. Altman
Stanford University, USA

Lawrence Hunter
University of Chicago, USA

Marylyn D. Ritchie
University of Pennsylvania, USA

Tiffany Murray
Stanford University, USA

Teri E. Klein
Stanford University, USA

World Scientific

NEW JERSEY • LONDON • SINGAPORE • BEIJING • SHANGHAI • HONG KONG • TAIPEI • CHENNAI • TOKYO

Published by

World Scientific Publishing Co. Pte. Ltd.

5 Toh Tuck Link, Singapore 596224

USA office: 27 Warren Street, Suite 401-402, Hackensack, NJ 07601

UK office: 57 Shelton Street, Covent Garden, London WC2H 9HE

Online ISSN: 2335-6936
Print ISSN: 2335-6928

British Library Cataloguing-in-Publication Data
A catalogue record for this book is available from the British Library.

BIOCOMPUTING 2026
Proceedings of the Pacific Symposium

Copyright © 2026 by World Scientific Publishing Co. Pte. Ltd.

All rights reserved. This book, or parts thereof, may not be reproduced in any form or by any means, electronic or mechanical, including photocopying, recording or any information storage and retrieval system now known or to be invented, without written permission from the publisher.

For photocopying of material in this volume, please pay a copying fee through the Copyright Clearance Center, Inc., 222 Rosewood Drive, Danvers, MA 01923, USA. In this case permission to photocopy is not required from the publisher.

ISBN 978-981-98-2475-5 (ebook)
ISBN 978-981-98-2474-8 (print)

Preface..... xi

AI AND MACHINE LEARNING IN CLINICAL MEDICINE: BRIDGING OR SEPARATING MODEL INTELLIGENCE AND HUMAN EXPERTISE

Session Introduction: 1
Fateme Nateghi Haredasht, Joseph D. Romano, Brett K Beaulieu-Jones, Dokyoon Kim, Alexander Ioannidis, Geoffrey H Tison, Roxana Daneshjou, Jonathan H. Chen

Inference Gap in Domain Expertise and Machine Intelligence in Named Entity Recognition: Creation of and Insights from a Substance Use-related Dataset..... 12
Sumon Kanti Dey, Jeanne M. Powell, Azra Ismail, Jeanmarie Perrone, Abeed Sarker

ColonCrafter: A Depth Estimation Model for Colonoscopy Videos Using Diffusion Priors 27
Romain Hardy, Tyler M. Berzin, Pranav Rajpurkar

A Clinician-Guided Framework for Endoscopic AI: Developing PanEndoAtlas and Benchmarking Foundation Models Across the Full GI Spectrum..... 42
Shreya Johri, Luyang Luo, Hong-Yu Zhou, Todd Brenner, Sami Elamin, Mark Enrik Geissler, Tyler M. Berzin, Pranav Rajpurkar

Higher-order Interaction Matters: Modeling Epidemics via Dynamic Hypergraph Neural Networks..... 57
Songyuan Liu, Shengbo Gong, Tianing Feng, Zewen Liu, Max S.Y Lau, Wei Jin

Scoring Physician Risk Communication in Prostate Cancer Using Large Language Models..... 71
Guillermo Lopez-Garcia, Dongfang Xu, Michael Luu, Renning Zheng, Timothy J. Daskivich, Graciela Gonzalez-Hernandez

SeizureFormer: A Multi-Scale Transformer for Seizure Risk Forecasting from RNS-Derived Biomarkers..... 85
Tianning Feng, Juntong Ni, Wei Jin, Ezequiel Gleichgerrcht

3DReasonKnee: Advancing Grounded Reasoning in Medical Vision Language Models 99
Sraavya Sambara, Sung Eun Kim, Xiaoman Zhang, Luyang Luo, Shreya Johri, Mohammed Baharoon, Du Hyun Ro, Pranav Rajpurkar

Abstention and Threshold Identification for Uncertainty Management in Clinical Decision Tools: A Case Study using Human-In-The-Loop Pediatric Autism Classifiers 114
Aiden Ko, Aaron Kline, Kaitlyn Dunlap, SaiMourya Surabhi, Parnian Azizian, Peter Y. Washington, Dennis P. Wall

Evaluation of Large Language Models as Emergency Department Revisit Predictors 130
Emma Chen, Luyang Luo, Fatma Gunturkun, Sraavya Sambara, Rushil Arora, Boyang Tom Jin, Pranav Rajpurkar, David A. Kim

Speaker Role Identification in Clinical Conversations..... 144
Andrew Zolensky, Kuk Jin Jang, Janice Sabin, Andrea Hartzler, Basam Alasaly, Sriharsha Mopidevi, Mark Liberman, Kevin Johnson

Learning Causally Predictable Outcomes from Psychiatric Longitudinal Data 158
Eric V. Strobl

Quantifying surprise in clinical care: Detecting highly informative events in electronic health records with foundation models 173
Michael C. Burkhart, Bashar Ramadan, Luke Solo, William F. Parker, Brett K. Beaulieu-Jones

Retrieval-Augmented Guardrails for AI-Drafted Patient-Portal Messages: Error Taxonomy Construction and Large-Scale Evaluation 189
Wenyuan Chen, Fateme Nateghi Haredasht, Kameron C. Black, François Grolleau, Emily Alsentzer, Jonathan H. Chen, Stephen P. Ma

Leveraging Large Language Models for Adverse Drug Event Detection: A Comparative Study of Token and Span-Based Named Entity Recognition 205
Howard Prioleau, Saurav Aryal, Jeremy Blackstone

Towards Automated Analysis of Gaze Behavior from Consumer VR Devices for Neurological Diagnosis 219
Lio Schmitz, Markus Plack, Berkan Koyak, Muhammad Ehsan Ullah, Ahmad Aziz, Reinhard Klein, Zorah Lähner, Hannah Dröge

Automated Chest X-ray Report Generation Remains Unsolved 236
Xiaoman Zhang, Julian Nicolas Acosta, Xiaoli Yang, Subathra Adithan, Luyang Luo, Hong-Yu Zhou, Joshua Miller, Ouwen Huang, Zongwei Zhou, Ibrahim Ethem Hamamci, Shruthi Bannur, Kenza Bouzid, Xi Zhang, Zaiqiao Meng, Aaron Nicolson, Bevan Koopman, Inhyeok Baek, Hanbin Ko, Mercy Prasanna Ranjit, Shaury Srivastav, Sriram Gnana Sambanthan, Pranav Rajpurkar

ReXVQA: A Large-scale Visual Question Answering Benchmark for Generalist Chest X-ray Understanding 251
Ankit Pal, Jung-Oh Lee, Xiaoman Zhang, Malaikannan Sankarasubbu, Seunghyeon Roh, Won Jung Kim, Meesun Lee, Pranav Rajpurkar

Detecting PTSD in Clinical Interviews: A Comparative Analysis of NLP Methods and Large Language Models 265
Feng Chen, Dror Ben-Zeev, Gillian Sparks, Arya Kadakia, Trevor Cohen

ED-Explain: Personalized Video Instructions for Patients Discharged from the Emergency Department 280
Luyang Luo, Emma Chen, Xiaoman Zhang, Julian Nicolas Acosta, Boyang Tom Jin, Fatma Gunturkun, Christian Rose, Carl Preiksaitis, Brian Suffoletto, Pranav Rajpurkar, David A. Kim

The Intention-Execution Disconnect in Medical AI: The ReXecution Framework for Evaluating Real-World Clinical Performance 294
Oishi Banerjee, Lucas Bijnens, Subathra Adithan, Pranav Rajpurkar

Leveraging Generative AI for Interpretable Clinical Decision Making Through Causal Graphs 309
Mehmet Eren Ahsen, Rand Kittani, Travis Gerke, Laya Krishnan, Sean Rogan, Erick R. Scott

Leveraging Large Language Models to Derive Multiple Sclerosis Progression Assessments from Clinical Notes: A Feasibility Study 324
Sy Hwang, Sunil Thomas, Heather Williams, Tom Hutchinson, Emily Schriver, Ashley Batugo, Amit Bar-Or, Vishakha Sharma, Frederik Buijs, Christopher Perrone, Danielle Mowery

WATCH-SS: Developing a Trustworthy and Explainable Modular Framework for Detecting Cognitive Impairment from Spontaneous Speech 338
Sydney Pugh, Matthew Hill, Sy Hwang, Rachel Wu, Kuk Jang, Stacy Iannone, Karen O'Connor, Kyra O'Brien, Eric Eaton, Kevin Johnson

MedAgentBench v2: Improving Medical LLM Agent Design 354
Eric Chen, Sam Postelnik, Kameron Black, Yixing Jiang, Jonathan Chen

Automated Evaluation of Large Language Model Response Concordance with Human Specialist Responses on Physician-to-Physician eConsult Cases 372
David JH Wu, Fateme Nateghi Haredasht, David Wu, Vishnu Ravi, Liam G. McCoy, Yingjie Weng, Kanav Chopra, Selin S. Everett, George Nageeb, Wenyuan Chen, Stephen P. Ma, Saloni Kumar Maharaj, Jessica Tran, Leah Rosengaus, Lena Giang, Olivia Jee, Ethan Goh, Jonathan H. Chen

MedFactEval and MedAgentBrief: A Framework and Workflow for Generating and Evaluating Factual Clinical Summaries 388
François Grolleau, Emily Alsentzer, Timothy Keyes, Philip Chung, Akshay Swaminathan, Asad Aali, Jason Hom, Tridu Huynh, Thomas Lew, April Liang, Weihan Chu, Natasha Steele, Christina Lin, Jingkun Yang, Kameron Black, Stephen Ma, Fateme N. Haredasht, Nigam H. Shah, Kevin Schulman, Jonathan H. Chen

Asking the Right Questions: Benchmarking Large Language Models in the Development of Clinical Consultation Templates 400
Liam G. McCoy, Fateme Nateghi Haredasht, Kanav Chopra, David Wu, David JH Wu, Abass Conteh, Sarita Khemani, Saloni Kumar Maharaj, Vishnu Ravi, Arth Pahwa, Yingjie Weng, Leah Rosengaus, Lena Giang, Kelvin Zhenghao Li, Olivia Jee, Daniel Shirvani, Ethan Goh, Jonathan H. Chen

BIOLOGICAL MOLECULAR FUNCTION: METHODS AND BENCHMARKS FOR FINDING FUNCTION IN BIOLOGICAL DARK MATTER

Session Introduction: 417
Jason McDermott, Yana Bromberg, Hannah Carter, Travis Wheeler

Implicitly and Differentiably Representing Protein Surfaces and Interfaces 425
Cory B. Scott, Charlie Rothschild, Benjamin E. Nye

Steering Protein Generative Models at Test-Time for Guided AAV2 Capsid Design 438
Ben Viggiano, Wenhui Sophia Lu, Xiaowei Zhang, Luis S. Mille-Fragoso, Xiaojing J. Gao, Euan Ashley, Wing Hung Wong

HALO: Hybrid Attention Model for Subcellular Localization 452
Shafayat Ahmed, Nazifa Ahmed Moumi, Liqing Zhang

PertSpectra: Interpretable Matrix Factorization for Predicting Functional Impact of Genetic Perturbation Experiments 465
Seowon Chang, Anna Shcherbina, Tal Ashuach, Shahin Mohammadi, Stephanie See, Ninad Ranadive, Emily Fox, Navpreet Ranu

Large Language Models Identify Causal Genes in Complex Trait GWAS 480
Suyash S. Shringarpure, Wei Wang, Sotiris Karagounis, Xin Wang, Anna C. Reisetter, Adam Auton, Aly A. Khan

Gene-R1: Reasoning with Data-Augmented Lightweight LLMs for Gene Set Analysis 494
Zhizheng Wang, Yifan Yang, Qiao Jin, Zhiyong Lu

LLM Agent Based Protein Function Prediction 508
Fernando Zhapa-Camacho, Olga Mashkova, Robert Hoehndorf, Maxat Kulmanov

FAIRNESS AND BIAS IN BIOMEDICAL AI/ML: DEFINING GOALS AND PUTTING THEM INTO PRACTICE

Session Introduction: 520
Nicole Martinez-Martin, Mildred Cho, Abdoul Jalil Djiberou Mahamadou, Madalena Ng

Using Large Language Models to Audit Model Healthcare Biases 524
Zara N. Ansari, Aaron Fanous, Jesutofunmi A. Omiye, Ank Agarwal, Roxana Daneshjou

From Detection to Mitigation: Addressing Bias in Deep Learning Models for Chest X-Ray Diagnosis 538
Clemence Mottez, Louisa Fay, Maya Varma, Sophie Ostmeier, Curtis Langlotz

Deciphering the Influence of Demographic Factors on the Treatment of Pediatric Patients in the Emergency Department 551
Helena Coggan, Anne Bischops, Pradip Chaudhari, Yuval Barak-Corren, Andrew M. Fine, Ben Y. Reis, Jaya Aysola, William G. La Cava

Barriers to Designing Inclusive Ecological Momentary Assessment and Wearable Data Collection Protocols for AI-Driven Substance Use Monitoring in Hawai'i 566
Yinan Sun, Aditi Jaiswal, Ali Kargarandehkordi, Christopher Slade, Roberto M. Benzo, Kristina T. Phillips, Peter Washington

Building Fair and Trustworthy Biomedical AI: A Tool for Identifying Key Decision Points 580
Nicole Foti, Janet K. Shim, Caitlin McMahon, Sandra Soo-Jin Lee

PRECISION MEDICINE: INTEGRATING LARGE-SCALE DATA AND INTERMEDIATE PHENOTYPES FOR UNDERSTANDING HEALTH AND TREATING DISEASE

Session Introduction: 596
Steven E. Brenner, Nilah M. Ioannidis, Tayo Obafemi-Ajayi, Anne O'Donnell-Luria

Integrating Polygenic Risk Improves Generative Forecasting of Disease Trajectories 600
Chris German, Suyash Shringarpure, Payam Dibaeinia, James Ashenhurst, Bertram L. Koelsch, Adam Auton, Aly A. Khan

Integrating Imaging-Derived Clinical Endotypes with Plasma Proteomics and External Polygenic Risk Scores Enhances Coronary Microvascular Disease Risk Prediction 612
Rasika Venkatesh, Tess Cherlin, Penn Medicine BioBank, Marylyn D. Ritchie, Marie A. Guerraty, Shefali S. Verma

Integrating Polygenic Scores with Clinical, Lifestyle, and Social Risk Factors to Improve Heart Failure Risk Prediction 629
Katie M. Cardone, Dokyoon Kim, Marylyn D. Ritchie

BioLM-NET: An Interpretable Deep Learning Model Combining Prior Biological Knowledge and Contextual LLM Gene Embeddings on Multi-Omics Data to Predict Disease 644
Jubair Ibn Malik Rifat, Thasina Tabashum, Md Marufi Rahman, Md Farhad Mokter, Sarthak Engala, Serdar Bozdag

Impact of Using PRS-CSx and Pruning and Thresholding for Polygenic Partitioning of Apparent Treatment Resistant Hypertension 664
Hannah M. Seagle, Jeewoo Kim, Alexis T. Akerele, VA Million Veteran Program, Adriana Hung, Jacklyn N. Hellwege, Todd L. Edwards

Prototype Learning to Create Refined Interpretable Digital Phenotypes from ECGs 679
Sahil Sethi, David Chen, Michael C. Burkhart, Nipun Bhandari, Bashar Ramadan, Brett Beaulieu-Jones

Deep Learning-based Classification of Patients with Postural Orthostatic Tachycardia Syndrome using Wearable ECG and Accelerometer Data 694
Hyunjun Choi, Nicholas Matsumoto, Xi Li, Debbie Teodorescu, Anxhela Kote, Min-Jing Yang, Xiao Liu, Miguel E. Hernandez, Jason H. Moore, Graciela Gonzalez-Hernandez, Peng-Sheng Chen

Patch-Level Phenotype Identification Via Weakly Supervised Neuron Selection in Sparse Autoencoders for CLIP-Derived Pathology Embeddings 708
Keita Tamura, Yao-zhong Zhang, Yohei Okubo, Seiya Imoto

DeepDiff-SHAP: Interpretable Deep Learning for Subgroup- Specific Causal Hypothesis Generation using Conditional SHAP 722
Aditya Sriram, Soyeon Kim, Joseph A. Carcillo, Hyun Jung Park

Literature-Driven Extraction and Computational Prediction of Causal Statements Linking Genetic Variants to Biological Processes, Pathways and Phenotypes 738
Jici Jiang, Predrag Radivojac, Benjamin M. Gyori

SYSTEMS BIOLOGY AND NETWORK ANALYSIS: FROM MULTI-OMICS INTEGRATION TO BIOLOGICAL MECHANISMS

Session Introduction: 752
Gurkan Bebek, Onur Mutlu, Iman Hajirasouliha, Joshua Welch, Serguei Pakhomov

Provenance Tracing in Network Diffusion Algorithms 755
Nure Tasnina, Mark Crovella, Simon Kasif, T. M. Murali

REPEL - Random Embedding Perturbation for Enhanced Learning of Protein Function 770
Di Zhou, Lenore Cowen, Kaiyi Wu, Xiaozhe Hu, Donna Slonim

Network Optimal Retrieval of Sparse Perturbations for Steady-State Control 784
Krithika Krishnan, Tiange Shi, Satyam Kumar, Han Yu, Rachael Hageman Blair

Discovery of Disease Relationships via Transcriptomic Signature Analysis Powered by Agentic AI 799
Ke Chen, Haohan Wang

A Random-Walk-Based Learning Framework to Uncover Novel Gene Candidates for Alzheimer's Disease Therapy 815
Alena Orlenko, Binglan Li, Neda Khanjani, Mythreye Venkatesan, Li Shen, Marylyn D. Ritchie, Zhiping Paul Wang, Tayo Obafemi-Ajayi, Jason H. Moore

DRIVE-KG: Enhancing Variant-Phenotype Association Discovery in Understudied Complex Diseases Using Heterogeneous Knowledge Graphs 830
Ananya Rajagopalan, Tram Anh Nguyen, Lindsay A. Guare, Andre Luis Garao Rico, Rasika Venkatesh, Lannawill Caruth, Regeneron Genetics Center, Penn Medicine BioBank, Anurag Verma, Marylyn D. Ritchie, Molly A. Hall, Joseph D. Romano, Shefali Setia-Verma

WORKSHOPS

Advances of AI Methods in Single Cell Spatial Omics 849
Lana Garmire, Xiuwei Zhang, Joshua Levy

AI for Health: Leveraging Artificial Intelligence to Revolutionize Healthcare 852
Ruowang Li, Brian D. Davison, Tiffani Bright, Lifang He

Applications of AI & ML in Biomanufacturing of Cell and Gene Therapies 855
Eric Neumann, Karen Weisinger, Tom Londo

The Evolving Cyberinfrastructure at the National Institutes of Health to Support Data and AI in Biomedical Research 859
Ojas A. Ramwala, Nick Weber, Sean D. Mooney

Trust, Reproducibility, and Progress: The Roles of Independent Blind Prediction and Assessment and Benchmarking in Computational Biology 865
Gaia Andreoletti, Serghei Mangul, Predrag Radivojac, Steven E Brenner

PACIFIC SYMPOSIUM ON BIOCOMPUTING 2026

2026 marks the 31st Pacific Symposium on Biocomputing (PSB)! As always, we gather on the Big Island to share the latest progress and challenges in biocomputing. It has been a challenging year for science in the United States, with cancelled federal grants, major cuts to important health and science agencies, public health recommendations with unclear evidence, and continued erosion in public trust of experts with actual, hard-won and documented expertise. With this backdrop, the mission of PSB to publish the most exciting emerging work in biocomputation is as important as ever. The continued emergence and dominance of AI in science is one bright spot that receives support from most corners, and those of us in the field are aware of the amazing capabilities (of course, not perfect and still needing refinement) of AI to augment discovery in science. In addition, AI still shows amazing promise to improve the delivery of healthcare—but with much work to be done to guarantee accuracy, fairness and workflow compatibility. Even when AI is not the headline, it is often serving a supporting role in application areas of great importance. As usual, the sessions and workshops in this year's PSB are at the frontiers of the ways in which computing technologies are revolutionizing the biosciences. We hope that these scientifically magical few days will restore and refresh your enthusiasm for and faith in the important work we all do.

In addition to being published by World Scientific and indexed in PubMed, the proceedings from all PSB meetings are available online at http://psb.stanford.edu/psb-online/. Since 1996, all PSB papers are indexed in PubMed. These papers are routinely cited in archival journal articles and routinely represent important early contributions in new subfields—many times before there is an established literature in more traditional journals; for this reason, many papers have garnered hundreds of citations.

The social media handle for PSB is @PacSymBiocomp and the hashtag for PSB 2026 is #PSB26.

The efforts of a dedicated group of session organizers have produced an outstanding program. The sessions of PSB 2026 and their hard-working organizers are as follows:

AI and Machine Learning in Clinical Medicine: Bridging or Separating Model Intelligence and Human Expertise?
Organizers: Jonathan Chen, Roxana Daneshjou, Fateme Nateghi Haredasht, Joseph D. Romano, Dokyoon Kim, Alexander Ioannidis, Brett K Beaulieu-Jones, Geoffrey H. Tison

Biological Molecular Function: Methods and Benchmarks for Finding Function in Biological Dark Matter
Organizers: Jason McDermott, Yana Bromberg, Hannah Carter, Travis Wheeler

Fairness and Bias in Biomedical AI/ML: Defining Goals and Putting Them into Practice
Organizers: Nicole Martinez-Martin, Mildred Cho, Abdoul Jalil Djiberou Mahamadou, Madalena Ng

Precision Medicine: Integrating Large Scale Data and Intermediate Phenotypes for Understanding Health and Treating Disease
Organizers: Nilah Ioannidis, Tayo Obafemi-Ajayi, Anne O'Donnell-Luria, Steven Brenner

Systems Biology and Network Analysis: From Multi-omics Integration to Biological Mechanisms
Organizers: Gurkan Bebek, Onur Mutlu, Iman Hajirasouliha, Joshua Welch, Serguei Pakhomov

We are excited to present five workshops in which investigators with a common interest come together to exchange results and new ideas in a format that is more informal than the peer-reviewed sessions. For this year, the workshops and their organizers are:

Advances of AI methods in Single Cell Spatial Omics
Organizers: Lana Garmire, Xiuwei Zhang, Joshua Levy

AI for Health: Leveraging Artificial Intelligence to Revolutionize Healthcare
Organizers: Ruowang Li, Tiffani Bright, Brian D. Davison, Lifang He

Applications of AI & ML in Biomanufacturing of Cell and Gene Therapies
Organizers: Eric Neumann, Karen Weisinger, Tom Londo

The Evolving Cyberinfrastructure at the National Institutes of Health to Support Data and AI in Biomedical Research
Organizers: Ojas A. Ramwala, Nick Weber, Sean D. Mooney

Trust, Reproducibility, and Progress: The Roles of Independent Blind Prediction and Assessment and Benchmarking in Computational Biology
Organizers: Gaia Andreoletti, Serghei Mangul, Mark Robinson, Predrag Radivojac, Steven E. Brenner

The PSB 2026 keynote speakers are Eric Green (Science keynote) and Luis Campos (Ethical, Legal and Social Implications keynote).

Tiffany Murray has managed the peer review process and assembly of the proceedings since 2001 and plays a key role in many aspects of the meeting. We are grateful for the long-time support of the National Institutes of Health[1], ISCB, and the National Science Foundation[2]. The Research Parasite Awards benefit from support from GigaScience, Jeff Stibel, Mr. and Mrs. Stephen Canon, and Drs. Casey and Anna Greene. The Research Symbiont Awards benefit from support from the Wellcome Trust and the DragonMaster Foundation.

We are particularly grateful to the PSB staff Tiffany Murray, Al Conde, Ryan Whaley, Mark Woon, Clarissa Klein, Randy Soares, Nicholas Murray, BJ Morrison McKay, Cynthia Paulazzo, Jackson Miller, and Heather Miller for their assistance. We also acknowledge the many busy

researchers who reviewed the submitted manuscripts on a very tight schedule. The partial list following this preface does not include many who wished to remain anonymous, and of course we apologize to any who may have been left out by mistake.

We look forward to a great meeting and to seeing you on the Big Island. Aloha!

Pacific Symposium on Biocomputing Co-Chairs,
October 13, 2025

Russ B. Altman
Departments of Bioengineering, Genetics, Medicine & Biomedical Data Science, Stanford University

Lawrence Hunter
Department of Pediatrics, University of Chicago

Marylyn D. Ritchie
Department of Public Health Sciences, Division of Biomedical Informatics and AI, Medical University of South Carolina

Teri E. Klein
Departments of Biomedical Data Science, Medicine & Genetics, Stanford University

Thanks to the reviewers…

Finally, we wish to thank the scores of reviewers. PSB aims for every paper in this volume to be reviewed by three independent referees. Since there is a large volume of submitted papers, paper reviews require a great deal of work from many people. We are grateful to all of you listed below and to anyone whose name we may have accidentally omitted or who wished to remain anonymous.

Vanessa Aguiar-Pulido
Rishita Anubhai
Vikas Bansal
Gurkan Bebek
Michael Beer
Filipa Blasco
Carly Bobak
Serdar Bozdag
Kelly Brock
Doug Brubaker
Douglas Brubaker
Emidio Capriotti
Hannah Carter
Christine Chang
Irene Chen
Jianlin Cheng
Mildred Cho
Sutanay Choudhury
Kritika Chugh
Ercument Cicek
John Cort
James Costello
Lenore Cowen
Jishnu Das
Clara De Paolis Kaluza
Mahshad Koohi Habibi
Dehkordi
Logan Dumitrescu
Song Feng
Jason Fries
Gaurav Gadhvi
Belinda Garana
Nika Mansouri Ghiasi
Sara Gosline
Arzu Guler
Pallavi Gupta
Melissa Gymrek
Iman Hajirasouliha
John Hanna
Dominik Heider
Gonzalo Ruz Heredia
Timothy Hohman
Fereydoun Hormozdiari
Justine Hsu
August Yue Huang
Steve Huang
Connah Johnson
Clara Kaluza
Dukka KC
Eileen Kim
Hoshin Kim
Hyun Jo Kim
Adam Klie
Konstantina Koliogeorgi
Mehmet Koyuturk
Heewook Lee
Yariv Levinson
Joshua Levy
Changye Li
Irene Li
Zheng Liu
Yunan Luo
Cong Ma
Abdoul Jalil Djiberou
Mahamadou
Yannick Mahlich
Lauren Mak
Nicole Martinez
Jason McDermott
Makaela Mews
Lieke Michielsen
Cristina Mitrea
Lummy Monteiro
Sean Mooney
Harun Mustafa
Madalena Ng
Cerag Oguztuzun
Daniel Olson
Oluwatosin Oluwadare
Ankit Pal
Daniele Papetti
Jiwoon Park
Ayan Paul
Adam Phillippy
William Phu
Dom Pimenta
Weizhou Qian
John Martin Rajamony
Suraj Rajendran
Prabakaran Ramakrishnan
Rashika Ramola
Antonio Rausell
Milad Razavi-Mohseni
Eeshaan Rehani
Nicolae Sapoval
Zhecheng Sheng
Mugdha Singh
Ritambhara Singh
Rohit Singh
Pankhuri Singhal
Donna K. Slonim
Ross Stewart
Budiwan Sumarsono
Zhaoyi Sun
Sobhan Shukueian
Tabrizi
Robert (Xiangru) Tang
Andrea Tangherloni
Oznur Tastan
Panagiotis
Theocharopoulos
Paraskevi V. Tsakmaki
Eliezer van Allen
Kathan Vyas

Alex Wagner
Yichen Wang
Wei Wei
Joshua Welch
Lonnie Welch
Travis Wheeler
Sam Windels
Jakob Woerner
Emily Wong
Han Yang
Vicky Yao
Jacqueline You
Mustafa Yurdakul
Simone Zaccaria
Daniel Zeiberg
Tarek Zikry
Amy Zimmerman
Md Muntasir Zitu

[1]Funding for this conference was made possible (in part) by R13LM006766 from the National Library of Medicine. The views expressed in written conference materials or publications and by speakers and moderators do not necessarily reflect the official policies of the Department of Health and Human Services; nor does mention by trade names, commercial practices, or organizations imply endorsement by the U.S. Government.

[2]Funding for this conference was made possible (in part) by Grant # 2531429 from the U.S. National Science Foundation. The views expressed in written conference materials or publications, and by speakers and moderators, does not necessarily reflect the official policies of the U.S. National Science Foundation; nor does mention by trade names, commercial practices, or organizations imply endorsement by the U.S. Government.

AI and Machine Learning in Clinical Medicine
Bridging or Separating Model Intelligence and Human Expertise

Fateme Nateghi Haredasht

Stanford Center for Biomedical Informatics Research,

Stanford University, Stanford, CA, USA

Email: fnateghi@stanford.edu

Joseph D. Romano

Department of Biostatistics, Epidemiology and Informatics,

University of Pennsylvania, Philadelphia, PA, USA

Email: joseph.romano@pennmedicine.upenn.edu

Brett K Beaulieu-Jones

Section of Computational Biomedicine and Biomedical Data Science,

University of Chicago, Chicago, IL, USA

Email: beaulieujones@uchicago.edu

Dokyoon Kim

Department of Biostatistics, Epidemiology and Informatics,

University of Pennsylvania, Philadelphia, PA, USA

Email:dokyoon.kim@pennmedicine.upenn.edu

Alexander Ioannidis

Department of Biomedical Data Science,

Stanford University, Stanford, CA, USA

Department of Biomolecular Engineering, University of California, Santa Cruz, Santa Cruz, CA, USA

Email: ioannid@stanford.edu

Geoffrey H Tison

Division of Cardiology, Center for Biosignal Research,

University of California, San Francisco, San Francisco, CA, USA

Email: geoff.tison@ucsf.edu

Roxana Daneshjou

Department of Biomedical Data Science, Stanford University, Stanford, CA, USA

Email: roxanad@stanford.edu

Jonathan H. Chen

Department of Medicine and Center for Biomedical Informatics Research,

Stanford University, Stanford, CA, USA

Email: jonc101@stanford.edu

© 2025 The Authors. Open Access chapter published by World Scientific Publishing Company and distributed under the terms of the Creative Commons Attribution Non-Commercial (CC BY-NC) 4.0 License.

Artificial Intelligence (AI) technologies continue to expand their role in clinical medicine, with large language models (LLMs) and multimodal systems now applied to communication, imaging, and predictive analytics. Advances in generative and retrieval-augmented methods have improved the accuracy and contextual grounding of clinical summaries, patient messaging, and decision support. At the same time, new benchmarks in imaging, vision, and spontaneous speech have underscored both progress and the persistence of unsolved challenges. Predictive modeling efforts highlight causality, longitudinal trajectories, and informative clinical events, while methodological contributions emphasize uncertainty management, abstention, and interpretable causal structures. Finally, frameworks for evaluation and governance address the crucial gap between laboratory performance and real-world deployment.

Keywords: Artificial Intelligence, clinical medicine, decision support systems, large language models

1. Introduction

Healthcare stands at a critical point where computational approaches to medical decision-making are becoming increasingly sophisticated and integrated into clinical practice. The past decade has witnessed notable advancements in artificial intelligence (AI) and machine learning methods applied to healthcare challenges (Davenport and Kalakota, 2019; Rajkomar, Dean and Kohane, 2019). These innovations span numerous domains, including medical imaging interpretation, clinical decision support, predictive analytics for patient outcomes, and natural language processing (NLP) of electronic health records (EHRs) (Noei *et al.*, 2016; Ashtari, Maes and Van Huffel, 2021; Ashtari *et al.*, 2022; Nateghi Haredasht and Vens, 2022; Ashtari *et al.*, 2023; Nateghi Haredasht *et al.*, 2023; Nateghi Haredasht, Fouladvand, *et al.*, 2024; Bedi *et al.*, 2025; Chang *et al.*, 2025; Lopez *et al.*, 2025).

The rapid emergence of large language models (LLMs) and foundation models in healthcare has particularly accelerated in recent years, promising to transform how clinicians interact with medical information and make decisions (Bommasani *et al.*, 2022; Thirunavukarasu *et al.*, 2023). Studies have demonstrated their potential for clinical documentation, summarization of medical literature, patient triaging, and even direct patient interaction (Patel *et al.*, 2019; Nori *et al.*, 2023). However, significant challenges remain regarding their reliability, interpretability, alignment with clinical workflows, and potential for harm when deployed in high-stakes healthcare environments (Wiens *et al.*, 2019; Sendak *et al.*, 2020).

This year's session at the 2026 Pacific Symposium on Biocomputing (PSB), titled "AI and Machine Learning in Clinical Medicine: Bridging or Separating Model Intelligence and Human Expertise", examines the evolving relationship between computational capabilities and human clinical judgment in healthcare settings (Nateghi Haredasht, Kim, *et al.*, 2024). The papers in this session explore various facets of this complex relationship, representing cutting-edge research across four major themes: (1) LLMs in clinical applications, (2) AI for medical imaging analysis and interpretation, (3) approaches to clinical decision support and risk prediction, and (4) clinical data analysis and patient care. Here, we highlight the accepted submissions for this session that provide insights as healthcare institutions aim to integrate AI tools into clinical workflows while preserving the essential human dimensions of medical care.

2. Artificial Intelligence in Clinical Medicine

2.1. Large Language Models (LLMs) in Clinical Applications

The emergence of LLMs has expanded the possibilities for AI applications in clinical medicine. Several papers in this session explore how these powerful models can be adapted, evaluated, and deployed to address healthcare challenges.

One study investigating named entity recognition (NER) for substance use-related information found that fine-tuned encoder-based models consistently outperform LLMs in precision and span accuracy, highlighting a persistent gap between human expert knowledge and current AI capabilities for complex tasks requiring deep domain understanding (Dey and et al., 2026). Similarly, work on adverse drug event detection demonstrated that specialized models like RoBERTa Large achieved superior performance in identifying complex and contextually ambiguous events, with ensemble methods further improving relation extraction for pharmacovigilance applications (Prioleau and et al., 2026).

In clinical communication assessment, a couple of papers have developed frameworks leveraging LLMs to evaluate physician-patient interactions. One approach uses rubric-based Chain-of-Thought prompting with few-shot learning to assess the quality of risk communication in prostate cancer consultations, achieving expert-level agreement and establishing a scalable foundation for evaluating physician-patient communication in oncology (Lopez-Garcia and et al., 2026).

For clinical decision support and prediction, several papers explored novel applications of foundation models. Burkhart et al. developed methods to quantify the "informativeness" of clinical events in EHRs by measuring divergence between model predictions and observed outcomes, identifying "surprising" events that are predictive of adverse outcomes such as mortality (Burkhart and et al., 2026). However, when evaluated on emergency department revisit prediction tasks using comprehensive clinical data, LLM-based approaches underperformed traditional machine learning models that used only structured EHR data, suggesting that current LLM reasoning approaches may have limitations for certain clinical prediction tasks (Emma Chen and et al., 2026)

The session features several important evaluation frameworks and benchmarks. The ReXrank Challenge presents a benchmark for chest X-ray report generation models, revealing that while AI systems perform well on normal cases, they still struggle significantly with abnormal findings, demonstrating that automated radiology report generation remains largely unsolved for clinically significant pathologies (Zhang and et al., 2026). Another research team introduced MedAgentBench v2, advancing benchmark methodologies for evaluating and improving LLM-based agents in medical contexts through refined prompt engineering, enhanced EHR interaction tools, and novel memory mechanisms that allow agents to learn from past errors (E. Chen and et al., 2026).

For improving clinical documentation quality, Grolleau et al. developed MedFactEval, a framework for scalable, fact-grounded evaluation using an "LLM Jury" to assess AI-generated clinical summaries, achieving nearly perfect agreement with physician panels (Grolleau and et al., 2026). Another work on eConsult templates showed that while models like o3 demonstrated

high comprehensiveness, they consistently struggled to prioritize the most clinically important questions, especially in narrative-heavy specialties (McCoy and et al., 2026). To address safety concerns, one team introduced a Retrieval-Augmented Error Checking pipeline that significantly improved error identification in AI-drafted patient-portal messages by incorporating local context retrieval (Chen and et al., 2026).

Across these diverse applications, we see both the potential and current limitations of LLMs in clinical medicine, with particular challenges remaining in achieving human-level domain expertise, prioritizing clinically relevant information, and ensuring factual accuracy in high-stakes healthcare applications.

2.2. Medical Imaging and Visual AI

Visual information processing represents another critical domain where AI is transforming clinical practice, from endoscopy to radiology to medical image interpretation. Research in this area focuses on developing AI systems that can enhance clinical workflows through improved visualization, interpretation, and analysis of medical imaging data.

In the field of endoscopic imaging, Hardy et al. have developed ColonCrafter, a diffusion-based depth estimation model designed to generate temporally consistent depth maps from monocular colonoscopy videos. Their approach leverages robust geometric priors learned from synthetic colonoscopy sequences while incorporating a novel style transfer technique to bridge the domain gap between synthetic training data and real clinical videos. This work enables important applications like improved 3D reconstruction of the colon and precise lesion localization, potentially enhancing the detection of subtle abnormalities during colonoscopy procedures (Hardy and et al., 2026).

Addressing the fragmentation in endoscopic AI development, Johri et al. introduce PanEndoAtlas, a clinician-guided dataset containing over 420,000 labeled endoscopic images compiled from 30 public datasets across 13 countries and 26 hospitals. This resource addresses the gap between current endoscopic AI capabilities and actual clinical needs. The team also presents PanEndoX, a benchmark suite of 10 clinically relevant tasks designed to evaluate the generalization capabilities of vision foundation models across the entire gastrointestinal spectrum, utilizing a hierarchical taxonomy for diagnostic reasoning that aligns with clinical practice (Johri and et al., 2026).

For musculoskeletal imaging, Sambara et al. have developed 3DReasonKnee, the first 3D grounded reasoning dataset specifically designed for medical image analysis. This resource comprises 494,000 quintuples derived from 7,970 3D knee MRI volumes, where each quintuple includes a 3D MRI volume, a diagnostic question, a 3D bounding box highlighting anatomical structures, clinician-generated reasoning steps, and structured severity assessments. This dataset serves as a testbed for advancing multimodal medical AI systems toward clinically aligned, localized decision-making in orthopedic imaging (Sambara and et al., 2026).

In chest radiology, Pal et al. present ReXVQA, a large-scale visual question answering benchmark featuring approximately 696,000 questions paired with 160,000 chest X-ray studies. Their work evaluates AI models on five core radiological reasoning skills: presence detection, location identification, negation understanding, differential diagnosis formulation, and geometric reasoning. Notably, their evaluation revealed that the best-performing AI model, MedGemma,

achieved superior accuracy compared to human radiology residents on randomly sampled cases, suggesting progress in automated chest X-ray interpretation capabilities (Pal and et al., 2026).

These advances in medical imaging AI collectively demonstrate progress toward systems that not only perform well on technical metrics but also align with clinical workflows and reasoning processes.

2.3. Clinical Decision Support and Risk Prediction

AI systems show promise for supporting clinical decision-making and predicting patient risks across various healthcare domains. The papers in this section explore approaches to modeling complex medical phenomena, predicting adverse events, managing uncertainty, and enhancing clinical communication.

In the domain of infectious disease modeling, Liu et al. introduce EpiDHGNN, a Human Contact-Tracing Hypergraph Neural Network framework that leverages hypergraphs to capture intricate, higher-order relationships at both location and individual levels. By modeling the complex dynamics of human interactions, their approach outperforms baseline models in critical epidemic management tasks such as source detection and forecasting, offering potential improvements for public health response systems (Liu and et al., 2026).

For neurological applications, Feng et al. present SeizureFormer, a Transformer-based model for long-horizon seizure risk forecasting (1–14 days) using structured biomarkers derived from responsive neurostimulation (RNS) systems. Their approach integrates multi-scale CNN patch embedding, cross-variable temporal convolution, and squeeze-and-excitation attention mechanisms to capture both short-term fluctuations and long-term seizure cycles. By achieving state-of-the-art performance on this challenging prediction task, SeizureFormer demonstrates the potential to enable more proactive seizure management strategies for patients with drug-resistant epilepsy (Feng and et al., 2026).

Schmitz et al. explore the use of consumer-grade virtual reality (VR) headsets for automated neurological assessment, specifically focusing on Parkinson's disease classification from eye-tracking data. By combining general oculomotor metrics with task-evoked features and learned representations, their approach achieves high discriminative performance in both binary and multi-class classification scenarios, suggesting a cost-effective and accessible approach to neurodegenerative disease assessment (Schmitz and et al., 2026).

In psychiatric applications, Strobl introduces DEBIAS (Durable Effects with Backdoor-Invariant Aggregated Symptoms), an algorithm designed to learn causally predictable outcomes from psychiatric longitudinal data. By optimizing outcome definitions to maximize causal identifiability, this approach learns clinically interpretable weights for outcome aggregation while minimizing both observed and latent confounding. The algorithm outperforms state-of-the-art methods in recovering causal effects for composite outcomes in depression and schizophrenia, addressing a challenge in psychiatric outcomes research (Strobl and et al., 2026).

Addressing the critical issue of uncertainty in clinical AI systems, Ko et al. investigate abstention mechanisms for AI-based diagnostic classifiers, using pediatric autism video assessments as a case study. Their work demonstrates that carefully selecting upper and lower confidence thresholds can improve clinical performance metrics without requiring model retraining, offering a practical and interpretable approach to tailoring model behavior for diverse

clinical contexts. This research highlights the importance of human-in-the-loop systems that can appropriately defer to human judgment in uncertain cases (Ko and et al., 2026).

Focusing on patient education, Luo et al. introduce ED-Explain, a system that transforms emergency department discharge instructions into personalized video presentations featuring a virtual healthcare provider. In evaluations by emergency physicians, these AI-generated video summaries received higher ratings for completeness, correctness, and patient accessibility compared to original text instructions (Luo and et al., 2026).

Finally, Ahsen et al. propose a computational framework that leverages generative AI to design interpretable structural causal models (SCMs) for clinical decision support. Their comparative analysis of transformer-based LLM against human experts on complex causal reasoning tasks revealed that both successfully designed clinically plausible causal diagrams with similar statistical performance (Ahsen and et al., 2026).

Collectively, these studies demonstrate how advanced AI techniques can enhance clinical decision-making across multiple dimensions: from modeling complex epidemiological patterns to forecasting individual patient risks, managing diagnostic uncertainty, improving patient communication, and providing interpretable decision support frameworks.

2.4. Clinical Data Analysis and Patient Care

Several papers in this session focus on methods for analyzing clinical data and improving patient care through AI, with particular emphasis on extracting meaningful information from unstructured data and evaluating AI systems in real-world clinical contexts.

Hwang et al. explore the application of LLMs for automating Multiple Sclerosis (MS) progression assessment from clinical notes. Their feasibility study examines LLMs' ability to derive Expanded Disability Status Scale (EDSS) and Functional Systems (FS) scores, metrics for monitoring MS progression. Their LLM-based solution demonstrated robust performance in classifying several FS subscores, particularly excelling in visual, sensory, and cerebellar domains, where it outperformed previous NLP systems. However, for overall EDSS classification, it did not exceed the performance of existing rules/CNN-based classifiers. This work highlights both the potential and current limitations of LLMs for extracting complex clinical assessments from unstructured text (Hwang and et al., 2026).

Pugh et al. introduce WATCH-SS (Warning Assessment and Alerting Tool for Cognitive Health from Spontaneous Speech), an innovative three-stage modular framework for detecting cognitive impairment from patients' spontaneous speech samples. This approach addresses the need for explainable AI in healthcare by leveraging detectors for five linguistic and acoustic indicators of cognitive impairment, aggregating their outputs into clinically interpretable features, and employing a predictive model for classification. The framework achieved a performance of AUC = 0.80 (Pugh and et al., 2026).

Addressing the crucial issue of real-world AI performance, Banerjee et al. present the ReXecution framework for clinician-centered assessments of medical AI assistants. Their evaluation of AI systems for chest X-ray interpretation in realistic clinical settings revealed a significant "intention-execution disconnect"—despite demonstrating considerable medical knowledge, ChatGPT-o3 and MedGemma frequently struggled to accurately interpret images and execute tasks, producing correct outputs in only 5-10% of cases. This stark finding highlights

the gap between AI system capabilities in controlled evaluation settings versus real-world clinical deployment, underscoring the need for more robust evaluation frameworks that reflect actual clinical usage scenarios (Banerjee and et al., 2026).

Wu et al. tackle the challenge of evaluating AI system performance in clinical consultation contexts by developing automated methods to assess concordance between AI-generated and human specialist responses in physician-to-physician electronic consultations (eConsults). Their study compared two approaches, "LLM-as-judge" and "decompose-then-verify", finding that the "LLM-as-judge" method achieved human-level concordance assessment with an F1-score of 0.89 and Cohen's κ of 0.75, comparable to inter-physician agreement (Wu and et al., 2026).

Zolensky et al. introduce methods for speaker role identification in clinical conversations, addressing a challenge in the automated analysis of doctor-patient interactions. Their work demonstrates techniques to identify different speakers and their roles in clinical dialogue, providing foundational capabilities for subsequent analyses of communication patterns, information exchange, and relationship dynamics in healthcare encounters (Zolensky and et al., 2026).

Finally, Chen et. al. evaluate multiple NLP techniques for classifying Post-Traumatic Stress Disorder (PTSD) from clinical interview transcripts. The study compares embedding-based methods (like SentenceBERT), fine-tuned transformers (like Mental-RoBERTa), and various LLM prompting strategies (zero-shot, few-shot). Key findings show that a SentenceBERT embedding model with logistic regression achieved the best overall performance, outperforming more complex models, and that few-shot LLM prompting with DSM-5 criteria also yielded competitive results (F. Chen and et al., 2026).

Collectively, these papers illustrate diverse approaches to leveraging AI for clinical data analysis and patient care improvement, while emphasizing the importance of explainability, trustworthiness, and realistic performance evaluation in healthcare AI systems. They highlight both significant progress and persistent challenges in developing AI tools that can effectively support clinical practice.

3. Conclusion

The papers presented in this session demonstrate significant progress in applying AI to clinical medicine while highlighting the fundamental challenge of creating systems that complement rather than replace human expertise. Three key themes emerge: the growing importance of multimodal reasoning capabilities that integrate diverse data sources; the persistent need for interpretability and trustworthiness in increasingly complex systems; and the critical importance of evaluating AI performance in realistic clinical contexts.

Looking forward, promising directions include the integration of causal reasoning, enhanced multimodal understanding, and robust uncertainty quantification methods. The central question posed by our session title—whether AI is bridging or separating model intelligence and human expertise—remains nuanced, but the most promising path appears to be designing AI systems that deliberately complement human capabilities. Such systems would address clinicians' cognitive limitations while leveraging their irreplaceable judgment, empathy, and contextual understanding. The research presented here represents meaningful progress toward achieving

productive human-AI collaboration in healthcare that enhances rather than diminishes the role of clinical expertise.

References

Ahsen and et al. (2026) "Leveraging Generative AI for Interpretable Clinical Decision Making Through Causal Graphs," in *Pacific Symposium on Biocomputing (PSB 2026)*.

Ashtari, P. *et al.* (2022) "New multiple sclerosis lesion segmentation and detection using pre-activation U-Net," *Frontiers in Neuroscience*, 16. Available at: https://doi.org/10.3389/fnins.2022.975862.

Ashtari, P. *et al.* (2023) "Factorizer: A scalable interpretable approach to context modeling for medical image segmentation," *Medical Image Analysis*, 84, p. 102706. Available at: https://doi.org/10.1016/j.media.2022.102706.

Ashtari, P., Maes, F. and Van Huffel, S. (2021) "Low-Rank Convolutional Networks for Brain Tumor Segmentation," in A. Crimi and S. Bakas (eds.) *Brainlesion: Glioma, Multiple Sclerosis, Stroke and Traumatic Brain Injuries*. Cham: Springer International Publishing, pp. 470–480. Available at: https://doi.org/10.1007/978-3-030-72084-1_42.

Banerjee and et al. (2026) "The Intention-Execution Disconnect in Medical AI: The ReXecution Framework," in *Pacific Symposium on Biocomputing (PSB 2026)*.

Bedi, S. *et al.* (2025) "MedHELM: Holistic Evaluation of Large Language Models for Medical Tasks." arXiv. Available at: https://doi.org/10.48550/arXiv.2505.23802.

Bommasani, R. *et al.* (2022) "On the Opportunities and Risks of Foundation Models." arXiv. Available at: https://doi.org/10.48550/arXiv.2108.07258.

Burkhart and et al. (2026) "Quantifying surprise in clinical care with foundation models," in *Pacific Symposium on Biocomputing (PSB 2026)*.

Chang, C.T. *et al.* (2025) "Red teaming ChatGPT in medicine to yield real-world insights on model behavior," *npj Digital Medicine*, 8(1), p. 149. Available at: https://doi.org/10.1038/s41746-025-01542-0.

Chen, E. and et al. (2026) "MedAgentBench v2: Improving Medical LLM Agent Design," in *Pacific Symposium on Biocomputing (PSB 2026)*.

Chen and et al. (2026) "Retrieval-Augmented Guardrails for AI-Drafted Patient-Portal Messages," in *Pacific Symposium on Biocomputing (PSB 2026)*.

Chen, F. and et al. (2026) "Detecting PTSD in Clinical Interviews: Comparative Analysis of NLP Methods and LLMs," in *Pacific Symposium on Biocomputing (PSB 2026)*.

Davenport, T. and Kalakota, R. (2019) “The potential for artificial intelligence in healthcare,” *Future Healthcare Journal*, 6(2), pp. 94–98. Available at: https://doi.org/10.7861/futurehosp.6-2-94.

Dey and et al. (2026) “Inference Gap in Domain Expertise and Machine Intelligence in Named Entity Recognition,” in *Pacific Symposium on Biocomputing (PSB 2026)*.

Emma Chen and et al. (2026) “Turning Large Language Models into Emergency Department Revisit Predictors,” in *Pacific Symposium on Biocomputing (PSB 2026)*.

Feng and et al. (2026) “SeizureFormer: A Multi-Scale Transformer for Seizure Risk Forecasting,” in *Pacific Symposium on Biocomputing (PSB 2026)*.

Grolleau and et al. (2026) “MedFactEval and MedAgentBrief: Framework for Generating and Evaluating Factual Clinical Summaries,” in *Pacific Symposium on Biocomputing (PSB 2026)*.

Hardy and et al. (2026) “ColonCrafter: A Depth Estimation Model for Colonoscopy Videos Using Diffusion Priors,” in *Pacific Symposium on Biocomputing (PSB 2026)*.

Hwang and et al. (2026) “Leveraging Large Language Models to Derive Multiple Sclerosis Progression Assessments from Clinical Notes,” in *Pacific Symposium on Biocomputing (PSB 2026)*.

Johri and et al. (2026) “A Clinician-Guided Framework for Endoscopic AI: Developing PanEndoAtlas,” in *Pacific Symposium on Biocomputing (PSB 2026)*.

Ko and et al. (2026) “Abstention and Threshold Identification for Uncertainty Management in Clinical Decision Tools,” in *Pacific Symposium on Biocomputing (PSB 2026)*.

Liu and et al. (2026) “Higher-order Interaction Matters: Modeling Epidemics via Dynamic Hypergraph Neural Networks,” in *Pacific Symposium on Biocomputing (PSB 2026)*.

Lopez, I. *et al.* (2025) “Clinical entity augmented retrieval for clinical information extraction,” *npj Digital Medicine*, 8(1), pp. 1–11. Available at: https://doi.org/10.1038/s41746-024-01377-1.

Lopez-Garcia and et al. (2026) “Scoring Physician Risk Communication in Prostate Cancer Using Large Language Models,” in *Pacific Symposium on Biocomputing (PSB 2026)*.

Luo and et al. (2026) “ED-Explain: Personalized Video Instructions for Patients Discharged from the Emergency Department,” in *Pacific Symposium on Biocomputing (PSB 2026)*.

McCoy and et al. (2026) “Asking the Right Questions: Benchmarking LLMs in Clinical Consultation Templates,” in *Pacific Symposium on Biocomputing (PSB 2026)*.

Nateghi Haredasht, F. *et al.* (2023) “Predicting outcomes of acute kidney injury in critically ill patients using machine learning,” *Scientific Reports*, 13, p. 9864. Available at: https://doi.org/10.1038/s41598-023-36782-1.

Nateghi Haredasht, F., Fouladvand, S., *et al.* (2024) "Predictability of buprenorphine-naloxone treatment retention: A multi-site analysis combining electronic health records and machine learning," *Addiction*, 119(10), pp. 1792–1802. Available at: https://doi.org/10.1111/add.16587.

Nateghi Haredasht, F., Kim, D., *et al.* (2024) "Session Introduction: AI and Machine Learning in Clinical Medicine: Generative and Interactive Systems at the Human-Machine Interface," in *Biocomputing 2025*. WORLD SCIENTIFIC, pp. 33–39. Available at: https://doi.org/10.1142/9789819807024_0003.

Nateghi Haredasht, F. and Vens, C. (2022) "Predicting Survival Outcomes in the Presence of Unlabeled Data," *Machine Learning*, 111(11), pp. 4139–4157. Available at: https://doi.org/10.1007/s10994-022-06257-x.

Noei, S. *et al.* (2016) "Classification of EEG signals using the Spatio-temporal feature selection via the elastic net," in *2016 23rd Iranian Conference on Biomedical Engineering and 2016 1st International Iranian Conference on Biomedical Engineering (ICBME)*. *2016 23rd Iranian Conference on Biomedical Engineering and 2016 1st International Iranian Conference on Biomedical Engineering (ICBME)*, pp. 232–236. Available at: https://doi.org/10.1109/ICBME.2016.7890962.

Nori, H. *et al.* (2023) "Capabilities of GPT-4 on Medical Challenge Problems." arXiv. Available at: https://doi.org/10.48550/arXiv.2303.13375.

Pal and et al. (2026) "ReXVQA: A Large-scale Visual Question Answering Benchmark for Chest X-ray Understanding," in *Pacific Symposium on Biocomputing (PSB 2026)*.

Patel, B.N. *et al.* (2019) "Human–machine partnership with artificial intelligence for chest radiograph diagnosis," *npj Digital Medicine*, 2(1), p. 111. Available at: https://doi.org/10.1038/s41746-019-0189-7.

Prioleau and et al. (2026) "Leveraging Large Language Models for Adverse Drug Event Detection," in *Pacific Symposium on Biocomputing (PSB 2026)*.

Pugh and et al. (2026) "WATCH-SS: A Trustworthy and Explainable Modular Framework for Detecting Cognitive Impairment," in *Pacific Symposium on Biocomputing (PSB 2026)*.

Rajkomar, A., Dean, J. and Kohane, I. (2019) "Machine Learning in Medicine," *The New England Journal of Medicine*, 380(14), pp. 1347–1358. Available at: https://doi.org/10.1056/NEJMra1814259.

Sambara and et al. (2026) "3DReasonKnee: Advancing Grounded Reasoning in Medical Vision Language Models," in *Pacific Symposium on Biocomputing (PSB 2026)*.

Schmitz and et al. (2026) "Towards Automated Analysis of Gaze Behavior from Consumer VR Devices for Neurological Diagnosis," in *Pacific Symposium on Biocomputing (PSB 2026)*.

Sendak, M.P. *et al.* (2020) "A Path for Translation of Machine Learning Products into Healthcare Delivery," *European Medical Journal* [Preprint]. Available at: https://doi.org/10.33590/emjinnov/19-00172.

Strobl and et al. (2026) "Learning Causally Predictable Outcomes from Psychiatric Longitudinal Data," in *Pacific Symposium on Biocomputing (PSB 2026)*.

Thirunavukarasu, A.J. *et al.* (2023) "Large language models in medicine," *Nature Medicine*, 29(8), pp. 1930–1940. Available at: https://doi.org/10.1038/s41591-023-02448-8.

Wiens, J. *et al.* (2019) "Do no harm: a roadmap for responsible machine learning for health care," *Nature Medicine*, 25(9), pp. 1337–1340. Available at: https://doi.org/10.1038/s41591-019-0548-6.

Wu and et al. (2026) "Automated Evaluation of Large Language Model Response Concordance with Human Specialist Responses on eConsult Cases," in *Pacific Symposium on Biocomputing (PSB 2026)*.

Zhang and et al. (2026) "Automated Chest X-ray Report Generation Remains Unsolved," in *Pacific Symposium on Biocomputing (PSB 2026)*.

Zolensky and et al. (2026) "Speaker Role Identification in Clinical Conversations," in *Pacific Symposium on Biocomputing (PSB 2026)*.

Inference Gap in Domain Expertise and Machine Intelligence in Named Entity Recognition: Creation of and Insights from a Substance Use-related Dataset

Sumon Kanti Dey,[1] Jeanne M. Powell,[1] Azra Ismail,[1] Jeanmarie Perrone,[2] Abeed Sarker[1,†]

[1]*Department of Biomedical Informatics, Emory University, Atlanta, GA 30322, USA*
[2]*Department of Emergency Medicine, Perelman School of Medicine, University of Pennsylvania, Philadelphia, PA 19104, USA*
[†]*E-mail: abeed.sarker@emory.edu*

Nonmedical opioid use is an urgent public health challenge, with far-reaching clinical and social consequences that are often underreported in traditional healthcare settings. Social media platforms, where individuals candidly share first-person experiences, offer a valuable yet underutilized source of insight into these impacts. In this study, we present a named entity recognition (NER) framework to extract two categories of self-reported consequences from social media narratives related to opioid use: *ClinicalImpacts* (e.g., withdrawal, depression) and *SocialImpacts* (e.g., job loss). To support this task, we introduce RedditImpacts 2.0, a high-quality dataset with refined annotation guidelines and a focus on first-person disclosures, addressing key limitations of prior work. We evaluate both fine-tuned encoder-based models and state-of-the-art large language models (LLMs) under zero- and few-shot in-context learning settings. Our fine-tuned DeBERTa-large model achieves a relaxed token-level F_1 of 0.61 [95% CI: 0.43–0.62], consistently outperforming LLMs in precision, span accuracy, and adherence to task-specific guidelines. Furthermore, we show that strong NER performance can be achieved with substantially less labeled data, emphasizing the feasibility of deploying robust models in resource-limited settings. Our findings underscore the value of domain-specific fine-tuning for clinical NLP tasks and contribute to the responsible development of AI tools that may enhance addiction surveillance, improve interpretability, and support real-world healthcare decision-making. The best performing model, however, still significantly underperforms compared to inter-expert agreement (Cohen's kappa: 0.81), demonstrating that a gap persists between expert intelligence and current state-of-the-art NER/AI capabilities for tasks requiring deep domain knowledge. The dataset, annotation guidelines, appendix, and training scripts are publicly available to support future research.*

Keywords: Named Entity Recognition; Substance Use; Clinical Impacts; Social Impacts; In-Context Learning; Large Language Models.

1. Introduction

Nonmedical use of opioids remains a pressing public health challenge in the United States (U.S.), with more than 8.6 million Americans affected [1]. Opioid-related overdoses have consistently remained a leading cause of accidental death in adults under 45 years of age, significantly reducing the average U.S. life expectancy [2]. In addition to fatal outcomes, nonmedical

*https://github.com/SumonKantiDey/Reddit_Impacts_NER

© 2025 The Authors. Open Access chapter published by World Scientific Publishing Company and distributed under the terms of the Creative Commons Attribution Non-Commercial (CC BY-NC) 4.0 License.

opioid use and addiction significantly disrupts social well-being and stability. People experiencing emotional distress or social instability, such as unemployment, housing insecurity, or family disruption, are more likely to initiate or escalate opioid use [3, 4]. Communities affected by the opioid epidemic often experience increased crime, educational challenges, and economic instability, further perpetuating cycles of disadvantage [5].

Nonmedical opioid use and subsequent impacts are underreported in clinical settings due to stigma, criminalization, and distrust of healthcare systems [6], leading to negative health outcomes [6, 7, 8]. Widespread underreporting creates significant blind spots in public health surveillance, impeding efforts to detect early warning signs and deliver timely interventions. In contrast, social media sites like Reddit provide a pseudonymous environment where people feel more comfortable disclosing sensitive information. Health-related disclosures can include patterns of substance use, clinical symptoms (e.g., withdrawal), overdose risk, and co-occurring mental health issues [9, 10]. Users also describe social consequences rarely captured in electronic health records [11], such as strained relationships, family disruption, financial hardship, unemployment, and social isolation. Analyzing these clinical and social impacts of opioid use reported on social media is crucial, as research has shown that the frequency and the content of opioid-related discussions online can mirror official epidemiological trends and provide timely insights for public health surveillance and intervention [12]. The enormity of the opioid crisis, which has ravaged the U.S. for almost three decades, requires innovative solutions [13], and the relative underutilization of social media data, which contains timely information directly posted by people with lived experiences, remains an untapped opportunity.

Extracting nuanced clinical and social impacts from informal, user-generated content poses significant challenges for natural language processing (NLP) models. Such content is highly unstructured, context-dependent, and contains abbreviations and ambiguities. Understanding the content, thus, requires deep contextual knowledge (e.g., through medical expertise or lived experience), which generic NLP systems, including large language models (LLMs) typically lack. Posts frequently express subjective, emotionally charged experiences, making it difficult for models to reliably map them to predefined categories [14]. There is a critical need to bridge the gap between expert-level domain-specific knowledge and NLP model capabilities in characterizing and extracting meaningful information from such user-generated content, so that surveillance systems can be deployed at scale to inform public health strategies, intervention planning, and, ultimately, reduce the burden of the substance-related overdose epidemic [15].

As an initial exploration of this challenge, our lab introduced a named entity recognition (NER) dataset—Reddit-Impacts [16]—which was the first to capture both clinical and social dimensions of substance use. Although promising, efforts employing transformer-based models and proprietary LLMs (GPT-3.5) revealed several critical limitations in the annotation and subsequent NLP system performances. A more detailed discussion about these limitations is provided in Appendix A. To address these shortcomings and enable the development/training of more effective NLP systems, we update the data set and develop an improved processing pipeline to automatically identify the clinical and social impacts of non-medical opioid use in Reddit narratives. Our contributions are summarized below:

(1) We release **RedditImpacts 2.0**, an improved, task-specific dataset featuring detailed an-

notation guidelines, consistent entity spans, and exclusive focus on first-person narratives.
(2) We propose an encoder-based framework for accurately extracting impact-related entities from unstructured social media narratives and systematically evaluate the effectiveness of various LLMs under zero- and few-shot in-context learning (ICL) settings.
(3) We introduce custom evaluation metrics designed to effectively measure the accuracy and reliability of models, ensuring they only identify self-reported social and clinical impacts.
(4) We conduct a targeted error analysis and data efficiency evaluation, demonstrating that strong, scalable performance can be achieved with substantially reduced labeled data, supporting responsible deployment in resource-limited and underserved settings.

Collectively, these contributions advance the development of human-aligned and trustworthy NLP systems to accurately interpret first-person opioid use narratives from social media.

Findings: Our findings reveal that LLMs underperform in the token-level NER task to identify clinical and social impacts of nonmedical opioid use in social media posts, whereas encoder-based models can be fine-tuned to achieve substantially better performance. Via targeted error analysis, we highlight areas where fine-tuned encoders and LLMs differ, illustrating specific strengths and pitfalls of each. We also show that strong model performance can be achieved with significantly small training data, emphasizing the feasibility, scalability, and responsible development of fine-tuned NER models in low-resource and data settings.

2. Related Work

NER involves identifying specific terms or phrases within texts, referred to as "entities". Traditionally, NER methods have concentrated on identifying narrow sets of predefined entities. In the biomedical field, for instance, entities include genes, diseases, chemicals, and proteins [17]. Compared to general or open-domain NER tasks, biomedical NER studies have received comparatively less scholarly attention because of the paucity of labeled data, the need for specialized computational models, and gaps in evaluation and benchmarking standards [18, 19, 20]. Biomedical NER involving social media data adds an additional layer of difficulty. Texts from such sources are characteristically informal, noisy, and linguistically diverse, making automated NER particularly difficult [21, 22]. Factors such as non-standard terminology, abbreviations, lack of context, and misspellings further amplify NER challenges [22, 23].

Recent advances have overcome many of the abovementioned challenges, demonstrating the successful use of advanced NER models, including neural network and transformer-based approaches, to extract entities such as drugs, diseases, and symptoms from posts on platforms like Reddit and online health forums [24, 16, 25]. Within the broader substance use sphere, transformer-based language models (BERT-base-NER, RoBERTa-base, BioBERT-base-cased, and Bio_ClinicalBERT) have been utilized to accurately identify opioid-related entities [25]. Scepanovic et al. [24] demonstrated that transformer-based models outperform traditional BiLSTM-CRF architectures in accurately extracting diverse medical entities such as symptoms, diseases, and drug names from social media posts, including Reddit.

The emergence of instruction-tuned LLMs, including Llama 3 [26], Gemma 3 [27], and GPT-4o [28], which have demonstrated exceptional performance in medical reasoning benchmarks, have also, in many cases, led to improvements in challenging NER tasks primarily

through innovative prompting strategies [29, 30, 31]. These prompting techniques enable models to generalize effectively to previously unseen scenarios with minimal contextual cues, reducing the need for extensive fine-tuning and thus facilitating efficient biomedical entity extraction. There is, however, still a research gap in NER for highly imbalanced datasets, descriptive entities, and in low-shot settings, as demonstrated by past work on the Reddit-Impacts dataset [16, 32].

3. Methodology

(a) Encoder-Based Pipeline for Impact Entity Recognition

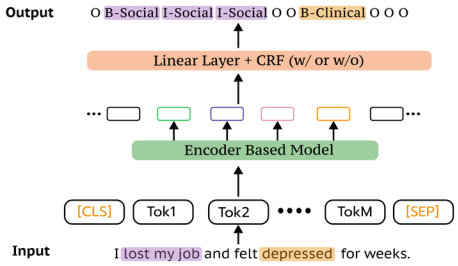

(b) LLM-Based Pipeline for Impact Entity Recognition

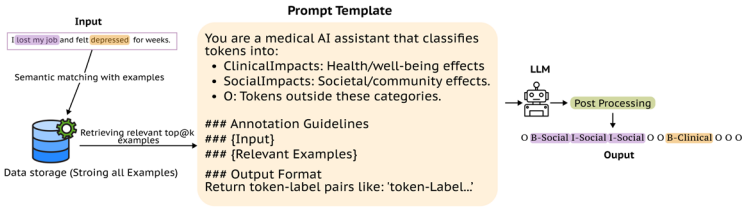

Fig. 1: NER framework for detecting *Social* and *Clinical Impacts* in user-generated text. In the output, Clinical corresponds to ClinicalImpacts and Social corresponds to SocialImpacts .

3.1. *Task Overview*

We formulate the NER task as a sequence-labeling problem using the BIO (Begin, Inside, Outside) tagging scheme. This scheme assigns one of three tags to each token: `B` to indicate the beginning of an entity, `I` for tokens that are inside an entity, and `O` for tokens that lie outside any entity span. Each tag is further associated with a specific entity type `X`, resulting in labels such as `B-X` (beginning of entity type `X`) and `O` (non-entity token).

Given a token sequence, $T = [t_1, t_2, \ldots, t_n]$ the model predicts a corresponding sequence of labels $L = [l_1, l_2, \ldots, l_n]$, where each $l_i \in \{\texttt{O}, \texttt{B-X}, \texttt{I-X}\}$. This formulation enables the model to learn both the boundary and the type of each entity span. In our study, we focus on two domain-specific entity types: **ClinicalImpacts**, representing physical or psychological consequences of substance use (e.g., *"hospitalized"*, *"depression"*), and **SocialImpacts**, which denote social, occupational, or relational consequences (e.g., *"lost job"*, *"arrested"*). An illustration of a BIO-tagged example with both entity types is shown in Table 1.

Table 1: Example of BIO-tagged tokens. The phrase *"lost my job"* is annotated as a `SocialImpacts` entity and *"depressed"* as a `ClinicalImpacts` entity.

Tokens	I	lost	my	job	and	felt	depressed	for	weeks	.
BIO Tag	O	**B-SocialImpacts**	**I-SocialImpacts**	**I-SocialImpacts**	O	O	**B-ClinicalImpacts**	O	O	O

3.2. *Data Annotation*

Named entities for very specialized problems are expected to be context-dependent, making annotation of such entities inherently complex [33]. This challenge is exacerbated in the context of social media data, where language is informal, unstructured, and shaped by personal, lived experiences. Posts related to opioid misuse often contain emotionally expressive narratives, fragmented grammar, and colloquial terms, making it difficult to consistently identify clinical and social impacts. To meet these complexities, this study included two experienced annotators with formal linguistic training. Both were guided by a comprehensive and detailed annotation manual, refined by a subject matter expert, specially designed to address the specific complexities of clinical and social impact mentions in opioid-related narratives. The full annotation guideline is provided in Appendix C.

The annotation process followed an iterative design. Initially, a 10% subset of the dataset was independently annotated by both annotators. This step was critical for aligning their interpretation of the guidelines, especially in handling variations in language and subtle distinctions in meaning. Discrepancies were resolved through discussion, leading to refinement of the guideline. We conducted iterative co-annotation until an agreement accuracy exceeding 95% was achieved. Once this threshold was met, the remaining data were divided between the two annotators for independent annotation.

We used Cohen's Kappa [34] across overlapping annotated samples to compute inter-annotator agreement. The resulting score of 81% indicated substantial agreement, reflecting almost-perfect agreement [35]. Descriptive statistics of the annotated dataset, including the total number of posts, tokens, and labeled entities, are summarized in Table 2.

Table 2: Statistics of the annotated Reddit-Impacts NER dataset.

Split	**Total Posts**	**SocialImpacts Entities**	**ClinicalImpacts Entities**	**Total Entities**	**Total Tokens**
Train	842	408	616	1024	17.2K
Dev	258	167	223	390	5.2K
Test	278	256	108	364	6.2K
Total	1378	831	947	1778	28.6K

3.3. *Experimental Setup*

For training our models, we merged the original training and development datasets to ensure we utilized the maximum amount of available data. We then set aside approximately 10% of this combined dataset as a validation set, resulting in roughly a 90/10 split between training and validation. The test set was kept separate to provide a reliable assessment of how well our models perform on completely unseen data. To support fine-tuning these models, we leveraged

a GPU equipped with 48GB of memory (e.g., NVIDIA RTX A6000). Detailed fine-tuning procedures and settings are provided in Appendix D.1.

3.4. *Modeling Approaches*

We evaluate three modeling paradigms for our SocialImpacts and ClinicalImpacts detection NER task: fine-tuning pre-trained language models (PLMs), augmenting PLMs with conditional random fields (CRF), and applying few-shot prompting techniques with large language models (LLMs). Each of these strategies has been extensively validated in recent NER research, motivating their adoption in our study [36, 37, 38, 39]. Figure 1 provides a visual summary of our overall modeling pipeline.

3.4.1. *Pre-trained language models (PLMs)*

We fine-tuned several transformer-based encoder derivatives, namely BERT [40], RoBERTa [41], DeBERTa [42], RoBERTaNER [a], and BioBERT [43]. We replace each model's standard classification head with a linear token-level classification layer predicting our BIO-formatted labels. Models are optimized using cross-entropy loss, AdamW optimizer, learning rate scheduling with linear warm-up, and early stopping based on validation-set F_1 score.

3.4.2. *PLM with CRF (PLM + CRF)*

Motivated by prior research demonstrating that adding CRF (Appendix B) layers significantly improve NER performance by capturing inter-label dependencies and ensuring valid BIO-tag transitions [44, 45], we extend each PLM by adding a CRF layer. The CRF replaces the softmax outputs and decodes the most probable sequence of labels through Viterbi decoding. Training is performed by minimizing the negative log-likelihood of the true sequences, further improving tag consistency and producing more coherent spans.

3.4.3. *Few-Shot Prompting with LLMs*

We explore zero- and few-shot prompting strategies. For each input sequence requiring labeling, we perform three key steps. First, we compute the semantic embedding of all training samples using sentence-BERT [46]. Second, we identify and select the top@K most semantically similar training examples based on cosine similarity to the input sequence. We then construct a comprehensive prompt, integrating a concise task description, explicit annotation guidelines (BIO scheme and definitions for ClinicalImpacts and SocialImpacts), the top@K dynamically selected exemplar token-label sequences, and the target input tokens to be annotated. This in-context learning approach leverages the robust semantic understanding and few-shot inference capabilities of LLMs, eliminating the need for task-specific parameter updates and providing a flexible inference method suited for low-resource or rapid-deployment scenarios. The prompt is detailed in Appendix D.2.

3.5. *Evaluation Metrics: Relaxed F_1 Score*

We evaluate model performance using a relaxed, token-level F_1 scoring method designed for entity recognition tasks involving partial matches. Our approach is inspired by partial-matching

[a]https://huggingface.co/Jean-Baptiste/roberta-large-ner-english

techniques used in biomedical NLP tasks [47, 48]. Unlike strict span-level matching, which considers only exact boundary matches, relaxed evaluation accounts for partial overlap between predicted and ground truth entity spans of the same type, capturing cases where predictions are approximately correct. This evaluation is especially suitable for informal, user-generated text where exact span boundaries may be difficult to capture. The specific evaluation strategy formulation is outlined below.

Let each labeled sequence consist of predicted and gold spans represented as:

$$G = \{g_1, g_2, \ldots, g_m\}, \quad P = \{p_1, p_2, \ldots, p_n\},$$

where each span g_i or p_j is defined as a triple (t, s, e), denoting the entity type t, start token index s, and end token index e.

We define token-level overlap between two spans g_i and p_j of the same entity type as:

$$\text{Overlap}(g_i, p_j) = \max(0, \min(e_g, e_p) - \max(s_g, s_p) + 1),$$

where (s_g, e_g) and (s_p, e_p) are the token span boundaries of the gold and predicted entities, respectively.

For each entity type T, we compute:

$$\text{TP}_T = \sum_{(g,p)\in\mathcal{M}_T} \text{Overlap}(g, p); \text{P}_T = \sum_{p_j\in P_T} (e_p - s_p + 1); \text{R}_T = \sum_{g_i\in G_T} (e_g - s_g + 1)$$

where $\mathcal{M}_T$ denotes the set of span pairs (g, p) of type T with non-zero token-level overlap.

Precision, recall, and F_1 score for entity type T are then defined as:

$$\text{Precision}_T = \frac{\text{TP}_T}{\text{P}_T}, \quad \text{Recall}_T = \frac{\text{TP}_T}{\text{R}_T}, \quad \text{F1}_T = \frac{2 \cdot \text{Precision}_T \cdot \text{Recall}_T}{\text{Precision}_T + \text{Recall}_T}.$$

We additionally compute a micro-averaged overall F_1 score by aggregating overlapping token counts across all entity types:

$$\text{Overall Precision} = \frac{\sum_T \text{TP}_T}{\sum_T \text{P}_T}, \quad \text{Overall Recall} = \frac{\sum_T \text{TP}_T}{\sum_T \text{R}_T},$$

$$\text{Overall F}_1 = \frac{2 \cdot \text{Overall Precision} \cdot \text{Overall Recall}}{\text{Overall Precision} + \text{Overall Recall}}$$

This relaxed overlap-based metric for NER is tailored to informal user-generated content, where exact boundary prediction is often difficult.

3.6. *Error Analysis*

To better understand the strengths and limitations of our models, we conducted a qualitative error analysis comparing the fine-tuned DeBERTa-large model (the best-performing model among fine-tuned PLMs) and GPT-4o with 3-shot prompting (the top-performing model among LLMs) on the task of extracting social and clinical impacts.

4. Results

Table 3 summarizes the overall token-level relaxed precision, recall, and F_1 scores with 95% confidence intervals (CI) for all models described in Section 3.4.

Among fine-tuned PLMs (Table 3(a)), **DeBERTa-large** achieved the highest overall performance, with an F_1 score of **0.61** (95% CI: [0.43, 0.62]), precision **0.75**, and recall 0.52, demonstrating significant improvement over prior approaches reported on this difficult NER task. Incorporating a CRF layer yielded mixed results across models. For DeBERTa-large, the F_1 score was lower with CRF at 0.57 [0.43-0.59], with overlapping confidence intervals suggesting statistically insignificant differences. For BERT-large, adding CRF similarly reduced F_1 from 0.56 [0.38–0.56] to 0.52 [0.36–0.52]. In contrast, RoBERTaNER-large with CRF achieved an F_1 of 0.56 [0.45–0.60], slightly higher than its no-CRF counterpart at 0.51 [0.39–0.53], reflecting modest improvements in recall. Overall, the effect of CRF was minimal and appeared to depend on the underlying architecture. BioBERT models generally achieved lower F_1 scores compared to other PLMs, reflecting possible limitations in transferring their specialized clinical language understanding to the informal language context of social media.

Table 3(b) presents the in-context learning performance of LLMs under zero-, 3-, and 5-shot settings. Among these LLMs, **GPT-4o** achieved the best overall few-shot prompting performance, with an F_1 score of **0.44** [95% CI: 0.37, 0.51] in the 3-shot setting, demonstrating balanced precision (0.42) and recall (0.46). Llama 3-70b also performed competitively, reaching an F_1 score of 0.41 in the 3- and 5-shot settings. Gemma 3-27b, while lower in absolute performance, showed a clear benefit from in-context examples, improving from an F_1 score of 0.32 [0.27-0.40] in a zero-shot setting to 0.34 [0.33-0.45] in the 3-shot setting.

These results collectively demonstrate that few-shot prompting using semantically similar examples enhances the performance of LLMs on token-level prediction tasks compared to zero-shot settings. Nevertheless, even the best-performing LLM (GPT4o, $F_1 = 0.44$) remained below the best fine-tuned encoder (DeBERTa-large, F_1=0.61), emphasizing the advantage of domain-specific fine-tuning for token-level NER tasks in this domain.

We also report entity-specific token label performance for the best-performing fine-tuned PLM (DeBERTa-large) and the top-performing few-shot LLM (GPT-4o with 3-shot prompting) in Table 4. In these two combinations, DeBERTa-large yielded the strongest performance on both ClinicalImpacts ($F_1 = 0.60$) and SocialImpacts ($F_1 = 0.50$). GPT-4o (3-shot) performed comparably on ClinicalImpacts ($F_1 = 0.51$), but underperformed on SocialImpacts ($F_1 = 0.26$), indicating varying levels of difficulty across entity types.

4.1. *Qualitative Error Analysis Results*

We identified four major categories of errors: label confusion, missed implicit entities, false positives due to negation/context errors, and violations of annotation guidelines.

Label confusion (Social vs. Clinical): GPT-4o frequently struggled to differentiate between social and clinical contexts. For instance, in the sentence *"When I was 21... on a therapeutic community"*, the model misclassified the phrase *"therapeutic community"* as a SocialImpact, whereas it was correctly annotated as a ClinicalImpact.

Missed implicit entities: Both models exhibited limitations in capturing impacts that

Table 3: Token-level relaxed precision, recall, and F_1 scores with 95% confidence intervals (CI) across two evaluation settings: **(a)** *Fine-tuned PLMs*–evaluated with and without Conditional Random Fields (CRF). **(b)** *In-Context Learning Performance of LLMs*–evaluated under zero-shot, 3-shot, and 5-shot settings using the most similar examples for prompting. The best-performing model is highlighted in **bold**, and the second-best is underlined.

(a) Fine-tuned Pretrained Language Models (PLMs).

Model	Precision	Recall	F_1	95% CI
BERT(large-uncased)	0.65	0.49	0.56	[0.38, 0.56]
BERT(large-uncased) + CRF	0.67	0.42	0.52	[0.36, 0.52]
RoBERTaNER(large)	0.67	0.42	0.51	[0.39, 0.53]
RoBERTaNER(large) + CRF	0.59	**0.54**	0.56	[0.45, 0.60]
DeBERTa(large)	**0.75**	0.52	**0.61**	[0.43, 0.62]
DeBERTa(large) + CRF	0.68	0.50	0.57	[0.43, 0.59]
BioBERT(large-cased)	0.60	0.39	0.47	[0.34, 0.52]
BioBERT(large-cased) + CRF	0.63	0.42	0.51	[0.35, 0.53]

(b) In-Context Learning Performance of LLMs under Zero-, 3-, and 5-shot Settings.

Model	Prompting	Precision	Recall	F_1	95% CI
Gemma 3-27b-it	0-shot	0.29	0.35	0.32	[0.27, 0.40]
	3-shot	0.26	**0.48**	0.34	[0.33, 0.45]
	5-shot	0.25	**0.48**	0.33	[0.32, 0.46]
Llama 3-70b instruct	0-shot	0.46	0.27	0.34	[0.28, 0.37]
	3-shot	**0.47**	0.37	0.41	[0.35, 0.45]
	5-shot	0.46	0.37	0.41	[0.33, 0.48]
GPT-4o	0-shot	0.43	0.37	0.40	[0.31, 0.43]
	3-shot	0.42	0.46	**0.44**	[0.39, 0.51]
	5-shot	0.39	**0.48**	0.43	[0.37, 0.51]

Table 4: Entity-specific token-level relaxed precision, recall, F_1-score with 95% CI for the top-performing fine-tuned PLM (DeBERTa-large) and few-shot LLM (GPT-4o, 3-shot).

Model	**Entity**	**Precision**	**Recall**	**F_1-score**	**95% CI**
DeBERTa(large)	SocialImpacts	0.63	0.41	0.50	[0.25, 0.62]
	ClinicalImpacts	0.80	0.56	0.66	[0.45, 0.67]
GPT-4o(3-shot)	SocialImpacts	0.28	0.25	0.26	[0.18, 0.34]
	ClinicalImpacts	0.46	0.56	0.51	[0.44, 0.60]

were implied rather than explicitly stated. In the sentence *"I was shocked... when I told them about my addiction and that I was seeking/needed help"*, DeBERTa successfully identified the ClinicalImpact *"addiction"*, but failed to detect the SocialImpact embedded in the phrase

"seeking/needed help". GPT-4o similarly failed, incorrectly labeling isolated words and missing the intended SocialImpacts entirely.

False positives due to context or negation errors: Both models occasionally produced false positives when failing to interpret negation or surrounding context accurately. In the sentence *"I am a recovering heroin addict with no criminal record but..."*, both DeBERTa and GPT-4o incorrectly labeled the phrase *"criminal record"* as a SocialImpact, despite the explicit negation ("no criminal record").

Guideline violations and overgeneralization errors: GPT-4o sometimes failed to adhere to annotation guidelines, including the instruction to annotate only first-person experiences. For example, in the sentence *"Helps with the restlessness and anxiety"*, the model labeled *"restlessness"* and *"anxiety"* as ClinicalImpacts, despite the absence of first-person framing. Moreover, GPT-4o exhibited overgeneralization, labeling ambiguous or emotionally charged terms, such as *"blindsided"*, *"pressuring"*, and *"treatment"*, as ClinicalImpacts, even when these were contextually neutral or not linked to direct impacts.

5. Discussion

5.1. *Bridging Expert Knowledge and Model Intelligence Remains a Challenge for Complex NER*

While our NER models demonstrated improvement over past efforts on the same, challenging dataset, there remains a significant gap between human-level agreement and model performance. Systematically improving the annotation guideline improved IAA, but models failed to fully capture the nuances of first-person reporting of clinical and social impacts of substance use. While our study explored strategies to bridge this gap using the Reddit-Impacts dataset, it generalizes to other NER tasks where deep domain expertise is necessary and in problems where annotated examples are lexically diverse and low due to dataset characteristics. In the context of substance use surveillance from social media data, improving NER performance may lead to the timely detection of emerging impacts of the continuously evolving overdose epidemic in the U.S. Our work may also shed light on how social media content reflects and shapes public perceptions of substance use over time, helping identify high-risk groups and the types of content they engage with, thereby informing development of more targeted and effective prevention strategies. Automated impact detection can further support the development of real-time support systems that connect users with peer or professional support during moments of crisis, thus strengthening clinical decision-making and public health intervention.

5.2. *Error Analysis*

Label confusion, prominent in GPT-4o, highlights its difficulty in distinguishing between structured clinical environments and broader social circumstances, particularly when terminologies overlap, although these subtle differences are evident to human experts. GPT-4o's overgeneralization errors also revealed its difficulty in handling subtle context-dependent biomedical terms. Model errors in detecting implicit entities revealed challenges in grasping context-dependent, nuanced language. Labeling errors in both models' ability to process negated constructs and assess contextual validity prior to labeling. Overall, while GPT-4o offers impressive generalization through prompting, it tends to misinterpret nuanced or implied information,

and is more prone to guideline violations and contextual errors. In contrast, the fine-tuned DeBERTa-large model demonstrated stronger alignment with domain-specific guidelines and span accuracy. It may be possible to employ ensembling approaches, such as adding a first-person report classifier prior to processing by an LLM, rather than a single-module pipeline to improve inference performance.

5.3. *Impact of In-Context Learning in LLMs*

Our findings indicate that ICL offers marginal performance gains in certain cases. For example, using 3-shot prompting resulted in a modest improvement of less than 4% in F_1 score across all LLMs compared to the zero-shot setting. However, when we increased the number of examples to 5, the overall performance declined by ≈1–2%, suggesting that additional examples may introduce noise or confuse the model's decision-making process in the NER detection task. The differences were not statistically significant, as indicated by overlapping 95%-CIs. Overall, we observe that while ICL may enhance performance to a limited extent, particularly when using well-selected and minimal examples, increasing the amount of text in the context window may overwhelm the model, leading to reduced inference performance.

5.4. *Sample Size Consideration for Fine-Tuning a Language Model*

Training a model for specialized tasks can be expensive due to the need for domain expert annotation—leading to substantial time and financial costs [49, 50]; expert annotators take 10-30 seconds per sentence to label named entities [51]. These challenges are further amplified for of user-generated biomedical data, which can be context-dependent, and emotionally nuanced, and where the demand for annotation quality is especially high. Consequently, developing models that can perform well even with limited annotated data is paramount.

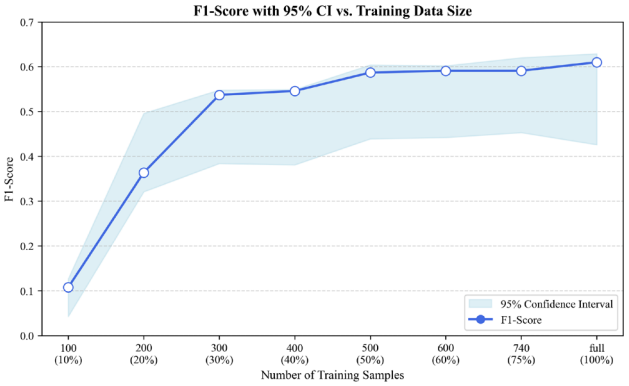

Fig. 2: F_1 score with 95% CIs across training data sizes. x-axis shows the number of training samples with the corresponding percentage of the full dataset; shaded area represents the 95% CI for each point.

We investigated the amount of annotated data required to achieve expert-level performance using the DeBERTa-large model, which attained the highest F_1 score. Our findings (Figure 2) demonstrate that F_1 score plateaus at approximately 50% of training data, with additional data yielding only minor improvements. This suggests that better strategies for incorporating domain knowledge may be more effective in improving performance than annotating more data.

5.5. *Domain-Specific Fine-Tuning Still Matters for Biomedical NER*

Our findings reinforce the growing evidence that prompting alone is insufficient for achieving state-of-the-art performance in biomedical NER. Despite the flexibility and generalization capabilities of LLMs, models like GPT-4o and Llama 3-70B underperformed compared to

domain-specific encoders fine-tuned on task-relevant labeled data. In our experiments, even the best-performing LLM using in-context learning (few-shot prompting) failed to match the F_1 score of the top fine-tuned encoder model, DeBERTa-large. These results align with some recent studies showing that LLMs, when used without task-specific fine-tuning, struggle to surpass traditional encoder architectures in specialized biomedical settings [39, 36]. One underlying limitation is that token-level NER tasks—particularly in biomedical contexts—require models that can interpret the structured label schemes such as BIO tags and manage domain-specific terminology, which may include rare and unseen tokens. Prompting strategies, which do not modify the model's internal weights, are often insufficient to capture these nuances. In contrast, fine-tuning involves updating the model's parameters through supervised training, which allows the model to learn domain-specific representations and labeling conventions more effectively. The relatively stable and accurate performance of fine-tuned PLMs in structured biomedical NER tasks highlights the continued importance of fine-tuning, particularly in domains where general-purpose LLMs still fall short.

5.6. *Limitations*

We acknowledge some limitations in our study. First, the dataset used for training is relatively small, resulting in suboptimal performance. Second, while our fine-tuned encoder-based models achieved strong performance, they are still struggle with capturing nuanced, context-dependent expression–especially when entities are implied rather than explicitly stated. Incorporating additional contextual signals or auxiliary tasks could further enhance the performance of the model. We also observed that social impacts are harder to detect than clinical impacts. This might be due to the fact that social impact expressions have higher lexical variability and non-clinical concepts are not as well defined as clinical ones. Lastly, though we evaluated LLMs under zero- and few-shot in-context learning settings, we did not explore instruction-tuned version of these models or feedback from error analysis to refine prompts. In future work, we aim to explore these approaches, along with multi-agent architectures, to better adapt LLMs for domain-specific entity recognition applicable to other types of texts (e.g., clinical notes).

6. Conclusion

We explored strategies for extracting social and clinical impacts from first-person narratives related to substance use, using the refined and high-quality RedditImpacts 2.0 dataset. Our best-performing fine-tuned encoder model, DeBERTa-large, achieved a relaxed token-level F_1 score of 61%, significantly outperforming the best-performing LLM (GPT-4o), which achieved an F_1 score of 44%—a 17% gap. This performance gap highlights the current limitations of prompting-based LLMs in specialized NER tasks without fine-tuning. Furthermore, our data efficiency analysis revealed that using only 50% of the balanced dataset was sufficient to achieve performance comparable to training on the full dataset, suggesting that high-quality, domain-specific annotations, even in moderate quantities, can yield strong results.

Acknowledgments

This publication was supported by the National Institute on Drug Abuse (NIDA) of the National Institutes of Health (NIH); award number R01DA057599. The content is solely the responsibility of the authors and does not necessarily represent the official views of the NIH.

References

[1] American Psychiatric Association, Opioid use disorder (2023), Accessed: 2025-06-06.

[2] Mayo Clinic, The role of healthcare professionals in opioid addiction prevention (n.d.), Accessed: 2025-06-06.

[3] M. Cerdá, N. Krawczyk, L. Hamilton, K. E. Rudolph, S. R. Friedman and K. M. Keyes, A critical review of the social and behavioral contributions to the overdose epidemic, *Annual review of public health* **42**, 95 (2021).

[4] C. Lin, S. J. Cousins, Y. Zhu, S. E. Clingan, L. J. Mooney, E. Kan, F. Wu and Y.-I. Hser, A scoping review of social determinants of health's impact on substance use disorders over the life course, *Journal of substance use and addiction treatment* , p. 209484 (2024).

[5] R. Darolia and C. Heflin, The social and community consequences of the opioid epidemic, *The ANNALS of the American Academy of Political and Social Science* **703**, 7 (2022).

[6] C. Strike, S. Robinson, A. Guta, D. H. Tan, B. O'Leary, C. Cooper, R. Upshur and S. Chan Carusone, Illicit drug use while admitted to hospital: Patient and health care provider perspectives, *Plos one* **15**, p. e0229713 (2020).

[7] S. Cooper and S. Nielsen, Stigma and social support in pharmaceutical opioid treatment populations: A scoping review, *International Journal of Mental Health and Addiction* **15**, 452 (2017).

[8] A. Cheetham, L. Picco, A. Barnett, D. I. Lubman and S. Nielsen, The impact of stigma on people with opioid use disorder, opioid treatment, and policy, *Substance abuse and rehabilitation* , 1 (2022).

[9] U. Lokala, O. C. Phukan, T. G. Dastidar, F. Lamy, R. Daniulaityte and A. Sheth, Detecting substance use disorder using social media data and the dark web: time-and knowledge-aware study, *JMIRx Med* **5**, p. e48519 (2024).

[10] A. Sarker, A. DeRoos and J. Perrone, Mining social media for prescription medication abuse monitoring: a review and proposal for a data-centric framework, *Journal of the American Medical Informatics Association* **27**, 315 (2020).

[11] S. Giorgi, D. B. Yaden, J. C. Eichstaedt, L. H. Ungar, H. A. Schwartz, A. Kwarteng and B. Curtis, Predicting us county opioid poisoning mortality from multi-modal social media and psychological self-report data, *Scientific reports* **13**, p. 9027 (2023).

[12] K. A. Carpenter, A. T. Nguyen, D. A. Smith, I. A. Samori, K. Humphreys, A. Lembke, M. V. Kiang, J. C. Eichstaedt and R. B. Altman, Which social media platforms facilitate monitoring the opioid crisis?, *PLOS Digital Health* **4**, p. e0000842 (2025).

[13] K. Humphreys, R. Saitz, N. D. Volkow, C. L. Shover, T. F. Babor, B. G. Carr, W. N. Evans, D. A. Fiellin, S. A. Glantz, W. Hall, D. Heller, D. H. Jernigan, R. J. MacCoun, B. K. Madras, S. Satel, B. Vicknasingam, S. E. Wakeman, R. West, D. P. Wilson, D. Ziedonis, L. R. Zindel, P. Das, O. A. Olukoya, S. L. Proctor, S. J. Tye, E. Wakeman and C. H. Wilkins, Responding to the opioid crisis in north america and beyond: recommendations of the stanford–lancet commission, *The Lancet* **399**, 555 (Feb 2022).

[14] G. Coppersmith, R. Leary, P. Crutchley and A. Fine, Natural language processing of social media as screening for suicide risk, *Biomedical informatics insights* **10**, p. 1178222618792860 (2018).

[15] D. Beyer, Joint economic committee releases new report on the economic toll of the opioid crisis (2023), Accessed: 2025-06-15.

[16] Y. Ge, S. Das, K. O'Connor, M. A. Al-Garadi, G. Gonzalez-Hernandez and A. Sarker, Reddit-impacts: A named entity recognition dataset for analyzing clinical and social effects of substance use derived from social media, *arXiv preprint arXiv:2405.06145* (2024).

[17] H. Cho and H. Lee, Biomedical named entity recognition using deep neural networks with contextual information, *BMC bioinformatics* **20**, 1 (2019).

[18] X. Dai, Recognising biomedical names: Challenges and solutions, *arXiv preprint arXiv:2106.12230* (2021).
[19] L. Luo, C.-H. Wei, P.-T. Lai, R. Leaman, Q. Chen and Z. Lu, Aioner: all-in-one scheme-based biomedical named entity recognition using deep learning, *Bioinformatics* **39**, p. btad310 (2023).
[20] S. Liu, A. Wang, X. Xiu, M. Zhong, S. Wu *et al.*, Evaluating medical entity recognition in health care: Entity model quantitative study, *JMIR Medical Informatics* **12**, p. e59782 (2024).
[21] P. Karisani and E. Agichtein, Did you really just have a heart attack? towards robust detection of personal health mentions in social media, in *Proceedings of the 2018 World Wide Web Conference*, 2018.
[22] A. Magge, A. Klein, A. Miranda-Escalada, M. A. Al-Garadi, I. Alimova, Z. Miftahutdinov, E. Farre, S. Lima-López, I. Flores, K. O'Connor *et al.*, Overview of the sixth social media mining for health applications (# smm4h) shared tasks at naacl 2021, in *Proceedings of the sixth social media mining for health (# SMM4H) workshop and shared task*, 2021.
[23] D. Weissenbacher, A. Sarker, A. Magge, A. Daughton, K. O'Connor, M. Paul and G. Gonzalez, Overview of the fourth social media mining for health (smm4h) shared tasks at acl 2019, in *Proceedings of the fourth social media mining for health applications (# SMM4H) workshop & shared task*, 2019.
[24] S. Scepanovic, E. Martin-Lopez, D. Quercia and K. Baykaner, Extracting medical entities from social media, in *Proceedings of the ACM conference on health, inference, and learning*, 2020.
[25] G. Sidorov, M. Ahmad, I. Ameer, M. Usman and I. Batyrshin, Opioid named entity recognition (oner-2025) from reddit, *arXiv preprint arXiv:2504.00027* (2025).
[26] A. Grattafiori, A. Dubey, A. Jauhri, A. Pandey, A. Kadian, A. Al-Dahle, A. Letman, A. Mathur, A. Schelten, A. Vaughan *et al.*, The llama 3 herd of models, *arXiv preprint arXiv:2407.21783* (2024).
[27] G. Team, A. Kamath, J. Ferret, S. Pathak, N. Vieillard, R. Merhej, S. Perrin, T. Matejovicova, A. Ramé, M. Rivière *et al.*, Gemma 3 technical report, *arXiv preprint arXiv:2503.19786* (2025).
[28] A. Hurst, A. Lerer, A. P. Goucher, A. Perelman, A. Ramesh, A. Clark, A. Ostrow, A. Welihinda, A. Hayes, A. Radford *et al.*, Gpt-4o system card, *arXiv preprint arXiv:2410.21276* (2024).
[29] Z. Zhan, S. Zhou, M. Li and R. Zhang, Ramie: Retrieval-augmented multi-task information extraction with large language models on dietary supplements, *Journal of the American Medical Informatics Association* **32**, 545 (March 2025).
[30] W. Zhou, S. Zhang, Y. Gu, M. Chen and H. Poon, Universalner: Targeted distillation from large language models for open named entity recognition, *arXiv preprint arXiv:2308.03279* (2023).
[31] C. Shyr, Y. Hu, L. Bastarache, A. Cheng, R. Hamid, P. Harris and H. Xu, Identifying and extracting rare diseases and their phenotypes with large language models, *Journal of Healthcare Informatics Research* **8**, 438 (2024).
[32] Y. Ge, Y. Guo, S. Das, M. A. Al-Garadi and A. Sarker, Few-shot learning for medical text: A review of advances, trends, and opportunities, *Journal of Biomedical Informatics* **144**, p. 104458 (August 2023), Epub 2023 Jul 23.
[33] N. Ding, G. Xu, Y. Chen, X. Wang, X. Han, P. Xie, H.-T. Zheng and Z. Liu, Few-nerd: A few-shot named entity recognition dataset, *arXiv preprint arXiv:2105.07464* (2021).
[34] J. Cohen, A coefficient of agreement for nominal scales, *Educational and psychological measurement* **20**, 37 (1960).
[35] A. J. Viera and J. M. Garrett, Understanding interobserver agreement: the kappa statistic, *Family Medicine* **37**, 360 (May 2005).
[36] Q. Lu, R. Li, A. Wen, J. Wang, L. Wang and H. Liu, Large language models struggle in token-level clinical named entity recognition, in *AMIA Annual Symposium Proceedings*, 2025.
[37] I. Keraghel, S. Morbieu and M. Nadif, A survey on recent advances in named entity recognition, *arXiv preprint arXiv:2401.10825* (2024).

[38] S. Wang, X. Sun, X. Li, R. Ouyang, F. Wu, T. Zhang, J. Li and G. Wang, Gpt-ner: Named entity recognition via large language models, *arXiv preprint arXiv:2304.10428* (2023).
[39] M. S. Obeidat, M. S. A. Nahian and R. Kavuluru, Do llms surpass encoders for biomedical ner?, *arXiv preprint arXiv:2504.00664* (2025).
[40] J. Devlin, M.-W. Chang, K. Lee and K. Toutanova, Bert: Pre-training of deep bidirectional transformers for language understanding, in *Proceedings of the 2019 conference of the North American chapter of the association for computational linguistics: human language technologies, volume 1 (long and short papers)*, 2019.
[41] Y. Liu, M. Ott, N. Goyal, J. Du, M. Joshi, D. Chen, O. Levy, M. Lewis, L. Zettlemoyer and V. Stoyanov, Roberta: A robustly optimized bert pretraining approach, *arXiv preprint arXiv:1907.11692* (2019).
[42] P. He, X. Liu, J. Gao and W. Chen, Deberta: Decoding-enhanced bert with disentangled attention, *arXiv preprint arXiv:2006.03654* (2020).
[43] J. Lee, W. Yoon, S. Kim, D. Kim, S. Kim, C. H. So and J. Kang, Biobert: a pre-trained biomedical language representation model for biomedical text mining, *Bioinformatics* **36**, 1234 (2020).
[44] T. H. Dang, H.-Q. Le, T. M. Nguyen and S. T. Vu, D3ner: biomedical named entity recognition using crf-bilstm improved with fine-tuned embeddings of various linguistic information, *Bioinformatics* **34**, 3539 (2018).
[45] Y. Qiu, L. Dong, W. Zhang, H. Xing and J. Huang, A diffusion enhanced crf and bilstm framework for accurate entity recognition, *Scientific Reports* **15**, p. 19670 (2025).
[46] N. Reimers and I. Gurevych, Sentence-bert: Sentence embeddings using siamese bert-networks, *arXiv preprint arXiv:1908.10084* (2019).
[47] G. H. B. Andrade, S. Yada and E. Aramaki, Comparative evaluation of boundary-relaxed annotation for entity linking performance, in *Proceedings of the 61st Annual Meeting of the Association for Computational Linguistics (Volume 1: Long Papers)*, 2023.
[48] I. Segura-Bedmar, P. Martínez and M. Herrero-Zazo, Semeval-2013 task 9: Extraction of drug-drug interactions from biomedical texts (ddiextraction 2013), in *Second Joint Conference on Lexical and Computational Semantics (* SEM), Volume 2: Proceedings of the Seventh International Workshop on Semantic Evaluation (SemEval 2013)*, 2013.
[49] Z. P. Majdik, S. S. Graham, J. C. Shiva Edward, S. N. Rodriguez, M. S. Karnes, J. T. Jensen, J. B. Barbour and J. F. Rousseau, Sample size considerations for fine-tuning large language models for named entity recognition tasks: methodological study, *Jmir ai* **3**, p. e52095 (2024).
[50] I. Lopez, A. Swaminathan, K. Vedula, S. Narayanan, F. Nateghi Haredasht, S. P. Ma, A. S. Liang, S. Tate, M. Maddali, R. J. Gallo *et al.*, Clinical entity augmented retrieval for clinical information extraction, *npj Digital Medicine* **8**, p. 45 (2025).
[51] Y. Chen, T. A. Lask, Q. Mei, Q. Chen, S. Moon, J. Wang, K. Nguyen, T. Dawodu, T. Cohen, J. C. Denny *et al.*, An active learning-enabled annotation system for clinical named entity recognition, *BMC medical informatics and decision making* **17**, 35 (2017).

ColonCrafter: A Depth Estimation Model for Colonoscopy Videos Using Diffusion Priors

Romain Hardy[1], Tyler M. Berzin MD[2], Pranav Rajpurkar PhD[1]
1. Department of Biomedical Informatics, Harvard Medical School
2. Center for Advanced Endoscopy, Beth Israel Deaconess Medical Center

Three-dimensional (3D) scene understanding in colonoscopy presents significant challenges that necessitate automated methods for accurate depth estimation. However, existing depth estimation models for endoscopy struggle with temporal consistency across video sequences, limiting their applicability for 3D reconstruction. We present ColonCrafter, a diffusion-based depth estimation model that generates temporally consistent depth maps from monocular colonoscopy videos. Our approach learns robust geometric priors from synthetic colonoscopy sequences, enabling reliable depth estimation across frames. We also introduce a style transfer technique that preserves geometric structure while adapting realistic clinical videos to match our synthetic training domain. ColonCrafter achieves state-of-the-art zero-shot performance on the C3VD dataset, outperforming both general-purpose and endoscopy-specific approaches. Although full trajectory 3D reconstruction remains a challenge, we demonstrate clinically relevant applications of ColonCrafter, including 3D point cloud generation and surface coverage assessment. Our code will be made publicly available at `https://github.com/rajpurkarlab/ColonCrafter`.

Keywords: colonoscopy, depth estimation, 3D reconstruction, diffusion models

1. Introduction

Colorectal cancer (CRC) remains a leading cause of cancer-related mortality, with 52,900 projected deaths in 2025 in the United States alone.[1] Colonoscopy serves as the gold standard for CRC screening and is designated as a first-tier test by the American College of Gastroenterology.[2] During this procedure, gastroenterologists navigate a flexible endoscope through the colon to identify and remove precancerous polyps and other lesions. However, the clinical effectiveness of colonoscopy is constrained by fundamental limitations in human visual perception and spatial reasoning within the complex three-dimensional colonic environment.

These limitations manifest in several critical ways that directly impact patient outcomes. Incomplete examinations occur due to poor visualization behind haustral folds, leading to miss rates of up to 26% for adenomas.[3–5] Clinicians struggle to relocate previously identified lesions during the same procedure or across multiple sessions, complicating treatment planning and follow-up care.[6] Perhaps most importantly, accurate measurement of polyp size—a critical factor in determining removal strategy and surveillance intervals—remains challenging using current two-dimensional visualization methods.[7,8] These challenges underscore a

© 2025 The Authors. Open Access chapter published by World Scientific Publishing Company and distributed under the terms of the Creative Commons Attribution Non-Commercial (CC BY-NC) 4.0 License.

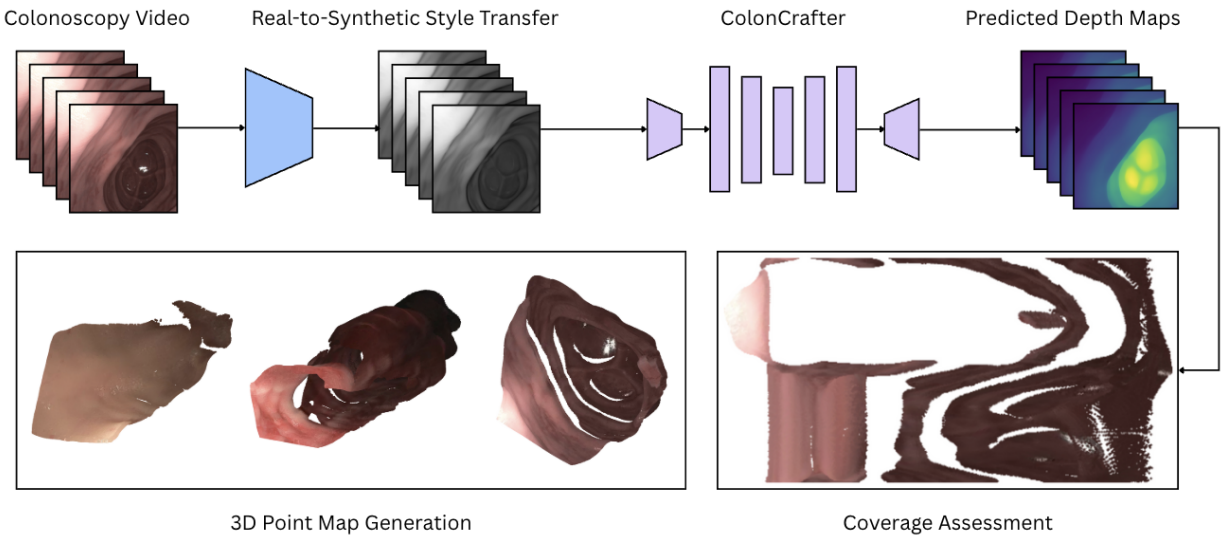

Fig. 1. Our approach incorporates two key components: (1) ColonCrafter, a diffusion-based depth estimation model trained on large-scale synthetic colonoscopy sequences, and (2) a domain adaptation technique that maps real colonoscopy frames into the synthetic training domain of ColonCrafter while preserving geometric structure. ColonCrafter outputs accurate, temporally consistent depth maps suitable for downstream 3D reconstruction and surface coverage assessment.

fundamental mismatch between the inherently three-dimensional nature of the colon and the two-dimensional visual information available to clinicians.

Bridging this gap between human expertise and the geometric complexity of colonoscopy requires computational tools that can augment clinical decision-making through precise three-dimensional scene understanding. 3D reconstruction of the colon could transform clinical practice by enabling complete surface coverage assessment,[9,10] accurate lesion localization and size measurement,[11] and robust lesion registration across multiple viewpoints and examination sessions. Such capabilities would complement rather than replace human expertise, providing clinicians with enhanced spatial awareness while preserving their critical role in clinical interpretation and decision-making.

However, achieving reliable 3D reconstruction from colonoscopy videos presents formidable technical challenges that render conventional computer vision approaches ineffective. The colonic environment systematically violates fundamental assumptions underlying traditional Simultaneous Localization and Mapping (SLAM) algorithms.[12,13] The mucosa lacks distinctive visual features necessary for robust tracking,[12,14] exhibits non-Lambertian reflectance with severe specular highlights,[6,15] and undergoes continuous deformation due to peristalsis and insufflation.[16,17] Additionally, rapidly changing illumination from the endoscope's point light source and erratic motion patterns—including rapid rotations, forward-backward movements, and frequent occlusions—further complicate reconstruction efforts.[13,18]

Recent advances in deep learning have enabled progress toward colonoscopy-specific depth estimation and SLAM systems.[16,19–21] Self-supervised approaches have shown promise by learning from unlabeled colonoscopy videos,[19,20,22] while others have leveraged synthetic data (i.e.,

computer-simulated videos with paired depth maps) to overcome the scarcity of ground-truth annotations.[23–25] Nevertheless, existing methods still struggle with long-term temporal consistency and often fail to generalize across the diverse appearance variations present in clinical data.[12,26,27] The persistent domain gap between synthetic training data and real colonoscopy imagery represents a critical barrier to clinical translation,[23,28,29] with models trained on synthetic data typically exhibiting poor performance when deployed on real clinical videos.[13,30]

To address these challenges and enable clinically meaningful AI-assisted colonoscopy, we present ColonCrafter (Figure 1), a diffusion-based depth estimation framework designed to generate temporally consistent depth maps from monocular colonoscopy videos. Our approach addresses the fundamental limitations of existing methods through three key innovations. First, we formulate monocular depth estimation (MDE) as a conditional generation task within a diffusion framework, enabling the model to learn robust priors over the complex appearance and geometry of colonic scenes. Second, we train our model on a large-scale dataset of synthetic colonoscopy sequences derived from computed tomography (CT) scans, providing rich supervision for reliable video-level reconstructions. Third, we introduce a style transfer technique that adapts real colonoscopy videos to match the appearance of our synthetic training domain while preserving the geometric structure essential for accurate depth estimation.

Our main contributions advance the integration of AI and clinical expertise in colonoscopy:

- We present the first diffusion-based depth estimation framework specifically designed for colonoscopy, capable of generating temporally consistent dense depth maps that enable robust 3D scene understanding.
- We develop a novel style transfer technique that bridges the domain gap between synthetic training data and real colonoscopy videos while preserving geometric cues essential for clinical applications.
- We demonstrate state-of-the-art zero-shot performance on the C3VD[9] benchmark, showing significant improvements in depth estimation accuracy compared to existing methods.

2. Methods

We introduce ColonCrafter, a diffusion-based depth estimation model tailored to colonoscopy. Given a monocular colonoscopy video sequence, ColonCrafter estimates temporally consistent dense depth maps, enabling 3D reconstruction of the colon surface. Our approach is based on a video diffusion model trained on a large-scale dataset of synthetic colonoscopy videos derived from CT scans. To overcome the domain gap between our synthetic training data and real-world clinical videos, we further propose a training-free style injection technique that converts any colonoscopy video to the style of our synthetic videos.

2.1. *Depth Estimation*

ColonCrafter is a conditional video diffusion model adapted from the DepthCrafter[31] architecture. Given an input RGB video $\mathbf{x} \in \mathbb{R}^{F\times H\times W\times 3}$, the primary objective of ColonCrafter is to predict a temporally consistent depth sequence $\mathbf{d} \in \mathbb{R}^{F\times H\times W}$. An overview of ColonCrafter is shown in Figure 2.

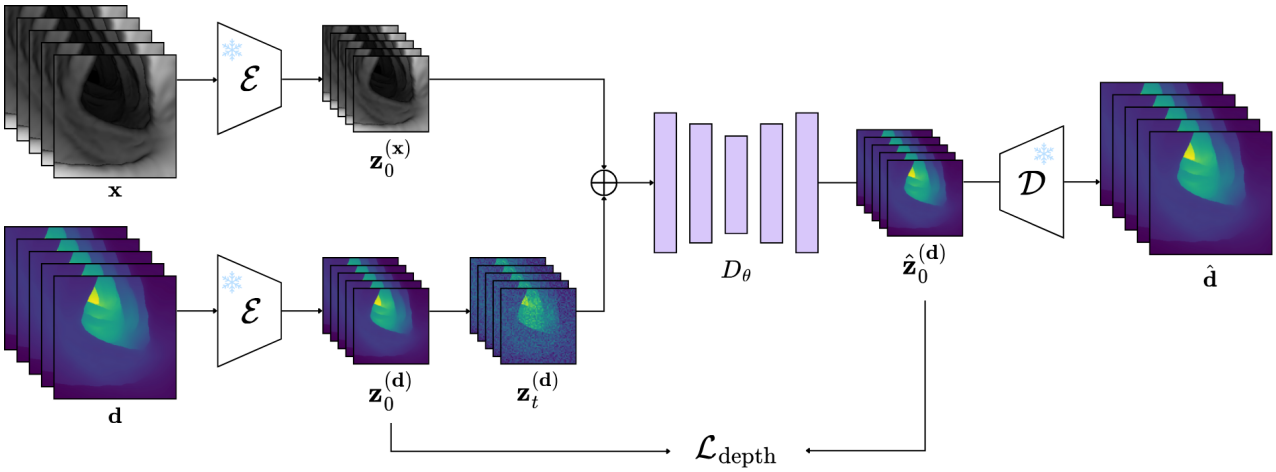

Fig. 2. Overview of the ColonCrafter architecture. The model uses a conditional diffusion framework in which paired colonoscopy videos and depth maps are projected into a latent space, and a spatio-temporal U-Net denoiser learns to recover clean depth latents from their noisy counterparts. Training is performed on synthetic colonoscopy sequences derived from CT scans to learn robust geometric priors.

As with DepthCrafter, we formulate this as a conditional generation task within the Elucidating Diffusion Models[32] framework. During training, the ground-truth depth sequence $\mathbf{d}$ is encoded to a lower-dimensional latent representation $\mathbf{z}_0^{(\mathbf{d})} = \mathcal{E}(\mathbf{d})$ using the encoder $\mathcal{E}$ of a pre-trained variational autoencoder (VAE). This latent code is then subjected to a forward diffusion process, which progressively adds noise over a continuous time variable t: $\mathbf{z}_t^{(\mathbf{d})} = \mathbf{z}_0^{(\mathbf{d})} + \sigma_t^2 \epsilon$, where $\epsilon \sim \mathcal{N}(0, I)$ is a Gaussian noise sample and σ_t^2 is the noise variance at time t. Finally, a spatio-temporal U-Net denoiser D_θ tries to predict the clean depth latent from the noisy latent: $\hat{\mathbf{z}}_0^{(\mathbf{d})} = D_\theta(\mathbf{z}_t^{(\mathbf{d})}; \sigma_t; \mathbf{z}_0^{(\mathbf{x})})$. Here, $\mathbf{z}_0^{(\mathbf{x})} = \mathcal{E}(\mathbf{x})$ is the encoded latent of the input video $\mathbf{x}$, and serves to condition the denoising process. The denoising objective is given by

$$\mathcal{L}_{\text{depth}} = \lambda_t \| D_\theta(\mathbf{z}_t^{(\mathbf{d})}; \sigma_t; \mathbf{z}_0^{(\mathbf{x})}) - \mathbf{z}_0^{(\mathbf{d})} \|_2^2 = \lambda_t \| \hat{\mathbf{z}}_0^{(\mathbf{d})} - \mathbf{z}_0^{(\mathbf{d})} \|_2^2, \tag{1}$$

where λ_t is the loss weight at time t. To obtain the predicted depth map $\hat{\mathbf{d}}$, we project $\hat{\mathbf{z}}_0^{(\mathbf{d})}$ back to pixel space using the VAE's frozen decoder $\mathcal{D}$, i.e. $\hat{\mathbf{d}} = \mathcal{D}(\hat{\mathbf{z}}_0^{(\mathbf{d})})$.

2.2. *Training Details*

2.2.1. *Synthetic Dataset Construction*

ColonCrafter is trained on 109,329 colonoscopy images that we synthetically generated from 5 CT scans[33] using standard segmentation and virtual fly-through rendering software.[34,35] An overview of our dataset construction methodology is shown in Figure 3.

2.2.2. *Model Fine-Tuning*

Rather than training ColonCrafter from scratch, we fine-tune the publicly available checkpoint of DepthCrafter using Low-Rank Adaptation (LoRA).[36] This approach allows us to reuse the high-level features learned during its pre-training phase, while simultaneously reducing the

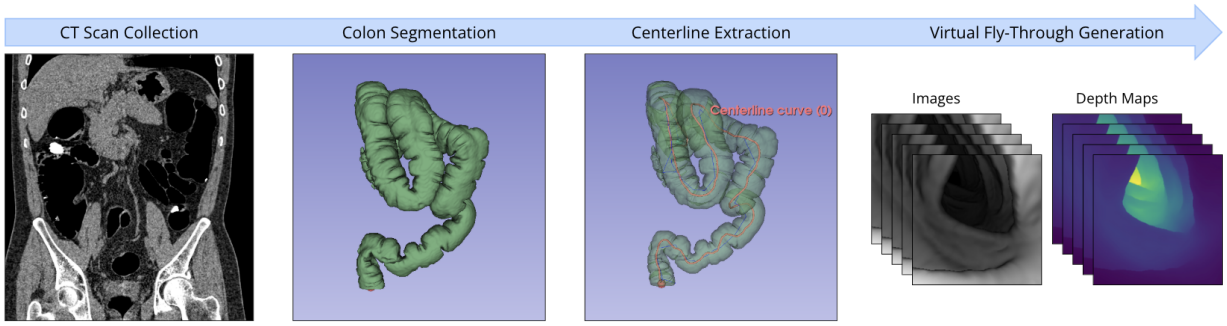

Fig. 3. Synthetic dataset construction pipeline. We segment the colonic volume from 5 CT scans, extract centerline paths, and render virtual fly-throughs to generate synthetic colonoscopy sequences with paired ground-truth depth maps.

computational cost of adapting the model to colonoscopy videos. In our implementation, we set the LoRA rank to 16 to give ColonCrafter sufficient expressive power and target the attention modules of the U-Net denoiser.

We fine-tune ColonCrafter on an NVIDIA A100 GPU for 50,000 steps using the AdamW[37] optimizer with a learning rate of 1.0×10^{-5} on a cosine schedule with warm-up. We set the batch size to 8 and the sequence length to 16 (similar to DepthCrafter), allowing ColonCrafter to effectively exploit temporal information. To improve generalization to complex colonoscopy trajectories, we introduce several data augmentation strategies. First, we randomly sample sequences so that camera translations between successive frames are not constant. Second, we randomly flip video segments to reflect the fact that colonoscopy trajectories are rarely straight paths in practice. Third, we randomly jitter the camera intrinsics to simulate variations in endoscopic equipment. Finally, we apply a random attenuation factor to vary input video brightness, creating lighting conditions representative of real colonoscopy procedures.

2.3. *Real-to-Synthetic Style Transfer*

Since ColonCrafter is trained on synthetic videos with different appearances from real colonoscopy videos, we propose a style transfer approach to bridge this gap. Previous works train dedicated neural networks using cycle consistency losses to convert between image domains.[38–40] However, such models must be trained on large corpora containing sufficiently varied synthetic and real colonoscopy examples, and are prone to destroying structural and lighting cues that are crucial for depth estimation and SLAM. To address these issues, we propose a dynamic style transfer approach that enforces content preservation when shifting from the real domain to the synthetic domain, as shown in Figure 4.

Specifically, we cast real-to-synthetic style transfer as a modulation of the denoising process within a pre-trained Stable Diffusion (SD) model, inspired by the work of Chung et al.[41] on artistic style transfer. Let $x^{(\mathbf{c})}$ be a colonoscopy video frame that we want to convert to the style of a synthetic video frame $x^{(\mathbf{s})}$. First, we project $(x^{(\mathbf{c})}, x^{(\mathbf{s})})$ to latent codes $(z_0^{(\mathbf{c})}, z_0^{(\mathbf{s})})$ using the VAE encoder of the SD model. Second, we invert the clean latents $(z_0^{(\mathbf{c})}, z_0^{(\mathbf{s})})$ to noisy latents $(z_T^{(\mathbf{c})}, z_T^{(\mathbf{s})})$ over T time steps. At each step $t \in [1, T]$, we store the intermediate queries $Q_t^{(\mathbf{c})}$ of

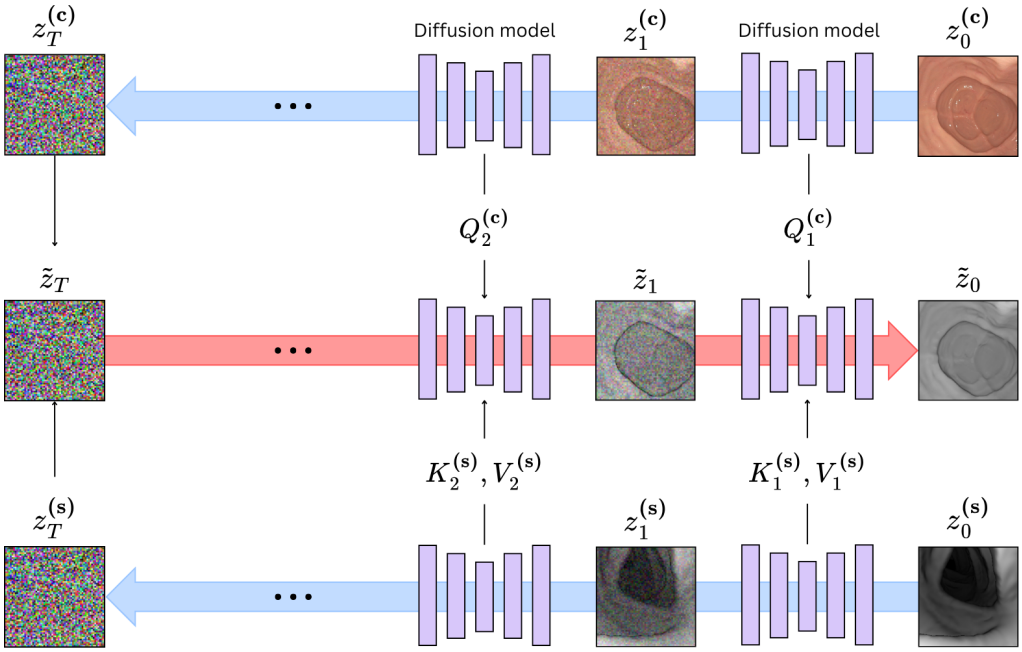

Fig. 4. Real-to-synthetic style transfer for colonoscopy videos. Given a real colonoscopy image to be converted into the style of a synthetic image, we first invert their latent representations over a sequence of time steps, storing the intermediate key, query, and value vectors at each step. Reverse diffusion with attention substitution produces an output that retains the real image's structure while adopting the synthetic style.

the content latent and the keys and values $(K_t^{(s)}, V_t^{(s)})$ of the style latent. We then carry out the reverse diffusion process with an initial latent input of $\tilde{z}_T = \text{AdaIN}(z_T^{(c)}, z_T^{(s)})$. For every step t of the reverse process and for selected self-attention layers in the frozen SD model, we substitute $(K_t^{(c)}, V_t^{(c)})$ with $(K_t^{(s)}, V_t^{(s)})$. By keeping the original content queries $Q_t^{(c)}$ fixed, we preserve the content cues of $x^{(c)}$ during denoising. After completing the reverse diffusion process, we obtain the style-transferred latent code $\tilde{z}^{(c)}$, which we decode into a full-resolution style-transferred image $\tilde{x}^{(c)}$ using the SD model's VAE decoder.

We also introduce three adjustments to facilitate specularity removal and enforce the preservation of depth cues. First, we mask pixels whose intensities exceed 3 standard deviations from the mean intensity of pixels in a 16×16 patch. During the reverse diffusion process, the SD model inpaints the masked patches to produce smooth style-transferred surfaces. Second, we apply a local histogram matching approach to align the intensities of the style-transferred videos with those of the original content videos. Third, we truncate the inversion process after $T' = \alpha T$ steps, where $\alpha = 0.4$. This approach allows us to reduce the amount of noise added during inversion, thus limiting content drift during the denoising process.

3. Experiments and Results

Datasets We evaluate ColonCrafter on 10 colonoscopy sequences from C3VD,[9] a dataset featuring realistic colon phantom models with corresponding ground-truth depth annotations. We preprocess all frames following the methodology of Huang et al.[42]

Baselines Our evaluation encompasses both general-purpose and endoscopy-specific depth estimation models. For general-purpose baselines, we include the publicly available checkpoints of DepthCrafter[31] and Depth-Anything.[43,44] For domain-specific comparisons, we evaluate against three endoscopy-tailored models: EndoDAC,[45] EndoSfM-Learner,[21] and EndoOmni.[46] To ablate our real-to-synthetic style transfer approach, we also evaluate ColonCrafter directly on the colonoscopy sequences without style transfer.

Evaluation Metrics We assess model performance using standard depth estimation metrics: absolute relative error (AbsRel), squared relative error (SqRel), root mean square error (RMSE), and the δ_1 accuracy measure. Rather than applying per-frame alignment, we compute global scale and shift parameters across each complete video sequence by solving:

$$\min_{\alpha,\beta\in\mathbb{R}} \sum_{p\in\Omega} \left[\alpha\hat{d}(p) + \beta - d(p)\right]^2, \tag{2}$$

where $\hat{d}(p)$ and $d(p)$ represent predicted and ground-truth depths at pixel p, respectively, with the summation spanning all pixels Ω in the evaluated sequence. To ensure fair comparison, we perform alignment in each model's native training domain—for example, we apply scale-shift alignment in the disparity domain for models trained on disparity data (such as DepthCrafter and ColonCrafter) before converting to the depth domain for final metric computation.

3.1. *Depth Estimation*

Table 1 presents the average zero-shot depth estimation performance of ColonCrafter on C3VD. ColonCrafter demonstrates excellent performance, outperforming both general-purpose and endoscopy-specific depth estimation models. Figure 5 shows qualitative examples of colonoscopy images from C3VD, their ground-truth depth maps, and the depth maps predicted zero-shot by ColonCrafter and other baseline methods.

Comparison with General-Purpose Models General-purpose depth estimation models show limited performance on colonoscopy sequences, reflecting the discrepancy between open-world and colonoscopy videos. This degradation stems from the unique visual characteristics of colonoscopy images: constrained lighting conditions, specular reflections, texture-poor surfaces, and limited field of view present fundamentally different challenges compared to natural outdoor scenes. Our colonoscopy-specific fine-tuning approach effectively addresses this discrepancy, improving δ_1 accuracy by more than 17% compared to the base DepthCrafter model. Notably, ColonCrafter outperforms most baseline methods even without style transfer, demonstrating that the model learns robust colonoscopy-specific geometric priors through synthetic data training alone.

Style Transfer Analysis Figure 6 qualitatively demonstrates our real-to-synthetic style transfer approach, showing original C3VD images (left), their style-transferred counterparts (middle), and the corresponding photometric intensity difference maps (right). The transformation successfully removes specular highlights and adjusts tissue appearance to match the synthetic training distribution while preserving essential anatomical structure and depth

Table 1. Zero-shot depth estimation performance on C3VD. We compare ColonCrafter with general-purpose and endoscopy-specific monocular depth estimation (MDE) models. ColonCrafter outperforms most baselines even without style transfer. Parentheses indicate 95% confidence intervals computed using 1,000-sample bootstrap resampling.

Model	$\delta_1 \uparrow$	**AbsRel** $\downarrow$	**SqRel** $\downarrow$	**RMSE (mm)** $\downarrow$
Depth-Anything-V1[43]	0.55 (0.45, 0.66)	0.28 (0.21, 0.34)	3.58 (1.83, 5.50)	10.08 (7.08, 13.24)
Depth-Anything-V2[44]	0.61 (0.52, 0.71)	0.24 (0.19, 0.28)	2.34 (1.55, 3.09)	8.20 (6.33, 9.87)
DepthCrafter[31]	0.59 (0.52, 0.65)	0.22 (0.19, 0.26)	2.65 (2.07, 3.14)	10.51 (9.09, 11.70)
EndoDAC[45]	0.50 (0.42, 0.61)	0.27 (0.22, 0.33)	4.45 (2.64, 6.63)	13.91 (10.45, 17.42)
EndoSfM-Learner[9]	0.56 (0.49, 0.64)	0.24 (0.21, 0.29)	3.49 (2.42, 4.68)	12.34 (9.81, 15.08)
EndoOmni[†46]	0.77 (0.72, 0.81)	0.15 (0.14, 0.16)	1.15 (0.88, 1.43)	6.91 (5.54, 8.20)
ColonCrafter	0.77 (0.66, 0.83)	0.16 (0.13, 0.20)	1.17 (0.81, 1.61)	6.42 (5.09, 7.62)
ColonCrafter + ST	0.79 (0.70, 0.86)	0.15 (0.12, 0.18)	1.09 (0.73, 1.45)	6.21 (5.01, 7.18)

ST: style transfer; †: Not strictly zero-shot (partially trained on C3VD).

cues. The intensity difference maps reveal that the most significant transformations occur in regions with strong specular reflections and lighting variations, while anatomically critical features such as tissue folds and surface geometry remain largely unchanged. Applying style transfer before inference aligns ColonCrafter with its synthetic training domain, leading to consistent gains across all depth evaluation metrics.

3.2. *Downstream Applications*

Point Cloud Generation ColonCrafter integrates seamlessly with established SLAM frameworks to produce consistent 3D colon reconstructions. Following the approach of Xu et al.,[47] we track feature points across successive frames using a pre-trained SpaTracker[48] model. We then estimate camera poses through bundle adjustment by minimizing the reprojection error across all tracked points and frame pairs:

$$\min_{W_1,\ldots,W_T} \sum_{i,j\in\{1,\ldots,T\}} \left[\pi_{K_j}(W_j W_i^{-1} \pi_{K_i}^{-1}(p_i, \hat{d}_i)) - p_j\right]^2. \tag{3}$$

Here, T represents the size of our tracking window, $\pi_{K_i}^{-1}$ denotes the backprojection operator that converts 2D pixel coordinates with depth $\hat{d}_i$ to 3D world coordinates using camera intrinsics K_i, and W_i represents the camera pose (transformation matrix) for frame i.

Figure 7 shows examples of 3D point clouds generated using ColonCrafter for six colon segments in C3VD. These reconstructions provide detailed structural representations of the colon anatomy, clearly delineating missed surface regions (appearing as white, empty spaces) and lesions. In the bottom right point cloud, we color points belonging to a polyp in blue, demonstrating how point clouds can be used for lesion registration. This capability has significant clinical potential for improving the accuracy of longitudinal lesion assessment by facilitating precise lesion tracking and size measurement in follow-up colonoscopies.

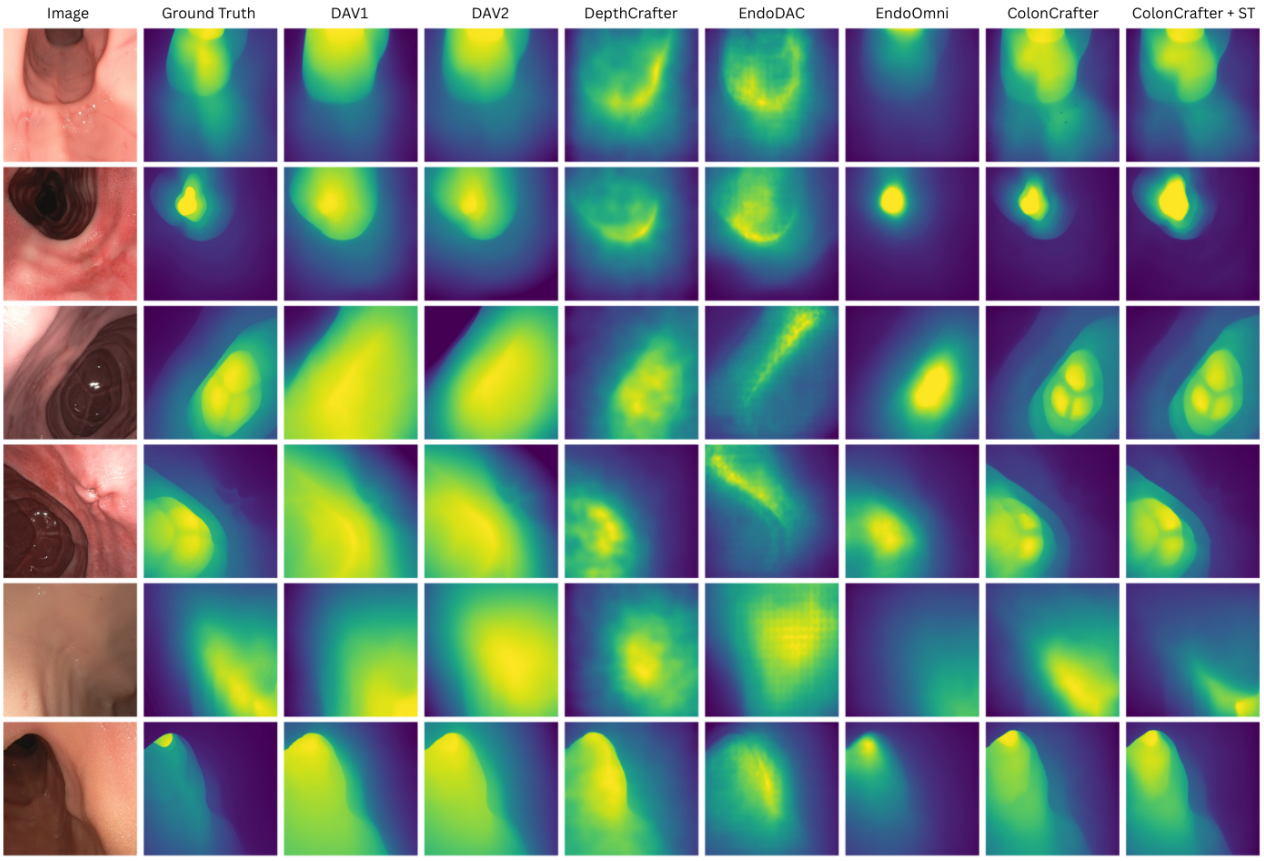

Fig. 5. Qualitative comparison of depth estimation on C3VD colonoscopy sequences. Each row shows the original colonoscopy image, the ground-truth depth map, and predictions from different methods: general-purpose models (DepthCrafter, Depth-Anything), endoscopy-specific approaches (EndoDAC, EndoOmni), and our ColonCrafter with and without style transfer (ST). ColonCrafter + ST yields the most accurate depth maps, with sharper boundaries, better preservation of fine geometric details, and improved handling of specular reflections that confuse other methods.

3.3. *Missing Surface Estimation*

Using the 3D reconstructions generated by ColonCrafter, we can assess unseen areas of the colon in an image sequence. For a given point cloud, we estimate its centerline using Principal Component Analysis, then "unroll" it into a 2D coverage map where the horizontal axis represents the distance along the centerline and the vertical axis represents the circumferential angle around it. Figure 8 shows coverage maps computed using ground-truth depths (left) and ColonCrafter predictions (right), demonstrating the model's ability to accurately identify missed surfaces.

4. Related Work

4.1. *Monocular Depth Estimation*

Monocular depth estimation (MDE) addresses the inherently ill-posed task of predicting dense depth maps from a single RGB image, where one image may correspond to infinitely many

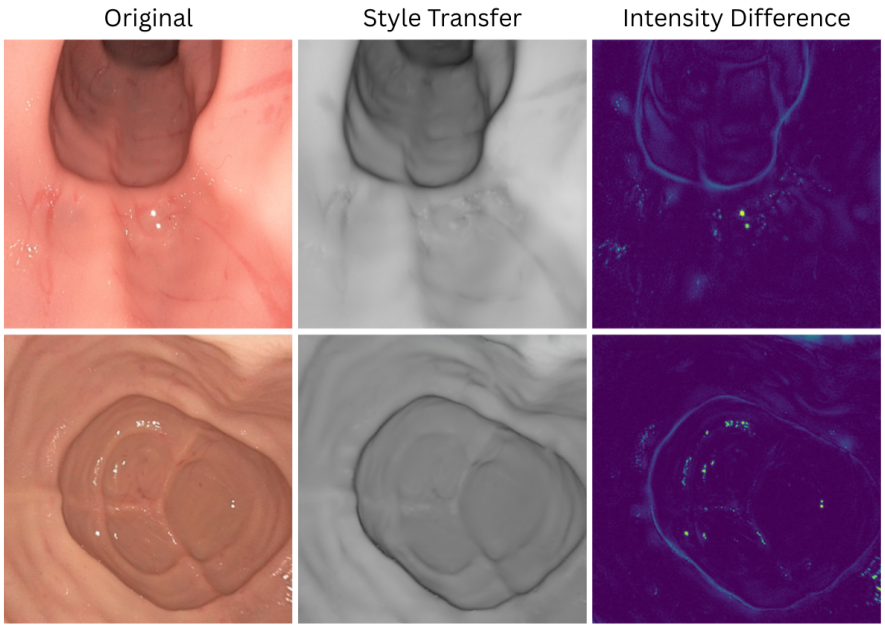

Fig. 6. Demonstration of real-to-synthetic style transfer on C3VD images. Each triplet shows: (left) the original image, (middle) the style-transferred version that mimics synthetic examples while preserving anatomical structure, and (right) the intensity difference map highlighting regions of greatest change. The transfer effectively removes specularities and adapts texture to match the synthetic domain, supporting improved depth estimation.

plausible 3D scenes. Classical geometric methods typically yield sparse reconstructions and are highly sensitive to illumination, motivating the development of learning-based approaches. Recent advances include open-world foundation models such as Depth-Anything[43,44] and DepthCrafter.[31] The latter exploits diffusion priors learned from large-scale video data, reducing the temporal inconsistencies common in single-frame models. In contrast, endoscopy-specific approaches such as EndoDAC[45] and EndoOmni[46] often rely on self-supervised or semi-supervised objectives to overcome the limited availability of ground-truth depth annotations. However, because they are primarily trained at the image level, these models still struggle to maintain temporal coherence across video sequences.

4.2. *Image Style Transfer*

An important challenge in endoscopic depth estimation is the mismatch between synthetic training data and real clinical images, which has motivated the use of style transfer for domain adaptation.[23,29,30,39,49] Most prior approaches adopt a synthetic-to-real strategy, training depth estimators directly on translated images to reduce distribution mismatch. In contrast, dynamic adaptation at inference time remains underexplored. Recent diffusion-based style transfer techniques offer a training-free alternative that preserves structural content while adjusting appearance for domain alignment.[41,50,51] For example, Chung et al.[41] manipulate self-attention layers of pre-trained diffusion models by substituting key-value pairs while preserving queries, thereby maintaining the original content during stylization. This property is

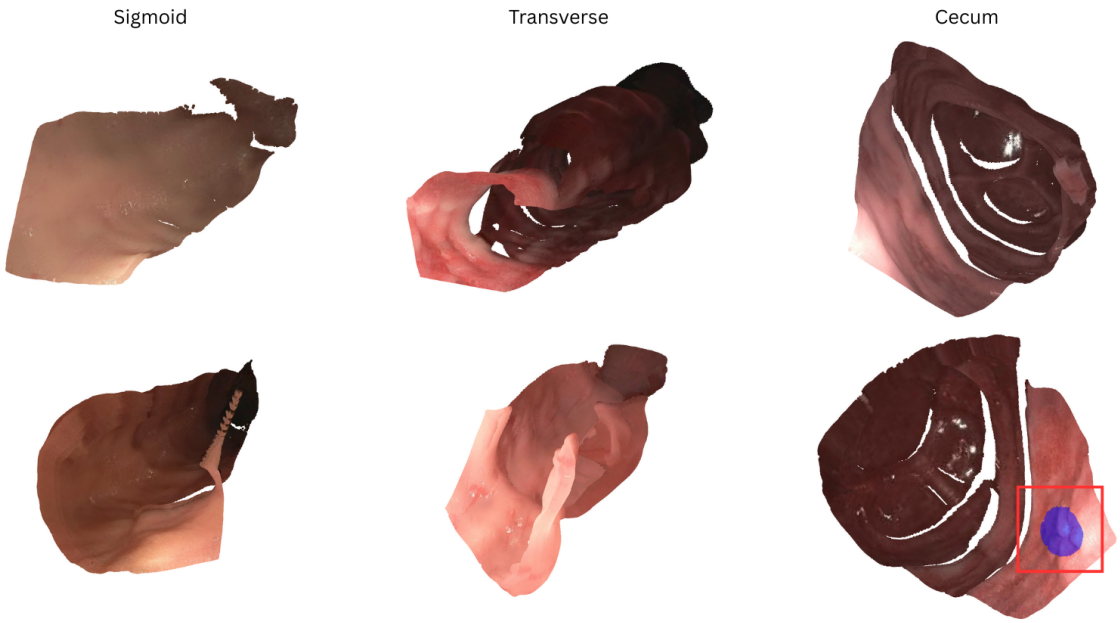

Fig. 7. 3D point cloud reconstructions of colon segments from C3VD using ColonCrafter depth predictions. Each point cloud represents the internal colon structure viewed from different perspectives, with white regions indicating areas not visible according to the reconstruction. Colored annotations highlight anatomical features and potential lesions on the point cloud.

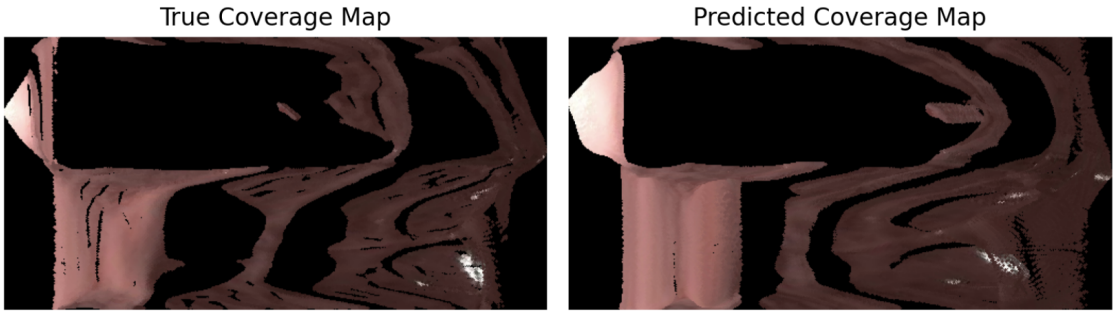

Fig. 8. Colon surface coverage analysis. Coverage maps show the surveyed areas of the colon surface "unrolled" into 2D representations, where the horizontal axis represents distance along the estimated centerline and the vertical axis represents circumferential angle. Black regions indicate areas unseen during the sequence, while colored regions represent seen surfaces. Comparison between ground-truth depth-based coverage (left) and ColonCrafter prediction-based coverage (right) demonstrates the model's relative accuracy in identifying unseen areas.

especially valuable in endoscopy, where retaining geometric cues is essential for accurate 3D reconstruction. Despite their promise, however, diffusion-based style transfer methods remain largely untested in endoscopic applications.

5. Discussion

Clinical Significance Our work addresses a fundamental challenge in colonoscopy: reconciling the three-dimensional structure of the colon with the two-dimensional visual information available to clinicians. ColonCrafter's ability to generate temporally consistent depth maps represents an important step toward augmenting clinical decision-making with computational tools. The observed improvements in depth estimation accuracy translate into practical benefits for lesion localization, size measurement, and coverage assessment during routine colonoscopic examinations.

Technical Contributions By adapting video diffusion models to the colonoscopy domain, we advance generative methods for medical depth estimation and achieve temporally consistent predictions that outperform both general-purpose and endoscopy-specific baselines. In parallel, our style transfer strategy offers a novel means of bridging domain gaps in medical imaging without the need for additional training data.

Limitations and Future Work Several limitations highlight directions for future development. First, while evaluation on C3VD phantom data provides initial validation, true clinical value requires testing on real patient procedures that include a wider range of anatomies and disease states. Second, ColonCrafter is not yet suited for full-length colonoscopy workflows, as it currently performs best on shorter video segments (with a runtime of 116 ms per frame on an A100 GPU at a resolution of 512×512), highlighting the need for further improvements in efficiency and robustness across different endoscopy systems. Finally, we plan to extend ColonCrafter into a semi-supervised framework that learns jointly from real and synthetic videos, reducing dependence on synthetic data and improving generalization to diverse clinical settings.

6. Conclusion

We introduced ColonCrafter, a novel diffusion-based depth estimation model for colonoscopy videos, achieving state-of-the-art zero-shot performance on a phantom dataset. By combining video diffusion modeling with a style transfer strategy, our method addresses the challenge of temporal consistency and bridges the domain gap between synthetic training data and real colonoscopy images. ColonCrafter outperforms both general-purpose and endoscopy-specific baselines, particularly in handling difficult visual conditions such as specular highlights and complex tissue geometry. Although the current framework is optimized for short video segments with smooth camera motion, it provides a strong foundation for future advances in computational colonoscopy. More broadly, it shows that synthetic data, when paired with domain adaptation, can support practical clinical applications including 3D reconstruction, lesion localization, and surface coverage analysis.

References

1. R. L. Siegel, T. B. Kratzer, A. N. Giaquinto, H. Sung and A. Jemal, Cancer statistics, 2025, *Ca* **75**, p. 10 (2025).
2. D. K. Rex, C. R. Boland, J. A. Dominitz, F. M. Giardiello, D. A. Johnson, T. Kaltenbach, T. R. Levin, D. Lieberman and D. J. Robertson, Colorectal cancer screening: recommendations for physicians and patients from the us multi-society task force on colorectal cancer, *Gastroenterology* **153**, 307 (2017).
3. S. Zhao, S. Wang, P. Pan, T. Xia, X. Chang, X. Yang, L. Guo, Q. Meng, F. Yang, W. Qian *et al.*, Magnitude, risk factors, and factors associated with adenoma miss rate of tandem colonoscopy: a systematic review and meta-analysis, *Gastroenterology* **156**, 1661 (2019).
4. A. C. Thompson, R. H. Jones, P. D. Poullos, S. Banerjee and L. K. Shin, Taller haustral folds in the proximal colon: A potential factor contributing to interval colorectal cancer, *Journal of Colon and Rectal Cancer* **1**, 45 (2016).
5. S. Mathew, S. Nadeem and A. Kaufman, Foldit: Haustral folds detection and segmentation in colonoscopy videos, in *International Conference on Medical Image Computing and Computer-Assisted Intervention*, 2021.
6. B. M. Shandro, K. Emrith, G. Slabaugh, A. Poullis and M. L. Smith, Optical imaging technology in colonoscopy: Is there a role for photometric stereo?, *World Journal of Gastrointestinal Endoscopy* **12**, p. 138 (2020).
7. S. A. O'Connor, D. G. Hewett, M. O. Watson, B. J. Kendall, L. F. Hourigan and G. Holtmann, Accuracy of polyp localization at colonoscopy, *Endoscopy international open* **4**, E642 (2016).
8. M. Izzy, M. A. Virk, A. Saund, J. Tejada, F. Kargoli and S. Anand, Accuracy of endoscopists' estimate of polyp size: A continuous dilemma, *World journal of gastrointestinal endoscopy* **7**, p. 824 (2015).
9. T. L. Bobrow, M. Golhar, R. Vijayan, V. S. Akshintala, J. R. Garcia and N. J. Durr, Colonoscopy 3d video dataset with paired depth from 2d-3d registration, *Medical image analysis* **90**, p. 102956 (2023).
10. R. Ma, R. Wang, S. Pizer, J. Rosenman, S. K. McGill and J.-M. Frahm, Real-time 3d reconstruction of colonoscopic surfaces for determining missing regions, in *International Conference on Medical Image Computing and Computer-Assisted Intervention*, 2019.
11. D. Soriero, P. Batistotti, R. Malinaric, D. Pertile, A. Massobrio, L. Epis, B. Sperotto, V. Penza, L. S. Mattos, M. Sartini *et al.*, Efficacy of high-resolution preoperative 3d reconstructions for lesion localization in oncological colorectal surgery—first pilot study, in *Healthcare*, (5)2022.
12. R. Ma, R. Wang, Y. Zhang, S. Pizer, S. K. McGill, J. Rosenman and J.-M. Frahm, Rnnslam: Reconstructing the 3d colon to visualize missing regions during a colonoscopy, *Medical image analysis* **72**, p. 102100 (2021).
13. M. V. Golhar, L. S. G. Fretes, L. Ayers, V. S. Akshintala, T. L. Bobrow and N. J. Durr, C3vdv2–colonoscopy 3d video dataset with enhanced realism, *arXiv preprint arXiv:2506.24074* (2025).
14. A. Schmidt, O. Mohareri, S. DiMaio, M. C. Yip and S. E. Salcudean, Tracking and mapping in medical computer vision: A review, *Medical Image Analysis* **94**, p. 103131 (2024).
15. S. Pyykölä, N. Joswig and L. Ruotsalainen, Non-lambertian surfaces and their challenges for visual slam, *IEEE Open Journal of the Computer Society* **5**, 430 (2024).
16. A. Mathew, L. Magerand, E. Trucco and L. Manfredi, Self-supervised monocular depth estimation for high field of view colonoscopy cameras, *Frontiers in Robotics and AI* **10**, p. 1212525 (2023).
17. J. Liu, K. R. Subramanian and T. S. Yoo, A robust method to track colonoscopy videos with non-informative images, *International journal of computer assisted radiology and surgery* **8**, 575 (2013).

18. H. Yao, R. W. Stidham, Z. Gao, J. Gryak and K. Najarian, Motion-based camera localization system in colonoscopy videos, *Medical image analysis* **73**, p. 102180 (2021).
19. K. Cheng, Y. Ma, B. Sun, Y. Li and X. Chen, Depth estimation for colonoscopy images with self-supervised learning from videos, in *Medical Image Computing and Computer Assisted Intervention–MICCAI 2021: 24th International Conference, Strasbourg, France, September 27–October 1, 2021, Proceedings, Part VI 24*, 2021.
20. S.-J. Hwang, S.-J. Park, G.-M. Kim and J.-H. Baek, Unsupervised monocular depth estimation for colonoscope system using feedback network, *Sensors* **21**, p. 2691 (2021).
21. K. B. Ozyoruk, G. I. Gokceler, T. L. Bobrow, G. Coskun, K. Incetan, Y. Almalioglu, F. Mahmood, E. Curto, L. Perdigoto, M. Oliveira *et al.*, Endoslam dataset and an unsupervised monocular visual odometry and depth estimation approach for endoscopic videos, *Medical image analysis* **71**, p. 102058 (2021).
22. A. Lou and J. Noble, Ws-sfmlearner: self-supervised monocular depth and ego-motion estimation on surgical videos with unknown camera parameters, in *Medical Imaging 2024: Image-Guided Procedures, Robotic Interventions, and Modeling*, 2024.
23. A. Rau, P. E. Edwards, O. F. Ahmad, P. Riordan, M. Janatka, L. B. Lovat and D. Stoyanov, Implicit domain adaptation with conditional generative adversarial networks for depth prediction in endoscopy, *International journal of computer assisted radiology and surgery* **14**, 1167 (2019).
24. F. Mahmood and N. J. Durr, Deep learning and conditional random fields-based depth estimation and topographical reconstruction from conventional endoscopy, *Medical Image Analysis* **48**, 230 (2018), Early work leveraging synthetic training data to compensate for scarcity of RGB-Depth pairs in endoscopy.
25. H. Itoh, H. R. Roth, L. Lu, M. Oda, M. Misawa, Y. Mori, S.-e. Kudo and K. Mori, Towards automated colonoscopy diagnosis: binary polyp size estimation via unsupervised depth learning, in *International conference on medical image computing and computer-assisted intervention*, 2018.
26. T. Teufel, H. Shu, R. D. Soberanis-Mukul, J. E. Mangulabnan, M. Sahu, S. S. Vedula, M. Ishii, G. Hager, R. H. Taylor and M. Unberath, Oneslam to map them all: a generalized approach to slam for monocular endoscopic imaging based on tracking any point, *International Journal of Computer Assisted Radiology and Surgery* **19**, 1259 (2024).
27. J. Xu, Q. Zhang, Y. Yu, R. Zhao, X. Bian, X. Liu, J. Wang, Z. Ge and D. Qian, Deep reconstruction-recoding network for unsupervised domain adaptation and multi-center generalization in colonoscopy polyp detection, *Computer methods and programs in biomedicine* **214**, p. 106576 (2022).
28. D. He, Z. Liu, X. Yin, H. Liu, W. Gao and Y. Fu, Synthesized colonoscopy dataset from high-fidelity virtual colon with abnormal simulation, *Computers in Biology and Medicine* **186**, p. 109672 (2025).
29. A. Dinkar Jagtap, M. Heinrich and M. Himstedt, Automatic generation of synthetic colonoscopy videos for domain randomization, *Current Directions in Biomedical Engineering* **8**, 121 (2022).
30. S. Wang, A. Paruchuri, Z. Zhang, S. McGill and R. Sengupta, Structure-preserving image translation for depth estimation in colonoscopy video, *arXiv preprint arXiv:2408.10153* (2024).
31. W. Hu, X. Gao, X. Li, S. Zhao, X. Cun, Y. Zhang, L. Quan and Y. Shan, Depthcrafter: Generating consistent long depth sequences for open-world videos, in *Proceedings of the Computer Vision and Pattern Recognition Conference*, 2025.
32. T. Karras, M. Aittala, T. Aila and S. Laine, Elucidating the design space of diffusion-based generative models, *Advances in neural information processing systems* **35**, 26565 (2022).
33. K. Smith, K. Clark, W. Bennett, T. Nolan, J. Kirby, M. Wolfsberger, J. Moulton, B. Vendt and J. Freymann, Data from ct colonography. the cancer imaging archive (2015).
34. A. Fedorov, R. Beichel, J. Kalpathy-Cramer, J. Finet, J.-C. Fillion-Robin, S. Pujol, C. Bauer,

D. Jennings, F. Fennessy, M. Sonka *et al.*, 3d slicer as an image computing platform for the quantitative imaging network, *Magnetic resonance imaging* **30**, 1323 (2012).
35. N. Ravi, J. Reizenstein, D. Novotny, T. Gordon, W.-Y. Lo, J. Johnson and G. Gkioxari, Accelerating 3d deep learning with pytorch3d, *arXiv:2007.08501* (2020).
36. E. J. Hu, Y. Shen, P. Wallis, Z. Allen-Zhu, Y. Li, S. Wang, L. Wang, W. Chen *et al.*, Lora: Low-rank adaptation of large language models., *ICLR* **1**, p. 3 (2022).
37. I. Loshchilov and F. Hutter, Decoupled weight decay regularization, *arXiv preprint arXiv:1711.05101* (2017).
38. F. Mahmood, R. Chen and N. J. Durr, Unsupervised reverse domain adaptation for synthetic medical images via adversarial training, *IEEE transactions on medical imaging* **37**, 2572 (2018).
39. S. Mathew, S. Nadeem, S. Kumari and A. Kaufman, Augmenting colonoscopy using extended and directional cyclegan for lossy image translation, in *Proceedings of the IEEE/CVF Conference on Computer Vision and Pattern Recognition*, 2020.
40. R. J. Chen, T. L. Bobrow, T. Athey, F. Mahmood and N. J. Durr, Slam endoscopy enhanced by adversarial depth prediction, *arXiv preprint arXiv:1907.00283* (2019).
41. J. Chung, S. Hyun and J.-P. Heo, Style injection in diffusion: A training-free approach for adapting large-scale diffusion models for style transfer, in *Proceedings of the IEEE/CVF conference on computer vision and pattern recognition*, 2024.
42. Y. Huang, B. Cui, L. Bai, Z. Chen, J. Wu, Z. Li, H. Liu and H. Ren, Advancing dense endoscopic reconstruction with gaussian splatting-driven surface normal-aware tracking and mapping, *arXiv preprint arXiv:2501.19319* (2025).
43. L. Yang, B. Kang, Z. Huang, X. Xu, J. Feng and H. Zhao, Depth anything: Unleashing the power of large-scale unlabeled data, in *Proceedings of the IEEE/CVF Conference on Computer Vision and Pattern Recognition*, 2024.
44. L. Yang, B. Kang, Z. Huang, Z. Zhao, X. Xu, J. Feng and H. Zhao, Depth anything v2, *Advances in Neural Information Processing Systems* **37**, 21875 (2024).
45. B. Cui, M. Islam, L. Bai, A. Wang and H. Ren, Endodac: Efficient adapting foundation model for self-supervised depth estimation from any endoscopic camera, in *International Conference on Medical Image Computing and Computer-Assisted Intervention*, 2024.
46. Q. Tian, Z. Chen, H. Liao, X. Huang, L. Li, S. Ourselin and H. Liu, Endoomni: Zero-shot cross-dataset depth estimation in endoscopy by robust self-learning from noisy labels, *arXiv preprint arXiv:2409.05442* (2024).
47. T.-X. Xu, X. Gao, W. Hu, X. Li, S.-H. Zhang and Y. Shan, Geometrycrafter: Consistent geometry estimation for open-world videos with diffusion priors, *arXiv preprint arXiv:2504.01016* (2025).
48. Y. Xiao, Q. Wang, S. Zhang, N. Xue, S. Peng, Y. Shen and X. Zhou, Spatialtracker: Tracking any 2d pixels in 3d space, in *Proceedings of the IEEE/CVF Conference on Computer Vision and Pattern Recognition*, 2024.
49. X. Xiong, A. D. Beltran, J. M. Choi, M. Niethammer and R. Sengupta, Pps-ctrl: Controllable sim-to-real translation for colonoscopy depth estimation, *arXiv preprint arXiv:2504.17067* (2025).
50. Y. Zhang, N. Huang, F. Tang, H. Huang, C. Ma, W. Dong and C. Xu, Inversion-based style transfer with diffusion models, in *Proceedings of the IEEE/CVF conference on computer vision and pattern recognition*, 2023.
51. Z. Wang, L. Zhao and W. Xing, Stylediffusion: Controllable disentangled style transfer via diffusion models, in *Proceedings of the IEEE/CVF International Conference on Computer Vision*, 2023.

A Clinician-Guided Framework for Endoscopic AI: Developing PanEndoAtlas and Benchmarking Foundation Models Across the Full GI Spectrum

Shreya Johri[1], Luyang Luo PhD[1], Hong-Yu Zhou PhD[1], Todd Brenner MD[2], Sami Elamin MD[2], Mark Enrik Geissler MD[2], Tyler M. Berzin MD[2]*, Pranav Rajpurkar PhD[1]*

1. Department of Biomedical Informatics, Harvard Medical School
2. Center for Advanced Endoscopy, Beth Israel Deaconess Medical Center and Harvard Medical School

Endoscopic procedures play a central role in the diagnosis and management of gastrointestinal (GI) diseases, yet the field lacks large-scale, clinically diverse benchmarks and unified datasets to evaluate vision foundation models. We introduce PanEndoSuite, the first unified ecosystem for endoscopic AI, developed through systematic collaboration between AI researchers and practicing gastroenterologists. PanEndoSuite consists of three complementary components: PanEndoAtlas, PanEndoX, and PanEndoFM. PanEndoAtlas is a harmonized dataset of over 420,000 labeled images from 30 public endoscopy datasets across 13 countries and 26 hospitals, creating a clinically-grounded hierarchical taxonomy that mirrors diagnostic reasoning patterns across 111 GI diseases. PanEndoX is a benchmark of 10 clinically grounded tasks, including hierarchical GI-tree classification, Barrett's esophagus grading, ulcerative colitis scoring, polyp subtyping, Boston Bowel Preparation Scale assessment, multi-organ disease classification, and anatomical landmark identification—designed to probe generalization across anatomical regions, disease presentations, and annotation granularities. PanEndoFM is a foundation model pretrained on a 10 million–image corpus curated from public data sources, spanning the entire GI tract. We benchmark PanEndoFM against two endoscopy-specific foundation models (EndoFM-LV, EndoSSL) and two general-purpose vision models (ViT-B/16, ResNet-50). PanEndoFM achieves the highest macro-AUC on 6 of 10 tasks, demonstrating broad clinical generalization; EndoFM-LV performs best on colon-focused tasks, EndoSSL excels in polyp subtyping, and ViT-B/16 shows strengths on small-intestine conditions. Together, PanEndoSuite establishes a foundation for building robust, generalist AI systems in gastrointestinal endoscopy that bridge current AI capabilities and clinical practice.

Keywords: Endoscopic Diagnosis; Vision Foundation Models; Datasets and Benchmark; PanEndoSuite; PanEndoAtlas; PanEndoFM

1. Introduction

Clinical integration of foundation models requires rigorous evaluation for real-world clinical use cases. Large and diverse datasets, along with robust benchmarks featuring clinically meaningful tasks, are essential to ensure this alignment. In domains like pathology and radiology, large-scale vision foundation models have demonstrated strong generalization with minimal

*Corresponding authors: pranav_rajpurkar@hms.harvard.edu, tberzin@bidmc.harvard.edu

© 2025 The Authors. Open Access chapter published by World Scientific Publishing Company and distributed under the terms of the Creative Commons Attribution Non-Commercial (CC BY-NC) 4.0 License.

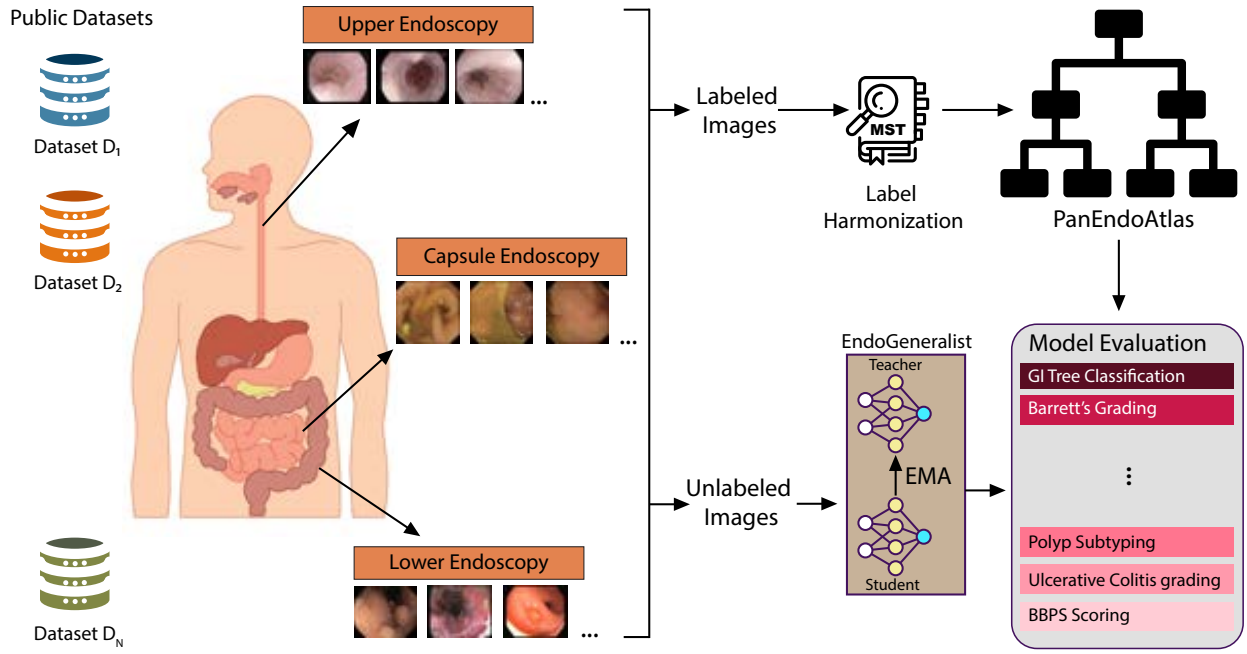

Fig. 1: PanEndoAtlas and PanEndoX Overview. PanEndoAtlas curates more than 420,000 labeled images spanning 111 GI abnormalities, from 13 countries and over 26 hospitals. PanEndoX is a benchmark suite of 10 clinically important GI tasks.

fine-tuning.[1–3] This progress has been accelerated by curated datasets and benchmarks designed to evaluate generalizability, robustness, and foundational capability.[4,5]

In contrast, gastroenterology lacks unified benchmarks despite the central role of endoscopy in diagnosing gastrointestinal (GI) diseases, including early cancer detection.[6,7] Diagnostic accuracy is often hampered by subtle disease presentations and clinician fatigue during high-throughput procedures.[8,9] Although several open-source and commercial vision models have been proposed for endoscopy,[10–14] their general-purpose utility remains unproven. Existing public datasets are fragmented, narrowly focused on common conditions such as colon polyps, and lack standardized annotations,[15–17] limiting clinical relevance and model generalization.

To address these limitations, we introduce PanEndoSuite, the first unified ecosystem for endoscopic AI, developed in collaboration between AI researchers and gastroenterologists. PanEndoSuite consists of three complementary components: PanEndoAtlas, PanEndoX and PanEndoFM. PanEndoAtlas is a harmonized dataset of more than 420,000 labeled images across 111 GI abnormalities, curated from 30 public datasets spanning 13 countries and 26 hospitals, with standardized hierarchical labels based on the MST-3.0 framework.[18] PanEndoX is a benchmark of 10 clinically grounded tasks including clinical disease classification, severity grading, and anatomical localization, to evaluate the foundational capabilities of endoscopic vision models. PanEndoFM is a vision foundation model pretrained via DINOv2[19] methodology on 10 million endoscopic images.

We benchmark PanEndoFM against two endoscopy-specific foundation models (EndoFM-LV, EndoSSL) and two general-purpose vision models (ViT-B/16, ResNet). PanEndoFM

achieves the highest AUC on 6 out of 10 benchmark tasks, demonstrating strong generalization across clinical scenarios. Additionally, we observe domain-specific strengths in other models, highlighting the influence of pretraining data on downstream performance. Together, these contributions establish PanEndoSuite as a foundation for building robust, generalist AI systems in gastrointestinal endoscopy that bridge current AI capabilities and clinical practice.

2. Related Work

Endoscopy Datasets: Public endoscopy datasets are fragmented and institution-specific, limiting their generalizability. Early datasets consisted of only a few hundred labeled images,[20,21] and while more recent efforts have scaled to several thousand examples,[22] they remain isolated contributions. Since 2012, over 25 public datasets have been released from more than 13 countries,[23] yet these are typically built independently, using different imaging protocols and patient populations, which hinders efforts to create unified training or evaluation sets.

Labeling across datasets is also highly inconsistent. While some groups maintain internal consistency within their own releases,[24,25] the broader landscape lacks a standardized annotation vocabulary. As a result, conceptually similar findings are labeled differently across datasets, or the same label is used for different anatomical contexts. For example, the label "polyp" may refer to lesions found in the colon, stomach, small intestine, or esophagus, creating semantic ambiguity. These inconsistencies make it difficult to merge datasets or perform cross-dataset evaluation without extensive re-labeling and clinical review.

Finally, current datasets are clinically narrow, with a strong bias toward colorectal polyps. Despite endoscopy being routinely used to diagnose and monitor over 100 distinct gastrointestinal conditions, most public datasets focus almost exclusively on polyp detection or segmentation.[15,16,26] A few recent datasets attempt to broaden disease coverage,[22] but they tend to be highly imbalanced, with a long tail of underrepresented conditions that models struggle to learn from. This limits the clinical relevance and diagnostic scope of models trained on existing resources.

To overcome these limitations, we introduce a large-scale benchmark dataset that is standardized, clinically diverse, and built using a hierarchical labeling system aligned with real-world endoscopic practice.

Endoscopy Foundation Models: A growing number of endoscopy foundation models have been developed using diverse pretraining strategies and datasets, yet their evaluations remain narrow in clinical scope. EndoSSL[10] used a masked siamese network pretrained on 2 million colonoscopy frames enriched for polyp-containing images, and was evaluated on polyp detection and classification tasks using single-center datasets focused exclusively on colon-polyps. EndoFM[11] scaled pretraining to 33,000 colonoscopy videos (5 million frames) and adopted a video transformer to capture spatiotemporal features for lesion detection and segmentation. Its variant, EndoFM-LV,[12] further extended training to over 12 million frames for longer video sequences. Both EndoFM and EndoFM-LV have been evaluated on tasks involving colon-polyp classification, detection, and segmentation. EndoMamba[13] adopted a state-space model architecture[42] in place of transformers,[43] and trained on combined 8 million

Table 1: Datasets encompassing PanEndoAtlas.

S.No.	Year	Dataset	Country	Hospital
1.	2012	ETIS-Larib[20]	France	Lariboisière Hospital-APHP
2.	2015	CVC-ClinicDB[21]	Spain	Hospital Clinic Barcelona
3.	2016	Kvasir[24]	Norway	Bærum Hospital
4.	2017	Nerthus[27]	Norway	Bærum Hospital
5.	2019	Kvasir-SEG[28]	Norway	Bærum Hospital
6.	2020	EDD2020[29]	France, Italy, UK	Ambroise Pare Hospital of Boulogne-Billancourt, Paris, France; Centro Riferimento Oncologico IRCCS, Aviano, Italy; Istituto Oncologico Veneto, Padova, Italy; John Radcliffe Hospital, Oxford, UK
7.	2020	HyperKvasir[25]	Norway	Bærum Hospital
8.	2020	CP-CHILD[30]	China	Hunan Children's Hospital
9.	2021	KvasirCapsule[31]	Norway	Bærum Hospital
10.	2021	KvasirCapsule-SEG[32]	Norway	Bærum Hospital
11.	2021	Kvasir-Sessile[33]	Norway	Bærum Hospital
12.	2021	KUMC[34]	US	University of Kansas Medical Center
13.	2021	SUN[35]	Japan	Showa University Northern Yokohama Hospital
14.	2021	CrohnIPI[36]	France	Nantes University Hospital
15.	2022	SUN-SEG[37]	Japan	Showa University Northern Yokohama Hospital
16.	2022	ERS[22]	Poland	Gdańsk University of Technology
17.	2023	PolypGen[15]	France, Italy, Norway, UK, Egypt	Ambroise Paré Hospital, Paris; Istituto Oncologico Veneto, Padova, Italy; Centro Riferimento Oncologico, IRCCS, Italy; Oslo University Hospital, Oslo; John Radcliffe Hospital, Oxford; University of Alexandria, Alexandria
18.	2023	GastroVision[38]	Norway, Sweden	Bærum Hospital, Karolinska University Hospital
19.	2023	MedFMC-Endo[39]	China	Renji Hospital
20.	2023	AICE[40]	Japan	Kyushu University Hospital
21.	2023	POLAR[41]	Netherlands, Spain	8 hospitals

still images and 10,000 videos. Its evaluations, like other models, have focused on colon-polyp tasks. Finally, EndoDINO,[14] a commercial model, trained DINOv2 on 10 million images, selected from a larger pool of 3.5 billion video frames, and performed validation on individual datasets. However, due to the unavailability of their model weights publicly, independent validation is limited.

Evaluation protocols across these models vary widely and remain constrained to colon-polyp related tasks and single-center datasets. The lack of standardization in validation data

and task diversity makes it difficult to perform fair comparisons or assess model generalization across different clinical settings and gastrointestinal conditions.

To address these gaps, we introduce a multi-center benchmark dataset that spans a broader spectrum of GI diseases and enables consistent, comprehensive evaluation of endoscopy foundation models across diverse diagnostic tasks.

3. Dataset

3.1. *PanEndoAtlas*

We introduce PanEndoAtlas which is a multi-source benchmark dataset designed to support standardized evaluation of AI models across a wide range of gastrointestinal endoscopy tasks. It comprises over 420,000 labeled images drawn from 21 public datasets, representing 13 countries and more than 26 clinical institutions (Table 1, Figure 2). The dataset spans all major anatomical regions of the GI tract, including the esophagus, stomach, small intestine, and colon, and includes a range of visual content, such as normal anatomy, pathological findings, therapeutic interventions, and quality control annotations.

Fig. 2: World map showing geographic distribution of PanEndoAtlas' constituent datasets across 13 countries and more than 26 clinical institutions. The dataset spans all major anatomical regions of the GI tract.

To unify the diverse label spaces in the constituent datasets, all annotations were systematically mapped into a standardized vocabulary inspired by MST-3.0 taxonomy.[18] These labels were further organized into a clinically-relevant four-level hierarchy to support training and evaluation of models on rare or sparsely represented categories (Figure 3).

- **Level 1: Anatomical Region.** Each image was assigned to one of four regions, upper GI (esophagus, stomach) or lower GI (small intestine, colon), based on available meta-

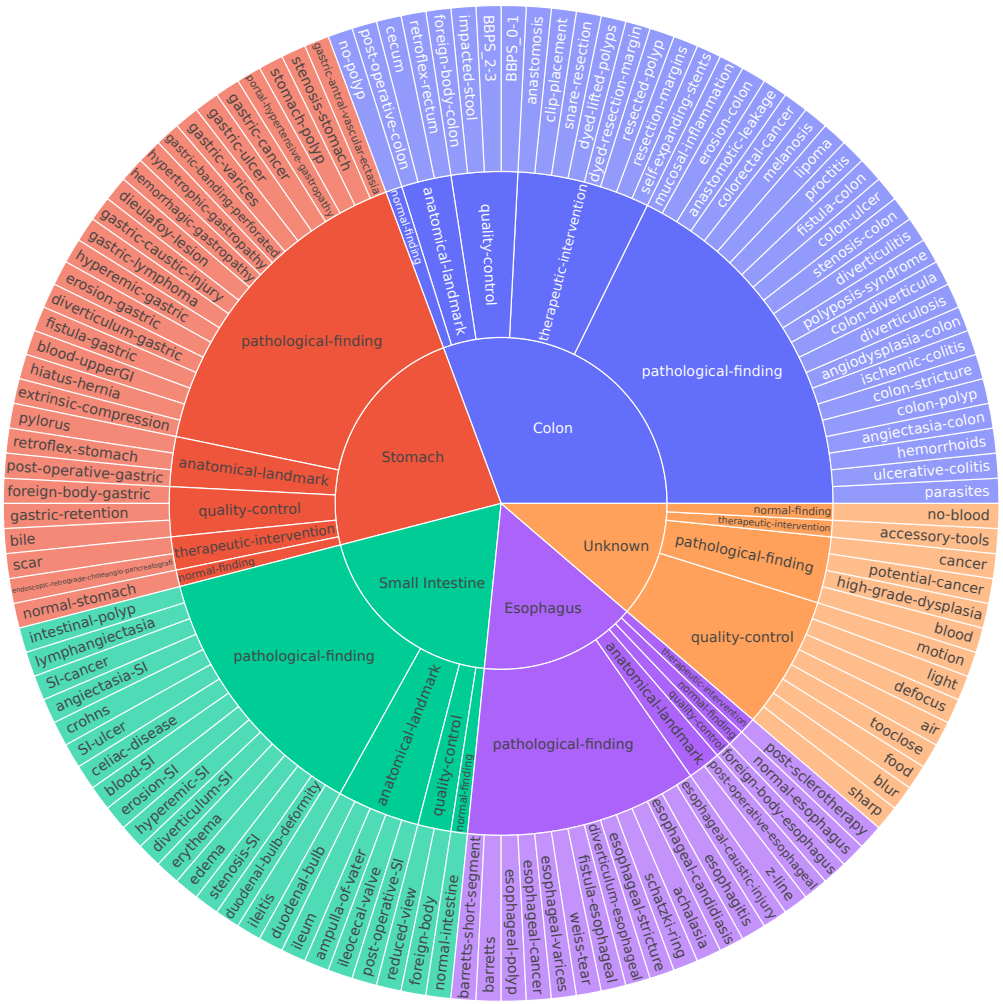

Fig. 3: PanEndoAtlas.

data, associated publications, or the type of imaging instrument used. Images with no definitive anatomical metadata were labeled as 'unknown'.

- **Level 2: Broad Clinical Category.** Images were categorized into one of five clinically relevant types: normal findings, anatomical landmarks, pathological findings, therapeutic procedures, and quality control measures.
- **Level 3: Fine-Grained Clinical Labels.** This level provides more specific diagnoses or findings within each broad category. Examples include pathological conditions such as polyps, ulcerative colitis, and Barrett's esophagus; anatomical landmarks such as the z-line, pylorus, and cecum; and procedural annotations such as polyp resection.
- **Level 4: Subtype and Severity Annotations.** Where available, additional clinical detail was included. For example, polyps were subclassified into adenomatous, hyperplastic, serrated, sessile and invasive-cancer. Ulcerative colitis cases included MAYO severity scores, and Barrett's esophagus cases were labeled according to subtype (e.g., short-segment, high-grade-dysplasia).

3.2. *Label Harmonization*

Each individual dataset in PanEndoAtlas had its own mapping dictionary, created in collaboration with a Gastroenterology Fellow. These mappings aligned original dataset labels with the standardized PanEndoAtlas schema, using three main sources: the original labels, dataset descriptions from the associated publications, and documentation from the datasets' GitHub repositories. During this process, two major types of ambiguity were resolved: location ambiguity, where anatomical location was absent from the label (e.g., 'polyp', 'ulcer'), and medical synonym ambiguity, where different terms referred to the same clinical condition or finding (e.g., 'angiodysplasia' and 'angiectasia'; 'diverticulosis', 'diverticulum', and 'diverticula'; 'edema', 'erosion', 'hyperemic', 'erythema', and 'mucosal inflammation').

Level-1 (Anatomical Region): Inferred using endoscope type and clinical label. Ambiguous cases (e.g., 'potential-cancer' in a study containing images from multiple GI regions) were labeled 'unknown'. All images have a level-1 label.

Level-2 (Broad Clinical Category): Derived from fine-grained labels or taken directly from existing annotations. All images have a valid level-2 label.

Level-3 (Fine-Grained Clinical Label): Harmonization occurred in two stages. First, labels were made anatomically specific (e.g., 'polyp' → 'colon-polyp', 'stomach-polyp' etc.). Second, clinically guided combinations were applied (e.g., BBPS-0 and BBPS-1 were combined into 'BBPS-0-1' since both indicate inadequate bowel preparation clinically). Distinctions were preserved when clinically meaningful e.g., 'colorectal-cancer' and 'colon-polyp' were merged for intramucosal cancers but kept separate for invasive lesions. All images have a level-3 label.

Level-4 (Subtype/Severity): Present in only some datasets; harmonized to standard terminology. Multiple grading systems were retained where relevant. Missing annotations were labeled 'None'. Tasks for subtype/severity were built from the subset with valid level-4 labels.

3.3. *Pretraining Dataset*

We assembled a pretraining corpus of 10 million unlabeled endoscopic images for training PanEndoFM. These images were sourced from five public datasets: ColonoscopicDS[44] , LDPolypVideo[26] , ERS[22] , RI-VCE[45] , and EndoFM-pretrain[11] . These span the full GI tract, including the esophagus, stomach, small intestine, and colon. It incorporates images captured using a variety of endoscopic instruments, such as colonoscopes, gastroscopes, and capsule endoscopes. The data reflect clinical and geographical diversity, with contributions from 5 countries, and capture variation in anatomical presentation, imaging protocols, disease states, and bowel preparation quality.

4. Methods

4.1. *PanEndoFM Pretraining*

We used a ViT-L architecture as the backbone for PanEndoFM, initialized with the official DINOv2 weights.[19] We then continued pretraining using DINOv2 methodology on the 10 million-image corpus described above. Model performance during pretraining was monitored

using Top-5 K-nearest neighbors (KNN) accuracy, computed over 100 neighbors using the Kvasir dataset,[24] which contains eight equally balanced classes. The best checkpoint was selected based on this validation metric. Training was conducted for two epochs, after which early stopping was triggered due to convergence in KNN accuracy. All other hyper-parameters were kept same as default.

4.2. *PanEndoX Benchmark*

We benchmark the performance of PanEndoFM against four additional models: 2 existing open-source endoscopy foundation models (EndoSSL, EndoFM-LV) and 2 general-purpose vision models (ViT-B/16, ResNet-50). We used linear probing, where the backbone was frozen and only a classification head was trained. This enabled a true assessment of image encoding generated by different vision encoders. A set of clinically relevant gastrointestinal (GI) tasks were used to assess the generalization ability (Table 2).

Baseline Methods: We adapted EndoFM-LV[12] and EndoSSL[10] foundation models for image-level evaluation. We further implemented the ViT-B/16 and ResNet-50 model architectures, initialized with ImageNet pretrained weights.

Dataset Splits: For each task, the data was split into training, validation, and test sets in a 75:10:15 ratio to support reproducibility. Splits were first performed at the dataset level, ensuring that all images from a given patient appeared in only one of the three sets. In cases where patient identifiers were not available, samples were randomly assigned. Within each dataset, label proportions were preserved across the splits to maintain class balance. Finally, the splits from individual datasets contributing to a given task were merged into a single unified file.

Hyper-parameter Search: All models, including baseline and comparison models, were fine-tuned using a hyperparameter search over learning rates $[1e^{-4}, 5e^{-5}, 1e^{-5}, 5e^{-6}, 1e^{-6}]$. The best model was selected based on validation AUC, and performance on independent test set is reported. Optimization was performed using AdamW (weight decay = 0.01) with a cosine learning rate scheduler ($\eta_{\min} = 1e^{-6}$, $T_{\text{mult}} = 2$). Other fine-tuning settings were held constant across experiments: batch size = 128, and early stopping after 10 epochs without improvement on the validation set.

Loss Function: We use binary cross-entropy (BCE) loss for our multi-label classification setup:

$$\mathcal{L}_{\text{BCE}}(y, \hat{y}) = -\left[y \log(\hat{y}) + (1 - y) \log(1 - \hat{y})\right], \tag{1}$$

where $y \in \{0, 1\}$ is the ground-truth label and $\hat{y} \in [0, 1]$ is the predicted probability.

To address class imbalance, the BCE loss is weighted using a log-scaled class prevalence term. The weight for class i is computed as:

$$w_i = \log\left(1 + \frac{N}{n_i}\right), \tag{2}$$

where N is the total number of samples and n_i is the number of samples belonging to class i. The resulting weighted BCE loss is:

$$\mathcal{L}(y, \hat{y}) = -w\left[y \log(\hat{y}) + (1 - y) \log(1 - \hat{y})\right], \tag{3}$$

Table 2: Task descriptions for PanEndoX Benchmark.

Task Name	**Description**
GI-Tree Classification	Hierarchical classification of GI anatomy, visual label type (e.g., normal, abnormal), and specific disease category.
Barrett's Grading	Grading of Barrett's esophagus severity: normal-barretts, barretts-short-segment, high-grade-dysplasia.
Ulcerative Colitis Grading	Inflammation severity scoring (MAYO-0, MAYO-1, MAYO-2).
Polyp Subtyping	Classification into the following subtypes: hyperplastic, adenomatous, serrated, or invasive-cancerous.
BBPS Scoring	Boston Bowel Preparation Scale scoring for colon cleanliness across three segments: BBPS-0-1 (well-prepared), BBSP-2-3 (not well-prepared), impacted-stool
Esophagus Disease Classification	Classification of esophageal diseases: esophagitis, esophageal-varices, esophageal-cancer, barretts, esophageal-candidiasis, esophageal-stricture, fistula-esophageal, esophageal-polyp, weiss-tear, diverticulum-esophageal, barretts-short-segment, achalasia, esophageal-caustic-injury.
Stomach Disease Classification	Classification of stomach diseases: portal-hypertensive-gastropathy, stomach-polyp, gastric-ulcer, erosion-gastric, gastric-varices, gastric-cancer, hyperemic-gastric, stomach-cancer, hemorrhagic-gastropathy, stenosis-stomach, gastric-lymphoma, hiatus-hernia, dieulafoy-lesion, gastric-caustic-injury
Small Intestine Disease Classification	Classification of small bowel conditions: erosion-SI, crohns, polyp-like, SI-ulcer, lymph-follicle, lymphangiectasia, angiectasia-SI, erythema, angiodysplasia-SI, blood-SI, stenosis-SI, submucosal-tumor, edema, intestinal-polyp, SI-cancer, hyperemic-SI, coeliac-disease, diverticulum-SI, duodenal-bulb-deformity
Colon Disease Classification	Classification of colonic diseases: colon-polyp, colorectal-cancer, ulcerative-colitis, colon-ulcer, angiodysplasia-colon, erosion-colon, diverticulosis, polyposis-syndrome, proctitis, lipoma, parasites, colon-stricture, fistula-colon, melanosis, hemorrhoids, ischemic-colitis, mucosal-inflammation, colon-diverticula, angiectasia-colon.
Stomach Anatomical Landmark Classification	Identification of anatomical landmarks in the stomach: non-landmark, pylorus, retroflex-stomach.

where w is the weight corresponding to the sample's class. For the GI-Tree classification task, the BCE loss was computed independently at each level of the hierarchy.

5. Results

We conducted a comprehensive evaluation of PanEndoFM, endoscopy-specific foundation models (EndoFM-LV, EndoSSL) and general-purpose vision models (ViT-B/16 and ResNet-50) on the PanEndoAtlas (Table 3). Performance was assessed using macro-AUC on the test set, which averages AUC across all classes to mitigate the effects of class imbalance and better

reflect model robustness in clinically heterogeneous settings.

We conducted a comprehensive evaluation of PanEndoFM, prior endoscopy-specific foundation models (EndoFM-LV, EndoSSL), and general-purpose vision models (ViT-B/16 and ResNet-50) on the PanEndoAtlas benchmark (Table 3). Performance was measured using macro-AUC, which averages AUC across all classes to mitigate class imbalance and provide a fairer measure of robustness in clinically heterogeneous settings. Across all 10 tasks, PanEndoFM ranked first on 6 tasks, second on 3 tasks, and third on 1 task, showing consistent superiority over both endoscopy-specific and general-purpose baselines.

PanEndoFM. PanEndoFM achieved the highest performance on the most comprehensive task, GI-Tree classification (111 classes, three-level hierarchy), with a macro-AUC of 0.648 (95% CI: 0.621–0.669), outperforming all other models. It also led performance on multiple upper GI tasks, including Barrett's grading (macro-AUC 0.775, 95% CI: 0.643–0.902) and esophageal disease classification (macro-AUC 0.772, 95% CI: 0.742–0.809). For stomach-related tasks, PanEndoFM achieved the best results in both disease classification (macro-AUC 0.539, 95% CI: 0.520–0.558) and anatomical landmark identification (macro-AUC 0.950, 95% CI: 0.943–0.956). It also topped ulcerative colitis grading with a macro-AUC of 0.571 (95% CI: 0.499–0.649). These results suggest that pretraining with broader anatomical coverage improves generalization across diverse disease types and organs.

Table 3: Macro-AUCs (95%CI) reported on test set for tasks in the PanEndoX Benchmark. Highest value is bolded, second highest is italicized.

Task Name	Classes	PanEndoFM	EndoFM-LV	EndoSSL	ViT-B/16	ResNet-50
GITree Classification	111 classes	**0.648 (0.621, 0.669)**	*0.570 (0.560, 0.578)*	0.551 (0.510, 0.599)	0.500 (0.491, 0.510)	0.515 (0.505, 0.526)
Barrett's Grading Classification	4 classes	**0.775 (0.643, 0.902)**	*0.733 (0.608, 0.850)*	0.581 (0.447, 0.719)	0.681 (0.559, 0.796)	0.707 (0.573, 0.843)
UCC Grading Classification	3 classes	**0.571 (0.499, 0.649)**	*0.565 (0.476, 0.650)*	0.507 (0.425, 0.583)	0.550 (0.470, 0.625)	0.525 (0.435, 0.614)
Polyp Subtyping Classification	4 classes	0.575 (0.562, 0.589)	0.500 (0.490, 0.511)	**0.704 (0.696, 0.712)**	0.542 (0.532, 0.552)	*0.643 (0.631, 0.655)*
BBPS Scoring Classification	3 classes	0.809 (0.773, 0.843)	**0.913 (0.885, 0.936)**	0.524 (0.479, 0.567)	*0.830 (0.800, 0.860)*	0.685 (0.648, 0.724)
Esophagus Disease Classification	13 classes	**0.772 (0.742, 0.809)**	0.590 (0.564, 0.612)	0.550 (0.519, 0.581)	*0.682 (0.645, 0.713)*	0.446 (0.418, 0.478)
Stomach Disease Classification	14 classes	**0.539 (0.520, 0.558)**	*0.539 (0.509, 0.582)*	0.521 (0.475, 0.554)	0.438 (0.410, 0.467)	0.498 (0.457, 0.536)
SI Disease Classification	20 classes	*0.594 (0.577, 0.612)*	0.481 (0.458, 0.507)	0.591 (0.573, 0.618)	**0.597 (0.577, 0.621)**	0.528 (0.509, 0.548)
Colon Disease Classification	30 classes	*0.552 (0.517, 0.586)*	**0.615 (0.583, 0.644)**	0.455 (0.430, 0.484)	0.494 (0.470, 0.519)	0.503 (0.467, 0.540)
Stomach Landmark Identification	3 classes	**0.950 (0.943, 0.956)**	0.869 (0.851, 0.886)	0.788 (0.749, 0.831)	*0.879 (0.866, 0.891)*	0.820 (0.800, 0.838)

EndoFM-LV. EndoFM-LV demonstrated strong performance on colon-focused tasks, outperforming all models on BBPS scoring (macro-AUC 0.913, 95% CI: 0.885–0.936) and colon disease classification (macro-AUC 0.615, 95% CI: 0.583–0.644). It also ranked second across five additional tasks. This advantage likely reflects its pretraining corpus, which was dominated

by colonoscopy videos, including HyperKvasir and SUN datasets. Because these datasets are also part of PanEndoAtlas, EndoFM-LV may benefit from pretraining-test overlap on colon-related tasks, inflating apparent generalization performance.

EndoSSL. EndoSSL performed best on polyp subtyping (macro-AUC 0.704, 95% CI: 0.696–0.712), consistent with its pretraining dataset being enriched for polyp-containing frames. However, it ranked outside the top two on most other tasks, particularly those involving non-colonic regions. This highlights the limitations of organ-specific pretraining strategies when models are applied to broader endoscopic practice.

General-purpose models. Interestingly, ViT-B/16 outperformed all models on small intestine disease classification (macro-AUC 0.597, 95% CI: 0.577–0.621) and achieved the second-highest performance on BBPS scoring, esophageal disease classification, and stomach landmark identification. We note that these tasks had least diversity in data sources.

Task-level difficulty. Macro-AUC values across multi-center tasks in PanEndoX were generally lower than those reported on single-center or task-specific datasets.[25] Easier tasks included anatomical landmark detection and bowel preparation scoring, where all models achieved relatively high performance. In contrast, grading-based tasks (e.g., ulcerative colitis grading, polyp subtyping) and multi-class disease classification tasks (e.g., GI-Tree) proved more difficult, with larger inter-model performance gaps. This spread highlights the value of PanEndoAtlas in exposing task difficulty and dataset diversity that are not captured by prior benchmarks.

Error analysis. Certain disease categories reflect intrinsic visual similarity rather than data scarcity and were often confused. For example, diverticulitis was frequently misclassified as diverticulosis, both involve diverticula; only inflamed ones count as diverticulitis. Similarly, ulcerative-colitis, ischemic-colitis, angiodysplastic-colitis, and infectious-colitis were often misclassified since all show inflamed, ulcerated mucosa, but with subtle cause-specific differences. Class-wise metrics for each task and model are provided in Supplementary Data.

Subgroup analysis. To assess generalization, we compared model performance on individual datasets against overall performance within each task. We observed substantial variance, with certain datasets consistently yielding higher metrics than others (Supplementary Data). The extent of this variance depended on the specific model–task combination, underscoring the strong influence of pretraining data on generalization performance. These findings demonstrate that reliance on single datasets can lead to overly optimistic performance estimates and reinforce the need for diverse, multi-center benchmarks.

Clinical interpretation. Although absolute improvements in macro-AUC may appear modest, they are clinically meaningful. Because macro-AUC weights rare and common diseases equally, even small gains can reduce missed diagnoses in less prevalent but high-risk conditions such as Barrett's esophagus or early gastric cancer. For tasks already approaching high accuracy (e.g., bowel preparation, anatomical landmark detection), incremental gains instead reflect greater robustness across institutions and devices.

6. Discussion

This work directly addresses the core limitations outlined in the introduction: the lack of large-scale, standardized, and clinically diverse benchmarks in endoscopy; the absence of clinically meaningful evaluation tasks; and the need to assess generalist versus specialist models in ways that reflect clinical reasoning.

First, PanEndoAtlas resolves the fragmentation of existing resources. Prior datasets have been narrowly focused, often on polyps, and inconsistent in their label vocabularies. By harmonizing 21 public datasets into a unified schema spanning 111 gastrointestinal abnormalities, PanEndoAtlas provides a standardized, hierarchical taxonomy that mirrors real diagnostic reasoning. This structure not only enables evaluation across rare and common conditions but also captures clinically relevant misclassifications that would be obscured in flat-label systems.

Second, PanEndoX introduces benchmarks grounded in clinical practice. The ten tasks span hierarchical classification, severity grading, disease subtyping, bowel preparation scoring, and anatomical landmark identification. Together, they probe the full spectrum of diagnostic reasoning in endoscopy—moving beyond single-center, polyp-focused tasks toward clinically meaningful evaluation. Our results demonstrate that task difficulty varies systematically, with multi-class grading and disease classification posing greater challenges than landmark detection or bowel preparation scoring. This reinforces the importance of diverse benchmarks for exposing gaps in model generalization.

Third, PanEndoFM demonstrates the value of broad, multi-organ pretraining for endoscopic AI. While prior models like EndoSSL and EndoFM-LV show strong performance on niche domains (polyp subtyping and colon disease tasks, respectively), PanEndoFM outperformed both endoscopy-specific and general-purpose models on six of ten tasks. Therefore, PanEndoSuite provides a rigorous foundation for evaluating generalization and robustness, thereby bridging AI development with real-world practice.

Limitations and future directions. We note that some prior endoscopy foundation models incorporated public datasets included in PanEndoAtlas for pretraining, even if labels were not used, partially limiting the independence of certain comparisons. Future work should establish clear dataset disjointness to enable standardized evaluation. We further note that a few of the images in the public datasets are low quality. We provide auto-generated quality annotations for each image in PanEndoAtlas.

7. Data and Code Availability

The dataset, code and supplementary data is publicly available is publicly available at: https://github.com/rajpurkarlab/panendosuite.

8. Acknowledgements

This work was supported by Harvard Medical School Dean's Innovation Fund for the Use of Artificial Intelligence.

References

1. R. J. Chen, T. Ding, M. Y. Lu, D. F. K. Williamson, G. Jaume, A. H. Song, B. Chen, A. Zhang, D. Shao, M. Shaban, M. Williams, L. Oldenburg, L. L. Weishaupt, J. J. Wang, A. Vaidya, L. P. Le, G. Gerber, S. Sahai, W. Williams and F. Mahmood, Towards a general-purpose foundation model for computational pathology, *Nature Medicine* **30**, p. 850–862 (March 2024).
2. M. Y. Lu, B. Chen, A. Zhang, D. F. K. Williamson, R. J. Chen, T. Ding, L. P. Le, Y.-S. Chuang and F. Mahmood, Visual language pretrained multiple instance zero-shot transfer for histopathology images, in *Proceedings of the IEEE/CVF Conference on Computer Vision and Pattern Recognition (CVPR)*, June 2023.
3. M. Paschali, Z. Chen, L. Blankemeier, M. Varma, A. Youssef, C. Bluethgen, C. Langlotz, S. Gatidis and A. Chaudhari, Foundation models in radiology: What, how, why, and why not, *Radiology* **314** (February 2025).
4. P. Neidlinger, O. S. M. E. Nahhas, H. S. Muti, T. Lenz, M. Hoffmeister, H. Brenner, M. van Treeck, R. Langer, B. Dislich, H. M. Behrens, C. Röcken, S. Foersch, D. Truhn, A. Marra, O. L. Saldanha and J. N. Kather, Benchmarking foundation models as feature extractors for weakly-supervised computational pathology (2024).
5. X. Zhang, H.-Y. Zhou, X. Yang, O. Banerjee, J. N. Acosta, J. Miller, O. Huang and P. Rajpurkar, Rexrank: A public leaderboard for ai-powered radiology report generation (2024).
6. D. A. Fisher, A. K. Shergill, D. S. Early, R. D. Acosta, V. Chandrasekhara, K. V. Chathadi, G. A. Decker, J. A. Evans, R. D. Fanelli, K. Q. Foley, L. Fonkalsrud, J. H. Hwang, T. Jue, M. A. Khashab, J. R. Lightdale, V. R. Muthusamy, S. F. Pasha, J. R. Saltzman, R. Sharaf and B. D. Cash, Role of endoscopy in the staging and management of colorectal cancer, *Gastrointestinal Endoscopy* **78**, p. 8–12 (July 2013).
7. L. Zhu, J. Qin, J. Wang, T. Guo, Z. Wang and J. Yang, Early gastric cancer: Current advances of endoscopic diagnosis and treatment, *Gastroenterology Research and Practice* **2016**, p. 1–7 (2016).
8. N. H. Kim, Y. S. Jung, W. S. Jeong, H.-J. Yang, S.-K. Park, K. Choi and D. I. Park, Miss rate of colorectal neoplastic polyps and risk factors for missed polyps in consecutive colonoscopies, *Intestinal Research* **15**, p. 411 (2017).
9. A. Turshudzhyan, H. Rezaizadeh and M. Tadros, Lessons learned: Preventable misses and near-misses of endoscopic procedures, *World Journal of Gastrointestinal Endoscopy* **14**, p. 302–310 (May 2022).
10. R. Hirsch, M. Caron, R. Cohen, A. Livne, R. Shapiro, T. Golany, R. Goldenberg, D. Freedman and E. Rivlin, Self-supervised learning for endoscopic video analysis (2023).
11. Z. Wang, C. Liu, S. Zhang and Q. Dou, Foundation model for endoscopy video analysis via large-scale self-supervised pre-train (2023).
12. Z. Wang, C. Liu, L. Zhu, T. Wang, S. Zhang and Q. Dou, Improving foundation model for endoscopy video analysis via representation learning on long sequences, *IEEE Journal of Biomedical and Health Informatics* , 1 (2025).
13. Q. Tian, H. Liao, X. Huang, B. Yang, D. Lei, S. Ourselin and H. Liu, Endomamba: An efficient foundation model for endoscopic videos (2025).
14. P. Dermyer, A. Kalra and M. Schwartz, Endodino: A foundation model for gi endoscopy (2025).
15. S. Ali, D. Jha, N. Ghatwary, S. Realdon, R. Cannizzaro, O. E. Salem, D. Lamarque, C. Daul, M. A. Riegler, K. V. Anonsen, A. Petlund, P. Halvorsen, J. Rittscher, T. de Lange and J. E. East, A multi-centre polyp detection and segmentation dataset for generalisability assessment, *Scientific Data* **10** (February 2023).
16. D. Jha, N. K. Tomar, V. Sharma, Q.-H. Trinh, K. Biswas, H. Pan, R. K. Jha, G. Durak, A. Hann, J. Varkey, H. V. Dao, L. Van Dao, B. P. Nguyen, N. Papachrysos, B. Rieders, P. T. Schmidt,

E. Geissler, T. Berzin, P. Halvorsen, M. A. Riegler, T. de Lange and U. Bagci, Polypdb: A curated multi-center dataset for development of ai algorithms in colonoscopy (2024).
17. M. Forootan, M. Rajabnia, A. R. Mafi, H. A. Tehrani, E. Ghadirzadeh, M. Setayeshfar, Z. Ghaffari, M. Tashakoripour, M. R. Zali and H. Bolhasani, Ercpmp: An endoscopic image and video dataset for colorectal polyps morphology and pathology (2023).
18. worldendo.org
`https://www.worldendo.org/assets-craft/pdf/resources/mst-3-0.pdf`, [Accessed 02-08-2025].
19. M. Oquab, T. Darcet, T. Moutakanni, H. Vo, M. Szafraniec, V. Khalidov, P. Fernandez, D. Haziza, F. Massa, A. El-Nouby, M. Assran, N. Ballas, W. Galuba, R. Howes, P.-Y. Huang, S.-W. Li, I. Misra, M. Rabbat, V. Sharma, G. Synnaeve, H. Xu, H. Jegou, J. Mairal, P. Labatut, A. Joulin and P. Bojanowski, Dinov2: Learning robust visual features without supervision (2023).
20. J. Silva, A. Histace, O. Romain, X. Dray and B. Granado, Toward embedded detection of polyps in wce images for early diagnosis of colorectal cancer, *International Journal of Computer Assisted Radiology and Surgery* **9**, p. 283–293 (September 2013).
21. J. Bernal, F. J. Sánchez, G. Fernández-Esparrach, D. Gil, C. Rodríguez and F. Vilariño, Wm-dova maps for accurate polyp highlighting in colonoscopy: Validation vs. saliency maps from physicians, *Computerized Medical Imaging and Graphics* **43**, p. 99–111 (July 2015).
22. J. Cychnerski, T. Dziubich and A. Brzeski, Ers: a novel comprehensive endoscopy image dataset for machine learning, compliant with the mst 3.0 specification (2022).
23. S. Zhu, J. Gao, L. Liu, M. Yin, J. Lin, C. Xu, C. Xu and J. Zhu, Public imaging datasets of gastrointestinal endoscopy for artificial intelligence: a review, *Journal of Digital Imaging* **36**, p. 2578–2601 (September 2023).
24. K. Pogorelov, K. R. Randel, C. Griwodz, S. L. Eskeland, T. de Lange, D. Johansen, C. Spampinato, D.-T. Dang-Nguyen, M. Lux, P. T. Schmidt, M. Riegler and P. Halvorsen, Kvasir: A multi-class image dataset for computer aided gastrointestinal disease detection, in *Proceedings of the 8th ACM on Multimedia Systems Conference*, MMSys'17 (ACM, June 2017).
25. H. Borgli, V. Thambawita, P. H. Smedsrud, S. Hicks, D. Jha, S. L. Eskeland, K. R. Randel, K. Pogorelov, M. Lux, D. T. D. Nguyen, D. Johansen, C. Griwodz, H. K. Stensland, E. Garcia-Ceja, P. T. Schmidt, H. L. Hammer, M. A. Riegler, P. Halvorsen and T. de Lange, Hyperkvasir, a comprehensive multi-class image and video dataset for gastrointestinal endoscopy, *Scientific Data* **7** (August 2020).
26. Y. Ma, X. Chen, K. Cheng, Y. Li and B. Sun, *LDPolypVideo Benchmark: A Large-Scale Colonoscopy Video Dataset of Diverse Polyps*, in *Lecture Notes in Computer Science*, (Springer International Publishing, 2021), p. 387–396.
27. K. Pogorelov, K. R. Randel, T. de Lange, S. L. Eskeland, C. Griwodz, D. Johansen, C. Spampinato, M. Taschwer, M. Lux, P. T. Schmidt, M. Riegler and P. Halvorsen, Nerthus: A bowel preparation quality video dataset, in *Proceedings of the 8th ACM on Multimedia Systems Conference*, MMSys'17 (ACM, June 2017).
28. D. Jha, P. H. Smedsrud, M. A. Riegler, P. Halvorsen, T. de Lange, D. Johansen and H. D. Johansen, Kvasir-seg: A segmented polyp dataset (2019).
29. S. Ali, B. Braden, D. Lamarque, S. Realdon, A. Bailey, R. Cannizzaro, N. Ghatwary, J. Rittscher, C. Daul and J. East, Endoscopy disease detection and segmentation (edd2020) (2020).
30. W. Wang, J. Tian, C. Zhang, Y. Luo, X. Wang and J. Li, An improved deep learning approach and its applications on colonic polyp images detection, *BMC Medical Imaging* **20** (July 2020).
31. P. H. Smedsrud, V. Thambawita, S. A. Hicks, H. Gjestang, O. O. Nedrejord, E. Næss, H. Borgli, D. Jha, T. J. D. Berstad, S. L. Eskeland, M. Lux, H. Espeland, A. Petlund, D. T. D. Nguyen, E. Garcia-Ceja, D. Johansen, P. T. Schmidt, E. Toth, H. L. Hammer, T. de Lange, M. A. Riegler and P. Halvorsen, Kvasir-capsule, a video capsule endoscopy dataset, *Scientific Data* **8** (May

2021).
32. D. Jha, N. K. Tomar, S. Ali, M. A. Riegler, H. D. Johansen, D. Johansen, T. de Lange and P. Halvorsen, Nanonet: Real-time polyp segmentation in video capsule endoscopy and colonoscopy (2021).
33. D. Jha, P. H. Smedsrud, D. Johansen, T. de Lange, H. D. Johansen, P. Halvorsen and M. A. Riegler, A comprehensive study on colorectal polyp segmentation with resunet++, conditional random field and test-time augmentation, *IEEE Journal of Biomedical and Health Informatics* **25**, p. 2029–2040 (June 2021).
34. K. Li, M. I. Fathan, K. Patel, T. Zhang, C. Zhong, A. Bansal, A. Rastogi, J. S. Wang and G. Wang, Colonoscopy polyp detection and classification: Dataset creation and comparative evaluations, *PLOS ONE* **16**, p. e0255809 (August 2021).
35. M. Misawa, S.-e. Kudo, Y. Mori, K. Hotta, K. Ohtsuka, T. Matsuda, S. Saito, T. Kudo, T. Baba, F. Ishida, H. Itoh, M. Oda and K. Mori, Development of a computer-aided detection system for colonoscopy and a publicly accessible large colonoscopy video database (with video), *Gastrointestinal Endoscopy* **93**, 960 (April 2021).
36. A. de Maissin, R. Vallée, M. Flamant, M. Fondain-Bossiere, C. L. Berre, A. Coutrot, N. Normand, H. Mouchère, S. Coudol, C. Trang and A. Bourreille, Multi-expert annotation of crohn's disease images of the small bowel for automatic detection using a convolutional recurrent attention neural network, *Endoscopy International Open* **09**, p. E1136–E1144 (June 2021).
37. G.-P. Ji, G. Xiao, Y.-C. Chou, D.-P. Fan, K. Zhao, G. Chen and L. Van Gool, Video polyp segmentation: A deep learning perspective, *Machine Intelligence Research* **19**, p. 531–549 (November 2022).
38. D. Jha, V. Sharma, N. Dasu, N. K. Tomar, S. Hicks, M. K. Bhuyan, P. K. Das, M. A. Riegler, P. Halvorsen, U. Bagci and T. de Lange, Gastrovision: A multi-class endoscopy image dataset for computer aided gastrointestinal disease detection (2023).
39. D. Wang, X. Wang, L. Wang, M. Li, Q. Da, X. Liu, X. Gao, J. Shen, J. He, T. Shen, Q. Duan, J. Zhao, K. Li, Y. Qiao and S. Zhang, A real-world dataset and benchmark for foundation model adaptation in medical image classification, *Scientific Data* **10** (September 2023).
40. A. Yokote, J. Umeno, K. Kawasaki, S. Fujioka, Y. Fuyuno, Y. Matsuno, Y. Yoshida, N. Imazu, S. Miyazono, T. Moriyama, T. Kitazono and T. Torisu, Small bowel capsule endoscopy examination and open access database with artificial intelligence: The see-artificial intelligence project, *DEN Open* **4** (June 2023).
41. Dekker, ClinicalTrials.gov — clinicaltrials.gov `https://clinicaltrials.gov/study/NCT03822390#more-information`, (2020), [Accessed 06-05-2024].
42. A. Gu and T. Dao, Mamba: Linear-time sequence modeling with selective state spaces (2023).
43. A. Vaswani, N. Shazeer, N. Parmar, J. Uszkoreit, L. Jones, A. N. Gomez, L. Kaiser and I. Polosukhin, Attention is all you need (2017).
44. P. Mesejo, D. Pizarro, A. Abergel, O. Rouquette, S. Beorchia, L. Poincloux and A. Bartoli, Computer-aided classification of gastrointestinal lesions in regular colonoscopy, *IEEE Transactions on Medical Imaging* **35**, p. 2051–2063 (September 2016).
45. A. Charoen, A. Guo, P. Fangsaard, S. Taweechainaruemitr, N. Wiwatwattana, T. Charoenpong and H. G. Rich, Rhode island gastroenterology video capsule endoscopy data set, *Scientific Data* **9** (October 2022).

Higher-order Interaction Matters: Modeling Epidemics via Dynamic Hypergraph Neural Networks

Songyuan Liu[1], Shengbo Gong[1], Tianning Feng[1],
Zewen Liu[1], Max S.Y. Lau, PhD[2], Wei Jin, PhD[1]
[1]*Department of Computer Science*
[2]*Department of Biostatistics and Bioinformatics*
Emory University, Atlanta, GA, USA

The ongoing need for effective epidemic modeling has driven advancements in capturing the complex dynamics of infectious diseases. Traditional models, such as Susceptible-Infected-Recovered, and graph-based approaches often fail to account for higher-order interactions and the nuanced structure pattern inherent in human contact networks. Higher-order interactions, such as those in schools, workplaces, or public transit, involve simultaneous contact among more than two individuals. This study introduces a novel Human Contact-Tracing Hypergraph Neural Network framework tailored for epidemic modeling called EpiDHGNN, leveraging the capabilities of hypergraphs to model intricate, higher-order relationships from both location and individual level. Both real-world and synthetic epidemic data are used to train and evaluate the model. Results demonstrate that EpiDHGNN consistently outperforms baseline models across various epidemic modeling tasks, such as source detection and forecast, by approximately 12.1% through effectively capturing the higher-order interactions and preserving the complex structure of human interactions. This work underscores the potential of representing human contact data as hypergraphs and employing hypergraph-based methods to improve epidemic modeling, providing reliable insights for public health decision-making.

Keywords: Epidemic Modeling; Hypergraph Neural Network; Contact Tracing

1. Introduction

Since the onset of the COVID-19 pandemic, there has been a growing interest in studying epidemiological models.[1–3] Understanding and managing infection outbreaks is crucial for public health. Traditional mechanistic models like Susceptible-Infected-Recovered (SIR), which mathematically describe the transmission mechanisms of infectious diseases, often suffer from limitations of oversimplified or fixed assumptions, leading to sub-optimal predictive power and inefficiency in capturing complex epidemic patterns.[4,5]

Motivated by these limitations, sequential models such as GRU[6] and LSTM[7] are used to model temporal relations. Compared to mechanistic models, sequential models have demonstrated superior performance in forecasting infection counts.[1,8,9] However, these models often struggle to incorporate spatial dependencies, such as human mobility patterns and geographical distributions, which play a crucial role in epidemiology modeling.[2] Mobility data captures

© 2025 The Authors. Open Access chapter published by World Scientific Publishing Company and distributed under the terms of the Creative Commons Attribution Non-Commercial (CC BY-NC) 4.0 License.

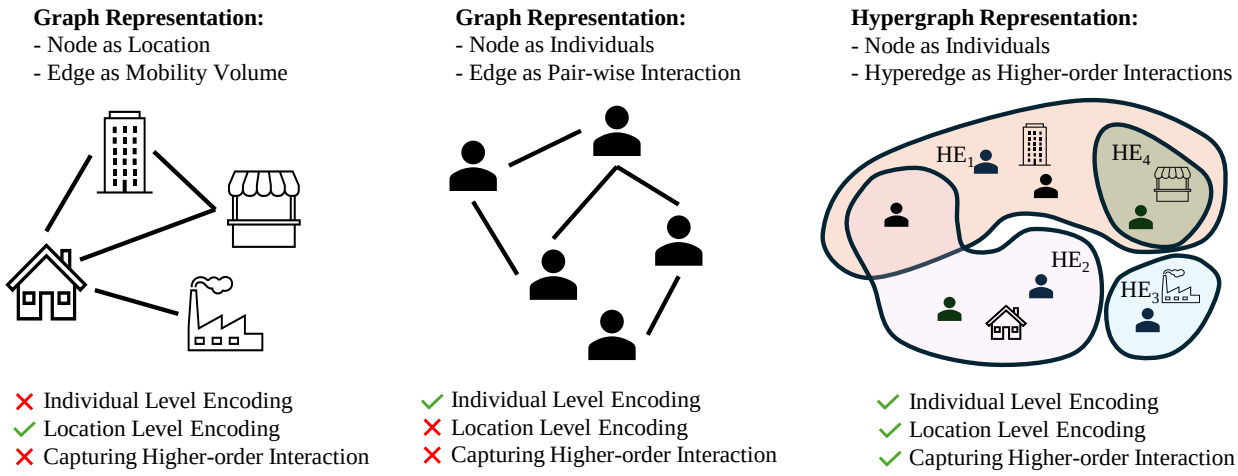

Fig. 1 Illustration of how various graph encoding methods can be employed to capture complex interactions. Hypergraphs, in particular, offer significant advantages over traditional graphs by retaining both individual-level and location-level information, while also capturing higher-order interactions. This enriched representation facilitates a more nuanced understanding of epidemic dynamics.

how individuals move and interact across different locations, influencing disease transmission dynamics beyond simple temporal trends. Accounting for this drawback, graph-based approaches have emerged as a popular tool in epidemic research. Graph Neural Networks (GNNs)[10,11] have become popular for their ability to model human mobility patterns. They achieve this by representing nodes as regions and weighted edges as mobility volume, effectively capturing movement between locations. Through a message-passing mechanism, GNNs enable nodes to share information with their neighbors, allowing for a more comprehensive understanding of mobility patterns. Additionally, by leveraging dynamic graph modeling and dynamic GNNs, they can further represent changes in human movement over time, enhancing their ability to model relational dynamics within mobility networks.[5,12,13]

Despite the utility of GNN-based methods, they primarily focus on pair-wise interactions and therefore neglect the higher-order interactions that are inherent in actual human contact networks.[14–16] Specifically, higher-order interactions refer to interactions or contacts that involve more than two individuals simultaneously in the context of epidemic modeling.[17] For example, public transportation, workplaces, and schools are shared spaces where groups of people interact following higher-order transmission dynamics. As illustrated in Figure 1, while standard graphs can model these interactions by representing individuals as nodes and forming fully connected subgraphs for each group, this approach is often inefficient and obscures the true higher-order structure. In contrast, hypergraphs provide a more natural and explicit way to represent higher-order interactions through hyperedges, eliminating the artificial clique. Additionally, hypergraphs can model overlapping interactions by representing locations as hyperedges, encompassing multiple individuals simultaneously. These enhancements can lead to more accurate and interpretable modeling of epidemics than standard graphs.[14,15,18]

Therefore, a fundamental limitation of prior graph-based approaches lies in their inability to simultaneously preserve both individual-level and location-level information, as well as their

failure to capture higher-order interactions. These shortcomings significantly hinder the accurate modeling of real-world human contact patterns, which are essential for understanding and predicting the spread of infectious diseases. However, learning on hypergraphs presents unique challenges. It is difficult to capture recurrent social contact patterns that occur at irregular intervals, as well as to learn disentangled yet interactive representations of individuals and locations. These challenges call for models that can handle dynamic, heterogeneous structures in human contact networks.

To address these, we propose **EpiDHGNN**, a novel framework that models human contact data as dynamic hypergraphs. This approach enables the encoding of complex, higher-order interactions and supports a more granular representation of epidemic dynamics. The major contributions of this paper are threefold:

(1) We propose a novel method to model human contact as dynamic hypergraphs, which encodes nodes as individuals and hyperedges as locations, leveraging both granular-level information and higher-order interactions.
(2) We develop EpiDHGNN, a model tailored for epidemic forecasting and source detection with a self-supervised contact-pattern awareness module, capturing the higher-order interactions and contact patterns that are inherent in human contacts.
(3) Extensive experiments are conducted to demonstrate the superiority of encoding human contact as hypergraphs, as well as the effectiveness of our proposed models in various epidemic tasks.

Our results indicate that EpiDHGNN significantly improve the performance. This advancement holds the potential to enhance infection control strategies in healthcare environments, ultimately contributing to better public health outcomes.

2. Related Work

Mechanistic Epidemic Modeling: In the past, when data was not sufficiently recorded, scientists were unable to build empirical models that successfully captured the dynamics of epidemics. Empirical models rely heavily on accurate and comprehensive data to make predictions and understand patterns. In contrast, mechanistic models[19,20] are designed to capture the underlying complexity of infections and the recovery processes of various diseases, even with limited data. Among these, the compartmental model, exemplified by the Susceptible-Infectious-Recovered (SIR) model,[21] is considered one of the most popular and successful. The model divides the population into compartments based on their disease status, allowing for a structured and systematic analysis of epidemic progression. It uses two parameters, β and γ, to account for the infection and recovery rates respectively. The model's ability to incorporate epidemiological principles makes it particularly valuable for understanding and predicting the course of infectious diseases.

Graphs for Epidemic Modeling: Recent advancements in dynamic graph modeling have underscored the utility of such models in epidemic source detection and spread prediction. Initially developed for traffic forecasting, dynamic graph models have been rapidly adapted to epidemiological contexts, where nodes represent geographical locations.[2,5,22,23] However, these methods overlook the higher-order interaction inherent in human contact networks.

Furthermore, previous works also focus on utilizing the dynamic message-passing (DMP) inference algorithm and network centrality as a tool for statistical inference to estimate the origin of an epidemic outbreak.[14,24,25] Such algorithms iteratively transmit messages along network edges, updating each node's state probabilities based on the states of its neighbors. However, they operate on static graphs, thereby overlooking the inherent dynamics of contact networks in human societies.

Hypergraphs for Epidemic Modeling: Similar to graphs, hypergraphs can be utilized in epidemic modeling while encompassing higher-order interactions.[26–28] In the pathogen propagation function proposed by Hypergraph-HeterSIS,[16] the infection state of each node is first aggregated to hyperedge, which is then followed by a nonlinear function f to remove linearity. The result is then mapped back to node level to provide the next step update. The method has been shown that hypergraph-based approaches are better at capturing the structural differences in contact networks and improving the accuracy of infection dynamics modeling. However, these approaches are based on variable calibration, therefore neglecting the higher-level representation generated through deep learning approaches.[15,29,30]

3. Formulation

3.1 Hypergraph: A hypergraph is a higher-order representation of a graph where an edge can connect any number of vertices. Formally, a hypergraph $G = (V, \mathcal{E}, \mathbf{X})$ consists of a set of nodes V, a set of hyperedges $\mathcal{E}$, where each hyperedge is a subset of V, and a feature matrix $\mathbf{X} \in \mathbb{R}^{|V| \times d}$, where each row encodes the node feature. The hypergraph structure can be described by an incidence matrix $\mathbf{H} \in \mathbb{R}^{|\mathcal{E}| \times N}$, where $\mathbf{H}_{i,j} = 1$ only when the node v_i is incident to the edge e_j.

3.2 Dynamic Hypergraph: A dynamic hypergraph is an extension of a hypergraph that evolves over time, consisting of a sequence of hypergraphs observed over T discrete time steps. Formally, a dynamic hypergraph is represented as $G^{(0:T)} = \{G^{(0)}, G^{(1)}, \ldots, G^{(T)}\}$, where each hypergraph $G^{(t)} = (V^{(t)}, \mathcal{E}^{(t)}, \mathbf{X}^{(t)})$ denotes the hypergraph at time step $t \in [0:T]$. Here, $V^{(t)}$ is the set of nodes, $\mathcal{E}^{(t)}$ is the set of hyperedges, and $\mathbf{X}^{(t)}$ denotes the node features at time t. It is worth noting that **both** the graph structure and node features are dynamic, since in some works, dynamic graphs have static features.

3.3 Epidemic Tasks: Consider an input of a dynamic hypergraph $G^{(0:T)} = \{G^{(0)}, \ldots, G^{(T)}\}$, where each node represents an individual and each hyperedge represents a location. At an arbitrary time step t, the nodes in a hyperedge $e^{(t)} \in \mathcal{E}^{(t)}$ represent a single contact between these entities. Each hypergraph $G^{(t)}$ is associated with an individual state matrix $\mathbf{X}^{(t)} \in \mathbb{R}^{N \times d}$, where d is the feature dimension of the individual. For example, in the SIR setting, d can consist of three dimensions, which correspond to the $\{\text{Suspected}, \text{Infected}, \text{Recovered}\}$ status of a specific individual.

Additionally, we define three time steps to clarify the time interval of our downstream epidemic tasks. [0 : tsh] where tsh stands for Time Step Hidden; [tsh : ks] where ks stands for Known Time Step; [ks : ps] where ps stands for Prediction Time Step. The three time steps are ordered such that $0 \leq \text{tsh} \leq \text{ks} \leq \text{ps} \leq T$. Note that for a time step $t \in T$, when $t < \text{tsh}$, only the contact hypergraph can be observed. When $\text{tsh} \leq t \leq \text{ks}$, both the contact

hypergraph and individual state can be observed. When $t >$ ps, neither contact hypergraph nor the individual state can be observed. An illustration of the three time steps is shown in Figure 2.

3.3.1 Source Detection: The source detection task focuses on identifying the initial node responsible for the spread of an epidemic, often referred to as "patient zero." Given the dynamic hypergraph $G^{(0:\text{ks})}$, or its incidence matrix $\mathbf{H}^{(0:\text{ks})}$, and the corresponding state matrix $\mathbf{X}^{(\text{tsh:ks})}$, we aim to infer the likelihood distribution over all nodes at the initial time step $T = 0$ using a model f parametrized by weight θ. Mathematically, we are interested in using f_θ to estimate the distribution:

$$f_\theta(\mathbf{H}^{(0:\text{ks})}, \mathbf{X}^{(\text{tsh:ks})}) \approx p(\mathbf{X}^{(0)} | \mathbf{H}^{(0:\text{ks})}, \mathbf{X}^{(\text{tsh:ks})}).$$

This task leverages both the structural properties of the hypergraph and the temporal evolution of the feature maps to backtrack the probable origin of the epidemic. The node labels y_{detect} are extracted from specific columns of $\mathbf{X}^{(0)}$ that represent the infection state — for example, **the "infected" column** in the case of the SIR model. To optimize the model, we use weighted binary cross-entropy loss between the predictions and node labels y_{detect}, where $w_1 = \frac{|V|}{|y_{\text{detect}}=1|}$ and $w_0 = \frac{|V|}{|y_{\text{detect}}=0|}$

$$\mathcal{L}_{\text{detect}}(\theta) = -\frac{1}{|V|} \sum_{v \in V} [w_1 \cdot y_{\text{detect}} \log(f_\theta) + w_0 (1 - y_{\text{detect}}) \log(1 - f_\theta)],$$

3.3.2 Infection Forecasting: Forecasting tasks in epidemics are usually defined as finding the total number of infections and recoveries in a range of future time steps. This is because previous approaches encode nodes as areas, neglecting the individual-level information. On the other hand, when using human contact hypergraphs, we can deduce a more fine-grained forecasting on an individual level. Therefore, we treat our forecast task as a binary node classification task. The node labels are defined as whether a node is in the "infected" state. Using the SIR model as an example, each node can be in one of three states, and only when it is in the "infected" state does the label become True. Here we are interested in using a model g parametrized by θ to estimate the distribution:

$$g_\theta(\mathbf{H}^{(0:\text{ks})}, \mathbf{X}^{(\text{tsh:ks})}) \approx p(\mathbf{X}^{(\text{ks+1,ps})} | \mathbf{H}^{(0:\text{ks})}, \mathbf{X}^{(\text{tsh:ks})})$$

Similar to source detection, we'll use the binary cross-entropy loss between the predictions and node labels y_{forecast}. The labels are extracted from specific columns of $\mathbf{X}^{(\text{ks+1:ps})}$ that represent the infection state, similar to source detection label extraction.

$$\mathcal{L}_{\text{forecast}}(\theta) = -\frac{1}{|V|} \sum_{v \in V} [y_{\text{forecast}} \log(g_\theta) + (1 - y_{\text{forecast}}) \log(1 - g_\theta)],$$

4. Method

In this section, we will formulate our proposed model EpiDHGNN, which serves as f_θ and g_θ defined in Section 3.3. Here we define $t \in T_{\text{interest}}$ where T_{interest} is the corresponding input interval for $\mathbf{H}$ defined in Sections 3.3.1 and 3.3.2.

EpiDHGNN is a novel dynamic hypergraph neural network that models epidemic dynamics by jointly capturing spatial, temporal, and structural contact patterns. As illustrated in

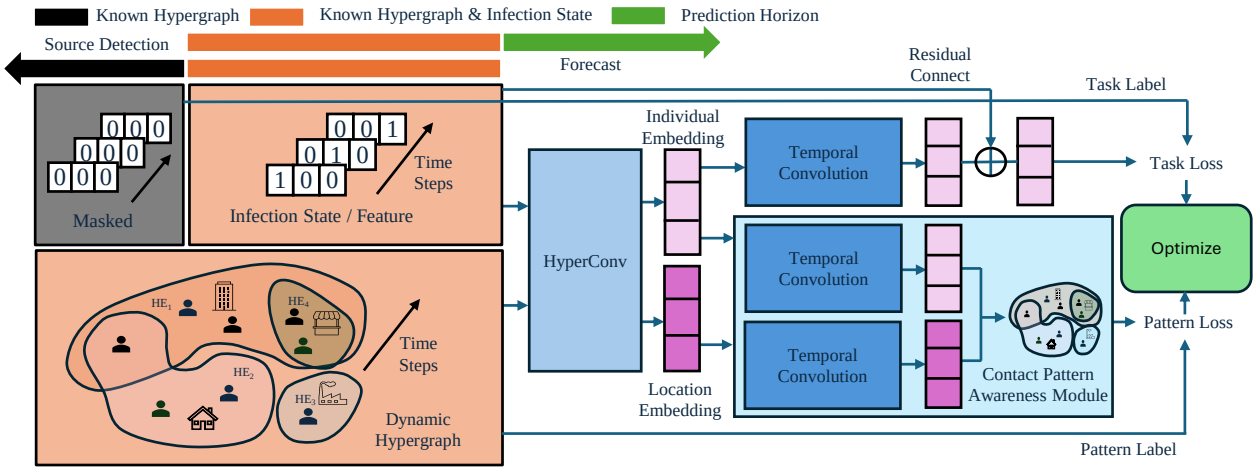

Fig. 2 Model Architecture of proposed EpiDHGNN model. The arrows in the top left corner refer to the three time steps defined in Section 3.3, where $[0 : tsh]$ is the black interval, $[tsh : ks]$ is the orange interval, and $[ks + 1 : ps]$ is the green interval. All individual state is masked to 0 in $[0 : tsh]$ as shown in the top left black module. Corresponding inputs for source detection and forecast, defined in Sections 3.3.1 and 3.3.2, are then fed to the model as input. The light blue HyperConv module is defined in Section 4.1; the dark blue temporal convolution module is defined in Section 4.1; and the contact pattern awareness module is defined in Section 4.2.

Figure 2, EpiDHGNN follows an encoder-decoder paradigm and integrates both supervised and self-supervised learning objectives to enhance the quality of node embeddings. The framework is composed of three key components: (1) a *Spatial-Temporal Encoder* based on hypergraph and temporal convolution that aggregates high-order relational information among individuals and captures progression patterns over time, (2) a novel self-supervised *Contact Pattern Awareness Module* that encourages structural consistency by reconstructing dynamic contact patterns. This architecture allows the model to learn robust spatiotemporal embeddings of infection states, improving performance on downstream tasks such as epidemic forecasting and source detection.

4.1 Spatio-Temporal Encoding: To capture spatial dependencies at each time step, we adopt the hypergraph convolution operator proposed in HGNN,[15] which aggregates information from high-order neighbors via node-edge-node message passing. Formally, a single hypergraph convolutional layer consists of:

$$\mathbf{X}_{\text{edge}}^{l+1,t} = \mathbf{D}_e^{-1}\mathbf{H}^{T,t}\mathbf{D}_v^{-1/2}\mathbf{X}_{\text{node}}^{l,t}\Theta, \tag{1}$$

$$\mathbf{X}_{\text{node}}^{l+1,t} = \mathbf{D}_v^{-1/2}\mathbf{H}^{t}\mathbf{W}\mathbf{D}_e^{-1}\mathbf{H}^{T,t}\mathbf{D}_v^{-1/2}\mathbf{X}_{\text{node}}^{l,t}\Theta, \tag{2}$$

where $\mathbf{H}^t$ is the incidence matrix at time t, $\mathbf{D}_v$ and $\mathbf{D}_e$ are diagonal node and edge degree matrices, $\mathbf{W}$ is an optional hyperedge weighting matrix, and Θ denotes learnable parameters. By stacking L such layers, the node embeddings can incorporate information from L-hop neighborhoods. After applying the convolution over all time steps, the node and edge embeddings are concatenated along the temporal axis:

$$\mathcal{X}_{\text{node}}^{L} = [\mathbf{X}_{\text{node}}^{L,t_0} \mid \mathbf{X}_{\text{node}}^{L,t_1} \mid \ldots], \quad \mathcal{X}_{\text{edge}}^{L} = [\mathbf{X}_{\text{edge}}^{L,t_0} \mid \mathbf{X}_{\text{edge}}^{L,t_1} \mid \ldots], \quad \forall t \in T_{\text{interest}}. \tag{3}$$

To capture temporal dependencies, we apply standard 1D convolution across the temporal axis, similar to the temporal convolutional networks introduced in[31] and later adapted for dynamic graphs in.[32] Letting time correspond to the width dimension, individuals to the height, and feature channels to the depth, the operation is defined as:

$$\hat{\mathbf{X}}_{\text{node}} = \sigma\left(\Phi^{k}_{\text{temporal}} \circledast \mathcal{X}^{L}_{\text{node}}\right), \tag{4}$$

where $\circledast$ denotes convolution, $\Phi^{k}_{\text{temporal}}$ is the convolution kernel of width k, and σ is a non-linear activation function. This enables the model to learn progression patterns across time.

4.2 Self-supervised Contact Pattern Awareness Module: In a societal setting, human interactions occur with varying probabilities based on social structures and daily routines. For instance, individuals are highly likely to engage in frequent interactions with family members or colleagues at home or in the workplace, while social encounters with friends or individuals sharing similar interests may occur less frequently, such as on a weekly or monthly basis in clubs or shopping centers. To leverage this information, we propose a self-supervised *Contact Pattern Awareness Module*, designed to predict human interactions within the epidemic framework. Given a sequence of k hypergraphs $\{G_t\}_{t=t_0}^{t_0+k-1}$ starting from a randomly selected time step t_0, the module aims to reconstruct the hypergraph at the final time step, G_{t_0+k}, using information from the preceding $k-1$ hypergraphs. Successful reconstruction enables HGNN to inject human-contact-aware inductive bias into the learned node embeddings $\mathcal{X}^{L}_{\text{node}}$, thereby improving performance in subsequent epidemic forecasting tasks.

To effectively capture these patterns, we utilize both the individual embeddings and location embeddings obtained from Section 4.1. These embeddings are then processed using the temporal convolution framework introduced in Section 4.2, enabling the model to extract temporal dependencies. Finally, the refined embeddings are passed through a fully connected layer to produce a confidence score for contact prediction. Mathematically, this operation is formulated as:

$$\mathbf{s} = \sigma\left(\text{MLP}\left(\Phi^{k}_{\text{pattern}} \circledast \mathcal{X}^{L}_{\text{node}} * \Phi^{k}_{\text{pattern}} \circledast \mathcal{X}^{L}_{\text{edge}}\right)\right), \tag{5}$$

where $*$ denotes element-wise multiplication and σ is a sigmoid activation. The output $\mathbf{s}$ is a predicted score for individual-location contact. The module is trained with binary cross-entropy loss on a balanced set of positive (observed) and negative (random) samples:

$$\mathcal{L}_{\text{pattern}} = -\frac{1}{N}\sum_{i=1}^{N}\left[y_i \log s_i + (1-y_i)\log(1-s_i)\right], \tag{6}$$

where $y_i \in \{0,1\}$ is the ground-truth label indicating whether contact occurred.

4.3 EpiDHGNN: Given an input sequence of dynamic hypergraphs $\{\mathbf{H}^t\}_{t=t_0}^{t_0+ks}$ and the corresponding individual features $\{\mathbf{X}^t\}_{t=t_0}^{t_0+ks}$, EpiDHGNN first encodes node representations using the spatial and temporal modules (Sections 4.1), and then incorporates initial state residuals before calculating task-specific loss. The overall loss is a combination of task-specific supervision and the self-supervised contact pattern loss:

$$\mathcal{L} = \alpha\ \mathcal{L}_{\text{task}} + (1-\alpha)\mathcal{L}_{\text{pattern}}, \tag{7}$$

where α is a weighting hyperparameter.

5. Experiment

In this section, we perform analysis on the datasets and conduct experiments to evaluate the proposed model. We focus on the following research questions:

- **RQ1**: Does EpiDHGNN outperforms baseline dynamic graph models in various tasks?
- **RQ2**: Does the contact pattern awareness module facilitate the performance of EpiDHGNN?
- **RQ3**: Is contact patterns successfully captured? To what aspect of the task does the module helps the most?
- **RQ4**: Beyond individual-level prediction, can EpiDHGNN capture population-level infection dynamics over time?

Data Description: We assess the performance of baseline models and our proposed model on both graph and hypergraph settings. Because of the privacy nature of human contact data, we used both real-world and synthetic data. The University of Virginia **UVA** dataset includes an extensive collection of clinical metadata sourced from the Epic-based SQL database at the UVA hospital. The interactions are derived from Electronic Healthcare Records (EHRs), which document the timing and locations of encounters between patients and healthcare workers (HCWs). We utilized the real-world infection case calibrated pathogen parameters provided by Anand etc.[16] to retrieve the patient infection states through simulations. The **EpiSim** dataset is based on the Mobility Intervention of Epidemic Simulator,[33] which models human movement and disease transmission. The *Human Mobility Model* simulates hourly movements from 8 A.M. to 10 P.M. On weekdays, individuals move from residential to work areas at time $T_d \sim U(a, b)$, stay for $T_w \sim U(c, d)$ hours, and may visit commercial areas before returning home. On weekends, they visit commercial areas at $T_e \sim U(g, h)$ with probability P_e, staying for $T_m \sim U(i, j)$ hours. The *Disease Transmission Model* includes *acquaintance* and *stranger* contacts. Each individual has fixed acquaintance contacts at home ($K_r \sim U(m, n)$) and work ($K_w \sim U(o, p)$). At each timestep, infection occurs with probability P_a from acquaintances and P_s from strangers. The simulator parameters are calibrated using the Covid-19 R_0 from WHO. The statistics for both datasets are shown in Table 1.

Table 1 Dataset Summary

Metric	**UVA**	**EpiSim**
Individuals	2,500	10,000
Locations	500	11
Time Steps	169	47
Contacts	94,134	664,177

Setup: In our experiment, we utilize a 2-layer HGNN to capture neighborhood information. We perform a grid search over key hyperparameters, including hidden dimensions, learning rate, weight decay, kernel size, and α. During training, we employ the ADAM optimizer with weight decay and gradient clipping activated to stabilize gradient updates and prevent exploding gradients. Models are trained for up to 100 epochs, with early stopping activated if the validation loss does not improve for 10 consecutive epochs. The experiments are conducted on a single NVIDIA Tesla V100 GPU with 16 GB of memory. Training time per epoch averages around 5 seconds. To enhance reproducibility, random seeds are fixed for data splitting, model initialization, and optimization processes. We run the baselines using the package EpiLearn.[34]

RQ1 - Performance: Our experimental results for both source detection and forecasting are presented in Table 2 and Table 3, respectively, with the best performance under

Table 2 Result of Forecast Task. Best Performance under each setting is bolded.

		UVA		EpiSim	
	PS	F1	AUROC	F1	AUROC
H2ABM	5	0.429 ± 0.067	0.602 ± 0.016	0.538 ± 0.083	0.703 ± 0.022
	10	0.258 ± 0.091	0.579 ± 0.070	0.378 ± 0.011	0.581 ± 0.048
	20	0.301 ± 0.061	0.552 ± 0.043	0.097 ± 0.064	0.484 ± 0.070
STGCN	5	0.526 ± 0.022	0.714 ± 0.035	0.632 ± 0.036	0.816 ± 0.029
	10	0.343 ± 0.028	0.688 ± 0.010	0.473 ± 0.025	0.692 ± 0.043
	20	0.398 ± 0.031	0.655 ± 0.031	0.195 ± 0.073	0.593 ± 0.010
ASTGCN	5	0.544 ± 0.038	0.731 ± 0.060	0.624 ± 0.030	0.801 ± 0.005
	10	0.376 ± 0.013	0.692 ± 0.012	0.489 ± 0.014	0.712 ± 0.009
	20	0.367 ± 0.009	0.652 ± 0.011	0.154 ± 0.045	0.612 ± 0.025
MSTGCN	5	**0.721 ± 0.063**	**0.846 ± 0.013**	0.869 ± 0.084	0.895 ± 0.010
	10	0.401 ± 0.041	0.647 ± 0.012	0.502 ± 0.042	0.729 ± 0.020
	20	0.358 ± 0.024	0.617 ± 0.065	0.223 ± 0.035	0.658 ± 0.056
EpiDHGNN	5	0.712 ± 0.023	0.837 ± 0.019	**0.918 ± 0.042**	**0.957 ± 0.065**
	10	**0.576 ± 0.012**	**0.750 ± 0.008**	**0.612 ± 0.001**	**0.874 ± 0.017**
	20	**0.454 ± 0.007**	**0.685 ± 0.008**	**0.298 ± 0.080**	**0.779 ± 0.071**

each setting highlighted in bold. The baseline models we chose includes: H2ABM groups interactions via hyperedges rather than pairwise edges to better capture collective dynamics; STGCN learns spatio-temporal dependencies using stacked temporal and spatial convolution blocks; MSTGCN serves as a multi-component spatial-temporal graph convolution network; and ASTGCN adds spatial-temporal attention mechanisms for dynamic weighting across time and space. Then, we evaluated the models under diverse conditions to assess their robustness. For source detection, we masked timesteps of varying lengths (5, 10, and 20) to examine the models' abilities to backtrack across different scenarios. Similarly, we tested forecasting performance using prediction horizons of 5, 10, and 20 timesteps. In most settings, EpiDHGNN outperforms the majority of baseline graph-based models, underscoring the advantages of hypergraph-based approaches in epidemic modeling through capturing the high-order contact interaction.

RQ2 - Ablation: We conducted an ablation study on the contact pattern awareness module to investigate Question 2. As shown in Table 4, removing this module led to a noticeable decline in performance, indicating its crucial role in capturing individual contact patterns. The results suggest that incorporating individual contact behaviors enhances the model's ability to encode social interactions more effectively, aligning with societal norms. This highlights the importance of modeling personalized contact dynamics in improving the overall predictive capability of our approach.

RQ3 - Module Effectiveness: To investigate whether the contact pattern is successfully

Table 3 Result of Source Detection Task. Best performance under each setting is bolded.

		UVA			EpiSim		
	TSH	MRR	Hit@1	Hit@3	MRR	Hit@1	Hit@3
H2ABM	5	0.291 ± 0.087	0.100 ± 0.061	0.450 ± 0.074	0.042 ± 0.082	0.092 ± 0.068	0.112 ± 0.095
	10	0.412 ± 0.070	0.265 ± 0.091	0.583 ± 0.060	0.079 ± 0.078	0.050 ± 0.084	0.145 ± 0.062
	20	0.382 ± 0.060	0.130 ± 0.080	0.551 ± 0.074	0.066 ± 0.085	0.044 ± 0.049	0.118 ± 0.073
STGCN	5	0.491 ± 0.056	0.300 ± 0.036	0.650 ± 0.057	0.242 ± 0.075	0.145 ± 0.052	0.282 ± 0.035
	10	0.462 ± 0.064	0.315 ± 0.074	0.633 ± 0.024	0.129 ± 0.039	0.100 ± 0.103	0.195 ± 0.052
	20	0.427 ± 0.033	0.175 ± 0.023	0.596 ± 0.078	0.111 ± 0.047	0.089 ± 0.042	0.163 ± 0.017
ASTGCN	5	0.501 ± 0.026	0.300 ± 0.078	0.650 ± 0.052	0.226 ± 0.036	0.167 ± 0.033	0.333 ± 0.042
	10	0.486 ± 0.046	0.250 ± 0.082	0.667 ± 0.022	0.141 ± 0.067	0.100 ± 0.027	0.133 ± 0.014
	20	0.416 ± 0.029	0.205 ± 0.058	0.650 ± 0.032	0.118 ± 0.087	0.076 ± 0.031	0.100 ± 0.087
MSTGCN	5	0.618 ± 0.026	0.417 ± 0.029	0.767 ± 0.076	0.333 ± 0.029	0.167 ± 0.032	0.400 ± 0.058
	10	0.561 ± 0.026	0.350 ± 0.050	0.733 ± 0.058	0.213 ± 0.058	0.100 ± 0.026	**0.200 ± 0.019**
	20	0.442 ± 0.029	0.150 ± 0.058	0.700 ± 0.052	0.192 ± 0.016	0.089 ± 0.100	0.193 ± 0.029
EpiDHGNN	5	**0.704 ± 0.033**	**0.517 ± 0.076**	**0.917 ± 0.029**	**0.401 ± 0.074**	**0.200 ± 0.100**	**0.500 ± 0.100**
	10	**0.662 ± 0.005**	**0.500 ± 0.015**	**0.783 ± 0.029**	**0.218 ± 0.037**	**0.133 ± 0.058**	0.167 ± 0.058
	20	**0.582 ± 0.031**	**0.350 ± 0.026**	**0.765 ± 0.050**	**0.219 ± 0.061**	**0.100 ± 0.100**	**0.200 ± 0.100**

Table 4 Ablation study on contact pattern awareness module.

			UVA		EpiSim	
		Setting	MRR	Hit@1	MRR	Hit@1
Detection	w/o CT module	tsh-5	0.692 ± 0.050	0.483 ± 0.104	0.381 ± 0.027	0.167 ± 0.058
		tsh-10	0.644 ± 0.032	0.467 ± 0.058	0.204 ± 0.020	0.100 ± 0.013
		tsh-20	0.558 ± 0.014	0.323 ± 0.029	0.197 ± 0.006	0.100 ± 0.100
	w/ CT module	tsh-5	**0.704 ± 0.033**	**0.517 ± 0.076**	**0.401 ± 0.074**	**0.200 ± 0.100**
		tsh-10	**0.662 ± 0.005**	**0.500 ± 0.005**	**0.218 ± 0.037**	**0.133 ± 0.058**
		tsh-20	**0.582 ± 0.031**	**0.350 ± 0.058**	**0.219 ± 0.061**	0.100 ± 0.092
			F1	AUROC	F1	AUROC
Forecast	w/o CT module	ps-5	0.709 ± 0.004	0.830 ± 0.003	0.891 ± 0.003	0.912 ± 0.007
		ps-10	0.571 ± 0.008	0.747 ± 0.006	0.513 ± 0.007	0.824 ± 0.005
		ps-20	0.439 ± 0.008	0.680 ± 0.004	0.253 ± 0.006	0.724 ± 0.009
	w/ CT module	ps-5	**0.712 ± 0.023**	**0.837 ± 0.019**	**0.918 ± 0.042**	**0.957 ± 0.006**
		ps-10	**0.576 ± 0.012**	**0.750 ± 0.008**	**0.612 ± 0.001**	**0.874 ± 0.004**
		ps-20	**0.454 ± 0.007**	**0.685 ± 0.008**	**0.298 ± 0.080**	**0.779 ± 0.071**

captured, we evaluate the module's performance in predicting contact existence at the location level. Specifically, locations are divided into four quantiles based on their contact intensity. For example, in the EpiSim dataset, households exhibit lower contact intensity compared to recreational locations. For each quantile, we report the prediction accuracy along with the overall accuracy in Table 5. The results suggest that the overall contact pattern is successfully reconstructed. While the UVA dataset shows little correlation between contact intensity and accuracy, the EpiSim dataset exhibits a strong negative correlation. This observation aligns with the underlying assumptions of our dataset. The UVA dataset includes hospital contacts,

which may fluctuate due to patient movement, whereas in the EpiSim dataset, locations with low contact intensity likely correspond to households, where visits occur with high frequency and regularity.

We further investigate the influence of the hyperparameter α, selecting values from 0.3, 0.5, 0.7, 0.9, 1.0, to assess its impact on overall model performance. Lower values of α were not considered, as $\alpha = 0.3$ already exhibited significantly diminished performance, failing to effectively capture the model's main task. As shown in Figure 3, our results indicate that α has little correlation with the final performance, suggesting that it can be treated as a tunable hyperparameter for future studies.

Additionally, we observe that the model with a high timestep hidden state (TSH20) consistently outperforms other configurations when incorporating α. This suggests that integrating contact pattern information is particularly beneficial for tasks requiring a longer temporal memory, as it helps the model better capture long-term dependencies in contact patterns. These findings highlight the importance of tuning α based on specific task requirements while reinforcing the advantage of incorporating contact-aware representations for long-horizon forecasting.

Table 5 Contact Pattern Prediction

	UVA		EpiSim	
Quantile	Range	F1	Range	F1
1	[:6]	0.795	[:616]	0.997
2	[6:11]	0.773	[616:1788]	0.852
3	[11:19]	0.809	[1788:1847]	0.820
4	[19:]	0.841	[1847:]	0.639
Overall	—	0.804	—	0.827

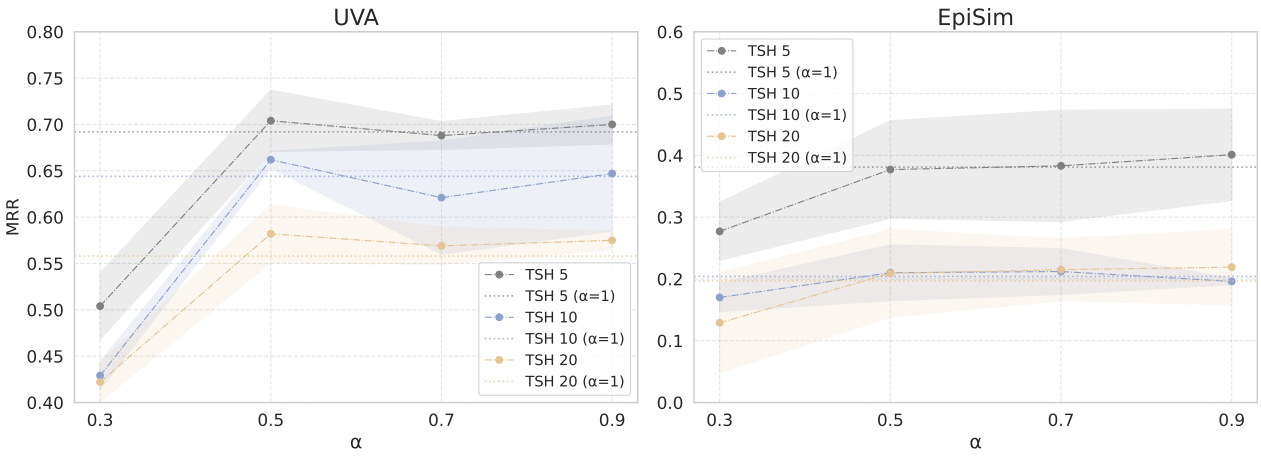

Fig. 3 Visualization of various α's impact on source detection performance

RQ4 - Generalizability: While we have demonstrated EpiDHGNN's ability to forecast an individual's probability of infection in RQ1, its effectiveness at capturing the population infection trend cannot be concluded. To address this, we aggregated the daily sum of infected individuals to generate population-level data across various prediction horizons with respect to time. As shown in Figure 4, EpiDHGNN accurately captures short-term infection dynamics and effectively tracks broader fluctuations at longer time steps, albeit with reduced precision.

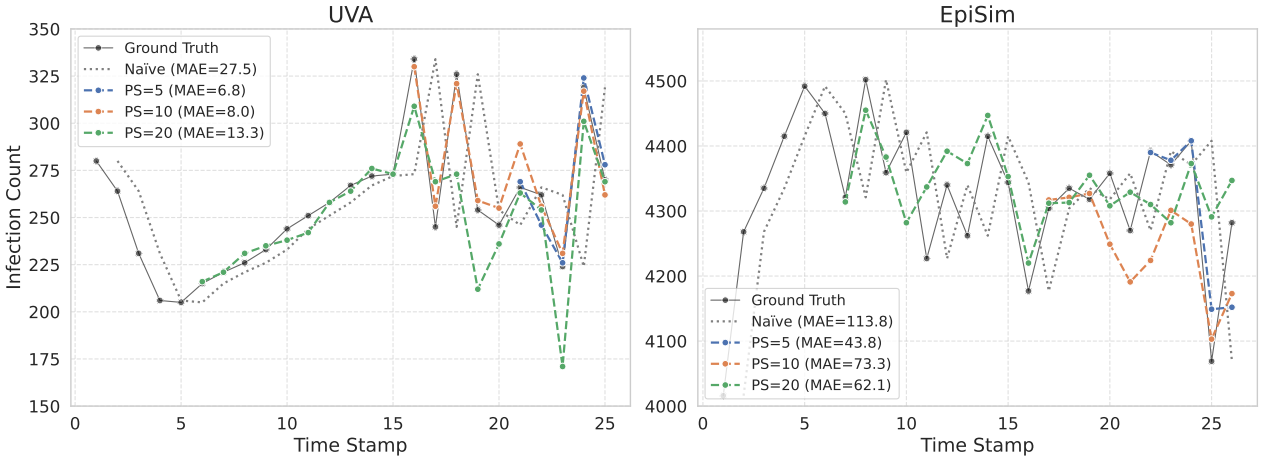

Fig. 4 Forecast generalizability analysis. The models can successfully the future infection dynamics within various PS. We also provide the Mean Absolute Error (MAE) of Naive Model (A naive time series model forecasts future values by assuming they will be the same as the most recent observed value) and our method.

6. Discussion & Conclusion

This study introduced the EpiDHGNN framework, demonstrating its ability to effectively capture the dynamics of epidemic spread through higher-order interactions in human contact networks. Through rigorous experimentation on both real-world and synthetic datasets, we validated the advantages of modeling human contact as a dynamic hypergraph, highlighting the importance of higher-order relationships and contact pattern in disease transmission.

Future improvements include exploring alternative model selections within the EpiDHGNN framework, leveraging its modular design for flexible layer substitutions. Advanced architectures in hypergraph-based learning will be investigated to enhance accuracy and efficiency. Additionally, real-world simulation remains challenging due to privacy concerns and data scarcity. Developing realistic synthetic algorithms that capture social clustering, geographic mobility, and temporal dynamics will refine simulations, improve model training, and provide a stronger benchmark for epidemic modeling.

In summary, this work underscores the power of hypergraph-based epidemic modeling and sets the stage for further exploration into both methodological advancements and data generation strategies. By enabling more accurate identification of transmission dynamics, these models hold promise for informing timely and targeted public health interventions, ultimately contributing to more effective epidemic response strategies at a broader societal level.

Acknowledgement

This research was supported by the U.S. National Science Foundation under Award No. 2504088 and by the National Institute of Allergy and Infectious Diseases of the NIH under Award No. R01AI189829. The content is the sole responsibility of the authors and does not necessarily represent the views of the NIH.

References

1. Rodríguez A, Kamarthi H, Agarwal P, Ho J, Patel M, Sapre S, et al.. Data-Centric Epidemic Forecasting: A Survey; 2022. Available from: https://arxiv.org/abs/2207.09370.
2. Liu Z, Wan G, Prakash BA, Lau MSY, Jin W. A Review of Graph Neural Networks in Epidemic Modeling; 2024.
3. Clement JC, Ponnusamy V, Sriharipriya KC, Nandakumar R. A Survey on Mathematical, Machine Learning and Deep Learning Models for COVID-19 Transmission and Diagnosis. IEEE Reviews in Biomedical Engineering. 2022;15:325-40.
4. Song S, Zong Z, Li Y, Liu X, Yu Y. Reinforced Epidemic Control: Saving Both Lives and Economy; 2020.
5. Deng S, Wang S, Rangwala H, Wang L, Ning Y. Graph Message Passing with Cross-location Attentions for Long-term ILI Prediction; 2019. Available from: https://arxiv.org/abs/1912.10202.
6. Chung J, Gulcehre C, Cho K, Bengio Y. Empirical Evaluation of Gated Recurrent Neural Networks on Sequence Modeling; 2014.
7. Yu Y, Si X, Hu C, Zhang J. A review of recurrent neural networks: LSTM cells and network architectures. Neural computation. 2019;31(7):1235-70.
8. Rodríguez A, Cui J, Ramakrishnan N, Adhikari B, Prakash BA. EINNs: epidemiologically-informed neural networks. In: Proceedings of the AAAI conference on artificial intelligence. vol. 37; 2023. p. 14453-60.
9. Liu Z, Ni J, Lau MSY, Jin W. CAPE: Covariate-Adjusted Pre-Training for Epidemic Time Series Forecasting; 2025. Available from: https://arxiv.org/abs/2502.03393.
10. Yu B, Yin H, Zhu Z. Spatio-Temporal Graph Convolutional Networks: A Deep Learning Framework for Traffic Forecasting. In: Proceedings of the 27th International Joint Conference on Artificial Intelligence; 2018. p. 3634-40.
11. Liu H, Zhu C, Zhang D, Li Q. Attention-based Spatial-Temporal Graph Convolutional Recurrent Networks for Traffic Forecasting; 2023. Available from: https://arxiv.org/abs/2302.12973.
12. Zheng Y, Jiang W, Zhou A, Hung NQV, Zhan C, Chen T. Epidemiology-informed Graph Neural Network for Heterogeneity-aware Epidemic Forecasting; 2024. Available from: https://arxiv.org/abs/2411.17372.
13. Qiu M, Tan Z, Bao BK. MSGNN: Multi-scale Spatio-temporal Graph Neural Network for epidemic forecasting. Data Mining and Knowledge Discovery. 2024 May;38(4):2348–2376. Available from: http://dx.doi.org/10.1007/s10618-024-01035-w.
14. Tan CW, Yu PD. Contagion Source Detection in Epidemic and Infodemic Outbreaks: Mathematical Analysis and Network Algorithms. Foundations and Trends® in Networking. 2023;13(2–3):107–251. Available from: http://dx.doi.org/10.1561/1300000068.
15. Feng Y, You H, Zhang Z, Ji R, Gao Y. Hypergraph Neural Networks; 2019.
16. Anand V, Cui J, Heavey J, Vullikanti A, Prakash BA. In: H²ABM: Heterogeneous Agent-based Model on Hypergraphs to Capture Group Interactions; 2024. p. 280-8. Available from: https://epubs.siam.org/doi/abs/10.1137/1.9781611978032.32.
17. Kim S, Lee SY, Gao Y, Antelmi A, Polato M, Shin K. A survey on hypergraph neural networks: An in-depth and step-by-step guide. In: Proceedings of the 30th ACM SIGKDD Conference on Knowledge Discovery and Data Mining; 2024. p. 6534-44.
18. Cao Q, Jiang R, Yang C, Fan Z, Song X, Shibasaki R. MepoGNN: Metapopulation Epidemic Forecasting with Graph Neural Networks. In: Amini MR, Canu S, Fischer A, Guns T, Kralj Novak P, Tsoumakas G, editors. Machine Learning and Knowledge Discovery in Databases. Cham: Springer Nature Switzerland; 2023. p. 453-68.
19. Lessler J, Cummings DA. Mechanistic Models of Infectious Disease and Their Impact on Public

Health. American Journal of Epidemiology. 2016 Mar;183(5):415-22. Epub 2016 Feb 17.
20. D'Agostino McGowan L, Grantz KH, Murray E. Quantifying Uncertainty in Mechanistic Models of Infectious Disease. American Journal of Epidemiology. 2021 Jan;190(7):1377–1385. Available from: http://dx.doi.org/10.1093/aje/kwab013.
21. Hethcote HW. The Mathematics of Infectious Diseases. SIAM Review. 2000;42(4):599-653.
22. Xie F, Zhang Z, Li L, Zhou B, Tan Y. EpiGNN: Exploring Spatial Transmission with Graph Neural Network for Regional Epidemic Forecasting; 2022. Available from: https://arxiv.org/abs/2208.11517.
23. Wan G, Liu Z, Lau MS, Prakash BA, Jin W. Epidemiology-aware neural ode with continuous disease transmission graph. arXiv preprint arXiv:241000049. 2024.
24. Lokhov AY, Mézard M, Ohta H, Zdeborová L. Inferring the Origin of an Epidemic with a Dynamic Message-Passing Algorithm. Phys Rev E. 2014;90(1):012801.
25. Yu PD, Tan CW, Fu HL. Epidemic Source Detection in Contact Tracing Networks: Epidemic Centrality in Graphs and Message-Passing Algorithms. IEEE Journal of Selected Topics in Signal Processing. 2022 feb;16(2):234-49. Available from: http://dx.doi.org/10.1109/JSTSP.2022.3153168.
26. Higham DJ, Kergorlay HLD. Disease extinction for susceptible-infected-susceptible models on dynamic graphs and hypergraphs. Chaos. 2022 8;32.
27. de Arruda GF, Petri G, Moreno Y. Social contagion models on hypergraphs. Phys Rev Res. 2020 Apr;2:023032. Available from: https://link.aps.org/doi/10.1103/PhysRevResearch.2.023032.
28. Ágnes Bodó, Katona GY, Simon PL. SIS epidemic propagation on hypergraphs; 2015.
29. Chien E, Pan C, Peng J, Milenkovic O. You are AllSet: A Multiset Function Framework for Hypergraph Neural Networks; 2022.
30. Agarwal S, Sawhney R, Thakkar M, Nakov P, Han J, Derr T. THINK: Temporal Hypergraph Hyperbolic Network. In: 2022 IEEE International Conference on Data Mining (ICDM). IEEE; 2022. p. 849-54.
31. Lea C, Vidal R, Reiter A, Hager GD. Temporal Convolutional Networks: A Unified Approach to Action Segmentation; 2016. Available from: https://arxiv.org/abs/1608.08242.
32. Guo S, Lin Y, Feng N, Song C, Wan H. Attention Based Spatial-Temporal Graph Convolutional Networks for Traffic Flow Forecasting. In: Proceedings of the AAAI Conference on Artificial Intelligence. vol. 33; 2019. p. 922-9.
33. Mobility Intervention of Epidemics; 2020. Accessed: 2025-02-13. Available from: https://hzw77-demo.readthedocs.io/en/latest/.
34. Liu Z, Li Y, Wei M, Wan G, Lau MSY, Jin W. EpiLearn: A Python Library for Machine Learning in Epidemic Modeling; 2024. Available from: https://arxiv.org/abs/2406.06016.

Scoring Physician Risk Communication in Prostate Cancer Using Large Language Models

Guillermo Lopez-Garcia, PhD
Department of Computational Biomedicine, Cedars-Sinai Medical Center, Los Angeles, CA, USA
E-mail: Guillermo.LopezGarcia@cshs.org

Dongfang Xu, PhD
Department of Computational Biomedicine, Cedars-Sinai Medical Center, Los Angeles, CA, USA
E-mail: Dongfang.Xu@cshs.org

Michael Luu, MPH
Department of Biostatistics, Cedars-Sinai Medical Center, Los Angeles, CA, USA
E-mail: Michael.Luu@cshs.org

Renning Zheng, BS
Department of Urology, Cedars-Sinai Medical Center, Los Angeles, CA, USA
Tsinghua Medicine, Tsinghua University Beijing, China
E-mail: Renning.Zheng@cshs.org

Timothy J. Daskivich, MD, MSHPM*
Department of Urology, Cedars-Sinai Medical Center, Los Angeles, CA, USA
E-mail: Timothy.Daskivich@cshs.org

Graciela Gonzalez-Hernandez, PhD*
Department of Computational Biomedicine, Cedars-Sinai Medical Center, Los Angeles, CA, USA
E-mail: Graciela.GonzalezHernandez@csmc.edu

Effective risk communication is essential to shared decision-making in prostate cancer care. However, the quality of physician communication of key concepts varies widely in real-world consultations. Manual evaluation of communication is labor-intensive and not scalable. We present a structured, rubric-based framework that uses large language models (LLMs) to automatically score the quality of risk communication in prostate cancer consultations.

*Co-Senior authors.

© 2025 The Authors. Open Access chapter published by World Scientific Publishing Company and distributed under the terms of the Creative Commons Attribution Non-Commercial (CC BY-NC) 4.0 License.

Using transcripts from 20 clinical visits, we curated and annotated 487 physician-spoken sentences that referenced five key concepts for shared decision-making: cancer prognosis, life expectancy, and three treatment side effects (erectile dysfunction, incontinence, and irritative urinary symptoms). Each sentence was assigned a score from 0 to 5 based on the precision and patient-specificity of communicated risk, using a validated scoring rubric. We modeled this task as five multiclass classification problems and evaluated both fine-tuned transformer baselines and GPT-4o with rubric-based and chain-of-thought (CoT) prompting. Our best performing approach, which combined rubric-based CoT prompting with few-shot learning, achieved micro averaged F1 scores between 85.0 and 92.0 across domains, outperforming supervised baselines and matching inter-annotator agreement. These findings establish a scalable foundation for AI-driven evaluation of physician–patient communication in oncology and beyond.

Keywords: Prostate cancer; physician-patient communication; risk communication; artificial intelligence; large language models; natural language processing; shared decision-making

1. Introduction

Effective communication of risk during treatment decision-making is essential for achieving high-quality, patient-centered care in oncology.[1,2] In prostate cancer, where multiple treatment options exist with similar oncologic outcomes but differing side-effect profiles, shared decision-making (SDM) is particularly critical.[3,4] To support this process, the American Urological Association (AUA) recommends that clinicians address five core domains during consultations: cancer severity, life expectancy (LE), cancer prognosis (CP), baseline function, and treatment side effects.[5] Among these, life expectancy,[6,7] cancer prognosis ,[8,9] and side effects represent the most critical factors patients must consider when evaluating treatment options.[10]

Despite the published guidelines, physician communication around these key concepts remains highly variable in both frequency and quality.[11] Recent analyses of prostate cancer consultations revealed that life expectancy, cancer prognosis, and side effects are often omitted entirely or discussed without sufficient quantification.[11,12] Even when mentioned, the level of detail ranges from general remarks to highly tailored, patient-specific risk estimates. This inconsistency poses challenges to effective shared decision-making, particularly given that many patients express a preference for quantified, personalized risk information.[7] Such variability not only undermines patient understanding but may contribute to poor decision quality and future regret,[12] highlighting the need for scalable tools to systematically assess the quality of physician risk communication.

While the value of high-quality risk communication is well recognized, practical methods for evaluating how effectively physicians communicate these key concepts are limited in real-world clinical settings.[13] Manual transcript coding remains the predominant approach for assessing communication, but this process is labor-intensive, costly, and not feasible at scale.[14] Recent advances in natural language processing (NLP)[15,16] offer new opportunities to automate these evaluations at scale, with greater efficiency and consistency.

Our recently published study[17] was the first to leverage natural language processing (NLP) to evaluate physician communication quality in prostate cancer consultations. In that work, we developed supervised machine learning models to accurately retrieve sentences pertaining

to five central decision-making domains—cancer severity, life expectancy, cancer prognosis, baseline function, and treatment side effects. We demonstrated that identifying the presence and frequency of such domain-specific content could serve as a proxy for broader consultation quality. However, the focus of that approach was limited to detecting whether key topics were discussed, without evaluating the depth, precision, or patient-specificity of how risks were communicated. In contrast, the present study moves beyond content retrieval to introduce a structured, rubric-based assessment of communication quality for each sentence. By assigning fine-grained quality scores that reflect not just topic presence but also the clarity, specificity, and quantitative precision of risk information, our framework offers a substantially more nuanced and actionable evaluation of physician–patient communication in prostate cancer care.

We introduce a novel framework for sentence-level scoring of communication quality using large language models (LLMs). Rather than merely detecting relevant content, we assess the precision and patient-specificity of each sentence using a validated scoring rubric .[14] Five key concepts central to shared decision making in prostate cancer are assessed: cancer prognosis, life expectancy, and three common treatment side effects: erectile dysfunction (ED), incontinence (INC), and irritative urinary symptoms (IUS). We formulate the task as five multiclass classification problems, one per key concept, where each sentence is assigned a numeric score (0–5) based on communication quality corresponding to the rubric .[14] To address this complex task, we evaluate two prompting strategies: rubric-only prompting and rubric-based chain-of-thought (CoT) prompting,[18] both in a few-shot in-context learning setting.[19]

By assigning quality scores grounded in established rubrics, we are able to capture not only whether key domains are discussed, but also the degree to which information is tailored, quantified, and relevant to individual patients. This enables systematic differentiation between vague, general statements and precise, patient-specific risk estimates—an essential distinction for understanding and improving shared decision-making. Leveraging the reasoning capabilities of advanced LLMs, our experiments demonstrate that rubric-informed assessment, particularly when combined with explicit chain-of-thought reasoning, allows models to approach expert-level performance even with limited annotated data.

Our contributions are threefold: (1) we develop a structured and reproducible annotation framework for scoring risk communication in prostate cancer based on previously validated rubrics;[14] (2) we demonstrate the effectiveness of GPT-4o in performing this scoring task using rubric-aligned CoT prompting; and (3) we compare LLM-based performance to supervised baselines and show that LLMs can achieve expert-level agreement, even with limited training data. Ultimately, this automated sentence-level assessment establishes a scalable foundation for evaluating and enhancing physician–patient communication quality in prostate cancer care and lays the groundwork for applications in a broad range of clinical settings.

2. Materials and Methods

2.1. *Data collection*

We collected the transcripts of 20 physician-patient encounters of men with newly diagnosed clinically localized prostate cancer. From each encounter, we extracted only the physician-spoken content and segmented it into individual sentences. Using our recently developed NLP-

based model,[13,17] we automatically identified the top five sentences per consultation that were most likely to contain relevant content for each of the five key concepts relevant to SDM: CP, LE, ED, INC, and IUS. This yielded an initial set of 100 candidate sentences for each concept. We then manually reviewed and removed sentences that were incorrectly identified by the model as relevant. After filtering, we retained 89 sentences for CP, 100 for LE, 99 for ED, 99 for INC, and 100 for IUS. To enrich the contextual information surrounding each selected sentence, we expanded it into a longer text window by combining three sentences before and after the selected sentence from the original transcript.

2.2. *Data Annotation*

To ensure high-quality data for developing and evaluating our scoring system, we created a structured annotation framework grounded in our previously validated methodology for assessing the quality of risk communication related to cancer prognosis, life expectancy, and treatment side effects for prostate cancer.[14] Our objective was to quantify the level of precision with which physicians conveyed risk-related information across the five key concepts in each selected sentence.

Each text fragment was assigned a numeric score from 0 to 5, with higher values indicating more patient-specific and quantitatively precise communication. Scores were assigned separately for each selected sentence of the five concepts.

Table 1 summarizes the scoring rubrics. For cancer prognosis, scores reflected the extent to which physicians quantified the risk of cancer-specific mortality, progression, or metastasis. Life expectancy scoring captured how physicians estimated patient longevity outside of their cancer diagnosis. Finally, the three treatment side effects—erectile dysfunction, urinary incontinence, and irritative urinary symptoms—shared a common rubric, focused on the specificity and clarity of communicated risk related to each outcome.

Two annotators with expertise in oncology and prior experience in prostate cancer communication research independently annotated all text fragments using the defined scoring rubrics for each concept. The annotation guidelines also included example text fragments to illustrate each score level. Annotations were performed using Microsoft Excel, which facilitated label entry and identification of disagreements. Discrepant labels were automatically detected by comparing the scores assigned by each annotator. All disagreements were reviewed in dedicated adjudication sessions, during which annotators discussed each case and reached consensus by referring to both the rubric criteria and the corresponding text fragments.

Table 2 presents the distribution of final annotated scores across the five key concepts. Prior to adjudication, inter-annotator agreement (IAA), computed as the micro-averaged F_1 score, was $F_1 = 85.39$ for CP, $F_1 = 83.00$ for LE, $F_1 = 83.84$ for ED, $F_1 = 84.85$ for INC, and $F_1 = 87.00$ for IUS. These scores reflect a moderate-to-strong level of agreement,[20] supporting the reliability of the annotation process.

2.3. *Approach*

In recent years, LLMs have demonstrated state-of-the-art performance across a wide range of NLP tasks, including classification, summarization, and reasoning tasks, without the need for

Table 1. Scoring rubric for Cancer Prognosis, Life Expectancy, and Side Effects. The rubrics of *Side Effects* column apply to ED, UI, and IUS.

Score	Cancer Prognosis	Life Expectancy	Side Effects
0	Not mentioned	Not mentioned	Not mentioned
1	Mention without quantification (e.g., general risk mentioned)	Mention without estimation	Name only (e.g., "erectile dysfunction")
2	Qualitative estimate only (e.g., "low risk")	Qualitative estimate only (e.g., "long life expectancy")	Qualitative terms only (e.g., "unlikely to affect you")
3	Numeric estimate without treatment comparison	Rough number of years (e.g., "20–30 years")	Numeric estimate without timeline (e.g., "30% will experience it")
4	Numeric estimate including risk with and without treatment	Probability of survival/mortality at a timepoint	Numeric estimate with timeline (e.g., "10% at 1 year")
5	Patient-specific numeric estimate at life expectancy, with and without treatment	Specific estimate based on patient factors (e.g., age, health status)	Patient-specific numeric estimate with timeline and reference to individual characteristics

Table 2. Distribution of annotated quality scores (0–5) across the five key concepts. Each row shows the number and proportion (%) of scored text fragments for a given score.

Score	CP		LE		ED		INC		IUS	
	Count	%	Count	%	Count	%	Count	%	Count	%
0	22	24.72%	32	32.00%	14	14.14%	23	23.23%	65	65.00%
1	2	2.25%	16	16.00%	28	28.28%	22	22.22%	13	13.00%
2	3	3.37%	5	5.00%	11	11.11%	18	18.18%	2	2.00%
3	25	28.09%	14	14.00%	16	16.16%	2	2.02%	6	6.00%
4	27	30.34%	–	–	21	21.21%	30	30.30%	11	11.00%
5	10	11.24%	33	33.00%	9	9.09%	4	4.04%	3	3.00%

supervised fine-tuning methods.[21] These models can be adapted to new tasks using *in-context learning* (ICL) techniques, where task-specific behavior is induced through natural language instructions and a small number of labeled examples embedded in the prompt (known as "few-shot prompting"[19]). Unlike traditional supervised learning, this approach does not require parameter updates or large amounts of labeled data, making it highly adaptable for low-resource or rapidly evolving domains.[22]

For our purpose, we harness the predictive capabilities of LLMs within a few-shot ICL framework for automatically scoring physician communication about key concepts in prostate cancer. We formulate the problem as five independent multiclass text classification tasks, one for each shared decision-making (SDM) concept: cancer prognosis, life expectancy, erectile dysfunction, urinary incontinence, and irritative urinary symptoms. Given a text fragment

from a prostate cancer consultation, the goal for each task is to assign a numeric score from 0 to 5, indicating the precision and patient-specificity with which the corresponding concept is discussed. We deployed two prompting strategies for automatic scoring: (1) a rubric-based strategy, where the model is expected to follow a set of explicit scoring rules; and (2) a rubric + chain-of-thought (CoT)[18] strategy, which further decomposes the scoring task into a sequence of structured reasoning steps. We detailed each strategy next.

2.3.1. *Rubric-based Prompting*

In the rubric-based strategy, we constructed prompts that directly instructed the model to assign a score based on the rubric definitions (see Section 2.2). Each prompt included task instructions, the full scoring rubric for the target key concept, and one or more few-shot examples consisting of a consultation fragment and its corresponding numeric score. The output format required the model to return only a numeric score from 0 to 5. An example of the rubric-based prompt used for scoring the cancer prognosis concept is shown in Table 3. The same structure was used to create prompts for the other four concepts, each time substituting in the appropriate rubric and task-specific few-shot examples.

2.3.2. *Rubric + Chain-of-Thought Prompting*

To encourage more interpretable and structured predictions, we also implemented a rubric + CoT prompting strategy. Chain-of-thought prompting is a technique that guides LLMs to reason through problems in a step-by-step manner, rather than producing an answer directly from the input.[18] This approach has been shown to improve performance in tasks that require multi-step reasoning, by explicitly decomposing complex decision-making into intermediate steps.[22] Here, we leverage CoT to augment the standard rubric-based prompt with an explicit set of reasoning instructions corresponding to each decision criterion in the scoring rubric. The model was instructed to reason through a series of decision steps that aligned with the structure of the 0–5 scoring rubric (see Table 1). Each step represented a condition that must be met to proceed to the next score level. The output format consisted of intermediate reasoning steps followed by the final score prediction. An example of the rubric + CoT prompt is shown in Table 4. The same structure was used for all five SDM key concepts, with each prompt adapted to reflect the decision criteria and rubric levels defined for that specific concept.

2.4. *Baseline*

To evaluate the performance of our LLM-based method, we compared it against a conventional supervised learning baseline using Bidirectional Encoder Representations from Transformers (BERT)-based models.[23] Unlike large autoregressive models such as GPT,[19] which are optimized for open-ended generation tasks, our baseline models are encoder-based transformers trained using a masked language modeling objective.[24] These models are more efficient to fine-tune and remain widely used for classification tasks in both general and domain-specific NLP applications. In this work, we fine-tuned BERT-based models within a multiclass text classification framework to predict physician communication scores across the five SDM key

Table 3. Example of rubric-based prompting for scoring the cancer prognosis concept. The prompt begins with task instructions and the scoring rubric, followed by a series of few-shot examples, each comprising a text fragment from a physician–patient consultation and its corresponding numeric score.

Instruction	You are an expert reviewer of physician–patient prostate-cancer consultations. Your task is to assign a single numeric score (0–5) for a given text segment **according to the cancer-prognosis rubric** below. Read the entire segment carefully, then follow the rubric exactly. **RUBRIC** • **Score 0:** No mention of prostate-cancer mortality, metastasis, or progression. • **Score 1:** Risk is mentioned, but not described qualitatively or numerically. • **Score 2:** Risk is described qualitatively only. • **Score 3:** Risk is quantified numerically **without** a comparison of risk with vs. without treatment. • **Score 4:** Risk is quantified numerically **and** includes a comparison of risk with vs. without treatment. • **Score 5:** Risk is quantified numerically, includes a treatment comparison, **and** is quoted at the patient's projected life expectancy.
Input	*Text:* "Well, we have data from about 25 years out from the diagnosis in cancers like this. And what we found in those trials is that **for cancer like you have, the risk of those cancers over, say, 25 years may be around 15 to 20 percent risk of dying of the cancer. And if you do treatment, the risk of dying of the cancer goes down to, say, something like five to 10 percent.** So it roughly cuts the risk of the cancer in half." *Provide a numeric score (0-5) based on the entire text segment:*
Output	**4**
...	...
Inference	*Text:* "This nomogram is saying that you're going to live 11 years. So, you're living to 71 years of age. None of us live forever, we all die of something, so the question is what is the likelihood you'll die of this cancer if you do nothing? And it's 47 percent." *Provide a numeric score (0-5) based on the entire text segment:*

concepts. Specifically, we evaluated the following two model variants:

RoBERTa-large A large-scale variant of the RoBERTa model, pretrained on 160 GB of general-domain text using a masked language modeling objective.[25] With approximately 355 million parameters, it removes BERT's next-sentence prediction objective and incorporates dynamic masking to improve contextual representations.

PubMedBERT-large A domain-specific transformer model with 335 million parameters, pretrained from scratch on PubMed abstracts.[26] Designed for biomedical NLP tasks, PubMedBERT is better suited to capture domain-specific terminology than general-domain models.

Table 4. Example of rubric + chain-of-thought prompting for scoring the cancer prognosis concept. Reasoning steps are required to justify the final numeric score.

Instruction	You are an expert reviewer of physician-patient prostate cancer consultations. Your task is to assign a single numeric score (0–5) for a given text segment **based on the cancer-prognosis rubric by following the structured reasoning steps below.** **STEP-BASED RUBRIC** • **Step 1:** Does the text mention risk of mortality, survival, or metastasis due to prostate cancer? – If no, **score 0** – If yes, proceed to step 2 • **Step 2:** Is the risk described qualitatively or numerically? – If risk is not quantified, **score 1** – If risk is described qualitatively, **score 2** – If risk is described numerically, proceed to step 3 • **Step 3:** Is a comparison made between risk with and without treatment? – If no, **score 3** – If yes, proceed to step 4 • **Step 4:** Is the risk quoted at the patient's projected life expectancy? – If no, **score 4** – If yes, **score 5**
Input	*Text:* "Well, we have data from about 25 years out from the diagnosis in cancers like this. And what we found in those trials is that **for cancer like you have, the risk of those cancers over, say, 25 years may be around 15 to 20 percent risk of dying of the cancer. And if you do treatment, the risk of dying of the cancer goes down to, say, something like five to 10 percent.** So it roughly cuts the risk of the cancer in half." *Provide step-by-step reasoning for the score (0–5) based on the entire text segment:*
Output	• **Step 1:** Yes, the text mentions "risk of dying of the cancer." • **Step 2:** A numerical risk is provided ("15 to 20 percent"). • **Step 3:** Yes, a comparison is made between with and without treatment ("goes down to 5 to 10 percent"). • **Step 4:** No, the risk is quoted at 25 years but not explicitly linked to the patient's life expectancy. **Score: 4**
...	...
Inference	*Text:* "This nomogram is saying that you're going to live 11 years. So, you're living to 71 years of age. None of us live forever, we all die of something, so the question is what is the likelihood you'll die of this cancer if you do nothing? And it's 47 percent." *Provide step-by-step reasoning for the score (0–5) based on the entire text segment:*

2.5. *Experiments*

We split each annotated dataset into training and testing sets using stratified sampling to preserve the distribution of scores (0–5). For each key concept, 40% of the data was used for

training and 60% for testing. Specifically, the number of examples used for training/testing per concept was: CP (35/54), LE (40/60), ED (39/60), INC (39/60), and IUS (40/60).

To construct the input text fragments used for both LLM prompting and baseline classifiers, we expanded each selected sentence by including the three preceding and three following sentences from the original consultation transcript. This 7-sentence context window was chosen based on prior experimentation, where we systematically compared different window sizes and found that including three sentences before and after led to the best scoring performance across key concepts.

Both prompting strategies were implemented using the GPT-4o model, accessed via the Microsoft Azure OpenAI API. To reduce response variability and encourage more deterministic scoring outputs, we set the generation *temperature* to 0.3 and the *top-p* sampling parameter to 0.4, based on initial experimentation. All other generation parameters were kept at their default values. We evaluated both few-shot and zero-shot variants of each prompting strategy:

Zero-shot prompting. The model received only task instructions, with no examples included in the prompt.

Few-shot prompting. Prompts included a small number of annotated examples spanning the full 0–5 score range. The number of examples per concept (6–10) was empirically selected based on training performance, with no consistent gains observed beyond these values: 10 for CP, 7 for LE, 7 for ED, 8 for INC, and 6 for IUS.

For baseline comparisons, we trained RoBERTa-large and PubMedBERT-large classifiers on the same 40% training splits. For each concept, we fine-tuned the models as 6-class (0–5 scores) classifiers using cross-entropy loss. Input text fragments were tokenized and padded to a maximum sequence length of 512 tokens. Models were trained for 10 epochs using a batch size of 6 and learning rate of 2×10^{-5}.

2.6. *Evaluation Metrics*

We evaluated the multiclass classification performance of the baseline models and generative approaches using standard metrics: Precision, Recall, and F_1-score. For each class label (scores 0 through 5), we define true positives (TP) as the number of fragments correctly classified with a given score, false positives (FP) as the number of fragments incorrectly predicted to have that score, and false negatives (FN) as the number of fragments with that score in the ground truth but misclassified by the model. *Precision* (P) measures the proportion of correct predictions for a given score among all instances predicted with that score ($P = \frac{TP}{TP+FP}$); *Recall* (R) measures the proportion of correct predictions for a given score among all true instances of that score ($R = \frac{TP}{TP+FN}$); and the *F_1-score* (F1) is the harmonic mean of precision and recall, balancing the trade-off between the two metrics ($F1 = 2 \times \frac{P \times R}{P+R}$). We evaluated each SDM key concept independently and report the micro-averaged F_1 score to aggregate performance across all classes for each concept.

3. Results

Table 5 presents the micro-averaged F_1 scores for both baseline classifiers and LLM-based prompting strategies across the five SDM key concepts. The results show that our best-

performing method (rubric + CoT with few-shot prompting) consistently outperforms both baseline classifiers and alternative prompting strategies. Specifically, this approach achieved the highest F_1 scores across all five concepts: cancer prognosis (92.00), life expectancy (86.67), erectile dysfunction (85.00), incontinence (85.00), and irritative urinary symptoms (91.67).

When comparing baseline classifiers to LLM-based approaches, we observe a substantial performance gap across all key concepts. While the fine-tuned transformer models achieved moderate F_1 scores, most notably RoBERTa-large on IUS and LE (78.33 and 73.33, respectively), they consistently underperformed relative to the prompting-based methods. This discrepancy is likely due to the limited size of the training datasets. With only 35 to 40 training fragments available per concept, the baseline models lacked sufficient data to effectively learn the complex and domain-specific scoring patterns required for this task. In contrast, the use of rubric-based and rubric + CoT prompting strategies enabled LLMs to effectively perform the scoring task with minimal reliance on annotated training data.

Comparing different prompting strategies, we observe two consistent trends. First, incorporating few-shot examples improves performance over zero-shot prompting. For instance, the rubric-only approach improved from 60.00 to 73.33 F_1 on ED and from 71.67 to 86.67 F_1 on LE when moving from zero-shot to few-shot prompting. Second, adding CoT reasoning further enhances performance. For example, rubric + CoT with zero-shot prompting achieved 78.00 F_1 on CP and 88.33 F_1 on IUS, outperforming rubric-only prompting in both zero-shot and few-shot settings.

Table 5. Micro-averaged F_1 scores (%) for baseline classifiers and LLM-based prompting strategies across the five key concepts. The best-performing method for each concept is shown in bold.

Approach	Model/Setting	CP	LE	ED	INC	IUS
Baseline	RoBERTa-large	42.00	73.33	41.67	53.33	78.33
	PubMedBERT-large	52.00	63.33	45.00	41.67	68.33
LLM (Rubric)	Zero-shot	58.00	71.67	60.00	63.33	78.33
	Few-shot	76.00	86.67	73.33	65.00	85.00
LLM (Rubric + CoT)	Zero-shot	78.00	76.67	70.00	78.33	88.33
	Few-shot	**92.00**	**86.67**	**85.00**	**85.00**	**91.67**

4. Discussion

Our findings show that rubric + CoT prompting is the most effective strategy for scoring physician communication and the most interpretable. By guiding the LLM to reason through each scoring criterion in a structured, stepwise manner, this approach makes the rationale behind each prediction transparent. In healthcare, such interpretability is critical not only to build trust in AI-assisted evaluations but also to support their integration into clinical practice. Interpretable scoring systems can also offer more actionable and targeted feedback to physicians, highlighting specific aspects of their communication that could be improved.

To examine the performance of this strategy, we conducted a detailed error analysis of the

LLM's predictions using rubric + CoT prompting with few-shot examples. The confusion matrices for each concept (Figure 1) show that, despite strong overall results, the LLM exhibited difficulty distinguishing between adjacent score levels for certain key concepts, particularly LE, ED, and INC.

For LE, the most frequent pattern included three instances where the LLM predicted a score of 5 instead of 3. In these cases, the text provided a rough estimate of years (e.g., "40 years") alongside general references to the patient's age (e.g., "you're 52"). However, such expressions lacked the detailed patient-specific estimate required for score 5.

In the case of ED, five errors involved the LLM predicting score 0 instead of 1. These fragments typically referenced surgical procedures or anatomical structures related to erectile function (e.g., "nerve-sparing techniques") without explicitly naming ED as a side effect. Although suggestive, the absence of direct mention led the LLM to conclude that the key concept was not discussed.

For INC, in four cases the LLM predicted score 1 instead of 2. These cases involved qualitative but vague language, often using generalized statements like "everybody has urinary incontinence", which the LLM interpreted as a mere mention rather than a qualitative risk estimate.

Importantly, many of the ambiguous cases that challenged the LLM also proved difficult for human annotators to score consistently. These fragments, often characterized by imprecise, indirect, or incomplete references to risk, were a common source of disagreement during the initial annotation phase. Given this context, the performance of our best LLM-based approach is particularly promising: its F_1 scores are broadly comparable to the pre-adjudication IAA values (see Section 2.2), suggesting that the system can approximate expert-level scoring in this complex classification task.

4.1. *Limitations and Future Work*

While our rubric + CoT prompting with the GPT-4o model achieves strong performance across all five key concepts, several limitations warrant further investigation. First, the dataset was drawn from a relatively small set of prostate cancer consultations (N=20), which may limit generalizability across institutions, clinicians, and patient populations. Future work will explore larger and more diverse corpora that encompass a wider range of provider communication styles and patient demographics. Second, our approach relies on the accuracy of a preceding NLP-based model used to identify candidate sentences for scoring.[17] While this model has been previously developed and validated to identify key concept-related sentences in prostate cancer consultations, any misclassifications at this selection stage may impact downstream scoring performance. Third, our study evaluated communication quality at the fragment level, using short, context-rich segments centered on key sentences. This design reflects how the system is intended to operate in clinical practice alongside our NLP-based content identifier. Nevertheless, ongoing efforts will focus on developing encounter-level scoring strategies—such as selecting the highest-scoring fragment—to better represent overall communication quality across a full consultation. Future work will also explore the integration of these components in real-world clinical workflows to evaluate physician risk communication at scale and ultimately

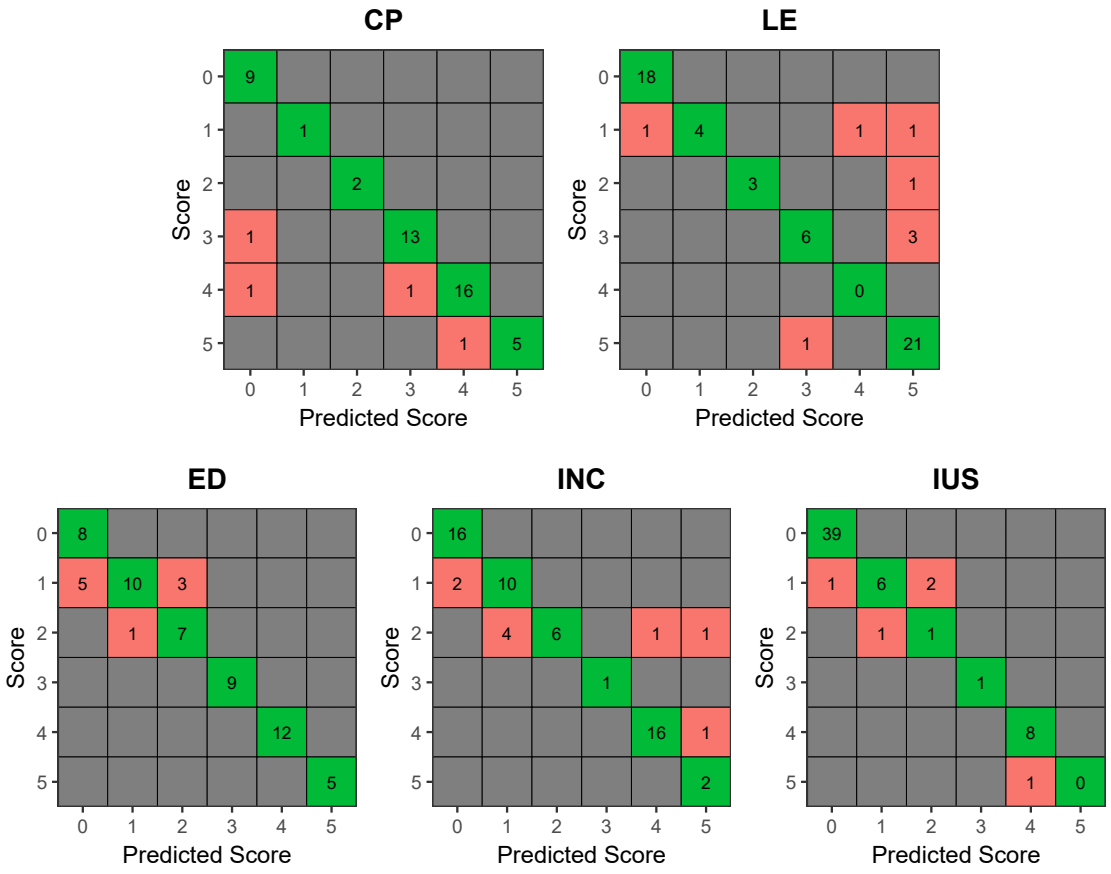

Fig. 1. Confusion matrices for each of the five key concepts using the best-performing system (rubric + CoT with few-shot prompting). Each matrix displays the distribution of predicted versus true scores (0–5).

support more informed, patient-centered decision making. Lastly, our methodology has thus far been applied only to prostate cancer, which may limit its applicability to other clinical domains. However, the underlying framework combining scoring rubrics with LLM-based approaches, has the potential to be adapted for risk communication assessment across other cancer types and medical decision-making contexts.

5. Conclusion

We present a novel framework for evaluating the quality of physician risk communication in prostate cancer consultations using LLMs. By combining validated scoring rubrics with CoT prompting, our method enables interpretable, sentence-level assessment of how precisely and patient-specifically key concepts are communicated. Across five clinically relevant domains, including cancer prognosis, life expectancy, and three side effects, our best-performing model achieved strong results and expert-level agreement. These findings highlight the potential of LLMs to support scalable, automated evaluations of physician–patient communication and lay the groundwork for real-time feedback tools to improve shared decision-making in oncology

and beyond.

Acknowledgments

This research was supported by the National Cancer Institute of the National Institutes of Health under Award Number R01CA290559 to TJD. The content is solely the responsibility of the authors and does not necessarily represent the official views of the National Institutes of Health.

References

1. T. J. Daskivich, M. S. Litwin and D. F. Penson, Effect of Age, Tumor Risk, and Comorbidity in a U.S. Population–Based Cohort of Men With Prostate Cancer, *Annals of Internal Medicine* **159**, p. 370 (2013).
2. L. F. van de Water, J. J. van Kleef, W. P. M. Dijksterhuis, I. Henselmans, H. G. van den Boorn, N. M. Vaarzon Morel, K. F. Schut, J. G. Daams, E. M. A. Smets and H. W. M. van Laarhoven, Communicating treatment risks and benefits to cancer patients: a systematic review of communication methods, *Quality of Life Research* **29**, 1747 (2020).
3. M. S. Litwin and H.-J. Tan, The Diagnosis and Treatment of Prostate Cancer: A Review, *JAMA* **317**, 2532 (06 2017).
4. T. J. Wilt, T. N. Vo, L. Langsetmo, P. Dahm, T. Wheeler, W. J. Aronson, M. R. Cooperberg, B. C. Taylor and M. K. Brawer, Radical Prostatectomy or Observation for Clinically Localized Prostate Cancer: Extended Follow-up of the Prostate Cancer Intervention Versus Observation Trial (PIVOT), *European Urology* **77**, 713 (2020).
5. D. V. Makarov, K. Chrouser, J. L. Gore, J. Maranchie, M. E. Nielsen, C. Saigal, C. Tessier and A. Fagerlin, AUA White Paper on Implementation of Shared Decision Making into Urological Practice, *Urology Practice* **3**, 355 (2016).
6. P. C. Albertsen, D. F. Moore, W. Shih, Y. Lin, H. Li and G. L. Lu-Yao, Impact of Comorbidity on Survival Among Men With Localized Prostate Cancer, *Journal of Clinical Oncology* **29**, 1335 (2011).
7. T. J. Daskivich, R. Gale, M. Luu, D. Khodyakov, J. T. Anger, S. J. Freedland and B. Spiegel, Patient Preferences for Communication of Life Expectancy in Prostate Cancer Treatment Consultations, *JAMA Surgery* **157**, 70 (01 2022).
8. A. Bill-Axelson, L. Holmberg, H. Garmo, K. Taari, C. Busch, S. Nordling, M. Häggman, S.-O. Andersson, O. Andrén, G. Steineck, H.-O. Adami and J.-E. Johansson, Radical Prostatectomy or Watchful Waiting in Prostate Cancer — 29-Year Follow-up, *New England Journal of Medicine* **379**, 2319 (2018).
9. R. D. Vromans, M. C. van Eenbergen, G. Geleijnse, S. Pauws, L. V. van de Poll-Franse and E. J. Krahmer, Exploring Cancer Survivor Needs and Preferences for Communicating Personalized Cancer Statistics From Registry Data: Qualitative Multimethod Study, *JMIR Cancer* **7**, p. e25659 (Oct 2021).
10. G. Elwyn, P. J. Barr and S. W. Grande, Patients recording clinical encounters: a path to empowerment? assessment by mixed methods, *BMJ Open* **5** (2015).
11. T. J. Daskivich, R. Gale, M. Luu, A. Naser-Tavakolian, A. Venkataramana, D. Khodyakov, J. T. Anger, E. Posadas, H. Sandler, B. Spiegel and S. J. Freedland, Variation in Communication of Competing Risks of Mortality in Prostate Cancer Treatment Consultations, *The Journal of Urology* **208**, 301 (2022).
12. T. J. Daskivich, A. Naser-Tavakolian, R. Gale, M. Luu, N. Friedrich, A. Venkataramana, D. Khodyakov, E. Posadas, H. Sandler, B. Spiegel and S. J. Freedland, Variation in communi-

cation of side effects in prostate cancer treatment consultations, *Prostate Cancer and Prostatic Diseases* **28**, 145 (2025).
13. T. Daskivich, M. Luu, R. Gale, D. Khodyakov, S. Freedland and B. Spiegel, MP24-03 Development and Validation of a Natural Language Processing System to Identify Information on Key Tradeoffs in Prostate Cancer Treatment Consultations, *Journal of Urology* **211**, p. e392 (2024).
14. A. Hernández Tirado, M. Luu, J. Tan and T. J. Daskivich, MP23-09 A Framework for Evaluating the Quality of Risk Communication in Prostate Cancer Treatment Consultations, *Journal of Urology* **213**, p. e798 (2025).
15. A. Jerfy, O. Selden and R. Balkrishnan, The Growing Impact of Natural Language Processing in Healthcare and Public Health, *INQUIRY: The Journal of Health Care Organization, Provision, and Financing* **61** (2024).
16. M. Cascella, F. Semeraro, J. Montomoli, V. Bellini, O. Piazza and E. Bignami, The Breakthrough of Large Language Models Release for Medical Applications: 1-Year Timeline and Perspectives, *Journal of Medical Systems* **48** (2024).
17. R. Zheng, N. A. Friedrich, M. Luu, R. Gale, D. Khodyakov, S. J. Freedland, B. Spiegel and T. J. Daskivich, Development and Validation of a Natural Language Processing System to Assess Quality of Physician Communication in Prostate Cancer Consultations, *Prostate Cancer and Prostatic Diseases* (2025).
18. J. Wei, X. Wang, D. Schuurmans, M. Bosma, b. ichter, F. Xia, E. Chi, Q. V. Le and D. Zhou, Chain-of-thought prompting elicits reasoning in large language models, in *Advances in Neural Information Processing Systems*, eds. S. Koyejo, S. Mohamed, A. Agarwal, D. Belgrave, K. Cho and A. Oh (Curran Associates, Inc., 2022).
19. T. Brown, B. Mann, N. Ryder, M. Subbiah, J. D. Kaplan, P. Dhariwal, A. Neelakantan, P. Shyam, G. Sastry, A. Askell, S. Agarwal, A. Herbert-Voss, G. Krueger, T. Henighan, R. Child, A. Ramesh, D. Ziegler, J. Wu, C. Winter, C. Hesse, M. Chen, E. Sigler, M. Litwin, S. Gray, B. Chess, J. Clark, C. Berner, S. McCandlish, A. Radford, I. Sutskever and D. Amodei, Language Models are Few-Shot Learners, in *Advances in Neural Information Processing Systems*, eds. H. Larochelle, M. Ranzato, R. Hadsell, M. Balcan and H. Lin (Curran Associates, Inc., 2020).
20. M. L. McHugh, Interrater reliability: the kappa statistic, *Biochemia Medica* **22**, 276 (2012).
21. T. Kojima, S. S. Gu, M. Reid, Y. Matsuo and Y. Iwasawa, Large language models are zero-shot reasoners, in *Advances in Neural Information Processing Systems*, eds. S. Koyejo, S. Mohamed, A. Agarwal, D. Belgrave, K. Cho and A. Oh (Curran Associates, Inc., 2022).
22. Y. Ge, Y. Guo, S. Das, M. A. Al-Garadi and A. Sarker, Few-shot learning for medical text: A review of advances, trends, and opportunities, *Journal of Biomedical Informatics* **144**, p. 104458 (2023).
23. J. Devlin, M.-W. Chang, K. Lee and K. Toutanova, BERT: Pre-training of Deep Bidirectional Transformers for Language Understanding, in *Proceedings of the 2019 Conference of the North American Chapter of the Association for Computational Linguistics: Human Language Technologies, Volume 1 (Long and Short Papers)*, (Association for Computational Linguistics, Minneapolis, Minnesota, June 2019).
24. A. Vaswani, N. Shazeer, N. Parmar, J. Uszkoreit, L. Jones, A. N. Gomez, L. u. Kaiser and I. Polosukhin, Attention is All you Need, in *Advances in Neural Information Processing Systems*, eds. I. Guyon, U. V. Luxburg, S. Bengio, H. Wallach, R. Fergus, S. Vishwanathan and R. Garnett (Curran Associates, Inc., 2017).
25. Y. Liu, M. Ott, N. Goyal, J. Du, M. Joshi, D. Chen, O. Levy, M. Lewis, L. Zettlemoyer and V. Stoyanov, RoBERTa: A Robustly Optimized BERT Pretraining Approach (2019).
26. R. Tinn, H. Cheng, Y. Gu, N. Usuyama, X. Liu, T. Naumann, J. Gao and H. Poon, Fine-tuning large neural language models for biomedical natural language processing, *Patterns* **4**, p. 100729 (2023).

SeizureFormer: A Multi-Scale Transformer for Seizure Risk Forecasting from RNS-Derived Biomarkers

Tianning Feng[3†], Juntong Ni[1†], Wei Jin[1], Ezequiel Gleichgerrcht[2]
[1]*Department of Computer Science, Emory University, Atlanta, GA, USA*
[2]*Department of Neurology, Emory University, Atlanta, GA, USA*
[3]*School of Engineering and Applied Science, University of Pennsylvania, Philadelphia, PA, USA*
[†]*E-mail: tfeng24@seas.upenn.edu, juntong.ni@emory.edu*
E-mail: wei.jin@emory.edu, eze.gleich@emory.edu

We present **SeizureFormer**, a Transformer-based model for long-horizon seizure risk forecasting (1–14 days) using structured biomarkers—interictal epileptiform activity (IEA) and long episodes (LE)—extracted from responsive neurostimulation (RNS) systems. Unlike prior models based on raw scalp EEG, SeizureFormer leverages stable RNS biomarkers and integrates multi-scale CNN patch embedding, cross-variable temporal convolution, and squeeze-and-excitation attention to capture both short-term fluctuations and long-term seizure cycles. Tested across five patients and multiple prediction windows (1–14 days), SeizureFormer achieved state-of-the-art performance with **mean ROC AUC** of *79.44%* and **mean PR AUC** of *76.29%* across five patients and four prediction windows. Compared to statistical, classical ML, and deep learning baselines, it demonstrates superior generalizability under class imbalance. Clinically, it enables actionable multi-day forecasting, supporting personalized and proactive intervention in epilepsy care by forecasting seizure-related events 1 to 14 days ahead.

Keywords: Seizure Forecasting; Epilepsy; Transformer; Deep Learning; RNS System

1. Introduction

Epilepsy is a chronic neurological disorder characterized by recurrent and unpredictable seizures, affecting over 50 million people worldwide.[1,2] A central clinical need is the ability to detect or forecast seizure risk in advance, enabling timely intervention and improved patient management.[2,3]

Seizure risk detection generally falls into two categories: seizure classification and seizure forecasting. Early research predominantly focused on seizure classification, which aims to detect ongoing or imminent seizures by identifying ictal or pre-ictal segments from recent EEG recordings. In contrast, seizure forecasting aims to estimate the probability of future seizure occurrence over longer horizons-often days in advance-without access to EEG signals from the forecasted time window, relying solely on historical neural activity.[4,5] While classification supports reactive interventions, forecasting offers a critical opportunity for preventive care and long-term planning.

Early efforts in seizure forecasting primarily relied on scalp EEG recordings combined

© 2025 The Authors. Open Access chapter published by World Scientific Publishing Company and distributed under the terms of the Creative Commons Attribution Non-Commercial (CC BY-NC) 4.0 License.

with statistical or deep learning models.[4,5] However, scalp EEG signals are inherently non-stationary and highly susceptible to physiological and environmental factors such as brain state transitions, medication effects, fatigue, and electrode shifts.[6,7] These fluctuations make it difficult to model consistent long-term patterns, often requiring frequent retraining and resulting in poor generalization across patients—especially for multi-day prediction settings.[8]

As an alternative, responsive neurostimulation (RNS) systems extract seizure-related signals such as interictal epileptiform activity (IEA) and long episodes (LE), which are validated seizure risk indicators that reflect sustained EEG abnormalities associated with cortical excitability.[9,10] These structured features offer a more stable and interpretable basis for seizure risk assessment compared to scalp EEG. Recent studies leveraging RNS biomarkers have explored statistical,[8] machine learning, and deep learning methods[11] for seizure risk forecasting, achieving promising results yet several critical limitations remain:

- **Limited multi-scale modeling ability:** RNS data exhibits multi-scale temporal patterns, including daily, weekly, and potentially longer-term rhythms.[12] However, existing work often fails to capture these complex temporal dependencies, focusing either on narrow time windows or specific periodicities.
- **Limited capacity to model both short-term and long-term dependencies:** Seizure risk is influenced by both immediate neural fluctuations and long-range historical patterns. While statistical models effectively capture long-term trends, they lack the resolution for short-term dynamics. Conversely, common deep learning models excel in local pattern recognition but struggle with integrating seizure periodicities across time scales.[8,11] A unified approach that can jointly model both short-term variability and long-term seizure cycles is needed.
- **Overreliance on raw RNS data, leading to high personalization requirements:** Many existing models rely heavily on raw RNS recordings, which are noisy, complex, and patient-specific. This often requires extensive per-patient training and limits generalizability.[9,10] Shifting towards more structured and stable biomarkers could improve model scalability and clinical applicability.

To address these challenges, we propose SeizureFormer—a deep learning model that jointly captures multi-scale seizure dynamics, bridges short- and long-term dependencies, and reduces reliance on raw patient-specific data. In essence, we are faced with three key challenges. **First, how to extract seizure-relevant features from time-series signals with varying periodicity?** We address this by employing a CNN-based patch embedding module with multiple kernel sizes, allowing the model to capture both short-term fluctuations and long-term cycles from the input signals. Additionally, we introduce a Cross-Variable Temporal 2D Conv (CVT-Conv) module to explicitly model local interactions and aggregate contextual information across different A+B pattern channels. The integration of these two modules is critical for effectively modeling epileptic activity across multiple temporal scales and compensating for the Transformer's limited inductive bias toward locality and temporal hierarchy. **Second, how to bridge the gap between short-term and long-term forecasting, which are often handled separately in prior work?** We tackle this by introducing a hierar-

chical Transformer architecture that jointly models local and global temporal dependencies, enabling unified forecasting across different time horizons. **Third, how to reduce model dependence on raw, highly individualized EEG signals?** Instead of using raw RNS data, we leveraged the RNS system's continuous monitoring of EEG-based hyperexcitable patterns (A/B spike detections and long episodes) to reduce the reliance on raw signal processing. Together, these components form SeizureFormer, a robust solution for generalized, multi-timescale seizure risk forecasting.

Our model demonstrates leading performance across multiple evaluation settings. Extensive experiments show that SeizureFormer achieves the highest **ROC AUC (79.44%)** and **PR AUC (76.29%)**, significantly outperforming baseline statistical and recurrent models. Furthermore, our approach extends seizure forecasting beyond conventional short-term windows, enabling **multi-day (1-14 days) risk estimation**, which is critical for clinical decision-making and patient management. Our contributions can be summarized as follows:

(1) We develop the first Transformer-based model for seizure risk forecasting, SeizureFormer, capable of capturing both short-term fluctuations and long-horizon seizure cycles. This enables accurate seizure forecasting across different time scales up to 14 days ahead, addressing the limitations of prior approaches.
(2) Our model relies on A+B spike patterns and Long Episodes (LE) as seizure risk proxies, reducing dependence on large volumes of raw EEG data while maintaining predictive robustness and generalizability.
(3) Extensive experiments demonstrate that SeizureFormer outperforms statistical and deep learning baselines in both short-term and long-term seizure forecasting, achieving superior predictive accuracy and clinical applicability.

2. Related Works

EEG-based Seizure Risk Forecasting: Traditional seizure forecasting models rely on scalp EEG data, using statistical and deep learning methods to estimate seizure risk. Statistical approaches such as Poisson regression, GLMs, and logistic regression model seizure probability through probabilistic frameworks.[13] Proix's study[8] showed that multi-day seizure cycles could be captured using Poisson regression on long-term iEEG, achieving above-chance forecasting in approximately 66% of patients. While effective for modeling cyclic trends, these methods struggle with the fine-grained temporal resolution required for real-time forecasting. To address this, deep learning models like RNNs, GRUs, and LSTMs have been applied to capture sequential dependencies in EEG signals.[14,15] Though they improve short-term prediction, they face limitations in modeling long-range patterns and generalizing across patients,[16] partly due to the variability of raw scalp EEG.[6,7] Recent studies have attempted to incorporate multi-day periodicity and additional physiological biomarkers such as heart rate (HR) and skin conductance (SC).[16] However, few approaches integrate both short-term fluctuations and long-term seizure cycles, limiting their clinical applicability.

RNS-Based Seizure Risk Forecasting: The RNS system, compared to raw scalp EEG, provides more stable and temporally correlated biomarkers such as interictal epileptiform ac-

tivity (IEA) and long episodes (LE),[9,10] making it a reliable source for seizure-related forecasting. Several studies have explored this potential: a past study[17] demonstrated the feasibility of using statistical and classical machine learning methods, including SVM and random forests, to forecast seizure frequency from long-term RNS recordings, capturing meaningful patient-specific temporal patterns with AUC ranging from 70% to 89%. Deep learning approaches have also been applied; for example, Constantino[18] and Peterson[11] utilized CNN-based models for seizure detection and onset prediction, achieving high accuracy on short-term tasks. While these studies show strong potential for leveraging structured RNS data, they still face limitations: most models heavily rely on patient-specific features and require extensive per-patient training due to the raw, individualized nature of RNS signals. Moreover, few models have explored unified architectures capable of simultaneously capturing short-term variability and long-term seizure periodicity from RNS-derived features.

Long-Term Seizure Risk Forecasting: Recent work has extended seizure prediction from short- to long-term horizons using RNS data. For example, Yang's study[19] showed that Poisson regression with SVMs achieves AUCs above 70% for up to 6-day forecasts, highlighting the potential of cyclic RNS features. However, most models target short or long-term patterns in isolation, and few explore learning both simultaneously. To address this, we propose a Transformer-based model that captures short-term fluctuations and long-range dependencies via multi-head self-attention. Compared to GRUs and LSTMs, Transformers mitigate vanishing gradients and better capture long-range periodicity through global attention mechanisms. We also benchmark statistical, classical ML, and deep learning baselines, showing that our approach achieves superior performance in modeling seizure dynamics across time scales.

3. Methods

In this section, we first present a general problem formulation for seizure risk forecasting. We then describe how RNS-derived features are utilized to support the forecasting process.

3.1. *Problem Formulation and Feature Selection*

Problem Formulation: We formulate seizure risk forecasting as a binary risk estimation task, where the objective is to predict whether a given day falls into a high-risk seizure period based on historical biomarkers of brain excitability. Given an input time series $\mathbf{X} = [\mathbf{x}_{t-n}, \mathbf{x}_{t-n+1}, ..., \mathbf{x}_t] \in \mathbb{R}^{n \times d}$, where $\mathbf{x}_t$ represents the extracted feature set at time t, d is the feature dimension (i.e., the number of input variables), and n is the sequence length, defining the number of past time steps. The goal is to estimate the seizure risk for the subsequent h days. In this study, we evaluate four forecasting horizons: $h \in 1, 3, 7, 14$.

$$y_h = f(\mathbf{x}_{t-n}, \mathbf{x}_{t-n+1}, ..., \mathbf{x}_t), \tag{1}$$

where $y_h \in \{0, 1\}$ is a binary label determined by the presence of long episodes.

RNS-Based Feature and Label Selection: Due to the non-stationary nature of raw scalp EEG, we chose to use data collected by the RNS system. While raw RNS data can still be

varying among different patients and across time, some clinically relevant biomarkers can be extracted from raw RNS data to represent seizure proxy in a more stable way. To capture these clinically relevant dynamics, we extract two structured biomarkers from the RNS system:

- **A+B Patterns (IEA Surrogate Biomarkers):** The RNS system continuously monitors electrocorticographic activity and detects patient-specific epileptiform discharges. These patterns provide a structured time-series representation of cortical excitability, making them a more stable biomarker for seizure forecasting compared to raw EEG. For each device with two channels, we extract Pattern A and B from both channels to get two combined features: *Pattern A + B on Channel 1* and *Pattern A + B on Channel 2*. These serve as the input features $\mathbf{x}_t \in \mathbb{R}^2$, and the full input sequence $\mathbf{X} = [\mathbf{x}_{t-n}, \ldots, \mathbf{x}_t] \in \mathbb{R}^{n\times 2}$ is used to predict the seizure risk label y_h.
- **Long Episodes (LEs) as Seizure Risk Indicators:** The RNS system also records Long Episodes (LEs), defined as sustained abnormal electrocorticographic activity exceeding a predefined duration threshold. Prior studies have shown that LE occurrences correlate strongly with seizure likelihood, making them an effective proxy for defining high-risk periods.[9] In our formulation, the binary label $y_h \in \{0, 1\}$ is determined based on LE activity: we assign $y_h = 1$ if the cumulative LE count or duration in the forecasting window exceeds a patient-specific threshold, indicating a high-risk period; otherwise, $y_h = 0$.

3.2. *Our Proposed Model: SeizureFormer*

Fig. 1. Overall framework of SeizureFormer.

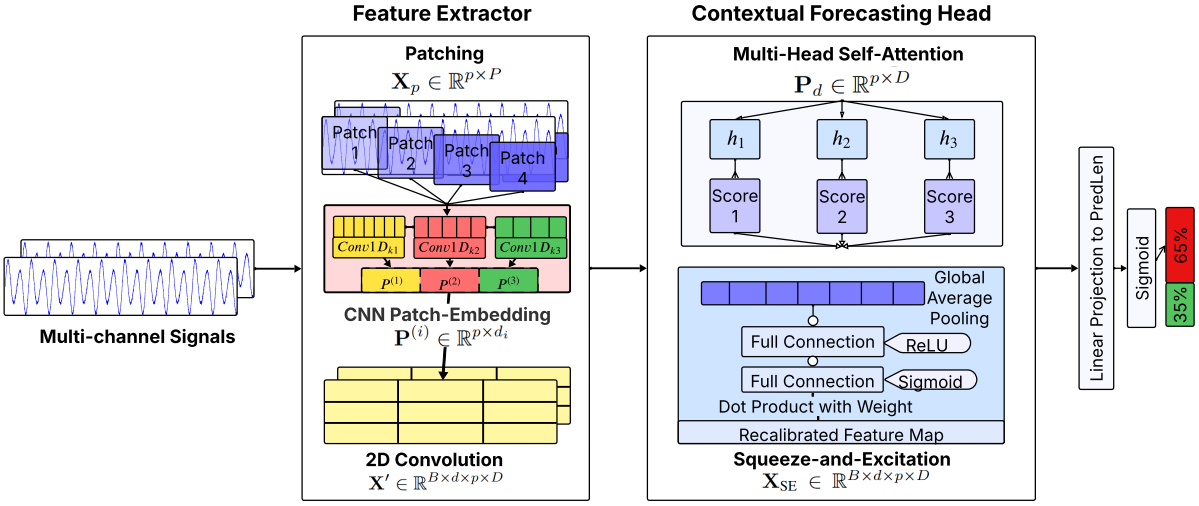

As shown in Fig. 1, *SeizureFormer* is composed of two functional components that first extract multi-scale temporal features and then model contextual risk dependencies for long-term seizure forecasting. Both of the modules will be explained below:

Multi-Scale Temporal Feature Extractor: The first stage of our model is the **Multi-Scale Temporal Feature Extractor**, which decomposes multichannel A+B signals into temporally and spatially enriched representations suitable for downstream modeling.

We begin by applying **patching** to each input channel independently. To effectively capture local seizure-relevant patterns, each univariate time series $\mathbf{X} \in \mathbb{R}^{N\times 1}$ is segmented into overlapping temporal windows, or patches, of length P and stride S:

$$\mathbf{X}_p = \{\mathbf{X}_{t:t+P} \mid t = 1, S, 2S, ..., N - P\}, \tag{2}$$

$$\mathbf{X}_p \in \mathbb{R}^{p\times P}, \tag{3}$$

where P is the *patch length*, S is the *stride*, and $p = \lfloor (N - P)/S \rfloor + 1$ is the number of resulting patches. This process reduces redundancy and enables the model to encode fine-grained temporal structure.

After patching, we perform **CNN patch embedding** to extract temporal features from each patch at multiple resolutions. This design mimics clinical intuition: seizures can manifest as both brief transients and prolonged patterns. Multi-kernel CNNs enable the model to concurrently detect different temporal signatures. The patch sequence $\mathbf{X}_p$ is processed by K parallel 1D convolutional layers with kernel sizes $\{k_1, \ldots, k_K\}$, each producing a feature map:

$$\mathbf{P}^{(i)} = \text{Conv1D}_{k_i}(\mathbf{X}_p), \tag{4}$$

$$\mathbf{P}^{(i)} \in \mathbb{R}^{p\times d_i}, \tag{5}$$

$$d_1 = \cdots = d_K, \quad i = 1, \ldots, K, \tag{6}$$

where $\text{Conv1D}_{k_i}(\cdot)$ denotes a convolution with kernel size k_i. The outputs are concatenated to form the final patch embedding:

$$\mathbf{P} = \text{Concat}\left(\mathbf{P}^{(1)}, \ldots, \mathbf{P}^{(K)}\right), \quad \mathbf{P} \in \mathbb{R}^{p\times d'}, \tag{7}$$

where $d' = \sum_{i=1}^{K} d_i$. To preserve the ordering of patches, we add a learnable position encoding:

$$\mathbf{P}_d = \mathbf{W}_P\mathbf{P} + \mathbf{W}_{\text{pos}}, \quad \mathbf{P}_d \in \mathbb{R}^{p\times D}, \tag{8}$$

where $\mathbf{W}_P$ is a trainable projection matrix and $\mathbf{W}_{\text{pos}}$ is a learnable position encoding.

Once patch-wise features have been extracted and embedded, we enhance the representation further using the **Cross-Variable Temporal 2D Conv** module. While the previous steps capture intra-channel patterns, this component explicitly models interactions across different A+B channelscapturing dependencies across spatially separated brain regions. This allows the model to learn coordinated dynamics that may underlie seizure generation. We first reshape the patch embeddings into a 4D tensor $\mathbf{X} \in \mathbb{R}^{B\times d\times p\times D}$, where B is the batch size, d is the number of channels, p is the number of patches, and D is the embedding dimension. Then, a 2D convolution is applied over the (d, p) grid:

$$\mathbf{X}' = \text{Conv2D}_{\mathcal{K}}(\mathbf{X}), \quad \mathbf{X}' \in \mathbb{R}^{B\times d\times p\times D}. \tag{9}$$

These enhancements introduce inductive biases that help the model learn local and inter-channel patterns.

Contextual Risk Modeling Module: The second component of SeizureFormer is the **Contextual Risk Modeling Module**, which integrates local features extracted by the previous stage and models global temporal dependencies to predict seizure risk.

Starting from the output of the previous convolutional step, we have a 4D tensor $\mathbf{X}' \in \mathbb{R}^{B\times d\times p\times D}$, where B is the batch size, d the number of channels, p the number of patches, and D the embedding dimension. To capture long-range dependencies across time for each channel, we apply **Multi-Head Self-Attention (MHSA)** to the patch dimension. For each attention head $j \in \{1, \ldots, h\}$, the output is computed as:

$$\begin{aligned} \mathrm{SA}_j(\mathbf{P}_d) &= \mathrm{softmax}\left(\frac{(\mathbf{P}_d\mathbf{W}_j^Q)(\mathbf{P}_d\mathbf{W}_j^K)^\top}{\sqrt{d_k}}\right)(\mathbf{P}_d\mathbf{W}_j^V), \\ MultiHead(\mathbf{P}_d) &= \left(\|_{j=1}^{h}\mathrm{SA}_j(\mathbf{P}_d)\right)\cdot\mathbf{W}^O, \end{aligned} \tag{10}$$

where $\mathbf{W}_j^Q, \mathbf{W}_j^K, \mathbf{W}_j^V$ are projection matrices for the queries, keys, and values respectively, $\mathbf{W}^O$ is the output projection, and $d_k = D/h$ is the per-head dimension. This mechanism allows the model to learn contextualized representations of each patch in the sequence.

Following attention, we further enhance the representation using a **Squeeze-and-Excitation Feature Recalibration** block. This lightweight module adaptively emphasizes the most seizure-relevant channels by learning to reweight their contributions based on global context. It first summarizing the information from each channel via global average pooling:

$$g_{b,d} = \frac{1}{p\cdot D}\sum_{a=1}^{p}\sum_{c=1}^{D}\mathbf{X}_{b,d,a,c}, \tag{11}$$

and then passing this summary through a two-layer feedforward network:

$$\mathbf{s} = \sigma\left(\mathbf{W}_2\cdot\mathrm{ReLU}(\mathbf{W}_1\mathbf{g})\right), \quad \mathbf{X}_{\mathrm{SE}} = \mathbf{X}'\cdot\mathbf{s}.\mathrm{unsqueeze(-1)}.\mathrm{unsqueeze(-1)}, \tag{12}$$

where $\mathbf{W}_1, \mathbf{W}_2$ are learnable parameters and σ is the sigmoid activation. This recalibration allows the model to focus on the most informative spatial patterns while suppressing less relevant activity, improving robustness to noise and channel variability.

The final step is **Seizure Risk Prediction**. We flatten the recalibrated tensor $\mathbf{X}_{\mathrm{SE}}$ to obtain a global representation $\mathbf{H}$, which is passed through a fully connected layer with dropout and sigmoid activation:

$$\hat{Y} = \sigma(\mathbf{W}\mathbf{H} + \mathbf{b}). \tag{13}$$

This produces a scalar probability representing the likelihood of a high-risk seizure period for the given input.

The model is trained using **binary cross-entropy loss**, which is well-suited for imbalanced binary classification tasks:

$$\mathcal{L} = -\frac{1}{M}\sum_{i=1}^{M}\left(y_i\log\hat{Y}_i + (1-y_i)\log(1-\hat{Y}_i)\right), \tag{14}$$

where y_i is the ground truth label, $\hat{Y}_i$ is the predicted probability, and M is the batch size.

4. Experimental Settings

4.1. *Datasets*

Our study uses electrocorticographic data from patients with implanted RNS devices. Rather than raw spectrograms, we extract IEA surrogate biomarkers as features and LEs as seizure risk indicators. The dataset comprises recordings from five patients, each identified by a unique RNS Patient ID, and collected at the Emory Epilepsy Center. The daily recordings span from 3,030 to 6,953 days per patient. These patients were selected based on the availability of ultra-long-term monitoring data and clinically validated seizure annotations. The dataset is partitioned into 70% training, 10% validation, and 20% testing sets.

4.2. *Data Preprocessing and Labeling*

To account for inter-patient variability and device reprogramming effects, we normalize the A+B pattern counts using patient-specific Z-scores:

$$Z_t = \frac{X_t - \mu}{\sigma}, \tag{15}$$

where X_t is the A+B count at time t, and μ, σ are the mean and standard deviation across all visits. High-risk days ($Y_t = 1$) are defined as days where the LE count exceeds 70% of the mean over the past 60 days, a threshold that approximates when patients typically transition into higher seizure vulnerability states. This adaptive strategy, informed by clinician input, reflects evolving seizure patterns and maintains robustness across clinical stages.

4.3. *Data Visulization*

To illustrate both macro-level trends and finer variability, we visualized 1000-day segments of normalized A+B patterns with corresponding LE risk labels in Fig.2.

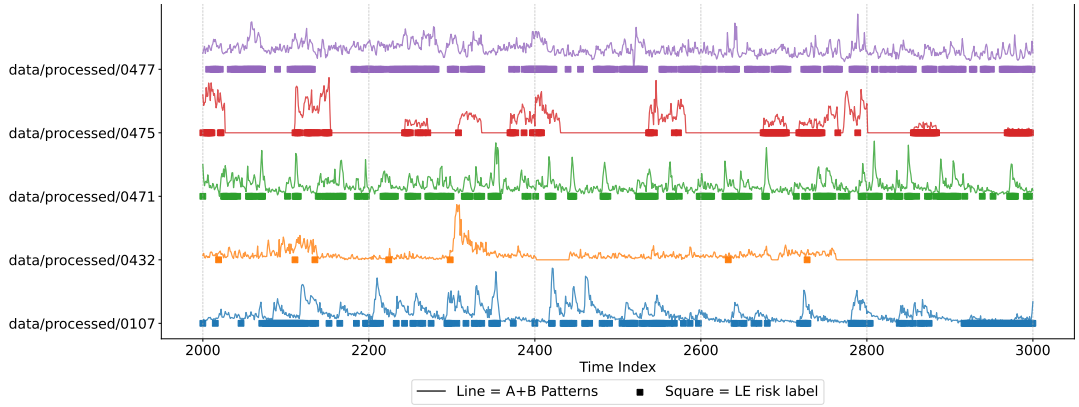

Fig. 2. A+B patterns and LE risk labels over a 1000-day period. The line represents normalized A+B patterns, while the square markers indicate high risk labels.

These samples were selected for their size and to represent diverse seizure risk profiles across patients. Fig. 2 shows that clear differences emerge across patients: *Patient 0475* and *Patient 0432* show periodic high-risk patterns—short cycles for 0475 and long, irregular ones

for 0432—affecting predictability. *Patient 0471* exhibits short, frequent cycles with high A+B variability, indicating unstable risk dynamics. In contrast, *Patients 0477* and *0107* show prolonged high-risk periods and noisy A+B patterns, suggesting persistent ictal-interictal states and increased forecasting difficulty.

4.4. *Evaluation Metrics*

According to the label distribution shown in Fig. 2, the label distribution for all patients is imbalanced. Thus we use Area Under the Receiver Operating Characteristic curve (ROC AUC) and Area Under the Precision-Recall curve (PR AUC) as the primary metrics.[20]

4.5. *Implementation Details*

Models undergo extensive hyperparameter tuning. We set the learning rate to 0.003, hidden dimension (D) to 128, batch size to 2048, and weight decay to 0.0001. The model uses 3 input channels ($enc_in = 3$), 2 decoder input channels ($dec_in = 2$), and 3 output channels ($c_out = 3$). The Transformer encoder comprises 3 layers with 2 attention heads and feedforward dimension 1024. Dropout is set to 0.2 to prevent overfitting. To address class imbalance, we apply class weighting in the loss function using a *pos_weight* derived from the ratio of negative to positive samples per patient. Experiments are conducted on an NVIDIA TITAN RTX (24GB VRAM) with CUDA 12.4. Models are trained for up to 30 epochs with early stopping (patience = 5), based on validation AUC.

4.6. *Baseline Models*

We compare SeizureFormer with baselines across three categories: statistical, machine learning, and deep learning. Statistical models, including Generalized Linear Models (GLM) and Poisson Regression,[21,22] provide interpretable baselines suited for structured medical data. For classical machine learning, we test Support Vector Machines (SVM)[23] and Logistic Regression,[22] which are effective for binary classification using structured features. Deep learning models include GRU-LSTM[24] for capturing long-range dependencies, DLinear[25] for decomposing trend and seasonality in time series, Informer,[26] which introduces a ProbSparse self-attention mechanism for efficient long-sequence forecasting, and PatchTST,[27] a Transformer-based model that leverages patching and global attention for improved forecasting.

5. Experimental Results

In this section, we present our experimental results, structured around four key research questions (RQs) to systematically evaluate the performance of our proposed model, SeizureFormer, in seizure risk forecasting.

(1) **RQ1:** Does SeizureFormer outperform baseline models?
(2) **RQ2:** How does the prediction window ($PredLen = 1, 3, 7, 14$ days) affect performance?
(3) **RQ3:** How do different patients' ictal patterns influence model performance?
(4) **RQ4:** How do different components affect the performance of SeizureFormer?

Table 1. Seizure Risk Forecasting Results. The table presents each model's seizure risk forecasting performance under different settings. Mean ROC AUC and Mean PR AUC are also calculated to show the overall performance of each model. The best performance is bold and the second best is underlined.

Patients		0107		0432		0471		0475		0477		Average	
Models	Pred	ROC	PR	ROC	PR	ROC	PR	ROC	PR	ROC	PR	ROC	PR
GLM	1	59.5%	37.6%	77.8%	19.6%	68.9%	55.9%	95.9%	88.7%	81.2%	67.1%		
	3	55.2%	51.5%	69.8%	21.8%	67.6%	76.3%	92.5%	86.8%	76.8%	75.8%	**71.32%**	**64.34%**
	7	58.7%	70.2%	53.4%	25.9%	67.5%	87.3%	90.2%	87.0%	80.4%	88.4%		
	14	58.2%	81.7%	21.5%	69.4%	95.3%	86.4%	84.1%	NA	NA	NA		
Poisson Regression	1	62.7%	48.8%	78.0%	27.1%	67.7%	54.7%	96.2%	90.8%	80.8%	65.9%		
	3	54.6%	51.3%	78.8%	33.5%	63.0%	73.6%	93.6%	88.5%	71.5%	69.4%	71.20%	65.24%
	7	59.8%	70.6%	72.1%	31.2%	59.6%	85.7%	90.5%	87.6%	76.9%	87.2%		
	14	65.0%	82.8%	38.2%	17.2%	61.6%	93.7%	82.2%	79.9%	NA	NA		
Logistic Regression	1	62.4%	44.9%	82.3%	22.3%	68.4%	54.8%	94.8%	87.1%	79.3%	62.6%		
	3	53.9%	49.1%	77.9%	28.2%	65.3%	73.8%	93.2%	87.6%	76.6%	74.6%	73.13%	64.94%
	7	55.3%	66.7%	70.9%	31.7%	68.7%	88.1%	90.4%	87.4%	81.3%	89.2%		
	14	59.1%	82.2%	54.3%	25.3%	69.8%	95.3%	85.6%	82.9%	NA	NA		
SVM	1	60.4%	39.4%	64.4%	16.4%	68.8%	55.2%	95.8%	88.5%	79.3%	63.0%		
	3	55.5%	51.3%	72.9%	22.9%	68.1%	76.1%	93.3%	87.9%	75.5%	71.8%	71.35%	63.92%
	7	57.3%	68.4%	62.1%	27.0%	67.5%	88.0%	90.6%	87.4%	81.3%	89.2%		
	14	57.7%	81.4%	50.8%	22.9%	69.0%	95.2%	85.4%	82.4%	NA	NA		
DLinear	1	70.9%	57.7%	46.2%	8.96%	68.9%	55.9%	96.9%	92.0%	81.8%	67.6%		
	3	52.9%	52.9%	73.4%	22.7%	69.4%	78.0%	93.6%	88.9%	79.3%	78.6%	72.83%	65.97%
	7	47.1%	61.6%	84.2%	37.2%	69.1%	89.5%	88.2%	85.1%	79.0%	89.6%		
	14	52.5%	77.5%	80.6%	35.6%	69.5%	95.2%	80.3%	78.9%	NA	NA		
GRU_LSTM	1	58.2%	81.7%	82.5%	32.4%	68.5%	56.3%	**97.6%**	93.3%	83.9%	68.4%		
	3	67.9%	66.2%	87.8%	54.3%	70.8%	78.7%	94.7%	88.9%	76.7%	73.5%	73.16%	71.05%
	7	64.5%	75.1%	76.8%	30.8%	58.4%	88.1%	90.2%	86.2%	50.0%	85.2%		
	14	45.6%	77.6%	35.1%	51.9%	51.9%	85.7%	82.6%	NA	NA	NA		
Informer	1	54.2%	64.1%	53.0%	54.7%	54.0%	67.7%	90.2%	89.3%	77.8%	66.7%		
	3	61.3%	66.9%	83.7%	28.8%	61.4%	68.8%	88.7%	82.7%	66.8%	66.8%	65.65%	69.82%
	7	67.7%	80.1%	54.2%	29.8%	58.7%	82.7%	85.4%	86.1%	56.6%	79.9%		
	14	65.1%	**88.0%**	46.2%	38.5%	42.3%	90.1%	84.9%	84.8%	NA	NA		
PatchTST	1	**74.2%**	63.9%	93.2%	62.4%	66.4%	46.0%	97.1%	91.7%	78.2%	62.7%		
	3	52.0%	45.4%	92.6%	59.6%	69.6%	76.4%	94.5%	89.9%	77.4%	78.7%	76.41%	73.07%
	7	53.7%	70.8%	87.4%	49.5%	73.1%	91.0%	91.2%	88.0%	78.8%	89.2%		
	14	28.9%	64.3%	83.9%	**78.5%**	**74.6%**	**95.9%**	85.0%	84.5%	NA	NA		
SeizureFormer	1	**74.2%**	53.5%	**94.7%**	61.6%	70.3%	59.2%	97.1%	**93.4%**	**84.8%**	73.0%		
	3	61.4%	68.1%	92.2%	77.8%	71.0%	76.7%	94.8%	90.8%	80.6%	80.7%	**79.44%**	**76.29%**
	7	47.7%	64.6%	87.9%	52.3%	71.8%	90.6%	92.7%	88.3%	81.6%	**90.7%**		
	14	64.7%	83.1%	85.5%	64.6%	73.3%	95.7%	86.0%	84.9%	NA	NA		

5.1. *RQ1: Overall Model Performance*

To evaluate whether SeizureFormer outperforms baseline models, we first analyze the overall model performance, disregarding the effects of prediction length (*PredLen*) and patient-specific variations. Table 1 presents the ROC AUC and PR AUC scores across all patients and *PredLen* values. SeizureFormer achieves the highest average ROC AUC (*79.44%*) and PR AUC (*76.29%*), surpassing all baseline models. The second-best performing model, PatchTST, achieves *76.41%* ROC AUC and *73.07%* PR AUC, while other deep learning models, such as GRU-LSTM, also demonstrate strong performance but fall short of SeizureFormer. Traditional statistical and classical machine learning models, including Logistic Regression, Poisson Regression, GLM, and SVM, yield lower mean PR AUC scores, reflecting their limited capacity to model complex temporal dynamics and address severe class imbalance. These results establish SeizureFormer as the most effective model overall, though further analysis is needed to

assess its robustness across different prediction lengths and patient cases. Examining patient-specific performance, SeizureFormer achieves top performance for four out of five patients, demonstrating strong generalization across different seizure patterns. For Patient *0477*, where long-term forecasting becomes challenging due to sparse or inconsistent label availability at longer prediction windows *PredLen = 14*, SeizureFormer still outperforms other models in shorter forecasts. GRU-LSTM exhibits strong performance in some cases but struggles with consistency, particularly for longer *PredLen*. These results confirm SeizureFormer as the most effective model for seizure risk forecasting.

5.2. *RQ2: Impact of Prediction Window*

To analyze the impact of prediction window length on model performance, we evaluate trends in both ROC AUC and PR AUC scores across different *PredLen* values. Table 1 provides the full performance breakdown. A general pattern emerges where shorter *PredLen* values (*1, 3* days) yield higher ROC AUC scores, while longer *PredLen* values (*7, 14* days) lead to higher PR AUC scores. For *PredLen = 1, 3* days, models show higher ROC AUC, with deep learning models (SeizureFormer, PatchTST, GRU-LSTM) performing consistently well. Traditional models (e.g., Poisson Regression, SVM) show weaker and less stable performance. For *PredLen = 7, 14* days, PR AUC improves, reflecting better long-term risk trend capture. Deep learning models handle class imbalance more effectively, with SeizureFormer exceeding *80%* PR AUC and GRU-LSTM often above *70%*. Statistical models frequently fall below *50%*. The trade-off between ROC AUC and PR AUC highlights the balance between short-term precision and long-term generalization. SeizureFormer performs robustly across all *PredLen* values. However, while most models benefit from longer prediction horizons, we observe a consistent PR AUC decline for **Patient 0475** (e.g., SeizureFormer: *93.4%→84.9%*, PatchTST: *78.2%→80.9%*, Poisson Regression: *90.8%→79.9%*, SVM: *88.5%→82.4%*). As shown in Fig.2, this patient's highly periodic seizure pattern likely causes temporal misalignment in long-window predictions, leading to false positives during low-risk phases and reduced PR AUC.

5.3. *RQ3: Inter-Patient Variation*

To investigate the impact of different patients' ictal patterns on model performance, we analyze how seizure forecasting varies across individuals. Given the variability in seizure occurrence and EEG characteristics, it is essential to assess whether certain models maintain consistent performance across different patients. Table 1 shows that forecasting performance varies widely across patients. Some (e.g., *0475*) consistently achieve high scores, while others (e.g., *0432*) show large fluctuations, indicating varying signal clarity and model sensitivity. SeizureFormer performs most consistently, while GRU-LSTM shows more variation. Statistical models often fail on patients with complex patterns. Model performance is strongly patient-dependent, with SeizureFormer generalizing better than other baselines.

5.4. *RQ4: Ablation Study of Model Components*

To assess each component's contribution, we performed ablation studies on **Patient 0477**, a representative case with stable high-risk dynamics. As shown in Table 2, we individually

Table 2. Ablation experiment results on Patient 0477. The best performance is bold and the second best is underlined.

Model Variant	**PredLen = 1**		**PredLen = 3**		**PredLen = 7**	
Metrics	ROC AUC	PR AUC	ROC AUC	PR AUC	ROC AUC	PR AUC
Full Model	**84.83%**	**73.03%**	**80.62%**	**80.70%**	<u>81.63%</u>	**90.70%**
w/o CNN Patch Embedding	<u>84.39%</u>	<u>71.89%</u>	73.31%	75.60%	64.61%	81.59%
w/o SE Block	82.80%	68.68%	<u>77.95%</u>	<u>78.21%</u>	**82.76%**	<u>90.20%</u>
w/o Cross-Variable Temporal convolution	77.71%	63.55%	77.66%	77.24%	75.69%	88.65%
w/o All Modules	76.35%	61.86%	70.87%	72.40%	72.97%	87.56%

removed three core modules—CNN Patch Embedding, Squeeze-and-Excitation (SE) Block, and Cross-Variable Temporal Convolution (CVT)—as well as all together. The table shows that removing any module reduces overall performance across multiple prediction lengths. Detailed comparisons reveal the following patterns:

- **CNN Patch Embedding** plays a critical role in long-horizon prediction. At *PredLen = 7*, removing it leads to the largest performance degradation: ROC AUC drops by 17.02% and PR AUC by 9.11%, confirming its effectiveness in capturing long-term features.
- **CVT (Cross-Variable Temporal Convolution)** is crucial for short-term forecasting. At *PredLen = 1*, its removal causes a 7.12% drop in ROC AUC and a 9.48% drop in PR AUC, indicating its importance in modeling high-resolution temporal dependencies.
- **SE Block** subtly improves short-horizon performance. At *PredLen = 1*, its removal results in a 2.03% drop in ROC AUC and a 4.35% drop in PR AUC. Interestingly, at *PredLen = 7*, its removal causes a slight increase in ROC AUC (+1.13%), likely due to reduced overfitting or over-suppression of weak channels. However, PR AUC still drops by 0.50%, which is more clinically relevant in imbalanced settings. This suggests that SE Block may help improve early seizure precision while trading off certain long-horizon sensitivity.

These findings highlight the complementary strengths of the three modules in addressing both short-term and long-term forecasting demands. Their combination enables *SeizureFormer* to achieve consistent performance across different horizons.

6. Conclusion

We present **SeizureFormer**, a Transformer-based model that advances seizure risk forecasting using RNS-derived IEA biomarkers. By integrating multi-kernel CNNs, cross-variable convolution, self-attention, and a squeeze-and-excitation module, it captures seizure-relevant temporal dynamics across multiple time scales. Experiments demonstrate state-of-the-art performance and strong generalizability across patients and forecasting horizons.

In clinical settings, SeizureFormer could enable proactive seizure management. For instance, if a forecast indicates elevated seizure risk over the next three days, clinicians might preemptively adjust medication, modify behavioral protocols, or recommend precautions. Such foresight empowers both patients and providers to make timely, informed decisions.

Future work will explore transfer learning across patients, dynamic biomarker adaptation, and integration with closed-loop neurostimulation for end-to-end seizure risk mitigation.

Acknowledgments

This research was partially supported by the U.S. National Science Foundation under Award No. 2437345. We would like to thank our collaborators and colleagues for their valuable feedback and discussions that helped improve this work.

References

1. World Health Organization, Epilepsy: A public health imperative (2023).
2. W. T. Kerr, K. N. McFarlane and G. F. Pucci, The present and future of seizure detection, prediction, and forecasting with machine learning, including the future impact on clinical trials, *Frontiers in Neurology* **15**, p. 1425490 (2024).
3. L. Kuhlmann, K. Lehnertz, M. P. Richardson *et al.*, Seizure prediction—ready for a new era, *Nature Reviews Neurology* **17**, 618 (2021).
4. L. Kuhlmann, K. Lehnertz, M. P. Richardson, B. Schelter and H. P. Zaveri, Eeg datasets for seizure detection and prediction—a review, *Seizure* **65**, 3 (2019).
5. X. Zhang, X. Zhang, Q. Huang and F. Chen, A review of epilepsy detection and prediction methods based on eeg signal processing and deep learning, *Frontiers in Neuroscience* **18**, p. 1468967 (2024).
6. K. Rasheed, A. Qayyum, J. Qadir, S. Sivathamboo, P. Kwan, L. Kuhlmann, T. O'Brien and A. Razi, Machine learning for predicting epileptic seizures using eeg signals: A review, *IEEE Reviews in Biomedical Engineering* **14**, 139 (2021).
7. L. Yang, R. E. Stirling, M. Kerr, J. J. Howbert and S. N. Baldassano, Seizure forecasting using a long-term implanted neurostimulator: data non-stationarity and model retraining, *arXiv preprint* (2022).
8. T. Proix, M. O. W. Thiele, V. R. Rao, T. K. Tcheng, W. Stacey, M. Guye, D. M. Kühn, M. L. V. Quyen, M. J. Stigler, O. Blanke, V. K. Jirsa and M. O. Baud, Forecasting seizure risk in adults with focal epilepsy: a development and validation study, *The Lancet Neurology* **20**, 127 (2021).
9. A. N. Khambhati, E. F. Chang, M. O. Baud and V. R. Rao, Hippocampal network activity forecasts epileptic seizures, *Nature Medicine* **30**, 2787 (OCT 2024).
10. H. Yang, J. Müller, M. J. Cook, P. Jiruska and A. Schulze-Bonhage, Seizure forecasting with ultra long-term eeg signals, *Clinical Neurophysiology* **146**, 56 (2024).
11. V. Peterson, D. A. Bickel, R. E. Gross, D. L. Kreil, M. J. Cook, G. Krauth and G. Klambauer, Deep net detection and onset prediction of electrographic seizure patterns in responsive neurostimulation, *Epilepsia* **64**, e1 (2023).
12. C. Schroeder, A. Nowacki, S. Chiang, M. Zamora and G. Worrell, Tracking seizure cycles in chronic intracranial eeg using wearable and implanted devices, *arXiv preprint* (2022).
13. M. G. Leguia *et al.*, Learning to generalize seizure forecasts: Comparison of generalized linear models and deep learning approaches, *Epilepsia* (2022).
14. P. Thodoroff, J. Pineau and A. Lim, Learning robust features using deep learning for automatic seizure detection, *International Conference on Machine Learning (ICML)* (2016).
15. S. Raghu, N. Sriraam, W. M. Temesgen and S. Rao, Deep learning for epilepsy: A review of recent advances and future challenges, *IEEE Transactions on Biomedical Engineering* (2019).
16. R. G. Andrzejak *et al.*, Seizure forecasting: Where do we stand?, *Epilepsia* (2023).
17. Y. Yang, S. B. Dumanis, K. A. Bujarski, G. A. Worrell, E. Geller, L. J. Hirsch, U. Seneviratne, M. J. Morrell and C. W. Bazil, Machine learning algorithms for seizure frequency forecasting using electrocorticographic data from a neurostimulator, *Epilepsy Behavior* **124**, p. 108347 (2021).
18. A. C. Constantino, N. D. Sisterson, N. Zaher, A. Urban, R. M. Richardson and V. Kokkinos,

Expert-level intracranial electroencephalogram ictal pattern detection by a deep learning neural network, *Frontiers in Neurology* **12**, p. 603868 (MAY 2021).
19. H. Yang, J. Müller and M. Eberlein, Seizure forecasting with ultra long-term eeg signals, *Clinical Neurophysiology* (2024).
20. T. Saito and M. Rehmsmeier, The precision-recall plot is more informative than the roc plot when evaluating binary classifiers on imbalanced datasets, *PLoS ONE* **10**, p. e0118432 (2015).
21. J. A. Nelder and R. W. M. Wedderburn, Generalized linear models, *Journal of the Royal Statistical Society: Series A (General)* **135**, 370 (1972).
22. J. M. Hilbe, *Logistic Regression Models* (Chapman and Hall/CRC, 2011).
23. C. Cortes and V. Vapnik, Support-vector networks, *Machine Learning* **20**, 273 (1995).
24. K. Cho, B. V. Merriënboer, C. Gulcehre, D. Bahdanau, F. Bougares, H. Schwenk and Y. Bengio, Learning phrase representations using rnn encoder-decoder for statistical machine translation, *arXiv preprint* (2014).
25. A. Zeng, Z. Zhang and Y. Xu, Dlinear: Modeling long-term temporal dependency with linear model for time series forecasting, *arXiv preprint* (2023).
26. H. Zhou, S. Zhang, J. Peng, S. Zhang, J. Li, H. Xiong and W. Zhang, Informer: Beyond efficient transformer for long sequence time-series forecasting, in *Proceedings of the AAAI Conference on Artificial Intelligence*, (12)2021. ProbSparse self-attention, self-attention distilling, generative decoder.
27. Z. Nie, J. Yoon and R. Zhang, Time-series representation learning via patch-based transformer, *Advances in Neural Information Processing Systems (NeurIPS)* (2022).

3DReasonKnee: Advancing Grounded Reasoning in Medical Vision Language Models

Sraavya Sambara[1*], Sung Eun Kim[1,2*], Xiaoman Zhang[1], Luyang Luo[1]
Shreya Johri[1], Mohammed Baharoon[1], Du Hyun Ro[2], Pranav Rajpurkar[1]
[1]*Department of Biomedical Informatics, Harvard Medical School, Boston, MA, USA*
[2]*Seoul National University Hospital, Seoul, South Korea*

Current Vision-Language Models (VLMs) struggle to ground anatomical regions in 3D medical images and reason about them in a step-by-step manner—a key requirement of real-world diagnostic assessment. This ability is essential for aligning model outputs with the diagnostic workflows clinicians use in practice, enabling trustworthy clinician-AI collaboration. Existing 3D datasets provide localization labels, but none support this "grounded reasoning" ability. To address this gap, we introduce **3DReasonKnee**, the first 3D grounded reasoning dataset for medical images, which provides 494k high-quality quintuples derived from 7,970 3D knee MRI volumes. Each quintuple includes: (1) the 3D MRI volume, (2) a diagnostic question targeting a specific anatomical region (3) a 3D bounding box localizing the relevant anatomical structures, (4) clinician-generated diagnostic reasoning steps that explicitly detail the 3D reasoning process, and (5) structured severity assessments for the relevant anatomical region. The meticulous creation and validation of 3DReasonKnee, involving over 450 hours of expert clinician time for manually segmenting MRIs and generating reasoning chains, ensures its superior quality and clinical relevance. We establish **ReasonKnee-Bench** to evaluate localization and diagnostic accuracy, providing novel insight into VLM ability to perform grounding and severity assessment across diverse anatomical regions and diagnostic inquiries. We benchmark five state-of-the-art VLMs, providing baseline performance for ReasonKnee-Bench. By providing this unique resource of expert-annotated 3D reasoning pathways, 3DReasonKnee serves as a repository of orthopedic surgeons' diagnostic expertise and offers a vital testbed for advancing multimodal medical AI systems towards 3D, clinically aligned, localized decision-making capabilities. The dataset can be found in HuggingFace: rajpurkarlab/3DReasonKnee.

1. Introduction

Medical VLMs Lack Fine-Grained 3D Grounded Reasoning. Recent progress in Medical Vision-Language models (VLMs) has demonstrated remarkable capabilities in versatile tasks requiring integrated reasoning across modalities, with models achieving state-of-the-art performance on visual question answering, report generation, and other global understanding tasks.[14,37] However, these models still fall short of clinician-level performance when confronted with problems demanding fine-grained diagnostic reasoning and assessment. Clinicians typically employ a region-first workflow (Figure 1), pinpointing relevant anatomical subregions, assessing them for abnormalities such as lesions or structural changes, and finally assign-

*These authors contributed equally to this work.

© 2025 The Authors. Open Access chapter published by World Scientific Publishing Company and distributed under the terms of the Creative Commons Attribution Non-Commercial (CC BY-NC) 4.0 License.

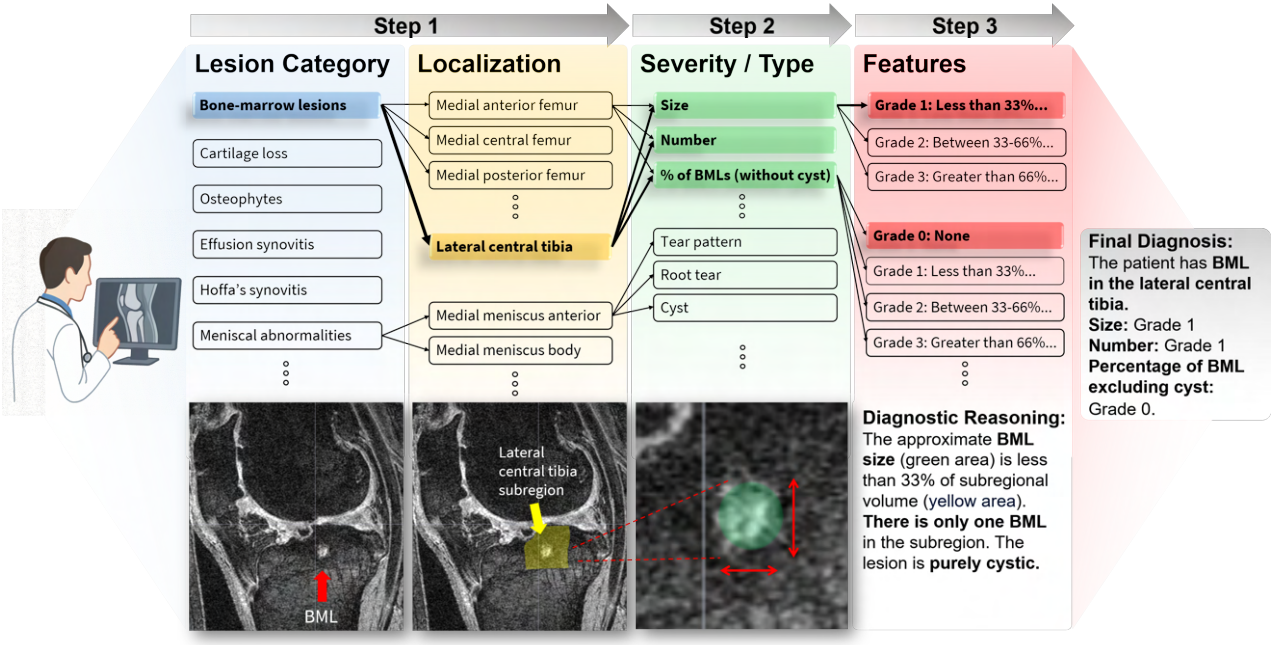

Fig. 1. Region-First Reasoning Workflow in Clinician Knee MRI Assessment. This schema illustrates the step-wise diagnostic process employed by clinicians, involving (Step 1) identification of lesion category and localization to specific anatomical subregions, (Step 2) assessment of severity and lesion type within the localized region, and (Step 3) characterization of specific features.

ing structured severity grades based on established clinical criteria. For instance, the MRI Osteoarthritis Knee Score (MOAKS) framework, as well as other semi-quantitative grading systems, necessitates this level of fine-grained analysis to evaluate specific knee structures and assign severity grades to features like bone marrow lesions and cartilage damage.[8,20] This "grounded" understanding of pathology within localized regions is crucial for accurate diagnosis, prognosis, and treatment planning in clinical settings. Bridging this gap between clinician reasoning and model intelligence is critical for enabling trustworthy clinical decision support and seamless integration of AI into diagnostic workflows.

3D Grounded Reasoning is Not Well-Supported by Existing Datasets. Advances in Chain-of-thought (CoT) prompting have proven effective in enabling models to break down complex problems into interpretable, step-by-step solution processes.[27,36] In 3D medical image analysis, diagnostic reasoning represents a structured cognitive process that extends far beyond simple pattern recognition. It requires precise spatial understanding across multiple planes to properly evaluate volumetric structures. However, instilling such reasoning capabilities in Medical VLMs for 3D medical data is hampered by a lack of suitable training data. While a growing number of datasets are facilitating the development of medical VLMs, such as MultiMedEval[21] for diverse evaluation and MedTrinity-25M[30] for large-scale pretraining, these resources often focus on 2D images with reasoning traces or 3D corpora emphasizing localization without detailed diagnostic rationale (Table 1). A significant gap remains in datasets that facilitate grounded reasoning on 3D medical images, particularly those combining volumetric data, integrated voxel-level localization, and expert-annotated reasoning chains.

Table 1. Representative datasets and benchmarks for medical VLMs. Dim. denotes dimensionality (2D vs. 3D). Grounding indicates the presence of spatial annotations (bounding boxes, masks, or voxel labels); refers to expert-authored diagnostic reasoning steps or structured interpretation pathways that mirror how clinicians synthesize visual findings into diagnostic conclusions

Dataset	Dim.	Modality	Size	Grounding	Reasoning
Path-VQA	2D	pathology images	32 k samples	×	×
Chest ImaGenome	2D	chest X-ray	242 k samples	✓	×
PadChest-GR	2D	chest X-ray	4,555 studies	✓	×
PubMedVision	2D	biomedical figures	1.3 M samples	×	×
RadRBench-CXR	2D	chest X-ray	59K samples	×	✓
GMAI-Reasoning10K	2D	mixed modalities	10K samples	×	✓
MedTrinity-25M	2D	mixed modalities	25M samples	✓	✓
M3D-RefSeg	3D	CT	210 vols	✓	×
MedMD RP3D	3D	CT/MR	51 k vols	×	×
RadGenome-Chest CT	3D	CT	1.3 M samples	✓	×
`3D ReasonKnee`	3D	knee MRI	494 k samples	✓	✓

Introducing 3DReasonKnee to Advance 3D Grounded Reasoning. Our work introduces 3DReasonKnee, the first 3D grounded reasoning dataset for medical images, comprising 494k high-quality quintuples spanning 7,970 unique MRIs. Each quintuple includes: (1) a 3D knee MRI volume, (2) a diagnostic question targeting a specific anatomical region, (3) a 3D bounding box localizing the relevant anatomical structures, (4) clinician-generated diagnostic reasoning steps detailing the 3D reasoning process, and (5) structured severity assessments for the relevant anatomical region. We frame 62 distinct clinical instruction tuning questions and provide volumetric bounding boxes for 22 distinct anatomical regions, drawing from the MOAKS framework. The creation of 3DReasonKnee involved over 450 clinician hours dedicated to manually labeling MRI data and generating detailed reasoning traces. In doing so, 3DReasonKnee provides a clinically aligned resource that supports interpretable model development and enables rigorous evaluation of model performance on narrowly defined diagnostic tasks. To leverage this rich data, we establish ReasonKnee-Bench to rigorously evaluate both localization and diagnostic accuracy in VLMs. Our evaluation metrics include diagnostic accuracy assessment and 3D IoU for the model-generated localization bounding boxes, providing new insights into VLM ability to perform grounding and severity assessment across diverse anatomical regions and diagnostic inquiries. We emphasize the significant potential of 3DReasonKnee, with its expert-annotated reasoning chains and validated localization labels serving as a valuable clinical gold standard, to drive advancements in VLM grounded reasoning capabilities. This work lays the foundation for VLMs that better reflect how clinicians localize and reason about findings in practice, an important step toward their reliable and interpretable use in diagnostic care.

2. Related Work

Existing Datasets and Benchmarks for Medical VLMs. A growing number of datasets and benchmarks are facilitating the development of medical vision-language models. Mul-

tiMedEval[21] offers a consolidated evaluation framework across various tasks and domains, with its VQA component utilizing 2D datasets such as PMC-VQA,[35] Path-VQA,[17] SLAKE,[15] and VQA-Rad.[12] MedTrinity-25M[30] introduces a large-scale multimodal dataset of 25 million image-text pairs for medical vision-language pretraining. GMAI-Reasoning10K[24] provides 10,000 medical reasoning examples with detailed CoT explanations for each VQA pair. RadRBench-CXR[5] offers 59K visual question answering samples with 301K clinically validated reasoning steps. OpenBiomedVid[25] introduces a biomedical video instruction tuning dataset from public educational videos. MedMD[28] includes 3D images and corresponding captions in its RP3D subset. Similarly, M3D-Data[1] introduces image-text pairs and instruction-response pairs tailored for 3D medical tasks, including voxel-level grounding in its M3D-RefSeg subset. RadGenome-ChestCT[34] presents 665K multi-granularity grounded reports and 1.3M VQA pairs of 25,692 3D chest CT volumes from CT-RATE.[7] Despite these advances, there remains a significant gap in datasets that facilitate grounded reasoning on 3D medical images, particularly those that combine volumetric data with expert-annotated reasoning chains. Our proposed 3D ReasonKnee addresses this gap by providing the largest 3D MRI dataset with integrated voxel-level localization, expert CoT rationales, and structured severity grades.

Medical VLMs: Capabilities and Gaps. The application of VLMs in the medical domain has led to models like MedVersa,[38] which explores versatile instruction following tasks for both 2D and 3D medical images. LLaVA-Med[13] adapts the LLaVA framework for biomedical images, but predominantly on 2D data and without explicit reasoning steps. MAIRA-2[3] focuses on grounded report generation, mainly for chest X-rays, underscoring the need for more spatially annotated datasets supporting grounding in medical imaging. While models like Med3DVLM[31] and M3D-LaMed[1] have been developed for 3D medical image analysis, leveraging datasets like M3D, they remain limited in diagnosis with vision-language reasoning. Other notable medical VLMs such as RadFM,[28] PMC-VQA,[35] MedPalm M,[26] and BiomedGPT [33] have advanced medical image understanding and report generation, but generally lack robust support for fine-grained 3D grounded reasoning with associated expert rationales. Therefore, the existing landscape of medical VLM datasets and models reveals a significant gap in resources that facilitate grounded reasoning on 3D medical images. 3DReasonKnee aims to bridge this gap by introducing the first large-scale 3D MRI dataset for knee imaging that simultaneously offers voxel-level localization and expert-annotated CoT rationales, intended to imbue VLMs with robust grounded reasoning abilities for this anatomical region.

General Vision Language Models with Chain-of-Thought Reasoning. The integration of CoT reasoning into vision-language models has emerged as a critical advancement for complex visual understanding tasks. LLaVA-CoT[32] pioneered a framework for teaching VLMs explicit multi-step reasoning, demonstrating significant performance improvements on multimodal reasoning benchmarks. GCoT[29] introduces grounded chain-of-thought reasoning, explicitly connecting visual regions to reasoning steps, enhancing both accuracy and interpretability in complex visual tasks. Other notable advances include Visual CoT,[23] which proposes a multi-turn processing pipeline that dynamically focuses on visual inputs and provides interpretable thought, and MM-CoT,[37] which incorporates language and vision modalities into a two-stage

framework that separates rationale generation and answer inference. SpatialRGPT[4] and RegionGPT[6] further enhance reasoning capabilities by grounding language outputs to specific visual regions. These advancements collectively demonstrate that explicit reasoning pathways significantly improve VLMs' performance on tasks requiring fine-grained visual analysis and multistep logical deduction. OpenAI's o3 and o4-mini models[19] have showcased remarkable multimodal reasoning capabilities, integrating images directly into their chain of thought. However, vision-language reasoning in the medical domain remains to be explored.

3. Dataset and Benchmark

3.1. *Problem Formulation: 3D Grounded Clinical Reasoning*

We formulate the problem as follows: Given a 3D knee MRI volume and a diagnostic question, the model must (1) localize the relevant anatomical region, (2) reason about abnormalities in that region, and (3) output a structured diagnosis that mirrors the MRI Osteoarthritis Knee Score (MOAKS) workflow. An example of quintuples can be found in Figure 2.

Each quintuple is represented as $\{I, Q, B, C, D\}$, where I is the 3D MRI volume, Q is the diagnostic question, B is the 3D bounding box, C is the CoT reasoning, and D is the set of diagnostic severity grades. This 3D knee MRI analysis framework processes the volume I and diagnostic question Q about a specific anatomical region and a single lesion category, then produces three outputs: a 3D bounding box B that precisely localizes the relevant region, a concise Chain of Thought reasoning chain C that transparently explains the analysis process, and a set of diagnostic severity grades D that directly answers the original question for that lesion category. For a given anatomical region and a target lesion category l, this category is associated with a specific set of attributes: $\{a_1, \ldots, a_m\}$. Each of these attributes has its own unique space of possible grades: $\{\mathcal{G}_l^{a_1}, \ldots, \mathcal{G}_l^{a_m}\}$. The structured diagnosis D is then represented as a set of severity grades, one for each attribute within that lesion category: $D = \{g_l^{a_1}, \ldots, g_l^{a_m}\}$. Here, each grade $g_l^{a_j}$ is selected from the corresponding unique grade space $\mathcal{G}_l^{a_j}$ of the attribute a_j for the lesion category l.

The model $\mathcal{M}$ predicts these three elements simultaneously, $(\hat{B}, \hat{C}, \hat{D}) = \mathcal{M}(I, Q)$, providing a structured diagnosis that mirrors the MOAKS workflow by first identifying the region of interest, then reasoning about the specific lesion category within that region, and finally outputting the predicted severity grade for each attribute associated with that category, drawing from its unique grade space.

3.2. *3DReasonKnee Construction Pipeline*

Our quintuplet dataset construction follows a systematic pipeline to create a comprehensive resource for 3D grounded clinical reasoning (see Figure 3).

Data Source. 3DReasonKnee builds upon the Osteoarthritis Initiative (OAI),[18] a NIH-sponsored longitudinal study with 4,796 subjects (58% female; age range: 45–79 years; mean age: 61.4 years) and over 45,000 MRI scans (https://nda.nih.gov/oai). We utilize 7,970 Double Echo Steady State (DESS) MRI sequences collected from baseline through 48-month follow-up, providing high-resolution volumetric data (160 slices per scan). These scans include ground

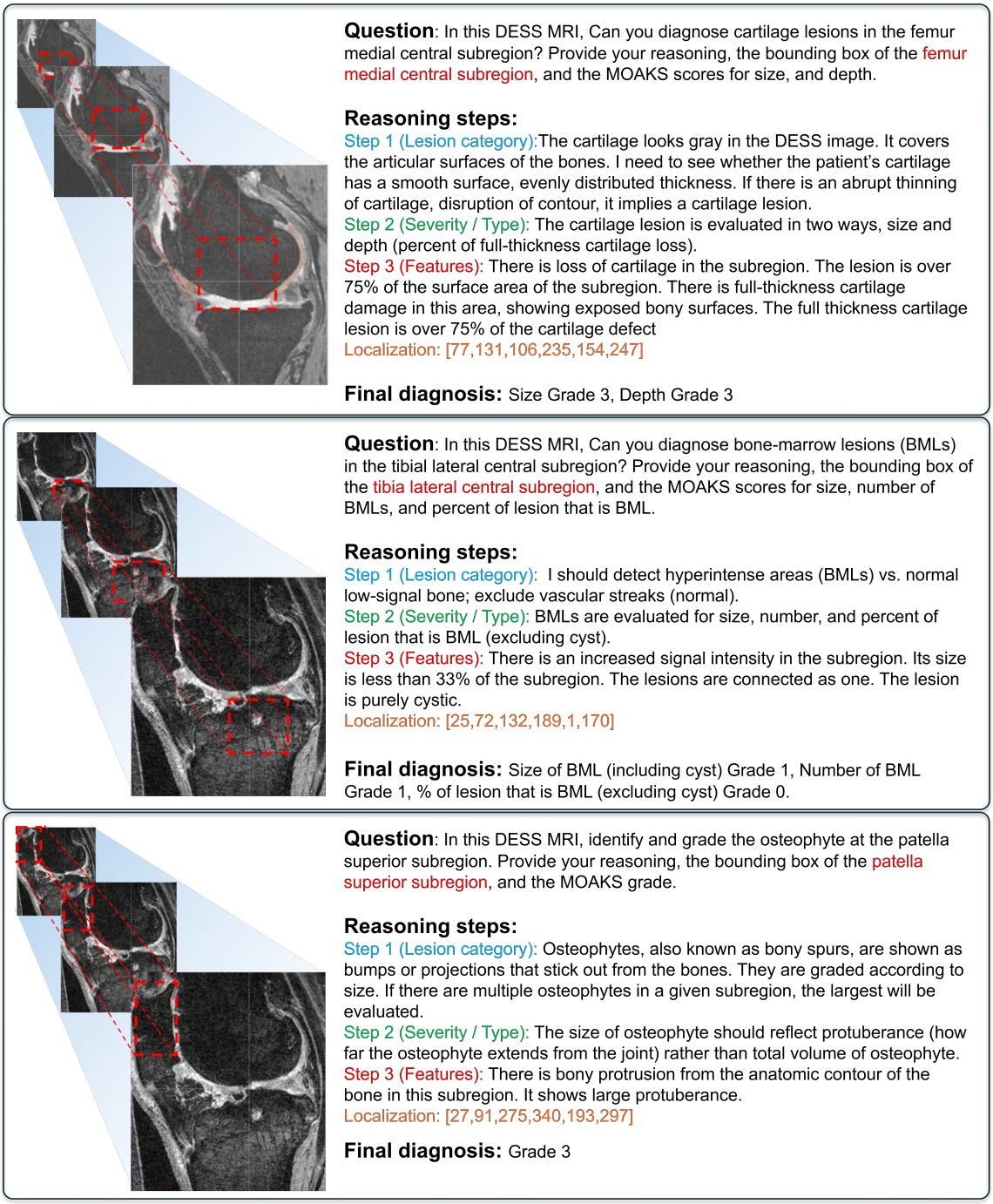

Fig. 2. Example of 3DReasonKnee with Chain-of-Thought.

truth scores included in the OAI using the MOAKS framework,[9] a comprehensive multi-label, multi-region scoring system for standardized knee osteoarthritis assessment. MOAKS evaluates: bone marrow lesions (15 subregions), cartilage lesions (14 subregions), osteophytes (16 subregions), meniscal damage (6 subregions), ligaments/tendons (3 structures), hoffa-synovitis, effusion-synovitis, and periarticular features.

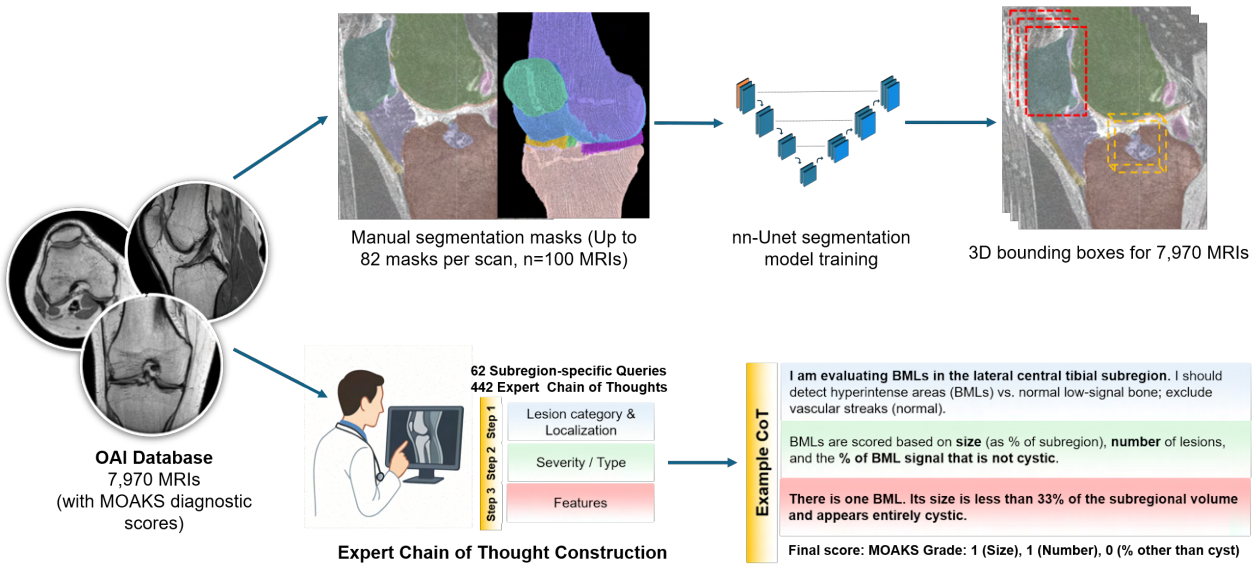

Fig. 3. Overview of the 3DReasonKnee Dataset Construction Pipeline. MRIs (n=100) underwent manual segmentation to train an nn-Unet model,[10] enabling automatic generation of 3D bounding boxes for all scans (n=7,970). Clinicians developed subregion-specific queries and structured CoT based on the MOAKS system.

3D Bounding Box Generation. Two board-certified radiologists and one orthopedic surgeon performed manual annotation of anatomical subregions using a specialized 3D annotation tool. Each scan required approximately **4.5 expert hours** for comprehensive annotation, resulting in a substantial time investment of over **450 hours** for the complete high-fidelity subset of 100 scans. We split the manual annotation data and used the standard nnU-Net pipeline[10] to build a segmentation model for all anatomical structures, subregions, and lesions. We then applied the trained nnU-Net to generate pseudo labels for all MRI scans with expert-adjudicated MOAKS assessments. As most of the current vision-language models primarily support bounding boxes rather than segmentation masks,[2,3] we extracted the largest connected component for each subregion from the model's output and generated axis-aligned 3D bounding boxes. This process created a comprehensive dataset where each scan is linked with its corresponding MOAKS and relevant anatomical subregions.

Expert Question Development & Chain-of-Thought Generation. A board-certified orthopedic surgeon with over seven years of experience in knee surgery developed a comprehensive set of 62 subregion-specific diagnostic queries, each aligned with distinct MOAKS components. For each targeted lesion and anatomical subregion combination, the clinician carefully formulated structured questions designed to prompt precise diagnostic evaluations. Subsequently, detailed step-by-step CoT were crafted to emulate the clinical reasoning pathway by clinicians. Specifically, the clinician first outlined the key pathological characteristics of each lesion type as observed on DESS MRI, emphasizing distinctive imaging features and points for distinguishing pathology from normal anatomy. In alignment with MOAKS criteria, the clinician then systematically translated these into reasoning steps, clearly articulating the conditions and rationale behind each grade.

Dataset Integration. We linked the 3D bounding box annotations with corresponding expert queries, reasoning chains, and MOAKS ground truth labels to create a comprehensive multimodal dataset enabling both localization and reasoning tasks.

3.3. *ReasonKnee-Bench: Evaluating 3D Multimodal Grounded Clinical Reasoning*

Our benchmark, ReasonKnee-Bench, comprehensively evaluates a vision-language model's ability to perform 3D multimodal grounded clinical reasoning for knee osteoarthritis MRI assessment, assessing both diagnostic accuracy and anatomical localization as detailed in the following:

(1) **Final Diagnostic Accuracy:** We assess the accuracy of predicted MOAKS severity grades, grouped into 7 major categories: Bone marrow lesions (BML), Cartilages, Osteophytes, Menisci, Ligaments & Tendons, Synovitis & Effusion, and Periarticular Features. We report classification accuracy for each.

(2) **Anatomical Subregion Localization:** We evaluate the accuracy of predicted 3D bounding boxes using the 3D Intersection over Union (IoU):

$$IoU_{3D} = \frac{Volume(B_p \cap B_{gt})}{Volume(B_p \cup B_{gt})},$$

where B_p is the predicted and B_{gt} is the ground truth bounding box.

By evaluating both localization and diagnostic accuracy, ReasonKnee-Bench provides a holistic assessment of a VLM's grounded reasoning ability – identifying the relevant 3D region and interpreting its visual information to reach a clinical diagnosis. The results in Table 2 and Table 3 offer an initial evaluation of existing models on this benchmark.

3.4. *Dataset Analysis*

Data Split. Our data set comprises 7,970 high-resolution DESS MRI scans split into training (5,977 scans, 75%), validation (797 scans, 10%), and test sets (1,196 scans, 15%) with no patient overlap.

Distribution of MOAKS Grades. The dataset exhibits natural clinical variation in the severity of the pathology in different anatomical regions (Figure 4a).

- **BML Size, Number, %**: The distribution indicates specific anatomical regions prone to developing BMLs, highlighting their relationship with OA progression. These regions include the medial aspect of the femur, the patella, and the area spanning from the tibia subspinous to the tibia medial central subregion.
- **Cartilage Lesion Size and Depth**: Cartilage damage is most pronounced in the patella and the femur medial central subregion, reflecting anatomical regions most susceptible to OA-related cartilage loss, with disproportionate involvement of specific articular surfaces.
- **Osteophyte Grade**: Osteophytes are more frequently observed in the medial compartment of the knee—specifically the femur medial, tibia medial, and patella medial subregions—reflecting the higher prevalence of medial knee OA in the population.

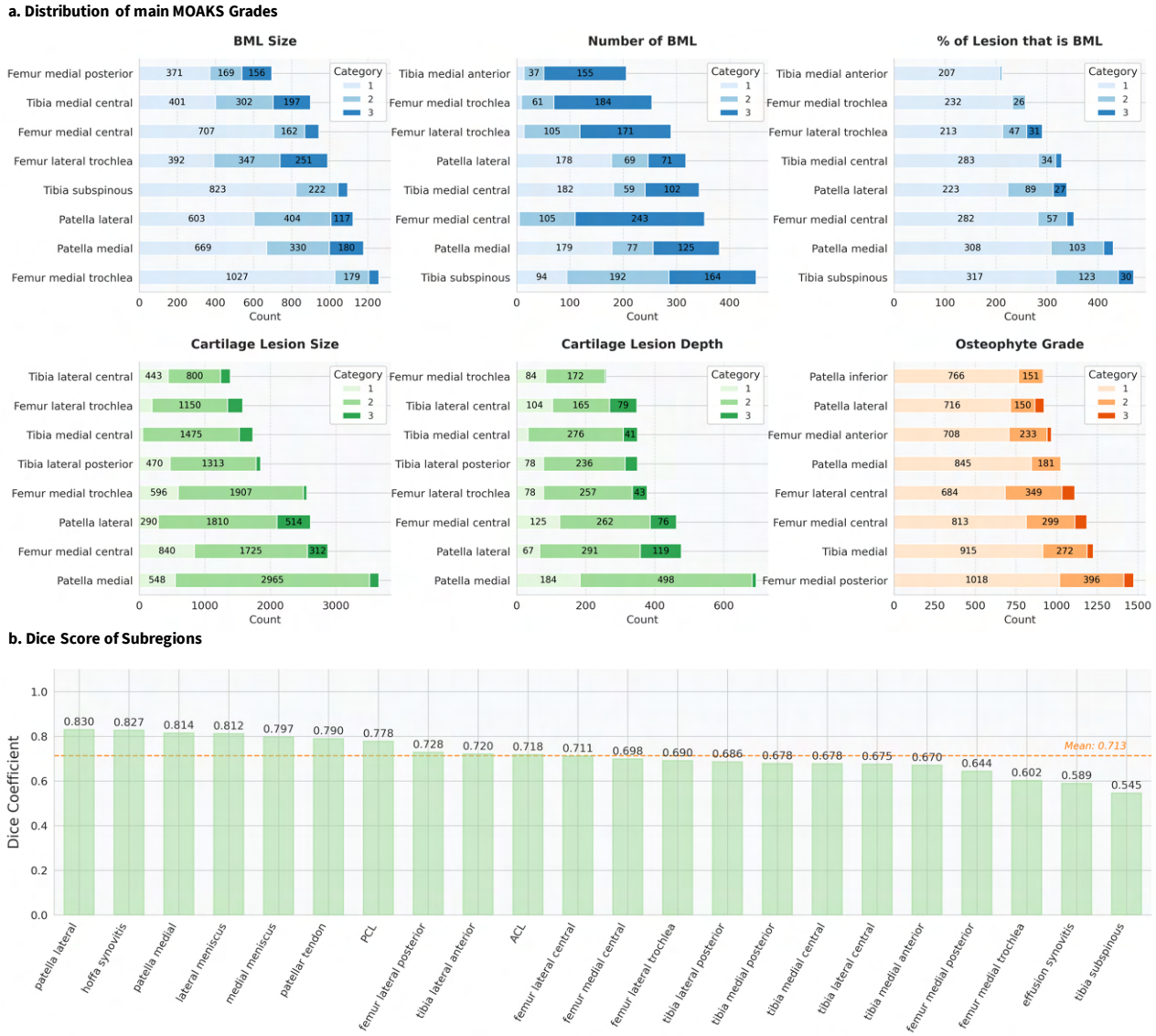

Fig. 4. Dataset distribution statistics. (a) Distribution of main MOAKS grades across different anatomical regions. The stacked bars indicate the frequency of different severity grades (1-3) for each anatomical location, with the remaining proportion representing grade 0. (b) Dice score of the nnU-Net model of all subregions.

3D Bounding Box Annotations. The 3D bounding box annotations provide precise spatial localization of relevant anatomical structures with comprehensive coverage across femoral, tibial, patellar, ligaments, and meniscal regions. The quality of these annotations is validated through Dice coefficient measurements against expert manual segmentations (Figure 4b). The mean Dice score of 0.717 across all regions indicates high precision in localization. The bounding boxes for subregions showed particularly strong performance in the lateral patella (0.830), the hoffa synovitis (0.827), and the medial patella (0.814) subregions. Even the worst performing subregion, such as the tibial subspinous (0.545) exceed acceptable thresholds for clinical relevance. Details can be found here (rajpurkarlab/3DReasonKnee).

4. Experiments and Baselines

Experimental Setup. We benchmarked various baseline models using 3DReasonKnee. Our selection spans specialized 3D Medical VLMs (Med3DVLM[31]), general-purpose VLMs with video input capabilities (Qwen2.5-VL-3B-Instruct, Qwen2.5-VL-7B-Instruct[2]), and state-of-the-art API-based models (o1, using the "2024-12-01-preview" version via Azure). Implementation details are available at rajpurkarlab/3DReasonKnee.

Experimental Settings. We evaluated the models under three different settings: zero-shot, zero-shot with instruction schema, and supervised fine-tuning, which allows us to quantify the inherent difficulty of the proposed tasks for them.

- **Zero-shot Inference.** For our zero-shot evaluation, we provide each model with the 3D MRI scan and a question prompt without any examples of the expected reasoning chain. For example, *"In this DESS MRI, identify and grade the osteophyte at the patella lateral subregion. Provide your reasoning, and the MOAKS grade."* The models rely solely on their pre-trained knowledge to analyze the 3D medical images, identify relevant anatomical structures, and generate appropriate clinical reasoning and MOAKS scores.
- **Zero-shot Inference with Instruction Schema.** In this enhanced zero-shot setting, we augment the base prompt with a structured instruction schema that outlines the expected reasoning process. For example, *"In this DESS MRI, identify and grade the osteophyte at the patella lateral subregion. Osteophytes are bony outgrowths at joint margins. Osteophytes are scored using MOAKS grading: Grade 0: None, Grade 1: Small, Grade 2: Medium, Grade 3: Large. If there are multiple osteophytes in a given subregion, the largest will be evaluated. The size of osteophyte should reflect protuberance (how far the osteophyte extends from the joint) rather than total volume of osteophyte. Provide your reasoning and the MOAKS grade."*. This instruction provides models with a systematic framework for interpreting 3D MRI data without prescribing specific findings, allowing us to evaluate how effectively models can apply structured reasoning processes to clinical assessment tasks.
- **Zero-shot Inference with Instruction Schema and Ground Truth Region.** In this setting, first, we augmented the zero-shot prompt with the structured instruction schema used in the previous baseline, explicitly outlining the expected reasoning process. Second, we cropped the input MRI volume to include only the ground-truth region of interest. By eliminating the need for the model to localize the relevant anatomical structure, this setting isolates its reasoning and grading capabilities.
- **Supervised Fine-tuning.** For the supervised approach, we fine-tune each baseline model on our training set. Models with the best performance on our validation set are used for evaluation.

Baselines. Table 2 summarizes the performance of different approaches on MOAKS component grading diagnostic accuracy, while Table 3 presents the localization performance across anatomical subregions. In zero-shot settings, even state-of-the-art models struggle with the complex task of MOAKS grading, with Qwen2.5VL-3B achieving only 0.158 overall accuracy.

Table 2. Results Summary of MOAKS Grading Performance. We report average accuracy on attributes for each lesion category (BML, Cartilage, Osteophyte, Meniscus, and Others) as well as the Overall average across all categories.

Model	Method	BML	Cartilage	Osteophyte	Meniscus	Others	Overall
Qwen2.5VL-3B	Zero-shot	0.081	0.253	0.251	0.093	0.159	0.158
Qwen2.5VL-7B	Zero-shot	0.642	0.309	0.348	0.347	0.469	0.470
o1	Zero-shot	0.479	0.553	0.353	0.332	0.476	0.477
Qwen2.5VL-3B	Instruction Zero-shot	0.092	0.149	0.253	0.205	0.146	0.146
Qwen2.5VL-7B	Instruction Zero-shot	0.629	0.466	0.342	0.297	0.503	0.504
o1	Instruction Zero-shot	0.635	0.579	0.345	0.391	0.567	0.568
Qwen2.5VL-7B	Instruction Zero-shot w/ GT region	0.697	0.549	0.338	0.166	0.563	0.556
Qwen2.5VL-3B	SFT w/o CoT	0.706	0.602	0.345	0.387	0.616	0.613
Med3DVLM	SFT w/o CoT	0.670	0.578	0.330	0.346	0.600	0.596
Qwen2.5VL-3B	SFT w/ CoT	0.667	0.600	0.342	0.340	0.590	0.588
Med3DVLM	SFT w/ CoT	0.671	0.579	0.333	0.343	0.605	0.581

Table 3. Results Summary of Anatomical Subregion Localization (IoU). Values represent average IoU scores for each subregion of each anatomical structure across different models.

Model	Patella	Femur	Tibia	Meniscus	ACL	PCL	Synovitis
Qwen2.5VL-3B	0.293	0.275	0.322	0.174	0.299	0.305	0.519
Med3DVLM	0.298	0.314	0.359	0.197	0.319	0.384	0.470

The larger Qwen2.5VL-7B model shows some improvement (0.470), comparable to the o1 model (0.477), but both fall short of clinically acceptable performance. Note that medical VLMs like Med3DVLM fail to follow the instructions and give valid outputs. For models that successfully follow instructions, prompting with structured instruction schemas significantly improves performance across models. When prompted with the instruction schema and the ground truth region, we observed a 0.05 increase in overall accuracy (0.556 vs. 0.504) compared to the Instruction Zero-shot baseline. This indicates that when the localization step is solved, the model's reasoning and final diagnostic grading improve. The o1 model showed the most substantial gains from instruction following, with overall accuracy increasing from 0.477 to 0.568 (+19.1%). This improvement was particularly pronounced for BML assessment, where accuracy increased from 0.479 to 0.635 (+15.6%). Supervised fine-tuning (SFT) yielded substantial performance improvements, with Qwen2.5VL-3B achieving 0.613 overall accuracy. While incorporating CoT reasoning during this SFT phase did not translate to accuracy gains in our initial experiments, the supervised models still significantly outperformed o1. We believe that the rich, expert-generated CoT annotations within our dataset hold considerable potential that may be more effectively unlocked with alternative training paradigms beyond standard supervised fine-tuning. Additionally, we observed a clear positive correlation between localization accuracy (IoU) and diagnostic accuracy for our supervised models, with the Med3DVLM model trained with CoT exhibiting the strongest positive correlation between these two metrics.

Failure Modes. Taken together, these two experiments provide an initial failure analysis across all the models evaluated. Grounding is a major failure point. Performance improves notably when the ground-truth region is provided, indicating that many errors arise from incorrect localization. Reasoning and grading remain challenging for certain categories. Even when localization is provided, categories such as Meniscus and Osteophyte still show low accuracy, suggesting that fine-grained reasoning about subtle lesion patterns is also a limitation.

5. Discussion

Our work lays the crucial groundwork for training grounded reasoning models in medical imaging. By demonstrating the current limitations of VLMs in this domain, 3DReasonKnee provides a vital resource to catalyze the development of models capable of reasoning through complex 3D medical data in a manner that mirrors the structured, region-first approach of clinicians. 3DReasonKnee provides a foundation for developing interpretable AI tools that integrate into diagnostic workflows and improve patient care. Future research directions stemming from this work are manifold. We believe this dataset shows promise for exploring reinforcement learning (RL) approaches, which can guide VLMs to diagnose by emulating the expert clinical process..[11,16,22] Notably, 3DReasonKnee features vision-language diagnostic problems paired with CoT rationales and a structured response format, a combination conducive to effective RL training. This dataset could serve as an SFT layer, establishing coherent thinking patterns and output structures, in conjunction with advanced RL techniques that strengthen both reasoning performance and generalization, as demonstrated in successful approaches like OpenAI o3. Another promising training avenue involves exploring novel training processes that directly embed both the full image and the localized subregion/lesion information, a strategy that has been eplored in 2D but is currently limited by computational constraints for 3D images.[23] Furthermore, the structured nature of 3DReasonKnee opens doors for investigating longitudinal reasoning, analyzing disease progression at different time points, and ultimately contributing to prognosis and treatment planning. Extending this framework to other medical imaging modalities beyond knee MRI and other joints such as hand and hip OA represents another significant future direction, paving the way for more broadly applicable and clinically impactful grounded reasoning models.[8,20]

6. Acknowledgments

This Research was supported by a grant of the Boston-Korea Innovative Research Project through the Korea Health Industry Development Institute(KHIDI), funded by the Ministry of Health & Welfare, Republic of Korea(grant no. : RS-2024-00403047). The OAI is a public-private partnership comprised of five contracts (N01- AR-2-2258; N01-AR-2-2259; N01-AR-2-2260; N01-AR-2-2261; N01-AR-2-2262) funded by the National Institutes of Health, a branch of the Department of Health and Human Services, and conducted by the OAI Study Investigators. Private funding partners include Merck Research Laboratories; Novartis Pharmaceuticals Corporation, GlaxoSmithKline; and Pfizer, Inc. Private sector funding for the OAI is managed by the Foundation for the National Institutes of Health.

References

1. Fan Bai, Yuxin Du, Tiejun Huang, Max Q-H Meng, and Bo Zhao. M3d: Advancing 3d medical image analysis with multi-modal large language models. *arXiv preprint arXiv:2404.00578*, 2024.
2. Shuai Bai, Keqin Chen, Xuejing Liu, Jialin Wang, Wenbin Ge, Sibo Song, Kai Dang, Peng Wang, Shijie Wang, Jun Tang, et al. Qwen2. 5-vl technical report. *arXiv preprint arXiv:2502.13923*, 2025.
3. Shruthi Bannur, Kenza Bouzid, Daniel C Castro, Anton Schwaighofer, Anja Thieme, Sam Bond-Taylor, Maximilian Ilse, Fernando Pérez-García, Valentina Salvatelli, Harshita Sharma, et al. Maira-2: Grounded radiology report generation. *arXiv preprint arXiv:2406.04449*, 2024.
4. An-Chieh Cheng, Hongxu Yin, Yang Fu, Qiushan Guo, Ruihan Yang, Jan Kautz, Xiaolong Wang, and Sifei Liu. Spatialrgpt: Grounded spatial reasoning in vision-language models. *Advances in Neural Information Processing Systems*, 37:135062–135093, 2025.
5. Ziqing Fan, Cheng Liang, Chaoyi Wu, Ya Zhang, Yanfeng Wang, and Weidi Xie. Chestx-reasoner: Advancing radiology foundation models with reasoning through step-by-step verification. *arXiv preprint arXiv:2504.20930*, 2025.
6. Qiushan Guo, Shalini De Mello, Hongxu Yin, Wonmin Byeon, Ka Chun Cheung, Yizhou Yu, Ping Luo, and Sifei Liu. Regiongpt: Towards region understanding vision language model. In *Proceedings of the IEEE/CVF Conference on Computer Vision and Pattern Recognition*, pages 13796–13806, 2024.
7. Ibrahim Ethem Hamamci, Sezgin Er, Furkan Almas, Ayse Gulnihan Simsek, Sevval Nil Esirgun, Irem Dogan, Muhammed Furkan Dasdelen, Bastian Wittmann, Enis Simsar, Mehmet Simsar, et al. A foundation model utilizing chest ct volumes and radiology reports for supervised-level zero-shot detection of abnormalities. *CoRR*, 2024.
8. Ida K. Haugen, Iris Eshed, Florence Gandjbakhch, Véronique Foltz, Mikkel Østergaard, Pernille Bøyesen, Paul Bird, Harry K. Genant, Charles G. Peterfy, and Philip G. Conaghan. The longitudinal reliability and responsiveness of the omeract hand osteoarthritis magnetic resonance imaging scoring system (hoamris). *The Journal of Rheumatology*, 2015. Accessed: Jul. 29, 2025.
9. David J Hunter, Ali Guermazi, Grace H Lo, Andrew J Grainger, Philip G Conaghan, Robert M Boudreau, and Frank W Roemer. Evolution of semi-quantitative whole joint assessment of knee oa: Moaks (mri osteoarthritis knee score). *Osteoarthritis and cartilage*, 19(8):990–1002, 2011.
10. Fabian Isensee, Paul F Jaeger, Simon AA Kohl, Jens Petersen, and Klaus H Maier-Hein. nnu-net: a self-configuring method for deep learning-based biomedical image segmentation. *Nature methods*, 18(2):203–211, 2021.
11. Yuxiang Lai, Jike Zhong, Ming Li, Shitian Zhao, and Xiaofeng Yang. Med-r1: Reinforcement learning for generalizable medical reasoning in vision-language models. *arXiv preprint arXiv:2503.13939*, 2025.
12. Jason J Lau, Soumya Gayen, Asma Ben Abacha, and Dina Demner-Fushman. A dataset of clinically generated visual questions and answers about radiology images. *Scientific data*, 5(1):1–10, 2018.
13. Chunyuan Li, Cliff Wong, Sheng Zhang, Naoto Usuyama, Haotian Liu, Jianwei Yang, Tristan Naumann, Hoifung Poon, and Jianfeng Gao. Llava-med: Training a large language-and-vision assistant for biomedicine in one day. *Advances in Neural Information Processing Systems*, 36:28541–28564, 2023.
14. Yifan Li, Zhixin Lai, Wentao Bao, Zhen Tan, Anh Dao, Kewei Sui, Jiayi Shen, Dong Liu, Huan Liu, and Yu Kong. Visual large language models for generalized and specialized applications. *arXiv preprint arXiv:2501.02765*, 2025.
15. Bo Liu, Li-Ming Zhan, Li Xu, Lin Ma, Yan Yang, and Xiao-Ming Wu. Slake: A semantically-labeled knowledge-enhanced dataset for medical visual question answering. In *2021 IEEE 18th*

international symposium on biomedical imaging (ISBI), pages 1650–1654. IEEE, 2021.
16. Qianchu Liu, Sheng Zhang, Guanghui Qin, Timothy Ossowski, Yu Gu, Ying Jin, Sid Kiblawi, Sam Preston, Mu Wei, Paul Vozila, et al. X-reasoner: Towards generalizable reasoning across modalities and domains. *arXiv preprint arXiv:2505.03981*, 2025.
17. Usman Naseem, Matloob Khushi, and Jinman Kim. Vision-language transformer for interpretable pathology visual question answering. *IEEE journal of biomedical and health informatics*, 27(4):1681–1690, 2022.
18. Michael Nevitt, David Felson, and Gayle Lester. The osteoarthritis initiative. *Protocol for the cohort study*, 1:2, 2006.
19. OpenAI. Introducing OpenAI o3 and o4-mini, 4 2025.
20. Frank W. Roemer, David J. Hunter, Andrea Winterstein, Luchi Li, Y. J. Kim, Jolanda Cibere, Thomas C. Mamisch, and Ali Guermazi. Hip osteoarthritis mri scoring system (hoams): Reliability and associations with radiographic and clinical findings. *Osteoarthritis and Cartilage*, 2011. Accessed: Jul. 29, 2025.
21. Corentin Royer, Bjoern Menze, and Anjany Sekuboyina. Multimedeval: A benchmark and a toolkit for evaluating medical vision-language models. *arXiv preprint arXiv:2402.09262*, 2024.
22. Thomas Schmied, Jörg Bornschein, Jordi Grau-Moya, Markus Wulfmeier, and Razvan Pascanu. Llms are greedy agents: Effects of rl fine-tuning on decision-making abilities. *arXiv preprint arXiv:2504.16078*, 2025.
23. Hao Shao, Shengju Qian, Han Xiao, Guanglu Song, Zhuofan Zong, Letian Wang, Yu Liu, and Hongsheng Li. Visual cot: Unleashing chain-of-thought reasoning in multi-modal language models. *arXiv e-prints*, pages arXiv–2403, 2024.
24. Yanzhou Su, Tianbin Li, Jiyao Liu, Chenglong Ma, Junzhi Ning, Cheng Tang, Sibo Ju, Jin Ye, Pengcheng Chen, Ming Hu, et al. Gmai-vl-r1: Harnessing reinforcement learning for multimodal medical reasoning. *arXiv preprint arXiv:2504.01886*, 2025.
25. Rahul Thapa, Andrew Li, Qingyang Wu, Bryan He, Yuki Sahashi, Christina Binder, Angela Zhang, Ben Athiwaratkun, Shuaiwen Leon Song, David Ouyang, et al. How well can general vision-language models learn medicine by watching public educational videos? *arXiv preprint arXiv:2504.14391*, 2025.
26. Tao Tu, Shekoofeh Azizi, Danny Driess, Mike Schaekermann, Mohamed Amin, Pi-Chuan Chang, Andrew Carroll, Charles Lau, Ryutaro Tanno, Ira Ktena, et al. Towards generalist biomedical ai. *Nejm Ai*, 1(3):AIoa2300138, 2024.
27. Jason Wei, Xuezhi Wang, Dale Schuurmans, Maarten Bosma, Fei Xia, Ed Chi, Quoc V Le, Denny Zhou, et al. Chain-of-thought prompting elicits reasoning in large language models. *Advances in neural information processing systems*, 35:24824–24837, 2022.
28. Chaoyi Wu, Xiaoman Zhang, Ya Zhang, Yanfeng Wang, and Weidi Xie. Towards generalist foundation model for radiology by leveraging web-scale 2d&3d medical data. *arXiv preprint arXiv:2308.02463*, 2023.
29. Qiong Wu, Xiangcong Yang, Yiyi Zhou, Chenxin Fang, Baiyang Song, Xiaoshuai Sun, and Rongrong Ji. Grounded chain-of-thought for multimodal large language models. *arXiv preprint arXiv:2503.12799*, 2025.
30. Yunfei Xie, Ce Zhou, Lang Gao, Juncheng Wu, Xianhang Li, Hong-Yu Zhou, Sheng Liu, Lei Xing, James Zou, Cihang Xie, and Yuyin Zhou. Medtrinity-25m: A large-scale multimodal dataset with multigranular annotations for medicine. In *The Thirteenth International Conference on Learning Representations*, 2025.
31. Yu Xin, Gorkem Can Ates, Kuang Gong, and Wei Shao. Med3dvlm: An efficient vision-language model for 3d medical image analysis. *arXiv preprint arXiv:2503.20047*, 2025.
32. Guowei Xu, Peng Jin, Li Hao, Yibing Song, Lichao Sun, and Li Yuan. Llava-o1: Let vision language models reason step-by-step. *arXiv preprint arXiv:2411.10440*, 2024.

33. Kai Zhang, Rong Zhou, Eashan Adhikarla, Zhiling Yan, Yixin Liu, Jun Yu, Zhengliang Liu, Xun Chen, Brian D Davison, Hui Ren, et al. A generalist vision–language foundation model for diverse biomedical tasks. *Nature Medicine*, pages 1–13, 2024.
34. Xiaoman Zhang, Chaoyi Wu, Ziheng Zhao, Jiayu Lei, Ya Zhang, Yanfeng Wang, and Weidi Xie. Radgenome-chest ct: A grounded vision-language dataset for chest ct analysis. *arXiv preprint arXiv:2404.16754*, 2024.
35. Xiaoman Zhang, Chaoyi Wu, Ziheng Zhao, Weixiong Lin, Ya Zhang, Yanfeng Wang, and Weidi Xie. Development of a large-scale medical visual question-answering dataset. *Communications Medicine*, 4(1):277, 2024.
36. Xuan Zhang, Chao Du, Tianyu Pang, Qian Liu, Wei Gao, and Min Lin. Chain of preference optimization: Improving chain-of-thought reasoning in llms. *Advances in Neural Information Processing Systems*, 37:333–356, 2024.
37. Zhuosheng Zhang, Aston Zhang, Mu Li, George Karypis, Alex Smola, et al. Multimodal chain-of-thought reasoning in language models. *Transactions on Machine Learning Research*.
38. Hong-Yu Zhou, Subathra Adithan, Julián Nicolás Acosta, Eric J Topol, and Pranav Rajpurkar. A generalist learner for multifaceted medical image interpretation. *arXiv preprint arXiv:2405.07988*, 2024.

Abstention and Threshold Identification for Uncertainty Management in Clinical Decision Tools: A Case Study using Human-In-The-Loop Pediatric Autism Classifiers

Aiden Ko, Aaron Kline, Kaitlyn Dunlap, SaiMourya Surabhi, Parnian Azizian
Department of Pediatrics (Clinical Informatics), Stanford University, Stanford, CA 94305, USA
Emails: aidensko@stanford.edu, akline@stanford.edu, Kaiti.dunlap@stanford.edu, mourya@stanford.edu, azizian@stanford.edu
Peter Y. Washington
Division of Clinical Informatics and Digital Transformation, Department of Medicine, University of California, San Francisco (UCSF), San Francisco, CA 94143, USA
Email: peter.washington@ucsf.edu
Dennis P. Wall
Departments of Pediatrics (Clinical Informatics), Biomedical Data Science, and Psychiatry and Behavioral Sciences, Stanford University, Stanford, CA 94305, USA
Email: dpwall@stanford.edu

Uncertainty quantification remains an underdeveloped aspect of AI-based clinical decision tools. As AI systems become increasingly prevalent in healthcare, it is essential not only to measure uncertainty but also to manage it in ways that support clinical decision-making. In this study, we investigate abstention as a practical mechanism for managing uncertainty in diagnostic classifiers. To stress-test this approach, we deliberately evaluate abstention performance on a purposefully noisy dataset of pediatric autism video assessments comprising heterogeneous video sources and a diverse range of human raters. We apply abstention strategies to existing autism classifiers trained on diagnostic assessment data, comparing baseline performance to a range of thresholding configurations that trade off retained sample coverage against key clinical metrics. We compare performance gains from prioritizing sensitivity or specificity to targeting a balanced increase in Youden's J to demonstrate a wide variety of use cases that abstention can enable. This work demonstrates a concrete use case of introducing abstention into the output range of clinical decision models, enabling both uncertainty quantification and management in diagnostic classifiers.

Keywords: Uncertainty Management; Human-In-The-Loop AI; Autism; Pediatrics;AI health; AI medicine; AI uncertainty

© 2025 The Authors. Open Access chapter published by World Scientific Publishing Company and distributed under the terms of the Creative Commons Attribution Non-Commercial (CC BY-NC) 4.0 License.

1. Introduction

Autism is a developmental disorder that is diagnosed by clinician observation and behavioral assessment. Current diagnostic approaches for autism rely on specialists who are outnumbered,[1] use myriad diagnostic aids, e.g. Autism Diagnostic Observation Schedule,[2] Autism Diagnostic Interview,[3] Social Responsiveness Scale,[4] with over 20 clinically recommended tools[5] that are time intensive (up to 8 hours of test time), subjective,[6, 7] disagree on outcome,[7] and that do not produce a numerical score that has consistent performance and reliability across the 1 in 31[8] who will be diagnosed with autism. The wait to access diagnostic assessments exceeds 12 months.[9] This delayed process has kept the average age of first diagnosis close to 5 years[10] (and 8 if from an underrepresented group[11]). Evidence supports the importance of early intervention. Like diagnosis, wait periods to access treatments often exceed 12 months,[12, 13] and are not quality monitored or modified with objective endpoints.

The difficulties navigating the healthcare system, variability in diagnostic practices, and consequent delays in diagnosis strongly underscores the need for an alternative system for diagnosis that is objective, quantified, reproducible, and consistent across geographies and demographics. Previous work has shown that machine learning models can effectively classify autism from neurotypical development when using an optimal feature set from clinical instrument data; our team previously trained models using data from 11,298 children with autism and 2,540 controls (including attention-deficit/hyperactivity disorder (ADHD), speech and language delays, and typical development) that resulted in 8 AI classifiers that use between 5 and 10 social-behavioral features each.[14-18] Together, the models use 30 different social-behavioral features. We have since tested the ability to run these models using human-labeled feature ratings on videos submitted by parents. Experiments show that video feature tagging by video analyst "crowdworkers"[19-28] requires a median of only 4 minutes and can be done with clinical accuracy >=92% in independent validation.[29-31,32] While the models were trained to produce binary outcomes, they produce point estimates that indicate the severity of the phenotype and range from severe forms of autism to typical development with no signs of developmental delay.

We seek to build upon this body of work by exploring the concept of uncertainty quantification and management in AI-powered diagnostic tools, with a specific emphasis on abstention-based thresholding as a way to make AI predictions more clinically interpretable and trustworthy. In clinical contexts like autism diagnosis, where behavioral variation is high, the incoming video quality can vary, symptom presentations may be complex, and even high-performing models may not perform at a level needed for clinical decision support. Forcing a model to make a binary decision in such cases can lead to overdiagnosis or missed opportunities for early intervention. This highlights the need for tools that can identify when they are uncertain and explicitly defer judgment, a concept known as abstention. Abstention allows models to say "I don't know" when presented with low-confidence inputs, enabling a safety-aware approach that aligns with clinical practice, where ambiguous cases are often escalated for further review.

This approach is especially relevant in behavioral health domains where ground truth is often fuzzy and diagnostic boundaries overlap. When implemented via thresholding on a model's probabilistic outputs, abstention can be tuned to meet the needs of a particular use case, for example by maximizing sensitivity for screening or maximizing Positive Predictive Value (PPV) for referral decisions. Despite its importance, abstention remains underutilized in diagnostic AI tools, and its integration with video-based autism assessment has not been systematically studied.

One prominent exception is CanvasDx, a machine learning-based medical device approved by the U.S. Food and Drug Administration (FDA) for autism diagnosis. This software device uses video submitted by a caregiver and human-provided feature ratings to produce a diagnostic classification using machine learning.[33, 34] As AI-informed clinical diagnostics are developed, it is critical to improve the quantification and management of uncertainty for these diagnostic tools.[35, 36] One key mechanism for improving these is adding an abstention mechanism with clinical performance-informed threshold values. CanvasDx improved its management of uncertainty using thresholding scores where if this score is above or below two prespecified thresholds, a positive autism or negative autism output is produced.[37, 38]

The focus of the current paper is to examine how we can apply such thresholding methods to a naturalistic but noisy set of video and ratings data that utilizes videos sourced from multiple settings (clinical, mobile game, and home, sourced from the U.S. and abroad) and ratings from raters of different backgrounds (cultural, geographic, professional). By testing performance on this larger dataset containing wildtype videos and nonexpert human ratings (as reflected in real-world scenarios), we perform a comprehensive evaluation of abstention as an uncertainty management mechanism and describe the tradeoffs between diagnostic coverage and performance on clinically informative performance metrics.

2. Methods

2.1 *Noisy Dataset Creation*

We sought to collect, aggregate, and curate a purposefully noisy and heterogeneous dataset as a representative but inherently challenging collection in which abstention for certain samples may be warranted. This combined dataset was collected through a series of studies conducted following approval by the Stanford University Institutional Review Board (IRB), protocol #39562. The data include videos submitted by parents/guardians of children with and without a diagnosis of autism via several different studies conducted by our team (N=665 videos) as well as videos sourced via Youtube.com (N=366 videos). Most videos in the dataset originated from smartphone videos taken by a parent of their child playing alone or with others. For these videos, parents were instructed to take short 1.5–5-minute videos of their children playing. Smaller subsets of videos were taken by clinical coordinators or behavioral therapists, following parent consent, of children waiting for therapy in a medical research center (N=217). Some of these clinically sourced videos are from Bangladesh.[31] Another subset of videos were collected via a mobile game app[39-41] where parents are

asked to play a charades style game with their child, while the phones front camera records the child acting out a prompt presented with a corresponding image (i.e., elephant, astronaut, playing basketball) (N=380). Our video dataset contained children who have been clinically confirmed to have a diagnosis of autism, another condition, such as speech language condition (SLC), or neurotypical development. For the purposes of this study, we classified videos as depicting a child with autism or a child without autism. Demographics including age and gender provided by the parent and/or clinician, and for Youtube videos, video meta data and descriptions were used to assign age and gender.

To safeguard against the potential for self-reporting bias in parent submitted video, we required the caregiver to confirm that their child's autism diagnosis came from a formal medical assessment[42] and asked parents to provide answers to a set of clinical instruments that included the Vineland Adaptive Behavior Scales-Parent Report,[43] Social Responsiveness Scale,[4] Mobile Autism Risk Assessment,[44] Social Communication Questionnaire,[45] and Autism Symptom Dimensions Questionnaire[46] to establish the autism diagnosis or lack thereof. Additionally, videos from YouTube and Caregivers were independently examined in a blinded fashion by a clinician with expertise in autism diagnosis to provide a clinical diagnostic impression.[22, 47] We required the parent reported diagnosis to match the clinician's observational diagnosis to include the video for analysis. This rigorous two-point consensus was used to ensure diagnostic ground truth while minimizing parental burden in the participation.

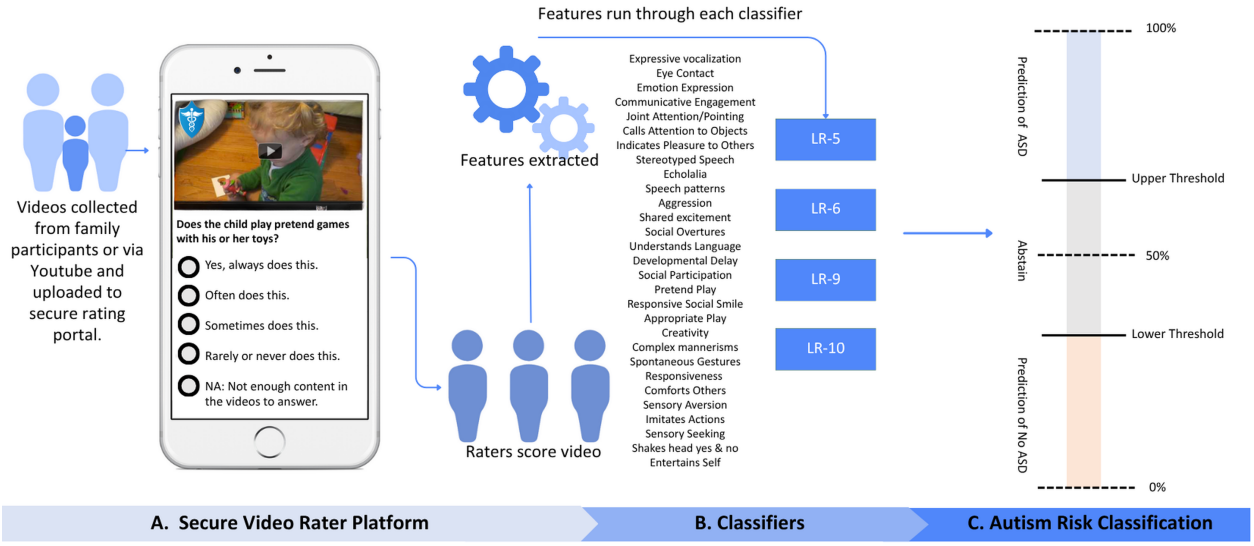

Figure 1. (A) Parents consented to participate in a study where they submitted short home videos of their child to be rated by human labelers in a secure rating platform. Video raters accessed a secure rating platform where 30 behavioral features were rated on a 4-point scale. (B) These features were then used in the following analysis by our previously developed machine learning classifiers to determine an autism risk classification. (C) The current study examines how we can determine and utilize thresholding values to tell the machine learning models to abstain when a certain level of uncertainty is reached.

Feature ratings were collected via a process we previously designed and evaluated (**Figure 1**) where raters recruited by our research lab under the same IRB protocol were asked to view a set of videos in a secure portal and rate a set of 30 features (i.e., answers to multiple choice questions that are clinically relevant to diagnosing autism).[26, 30] Video raters composed of clinicians (N=56 raters and N=3,025 sets of 30-feature ratings) and non-clinician students and crowdworkers (N=50 raters and N=5119 sets of 30 feature ratings) provided numerically coded responses to each of the 30 questions necessary to create the feature vectors for input into the models.

2.2 *Thresholding Experiments*

We leveraged an established and previously-validated set of binary logistic regression (LR) autism classifiers that have previously demonstrated high performance in more homogenous video and rater settings.[26, 30, 31] These models were trained on medical records generated through the clinical administration of popular autism instruments, with training feature sets ranging in size from 30 to over 100. Each identified a specific subset of behavioral features particularly salient to their performance. Given this, we use a short form notation to indicate the number of features for each of the models used in our evaluations, namely LR5, LR6, LR9 and LR10.

We then supplied the ratings from the dataset described above as inputs for inference to the models, taking the median of all ratings available for each video, due to the crowdsourced nature of the ratings and the potential for outliers. The results serve as baseline performance for the thresholding experiments, representing the initial metrics based on a default single 0.5 threshold.

We then introduced an abstention window by replacing that single threshold with dual thresholds t_L and t_U. For each prediction p_i that the model makes, if $p_i < t_L$, we consider it a negative diagnosis, whereas if $p_i > t_U$, we consider it a positive diagnosis. If p_i instead falls on or between the two thresholds, we consider it an abstention. In turn, we can reevaluate each model with different threshold pairs to demonstrate the modified performance alongside an abstention rate (= abstained cases/total cases).

We first measure baseline performance on our dataset using the logistic regression models. Then, to better understand how abstention might improve clinical performance, we conducted a comprehensive grid search over possible upper and lower decision thresholds for each model. Rather than fixing a single decision boundary (e.g., 0.5), we examined the full landscape of trade-offs between diagnostically-relevant performance metrics (sensitivity, specificity, Positive Predictive Value (PPV), and Negative Predictive Value (NPV)) and the rate at which the model abstains from making a prediction. In the grid search, we set the minimum value as the lowest predicted probability (p_{min}) and the maximum value as the highest (p_{max}). We utilized 2000 evenly spaced steps between p_{min} and p_{max} to iterate through all pairs of t_L and t_U along those steps, generating millions of threshold combinations. For each valid combination (where $t_L < t_U$), we calculated the same performance metrics as before, as well as the abstention rate.

This enables us to ask, for example: if we want a classifier that achieves 80% sensitivity and 80% specificity, what is the minimum abstention rate required to meet that target? Or

alternatively: if we can tolerate an abstention rate of up to 25%, what is the best performance we can achieve? By evaluating these scenarios across all valid threshold pairs, we create a flexible framework for tailoring model behavior to different clinical priorities.

3. Results

3.1 *Dataset Compilation*

In the dataset, we identified a total of 8144 sets of ratings across 1031 unique children after preprocessing for videos deemed 'unscorable' by raters and duplicate entries. Of those, 588 children had a confirmed positive ASD diagnosis while 443 did not, including those who were neurotypical or had other diagnoses that were not ASD (**Table 1**). Several children in our dataset had video ratings from multiple independent raters (**Figure 2**).

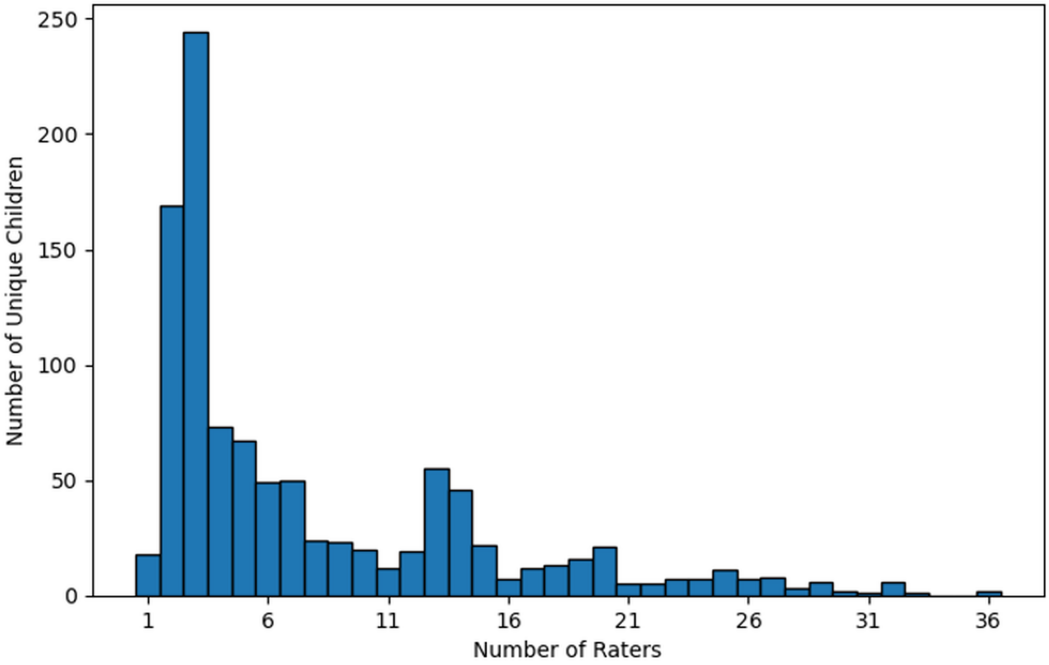

Figure 2. Frequency distribution of the number of raters per child, where the majority of children were given at least three sets of ratings.

Table 1. Demographic characteristics of the children in the video ratings utilized in the analysis.

	Number of Children	**Average Age (Months)**	**Gender Distribution**
Autism	588	65.07 (SD=29.77)	M: 456; F: 132
Non-Autism	443 (38% with other DD)	60.04 (SD=123.14)	M: 257; F:186
Total	1031	62.91 (SD=83.8)	M: 713; F: 318

3.2 *Baseline Classification*

As seen in **Table 2,** accuracies for our baseline classification ranged from 62% to 72%, with LR9 achieving the highest accuracy (71.87%) and sensitivity (82.31%) but lower specificity (58.01%). The other models demonstrated more balanced sensitivity and specificity, though at slightly lower overall accuracy. These results suggest that while our baseline classifiers perform reasonably well given the noisiness (by design) of the video data and human ratings, the addition of abstention may boost performance into more clinically acceptable levels.

Table 2. Baseline performance of logistic regression binary classifiers on the curated collection of 1031 naturalistic video samples.

Model	Accuracy	Sensitivity	Specificity	PPV	NPV
LR5	62.08%	56.12%	69.98%	71.27%	54.58%
LR6	68.57%	66.50%	71.33%	75.48%	61.60%
LR9	71.87%	82.31%	58.01%	72.24%	71.19%
LR10	66.92%	64.63%	69.98%	74.07%	59.85%

3.3 *Thresholding Experiments*

First, we ran a preliminary empirical scan of the data in which we moved the thresholds incrementally further apart for all 4 models. This showed that the general behavior remained consistent across models and further showed for all 4 models a near linear relationship between the threshold width ($t_U - t_L$) and the abstention rate, indicating that widening the distance, and consequently decreasing coverage, expectedly improves performance metrics. We then chose LR6 for the additional in-depth evaluation steps described below due to the fact that it showed the greatest equivalence between sensitivity and specificity, likely offering more room and opportunity to study the impact of uncertainty management on performance (while LR9 showed the highest baseline accuracy (Table 2), its performance favors positives (given the high sensitivity and comparably low specificity), making it potentially less balanced overall).

We evaluated LR6 over a grid of performance targets. For each metric pair (Sensitivity/Specificity and NPV/PPV), we varied the target values from 0.5 to 1.0 in increments of 0.0025, calculating the minimum abstention rate required to simultaneously satisfy both target constraints at each point. Subsequently, we calculated a maximum performance we can achieve under a clinically viable abstention rate. We choose Youden's J (*sensitivity* + *specificity* - 1) as a balanced metric for performance for each set of thresholds and iterate through a set of abstention ceilings, finding the set of thresholds that achieved the maximum Youden's J. Additionally, we set

a sensitivity requirement and measure the effect of the ceiling on the best possible specificity and vice versa.

Table 3. LR6 model performance with optimized thresholds (t_L,t_U) under varying abstention ceilings, searching for the highest Youden's J.

Abstain ceiling	Accuracy (%)	Sensitivity (%)	Specificity (%)	Youden's J	t_L	t_U
Baseline	68.57	66.50	71.33	.3783	N/A	N/A
0.1	71.77	71.37	72.28	.4365	0.4027	0.5480
0.2	73.58	69.89	78.33	.4822	0.3685	0.6923
0.3	76.31	74.45	78.78	.5323	0.2966	0.7530
0.4	79.64	85.87	70.52	.5639	0.1944	0.7060
0.5	81.59	86.38	74.88	.6126	0.1645	0.8459

Table 4. LR6 model performance with optimized thresholds (t_L,t_U) under varying abstention ceilings and a baseline condition for sensitivity/specificity while searching to maximize the other.

Abstain ceiling	Additional Condition	Accuracy (%)	Sensitivity (%)	Specificity (%)	t_L	t_U
Baseline	N/A	68.57	66.50	71.33	N/A	N/A
0.1	Sensitivity>=71.33	71.58	71.70	71.43	0.3944	0.5382
0.2	Sensitivity>=71.33	73.70	75.43	71.47	0.3235	0.5867
0.3	Sensitivity>=71.33	75.90	79.15	71.33	0.2384	0.6532
0.4	Sensitivity>=71.33	78.04	82.51	71.43	0.2032	0.7060
0.5	Sensitivity>=71.33	81.48	88.05	71.43	0.1640	0.7593
0.1	Specificity>=66.50	70.72	66.73	75.79	0.4619	0.5969
0.2	Specificity>=66.50	72.92	66.60	81.04	0.4155	0.7354
0.3	Specificity>=66.50	74.52	67.26	83.08	0.3524	0.8400
0.4	Specificity>=66.50	75.08	66.56	84.54	0.3206	0.8841

Abstain ceiling	Additional Condition	Accuracy (%)	Sensitivity (%)	Specificity (%)	t_L	t_U
Baseline	N/A	68.57	66.50	71.33	N/A	N/A
0.1	Sensitivity>=71.33	71.58	71.70	71.43	0.3944	0.5382
0.2	Sensitivity>=71.33	73.70	75.43	71.47	0.3235	0.5867
0.3	Sensitivity>=71.33	75.90	79.15	71.33	0.2384	0.6532
0.4	Sensitivity>=71.33	78.04	82.51	71.43	0.2032	0.7060
0.5	Specificity>=66.50	77.76	66.67	89.58	0.2643	0.9320

As displayed in **Table 3**, increasing the maximum tolerated abstention rate allows the model to achieve a significantly higher optimal performance. The maximum Youden's J consistently improves with higher ceilings, and each ceiling shows a significant increase in performance over the baseline in terms of sensitivity and specificity. We can also see in **Table 4** how setting a baseline for sensitivity or specificity and maximizing the other displays monotonic growth as the abstention ceiling is raised. Moreover, a particularly compelling point can be found at the 30% ceiling in the Youden's J optimization, as this level of data coverage would make it viable in clinical contexts while also displaying a clear performance benefit: both sensitivity and specificity are enhanced, rising to 74.5% and 78.8% respectively, compared to the baseline's 66.5% and 71.3%.

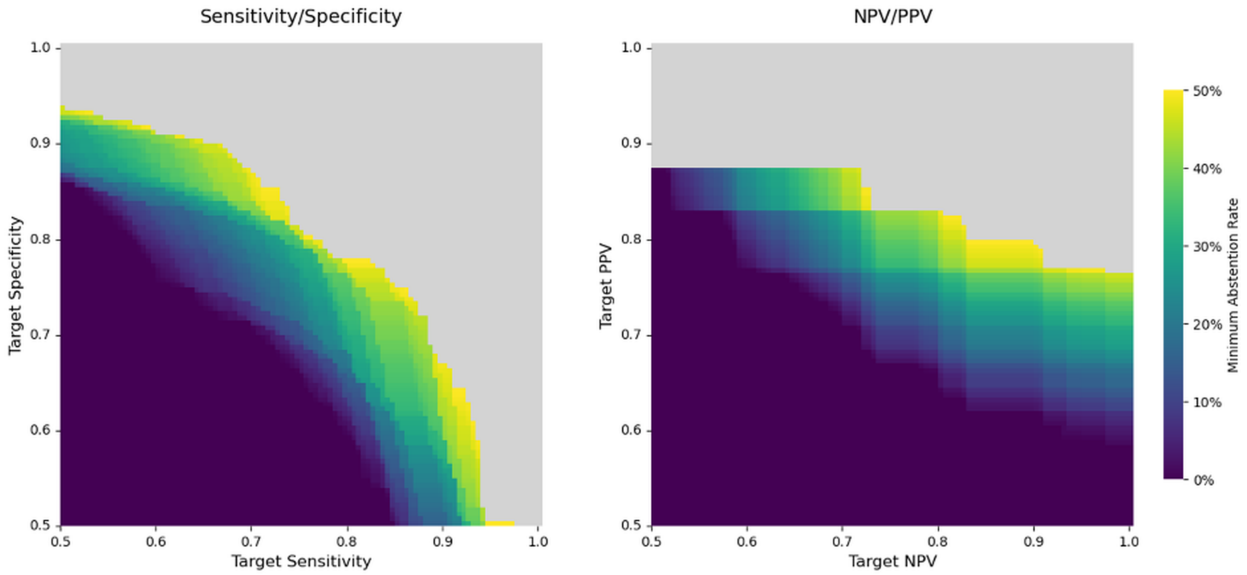

Figure 3. Performance trade-off landscapes for the LR6 model, showing achievable targets at an abstention rate of 50% or less. The grey area represents target combinations that are either impossible to achieve or require an abstention rate greater than 50%.

We also plot the results of our model evaluation over ranges of performance targets in **Figure 3.** This illustrates a promising result, displaying the minimum abstention rate required to simultaneously achieve target performance levels for two key pairs of metrics: sensitivity/specificity (left) and NPV/PPV (right). While some targets are not feasible with any threshold pair at all, we also intentionally drop any data points where the minimum required abstention is greater than 50% as a reasonable ceiling for a scenario where a model would be clinically viable.

Figure 3 demonstrates that the model's performance can be significantly improved over the baseline performance in **Table 2** by allowing it to abstain from making predictions on low-confidence samples. For instance, in the left panel, achieving an approximate balanced 80% sensitivity and 80% specificity requires an abstention rate of approximately 20-30%. Pushing for higher targets, such as 90% in both metrics, drastically pushes the abstention rate past 40%, or it may not be possible within our parameters.

A particularly promising result is seen in the NPV/PPV plot. The model can achieve a high target NPV (e.g., 0.95) while maintaining a moderate but still clinically useful target PPV (e.g., 0.75) with a minimal abstention rate of less than 20%, demonstrating its potential promise as a triaging tool, confidently identifying negative cases while flagging a smaller, manageable subset of potential positive cases for further review. This is particularly valuable in the context of autism, where it could help reduce the backlog of patients waiting for full evaluation by prioritizing those that pass this initial screening.

4. Discussion

We demonstrate that abstention-based thresholding can serve as a flexible mechanism for managing uncertainty in AI-based clinical diagnostic tools, and the possibilities that this dual-threshold approach can provide in the context of pediatric autism classification. By applying abstention strategies to video-based autism classifiers trained on traditional instruments, we were able to explore trade-offs between PPV, NPV, and the proportion of samples retained for classification. Our results show that carefully selecting upper and lower thresholds can meaningfully shift clinical performance metrics without retraining the underlying model, offering a post-hoc yet clinically interpretable mechanism to tailor model behavior to the needs of diverse deployment contexts. These findings build on prior work in medical AI that emphasizes the importance of communicating uncertainty[36, 37] by offering a concrete pathway to operationalize it within the diagnostic process.

Additionally, our results demonstrate that dynamic thresholding can permit us to utilize the existing models in many different contexts. For instance, as described above, it could be employed as a triage tool, with a fixed high NPV and trading off PPV to fit abstention requirements. Another use case would be as a “first pass” model, requiring a high PPV and NPV but also accepting a

large abstention rate. This would permit one to filter for “easier” cases (i.e. cases where a model has high confidence) cheaply then transfer the remaining cases to a more resource intensive next step. Overall, working with abstention allows us to explore a plethora of new applications for a single model, all without requiring retraining.

There are limitations worth highlighting that will be the target of future work. First, our dataset, though diverse and significantly larger than in prior work, is still constrained by the availability of labeled videos with verified diagnoses. Publicly available videos, especially those sourced from platforms like YouTube, often lack complete demographic or clinical metadata, limiting the ability to perform stratified or subgroup analyses. Second, the crowdsourced ratings used to construct the input features, although aggregated, may contain suboptimal variations in rater quality. While we employed clinicians and trained raters in many instances, we did not systematically quantify or control for inter-rater reliability across the full dataset. This introduces uncertainty that may impact classifier threshold optimization. Given that the goal of this study was to demonstrate the general tradeoffs of sweeping across a wide span of threshold points and abstention windows, as opposed to the identification of specific points for clinical decision making based on thresholds aligned with real-world distribution, we used pre-existing classifiers without additional calibration. However, we acknowledge that model calibration is a critical step for any future work that would target such real-world clinical goals. Furthermore, we note that future work exploring feature importance contributing to abstain decisions would provide additional insight into specific factors that drive models to identify samples as indeterminate, resulting in increased model explainability, a key facet of uncertainty management. Finally we acknowledge that selecting thresholds and evaluating performance on the same inference outputs could introduce optimistic bias. Although inference was performed using frozen classifiers that were previously trained on an entirely different dataset, and our thresholds were utilized to examine the tradeoffs of abstain windows and performance, future work will benefit from use of a dedicated evaluation dataset and/or nested-cross validation.

The paradigm of abstention in clinical informatics leads to several opportunities for future work. A natural follow up of this work is to study patient and clinician-facing consequences of abstention from a human-centered design perspective (e.g., user trust, follow-up burden, and missed diagnosis costs). Future work should incorporate decision-analytic frameworks or prospective studies to align abstention behavior and threshold selection with clinical utility and patient outcomes. In addition, adaptive thresholding strategies that respond to contextual features, such as demographic variables, symptom severity, or prior history, may enable more personalized uncertainty management decision making. Exploring abstention in multi-class or multi-label diagnostic settings, including differential diagnosis among overlapping developmental conditions, would enable abstention management in more challenging diagnostic scenarios (e.g., distinguishing between autism vs. ADHD vs. both vs. none).[48, 49] Finally, we plan to explore the concept of abstention in less noisy contexts, such as by using a single source of videos and a highly filtered subset of human raters.

5. Conclusion

Abstention is a powerful mechanism for enhancing the quantification and management of uncertainty in AI-based clinical diagnostic tools. We demonstrated how adjusting classification thresholds on models trained with traditional autism measurement tools can meaningfully trade off between performance metrics, such as PPV, NPV, and coverage, without requiring retraining or architectural changes. These thresholding strategies provide more "degrees of freedom" to align model outputs with diverse clinical success criteria, depending on the setting, population, and tolerance for false positives or negatives.

As AI tools increasingly move from research settings into regulated clinical workflows, it is essential to develop and formalize strategies for managing uncertainty in ways that are interpretable, clinically relevant, and adaptable. Abstention offers one such strategy, enabling systems to defer low-confidence predictions and support safer, more trustable decision-making. Future work should build upon this paradigm by integrating abstention into clinician-facing interfaces, evaluating its real-world impact, and developing guidelines that support its responsible use across a range of clinical domains.

6. Acknowledgements

This work was funded by National Institutes of Health, under awards R01LM013364 and R01LM014342, and Stanford Center for Digital Health. PW acknowledges funding from the National Institutes of Health (NIH) via the NIH Director's New Innovator Award (award DP2-EB035858). We acknowledge the use of ChatGPT in polishing sections of the manuscript for readability; all emitted outputs were thoroughly reviewed and edited by the coauthors.

References

1. Thomas KC, Ellis AR, Konrad TR, Holzer CE, Morrissey JP. County-level estimates of mental health professional shortage in the United States. Psychiatr Serv. 2009;60(10):1323-8. Epub 2009/10/03. doi: 10.1176/ps.2009.60.10.1323. PubMed PMID: 19797371.
2. Gotham K, Risi S, Pickles A, Lord C. The Autism Diagnostic Observation Schedule: revised algorithms for improved diagnostic validity. J Autism Dev Disord. 2007;37(4):613-27. Epub 2006/12/21. doi: 10.1007/s10803-006-0280-1. PubMed PMID: 17180459.
3. Lord C, Rutter M, Le Couteur A. Autism Diagnostic Interview-Revised: a revised version of a diagnostic interview for caregivers of individuals with possible pervasive developmental disorders. J Autism Dev Disord. 1994;24(5):659-85. Epub 1994/10/01. PubMed PMID: 7814313.
4. Constantino JN, Gruber CP. Social responsiveness scale, second edition (SRS-2): Western Psychological Services Los Angeles, CA; 2012.
5. Falkmer T, Anderson K, Falkmer M, Horlin C. Diagnostic procedures in autism spectrum disorders: a systematic literature review. European Child & Adolescent Psychiatry. 2013;22(6):329-40. doi: 10.1007/s00787-013-0375-0.
6. Lebersfeld JB, Swanson M, Clesi CD, O'Kelley SE. Systematic Review and Meta-Analysis of the Clinical Utility of the ADOS-2 and the ADI-R in Diagnosing Autism Spectrum Disorders in Children. Journal of Autism and Developmental Disorders. 2021;51(11):4101-14. doi: 10.1007/s10803-020-04839-z.
7. Kamp-Becker I, Albertowski K, Becker J, Ghahreman M, Langmann A, Mingebach T, Poustka L, Weber L, Schmidt H, Smidt J, Stehr T, Roessner V, Kucharczyk K, Wolff N, Stroth S. Diagnostic accuracy of the ADOS and ADOS-2 in clinical practice. European Child & Adolescent Psychiatry. 2018;27(9):1193-207. doi: 10.1007/s00787-018-1143-y.
8. Shaw KA. Prevalence and Early Identification of Autism Spectrum Disorder Among Children Aged 4 and 8 Years—Autism and Developmental Disabilities Monitoring Network, 16 Sites, United States, 2022. MMWR Surveillance Summaries. 2025;74.
9. Shannon J, Salomon M, Kraft C, Chettiath T, Taraman S, Badesch S, editors. Wait Times and Processes for Autism Diagnostic Evaluations: A First Report Survey of Autism Centers in the US. JOURNAL OF DEVELOPMENTAL AND BEHAVIORAL PEDIATRICS; 2024: LIPPINCOTT WILLIAMS & WILKINS TWO COMMERCE SQ, 2001 MARKET ST, PHILADELPHIA ….
10. National Autism Data Center AJ. How early does diagnosis happen? Autism by the Numbers supported by Autism Speaks. In: Institute DA, editor.
11. Mandell DS, Listerud J Fau - Levy SE, Levy Se Fau - Pinto-Martin JA, Pinto-Martin JA. Race differences in the age at diagnosis among medicaid-eligible children with autism(0890-8567 (Print)).
12. Gordon-Lipkin E, Foster J, Peacock G. Whittling Down the Wait Time: Exploring Models to Minimize the Delay from Initial Concern to Diagnosis and Treatment of Autism Spectrum Disorder. Pediatr Clin North Am. 2016;63(5):851-9. Epub 2016/08/28. doi: 10.1016/j.pcl.2016.06.007. PubMed PMID: 27565363; PMCID: PMC5583718.
13. Vu M, Duhig AM, Tibrewal A, Campbell CM, Gaur A, Salomon C, Gupta A, Kruse M, Taraman S. Increased delay from initial concern to diagnosis of autism spectrum disorder and associated health care resource utilization and cost among children aged younger than 6 years in the United States(2376-1032 (Electronic)).

14. Duda M, Ma R, Haber N, Wall DP. Use of machine learning for behavioral distinction of autism and ADHD. Transl Psychiat. 2016;6(2):e732. doi: ARTN e732
10.1038/tp.2015.221. PubMed PMID: WOS:000373892800003.
15. Kosmicki JA, Sochat V, Duda M, Wall DP. Searching for a minimal set of behaviors for autism detection through feature selection-based machine learning. Transl Psychiat. 2015;5(2):e514. doi: ARTN e514
10.1038/tp.2015.7. PubMed PMID: WOS:000367652200002.
16. Levy S, Duda M, Haber N, Wall DP. Sparsifying machine learning models identify stable subsets of predictive features for behavioral detection of autism. Mol Autism. 2017;8:1-17.
17. Wall DP, Dally R, Luyster R, Jung JY, Deluca TF. Use of artificial intelligence to shorten the behavioral diagnosis of autism. Plos One. 2012;7(8):e43855. Epub 2012/09/07. doi: 10.1371/journal.pone.0043855. PubMed PMID: 22952789; PMCID: PMC3428277.
18. Wall DP, Kosmicki J, DeLuca TF, Harstad E, Fusaro VA. Use of machine learning to shorten observation-based screening and diagnosis of autism. Transl Psychiat. 2012;2(4):e100. doi: ARTN e100
10.1038/tp.2012.10. PubMed PMID: WOS:000306218400003.
19. Washington P. A Perspective on Crowdsourcing and Human-in-the-Loop Workflows in Precision Health. J Med Internet Res. 2024;26:e51138. Epub 11.4.2024. doi: 10.2196/51138. PubMed PMID: 38602750.
20. Washington P, Chrisman B, Leblanc E, Dunlap K, Kline A, Mutlu C, Stockham N, Paskov K, Wall DP. Crowd annotations can approximate clinical autism impressions from short home videos with privacy protections. Intelligence-Based Medicine. 2022;6:100056. doi: https://doi.org/10.1016/j.ibmed.2022.100056.
21. Washington P, Kalantarian H, Tariq Q, Schwartz J, Dunlap K, Chrisman B, Varma M, Ning M, Kline A, Stockham N, Paskov K, Voss C, Haber N, Wall DP. Validity of Online Screening for Autism: Crowdsourcing Study Comparing Paid and Unpaid Diagnostic Tasks. J Med Internet Res. 2019;21(5):e13668. Epub 2019/05/28. doi: 10.2196/13668. PubMed PMID: 31124463.
22. Washington P, Leblanc E, Dunlap K, Kline A, Mutlu C, Chrisman B, Stockham N, Paskov K, Wall DP. Crowd Annotations Can Approximate Clinical Autism Impressions from Short Home Videos with Privacy Protections. medRxiv. 2021:2021.07.01.21259683. doi: 10.1101/2021.07.01.21259683.
23. Washington P, Leblanc E, Dunlap K, Penev Y, Kline A, Paskov K, Sun MW, Chrisman B, Stockham N, Varma M. Precision telemedicine through crowdsourced machine learning: testing variability of crowd workers for video-based autism feature recognition. Journal of personalized medicine. 2020;10(3):86.
24. Washington P, Leblanc E, Dunlap K, Penev Y, Varma M, Jung J-Y, Chrisman B, Sun MW, Stockham N, Paskov KM, Kalantarian H, Voss C, Haber N, Wall DP. Selection of trustworthy crowd workers for telemedical diagnosis of pediatric autism spectrum disorder. Biocomputing 2021: WORLD SCIENTIFIC; 2020. p. 14-25.
25. Washington P, Tariq Q, Leblanc E, Chrisman B, Dunlap K, Kline A, Kalantarian H, Penev Y, Paskov K, Voss C, Stockham N, Varma M, Husic A, Kent J, Haber N, Winograd T, Wall DP. Crowdsourced feature tagging for scalable and privacy-preserved autism diagnosis. medRxiv. 2020:2020.12.15.20248283. doi: 10.1101/2020.12.15.20248283.
26. Washington P, Tariq Q, Leblanc E, Chrisman B, Dunlap K, Kline A, Kalantarian H, Penev Y, Paskov K, Voss C, Stockham N, Varma M, Husic A, Kent J, Haber N, Winograd T, Wall DP.

Crowdsourced privacy-preserved feature tagging of short home videos for machine learning ASD detection. Scientific Reports. 2021;11(1):7620. doi: 10.1038/s41598-021-87059-4.
27. al. PWe. Evaluating Privacy-Preserving Mechanisms for Crowdsourcing Pediatric Autism Diagnoses from Home Video. Under review. 2020.
28. Wall DP, Kosmicki J, Deluca TF, Harstad E, Fusaro VA. Use of machine learning to shorten observation-based screening and diagnosis of autism. Transl Psychiatry. 2012;2:e100. Epub 2012/07/27. doi: 10.1038/tp.2012.10. PubMed PMID: 22832900; PMCID: 3337074.
29. Fusaro VA, Daniels J, Duda M, DeLuca TF, D'Angelo O, Tamburello J, Maniscalco J, Wall DP. The Potential of Accelerating Early Detection of Autism through Content Analysis of YouTube Videos. Plos One. 2014;9(4):e93533. doi: ARTN e93533
10.1371/journal.pone.0093533. PubMed PMID: WOS:000336863900022.
30. Tariq Q, Daniels J, Schwartz JN, Washington P, Kalantarian H, Wall DP. Mobile detection of autism through machine learning on home video: A development and prospective validation study. Plos Med. 2018;15(11):e1002705. doi: 10.1371/journal.pmed.1002705; PMCID: PMC6258501.
31. Tariq Q, Fleming SL, Schwartz JN, Dunlap K, Corbin C, Washington P, Kalantarian H, Khan NZ, Darmstadt GL, Wall DP. Detecting Developmental Delay and Autism Through Machine Learning Models Using Home Videos of Bangladeshi Children: Development and Validation Study. J Med Internet Res. 2019;21(4):e13822. Epub 24.04.2019. doi: 10.2196/13822. PubMed PMID: 31017583; PMCID: PMC6505375.
32. Tariq Q, Daniels J, Schwartz JN, Washington P, Kalantarian H, Wall DP. Mobile detection of autism through machine learning on home video: A development and prospective validation study. PLoS Med. 2018;15(11):e1002705. Epub 2018/11/28. doi: 10.1371/journal.pmed.1002705. PubMed PMID: 30481180; PMCID: PMC6258501 following competing interests: DPW is the scientific founder of Cognoa, a company focused on digital pediatric healthcare; the approach and findings presented in this paper are independent from/not related to Cognoa. All other authors have declared no competing interests exist.
33. Megerian JT, Dey S, Melmed RD, Coury DL, Lerner M, Nicholls C, Sohl K, Rouhbakhsh R, Narasimhan A, Romain J, Golla S, Shareef S, Ostrovsky A, Shannon J, Kraft C, Liu-Mayo S, Abbas H, Gal-Szabo DE, Wall DP, Taraman S. Performance of Canvas Dx, a Novel Software-based Autism Spectrum Disorder Diagnosis Aid for Use in a Primary Care Setting (P13-5.001). Neurology. 2022;98(18_supplement):1025. doi: doi:10.1212/WNL.98.18_supplement.1025.
34. Shannon J, Taraman S, Liu-Mayo S, Salomon M, Seal M, Kraft C, Wall D, editors. Exploring the real-world performance of an artificial intelligence-based diagnostic device for autism: an aggregate analysis of early Canvas Dx prescription and output data. ANNALS OF NEUROLOGY; 2023: WILEY 111 RIVER ST, HOBOKEN 07030-5774, NJ USA.
35. Abdar M, Khosravi A, Islam SMS, Acharya UR, Vasilakos AV. The need for quantification of uncertainty in artificial intelligence for clinical data analysis: increasing the level of trust in the decision-making process. IEEE Systems, Man, and Cybernetics Magazine. 2022;8(3):28-40. doi: 10.1109/MSMC.2022.3150144.
36. Kompa B, Snoek J, Beam AL. Second opinion needed: communicating uncertainty in medical machine learning. Npj Digit Med. 2021;4(1):4. doi: 10.1038/s41746-020-00367-3.
37. Wall DP, Liu-Mayo S, Salomon C, Shannon J, Taraman S. Optimizing a de novo artificial intelligence-based medical device under a predetermined change control plan: Improved ability to

detect or rule out pediatric autism. Intelligence-Based Medicine. 2023;8:100102. doi: https://doi.org/10.1016/j.ibmed.2023.100102.
38. Salomon C, Heinz K, Aronson-Ramos J, Wall DP. An analysis of the real world performance of an artificial intelligence based autism diagnostic. Scientific Reports. 2025;15(1):29503. doi: 10.1038/s41598-025-15575-8.
39. Kalantarian H, Jedoui K, Washington P, Tariq Q, Dunlap K, Schwartz J, Wall DP. Labeling images with facial emotion and the potential for pediatric healthcare. Artificial Intelligence in Medicine. 2019;98:77-86. doi: https://doi.org/10.1016/j.artmed.2019.06.004.
40. Kalantarian H, Washington P, Schwartz J, Daniels J, Haber N, Wall DP. Guess What? Journal of Healthcare Informatics Research. 2018. doi: 10.1007/s41666-018-0034-9.
41. Washington P, Kalantarian H, Kent J, Husic A, Kline A, Leblanc E, Hou C, Mutlu OC, Dunlap K, Penev Y, Varma M, Stockham NT, Chrisman B, Paskov K, Sun MW, Jung J-Y, Voss C, Haber N, Wall DP. Improved Digital Therapy for Developmental Pediatrics Using Domain-Specific Artificial Intelligence: Machine Learning Study. JMIR Pediatr Parent. 2022;5(2):e26760. Epub 8.4.2022. doi: 10.2196/26760. PubMed PMID: 35394438.
42. Fombonne E, Coppola L, Mastel S, O'Roak BJ. Validation of Autism Diagnosis and Clinical Data in the SPARK Cohort. Journal of Autism and Developmental Disorders. 2022;52(8):3383-98. doi: 10.1007/s10803-021-05218-y.
43. Sparrow SS, Cicchetti DV, Balla DA, Doll EA. Vineland adaptive behavior scales: Survey forms manual: American Guidance Service; 2005.
44. Duda M, Daniels J, Wall DP. Clinical Evaluation of a Novel and Mobile Autism Risk Assessment. J Autism Dev Disord. 2016;46(6):1953-61. Epub 2016/02/14. doi: 10.1007/s10803-016-2718-4. PubMed PMID: 26873142; PMCID: PMC4860199.
45. Lord C, Rutter M. Social communication questionnaire (SCQ). Torrance, CA: WPS. 2003.
46. Frazier TW, Dimitropoulos A, Abbeduto L, Armstrong-Brine M, Kralovic S, Shih A, Hardan AY, Youngstrom EA, Uljarević M, Team VB. Psychometric evaluation of the Autism Symptom Dimensions Questionnaire. Developmental Medicine & Child Neurology. 2025;67(6):758-69.
47. Canale RR, Larson C, Thomas RP, Barton M, Fein D, Eigsti I-M. Investigating frank autism: clinician initial impressions and autism characteristics. Mol Autism. 2024;15(1):48. doi: 10.1186/s13229-024-00627-z.
48. Jaiswal A, Wall DP, Washington P, editors. Challenges in the Differential Classification of Individual Diagnoses from Co-Occurring Autism and ADHD Using Survey Data. 2024 IEEE EMBS International Conference on Biomedical and Health Informatics (BHI); 2024: IEEE.
49. Jaiswal A, Kruiper R, Rasool A, Nandkeolyar A, Wall DP, Washington P. Digitally Diagnosing Multiple Developmental Delays Using Crowdsourcing Fused With Machine Learning: Protocolfor a Human-in-the-Loop Machine Learning Study. JMIR Res Protoc. 2024;13:e52205. Epub 8.2.2024. doi: 10.2196/52205. PubMed PMID: 38329783.

Evaluation of Large Language Models as Emergency Department Revisit Predictors

Emma Chen[1,2†], Luyang Luo[1†], Fatma Gunturkun[3], Sraavya Sambara[1], Rushil Arora[3], Boyang Tom Jin[3], Pranav Rajpurkar[1,*], and David A Kim[3,*]

[1]*Department of Biomedical Informatics, Harvard Medical School, Boston, MA, USA*
[2]*Harvard John A. Paulson School Of Engineering And Applied Sciences, Cambridge, MA, USA*
[3]*Stanford University, Stanford, CA, USA*
[†]*These authors contributed equally to this work*
[*]*Corresponding authors*
E-mail: yingchen@g.harvard.edu, pranav_rajpurkar@hms.harvard.edu, davidak@stanford.edu

Large Language Models (LLMs) have shown promise in clinical reasoning and question answering, yet their effectiveness for real-world clinical prediction remains an open question. We present the first large-scale study evaluating LLMs for predicting 30-day emergency department (ED) revisits using 138,010 visits from the Adult Emergency Department at Stanford. We assessed two modeling paradigms: (1) direct prediction, where the LLM generates revisit risk assessments in natural language, and (2) embedding-based approaches that leverage LLM-derived vector representations (LLM2Vec) of patient data for downstream modeling. Retrieval augmentation improved direct prediction performance (e.g., Claude 3.7 F1 from 0.3755 (95% CI [0.3647, 0.3864]) to 0.4160 (95% CI [0.4024, 0.4294])), and embedding-based methods consistently outperformed direct approaches, with LLM2Vec achieving F1=0.4505 (95% CI [0.4345, 0.4666]). Despite having access to comprehensive structured and unstructured clinical data, all LLM approaches (F1=0.3022-0.4505) failed to exceed a traditional LightGBM model using only structured data (F1=0.4614 (95% CI [0.4496, 0.4789])). Through systematic analysis of the reasoning chains in 17,488 predictions, we suggest potential failure patterns: reasoning may systematically degrade performance through overweighting medical histories and similar visits, neglecting protective factors, and risk aversion. Our work establishes essential baseline performance while revealing fundamental limitations in current-generation LLMs for clinical prediction tasks.

Keywords: Large Language Models, Emergency Medicine, Clinical Prediction

1. Introduction

Large Language Models (LLMs) have demonstrated impressive medical knowledge, with models like Med-PaLM 2 surpassing physician performance on medical licensing examinations.[1,2] These advances have generated considerable interest in applying LLMs to clinical prediction tasks, where their ability to process unstructured clinical text and leverage pretrained medical knowledge could address longstanding challenges in healthcare.

The Promise and Challenge of LLMs for Clinical Prediction. Emergency department (ED) revisit prediction represents a compelling application for LLMs. Twenty percent

©2025 The Authors. Open Access chapter published by World Scientific Publishing Company and distributed under the terms of the Creative Commons Attribution Non-Commercial (CC BY-NC) 4.0 License.

of discharged ED patients return within 30 days, often due to incomplete evaluation, premature discharge, or inadequate follow-up.[3] Predicting these revisits is challenging because the underlying drivers are multifactorial—spanning clinical, behavioral, and social factors often embedded in unstructured clinical notes and distributed across temporally separated encounters. LLMs are uniquely positioned to address this complexity through their ability to: (1) leverage rich medical knowledge from pretraining, (2) process unstructured inputs like clinical notes and radiology reports, and (3) model longitudinal patient histories across multiple visits.[4–6]

Research Questions and Approach. To evaluate LLM potential for clinical prediction, this study addresses three fundamental questions: (1) What performance can current frontier LLMs achieve in 30-day ED revisit, and how does that compare to a traditional machine learning approach? (2) What LLM modeling paradigms are suitable for predicting 30-day ED revisit? (3) What clinical knowledge do LLMs use when making predictions, and how does reasoning affect this process? Our systematic evaluation across multiple state-of-the-art models and integration strategies provides crucial insights into both the capabilities and limitations of current LLM approaches for complex clinical prediction tasks.

Key Contributions. Our work makes four contributions to understanding LLMs in clinical prediction:

- **Comprehensive evaluation framework:** Using 138,010 ED visits, we establish the first large-scale benchmark comparing direct prediction and embedding-based approaches across multiple state-of-the-art models.
- **Open challenge identification:** We demonstrate that current-generation LLMs cannot exceed traditional machine learning approaches in 30-day ED revisit prediction, even when given access to both structured and unstructured data while the traditional approach uses only structured features.
- **Modeling strategy insights:** We highlight the importance of retrieval augmentation for improving LLM performance. We also show that embedding-based approaches consistently outperform direct prediction, suggesting that LLMs' primary value may lie in representation learning rather than end-to-end reasoning for complex prediction tasks.
- **Systematic analysis of reasoning failures:** Through detailed examination of 17,488 predictions, we identify patterns suggesting how reasoning may degrade LLM performance through systematic biases, including risk aversion and medical history overweighting.

2. Related Work

2.1. *Structured Electronic Health Record (EHR) Foundation Models*

Transformer-based foundation models trained on structured EHR data have emerged as a promising approach to clinical prediction. These models treat EHR sequences as analogous to natural language, encoding events as tokens and leveraging pretraining objectives such as masked event prediction or time-to-event modeling. For example, CLMBR (Clinical Language Model-Based Representations) demonstrated that pretraining on longitudinal structured data improves robustness and sample efficiency in downstream clinical tasks.[7] Similarly, MOTOR

(Many Outcome Time Oriented Representations) introduces a self-supervised time-to-event modeling framework and achieves state-of-the-art performance across 19 clinical tasks using over 9 billion clinical events from 55 million patients.[8] These methods offer robustness to temporal distribution shifts and perform well under limited supervision. However, they require large-scale, site-specific pretraining, and typically exclude unstructured data such as clinical notes or radiology reports.

2.2. *LLMs for Clinical Reasoning and Outcome Prediction*

In parallel, LLMs pretrained on general-domain text have demonstrated impressive capabilities in clinical reasoning and medical question answering.[9] Med-PaLM and Med-PaLM 2, for example, surpass the passing threshold on the US Medical Licensing Examination (USMLE) and outperform physicians on key clinical axes such as reasoning, factual accuracy, and safety.[1,2] Similarly, NYUTron shows that LLMs trained on unstructured clinical notes can serve as general-purpose predictive engines, achieving AUCs between 78.7-94.9% across five clinical and operational tasks within a real-world health system.[10] These results underscore the potential of LLMs to extract high-value representations from unstructured data and generalize across a wide range of clinical contexts with minimal task-specific tuning.[5,11]

The potential of LLMs in clinical prediction is enhanced by recent developments that convert LLMs into effective embedding generators. These techniques, such as LLM2Vec, transform decoder-only LLMs into bidirectional text encoders capable of generating dense vector representations from multimodal EHR inputs for downstream ML tasks.[12] In parallel, specialized text embedding models like Voyage-3-Large (Voyage AI Innovations, Inc.) have emerged as strong baselines for general-purpose text representation learning, offering state-of-the-art performance across diverse text understanding tasks.

2.3. *LLMs for Clinical Outcome Prediction in Emergency Settings*

Several recent studies have explored the use of LLMs for clinical outcome prediction in emergency settings. Gebrael et al. evaluated ChatGPT's ability to triage patients with metastatic prostate cancer in the ED and found high sensitivity in identifying cases requiring admission, along with improved comprehensiveness and accuracy of diagnostic suggestions compared to physicians.[13] Glicksberg et al. investigated GPT-4 for predicting hospital admissions from ED encounters, comparing its performance to traditional ML models with and without prompting and numerical probabilities.[14] Both studies highlight LLMs' potential to support clinical decision-making in emergency care, especially when structured and unstructured data are combined. However, these works rely on naïve prompting strategies and do not explore the use of LLM-derived embeddings or fine-grained modeling of revisit risk. Moreover, they focus on admission prediction rather than revisit forecasting, which is a simpler task whose outcome is known within hours rather than days or weeks.

3. Methods

To evaluate the readiness of LLMs for clinical prediction tasks, we evaluated five approaches for predicting 30-day ED revisit risk. Our methods fall into two main categories: (1) direct

prediction, where the LLM generates revisit risk assessments through its generated text outputs, and (2) embedding-based approaches that use LLM-generated vector representations of patient data for modeling. (Figure 1)

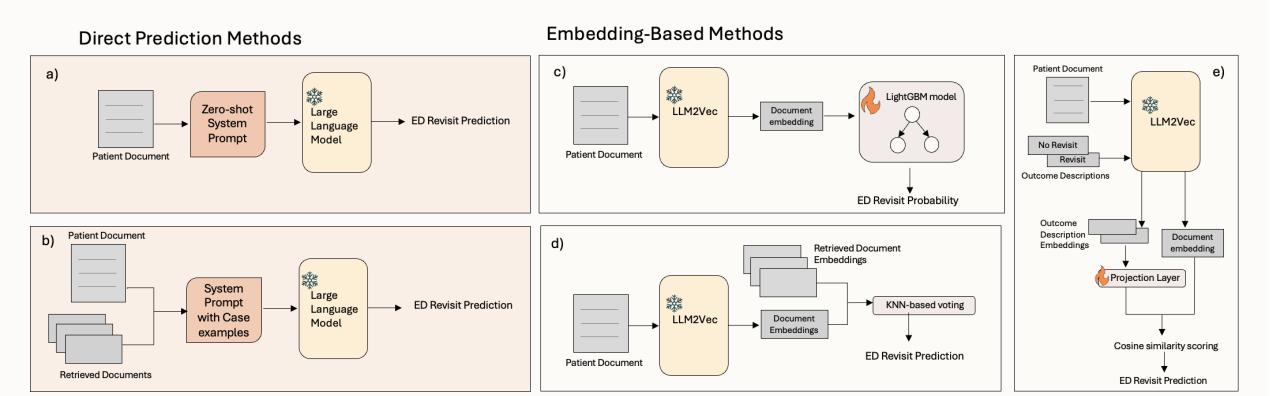

Fig. 1. Overview of Large Language Model (LLM) utilization for 30-day Emergency Department (ED) revisit prediction. Our approach explores two primary paradigms: (a, b) Direct Prediction Methods, where LLMs generate revisit risk assessments directly via text outputs, leveraging (a) zero-shot prompting or (b) retrieval-augmented prompting with case examples. (c, d, e) Embedding-Based Methods generate LLM-derived vector representations (e.g., using LLM2Vec) of patient visit data for downstream modeling, including (c) LightGBM classification, (d) k-Nearest Neighbors (KNN) based lookup, and (e) cosine similarity scoring with retrieved outcome descriptions. Each method processes a "Patient Document" representing the patient's visit data.

3.1. *Data*

We studied 138,010 discharged ED visits from 87,112 adult ED patients, from the Adult Emergency Department at Stanford , between February 1st, 2021, and February 28th, 2024. The dataset is split chronologically into 100,987, 19,535, and 17,488 visits for training, validation, and test sets, with no patient overlap between splits. 30-day ED revisit rates in the train, validation, and test splits are 17.45%, 15.77%, and 16.45%, respectively.

The dataset contains both structured and unstructured elements from the EHR. Visit-level data includes patient demographics (age, gender, race, ethnicity), socioeconomic indicators (payor information), and visit outcomes (length of stay, disposition). Vital signs (heart rate, respiratory rate, oxygen saturation, temperature, systolic blood pressure, diastolic blood pressure) are summarized by minimum, maximum, triage, and final values throughout the visit. Orders data captures procedure and medication orders placed during the visit. Laboratory results contain both categorical interpretations (normal/abnormal) and numerical values with reference ranges. Home medication data includes generic and brand names with medication classifications. Radiology data consists of study types and de-identified free-text narrative impressions. Past medical history combines ICD-10 diagnosis codes and descriptions, Clinical Classification Software (CCS) categories, and diagnosis dates. Past ED visit history includes temporal patterns of ED utilization, with chief complaints, diagnoses, and dispositions. Hospital admission data includes admit service, level of care, and hospital length of stay. While we only predict revisits for ED patients discharged home, our predictions draw on informa-

tion from all their previous ED visits, regardless of whether those visits ended in discharge or admission. (Supplement: Table 1)

3.2. *Prediction Using Structured EHR Data*

To provide a traditional machine learning baseline, we trained a LightGBM[15] model using a binary classification objective on the structured EHR only, totaling 2,221 features. Specifically, we included five demographic variables, admission types, diagnosis codes mapped to 278 Clinical Classifications Software categories, 46 distinct chief complaints, 1,675 clinical orders (e.g., medications, procedures), seven triage measurements, 181 laboratory test results (each encoded as abnormal = 1 or normal = 0), and 36 summary features derived from vital signs (e.g., minimum or maximum heart rate). Additionally, two aggregated temporal features were derived to represent the number of ED visits and inpatient admissions within the six months preceding each index visit. The model's outputs are thresholded at the value that maximizes F1 on the validation set.

3.3. *Visit Documents*

We developed a rule-based approach to convert the raw EHR data, including both structured and unstructured elements, into a comprehensive visit document for each ED encounter. Each document begins with patient demographics and medical history, followed by current medications. Previous ED visits from the past six months are summarized with their chief complaints, diagnoses, and dispositions, including hospital admissions when applicable. The current visit section includes arrival information, chief complaint, vital signs (with triage, final, minimum, and maximum values), visit timeline (arrival, rooming, disposition decision, and departure times), procedural and medication orders, laboratory and imaging results, diagnosis, and disposition details. For visits resulting in admission, additional details about admit time, service, and level of care are included. Laboratory results are categorized by abnormality status (critical, abnormal, normal) to highlight significant findings. Timing information is in the format of time, day of the week, and month. (Supplement: Table 1, Figure 1)

3.4. *Direct LLM Prediction Methods*

We implemented two approaches where the LLM directly predicts revisit risk through text generation. We evaluated several state-of-the-art LLMs with different characteristics. Reasoning models included Claude 3.7 (claude-3-7-sonnet-20250219-v1), a multimodal model with an optional reasoning mode designed to enhance step-by-step analytical thinking, which we evaluated in both standard and reasoning mode; OpenAI o3-mini (2024-12-01-preview), a smaller, more efficient variant from OpenAI's o3 series; and Deepseek R1 (v1), a specialized model from Deepseek AI that employs structured reasoning techniques. Models without explicit reasoning modes included GPT-4o (2024-10-21), OpenAI's multimodal model optimized for instruction-following and responsiveness, but without a dedicated reasoning mode that emphasizes step-by-step analytical processing.

Zero-Shot Direct Prediction In our baseline direct prediction approach, we prompted the LLM to assess ED revisit risk without providing examples. Additionally, we calculated the prevalence of 30-day revisits in the training data and included that in the prompt:

```
You are an expert in emergency department patient risk assessment. Given a
    patient's current ED visit data, evaluate their risk of returning to the ED
    within 30 days. Assess the patient's 30-day ED revisit risk as HIGH or LOW.
    If the revisit risk is HIGH, provide the most likely chief complaint for a
    potential return visit. Consider that the 30-day ED revisit prevalence in
    this hospital is 17.45%. Pay special attention to patterns in previous visits
    , particularly repeated visits for similar complaints. Return your assessment
     in JSON format: {"risk": "HIGH" or "LOW", "risk_factors": {"list key factors
     driving the risk assessment"}}.
```

Retrieval-Augmented Generation We enhanced the direct prediction approach by implementing Retrieval-Augmented Generation (RAG), where each prediction was informed by similar cases. We used a pretrained embedding model (LLM2Vec-Meta-Llama-3-8B-Instruct-mntp-unsup-simcse) to generate embeddings for visit documents and retrieved the 10 most relevant cases from the training set for each test patient based on cosine similarity. These retrieved cases were then provided to the LLM as few-shot examples to augment the same prompt used by zero-shot direct prediction:

```
Following are 10 examples:
###
{patient's EHR data using the same template}
30-day revisit: {'Yes' or 'No'}
####
...
Now, assess the following case:
```

3.5. *Text Embedding-Based Prediction Methods*

We implemented three distinct methods using LLM-derived embeddings to predict ED revisit disposition. For our primary experiments, we used LLM2Vec-Meta-Llama-3-8B-Instruct-mntp-unsup-simcse, which converts a Llama 3 8B instruction-tuned model into a text embedding model. To establish a performance baseline, we repeated all experiments using Voyage-3-Large, a state-of-the-art general-purpose text embedding model.

Embedding Similarity Classification Our first approach uses semantic similarity to classify outcomes by comparing visit document embeddings with outcome description embeddings. We created natural language descriptions for each possible outcome and measured how closely each visit's embedding matched these outcome descriptions. The outcome descriptions were:

- No revisit with 30 days: "No return visits to the Emergency Department occur within 30 days following the current Emergency Department visit."
- Revisit within 30 days: "A return visit to the Emergency Department occurs within 30 days following the current Emergency Department visit for any reason."

Predictions were made by computing cosine similarities between the patient visit embedding and each outcome description embedding, with the highest similarity score determining the predicted outcome. Formally, for patient visit embedding $\mathbf{p}$ and outcome description em-

bedding $\mathbf{o}$, the cosine similarity is calculated as:

$$\cos(\mathbf{p}, \mathbf{o}) = \frac{\mathbf{p} \cdot \mathbf{o}}{\|\mathbf{p}\|\|\mathbf{o}\|} = \frac{\sum_{i=1}^{n} p_i o_i}{\sqrt{\sum_{i=1}^{n} p_i^2} \sqrt{\sum_{i=1}^{n} o_i^2}} \quad (1)$$

where $\mathbf{p} \cdot \mathbf{o}$ represents the dot product of the two vectors, and $||\mathbf{p}||$ and $||\mathbf{o}||$ represent their Euclidean norms (magnitudes). To enhance the discriminative power of our model, we train a single linear projection layer for the outcome embeddings. This projection is implemented as $\mathbf{o}_{\text{proj}} = W_{\text{projection}} \cdot \mathbf{o}$, where $W_{\text{projection}}$ is a learnable weight matrix. This projection helps to align the outcome embeddings with the relevant semantic features in the patient data space.

LLM Embeddings with LightGBM For our second approach, we trained a LightGBM model on the patient document embeddings to predict 30-day ED revisit. We selected LightGBM[15] due to its widespread use and demonstrated strong performance in predicting hospital admissions and readmissions across various clinical settings.[16–18]

K-Nearest Neighbor Prediction Our third embedding-based approach used k nearest-neighbor (KNN) retrieval to identify similar cases for prediction. We created patient document embeddings for visits in the training set. These embeddings were stored in a FAISS (Facebook AI Similarity Search) vector database for efficient similarity search. During prediction, we retrieved the k most similar cases based on cosine similarity between the document embedding of the patient in query and those in the vector store. Note that because there is no patient overlap between splits, the retrieved cases will only belong to patients different from the one we are making predictions for. To predict the probability of 30-day ED revisits, we calculated the proportion of similar cases in the training set that resulted in revisits, with Laplace smoothing applied to avoid zero probabilities:

$$P(\text{revisit}) = \frac{\text{count of revisit neighbors} + 1}{\text{total neighbors} + 2}$$

We experimented with multiple k values (10, 20, 30, 50, 100, 500, 1000, 2000, 5000, 10000) to find the optimal neighborhood size using the validation set.

4. Results

4.1. *Overall Performance Comparison*

All performance metrics are reported with 95% confidence intervals computed using bootstrap resampling with 1,000 iterations. Among LLM-based approaches, embedding methods consistently outperformed direct prediction. LLM-derived embeddings (LLM2Vec) achieved competitive performance at F1=0.4505 (95% CI [0.4345, 0.4666]) compared to Voyage-3-Large (F1=0.4608 (95% CI [0.4375, 0.4667])). Notably, RAG provided consistent improvements across all direct prediction models. However, we also found that a structured EHR baseline achieved performance (F1=0.4614 (95% CI [0.4496, 0.4789])) that exceeded LLM-based methods (F1=0.3022-0.4505). (Figure 2, Supplement: Table 2-7)

4.2. *Direct Prediction Performance*

Figure 3 demonstrate the performance of various LLMs in directly predicting ED revisits without additional context. F1 scores ranged from 0.3022 to 0.3889, with o3-mini achieving

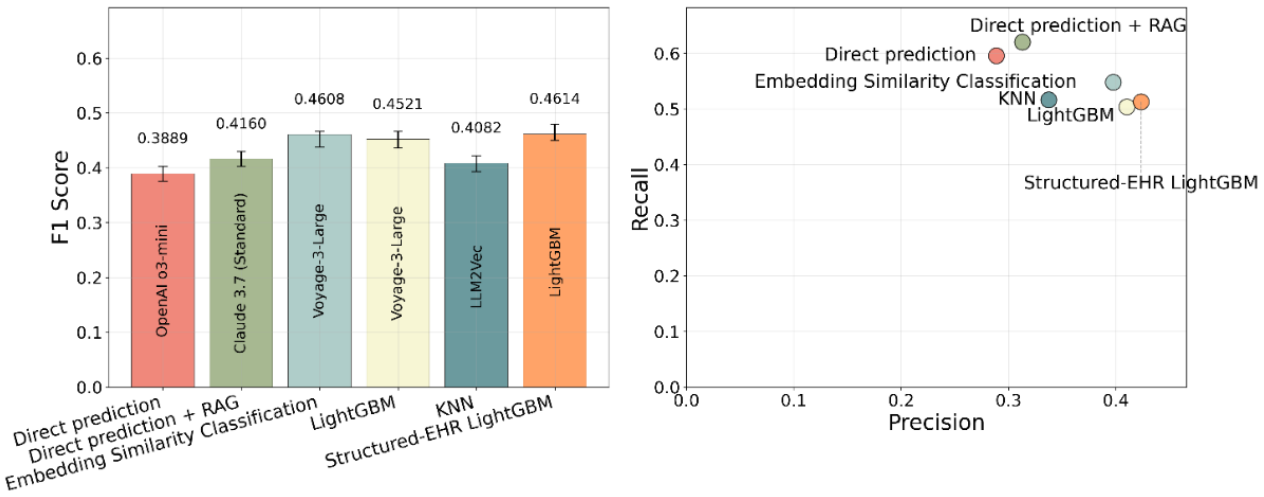

Fig. 2. Comparison of the best model across modeling paradigms.

the highest performance among zero-shot approaches. The precision-recall breakdown reveals that models exhibited different operational characteristics, with Deepseek R1 and Claude 3.7 (reasoning) favoring high recall (>85%) at the expense of precision (<20%), while GPT-4o and Claude 3.7 (standard) achieved a more balanced precision-recall profile.

Incorporating retrieval augmentation with the top 10 similar cases substantially improved performance across all models. The most significant gains were observed in GPT-4o (from F1=0.3403 to 0.3867) and Claude 3.7 (standard), with the latter achieving the highest overall F1 score of 0.4160 (95% CI [0.4024, 0.4294]) among direct prediction methods. This improvement suggests that providing LLMs with similar cases enables them to identify relevant patterns that enhance prediction accuracy, potentially mirroring how clinicians draw upon their experience with similar patients. (Figure 3; Supplement: Table 2,3)

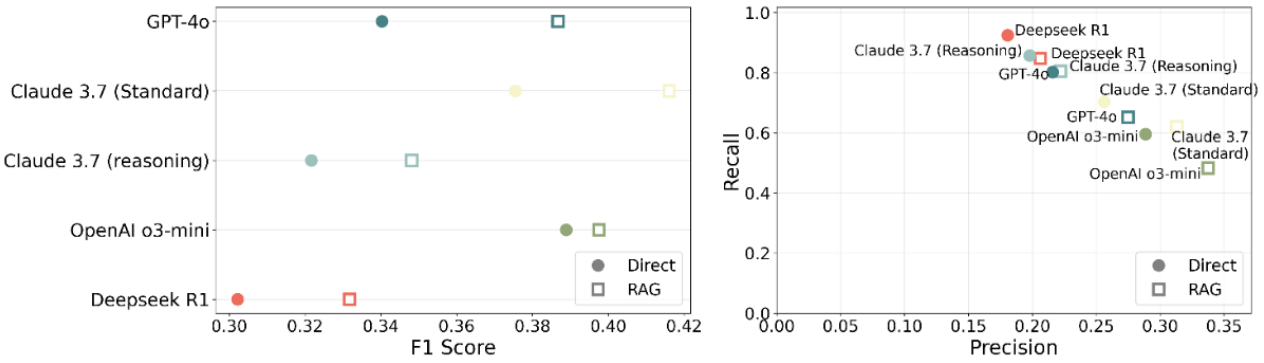

Fig. 3. Performance of direct prediction with and without retrieval augmentation (RAG) across LLMs.

4.3. *Embedding-Based Method Performance*

Figure 4 present the performance of different embedding approaches across three prediction methods: embedding similarity classification, LightGBM, and KNN-based prediction. Embedding similarity classification achieved the highest performance across all metrics (F1,

precision@recall=0.95, precision@recall=0.85) for both embedding models. Voyage-3-Large achieved the highest performance in both similarity classification (F1=0.4608 (95% CI [0.4375, 0.4667])) and LightGBM (F1=0.4521 (95% CI [0.4358, 0.4667])) approaches. However, LLM2Vec demonstrated competitive performance with F1=0.4505 (95% CI [0.4345, 0.4666]) in similarity classification and F1=0.4386 (95% CI [0.4231, 0.4531]) in LightGBM, showing that the performance gap between LLM-derived and specialized embedding models is relatively modest. (Supplement: Table 4-6)

For our KNN approach, we observed performance variations across different neighborhood sizes. With LLM2Vec embeddings, performance improved as k increased from 10 (F1=0.3688 (95% CI [0.3536, 0.3838])) to 500 (F1=0.4082 (95% CI [0.3927, 0.4218])), before declining with larger k values. Similarly, with Voyage-3-Large embeddings, performance peaked at k=100 (F1=0.4002 (95% CI [0.3849, 0.4137])). The inverted-U performance curve across k values suggests a trade-off between capturing relevant cases and introducing noise, indicating that while a moderate number of similar cases provides useful signal for revisit prediction, extremely large neighborhood sizes dilute this signal by incorporating less relevant cases. The competitive performance of simple KNN approaches (F1 >0.4) validates that both LLM2Vec and Voyage-3-Large capture clinically relevant patient similarity—when patients are similar in embedding space, their revisit outcomes are also similar, making the prevalence of revisits among retrieved neighbors a reliable predictor. (Supplement: Table 6)

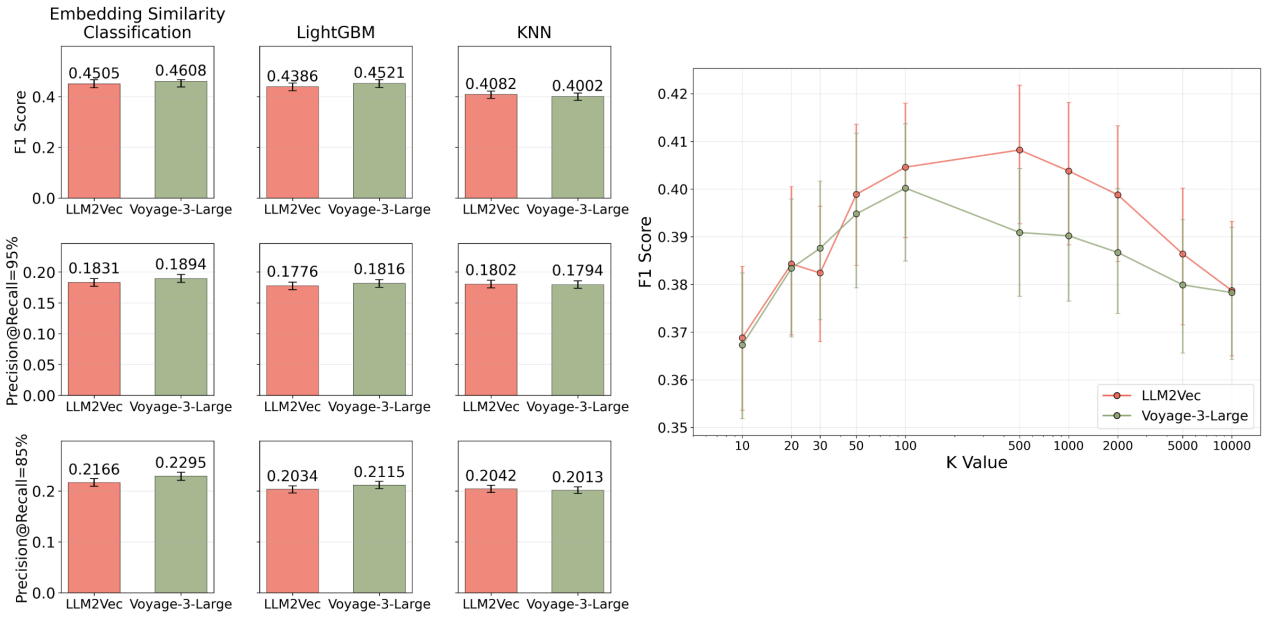

Fig. 4. Performance of embedding-based methods (similarity classification, LightGBM, KNN) using LLM2Vec and Voyage-3-Large (left) and the impact of k on performance for KNN (right).

4.4. *The Challenge of Reasoning: When Sophisticated Models Perform Worse*

Contrary to expectations, explicit reasoning modes didn't consistently improve prediction performance. This finding is particularly striking given that reasoning capability is often con-

sidered a hallmark of advanced LLMs. We conducted a quantitative and qualitative analysis on the responses of Claude 3.7 with RAG in the reasoning mode because it allows a controlled comparison against the standard mode to evaluate the impact of reasoning. (Supplement C,D)

4.4.1. *Reasoning Mode Performance Patterns*

Claude 3.7's standard mode (F1=0.3755 (95% CI [0.3647, 0.3864])) outperformed its reasoning counterpart (F1=0.3217 (95% CI [0.3125, 0.3311])). To understand this phenomenon, we analyzed prediction changes when reasoning was enabled, focusing on the 4,891 cases where Claude 3.7's predictions differed between standard and reasoning modes.

The analysis revealed a systematic bias: the reasoning mode predominantly changed predictions toward higher risk. Of cases where predictions were flipped after enabling reasoning:

- Correct improvements: 542 cases changed from Low to High risk correctly, 69 cases changed from High to Low risk correctly
- Incorrect changes: 4,271 cases changed from Low to High risk incorrectly, 9 cases changed from High to Low risk incorrectly

4.4.2. *Systematic Analysis of Reasoning Failures*

We conducted a comprehensive qualitative analysis using GPT-4o to examine Claude 3.7's reasoning chains on cases where reasoning changed the prediction. Summarizing the qualitative analysis with Claude Sonnet 4 suggest several factors that may cause reasoning-mode failures:

When Reasoning Hurts Performance (4271 cases): The most common failure occurred when correct low-risk predictions became incorrect high-risk predictions. Key patterns included:

- *Medical history overweighting*: Excessive emphasis on chronic conditions and complex medical histories while undervaluing protective factors, including no prior ED visits, normal test results, stable vital signs, and etc. (87.59% cases)
- *Risk aversion*: The step-by-step reasoning made the model more conservative, favoring high-risk predictions to avoid missing potential problems (76.96% cases)
- *Statistical misinterpretation*: Focus on small percentages of similar cases that experienced revisits while ignoring that the majority did not return (41.65% cases)

When Reasoning Helps Performance (542 cases): Reasoning successfully identified missed high-risk cases by:

- *Capturing subtle risk factors*: Noticing demographic and social predictors, such as insurance status, medication adherence issues, that affect follow-up (90.04%)
- *Identifying untreated conditions*: Finding abnormal laboratory results with no or inadequate corresponding interventions (63.28% cases)
- *Leveraging temporal patterns*: Finding escalating patterns by connecting current visit to recent ED visits for related complaints (26.38% cases)
- *Catching concerning vital signs*: Noticing worsening vitals at discharge, such as low SpO2, persistent tachycardia, that signal instability (25.46% cases)
- *Recognizing diagnostic mismatches*: Identifying cases where discharge diagnoses didn't match presenting symptoms (10.52% cases)

4.4.3. *Factors Underlying LLM Predictions*

To characterize what factors drive LLM predictions, we used OpenAI's text-embedding-3-large to embed the "*risk_factors*" in Claude 3.7's responses and applied k-means clustering, identifying 56 factor groupings. The full list with random samples from each grouping can be found in Supplement Table 8. The five most frequently considered factors align with established revisit prediction literature: (1) Population Revisit Patterns - comparisons to similar cases and hospital baseline rate (n=3530), (2) Very Recent Prior Visits - ED visits within days/weeks of current presentation (n=2755), (3) Frequent ED Utilization - patterns of multiple recent visits (n=1857), (4) ED Length of Stay - duration of encounters (n=1821), and (5) Ongoing Treatment Protocols - continued therapies requiring follow-up (n=1757).[19–21]

To understand whether the LLM utilized the provided similar cases for prediction, we prompted GPT-4o to classify any references to the retrieved cases in the reasoning chain, showing that 99.15% of the cases have references. Besides, the k-mean clustering above shows that comparisons to similar cases and hospital baseline revisit rates is the most used risk factor, confirming again that the LLM really reasons over similar cases.

5. Discussion

Current LLMs Cannot Exceed Traditional Approaches Despite Capability to Process Richer Data Our study reveals a striking finding that despite providing LLMs with comprehensive structured and unstructured clinical data, all LLM-based approaches (F1=0.3022-0.4505) failed to exceed a simple LightGBM model trained only on structured EHR features (F1=0.4614 (95% CI [0.4496, 0.4789])). While LLMs showed varying effectiveness depending on integration strategies, the fundamental limitation persists across all approaches, challenging assumptions about LLMs' readiness for complex clinical prediction tasks.

Zero-Shot Prediction Demonstrates High Recall but Limited Precision Direct zero-shot prediction using LLMs yielded modest performance (F1 scores 0.3022-0.3889), with these models demonstrating a tendency toward high recall at the expense of precision. This overestimate of revisit risk is potentially caused by the characteristics of ED patients who typically have multiple comorbidities and acute presentations. The clinical consequence of such behavior would be an excessive number of false positives, limiting practical utility in resource-constrained healthcare environments where targeted interventions must be allocated efficiently.

Retrieval-Based Methods Offer Interpretability and Clinically Meaningful Context Notably, our simple KNN approaches using LLM embeddings achieved competitive performance (F1=0.4082 (95% CI [0.3927, 0.4218]) and 0.4002 (95% CI [0.3849, 0.4137]) for LLM2Vec and Voyage-3-Large respectively), suggesting the similar cases are clinically informative. This approach combines reasonable performance with high interpretability, as similar cases can be presented alongside predictions to provide clinicians with concrete examples informing the risk assessment. Such transparency may enhance clinical trust and adoption while enabling physicians to incorporate their judgment when similar cases reveal important nuances not captured in the prediction itself.

Retrieval augmentation with similar cases significantly improved LLM performance across

all models evaluated. This enhancement was particularly pronounced for Claude 3.7 (standard mode with reasoning disabled) and GPT-4o. The consistent benefit of retrieval augmentation suggests that LLMs can effectively leverage pattern recognition from relevant cases—a process that mirrors clinical reasoning, where physicians draw upon their experience with similar patients to inform prognostication. This finding aligns with recent work showing that case-based reasoning can enhance clinical decision support systems.[14]

Embedding-Based Models Yield Strong Performance with Tradeoffs in Interpretability Embedding-based approaches demonstrated superior performance compared to direct prediction methods, with LLM2Vec embeddings achieving F1 scores exceeding 0.45 when combined with embedding similarity classification. However, this performance gain comes with a tradeoff in interpretability—while direct LLM predictions can include explanatory text and reference similar cases, methods built on embeddings function as relative black boxes from a clinical perspective.

Our analysis of LLM reasoning suggests a potential paradox The very capability that makes LLMs appear more "intelligent"—their ability to engage in step-by-step reasoning—may systematically degrade prediction performance in clinical contexts. Through automated analysis of reasoning chains, we observed that explicit reasoning appears more risk averse and may overly focus on small percentages of similar cases that experienced revisits while potentially ignoring that the majority did not return. It also seems to overweight complex medical histories and seek confirmatory evidence for identified risk factors, while potentially discounting contradictory evidence and protective factors. These potential confirmation biases in LLM reasoning may mirror well-documented challenges in human clinical decision-making,[22] though further validation with human expert review is needed to confirm these patterns.

Limitations and Future Directions Our dataset includes EHR components unavailable in MIMIC-IV-ED, the only publicly available ED dataset, precluding external validation. We focused on binary revisit prediction rather than more clinically actionable outcomes such as preventable returns or severity-stratified revisits. Our outcome data captures only Stanford ED revisits, potentially missing visits to other emergency departments; however, this limitation affects all methods equally and should not bias comparative performance. We did not prospectively evaluate the impact of these predictions on clinical decision-making or patient outcomes. Our models use complete ED visit data available at discharge, limiting immediate applicability for pre-emptive interventions during the visit, though many interventions can be delivered after discharge (e.g., expedited clinic or telemedicine follow-up), and LLMs' flexible input format enables adaptation to earlier time points during visits at potential cost to accuracy. While our findings reveal fundamental limitations of current LLMs for this task, targeted post-training approaches warrant investigation. Supervised fine-tuning or reinforcement learning from human feedback (RLHF/DPO[23,24]) incorporating physician evaluations could potentially improve both prediction accuracy and clinical alignment.

Supplement `https://github.com/dkimlab/PSB_2026_EDLLM_Supplement`

Acknowledgement This research was supported in part by the National Institutes of Health, grant number 1R01HL172794.

References

1. K. Singhal, T. Tu, J. Gottweis, R. Sayres, E. Wulczyn, L. Hou, K. Clark, S. Pfohl, H. Cole-Lewis, D. Neal, M. Schaekermann, A. Wang, M. Amin, S. Lachgar, P. Mansfield, S. Prakash, B. Green, E. Dominowska, B. Aguera y Arcas, N. Tomasev, Y. Liu, R. Wong, C. Semturs, S. S. Mahdavi, J. Barral, D. Webster, G. S. Corrado, Y. Matias, S. Azizi, A. Karthikesalingam and V. Natarajan, Towards Expert-Level Medical Question Answering with Large Language Models (2023), arXiv preprint arXiv:2305.09617. https://arxiv.org/abs/2305.09617.
2. K. Singhal, S. Azizi, T. Tu, S. S. Mahdavi, J. Wei, H. W. Chung, N. Scales, A. Tanwani, H. Cole-Lewis, S. Pfohl, P. Payne, M. Seneviratne, P. Gamble, C. Kelly, A. Babiker, N. Schärli, A. Chowdhery, P. Mansfield, D. Demner-Fushman, B. Agüera y Arcas, D. Webster, G. S. Corrado, Y. Matias, K. Chou, J. Gottweis, N. Tomasev, Y. Liu, A. Rajkomar, J. Barral, C. Semturs, A. Karthikesalingam and V. Natarajan, Large language models encode clinical knowledge, *Nature* **620**, 172 (2023), https://www.nature.com/articles/s41586-023-06291-2.
3. J. S. Dhaliwal and A. K. Dang, Reducing Hospital Readmissions, in *StatPearls [Internet]*, (StatPearls Publishing, Treasure Island (FL), 2024) Last updated June 7, 2024. https://www.ncbi.nlm.nih.gov/books/NBK606114/.
4. H. Ahsan, D. J. McInerney, J. Kim, C. Potter, G. Young, S. Amir and B. C. Wallace, Retrieving Evidence from EHRs with LLMs: Possibilities and Challenges, *Proceedings of Machine Learning Research* **248**, 489 (2024), PMID: 39224857, PMCID: PMC11368037. https://pubmed.ncbi.nlm.nih.gov/39224857/.
5. G. Wang, G. Yang, Z. Du, L. Fan and X. Li, CLINICALGPT: Large Language Models Finetuned with Diverse Medical Data and Comprehensive Evaluation (2023), arXiv:2306.09968 [cs.CL]. https://arxiv.org/abs/2306.09968.
6. Q. Shen, X. Zhang, H. Ren, Q. Guo and Z. Yi, Knowledge-embedded large language models for emergency triage, *Knowledge-Based Systems* **283**, p. 110574 (2025), https://www.sciencedirect.com/science/article/abs/pii/S0950705125004782.
7. E. Steinberg, K. Jung, J. A. Fries, C. K. Corbin, S. R. Pfohl and N. H. Shah, Language Models Are An Effective Patient Representation Learning Technique For Electronic Health Record Data (2020), arXiv:2001.05295 [cs.CL]. https://arxiv.org/abs/2001.05295.
8. E. Steinberg, J. Fries, Y. Xu and N. Shah, MOTOR: A Time-To-Event Foundation Model For Structured Medical Records (2023), arXiv:2301.03150 [cs.LG]. https://arxiv.org/abs/2301.03150.
9. C. Y. K. Williams, B. Y. Miao, A. E. Kornblith and A. J. Butte, Evaluating the use of large language models to provide clinical recommendations in the Emergency Department, *Nature Communications* **15**, 1 (2024), https://www.nature.com/articles/s41467-024-52415-1.
10. L. Y. Jiang, X. C. Liu, N. Pour Nejatian, M. Nasir-Moin, D. Wang, A. Abidin, K. Eaton, H. A. Riina, I. Laufer, P. Punjabi *et al.*, Health system-scale language models are all-purpose prediction engines, *Nature* **619**, 357 (2023), https://www.nature.com/articles/s41586-023-06160-y.
11. H. Wang, C. Liu, N. Xi, Z. Qiang, S. Zhao, B. Qin and T. Liu, HuaTuo: Tuning LLaMA Model with Chinese Medical Knowledge (2023), arXiv:2304.06975 [cs.CL]. https://arxiv.org/abs/2304.06975.
12. P. BehnamGhader, V. Adlakha, M. Mosbach, D. Bahdanau, N. Chapados and S. Reddy, LLM2Vec: Large Language Models Are Secretly Powerful Text Encoders, in *Proceedings of the Conference on Language Modeling (COLM)*, 2024. arXiv preprint arXiv:2404.05961. https://arxiv.org/abs/2404.05961.
13. G. Gebrael, K. K. Sahu, B. Chigarira, N. Tripathi, V. M. Thomas, N. Sayegh, B. L. Maughan, N. Agarwal, U. Swami and H. Li, Enhancing Triage Efficiency and Accuracy in Emergency Rooms for Patients with Metastatic Prostate Cancer: A Retrospective Analysis of Artificial Intelligence-

Assisted Triage Using ChatGPT 4.0, *Cancers* **15**, p. 3717 (2023), https://pubmed.ncbi.nlm.nih.gov/37509379/.
14. B. S. Glicksberg, P. Timsina, D. Patel, A. Sawant, A. Vaid, G. Raut, A. W. Charney, D. Apakama, B. G. Carr, R. Freeman *et al.*, Evaluating the accuracy of a state-of-the-art large language model for prediction of admissions from the emergency room, *Journal of the American Medical Informatics Association* **31**, 1921 (2024).
15. G. Ke, Q. Meng, T. Finley, T. Wang, W. Chen, W. Ma, Q. Ye and T.-Y. Liu, Lightgbm: A highly efficient gradient boosting decision tree, in *Advances in Neural Information Processing Systems 30*, 2017.
16. Y. Hu, F. Ma, M. Hu, B. Shi, D. Pan and J. Ren, Development and validation of a machine learning model to predict the risk of readmission within one year in HFpEF patients: Short title: Prediction of HFpEF readmission, *International Journal of Medical Informatics* **194**, p. 105703 (2025).
17. J. Miao, C. Zuo, H. Cao, Z. Gu, Y. Huang, Y. Song and F. Wang, Predicting ICU readmission risks in intracerebral hemorrhage patients: Insights from machine learning models using MIMIC databases, *Journal of the Neurological Sciences* **456**, p. 122849 (2024).
18. C. Brossard, C. Goetz, P. Catoire, L. Cipolat, C. Guyeux, C. Gil Jardine, M. Akplogan and L. Abensur Vuillaume, Predicting emergency department admissions using a machine-learning algorithm: a proof of concept with retrospective study, *BMC Emergency Medicine* **25**, p. 3 (2025).
19. S. Janda and J. Sansuk, Factors Associated with Re-attendance at Emergency Departments Among Older Adults: A Cross-Sectional Analytical Study, *Inquiry* **62**, p. 469580251349652 (2025), https://doi.org/10.1177/00469580251349652.
20. I. Dufour, M. C. Chouinard, N. Dubuc, J. Beaudin, S. Lafontaine and C. Hudon, Factors associated with frequent use of emergency-department services in a geriatric population: a systematic review, *BMC Geriatrics* **19**, p. 185 (2019), https://doi.org/10.1186/s12877-019-1197-9.
21. P. Tangkulpanich, C. Yuksen, W. Kongchok and C. Jenpanitpong, Clinical predictors of emergency department revisits within 48 hours of discharge; a case control study, *Archives of academic emergency medicine* **9**, p. e1 (2020).
22. B. Sætrevik, V. T. Seeligmann, T. F. Frotvedt and Ø. Keilegavlen Bondevik, Anchoring, confirmation and confidence bias among medical decision-makers, *Collabra: Psychology* **10**, p. 126223 (2024).
23. P. Christiano, J. Leike, T. B. Brown, M. Martic, S. Legg and D. Amodei, Deep reinforcement learning from human preferences (2023).
24. R. Rafailov, A. Sharma, E. Mitchell, S. Ermon, C. D. Manning and C. Finn, Direct preference optimization: Your language model is secretly a reward model (2024).

Speaker Role Identification in Clinical Conversations*

[1]Andrew Zolensky, [2]Kuk Jin Jang , [3]Janice Sabin, [3]Andrea Hartzler, [1]Basam Alasaly, [1]Sriharsha Mopidevi, [4,5]Mark Liberman, [1,4,6]Kevin Johnson

[1]*Department of Biostatistics, Epidemiology, and Informatics, University of Pennsylvania, Philadelphia, PA, USA*

[2]*Department of Computer Engineering, Hongik University, Seoul, South Korea*

[3]*Biomedical Informatics and Medical Education, University of Washington, Seattle, WA, USA*

[4]*Department of Computer Science, University of Pennsylvania, Philadelphia, PA, USA*

[5]*Department of Linguistics, University of Pennsylvania, Philadelphia, Pennsylvania, USA*

[6]*Annenberg School for Communication, University of Pennsylvania, Philadelphia, Pennsylvania, USA*

Email: Andrew.Zolensky@PennMedicine.upenn.edu, jangkj@hongik.ac.kr, sabinja@uw.edu, andreah@uw.edu, Basam.Alasaly@PennMedicine.upenn.edu, Sriharsha.Mopidevi@PennMedicine.upenn.edu, myl@cis.upenn.edu, Kevin.Johnson1@PennMedicine.upenn.edu

Patient-clinician communication research is crucial for understanding interaction dynamics and for predicting outcomes that are associated with clinical discourse. Traditionally, interaction analysis is conducted manually because of challenges such as Speaker Role Identification (SRI), which must reliably differentiate between doctors, medical assistants, patients, and other caregivers in the same room. Although automatic speech recognition with diarization can efficiently create a transcript with separate labels for each speaker, these systems are not able to assign roles to each person in the interaction. Previous SRI studies in task-oriented scenarios have directly predicted roles using linguistic features, bypassing diarization. However, to our knowledge nobody has investigated SRI in clinical settings. We explored whether Large Language Models (LLMs) such as BERT could accurately identify speaker roles in clinical transcripts, with and without diarization. We used veridical turn segmentation and diarization identifiers, fine-tuning each model at varying levels of identifier corruption to assess impact on performance. Our results demonstrate that BERT achieves high performance with linguistic signals alone (82% accuracy/82% F1-score), while incorporating accurate diarization identifiers further enhances accuracy (95%/95%). We conclude that fine-tuned LLMs are effective tools for SRI in clinical settings.

Keywords: Speaker Role Identification, Clinical Conversations, Large Language Models, Natural Language Processing

1. Introduction

Patient-clinician interaction forms a central component of healthcare, generating medically relevant data and situating interventions. Effective communication between clinicians and patients impacts

* This work was supported by the National Institutes of Health under Award Number DP1-LM-014558. The content herein is the sole responsibility of the authors and does not necessarily reflect the views of the National Institutes of Health.

© 2025 The Authors. Open Access chapter published by World Scientific Publishing Company and distributed under the terms of the Creative Commons Attribution Non-Commercial (CC BY-NC) 4.0 License.

healthcare utilization, medical adherence, and various other positive and negative functional outcomes [1][2][3]. Health systems recognize the critical role of communication by adopting research-informed guidelines for judging quality of patient-clinician communication, such as the Six Core Competencies for medical professionals defined by the Accreditation Council for Graduate Medical Education [4][5]. One such competency is Interpersonal and Communication Skills (ICS), including "effective information exchange and teaming with patients, their families, and other health professionals." Similarly, effective communication is central to Patient-Centered Care (PCC), a model in which patient participation and decision-sharing are key [3][6]. Nevertheless, precisely evaluating what constitutes "effective communication" is an ongoing research challenge [7].

Evaluating communication requires electronic representations of recorded conversations, which can be provided as textual transcripts derived from speech-to-text applications. For these transcripts to be useful for further research, it is necessary to accurately attribute each utterance to the correct participant, a process we refer to as Speaker Role Identification (SRI). Typical roles in a clinical setting include "physician," "medical assistant," and "patient."

Diarization tools, often included with automated transcription services, label audio by distinguishing between speakers based on acoustic features. To do so, diarization pipelines segment audio into turns using voice activity detection and then utilize clustering algorithms to group utterances based on spectrographic representations [8]. However, these tools assign generic diarization identifiers such as "Speaker 1" or "Speaker 2," without mapping them to functional roles like "physician" or "patient". As a result, SRI researchers have employed pipelines that use diarization identifiers to group utterances into disjoint sets, then employ either structural heuristics or lexical modeling on each group to infer speaker roles [9][10]. However, diarization errors may propagate through these pipelines and significantly undermine the accuracy of SRI.

Furthermore, reliance on audio cues causes diarization algorithms to overlook valuable linguistic information present in the transcript, which might be useful for downstream SRI, such as role-specific vocabulary. Research on SRI in parallel sources of conversational data, such as call-center dialogues [9], Air Traffic Control [11], and at-home care [12], suggests that roles may be robustly identified solely from the textual content of transcribed utterances using Support Vector Machines [12], Bi-LSTMs, CNNs, and Transformers [9][11], without the use of any diarization identifiers. Transformers can attend to previous utterance context in addition to the target utterance, allowing for more flexible utterance grouping strategies. However, these studies overlook the possibility that diarization identifiers can be useful as categorical inputs to models.

Our primary aim is to test the viability of SRI in the context of clinical conversations by using Large Language Models (LLMs), as these have shown improvements in a broad set of natural language processing (NLP) tasks over traditional, task-specific architectures [18], and have been used successfully for SRI in other domains [19]. We fine-tune BERT, an LLM based on the encoder-only transformer architecture [18], to perform SRI on a conversational dataset of over 25,000 utterances from doctors, patients, medical assistants, and others, made during recorded, out-patient clinical visits. To establish baselines for comparison, we also train decision trees and gradient boosted decision trees. Additionally, we assess the effect of varying multiple design hyperparameters that have been evaluated in the SRI literature, including use of heuristic and linguistic features, and assess the impact of various contextual grouping strategies based on

proximity to target utterance and use of diarization identifiers. Lastly, we quantify the performance impact of diarization use and error for each method.

2. Previous Works

SRI has been applied to several domains over the years but has seen limited references in clinical informatics. Most SRI applications relate to social signal processing and arise in studies of task-specific communication. In each of these domains, SRI has been motivated by the need for richer representation of conversational datasets. It generally supports indexing and retrieval functions for large human conversation datasets [16].

Early work on SRI was done on conversational data for radio broadcast, television news, and talk shows [13][14][15]. Other SRI work has occurred in domains such as Air Traffic Control, where it has been used to differentiate between pilots and ATC officials [11]. Recently, SRI has also been applied to differentiate between social roles in work-related meetings [16], to distinguish between assistant and customer in call-center conversations [9], and to distinguish between study participants and administrators in conversations related to clinical trials for autism spectrum disorder [10]. Lastly, in at-home health settings, SRI has been applied successfully to predict caregiver and patient roles [12].

SRI has been approached using several feature representations. The best-performing models to date utilize features extracted via Automated Speech Recognition (ASR) software and other structural features from conversations [12][14][15], spectrographic and prosodic features [11][16], and in some cases video signals as well [13]. However, it remains possible to achieve high performance using text alone [9][11][12]. SRI has also been performed using a variety of methods mentioned previously.

Research exists in non-clinical domains, including at-home care settings, but SRI has not yet been applied in clinical conversations between doctors and patients. Additionally, the possibility of incorporating diarization identifiers remains underexplored. Most models ignore diarization identifiers, or use them for grouping utterances, without allowing downstream models to directly attend to them.

From an implementation standpoint, the text-only transformer model is the simplest approach that preserves the ability to fit arbitrarily complex semantic patterns. We hypothesize that lexical signals alone are sufficient to identify speaker roles in clinical visit conversations, and that inclusion of diarization identifiers as model inputs will further improve performance. To test this, we applied BERT to a clinical conversation dataset, evaluating its effectiveness in identifying the roles of patient, doctor, and medical assistant.

3. Materials & Methods

3.1. *Task Definition*

The task of SRI consists of accurately identifying one speaker role label for each utterance in a recorded conversation. We define a conversation as a textual transcript consisting of a list of utterances. Each utterance is represented as a sequence of tokens, and every token is drawn from a

specified vocabulary. Each utterance corresponds to one a speaker role, which in our case is one of: "patient," "doctor," "medical assistant," or "other." The task of SRI is, given a textual transcript, uncover the speaker role associated with each utterance.

Although it is possible to use the entire conversation as context for each utterance, in this study, we consider only previous utterances within a specified number of utterances of the target utterance as context. A sliding window, which we call a "context window", is applied to ease computation and ensure inputs fit fully within LLM context limits. Restriction to the previous context is done to leave it unambiguous which is the target utterance (the last utterance in the window). The number of utterances in the window, including the target utterance, is called the "context size". This is treated as an independent variable in our experiments.

3.2. *Dataset*

We used 117 manually transcribed clinical visit transcripts from the Establishing Focus (EF) Study [17], comprising a total of 27,505 usable utterances across 117 patients and 27 providers, each labeled with speaker role (doctor, patient, medical assistant, and others). The EF study was a randomized control trial designed to assess the impact of specialized clinician training in agenda-setting on communication behaviors and functional outcomes of clinical visits. Participating clinicians were trained and had their visits audio-taped six months afterwards (March 2004-March 2005). Recordings spanned 1460 patients and 48 clinicians. The clinical population was generated via convenience sampling of 12 community-based primary care clinics in the Puget Sound area of Washington. Consented patients were over the age of 18 and had previous visits with the clinician. Encounters shorter than three minutes were removed from the dataset. Encounters lasted an average duration of 32 minutes, 58 seconds (std. dev. = 14 minutes, 40 seconds).

3.3. *Pre-Processing*

Transcript pre-processing was performed using the Python docx module, version 1.2.0. The steps are shown in Figure 1. An example of a transcript prior to processing is shown in Figure 2. Human transcribers inserted paragraph breaks between successive transcribed speaker turns, which consist of a speaker label and an utterance, allowing them to be easily extracted using the docx module. For each extracted turn, we normalized spacing by replacing tab characters with a single white space and stripping leading and trailing whitespaces from the result. Next, if a turn began with an open parentheses or bracket, we dropped it from the transcript, as it was most likely a description of non-verbal activity, such as "(MA enters the room)". To separate the utterance and the speaker label, we split each remaining turn on the colon character (":"). If this failed to extract two separate items for a given utterance, we attempted to split on semi-colons (";"), and lastly on spaces (" "), in case transcribers forgot to include relevant punctuation. If all these methods failed, the turn was dropped from the transcript. If speaker label extraction succeeded, we removed all non-alphanumeric characters from the speaker label, stripped trailing and leading whitespaces, and converted it to lowercase before saving both the speaker label and the utterance.

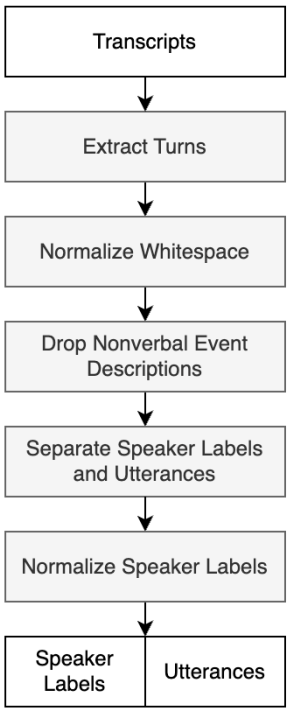

Fig. 1. Diagram displaying pre-processing steps taken for transcript data prior to modeling.

Next, we collected all extracted speaker labels across our corpus, removed duplicates, and manually pruned the results to remove malformed labels (e.g. (e.g., “Case ID Number,” “Stop Time,” and “Patient”, the latter likely coming from lines such as “Patient 50768 checking in at 12:42,” rather than from actual utterance labels, which would have been coded as “PT”). For malformed labels, we also excluded the associated utterances from our dataset. We then categorized each distinct speaker label in the resulting set to one of “patient,” “doctor,” “medical assistant,” or “other”, and applied this mapping to our dataset to normalize the speaker labels.

To compute features for each utterance in each transcript, we computed the “line number,” or number of preceding utterances in the transcript plus one, for that utterance, and stored it along with the utterance content and the speaker role. Additionally, we computed the “second-person pronoun proportion,” the percentage of pronouns from that utterance that were second person, as opposed to first or third person. This was computed by searching for exact matches between a listed set of pronouns and the words in each utterance.

```
0768.05-01-04

Patient 50768 checking in at 12:42

(MA and PT enter 0:56)

MA: I'll just meet you in the lobby when you're done. I'll have a little
packet for you. Thanks T.

PT: All right, I'll send it off today.

MA: Oh, perfect. Okay.

PT: Soon as I get home, [and get my glasses.]

MA: [All right.] Great.

(MA exits 1:06)

PT: Shoo, lordy, lordy, lordy (whisper).

(2 minute 30 second pause; MA enters 2:36)

MA: That's yours, and it's all ready, there's no additional postage
necessary, just drop it in [the mail,]

PT: [Oh, okay.]
```

Fig. 2. An example transcript from the EF dataset. Only the beginning is shown. Identifiable information has been replaced with dummy values.

3.4. *Diarization Error Simulation*

We investigated whether numeric speaker identities computed via diarization software would provide models with helpful signals for reliably identifying speaker roles throughout transcripts, and if so, to what degree errors in diarization pipelines would adversely impact downstream SRI performance. Rather than relying on open source diarization tools that would provide us with a definite accuracy, we used our ground truth labels to simulate diarization at varying degrees of corruption. We did so by assigning each speaker role within a transcript to a numeric identifier and then randomly reassigning a pre-specified percentage of the numeric identifiers from the pool of identifiers in the conversation. We refer to this percentage as the "error rate". The error rates we tested were 0%, 10%, 25%, and 50%.

3.5. *Models*

Three main model types were evaluated:

- Gradient-boosted decision tree classifiers using the Gini criterion as purity measure/objective function, a max depth of two, and 100 estimators, trained on the proportion of second-person pronouns in each utterance, as well as the utterance line number.
- Gradient-boosted decision tree classifiers using the Gini criterion as purity measure/objective function, a max depth of five, and 100 estimators, learning rate of 0.1, trained on the lexical content of the utterance using a bag of words approach.
- BERT-base-cased models with a multiclass classification head fine-tuned on the utterance content (sequence data) with utterance line number appended at the end, to classify speaker role.

We refer to instances of our first model type as “heuristics-based” models, and instances of the second and third types as “linguistic-based” models. For both the heuristics-based and linguistic-based boosted decision trees, we trained decision trees with identical max depth and purity settings for comparison.

All tree-based models were trained using scikit-learn, version 1.6.1. For BERT models, the tokenizer, model, and configuration files were loaded from the Hugging Face Transformers Library, version 4.48.0. The models were fine-tuned using the Hugging Face Trainer class.

All models were evaluated under differing context sizes, parametrized by the number of preceding utterances. Models received a sliding window of utterances and predicted the speaker of the final utterance. Inputs to BERT models were trimmed to avoid exceeding the token limit of 512 tokens for the model.

3.6. *Overview of Experiments*

Our primary aim was to evaluate the effectiveness of LLMs for SRI in clinical conversations. We also compared several methodological choices from the SRI literature, such heuristics-based versus linguistic-based models, basic machine learning versus LLMs, use of diarization identifiers, and using diarization identifiers to group utterances versus as direct model inputs.

To compare heuristic and linguistic approaches, we trained decision trees and boosted decision trees under two schemes: (1) models using bag-of-words features, and (2) models using simple heuristics; namely, pronoun proportion and utterance line number.

To evaluate the use of diarization identifiers for BERT, we experimented with three separate approaches, each attending to only a “context window” of previous utterances:

- BERT with no additional speaker information.
- BERT where the context window is filtered to only include utterances with the same diarization identifier as the target utterance. We call this a “grouping-based” model.
- BERT where the diarization identifier for each utterance is prefixed to that utterance, in the form “speaker<identifier>: ”. We call this a “token-based” model.

This allowed us to compare LLM models without diarization, LLMs with grouped context based on speaker, and LLMs with diarization identifiers as tokens.

For tree-based models, diarization was handled differently, as the token-based strategy does not apply to bag-of-words features. Tree models which did not use diarization only attended to the target utterance without conversational context. For all other tree models, a grouping-based strategy was used. For heuristics-based trees, feature values were averaged over utterances from the same speaker within the context window; for linguistic-based trees, features were aggregated as the union of all words used by the same speaker within the context window.

3.7. *Training and Optimization*

Our dataset was split into training (70%), validation (15%), and testing (15%) subsets at the level of conversation id prior to all experiments. Proportion of utterances due to patients, doctors, medical

assistants, and others in the dataset was 49%, 40%, 11%, and 0% (0.001% unrounded), respectively, and was preserved in each subset. All models were trained for exactly one epoch. BERT models were trained using the AdamW optimizer with a learning rate of 5e-05, and batch size of 32. No prompts were used.

3.8. *Evaluation*

Performance was assessed using accuracy and weighted F1 score on the testing dataset averaged across all speaker categories. Accuracy was computed as the number of ground truth labels predicted correctly. The F1 score, computed as the harmonic mean of precision and recall for a single class, was averaged across classes using weights proportional to the support to obtain the weighted F1 score. The weighted F1 score was chosen to aggregate per-class performance in a way that reflects the real-world distribution of utterances by speaker role in clinical environments.

3.9. *Computational Environment*

All experiments were performed on a dedicated GPU compute cluster, equipped with 4 vCPUs, 28 GB system memory, and a single NVIDIA T4 GPU (16 GB GDDR6). The software stack included Databricks Runtime 17.0.

3.10. *Ethics*

This study utilized transcripts containing protected health information (PHI) from the EF dataset [17], under a Data Use Agreement between the University of Washington (UW) and the University of Pennsylvania (UPenn). The protocol was approved by the UW IRB (STUDY000005436), listing UPenn as the relying institution via the SMART Master Reliance Agreement. All data were stored in secure, access-controlled environments only accessible to authorized study personnel. All handling of PHI was conducted in compliance with HIPAA and relevant institutional policies, as reflected in the IRB determination (exempt). Re-consent of participants was not required per IRB approval. Data used and machine learning models developed in this work are not publicly released to maintain the safety of participant data.

4. Results

4.1. *Model Class*

Accuracy and F1 scores for all models are shown in Table 1. The BERT models scored higher than the decision trees and boosted trees with respect to both accuracy and F1 for each setting of context size and diarization error rate. BERT models achieved balanced accuracy and F1 scores. Tree models achieved mostly balanced scores, but many of them displayed F1 scores anywhere from 2-6% lower than corresponding accuracy scores.

While BERT models outperformed decision tree models overall, the best-performing decision tree model, which was the linguistic-based decision tree with context size 10 utterances and 0% error rate (82%/80% accuracy/F1), outperformed the token-based BERT model trained with context size one utterance and no diarization (73%/73%), and performed on par with the token-based BERT

model with two utterances and no diarization. The heuristics-based decision tree model with identical settings also matched the same BERT model in F1 score and accuracy.

Table 1. Accuracy and F1 scores for BERT, decision-tree, and gradient-boosted decision tree models across alternative input and experimental hyperparameter settings. The column "Diarization Use" indicates whether grouping-based or token-based methods were used. "Inputs" indicates whether heuristics-based features or linguistic-based features were used, the latter encompassing bag of words features and text sequences. "Context Size" indicates the number of preceding utterances, including the target utterance, that were used in the context window. "Diarization Error" refers to experiments that used diarization and varying error levels, and the "No Diarization" refers to models that do not use diarization.

				Diarization Error				No Diarization
Model	Diarization Use	Inputs	Context Size	50% error	25% error	10% error	0% error	
Decision Tree	N/A	Heuristics	1	N/A	N/A	N/A	N/A	0.62/0.58
Decision Tree	Grouped	Heuristics	2	0.58/0.54	0.60/0.56	0.61/0.58	0.62/0.59	N/A
Decision Tree	Grouped	Heuristics	5	0.62/0.61	0.67/0.66	0.70/0.70	0.71/0.71	N/A
Decision Tree	Grouped	Heuristics	10	0.64/0.63	0.70/0.69	0.74/0.73	**0.76/0.76**	N/A
Decision Tree	N/A	Bag of Words	1	N/A	N/A	N/A	N/A	0.62/0.57
Decision Tree	Grouped	Bag of Words	2	0.55/0.51	0.58/0.54	0.60/0.55	0.62/0.56	N/A
Decision Tree	Grouped	Bag of Words	5	0.58/0.56	0.62/0.60	0.67/0.64	0.71/0.68	N/A
Decision Tree	Grouped	Bag of Words	10	0.55/0.53	0.62/0.59	0.68/0.66	**0.73/0.71**	N/A
Boosted Trees	N/A	Heuristics	1	N/A	N/A	N/A	N/A	0.62/0.59
Boosted Trees	Grouped	Heuristics	2	0.58/0.55	0.60/0.57	0.61/0.58	0.62/0.59	N/A
Boosted Trees	Grouped	Heuristics	5	0.63/0.62	0.67/0.66	0.71/0.70	0.72/0.71	N/A
Boosted Trees	Grouped	Heuristics	10	0.65/0.64	0.71/0.70	0.74/0.74	**0.77/0.77**	N/A
Boosted Trees	N/A	Bag of Words	1	N/A	N/A	N/A	N/A	0.65/0.61
Boosted Trees	Grouped	Bag of Words	2	0.56/0.52	0.60/0.56	0.63/0.59	0.65/0.61	N/A
Boosted Trees	Grouped	Bag of Words	5	0.63/0.61	0.67/0.64	0.72/0.70	0.76/0.74	N/A
Boosted Trees	Grouped	Bag of Words	10	0.58/0.55	0.67/0.65	0.76/0.74	**0.82/0.80**	N/A
BERT	N/A	Sequence	1	N/A	N/A	N/A	N/A	0.73/0.73
BERT	Token	Sequence	2	0.86/0.86	0.90/0.90	0.90/0.90	**0.95/0.95**	0.82/0.82
BERT	Token	Sequence	5	0.86/0.86	0.89/0.89	0.92/0.92	**0.95/0.95**	0.80/0.80
BERT	Token	Sequence	10	0.71/0.71	0.75/0.76	0.81/0.81	0.84/0.84	0.68/0.68
BERT	N/A	Sequence	1	N/A	N/A	N/A	N/A	N/A
BERT	Grouped	Sequence	2	0.69/0.67	0.69/0.67	0.68/0.66	0.70/0.68	N/A
BERT	Grouped	Sequence	5	0.71/0.70	0.74/0.74	0.79/0.78	0.83/0.83	N/A
BERT	Grouped	Sequence	10	0.70/0.69	0.76/0.76	0.82/0.82	**0.88/0.88**	N/A

4.2. *Heuristics vs. Lexical Content*

Features utilized by the heuristics-based decision tree are shown in Figure 3. First-person pronouns were more associated with patients than medical professionals. Line number was useful for distinguishing between doctors and medical assistants. Linguistic-based boosted decision trees scored higher than heuristics-based boosted decision trees with respect to both accuracy and F1 for each setting of context size and diarization error rate. However, the opposite was the case for the regular decision trees.

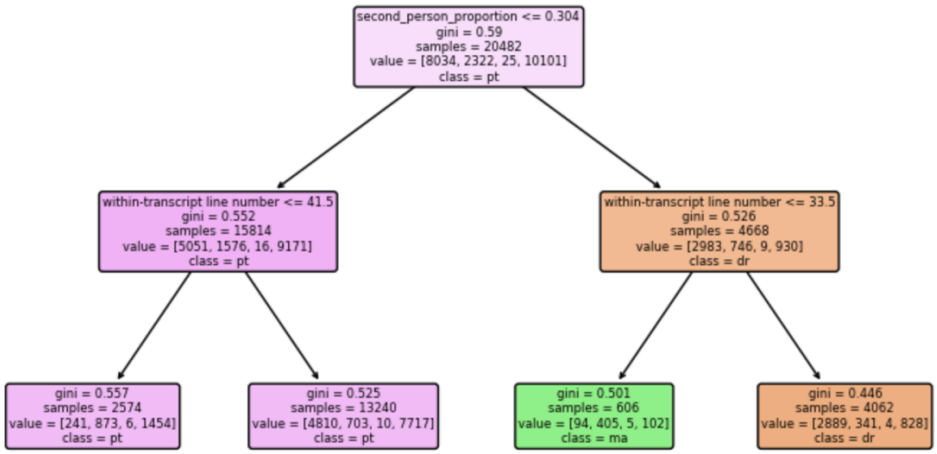

Fig. 3. Visualization of Decision Tree trained with 5-utterance context and 100% diarization accuracy. Individual nodes contain the condition (variable and threshold) for moving left (top line), along with the value of the gini purity measure of the applicable records (gini), the number of such records (samples), the ground-truth distribution of the records (value), and the majority class (class).

4.3. *Diarization-Based Grouping vs. Diarization-Based Tokens*

The token-based BERT model outperformed the grouping-based BERT model respect to both accuracy and F1 score at all settings of context size and diarization error rate. The best token-based BERT model achieved both an accuracy and F1 score 95%, whereas the most performant grouping-based BERT model scored 88% on both.

4.4. *Context Size*

Increasing context size beyond a single utterance improved performance of the token-based BERT model. Increasing it to 5 improved performance for some levels of diarization error rate (10%) but decreased it for others (25%, no diarization) and left others unaltered (0%, 50%). However, increasing context size to 10 utterances degraded results. For all other models, increasing context size when diarization error rate was below 50% always increased accuracy and F1 score.

4.5. *Diarization and Accuracy*

Diarization was seen to improve performance for all models when it remained accurate. BERT models which did not use diarization performed uniformly worse than counterparts trained with accurate diarization with respect to accuracy and F1 score. For example, the token-based BERT model with context size 2 scored 82% accuracy, 82% F1 score with no diarization, but achieved a balanced 95%, 90%, 90%, and 86% accuracy and F1 score for settings with 0%, 10%, 25%, and 50% diarization error rate, respectively. Tree-based models also benefited from the combination of context and diarization.

All diarization-based models showed similar patterns of partial reliance on diarization performance, with differences in F1 score between the setting with 0% diarization error rate and 50% diarization error rate ranging from 4% to 18%. There is no clear trend relating the model type and robustness to diarization error.

5. Discussion

The purpose of our study was to investigate the potential for LLMs to perform SRI in clinical conversations involving patients, doctors, and medical assistants, and to compare aspects of model design with respect to performance. We find that LLMs can accurately identify who is speaking in clinical conversations using SRI, and furthermore that they benefit from the use of accurate diarization despite remaining robust to errors. This contributes to the growing literature on SRI by demonstrating its possibility in clinical settings and providing helpful comparisons of design considerations. Despite being the first of their kind for clinical SRI in clinical conversations, our models perform on par with recent text transformer-based SRI models trained in other domains such as Air Traffic Control [11].

Comparison of boosted decision tree models and LLMs reveal that model class makes a large difference in downstream performance, with LLM models outperforming boosted decision tree models for SRI in clinical conversations. Comparison of decision tree models and boosted decision trees reveals the same finding. This is likely a result of the fact that boosted decision trees can approximate a wider range of functions than decision trees, and LLMs a yet wider range, allowing them to model the intricate semantic dependencies between speaker role and conversational utterances with increasing intricacy. LLM superiority likely also results from the fact that LLM embeddings encode richer semantic information than bag-of-words features, including positional information and synonymy relations.

Comparison of the boosted decision tree trained using second-person pronoun proportions versus using bag-of-words reveals that pronoun-usage heuristics underperform lexical approaches for SRI in our clinical conversation dataset. This is because the latter permits learning a more general set of role-specific keywords, including but not limited to tendencies in pronoun usage. Nevertheless, pronoun usage trends are important for performance in lexical approaches: presence of the word “you” serves as the primary split in all our learned decision trees. The fact that decision trees performed better with heuristics is not evidence that lexical approaches underperform heuristics due to the tendency for decision trees to overfit in the presence of complex data types such as text [20].

LLM models which employed diarization outperformed LLM models which did not, as long as diarization identifiers remained accurate, indicating that diarization identifiers can be useful as input signals to SRI pipelines, as long as accuracy is maintained. Decision trees which were able to attend to context in the presence of diarization identifiers outperformed single-utterance decision trees as well, demonstrating that use of diarization-based grouping methods can allow decision trees to benefit from larger context sizes effectively.

Amongst LLM models which attended to diarization, the grouping-based models underperformed relative to the token-based models. This indicates that models benefit from being

able to flexibly attend to diarization signals rather than being constrained by them to analyze utterance groups which may or may not be malformed due to diarization errors.

For all grouping-based models, increasing context size had a positive impact on performance. However, for the LLM models trained without diarization-based grouping, increasing context past a certain point had the tendency to degrade performance. Interestingly, this trend persisted in the absence of diarization. This suggests that excessive context has the tendency to degrade results when adequate filtering steps are not taken to minimize input sizes. Despite potential inaccuracies, diarization-based grouping can act as a filtering mechanism to reduce input token sizes.

All models which used diarization benefited from increased diarization accuracy. Interestingly, the token-based LLM did not have a more robust performance against diarization inaccuracy compared to grouping-based methods, indicating that diarization errors may propagate through LLMs regardless of whether grouping is used or not.

6. Limitations

While the current study has revealing findings concerning design and implementation of SRI systems in clinical settings, there exist limitations which will need to be addressed in future works. First, our analysis was limited to a single dataset of clinical conversations, leaving questions about generalizability across specialty and institution. Second, our experiments only simulated one aspect of diarization error; namely, when diarization identifiers are inconsistent. However, future experiments should also simulate errors in segmentation due to voice activity detection, which is another component of diarization. Lastly, our experiments only use one candidate LLM, which can potentially limit generalizability to other models. However, given the number of open-source LLMs and the fact that many of them are comparable to and more performant than BERT in a wide array of NLP tasks, we hypothesize that our results are broadly applicable to performant LLMs and may even act as a lower bound on possible performance.

7. Conclusion

We demonstrate that semantic cues alone can identify speaker roles in clinical conversations. These are more powerful than specific communication heuristics. While diarization is useful for various model types depending on how it is incorporated, our LLM-based approach is robust to diarization errors and even remains performant in the absence of diarization. Further, non-LLM based approaches which use simple techniques such as bag-of-words also perform well in the context of clinical SRI and remain somewhat robust to diarization errors. Lastly, LLM approaches which attend to a target utterance in the context of previous utterances enriched with diarization labels are shown to be superior to utterances which analyze disjoint groups of diarized utterances separately, whether diarization is accurate. These findings support the viability of SRI pipelines for clinical interaction analysis using transcribed conversations and have implications for the implementation of conversational analysis in clinical systems. Applications of this technology allow speaker role-based segmentation of visits at scale, providing a possible foundation for downstream modeling, such as speaker-based sentiment analysis and measurement of communication quality for clinical professionals.

References

1. Fawole, Oluwakemi A. et al. “A systematic review of communication quality improvement interventions for patients with advanced and serious illness.” *Journal of general internal medicine* vol. 28,4 (2013): 570-7. doi:10.1007/s11606-012-2204-4
2. Crampton, Noah H. et al. “Computers in the clinical encounter: a scoping review and thematic analysis.” *Journal of the American Medical Informatics Association : JAMIA* vol. 23,3 (2016): 654-65. doi:10.1093/jamia/ocv178
3. Beck, Rainer S. et al. “Physician-patient communication in the primary care office: a systematic review.” *The Journal of the American Board of Family Practice* vol. 15,1 (2002): 25-38.
4. Kavic, Michael S. “Competency and the six core competencies.” *JSLS : Journal of the Society of Laparoendoscopic Surgeons* vol. 6,2 (2002): 95-7.
5. Nasca, Thomas J et al. “The next GME accreditation system--rationale and benefits.” *The New England journal of medicine* vol. 366,11 (2012): 1051-6. doi:10.1056/NEJMsr1200117
6. Epstein, Ronald M., and Richard L. Street Jr. “The values and value of patient-centered care.” *Annals of family medicine* vol. 9,2 (2011): 100-3. doi:10.1370/afm.1239
7. Brockway, Christine. "Evaluating Effective Communication in Clinical and Simulation." *Clinical Simulation in Nursing*, vol. 98, Jan. 2025, article no. 101669. https://doi.org/10.1016/j.ecns.2024.101669.
8. Park, Tae Jin, et al. “A Review of Speaker Diarization: Recent Advances with Deep Learning.” *Computer Speech & Language*, vol. 72, Mar. 2022, article no. 101317, https://doi.org/10.1016/j.csl.2021.101317.
9. Nghiem, Minh-Quoc, et al. "Speaker Role Identification in Call Centre Dialogues: Leveraging Opening Sentences and Large Language Models." *Proceedings of the 24th Annual Meeting of the Special Interest Group on Discourse and Dialogue*, edited by Svetlana Stoyanchev et al., Association for Computational Linguistics, 2023, pp. 388–392. https://doi.org/10.18653/v1/2023.sigdial-1.35.
10. O'Sullivan, James et al. “Automatic speaker diarization for natural conversation analysis in autism clinical trials.” *Scientific reports* vol. 13,1 10270. 24 Jun. 2023, doi:10.1038/s41598-023-36701-4
11. Guo, Dongyue, et al. “A Comparative Study of Speaker Role Identification in Air Traffic Communication Using Deep Learning Approaches.” *ACM Transactions on Asian and Low-Resource Language Information Processing*, vol. 22, no. 4, Apr. 2023, article 102, https://doi.org/10.1145/3572792.
12. Zolnoori, Maryam et al. “Is the patient speaking or the nurse? Automatic speaker type identification in patient-nurse audio recordings.” *Journal of the American Medical Informatics Association : JAMIA* vol. 30,10 (2023): 1673-1683. doi:10.1093/jamia/ocad139
13. Cheema, Gullal S., et al. "Identification of Speaker Roles and Situation Types in News Videos." *Proceedings of the 2024 International Conference on Multimedia Retrieval,*

Association for Computing Machinery, 2024, pp. 506–514. https://doi.org/10.1145/3652583.3658101.
14. Barzilay, Regina, et al. “The Rules Behind Roles: Identifying Speaker Role in Radio Broadcasts.” *Proceedings of the Seventeenth National Conference on Artificial Intelligence and Twelfth Conference on Innovative Applications of Artificial Intelligence*, AAAI Press, 2000, pp. 679–684.
15. Hutchinson, Brian, et al. “Unsupervised Broadcast Conversation Speaker Role Labeling.” *2010 IEEE International Conference on Acoustics, Speech and Signal Processing*, Dallas, TX, USA, 2010, pp. 5322–5325. IEEE. doi:10.1109/ICASSP.2010.5494958.
16. Sapru, Ashtosh, and Fabio Valente. “Automatic Speaker Role Labeling in AMI Meetings: Recognition of Formal and Social Roles.” *2012 IEEE International Conference on Acoustics, Speech and Signal Processing (ICASSP)*, Kyoto, Japan, 2012, pp. 5057–5060. IEEE. doi:10.1109/ICASSP.2012.6289057
17. Robins L, Brock D, Mauksch L. Effects of Establishing Focus in the Medical Interview. Final Progress Report. AHRQ Grant Number R01HS013172 (PI: Robins, L). Retrieved from: https://www.ahrq.gov/sites/default/files/2024-07/robins-report.pdf
18. Devlin, Jacob, et al. “BERT: Pre-training of Deep Bidirectional Transformers for Language Understanding.” *Proceedings of the 2019 Conference of the North American Chapter of the Association for Computational Linguistics: Human Language Technologies*, vol. 1, 2019, pp. 4171–4186. Association for Computational Linguistics.
19. Vaswani, Ashish, et al. “Attention is All You Need.” *Proceedings of the 31st International Conference on Neural Information Processing Systems*, Long Beach, California, 2017, Curran Associates Inc., pp. 6000–6010.
20. Halabaku, Erblin, and Eliot Bytyçi. “Overfitting in Machine Learning: A Comparative Analysis of Decision Trees and Random Forests.” *Intelligent Automation & Soft Computing*, vol. 39, no. 6, 2024, pp. 987–1006. https://doi.org/10.32604/iasc.2024.059429.

Learning Causally Predictable Outcomes from Psychiatric Longitudinal Data

Eric V. Strobl

Departments of Biomedical Informatics & Psychiatry, University of Pittsburgh, Pittsburgh, Pennsylvania 15206, United States of America

Causal inference in longitudinal biomedical data remains a central challenge, especially in psychiatry, where symptom heterogeneity and latent confounding frequently undermine classical estimators. Most existing methods for treatment effect estimation presuppose a fixed outcome variable and address confounding through observed covariate adjustment. However, the assumption of unconfoundedness may not hold for a fixed outcome in practice. To address this foundational limitation, we directly optimize the outcome definition to maximize causal identifiability. Our DEBIAS (Durable Effects with Backdoor-Invariant Aggregated Symptoms) algorithm learns non-negative, clinically interpretable weights for outcome aggregation, maximizing durable treatment effects and empirically minimizing both observed and latent confounding by leveraging the time-limited direct effects of prior treatments in psychiatric longitudinal data. The algorithm also furnishes an empirically verifiable test for outcome unconfoundedness. DEBIAS consistently outperforms state-of-the-art methods in recovering causal effects for clinically interpretable composite outcomes across comprehensive experiments in depression and schizophrenia. R code is available at `github.com/ericstrobl/DEBIAS`.

Keywords: causal inference, psychiatry, longitudinal data, outcome learning, latent confounding, empirical unconfoundedness, composite outcomes

1. Introduction

Causal inference seeks to identify cause-and-effect relationships from data, enabling scientific discovery and effective intervention design.[1,2] In psychiatry, most causal knowledge has come from randomized clinical trials (RCTs), but RCTs are often infeasible or unethical to perform. For example, we cannot randomize individuals to different income levels to study the effects of poverty on mental health. Meanwhile, rich longitudinal observational datasets that provide far greater temporal and phenotypic resolution than cross-sectional studies[3] or electronic health records[4] are increasingly accessible through protected repositories in psychiatry. However, inferring causality from such data remains difficult in the absence of randomized assignment.

One of the primary obstacles to causal inference from observational data is latent confounding,[1] where unmeasured variables $\boldsymbol{C}$ may influence both treatment T_2 and outcomes $(\boldsymbol{Y}_3, \ldots, \boldsymbol{Y}_m)$, biasing causal effect estimates (Figure 1 (a)). Here, subscripts denote time steps in the longitudinal data, so T_1 and T_2 refer to treatments at different times, and $\boldsymbol{Y}_i$ represents the vector of *multiple* clinical rating scale items measured at time i. While standard practice adjusts for observed confounders $\boldsymbol{X}$ in regression models, this ignores clinical

© 2025 The Authors. Open Access chapter published by World Scientific Publishing Company and distributed under the terms of the Creative Commons Attribution Non-Commercial (CC BY-NC) 4.0 License.

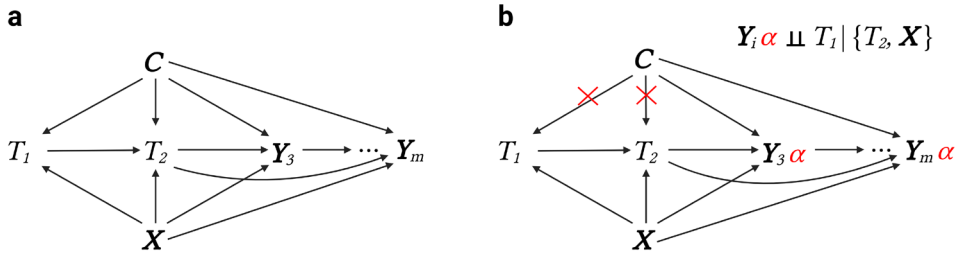

Fig. 1. **Main idea.** (a) Causal diagram where T_2 denotes current treatment assignment, T_1 denotes historical treatment assignment (not necessarily representing the same treatments as in T_2), each $\boldsymbol{Y}_i$ represents multiple items of a clinical rating scale, $\boldsymbol{X}$ indicates observed confounders available for adjustment, and $\boldsymbol{C}$ denotes latent confounders. In this structure, T_1 has time-limited direct effects: its influence on $\boldsymbol{Y}_3, \ldots, \boldsymbol{Y}_m$ is entirely indirect – mediated through T_2 – with no direct arrows from T_1 to the later outcomes. Moreover, $\boldsymbol{Y}_i$ is either unweighted or combined in a non-optimized manner, such as using total severity scores. (b) We learn non-negative weights $\alpha \geq 0$ to form the weighted severity scores $\boldsymbol{Y}_3\alpha, \ldots, \boldsymbol{Y}_m\alpha$ such that $\boldsymbol{Y}_i\alpha \perp\!\!\!\perp T_1 \mid \{T_2, \boldsymbol{X}\}$ for each time step. This outcome projection removes the statistical influence of spurious backdoor associations between T_2 (as well as T_1) and the outcomes, as indicated by the red crosses.

knowledge that many historical treatments T_1 have only *time-limited direct causal effects* and thus do not directly impact later outcomes[a]. Instead, any effect of T_1 on outcomes $\boldsymbol{Y}_3, \ldots, \boldsymbol{Y}_m$ occurs indirectly – mediated through T_2 – with no direct causal arrows from T_1 to the later outcomes (Figure 1 (a)). For instance, antidepressants do not directly affect symptom severity a year after discontinuation in active major depression.[5]

We propose to incorporate the prior knowledge of short-term treatment effects by searching for a non-negative weight vector α such that the aggregated outcome $\boldsymbol{Y}_i\alpha$ is conditionally independent of past treatment T_1, given current treatment T_2 and $\boldsymbol{X}$, for all time steps. The non-negativity constraint on α ensures that $\boldsymbol{Y}_i\alpha$ remains a clinically interpretable *severity score*, preserving the additive contribution of each symptom without introducing cancellation effects. Moreover, in this longitudinal setting, conditioning on the current treatment T_2 activates the collider on the path $T_1 \rightarrow T_2 \leftarrow \boldsymbol{C} \rightarrow \boldsymbol{Y}_i$ for any latent confounders $\boldsymbol{C}$ that affect T_2 and $\boldsymbol{Y}_i$. As a result, achieving conditional independence between T_1 and $\boldsymbol{Y}_i\alpha$ (after adjusting for T_2 and $\boldsymbol{X}$) eliminates the statistical influence transmitted along $\boldsymbol{C}$-mediated non-causal paths linking T_2 (and T_1) to each $\boldsymbol{Y}_i\alpha$, thereby enabling unbiased inference of the causal effect of T_2 on each $\boldsymbol{Y}_i\alpha$ (e.g., Figure 1 (b)). Applying the same α across all time points ultimately yields a single, durable, and empirically unconfounded severity score, enabling credible causal inference for a structured combination of items – even when such inference is infeasible for other combinations.

We specifically make the following contributions in this work:

[a]We relax this assumption in Supplementary Materials 8.1, where we also provide more technical discussion. Supplementary Materials link: https://github.com/ericstrobl/DEBIAS/tree/main/PDF

(1) We introduce a principled approach for learning outcome scores as non-negative combinations of clinical rating scale items, maximizing the correlation between current treatment and subsequent outcomes across time.
(2) We propose a novel regularization criterion that minimizes latent confounding bias by leveraging the time-limited direct effects of past treatments.
(3) We generalize the framework to extract not just a single score, but all unconfounded severity scores, each defined by a distinct non-negative weight vector and interpretable as a composite severity score.
(4) We instantiate the above concepts into a single algorithm, Durable Effects with Backdoor-Invariant Aggregated Symptoms (DEBIAS), which employs cross-validation to minimize latent confounding and maximize correlation.
(5) We demonstrate that DEBIAS effectively eliminates latent confounding and consistently outperforms existing algorithms in depression and schizophrenia.

Collectively, these advances enable robust causal inference from complex longitudinal datasets by learning *multiple* durable severity scores that are empirically unconfounded, even in the presence of latent sources of bias.

2. Related Work

We introduce the term *outcome learning* to describe algorithmic identification of the optimal set or combination of outcome variables for a given analytical task. Traditionally, investigators predefine a single clinically meaningful outcome for prediction,[6,7] which is effective when the target is clear, but problematic in complex diseases like depression or psychosis where symptoms are heterogeneous and not easily summarized by a single composite measure.

Recent algorithms in precision psychiatry attempt to learn multiple outcome measures tailored to specific analytical goals. For example, the Supervised Varimax algorithm constructs outcome measures that maximally differentiate psychiatric treatments in RCTs,[6,7] and the method has been modified to detect subtle differences between subgroups within patient populations.[8] The Sparse Canonical Outcome Regression (SCORE) algorithm, in contrast, optimizes multiple outcome measures for predictability rather than discrimination between groups.[9] Thus, different outcome learning approaches have emerged depending on whether the goal is to distinguish treatments, differentiate patient subgroups, or maximize predictability. Importantly, none of these existing methods explicitly optimize outcome measures to enable causal inference – a gap the DEBIAS algorithm is designed to fill.

Almost all existing causal inference methods address confounding by transforming or leveraging observed covariates but leave outcome variables fixed. For example, Difference-in-Differences relies on observed covariates to support the parallel trends assumption,[10] and Inverse Probability of Treatment Weighting (IPTW) uses propensity scores based on observed covariates to balance treatment groups.[11] In principle, IPTW can be combined with outcome-learning methods such as Non-Negative Canonical Correlation Analysis (NNCCA),[12] but such strategies still rest on the assumption that adjustment for observed covariates is sufficient to re-

move confounding. More recent approaches – including meta-learners[13,14] and causal forests[15] – extend this logic by using flexible machine learning models to control for high-dimensional covariates and estimate the conditional average treatment effect (CATE). Yet, all these methods implicitly assume that confounding can only be addressed by modifying the set of predictors, rather than the outcomes themselves.

Instrumental variable (IV) methods provide an alternative approach by leveraging external sources of variation to identify causal effects.[16] However, they depend on the strong assumption of no latent confounding linking the instrument (e.g., T_1) to the outcome – an assumption that is rarely plausible in complex observational settings. In practice, observed covariates and putative instruments are frequently inadequate to eliminate confounding for all outcome variables. Moreover, no empirical test can definitively establish that all sources of bias have been addressed by observed covariates.[1] Our approach instead relaxes the requirement by finding projections of the outcomes that minimize confounding, thereby retaining robustness even in the presence of residual latent confounders.

In summary, outcome learning methods in psychiatry have so far focused on RCT settings, subgroup differentiation, or improving predictivity rather than optimizing for causal inference from observational data. Meanwhile, causal inference algorithms have almost exclusively targeted the covariate space, neglecting the potential of outcome transformation. To our knowledge, DEBIAS is the first method to empirically learn outcome definitions specifically for causal inference within a unified, testable, and interpretable framework.

3. Assumptions

We adopt the potential outcomes framework to rigorously formalize causal inference in longitudinal data. While Figure 1 illustrates the case of two treatment time points (T_1 and T_2) for simplicity, our general framework allows the treatment of interest T_p to occur at any time step p, with the possibility of multiple prior treatments T_j for all $j < p$. Moreover, to unambiguously distinguish between temporal indices and hypothetical interventions in the outcomes, we denote by $\boldsymbol{Y}_i(t_p)$ the observed or potential outcome vector at time point i, under the hypothetical scenario in which treatment $T_p = t_p$ was assigned at time $p < i$. This notation enables a clear analysis of intervention effects across time.

Our methodology is predicated upon three standard assumptions from the causal inference literature:[1]

(1) **Consistency**: If a unit receives treatment t_p, then the observed outcome at time i coincides with the potential outcome under t_p; that is, $\boldsymbol{Y}_i = \boldsymbol{Y}_i(t_p)$ when $T_p = t_p$.
(2) **Stable Unit Treatment Value Assumption (SUTVA)**: The potential outcomes for any unit are unaffected by the treatment assignments of other units (i.e., there is no interference), and each treatment condition is consistently and uniquely defined.
(3) **Positivity**: The conditional density of treatment assignment is strictly positive; that is, $p(T_p = t_p \mid T_1, \boldsymbol{X}) > 0$ for all $(T_1, \boldsymbol{X}, t_p)$ within the support of the data. Similarly, $p(T_j = t_j \mid T_p, \boldsymbol{X}) > 0$ for all $j < p$ and all $(T_p, \boldsymbol{X}, t_j)$ in the support.

Most existing studies also assume *unconfoundedness* (ignorability), where $\boldsymbol{Y}_i(t_p)\alpha \perp\!\!\!\perp T_p|\boldsymbol{X}$

for some fixed weight vector $\alpha \geq 0$ and all t_p. For example, $\boldsymbol{Y}_i(t_p)\alpha$ with $\alpha = 1$ corresponds to the total score at time point i that would be observed if $T_p = t_p$. However, in practice, a potential outcome $\boldsymbol{Y}_i(t_p)\alpha$ may remain probabilistically dependent on T_p given $\boldsymbol{X}$ due to confounding from latent variables like $\boldsymbol{C}$ (Figure 1 (a)).[17] The dependence can also extend to earlier treatments T_j for all $j < p$ because the factors influencing earlier treatment assignments frequently continue to affect the assignment of treatment at the time point of interest.

We forego the standard unconfoundedness assumption and instead propose to *learn* α such that the antecedent in the following assumption holds:

(4) **Projected Unconfoundedness**: If there exists $\alpha \geq 0$ such that $\boldsymbol{Y}_i(T_p)\alpha \perp\!\!\!\perp \{T_1, \ldots, T_{p-1}\} | T_p \cup \boldsymbol{X}$ for all $i > p$, then $\boldsymbol{Y}_i(t_p)\alpha \perp\!\!\!\perp T_p | \boldsymbol{X}$ for all $i > p$ and all t_p.

This condition is justified by the temporal and graphical structure of confounding in longitudinal data. Specifically, latent factors $\boldsymbol{C}$ – such as historical severity or health insurance status – often exert influence on historical treatments $T_1, \ldots, T_{p-1}$ and the treatment of interest T_p, as depicted in Figure 1 (a). Moreover, historical treatments frequently have a direct causal effect on T_p but are time-limited without direct effects on $\boldsymbol{Y}_i$ for any $i > p$. This induces a graphical structure where T_p functions as a collider on backdoor paths of the form $T_j \to T_p \leftarrow \boldsymbol{C} \to \boldsymbol{Y}_i\alpha$ for some $j < p$. By choosing α such that $\boldsymbol{Y}_i(T_p)\alpha \perp\!\!\!\perp \{T_1, \ldots, T_{p-1}\} | T_p \cup \boldsymbol{X}$, we eliminate statistical dependence induced by latent confounders, thereby removing bias from unmeasured confounding along non-causal paths (Figure 1 (b)). Consequently, the standard unconfoundedness condition is restored for the specific learned outcome $\boldsymbol{Y}_i\alpha$, enabling unbiased causal effect estimation of T_p on $\boldsymbol{Y}_i\alpha$ for each time point $i > p$. See Supplementary Materials 8.1 for an even more general treatment that requires time-limited direct effects for only a subset of items.

Notice that our outcome-centric strategy departs from conventional approaches that presume no unmeasured confounding for combinations of all outcome items, such as total severity scores or remission rates – a strong and generally untestable assumption. Our approach algorithmically learns a non-negative weight vector α that is typically sparse in practice, so the resulting outcome score depends only on a small subset of items. Accordingly, the projected unconfoundedness condition and resulting causal guarantees apply specifically to this empirically identified subset of outcomes, rather than to composite measures constructed a priori without regard to confounding structure. This yields both improved interpretability and greater robustness to latent confounding, as the learned outcome focuses on those items for which credible causal inference is feasible.

4. Maximizing Correlation to Causally Distinguish Patients

In causal inference, larger values of $\boldsymbol{Y}_i(T_p)$ are conventionally interpreted as improvement, whereas most clinical rating scales assign higher scores to greater symptom severity. To align these conventions, we multiply each rating item by -1 so that higher values indicate improvement. The canonical quantity for binary treatment assignment with an outcome composite is then the average treatment effect (ATE):

$$\text{ATE}_\alpha = \mathbb{E}[\boldsymbol{Y}_i(1)\alpha] - \mathbb{E}[\boldsymbol{Y}_i(0)\alpha],$$

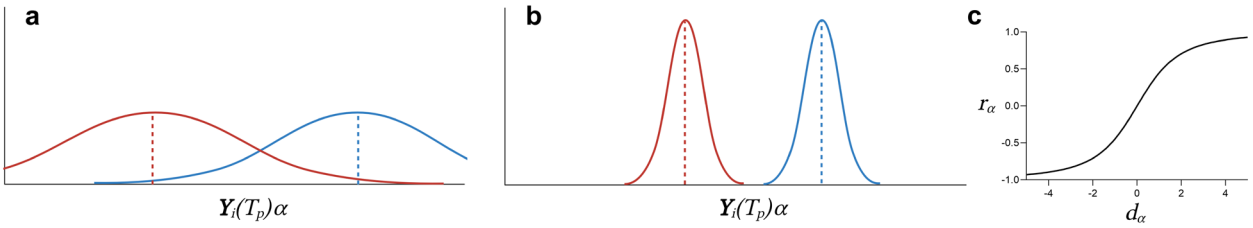

Fig. 2. **Comparison of effect size measures.** (a) The ATE quantifies the raw difference in group means (red vs. blue), without accounting for within-group variability or distributional overlap. (b) Cohen's d and Pearson's correlation coefficient both capture the separability of groups by standardizing the mean difference using the pooled within-group standard deviation; separability increases as within-group variance decreases and group means diverge. (c) Although Cohen's d and correlation are monotonically related under binary treatment, only correlation extends naturally to ordinal (more than two levels) or continuous treatment variables, making it more broadly applicable.

where $\boldsymbol{Y}_i(1)\alpha$ and $\boldsymbol{Y}_i(0)\alpha$ denote the potential outcomes under treatment and control, projected via $\alpha \geq 0$. The goal is to identify α that maximizes the treatment effect along a learned score. However, maximizing the ATE alone does not account for the variance of $\boldsymbol{Y}_i(T_p)\alpha$ within each treatment group. As a result, even if the group means are well separated, the individual outcomes may still overlap substantially due to high within-group variance (Figure 2 (a)), rendering it difficult to predict which patients will benefit from treatment in practice.

The separation between treatment assignments must be meaningful relative to the within-group variability of outcomes. Let $p = P(T = 1)$ denote the proportion of individuals assigned to the treatment group, and $1-p = P(T = 0)$ the proportion in the control group. One classical approach to quantifying such standardized separation is to maximize Cohen's d:

$$d_\alpha = \frac{\text{ATE}_\alpha}{\sqrt{p\text{Var}(\boldsymbol{Y}_i(1)\alpha) + (1-p)\text{Var}(\boldsymbol{Y}_i(0)\alpha)}},$$

where the denominator represents the pooled within-group variance.[18] Cohen's d thus quantifies the magnitude of group separation relative to internal variability. Maximizing d aligns the learned outcome score with maximal distinguishability of treatment groups (Figure 2 (b)).

Cohen's d is unfortunately limited to binary treatment assignment, but the measure admits a monotonic transformation into Pearson's correlation coefficient:[19]

$$r_\alpha = \frac{\sqrt{p(1-p)} \cdot d_\alpha}{\sqrt{1 + p(1-p) \cdot d_\alpha^2}}.$$

This is a bijective mapping that preserves the ranking of outcome scores (Figure 2 (c)), so maximizing d_α necessarily maximizes r_α and vice versa. Importantly, while Cohen's d is limited to binary comparisons, Pearson's correlation generalizes naturally to ordinal and continuous treatment variables (e.g., income levels or medication dosages), thereby offering a more versatile and broadly applicable objective. Accordingly, we adopt the correlation coefficient as our primary optimization criterion, given its capacity to maximally distinguish between treatment conditions regardless of whether the treatment variable is discrete or continuous.

5. Algorithm

5.1. *First Learned Severity Score*

We now describe the DEBIAS algorithm. The algorithm begins by constructing the first non-negatively weighted outcome score that is durably responsive to treatment and robust to confounding. As detailed in Section 4, our objective is to maximize the correlation between T_p and each outcome measure $\boldsymbol{Y}_i\alpha$ for $i > p$. This leads to the following optimization problem:

$$\underset{\alpha\geq 0,\|\alpha\|_1=1}{\arg\max} \sum_{i=p+1}^{m} \Big[\underbrace{\operatorname{cor}(\boldsymbol{Y}_i\alpha, T_p|T_1, \boldsymbol{X})}_{(a)} - \underbrace{\frac{\lambda}{p-1}\sum_{j=1}^{p-1}\operatorname{cor}^2(\boldsymbol{Y}_i\alpha, T_j|T_p, \boldsymbol{X})}_{(b)} \Big], \tag{1}$$

where we enforce $\|\alpha\|_1 = 1$ to ensure uniqueness of the solution.

The **main correlation** term in (a) seeks to maximize the durable partial correlation between the learned outcome and the target treatment across all future time points, adjusting for $\boldsymbol{X}$ to account for observed confounders. We also adjust for the most distant prior treatment T_1 to ensure the algorithm remains robust when treatment assignment is constant over time; without this step, the confounding penalty in (b) – explained below – becomes vacuously zero and cannot control for confounding. Including T_1 as a covariate in (a) ensures the correlation objective is also zero in such cases, preventing spurious associations when there is no temporal variation in treatment.

The **confounding penalty** in (b) targets association arising from latent confounding. Here, $\sum_{j=1}^{p-1}\operatorname{cor}^2(\boldsymbol{Y}_i\alpha, T_j|T_p, \boldsymbol{X}) = 0$ is a necessary condition for $\boldsymbol{Y}_i(T_p)\alpha \perp\!\!\!\perp \{T_1, \ldots, T_{p-1}\}|T_p \cup \boldsymbol{X}$ in the projected unconfoundedness condition (Section 3). Minimizing this penalty thus addresses confounding and also serves as a regularizer in finite samples: if the empirical squared partial correlation is large, it counteracts over-optimistic correlations in (a). Notably, this approach uses a linear approximation to conditional independence, enabling empirical unconfoundedness and statistical hypothesis testing of latent confounding; while not equivalent to full conditional independence, partial decorrelation is often sufficient for practical purposes in high-dimensional observational data.

To balance predictive accuracy and robustness, we optimize λ by cross-validation over a predefined grid and select the value that maximizes the correlation in (a), *provided* that the p-value associated with the squared correlation in (b) exceeds a specified threshold (default 0.05), meaning we cannot reject the null hypothesis of no partial association. In this way, the penalty both mitigates confounding and regularizes the model to avoid overfitting.

5.2. *Sequential Extraction of Severity Scores*

The optimization problem in Expression (1) only produces a single set of non-negative weights, α_1. However, our goal is to identify all α that maximize persistent correlation with treatment while minimizing confounding. We thus introduce an additional **diversity-promoting penalty** term (c) that encourages each new score to be as clinically distinct as possible from

all previously extracted scores:

$$\underset{\alpha\geq 0,\|\alpha\|_1=1}{\arg\max} \sum_{i=p+1}^{m} \Bigg[\mathrm{cor}(\boldsymbol{Y}_i\alpha, T_p|T_1, \boldsymbol{X}) - \frac{\lambda}{p-1}\sum_{j=1}^{p-1} \mathrm{cor}^2(\boldsymbol{Y}_i\alpha, T_j|T_p, \boldsymbol{X}) \\ \underbrace{- \frac{1}{K-1}\sum_{k=1}^{K-1}\left(\frac{\alpha_k^T M_i \alpha}{\sqrt{\alpha_k^T M_i \alpha_k}\sqrt{\alpha^T M_i \alpha}}\right)}_{(c)} \Bigg], \tag{2}$$

where $K \geq 2$ denotes the total number of learned scores including the current score under optimization. The diversity-promoting penalty measures the correlation-weighted cosine similarity between the current score α and each previously discovered score α_k, where M_i is the correlation matrix of the outcome variables $\boldsymbol{Y}_i$. This similarity ranges from -1 to 1 like the main correlation term, so the penalty is naturally scale-matched to the main objective and does not require a separate hyperparameter for balancing its influence.

We intentionally do *not* square the correlation-weighted cosine similarity so that the optimization procedure favors negative similarity values when permitted by the data and the non-negativity constraint. Recall that (1) the individual items in $\boldsymbol{Y}_i$ represent *pathological* symptoms, where higher values indicate worse clinical severity, and (2) each item was sign-flipped in Section 4 so that higher values instead denote clinical *improvement*, aligning with the causal interpretation of treatment effects. Within this transformed space, all weights in α are constrained to be non-negative, ensuring that learned outcome scores reflect additive improvements across symptoms without cancellation. These two conditions impose a directional structure: outcome scores represent strictly non-negative combinations of improvements in underlying pathologies. Consequently, a negative correlation-weighted cosine similarity between scores becomes possible only when the symptom correlation matrix M_i contains sufficiently negative off-diagonal elements – i.e., when some symptoms improve inversely with others. In such cases, the algorithm can extract new scores that are anti-aligned with prior ones within the non-negative feasible region, capturing distinct, clinically interpretable axes of symptom variation.

For example, manic and depressive symptoms in bipolar disorder are clearly clinically distinct yet strongly negatively correlated. In this context, DEBIAS may recover one composite score weighted toward manic symptoms and another toward depressive symptoms, both with non-negative weights and exhibiting negative correlation-weighted cosine similarity. In contrast, minimizing the *squared* correlation-weighted cosine similarity only enforces orthogonality, which can result in a new score that emphasizes peripheral symptoms – such as chronic irritability, distractibility, or somatic complaints – rather than capturing the strong negative correlation between core mood domains. The diversity-promoting penalty thus directly exploits the negative correlation structure to extract outcome scores that are clinically distinct, rather than conflating mathematical orthogonality with clinical distinctiveness.

We ultimately solve the optimization problem in Expressions (1) and (2) by projected gradient ascent using backtracking line search with the Armijo condition[20] (Supplementary Materials 8.2). Computational complexity analysis revealed that DEBIAS scales linearly with

the number of subjects and time points, but quadratically with the number of outcome items, covariates, and summary scores (Supplementary Materials 8.3).

6. Results

6.1. *Comparator Algorithms*

We ran DEBIAS with 5-fold cross-validation evaluating λ over the grid $0, 1, \ldots, 10$. We extracted $s = 3$ severity scores. We compared DEBIAS against the following algorithms:

(1) **Non-Negative Canonical Correlation Analysis (NNCCA) with IPTW**:[12] NNCCA estimates time point-specific outcome weights by independently maximizing the IPTW-weighted correlation at each time point: $\max_{\alpha \geq 0} \mathrm{cor}_w(\boldsymbol{Y}_i \alpha, T_p)$. NNCCA further applies a weighted deflation procedure to iteratively extract approximately orthogonal sets of non-negative outcome weights.

(2) **R-Learner with Extreme Gradient Boosting (RBoost)**:[13] RBoost first estimates the baseline outcome function and the propensity score using XGBoost,[21] and then computes residualized outcomes and residualized treatment assignments. Next, the algorithm fits a model for the CATE by regressing the residualized outcomes onto the residualized treatments using XGBoost. This orthogonalization-based procedure improves robustness to model misspecification and enables efficient use of modern machine learning methods for CATE estimation. We used 3 folds for cross-fitting and cross-validation, 100 trees, 3 search rounds, and 5 early stopping rounds.

(3) **Causal Forests (CF)**:[15] Causal forests estimate the CATE by building an ensemble of honest causal trees, each of which partitions the feature space into locally estimate treatment effects. Honesty is ensured by splitting the data into separate subsamples for tree construction and effect estimation. Averaging over the ensemble yields a flexible, nonparametric estimator with valid asymptotic inference. We learned 2000 trees and otherwise used default parameters.

We further assessed DEBIAS against **three ablated variants**: (i) replacing the correlation objective with mean squared error (MSE), (ii) removing the confounding penalty in Expression (2) ($\lambda = 0$), and (iii) replacing the correlation objective and removing the confounding penalty. Notably, the variant with the confounding penalty removed can be considered a variant of the SCORE algorithm,[9] except that we employ a diversity-promoting penalty (correlation-weighted cosine similarity) instead of deflation to extract multiple scores when treatment is univariate (a setting where deflation fails). All ablated variants used the same cross-validation protocol, λ grid, and number of scores as DEBIAS.

DEBIAS differs from existing comparator methods along several key dimensions. First, while all comparators adjust only for observed confounding, DEBIAS uniquely leverages the temporal structure of longitudinal data and the time-limited nature of treatments to additionally reduce the influence of latent confounding. Second, DEBIAS is the only method capable of extracting multiple interpretable severity scores in the setting of binary treatment assignment, owing to its use of a diversity-promoting penalty rather than deflation. Although NNCCA can also produce multiple scores, these do not correspond to strict severity scores and

lack a clear causal interpretation. Third, DEBIAS estimates non-negative outcome weights by jointly utilizing all future time points, thereby borrowing statistical strength across the outcome trajectory. In contrast, NNCCA, RBoost, and CF estimate effects or representations independently at each time point, precluding information sharing across time. Taken together, DEBIAS is the only approach that integrates temporal consistency and confounding control – both observed and latent – to derive outcome scores that are both longitudinally predictive and causally valid.

6.2. *Evaluation Metrics*

As detailed in Section 4, our primary goal is to assess how effectively each method differentiates patients based on treatment assignment, motivating the use of **partial correlation** $\text{cor}(\widehat{m}_i, T_2 \mid T_1, \boldsymbol{X})$ as the main performance metric for each time point $i > 2$; here, $\widehat{m}_i$ represents the learned outcome at time i – specifically, $\boldsymbol{Y}_i\alpha$ for DEBIAS and NNCCA, or the estimated CATE of the total severity score for RBoost and CF. However, naive correlation is only meaningful in the absence of confounding. To address this limitation, we additionally evaluate all algorithms using the **confounding p-value** derived from the squared partial correlation, $\text{cor}^2(\widehat{m}_i, T_1 \mid T_2, \boldsymbol{X})$. This squared partial correlation quantifies the residual association between the model output and historical exposures, reflecting the extent of any remaining confounding bias. We further evaluated each method by the **sum of confounded coefficients**, or the sum of the coefficients associated with outcome items known to suffer from latent confounding; methods that achieve a low total are preferred, as they minimize reliance on confounded information. Finally, we compare all algorithms in terms of **run-time** to evaluate computational efficiency.

We evaluated all metrics using 1,000 bootstrap replicates, where we sampled with replacement such that approximately 63.2% of the samples acted as the training set and the remaining 36.8% as the held-out test set in each replicate. We computed all performance measures exclusively on the test samples. For all comparisons of relative algorithm performance, we applied two-sided paired t-tests and interpreted significance at a Bonferroni-corrected threshold of $0.05/u$, where u denotes the total number of comparator algorithms.

6.3. *Adolescent Depression*

We evaluated each algorithm's ability to maximize correlation and minimize confounding using data from the Treatment for Adolescents with Depression Study (TADS; ClinicalTrials.gov ID NCT00006286), an RCT assessing the efficacy of cognitive-behavioral therapy (CBT), fluoxetine, their combination, and placebo in adolescent major depressive disorder.[22] We excluded the placebo group since patients received placebo for only 8 weeks before transitioning to standard care, whereas 323 patients in the other groups maintained their assigned treatments for a 36-week duration.

NNCCA, CF, and RBoost are canonically applied to binary treatment variables; therefore, treatment groups were dichotomized as medication (fluoxetine or combination therapy) versus CBT to facilitate a fair comparison across methods. The resulting medication indicator was used as the current treatment variable, $T_p = T_2$. The prior treatment indicator, T_1, was defined as a binary variable indicating whether the patient had received any mental health services

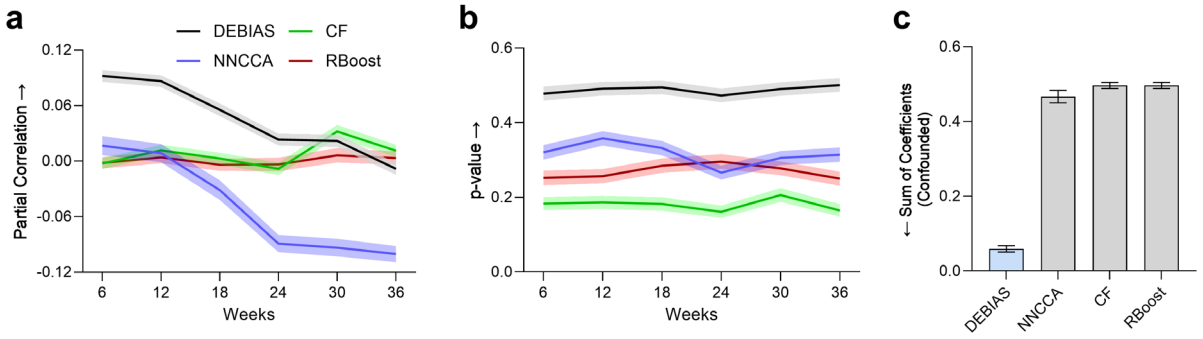

Fig. 3. **Accuracy results for the first score in the TADS dataset.** (a) DEBIAS achieved the highest correlation with outcomes from weeks 6-24, despite incorporating regularization to mitigate latent confounding bias. (b) DEBIAS also attained the largest mean p-value associated with the squared correlation coefficient, reflecting reduced confounding influence relative to competing methods. (c) The sum of the outcome coefficients assigned by DEBIAS to confounded items was also the smallest among all methods. Error bands and bars denote 95% confidence intervals of the mean.

prior to treatment assignment, as measured by the Child and Adolescent Services Assessment (CASA),[23] given its likely correlation with T_2. The outcome vector $\boldsymbol{Y}_i$ comprised the change from baseline in each item of the Children's Depression Rating Scale–Revised (CDRS-R).[24]

Although the original RCT design ensures perfect control of confounding, we introduced an artificial latent confounder, $\boldsymbol{C}$, sampled from a standard normal distribution. We then additively incorporated $\boldsymbol{C}$ into T_1, T_2, and a randomly selected subset of 5 to 12 items within each outcome vector $\boldsymbol{Y}_i$, using time-varying weights for each item and time point sampled uniformly from $[0.2, 1]$. We then re-binarized T_1 and T_2 by thresholding at the value 0.25. Crucially, this experimental setup provides ground-truth knowledge regarding which $\boldsymbol{Y}_i$ items are confounded to compute the sum of confounded coefficients metric. All analyses included age and biological sex as observed covariates in $\boldsymbol{X}$.

Figure 3 presents the primary results. DEBIAS achieved the highest correlation coefficients among all methods across the first 24 weeks (Figure 3 (a)). This superior performance reflects the enforcement of a consistent set of non-negative weights α, which facilitates information sharing across time points. In later weeks, all algorithms exhibited a decline toward zero or negative correlations, reflecting the true convergence of treatment effects among fluoxetine, CBT, and combination therapy.[22] We conclude that DEBIAS maximizes outcome predictability relative to all comparators.

DEBIAS also yielded the largest p-values associated with the squared correlation regularization term, indicating effective mitigation of latent confounding effects (Figure 3 (b)). Inspection of the outcome coefficients revealed that DEBIAS preferentially assigned the smallest weights to the confounded outcomes, providing further evidence of superior confounding control (Figure 3 (c)). Collectively, these results demonstrate that DEBIAS achieves both maximal correlation and minimal confounding in the TADS dataset. Ablation results against three variants in Supplementary Figure 6 confirmed that both correlation maximization and confounding minimization are essential for DEBIAS to achieve optimal performance, even for

the scores beyond the first. Finally, DEBIAS completed within 10 seconds on average in this dataset (Supplementary Figure 7).

6.4. *Chronic Schizophrenia*

We next evaluated each algorithm's ability to learn causally predictable outcomes in schizophrenia. We downloaded data from the Clinical Antipsychotic Trials of Intervention Effectiveness (CATIE; NCT00014001), which was a large RCT comparing the effectiveness of antipsychotic medications in adults with chronic schizophrenia.[25] We restricted our analysis to 664 subjects treated with olanzapine (coded as $T_2 = T_p = 1$) or quetiapine ($T_2 = 0$), in order to maximize the contrast in antipsychotic efficacy for core psychotic symptoms; olanzapine is widely regarded as one of the most effective antipsychotics, whereas quetiapine is generally considered among the least effective.[26] We set T_1 to the number of prior inpatient psychiatric visits, since this variable influences antipsychotic prescribing in patients with schizophrenia.[27] We introduced time-varying confounding by additively including a standard normal latent confounder in T_1, T_2, and a uniformly selected subset of 15 to 25 items within each outcome vector $\boldsymbol{Y}_i$. Each outcome vector represented the change from baseline for the 30 individual items of the Positive and Negative Syndrome Scale (PANSS) measured across 15 months.[28]

We present the results in Figure 4. DEBIAS once again achieved the highest correlation with treatment assignment among all competing methods (Figure 4 (a)). The algorithm also improved confounding control, as evidenced by a markedly higher p-value for the confounding penalty and a much lower total sum of non-negative coefficients assigned to confounded outcome items. These results indicate that DEBIAS consistently maximized out-of-sample correlation and minimized confounding, paralleling its performance in the TADS dataset. Ablation analyses further demonstrated that both the correlation maximization objective and the confounding penalty were necessary to achieve optimal results across multiple extracted scores

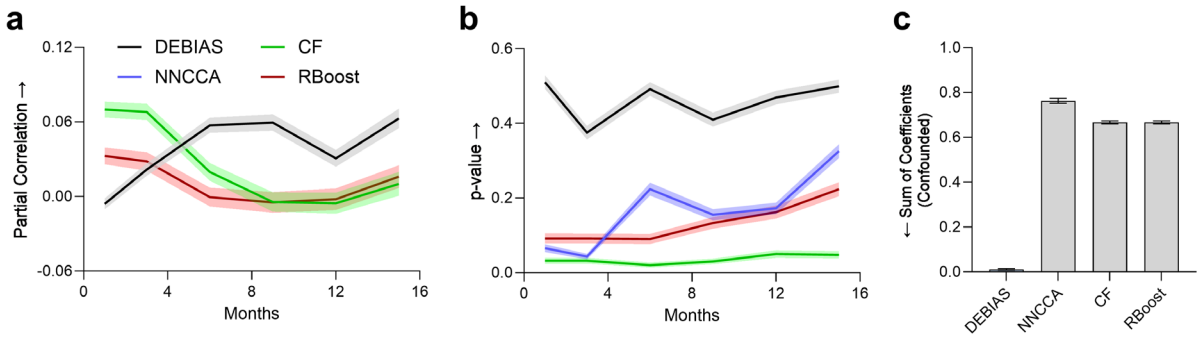

Fig. 4. **Accuracy results for the first score in the CATIE dataset.** (a) DEBIAS attained the highest correlation with treatment assignment as treatment effects diverged over time. The correlation achieved by NNCCA was consistently poor (below -0.20 on average) and therefore omitted from the plot to focus on the competitive algorithms. (b) Compared to all other methods, DEBIAS exhibited substantially superior control of confounding, as reflected by higher p-values for the squared correlation coefficient. (c) DEBIAS also assigned markedly lower non-zero coefficients to confounded outcome items, indicating greater selectivity and robustness to confounding.

(Supplementary Figure 8). Finally, DEBIAS completed its computation within 20 seconds on this dataset (Supplementary Figure 9).

7. Discussion

We introduced the DEBIAS algorithm, which learns combinations of symptom severity items that maximize predictability and minimize latent confounding bias, enabling robust causal inference from psychiatric longitudinal data. Unlike conventional approaches that rely on fixed, user-defined outcomes and assume adequate adjustment for confounding, DEBIAS is the first method to algorithmically identify outcome measures empirically amenable to valid causal inference even with latent confounders. Experiments in adolescent depression and chronic schizophrenia demonstrated that DEBIAS recovers causally predictable severity scores by leveraging the time-limited direct effects of past treatments, a critical advantage when comprehensive covariate collection is infeasible. DEBIAS thus represents a paradigm shift, showing that identifying suitable outcomes for causal inference can be just as important as adjusting for observed confounders in complex real-world settings.

Our work has several limitations. First, DEBIAS is purposefully designed as a linear method to emphasize foundational conceptual advances in causal inference rather than algorithmic complexity. While linear decorrelation is often practically effective for removing confounding, it does not guarantee conditional independence in the strict mathematical sense. Thus, extending DEBIAS to nonlinear settings, where more general forms of dependence can be addressed, remains important for future research. Second, we currently treat T_1 as a historical treatment with time-limited direct effects, an assumption justified for most psychiatric medications. The assumption may be violated for interventions such as CBT, which is believed to exert long-lasting effects by imparting enduring skills.[29] However, in practice, the presence of persistent symptoms among non-remitting patients included in clinical longitudinal datasets suggests that any enduring direct effects of prior therapy are likely minimal in this cohort. Our experimental results further support this claim: DEBIAS consistently achieved the lowest levels of confounding across all methods, despite not explicitly manipulating or blocking potential pathways of the form $T_1 \to \boldsymbol{Y}_3, \ldots, \boldsymbol{Y}_m$. This empirical finding suggests that the time-limited direct effects assumption and corresponding regularization strategy are reasonable and effective. Time-limited direct effects on all outcome items are also not required for our identification strategy, as discussed in Supplementary Materials 8.1. Third, outcome learning opens avenues for novel approaches to confounding adjustment and offers potential applications in domains beyond psychiatry, such as the construction of composite endpoints in endocrinology or the definition of multi-omic phenotypes in oncology. Systematically exploring these alternatives represents a particularly promising avenue for future research.

In summary, DEBIAS represents a substantial advance in outcome learning for causal inference, delivering clinically interpretable measures from data readily available in psychiatric research. This enables more accurate and unbiased causal inference for important real-world applications that may ultimately improve mental healthcare.

References

1. G. W. Imbens and D. B. Rubin, *Causal inference in statistics, social, and biomedical sciences* (Cambridge University Press, 2015).
2. P. Spirtes, C. Glymour and R. Scheines, *Causation, Prediction, and Search*, 2nd edn. (MIT press, 2000).
3. D. Hedeker and R. D. Gibbons, *Longitudinal Data Analysis* (John Wiley & Sons, 2006).
4. B. A. Goldstein, A. M. Navar, M. J. Pencina and J. P. Ioannidis, Opportunities and challenges in developing risk prediction models with electronic health records data: a systematic review, *Journal of the American Medical Informatics Association: JAMIA* **24**, p. 198 (2016).
5. A. J. Rush, M. H. Trivedi, S. R. Wisniewski, A. A. Nierenberg, J. W. Stewart, D. Warden, G. Niederehe, M. E. Thase, P. W. Lavori, B. D. Lebowitz *et al.*, Acute and longer-term outcomes in depressed outpatients requiring one or several treatment steps: a star* d report, *American Journal of Psychiatry* **163**, 1905 (2006).
6. E. V. Strobl and S. Kim, Learning outcomes that maximally differentiate psychiatric treatments, *medRxiv* , 2024 (2024).
7. E. V. Strobl, Consistent differential effects of bupropion and mirtazapine in major depression, *Journal of Affective Disorders* , p. 119551 (2025).
8. E. V. Strobl, Unique behavior profiles that specify mental distress in autism, *medRxiv* , 2025 (2025).
9. E. V. Strobl, Predicting the predictable in the psychiatric high risk, *Proceedings of the Machine Learning for Healthcare Conference* (2025, accepted).
10. O. Ashenfelter and D. Card, Using the longitudinal structure of earnings to estimate the effect of training programs, *The Review of Economics and Statistics* **67**, 648 (1985).
11. J. M. Robins, M. A. Hernan and B. Brumback, Marginal structural models and causal inference in epidemiology, *Epidemiology* **11**, 550 (2000).
12. C. Sigg, B. Fischer, B. Ommer, V. Roth and J. Buhmann, Nonnegative cca for audiovisual source separation, 253 (2007).
13. X. Nie and S. Wager, Quasi-oracle estimation of heterogeneous treatment effects, *Biometrika* **108**, 299 (2021).
14. S. R. Künzel, J. S. Sekhon, P. J. Bickel and B. Yu, Metalearners for estimating heterogeneous treatment effects using machine learning, *Proceedings of the National Academy of Sciences* **116**, 4156 (2019).
15. S. Wager and S. Athey, Estimation and inference of heterogeneous treatment effects using random forests, *Journal of the American Statistical Association* **113**, 1228 (2018).
16. J. D. Angrist, G. W. Imbens and D. B. Rubin, Identification of causal effects using instrumental variables, *Journal of the American Statistical Association* **91**, 444 (1996).
17. T. S. Richardson and J. M. Robins, Single world intervention graphs (swigs): A unification of the counterfactual and graphical approaches to causality, *Center for the Statistics and the Social Sciences, University of Washington Series. Working Paper* **128**, p. 2013 (2013).
18. J. Cohen, *Statistical power analysis for the behavioral sciences* (Routledge, 2013).
19. M. W. Lipsey and D. B. Wilson, *Practical meta-analysis.* (SAGE publications, Inc, 2001).
20. L. Armijo, Minimization of functions having lipschitz continuous first partial derivatives, *Pacific Journal of Mathematics* **16**, 1 (1966).
21. T. Chen and C. Guestrin, Xgboost: A scalable tree boosting system, 785 (2016).
22. J. March, S. Silva, S. Petrycki, J. Curry, K. Wells, J. Fairbank, B. Burns, M. Domino, S. McNulty, B. Vitiello *et al.*, Fluoxetine, cognitive-behavioral therapy, and their combination for adolescents with depression: Treatment for adolescents with depression study (tads) randomized controlled trial., *JAMA* **292**, 807 (2004).

23. B. H. Ascher, E. M. Z. Farmer, B. J. Burns and A. Angold, The child and adolescent services assessment (casa) description and psychometrics, *Journal of Emotional and Behavioral Disorders* **4**, 12 (1996).
24. E. O. Poznanski, J. A. Grossman, Y. Buchsbaum, M. Banegas, L. Freeman and R. Gibbons, Children's depression rating scale–revised, *Journal of the American Academy of Child Psychiatry* (1995).
25. J. A. Lieberman, T. S. Stroup, J. P. McEvoy, M. S. Swartz, R. A. Rosenheck, D. O. Perkins, R. S. Keefe, S. M. Davis, C. E. Davis, B. D. Lebowitz *et al.*, Effectiveness of antipsychotic drugs in patients with chronic schizophrenia, *New England Journal of Medicine* **353**, 1209 (2005).
26. S. Leucht, A. Cipriani, L. Spineli, D. Mavridis, D. Örey, F. Richter, M. Samara, C. Barbui, R. R. Engel, J. R. Geddes *et al.*, Comparative efficacy and tolerability of 15 antipsychotic drugs in schizophrenia: a multiple-treatments meta-analysis, *The Lancet* **382**, 951 (2013).
27. J. Tiihonen, E. Mittendorfer-Rutz, M. Majak, J. Mehtälä, F. Hoti, E. Jedenius, D. Enkusson, A. Leval, J. Sermon, A. Tanskanen *et al.*, Real-world effectiveness of antipsychotic treatments in a nationwide cohort of 29 823 patients with schizophrenia, *JAMA Psychiatry* **74**, 686 (2017).
28. S. R. Kay, A. Fiszbein and L. A. Opler, The positive and negative syndrome scale (panss) for schizophrenia, *Schizophrenia Bulletin* **13**, 261 (1987).
29. S. D. Hollon, M. O. Stewart and D. Strunk, Enduring effects for cognitive behavior therapy in the treatment of depression and anxiety, *Annu. Rev. Psychol.* **57**, 285 (2006).
30. M. T. Treadway and D. H. Zald, Reconsidering anhedonia in depression: lessons from translational neuroscience, *Neuroscience & Biobehavioral Reviews* **35**, 537 (2011).

Quantifying surprise in clinical care: Detecting highly informative events in electronic health records with foundation models

Michael C. Burkhart, Bashar Ramadan, Luke Solo, William F. Parker, and Brett K. Beaulieu-Jones

Department of Medicine, University of Chicago,
Chicago, Illinois, USA
E-mail: {burkh4rt,basharramadan,lsolo,wparker,beaulieujones}@uchicago.edu

We present a foundation model-derived method to identify highly informative tokens and events in electronic health records. Our approach considers incoming data for the entire context of a patient's hospitalization to find surprising events. Context enables flagging anomalous events that rule-based approaches would consider within a normal range. We demonstrate that the events our model flags are significantly more useful than average events for predicting downstream patient outcomes and show that a fraction of events we identify as unsurprising can be safely dropped without an adverse impact on performance. Finally, we show how informativeness can help interpret the predictions of prognostic models trained on foundation model-derived representations.

Keywords: Foundation models; Electronic health records; Information quantification; Model explainability.

© 2025 The Authors. Open Access chapter published by World Scientific Publishing Company and distributed under the terms of the Creative Commons Attribution Non-Commercial (CC BY-NC) 4.0 License.

1. Introduction

Healthcare generates a stream of data, including vitals, labs, medications, and respiratory support. Clinical decision making requires parsing and understanding this information and its importance in the context of each patient's medical history. Oftentimes, event summaries like automatically-collected vitals provide little additional knowledge about a patient.[2,58] Clinicians are commonly notified regardless, resulting in increased cognitive burden and alarm fatigue.[51] For over a decade now, the Joint Commission has included "reduc[ing] patient harm associated with clinical alarm systems" as a National Patient Safety Goal [52, NPSG.06.01.01, since 2014]. In this paper, we investigate the extent to which foundation model (FM)-derived estimates of event information can be used to highlight the most important events in a patient's record. In essence, we explore which events are surprising to the FM based on a comparison between what the model expects to happen next and what is observed. Identifying important or surprising events has the potential to substantially improve our understanding of healthcare delivery and better inform clinicians about the status of their patients.

Divergence between the model's expectation and the actual observation or informativeness broadly indicates one of three things: (1) practice variation, when a clinician makes a decision which deviates from what is typically done in similar contexts in the training data (e.g., prescribing a medication off-label); (2) an unexpected change in patient condition that would generally be observed in clinical measurements (e.g., a lab result which indicates a change in patient state that could not be predicted using observed covariates); or (3) issues of data quality which could be present in either orders or patient measurements (e.g., a typo when entering a value). In all three cases, there is the potential to learn substantially from the model's "surprise," to potentially reduce clinical errors, and to rapidly and succinctly surface the most important information for a clinician. This could be used to both better inform the time-sensitive decision-making that often occurs in the hospital setting as well as to provide a summary of the most important information about a patient for downstream analyses like phenotyping or sub-population identification.

While this work focuses on patients receiving critical care in the inpatient setting, the approach aims to be one which can be generalized to many healthcare settings with longitudinal data and outcomes. This work operates at the level of Electronic Health Records (EHRs) corresponding to individual hospitalization stays. For each hospitalization, we form a sequence of tokens that describe the admitted patient, along with their admission type, and then chronicle vitals, administered medications, lab results, assessments, and a few other categories of data as they become available, ending with a token for discharge.[9,33,49] We perform self-supervised training of a foundation model (FM) to predict the next token in one of these sequences given all previous tokens. Such models have proven remarkably effective across a number of fields[4,41,50] but most importantly in our case for predicting a variety of downstream clinical outcomes.[56,57] Furthermore, these models are generative[34] in the sense that they estimate the joint probability distribution on these sequences. Given a trained model and a novel sequence, we can estimate the context-aware (conditional) information of each token. We call a series of tokens that become available at the same time "an event" and calculate context-aware information for each event. We show that highly informative tokens and events are more

predictive of downstream outcomes and tend to result in greater changes to the model-derived understanding of a patient's current condition.

In this paper, we present the first comprehensive study of FM-derived information quantification for tokens and events in EHRs. Our main contributions are as follows:

(1) We propose a principled FM-derived method to identify highly informative tokens and events in a patient's EHR. As opposed to classical rules-based methods, our context-informed approach identifies anomalous labs and assessments even when a patient has values within what would be considered a normal range. As opposed to the variable importance methods applied to classifiers trained for specific outcomes, our method defines informativeness in terms of the sequences themselves.
(2) We illustrate how the occurrence of highly informative events impacts a patient's prognosis and alters the FM-derived representation that is commonly used for making downstream predictions. In terms of interpretability, this allows us to provide a list of events deemed most informative to the FM. We show that dropping these events from a patient's timeline impacts the performance of downstream prognostic models. Conversely, we show that events carrying the least information can be dropped without sacrificing predictive performance.

2. Related work

Early approaches to modeling sequential data derived from EHRs focused on recurrent neural networks (RNNs) including Long Short-Term Memory [22, LSTM] networks.[5,10,30,39] Approaches shifted from RNNs to transformers[53] beginning with variations on BERT,[11] including BEHRT[29] and Med-BERT.[40] Subsequently, Foresight[27] and ETHOS[42,43] both used generative pretrained transformer [38, GPT] architectures. Wornow, et al. provided a detailed review of FMs for EHRs up to 2023.[57] More recently, Mamba,[19] a selective state-space model, has found applications in ClinicalMamba[59] and EHRMamba.[13]

Some efforts have been made to better understand these types of models. Beaulieu-Jones, et al.[6] noted that sequential EHR models can learn both from the patient's actual state (e.g. the result of a particular lab) and from clinicians' actions (e.g. the fact that a particular lab was ordered). They found that models trained on demographics, admissions data, and charges from the first day of admission (clinician-initiated actions) performed competitively against models trained on full sequences of EHR data. In doing so, they raised an important point about understanding which tokens and events in a patient's sequence drive a model's understanding of that sequence.

Wornow et. al[55] studied, among other things, how sequences derived from EHRs differ from natural language (written English). They showed how EHRs exhibit copy-forwarding of chronic diagnoses, irregular spacing between tokens, and increased perplexity of tokens over time due to disease progression. Their definition of perplexity relates closely to our definition of informativeness, but they did not investigate which types of tokens tend to carry more information, nor did they consider subsequences. In contrast to this work, they focused on much longer-term time horizons consisting of multiple clinical encounters, whereas we focus on single hospitalizations.

3. Methods

3.1. *Data*

We considered 422,765 hospitalizations for adults (age 18 or older) from the Beth Israel Deaconess Medical Center between 2008–2019 (MIMIC-IV-3.1[25]) and 50,440 hospitalizations from the UCMC health system between March 2020–March 2022. We restricted our analysis to patients with stays of at least 24 hours. We formatted EHR data from each health system into the CLIF standard.[44] The MIMIC patients were partitioned into training, validation, and test sets at a 70%-10%-20% rate. We then collected each hospitalization for patients in a given set. In this way, hospitalization records in the test set corresponded to patients with no hospitalizations in the training or validation sets to avoid any potential information leakage. The UCMC data was primarily used as a held-out test set, and so was partitioned at a 5%-5%-90% rate according to the time of each patient's first hospitalization, with training patients coming first, followed by validation and then test.

3.2. *Tokenization*

We converted each hospitalization event from the CLIF standard into a sequence of tokens (represented computationally as non-negative integers) as follows. For a given sequence, the first token always corresponds to a timeline start token. The next three tokens contain patient-level demographic information on race, ethnicity, and sex. The following two tokens correspond to admission-specific information, namely patient age converted to a decile and admission type. Taken together, we refer to the 5 tokens occurring immediately after the timelines start token as the *admission prefix*. Tokens corresponding to a variety of events for a hospitalization are then inserted in the same order in which these events occurred. Transfers are encoded with their standardized location category. Labs are encoded with two tokens and inserted at the time results become available: one for lab category, and a second for the deciled lab value in the training set within that category. We call this strategy, of tokenizing categories and binning their corresponding values according to the training value of the deciles, category-value tokenization. See Figure 1 for an illustration. A handful of other tables receive this type of tokenization: vitals and results according to vital category, medication and dosage by medication category, assessment and results by assessment category. Respiratory information is recorded at the beginning of respiratory support; the encoded information is mode category and device category. We include a token indicating if a patient is placed into a prone position. All hospitalization-related data is encoded this way and inserted in chronological order. Tokens that arrive synchronously correspond to an event and always appear coterminously in a sequence. Timelines then end with a token for discharge category and a dedicated timeline end token. We did not use time-spacing or artificial time tokens[36] as recent studies suggest they do not improve performance.[55]

3.3. *Context-aware information*

Consider the set V^T of length-T sequences of tokens drawn from some vocabulary V. Such sequences correspond directly to tokenized EHR data as described in the previous subsection.

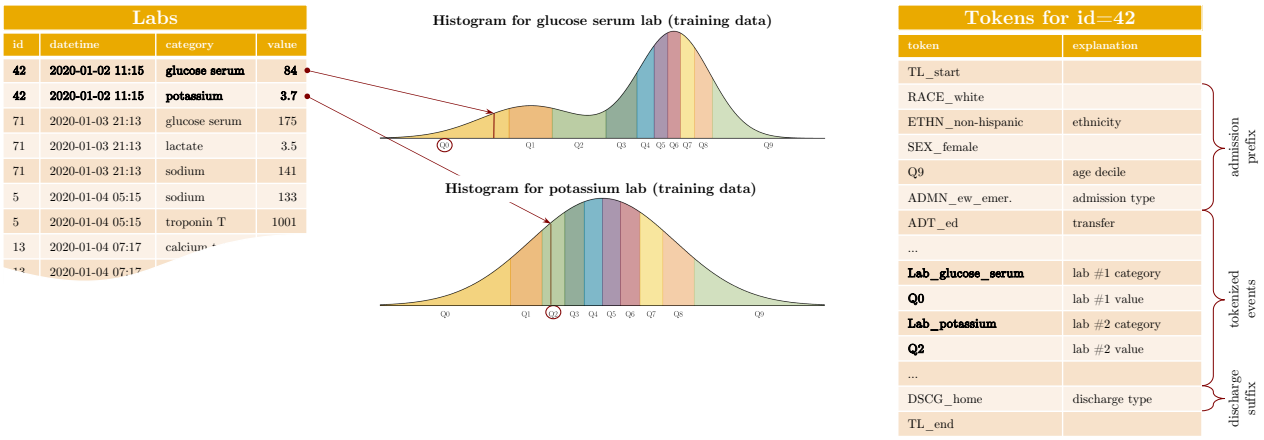

Figure 1. *Category-value tokenization.* We convert lab results into tokens as follows. For each lab category, we determine decile cutoffs (center) using all results corresponding to that lab category available in the training dataset. Each lab value is then encoded as a decile (with `Q0` corresponding to the lowest decile, `Q1` to the next, and so on up to `Q9`) and inserted into the corresponding hospitalization in temporal order.

For a given sequence $x = (x_1, \ldots, x_T)$ and indices $1 \leq u \leq v \leq T$, we let $x_{u:v} = (x_u, x_{u+1}, \ldots, x_v)$ correspond to the subsequence and $x_{<u} = x_{1:u-1}$ to the context at u for $u > 1$. If p is a probability distribution on V^T, we let $p(x_{u:v}) = \mathbb{P}_{X\sim p}(X_{u:v} = x_{u:v})$ denote the marginal distribution and $p(x_{u:v}|x_{y:z}) = \mathbb{P}_{X\sim p}(X_{u:v} = x_{u:v}|X_{y:z} = x_{y:z})$ denote the conditional for indices u, v, y, z. We adopt the convention that $p(x_{u:v}|x_{<1}) = p(x_{u:v})$. With these definitions, the Shannon self-information[46] of a certain realized subsequence $x_{u:v}$ under p is given by $I_p(x_{u:v}) = -\log_2 p(x_{u:v})$. The *context-aware information* associated to a realized subsequence $x_{u:v} \in V$ and context $x_{<u} \in V^{u-1}$ is defined analogously, by

$$\boxed{I_p(x_{u:v}|x_{<u}) = -\log_2 p(x_{u:v}|x_{<u}).} \tag{1}$$

In the case of a single token x_t, we have $t = u = v$ and refer to $I_p(x_t|x_{<t}) = -\log_2 p(x_t|x_{<t})$ as tokenwise context-aware information. As $p(x_{u:v}|x_{<t}) = \prod_{t=u}^{v} p(x_t|x_{<t})$, it follows that

$$I_p(x_{u:v}|x_{<u}) = \textstyle\sum_{t=u}^{v} I_p(x_t|x_{<t}). \tag{2}$$

Thus, context-aware information is additive.

This quantity plays a pivotal role in the training of standard models. A model is a parameterized distribution p_θ on V^T. Training attempts to find parameters θ that minimize the relative entropy (or Kullback–Leibler divergence[28]) between the empirical distribution $\hat{p}$ given by the training set and p_θ,

$$D(\hat{p}||p_\theta) = \underbrace{\mathbb{E}_{X_{1:T}\sim\hat{p}}[I_{p_\theta}(X_{1:T})]}_{H(\hat{p},p_\theta)} - \underbrace{\mathbb{E}_{X_{1:T}\sim\hat{p}}[I_{\hat{p}}(X_{1:T})]}_{H(\hat{p})}. \tag{3}$$

Here, $H(\hat{p}, p_\theta)$ is the cross-entropy between $\hat{p}$ and p_θ and $H(\hat{p})$ is the entropy of $\hat{p}$. As this latter term is independent of θ, it may be disregarded during training / optimization. By (2), we have the simplification $H(\hat{p}, p_\theta) = \sum_{t=1}^{T} \mathbb{E}_{X_{1:T}\sim\hat{p}}[I_{p_\theta}(X_t|X_{<t})]$. We see that the training process optimizes θ to minimize the expected tokenwise context-aware information over the training set.

In more general terms, training finds the model p_θ that makes the training set least surprising. This is equivalent to maximum likelihood estimation [17, §5.5]. Upon completion of training, p_{θ_*} with optimized parameters θ_* serves as our best approximation to p and can be used to calculate the context-aware information (1) in new timelines for tokens and subsequences.

3.4. *Model architecture and training*

For our parameterized distribution p_θ on sequences of tokens/integers, we train a model from scratch based on the Llama-3.2 model architecture[18] with a hidden size of 1024, intermediate size of 2048, 8 hidden layers, and 8 attention heads, for a total of 67.3 million parameters. Wornow, et al.'s [55, Fig. 1B] architecture comparison indicates that the Llama architecture performs favorably to GPT,[38] Hyena,[37] and Mamba[19] architectures for context lengths of 1000-2000 tokens, such as we use here.

As our vocabulary is created during the tokenization process, we train models from scratch, as opposed to fine-tuning models that have been pre-trained on a tokenized natural language vocabulary. We train weights to minimize (3) with AdamW,[32] a variant of Adam[26] with decoupled weight decay.[21] Training batches were formed by packing tokenized sequences into a $b \times 1024$-dimensional array in row-major order where b is the batch size.[a] We used tree-structured Parzen estimators[1] to tune the learning rate (between $5 \cdot 10^{-5}$ and $5 \cdot 10^{-4}$, inclusive) and effective batch size (between 32 and 96, inclusive). Models were trained on a single compute node with 8×A100 (40GB PCIe) GPUs, connected with 2×16-core 3.0-GHz AMD Milan processors. The model having best-performing loss on the MIMIC evaluation set was selected and provides the p used to calculate context-aware information for the remainder of the paper.

3.5. *Representation-based prognostic models*

As a causal language model or state space-based model processes a sequence $x_{1:T}$ of tokens, it forms a representation $R(x_{1:t}) \in \mathbb{R}^d$ of the subsequence encountered up to the tth token for each $1 \leq t \leq T$, where d tends to be at least a few hundred dimensions. In Llama models, we take the last hidden state to be our representation, with d equal to the "hidden size" parameter, in our case set to 1024. In many FM-based works,[13,48,55] these representations or a function of them provide the basis for all subsequent prognostic predictions. For example, the representation $R(x_{1:t_0})$ of a patient's timeline that contains all tokens occurring prior to some cutoff time will then be used as features in a logistic regression model to predict outcomes for that patient occurring after the cutoff time. All patients start with the same representation, i.e. $R(x_1)$ corresponds to the representation associated to the "timeline start" token. As tokens are added to each timeline, these representations diverge. We are generally interested in the relationship between informativeness and corresponding changes in representation space at both the token

[a]Note, because of this packing strategy, the model does not learn that our sequences always start with the timeline start token. By convention, the true $p(x_1)$ is an indicator function on the timeline start token, so that $I_p(x_1)$ should be $-\log_2 1 = 0$. (Deterministic tokens do not carry information.) The model should learn that the first token after the start token should be a race token, and then an ethnicity token, and so on, because for these predictions, context is supplied.

and event levels of granularity. Establishing a strong relationship between information content and changes in representation could help to explain the predictions of representation-based prognostic models. To this end, we define the magnitude of the change in representation space when token x_t is added as

$$\Delta_t = \|R(x_{1:t}) - R(x_{1:t-1})\| \tag{4}$$

where the norm is taken to be the standard Euclidean norm and define the path length in representation space corresponding to a subsequence $x_{u:v}$ as

$$\Delta_{u:v} = \sum_{t=u}^{v} \Delta_t. \tag{5}$$

3.6. *Redaction experiment*

We restrict our cohort to patients who are admitted to the ICU within the first 24 hours of their admission. We consider two outcomes: *inpatient mortality*, defined as patient death prior to discharge from the hospital, and *long length-of-stay*, defined as discharge occurring ≥ 7 days after admission.

For each timeline truncated at the 24 hour mark, we calculate context-aware information for each event. For each of 10%, 20%, 30%, & 40%, we drop that percentage of either the most or the least informative events, or that percentage of events chosen at random. We do this for each combination of percentage and method (most, least, random), creating 12 partially redacted versions of the original 24-hour timelines.

For each data version, we extract 24-hour representations $R(x_{1:t_0})$ using our model, where $t_0 \leq 1024$ corresponds to the last token to arrive within 24 hours of admission. Note that, in an abuse of notation, t_0 depends on the hospitalization sequence x. Much more information is collected for some patients in the first 24 hours than for others. We then train a logistic regression classifier to predict each outcome (inpatient mortality and long length-of-stay) given the 24-hour representations on the training portion of the MIMIC dataset. We apply each model to the respective versions of both the MIMIC and UCMC test sets.

We perform bootstrap resampling to estimate 95% confidence intervals for test set-based variability in the ROC-AUC [12, *cf.* §13.3]. This method takes a fixed classification model and forms an empirical distribution of performance metrics by resampling test data 10,000 times.

We also use bootstrap sampling to estimate p-values for the hypothesis test of $H_0 : \mathrm{AUC}_0 = \mathrm{AUC}_1$ against the one-sided alternative $H_a : \mathrm{AUC}_0 > \mathrm{AUC}_1$, where AUC_0 corresponds to the original AUC and AUC_1 to the AUC from a fixed classifier built and tested on redacted timelines [12, Algorithm 16.1]. This method compares the observed difference in AUC performance against differences obtained from 10,000 resamplings under the hypothesis that predictions from the two classifiers are exchangeable. This bootstrapping approach also only simulates variability in the test set given fixed classifiers.

4. Results

4.1. *Highlighted timelines*

We present the first 210 tokens from three timelines in row-major order along with comments as Figures 2-4. Starting from the upper left-hand corner, each row can be read off from left to right.

TL_START	RACE_white	ETHN_non-hispanic	SEX_male	Q4	ADMN_observation_admi
ADT_ed	ADT_ward	LAB_hemoglobin	Q5	LAB_platelet_count	Q1
LAB_bicarbonate	Q8	LAB_chloride	Q5	LAB_creatinine	Q4
LAB_glucose_serum	Q2	LAB_magnesium	Q8	LAB_potassium	Q3
LAB_sodium	Q7	LAB_bun	Q2	LAB_calcium_total	Q8
LAB_phosphate	Q5	LAB_ldh	Q9	LAB_troponin_t	Q9
LAB_basophils_percent	Q3	LAB_eosinophils_percent	Q2	LAB_lymphocytes_percent	Q1
LAB_monocytes_percent	Q0	LAB_neutrophils_percent	Q0	LAB_basophils_absolute	Q3
LAB_hemoglobin	Q5	LAB_platelet_count	Q1	LAB_inr	Q4
LAB_pt	Q3	LAB_troponin_t	Q9	LAB_bicarbonate	Q8
LAB_chloride	Q5	LAB_creatinine	Q5	LAB_glucose_serum	Q3
LAB_magnesium	Q7	LAB_potassium	Q1	LAB_sodium	Q7
LAB_bun	Q3	LAB_calcium_total	Q7	LAB_phosphate	Q7
LAB_ldh	Q9	LAB_basophils_percent	Q3	LAB_eosinophils_percent	Q2
_AB_lymphocytes_percent	Q1	LAB_monocytes_percent	Q0	LAB_neutrophils_percent	Q0
LAB_basophils_absolute	Q3	LAB_alt	Q7	LAB_alkaline_..phatase	Q0
LAB_ast	Q7	LAB_bilirubin_total	Q2	LAB_bicarbonate	Q6
LAB_chloride	Q8	LAB_creatinine	Q5	LAB_glucose_serum	Q3
LAB_magnesium	Q7	LAB_potassium	Q2	LAB_sodium	Q7
LAB_bun	Q3	LAB_calcium_total	Q3	LAB_phosphate	Q6
LAB_ldh	Q9	LAB_troponin_t	Q9	LAB_hemoglobin	Q2
LAB_platelet_count	Q1	LAB_basophils_percent	Q3	LAB_eosinophils_percent	Q2
_AB_lymphocytes_percent	Q0	LAB_monocytes_percent	Q0	LAB_neutrophils_percent	Q0
LAB_basophils_absolute	Q3	LAB_hemoglobin	Q2	LAB_bicarbonate	Q5
LAB_chloride	Q7	LAB_creatinine	Q5	LAB_glucose_serum	Q5
LAB_magnesium	Q7	LAB_potassium	Q4	LAB_sodium	Q6
LAB_bun	Q3	LAB_calcium_total	Q3	LAB_phosphate	Q5
LAB_alt	Q7	LAB_alkaline_..phatase	Q0	LAB_ast	Q6
LAB_bilirubin_total	Q1	LAB_ldh	Q9	LAB_inr	Q5
LAB_pt	Q5	LAB_ptt	Q3	LAB_basophils_percent	Q3
LAB_eosinophils_percent	Q2	LAB_lymphocytes_percent	Q1	LAB_monocytes_percent	Q1
LAB_neutrophils_percent	Q0	LAB_basophils_absolute	Q3	LAB_platelet_count	Q1
LAB_troponin_t	Q9	LAB_hemoglobin	Q1	LAB_platelet_count	Q1
LAB_inr	Q5	LAB_pt	Q5	LAB_ptt	Q5
LAB_troponin_t	Q9	LAB_basophils_percent	Q3	LAB_eosinophils_percent	Q2

Figure 2. Timeline highlighted by tokenwise context-aware information for MIMIC hospitalization 24640534 (first 210 tokens). This white, non-Hispanic male of age ~ 60 was admitted to the ED for observation. He had no previous admission history within MIMIC. His stay was 37 days 22 hours in duration. After the stay, he subsequently received ICD-10 diagnoses C9200 for 'Acute myeloblastic leukemia, not having achieved remission' and I214 for 'Non-ST elevation (NSTEMI) myocardial infarction', among others. (Full diagnostic list in appendix.) The model successfully identified low lymphocytes as being potentially clinically relevant (`Lab_lymphocytes_percent`, `Q1`), but overlooked the low neutrophils (`Lab_neutrophils_percent`, `Q0`) and high troponin T (`Lab_troponin_t`, `Q9`).

We see that informative tokens sometimes correspond to lab events or vitals readings that have a direct bearing on the patient's current state. Examples include the lymphocytes percentage lab in Figure 2, arterial PCO_2 in Figure 3, and blood pressure readings in Figure 4. Informative tokens can also correspond to clinician-initiated events, such as the CAM assessment[24] in Figure 3 following a low RASS[45] score. (If the RASS score were -4 as opposed to -3, typically the CAM assessment would not be made until later.) Finally, informative tokens can correspond to measurements that seem implausible and may be worth further investigation, such as the Braden scores[7] in Figure 4.

4.2. *Counts of highly informative tokens and events anticipate negative outcomes*

We consider $T_{\geq 95}$, the number of tokens exceeding the 95th percentile for informativeness, $E_{\geq 95,<99}$, the number of events in the 95th to the 99th percentile, and $E_{\geq 99}$, the number of events exceeding the 99th percentile for informativeness. For these definitions, we restrict to tokens and events that occur within the first 24 hours of admission.

In a logistic regression model for inpatient mortality in the MIMIC test set, we find that $T_{\geq 95}$ $(\hat{\beta} = 0.0269, p < 0.001)$, $E_{\geq 95,<99}$ $(\hat{\beta} = 0.3015, p < 0.001)$, and $E_{\geq 99}$ $(\hat{\beta} = 0.2480, p < 0.001)$ all have positive coefficients and are highly significant. Similarly for long length of stay, we find that

TL_START	RACE_unknown	ETHN_unknown	SEX_female	Q4	ADMN_ew_emer.
ADT_ed	LAB_pco2_arterial	Q9	LAB_ph_arterial	Q0	LAB_po2_arterial
Q0	LAB_so2_arterial	Q0	VTL_weight_kg	Q0	VTL_height_cm
Q2	ADT_icu	MED_propofol	Q6	MED_fentanyl	Q5
RESP_mode_pre..control	RESP_devc_imv	MED_fentanyl	Q6	ASMT_rass	Q1
ASMT_cat_cam_loc	ASMT_val_yes	ASMT_cat_cam_..tention	ASMT_val_yes	ASMT_cat_cam_mental	ASMT_val_yes
ASMT_cat_cam_total	ASMT_val_positive	ASMT_gcs_total	Q9	ASMT_gcs_motor	Q0
ASMT_gcs_verbal	Q3	ASMT_gcs_eye	Q1	MED_fentanyl	Q7
VTL_temp_c	Q4	LAB_lactate	Q0	LAB_pco2_arterial	Q9
LAB_ph_arterial	Q0	LAB_po2_arterial	Q1	LAB_ph_venous	Q0
LAB_pco2_venous	Q9	VTL_spo2	Q7	VTL_sbp	Q6
VTL_map	Q8	VTL_dbp	Q8	VTL_heart_rate	Q8
VTL_respiratory_rate	Q0	LAB_hemoglobin	Q8	LAB_platelet_count	Q6
VTL_spo2	Q9	VTL_weight_kg	Q0	VTL_heart_rate	Q7
VTL_respiratory_rate	Q7	RESP_mode_None	RESP_devc_imv	VTL_sbp	Q0
VTL_map	Q1	VTL_dbp	Q3	LAB_inr	Q2
LAB_pt	Q2	LAB_ptt	Q4	LAB_bicarbonate	Q1
LAB_chloride	Q2	LAB_creatinine	Q9	LAB_glucose_serum	Q6
LAB_magnesium	Q8	LAB_potassium	Q7	LAB_sodium	Q1
LAB_bun	Q7	LAB_calcium_total	Q8	LAB_phosphate	Q9
MED_norepinephrine	Q3	MED_midazolam	Q5	LAB_lactate	Q1
LAB_pco2_arterial	Q5	LAB_ph_arterial	Q4	LAB_po2_arterial	Q8
ASMT_gcs_total	Q9	ASMT_gcs_motor	Q0	ASMT_gcs_verbal	Q3
ASMT_gcs_eye	Q1	ASMT_braden_activity	Q6	ASMT_braden_friction	Q1
ASMT_braden_mobility	Q5	ASMT_braden_moisture	Q5	ASMT_braden_nutrition	Q5
ASMT_braden_sensory	Q3	ASMT_braden_total	Q1	MED_norepinephrine	Q4
MED_norepinephrine	Q5	RESP_mode_pre..control	RESP_devc_None	VTL_spo2	Q9
VTL_heart_rate	Q6	VTL_respiratory_rate	Q7	MED_midazolam	Q4
VTL_sbp	Q4	VTL_map	Q7	VTL_dbp	Q7
VTL_spo2	Q9	VTL_heart_rate	Q7	VTL_respiratory_rate	Q7
VTL_sbp	Q7	VTL_map	Q8	VTL_dbp	Q8
MED_norepinephrine	Q4	MED_norepinephrine	Q0	ASMT_rass	Q1
VTL_spo2	Q9	VTL_heart_rate	Q8	VTL_respiratory_rate	Q7
VTL_sbp	Q0	VTL_map	Q2	VTL_dbp	Q3
VTL_spo2	Q9	VTL_heart_rate	Q8	VTL_respiratory_rate	Q7

Figure 3. Timeline highlighted by tokenwise context-aware information for MIMIC hospitalization 26886976 (first 210 tokens). This female of unknown race and ethnicity was admitted to the ED at age $\sim$ 73. Her 12 day 2 hour hospital stay ended in death. Afterwards, she subsequently received ICD-10 diagnoses A4189 for 'Other specified sepsis', R6521 for 'Severe sepsis with septic shock', and N179 for 'Acute kidney failure, unspecified', in addition to other diagnoses. After the patient received a low Richmond Agitation-Sedation Scale score [45, RASS] with (`ASMT_rass`, `Q1`) indicating a high likelihood of coma, the model finds the administration of the Confusion Assessment Method [24, CAM] (`ASMT_cat_cam_loc`) to evaluate delirium to be surprising/ informative. The model also finds the high arterial PCO_2 (`LAB_pco2_arterial`, `Q9`) to be of interest.

$T_{\geq 95}$ ($\hat{\beta} = 0.0163, p < 0.001$), $E_{\geq 95,<99}$ ($\hat{\beta} = 0.2872, p < 0.001$), and $E_{\geq 99}$ ($\hat{\beta} = 0.1236, p < 0.001$) are positively and significantly associated. In the UCMC test dataset (where percentiles are based on statistics from the UCMC data), $T_{\geq 95}$ ($\hat{\beta} = 0.0148, p < 0.001$), $E_{\geq 95,<99}$ ($\hat{\beta} = 0.1684, p < 0.001$), and $E_{\geq 99}$ ($\hat{\beta} = 0.4798, p < 0.001$) all associate with inpatient mortality. Similarly, $T_{\geq 95}$ ($\hat{\beta} = 0.0165, p < 0.001$), $E_{\geq 95,<99}$ ($\hat{\beta} = 0.1292, p < 0.001$), and $E_{\geq 99}$ ($\hat{\beta} = 0.4727, p < 0.001$) associate positively with long length of stay.

4.3. *Informative tokens tend to result in larger changes to a patient's latent representation*

In our MIMIC test set, a simple linear regression for Δ_t from (4) given informativeness $I_p(x_t|x_{<t})$ yields $\hat{\beta} = 0.548, p < 0.001$ with $R^2 = 0.212$. For a breakdown of average Δ_t vs. average informativeness by token type, see Figure 5. Positioning and transfer tokens tend to carry less information, while assessment, lab, and quantile `Q` tokens tend to carry more.

At the level of events $x_{u:v}$, a regression for path length $\Delta_{u:v}$ from (5) given event-level informativeness $I_p(x_{u:v}|x_{<u})$ yields $\hat{\beta} = 2.081, p < 0.001$ with $R^2 = 0.997$ (see also Figure 6). More informative events trace out longer paths in representation space. Perhaps surprisingly, there does not appear to be a strong linear relationship between event informativeness and

TL_START	RACE_white	ETHN_non-hispanic	SEX_female	Q4	ADMN_urgent
ADT_ward	ADT_ward	ADT_ward	LAB_lactate	Q5	LAB_pco2_arterial
Q9	LAB_ph_arterial	Q0	LAB_po2_arterial	Q3	LAB_bicarbonate
Q9	LAB_chloride	Q0	LAB_creatinine	Q6	LAB_glucose_serum
Q4	LAB_magnesium	Q2	LAB_sodium	Q1	LAB_bun
Q3	LAB_phosphate	Q8	LAB_potassium	Q9	RESP_mode_other
RESP_devc_None	VTL_weight_kg	Q0	VTL_height_cm	Q2	ADT_icu
VTL_temp_c	Q0	RESP_mode_None	RESP_devc_nippv	VTL_sbp	Q9
VTL_map	Q9	VTL_dbp	Q8	VTL_heart_rate	Q8
VTL_temp_c	Q5	ASMT_rass	Q4	ASMT_cat_cam_loc	ASMT_val_no
ASMT_cat_cam_..tention	ASMT_val_yes	ASMT_cat_cam_mental	ASMT_val_yes	ASMT_cat_cam_total	ASMT_val_positive
ASMT_cat_cam_thinking	ASMT_val_yes	ASMT_gcs_total	Q2	ASMT_gcs_motor	Q9
ASMT_gcs_verbal	Q9	ASMT_gcs_eye	Q3	ASMT_braden_activity	Q8
ASMT_braden_friction	Q7	ASMT_braden_mobility	Q9	ASMT_braden_moisture	Q9
ASMT_braden_nutrition	Q5	ASMT_braden_sensory	Q7	ASMT_braden_total	Q7
VTL_spo2	Q9	VTL_respiratory_rate	Q2	VTL_spo2	Q9
VTL_heart_rate	Q8	VTL_respiratory_rate	Q6	VTL_sbp	Q8
VTL_map	Q7	VTL_dbp	Q5	VTL_spo2	Q9
VTL_heart_rate	Q7	VTL_respiratory_rate	Q5	RESP_mode_other	RESP_devc_nippv
VTL_sbp	Q7	VTL_map	Q6	VTL_dbp	Q5
LAB_lactate	Q3	LAB_pco2_arterial	Q9	LAB_ph_arterial	Q0
LAB_po2_arterial	Q0	LAB_ph_venous	Q0	LAB_pco2_venous	Q9
LAB_hemoglobin	Q7	LAB_platelet_count	Q9	LAB_inr	Q4
LAB_pt	Q2	LAB_ptt	Q4	LAB_bicarbonate	Q6
LAB_chloride	Q1	LAB_creatinine	Q5	LAB_glucose_serum	Q7
LAB_magnesium	Q1	LAB_sodium	Q1	LAB_bun	Q4
LAB_calcium_total	Q9	LAB_phosphate	Q8	LAB_alt	Q1
LAB_alkaline_..phatase	Q4	LAB_ast	Q2	LAB_bilirubin_total	Q1
LAB_ldh	Q7	LAB_potassium	Q9	VTL_spo2	Q0
VTL_heart_rate	Q7	VTL_respiratory_rate	Q8	RESP_mode_None	RESP_devc_None
VTL_sbp	Q7	VTL_map	Q9	VTL_dbp	Q9
VTL_spo2	Q5	VTL_heart_rate	Q8	VTL_respiratory_rate	Q3
VTL_temp_c	Q0	VTL_sbp	Q8	VTL_map	Q6
VTL_dbp	Q6	VTL_spo2	Q1	VTL_heart_rate	Q8
VTL_respiratory_rate	Q7	ASMT_gcs_total	Q2	ASMT_gcs_motor	Q9

Figure 4. Timeline highlighted by tokenwise context-aware information for MIMIC hospitalization 29022625 (first 210 tokens). This $\sim$ 55 year old white female had previously been seen for a myriad of conditions (see appendix). After a a 30 day 20 hour stay, she received new diagnoses of K2211 for 'Ulcer of esophagus with bleeding', J9601 for 'Acute respiratory failure with hypoxia', J9602 for 'Acute respiratory failure with hypercapnia', A419 for 'Sepsis, unspecified organism', J90 for 'Pleural effusion, not elsewhere classified', E872 for 'Acidosis', and J95851 for 'Ventilator associated pneumonia', among others. The model notices that the Braden scores seem implausibly high, and highlights the hypercarbia (`LAB_pco2_arterial`, `Q9`). It seems to miss the hypoxia (`VTL_spo2`, `Q0`); however, SPO_2 readings up to 93.0 are placed in decile `Q0` so this may be due to the tokenization strategy. The model also emphasizes the patient's rising blood pressure (`VTL_sbp`) over time.

total distance moved in representation space during the course of an event $x_{u:v}$, i.e. $\|R(x_{1:v}) - R(x_{1:u-1})\|$.

4.4. *Redacting informative events significantly reduces prognostic ability*

Results from our redaction experiment (described in §3.6) indicate that dropping highly informative events from a patient's timeline significantly impairs representation-based classifier performance in the MIMIC test set. For ROC-AUC, we find statistically significant performance disparities when dropping as few as 20% of the most informative events. Conversely, events carrying little information can readily be dropped from a timeline without significantly impacting predictive performance. For representation-based logistic regression models trained on the MIMIC training set, predictive performance on the MIMIC and UCMC test sets are available in Table 1. In addition to ROC-AUC, we report PR-AUC, the area under the precision-recall curve, and the Brier score,[8] which corresponds to the mean squared error between predicted probabilities and boolean realizations in online Appendix E. Higher ROC-AUC and PR-AUC values and lower Brier scores correspond to better performing models.

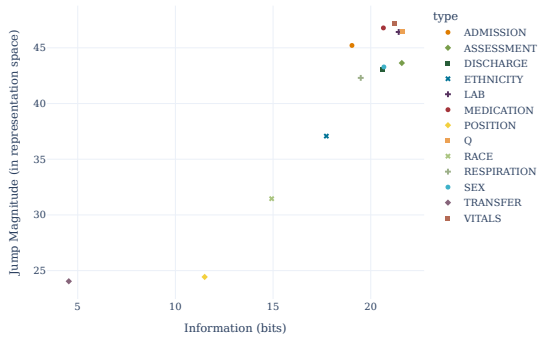

Figure 5. Average Δ_t versus average token-wise informativeness by token type for the 24.7 million tokens x_t in the MIMIC test set.

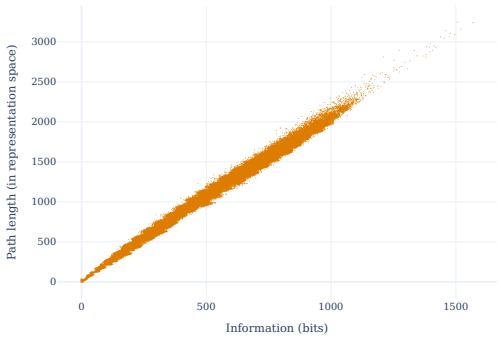

Figure 6. Path length $\Delta_{u:v}$ versus eventwise informativeness for the 2.8 million events $x_{u:v}$ in the MIMIC test set.

5. Discussion

In this work, we developed a method to quantify the informativeness of clinical events as observed in EHRs based on their tokenized representation.[b] We found that highly informative tokens can correspond to measurements of clinical significance, to clinician-initiated events or lab orders, and in some cases to records that seem *prima facie* to be data-entry errors.[35] Tokens that carry more information tend to precipitate larger changes in a patient's latent representation and events that carry more information tend to have longer paths in representation space. Counts of highly informative / surprising tokens and events in the first 24 hours of a patient's stay relate to an increased risk of future negative outcomes like death or long length-of-stay. Redacting highly informative events reduces the predictive performance of representation-based classifiers, while redacting a fraction of relatively uninformative events tends to not result in significant performance drops.

5.1. *Broad applicability beyond clinical prediction*

The FM-derived informativeness measure extends well beyond traditional clinical prediction tasks and opens new avenues for AI applications to healthcare. Context-aware information quantification provides a principled framework for addressing downstream challenges that have historically relied on heuristic approaches.

Our informativeness metric could provide a data-driven solution to clinical alarm fatigue through dynamic alerting systems that prioritize notifications based on contextual surprise rather than static thresholds. For example, a blood pressure of 118/86 mmHg might be routine in most contexts, but could be highly informative if it represents a rapid drop in a patient

[b]Shannon famously estimated the average information content of words in written English to be around 11.82 bits [47, Eq. 7]. Under the assumption that our model p trained on the MIMIC training set adequately approximates the empirical distribution $\hat{p}$, we can average $I_p(x_t|x_{<t})$ over x_t in the MIMIC test set to roughly approximate that tokens in our timelines each carry around 21.23 bits of information on average.

Table 1. ROC-AUC for the two classification tasks on ICU patients in the MIMIC and UCMC test sets. Stars correspond to the significance level of a hypothesis test against the one-sided alternative that the model trained on the original data performs better. A single asterisk * corresponds to $p < 0.05$, two ** to $p < 0.01$ and three *** to $p < 0.001$.

version		Inpatient mortality		Long length-of-stay	
method	pct.	MIMIC	UCMC	MIMIC	UCMC
original	—	0.869 ± 0.009	0.839 ± 0.013	0.740 ± 0.008	0.661 ± 0.011
top	10	0.860 ± 0.010	0.830 ± 0.013	0.735 ± 0.009	0.671 ± 0.011
	20	0.848 ± 0.011 **	0.814 ± 0.014 **	0.726 ± 0.009 **	0.653 ± 0.012
	30	0.833 ± 0.012 ***	0.812 ± 0.013 **	0.720 ± 0.009 **	0.642 ± 0.011 *
	40	0.823 ± 0.011 ***	0.818 ± 0.012 *	0.714 ± 0.009 ***	0.649 ± 0.012
bottom	10	0.867 ± 0.010	0.834 ± 0.011	0.736 ± 0.012	0.659 ± 0.013
	20	0.866 ± 0.009	0.834 ± 0.012	0.732 ± 0.010	0.667 ± 0.012
	30	0.862 ± 0.011	0.829 ± 0.012	0.726 ± 0.009 *	0.667 ± 0.013
	40	0.859 ± 0.012	0.829 ± 0.011	0.724 ± 0.008 **	0.664 ± 0.011
random	10	0.866 ± 0.008	0.838 ± 0.012	0.737 ± 0.006	0.664 ± 0.012
	20	0.863 ± 0.008	0.835 ± 0.011	0.733 ± 0.009	0.667 ± 0.012
	30	0.865 ± 0.010	0.835 ± 0.014	0.728 ± 0.007	0.674 ± 0.009
	40	0.861 ± 0.011	0.835 ± 0.011	0.727 ± 0.008 *	0.674 ± 0.011

being treated for an ischemic stroke or hypertensive emergency. In these conditions, a slower reduction in blood pressure is preferred to avoid complications, making a rapid drop worthy of alerting a clinician. Traditional rule-based clinical decision support alerts would likely consider this a normal reading and therefore fail to identify a potentially concerning change. The ability to use context to differentiate this alarming event from a similar, but clinically appropriate, change in another patient distinguishes FM-based approaches.[23]

Detecting data entry errors represents another potential application. Traditional validation of data entry quality is dedicated to verification of abnormal values, but our approach could identify contextually implausible entries that fall within normal ranges. Overall, surprise quantification could help automate much of the manual chart review process currently required for quality assurance. For clinical research, informativeness patterns could enable novel patient phenotyping approaches. Rather than relying on pre-specified diagnostic codes, researchers could identify patient subgroups characterized by similar patterns of surprising events, potentially revealing previously unrecognized disease subtypes or complex pathologies difficult to capture with traditional algorithms. So-called events-based models[14,61] have already proven remarkably effective at both subtyping and staging neurodegenerative disease,[3,54,60] but could in the future find broader applications.

At the health system level, patterns of informativeness could inform resource allocation decisions. Units characterized by high rates of surprising events might require additional staffing or monitoring capabilities. Our finding that surprising events correlate with negative outcomes suggests informativeness patterns could serve as early warning indicators for periods of increased clinical risk. Furthermore, cases highlighted by our informativeness measure could

serve as valuable educational resources. Clinical scenarios with highly informative events represent situations where standard protocols might be insufficient, making them ideal for training clinicians to recognize complex presentations.

Quantifying the information in EHRs could help clinicians quickly detect anomalous events and identify data entry errors. FMs trained on tokenized EHRs have already demonstrated remarkably good performance on prognostic tasks. Finding ways to better understand and interpret predictions made from these models through informativeness quantification represents a significant step toward more transparent and actionable clinical AI systems. The broad applicability of this informativeness framework across diverse healthcare challenges suggests that context-aware information quantification could become a foundational tool for healthcare analytics, complementing traditional approaches with a more nuanced understanding of clinical surprise and significance.

5.2. *Limitations and directions for future work*

We are actively working to improve our approach to tokenization. Our decision to encode labs and medications at a broad categorical level significantly reduces the overall vocabulary,[c] allowing more efficient training on a relatively small dataset. However, it can merge clinically distinct items into the same token. For instance, potassium measured from whole blood versus serum is treated in the same manner, obscuring an important factor for distinguishing pseudo-hyperkalemia from life-threatening hyperkalemia. Our approach to tokenizing values by decile within each category is standard,[43,55] but sometimes results in deciles that straddle clinically relevant thresholds. Future work may explore tokenization strategies that incorporate lab reference values. We also intend to develop methods to distinguish between the various types of surprising events identified in this work (e.g. to differentiate changes in a patient's condition from data entry errors). Manual chart review would be required to support claims of data entry errors. Finally, we also intend to compare our approach to attention-based mechanisms for identifying important tokens.[15,20,31]

Data and code availability. The MIMIC-IV-3.1 dataset[25] is available to credentialed users on Physionet.[16] The UCMC dataset is available in the CLIF format for federated, privacy-preserving analyses. Reasonable requests may be directed to WFP. Github hosts code to reproduce the results found here.[d] The arXiv version[e] of this work contains an appendix with a listing of the vocabulary, all learned decile cutoffs, additional examples, and detailed results.

Acknowledgments. This work was funded in part by the National Institutes of Health, specifically the National Institute of Neurological Disorders and Stroke grant R00NS114850 to BKB and National Library of Medicine grant R01LM014263 to WFP. This project would not have been possible without the support of the Center for Research Informatics at the University of Chicago and particularly the High-Performance Computing team.

[c]We used 208 unique tokens while Renc et al.[42] used 4,495 and Wornow et al.[55] used 39,818.
[d]See: `https://github.com/bbj-lab/Quantifying-Surprise-EHRs`
[e]See: `https://arxiv.org/abs/2507.22798`

Bibliography

1. T. Akiba, S. Sano, T. Yanase, T. Ohta, and M. Koyama. Optuna: A next-generation hyperparameter optimization framework. In *KDD*, 2019.
2. H. R. Anderson, A. C. Borgen, R. Christnacht, J. Ng, J. G. Weller, H. N. Davison, et al. Stats on the desats: Alarm fatigue and the implications for patient safety. *BMJ Open Qual.*, 12(3), 2023.
3. D. Archetti, A. L. Young, N. P. Oxtoby, D. Ferreira, G. Mårtensson, E. Westman, D. C. Alexander, G. B. Frisoni, and A. Redolfi. Inter-cohort validation of Sustain model for Alzheimer's disease. *Front. Big Data*, 2021.
4. M. Awais, M. Naseer, S. Khan, R. M. Anwer, H. Cholakkal, M. Shah, M.-H. Yang, and F. S. Khan. Foundation models defining a new era in vision: A survey and outlook. *IEEE Trans. Pattern Anal. Mach. Intell.*, 47(4):2245–2264, 2025.
5. B. K. Beaulieu-Jones, P. Orzechowski, and J. H. Moore. Mapping patient trajectories using longitudinal extraction and deep learning in the MIMIC-III critical care database. In *PSB*, pages 123–132, 2018.
6. B. K. Beaulieu-Jones, W. Yuan, G. A. Brat, A. L. Beam, G. Weber, M. Ruffin, and I. S. Kohane. Machine learning for patient risk stratification: standing on, or looking over, the shoulders of clinicians? *npj Digit. Med.*, 4(1):62, 2021.
7. N. Bergstrom, B. J. Braden, A. Laguzza, and V. Holman. The Braden scale for predicting pressure sore risk. *Nurs. Res.*, 36(4):205–210, 1987.
8. G. W. Brier. Verification of forecasts expressed in terms of probability. *Mon. Weather Rev.*, 78(1):1–3, 1950.
9. M. C. Burkhart, B. Ramadan, Z. Liao, K. Chhikara, J. C. Rojas, W. F. Parker, and B. K. Beaulieu-Jones. Foundation models for electronic health records: representation dynamics and transferability. arXiv:2504.10422, 2025.
10. E. Choi, M. T. Bahadori, A. Schuetz, W. F. Stewart, and J. Sun. Doctor AI: Predicting clinical events via recurrent neural networks. arXiv:1511.05942, 2016.
11. J. Devlin, M.-W. Chang, K. Lee, and K. Toutanova. BERT: Pre-training of deep bidirectional transformers for language understanding. In *NAACL-HLT*, pages 4171–4186, 2019.
12. B. Efron and R. J. Tibshirani. *An Introduction to the Bootstrap*, volume 57 of *Monographs on Statistics and Applied Probability*. Chapman and Hall, 1993.
13. A. Fallahpour, M. Alinoori, W. Ye, X. Cao, A. Afkanpour, and A. Krishnan. EHRMamba: Towards generalizable and scalable foundation models for electronic health records. In *ML4H*, volume PMLR 259, pages 291–307, 2025.
14. H. M. Fonteijn, M. Modat, M. J. Clarkson, J. Barnes, M. Lehmann, N. Z. Hobbs, et al. An event-based model for disease progression and its application in familial Alzheimer's disease and Huntington's disease. *NeuroImage*, 60(3):1880–1889, 2012.
15. S. Ge, Y. Zhang, L. Liu, M. Zhang, J. Han, and J. Gao. Model tells you what to discard: Adaptive KV cache compression for LLMs. In *ICLR*, 2024.
16. A. L. Goldberger, L. A. N. Amaral, L. Glass, J. M. Hausdorff, P. C. Ivanov, R. G. Mark, et al. Physiobank, physiotoolkit, and physionet. *Circulation*, 101(23), 2000.
17. I. Goodfellow, Y. Bengio, and A. Courville. *Deep Learning*. Adaptive Computation and Machine Learning. MIT Press, Cambridge, MA, 2016.
18. A. Grattafiori, A. Dubey, A. Jauhri, A. Pandey, A. Kadian, A. Al-Dahle, et al. The Llama 3 herd of models. arXiv 2407.21783, 2024.
19. A. Gu and T. Dao. Mamba: Linear-time sequence modeling with selective state spaces. In *COLM*, 2024.
20. Z. Guo, H. Kamigaito, and T. Watanabe. Attention score is not all you need for token importance indicator in KV cache reduction: Value also matters. In *Conference on Empirical Methods in*

Natural Language Processing, 2024.
21. S. Hanson and L. Pratt. Comparing biases for minimal network construction with back-propagation. In *Adv. Neur. Inf. Proc. Sys.*, 1988.
22. S. Hochreiter and J. Schmidhuber. Long short-term memory. *Neural Comput.*, 9(8):1735–1780, 1997.
23. M. D. Howell, G. S. Corrado, and K. B. DeSalvo. Three epochs of artificial intelligence in health care. *JAMA*, 331(3):242–244, 2024.
24. S. K. Inouye, C. H. van Dyck, C. A. Alessi, S. Balkin, A. P. Siegal, and R. I. Horwitz. Clarifying confusion: The confusion assessment method. *Ann. Intern. Med.*, 113(12):941–948, 1990.
25. A. E. W. Johnson, L. Bulgarelli, L. Shen, A. Gayles, A. Shammout, S. Horng, et al. MIMIC-IV, a freely accessible electronic health record dataset. *Sci. Data*, 10, 2023.
26. D. P. Kingma and J. Ba. Adam: A method for stochastic optimization. In *ICLR*, 2015.
27. Z. Kraljevic, D. Bean, A. Shek, R. Bendayan, H. Hemingway, J. A. Yeung, et al. Foresight-a generative pretrained transformer for modelling of patient timelines using electronic health records: a retrospective modelling study. *Lancet Digit. Health*, 6(4), 2024.
28. S. Kullback and R. A. Leibler. On information and sufficiency. *Ann. Math. Statistics*, 22:79–86, 1951.
29. Y. Li, S. Rao, J. A. Solares, A. Hassaine, R. Ramakrishnan, D. Canoy, Y. Zhu, K. Rahimi, and G. Salimi-Khorshidi. BEHRT: Transformer for electronic health records. *Sci. Rep.*, 10, 2020.
30. Z. C. Lipton, D. C. Kale, C. Elkan, and R. Wetzel. Learning to diagnose with LSTM recurrent neural networks. arXiv:1511.03677, 2017.
31. Z. Liu, A. Desai, F. Liao, W. Wang, V. Xie, Z. Xu, A. Kyrillidis, and A. Shrivastava. Scissorhands: Exploiting the persistence of importance hypothesis for LLM KV cache compression at test time. In *Adv. Neur. Inf. Proc. Sys.*, volume 36, pages 52342–52364, 2023.
32. I. Loshchilov and F. Hutter. Decoupled weight decay regularization. In *ICLR*, 2019.
33. M. McDermott, B. Nestor, P. Argaw, and I. S. Kohane. Event stream GPT: A data pre-processing and modeling library for generative, pre-trained transformers over continuous-time sequences of complex events. In *Adv. Neur. Inf. Proc. Sys.*, volume 36, pages 24322–24334, 2023.
34. A. Ng and M. Jordan. On discriminative vs. generative classifiers: A comparison of logistic regression and naive Bayes. In *Adv. Neur. Inf. Proc. Sys.*, volume 14, pages 841–848, 2002.
35. H. Niu, O. A. Omitaomu, M. A. Langston, M. Olama, O. Ozmen, H. B. Klasky, A. Laurio, M. Ward, and J. Nebeker. EHR-BERT: A BERT-based model for effective anomaly detection in electronic health records. *J. Biomed. Inf.*, 150:104605, 2024.
36. C. Pang, X. Jiang, K. S. Kalluri, M. Spotnitz, R. Chen, A. Perotte, and K. Natarajan. CEHR-BERT: Incorporating temporal information from structured EHR data to improve prediction tasks. In *Proceedings of Machine Learning for Health*, volume PMLR 158, pages 239–260, 2021.
37. M. Poli, S. Massaroli, E. Nguyen, D. Y. Fu, T. Dao, S. Baccus, Y. Bengio, S. Ermon, and C. Ré. Hyena hierarchy: towards larger convolutional language models. In *ICML*, 2023.
38. A. Radford, K. Narasimhan, T. Salimans, and I. Sutskever. Improving language understanding by generative pre-training. OpenAI, 2018.
39. A. Rajkomar, E. Oren, K. Chen, A. M. Dai, N. Hajaj, M. Hardt, P. J. Liu, X. Liu, J. Marcus, M. Sun, et al. Scalable and accurate deep learning with electronic health records. *npj Digit. Med.*, 1(1):18, 2018.
40. L. Rasmy, Y. Xiang, Z. Xie, C. Tao, and D. Zhi. Med-BERT: pretrained contextualized embeddings on large-scale structured electronic health records for disease prediction. *npj Digit. Med.*, 4(1):86, 2021.
41. M. Raza, Z. Jahangir, M. B. Riaz, M. J. Saeed, and M. A. Sattar. Industrial applications of large language models. *Sci. Rep.*, 15, 2025.
42. P. Renc, M. K. Grzeszczyk, N. Oufattole, D. Goode, Y. Jia, S. Bieganski, M. B. A. McDermott,

J. Was, A. E. Samir, J. W. Cunningham, D. W. Bates, and A. Sitek. Foundation model of electronic medical records for adaptive risk estimation. arXiv:2502.06124, 2025.
43. P. Renc, Y. Jia, A. E. Samir, J. Was, Q. Li, D. W. Bates, and A. Sitek. Zero shot health trajectory prediction using transformer. *npj Digit. Med.*, 7, 2024.
44. J. C. Rojas, P. G. Lyons, K. Chhikara, V. Chaudhari, S. V. Bhavani, M. Nour, K. G. Buell, K. D. Smith, C. A. Gao, S. Amagai, et al. A common longitudinal intensive care unit data format (CLIF) for critical illness research. *Intensive Care Med.*, 2025.
45. C. N. Sessler, M. S. Gosnell, M. J. Grap, G. M. Brophy, P. V. O'Neal, K. A. Keane, E. P. Tesoro, and R. K. Elswick. The Richmond agitation–sedation scale. *Am. J. Respir. Crit. Care Med.*, 166(10):1338–1344, 2002.
46. C. E. Shannon. A mathematical theory of communication. *Bell System Tech. J.*, 27:379–423,623–656, 1948.
47. C. E. Shannon. Prediction and entropy of printed English. *Bell System Tech. J.*, 30(1):50–64, 1951.
48. E. Steinberg, J. A. Fries, Y. Xu, and N. Shah. MOTOR: A time-to-event foundation model for structured medical records. In *ICLR*, 2024.
49. E. Steinberg, K. Jung, J. A. Fries, C. K. Corbin, S. R. Pfohl, and N. H. Shah. Language models are an effective representation learning technique for electronic health record data. *J. Biomed. Inf.*, 113, 2021.
50. J. Sun, C. Zheng, E. Xie, Z. Liu, R. Chu, J. Qiu, J. Xu, M. Ding, H. Li, M. Geng, et al. A survey of reasoning with foundation models: Concepts, methodologies, and outlook. *ACM Comput. Surv.*, 57(11), 2025.
51. The Joint Commission. Medical device alarm safety in hospitals. *Sentinel Event Alert*, (50), 2013.
52. The Joint Commission. *Hospital: 2025 National Patient Safety Goals*. 2024.
53. A. Vaswani, N. Shazeer, N. Parmar, J. Uszkoreit, L. Jones, A. N. Gomez, Ł. Kaiser, and I. Polosukhin. Attention is all you need. In *Adv. Neur. Inf. Proc. Sys.*, volume 30, 2017.
54. J. W. Vogel, A. L. Young, N. P. Oxtoby, R. Smith, R. Ossenkoppele, O. T. Strandberg, et al. Four distinct trajectories of tau deposition identified in Alzheimer's disease. *Nat. Med.*, 27(5):871–881, 2021.
55. M. Wornow, S. Bedi, M. A. F. Hernandez, E. Steinberg, J. Fries, C. Ré, O. Koyejo, and N. H. Shah. Context clues: Evaluating long context models for clinical prediction tasks on EHRs. In *ICLR*, 2025.
56. M. Wornow, R. Thapa, E. Steinberg, J. A. Fries, and N. Shah. EHRSHOT: An EHR benchmark for few-shot evaluation of foundation models. In *Neurips Datasets and Benchmarks Track*, volume 36, pages 67125–67137, 2023.
57. M. Wornow, Y. Xu, R. Thapa, B. Patel, E. Steinberg, S. Fleming, M. A. Pfeffer, J. Fries, and N. H. Shah. The shaky foundations of large language models and foundation models for electronic health records. *npj Digit. Med.*, 6(1):135, 2023.
58. D. Xu, F. Liu, X. Ding, J. Ma, Y. Suo, Y.-Y. Peng, J. Li, and X. Fu. Exploring ICU nurses' response to alarm management and strategies for alleviating alarm fatigue: a meta-synthesis and systematic review. *BMC Nursing*, 24, 2025.
59. Z. Yang, A. Mitra, S. Kwon, and H. Yu. ClinicalMamba: A generative clinical language model on longitudinal clinical notes. In *Proceedings of the 6th Clinical NLP Workshop*, pages 54–63, 2024.
60. A. L. Young, R. V. Marinescu, N. P. Oxtoby, M. Bocchetta, K. Yong, N. C. Firth, et al. Uncovering the heterogeneity and temporal complexity of neurodegenerative diseases with subtype and stage inference. *Nat. Commun.*, 9(1), 2018.
61. A. L. Young, N. P. Oxtoby, P. Daga, D. M. Cash, N. C. Fox, S. Ourselin, J. M. Schott, and D. C. Alexander. A data-driven model of biomarker changes in sporadic Alzheimer's disease. *Brain*, 137(9):2564–2577, 2014.

Retrieval-Augmented Guardrails for AI-Drafted Patient-Portal Messages: Error Taxonomy Construction and Large-Scale Evaluation

Wenyuan Chen[1*], Fateme Nateghi Haredasht[1*], Kameron C Black[2], François Grolleau[1], Emily Alsentzer[3], Jonathan H Chen[1,2,4**], Stephen P Ma[2**]

[1]*Stanford Center for Biomedical Informatics Research, Stanford, CA, USA*

[2]*Department of Medicine, Stanford University, Stanford, CA, USA*

[3]*Department of Biomedical Data Science, Stanford University, Stanford, CA, USA*

[4]*Stanford Clinical Excellence Research Center, Stanford University, Stanford, CA, USA*

**Equal Contribution*

***Equal Contribution*

Email: wenyuanc@stanford.edu , fnateghi@stanford.edu , spma@stanford.edu

Asynchronous patient–clinician messaging via EHR portals is a growing source of clinician workload, prompting interest in large language models (LLMs) to assist with draft responses. However, LLM outputs may contain clinical inaccuracies, omissions, or tone mismatches, making robust evaluation essential. Our contributions are threefold: (1) we introduce a clinically grounded error ontology comprising 5 domains and 59 granular error codes, developed through inductive coding and expert adjudication; (2) we develop a Retrieval-Augmented Error Checking (RAEC) pipeline that leverages semantically similar historical message–response pairs to improve judgment quality; and (3) we provide a two-stage prompting architecture using DSPy to enable scalable, interpretable, and hierarchical error detection. Our approach assesses the quality of drafts both in isolation and with reference to similar past message–response pairs retrieved from institutional archives. Using a two-stage DSPy pipeline, we compared baseline and reference-enhanced evaluations on over 1,500 patient messages. Retrieval context improved error identification in domains such as clinical completeness and workflow appropriateness. Human validation on 100 messages demonstrated superior agreement (concordance = 50% vs. 33%) and performance (F1 = 0.500 vs. 0.256) of context-enhanced labels vs. baseline, supporting the use of our RAEC pipeline as AI guardrails for patient messaging.

Keywords: Large Language Models (LLMs); clinical AI evaluation; error taxonomy; retrieval-augmented generation; AI safety

© 2025 The Authors. Open Access chapter published by World Scientific Publishing Company and distributed under the terms of the Creative Commons Attribution Non-Commercial (CC BY-NC) 4.0 License.

1. Introduction

Asynchronous, text-based communication between patients and clinicians via government-mandated secure portals has become an integral component of contemporary care delivery since its launch in the early 2000s,[1-4] improving access, continuity, and patient engagement across diverse health-care settings,[5-7] but staffing has not kept pace; delayed replies, clinician burnout, and safety risks are rising.[8] To cope with the accelerating volume of inbox messages—especially in resource-constrained clinics—health systems are experimenting with large language models (LLMs) that draft replies for clinician review .

Despite their promise, state-of-the-art LLMs can still produce hallucinations and clinically consequential errors.[9-10] Current monitoring approaches predominantly rely on clinician oversight at the point of care and retrospective manual reviews by dedicated reviewers. Unfortunately, these strategies are neither scalable nor capable of preventing real-time patient harm.[11-12] Moreover, errors in generated clinical text remain a major obstacle to the broader adoption of generative AI technologies in healthcare. There is an urgent need for automated, real-time safety mechanisms to detect and mitigate these errors as they occur, ensuring safe and effective deployment in clinical practice.[13]

In response to these challenges, we developed a real-time, multi-agent framework called Retrieval-Augmented Error Checking (RAEC) to evaluate and explain potential errors in LLM-generated patient messages before they reach clinicians or patients. RAEC combines three core innovations: (1) a comprehensive, clinician-vetted error ontology; (2) retrieval of local historical message context to personalize error detection; and (3) a team of agentic LLM evaluators that classify and justify errors at inference time. We hypothesize that incorporating historical context from individual clinicians will improve the system's accuracy and specificity in identifying clinically meaningful errors.

To test this hypothesis, we benchmark RAEC's performance against a rigorously curated, human-labeled reference standard. The pipeline ingests de-identified clinician–patient message pairs, filters and re-ranks candidates based on structured metadata, and passes retrieved examples to LLM agents for classification and explanation. By providing a scalable safety layer for LLM-powered messaging, RAEC supports safer, more context-aware AI deployment, with the potential to reduce clinician workload and improve communication quality across diverse care settings.

2. Related Work

The current evaluation of generative artificial intelligence (AI) in clinical contexts has significant limitations. Traditional surface-level metrics such as BLEU and ROUGE do not capture the nuanced clinical implications or real-world applicability of AI-generated outputs. Human review, while more accurate, is not scalable for large datasets or routine clinical deployment. Modular large language model (LLM) "judge" systems like G-Eval and RubricEval have been introduced to assess outputs across multiple quality dimensions using specialized prompts, but these typically evaluate text in isolation and lack alignment with real-world clinical scenarios or local practice standards.[14-15]

Recent advances in retrieval-augmented generation (RAG) have demonstrated that grounding LLM outputs in external knowledge, such as clinical guidelines, medical textbooks, or up-to-date literature, can substantially improve factuality, reduce hallucinations, and enhance alignment with

clinical best practices.[16] For example, RAG has been shown to improve factual accuracy and clinical alignment in specialty applications such as gastrointestinal symptom triage chatbots and orthopedic exam question answering.[17-18] These approaches allow LLMs to ground their responses in up-to-date, guideline-based information, reducing hallucinations and improving alignment with clinical best practices.[19-21]

However, the application of retrieval for post-hoc error checking—especially with personalization to local clinical practice—remains underexplored. Combining modular LLM agents with retrieval-augmented error checking that leverages locally relevant examples addresses this gap, enhancing both the accuracy and real-world applicability of AI-assisted clinical messaging. This approach is supported by recent systematic reviews, which emphasize the need for robust, context-aware, and standardized evaluation frameworks to ensure safe and effective LLM integration in clinical workflows.[21-22]

Our work addresses this gap in two ways. First, we construct a comprehensive, inductively derived error taxonomy specifically for AI-generated patient portal messages, enabling fine-grained and structured evaluation. Second, we introduce a novel Retrieval-Augmented Error Checking (RAEC) framework—not to improve generation, but to improve evaluation. Instead of supplying reference documents to help draft a response, our system retrieves five similar, previously answered patient-clinician message pairs from a large institutional archive. These exemplars are used as context for an LLM-based judge to assess whether the draft response contains omissions, inappropriate recommendations, or other clinical flaws. This grounding in local precedent significantly reshapes error detection patterns, redirecting attention from superficial factual discrepancies to actionable guidance and completeness, and offers a scalable path toward safer LLM integration in clinical communication.

3. Data

3.1. *Raw Corpus and Preprocessing*

We extracted 246,588 patient–clinician message threads from the Epic-based Stanford Health Care (SHC) enterprise EHR system, spanning a 3-month period from October 2024 to January 2025. These threads were pulled from the secure patient portal infrastructure and represent all asynchronous outpatient communications during that period. Each thread record includes structured metadata (timestamps, department and provider identifiers) along with the full text of the patient's new inquiry, the initial LLM-generated draft, and the final clinician-edited reply.

To ensure high-quality comparisons between AI drafts and human-edited responses, we focused on message triplets (patient query, LLM draft, clinician reply) that clearly represented a single, discrete communication turn. We excluded system messages, administrative events, and cases with missing or NULL content in any of the three key fields. Duplicates were collapsed based on identical text/timestamp pairs, and the earliest valid message was retained. This yielded a clean working corpus of 146,681 unique message triplets (220,739 total messages) across 11 clinical specialties, including Family Medicine, Primary Care, Internal Medicine, Oncology, Hematology, Geriatrics, Gastroenterology, Express Care, Radiation Oncology, Sports Medicine, and Coordinated Care.

For downstream evaluation, we retained only variables essential for automated error labeling and validation: Patient Message, LLM Prompt, LLM Draft, Clinician Reply, Date Sent, Recipient Name, Message Sender, Department, Specialty, and a pseudonymized thread identifier. All extraneous metadata was removed to reduce privacy exposure and enhance reproducibility.

3.2. *Sampling Strategy and Dataset Splits*

From the cleaned corpus, we first extracted a stratified random sample of 1,000 messages, maintaining the same specialty distribution observed in the full dataset, and dedicated this set exclusively to the inductive coding procedure that generated the error taxonomy (see § 4.1.). After removing these cases, we again performed stratified random sampling—preserving the specialty proportions—to select 1570 additional messages for automated evaluation by the LLM guardrail. Finally, we performed independent physician review on a 100-message subset of this evaluation cohort (using 1:1 sampling for messages with at least one error identified by automated LLM guardrail vs messages with no errors); the manually reviewed labels from this set serve as the ground truth references in all validation analyses.

4. Methods

4.1. *Construction of a Clinical Error Taxonomy*

For our initial seed error taxonomy, physicians and researchers with experience studying AI-generated draft replies to patient messages brainstormed common discrepancies observed in patient communication and organized the resulting items into an initial hierarchy. To refine and expand it, we had an LLM perform inductive coding on a stratified sample of 1,000 message triplets (patient query, LLM draft, and clinician-edited reply), maintaining specialty proportions from the full corpus (see § 3.2. . For this process, we used the OpenAI o3-mini reasoning model in a looped prompt–response design: for each message, the model labeled errors using the current taxonomy and proposed new error codes when existing ones didn't fit. The inductive codes were then reviewed in conjunction with the original codes by a board-certified physician. Simple, duplicative codes were manually resolved whereas overly broad codes/new thematic elements prompted the generation of additional codes and extensive reorganization of subdomains. This process involved additional manual inductive coding of 100 example messages for refinement before the taxonomy was finalized.

4.2. *Baseline: LLM Guardrail (No Retrieval)*

We implemented a two-stage LLM-based guardrail system using Declarative Self-improving Python (DSPY),[23] a modular orchestration framework for prompt-driven pipelines. In the baseline configuration, the model receives the patient message, the corresponding LLM-generated draft response, and structured EHR metadata available at the time of response drafting (e.g., patient name, department, last note, thread history, etc), with no additional retrieved context provided.

In the first stage, the LLM functions as an error identifier. It determines whether any error is present in the draft response and if so, produces a short summary, along with a free-text explanation of its reasoning. If an error is identified, the system proceeds to the second stage, where the model

classifies the error using a structured taxonomy. Specifically, the LLM is provided with the full set of domain, subdomain, and error code definitions, and it returns a structured JSON output that includes the selected error code(s), associated confidence scores, and justification.

4.3. *Enhanced: Retrieval-Augmented Error Checking Guardrail (RAEC)*

In the enhanced configuration of our evaluation pipeline, we activate a retrieval-augmented mode, referred to as RAEC (Retrieval-Augmented Error Checking). In this setting, the LLM receives not only the patient message, draft response, and structured metadata, but also a curated set of up to five similar message–response pairs drawn from the historical archive of clinician-authored replies (see§ 4.3.1. to 4.3.3.). These retrieved examples serve as contextual reference points to inform the LLM's assessment of whether the current draft aligns with how similar cases were handled by real clinicians in the past. Importantly, the model is not prompted to quote, imitate, or directly compared to these examples; instead, they are offered purely to ground the model's clinical reasoning in precedent.

The remainder of the pipeline remains identical to the baseline setup. The LLM still performs a two-stage evaluation: first, detecting the presence of errors, then assigning structured error codes based on the established taxonomy. By keeping the task structure fixed and only varying the availability of reference examples, we are able to isolate the impact of contextual grounding on the model's ability to identify safety-relevant flaws in its own output.

4.3.1. *Message-Response Embeddings*

To support the retrieval-augmented error checking, we embedded all 220,739 messages from 146,681 patient–clinician threads using the all-mpnet-base-v2 model from SentenceTransformers.[24] These 768-dimensional vectors were stored alongside structured metadata such as recipient name, department, and specialty, for filtering purposes, enabling scalable and low-latency retrieval.

4.3.2. *Message-Response Retrieval*

To ensure relevance, the retrieval process filters candidates by matching physician, department, and specialty metadata, and then ranks them based on cosine similarity between the query patient message and the archived patient messages, using sentence embeddings derived from the all-mpnet-base-v2 model in the SentenceTransformers library.[24-25] Once a top match is selected, its corresponding clinician response is retrieved as part of the reference pair. Only the top five message–response pairs are presented to the LLM, formatted as background context.

4.3.3. *Message-Response Retrieval Evaluation*

To evaluate this retrieval mechanism, a board-certified physician reviewed a random sample of 56 queries and their associated retrieved sets. For each query, the reviewer assigned a binary usefulness score to each set of the five retrieved examples and provided an ordinal re-ranking of their relative clinical helpfulness. Retrieval quality was quantified via two metrics: Mean Usefulness (average fraction of retrieved messages marked helpful per query) and Kendall's τ (correlation between similarity-based and physician rankings).

4.4. *Physician Validation of Assigned Error Labels*

To rigorously assess the accuracy of the LLM-generated error labels, and assess the value of the retrieval augmentation process, we conducted a validation study using a subset of 100 messages from the evaluation cohort. Each patient message and corresponding LLM draft along with EHR context was reviewed by a board-certified physician. Using the final error taxonomy, they identified and labeled all applicable errors. These physician annotations were then treated as the reference standard against which both the baseline and retrieval-augmented guardrail outputs were evaluated.

For our primary outcome, we define message-level concordance as the absolute agreement between the LLM-based annotations (Baseline and Enhanced) with the Physician annotations at the various hierarchical levels of the taxonomy (domain, subdomain, or error code). More precisely, let $V(x)$ be the set of labels assigned to index x by a source at a given level (e.g., domains assigned to index x). Then for each index and hierarchical level, concordance is defined as:

- *Concordant* = 1, if $V_{physician}(x) == V_{llm}(x)$
- *Concordant* = 0, otherwise

We computed counts and percentages of concordant cases for both Baseline and Enhanced guardrails and performed a statistical comparison of the two using McNemar's test.

We then computed standard performance metrics for all individual labels at all three hierarchical levels including sensitivity (recall), specificity, positive predictive value (precision), negative predictive value, and F1-score (harmonic mean of precision and recall). The denominator for true negatives included all index-label combinations including those not labeled by any source.

5. Results

5.1. *Inductive Coding and Error Taxonomy*

The tree diagram in Figure 1 traces the trajectory of the taxonomy across three phases. The physician seeded draft began with 6 domains, 27 subdomains, and 37 error codes. While the o3mini inductive loop annotated the stratified 1 000 message samples, it proposed 13 additional codes. After human review (see § 4.1), our final taxonomy resulted in 5 domains, 24 subdomains, and 59 error codes.

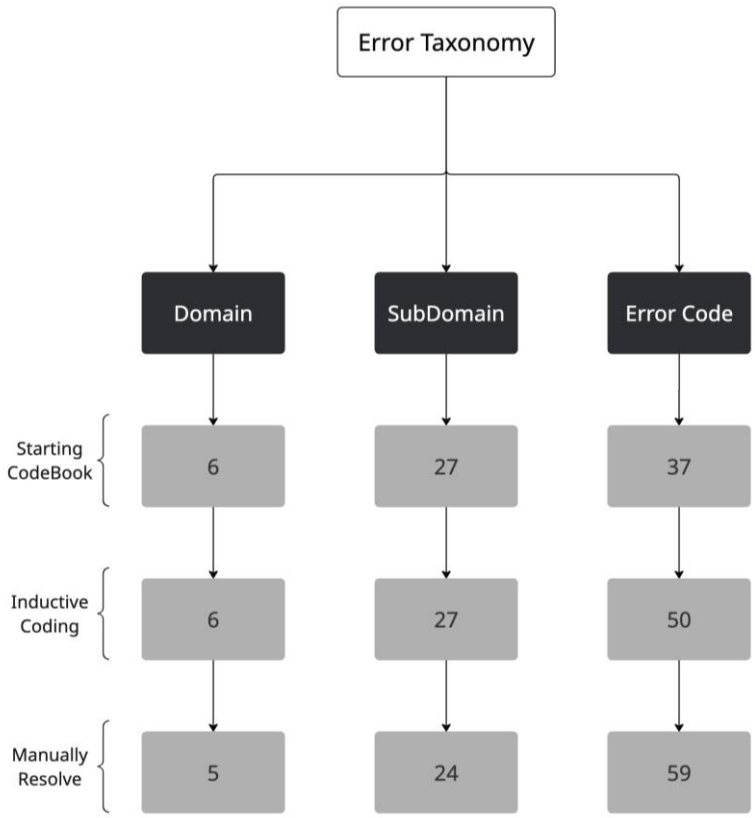

Figure 1: Schematic of error taxonomy development and refinement.

5.2. *Reference Retrieval Performance*

A board-certified physician adjudicated a random sample of 56 queries (280 retrieved message–response pairs). On average, 85.7 % of the queries returned clinically helpful references (Mean Usefulness = 0.86). The average Kendall's τ of 0.77 confirms strong agreement between the similarity-based ranking and the physician's preferred ordering, demonstrating that the retrieval stage both identifies and prioritizes exemplars likely to aid downstream error detection.

5.3. *Physician Validation and Comparison of Baseline vs Enhanced Guardrails*

5.3.1. *Error Counts*

In terms of basic summary counts (Table 1) for the 100 unique message indices evaluated using all three workflows (Baseline, Enhanced, and Physician), we found that Physicians flagged errors in more cases overall compared to the baseline and enhanced LLM judges (57 cases vs. 43 and 36, respectively). At a domain level, physicians tended to flag more errors in clinical reasoning and fewer errors in communication quality and readability. At the level of individual subdomains and error codes, the major changes occurred at the level of workflow recommendations (large increase in workflow violations) and communication clarity (large decrease in messages flagged as ambiguous or conflicting instructions). The other three error domains occurred infrequently, but physicians generally flagged fewer errors in those areas as well.

Table 1: Comparison of error counts identified by Physicians vs Baseline and Enhanced guardrails.

Category	Baseline	Enhanced	Physician
Cases with ≥1 error	43	36	57
Error rate (%)	43.0%	36.0%	57.0%
Domain-level error counts			
Accessibility	1	0	1
Bias & Stigmatization	5	4	2
Clinical Reasoning	43	36	54
Communication Quality & Readability	37	32	16
Privacy & Security	4	7	0

5.3.2. *Message-Level Concordance*

The Enhanced guardrails were more frequently concordant with the Physician labels than the Baseline guardrails at the level of domains, subdomains, and error codes (Table 2).

Table 2: Comparison of Physician concordance rates between Baseline and Enhanced guardrails. Statistical significance was calculated using McNemar's test.

Level	Baseline Concordance	Enhanced Concordance	P-value
Domains	45 (45.0%)	56 (56.0%)	0.0371
Subdomains	35 (35.0%)	50 (50.0%)	0.0007
Error Codes	33 (33.0%)	50 (50.0%)	0.0002

We also perform subgroup analysis for individual domains, subdomains, and error codes (data not shown), with generally improved concordance for the Enhanced guardrails compared to the Baseline guardrails.

5.3.3. *Error-Level Performance*

Table 3: Performance metrics for Baseline and Enhanced guardrails at identification of the correct domains, subdomains, and error codes

	Domain Level		Subdomain Level		Error Code Level	
	Baseline	**Enhanced**	**Baseline**	**Enhanced**	**Baseline**	**Enhanced**
TP	42	47	36	55	30	59
FP	48	32	86	58	102	75
FN	31	26	58	39	72	43
TN	379	395	1420	1448	3496	3423
Sensitivity	0.575	0.644	0.383	0.585	0.294	0.578
Specificity	0.888	0.925	0.943	0.961	0.972	0.979
PPV	0.467	0.595	0.295	0.487	0.227	0.44
NPV	0.924	0.938	0.961	0.974	0.98	0.988
Accuracy	0.842	0.884	0.91	0.939	0.953	0.967
F1	0.515	0.618	0.333	0.531	0.256	0.500

Next, we measured the overall performance of our guardrails at identifying the correct domains, subdomains, and error codes (Table 3). In comparison to the Baseline guardrails where both precision (PPV) and recall (Sensitivity) drop significantly (0.467 to 0.227 and 0.575 to 0.294, respectively) as the granularity increases from domain to error code, the Enhanced guardrails maintain much better performance (0.595 to 0.44 and 0.644 to 0.578, respectively). This is also reflected in the gap between their F1 scores as granularity increases (0.618 vs 0.515 at the domain level, increasing to 0.500 vs. 0.256 at the error code level).

5.3.4. *Impact of Enhanced Guardrails compared to Baseline*

We then compared error identification between baseline and retrieval-enhanced guardrail configurations across the full 1570 message cases to better determine the potential impact on downstream clinical workflows between the two models if they were to be deployed into production.

The baseline model identified 350 cases with at least one associated error, whereas the enhanced retrieval-augmented guardrail reduced this count to 307, reflecting our prior observations about increased specificity. This was also reflected at the level of individual errors, where the baseline model flagged a total of 1,170 errors, while the retrieval-augmented guardrail identified 1,025.

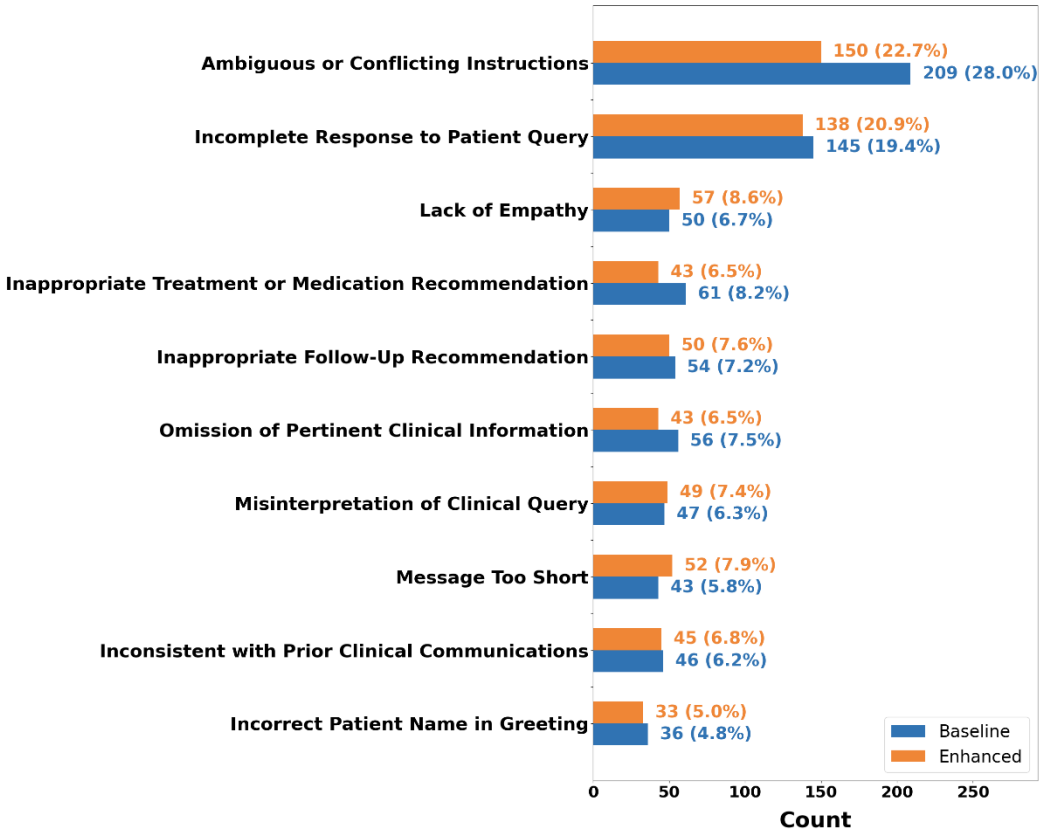

Figure 2: Relative frequencies of the top 10 most common error codes in baseline and enhanced models

When comparing error distributions (Figure 2), the Enhanced guardrail dramatically decreases the number of messages flagged as *Ambiguous or Conflicting Instructions* (28% to 22.7%). Out of the other 10 most common error codes, there were small increases in *Lack of Empathy* (6.7% to

8.6%), *Misinterpretation of Clinical Query* (6.3% to 7.4%), and *Message Too Short* (5.8% to 7.9%). The other error codes all showed small decreases, consistent with overall increase in specificity for the Enhanced guardrail.

5.4. *Adapted vs Nonadapted Drafts*

Finally, to further validate our pipeline and demonstrate its utility, we utilize the Enhanced guardrails to analyze differences in the frequency of errors between messages where the drafts were used vs. messages where the drafts were not used for the same overall set of 1570 messages. We identified a decrease in the error rate for utilized drafts (36 errors across 132 messages = 0.27 errors per draft) vs. discarded drafts (989 errors across 1438 messages = 0.69 errors per draft).

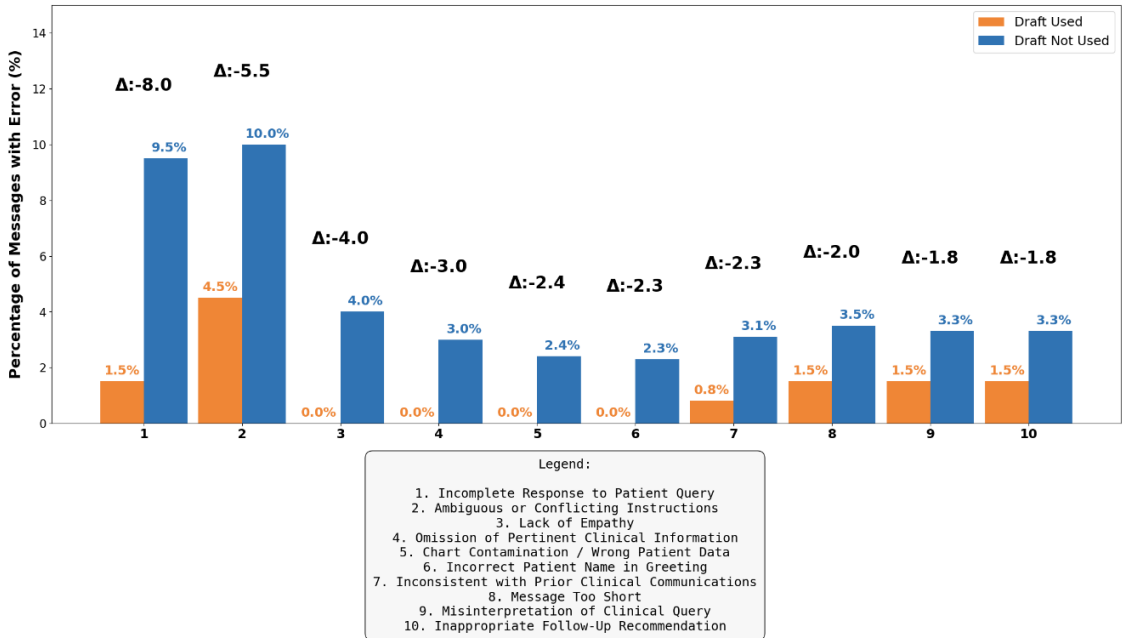

Figure 3: Error codes with the largest absolute drop in frequency for utilized drafts

We also ranked the individual error codes by their absolute change in frequency comparing utilized drafts vs. discarded drafts. The labels with the largest drop in frequency for utilized drafts (Figure 3) included instances where the reply to the patient was clearly incorrect (*Incomplete Response to Patient Query* at -8.0 pp, *Chart Contamination/Wrong Patient Data* at -2.4 pp, *Incorrect Patient Name in Greeting* at -2.3 pp) or lacked empathy (*Lack of Empathy* at -*4.0* pp).

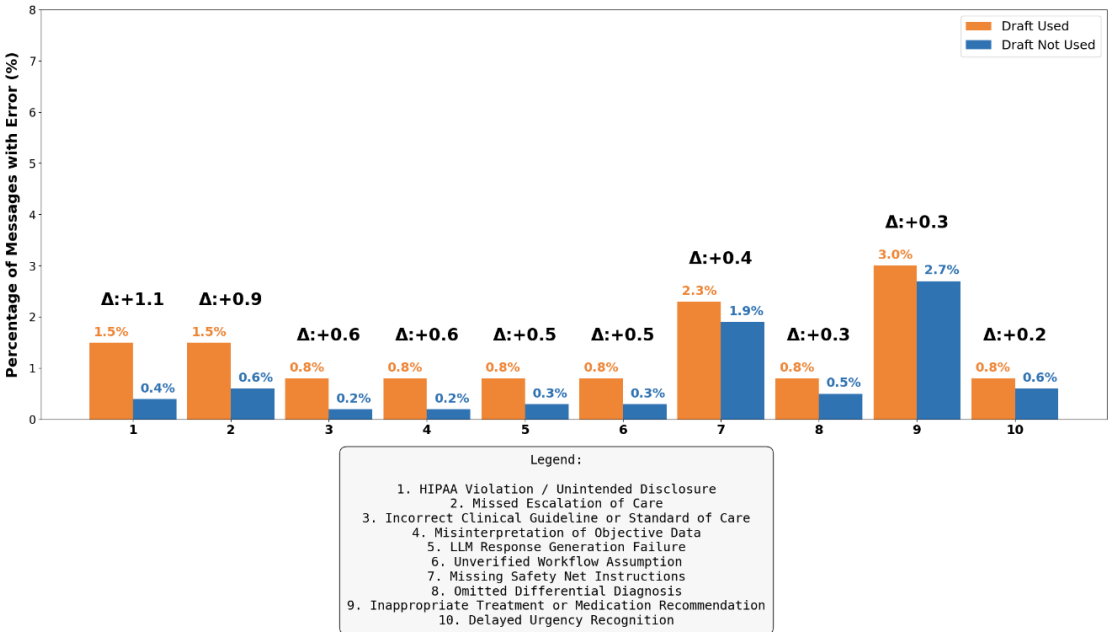

Figure 4: Error codes with the largest absolute increase in frequency for utilized drafts

In contrast, the error codes that were more common when drafts were used (Figure 4) included several subtle clinical errors including errors of omission (*Missed Escalation of Care* at +1.1 pp, *Incorrect Clinical Guideline or Standard of Care* at +0.9 pp, *Missed Safety Net Instructions* at +0.4 pp, *Omitted Differential Diagnosis* at +0.3).

6. Discussion

This study introduced and rigorously evaluated our Retrieval Augmented Error Checking (RAEC) pipeline, a modular framework for the evaluation of clinician replies to patient messages that synthesizes three separate innovations: 1) a comprehensive error taxonomy, 2) local context retrieval, and 3) an agentic two-stage LLM pipeline using DSPy to deliver real-time quality assurance for AI generated patient messages.

The lack of a comprehensive error taxonomy constitutes a major gap in the field for the evaluation of AI-generated draft replies, which currently relies on superficial metrics such as edit distances. We utilize machine-assisted inductive coding in conjunction with manual refinement to create an empirically grounded clinician validated taxonomy, allowing us to distinguish between superficial communication lapses vs. deeper clinical inaccuracies. Embedding this taxonomy within RAEC enabled nuanced, structured error detection with clear clinical interpretability.

We found that augmentation through local context retrieval was critically important for the performance of our LLM guardrails, with the Enhanced guardrail achieving much higher message-level concordance with Physician labels compared to the Baseline guardrail as well as much better performance for individual error detection across all traditional metrics. This improvement was most evident when identifying individual error codes but was present even when evaluating performance with less granularity at the level of general error domains. Importantly, we identified simultaneous improvements in both precision and recall meaning that in clinical practice, the Enhanced guardrail

would simultaneously identify more errors (potentially preventing more harm to patients) while also decreasing the burden on clinicians (who will need to perform follow-up review of false positives). Subgroup analysis at the level of individual errors revealed that the use of Enhanced guardrails markedly reduced the total number of flagged messages and errors, with a major reduction in errors flagged as *Ambiguous or Conflicting Instructions*, which was noted to be an important source of false positives (see § 5.3.1.). The use of retrieved context also resulted in slight increases in error counts for *Lack of Empathy*, and *Message Too Short*, which may reflect differences in clinician writing style in the retrieved context and has been identified as a major barrier to utilization of AI-generated draft replies.[26]

Despite this improvement in performance, we identified several opportunities for improvement based on the major shifts in error counts between the Enhanced guardrail labels and the Physician labels. Workflow violations were a notable blind spot for LLMs, which makes sense given that many of these workflows consist of tribal knowledge that are sometimes not even documented internally. While examples of these workflows were sometimes apparent in the retrieved reference pairs, they were not always detected by the Enhanced guardrails. On the other end of the spectrum, the LLMs frequently flagged messages as ambiguous or conflicting that were actually straightforward, which will likely require adjustments to the taxonomy definitions to adjust the threshold for meeting this error definition. In general, physicians more frequently flagged issues in clinical reasoning and less frequently identified problems related to communication quality and readability. This suggests that human reviewers may be more attuned to clinical nuances and interpretive gaps, while LLM-based systems may be better at identifying stylistic differences.

Finally, we further validated the performance of our pipeline and demonstrated additional utility by applying our Enhanced guardrails towards the analysis of clinician behavior through the comparison of error rates stratified by draft utilization. Our priori expectations were that better drafts would be more likely to be used by our clinicians and that obvious surface flaws would deter adoption whereas more subtle clinical reasoning errors might slip through. Our results confirmed our intuition, with a much lower overall error rate for utilized drafts (60% relative reduction from 0.69 errors/draft to 0.27 errors/draft), passing an essential sanity check for our pipeline. Moreover, we also identified relatively more errors related to subtle clinical reasoning when drafts were used, including missed escalations of care, safety net instructions, and considering a broader differential. These errors of omission are notoriously challenging to address as they require busy clinicians to go beyond directly replying to the patient message and spontaneously apply other frameworks/checklists.

7. Future Work

Despite these encouraging findings, the present work has important limitations that suggest clear avenues for refinement. First, the inductive coding phase drew on a corpus of only 1,000 message threads. Although this sample was adequate to capture the dominant error modes, it left several infrequent—but clinically meaningful—codes with sparse or no few shot exemplars. Enlarging the annotated corpus and engaging professional ontology engineers will be essential to expanding coverage of the “long tail” of rare errors. Second, our retrieval module relies on cosine similarity over allmpnetbasev2 sentence embeddings—a practical but generic choice. While this straightforward approach performed remarkably well at identifying and ranking relevant context as adjudicated by an independent physician, future iterations should explore domain adapted

encoders, hybrid lexical–semantic rankers, or clinically informed rescoring schemes to surface even more contextually relevant exemplars. Third, we currently embed each patient message as a single text block for the purposes of retrieval. This strategy can obscure multiple clinical concerns that are often packed into a single thread. Tokenizing messages into topic coherent spans and retrieving context at sub-message granularity may further improve the guardrail's sensitivity to nuanced errors arising in complex, multi-issue communications. Fourth, our current validation relies on a single physician; future work will involve recruiting additional physicians as well as other stakeholders and systematically assessing inter-rater agreement. Finally, our current pipeline is intended for human review but the final goal will be to integrate AI guardrails into our live clinical setting where they can catch errors in AI-generated draft messages and provide closed loop feedback directly to the draft generation LLM, which will require additional optimization

8. Conclusion

Collectively, these findings establish RAEC as a robust, scalable solution for mitigating clinical risk in AI assisted messaging. By uniting a structured error taxonomy, local context retrieval, and modular LLM agents, the framework systematically produces contextually grounded judgments aligned with clinician expertise that elevates clinically salient errors while reducing noise—ultimately enhancing patient safety while alleviating the growing burden of asynchronous communication.

Reference

1. U.S. Department of Health and Human Services. (2003). Security Standards for the Protection of Electronic Protected Health Information: Final rule. 45 CFR Parts 160 and 164. Federal Register, 68(34), 8334–8381.

2. Centers for Medicare & Medicaid Services. (2014). Clinical Laboratory Improvement Amendments (CLIA) of 1988: Laboratory Requirements—Direct Patient Access to Laboratory Test Reports; Final rule. 42 CFR Part 493. Federal Register, 79(45), 7289–7316.

3. U.S. Department of Health and Human Services, Office for Civil Rights. (2013). Modifications to the HIPAA Privacy, Security, Enforcement, and Breach Notification Rules under the Health Information Technology for Economic and Clinical Health Act and the Genetic Information Nondiscrimination Act; Other Modifications to the HIPAA Rules; Final rule. Federal Register, 78(17), 5566–5702.

4. Serrato, C. A., Retecki, S., & Schmidt, D. E. (2007). MyChart—a new mode of care delivery: 2005 personal health link research report. The Permanente Journal, 11(2), 14.

5. Martinez KA, Schulte R, Rothberg MB, Tang MC, Pfoh ER. Patient Portal Message Volume and Time Spent on the EHR: an Observational Study of Primary Care Clinicians. J Gen Intern Med. 2024;39(4):566-572. doi:10.1007/s11606-023-08577-7

6. Rotenstein LS, Melnick ER, Jeffery M, et al. Association of Primary Care Physicians' Electronic Inbox Activity Patterns with Patients' Likelihood to Recommend the Physician. J Gen Intern Med. 2024;39(1):150-152. doi:10.1007/s11606-023-08417-8

7. Carini E, Villani L, Pezzullo AM, et al. The Impact of Digital Patient Portals on Health Outcomes, System Efficiency, and Patient Attitudes: Updated Systematic Literature Review. J Med Internet Res. 2021;23(9):e26189. doi:10.2196/26189

8. Chavez A, Bracamonte J, Kresin M, Yardley M, Grover M. High Volume Portal Usage Impacts Practice Resources. J Am Board Fam Med. 2020;33(3):452-455. doi:10.3122/jabfm.2020.03.190401

9. Manakul P, Liusie A, Gales MJF. SelfCheckGPT: Zero-Resource Black-Box Hallucination Detection for Generative Large Language Models. Published online October 11, 2023. doi:10.48550/arXiv.2303.08896

10. Chen S, Guevara M, Moningi S, et al. The effect of using a large language model to respond to patient messages. The Lancet Digital Health. 2024;6(6):e379-e381. doi:10.1016/S2589-7500(24)00060-8

11. Biro JM, Handley JL, Malcolm McCurry J, et al. Opportunities and risks of artificial intelligence in patient portal messaging in primary care. npj Digit Med. 2025;8(1):222. doi:10.1038/s41746-025-01586-2

12. Adler-Milstein J, Redelmeier DA, Wachter RM. The Limits of Clinician Vigilance as an AI Safety Bulwark. JAMA. 2024;331(14):1173-1174. doi:10.1001/jama.2024.3620

13. Inan H, Upasani K, Chi J, et al. Llama Guard: LLM-based Input-Output Safeguard for Human-AI Conversations. Published online December 7, 2023. doi:10.48550/arXiv.2312.06674

14. Abbasian M, Khatibi E, Azimi I, et al. Foundation metrics for evaluating effectiveness of healthcare conversations powered by generative AI. NPJ Digit Med. 2024;7(1):82. doi:10.1038/s41746-024-01074-z

15. Shool S, Adimi S, Saboori Amleshi R, Bitaraf E, Golpira R, Tara M. A systematic review of large language model (LLM) evaluations in clinical medicine. BMC Med Inform Decis Mak. 2025;25(1):117. doi:10.1186/s12911-025-02954-4

16. Lopez I, Swaminathan A, Vedula K, et al. Clinical entity augmented retrieval for clinical information extraction. npj Digit Med. 2025;8(1):45. doi:10.1038/s41746-024-01377-1

17. Zhou Q, Liu C, Duan Y, et al. GastroBot: a Chinese gastrointestinal disease chatbot based on the retrieval-augmented generation. Front Med (Lausanne). 2024;11:1392555. doi:10.3389/fmed.2024.1392555

18. Eskenazi J, Krishnan V, Konarzewski M, Constantinescu D, Lobaton G, Dodds SD. Evaluating retrieval augmented generation and ChatGPT's accuracy on orthopaedic examination assessment questions. Ann Jt. 2025;10:12. doi:10.21037/aoj-24-49

19. Malik S, Frey LJ, Gutman J, Mushtaq A, Warraich F, Qureshi K. Evaluating Artificial Intelligence-Driven Responses to Acute Liver Failure Queries: A Comparative Analysis Across Accuracy, Clarity, and Relevance. Am J Gastroenterol. Published online December 17, 2024. doi:10.14309/ajg.0000000000003255

20. Woo JJ, Yang AJ, Olsen RJ, et al. Custom Large Language Models Improve Accuracy: Comparing Retrieval Augmented Generation and Artificial Intelligence Agents to Noncustom Models for Evidence-Based Medicine. Arthroscopy. 2025;41(3):565-573.e6. doi:10.1016/j.arthro.2024.10.042

21. Sandhu A, Kim EJ, Urueta Portillo D, Powers B, Rodriguez R. Open-source modular AI coupled with agentic AI for comprehensive breast cancer note generation and guideline-directed treatment comparison. JCO. 2025;43(16_suppl). doi:10.1200/JCO.2025.43.16_suppl.e13685

22. Bedi S, Liu Y, Orr-Ewing L, et al. Testing and Evaluation of Health Care Applications of Large Language Models: A Systematic Review. JAMA. 2025;333(4):319-328. doi:10.1001/jama.2024.21700

23. Khattab O, Singhvi A, Maheshwari P, et al. DSPy: Compiling Declarative Language Model Calls into Self-Improving Pipelines. Published online October 5, 2023. doi:10.48550/arXiv.2310.03714

24. Song K, Tan X, Qin T, Lu J, Liu TY. MPNet: Masked and Permuted Pre-training for Language Understanding. Published online November 2, 2020. doi:10.48550/arXiv.2004.09297

25. Reimers N, Gurevych I. Sentence-BERT: Sentence Embeddings using Siamese BERT-Networks. Published online August 27, 2019. doi:10.48550/arXiv.1908.10084

26. Garcia P, Ma SP, Shah S, et al. Artificial Intelligence-Generated Draft Replies to Patient Inbox Messages. JAMA Netw Open. 2024;7(3):e243201. doi:10.1001/jamanetworkopen.2024.3201

Leveraging Large Language Models for Adverse Drug Event Detection: A Comparative Study of Token and Span-Based Named Entity Recognition

Howard Prioleau†, Saurav K. Aryal, and Jeremy Blackstone
EECS, Artificial Intelligence for Positive Change (AI4PC) Lab, Howard University, Washington, DC 20059, USA
†*E-mail: howard.prioleau@bison.howard.edu*
https://ai4pc.howard.edu/

Adverse Drug Events (ADEs) pose a persistent threat to patient safety and public health. This study investigates the use of large language models (LLMs) fine-tuned for both token classification and span-based named entity recognition (NER) to improve ADE detection in clinical text. Using the 2018 n2c2 Track 2 dataset, we evaluate models under both predefined (gold label) and end-to-end settings. RoBERTa Large consistently outperforms other models, particularly in identifying ADEs, which remain more challenging due to their contextual ambiguity. Token-based models generally deliver stronger performance than span-based approaches, and ensemble methods, especially majority voting and XGBoost-based aggregation, further enhance end-to-end relation extraction by mitigating individual model weaknesses. These findings highlight the potential of fine-tuned LLMs, augmented by strategic ensembling, to advance clinical NLP pipelines and support safer, more personalized healthcare.

Keywords: Artificial intelligence, Large language models, Clinical Notes, Adverse Drug Events, n2c2

1. Introduction

Adverse Drug Events (ADEs), defined as "harm caused by the use of a drug",[1] continue to pose a critical threat to patient safety and the healthcare system at large. In 2023, the FDA's Adverse Event Reporting System (FAERS) documented over 2.15 million ADE cases, including nearly 163,000 associated deaths. The economic impact is equally stark, with estimated costs reaching up to $30 billion annually in the United States alone.[2] These figures have doubled over the past decade and are expected to rise, highlighting the urgent need for more effective detection methods. Beyond the financial and human costs, ADEs erode public trust in medical institutions, potentially deterring individuals from adhering to treatments or seeking timely care.[3,4]

While pre-market clinical trials aim to identify potential drug risks, many ADEs surface only after widespread public use, particularly in vulnerable groups such as the elderly.[3] Factors like genetic variability, comorbidities, and even psychosomatic effects like the nocebo phenomenon contribute to the complexity of ADE identification.[5] Developing systems that

© 2025 The Authors. Open Access chapter published by World Scientific Publishing Company and distributed under the terms of the Creative Commons Attribution Non-Commercial (CC BY-NC) 4.0 License.

can detect ADEs at the individual level is therefore essential, but the fragmented and unstructured nature of clinical documentation challenges such efforts.

This research focuses on improving adverse drug event (ADE) detection using large language models (LLMs) fine-tuned for token classification and span-based named entity recognition (NER). The goal is to accurately identify Drug and ADE mentions in clinical text, and then perform relationship extraction (RE) to determine which drugs are associated with which ADEs. Token classification enables efficient sequence labeling, while span-based methods are better suited for handling overlapping or discontinuous entities common in medical narratives. This dual modeling strategy addresses challenges posed by variable document lengths, complex entity structures, and annotation inconsistencies. To further enhance performance and robustness, we explore ensemble methods that combine diverse model predictions, revealing that aggregating complementary strengths yields more reliable end-to-end relation extraction. Using the n2c2 dataset as a benchmark, our findings demonstrate the potential of LLMs, especially when combined through ensemble strategies, to refine ADE detection and support safer, more personalized clinical decision-making.

2. Relevant Works

This section explores key developments in ADE detection and medical Natural Language Processing (NLP), focusing on Token and sequence classification techniques and relation extraction.

2.1. *ADE Detection Task*

Early research in ADE detection began with the development of the ADE Corpus,[6] which comprises 2,972 curated medical documents containing manual annotations for drugs, adverse effects, dosages, and their interrelations. This corpus resulted in a total of 20,967 sentences, with 4,272 labeled as Positive for containing at least one mention of a drug-related adverse effect, and the remaining 16,695 labeled as Negative, indicating the absence of such mentions. Building upon this foundation, the TAC 2017 shared task[7] introduced an initiative focused on extracting adverse reactions from structured drug labels and mapping them to standardized MedDRA terms. However, the XML format used in this task imposed a rigid document structure, which limited the retention of nuanced contextual information found in natural clinical narratives. This constraint reduced the effectiveness of relation extraction by stripping away the free-form, real-world textual cues essential for accurately identifying ADEs.

To overcome these limitations, the 2018 National NLP Clinical Challenges Track 2 (n2c2) task[8] offered a more comprehensive and clinically realistic dataset. As the primary data source for this study, the n2c2 dataset significantly broadened the annotation schema to include not only drugs and ADEs but also associated attributes such as strength, form, dosage, frequency, route, duration, and reason. Moreover, it required the identification of relationships among these entities, enhancing the potential for more precise drug-event linkage. Importantly, the data preserved the original structure of electronic health records (EHRs), maintaining the contextual richness and linguistic complexity inherent to clinical documentation. This design makes the n2c2 dataset particularly well-suited for advancing ADE detection models in real-

world healthcare settings.

2.2. *Named Entity Recognition*

NER is a fundamental component of NLP, playing a crucial role in the transformation of unstructured text into structured information. In the medical domain, NER is particularly valuable for identifying key clinical entities such as diseases, medications, procedures, and other relevant concepts. Large language model (LLM) generation-based methods have also been explored for NER,[9,10] but these approaches introduce their own challenges, such as instability and difficulty in evaluation. In this work, we focus on the two more established approaches to NER: token classification and span classification, each offering distinct advantages depending on the complexity and structure of the entities being extracted.

2.2.1. *Token Classification*

Prior to the widespread adoption of large language models (LLMs), state-of-the-art token classification for ADE detection relied heavily on Bidirectional Long Short-Term Memory networks (BiLSTMs). One notable example is the work by,[11] which proposed a cascaded architecture consisting of three sequential stages, each employing BiLSTM-CRF models trained on distinct, non-overlapping entity types. These models incorporated a combination of character-level representations (via CNN or LSTM), word embeddings, and handcrafted linguistic features. An ensemble layer in the final stage aggregated predictions from the earlier stages, resulting in an overall F1 score of 92.87% and an ADE-specific F1 of 38.75%. The shift from BiLSTM-based architectures to LLMs, particularly those with domain-specific pretraining, has significantly enhanced token classification performance, especially for complex and context-dependent entities like ADEs.

A leading example of this evolution is the MC-DRE model,[12] which achieves state-of-the-art performance on the n2c2 dataset. MC-DRE leverages PubMedBERT, a domain-adapted LLM, within a multi-aspect cross-integration framework. This architecture integrates semantic, syntactic, and domain-specific representations using a combination of key-value attention mechanisms, feedforward networks, and cross-learning strategies. The model is further strengthened by auxiliary tasks, such as part-of-speech tagging and general medical NER, along with the use of BIOHD tagging to effectively capture discontinuous entities. As a result, MC-DRE achieves an impressive 98.38% overall F1 and a 61.59% F1 specifically for ADE detection.

2.2.2. *Span Classification*

Span-based classification has gained traction as a powerful alternative to token-level approaches for NER and RE, particularly in addressing overlapping, nested, or discontinuous entities. Unlike traditional sequence tagging, span classification directly predicts entity spans and their corresponding types, allowing for greater flexibility and improved handling of complex clinical text. One prominent model in this area is SpanBERT,[13] which introduced span-level pretraining objectives designed to enhance span representations. Rather than masking indi-

vidual tokens, SpanBERT masks contiguous spans of text and incorporates a span-boundary objective that trains the model to predict the full content of a masked span based solely on its boundary tokens. This approach allows the model to better capture dependencies within and between spans, resulting in notable improvements on span-centric tasks such as question answering and coreference resolution.

Building on this foundation, Packed Levitated Marker (PL-Marker)[14] improves span and span-pair modeling with a marker-based representation method. Instead of processing each span pair separately, PL-Marker groups together spans that share similar boundaries, allowing the model to encode them jointly and improve both boundary precision and contextual understanding. For span-pair classification tasks such as RE, it applies a subject-oriented packing strategy that links one subject span with multiple related object spans. The approach uses levitated markers, which preserve the original token positions while enabling span-specific attention, making it possible to encode many span candidates in parallel. Experiments show that this design yields up to a 4.3% strict F1 improvement over prior state-of-the-art RE models on ACE04 and ACE05 datasets, and also outperforms strong baselines on multiple NER benchmarks.

2.3. *Relation Extraction*

Relation extraction is often simpler than NER when working with gold entities, as it typically involves determining if a specific relationship exists between given entity pairs, formatted as binary questions or multi-output options. Techniques for RE leverage this reduced complexity to achieve high performance.[15] implemented two random forest classifiers first to detect the existence of relations and then classify their types, achieving a 95% F1 and[11] used SVM classifiers with n-grams, token-level distance, and semantic types as features, considering all drug-entity pairs within one sentence as candidates which achieved a 94% F1. These tasks can also be performed jointly using models like BiLSTM-CRFs, which combine bidirectional long short-term memory networks (BiLSTMs) with conditional random fields (CRFs) to simultaneously handle NER and RE.

3. Methodology

3.1. *Dataset*

This study uses the n2c2 dataset,[8] consisting of 505 discharge summaries from the Medical Information Mart for Intensive Care III (MIMIC-III) database. These medical documents were annotated by seven domain experts, including four physician assistant students and three nurses, for entities such as drugs, adverse drug events (ADEs), strength, form, dosage, frequency, route, duration, and reasons using specific entity tags and attributes.

3.2. *Pre-processing*

Due to the highly structured nature of medical notes, pre-processing was essential to make the text more conducive to entity extraction. Due to the considerable length of the medical notes, we first split each note into sentences using the NLTK project's punkt sentence splitter.[16] This

pre-processing step was necessary because the models struggled to classify tokens effectively when handling very long sequences. We then mapped every token of the sentences to its own entity classification where "ADE" and "Drug" were preserved, while all other entities were consolidated under a generic 'other' label, simplifying the focus on the primary entities of interest.

Our dataset consists of annotated entities across three categories: 'Other', 'Drug', and 'ADE'. The training set contains 96,350 'Other', 18,039 'Drug', and 1,665 'ADE' entities, while the test set includes 74,765 'Other', 11,905 'Drug', and 1,057 'ADE' entities. This distribution highlights a significant class imbalance, with ADE instances being markedly underrepresented. Such imbalance has been shown to negatively affect model performance in prior work, particularly in the reliable detection of ADEs.

3.3. *Modeling*

Table 1: Release year and parameter size of selected models

Model	Release Year	Parameter Size
Qwen2.5-0.5B[17]	2025	500M
RoBERTa-large[18]	2019	355M
ModernBERT-base[19]	2025	149M
BERT-base-cased[20]	2018	110M

This section covers the modeling approaches for each task: Token Classification, Span Classification, and Relationship Extraction. Across these three tasks, we selected four LLMs with different architectures and release years to capture variation in both model design and historical development. The 4 models are showcased here 1, to see if any patterns emerge from model size to when they were trained. The 4 models were: Qwen2.5-0.5B,[17] Roberta-large,[18] ModernBERT-base,[19] and bert-base-cased.[20]

3.3.1. *Token Classification*

For the Token Classification task, sentences from the annotated dataset were tokenized using the tokenizer corresponding to each model. Specifically, sentences longer than 64 tokens were split into overlapping chunks with a maximum token length of 64 and an overlap of 50%. Overall, this approach improved modeling efficiency and ensured more consistent processing times by reducing variability in sentence length and minimizing the need for padding with zeros.

Each token in these sentences was assigned to one of three predefined classes: ADE, Drug, or Other, as illustrated in Figure 1. We used Hugging Face's Trainer[21] API for training and evaluation. The models were fine-tuned for five epochs with a batch size of 32, a learning rate of 2e-5, and mixed-precision training (bf16) enabled for improved computational performance.

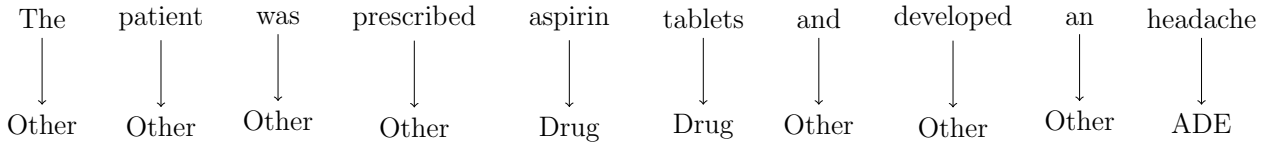

Fig. 1: Token classification for: *"The patient was prescribed aspirin tablets and developed an headache"*. Tokens: **Drug** = "aspirin", "tablets"; **ADE** = "headache"; others = **Other**.

3.3.2. *Span Classification*

For the Span Classification task, we used the Hugging Face implementation of SpanMarker,[22] based on the Packed Levitated Marker (PL-Marker) framework. We initialized the model with bert-base-cased and roberta-large encoders, which were the only ones compatible with SpanMarker due to tokenizer constraints. Attempts to use Qwen2.5-0.5B and ModernBERT-base were unsuccessful, as they do not support the marker-style span encoding required by the architecture. As a result, only encoders with standard Hugging Face tokenizer support were used.

Each candidate span was classified as ADE, Drug, or Other by aggregating token-level predictions into labeled spans, as illustrated in Figure 2. Fine-tuning was performed for five epochs using the Hugging Face Trainer API with a batch size of 32, a learning rate of 5e-5, and mixed-precision training (bf16) to improve efficiency. These settings were kept consistent across encoders to ensure comparability.

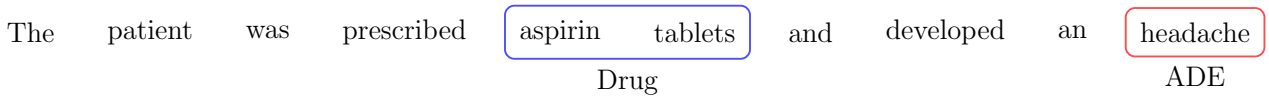

Fig. 2: Span classification for: *"The patient was prescribed aspirin tablets and developed an headache"*. Spans: **Drug** = "aspirin tablets"; **ADE** = "headache".

3.3.3. *Relationship Extraction*

Relationship extraction involves identifying and classifying relationships between drug entities and their corresponding adverse events. The relationship extraction problem was transformed into a binary classification scenario by selecting sentences containing both drug and adverse event mentions, masking these specific entities, and then classifying whether the masked drug-ade pairs were related or unrelated.

This approach was implemented through two distinct experiments: the Golden Labels experiment and the End-to-End experiment. In the Golden Labels experiment, entity spans were predefined (gold standard), and models were tasked with classifying these specified drug-event pairs. In the end-to-end experiment, the models first predicted entities in the test set and then these predicted entities were classified using the models previously trained on gold-standard relation labels.

3.3.4. *Ensembling*

To explore how much additional performance could be gained by leveraging the multiple models we trained, we implemented various token-level ensembling techniques. This effort was motivated by prior work that demonstrated the potential of ensemble approaches in natural language processing tasks,[23] in health-related applications,[24] and more specifically in the ADE extraction domain.[25] We applied voting-based methods, including *majority voting*, where the most frequent label among models was selected, and *minority voting*, which emphasized outlier predictions. Confidence-based techniques were also tested, such as selecting the *most confident prediction* based on the highest individual model probability, and computing the *sum of probabilities* across models to determine the dominant class. Additionally, we trained meta-classifiers including Decision Trees, Random Forests, Support Vector Machines (SVM), LightGBM, XGBoost, Logistic Regression, CatBoost, and Multi-Layer Perceptrons (MLP) on the binary outputs (votes), class probabilities, or a combination of both. This comprehensive framework enabled us to assess the extent to which ensemble methods could enhance token-level ADE classification performance.

3.4. *Evaluation*

Model performance across all tasks was assessed using standard metrics commonly used in NLP research. The evaluation criteria for each task are briefly summarized below.

3.4.1. *Token Classification*

Token classification performance was evaluated at the token level using precision, recall, accuracy, and F1-score metrics.

3.4.2. *Span Classification*

Span classification metrics included precision, recall, and F1-score, which were calculated after mapping span-level predictions back to token-level annotations. A prediction was considered correct only if the predicted span boundaries and associated labels exactly matched the corresponding ground truth tokens for ADE or Drug entities.

3.4.3. *Relationship Extraction*

Relationship extraction was evaluated using precision, recall, and F1-score. Correct predictions required accurately identifying pairs of Drug and ADE entities along with their correct relationship according to the annotated dataset.

In Figure 3, details how performance is evaluated in the End to End setting. Since the evaluation depends on the model's predicted entities and relations, some true Drug ADE pairs cannot be evaluated because the corresponding entities were never identified by the model. In such cases, these missed pairs are counted as false negatives to reflect the model's end to end limitations.

For Token and Span Classification the macro average will be reported due to the imbalanced nature of the dataset we want to treat all classes as equal when it comes to gauge

Actual\Predicted	Related	Not Related
Related	**True Positive (TP)** Drug-ADE pair is related and correctly predicted as related	**False Negative (FN)** Drug-ADE pair is related but predicted as not related (or entity in pair was not predicted)
Not Related	**False Positive (FP)** Drug-ADE pair is not related but predicted as related	**True Negative (TN)** Drug-ADE pair is not related and correctly predicted as not related

Fig. 3: Confusion matrix for Drug–ADE relationship extraction showing classification categories with criteria for Relation

performance.

4. Results

4.1. *Token & Span Classification*

model name	Exp. Type	ADE-f1	ADE-pr	ADE-re	Drug-f1	Drug-pr	Drug-re	macro-f1
ModernBERT	token	0.49258	0.66083	0.39262	0.94026	0.95026	0.93047	0.80990
Roberta large	token	**0.54813**	0.61730	**0.49290**	**0.94612**	0.94549	**0.94676**	**0.83043**
bert_base_cased	token	0.46102	0.56612	0.38884	0.93781	0.93979	0.93584	0.79849
Qwen2.5	token	0.21021	0.48299	0.13434	0.79887	0.85807	0.74731	0.66714
bert_base_cased	span	0.42832	0.56135	0.34626	0.93247	0.94275	0.92241	0.78575
Roberta large	span	0.47740	0.57199	0.40965	0.94052	0.94219	0.93886	0.80488
majority_vote	ensemble	0.50898	0.73656	0.38884	0.94579	0.95860	0.93332	0.81730
minority_vote	ensemble	0.32744	0.32205	0.33302	0.76664	0.81949	0.72019	0.69496
highest_proba_vote	ensemble	0.33554	0.75497	0.21570	0.93311	0.95839	0.90914	0.75509
sum_proba_vote	ensemble	0.42004	0.76500	0.28950	0.94584	0.96084	0.93131	0.78765
meta_vote_XGB	ensemble	0.50234	0.65899	0.40587	0.94013	0.96146	0.91972	0.81312
meta_proba_LGBM	ensemble	0.44869	0.68750	0.33302	0.94599	0.96069	0.93173	0.79724
meta_vote_and_proba_MLP	ensemble	0.37536	**0.77286**	0.24787	0.94166	**0.96616**	0.91837	0.77131

Table 2: Test set performance of token, span, and ensemble models for ADE and Drug classification using per-class and macro-averaged metrics. Only the best macro-F1 per meta-ensemble strategy is shown.

Table 2 presents performance metrics for all evaluated models across token-based, span-based, and ensemble approaches for ADE and Drug entity recognition. Among the individual models, Roberta large (token) achieves the best overall performance, with the highest macro-F1 score and leading F1 for both ADE and Drug classes. It balances precision and recall particularly well, demonstrating strong generalization to both frequent and less frequent entities. In contrast, ModernBERT yields the highest precision for both classes, especially ADE, but this comes at the cost of reduced recall, resulting in a slightly lower macro-F1. BERT base cased, across both token and span variants, maintains consistent performance, though it underperforms relative to Roberta in ADE recognition. Qwen2.5 shows the weakest performance

overall, struggling particularly with ADE recall, which substantially limits its macro-F1 despite acceptable Drug classification. This suggests that while high Drug precision is relatively easy to achieve, due to consistent lexical cues and training frequency. ADE extraction remains a more discriminative benchmark of model capability.

When comparing token-based to span-based approaches, token models generally outperform span models across both entity types, especially in ADE F1 and macro-F1. This is likely due to finer token-level supervision and broader compatibility with standard pre-trained architectures. For example, span-based RoBERTa lags behind its token counterpart in ADE and macro-F1, despite comparable Drug performance. Still, span models remain competitive for Drug entities and may be useful where precise boundary detection is critical. Ensemble methods provide a strong alternative, with strategies such as majority_vote and meta_vote_XGB surpassing most single models in macro-F1 and narrowing the precision–recall gap for ADEs. Notably, some ensembles (e.g., meta_vote_and_proba_MLP) achieve very high precision at the cost of recall, while minority_vote sometimes identifies difficult ADEs missed by the majority, though with low consensus and reliability. These results suggest that model diversity can uncover challenging cases that uniform agreement overlooks, highlighting the importance of complementary perspectives in ensemble design.

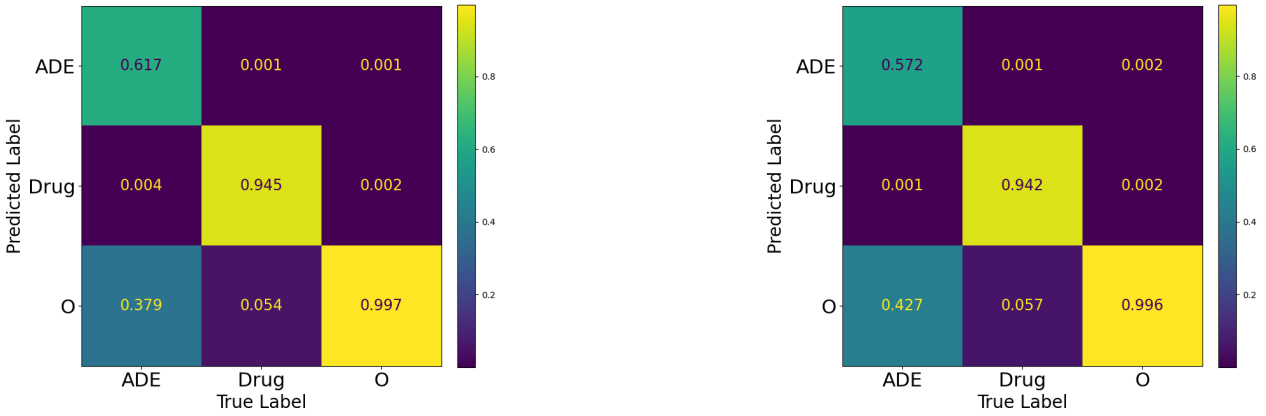

(a) Token Classification Roberta Large

(b) Span Classification Roberta Large

Fig. 4: Confusion matrices for Token Classification models on the test set.

Figures 4a and 4b present a comparison of Roberta large's performance in token-based versus span-based classification, using column-normalized confusion matrices to show per-class precision. In the token classification setting, Roberta large demonstrates strong performance, particularly for the Drug class, with minimal confusion and high precision, while still exhibiting some misclassification of ADE instances as Other. In the span-based setting, this challenge becomes more pronounced: the model's precision for ADE decreases noticeably, with a larger proportion of predictions incorrectly assigned to the Other class, despite maintaining reliable precision for Drug entities. Notably, ADE predictions are rarely confused with Drug, suggesting

that while the model retains a semantic distinction between the two, it is less confident in identifying ADE spans. This performance gap mirrors the quantitative trends observed in Table 2, where the span-based Roberta model underperforms its token counterpart in ADE F1 and macro-F1. These results indicate that token-level classification offers improved precision for rare and syntactically diverse classes like ADE, likely due to denser contextual supervision, whereas span-level approaches may introduce greater uncertainty for minority labels, despite their utility in precise boundary modeling.

4.2. *Relationship Extraction*

There will be 2 sections from the Golden Label RE and End to End RE

4.2.1. *Golden Label*

Model	Accuracy	Macro-pr	Macro-re	Macro-F1
ModernBERT	0.7607	0.7185	0.6750	0.6875
Qwen2.5	0.7451	0.6981	0.7005	0.6992
RoBERTa Large	0.7671	0.7249	0.6930	0.7040
BERT Base Cased	**0.7814**	**0.7405**	**0.7410**	**0.7407**

Table 3: Relation classification performance on the test set using golden labels. Metrics include macro-averaged precision, recall, and F1.

As shown in Table 3, BERT base cased achieves the highest performance across all metrics for relation classification using golden entity labels, outperforming RoBERTa Large, ModernBERT, and Qwen2.5. This result suggests that strong performance in relation extraction does not necessarily correlate with superior entity recognition, as the best-performing model here differs from those leading in token or span classification tasks, highlighting the distinct challenges and model strengths required for each subtask.

4.2.2. *End to End*

Model / Method	Exp. Type	Accuracy	Macro pr	Macro re	Macro F1
ModernBERT	token	0.2470	0.2304	0.2253	0.2277
Roberta large	token	0.2876	0.2715	0.2439	0.2542
Roberta large	span	0.2751	0.2556	0.2413	0.2474
BERT base cased	token	**0.3213**	**0.2766**	**0.2762**	**0.2764**
BERT base cased	span	0.3005	0.2564	0.2718	0.2630
Qwen2.5	token	0.1601	0.1309	0.2119	0.1469
Majority Vote	Ensemble	**0.3262**	**0.2808**	**0.2901**	**0.2850**
XGB Vote	Ensemble	0.3199	0.2750	0.2868	0.2802
MLP Vote and Proba	Ensemble	0.1175	0.0865	0.1339	0.1051

Table 4: End-to-End Relation Classification Metrics on the Test Set

Table 4 presents performance metrics for the classification of end-to-end relationships, where the models must identify both entities and their relationships without access to gold spans. All models show a drop in performance compared to the golden label setting, reflecting the compounded difficulty of the task, since a correct relation prediction requires both the Drug and ADE entities to be correctly identified, and errors in entity detection directly suppress overall performance. Although BERT base cased achieves the strongest individual performance, ensemble methods such as majority vote and XGB voting further improve results across all metrics, highlighting the benefit of leveraging diverse model outputs to mitigate individual weaknesses. These ensembles demonstrate greater stability and robustness, especially in handling harder ADE cases, where entity-level errors otherwise propagate into relation misclassifications. Conversely, weaker ensemble strategies like MLP Vote and Proba show poor generalization, suggesting that not all aggregation methods are equally effective under noisy conditions. In general, these results underscore the critical role of accurate entity recognition in end-to-end settings and the potential of ensemble learning to improve reliability in the extraction of complex biomedical relationships.

5. Discussion

Across all tasks, models consistently struggled more with identifying ADE entities than Drug entities, with ADE recall notably lower despite strong Drug performance. This highlights the linguistic complexity and context dependence of ADE mentions. Model performance did not align with size or recency: for example, Qwen2.5 underperformed while the smaller BERT-base-cased remained competitive, suggesting that architecture and task alignment matter more than scale. RoBERTa Large emerged as the strongest overall model, particularly for ADE detection, likely due to its pretraining strategy with dynamic masking on a diverse corpus.

Token-based models generally outperformed span-based ones for ADEs, while span models remained competitive for Drug recognition where boundary precision is important. Ensemble methods, especially majority voting and XGB-based approaches, improved stability in end-to-end relation extraction by mitigating error propagation from entity recognition. The sharp performance drop in the end-to-end setting underscored the dependence of relation classification on accurate entity detection. Notably, minority-vote ensembles occasionally identified difficult ADE cases missed by the majority, emphasizing the value of model diversity. Overall, these findings show that robust entity recognition, supported by effective ensemble strategies, is key to reliable biomedical NLP systems.

6. Conclusion

This study evaluated the effectiveness of fine-tuned LLMs for ADE detection through entity recognition and relation extraction in clinical text. Using both token and span classification approaches on the n2c2 dataset, we found that models like RoBERTa Large consistently outperformed others, particularly in handling the contextual complexity of ADEs. While Drug entities were identified reliably across models, ADE detection remained more challenging, highlighting the importance of contextual modeling. Notably, our results show that entity

recognition and relation extraction success do not always align across models, underscoring the distinct demands of each task. Ensemble methods, especially majority voting and XGB-based strategies, proved to be effective in boosting end-to-end relation extraction by leveraging complementary model predictions and mitigating individual weaknesses. These findings reinforce the value of ensembling and task-specific modeling in building robust biomedical NLP systems and point toward practical strategies for improving clinical information extraction pipelines.

7. Limitations and Future Work

While RoBERTa Large showed strong performance and the study produced valuable insights, several limitations warrant consideration. Models consistently struggled to identify ADE entities, likely due to class imbalance and their linguistic variability, which was reflected in lower recall scores. In addition, architectural constraints prevented a uniform comparison across models, as some could not be evaluated in both token and span settings. Finally, the Relationship Extraction model could be optimized to leverage the best performer and not the same model making the initial entity predictions.

Future work should prioritize improving ADE recognition through methods that address class imbalance and context sensitivity. Multi-task learning and modular pipeline designs may help reduce the impact of upstream errors by coupling entity and relation prediction. Incorporating external biomedical resources for pretraining could improve model performance. Expanding the usable corpus of ADE datasets that represent real-world data would also be beneficial. In addition, adopting a two-step approach similar to strategies used in multilingual sentiment classification[26] could help cut down on over-prediction by first determining whether a sentence contains an ADE before applying fine-grained extraction.

8. Acknowledgments

This research was supported by the Office of Naval Research, Department of the Navy (FAIN N00014-22-1-2714), the Office of the Director, National Institutes of Health (NIH) Common Fund under award number 1OT2OD032581-01, and the Amazon Research Award. Any opinions, findings, and conclusions or recommendations expressed in this material are those of the authors and do not necessarily reflect the views or official policies of the Office of Naval Research, the U.S. Government, AIM-AHEAD, the National Institutes of Health, or Amazon.

References

1. J. R. Nebeker, P. Barach and M. H. Samore, Clarifying adverse drug events: a clinician's guide to terminology, documentation, and reporting, *Annals of internal medicine* **140**, 795 (2004).
2. J. Sultana, P. Cutroneo and G. Trifirò, Clinical and economic burden of adverse drug reactions, *Journal of Pharmacology and Pharmacotherapeutics* **4**, S73 (2013).
3. K. M. Cresswell, B. Fernando, B. McKinstry and A. Sheikh, Adverse drug events in the elderly, *British medical bulletin* **83**, 259 (2007).
4. D. Balog-Way, D. Evensen, R. Löfstedt and F. Bouder, Effects of public trust on behavioural intentions in the pharmaceutical sector: data from six european countries, *Journal of Risk Research* **24**, 645 (2021).

5. K. Faasse and K. J. Petrie, The nocebo effect: patient expectations and medication side effects, *Postgraduate medical journal* **89**, 540 (2013).
6. H. Gurulingappa, A. M. Rajput, A. Roberts, J. Fluck, M. Hofmann-Apitius and L. Toldo, Development of a benchmark corpus to support the automatic extraction of drug-related adverse effects from medical case reports, *Journal of Biomedical Informatics* **45**, 885 (2012), Text Mining and Natural Language Processing in Pharmacogenomics.
7. K. Roberts, D. Demner-Fushman and J. M. Tonning, Overview of the tac 2017 adverse reaction extraction from drug labels track. (2017).
8. S. Henry, K. Buchan, M. Filannino, A. Stubbs and O. Uzuner, 2018 n2c2 shared task on adverse drug events and medication extraction in electronic health records, *Journal of the American Medical Informatics Association* **27**, 3 (2020).
9. H. Prioleau and S. Aryal, Entity only vs. inline approaches: Evaluating llms for adverse drug event detection in clinical text (student abstract), in *Proceedings of the AAAI Conference on Artificial Intelligence*, (28)2025.
10. H. Prioleau, S. K. Aryal and L. Burge, Evaluating llama-3.1 for adverse drug event entity and relationship extraction across prompting techniques, in *International Conference on Advances in Computing Research*, 2025.
11. H.-J. Dai, C.-H. Su and C.-S. Wu, Adverse drug event and medication extraction in electronic health records via a cascading architecture with different sequence labeling models and word embeddings, *Journal of the American Medical Informatics Association* **27**, 47 (2020).
12. J. Yang, S. C. Han, S. Long, J. Poon and G. Nenadic, Mc-dre: Multi-aspect cross integration for drug event/entity extraction, 4385 (2023).
13. M. Joshi, D. Chen, Y. Liu, D. S. Weld, L. Zettlemoyer and O. Levy, Spanbert: Improving pre-training by representing and predicting spans, *Transactions of the association for computational linguistics* **8**, 64 (2020).
14. D. Ye, Y. Lin, P. Li and M. Sun, Packed levitated marker for entity and relation extraction, *arXiv preprint arXiv:2109.06067* (2021).
15. A. B. Chapman, K. S. Peterson, P. R. Alba, S. L. DuVall and O. V. Patterson, Hybrid system for adverse drug event detection, in *Proceedings of the 1st International Workshop on Medication and Adverse Drug Event Detection*, eds. F. Liu, A. Jagannatha and H. Yu, Proceedings of Machine Learning Research, Vol. 90 (PMLR, 04 May 2018).
16. S. Bird, E. Klein and E. Loper, *Natural language processing with Python: analyzing text with the natural language toolkit* (" O'Reilly Media, Inc.", 2009).
17. Q. Team, Qwen2.5: A party of foundation models (September 2024).
18. Y. Liu, M. Ott, N. Goyal, J. Du, M. Joshi, D. Chen, O. Levy, M. Lewis, L. Zettlemoyer and V. Stoyanov, Roberta: A robustly optimized BERT pretraining approach, *CoRR* **abs/1907.11692** (2019).
19. B. Warner, A. Chaffin, B. Clavié, O. Weller, O. Hallström, S. Taghadouini, A. Gallagher, R. Biswas, F. Ladhak, T. Aarsen, N. Cooper, G. Adams, J. Howard and I. Poli, Smarter, better, faster, longer: A modern bidirectional encoder for fast, memory efficient, and long context finetuning and inference (2024).
20. J. Devlin, M. Chang, K. Lee and K. Toutanova, BERT: pre-training of deep bidirectional transformers for language understanding, *CoRR* **abs/1810.04805** (2018).
21. T. Wolf, L. Debut, V. Sanh, J. Chaumond, C. Delangue, A. Moi, P. Cistac, T. Rault, R. Louf, M. Funtowicz *et al.*, Huggingface's transformers: State-of-the-art natural language processing, *arXiv preprint arXiv:1910.03771* (2019).
22. T. Aarsen, F. M. del Prado Martin, D. V. Suero and H. Oosterhuis, Spanmarker for named entity recognition (2023).
23. S. K. Aryal, H. Prioleau, G. Washington and L. Burge, Evaluating ensembled transformers for

multilingual code-switched sentiment analysis, in *2023 International Conference on Computational Science and Computational Intelligence (CSCI)*, 2023.
24. S. K. Aryal, U. Shah, H. Prioleau and L. Burge, Ensembling and modeling approaches for enhancing alzheimer's disease scoring and severity assessment, in *2023 International Conference on Computational Science and Computational Intelligence (CSCI)*, 2023.
25. S. K. Aryal and H. Prioleau, Ad-hoc ensemble approach for detecting adverse drug events in electronic health records, *Journal of Computing Sciences in Colleges* **40**, 238 (2024).
26. S. Aryal and H. Prioleau, Howard university computer science at semeval-2023 task 12: A 2-step system design for multilingual sentiment classification with language identification, in *Proceedings of the 17th International Workshop on Semantic Evaluation (SemEval-2023)*, 2023.

Towards Automated Analysis of Gaze Behavior from Consumer VR Devices for Neurological Diagnosis

Lio Schmitz[1,†], Markus Plack[1], Berkan Koyak[2], Muhammad Ehsan Ullah[2], Ahmad Aziz[2], Reinhard Klein[1], Zorah Lähner[1], Hannah Dröge[1]

[1] *Visual Computing Group, University of Bonn, Friedrich-Hirzebruch-Allee 8, 53115 Bonn, Germany*
[†] *E-mail: lschmitz@cs.uni-bonn.de*
www.uni-bonn.de

[2] *German Center for Neurodegenerative Diseases (DZNE), Center of Neurology, Department of Parkinson, Sleep and Movement Disorders, University Hospital Bonn, Venusberg-Campus 1, 53127 Bonn, Germany*
www.ukbonn.de

Recent studies have demonstrated that eye tracking is a valuable tool in the detection, classification and staging of neurodegenerative diseases such as Parkinson's Disease (PD). However, traditional methods for capturing gaze data often rely on expensive and non-engaging clinical equipment such as video-oculography, limiting their accessibility and scalability. In this work, we investigate the feasibility of using eye tracking data collected via consumer-grade virtual reality (VR) headsets to support neurological diagnostics in a more accessible and user-friendly manner.

This approach enables large-scale, low-cost, and remote assessments, which are particularly valuable in early detection and monitoring of neurodegenerative conditions. We show that relevant oculomotor features extracted from VR-based eye tracking can be used for predictive assessment. Despite the inherent noise and lower precision of consumer devices, careful preprocessing and robust feature engineering, including deep learning embeddings, mitigate these limitations. Our results demonstrate that both handcrafted and learned features from gaze behavior enable promising levels of classification performance. This research represents an important step towards scalable, automated, and accessible diagnostic tools for neurodegenerative diseases using ubiquitous VR technology.

Keywords: Machine Learning; Eye tracking; Virtual reality; Parkinson's Disease

1. Introduction

Eye tracking data has been shown to be a valuable tool in many medical applications, such as detecting concussions in athletes[1–4] or studying behavior to, *e.g.* , identify ADHD in children.[5–8] Many conditions that affect oculomotor function are marked by eye movement abnormalities such as slowed saccades, fixation instability, square wave jerks, impaired smooth pursuit, gaze-evoked nystagmus, vertical gaze palsy, reduced optokinetic nystagmus (OKN) and

© 2025 The Authors. Open Access chapter published by World Scientific Publishing Company and distributed under the terms of the Creative Commons Attribution Non-Commercial (CC BY-NC) 4.0 License.

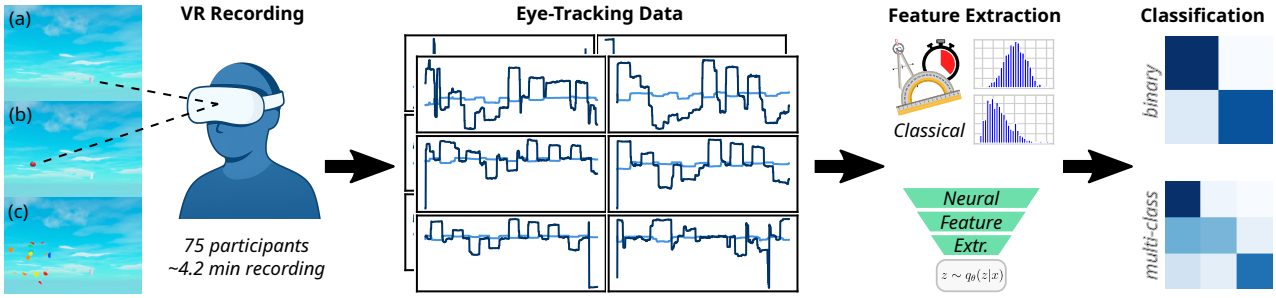

Fig. 1. Overview of our approach. We use raw eye tracking data (center) from a game-like VR experiment (left), where the user gaze starts in a resting position (a) and has to focus on dynamically appearing objects (b). Upon successful fixation, these objects playfully "explode" into confetti, providing immediate visual feedback (c). From multiple repetitions with different target locations we extract various types of features and perform classification (right).

vestibuloocular reflex (VOR) gain as can be observed for Parkinson's disease (PD), atypical Parkinsonian disorders such as multiple system atrophy (MSA), progressive supranuclear palsy (PSP) and corticobasal degeneration (CBD), spinocerebellar ataxias (SCA), Huntington's disease (HD), frontotemporal dementia (FTD), Alzheimer's Disease and schizophrenia.[9,10] Of those, PD features decreased saccade amplitudes, quantified as task-specific hypometria, as a probable reflection of early nigrostriatal degeneration, whilst increased saccadic latency, and antisaccade errors, attributed to the non-dopaminergic degeneration of higher-level eye movement related circuits later in the disease course, thereby linking eye-tracking metrics to cognitive decline.[11–13] Oculomotor signatures – such as asymmetry of corrective saccades and VOR gain measured by video head-impulse tests (vHIT) to distinguish central causes (e.g., posterior circulation strokes or cerebellar ataxia, neuropathy and vestibular areflexia syndrome [CANVAS]) from peripheral vestibulopathies (e.g., vestibular neuritis), as well as slow or absent vertical saccades to differentiate early PSP from PD – highlight the broader diagnostic utility of eye tracking across diverse disorders, without the need for costly diagnostic measures such as alpha – synuclein seed amplification assays or PET-CT scans.[14–17]

At the same time, consumer-grade eye tracking hardware (webcams, phone cameras, VR headsets) has become more accessible and demonstrated potential for unintrusive, remote eye-tracking assessments, thus offering scalable tools to complement traditional methods for early detection and monitoring.[18,19] This enables remote assessment of problems and widely accessible diagnostic tools. However, it remains unclear whether these devices can measure data that is qualitatively sufficient for diagnostics.

In the following, we will focus on eye tracking data obtained from a virtual reality (VR) headset in the prediction of PD. VR headsets have several advantages over traditional camera recordings, *e.g.* eye tracking independent of head movement which allows for more reliable handling of movement artifacts, a built-in calibration for faster setup, and complete control over the visual environment which allows for repeatable, immersive experimental conditions with complete control over both foreground and background stimuli. By contrast, conventional camera-based systems typically require stricter environmental control and are more sensitive to external distractions. And, even though they are less common than phone cameras, they

can be bought at a reasonable price nowadays. By developing an automated analysis and classification of this data, we can simplify assessment of movement disorders such as PD. The experiment tracks the gaze of patients and healthy controls as they look at different objects in the form of fruits, according to simple instructions: The user's task is to look at pseudo-randomly appearing objects (see Fig. 1), starting from a reference resting position, in order to explode them and increase a score with each successfully performed action. This approach leverages gamification to enhance engagement, making the task more enjoyable and potentially more effective in sustaining user attention and compliance.

We analyze the applicability of three classes of features for predicting the diagnosis of PD using eye tracking data. *General features*, such as those established in prior work,[20] can easily be extracted but may underperform with low-quality or noisy recordings. *Task-evoked features* like reaction time, derived directly from the experimental setup, can capture meaningful responses but require careful computation and may still have limited predictive power (compare Fig. 4). *Learning-based features* obtained through neural network training offer a data-driven approach that may uncover latent patterns not accessible through traditional methods. We demonstrate that combining and selectively integrating these feature types yields improved predictive performance. This classification can potentially become a tool to help identify early oculomotor changes of movement disorders and monitor disease progression in a cost-effective, reproducible, and scalable fashion.

Contributions. This work takes a step towards accessible and automated analysis of eye tracking data from consumer-grade VR devices for the detection of oculomotor dysfunction. We explore the potential of such data for distinguishing PD from healthy controls and other movement disorders. In summary, our contributions are

- We design a gamified eye tracking experiment in virtual reality to capture controlled gaze behavior in a reproducible setting while remaining accessible and engaging through consumer VR hardware.
- We evaluate multiple feature classes for PD classification: (i) general statistical features, (ii) task-evoked metrics derived from the experimental design, and (iii) deep features learned via a supervised variational autoencoder.
- We demonstrate that combining these feature types improves classification performance across multiple metrics and extends to multiclass scenarios involving spinocerebellar ataxia patients.

2. Related Work

In this section, we discuss prior work from two intersecting areas: (1) the application of eye tracking in medical diagnostics, particularly for movement disorders, and (2) machine learning methods for oculographic data in both traditional and immersive environments.

2.1. *Ophthalmology for Diagnostics*

Eye movement behavior has long been studied as a non-invasive window into motor, coordinative, and cognitive function.[21,22] In clinical contexts, eye tracking has been used to assess

cognitive abilities, such as in dementia screening,[23] as well as to evaluate social behaviors,[24] and neurological conditions such as Parkinson's disease (PD).[11,25–27] Moreover, it has also been used to differentiate PD from related disorders like Progressive Supranuclear Palsy.[28] Eye tracking has found applications outside of neurodegenerative disease as well and has shown promise in concussion assessment, particularly in sports contexts.[1–4] Additionally, it has been explored as a tool for screening and diagnosing neurodevelopmental disorders, including attention-deficit/hyperactivity disorder (ADHD) and autism spectrum disorder.[5–8] Beyond patient diagnosis, several studies investigate eye movements in decision making and clinical reasoning,[29–32] for instance by analyzing the connection between time-related costs in decision processes and eye movement[29] or exploring the relationship between diagnostic performance and visual search behaviors of the radiologists.[32]

A variety of eye tracking tools have supported these investigations. High-fidelity systems such as the EyeLink 1000[20,29] and the iView X Hi-Speed[25] are commonly used in controlled lab settings. More recent efforts have also examined the feasibility of webcam-based eye tracking for remote cognitive assessments, despite current limitations in resolution and precision.[33] Immersive and extended reality platforms have opened new avenues for eye tracking in clinical research. In mixed reality, Daniol et al.[34] used the Microsoft HoloLens 2 to analyze eye tracking patterns in PD patients. In the virtual reality (VR) domain, Orlosky et al.[35] recorded eye movements of PD patients during VR tasks for subsequent clinical evaluation. Other VR-based efforts include tools for post-COVID symptom assessment[36] and dementia screening.[23] Adhanom et al.[37] provide a comprehensive review of eye tracking applications in VR. In our work, we also use immersive VR with the Meta Quest Pro headset to capture oculographic data from patients with PD.

2.2. *Machine Learning for Oculometrics*

Machine learning and deep learning techniques have been increasingly applied to eye tracking data across a range of medical contexts. Recent studies demonstrate their utility in detecting PD and monitoring its progression, highlighting the potential of eye tracking as a non-invasive digital biomarker.[38,39] These approaches typically operate on small-scale datasets and employ classifiers such as Naïve Bayes, Decision Trees, and Random Forests.[40,41] Other work extracts a feature set from video-based eye trackers, and trains an ensemble classifier composed of Support Vector Machines, Logistic Regression, and Random Forest models.[42] Additionally, tablet-based eye tracking has been used both to differentiate Parkinson's patients from healthy controls using Logistic Regression,[43] and to predict the severity of motor symptoms (e.g., MDS-UPDRS scores) using SVM classifiers.[44] There are specific eye movement abnormalities in PD patients, which leverage many of these approaches; an overview can be found in.[12,45]

Recently, deep learning models have been increasingly applied to PD detection and monitoring using eye tracking data. Mao *et al.*[46] proposed a classification pipeline that combines deep learning with ensemble methods to identify neurological disorders, using features such as pupil position extracted from 30 Hz infrared video eye tracking data. Their approach utilizes a long short-term memory (LSTM) network for initial temporal modeling, followed by a decision-tree ensemble (Random Forest) for final classification. Vodrahalli *et al.*[47] used a

500 Hz binocular infrared eye tracking system to detect eye movement disorders, including PD. Their method generates convolutional neural network (CNN) embeddings from gaze data recorded while patients read numbers on a page, which are then classified using a Random Forest model. Similarly, Uribarri et al.[48] applied state-of-the-art deep learning architectures to classify PD using 300 Hz eye tracking data. They used near-infrared illumination to track pupil movements, focusing their predictions on short fixation intervals. Reiner et al.[49] employed a Tobii Fusion Pro remote eye tracker to collect oculometric data, which was processed using a deep learning pipeline designed for visual feature extraction. In a related effort, Jiang et al.[50] developed a custom deep neural network for automated PD classification using eye tracking data acquired with an HTC Vive Pro Eye VR headset featuring integrated Tobii tracking with 120 Hz.[51] Deep learning-based eye tracking analysis has also been employed to detect other neurodegenerative and developmental conditions, including Alzheimer's disease,[52,53] dyslexia,[54–58] and autism spectrum disorder.[59–61]

In contrast to prior work, our approach targets PD (and spinocerebellar ataxia) classification using eye tracking data from consumer-grade VR hardware with lower sampling rates of 70 Hz. We employ a structured, gamified task and a robust feature extraction pipeline, showing that even under these constrained conditions, effective classification is possible. This performance is supported in part by higher-order statistical features (e.g., skewness, kurtosis), learned features, and task-evoked metrics that capture subtle but clinically relevant variations in gaze behavior.

3. Experimental Setup

In this work, we explore the potential of using eye tracking data from widely available VR headsets to enable more accessible approaches to support neurological diagnostics. To this end, we use a dataset collected in a virtual reality (VR) environment with the Meta Quest Pro, a consumer-grade headset featuring integrated infrared-based eye tracking. Despite its accessibility, the system introduces challenges related to signal noise and reduced accuracy in peripheral regions, which must be considered during data preprocessing and model design.

The AVERT-MD (Avatar Evaluation in Real-Time for Movement Disorders) study has been granted ethical approval by the institutional review board of the University Hospital Bonn in compliance with the Helsinki Declaration (File number: 2024-367-BO). All participants are recruited either from the Department of Parkinson, Sleep and Movement Disorders at the University Hospital Bonn or from the observational study cohorts of the German Center for Neurodegenerative Diseases (DZNE): healthy individuals (DANCER), Parkinson's disease (DESCRIBE-PD), and spinocerebellar ataxia (SCA-Registry). Participants with congenital nystagmus, age-related macular degeneration, or head tremor were excluded from study participation. After providing written informed consent, demographic data were collected, and participants underwent clinical motor assessments consisting of the Movement Disorder Society's Unified Parkinson's Disease Rating Scale (MDS-UPDRS) and the Scale for the Rating and Assessment of Ataxia (SARA), which were administered by a movement disorders specialist certified in the aforementioned clinical assessment scales. At the beginning of the VR game, an instructional text will be shown to participants in VR, and the test will be run

without any interference from the examiner, only to be repeated in case of involuntary head movements.

The dataset is recorded through a controlled gaze-tracking task in which individual objects in the form of fruits appear sequentially at varying positions in the user's field of view. Participants are instructed to fixate on each new target upon its appearance, which is marked by the explosion of the object, followed by return to a centrally located reference object. The timing of each trial is participant-dependent and dynamically gated by real-time gaze detection, resulting in session durations in the order of several minutes. Each session yields continuous recordings of gaze vectors, the participant's positions, and 3D object coordinates for both central and target stimuli. The dataset includes recordings from 75 participants, comprising 33 individuals with Parkinson's disease (PD), mainly of Stage I or II of the Hoehn and Yahr staging system, which is well representative of the early stages of PD, 27 healthy controls (HC), and 15 individuals diagnosed with Ataxia, a separate neurological disorder characterized by motor impairments. The PD participants had an average UPDRS III score of 16.86 with a standard deviation of 10.27, and the PD group's male predominance reflects projected global prevalence ratios, rising from 1.46 in 2021 to 1.64 in 2050.[62] Recordings were performed at a 70 Hz sampling rate using the native Quest Pro SDK, without additional hardware modifications, resulting in 75 VR sequences with consistent task structure and spatial alignment.

By using the Meta Quest Pro, a widely available consumer VR headset with built-in eye tracking, the setup enables scalable data collection without the need for specialized hardware or lab environments. Note that the system has only been tested with this VR headset model, so its generalizability to other devices remains unclear.

4. Feature Extraction

To analyze gaze behavior, we extracted a range of features from the raw eye tracking data. These include handcrafted features based on task-evoked reaction metrics such as saccadic latency and velocity, spontaneous fixations and saccades, and higher-level representations learned via deep neural networks.

4.1. *Task-Evoked Saccadic Response Features*

To systematically analyze response dynamics in the eye movement behavior of the participants, we calculated two primary metrics from the gaze data: the *saccadic latency* (sl) and the *saccadic velocity* (sv). The saccadic latency refers to the time from appearance of the target to the start of the participants eye movement, as illustrated in Fig. 2. From the duration of the saccade and the distance to the target at movement start, we compute the saccadic velocity, the angular velocity of the eye movement in degrees per second.

To determine the initiation of eye movement toward the target, we analyze the angular distance between the gaze and the target object over time. As shown in Fig. 2, the angular distance remains approximately constant prior to movement initiation, reflecting gaze stability at a non-target location. Movement onset is identified as the point where the angular distance begins to decrease sharply. While methods based on fixed angular or velocity thresholds were

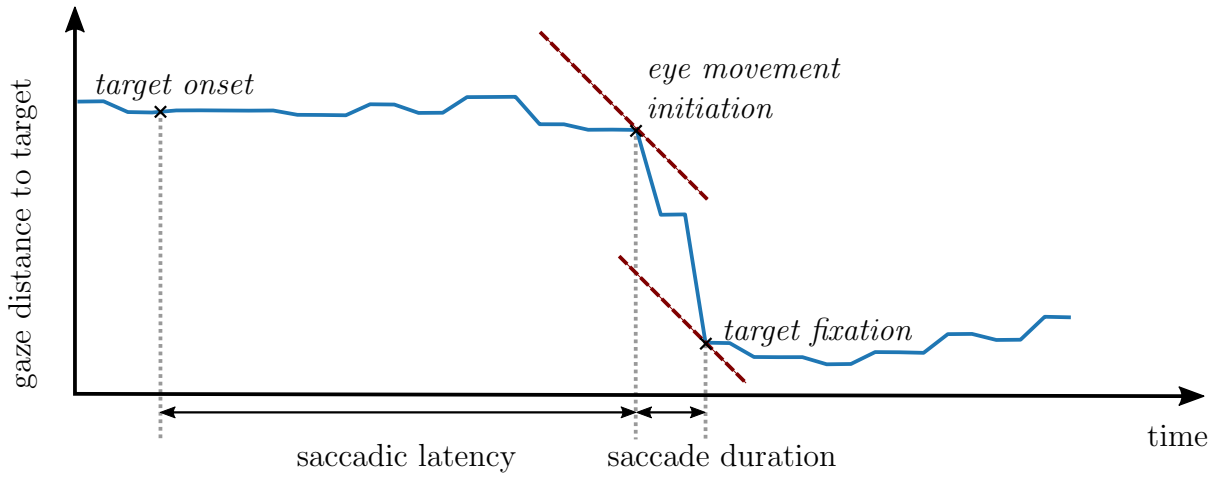

Fig. 2. Timeline illustrating the visual response to a stimulus. Eye movement initiation and target fixation are detected based on angular distance to the target over time. The blue curve represents the angular distance between the gaze and the target object. Eye movement initiation is defined as the point of closest approach to a reference line with a 45° negative slope. Target fixation is identified as the point where the gaze intersects a 45° positive slope reference line.

found to be sensitive to noise and inter-subject variability, we fit a reference line with a fixed slope of 45° to the angular distance profile and define the initiation point as the location of closest approach to this line. Fixation is defined similarly as the point, where the gaze intersects a 45° positive slope reference line. From the saccade duration, the saccadic velocity is calculated using the angular distance between the central fixation point and the target.

To prepare the data for classification, we extract statistical features from saccadic latency and velocity measurements recorded during the experiment. Each participant was exposed to $n = 127$ object appearances, with each trial $i \in \{1, \ldots, n\}$ yielding a pair of scalar values (ℓ_i, v_i) corresponding to their saccadic latency/sl and velocity/sv.

To generate meaningful participant-level features that characterize the empirical distributions of these sequences, we computed a set of descriptive statistics based on statistical moments over $\boldsymbol{\ell} = (\ell_1, \ldots, \ell_n)$ and $\boldsymbol{v} = (v_1, \ldots, v_n)$. The first and second central moments, representing the sample *mean* $\mu(x)$ and *variance* $\sigma(x)^2$,

$$\mu(x) = \frac{1}{n}\sum_{i=1}^{n} x_i, \quad \sigma(x)^2 = \frac{1}{n}\sum_{i=1}^{n}(x_i - \mu(x))^2, \tag{1}$$

quantify the average saccadic latency or velocity and the overall variability in oculomotor responses, respectively. The *standard deviation* $\sigma(x)$ is simply the square root of the variance. The third and fourth standardized moments, corresponding to *skewness* and *kurtosis*, respectively,

$$\text{skew}(x) = \frac{1}{n}\sum_{i=1}^{n}\left(\frac{x_i - \mu(x)}{\sigma(x)}\right)^3, \quad \text{kurt}(x) = \frac{1}{n}\sum_{i=1}^{n}\left(\frac{x_i - \mu(x)}{\sigma(x)}\right)^4, \tag{2}$$

whereby skewness quantifies the asymmetry of the distribution, with positive values indicating a longer right tail, while kurtosis measures the heaviness of the tails and sharpness of the peak,

relative to a normal distribution. To complement these moment-based features, we computed robust statistics that are less sensitive to outliers. The *median* offers a robust measure of central tendency, and represents the 50th percentile of the sequence, and the *interquartile range* $\mathrm{IQR} = Q_3 - Q_1$ is the difference between the 75th and 25th percentiles and captures the spread of the central 50% of observations. We also included the *minimum* and *maximum* values $\min(x) = \min_i x_i, \quad \max(x) = \max_i x_i$, which highlight the extremal responses and indicate anomalously fast or slow responses. The *range* $\mathrm{range}(x) = \max(x) - \min(x)$ measures the spread between the most extreme observations, reflecting the total span of variation.

Each statistic is computed independently for the saccadic latency vector $\boldsymbol{\ell}$ and the movement speed vector $\boldsymbol{v}$, resulting in a total of 18 features per participant.

4.2. *General Fixation and Saccade Features*

Saccadic eye movements and visual fixation provide important insights into motor and cognitive function, particularly in Parkinson's disease.[45,63] Therefore, we evaluated a variety of fixation- and saccade-based features from the gaze data. Fixations and saccades were identified using the Buscher method,[64] which classifies a fixation as a cluster of gaze points within a 1° visual angle for at least 100 ms. Saccades were inferred as the rapid transitions between consecutive fixations during free viewing. Similar to Jiang *et al.*[50] we extracted the total number of fixations (TNF), total duration of fixations (TDF), mean duration of fixations (MDF), and their number, as well as the scan path length (SL) and its duration (SD), and the rate of saccade/fixation. We compute them for both the interval of the target visibility and the complete recording. To extract additional insights into the feature distribution, we also compute statistical features as described in Sec. 4.

4.3. *Deep Feature Extraction*

To capture higher-level representations of gaze behavior beyond handcrafted features, we employ a deep neural network on the gaze data as shown in Fig. 3. We use a 1D convolutional neural network encoder with residual connections to extract features from the input. To summarize the temporal dynamics of the extracted features, we apply attention inspired average pooling. These pooled features are passed through a reparameterization layer, yielding latent representations which are subsequently processed by a classification module. The model outputs a 4-dimensional latent embedding $z \sim q_\theta(z|x)$ that captures the underlying structure of gaze behavior and is used for subsequent classification.

Model parameters θ and ϕ are optimized by minimizing a composite loss function that combines a cross-entropy loss with a regularization term based on the Kullback–Leibler (KL) divergence,

$$\min_{\theta,\phi} \; \mathcal{L}_{\mathrm{CE}}\left(\mathcal{G}_\phi(z), y\right) + \lambda \cdot \mathcal{L}_{\mathrm{KL}}\left(q_\theta(z|x)|p(z)\right), \tag{3}$$

where x is the input, y is the ground-truth label, and $\mathcal{G}_\phi(z)$ denotes the classification head applied to the sampled latent representation. The KL divergence term encourages the approximate posterior $q_\theta(z|x)$ to remain close to the prior $p(z) = \mathcal{N}(0, I)$.

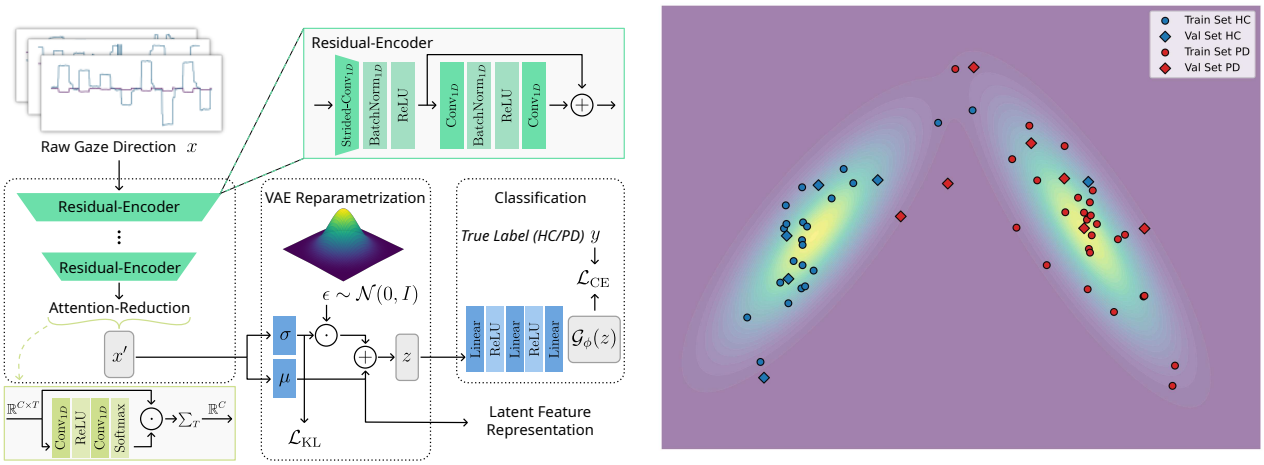

(a) Neural Network Architecture **(b)** Feature Space Visualization

Fig. 3. (a) Architecture of the 1D convolutional network for gaze representation learning. (b) PCA projection of the learned feature space showing task-specific clustering.

5. Experiments

We now assess the ability of the features introduced in Sec. 4 to discriminate between healthy individuals (HC) and those with Parkinson's disease (PD) by evaluating their performance in a binary classification task using standard machine learning classifiers. We then extend this analysis to a more challenging three-class classification problem by additionally including spinocerebellar ataxia participants.

5.1. *Prediction of Parkinson's Disease*

To identify the most discriminative features, we begin with a statistical analysis based on the independent two-sample t-test, comparing feature distributions between PD and HC groups. Features yielding p-values less than 0.05 are considered statistically significant and are hypothesized to contribute meaningfully to classification. Fig. 4 illustrates the mean and standard deviation of the normalized feature space and shows significant differences across several features, with varying levels of significance indicated by asterisks.

Next, we evaluate the ability of several machine learning models to distinguish between HC and PD participants, using both the statistical features extracted from saccadic latencies and velocity, as well as the general fixation and saccade features (Sec. 4). For each model, we use Sequential Feature Selector from scikit-learn[65] to identify optimal feature subsets. Classification performance is assessed using stratified k-fold cross-validation with randomized splits (four independent seeds) to ensure robustness. We evaluate nine representative machine learning models: Logistic Regression, Linear Discriminant Analysis (LDA), Support Vector Machine (SVM) with a linear and radial basis function (RBF) kernel, Random Forest, Gradient Boosted Trees (GBT), k-nearest neighbors (KNN), and perceptron. Tab. 1 reports performance metrics for all classifiers, including weighted accuracy, precision, recall, F1 score, and ROC AUC, based on classification results using both generic and task-evoked features. We

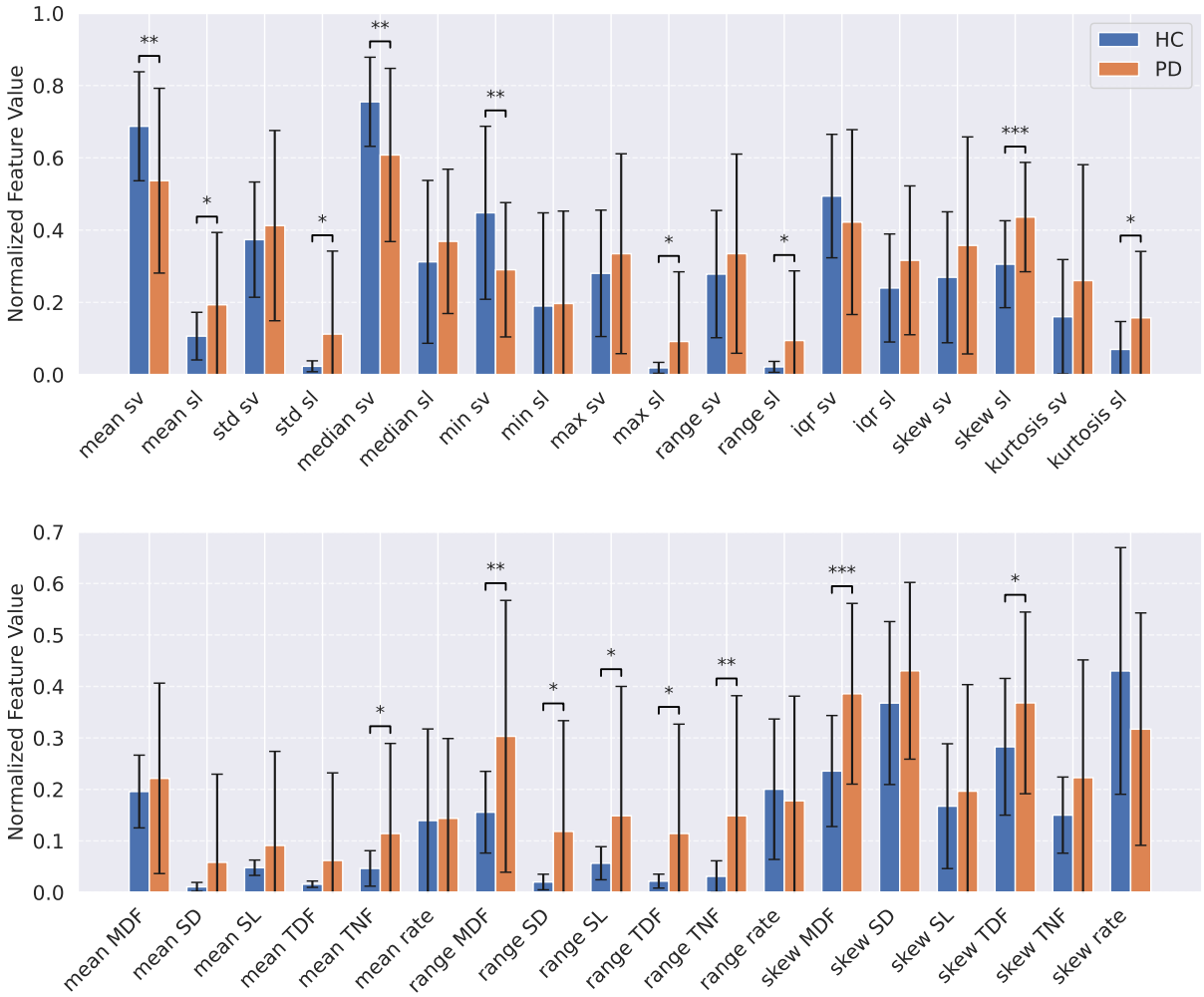

Fig. 4. Mean and standard deviation of normalized (task-evoked and general) feature spaces for Parkinson's disease and healthy controls. Significance levels are based on t-test p-values across features, indicating statistical differences: $^{*}p < 0.05$, $^{**}p < 0.01$, $^{***}p < 0.001$.

additionally report weighted accuracy without the higher-order statistical features (denoted as Accuracy*). To further analyze classifier performance, we visualize the confusion matrices for the three best-performing models in Fig. 5. These show well each model distinguishes between PD and HC participants, highlighting common misclassification patterns.

To assess how well the learned latent representations separate classes, we apply the Naive Bayes classifiers to the deep features extracted from a deep neural network (compare Sec. 4.3). We evaluate the latent representations as complementary information by concatenating the latent vectors $z \sim q_\theta(z|x)$ with the most informative handcrafted features $f \in \mathbb{R}^d$, selected through sequential feature selection. The increased accuracy observed in Tab. 1 for Naive Bayes^{a+emb} shows that the learned feature space is able to capture additional discriminative information not present in classical features. In parallel, we evaluate the performance of the full neural architecture in an *end-to-end supervised learning* setup, which demonstrates perfor-

Table 1. Performance comparison of models using sequentially selected features. Superscripts indicate the specific set of selected features used by each model, and "Accuracy*" reports the model's classification accuracy without the use of higher statistical features. Here, *sv* refers to saccadic velocity and *sl* to saccadic latency. The tag *vis* marks features computed only when the object was visible; features without this tag are calculated across the entire dataset.

Model	Accuracy	Precision	Recall	F1 Score	ROC AUC	Accuracy*
Naive Bayes [a]	0.824	0.913	0.756	0.808	0.873	0.713
Random Forest [b]	0.804	0.829	0.824	0.818	0.836	0.758
GBT [c]	0.772	0.823	0.780	0.780	0.821	0.754
LDA [d]	0.748	0.796	0.713	0.737	0.737	0.697
SVM RBF Kernel [e]	0.743	0.868	0.614	0.703	0.715	0.723
KNN [f]	0.710	0.798	0.643	0.692	0.679	0.683
Logistic Regression [g]	0.681	0.733	0.671	0.681	0.771	0.646
SVM Linear Kernel [h]	0.667	0.756	0.571	0.624	0.722	0.679
Perceptron [i]	0.648	0.746	0.637	0.647	0.724	0.558
Naive Bayes [a+emb]	0.831	0.859	0.821	0.816	0.871	—
End-to-end	0.741	0.773	0.738	0.731	0.768	—

[a] mean sv, max sv, median TNF vis, range MDF vis, kurtosis rate vis, range rate
[b] min sl, iqr sv, kurtosis sv, iqr TDF vis, median TNF vis, median TDF, mean SL, mean SD, median SD
[c] min TNF vis, mean SL, max SD
[d] std sl, kurtosis sv, mean TNF vis, median TNF vis, range MDF vis, median SL vis, iqr TNF, kurtosis MDF
[e] median sv, iqr ms, kurtosis sl, mean SL, median SL, max SL, range SL, kurtosis SD
[f] median SL
[g] median TNF vis, kurtosis TNF
[h] range sl, max MDF vis, range MDF vis, range rate vis, mean TDF, median SL
[i] std sl, skew sl, kurtosis sl vis, range SD vis, min rate vis, iqr rate vis, mean TDF, kurtosis TNF

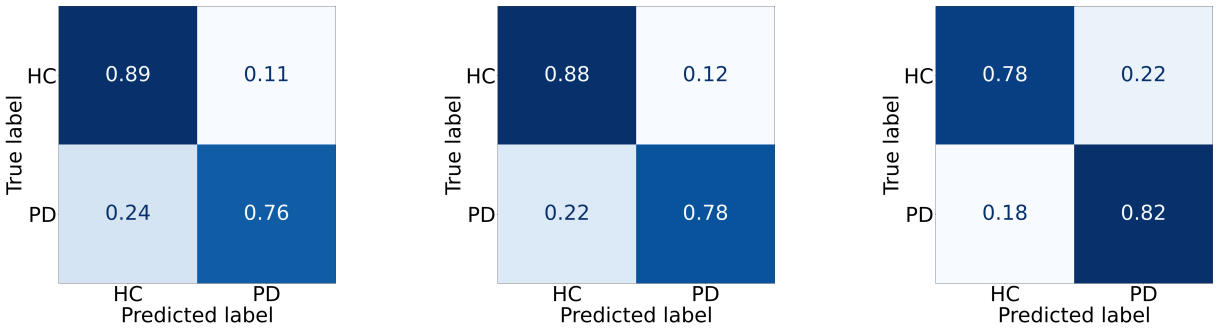

(a) Naive Bayes **(a)** Naive Bayes + Emb **(c)** Random Forest

Fig. 5. Confusion matrices for the top three binary classifiers. Each matrix summarizes the classification performance for distinguishing between HC and PD participants.

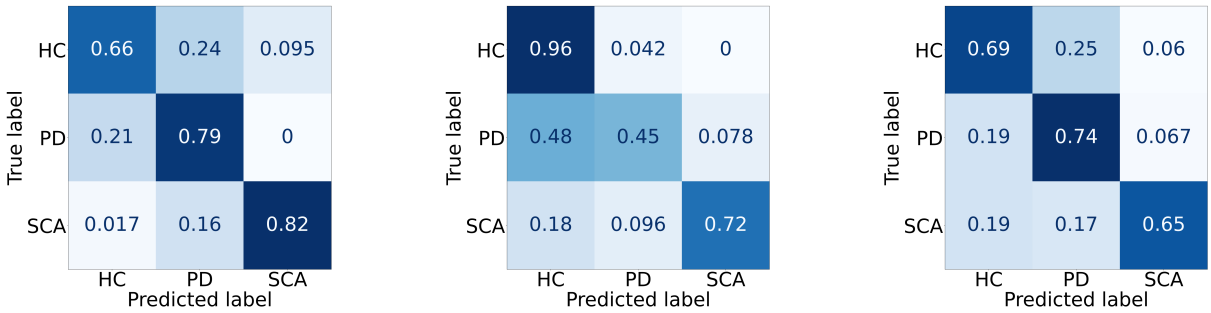

(a) LDA **(b)** Naive Bayes **(c)** Random Forest

Fig. 6. Confusion matrices for the top three classifiers in the multiclass case. Each matrix summarizes the classification performance for distinguishing between healthy controls, Parkinson's disease and Ataxia participants. Diagonal elements represent correctly classified instances, while off-diagonal entries indicate misclassifications.

mance competitive with classical approaches. We believe that with a larger training dataset, this potential could be further leveraged, leading to greater performance gains. To interpret the learned embedding space, we project latent vectors to two dimensions using PCA. As shown in Fig. 3(b), samples cluster clearly by diagnostic label, highlighting that the latent space encodes disease-specific behavioral patterns.

5.2. *Discrimination of Neurodegenerative Diseases*

To evaluate the scalability of our approach, we extend the classification task to a three-class setting by incorporating spinocerebellar ataxias (SCA) as an additional target class. SCAs are a group of hereditary neurodegenerative disorders whose hallmark is the neurodegeneration of Purkinje cells in the cerebellum, as well as the deep cerebellar nuclei and brainstem, leading to discoordination of oculomotion, speech, standing, gait, and fine motor skills. The resulting task requires models to distinguish between oculometric signatures across three groups: HC, PD, and SCA. We adopt the same feature selection and cross-validation strategy used in the binary task, and account for class imbalance by using balanced class weights due to the smaller number of SCA participants. As shown in Tab. 2 and in Fig. 6, all models exhibit a decrease in absolute classification metrics, reflecting the increased difficulty of multi-class discrimination. Nevertheless, classifiers continue to perform above chance, confirming that the extracted features retain discriminative power across heterogeneous movement disorders.

6. Discussion

We highlight the feasibility of using consumer-grade VR headsets for automated neurological assessment, focusing on Parkinson's disease (PD) classification from eye tracking data. Our approach combines a controlled VR gaze task with a diverse feature extraction strategy that includes both statistical metrics and learned representations, addressing the limitations of noisy, low-resolution hardware and a limited dataset. We demonstrate that combining general oculomotor metrics with task-evoked feature computation of saccadic latency and velocity

Table 2. Multiclass performance comparison of models using sequentially selected features. Superscripts indicate the specific set of selected features used by each model, where *sv* refers to saccadic velocity and *sl* to saccadic latency. *vis* marks features computed only when the object was visible.

Model	Accuracy	Precision	Recall	F1 Score
LDA [a]	0.759	0.804	0.733	0.734
Naive Bayes [b]	0.708	0.774	0.642	0.629
Random Forest [c]	0.693	0.740	0.667	0.661
Gradient Boosted Trees [d]	0.692	0.751	0.692	0.686
SVM (RBF Kernel) [e]	0.591	0.551	0.579	0.523
Logistic Regression [f]	0.583	0.653	0.613	0.598
SVM (Linear Kernel) [g]	0.558	0.623	0.625	0.597
Perceptron [h]	0.516	0.589	0.525	0.510

[a] median sl, kurtosis sv, std TDF vis, median TNF vis, median MDF vis, skew MDF vis, max SD vis, iqr TDF, median SD, skew rate
[b] kurtosis v, median TDF vis, iqr TDF vis, kurtosis MDF vis, kurtosis TDF, min TNF
[c] median TDF vis, max MDF vis, kurtosis MDF vis, mean SL vis, mean SD vis, median SD vis, std rate, max rate, range rate
[d] max MDF vis, kurtosis MDF vis, mean SD vis, min TNF
[e] mean sl, median sl, median TDF vis, min TDF vis, max MDF vis, range MDF vis, median&min SD vis, mean MDF, median MDF
[f] median sl, min sl, min TDF vis, median TNF vis, range MDF, skew MDF, kurtosis MDF, skew rate
[g] median TDF vis, min TDF vis, skew MDF vis, skew SL vis, skew TDF, skew MDF, min SD
[h] mean sl, skew MDF vis, std SD vis, min SD vis, min rate vis, std rate, min rate, max rate, iqr rate

results in high discriminative performance. In particular, features based on higher-order statistics such as skewness and kurtosis contribute meaningfully to classification, indicating that distributional shape carries relevant diagnostic information not captured by simple averages. Deep learning has also proven to be a valuable tool for extracting additional features, and we believe that with a larger dataset, its contribution could be even more substantial. Finally, we show that our experimental setup is scalable, achieving robust performance not only in binary classification but also in more complex multi-class scenarios.

Note, that this approach does not yet provide sufficiently reliable confidence estimates to serve as a standalone diagnostic tool and remains a research prototype that can offer supportive measures. Integration into clinical practice requires privacy-compliant handling of eye-tracking data, clear communication to patients about possible insurance implications of early PD diagnosis, and approval of consumer VR devices as medical devices, which demands transparent data curation and close collaboration between clinicians and data scientists. Its main potential lies in the quantitative monitoring of PD symptoms, for example, to assess current symptom levels, track treatment response, and to assist differential diagnosis.

Acknowledgments

This work has been funded by the Ministry of Culture and Science North Rhine-Westphalia under grant number PB22-063A (InVirtuo 4.0: Experimental Research in Virtual Environments). Lio Schmitz and Zorah Lähner have been funded by the Federal Ministry of Research, Technology and Space of Germany and the state of North Rhine-Westphalia as part of the Lamarr Institute for Machine Learning and Artificial Intelligence.

References

1. N. Snegireva, W. Derman, J. Patricios and K. Welman, Eye tracking technology in sports-related concussion: a systematic review and meta-analysis, *Physiological measurement* **39**, p. 12TR01 (2018).
2. N. Snegireva, W. Derman, J. Patricios and K. E. Welman, Awareness and perceived value of eye tracking technology for concussion assessment among sports medicine clinicians: a multinational study, *The Physician and Sportsmedicine* **48**, 165 (2020).
3. C. N. Feller, M. Goldenberg, P. D. Asselin, K. Merchant-Borna, B. Abar, C. M. C. Jones, R. Mannix, K. Kawata and J. J. Bazarian, Classification of comprehensive neuro-ophthalmologic measures of postacute concussion, *JAMA network open* **4**, e210599 (2021).
4. N. Snegireva, W. Derman, J. Patricios and K. Welman, Eye tracking to assess concussions: an intra-rater reliability study with healthy youth and adult athletes of selected contact and collision team sports, *Experimental brain research* **239**, 3289 (2021).
5. J. H. Yoo, C. Kang, J. S. Lim, B. Wang, C.-H. Choi, H. Hwang, D. H. Han, H. Kim, H. Cheon and J.-W. Kim, Development of an innovative approach using portable eye tracking to assist adhd screening: a machine learning study, *Frontiers in Psychiatry* **15**, p. 1337595 (2024).
6. L. Merzon, K. Pettersson, E. T. Aronen, H. Huhdanpää, E. Seesjärvi, L. Henriksson, W. J. MacInnes, M. Mannerkoski, E. Macaluso and J. Salmi, Eye movement behavior in a real-world virtual reality task reveals adhd in children, *Scientific reports* **12**, p. 20308 (2022).
7. L. Chetcuti, K. J. Varcin, M. Boutrus, J. Smith, C. A. Bent, A. J. Whitehouse and K. Hudry, Feasibility of a 2-minute eye-tracking protocol to support the early identification of autism, *Scientific Reports* **14**, p. 5117 (2024).
8. R. K. Wang, K. Kwong, K. Liu and X.-J. Kong, New eye tracking metrics system: the value in early diagnosis of autism spectrum disorder, *Frontiers in Psychiatry* **15**, p. 1518180 (2024).
9. S. Hutton and C. Kennard, Oculomotor abnormalities in schizophrenia: a critical review, *Neurology* **50** (1998).
10. E. Pretegiani and L. M. Optican, Eye movements in parkinson's disease and inherited parkinsonian syndromes, *Front Neurol.* (2017).
11. P. Diotaiuti, G. Marotta, F. Di Siena, S. Vitiello, F. Di Prinzio, A. Rodio, T. Di Libero, L. Falese and S. Mancone, Eye tracking in parkinson's disease: A review of oculomotor markers and clinical applications, *Brain Sciences* **15**, p. 362 (2025).
12. C. A. Antoniades and M. Spering, Eye movements in parkinson's disease: from neurophysiological mechanisms to diagnostic tools, *Trends in Neurosciences* **47**, 71 (2024).
13. T. J. Anderson and M. R. MacAskill, Eye movements in patients with neurodegenerative disorders, *Nature Reviews Neurology* **9**, 74 (2013).
14. S.-H. Kim, S.-U. Lee, B.-H. Cho, K.-H. Cho, S. Yu, B.-J. Kim and J.-S. Kim, Analyses of head-impulse tests in patients with posterior circulation stroke and vestibular neuritis, *Neurology* **100**, e2374 (2023).
15. L. Chen, M. Todd, G. M. Halmagyi and S. Aw, Head impulse gain and saccade analysis in pontine-cerebellar stroke and vestibular neuritis, *Neurology* **83**, 1513 (2014).
16. G.-S. Nam, H.-J. Shin, J.-J. Kang, N.-R. Lee and S.-Y. Oh, Clinical implication of corrective saccades in the video head impulse test for the diagnosis of posterior inferior cerebellar artery infarction, *Frontiers in Neurology* **12**, p. 605040 (2021).
17. C. Antoniades and C. Kennard, Ocular motor abnormalities in neurodegenerative disorders, *Eye* **29**, 200 (2015).
18. K. Krafka, A. Khosla, P. Kellnhofer, H. Kannan, S. Bhandarkar, W. Matusik and A. Torralba, Eye tracking for everyone, in *Proceedings of the IEEE Conference on Computer Vision and Pattern Recognition (CVPR)*, (IEEE, 2016).

19. B. J. Hou, Y. Abdrabou, F. Weidner and H. Gellersen, Unveiling variations: A comparative study of vr headsets regarding eye tracking volume, gaze accuracy, and precision, in *Proceedings of the IEEE Conference on Virtual Reality and 3D User Interfaces Abstracts and Workshops (VRW)*, (IEEE, 2024).
20. I. Rigas, L. Friedman and O. Komogortsev, Study of an extensive set of eye movement features: Extraction methods and statistical analysis, *Journal of Eye Movement Research* **11**, 10 (2018).
21. Y. Terao, H. Fukuda and O. Hikosaka, What do eye movements tell us about patients with neurological disorders?—an introduction to saccade recording in the clinical setting—, *Proceedings of the Japan Academy, Series B* **93**, 772 (2017).
22. L. Graham, R. Vitorio, R. Walker, G. Barry, A. Godfrey, R. Morris and S. Stuart, Digital eye-movement outcomes (demos) as biomarkers for neurological conditions: a narrative review, *Big Data and Cognitive Computing* **8**, p. 198 (2024).
23. Y. Xu, C. Zhang, B. Pan, Q. Yuan and X. Zhang, A portable and efficient dementia screening tool using eye tracking machine learning and virtual reality, *NPJ Digital Medicine* **7**, p. 219 (2024).
24. T. W. Frazier, M. Strauss, E. W. Klingemier, E. E. Zetzer, A. Y. Hardan, C. Eng and E. A. Youngstrom, A meta-analysis of gaze differences to social and nonsocial information between individuals with and without autism, *Journal of the American Academy of Child & Adolescent Psychiatry* **56**, 546 (2017).
25. M. R. MacAskill, C. F. Graham, T. L. Pitcher, D. J. Myall, L. Livingston, S. van Stockum, J. C. Dalrymple-Alford and T. J. Anderson, The influence of motor and cognitive impairment upon visually-guided saccades in parkinson's disease, *Neuropsychologia* **50**, 3338 (2012).
26. S. Stuart, R. A. Lawson, A. J. Yarnall, J. Nell, L. Alcock, G. W. Duncan, T. K. Khoo, R. A. Barker, L. Rochester, D. J. Burn *et al.*, Pro-saccades predict cognitive decline in parkinson's disease: Icicle-pd, *Movement Disorders* **34**, 1690 (2019).
27. J. Waldthaler, L. Stock, C. Krüger-Zechlin, Z. Deeb and L. Timmermann, Cluster analysis reveals distinct patterns of saccade impairment and their relation to cognitive profiles in parkinson's disease, *Journal of Neuropsychology* **17**, 251 (2023).
28. S. Marx, G. Respondek, M. Stamelou, S. Dowiasch, J. Stoll, F. Bremmer, W. H. Oertel, G. U. Höglinger and W. Einhäuser, Validation of mobile eye-tracking as novel and efficient means for differentiating progressive supranuclear palsy from parkinson's disease, *Frontiers in behavioral neuroscience* **6**, p. 88 (2012).
29. J. E. Choi, P. A. Vaswani and R. Shadmehr, Vigor of movements and the cost of time in decision making, *Journal of neuroscience* **34**, 1212 (2014).
30. M. O. Al-Moteri, M. Symmons, V. Plummer and S. Cooper, Eye tracking to investigate cue processing in medical decision-making: A scoping review, *Computers in Human Behavior* **66**, 52 (2017).
31. K. Blondon, R. Wipfli and C. Lovis, Use of eye-tracking technology in clinical reasoning: a systematic review, *Digital Healthcare Empowering Europeans* , 90 (2015).
32. A. Van der Gijp, C. Ravesloot, H. Jarodzka, M. Van der Schaaf, I. Van der Schaaf, J. P. van Schaik and T. J. Ten Cate, How visual search relates to visual diagnostic performance: a narrative systematic review of eye-tracking research in radiology, *Advances in Health Sciences Education* **22**, 765 (2017).
33. G. E. Juantorena, F. Figari, A. Petroni and J. E. Kamienkowski, Web-based eye-tracking for remote cognitive assessments: The anti-saccade task as a case study, *bioRxiv* , 2023 (2023).
34. M. Daniol, D. Hemmerling, J. Sikora, P. Jemiolo, M. Wodzinski and M. Wojcik-Pedziwiatr, Eye-tracking in mixed reality for diagnosis of neurodegenerative diseases, in *Proceedings of the 46th Annual International Conference of the IEEE Engineering in Medicine and Biology Society (EMBC)*, (IEEE, 2024).

35. J. Orlosky, Y. Itoh, M. Ranchet, K. Kiyokawa, J. Morgan and H. Devos, Emulation of physician tasks in eye-tracked virtual reality for remote diagnosis of neurodegenerative disease, *IEEE transactions on visualization and computer graphics* **23**, 1302 (2017).
36. W. Mehringer, M. Stoeve, D. Krauss, M. Ring, F. Steussloff, M. Güttes, J. Zott, B. Hohberger, G. Michelson and B. Eskofier, Virtual reality for assessing stereopsis performance and eye characteristics in post-covid, *Scientific Reports* (2023).
37. I. B. Adhanom, P. MacNeilage and E. Folmer, Eye tracking in virtual reality: a broad review of applications and challenges, *Virtual Reality* **27**, 1481 (2023).
38. A. W. Przybyszewski, A. Śledzianowski, A. Chudzik, S. Szlufik and D. Koziorowski, Machine learning and eye movements give insights into neurodegenerative disease mechanisms, *Sensors* **23**, p. 2145 (2023).
39. A. Chudzik, A. Śledzianowski and A. W. Przybyszewski, Machine learning and digital biomarkers can detect early stages of neurodegenerative diseases, *Sensors* **24**, p. 1572 (2024).
40. A. W. Przybyszewski, M. Kon, S. Szlufik, A. Szymanski, P. Habela and D. M. Koziorowski, Multimodal learning and intelligent prediction of symptom development in individual parkinson's patients, *Sensors* **16**, p. 1498 (2016).
41. A. Sledzianowski, A. Szymanski, A. Drabik, S. Szlufik, D. M. Koziorowski and A. W. Przybyszewski, Measurements of antisaccades parameters can improve the prediction of parkinson's disease progression, in *Proceedings of the Asian Conference on Intelligent Information and Database Systems*, (Springer, 2019).
42. D. C. Brien, H. C. Riek, R. Yep, J. Huang, B. Coe, C. Areshenkoff, D. Grimes, M. Jog, A. Lang, C. Marras *et al.*, Classification and staging of parkinson's disease using video-based eye tracking, *Parkinsonism & Related Disorders* **110**, p. 105316 (2023).
43. É. de Villers-Sidani, P. Voss, D. Guitton, J. M. Cisneros-Franco, N. A. Koch and S. Ducharme, A novel tablet-based software for the acquisition and analysis of gaze and eye movement parameters: a preliminary validation study in parkinson's disease, *Frontiers in Neurology* **14**, p. 1204733 (2023).
44. N. A. Koch, P. Voss, J. M. Cisneros-Franco, A. Drouin-Picaro, F. Tounkara, S. Ducharme, D. Guitton and É. de Villers-Sidani, Eye movement function captured via an electronic tablet informs on cognition and disease severity in parkinson's disease, *Scientific Reports* **14**, p. 9082 (2024).
45. Y. R. Sun, S. B. Beylergil, P. Gupta, F. F. Ghasia and A. G. Shaikh, Monitoring eye movement in patients with parkinson's disease: what can it tell us?, *Eye and Brain* , 101 (2023).
46. Y. Mao, Y. He, L. Liu and X. Chen, Disease classification based on eye movement features with decision tree and random forest, *Frontiers in Neuroscience* **14**, p. 798 (2020).
47. K. Vodrahalli, M. Filipkowski, T. Chen, J. Zou and Y. J. Liao, Predicting visuo-motor diseases from eye tracking data, in *PACIFIC SYMPOSIUM ON BIOCOMPUTING 2022*, (World Scientific, 2021).
48. G. Uribarri, S. E. von Huth, J. Waldthaler, P. Svenningsson and E. Fransén, Deep learning for time series classification of parkinson's disease eye tracking data, *arXiv preprint arXiv:2311.16381* (2023).
49. J. Reiner, L. Franken, E. Raveh, I. Rosset, R. Kreitman, E. Ben-Ami and R. Djaldetti, Oculometric measures as a tool for assessment of clinical symptoms and severity of parkinson's disease, *Journal of Neural Transmission* **130**, 1241 (2023).
50. M. Jiang, Y. Liu, Y. Cao, S. Xia, F. Teng, W. Zhao, Y. Lin and W. Liu, Diagnosis of parkinson's disease by eliciting trait-specific eye movements in multi-visual tasks, *Journal of Translational Medicine* **23**, p. 65 (2025).
51. I. Schuetz and K. Fiehler, Eye tracking in virtual reality: Vive pro eye spatial accuracy, precision, and calibration reliability, *Journal of Eye Movement Research* **15**, 10 (2022).

52. F. Zuo, P. Jing, J. Sun, J. Duan, Y. Ji and Y. Liu, Deep learning-based eye-tracking analysis for diagnosis of alzheimer's disease using 3d comprehensive visual stimuli, *IEEE Journal of Biomedical and Health Informatics* **28**, 2781 (2024).
53. J. Sun, Y. Liu, H. Wu, P. Jing and Y. Ji, A novel deep learning approach for diagnosing alzheimer's disease based on eye-tracking data, *Frontiers in Human Neuroscience* **16**, p. 972773 (2022).
54. L. Rello and M. Ballesteros, Detecting readers with dyslexia using machine learning with eye tracking measures, in *Proceedings of the 12th International Web for All Conference*, (ACM, 2015).
55. I. A. Vajs, G. S. Kvaščev, T. M. Papić and M. M. Janković, Eye-tracking image encoding: Autoencoders for the crossing of language boundaries in developmental dyslexia detection, *IEEE Access* **11**, 3024 (2023).
56. B. Nerušil, J. Polec, J. Škunda and J. Kačur, Eye tracking based dyslexia detection using a holistic approach, *Scientific Reports* **11**, p. 15687 (2021).
57. I. Vajs, V. Ković, T. Papić, A. M. Savić and M. M. Janković, Dyslexia detection in children using eye tracking data based on vgg16 network, in *2022 30th European Signal Processing Conference (EUSIPCO)*, (IEEE, 2022).
58. A. E. El Hmimdi, Z. Kapoula and V. Sainte Fare Garnot, Deep learning-based detection of learning disorders on a large scale dataset of eye movement records, *BioMedInformatics* **4**, 519 (2024).
59. M. Elbattah, J.-L. Guérin, R. Carette, F. Cilia and G. Dequen, Nlp-based approach to detect autism spectrum disorder in saccadic eye movement, in *2020 IEEE Symposium Series on Computational Intelligence (SSCI)*, (IEEE, 2020).
60. S. Chen and Q. Zhao, Attention-based autism spectrum disorder screening with privileged modality, in *Proceedings of the IEEE/CVF International Conference on Computer Vision (ICCV)*, (IEEE, 2019).
61. M. Jiang and Q. Zhao, Learning visual attention to identify people with autism spectrum disorder, in *Proceedings of the IEEE International Conference on Computer Vision (ICCV)*, (IEEE, 2017).
62. D. Su, Y. Cui, C. He, P. Yin, R. Bai, J. Zhu, J. S. Lam, J. Zhang, R. Yan, X. Zheng *et al.*, Projections for prevalence of parkinson's disease and its driving factors in 195 countries and territories to 2050: modelling study of global burden of disease study 2021, *bmj* **388** (2025).
63. A. Srivastava, R. Sharma, S. K. Sood, G. Shukla, V. Goyal and M. Behari, Saccadic eye movements in parkinson's disease, *Indian journal of ophthalmology* **62**, 538 (2014).
64. G. Buscher, A. Dengel and L. van Elst, Eye movements as implicit relevance feedback, in *CHI'08 extended abstracts on Human factors in computing systems*, 2008 pp. 2991–2996.
65. F. Pedregosa, G. Varoquaux, A. Gramfort, V. Michel, B. Thirion, O. Grisel, M. Blondel, P. Prettenhofer, R. Weiss, V. Dubourg *et al.*, Scikit-learn: Machine learning in python, *the Journal of machine Learning research* **12**, 2825 (2011).

Automated Chest X-ray Report Generation Remains Unsolved

Xiaoman Zhang[1], Julian Nicolas Acosta[1], Xiaoli Yang[1], Subathra Adithan[1], Luyang Luo[1], Hong-Yu Zhou[1], Joshua Miller[2], Ouwen Huang[2,3,4], Zongwei Zhou[5], Ibrahim Ethem Hamamci[6], Shruthi Bannur[7], Kenza Bouzid[7], Xi Zhang[8], Zaiqiao Meng[8], Aaron Nicolson[9], Bevan Koopman[9], Inhyeok Baek[10], Hanbin Ko[11], Mercy Prasanna Ranjit[12], Shaury Srivastav[12], Sriram Gnana Sambanthan[13] and Pranav Rajpurkar[1]

[1]*Department of Biomedical Informatics, Harvard Medical School, Boston, MA, USA*

[2]*Gradient Health, Durham, NC, USA*

[3]*Department of Statistical Science, Duke University, Durham, NC, USA*

[4]*Laplace Institute, Durham, NC, USA*

[5]*Department of Computer Science, Johns Hopkins University, MD, USA*

[6]*University of Zurich, Switzerland*

[7]*Microsoft Research Health Futures, USA*

[8]*University of Glasgow, UK*

[9]*Australian e-Health Research Centre, CSIRO Health and Biosecurity, Brisbane, Australia*

[10]*Seoul National University, South Korea*

[11]*Seoul National University Graduate School, South Korea*

[12]*Microsoft Research India, India*

[13]*Indian Institute of Technology Madras, Chennai, India*

Accurate interpretation of chest radiograph images and generation of narrative reports is essential for patient care but places a heavy burden on radiologists and clinical experts. While AI models for automated report generation show promise, standardized evaluation frameworks remain limited. Here we present the ReXrank Challenge V1.0, a competition in the generation of chest radiograph reports utilizing ReXGradient, the largest test dataset consisting of **10,000** studies across 67 sites. The challenge attracted diverse participants from academic institutions, industry, and independent research teams, resulting in 8 new submissions alongside 16 state-of-the-art models previously benchmarked. Through comprehensive evaluation using multiple metrics, we analyzed model performance across various dimen-

© 2025 The Authors. Open Access chapter published by World Scientific Publishing Company and distributed under the terms of the Creative Commons Attribution Non-Commercial (CC BY-NC) 4.0 License.

sions: differences between normal and abnormal studies, generalization capabilities across healthcare sites, and error rates in identifying clinical findings. This benchmark reveals that automated chest X-ray report generation remains fundamentally unsolved, with significant performance gaps between normal and abnormal studies, where even top-performing models achieve less than 45% error-free reporting on abnormal cases, and substantial variability across healthcare institutions, indicating that robust, clinically-ready systems require continued development before widespread deployment.

Keywords: Radiology Report Generation; Benchmark.

1. Introduction

Automating radiology report generation has the potential to dramatically improve clinical workflow efficiency, reduce reporting delays, and ensure consistent quality in radiology services in diverse healthcare settings.[1,2] However, creating AI systems that can match the accuracy and nuance of expert radiologists requires overcoming substantial technical and clinical hurdles.

Previous approaches to automated radiology report generation have shown promise, but have not yet achieved the reliability required for widespread clinical applications.[3,4] The field faces several critical obstacles to progress. Existing model comparisons typically employ inconsistent data splits and lack standardized evaluation metrics, preventing reliable comparative analysis across different model architectures. Additionally, commonly used public datasets often serve dual purposes as both training and evaluation data, failing to adequately test the models' ability to generalize to new, unseen distributions.[5–7] To address these challenges, a standardized evaluation framework called ReXrank[8] was recently proposed, establishing a common benchmark for 16 state-of-the-art models across identical evaluation settings. Although this initiative represents an important step forward, further work is needed to push the domain toward clinical applicability.

To further advance the field, we hosted the **ReXrank Challenge V1.0**, a comprehensive competition to evaluate AI-powered chest X-ray report generation models, which ran from December 1, 2024, to March 15, 2025. This challenge builds on the foundation of the ReXrank leaderboard, 8 new submissions were received during the challenge period, each employing distinctive approaches and training sets to the task of generating accurate and clinically relevant radiology reports from chest radiographs. These submissions, along with 16 state-of-the-art models previously benchmarked in the initial ReXrank evaluation, were evaluated as part of the ReXrank Challenge V1.0

In this paper, we present results from the ReXrank Challenge V1.0, providing a comprehensive benchmark for AI-powered chest X-ray report generation. We evaluated all participating models using an expanded set of metrics that included traditional measures (BLEU,[9] BertScore,[10] SembScore,[11] RadGraph,[12] RadCliQ,[12] RaTEScore[13]) as well as newer LLM-based metrics (GREEN,[14] FineRadScore[15]). We perform detailed analyses of model performance across various clinically relevant dimensions, including normal and abnormal studies, performance variations across different medical sites, and error patterns of the model's prediction. These stratified evaluations provide critical insight into the real-world applicability of these models and highlight areas where further development is needed.

Our comprehensive benchmark provides several key insights for medical ML applications:

- Top models achieving over 80-90% no significant error rates on normal studies while struggling with abnormal cases (MedVersa leading with 43.32% no significant error rate but only 11.70% no actionable error rate). This substantial performance gap highlights that automated radiology report generation remains an unsolved problem, particularly for clinically significant abnormal findings.
- Model performance varies dramatically across different healthcare sites, even for top-performing models such as MedVersa, MAIRA-2 and Libra, indicating that achieving robust cross-institutional generalization remains a significant challenge that requires diverse training data and targeted adaptation techniques.
- Current evaluation metrics show low consistency, especially traditional metrics that correlate poorly with newer LLM-based metrics, highlighting the need for evaluation approaches that better align with clinical needs.

2. Related Work

The automated generation of radiology reports has emerged as a significant research area addressing the growing demand for imaging services that exceeds radiologist capacity. The field has evolved from recurrent neural networks to Transformer-based architectures,[5] with recent systems incorporating LLMs such as LLaMA[16] and Vicuna-7B.[17] Non-LLM approaches include BiomedGPT,[18] CheXpertPlus,[6] CvT2DistilGPT2,[19] and RGRG,[20] while LLM-based systems like CheXagent,[21] RaDialog,[22] MAIRA-2,[4] MedVersa,[23] RadFM,[24] and Libra[25] have transformed the field through visual instruction tuning. The evaluation of automated radiology reports presents unique challenges, as traditional natural language generation metrics do not account for clinical significance. Specialized metrics have been developed, including CheXbert,[11] which evaluates reports based on the presence of specific pathologies, and RadGraph-F1,[12] which measures the overlap in clinical entities and relations between generated and reference reports. More recently, ReXrank[8] has been introduced as a public leaderboard and challenge for assessing AI-powered radiology report generation. ReXrank incorporates various datasets, including MIMIC-CXR,[26] IU-Xray,[27] and CheXpert Plus,[6] and employs eight different evaluation metrics to provide a comprehensive assessment of model performance.

3. Overview

3.1. *Challenge Design*

The ReXrank Challenge, which ran from December 1, 2024, to March 15, 2025, was designed as a comprehensive competition for evaluating AI-powered chest X-ray report generation models. This challenge aimed to benchmark model performance across multiple critical dimensions, including linguistic quality, clinical accuracy, and generalization capability across diverse clinical settings.

3.2. *Datasets*

The ReXrank Challenge leveraged both public and private datasets for robust report generation assessment. The private ReXGradient dataset, comprising 10,000 studies collected from 67 U.S. medical institutions, represents one of the largest and most geographically diverse evaluation sets available. For public evaluation, we utilized the official test splits of MIMIC-CXR (2,347 studies)[26] and IU-Xray (590 studies),[27] along with CheXpert Plus's validation set (200 studies),[6] as no official test split was available. Each study may contain multiple images, all of which were utilized in our evaluation. We specifically focused on the generation of "Findings" section of reports and filtered out any reports that lacked this section, reducing the CheXpert Plus evaluation set to 62 studies with available findings sections.

3.3. *Models*

During the challenge period, we received 8 model submissions from 5 institutions, including Libra,[25] CXRMate,[28] CXRMate-ED,[29] CXRMate-RRG24,[30] RadPhi3.5Vision,[31] DD-LLaVA-X, MoERad-IU, and MoERad-MIMIC. We compared these submissions with **16** previously benchmarked report generation models from 10 different institutions:[8] BiomedGPT-IU,[32] CheXagent,[21] CheXpertPlus-CheX,[6] CheXpertPlus-CheX-MIMIC,[6] CheXpertPlus-MIMIC,[6] CvT2DistilGPT2-IU,[5] CvT2DistilGPT2-MIMIC,[5] GPT4V,[33] LLM-CXR,[34] MAIRA-2,[4] MedVersa,[23] RadFM,[24] RaDialog,[22] RGRG,[20] VLCI-IU,[7] and VLCI-MIMIC.[7] The detailed evaluation setup of each models can be found in the appendix.

3.4. *Metrics*

The ReXrank Challenge employed **8** distinct metrics to comprehensively assess the quality of generated radiology reports. These included traditional text generation metrics such as BLEU-2[9] and BERTScore,[10] alongside domain-specific metrics designed for radiology report evaluation, including SembScore,[11] RadGraph-F1,[35] RadCliQ-v1,[35] and RaTEScore.[13] The framework also incorporated recently developed LLM-based metrics, including GREEN,[14] FineRadScore,[15] which focus on identifying clinically significant errors. Each metric evaluated different aspects of the generated reports, from textual similarity to clinical accuracy, enabling a thorough and multifaceted assessment of model performance. The detailed information can be found in the appendix.

4. Results

4.1. *Model Results Summary*

The comprehensive evaluation across multiple datasets revealed several key insights about current chest X-ray report generation capabilities. No single model dominated across all metrics, suggesting that different evaluation metrics capture complementary aspects of report quality from linguistic similarity (BLEU, BertScore) to clinical accuracy (SembScore, RadCliQ-V1, RadGraph, RATEScore) and error detection (FineRadScore, GREEN). MedVersa emerged as the top-performing model on both ReXGradient and MIMIC-CXR datasets, achieving the

highest 1/FineRadScore (0.475 and 0.365, respectively) and excelling in multiple metrics including BertScore and SembScore. On the IU-Xray dataset, CheXpertPlus-MIMIC achieved the highest 1/FineRadScore (0.622), while CXRMate-ED led on the CheXpert Plus dataset (0.367). Among the newly submitted models, Libra and CXRMate-ED demonstrated strong performance, with Libra achieving the highest BLEU score (0.246) on MIMIC-CXR and CXRMate-ED showing remarkable consistency across diverse institutional datasets. MoERad-IU excelled on the IU-Xray dataset, achieving the highest scores in BLEU (0.277), SembScore (0.641), RadGraph (0.341), and 1/RadCliQ-V1 (1.922). Notably, specialist models trained on specific datasets generally performed best on their corresponding test sets, highlighting the challenge of developing models that generalize across institutions.

Table 1. Comprehensive evaluation of medical report generation models on ReXGradient. Models are ranked by 1/FineRadScore. The best results for each metric are shown in **bold** (n=10,000).

Model-Name	BLEU	BertScore	SembScore	RadGraph	1/RadCliQ-V1	RATEScore	GREEN	1/FineRadScore
MedVersa	0.210	0.431	**0.498**	0.202	1.008	0.527	0.532	**0.475**
MAIRA-2	0.205	**0.436**	0.462	0.187	0.963	0.559	0.531	**0.475**
Libra	0.176	0.408	0.474	0.169	0.913	0.544	0.549	0.473
CXRMate-ED	0.202	0.398	0.415	0.187	0.872	0.564	0.518	0.472
CheXpertPlus-MIMIC	0.154	0.341	0.440	0.131	0.778	0.501	0.517	0.471
MoERad-IU	**0.227**	0.434	0.446	**0.247**	**1.018**	**0.575**	0.494	0.468
CvT2DistilGPT2-MIMIC	0.186	0.374	0.458	0.175	0.866	0.522	0.510	0.468
CXRMate	0.169	0.363	0.479	0.174	0.863	0.545	**0.550**	0.466
CheXpertPlus-CheX-MIMIC	0.169	0.372	0.440	0.153	0.828	0.516	0.486	0.463
DD-LLaVA-X	0.166	0.387	0.469	0.174	0.886	0.542	0.504	0.459
CXRMate-RRG24	0.150	0.327	0.462	0.152	0.792	0.518	0.408	0.458
RadPhi3.5Vision	0.209	0.383	0.488	0.169	0.891	0.544	0.453	0.458
RGRG	0.190	0.391	0.470	0.169	0.888	0.540	0.487	0.458
CvT2DistilGPT2-IU	0.176	0.394	0.405	0.166	0.839	0.518	0.467	0.456
CheXagent	0.093	0.305	0.366	0.080	0.674	0.428	0.241	0.455
RaDialog	0.188	0.402	0.450	0.158	0.876	0.522	0.435	0.454
VLCI-MIMIC	0.158	0.310	0.400	0.122	0.720	0.487	0.473	0.453
VLCI-IU	0.214	0.365	0.466	0.213	0.894	0.571	0.532	0.451
BioMedGPT-IU	0.099	0.317	0.437	0.157	0.771	0.472	0.388	0.450
MoERad-MIMIC	0.145	0.351	0.406	0.116	0.756	0.508	0.431	0.446
RadFM	0.157	0.365	0.392	0.135	0.775	0.504	0.406	0.437
GPT4V	0.075	0.214	0.337	0.138	0.629	0.470	0.497	0.428
CheXpertPlus-CheX	0.144	0.361	0.428	0.124	0.785	0.475	0.407	0.414
LLM-CXR	0.043	0.182	0.142	0.029	0.507	0.317	0.044	0.326

4.2. *Performance Comparison Across Normal and Abnormal Studies*

Our analysis of model performance on the ReXGradient dataset reveals significant differences when comparing normal versus abnormal chest X-ray studies. The results are summarized in the Appendix tables. For abnormal studies, MedVersa emerged as the top-performing model, achieving the highest scores in SembScore (0.425), RadGraph (0.169), 1/RadCliQ-v1 (0.856), and 1/FineRadScore (0.396). This suggests MedVersa has superior capability in detecting and describing pathological findings, which is critical for clinical utility. In normal studies, MAIRA-2 achieved the highest 1/FineRadScore (0.734), indicating strong clinical accuracy with minimal required corrections, and it ranked 4th in abnormal studies with 1/FineRadScore (0.392). Models like MoERad-IU demonstrated superior performance across multiple metrics for normal studies, achieving the highest scores in BLEU (0.353), BertScore (0.532), RadGraph (0.367), 1/RadCliQ-v1 (2.061), and RATEScore (0.710). While for abnormal studies,

Table 2. Comprehensive evaluation of medical report generation models on MIMIC-CXR. Models are ranked by 1/FineRadScore. The best results for each metric are shown in **bold**($n = 2,347$).

Model-Name	BLEU	BertScore	SembScore	RadGraph	1/RadCliQ-V1	RATEScore	GREEN	1/FineRadScore
MedVersa	0.209	**0.448**	**0.466**	**0.273**	**1.103**	**0.550**	**0.374**	**0.365**
CheXpertPlus-MIMIC	0.145	0.361	0.375	0.170	0.788	0.485	0.311	0.363
CheXpertPlus-CheX-MIMIC	0.142	0.367	0.379	0.181	0.805	0.490	0.305	0.363
CvT2DistilGPT2-MIMIC	0.126	0.331	0.329	0.149	0.719	0.432	0.268	0.362
Libra	**0.246**	0.431	0.405	0.222	0.944	0.529	0.351	0.362
CXRMate	0.198	0.367	0.423	0.220	0.870	0.521	0.338	0.362
DD-LLaVA-X	0.154	0.348	0.402	0.182	0.801	0.505	0.301	0.361
RaDialog	0.127	0.363	0.387	0.172	0.799	0.485	0.273	0.359
MAIRA-2	0.088	0.308	0.339	0.131	0.694	0.517	0.224	0.359
CXRMate-RRG24	0.198	0.367	0.423	0.220	0.870	0.521	0.338	0.359
CXRMate-ED	0.208	0.383	0.396	0.223	0.872	0.531	0.327	0.358
VLCI-MIMIC	0.136	0.304	0.305	0.140	0.680	0.450	0.256	0.357
RadPhi3.5Vision	0.223	0.386	0.431	0.207	0.888	0.534	0.294	0.356
CheXagent	0.113	0.346	0.347	0.148	0.741	0.474	0.257	0.355
MoERad-MIMIC	0.163	0.341	0.334	0.143	0.726	0.465	0.240	0.354
RGRG	0.130	0.348	0.344	0.168	0.755	0.491	0.273	0.352
CheXpertPlus-CheX	0.077	0.314	0.325	0.142	0.698	0.469	0.225	0.351
RadFM	0.087	0.313	0.259	0.109	0.650	0.450	0.185	0.351
VLCI-IU	0.075	0.263	0.212	0.109	0.599	0.449	0.210	0.347
CvT2DistilGPT2-IU	0.055	0.303	0.191	0.103	0.613	0.448	0.164	0.347
MoERad-IU	0.064	0.321	0.213	0.122	0.643	0.455	0.174	0.347
GPT4V	0.068	0.207	0.214	0.084	0.558	0.423	0.161	0.343
BioMedGPT-IU	0.020	0.192	0.224	0.059	0.544	0.360	0.123	0.341
LLM-CXR	0.037	0.181	0.156	0.046	0.516	0.341	0.043	0.307

Table 3. Comprehensive evaluation of medical report generation models on IU-Xray. Models are ranked by 1/FineRadScore. The best results for each metric are shown in **bold** ($n = 590$).

Model-Name	BLEU	BertScore	SembScore	RadGraph	1/RadCliQ-V1	RATEScore	GREEN	1/FineRadScore
CheXpertPlus-MIMIC	0.178	0.386	0.593	0.169	0.988	0.585	0.661	**0.622**
CvT2DistilGPT2-MIMIC	0.199	0.422	0.609	0.209	1.126	0.606	0.682	0.608
MAIRA-2	0.219	0.477	0.604	0.233	1.298	0.627	0.194	0.599
CXRMate-RRG24	0.245	0.456	0.638	0.302	1.458	0.666	0.680	0.598
CXRMate-ED	0.225	0.464	0.557	0.249	1.220	0.655	0.685	0.597
RGRG	0.216	0.437	0.602	0.223	1.174	0.620	0.665	0.596
Libra	0.192	0.461	0.616	0.210	1.226	0.623	0.674	0.593
MoERad-IU	**0.277**	0.525	**0.641**	**0.341**	**1.922**	**0.684**	0.665	0.587
MoERad-MIMIC	0.171	0.420	0.559	0.178	1.020	0.603	0.584	0.579
CheXpertPlus-CheX-MIMIC	0.198	0.453	0.593	0.211	1.179	0.618	0.648	0.576
DD-LLaVA-X	0.189	0.443	0.600	0.233	1.204	0.636	0.671	0.574
CheXagent	0.116	0.353	0.488	0.139	0.827	0.503	0.389	0.574
RadFM	0.200	0.459	0.566	0.230	1.187	0.627	0.615	0.572
MedVersa	0.206	**0.527**	0.606	0.235	1.460	0.650	0.631	0.569
CXRMate	0.181	0.418	0.625	0.213	1.146	0.637	**0.730**	0.565
CvT2DistilGPT2-IU	0.244	0.482	0.548	0.265	1.283	0.620	0.686	0.563
RadPhi3.5Vision	0.248	0.433	0.607	0.220	1.166	0.634	0.597	0.552
VLCI-IU	0.268	0.455	0.619	0.288	1.381	0.679	0.698	0.551
GPT4V	0.076	0.274	0.405	0.146	0.708	0.517	0.651	0.550
CheXpertPlus-CheX	0.157	0.413	0.495	0.153	0.920	0.534	0.541	0.548
BioMedGPT-IU	0.142	0.375	0.522	0.213	0.956	0.543	0.523	0.543
RaDialog	0.201	0.444	0.544	0.205	1.086	0.586	0.586	0.543
VLCI-MIMIC	0.139	0.364	0.483	0.220	0.913	0.578	0.474	0.488
LLM-CXR	0.033	0.186	0.057	0.023	0.486	0.280	0.025	0.302

it ranked 13th with a 1/FineRadScore of 0.379 and a 1/RadCliQ-v1 score of 0.755, showing a substantial performance drop when handling pathological cases. Most models performed substantially better on normal cases compared to abnormal ones, with average 1/RadCliQ-v1 scores approximately 40-50% higher for normal studies. This pattern is consistent with pre-

Table 4. Comprehensive evaluation of medical report generation models on CheXpert Plus. Models are ranked by 1/FineRadScore. The best results for each metric are shown in **bold** ($n = 62$).

Model-Name	BLEU	BertScore	SembScore	RadGraph	1/RadCliQ-V1	RATEScore	GREEN	1/FineRadScore
CXRMate-ED	0.157	0.324	0.316	0.175	0.723	0.498	0.265	**0.367**
RadPhi3.5Vision	**0.198**	0.353	**0.437**	0.217	**0.860**	0.510	0.243	0.356
MAIRA-2	0.163	**0.359**	0.355	0.189	0.788	0.485	0.273	0.352
CXRMate-RRG24	0.157	0.315	0.411	**0.218**	0.801	**0.521**	**0.276**	0.350
CheXpertPlus-CheX-MIMIC	0.153	0.335	0.404	0.207	0.808	0.497	0.274	0.348
CXRMate	0.135	0.289	0.327	0.138	0.678	0.425	0.235	0.348
CvT2DistilGPT2-MIMIC	0.124	0.267	0.266	0.119	0.626	0.420	0.215	0.346
CheXpertPlus-MIMIC	0.140	0.292	0.294	0.134	0.663	0.430	0.238	0.344
Libra	0.165	0.343	0.318	0.171	0.738	0.477	0.265	0.344
DD-LLaVA-X	0.085	0.318	0.385	0.172	0.753	0.476	0.206	0.343
MoERad-MIMIC	0.122	0.267	0.300	0.120	0.641	0.434	0.166	0.343
CheXpertPlus-CheX	0.150	0.342	0.377	0.191	0.786	0.487	0.237	0.343
MedVersa	0.129	0.323	0.344	0.147	0.719	0.470	0.243	0.343
CheXagent	0.123	0.278	0.269	0.125	0.638	0.434	0.183	0.341
MoERad-IU	0.075	0.284	0.175	0.102	0.595	0.390	0.127	0.341
VLCI-IU	0.106	0.220	0.170	0.094	0.555	0.418	0.194	0.339
GPT4V	0.081	0.215	0.234	0.082	0.568	0.415	0.152	0.339
RGRG	0.154	0.315	0.274	0.140	0.674	0.453	0.216	0.337
RadFM	0.081	0.235	0.216	0.080	0.572	0.396	0.096	0.333
RaDialog	0.131	0.312	0.353	0.138	0.709	0.445	0.211	0.333
CvT2DistilGPT2-IU	0.084	0.267	0.155	0.098	0.577	0.382	0.147	0.332
VLCI-MIMIC	0.120	0.229	0.251	0.101	0.589	0.384	0.165	0.330
BioMedGPT-IU	0.022	0.200	0.241	0.056	0.552	0.351	0.118	0.320
LLM-CXR	0.041	0.162	0.211	0.037	0.519	0.321	0.022	0.291

vious research showing that AI systems typically find it easier to describe normal anatomical structures than to detect and characterize pathological findings.

4.3. *Error Rates Analysis Across Normal and Abnormal Studies*

Figure 1 presents a comprehensive comparison of error rates across multiple AI models when generating radiology reports for both abnormal and normal chest X-ray studies from the ReXGradient dataset. The visualization reveals several important patterns. All models demonstrate significantly higher no actionable error rates for normal studies compared to abnormal ones, with most models achieving 60-75% no actionable error rates for normal studies but only 5-15% for abnormal studies. For abnormal studies, MedVersa performs best with a 43.32% no significant error rate, closely followed by CXRMate-ED (43.05%) and MAIRA-2 (41.98%). However, when examining the no actionable error rate (dark blue bars), these values drop dramatically to only 11.70%, 13.00%, and 10.78% respectively, highlighting how frequently these models make at least some errors in abnormal cases. Performance on normal studies is consistently stronger across all models. MAIRA-2 achieves the highest no significant error rate at 91.95%, followed by Libra (89.10%) and MedVersa (89.01%). The no-error rates for normal studies are also substantially higher, with many models exceeding 60-70%. There's considerable variability in model performance rankings between abnormal and normal categories. While some models like MedVersa and MAIRA-2 maintain strong performance in both categories, others show notable differences. For instance, MoERad-IU performs relatively well on normal studies (90.21% no significant error rate) but drops significantly for abnormal studies (38.06%). This analysis underscores the persistent challenge in developing AI systems that can accurately report abnormal findings in chest X-rays.

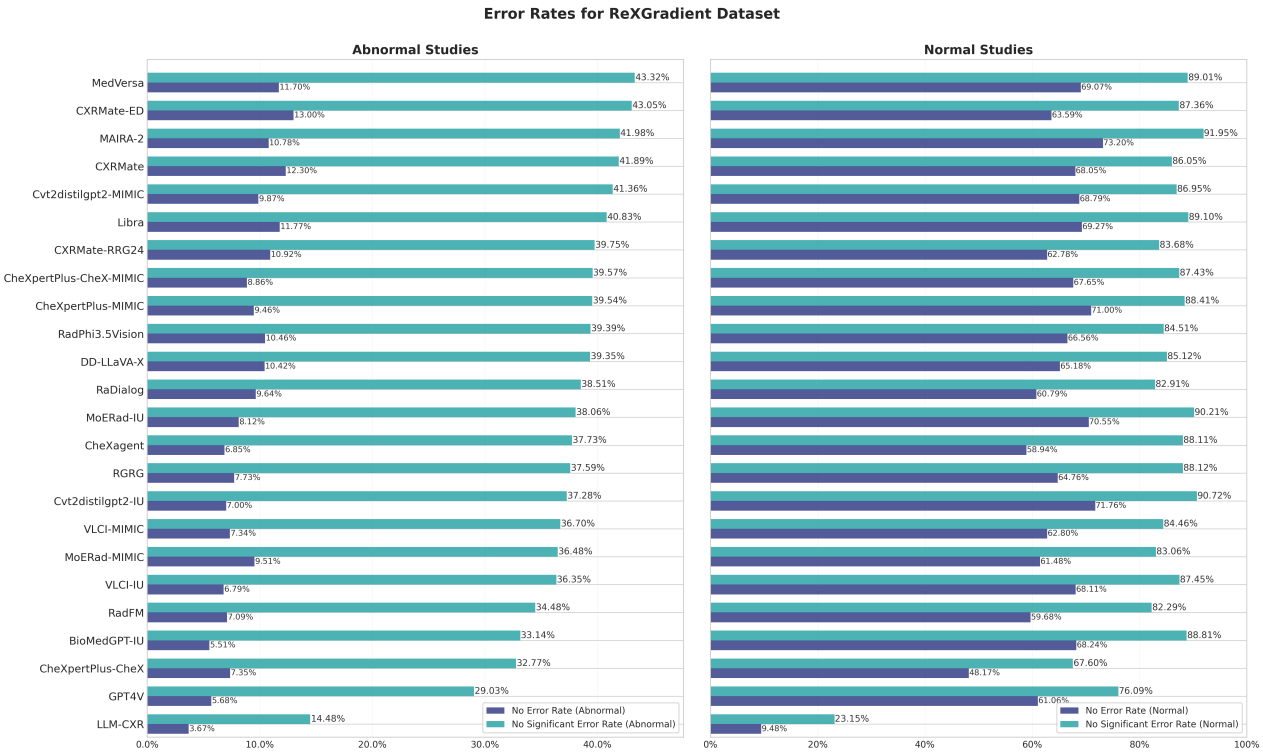

Fig. 1. Comparison of error rates for AI-generated radiology reports on the ReXGradient Dataset. The chart shows no-actionable-error rates (dark blue) and no-significant-error rates (teal) for both abnormal studies (left) and normal studies (right).

4.4. *Analysis of Results on Different Sites*

Figure 2 shows model performance variability across the 30 different healthcare sites represented in the ReXGradient dataset. As shown, MAIRA-2 and Libra demonstrate the most robust performance across sites, ranking in the top positions for the majority of sites. MAIRA-2 particularly excels, achieving first place in 8 sites and rarely falling below 6th place except for a few outliers. CheXpertPlus-MIMIC and MedVersa show generally strong performance but with noticeable variability. MedVersa, for instance, ranks first in several sites (particularly sites 1, 14, 19) but unexpectedly drops to much lower rankings (17th, 19th, 20th) in others (sites 10, 22, 28). The considerable performance fluctuation of models across different sites highlights the challenge of developing AI systems that generalize well across diverse clinical settings. For example, CXRMate performs excellently in some sites (ranked 1st in sites 4, 14, 16) but poorly in others (21st in institution 26). The substantial rank variability for most models (except the very top and bottom performers) suggests that current AI approaches for radiology report generation face significant challenges in generalizing across different institutional data distributions, which may reflect variations in patient demographics, imaging protocols, or radiologist reporting styles. Some models show similar performance patterns across certain groups of sites, potentially indicating similarities in those sites' data characteristics. For example, MAIRA-2 performs particularly well in sites 0-6 but shows more variable performance in sites 10-15. This analysis underscores the importance of evaluating AI models

across diverse institutional datasets before deployment in clinical settings, as performance can vary dramatically depending on the specific healthcare environment.

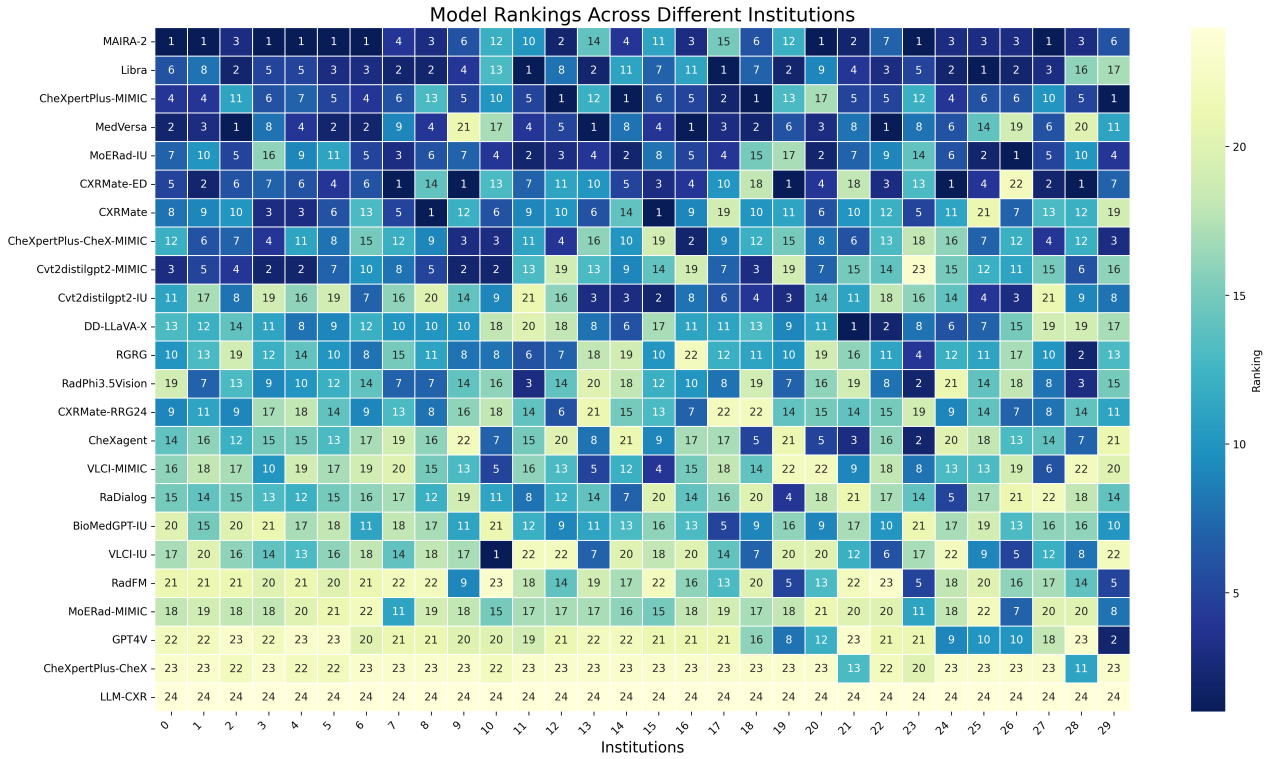

Fig. 2. Model Rankings Across Different Sites. The heatmap displays the performance ranking of 24 AI models (rows) across top 30 different healthcare sites (columns) in the ReXGradient dataset, with darker blue representing better rankings (1 being the best).

4.5. *Analysis of Current Evaluation Metrics*

Our analysis of the correlation between different evaluation metrics across multiple chest X-ray datasets reveals important insights about their relationships and potential redundancies. Figure 3 presents the correlation matrices for ReXGradient, MIMIC-CXR, IU X-ray, and CheXpert Plus datasets. We observe strong positive correlations (>0.75) between traditional text matching and NER-based metrics, particularly between BertScore and 1/RadCliQ-v1 (0.90), as well as between RadGraph and 1/RadCliQ-v1 (0.84) on IU X-ray. This suggests these conventional metrics may capture similar aspects of report quality. However, the LLM-based metrics, GREEN and 1/FineRadScore, show weaker correlations with traditional metrics (mostly < 0.60) and moderate correlation with each other (0.59), suggesting they capture unique dimensions of report quality that text matching and NER-based approaches miss. Notably, correlation patterns remain remarkably consistent across all four datasets, indicating the robustness of these relationships regardless of the data source. These findings highlight the complementary nature of LLM-based and traditional evaluation approaches, suggesting that comprehensive assessment of radiology reports requires metrics from both categories.

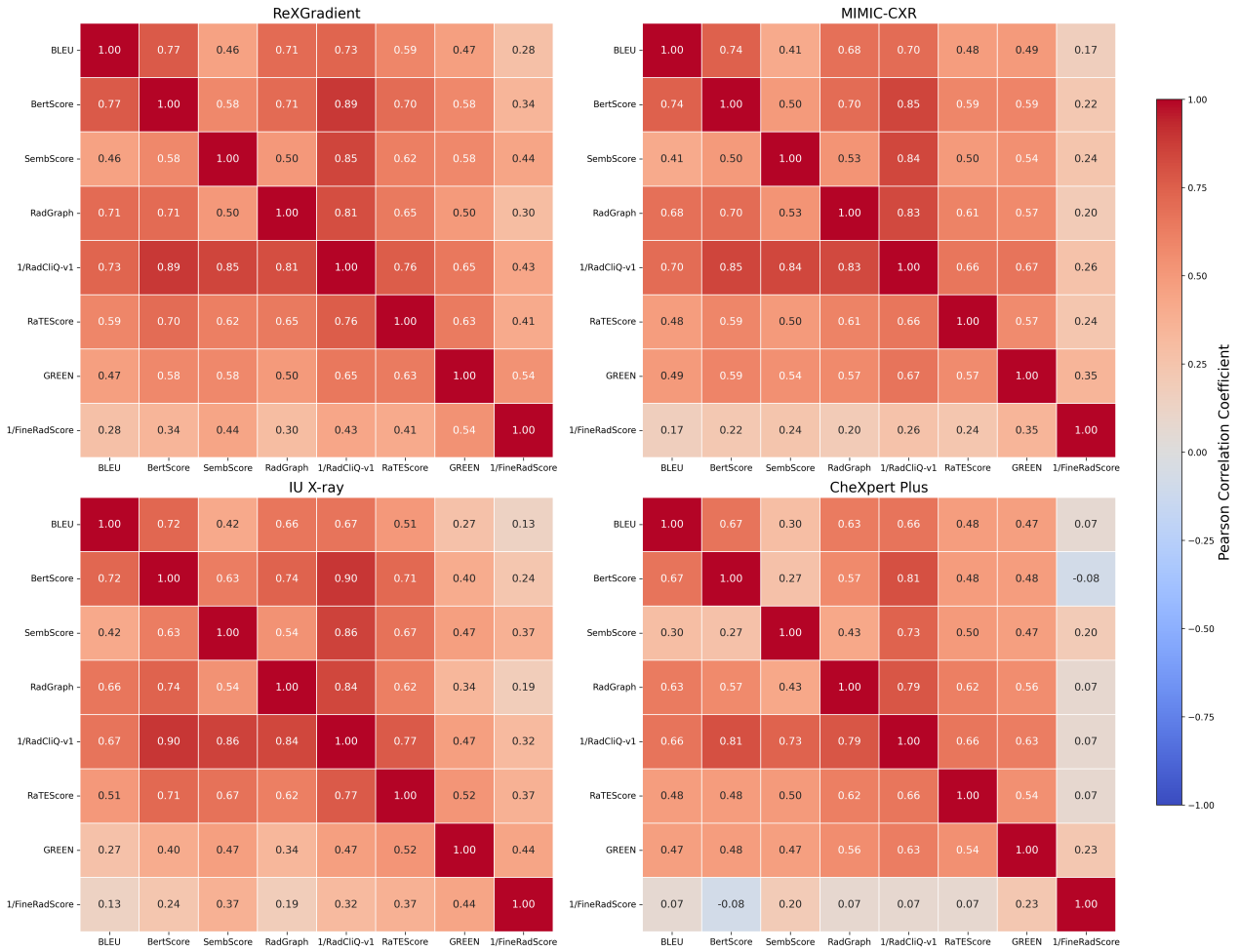

Fig. 3. Pearson correlation coefficients between eight evaluation metrics for the ReXGradient, MIMIC-CXR, IU X-ray, and CheXpert Plus datasets.

5. Discussion

Our comprehensive evaluation of AI-powered chest X-ray report generation models offers important insights into the current state of automated radiology reporting and reveals several key implications for both technical development and clinical implementation. The ReXrank Challenge demonstrates substantial progress in the field, with top-performing models like MedVersa, MAIRA-2, and Libra achieving impressive metrics across diverse institutional datasets. However, the significant performance gap between normal and abnormal studies—with even the best models showing no significant error rates below 45% for abnormal cases compared to over 90% for normal studies, highlights a fundamental challenge: current AI systems excel at identifying normal studies but struggle significantly with accurate pathology detection and characterization.

Technical Implications. Our analysis of model performance across multiple healthcare sites reveals substantial variability, with most models showing inconsistent rankings across different sites. This finding underscores the critical importance of developing robust cross-institutional generalization capabilities. Models trained on diverse datasets (e.g., MedVersa, MAIRA-2) demonstrated more consistent performance compared to those trained on homogeneous datasets (e.g., Libra), suggesting that exposure to varied reporting styles and patient populations may improve generalization. Our evaluation metric analysis reveals important insights for model assessment. The relatively weak correlation between LLM-based metrics (GREEN, FineRadScore) and general lexical metrics (BLEU, BERTScore) suggests they capture complementary aspects of report quality. This reveals a significant limitation of general lexical metrics that prioritize stylistic consistency over clinical accuracy. There remains substantial room for improvement in developing metrics that better align with clinical needs, such as HeadCT-ONE,[36] which utilizes ontology normalization to make evaluation more robust to variations in radiological language while allowing customizable weighting of different clinical entities.

Clinical Implications. The observed error rates, particularly in abnormal studies where fewer than 45% of cases are error-free, indicate that the technology is not yet ready for fully autonomous reporting. Nevertheless, these models show considerable promise as assistive tools that can generate preliminary report drafts for radiologist verification and refinement. This collaborative approach has the potential to simultaneously reduce radiologist workload and enhance clinical accuracy, as multiple recent studies have substantiated .[3,37,38]

Future Directions Our findings suggest several promising directions for advancing automated radiology report generation:

- **Improving abnormality detection.** Future research should focus specifically on enhancing model performance for abnormal studies, perhaps through preference fine-tuning,[39] or two-stage approaches combining classification/segmentation with report generation.[40]
- **Cross-institutional robustness:** Developing techniques to improve generalization across diverse clinical settings represents a critical research priority. This might include domain adaptation methods, adversarial training to reduce institutional bias, or federated learning approaches that preserve privacy while leveraging multi-institutional data.[41] Initiatives such as MAIDA,[42] which coordinates data sharing from 69 hospitals across 28 countries, offer promising frameworks for collaborative data sharing that could help address these challenges while ensuring diverse representation across global healthcare environments.
- **Enhanced evaluation frameworks:** The complementary nature of different evaluation metrics suggests value in developing more comprehensive assessment frameworks that combine strengths of traditional and LLM-based approaches while addressing their respective limitations.

- **Human-AI collaboration:** Given the performance gap between normal and abnormal cases, research into effective human-AI collaboration workflows could help optimize the clinical utility of these systems while ensuring patient safety.

Limitations. Our study has several important limitations to consider. First, while ReXGradient represents one of the largest and most diverse evaluation datasets to date, it still cannot fully capture the heterogeneity of chest X-ray imaging and reporting practices globally. Cultural and regional variations in radiology practice may impact the generalizability of our findings. Second, our evaluation framework did not systematically account for the presence of prior studies. Some models are designed to incorporate prior imaging and reports as additional context, but our standardized evaluation did not consistently leverage this capability across all models. Additionally, ground truth reports often contain references to prior studies and temporal changes that may be difficult for models to generate without access to the relevant prior information. This limitation may disadvantage models designed to utilize longitudinal data and could explain some performance variations across different clinical scenarios. Third, our evaluation relied on comparing AI-generated reports to human-written references, which inherently assumes that the reference reports are optimal. However, inter-radiologist variability in reporting style and content means that valid alternative phrasings or observations might be unfairly penalized by reference-based metrics. Fourth, while we employed multiple evaluation metrics to assess different aspects of report quality, these metrics cannot fully capture the clinical utility of generated reports. Important factors like actionability, clinical relevance, and communication effectiveness are challenging to quantify with automated metrics. Finally, our analysis focused on English-language reports, limiting generalizability to non-English healthcare settings. Language-specific nuances and reporting conventions may impact both model performance and metric reliability in other languages. Despite these limitations, the ReXrank Challenge provides valuable insights into the current capabilities and limitations of AI-powered chest X-ray report generation, establishing important benchmarks and highlighting critical areas for future research and development.

Acknowledgement

This work was supported by the Biswas Family Foundation's Transformative Computational Biology Grant in Collaboration with the Milken Institute.

References

1. V. M. Rao, M. Hla, M. Moor, S. Adithan, S. Kwak, E. J. Topol and P. Rajpurkar, Multimodal generative ai for medical image interpretation, *Nature* **639**, 888 (2025).
2. M. Moor, O. Banerjee, Z. S. H. Abad, H. M. Krumholz, J. Leskovec, E. J. Topol and P. Rajpurkar, Foundation models for generalist medical artificial intelligence, *Nature* **616**, 259 (2023).
3. R. Tanno, D. G. Barrett, A. Sellergren, S. Ghaisas, S. Dathathri, A. See, J. Welbl, C. Lau, T. Tu, S. Azizi *et al.*, Collaboration between clinicians and vision–language models in radiology report generation, *Nature Medicine* **31**, 599 (2025).
4. S. Bannur, K. Bouzid, D. C. Castro, A. Schwaighofer, S. Bond-Taylor, M. Ilse, F. Pérez-García, V. Salvatelli, H. Sharma, F. Meissen *et al.*, Maira-2: Grounded radiology report generation, *arXiv preprint arXiv:2406.04449* (2024).

5. A. Nicolson, J. Dowling and B. Koopman, Improving chest x-ray report generation by leveraging warm starting, *Artificial intelligence in medicine* **144**, p. 102633 (2023).
6. P. Chambon, J.-B. Delbrouck, T. Sounack, S.-C. Huang, Z. Chen, M. Varma, S. Q. Truong, C. T. Chuong and C. P. Langlotz, Chexpert plus: Hundreds of thousands of aligned radiology texts, images and patients, *arXiv preprint arXiv:2405.19538* (2024).
7. W. Chen, Y. Liu, C. Wang, J. Zhu, S. Zhao, G. Li, C.-L. Liu and L. Lin, Cross-modal causal intervention for medical report generation, *arXiv preprint arXiv:2303.09117* (2023).
8. X. Zhang, H.-Y. Zhou, X. Yang, O. Banerjee, J. N. Acosta, J. Miller, O. Huang and P. Rajpurkar, Rexrank: A public leaderboard for ai-powered radiology report generation, *arXiv preprint arXiv:2411.15122* (2024).
9. K. Papineni, S. Roukos, T. Ward and W.-J. Zhu, Bleu: a method for automatic evaluation of machine translation, in *Proceedings of the 40th annual meeting of the Association for Computational Linguistics*, (Association for Computational Linguistics, 2002).
10. T. Zhang, V. Kishore, F. Wu, K. Q. Weinberger and Y. Artzi, Bertscore: Evaluating text generation with bert, *arXiv preprint arXiv:1904.09675* (2019).
11. A. Smit, S. Jain, P. Rajpurkar, A. Pareek, A. Y. Ng and M. P. Lungren, Chexbert: combining automatic labelers and expert annotations for accurate radiology report labeling using bert, *arXiv preprint arXiv:2004.09167* (2020).
12. S. Jain, A. Agrawal, A. Saporta, S. Q. Truong, D. N. Duong, T. Bui, P. Chambon, Y. Zhang, M. P. Lungren, A. Y. Ng *et al.*, Radgraph: Extracting clinical entities and relations from radiology reports, *arXiv preprint arXiv:2106.14463* (2021).
13. W. Zhao, C. Wu, X. Zhang, Y. Zhang, Y. Wang and W. Xie, Ratescore: A metric for radiology report generation, *medRxiv* , 2024 (2024).
14. S. Ostmeier, J. Xu, Z. Chen, M. Varma, L. Blankemeier, C. Bluethgen, A. E. Michalson, M. Moseley, C. Langlotz, A. S. Chaudhari *et al.*, Green: Generative radiology report evaluation and error notation, *arXiv preprint arXiv:2405.03595* (2024).
15. A. Huang, O. Banerjee, K. Wu, E. P. Reis and P. Rajpurkar, Fineradscore: A radiology report line-by-line evaluation technique generating corrections with severity scores, *arXiv preprint arXiv:2405.20613* (2024).
16. H. Touvron, T. Lavril, G. Izacard, X. Martinet, M.-A. Lachaux, T. Lacroix, B. Rozière, N. Goyal, E. Hambro, F. Azhar *et al.*, Llama: Open and efficient foundation language models, *arXiv preprint arXiv:2302.13971* (2023).
17. L. Zheng, W.-L. Chiang, Y. Sheng, S. Zhuang, Z. Wu, Y. Zhuang, Z. Lin, Z. Li, D. Li, E. Xing *et al.*, Judging llm-as-a-judge with mt-bench and chatbot arena, *Advances in Neural Information Processing Systems* **36**, 46595 (2023).
18. Y. Luo, J. Zhang, S. Fan, K. Yang, Y. Wu, M. Qiao and Z. Nie, Biomedgpt: Open multimodal generative pre-trained transformer for biomedicine, *arXiv preprint arXiv:2308.09442* (2023).
19. O. Alfarghaly, R. Khaled, A. Elkorany, M. Helal and A. Fahmy, Automated radiology report generation using conditioned transformers, *Informatics in Medicine Unlocked* **24**, p. 100557 (2021).
20. T. Tanida, P. Müller, G. Kaissis and D. Rueckert, Interactive and explainable region-guided radiology report generation, in *Proceedings of the IEEE/CVF Conference on Computer Vision and Pattern Recognition*, (Association for Computational Linguistics, 2023).
21. Z. Chen, M. Varma, J.-B. Delbrouck, M. Paschali, L. Blankemeier, D. Van Veen, J. M. J. Valanarasu, A. Youssef, J. P. Cohen, E. P. Reis *et al.*, Chexagent: Towards a foundation model for chest x-ray interpretation, *arXiv preprint arXiv:2401.12208* (2024).
22. C. Pellegrini, E. Özsoy, B. Busam, N. Navab and M. Keicher, Radialog: A large vision-language model for radiology report generation and conversational assistance, *arXiv preprint arXiv:2311.18681* (2023).
23. H.-Y. Zhou, S. Adithan, J. N. Acosta, E. J. Topol and P. Rajpurkar, A generalist learner for

multifaceted medical image interpretation, *arXiv preprint arXiv:2405.07988* (2024).
24. C. Wu, X. Zhang, Y. Zhang, Y. Wang and W. Xie, Towards generalist foundation model for radiology, *arXiv preprint arXiv:2308.02463* (2023).
25. X. Zhang, Z. Meng, J. Lever and E. S. Ho, Libra: Leveraging temporal images for biomedical radiology analysis, *arXiv preprint arXiv:2411.19378* (2024).
26. A. E. Johnson, T. J. Pollard, S. J. Berkowitz, N. R. Greenbaum, M. P. Lungren, C.-y. Deng, R. G. Mark and S. Horng, Mimic-cxr, a de-identified publicly available database of chest radiographs with free-text reports, *Scientific data* **6**, p. 317 (2019).
27. D. Demner-Fushman, M. D. Kohli, M. B. Rosenman, S. E. Shooshan, L. Rodriguez, S. Antani, G. R. Thoma and C. J. McDonald, Preparing a collection of radiology examinations for distribution and retrieval, *Journal of the American Medical Informatics Association* **23**, 304 (2016).
28. A. Nicolson, J. Dowling, D. Anderson and B. Koopman, Longitudinal data and a semantic similarity reward for chest x-ray report generation, *Informatics in Medicine Unlocked* **50**, p. 101585 (2024).
29. A. Nicolson, S. Zhuang, J. Dowling and B. Koopman, The impact of auxiliary patient data on automated chest x-ray report generation and how to incorporate it, *arXiv preprint arXiv:2406.13181* (2024).
30. A. Nicolson, J. Liu, J. Dowling, A. Nguyen and B. Koopman, e-health csiro at rrg24: entropy-augmented self-critical sequence training for radiology report generation, *arXiv preprint arXiv:2408.03500* (2024).
31. M. Ranjit, S. Srivastav and T. Ganu, Radphi-3: Small language models for radiology, *arXiv preprint arXiv:2411.13604* (2024).
32. K. Zhang, R. Zhou, E. Adhikarla, Z. Yan, Y. Liu, J. Yu, Z. Liu, X. Chen, B. D. Davison, H. Ren *et al.*, A generalist vision–language foundation model for diverse biomedical tasks, *Nature Medicine* , 1 (2024).
33. Z. Yang, L. Li, K. Lin, J. Wang, C.-C. Lin, Z. Liu and L. Wang, The dawn of lmms: Preliminary explorations with gpt-4v (ision), *arXiv preprint arXiv:2309.17421* **9**, p. 1 (2023).
34. S. Lee, W. J. Kim, J. Chang and J. C. Ye, Llm-cxr: Instruction-finetuned llm for cxr image understanding and generation, *arXiv preprint arXiv:2305.11490* (2023).
35. F. Yu, M. Endo, R. Krishnan, I. Pan, A. Tsai, E. P. Reis, E. K. U. N. Fonseca, H. M. H. Lee, Z. S. H. Abad, A. Y. Ng *et al.*, Evaluating progress in automatic chest x-ray radiology report generation, *Patterns* **4** (2023).
36. J. N. Acosta, X. Zhang, S. Dogra, H.-Y. Zhou, S. Payabvash, G. J. Falcone, E. K. Oermann and P. Rajpurkar, Headct-one: Enabling granular and controllable automated evaluation of head ct radiology report generation, *arXiv preprint arXiv:2409.13038* (2024).
37. J. N. Acosta, S. Dogra, S. Adithan, K. Wu, M. Moritz, S. Kwak and P. Rajpurkar, The impact of ai assistance on radiology reporting: A pilot study using simulated ai draft reports, *arXiv preprint arXiv:2412.12042* (2024).
38. E. K. Hong, B. Roh, B. Park, J.-B. Jo, W. Bae, J. Soung Park and D.-W. Sung, Value of using a generative ai model in chest radiography reporting: a reader study, *Radiology* **314**, p. e241646 (2025).
39. D. Hein, Z. Chen, S. Ostmeier, J. Xu, M. Varma, E. P. Reis, A. E. Michalson, C. Bluethgen, H. J. Shin, C. Langlotz *et al.*, Preference fine-tuning for factuality in chest x-ray interpretation models without human feedback, *arXiv preprint arXiv:2410.07025* (2024).
40. P. R. Bassi, M. C. Yavuz, K. Wang, X. Chen, W. Li, S. Decherchi, A. Cavalli, Y. Yang, A. Yuille and Z. Zhou, Radgpt: Constructing 3d image-text tumor datasets, *arXiv preprint arXiv:2501.04678* (2025).
41. P. R. Bassi, W. Li, Y. Tang, F. Isensee, Z. Wang, J. Chen, Y.-C. Chou, Y. Kirchhoff, M. R. Rokuss, Z. Huang *et al.*, Touchstone benchmark: Are we on the right way for evaluating ai

algorithms for medical segmentation?, *Advances in Neural Information Processing Systems* **37**, 15184 (2024).
42. A. Saenz, E. Chen, H. Marklund and P. Rajpurkar, The maida initiative: establishing a framework for global medical-imaging data sharing, *The Lancet Digital Health* **6**, e6 (2024).

ReXVQA: A Large-scale Visual Question Answering Benchmark for Generalist Chest X-ray Understanding

Ankit Pal[1,3], Jung-Oh Lee[2], Xiaoman Zhang[3], Malaikannan Sankarasubbu[1], Seunghyeon Roh[2], Won Jung Kim[2], Meesun Lee[2], Pranav Rajpurkar[3]

[1]*Saama AI Research, Saama Technologies, India*
E-mail: {ankit.pal, malaikannan.sankarasubbu}@saama.com

[2]*Seoul National University, Seoul, South Korea*
E-mail: {pisceanoh, seunghyeon.roh, wonjung.kim, meesun.lee}@snu.ac.kr

[3]*Department of Biomedical Informatics, Harvard Medical School, Boston, MA, USA*
E-mail: {xiaoman.zhang, pranav.rajpurkar}@hms.harvard.edu

Dataset hf.co/datasets/rajpurkarlab/ReXVQA

Supplementary Material Github Appendix.pdf

We present ReXVQA, the largest and most comprehensive benchmark for visual question answering (VQA) in chest radiology, comprising 694,841 questions paired with 160,000 chest X-rays studies across training, validation, and test sets. Unlike prior efforts that rely heavily on template based queries, ReXVQA introduces a diverse and clinically authentic task suite reflecting five core radiological reasoning skills: presence assessment, location analysis, negation detection, differential diagnosis, and geometric reasoning. We evaluate eight state-of-the-art multimodal large language models, including MedGemma-4B-it, Qwen2.5-VL, Janus-Pro-7B, and Eagle2-9B. The best-performing model (MedGemma) achieves 83.24% overall accuracy. To bridge the gap between AI performance and clinical expertise, we conducted a comprehensive human reader study involving 3 senior radiology residents on 200 randomly sampled cases. Our evaluation demonstrates that MedGemma achieved superior performance (83.84% accuracy) compared to human readers (best radiology resident: 77.27%), representing a significant milestone where AI performance exceeds human evaluation on chest X-ray interpretation. The reader study reveals distinct performance patterns between AI models and radiology residents, with strong inter-reader agreement among the human readers while showing more variable agreement patterns between human readers and AI models. ReXVQA establishes a new standard for evaluating generalist radiological AI systems, offering public leaderboards, fine-grained evaluation splits, structured explanations, and category-level breakdowns. This benchmark lays the foundation for next-generation AI systems capable of mimicking expert-level clinical reasoning beyond narrow pathology classification.

1. Introduction

Chest X-ray (CXR) interpretation requires a radiologist to perform diverse cognitive tasks - from localizing findings *where is the reticular opacity?* to comparative analysis *has the hilar*

© 2025 The Authors. Open Access chapter published by World Scientific Publishing Company and distributed under the terms of the Creative Commons Attribution Non-Commercial (CC BY-NC) 4.0 License.

enlargement progressed? to offering differential diagnoses *what are the likely causes of these peripheral findings?* A truly generalist CXR AI system would need similar capabilities: flexibly answering questions about location, relationships, measurements, and diagnostic reasoning rather than just detecting predefined pathologies.

Current CXR AI approaches, while impressive at disease classification, operate within narrow constraints. Systems have progressed from detecting a handful of conditions to impressive performance on multi-label classification of up to 130 pathologies, achieving near-radiologist performance on specific tasks.[14,16,18] However, they remain fundamentally limited to a fixed set of predetermined labels and cannot engage in the broader analytical reasoning that characterizes expert radiological assessment.

The emergence of multimodal Large Language Models (LLMs) offers a promising path toward such generalist medical AI systems.[12] These models can process both images and natural language, potentially enabling them to engage in the kind of flexible visual reasoning and natural dialogue that characterizes clinical practice. Early results show these models can understand basic medical concepts and engage in simple diagnostic reasoning when prompted with medical images.[13,15] However, systematically evaluating these models' capabilities across clinically meaningful tasks remains challenging. While recent datasets have scaled in size and scope, most rely on templated question generation and lack the diversity and complexity of real clinical reasoning, limiting their effectiveness as generalist benchmarks.

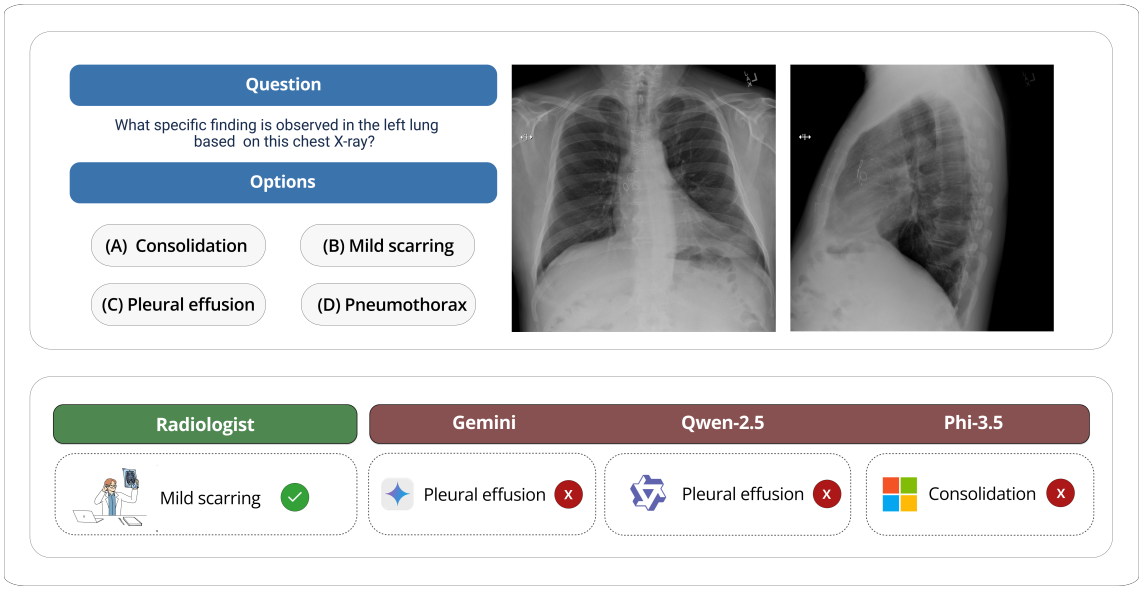

Fig. 1. Sample from the ReXVQA dataset, where human readers correctly identified mild scarring in the left lung base (correct answer B), while three state-of-the-art LVMs (Gemini, Qwen-2.5, and Phi-3.5) provided incorrect assessments, misidentifying the condition as pleural effusion or consolidation.

To address these limitations, we introduce ReXVQA, a benchmark of approximately 694,841 multiple-choice questions (MCQs) questions paired with 160,000 chest X-rays sourced from four U.S. health systems. Unlike previous datasets, ReXVQA evaluates five distinct cog-

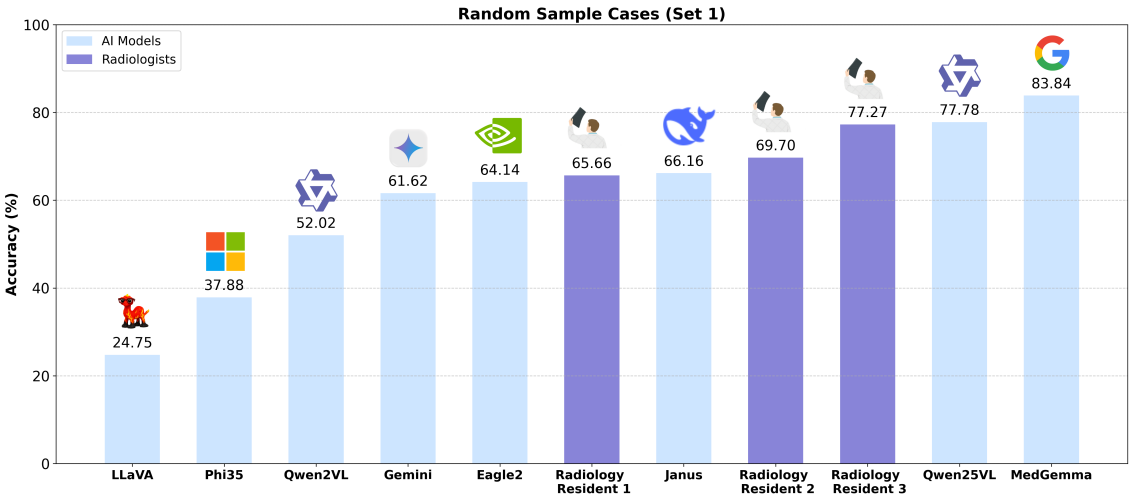

Fig. 2. Performance comparison of AI models and human readers across 200 random sampled cases. The bar chart shows overall accuracy (%) for eight AI models (Eagle2, Gemini, Janus, LLaVA, Phi35, Qwen2VL, Qwen25VL, and MedGemma) and three senior radiology residents.

nitive abilities that mirror clinical workflows, with questions distributed as follows: negation assessment (36.5% of questions), presence assessment (36.1%), differential diagnosis (20.9%), location and distribution assessment (6.1%), and geometric information analysis (0.4%). Questions are generated through a rigorous three-layer pipeline with expert-refined prompts developed over multiple rounds of radiologist feedback, ensuring they reflect authentic clinical reasoning patterns rather than artificial templates. Figure 1 shows one random sample from the dataset.

Our evaluation of eight state-of-the-art multimodal LLMs reveals significant advances in medical AI capabilities, with MedGemma demonstrating exceptional performance across all radiological reasoning tasks. MedGemma achieves superior performance in negation assessment (85.03%), presence assessment (85.21%), and location and distribution assessment (83.47%). The model shows remarkable capabilities across anatomical structures, achieving 91.84% on rib detection, 97.03% on heart findings, and 92.68% on spine assessment. Our reader study demonstrates a significant milestone: MedGemma surpasses senior radiology residents' performance on randomly sampled cases (83.84% vs. best reader: 77.27%), representing the first instance where AI consistently exceeds expert human evaluation in chest X-ray interpretation (Figure 2). These results demonstrate substantial progress toward generalist medical AI systems capable of expert-level clinical reasoning across diverse diagnostic tasks.

Our comprehensive evaluation of multimodal LLMs for chest X-ray interpretation provides several key insights for medical ML applications:

- **Task-specific cognitive capabilities:** Our finding that the best model (MedGemma) achieves 85.03% accuracy on negation tasks but only 76.71% in differential diagnosis demonstrates that medical AI requires explicit design for different cognitive skills rather than treating all diagnostic reasoning as a uniform task.
- **Expert-guided dataset creation methodology:** Our three-layer pipeline with ra-

diologist validation offers a replicable approach for developing clinically representative datasets in other medical domains where direct annotation is costly or impractical.

- **Category-specific performance patterns:** Our detailed analysis across anatomical structures demonstrates that architectural decisions significantly impact performance on specific medical findings (e.g., while Janus-Pro-7B shows competitive performance on some skeletal structures, MedGemma demonstrates superior performance across nearly all anatomical categories including 94.04% on bone assessment and 97.03% on heart findings), suggesting specialized architectures may be more effective than general-purpose approaches for clinical applications.

2. Related Work

Early efforts in medical visual question answering (VQA) laid important groundwork but were limited in scope and complexity. VQA-RAD[10] introduced just 3,515 questions over 315 images, focusing primarily on basic anatomical queries. Similarly, ImageCLEF VQA-Med[1] offered binary questions like *"Is there something wrong in the image?"* suitable for feasibility studies but inadequate for training generalist systems. More recent datasets have expanded the scale and sophistication of medical VQA. PMC-VQA [19] introduced 227K question-answer pairs with free-text answer based on 149K diverse medical images from PubMed papers. MIMIC-CXR-VQA[5] provided 377K questions derived from radiology reports, but relied heavily on templated generation. Medical-Diff-VQA[7] took a novel approach by focusing on temporal reasoning over paired images, generating 700K questions for comparative assessment. MIMIC-Ext-MIMIC-CXR-VQA[3] improved the linguistic variety with paraphrased templates, while GEMeX[11] offered 1.6M multimodal questions with explanations. Despite these advances, most current datasets depend on rigid templates and fail to capture the flexible, multistep reasoning processes typical in radiology. Our work builds on this foundation but takes a distinct approach constructing questions via expert-refined prompts validated by radiologists to better reflect real clinical reasoning patterns and assess diverse cognitive capabilities.

3. The ReXVQA Dataset

In this section, we present the properties of ReXVQA dataset, a comprehensive multimodal benchmark for evaluating LLMs in radiology. We selected the MCQ format for its significant advantages over long-form assessment methodologies, as detailed in Table A.1 supplementary material. We discuss the data collection methodology, the preparation process, and the resulting dataset characteristics. A detailed visualization of the multi-stage MCQ generation pipeline used to create the ReXVQA dataset is provided in the supplementary material

3.1. *Task Definition*

The ReXVQA task can be formalized as $\mathbf{X}_i = (\mathbf{I}_i, \mathbf{Q}_i, \mathbf{O}_i)$, where $\mathbf{I}_i$ represents the i-th X-ray image input, $\mathbf{Q}_i$ represents the i-th question text, and $\mathbf{O}_i$ represents the set of candidate options. For each question-image pair, multiple candidate answers are provided as $\mathbf{O}_i = \{\mathbf{O}_{i1}, \mathbf{O}_{i2}, \mathbf{O}_{i3}, \mathbf{O}_{i4}\}$. The task requires models to analyze both the visual input $\mathbf{I}_i$ and

the textual question $\mathbf{Q}_i$ to select the correct answer(s) from the option set. The ground truth label for each data point is defined as $y \in \mathbb{R}^1$ where $y^i = \{\mathbf{0}, \mathbf{1}, \mathbf{2}, \mathbf{3}\}$. The objective is to learn a prediction function $f : (I, Q) \rightarrow y$ that can effectively combine visual and textual information to make accurate diagnostic and clinical judgments. In addition, models are required to provide explanations $\mathbf{E}$ for their choices, making the complete prediction tuple $(\mathbf{y}, \mathbf{E})$. This explanation component allows for evaluation of the model's reasoning process and clinical understanding beyond mere answer selection.

MCQ Format Justification. We adopted the four-option MCQ format for several reasons. It mirrors established practices in medical education and board exams (e.g., USMLE, radiology boards), providing familiarity and clinical relevance. MCQs also enable systematic assessment of cognitive skills with objective, reproducible scoring, while the four-option design balances complexity and cognitive load.

Table A.1 in the supplementary material details the advantages of MCQs over long-form assessments, including scalability, consistent scoring, and precise analysis of reasoning patterns. While long-form responses capture nuanced clinical reasoning, they face challenges in standardized evaluation and cross-model comparison. Our approach focuses on systematically evaluating core radiological reasoning, with expert-validated questions ensuring clinical authenticity.

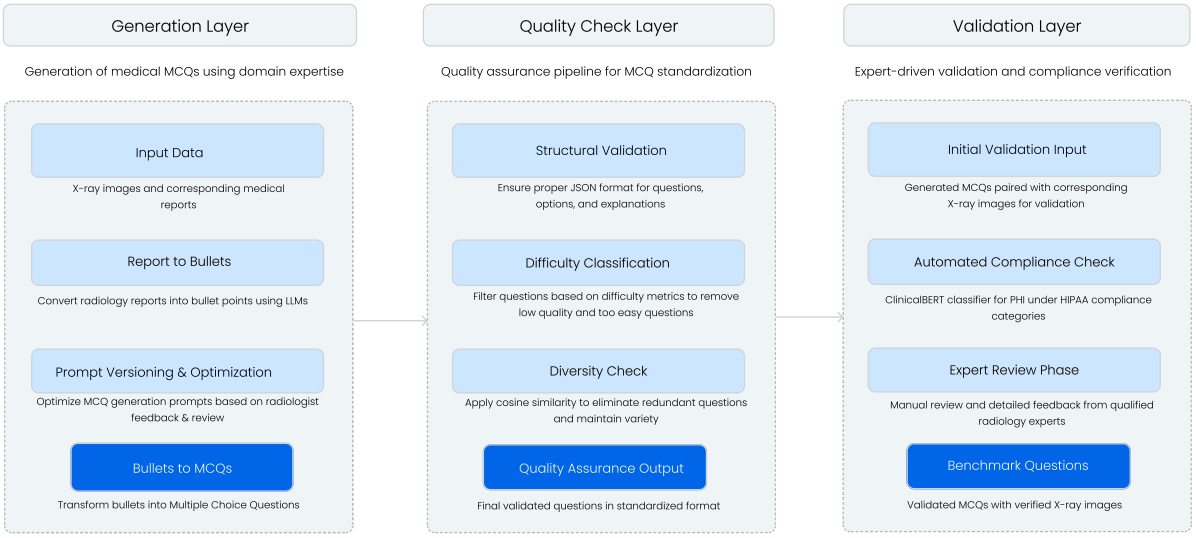

Fig. 3. **Expert-Guided Medical MCQ Generation Pipeline:** We propose a three-layer approach combining computational processes and expert oversight for creating high-quality radiology MCQs.

3.2. *Source Dataset*

The source dataset, ReXGradient-160K,[17] comprises 170,000 chest X-ray studies with paired radiological reports from 109,722 unique patients across 4 U.S. health systems. This dataset represents the largest publicly available chest X-ray dataset to date in terms of patient count. The dataset is divided into public training (140,000 studies), public validation (10,000 studies), and public test (10,000 studies) sets, with an additional private test set, (10,000 studies).

Equipment Diversity The dataset encompasses chest X-rays acquired using equipment from multiple manufacturers including SIEMENS, FUJI, SAMSUNG, VIDAR, TOSHIBA, and GE. These manufacturers are distributed across all four hospital systems rather than being system-specific, reflecting real-world clinical diversity and enhancing model generalizability across different imaging technologies and acquisition protocols.

Expert Review Phase. Our expert review process incorporates a quality assurance protocol involving a board-certified radiologist. In total, 520 multiple-choice questions (MCQs) were reviewed. 300 were qualitatively assessed during initial development process to examine the LLM's question-answering quality, and 220 were evaluated quantitatively with error classification after refining prompts and models. These 220 questions spanned varying difficulty levels and included a dedicated image alignment assessment. The evaluation emphasized four critical dimensions: clinical quality, explanation clarity, factual correctness, and image alignment. The image alignment analysis revealed only one case (0.5%) of content-radiograph misalignment due to a source data discrepancy, suggesting minimal inconsistency resulting from our report-based approach. Figure A.1 in the supplementary material illustrates the radiology image tagging platform used for expert annotation.

Expert Review Outcomes. The quantitative expert review of 220 sample questions revealed several issues requiring correction. Specifically, 10.8% of questions had multiple valid answers, 6.7% contained unnecessary comparison-related content, 5% required improvements to ensure clinical validity, and 3.3% included hallucinated information about findings not described in the radiology reports. The most common issue occurred with negation-type questions, where multiple valid answers arose for findings that were absent in the original reports. To address these concerns, we implemented multiple validation steps, including careful cross-checking of the original reports and generated questions to remove comparison-related content and eliminate questions with multiple valid answers. This feedback directly informed our prompt engineering iterations, leading to refined question generation strategies, simplified medical language, standardized anatomical terminology, and ultimately proving highly effective, Only two errors were identified in a subsequent reader study involving 300 questions.

Benchmark Question Finalization. After rigorous multi-stage validation and quality control, questions meeting all quality criteria are incorporated into the final ReXVQA benchmark, facilitating detailed analysis of model performance across different dimensions of radiological expertise.

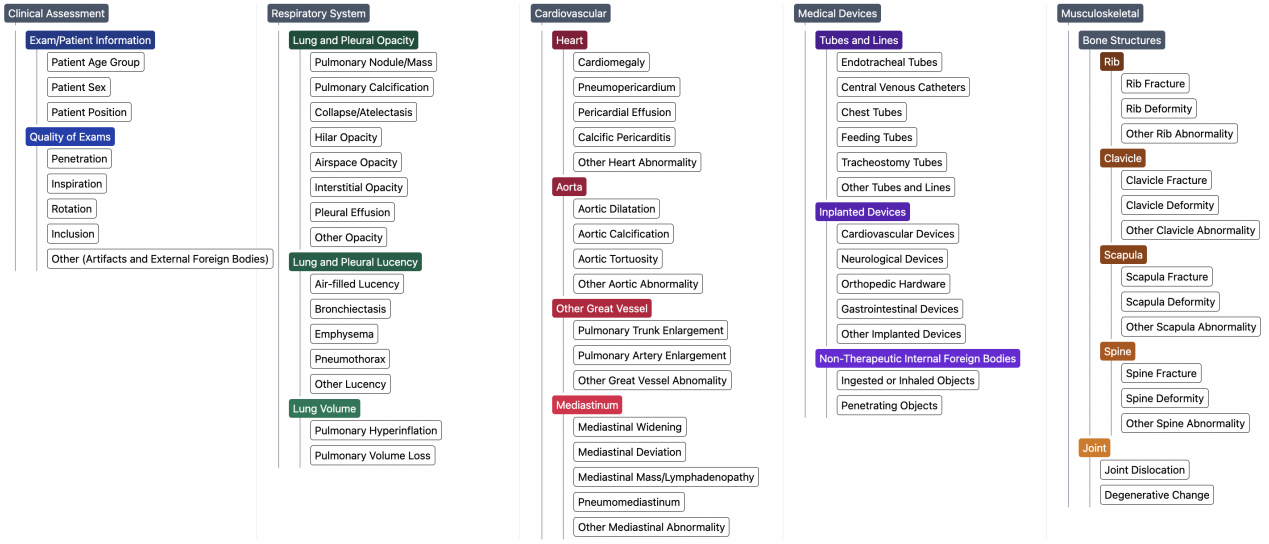

Fig. 4. **Hierarchical Taxonomy of Chest X-Ray Categories.** This expert-validated classification system, developed in collaboration with radiologists, organizes chest X-ray findings into five major domains: Clinical Assessment, Respiratory System, Cardiovascular, Medical Devices, and Musculoskeletal findings. The taxonomy serves as a structured foundation for Expert-Guided Medical MCQ generation, ensuring comprehensive coverage and clinical relevance.

3.3. *Cognitive Framework Development*

The five cognitive abilities evaluated in ReXVQA were informed by established question types in medical VQA literature and clinical practice patterns. Presence and negation assessment reflect the most common question types in VQA-RAD[9] and MIMIC-Ext-MIMIC-CXR-VQA,[4] with negation detection being clinically critical.[6] Location assessment aligns with anatomy-focused questions in prior datasets,[4,8] while differential diagnosis corresponds to abnormality detection tasks in VQA-Med.[2] Geometric analysis addresses quantitative measurements relevant to clinical assessment.[4]

Through radiologist consultation during prompt development, we validated these abilities as reflecting core radiological reasoning patterns, with task distribution prioritizing fundamental skills (∼73% for presence/negation) while ensuring representation of specialized assessment capabilities.

3.4. *Dataset Statistics*

For ReXVQA, we follow the same split as the source dataset. The private test set is reserved for independent evaluation through our leaderboard system, ensuring unbiased assessment of model performance. The dataset consists of 572,419 VQA pairs for training, 40,878 for validation, 40,826 for public testing, and 41,007 for private testing. The ReXVQA dataset encompasses a diverse range of radiological aspects, carefully structured to evaluate different dimensions of multimodal LLM capabilities in medical imaging interpretation.

3.4.1. *Task Distribution Analysis*

Our dataset incorporates five distinct task types across training, validation, test, and private test sets, with remarkably consistent distributions. As shown in Table 1, Negation Assessment and Presence Assessment together comprise approximately 72% of all tasks, highlighting their fundamental importance in radiological interpretation. Differential Diagnosis represents about 21% of tasks, while Location and Distribution Assessment (approximately 6%) and Geometric Information Assessment (less than 0.5%) target more specialized interpretative skills. This distribution reflects the hierarchical nature of radiological reasoning, from basic detection to complex spatial and differential analysis.

Table 1. Distribution of task categories across datasets. Private test set (41,007 cases) is reserved for leaderboard evaluation and not included in the publicly available dataset.

Category	**Train**	**Valid**	**Test**	**Private**
	Count (%)	Count (%)	Count (%)	Count (%)
Task Categories				
Negation Assessment	209,053 (**36.5**)	15,007 (**36.7**)	15,369 (**37.9**)	15,408 (**37.6**)
Presence Assessment	206,880 (**36.1**)	14,698 (**36.0**)	14,078 (**34.7**)	14,452 (**35.2**)
Differential Diagnosis	119,111 (**20.9**)	8,578 (**21.0**)	8,563 (**21.1**)	8,585 (**20.9**)
Location & Distribution	34,829 (**6.1**)	2,404 (**5.9**)	2,365 (**5.8**)	2,383 (**5.8**)
Geometric Information	2,546 (**0.4**)	171 (**0.4**)	182 (**0.5**)	179 (**0.4**)
Total	572,419	40,858	40,557	41,007

3.4.2. *Anatomical Category Distribution*

Analysis across the dataset reveals a diverse but clinically realistic distribution of anatomical categories. Lung and Pleural Opacity dominates (30.2-30.4%), reflecting the prevalence of this finding in chest radiography, followed by Heart assessments (14.6-15.0%) and Negation (13.2-13.5%). The distribution encompasses supportive devices such as Tubes and Lines (5.0-5.2%), along with Other Pulmonary Diagnosis (4.2-4.5%). The dataset maintains balanced representation across critical diagnostic areas, including Infectious Disease (2.3-2.5%), Pulmonary Vascularity (1.8%), and Cardiac Disease (0.35%), while also covering essential supporting structures such as Spine, Ribs, and Mediastinum. Importantly, the distribution captures both common conditions and rare but clinically significant findings like Pulmonary Neoplasm (0.32-0.35%) and Lymphoproliferative Disease (0.02-0.03%), along with technical quality assessments (3.4-3.6%). This distribution mirrors real-world clinical prevalence while ensuring sufficient representation for comprehensive model evaluation. Table A.2 in the supplementary material presents the taxonomy of medical conditions in our dataset, categorizing them into nine main classes with their respective subcategories.

4. Experiments

4.1. *Baseline Models*

The primary objective of our baseline experiments is to evaluate the performance of current state-of-the-art multimodal LLMs on ReXVQA, specifically focusing on their ability to handle complex radiological MCQs designed for medical professionals. We selected models with varying architectures, training approaches, and accessibility to provide a comprehensive benchmark. Our evaluation includes both commercial and open-source models, representing the current landscape of multimodal AI capabilities in medical imaging. Notably, MedGemma represents a medical-domain-specific model, allowing us to compare general-purpose multimodal models against specialized medical AI systems.

For brevity, we refer to the evaluated models using the following short names throughout the paper: Phi35 (Phi-3.5-vision-instruct), Qwen2VL (Qwen2-VL), Qwen25VL (Qwen2.5-VL), Gemini (Gemini 1.5 Pro), Eagle2, Janus, LLaVA, and MedGemma. A detailed description of each model, including architecture and training background, is provided in the supplementary material. Importantly, none of the evaluated models overlap with the LLM used for dataset generation (GPT-4o), ensuring unbiased evaluation without data leakage or model-specific advantages.

4.2. *Evaluation Framework*

Our evaluation framework implements a standardized protocol for assessing model performance. For each query, models receive an X-ray image, accompanied by a question in natural language and four multiple-choice options. Models must provide their selected option and a detailed explanation justifying their choice for their prediction. We employ the standard accuracy as the evaluation metric.

Image Input Specifications. Models receive chest X-ray images in PNG format (converted from original DICOM files). For the public dataset, images are provided at 1/4 of original resolution to balance computational efficiency with diagnostic detail preservation. This preprocessing maintains clinically relevant features while enabling scalable evaluation across multiple models. For studies containing multiple radiographic views (as occurs in real-world radiology practice), models are provided with all available images paired with each question, enabling comprehensive assessment across different anatomical projections.

5. Results and Analysis

The comprehensive evaluation of eight state-of-the-art multimodal models revealed significant variations in their ability to interpret chest X-rays across different clinical domains. MedGemma demonstrated exceptional performance, achieving 83.24% overall accuracy and establishing a new benchmark for multimodal medical image interpretation. This represents a substantial improvement over previous leading models, with Janus-Pro-7B following at 66.56%, followed closely by Qwen25VL (65.55%) and Eagle2 (64.43%) as shown in Table 2. Gemini achieves a respectable 63.31%, while LLaVA struggles notably with only 26.61% accuracy, highlighting the considerable challenges in multimodal medical image interpretation.

Table 2. Evaluation of models on various diagnostic and assessment metrics. Failed Extractions shows the percentage of test cases where models failed to provide valid responses in the required format (out of 41,007 private test cases). ↑ indicates higher is better, ↓ indicates lower is better.

Model	Overall Accuracy ↑	Differential Diagnosis ↑	Geometric Information ↑	Location and Distribution ↑	Negation Assessment ↑	Presence Assessment ↑	Failed Extractions ↓
LLaVA	26.61	21.61	23.46	27.61	24.02	36.33	2.37
Phi35	47.49	62.24	22.15	37.11	79.50	36.44	0.05
Qwen2VL	54.70	52.65	44.94	54.05	62.69	59.15	0.01
Gemini	63.31	62.21	46.89	59.60	85.68	62.17	**0.0**
Eagle2	64.43	68.17	56.98	56.95	**86.32**	53.75	**0.0**
Qwen25VL	65.55	63.61	66.48	63.24	83.27	51.14	**0.0**
Janus-Pro-7B	66.56	56.34	75.42	64.62	75.73	60.70	**0.0**
MedGemma	**83.24**	**76.71**	**80.45**	**83.47**	85.03	**85.21**	**0.0**

5.1. *Task-Specific Performance Analysis*

The models demonstrate distinct strengths across different radiological reasoning tasks, with MedGemma leading in four out of five major categories as shown in Table 2. Based on our analysis of model architectures and performance patterns:

- **Differential Diagnosis**: MedGemma achieves the highest performance at 76.71%, substantially outperforming second model Eagle2 with accuracy 68.17%. This superior performance suggests MedGemma's specialized medical training enables more sophisticated clinical reasoning for distinguishing between similar conditions.
- **Geometric Information Assessment**: MedGemma excels with 80.45% accuracy, surpassing Janus-Pro-7B's 75.42%. This improvement indicates enhanced capabilities for spatial representation and precise measurement interpretation in radiological contexts.
- **Location and Distribution Assessment**: MedGemma leads significantly at 83.47%, well above Janus-Pro-7B's 64.62% and Qwen25VL's 63.24%. This performance suggests superior positional representation mechanisms for localizing findings within complex radiological images.
- **Negation Assessment**: Eagle2 achieves the best performance at 86.32%, closely followed by Gemini (85.68%) and MedGemma (85.03%). The top three models demonstrate consistently high standards for identifying absence of findings a critical skill in avoiding false positives.
- **Presence Assessment**: MedGemma demonstrates exceptional capability at 85.21%, substantially exceeding Gemini's previous best of 62.17%. This dramatic improvement suggests superior feature extraction capabilities for detecting radiological abnormalities within complex backgrounds.

5.2. *Category-wise Performance Analysis*

Table 3 & Table A.3 in the supplementary material presents a detailed breakdown of model performance across key radiological categories, with MedGemma consistently outperforming other models across most categories, achieving an average performance of 83.24%.

Table 3. Comprehensive performance comparison of models across key radiological categories (values shown in %). Bold numbers indicate best performance per category. Abbreviations: P.O. = Pleural Opacity, P.L. = Pleural Lucency and Q2 & Q25 = Qwen2 & Qwen25

Category	Gemini	Eagle2	Janus	LLaVA	Q2VL	Q25VL	Phi35	MedGemma
Clinical Assessment								
Quality of Exams	70.30	62.50	51.64	10.30	40.50	60.92	35.10	**71.23**
Respiratory System								
Lung & P.O	72.24	72.19	68.70	32.98	60.73	64.77	58.14	**80.44**
Lung & P.L	80.00	64.65	58.59	19.34	61.62	78.64	58.82	**87.88**
Lung Volume	65.44	58.22	51.64	39.72	52.11	60.92	28.25	**78.64**
Cardiovascular								
Heart	80.29	81.71	72.01	26.01	60.31	84.83	62.73	**97.03**
Aorta	76.65	41.04	60.14	6.84	72.17	34.79	33.05	**87.86**
Other Great Vessel	**73.33**	60.00	60.00	13.33	60.00	60.00	45.45	**73.33**
Medical Devices								
Tubes and Lines	59.45	58.26	58.87	22.81	48.78	65.04	32.10	**83.86**
Implanted Devices	54.46	52.64	60.79	29.50	52.40	53.48	43.16	**73.14**
Pathologies								
Infectious Disease	71.55	63.24	66.77	56.63	51.02	67.74	42.13	**77.61**
Pulmonary Neoplasm	78.46	66.92	81.95	39.29	63.91	73.68	69.44	**88.72**
Negation	61.05	71.73	58.19	15.00	56.37	61.49	**78.96**	74.76
Musculoskeletal								
Rib	88.90	83.93	89.80	36.92	86.35	79.21	78.56	**91.84**
Spine	78.84	62.30	86.43	64.84	73.73	50.10	57.94	**92.68**
Clavicle	75.93	57.14	75.00	23.21	71.43	33.93	51.02	**92.73**
Joint	51.96	42.31	70.19	47.06	66.35	36.54	42.22	**88.46**
Average	74.00	67.00	67.00	38.00	64.00	66.00	50.00	**83.24**

Clinical Assessment. In exam quality interpretation, MedGemma demonstrates superior capabilities (71.23%), followed by Gemini (70.30%), Eagle2 (62.50%) and Qwen25VL (60.92%). LLaVA's performance (10.30%) suggests significant limitations in understanding technical image characteristics. This disparity indicates that advanced multimodal architectures are essential for capturing the nuanced details required for technical quality assessment.

Respiratory System. Respiratory findings analysis reveals consistent performance patterns across subcategories. MedGemma leads in all three respiratory metrics, achieving 80.44% for lung and pleural opacities, 87.88% for pleural lucencies, and 78.64% for lung volume assessment. The substantial performance gap between top models and LLaVA (19.34-39.72%) underscores the complexity of pulmonary pattern recognition.

Cardiovascular Imaging. Cardiovascular interpretation presents interesting variations across subcategories. MedGemma leads in heart finding analysis (97.03%), substantially exceeding Qwen25VL's 84.83%. and 87.86% for aortic assessment (compared to Gemini's

76.65%). This consistent excellence across different vascular structures suggests robust architectural capabilities for cardiovascular imaging, addressing the previous inconsistencies observed among other models.

Medical Devices Detection. MedGemma significantly advances medical device recognition with 83.86% for tubes and lines detection and 73.14% for implanted devices. These improvements suggest that specialized medical training helps models better understand artificial structures despite their variable appearance and positioning.

Pathologies. MedGemma demonstrates superior pathology identification capabilities: 88.72% for pulmonary neoplasms, 77.61% for infectious diseases, and 74.76% for negation assessment (Phi35 maintains a slight edge at 78.96%). These results confirm that medical domain specialization enhances pattern recognition for diverse pathological conditions.

Musculoskeletal Findings. MedGemma achieves exceptional performance in skeletal structure assessment, leading all categories: 91.84% for rib interpretation, 92.68% for spine assessment, 92.73% for clavicle detection, and 88.46% for joint interpretation. These results demonstrate that even for high-contrast bony structures that were already well-recognized by previous models, specialized medical training can yield substantial improvements.

6. Reader Studies

6.1. *Overall Performance Analysis*

Our reader study evaluated the diagnostic performance of AI models compared to three radiology residents in their 3rd or 4th year of training, using 200 randomly sampled chest X-ray cases. The results reveal that current AI models can achieve competitive performance with human readers in standard diagnostic tasks, although there are significant variations between different models. Among the AI models tested, MedGemma demonstrated the highest overall accuracy at 83.84%, substantially outperforming all other models and human readers. Qwen25VL achieved 77.78% accuracy, closely matching the performance of the top human reader (Reader 3 at 77.27%). Reader 2 achieved 69.70% accuracy, while Reader 1 performed at 65.66%, comparable to several AI models, including Janus (66.16%) and Eagle2 (64.14%). The performance distribution shows a clear hierarchy, with some models like LLaVA (24.75%) and Phi35 (37.88%) demonstrating significantly lower accuracy, indicating substantial variability in current AI model capabilities for medical image interpretation.

This variability is further reflected in the interrater agreement patterns across models and human readers (see Section A.4 and Figure A.3 in the supplementary material)

Acknowledgement

This work was supported by the Biswas Family Foundation's Transformative Computational Biology Grant in Collaboration with the Milken Institute.

References

1. Asma Ben Abacha, Vivek Datla, Sadid A. Hasan, Dina Demner-Fushman, and Henning Müller. Overview of the vqa-med task at imageclef 2020: Visual question answering and generation in the medical domain. In *Conference and Labs of the Evaluation Forum*, 2020.
2. Asma Ben Abacha, Sadid A. Hasan, Vivek Datla, Joey Liu, Dina Demner-Fushman, and Henning Müller. Vqa-med: Overview of the medical visual question answering task at imageclef 2019. In *Conference and Labs of the Evaluation Forum*, 2019.
3. Seongsu Bae, Daeun Kyung, Jaehee Ryu, Eunbyeol Cho, Gyubok Lee, Sunjun Kweon, Jungwoo Oh, Lei Ji, Eric Chang, Tackeun Kim, and Edward Choi. Mimic-ext-mimic-cxr-vqa: A complex, diverse, and large-scale visual question answering dataset for chest x-ray images, 2024.
4. Seongsu Bae, Daeun Kyung, Jaehee Ryu, Eunbyeol Cho, Gyubok Lee, Sunjun Kweon, Jungwoo Oh, Lei Ji, Eric Chang, Tackeun Kim, and Edward Choi. MIMIC-Ext-MIMIC-CXR-VQA: A Complex, Diverse, And Large-Scale Visual Question Answering Dataset for Chest X-ray Images (version 1.0.0). `https://doi.org/10.13026/deqx-d943`, July 2024. PhysioNet. RRID:SCR_007345.
5. Seongsu Bae, Daeun Kyung, Jaehee Ryu, Eunbyeol Cho, Gyubok Lee, Sunjun Kweon, Jungwoo Oh, Lei Ji, Eric Chang, Tackeun Kim, et al. Ehrxqa: A multi-modal question answering dataset for electronic health records with chest x-ray images. *Advances in Neural Information Processing Systems*, 36, 2024.
6. Sergey Goryachev, Margarita Sordo, Qing T. Zeng, and Long H. Ngo. Implementation and evaluation of four different methods of negation detection. 2007.
7. Xinyue Hu, Lin Gu, Qi A. An, Mengliang Zhang, Liangchen Liu, Kazuma Kobayashi, Tatsuya Harada, Ronald M. Summers, and Yingying Zhu. Expert knowledge-aware image difference graph representation learning for difference-aware medical visual question answering. *Proceedings of the 29th ACM SIGKDD Conference on Knowledge Discovery and Data Mining*, 2023.
8. Xinyue Hu, Lin Gu, Qiyuan An, Mengliang Zhang, liangchen liu, Kazuma Kobayashi, Tatsuya Harada, Ronald Summers, and Yingying Zhu. Medical-Diff-VQA: A Large-Scale Medical Dataset for Difference Visual Question Answering on Chest X-Ray Images (version 1.0.1). `https://doi.org/10.13026/e6dd-cn74`, Feb 2025. PhysioNet. RRID:SCR_007345.
9. Jason J. Lau, Soumya Gayen, Asma Ben Abacha, and Dina Demner-Fushman. A dataset of clinically generated visual questions and answers about radiology images. 2018.
10. Jason J. Lau, Soumya Gayen, Asma Ben Abacha, and Dina Demner-Fushman. Descriptor : A dataset of clinically generated visual questions and answers about radiology images. 2018.
11. Bo Liu, Kevin Yingyin Zou, Li-Ming Zhan, Zexin Lu, Xiaoyu Dong, Yidi Chen, Chengqiang Xie, Jiannong Cao, Xiao-Ming Wu, and Huazhu Fu. Gemex: A large-scale, groundable, and explainable medical vqa benchmark for chest x-ray diagnosis. *ArXiv*, abs/2411.16778, 2024.
12. Michael Moor, Oishi Banerjee, Zahra F H Abad, Harlan M. Krumholz, Jure Leskovec, Eric J. Topol, and Pranav Rajpurkar. Foundation models for generalist medical artificial intelligence. *Nature*, 616:259–265, 2023.
13. Ankit Pal and Malaikannan Sankarasubbu. Gemini goes to med school: Exploring the capabilities of multimodal large language models on medical challenge problems & hallucinations. In *Clinical Natural Language Processing Workshop*, 2024.
14. Ekin Tiu, Ellie Talius, Pujan Patel, Curtis P Langlotz, Andrew Y Ng, and Pranav Rajpurkar. Expert-level detection of pathologies from unannotated chest x-ray images via self-supervised learning. *Nature biomedical engineering*, 6(12):1399–1406, 2022.
15. Sheng Wang, Zihao Zhao, Ouyang Xi, Tianming Liu, Qian Wang, and Dinggang Shen. Interactive computer-aided diagnosis on medical image using large language models. *Communications Engineering*, 3, 2024.

16. Chaoyi Wu, Xiaoman Zhang, Ya Zhang, Yanfeng Wang, and Weidi Xie. Medklip: Medical knowledge enhanced language-image pre-training for x-ray diagnosis. In *Proceedings of the IEEE/CVF International Conference on Computer Vision*, pages 21372–21383, 2023.
17. Xiaoman Zhang, Julián N. Acosta, Josh Miller, Ouwen Huang, and Pranav Rajpurkar. Rexgradient-160k: A large-scale publicly available dataset of chest radiographs with free-text reports. In *arXiv:2505.00228v1*, 2025.
18. Xiaoman Zhang, Chaoyi Wu, Ya Zhang, Weidi Xie, and Yanfeng Wang. Knowledge-enhanced visual-language pre-training on chest radiology images. *Nature Communications*, 14(1):4542, 2023.
19. Xiaoman Zhang, Chaoyi Wu, Ziheng Zhao, Weixiong Lin, Ya Zhang, Yanfeng Wang, and Weidi Xie. Development of a large-scale medical visual question-answering dataset. *Communications Medicine*, 4(1):277, 2024.

Detecting PTSD in Clinical Interviews: A Comparative Analysis of NLP Methods and Large Language Models

Feng Chen[1,2], Dror Ben-Zeev[2], Gillian Sparks[2], Arya Kadakia[2], Trevor Cohen[1,2]

[1]*Department of Biomedical Informatics and Health Education, University of Washington, Box 358047 Seattle, WA 98195, USA*

[2]*Behavioral Research in Technology and Engineering (BRiTE) Center, Department of Psychiatry and Behavioral Sciences, University of Washington, 3751 W Stevens Wy NE Seattle, WA 98195, USA*

Email: fengc9@uw.edu, dbenzeev@uw.edu, gsparks@uw.edu, arya1kadakia@gmail.com, cohenta@uw.edu

Post-Traumatic Stress Disorder (PTSD) remains under-detected in clinical settings, presenting opportunities for automated detection to identify at-risk patients. This study evaluates natural language processing approaches for binary PTSD classification from clinical interview transcripts using the DAIC-WOZ dataset, which contains semi-structured interviews with standardized psychological assessments. We compared embedding-based methods (SentenceBERT/LLaMA with logistic regression), general and mental health-specific transformer models (BERT/RoBERTa), and large language model prompting strategies (zero-shot/few-shot/chain-of-thought). SentenceBERT embeddings with logistic regression achieved the highest overall performance (AUPRC=0.758±0.128), outperforming domain-specific end-to-end fine-tuning models like Mental-RoBERTa (AUPRC=0.675±0.084 vs. RoBERTa-base 0.599±0.145). Few-shot prompting using DSM-5 criteria and two examples yielded competitive results (AUPRC=0.737). Performance varied significantly across symptom severity and comorbidity status with depression, with higher accuracy for severe PTSD cases and patients with comorbid depression. Our findings highlight the potential of embedding-based methods and LLMs for scalable screening while underscoring the need for improved detection of nuanced presentations.

Keywords: Post-Traumatic Stress Disorder, Natural Language Processing, Large language models, Mental health detection, Clinical Interview

© 2025 The Authors. Open Access chapter published by World Scientific Publishing Company and distributed under the terms of the Creative Commons Attribution Non-Commercial (CC BY-NC) 4.0 License.

1. Introduction

Post-Traumatic Stress Disorder (PTSD) affects approximately 6% of the U.S. population, with significantly higher rates among veterans and trauma survivors.[1] Despite its prevalence, PTSD remains under-detected in primary care settings, with studies suggesting that around 30% of cases go unrecognized.[2] Traditional screening approaches rely on structured clinical interviews and self-report measures, which require substantial clinical expertise and patient engagement. The development of automated screening tools could significantly improve detection rates, particularly in resource-constrained settings where mental health specialists are limited.

Recent advances in natural language processing (NLP) and large language models (LLMs) offer promising avenues for mental health assessment through analysis of patient language.[3, 4] While numerous studies have explored computational approaches to mental health detection, most have focused on depression and anxiety, with relatively less attention paid to PTSD.[4, 5] Furthermore, existing PTSD detection research has predominantly relied on social media data or surveys rather than clinical interview, limiting applicability at the point of care.[6] Prior work in clinical NLP has explored various approaches including transformer-based models like BERT and RoBERTa, embedding-based methods using SentenceBERT, and prompting strategies with large language models. Traditional transformer models trained on general text corpora which may have limited capability to capture the nuanced linguistic markers of PTSD, such as trauma-specific disfluencies, avoidance semantics, or fragmented narrative coherence. Though domain-adapted variants like Mental-BERT show promise for depression classification, their efficacy for PTSD detection remains unproven.[7] Embedding-based approaches using SentenceBERT have demonstrated effectiveness for depression detection tasks.[8] while instruction-tuned large language models offer potential for clinical assessment through prompting strategies that leverage clinical knowledge without requiring extensive labeled training data.[9, 10] However, these approaches have rarely been applied to PTSD detection in clinical interview settings, representing a significant gap in the literature.

The Distress Analysis Interview Corpus - Wizard of Oz (DAIC-WOZ) dataset provides a unique opportunity to develop and evaluate computational methods for PTSD detection in a simulated clinical context.[11-13] This dataset contains semi-structured clinical interviews conducted by a virtual interviewer with standardized psychological assessments as ground truth. While previous studies using this dataset have primarily focused on depression detection or multimodal approaches combining audio, visual, and linguistic features, the potential of advanced NLP techniques specifically for PTSD detection remains underexplored.[14]

To address this gap, this study bridges critical gaps in computational PTSD detection through a multifaceted NLP framework that advances both methodological innovation and clinical relevance. Our research investigates three key aspects: First, we examine the efficacy of various language representation approaches for PTSD detection with models fine-tuned on labeled data, comparing general versus domain-specific pre-trained transformer models (BERT and RoBERTa compared with Mental-BERT and Menta-RoBERTa) with embedding-based methods using more recent architectures (SentenceBERT and LLaMA). This comparison aims to identify whether domain adaptation or architectural differences have greater impact on PTSD classification performance. Second, we explore different LLM prompting strategies (zero-shot, few-shot, and chain-of-thought)

for PTSD classification, which to our knowledge represents the first application of instruction-tuned LLMs to PTSD detection in clinical interviews. This approach investigates whether LLMs can leverage clinical knowledge encoded during pre-training without requiring extensive labeled data. By comprehensively comparing these approaches, we contribute benchmark results for future research on automated PTSD detection using transcripts from clinical interviews. Third, we analyze how model predictions vary across symptom severity levels and comorbidity with depression, seeking to understand if computational approaches face similar challenges to human clinicians in distinguishing PTSD from related conditions, and in detecting subclinical or borderline cases.

This work has implications for the development of automated PTSD screening tools in mental health settings. By leveraging advanced NLP techniques for PTSD detection, our research may help address the significant gap in PTSD screening and assessment, particularly in primary care and other settings where specialized mental health resources are limited.

2. Methods

2.1. *Dataset*

For this study, we utilized the DAIC-WOZ dataset, a specialized collection of clinical interviews designed for psychological assessment research. The corpus contains semi-structured clinical interviews conducted by a virtual interviewer named Ellie, whose responses were controlled by human operators following a consistent protocol. The DAIC-WOZ dataset comprises multimodal data from 189 participants, including audio, video, and transcribed textual data. Each interview followed a clinical protocol designed to elicit information relevant to psychological assessment, beginning with neutral rapport-building questions before progressing to more specific inquiries about symptoms related to psychological distress. Pre-interview, participants completed standardized psychological assessments, including the PTSD Checklist-Civilian Version (PCL-C), which was used to establish ground truth diagnostic labels.[12] Among 189 participants, 56 (29.6% of the sample) met criteria for PTSD, while the remaining 133 were non-PTSD participants. Additionally, participants completed the Patient Health Questionnaire-8 (PHQ8) for depression assessment, enabling analysis of comorbid conditions. Among them, 42 (22.2% of the sample) were diagnosed as having depression and 147 were categorized as non-depressed participants.

2.2. *Data Preprocessing and Model Architecture*

This study focused on exploring the predictive power of natural language from clinical interviews. For our analysis, we focused exclusively on the patient-side transcripts, extracting only the verbal content produced by participants while excluding interviewer questions and prompts. This approach allowed us to isolate linguistic features directly attributable to the participants, minimizing potential confounding from interviewer speech patterns or question framing, which have been shown to influence model predictions of depression.[14]

For our baseline approach, we employed BERT (Bidirectional Encoder Representations from Transformers),[15] a pre-trained language model that generates contextual word embeddings capturing semantic information. We experimented with both a general domain “bert-base-uncased” model and

a domain-specific "mental-bert" variant, that has undergone additional pre-training using mental health-related posts collected from Reddit.[7] To address BERT's 512-token input limitation with lengthy clinical transcripts, we developed a chunking strategy that segmented each transcript into 512-token portions. From each chunk, we extracted the representation from the [CLS] token, which provides a 768-dimensional vector serving as an aggregate representation of that segment. To create a fixed-length representation for the variable-length transcripts, we computed the mean of all chunk embeddings, thereby preserving information from the entire transcript while maintaining consistent dimensions for the downstream classifier. We also implemented RoBERTa, which was trained with a larger corpus than BERT and with augmented training objectives,[16] utilizing both "roberta-base" and "mental-roberta" variants.[7] Models were trained for 10 epochs using AdamW optimizer with weight decay regularization,[17 18] with a learning rate of 2e−5, batch size of 4, and binary cross-entropy loss. To address class imbalance, we implemented weighted random sampling during training, assigning weights inversely proportional to class frequencies to ensure balanced representation of PTSD and non-PTSD cases in each mini-batch.[19] A linear layer with sigmoid activation was used as a classification layer for binary classification.

In addition to end-to-end fine-tuning approaches, we implemented embedding-based PTSD classification using representations generated from SentenceBERT and LLaMA followed by logistic regression. Embedding-based approaches produces semantically meaningful sentence embeddings directly without task-specific fine-tuning like BERT, making it computationally efficient for classification tasks. For SentenceBERT, we utilized the "paraphrase-multilingual-mpnet-base-v2" model, which produces 768-dimensional vectors for each text segment under 128 words.[20] Similar to our BERT implementation, we chunked transcripts and applied mean pooling to generate transcript-level embeddings. For LLaMA embeddings, we used pre-computed 16,384-dimensional vectors that were generated through mean pooling across entire transcripts without chunking, leveraging the model's ability to handle longer sequences effectively. Both embedding approaches were followed by logistic regression classification using scikit-learn's implementation (C=1.0, liblinear solver, maximum 1000 iterations). For the logistic regression models, balanced class weights were automatically computed as inversely proportional to class frequencies in the training data, effectively upweighting the minority PTSD class during optimization.

All models were evaluated using the same 5-fold stratified cross-validation to ensure robust and unbiased performance estimation across different data splits and across all methodologies.

2.3. *Large Language Models Approach*

We then explored the use of Large Language Models (LLMs) for PTSD prediction through various prompting strategies. We used LLaMA 3.1 with 405B parameters, a state-of-the-art open weight large language model, for this task in comparison with the fine-tuned models.[21, 22] This approach allowed us to assess whether LLMs could effectively identify linguistic markers of PTSD in patient speech without fine-tuning on labeled data. For our zero-shot learning approach, we developed a clinically informed prompt that framed the task as a diagnostic assessment performed by a psychiatrist specializing in trauma. The prompt incorporates the DSM-5 diagnostic criteria for PTSD,[23] which cover four key symptom clusters: intrusion symptoms, avoidance, negative alterations in cognitions and mood, and alterations in arousal and reactivity. We excluded the PTSD diagnostic Criterion A (exposure to traumatic events) as our analysis focused on linguistic markers

of current PTSD symptomatology that would be observable in the interview transcripts. This approach augments the LLM's ability to perform psychiatric assessment by providing explicit diagnostic criteria, without requiring examples from our dataset.

For few-shot learning, we enhanced the prompt by including a small number of labeled examples from our dataset. We selected the positive case with the highest PCL-C (PTSD Checklist – Civilian Version)[24] score and the first negative case with the lowest score we encountered in the dataset to serve as anchors for the classification task. These examples provided the model with concrete instances of how PTSD manifests linguistically in our specific clinical interview context.

We further incorporated a chain-of-thought methodology where the model was instructed to produce a step-by-step reasoning process before making the final classification. The prompt directs the model to first analyze the transcript for specific PTSD indicators across all symptom clusters, then synthesize this information into a brief rationale (under 100 words) justifying the classification decision, and finally output a binary classification (0 for no PTSD, 1 for PTSD). Our implementation followed a two-stage process: first, we used the chain-of-thought prompt to generate the detailed reasoning, then extracted this reasoning and fed it into a separate zero-shot classification prompt to obtain the final binary classification result and probability scores. Through this approach we aimed to improve classification accuracy by encouraging more structured analytical reasoning that mimics clinical diagnostic processes. The detailed prompt can be found in Table 1.

Table 1. Prompt Structure for PTSD prediction

Component	Prompt
Role specification	You are a highly experienced psychiatrist specializing in trauma and mental health disorders.
Task description	Your task is to analyze patient transcripts—containing only the patient's speech—and classify whether the patient has PTSD or not.
DSM-5 Criteria	According to the DSM-5 diagnostic criteria, PTSD is characterized by: a. Intrusion Symptoms: At least one symptom such as recurrent, involuntary, and intrusive distressing memories of the traumatic event(s); recurrent distressing dreams related to the event(s); dissociative reactions (e.g., flashbacks) in which the event seems to recur; intense or prolonged psychological distress at exposure to internal or external cues that symbolize or resemble the traumatic event(s); or marked physiological reactions to such cues. b. Avoidance: Persistent avoidance of stimuli associated with the traumatic event(s), evidenced by efforts to avoid distressing memories, thoughts, or feelings about or closely associated with the event(s) and/or avoidance of external reminders (people, places, conversations, activities, objects, or situations) that trigger these memories. c. Negative Alterations in Cognitions and Mood: Two or more symptoms such as inability to remember an important aspect of the traumatic event(s) (typically due to dissociative amnesia); persistent and exaggerated negative beliefs or expectations about oneself, others, or the world; persistent, distorted cognitions about the cause or consequences of the traumatic event(s) leading to self-blame or blaming others; persistent negative emotional state (e.g., fear, horror, anger, guilt, or shame); markedly diminished interest in significant activities; feelings of detachment or estrangement from others; or a persistent inability to experience positive emotions. d. Alterations in Arousal and Reactivity: Two or more symptoms such as irritable behavior and angry outbursts (with little or no provocation); reckless or self-destructive behavior; hypervigilance; exaggerated startle response; problems with concentration; or sleep disturbances.
Output format (Answer)	Based on these criteria and your analysis of linguistic patterns, coherence, sentiment, and emotional expressions in the transcript, output 0 if there is no indication of PTSD and 1 if PTSD is present. Provide only the classification result (0 or 1) without any additional explanation.
Output format (Answer + reasoning)	Based on these criteria and your analysis of linguistic patterns, coherence, sentiment, and emotional expressions in the transcript, output 0 if there is no indication of PTSD and 1 if PTSD is present. Format Your Output as Follows: - The classification at the start in the format: “Final Classification: 0” or “Final Classification: 1”. - Step-by-step reasoning for the classification in less than 100 words.
Few-shot examples	Here are two examples, one positive and one negative: Transcript for a participant with PTSD: xxx. Classification: 1; Transcript for a participant without PTSD: xxx. Classification: 0

2.4. *Performance Evaluation*

For each model, we report multiple complementary metrics to provide a comprehensive view of predictive performance. Area Under the Precision-Recall Curve (AUPRC) was selected as our primary metric due to its robust performance in imbalanced datasets, providing better discriminant ability for rare-case scenarios compared to AUROC.[25] AUPRC is particularly valuable in clinical settings where identifying positive cases (PTSD patients) is the primary concern, as it focuses on precision and recall trade-offs across different classification thresholds.

We also report Area Under the Receiver Operating Characteristic curve (AUROC) to evaluate discrimination performance across all possible classification thresholds, and balanced accuracy to account for potential class imbalance in our dataset. Balanced accuracy estimates the arithmetic mean of sensitivity and specificity, giving equal weight to performance on positive and negative classes regardless of their proportional representation. For all models, we determined optimal classification thresholds using the Equal Error Rate (EER) method, where the false positive rate equals the false negative rate. This threshold was then applied to calculate balanced accuracy, ensuring fair performance comparison across different model architectures.

For LLM-based prompting approaches, we implemented specialized methods to derive probability scores for metric calculation. For the zero-shot and few-shot approaches, we extracted logits from the model for both class labels (0 and 1) and converted to probabilities using SoftMax normalization. This approach provides a continuous measure of the model's confidence in each classification. For the chain-of-thought approach we employed a two-stage process, first collecting the reasoning output without the final classification, then feeding this reasoning back to the model to obtain logits for possible classifications. These logits were then normalized to probabilities for AUROC and AUPRC calculation. This methodology ensured comparable measurements across all model types despite their fundamental differences in classification approaches.

2.5. *Comorbidity and Severity Analysis*

To investigate the relationship between PTSD and depression diagnoses, we conducted a comprehensive stratified analysis by comorbidity status and symptom severity. For comorbidity analysis, we examined prediction performance separately for patients with and without comorbid depression, allowing us to assess whether models performed differently across these clinically distinct subgroups. This analysis was conducted using AUPRC as the primary metric to maintain consistency with our overall evaluation framework.

For severity analysis, we stratified participants into discrete PCL-C severity bins designed to have approximately equal sample sizes within each group, ensuring robust statistical comparisons across severity levels. For PTSD-positive participants, we created four severity bins: 39-46 (lowest severity), 47-53, 54-62, and 63-85 (highest severity). For PTSD-negative participants, we established four corresponding bins: 17-19 (lowest scores), 20-25, 26-30, and 31-56 (highest scores approaching clinical threshold). This overlap in score ranges between diagnostic groups, present in the original data, underscores the complexity of PTSD diagnosis and explains some of the

classification challenges observed in our models. We calculated classification accuracy for each model within these severity bins to determine how symptom intensity affected model performance across the spectrum of PTSD presentations. The analysis was performed across all three approaches: end-to-end, embedding-based and prompt-based models, to identify consistent patterns and understand the challenges models face across different clinical presentations of PTSD.

3. Results

3.1. *Supervised Learning Approaches*

3.1.1. End-to-End Fine-tuning Models

The performance of different end-to-end fine-tuning BERT-based models for PTSD classification is presented in Table 2. Our analysis revealed substantial performance differences between models pre-trained on general text corpora versus those specialized for mental health domains.

The domain-specific models consistently outperformed their general-domain counterparts across all evaluation metrics. Mental-BERT achieved an AUPRC of 0.647±0.101, representing a 24.0% improvement over BERT-base (0.522±0.092). Similarly, Mental-RoBERTa demonstrated superior performance with an AUPRC of 0.675±0.084, a 12.7% increase from RoBERTa-base (0.599±0.145).

Mental-RoBERTa achieved the highest AUPRC performance (0.675±0.084) among all end-to-end fine-tuning approaches, establishing it as the best-performing transformer-based model for PTSD detection. Notably, while RoBERTa variants typically outperform BERT models in many natural language processing tasks due to their more robust pre-training, in our experiments the advantage of Mental-RoBERTa over Mental-BERT was modest: only outperformed in AUPRC but underperformed in AUC and balanced accuracy. The domain of pre-training emerged as the dominant factor influencing performance, with both mental health-specific models substantially outperforming their general-domain counterparts.

Table 2. Performance comparison of general and mental health-specific BERT and RoBERTa for PTSD detection

	BERT-base	**Mental-BERT**	**RoBERTa-base**	**Mental-RoBERTa**
AUPRC	0.522±0.0 92	0.647±0.101	0.599±0.145	**0.675±0.084**
AUC	0.723±0.108	**0.794±0.059**	0.723±0.107	0.786±0.046
Balanced Acc	0.702±0.101	**0.739±0.091**	0.662±0.088	0.695±0.092

3.1.2. Embedding-based Models

We then evaluated embedding-based classification using frozen pre-trained representations followed by logistic regression to assess whether this two-stage approach could outperform end-to-end fine-tuning within the supervised learning category.

The SentenceBERT embedding + LR approach achieved an AUPRC of 0.758±0.128, representing a 12.3% improvement over the best end-to-end model (Mental-RoBERTa: 0.675±0.084). This approach also demonstrated strong discriminative ability with an AUROC of 0.856±0.069 and balanced accuracy of 0.801±0.097. The LLaMA embedding + LR method also showed competitive performance with an AUPRC of 0.693±0.094, AUROC of 0.835±0.046, and

balanced accuracy of 0.747±0.029, similarly exceeding Mental-RoBERTa's performance across all metrics (as shown in Table 3).

Both embedding-based approaches outperformed end-to-end fine-tuning, with SentenceBERT + LR demonstrating the strongest performance among supervised learning methods. This finding suggests that pre-trained sentence-level embeddings, when combined with logistic regression on a small dataset, can capture linguistic patterns associated with PTSD more effectively than end-to-end fine-tuning. The strong performance of both embedding approaches indicates that frozen language model representations contain rich semantic information that can be effectively leveraged by simpler linear classifiers. Moreover, the computational efficiency of embedding-based approaches makes them particularly attractive for clinical applications, as they eliminate the need for resource-intensive fine-tuning while delivering superior performance within the supervised learning category.

3.2. *Instruction-Tuned Language models*

We evaluated various prompting strategies for PTSD classification using LLaMA 3.1 to assess whether large language models could achieve competitive performance without requiring labeled training data or domain-specific fine-tuning.

Zero-shot classification using LLaMA prompted with DSM-5 criteria achieved an AUPRC of 0.701, AUROC of 0.841, and balanced accuracy of 0.751 (Table 3). This approach leveraged the model's pre-trained knowledge by providing explicit psychiatric diagnostic criteria in the prompt, demonstrating that LLMs can effectively utilize clinical guidelines to identify linguistic markers of PTSD without any training examples from our dataset.

Adding one positive and one negative example case to the prompt improved performance across most metrics. The few-shot approach achieved an AUPRC of 0.737, balanced accuracy of 0.804, and the highest AUROC of 0.875 among all instruction-tuned methods (Table 3). The superior AUROC performance indicates exceptional discriminative ability, suggesting that strategically selected examples enhance the model's ability to distinguish between PTSD and non-PTSD cases.

Chain-of-thought prompting, which required the model to provide step-by-step diagnostic reasoning before classification, achieved an AUPRC of 0.579, AUROC of 0.705, and balanced accuracy of 0.681 (Table 3). This approach showed the lowest performance among instruction-tuned methods, indicating that explicit diagnostic reasoning steps do not improve PTSD classification accuracy in this context.

3.3. *Cross-Method Performance*

Table 3 presents a comprehensive comparison across all approaches. SentenceBERT + LR achieved the highest AUPRC (0.758±0.128) among all methods, representing the best overall performance for PTSD detection. However, few-shot prompting demonstrated the best discriminative ability (AUROC: 0.875) and competitive balanced accuracy (0.804).

Within supervised learning approaches, embedding-based methods consistently outperformed end-to-end fine-tuning, with both SentenceBERT + LR and LLaMA + LR exceeding Mental-RoBERTa across all metrics. Among instruction-tuned approaches, the strong performance of zero-

shot and few-shot approaches demonstrates that these models have successfully encoded substantial domain knowledge relevant to mental health assessment during pre-training, enabling competitive performance without labeled training data.

The results reveal distinct trade-offs between approach categories: supervised learning methods achieved the highest performance but require labeled training data, while instruction-tuned approaches achieved competitive performance with few trained data but need substantial computational resources to host the large models, offering advantages in scenarios where clinical training data is scarce or unavailable.

Table 3. Performance comparison of fine-tuning, embedding-based, and prompting approaches for PTSD detection

	End-to-end	**Embedding-based**		**Prompt-based**		
	Mental RoBERTa	SBERT + LR	LLaMA + LR	LLaMA ZS	LLaMA FS	LLaMA CoT
AUPRC	0.675±0.084	**0.758±0.128**	0.693±0.094	0.701	0.737	0.579
AUC	0.786±0.046	0.856±0.069	0.835±0.046	0.841	**0.875**	0.705
Balanced Acc	0.695±0.092	0.801±0.097	0.747±0.029	0.751	**0.804**	0.681

3.4. *Model Predictions Patterns: Severity and Comorbidity Effects*

3.4.1. Severity Analysis

Results of our evaluation of model performance across different PTSD severity levels, based on PCL-C self-report scores, are shown in Figure 1. All six approaches (Mental-RoBERTa, SentenceBERT + LR, LLaMA + LR, and the three LLaMA prompting methods) exhibit similar performance patterns across PTSD severity levels, suggesting consistent challenges in classification based on symptom intensity.

For PTSD-positive participants, most models demonstrated improved accuracy with increasing severity. Several approaches achieved perfect or near-perfect accuracy for the most severe cases (63-85 range): LLaMA + LR (100%), few-shot (100%), Mental-RoBERTa (92.9%), zero-shot (92.9%), and chain-of-thought (92.9%), while SentenceBERT + LR achieved 85.7%. These findings suggest that extreme cases at both ends of the severity spectrum (very low or very high PCL-C scores) are easier for models to classify correctly, while cases with moderate severity present the greatest challenge.

Conversely, for PTSD-negative participants, all models showed declining accuracy with increasing severity scores, indicating that PTSD-negative participants with more severe symptoms are more likely to be inaccurately classified as having PTSD. Accuracy dropped substantially from the lowest severity bin (17-19) to the highest bin (31-56) across all approaches: Mental-RoBERTa (80.6% to 46.9%), SentenceBERT + LR (83.3% to 59.4%), LLaMA + LR (86.1% to 56.2%), zero-shot (88.9% to 59.4%), few-shot (94.4% to 62.5%), and chain-of-thought (72.2% to 56.2%). This suggests that subclinical cases approaching the diagnostic threshold pose greater classification challenges, likely due to their linguistic similarities with mild PTSD presentations.

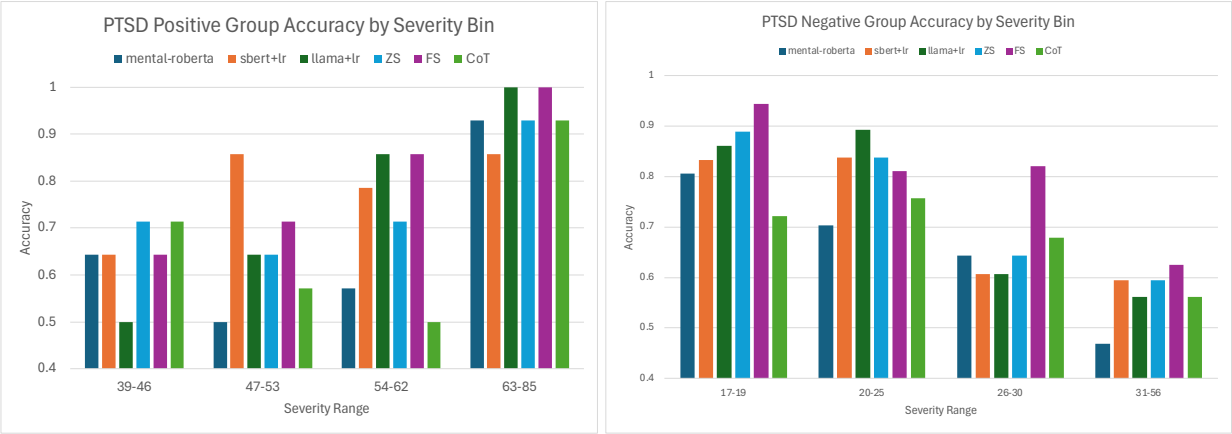

Figure 1. Accuracy of PTSD prediction by PCL-C severity score

3.4.2. Comorbidity Analysis

We then evaluated the predictive accuracy for PTSD while considering the influence of depression comorbidity, with results shown in Table 4. A striking finding emerged when comparing model performance across depression comorbidity groups using AUPRC as the evaluation metric. For patients with comorbid depression, all models demonstrated remarkably high AUPRC scores: few-shot achieving 0.961, Mental-RoBERTa reaching 0.953, SentenceBERT + LR achieving 0.925, zero-shot reaching 0.915, LLaMA + LR achieving 0.879, and chain-of-thought reaching 0.859. In contrast, performance was substantially lower for PTSD classification among patients without depression, with AUPRC scores ranging from 0.381 to 0.574 across all models.

This performance pattern was consistent across all methodologies, suggesting that the observed performance disparity reflects a complex interplay between comorbidity status and symptom severity. Supporting this interpretation, our correlation analysis revealed strong associations between PTSD and depression severity scores (overall Spearman $\rho = 0.8426$, $p < 0.001$). Further analysis revealed that participants with depression exhibited significantly more severe PTSD symptoms, with a median PCL-C score of 59.5 compared to PTSD participants without comorbid depression (median = 49.5; Welch's t-test: $t=3.620$, $p<0.001$).

Table 4. AUPRC comparison of PTSD prediction in patient with/without depression

AUPRC	Overall	patient with depression	Patient without depression
Mental RoBERTa	0.675±0.084	0.953±0.048	0.521±0.171
SBERT + LR	0.758±0.128	0.925±0.073	0.574±0.137
LLaMA + LR	0.693±0.094	0.879±0.070	0.562±0.100
LLaMA zs	0.701	0.915	0.492
LLaMA fs	0.737	0.961	0.467
LLaMA cot	0.579	0.859	0.381

4. Discussion

Our findings demonstrate the potential of advanced NLP approaches for detecting PTSD from clinical interview transcripts, while also revealing important challenges and considerations for

clinical implementation. The results highlight several key insights at the intersection of computational linguistics and mental health assessment.

Among supervised learning methods, embedding-based approaches demonstrated superior performance over end-to-end fine-tuning. The SentenceBERT embedding + logistic regression approach achieved the highest AUPRC performance (0.758±0.128), outperforming the best end-to-end model (Mental-RoBERTa: 0.675±0.084). This suggests that decoupling embedding generation from classification through a two-stage approach offers significant advantages for PTSD classification from clinical transcripts, particularly when working with limited labeled data. The effectiveness of logistic regression with balanced class weights demonstrates that sophisticated neural network architectures are not always necessary for clinical text classification when high-quality embeddings are available.

Within end-to-end fine-tuning approaches, domain-specific models (Mental-BERT and Mental-RoBERTa) substantially outperformed their general-domain counterparts (BERT-base and RoBERTa-base), underscoring the importance of domain adaptation in mental health applications. This finding aligns with prior work in clinical NLP that has shown domain-specific language representations better capture the nuanced linguistic patterns associated with psychological distress.[7, 26] The superior performance of mental health-specific models suggests that these pre-trained representations more effectively encode the subtle linguistic markers of PTSD.

Our exploration of more complex supervised learning approaches—including BERT/Mental BERT embeddings, deep feed-forward neural networks and complex pooling strategies—did not yield performance improvements over the embedding + logistic regression approach, suggesting that for clinical interview transcripts, simpler approaches may be more robust and generalizable.

Among instruction-tuned approaches, our exploration of LLM prompting strategies revealed that zero-shot classification using clinical criteria can achieve competitive performance without any training examples, highlighting the potential of instruction-tuned LLMs to leverage encoded linguistic information.[3] This finding has significant implications for low-resource scenarios where labeled clinical data is scarce or unavailable. The few-shot approach achieved the highest discriminative ability (AUROC: 0.875) among all instruction-tuned methods, suggesting that strategically selected examples can enhance LLM performance for clinical classification tasks, consistent with findings in other clinical NLP applications.[10]

Contrary to expectations, the chain-of-thought reasoning strategy showed lower performance despite its more structured analytical process. This pattern contrasts with findings in other domains where chain-of-thought reasoning typically enhances performance.[9] This could indicate that the linguistic markers of PTSD in transcripts are detected by LLMs more through implicit pattern recognition than through the explicit application of diagnostic criteria in a sequential reasoning process.

The substantial performance differences observed across symptom severity levels and comorbidity status represent particularly clinically relevant findings. Most models exhibited a clear bidirectional pattern: declining accuracy with increasing severity for PTSD-negative cases and improving accuracy with increasing severity for PTSD-positive cases. This severity-dependent performance mirrors challenges faced by human clinicians, where clear-cut cases are more readily identified than those with moderate or subclinical presentations.[27] This diagnostic complexity is

further illustrated by the inconsistencies between PTSD diagnoses and patient-submitted PCL-C scores observed in the DAIC-WOZ dataset. Such inconsistencies typically arise because clinical interviews and self-report measures often diverge in moderate severity cases—clinicians may apply diagnostic thresholds differently than standardized cutoffs used in self-report scales, and patients' subjective experiences of symptoms may not align with clinically observable manifestations, creating a challenging middle ground where diagnostic agreement is lowest.

The markedly higher performance for patients with comorbid depression raises important considerations for clinical implementation. This enhanced model performance in comorbid cases likely reflects the more readily detectable transdiagnostic symptoms—such as emotional dysregulation, sleep disturbances, and cognitive difficulties—that represent cross-cutting dimensional constructs consistent with Research Domain Criteria (RDoC) frameworks.[28, 29] These shared symptom dimensions create stronger, more detectable linguistic signals when both conditions are present at higher severity levels. Rather than representing confounding between conditions, the substantial overlap in severe presentations indicates that comorbid cases manifest more pronounced psychological distress across multiple symptom domains, creating a more robust linguistic signature that facilitates computational detection.[30] This interpretation is strongly supported by the consistent pattern observed across all model architectures and prompting strategies, suggesting a fundamental linguistic phenomenon rather than a model-specific limitation.

This finding has two primary clinical implications. First, automated screening tools based on current approaches may be most effective as part of a staged screening process, where they are used to identify potential cases for further clinical assessment rather than as standalone diagnostic tools. This approach could provide value in places where mental health specialists are limited, serving as an efficient tool to flag cases requiring clinical attention. Second, these tools may require specific calibration for different patient populations, considering both symptom severity and comorbidity profiles. The development of more sophisticated models that can distinguish PTSD-specific linguistic markers from general indicators of psychological distress remains an important direction for future research.

5. Limitations and Future Directions

Several limitations should be considered when interpreting our findings. First, this study relied on a single dataset (DAIC-WOZ) with a relatively small sample size (189 participants), which may limit the generalizability of our findings. The limited sample size may explain why embedding-based approaches outperformed end-to-end fine-tuning approaches, as the latter require training the entire neural network and may be more prone to overfitting with insufficient training data. Second, the chunking and mean-pooling approach used to handle long transcripts may obscure the detection of temporal patterns that could be diagnostically relevant for PTSD, such as fragmented narratives when discussing traumatic events. While we explored alternative pooling strategies including attention-based and hierarchical long short-term memory pooling mechanisms, these did not improve performance over simple mean pooling. Third, while our approach incorporates DSM-5 criteria in prompting strategies, the linguistic patterns captured by computational models may not fully align with the clinical reasoning process used in traditional diagnostic approaches. Fourth, our

few-shot prompting strategy used a simple selection method (highest and lowest PCL-C scores), which may not represent optimal example selection for enhancing model performance. More sophisticated example selection strategies based on linguistic diversity, diagnostic complexity, or active learning principles could potentially improve few-shot performance. Fifth, our evaluation was limited to a single LLM architecture (LLaMA 3.1), and performance may vary across different instruction-tuned models such as GPT-4, or other state-of-the-art LLMs. Finally, the DAIC-WOZ dataset, while valuable for its standardized interview format, may not fully represent the diversity of PTSD presentations across different trauma types, cultural backgrounds, and demographic groups. Evaluation on structured interview data may also limit generalizability to unstructured conversations. Future validation in diverse clinical settings and interview styles is essential to establish broader clinical utility.

Our work suggests several promising directions for future research. First, evaluation on larger, more diverse clinical datasets is needed to validate our findings and assess the scalability of embedding-based approaches. Second, multimodal approaches that combine linguistic analysis with audio and visual features could potentially enhance detection accuracy, particularly for patients who may not express their psychological distress linguistically. Third, developing more sophisticated sequence modeling approaches that can capture temporal dynamics while maintaining the efficiency of embedding-based methods represents an important technical challenge. Finally, future work should explore how these computational approaches can be integrated into clinical workflows to augment rather than replace clinician judgment, including developing interpretable models that provide clinicians with transparent reasoning for their predictions.

6. Conclusion

Our comprehensive evaluation of language modeling approaches for PTSD detection demonstrates both the potential and limitations of current computational methods. embedding-based methods, particularly SentenceBERT combined with logistic regression (AUPRC=0.758±0.128), outperform both domain-specific end-to-end fine-tuning and large language model prompting strategies. While domain-specific pre-training showed clear benefits over general models, and prompt-based approaches achieved competitive performance without requiring labeled data (few-shot AUROC=0.875), all methods demonstrated substantially higher performance for patients with comorbid depression and performed worse with moderate-severity cases, suggesting current approaches may detect general psychological distress rather than PTSD-specific markers. These findings provide practical insights for clinical implementation, highlighting the computational efficiency and clinical viability of embedding-based approaches while underscoring the need for more nuanced methods to address the significant challenges in PTSD recognition and facilitate earlier intervention for those affected by this widespread condition.

Acknowledgements

This study was supported by National Institute of Mental Health U01MH135901. We would like to thank John Gratch, Jill Boberg, and their colleagues at the USC Institute for Creative Technologies for making this dataset available to the scientific community.

References

1.Affairs USDoV. How Common Is PTSD in Adults? National Center for PTSD2025 [Available from: https://www.ptsd.va.gov/understand/common/common_adults.asp.
2.Zammit S, Lewis C, Dawson S, et al. Undetected post-traumatic stress disorder in secondary-care mental health services: Systematic review. The British Journal of Psychiatry. 2018;212(1):11-8.
3.Stade EC, Stirman SW, Ungar LH, et al. Large language models could change the future of behavioral healthcare: a proposal for responsible development and evaluation. NPJ Mental Health Research. 2024;3(1):12.
4.Xu X, Yao B, Dong Y, et al. Mental-llm: Leveraging large language models for mental health prediction via online text data. Proceedings of the ACM on Interactive, Mobile, Wearable and Ubiquitous Technologies. 2024;8(1):1-32.
5.Omar M, Soffer S, Charney AW, et al. Applications of large language models in psychiatry: a systematic review. Frontiers in psychiatry. 2024;15:1422807.
6.Bartal A, Jagodnik KM, Chan SJ, Dekel S. AI and narrative embeddings detect PTSD following childbirth via birth stories. Scientific Reports. 2024;14(1):8336.
7.Ji S, Zhang T, Ansari L, et al. Mentalbert: Publicly available pretrained language models for mental healthcare. arXiv preprint arXiv:211015621. 2021.
8.Ogunleye B, Sharma H, Shobayo O. Sentiment Informed Sentence BERT-Ensemble Algorithm for Depression Detection. Big Data and Cognitive Computing. 2024;8(9):112.
9.Wei J, Wang X, Schuurmans D, et al. Chain-of-thought prompting elicits reasoning in large language models. Advances in neural information processing systems. 2022;35:24824-37.
10.Liu H, Zhang W, Xie J, et al. Few-shot learning for chronic disease management: Leveraging large language models and multi-prompt engineering with medical knowledge injection. arXiv preprint arXiv:240112988. 2024.
11.Gratch J, Artstein R, Lucas GM, et al., editors. The distress analysis interview corpus of human and computer interviews. LREC; 2014: Reykjavik.
12.DeVault D, Artstein R, Benn G, et al., editors. SimSensei Kiosk: A virtual human interviewer for healthcare decision support. Proceedings of the 2014 international conference on Autonomous agents and multi-agent systems; 2014.
13.Ringeval F, Schuller B, Valstar M, et al., editors. AVEC 2019 workshop and challenge: state-of-mind, detecting depression with AI, and cross-cultural affect recognition. Proceedings of the 9th International on Audio/visual Emotion Challenge and Workshop; 2019.
14.Burdisso S, Reyes-Ramírez E, Villatoro-Tello E, et al. DAIC-WOZ: On the Validity of Using the Therapist's prompts in Automatic Depression Detection from Clinical Interviews. arXiv preprint arXiv:240414463. 2024.
15.Devlin J, Chang M-W, Lee K, Toutanova K, editors. Bert: Pre-training of deep bidirectional transformers for language understanding. Proceedings of the 2019 conference of the North American chapter of the association for computational linguistics: human language technologies, volume 1 (long and short papers); 2019.
16.Liu Y, Ott M, Goyal N, et al. Roberta: A robustly optimized bert pretraining approach. arXiv preprint arXiv:190711692. 2019.
17.Loshchilov I, Hutter F. Decoupled weight decay regularization. arXiv preprint arXiv:171105101. 2017.

18.Kingma DP, Ba J. Adam: A method for stochastic optimization. arXiv preprint arXiv:14126980. 2014.
19.Cui Y, Jia M, Lin T-Y, et al., editors. Class-balanced loss based on effective number of samples. Proceedings of the IEEE/CVF conference on computer vision and pattern recognition; 2019.
20.Reimers N, Gurevych I. Sentence-bert: Sentence embeddings using siamese bert-networks. arXiv preprint arXiv:190810084. 2019.
21.Touvron H, Lavril T, Izacard G, et al. Llama: Open and efficient foundation language models. arXiv preprint arXiv:230213971. 2023.
22.Grattafiori A, Dubey A, Jauhri A, et al. The llama 3 herd of models. arXiv preprint arXiv:240721783. 2024.
23.Regier DA, Kuhl EA, Kupfer DJ. The DSM‐5: Classification and criteria changes. World psychiatry. 2013;12(2):92-8.
24.Andrykowski MA, Cordova MJ, Studts JL, Miller TW. Posttraumatic stress disorder after treatment for breast cancer: Prevalence of diagnosis and use of the PTSD Checklist—Civilian Version (PCL—C) as a screening instrument. Journal of consulting and clinical psychology. 1998;66(3):586.
25.Saito T, Rehmsmeier M. The precision-recall plot is more informative than the ROC plot when evaluating binary classifiers on imbalanced datasets. PloS one. 2015;10(3):e0118432.
26.Su C, Xu Z, Pathak J, Wang F. Deep learning in mental health outcome research: a scoping review. Translational psychiatry. 2020;10(1):116.
27.Palm KM, Strong DR, MacPherson L. Evaluating symptom expression as a function of a posttraumatic stress disorder severity. Journal of Anxiety Disorders. 2009;23(1):27-37.
28.Insel T, Cuthbert B, Garvey M, et al. Research domain criteria (RDoC): toward a new classification framework for research on mental disorders. American Psychiatric Association; 2010. p. 748-51.
29.Dalgleish T, Black M, Johnston D, Bevan A. Transdiagnostic approaches to mental health problems: Current status and future directions. Journal of consulting and clinical psychology. 2020;88(3):179.
30.Todorov G, Mayilvahanan K, Cain C, Cunha C. Context-and subgroup-specific language changes in individuals who develop PTSD after trauma. Frontiers in Psychology. 2020;11:989.

ED-Explain: Personalized Video Instructions for Patients Discharged from the Emergency Department

Luyang Luo[1*], Emma Chen[1*], Xiaoman Zhang[1], Julian Nicolas Acosta[1], Boyang Tom Jin[2], Fatma Gunturkun[3], Christian Rose[3], Carl Preiksaitis[3], Brian Suffoletto[3], Pranav Rajpurkar[1†], David A Kim[3†]

[1]*Department of Biomedical Informatics, Harvard Medical School*
[2]*Department of Computer Science, Stanford University*
[3]*Department of Emergency Medicine, Stanford University School of Medicine*

This paper presents ED-Explain, an integrated, AI-driven system that transforms emergency department (ED) discharge instructions and electronic health records into personalized video presentations featuring a virtual healthcare provider. By leveraging multimodal ED data, large language models, and video generation, we aimed to produce accessible discharge instructions tailored to patients' ED visits. Four board-certified Emergency Medicine physicians reviewed 39 pairs of original and ED-Explain-produced discharge instructions. AI video summaries received significantly higher ($p<0.001$) average ratings (1-5) of completeness (4.1 vs. 3.1), correctness (3.9 vs. 3.5) and patient accessibility (3.4 vs. 2.9). Physicians expressed reservations about 13.3% of ED-Explain's discharge instructions for patient viewing, and only 4.6% of ED-Explain's instructions were found inappropriate for use with patients. Physician feedback suggests that AI-enhanced video discharge summaries have potential to improve communication of discharge information to ED patients, though patient-centered evaluation is needed. This work contributes to the growing field of AI-assisted healthcare communication and offers insights into the potential for AI to improve physician-patient communication and patient self-efficacy.

Keywords: Patient-centered Understanding; AI-generated Discharge Instruction.

1. Introduction

Background and motivation. Emergency department (ED) discharge represents a critical yet vulnerable transition point in patient care. The ED environment-characterized by high patient volumes, heterogeneous clinical presentations, time pressure, and frequent interruptions—creates substantial barriers to effective physician-patient communication. These communication challenges have serious consequences: between 41% and 78% of patients fail to adequately understand their diagnosis, treatment plan, or follow-up instructions upon leaving the ED.[1–8] More concerning, many patients overestimate their own comprehension,[5] creating a dangerous gap between perceived and actual understanding. Despite recognition of these problems and numerous efforts to improve discharge communication,[8–10] practical implementation has been limited by the requirement of substantial additional time from already-overburdened

© 2025 The Authors. Open Access chapter published by World Scientific Publishing Company and distributed under the terms of the Creative Commons Attribution Non-Commercial (CC BY-NC) 4.0 License.

* These authors contributed equally. † Co-senior authorship.

healthcare providers, making widespread adoption impractical in busy ED settings.

AI in provider-patient communication. Recent advances in artificial intelligence (AI) offer a potential solution. Large language models (LLMs) have demonstrated capability in simplifying complex medical information, including radiology reports[11] and consent documents.[12] A cross-sectional study by Kumar et al.[13] showed that GPT-4-based plain language translation of discharge materials significantly improved both objective and subjective patient comprehension. However, existing research has focused primarily on simplifying text-based materials without leveraging the established benefits of multimodal communication. Evidence from multiple domains suggests that video-based patient education can be more effective than written materials alone. Synchronized visual and verbal explanations improve patient comprehension and satisfaction.[10,14] In radiology, "ReXplain"[15] demonstrated the feasibility of AI-generated video reports with high ratings from radiologists. However, creating personalized video content manually remains time-intensive and impractical for routine clinical use.

Our approach and contributions. In this paper, we present ED-Explain, an integrated, AI-driven system that transforms multimodal visit data and original text discharge instructions into personalized, plain-language video presentations from a virtual healthcare provider. ED-Explain combines multimodal structured and free-text data, LLMs, and video generation to create engaging, accessible discharge instructions tailored to the patient encounter. 39 pairs of original and ED-Explain-generated discharge instructions, Emergency physicians rated the AI-generated discharge instructions as significantly more complete, correct, and accessible than the original discharge instruction. The physicians also deemed that ED-Explain could benefit both patients and providers if deployed. Our contributions include: (1) a multimodal approach that synthesizes diverse ED data types into coherent patient-friendly narratives, (2) empirical evidence that AI-generated instructions can exceed the quality of standard discharge materials as judged by emergency physicians, and (3) insights into physician perspectives on implementation challenges and opportunities.

2. Related Works

2.1. *Health Literacy and Outcomes*

The underlying issue extends beyond the ED environment to the broader challenge of health literacy—defined as the ability to obtain, process, and understand basic health information needed to make appropriate health decisions.[16] According to the Centers for Disease Control and Prevention, nearly nine out of ten adults struggle to understand and use health information when it contains unfamiliar or complex medical terminology,[17] highlighting the critical need for clearer communication strategies. This health literacy challenge is strongly associated with higher rates of hospital admission and readmission, increased healthcare costs, and higher all-cause mortality.[18] These consequences disproportionately affect marginalized populations, including older adults, racial and ethnic minorities, patients with limited English proficiency, and those with limited education.[19] Moreover, health literacy influences health outcomes through a multidimensional causal pathway.[20] The strongest evidence for its impact

appears at the most proximal (health knowledge) and distal (mortality) ends of this pathway, with less consistent evidence for intermediary outcomes such as self-management behaviors.[16] While health literacy directly influences knowledge acquisition, the translation of this knowledge into improved health behaviors and outcomes is mediated by additional factors including motivation, resources, and system-level barriers.

2.2. *Interventions to Improve Discharge Communication*

Various approaches have been proposed to enhance patient understanding of discharge instructions, ranging from improved written materials to multimodal communication strategies. DeSai et al.[9] evaluated the impact of simplified discharge instructions, finding significant improvements in patient comprehension. Teach-back methods, in which patients are asked to repeat instructions in their own words, have shown promise in improving comprehension. Slater et al.[8] found that incorporating teach-back methods into the discharge process improved retention of key domains of emergency department discharge instructions, particularly regarding follow-up appointments and medication management. In a systematic review, Oh et al.[21] further demonstrated that discharge education with the teach-back method was associated with reduced 30-day readmission rates, suggesting clinical benefits beyond improved comprehension.

Multimodal communication approaches that combine visual, auditory, and textual elements have emerged as a promising direction for improving patient comprehension. Bloch et al.[10] conducted a randomized controlled trial demonstrating that video discharge instructions improved caregivers' understanding of their child's emergency department visit compared to standard written instructions. The effect was particularly pronounced for follow-up care instructions, where comprehension improved from 59% to 91%. Building on this foundation, Wray et al.[22] developed and evaluated standardized discharge instruction videos for common emergency department conditions, finding that they improved patient satisfaction and reduced callbacks for clarification. However, these standardized videos lacked personalization to individual patient circumstances, potentially limiting their effectiveness for complex cases.

In the field of radiology, Recht et al.[14] found that video reports created by radiologists, featuring explanations and visual guidance, were strongly preferred by patients over written reports alone. Similarly, Balkman et al.[23] demonstrated that audio/video reporting workflows supplementing standardized radiology reports improved patient comprehension and satisfaction. However, both approaches required substantial radiologist time for video creation, limiting their scalability in practice. Neto et al.[24] further established the value of audiovisual reports in emergency musculoskeletal radiology, finding that patients preferred them over traditional reports and demonstrated improved understanding of their conditions. The authors noted that the production of such videos required specialized software and significant radiologist time, highlighting the need for more efficient production methods.

2.3. *AI Applications in Healthcare Communication*

Recent advances in large language models (LLMs) have created new opportunities for improving healthcare communication. LLMs demonstrate capability in translating medical terminol-

ogy into patient-friendly language while maintaining clinical accuracy. Large language models, such as GPT-4, have shown promise in simplifying radiology reports and medical consent, as well as translating appropriate patient instructions for incidental findings, though instances of hallucination underscore the need for clinical oversight.[12,13,25] Cross-sectional evaluation of GPT-4-based clinical note translation revealed significant improvements in patient comprehension, with larger gains among traditionally underserved populations.[13] Beyond text-only applications, multimodal approaches are emerging. "ReXplain" integrates language models with image segmentation and avatar generation to transform radiology reports into patient-friendly videos. Initial feedback from radiologists suggests this approach effectively simulates one-on-one consultation.[15] These developments highlight AI's growing role in bridging communication gaps between healthcare providers and patients.

Clough et al.[26] conducted a pilot study evaluating AI-generated discharge summaries based on mock patient vignettes, finding that all AI-generated summaries were deemed acceptable by general practitioners, compared to 92% of summaries written by junior doctors. Similarly, Kim et al.[27] developed and validated patient-friendly discharge summaries based on GPT technology in Korea, demonstrating high acceptance among both patients and physicians. However, Williams et al.[28] observed instances of hallucination or omission of clinically significant facts in LLM-generated discharge summaries for complex cases, highlighting the need for improved factual grounding.

2.4. *Gaps in the Current Literature*

Despite advances in AI for healthcare communication, significant gaps remain that limit clinical impact. First, many of previous studies have approached discharge summary generation as technical challenges focused on clinical accuracy rather than patient comprehension. Second, translation-based approaches remain constrained by the quality and structure of original documents, merely simplifying language without addressing possible organizational flaws. Third, research has remained almost exclusively text-based, failing to leverage the established benefits of multimodal communication, despite evidence that video formats significantly enhance understanding of complex medical concepts.[10,14,15,29] These limitations collectively highlight the need for an approach that fundamentally reimagines discharge communication through multimodal formats while directly measuring impact on clinical outcomes.

3. Method

ED Visit Data. Discharge instructions are particularly important for patients at high risk of complications and return visits. Therefore, we randomly sampled 50 ED visits from the Stanford Adult Emergency Department (2020–2024) followed by a return visit within 30 days of the original encounter. We excluded 11 cases lacking original discharge instructions, which produced a final cohort of 39 ED visits. Data are de-identified following the approach by Kansal et al.[30]

Multimodal Visit Documentation. The term "multimodal" in this study refers to the integration of multiple types of electronic health record data, specifically structured data fields

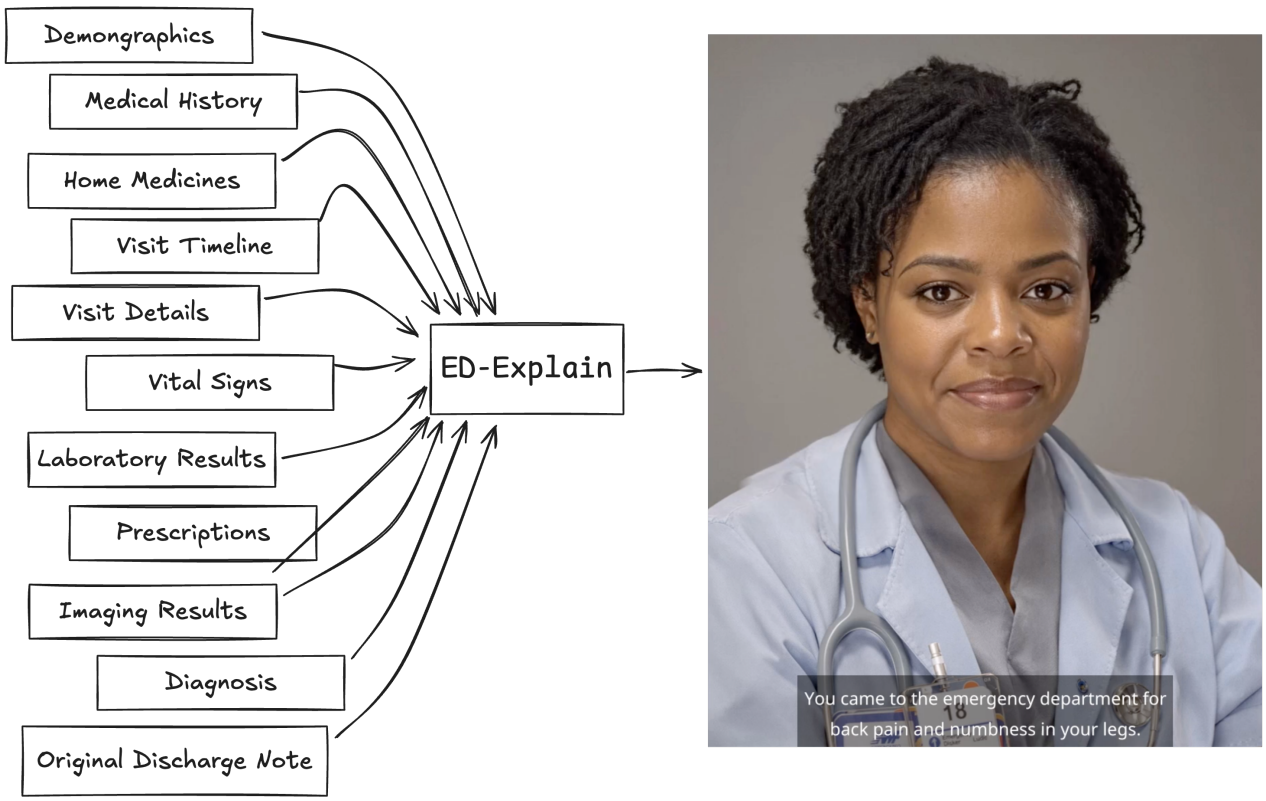

Fig. 1. **ED-Explain workflow**. We produced structured visit documents containing patient demographics, past medical history, home medications, vital signs, laboratory and imaging results, diagnoses, prescriptions, and original ED discharge instructions. ED-Explain converted visit documents into video discharge instructions featuring a virtual healthcare provider.

(such as vitals) and unstructured free-text narratives. This approach differs from multimodal AI systems that process images, audio, or video.

We first convert de-identified multimodal visit data into a single visit document. Structured data included: patient demographics (age, gender, payor), home medications, past medical history, visit metadata (chief complaint; triage information; diagnosis, arrival, disposition, and departure times), orders (medications, laboratory and imaging tests, consults), laboratory results, and vital signs. De-identified free-text data included: radiology report impressions, and the original text of discharge instructions given to patients upon discharge from the ED.

Home medications included names and medication classes. Past medical history included ICD-10 codes, descriptions, and Clinical Classification Software (CCS) categories. Vital signs—including heart rate, respiratory rate, oxygen saturation, temperature, systolic blood pressure, and diastolic blood pressure—are summarized by minimum, maximum, and final recorded values from the visit. Laboratory results were represented both categorically (normal/abnormal/critical) and as numerical values with reference ranges. Imaging results included study types and de-identified free-text narrative impressions.

Visit documents also included details of previous visits to capture patterns of healthcare utilization, including chief complaints, diagnoses, and dispositions.

Discharge Instruction Translating Prompt

You are helping explain what happened in the emergency department visit for the patient. You will be given a note recording the patient's visit and discharge summary. Help explain the note as follows:
(1) Briefly summarize the reason for the visit and what was found
(2) Provide a coherent narrative of what happened during the ED visit in chronological order, highlighting key events with general timing (e.g., "Initially," "Later," "Following that," "Toward the end of your visit")
(3) Note any specific findings that require follow up
(4) Any actions the patient should take
(5) Scheduled follow up plan
(6) Reasons to return to ED

Requirements:
*Begin with a coherent story introduction: "You came to the emergency department for [chief complaint]."
*Then provide a smooth narrative of the ED visit: "When you first arrived, [initial assessments/procedures]. After that, [subsequent events]. Based on these initial findings, [additional tests/interventions] were performed. The results showed [relevant findings]."
*Include approximate timing where meaningful (e.g., "Shortly after arrival," "Several hours into your visit," "Before discharge"), but prioritize the flow of the story over precise timestamps.
*Include relevant test results, noting both normal and abnormal findings within the narrative context they occurred.
*Discuss trends in serial results when applicable, and where results fall in the patient's past distribution of results.
*All explanations should be conversational. *Try your best to generate the explanation in a way that can be understood by a layman with an eighth-grade reading level.
*Try your best to make the explanation concise while maintaining clarity.
*When there are abbreviations, expand them. *Do not suggest anything except for those already mentioned in the report.

Example:
"You came to the emergency department late last night for chest pain and shortness of breath.

When you first arrived, the nursing team checked your vital signs and found your heart rate was slightly elevated. The doctor then examined you and ordered several tests to check your heart and lungs. First, you had an electrocardiogram (ECG) to check your heart rhythm, which was normal. Shortly after, blood samples were taken to check for signs of heart damage.

Later in your visit, you had a chest X-ray. When all your test results came back, your ECG and blood tests were reassuring against heart attack, but your chest X-ray showed a likely pneumonia, as well as a pulmonary nodule (small spot on the lung) that should be followed by your primary care physician. You were then given your first dose of antibiotics through an IV before the doctor discussed your diagnosis and treatment plan.

Take Amoxicillin (antibiotic) twice daily for 7 days. Take Tylenol 1000mg and Ibuprofen 400mg every 6 hours as needed for pain or fever.

Follow up with your primary care physician within 1 week. Return to the emergency department for worsening shortness of breath, persistent fever above 101°F, or loss of consciousness."

Please generate a discharge summary based on the following information:
MEDICAL DOCUMENT:{patient_document}
ORIGINAL DISCHARGE INSTRUCTION:{original_discharge_instruction}

Fig. 2. **Discharge Instruction Translating Prompt** used in this study to translate original discharge summary and electronic health records into patient-friendly narratives. {} represents placeholders for inputs.

ED-Explain (Video Discharge Instructions). [a] Fig. 1 illustrates the framework of ED-Explain. The system prompts OpenAI o3-mini (2024-12-01-preview) to explain the patient's ED visit and discharge instructions by synthesizing the de-identified multimodal visit data and original discharge instructions in patient-friendly language, while preserving critical clinical information. A structured prompt guides the model to create a coherent narrative of the ED visit, including the reason for the visit, key events and outcomes, specific findings requiring follow-up, and recommended patient actions, follow-up, and reasons to return to the ED. ED-Explain aims for better readability while maintaining clinical accuracy. The patient-accessible text is checked for complete de-identification, then converted via HeyGen (`https://www.heygen.com/`) to a video featuring a virtual healthcare provider who delivers the information in a conversational manner. The prompt for translating the discharge instructions can be found in Fig. 2.

Physician Evaluation. We presented four board-certified Emergency Physicians with the structured and unstructured visit data, the multimodal visit document, the original ED note and discharge instructions, and ED-Explain's AI-generated text and video discharge instructions. These materials were presented on a standardized rating dashboard. The evaluation included structured ratings (1-5) of completeness, correctness, and patient accessibility for original text and ED-Explain text and video discharge instructions. For the videos, physicians provided additional assessments of potential patient acceptability, potential to improve comprehension and adherence, potential to supplementing or replace existing discharge instructions, and appropriateness for supervised and unsupervised viewing by patients. These supplementary metrics were scored on a 5-point Likert scale (1=very unlikely, 2=unlikely, 3=maybe, 4=likely, 5=very likely).

4. Results

Three physicians completed numeric ratings of individual pairs of discharge instructions. Sixteen pairs were rated by two physicians and 23 pairs were rated by one. All four physicians completed the open-ended survey.

4.1. *Comparison of Text and ED-Explain-generated Discharge Instructions*

Fig.3 A shows mean completeness, correctness, and accessibility ratings, with ED-Explain discharge instructions rated superior to the original written instructions across all three criteria. The largest difference was observed in completeness, with AI instructions receiving a mean rating of 4.1 for completeness, compared to 3.1 for original instructions. For correctness, AI video instructions scored 3.9, compared to 3.5 for original instructions. AI instructions averaged 3.4 in ratings of patient accessibility, compared to 2.9 for original instructions. All differences were significant at $p<0.001$ by Wilcoxon signed-rank test. These results suggest that multimodal AI discharge instructions can both preserve clinical accuracy and enhance

[a] A sample video can be found via
`https://drive.google.com/file/d/1_B1OdR0fiB1nia9SNiwp3CcXhDA-QJk5/view?usp=sharing`

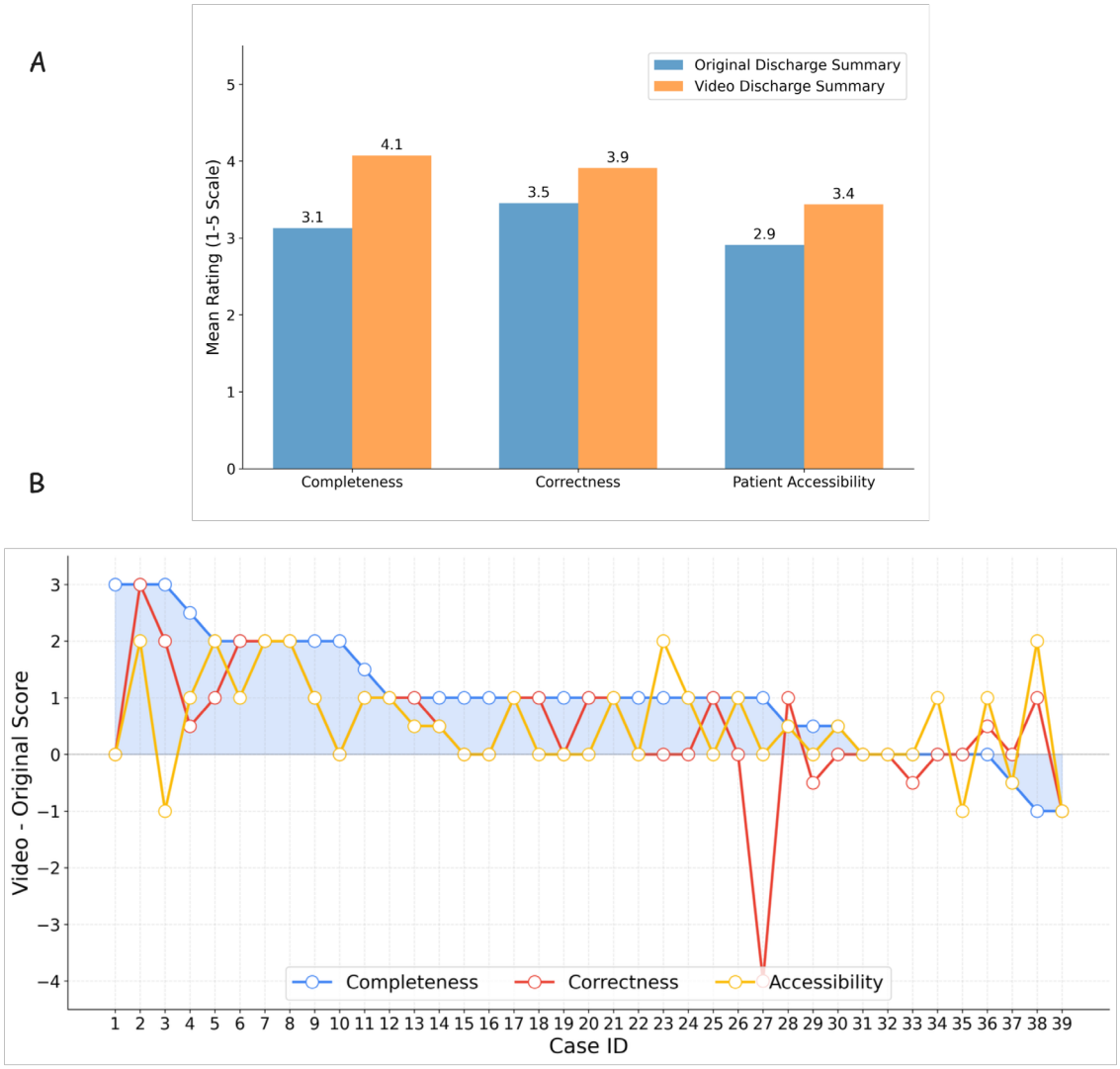

Fig. 3. **(A)** Mean physician ratings (1-5 scale) of completeness, correctness, and patient accessibility of original text (blue) and ED-Explain (orange) discharge instructions . **(B)** Case-level differences between original and AI-generated discharge instruction scores across all 39 evaluated cases, with positive values indicating that ED-Explain was rated superior in completeness (blue), correctness (red), or accessibility (orange) compared to original discharge instructions.

accessibility to patients.

We averaged the scores for each case to analyze case-level differences in ratings (Fig. 3 B). In 30 of 39 cases (76.9%), AI discharge instructions were rated more complete than the original instructions (improvements ranging from 0.5 to 3.0 points on a 5-point scale). In 20 of 39 cases (51.3%), ED-Explain was rated more correct than original instructions, though with more modest gains (typically between 0.5 and 2.0 points). For patient accessibility, ED-Explain was found superior to the original instructions in 21 of 39 cases (53.8%), with differences of 0.5 to 2.0 points.

In 8 of 39 cases (20.5%), the AI discharge instructions were found inferior to the original

instructions in at least one dimension. The most serious instance of AI underperformance was in correctness for a case involving a complex therapeutic regimen not accurately captured by the AI-generated instructions, highlighting an area for improvement.

4.2. *Video Assessment*

Survey results (Fig. 4) provide insights into physicians' perspectives on the practical implementation of video discharge instructions.

Physicians believed it was "likely" that the generated videos could improve patient understanding in 44.4% of cases, and responded "maybe" in 51.1% of cases. Only 4.5% of cases were rated as "unlikely" to improve understanding. This distribution suggests cautions optimism from physicians about the real-world patient education impact of the AI discharge instructions. Physicians responded that they would consider supplementing traditional discharge instructions with AI videos in 40.9% of cases, and responded "maybe" for another 54.5%. Only 4.6% of videos ratings were deemed clearly unsuitable for use. Physicians were less amenable to completely replacing text instructions, with only 18.2% of cases rated as suitable for video instructions alone.

When asked about patient supervision requirements, physicians found 60.0% of examples suitable for independent viewing by patients (8.9% "very likely" and 51.1% "likely"). Few videos were rated as unsuitable for patient viewing with or without supervision. When asked whether the ED-Explain-generated discharge instruction videos would better help patients follow discharge instructions, physicians found this outcome "likely" for 22.7%, were uncertain for the majority (72.7%), and doubtful about 4.6%. Similarly, when asked if video format would be preferred by patients, physicians responded affirmatively in 27.3% of cases, were uncertain for 68.2%, and skeptical for 4.5%.

These results indicate that physicians see potential in AI video discharge instructions.

4.3. *Qualitative Findings from Physician Feedback*

Four physicians provided their opinions on the perceived value and potential implementation challenges of ED-Explain-generated video discharge instructions. Responses were collected through open-ended survey questions focused on utility, improvements, clinical integration, and anticipated barriers. We summarize key themes from this feedback.

Perceived Value of Video Discharge Instructions. Physicians identified several aspects of the AI-generated discharge videos as particularly valuable. The narrative format was highlighted as a significant improvement, with one physician noting that the videos offered "a more comprehensive explanation of what actually occurred during the ED encounter." Another physician valued how the AI system could "assimilate multiple forms of data and fit them to a theme" while maintaining "the right balance between specific and general data." The potential beneficiaries of such a system were primarily identified as patients with limited health literacy and those who had complex ED encounters:

> "I think patients with poor health literacy and a poor understanding of what took place during an ED encounter [would benefit most]."

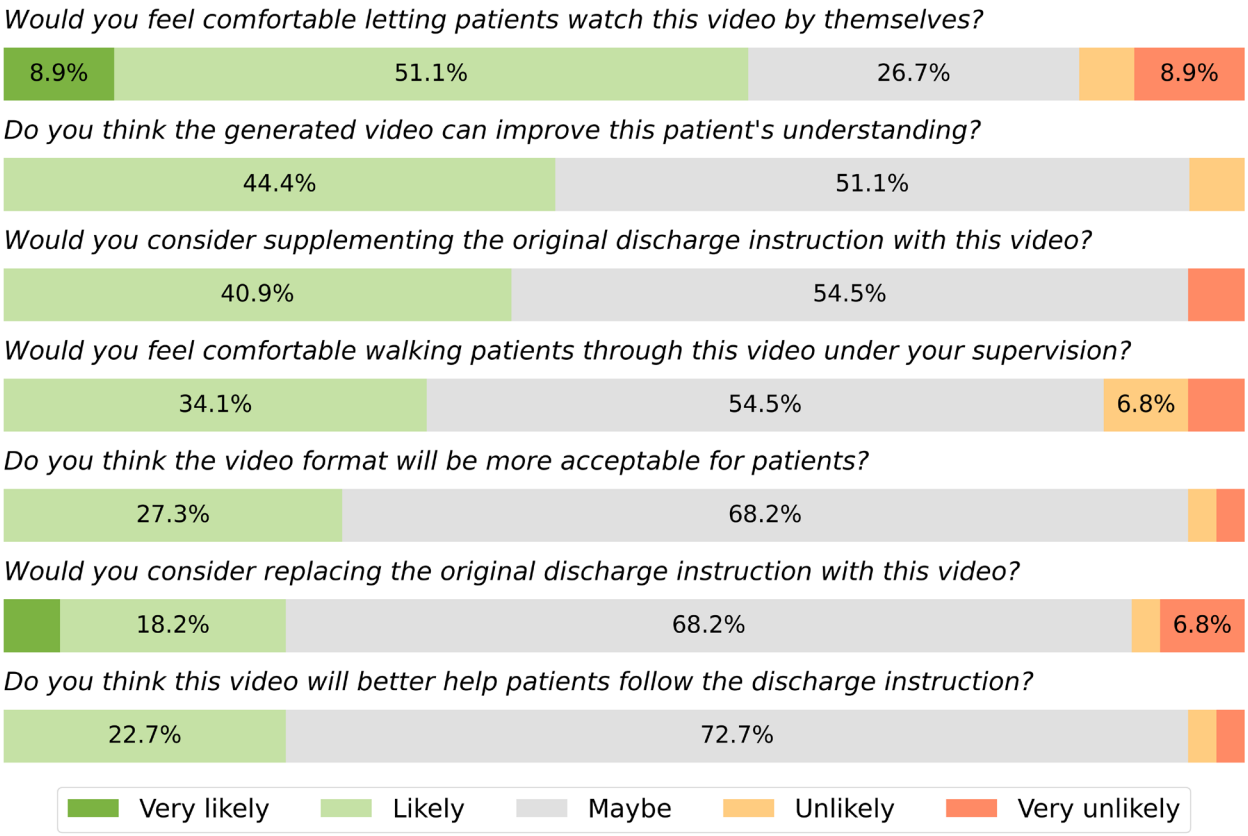

Fig. 4. **Physician perspectives on implementing ED-Explain video discharge instructions in clinical practice.** The bar chart displays survey responses from Emergency Physicians (n=4) evaluating seven key implementation questions. Color-coded segments represent the distribution of responses on a 5-point Likert scale from "Very likely" (dark green) to "Very unlikely" (red).

Additionally, physicians recognized value for family members and caregivers who may not have been present for the ED visit, with one physician suggesting that "patients should be allowed to forward it to their family and/or caregivers."

Implementation Considerations. When asked about implementation in clinical practice, physicians envisioned using the system primarily at the end of visits, with one suggesting they would have patients "review/watch the video prior to me being available to answer additional questions/clarify points." Similarly, another physician would consider having the patient "interface with it toward end of visit/end of visit" and "then ask them if they had questions." Anticipated institutional barriers centered on safety and risk management:

> "There will likely be data privacy concerns. I would imagine some physicians might be concerned about inaccuracies presented in the AI instructions."

Another physician highlighted the fear of malpractice risk "if the AI gets something wrong," while a third emphasized that such a system will "ALWAYS need a human-in-the-loop." The most valuable potential outcomes identified by physicians included improved patient

understanding, better adherence to treatment plans, reduced revisits, and time savings for physicians. As one physician summarized:

> "Patients have very poor understanding of discharge instructions, which often impairs follow up, treatment adherence, and increases revisits to the hospital. Improving all of those factors would be beneficial."

These qualitative insights provide important context for understanding the potential real-world implementation challenges and benefits of ED-Explain. While physicians see significant value in the approach, careful attention to content organization, customization, and risk management will be essential for successful clinical deployment.

Suggested Improvements. Specific suggestions for improving the video discharge instructions are focused on content organization, presentation, and customization:

(1) **Content organization**: Most physicians recommended better structuring of information, with one suggesting to start with "a brief summary of the entire visit, then give more details" and another recommending separating content into "sections that the patient can expand based on their interest."
(2) **Simplification**: Physicians noted that some aspects were "too detailed and may detract from the main message," with specific recommendations to "remove ICD codes," "remove dosages," and eliminate "generic boilerplate phrases."
(3) **Presentation format**: Feedback on the avatar itself was mixed, with one physician finding "the AI face mannerisms were distracting" while others focused more on content than delivery method.
(4) **Customization**: Physicians suggested adapting content to "patient-preferred language" and providing "specific resources/recommendations based on patient location and best-practice guidelines."

Key Stakeholders and Adoption. When asked which stakeholders would be most interested in adopting such a system, providers identified several key groups:

> "If done in the correct way that would reduce the burden on physicians they would be a major stakeholder. Demonstrating better adherence to follow up recommendations and decreased revisits would be major things for the hospital/healthcare system."

Other providers specifically mentioned discharge coordinators and planners as well as callback services, walk in clinics, and ED care providers as primary stakeholders. A provider suggested that "with improvements to clarity and reliability, everyone would be interested in adoption."

5. Limitations and Future Directions

Our study has limitations. First, our evaluation focused on physician assessment alone and was not blinded—physicians knew which instructions were AI-generated and thus could potentially influence ratings. Additionally, this was a retrospective study from a single academic medical center. However, this study represents a crucial first step in demonstrating that AI-

generated discharge instructions can meet clinical standards in real-world practice. By establishing physician acceptance and clinical appropriateness, this work provides the essential foundation needed to advance to patient-centered studies. Future studies would assess acceptability to diverse patient populations. Second, the cases in which AI-generated discharge instructions were rated inferior to original instructions highlight the need for improved handling of complex therapeutic regimens. Third, this was a retrospective study on de-identified data. Future research should assess long-term patient retention of discharge information and its impact on adherence to treatment plans. Finally, an important practical consideration for implementing ED-Explain is the time and cost associated with video generation. Current commercial video generation platforms require several to tens of minutes per video, which could constrain scalability in high-volume ED settings. However, the rapidly evolving video generation technology is expected to substantially reduce processing time and cost, making real-time generation[31] at scale feasible for widespread clinical deployment.

6. Discussion

Our results suggest that ED-Explain-generated video discharge instructions can enhance communication of discharge information compared to conventional written instructions. The AI-generated instructions' superior ratings for completeness, correctness, and patient accessibility align with previous research on video discharge.[10] The cautious physician reception, with most responses falling into the "maybe" category, suggests a need for iterative implementation under clinical supervision, rather than wholesale replacement of text instructions. This aligns with previous findings,[26] which emphasized the importance of physician oversight for AI-generated patient information. The positive physician feedback on narrative format and comprehensive explanation indicates that our approach can address known challenges in discharge communication while preserving clinical accuracy. The minimal outright opposition to implementation (only 13.3% of cases provoking reservations about patient viewing, and 4.6% firm opposition to patient viewing) indicates openness to this approach.

In summary, ED-Explain demonstrates the potential to enhance patient comprehension of discharge instructions through AI-generated video that synthesizes structured and unstructured visit data. Physicians found ED-Explain's multimodal discharge instructions to be more complete, correct, and accessible than conventional text-only discharge instructions. While the value of this approach is recognized, implementation will require appropriate clinical oversight. At present, AI-generated discharge instructions are more suitable as a supplement to standard instructions than as a replacement. AI-driven healthcare communication tools can bridge the gap between complex medical information and patient understanding. As healthcare systems seek to improve patient-specific personalization, ED-Explain represents a scalable solution to persistent challenges in discharge communication, a high-risk, high-impact aspect of health care. Future work should focus on patient reception and outcomes, improved performance on complex cases, and clinical workflows to maximize the benefits of the technology while maintaining the highest standards of quality and safety.

Acknowledgment: This research was supported in part by the National Institutes of Health, grant number 1R01HL172794.

References

1. M. Mahajan, J. A. Hogewoning, J. J. A. Zewald, M. Kerkmeer, M. Feitsma and D. A. van Rijssel, The impact of teach-back on patient recall and understanding of discharge information in the emergency department: the emergency teach-back (em-teba) study, *International Journal of Emergency Medicine* **13**, 1 (2020).
2. H. Sheikh, A. Brezar, A. Dzwonek, L. Yau and L. A. Calder, Patient understanding of discharge instructions in the emergency department: do different patients need different approaches?, *International journal of emergency medicine* **11**, p. 5 (2018).
3. H. Marty, Y. Bogenstätter, G. Franc, F. Tschan and H. Zimmermann, How well informed are patients when leaving the emergency department? comparing information provided and information retained, *Emergency Medicine Journal* **30**, 53 (2013).
4. K. G. Engel, B. A. Buckley, V. E. Forth, D. M. McCarthy, E. P. Ellison, M. J. Schmidt and J. G. Adams, Patient understanding of emergency department discharge instructions: where are knowledge deficits greatest?, *Academic Emergency Medicine* **19**, E1035 (2012).
5. K. G. Engel, M. Heisler, D. M. Smith, C. H. Robinson, J. H. Forman and P. A. Ubel, Patient comprehension of emergency department care and instructions: are patients aware of when they do not understand?, *Annals of emergency medicine* **53**, 454 (2009).
6. J. A. Crane, Patient comprehension of doctor-patient communication on discharge from the emergency department, *The Journal of emergency medicine* **15**, 1 (1997).
7. M. W. Musso, J. N. Perret, T. Sanders, R. Daray, K. Anderson, M. Lancaster, D. Lim and G. N. Jones, Patients' comprehension of their emergency department encounter: a pilot study using physician observers, *Annals of emergency medicine* **65**, 151 (2015).
8. B. A. Slater, Y. Huang and P. Dalawari, The impact of teach-back method on retention of key domains of emergency department discharge instructions, *The Journal of emergency medicine* **53**, e59 (2017).
9. C. DeSai, K. Janowiak, B. Secheli, E. Phelps, S. McDonald, G. Reed and A. Blomkalns, Empowering patients: simplifying discharge instructions, *BMJ Open Quality* **10**, p. e001419 (2021).
10. S. A. Bloch and A. J. Bloch, Using video discharge instructions as an adjunct to standard written instructions improved caregivers' understanding of their child's emergency department visit, plan, and follow-up: a randomized controlled trial, *Pediatric emergency care* **29**, 699 (2013).
11. K. Jeblick, B. Schachtner, J. Dexl, A. Mittermeier, A. T. Stüber, J. Topalis, T. Weber, P. Wesp, B. O. Sabel, J. Ricke *et al.*, Chatgpt makes medicine easy to swallow: an exploratory case study on simplified radiology reports, *European radiology* **34**, 2817 (2024).
12. F. N. Mirza, O. Y. Tang, I. D. Connolly, H. A. Abdulrazeq, R. K. Lim, G. D. Roye, C. Priebe, C. Chandler, T. J. Libby, M. W. Groff *et al.*, Using chatgpt to facilitate truly informed medical consent, *NEJM AI* **1**, p. AIcs2300145 (2024).
13. A. Kumar, H. Wang, K. W. Muir, V. Mishra and M. Engelhard, A cross-sectional study of gpt-4–based plain language translation of clinical notes to improve patient comprehension of disease course and management, *NEJM AI* **2**, p. AIoa2400402 (2025).
14. M. P. Recht, M. Westerhoff, A. M. Doshi, M. Young, D. Ostrow, D.-m. Swahn, S. Krueger and S. Thesen, Video radiology reports: a valuable tool to improve patient-centered radiology, *American Journal of Roentgenology* **219**, 509 (2022).
15. L. Luo, J. Vairavamurthy, X. Zhang, A. Kumar, R. R. Ter-Oganesyan, S. T. Schroff, D. Shilo, R. Hossain, M. Moritz and P. Rajpurkar, Rexplain: Translating radiology into patient-friendly video reports, *arXiv preprint arXiv:2410.00441* (2024).
16. R. O'Conor, A. Moore and M. S. Wolf, Health literacy and its impact on health and healthcare outcomes, in *Health literacy in clinical practice and public health*, (IOS Press, 2020) pp. 3–21.
17. CDC Health Literacy, Talking points about health literacy (October 2024), Accessed: April 11,

2025.
18. N. D. Berkman, S. L. Sheridan, K. E. Donahue, D. J. Halpern and K. Crotty, Low health literacy and health outcomes: an updated systematic review, *Annals of internal medicine* **155**, 97 (2011).
19. S. A. Fleary and R. Ettienne, Social disparities in health literacy in the united states, *HLRP: Health Literacy Research and Practice* **3**, e47 (2019).
20. M. K. Paasche-Orlow and M. S. Wolf, The causal pathways linking health literacy to health outcomes, *American journal of health behavior* **31**, S19 (2007).
21. E. G. Oh, H. J. Lee, Y. L. Yang and Y. M. Kim, Effectiveness of discharge education with the teach-back method on 30-day readmission: a systematic review, *Journal of patient safety* **17**, 305 (2021).
22. A. Wray, R. Goubert, R. Gadepally, M. Boysen-Osborn, W. Wiechmann and S. Toohey, Utilization of educational videos to improve communication and discharge instructions, *Western Journal of Emergency Medicine* **22**, p. 644 (2021).
23. J. D. Balkman and A. H. Siegel, An audio/video reporting workflow to supplement standardized radiology reports, *Journal of digital imaging* **29**, 153 (2016).
24. L. P. Neto, I. R. Godoy, A. F. Yamada, H. Carrete, D. Jasinowodolinski and A. Skaf, Evaluation of audiovisual reports to enhance traditional emergency musculoskeletal radiology reports, *Journal of Digital Imaging* **32**, 1081 (2019).
25. K.-m. C. Woo, G. W. Simon, O. Akindutire, Y. Aphinyanaphongs, J. S. Austrian, J. G. Kim, N. Genes, J. A. Goldenring, V. J. Major, C. S. Pariente *et al.*, Evaluation of gpt-4 ability to identify and generate patient instructions for actionable incidental radiology findings, *Journal of the American Medical Informatics Association* **31**, 1983 (2024).
26. R. A. J. Clough, W. A. Sparkes, O. T. Clough, J. T. Sykes, A. T. Steventon and K. King, Transforming healthcare documentation: harnessing the potential of ai to generate discharge summaries, *BJGP open* **8** (2024).
27. H. Kim, H. M. Jin, Y. B. Jung and S. C. You, Patient-friendly discharge summaries in korea based on chatgpt: software development and validation, *Journal of Korean Medical Science* **39** (2024).
28. C. Y. Williams, J. Bains, T. Tang, K. Patel, A. N. Lucas, F. Chen, B. Y. Miao, A. J. Butte and A. E. Kornblith, Evaluating large language models for drafting emergency department discharge summaries, *medRxiv* (2024).
29. H. Newnham, A. Barker, E. Ritchie, K. Hitchcock, H. Gibbs and S. Holton, Discharge communication practices and healthcare provider and patient preferences, satisfaction and comprehension: a systematic review, *International Journal for Quality in Health Care* **29**, 752 (2017).
30. A. Kansal, E. Chen, T. Jin, P. Rajpurkar and D. Kim, Multimodal clinical monitoring in the emergency department (mc-med), *PhysioNet, v1* **10** (2025).
31. A. Kodaira, T. Hou, J. Hou, M. Tomizuka and Y. Zhao, Streamdit: Real-time streaming text-to-video generation, *arXiv preprint arXiv:2507.03745* (2025).

The Intention-Execution Disconnect in Medical AI: The ReXecution Framework for Evaluating Real-World Clinical Performance

Oishi Banerjee[1*], Lucas Bijnens[1,2*], Subathra Adithan[3] and Pranav Rajpurkar[1†]

[1] *Department of Biomedical Informatics, Harvard Medical School, Boston, MA, USA*
[2] *Department of Imaging and Pathology, KU Leuven, Leuven, Belgium*
[3] *Department of Radiodiagnosis, Jawaharlal Institute of Postgraduate Medical Education and Research, Puducherry, India*
[†] *Corresponding Author E-mail: pranav_rajpurkar@hms.harvard.edu*

* Both authors contributed equally to this work.

© 2025 The Authors. Open Access chapter published by World Scientific Publishing Company and distributed under the terms of the Creative Commons Attribution Non-Commercial (CC BY-NC) 4.0 License.

Abstract: We present the ReXecution framework for conducting clinician-centered assessments of medical AI assistants, providing detailed insights into their reliability in realistic clinical settings. Using this framework, we assessed AI assistants for chest X-ray (CXR) interpretation, exploring the gap between current model capabilities and real-world radiological needs. Unlike prior benchmarks that rely on automatically generated questions with limited clinical relevance, our dataset consists of 100 expert-curated tasks that radiologists might realistically present to an AI assistant in their day-to-day workflow. Through detailed manual review by a radiologist, we evaluated two leading foundation models, ChatGPT-o3 and MedGemma, on our tasks. While both models demonstrated considerable medical knowledge and reasoning capabilities on our tasks, they frequently struggled to interpret images and execute tasks accurately, producing correct outputs in only 5-10% of cases. Our detailed manual evaluation highlights a critical mismatch: models often abstractly understand radiology concepts but cannot reliably execute their plans when interpreting specific medical images. This work identifies key gaps in current models' ability to serve as comprehensive radiology assistants and provides insights into how the development and evaluation of models can better align with real-world clinician needs, enabling seamless clinician-AI collaboration.

Keywords: Clinician-AI Collaboration, Radiologist-Centered Evaluation, Vision-Language Models, AI for Chest X-Rays

1. Introduction

Artificial intelligence (AI) for medicine has rapidly progressed from narrow classifiers to large-scale vision-language models (VLMs) that promise to function as generalist assistants for clinicians.[1,2] In radiology, some recent studies have found that AI foundation models can match or even exceed clinician performance on chest X-ray (CXR) interpretation tasks.[3] Such VLMs may collaborate with clinicians as interactive chatbots, providing measurements and other useful information as radiologists interpret a study.[4] Alternatively, models might perform useful tasks in the background before a clinician even reaches a study, flagging urgent cases or preemptively commenting on images according to a user's standing instructions.[5]

Several large-scale, automatically generated benchmarks have been constructed to evaluate assistive models on CXR tasks,[3,6,7] but these benchmarks prioritize scalability and automated scoring over clinical realism. Most are constructed from templates or report-mined labels, producing short-answer or multiple-choice tasks with clear-cut ground truths. While useful for coverage and automated scoring, such benchmarks overlook additional information encoded in the images, feature frequently unrealistic questions and answers, and ultimately diverge from how radiologists would actually interact with an AI assistant.

For instance, some benchmark questions are too trivial to require large VLMs (e.g., inferring patient sex from the image), while others are overly specific or complicated (e.g., "Q: Does the left mid lung zone contain either low lung volumes or calcified nodule? A: Yes.").[6] Moreover, such short ground-truth answers can obscure whether a model arrived at the correct response through accurate reasoning, chance, or shortcuts. The resulting benchmarks do not accurately represent the open-ended questions and complex reasoning processes that arise in clinical practice (Figure 1a).

To address these shortcomings, clinician-centered evaluation procedures are needed. In this exploratory study, we evaluate the capabilities of cutting-edge vision-language models, testing them on a complex, clinically relevant dataset created through radiologist-AI collaboration. We score model outputs on several dimensions, assessing both their "intentions"—their general medical knowledge and abstract planning capabilities—as well as their "execution" when interpreting specific images and making practical judgments. Our data curation and scoring processes comprise the ReXecution (*Re*alistic Intention-*Execution* Assessment) framework (Figure 1b), which can be extended beyond radiology to conduct clinician-centered assessments in other domains of medicine.

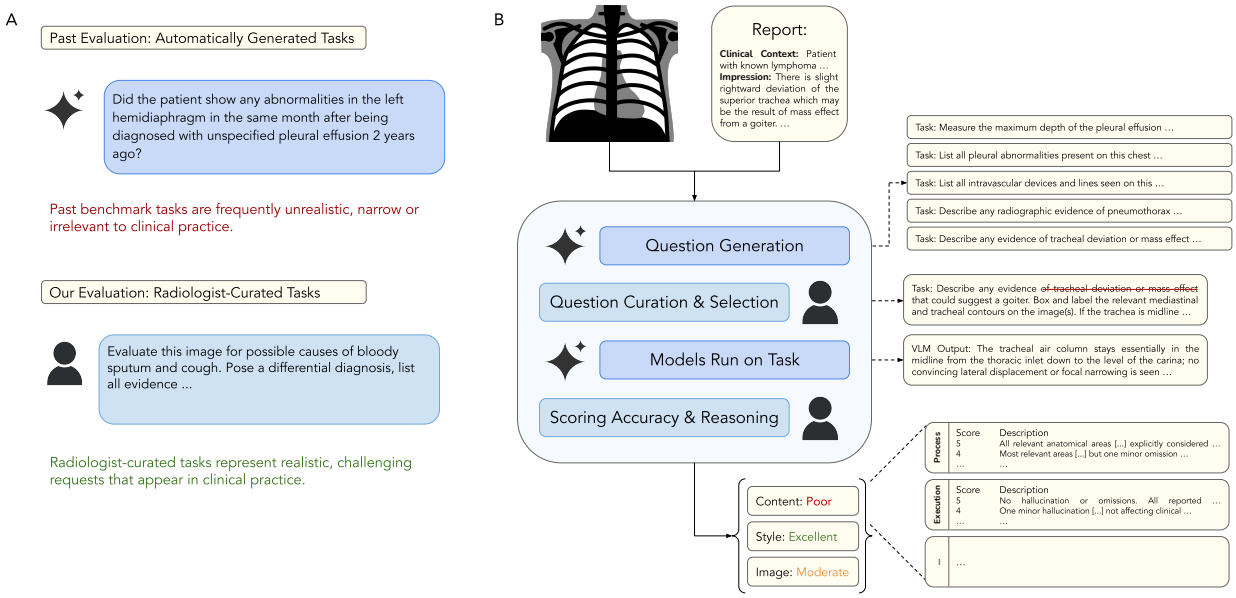

Fig. 1: The ReXecution framework emphasizes (a) realistic task design and (b) clinician-led data curation and scoring, providing detailed insights into how models reason in clinical settings. [a]

By applying this framework to chest X-ray interpretation, we make two primary contributions:

(1) We curated a high-quality dataset with 100 challenging, realistic evaluation tasks. Selected from a list of automatically-generated candidates, each task was reviewed and edited by a radiologist to ensure that it would plausibly occur in clinical practice—either when actively interacting with a chatbot or when specifying tasks for an agent to perform independently in the background.
(2) Using our dataset, we tested ChatGPT-o3, a leading general-purpose foundation model, and MedGemma, a top medical foundation model trained heavily on chest X-ray inter-

[a]Figure 1a's "past evaluation" question comes from an existing benchmark linking EHR and CXR data.[8] We removed a patient identification number but otherwise preserved the text.

pretation. As our tasks elicited lengthy, nuanced answers, we manually evaluated model performance. We obtained rich qualitative insights into radiologist experiences with AI assistants, while also compiling descriptive statistics that highlight model weaknesses.

(3) We found that both models demonstrate sophisticated medical knowledge, accurately understand complex questions, and plan multi-step strategies to answer them. However, they struggled to execute those strategies due to the "visual" component of visual question-answering, frequently misreading chest X-rays and ultimately arriving at incorrect conclusions. Our findings indicate that, despite achieving expert-level performance on certain tasks, AI models still fall short of providing truly comprehensive assistance to clinicians.

2. Related Works

Prior visual question-answering datasets for chest X-ray interpretation have typically mined large numbers of questions from radiology reports, weakly labeled bounding boxes, or other metadata. The recently released ReXVQA benchmark features approximately 696,000 LLM-generated multiple-choice questions based on radiology reports. On a subset of 200 questions, this benchmark found that MedGemma outperformed radiology residents with an accuracy of 83.8%, though its performance varied depending on the type of task.[3]

Building on an earlier dataset,[8] MIMIC-Ext-MIMIC-CXR-VQA generated approximately 377,000 CXR questions by filling templates using AI-generated bounding boxes and keywords extracted from radiology reports. About two-thirds of MIMIC-Ext-MIMIC-CXR-VQA questions require yes/no or multiple-choice answers, while the rest expect a short list of abnormalities or locations.[6] More recently, Medical-CXR-VQA and MIMIC-Diff-VQA each presented approximately 700,000 questions, generated through a similar methodology.[7,9]

The GEMeX benchmark contains about 1,600,000 LLM-generated questions based on radiology reports and bounding boxes, as well as a GPT-based scoring metric.[10] While GEMeX also focuses on multiple-choice questions or brief answers, it expands on prior benchmarks by accepting multimodal outputs with both text and bounding boxes and by including more of an emphasis on causal reasoning (e.g. "What implications does the tortuous aorta have?").

While these recent datasets have been automatically constructed, the earlier SLAKE and VQA-RAD datasets contain tens of thousands of clinician-written questions for several radiology modalities including chest X-rays. These questions also expect short, often one-word answers that can be easily be automatically scored.[11,12] Outside visual question-answering, there have been attempts to automatically score longer free-text responses in the field of radiology report generation, yet automated metrics have struggled to evaluate complex descriptions of chest X-rays, offering only moderate correlations with expert opinions.[13,14]

3. Methods

3.1. *ReXecution Data Curation*

The first step of our framework is the construction of a dataset that reflects real-world clinical workflows while leveraging LLMs for efficiency. To this end, we developed a pipeline (Figure 1) to generate high-level, clinically relevant tasks for CXR interpretation through clinician-AI

collaboration. We randomly sampled 100 chest X-ray studies from the test set of *MIMIC-CXR-JPG*, a large public dataset of CXRs and associated reports from Beth Israel Deaconess Medical Center in Boston, MA.[15]

For each study, we prompted GPT-o4-mini (Supplementary Table 1) to propose five candidate tasks across three categories. We selected these categories to require complex clinical reasoning and the integration of multiple imaging findings:

(1) *Broad abnormality query.* "Describe all pleural abnormalities", "List all visible tubes and lines and assess for complications", etc.
(2) *High-level diagnostic reasoning.* "Gather evidence of congestive heart failure", "Perform differential diagnosis for a lobar opacity", etc.
(3) *Measurements and temporal comparisons.* "Measure the cardiothoracic ratio", "Assess effusion size compared to prior", etc.

We prompted the model to generate questions that were relevant to the indication or findings from each case's radiology report. Indications are provided before performing the imaging study and describe the symptoms or other clinical motivation for the study. Findings are reported after the study is performed and represent a radiologist's interpretation of the images. By drawing questions from not only the radiology report but also the clinical context, we cover multiple phases in the clinical workflow—both before and after the radiologist starts working on the imaging study.

After generating questions, we prompted GPT-o4-mini (Supplementary Table 1) to score all questions on 5-point Likert scales, based on whether it (i) is clinically relevant, (ii) is answerable from CXR alone, and (iii) requires reasoning beyond simple pattern matching. Additionally, the LLM assigned multiple types of content tags (e.g., areas of interest, main pathology). The tagging and scoring system are described in more detail in the appendix (Supplementary Table 2).

A radiologist then selected a final question for each case, considering high-scoring candidates first and re-scoring selected questions to verify that they aligned with our goals. During this process, they verified that selected questions were clinically important and clearly phrased. They also leveraged the content tags to ensure that the selected question pool covered a large variety of medical topics and tasks, reflecting realistic caseloads. Where needed, the radiologist rephrased questions or wrote new ones to maintain quality, diversity and clinical relevance. Additionally, while most questions (n=89) concerned a single case, the radiologist verified whether MIMIC-CXR contained a sufficiently recent prior study for questions covering disease progression over time.

The resulting tasks covered a wide range of clinical use cases. Based on the content tags, many areas of interest were represented: lung parenchyma (37%), pleura (15%), cardiac silhouette and mediastinum (14%), hilar regions (11%), devices (9%), osseous structures (4%), diaphragm and soft tissues (6%), and airways (3%). Pathology tags covered pneumonia, effusions, atelectasis, lymphadenopathy, pneumothorax as well as some rarer pathologies—aligning with the clinical distribution seen in routine radiology practice.

A score histogram (Supplementary Figure 1a) shows the distribution of quality scores

across the selected question set, indicating the overall high quality of the included items. For more details on the variation in our dataset, breakdown plots are provided in the appendix (Supplementary Figure 1b).

3.2. *Vision-Language Models*

We evaluated two state-of-the-art VLMs that represent different development paradigms:

- **ChatGPT-o3 (OpenAI, closed-source generalist)**. The strongest reasoning model in the GPT family at time of writing. It is a multimodal foundation model capable of ingesting multiple images and producing both text and figures.
- **MedGemma-4b-it (Google, open-source medical)**. A vision-language model fine-tuned on medical imaging with strong performance on multiple-choice CXR benchmarks. We selected MedGemma specifically for its strong performance on ReXVQA, a multiple-choice benchmark where it was found to exceed the performance of radiology residents.[3] It is optimized for processing one input image at a time and returns text-only outputs.

For ChatGPT-o3, we provided all available CXR views and instructed the model to generate bounding-box annotations for localized findings. If no abnormalities were found, the model was not required to draw boxes; when ChatGPT-o3 found abnormalities but did not annotate them, we did not force it to generate bounding boxes. For MedGemma, we provided a single PA (or AP if unavailable) image per case, or both images only for temporal comparisons. No bounding boxes were requested as this is not supported by MedGemma. Except for the bounding box directions, the prompts were harmonized across the models to reduce bias.

3.3. *ReXecution Metrics*

In our framework, we assess text outputs on four dimensions (Figure 2) that capture both a model's abstract medical knowledge and concrete visual abilities. Each text output was scored by a radiologist on each dimension:

(1) *Process.* Did the model correctly interpret the task and plan an appropriate strategy? (e.g., while gathering evidence of cancer, but only looking for lung lesions without considering bone lesions)
(2) *Execution.* Did it accurately identify and describe image findings without hallucinations or omissions? (e.g., attempting to look for lung lesions, but hallucinating a granulomatous lesion)
(3) *Synthesis.* Did it integrate findings into sound, clinically appropriate conclusions, accounting for uncertainty? (e.g., claiming that a granuloma is suggestive of cancer while ignoring more plausible explanations such as infection)
(4) *Language.* Was the response clear, concise, and professional? (e.g., rambling and repeating itself when answering a question)

In practice, radiologists would struggle to use a model with poor Execution or Synthesis scores, and they would struggle to trust a model with poor Process scores even if it sometimes guessed at correct answers. We therefore calculate an aggregated *Content* score, which judges

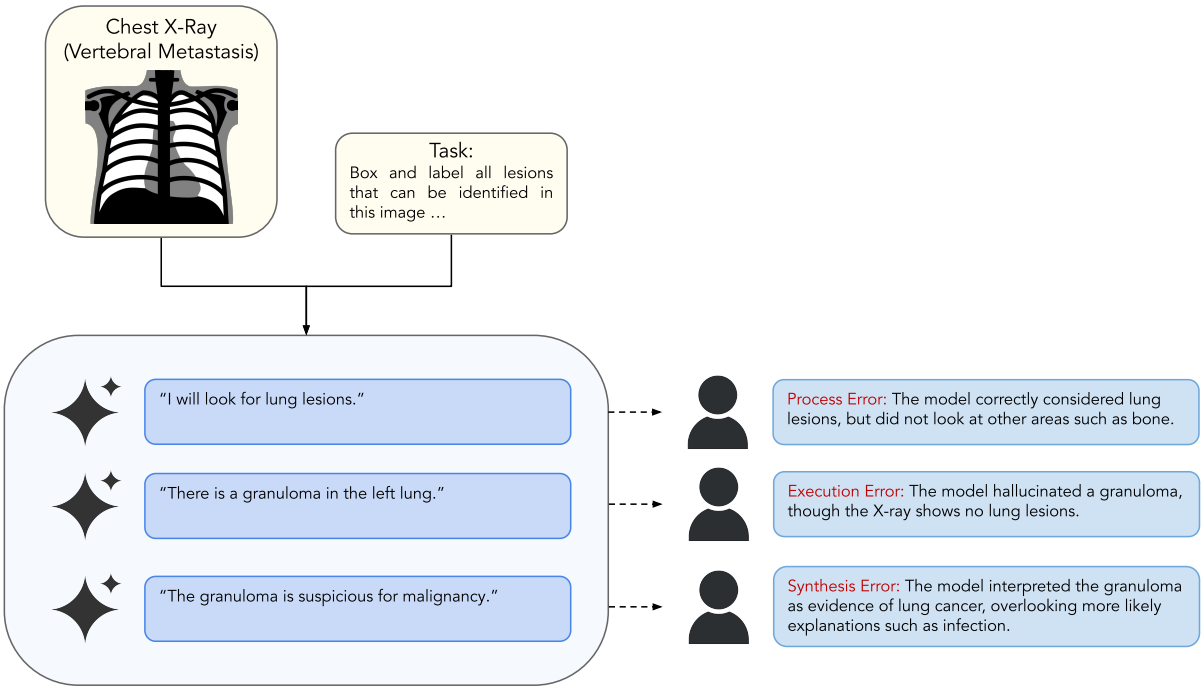

Fig. 2: Demonstration of different content error types. The ReXecution framework judges content on Process, Execution, and Synthesis.

output content based on its weakest link. The Content score is equal to the minimum of the Process, Execution, and Synthesis scores. In other words, an output cannot receive a Content score of 5 unless it successfully performs all relevant tasks required to answer the question correctly—ranging from question comprehension, detection of findings, to reasoning about their clinical implications.

Additionally, image outputs from ChatGPT-o3 were scored on two dimensions by a radiologist. *Image Content* scores reflect whether the model correctly localizes the regions it is attempting to box. If a model attempts to label a pleural effusion but instead boxes a lower part of the hemidiaphragm, this error would be considered an Image Content issue. *Image Style* scores reflect whether the model plans out a useful illustration, attempting to box findings mentioned in the text without cluttering the image with unrelated boxes. If a model boxes and labels a pacemaker when asked to calculate the cardiothoracic ratio, this unnecessary addition would be considered an Image Style issue.

Scoring for each dimension followed a customized 5-point scale (1 = poor, 5 = excellent). The full rubric is provided in the appendix (Supplementary Table 2).

3.4. *Statistical Analysis*

For each of the five text scores, we tested whether there was a significant difference between ChatGPT-o3 and MedGemma by applying the Wilcoxon signed-rank test for paired non-parametric comparisons and controlling for multiple testing using the Benjamini–Hochberg

false discovery rate procedure. We did not run statistical tests between different score types (e.g. Content vs. Language) because each dimension was measured using custom criteria, making formal statistical comparisons infeasible. Aggregate means are reported with standard deviations.

3.5. *Inter-Reader Agreement*

To gauge the reproducibility of our evaluation rubric, a senior radiologist independently re-scored roughly a quarter of the dataset. They labeled 51 model outputs, 15 of which contained boxed images from ChatGPT-o3. Agreement with the primary reader was quantified using quadratic-weighted Cohen's κ (QWK), appropriate for our five-point ordinal scale, and mean absolute differences (MAD). Where both readers provided scores, we used the average of the two scores for our final results to provide more robust performance metrics.

4. Results

4.1. *Quantitative Overview of Text Content and Language*

We found that both models struggled to produce factually accurate answers (Table 1). ChatGPT-o3 received an average Content score of 2.71, with 10.0% of outputs receiving a 5. MedGemma received an average Content score of 2.84, with only 4.9% of outputs receiving a score of 5. MedGemma's failure to generate an answer for 19 tasks was concerning. The underlying issue was a built-in limit on the number of tokens it can process at once, which was triggered by tasks that elicited particularly detailed answers. However, both models generally maintained a professional writing style and used appropriate radiological vocabulary, with 56.8% of MedGemma outputs and 31.0% of ChatGPT-o3 outputs receiving Language scores of 5. When comparing ChatGPT-o3 and MedGemma's performance, we tested only data points that received outputs from both models and found no statistically significant difference.

Metric	ChatGPT-o3 (n = 100)	MedGemma (n = 81)	p_{adj}
Content	2.71 ± 1.31	2.84 ± 1.14	0.52
Language	4.15 ± 0.73	4.33 ± 0.96	0.66

Table 1: Aggregate metrics for content and language clarity.

4.2. *Breakdown of Content Errors*

Errors were frequent across all four content categories (Table 2), driving the low overall content scores seen above. We noted that both models received their highest average scores in Process and their lowest average scores in Execution, with gaps of .65 for MedGemma and 1.27 for ChatGPT-o3. Differences in error distributions also differed strikingly across categories (Figure 3). Only 5.0% of MedGemma's Process scores and 8.0% of ChatGPT-o3's Process scores fell under 3, compared to 34.5% of MedGemma's Execution scores and 42% of ChatGPT-o3's

Execution scores. Synthesis scores were left-skewed like Process scores, indicating that scores were rarely very poor. After correcting for multiple-hypothesis testing, we again found no statistically significant difference between ChatGPT-o3 and MedGemma.

Metric	ChatGPT-o3 (n = 100)	MedGemma (n = 81)	p_{adj}
Process	4.17 ± 0.95	3.91 ± 0.94	0.10
Execution	2.90 ± 1.44	3.26 ± 1.27	0.19
Synthesis	3.85 ± 1.06	3.49 ± 1.21	0.10

Table 2: Content metric breakdown in individual task performances.

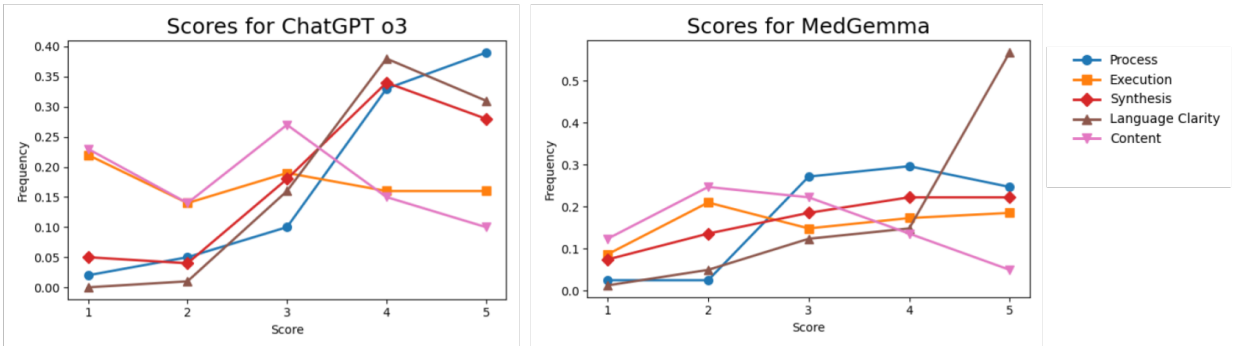

Fig. 3: Score distributions showing both models avoided low scores on Process but had a large spread in Execution scores and rarely reach an overall Content score of 5.

4.3. *Overview of ChatGPT-o3 Image Quality*

For 62 tasks, ChatGPT-o3 successfully produced images, otherwise deciding that no image was necessary or failing to follow that part of the instructions. Upon assessment of these images, we found frequent errors in ChatGPT-o3's boxes and labels, with an average Image Content score of 3.06±1.22. Only 10.1% of images received a 5 for Image Content, indicating that most images contained a misplaced box or label. ChatGPT-o3 performed better at Image Style with an average score of 3.63±1.33. 36.2% of images received an Image Style score of 5, indicating that ChatGPT-o3 generally showed better judgment when planning what to box and label.

4.4. *Qualitative Observations*

As suggested by the quantitative findings, we found that both models showed strong theoretical knowledge while struggling to interpret images correctly in practice, yet we also observed distinct behavioral patterns and failure modes across the two models (Figure 4). ChatGPT-o3 often found the correct regions of interest but misclassified the abnormality type. It was also prone to making mistakes on laterality, mixing up the left and right sides of the image; this

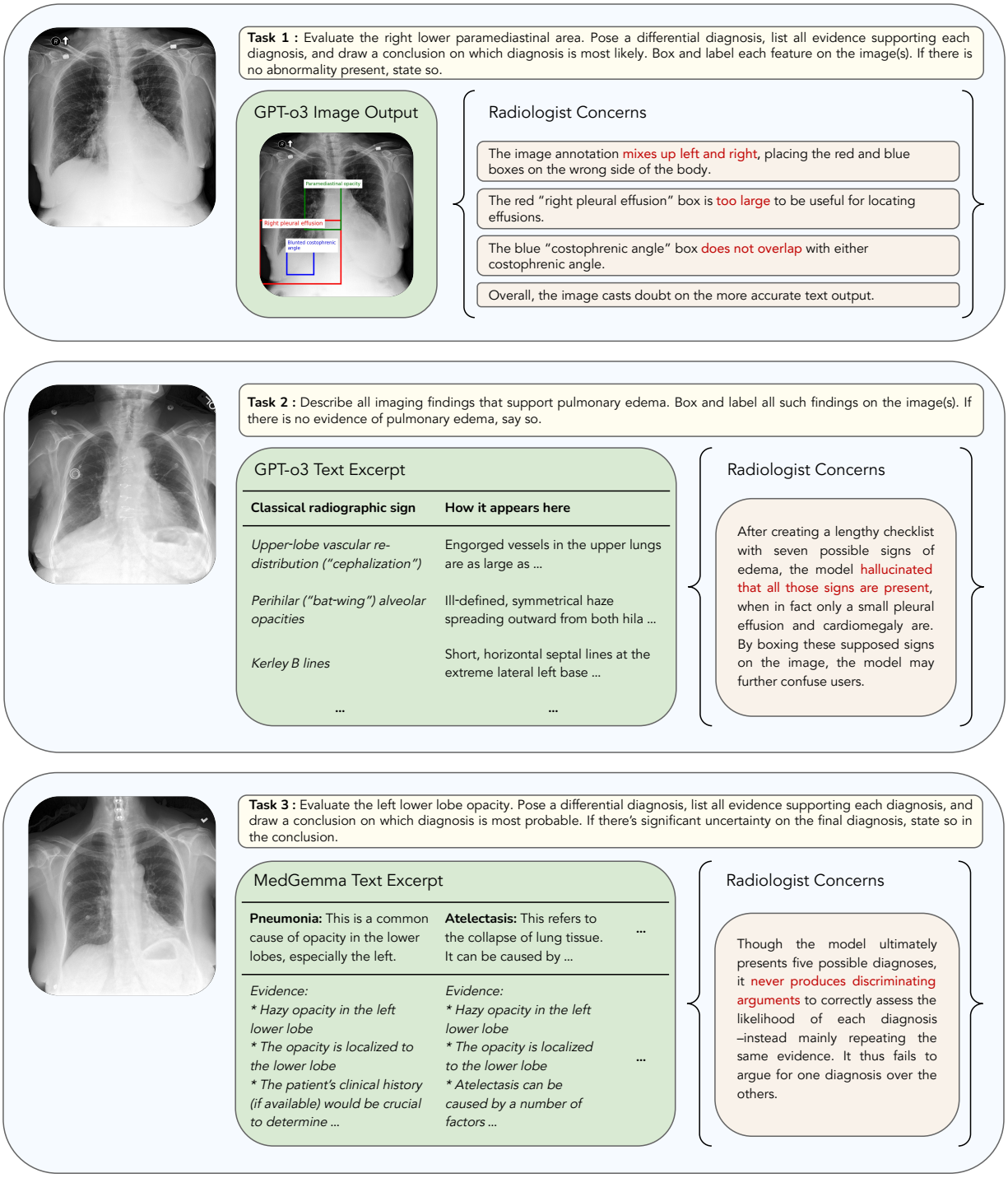

Fig. 4: Error examples highlighting radiologist's concerns on three cases.

pattern has definite potential to mislead clinicians, who can also struggle with this aspect of radiological imaging. Often, ChatGPT-o3 tended to explain its reasoning in depth, even when arriving at incorrect conclusions. This verbosity aided transparency but occasionally reduced

clarity, confusing clinicians or slowing them down.

On the other hand, we found that MedGemma tended toward brevity, providing little insight into its reasoning, providing insufficient detail and under-reporting secondary findings. For example, when asked to gather all evidence of a pathology, the model described some findings like pleural effusions and consolidation while neglecting other findings such as rib crowding or volume loss. It also gave overly broad descriptions of abnormalities, such as stating that an "opacity" is present without further specifying that the opacity was an "air-bronchogram." For 19 tasks, MedGemma failed to finish generating answers due to an excessive token count; it is possible that those answers would have contained the desired level of detail if they had been successfully generated.

4.5. *Inter-Reader Agreement*

Moderate agreement was obtained for Execution ($\kappa = 0.57$), and Image Style ($\kappa = 0.48$). We observed lower rates of agreement on other dimensions (Table 3). Low rates of agreement were likely driven in part by the lack of variance in our score distributions; for example, nearly all Process scores fell into the range of 3-5, leading to lower Cohen's κ values. We note that mean absolute differences were under 1 for all text content categories; even when their orderings across cases differed, reader scores for any individual case were typically close together, as seen on Figure 5.

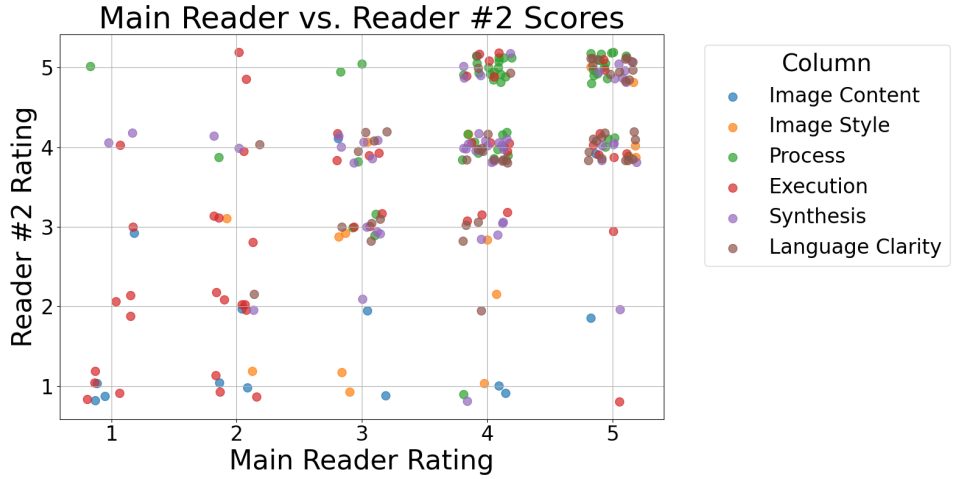

Fig. 5: Plot of both readers' scores, which generally differ by a maximum of one category.

5. Discussion

This study presented the ReXecution framework and evaluated the performance of two leading foundation models on expert-curated questions that reflect the interpretive demands that AI assistants would face in real-world radiology practice. Our evaluation set was built to mirror everyday radiological workstation questions requiring complex, detailed answers—contrasting with current benchmarks that rely on automatically generated multiple-choice or short-answer

Evaluation Category	QWK	MAD	Main Reader ($\mu \pm \sigma$)	Reader #2 ($\mu \pm \sigma$)
Process	0.215	0.667	4.118 ± 0.840	4.510 ± 0.784
Execution	0.573	0.882	2.961 ± 1.399	3.176 ± 1.337
Synthesis	0.291	0.706	3.824 ± 1.014	3.902 ± 0.878
Language	0.560	0.510	4.235 ± 0.862	4.078 ± 0.771
Image Content	0.327	1.200	2.733 ± 1.438	1.933 ± 1.223
Image Style	0.484	1.000	3.667 ± 1.047	2.933 ± 1.438

Table 3: Quadratic Weighted Kappa (QWK), Mean Absolute Difference (MAD), and reader score distributions (mean ± SD) for each evaluation category.

questions and fall short of modeling clinical settings. Through expert review of tasks and model answers, we gathered rich qualitative information on how current AI models would perform when supporting radiologists at the workstation.

Our findings reveal important insights into both the promise and the limitations of present-day foundation models in radiology. When performing our tasks, both ChatGPT-o3 and MedGemma displayed strong medical knowledge and abstract reasoning, with ChatGPT-o3's detailed explanations proving particularly useful. However, both struggled to execute their plans due to weaker image understanding—they often knew what to do, but not how to do it. Quantitatively, Process scores topped Execution scores by 0.65 points for MedGemma and 1.27 points for ChatGPT-o3, underscoring a gap between planning and pixel-level perception. Average Content scores were only 2.7-2.8 out of 5, and $\leq 10\%$ of answers were marked as completely correct. In addition to observing errors in text outputs, we noted frequent errors in ChatGPT-o3's image outputs. Only 10.1% of 62 annotated images showed perfect localization, while nearly half of the figures were stylistically sound but spatially inaccurate. Ideally, image outputs would improve explainability and help users find subtle findings mentioned by text outputs, yet current image annotations are as likely to decrease trust in correct text outputs or confuse users.

We found no statistically significant differences between ChatGPT-o3, a leading general-purpose model, and MedGemma, a cutting-edge foundation model trained specifically for medical imaging tasks. While the two models demonstrated qualitatively different patterns of behavior, both impressed readers with their abstract medical knowledge regardless of their mistakes and occasional unreliable conclusions.

We observed interesting practical differences when using models, beyond the fact that only ChatGPT-o3 could illustrate its outputs. MedGemma was constrained in its inputs, officially recommending that users only provide one image at a time. This constraint substantially restricts the amount of relevant information users can provide, since imaging studies routinely contain chest X-rays taken from different views. MedGemma was also limited in the number of tokens it could process at once and thus failed to perform tasks that elicited longer, more complex outputs. To keep up with the offerings of large, general-purpose models, medical foundation models must make use of multimodal data and increasing amounts of context. The main usability issue we encountered with ChatGPT-o3 was that it sometimes failed to

follow the "bounding box" parts of our instructions, outputting only a text output. In some instances, it completely ignored that part of our instruction, while in others it acknowledged the request but requested guidance on what to draw. While this behavior might be acceptable from an interactive chatbot, it could also prove frustrating in situations where models are expected to act independently and follow instructions the first time.

Broadly speaking, our findings complicate recent claims that chest X-ray models are reaching expert-level performance on classification and even radiology report generation. For example, a recent multiple-choice benchmark found that MedGemma achieved 83.8% accuracy on multiple-choice chest X-ray questions,[3] yet only 4.9% of MedGemma's outputs were free of content errors on our complex tasks. With a focus on radiologist-centered evaluation, our work shows the importance of "stress-testing" models on difficult, clinically relevant tasks, revealing shortcomings in model performance before they enter real-world workflows. More work is needed to help models match their theoretical prowess with concrete skills, perhaps by focusing on fine-grained image localization tasks and on findings like rib crowding or air bronchograms that—though common—may be overlooked by existing labeled datasets. Such advances can bridge the gap between current AI capabilities and real-world clinical needs, allowing models to provide comprehensive support and achieve true clinician-AI collaboration.

6. Limitations

While we cover a large range of tasks related to abnormality detection, diagnostic support, and measurement, we omitted some clinically relevant use cases, such as "quality control" tasks for flagging otherwise low-quality chest X-rays. We also did not include "unanswerable" questions that required models to request more information or refrain from answering. Since our focus was on posing realistic questions, we did not design questions to purposefully mislead the model by emphasizing irrelevant or counterintuitive details, though such "trick" questions may have revealed important biases and merit consideration in other work.

We occasionally encountered ambiguous edge cases when scoring answer content, as it is not always clear whether an error arises from the "Process", "Execution", or "Synthesis" phase; we attempted to mitigate this issue by aggregating those scores in a single "Content" score to penalize all content-related errors on a task, no matter the phase. Score subjectivity was also reflected in the fair-to-moderate inter-reader agreement—demonstrating inherent subjectivity in clinician evaluation and emphasizing the need for multi-reader evaluation. Finally, our semi-automated pipeline required considerable radiologist effort, even with only 100 studies. Future work may leverage LLMs more heavily, improving scalability while maintaining realism.

7. Supplementary Materials

Materials are available at https://rajpurkarlab.github.io/rexecution-supplementals/.

8. Acknowledgments

We thank Sung Eun Kim and Xiaoman Zhang for feedback. This work was supported by Biswas Family Foundation's Transformative Computational Biology Grant in collaboration with the Milken Institute. L.B. was supported by Junior Orsi and Barco.

References

1. A. Sellergren, S. Kazemzadeh, T. Jaroensri, A. Kiraly, M. Traverse, T. Kohlberger, S. Xu, F. Jamil, C. Hughes, C. Lau, J. Chen, F. Mahvar, L. Yatziv, T. Chen, B. Sterling, S. A. Baby, S. M. Baby, J. Lai, S. Schmidgall, L. Yang, K. Chen, P. Bjornsson, S. Reddy, R. Brush, K. Philbrick, M. Asiedu, I. Mezerreg, H. Hu, H. Yang, R. Tiwari, S. Jansen, P. Singh, Y. Liu, S. Azizi, A. Kamath, J. Ferret, S. Pathak, N. Vieillard, R. Merhej, S. Perrin, T. Matejovicova, A. Ramé, M. Riviere, L. Rouillard, T. Mesnard, G. Cideron, J. bastien Grill, S. Ramos, E. Yvinec, M. Casbon, E. Buchatskaya, J.-B. Alayrac, D. Lepikhin, V. Feinberg, S. Borgeaud, A. Andreev, C. Hardin, R. Dadashi, L. Hussenot, A. Joulin, O. Bachem, Y. Matias, K. Chou, A. Hassidim, K. Goel, C. Farabet, J. Barral, T. Warkentin, J. Shlens, D. Fleet, V. Cotruta, O. Sanseviero, G. Martins, P. Kirk, A. Rao, S. Shetty, D. F. Steiner, C. Kirmizibayrak, R. Pilgrim, D. Golden and L. Yang, Medgemma technical report (2025).
2. H.-Y. Zhou, J. N. Acosta, S. Adithan, S. Datta, E. J. Topol and P. Rajpurkar, Medversa: A generalist foundation model for medical image interpretation (2025).
3. A. Pal, J.-O. Lee, X. Zhang, M. Sankarasubbu, S. Roh, W. J. Kim, M. Lee and P. Rajpurkar, Rexvqa: A large-scale visual question answering benchmark for generalist chest x-ray understanding (2025).
4. M. Moor, O. Banerjee, Z. Abad, H. Krumholz, J. Leskovec, E. Topol and P. Rajpurkar, Foundation models for generalist medical artificial intelligence, *Nature* **616**, 259 (04 2023).
5. J. Huang, M. T. Wittbrodt, C. N. Teague, E. Karl, G. Galal, M. Thompson, A. Chapa, M.-L. Chiu, B. Herynk, R. Linchangco, A. Serhal, J. A. Heller, S. F. Abboud and M. Etemadi, Efficiency and quality of generative ai–assisted radiograph reporting, *JAMA Network Open* **8**, e2513921 (06 2025).
6. S. Bae, D. Kyung, J. Ryu, E. Cho, G. Lee, S. Kweon, J. Oh, L. Ji, E. Chang, T. Kim and E. Choi, Mimic-ext-mimic-cxr-vqa: A complex, diverse, and large-scale visual question answering dataset for chest x-ray images `https://physionet.org/content/mimic-cxr-vqa/1.0.0/`, (2024), Published July 19, 2024.
7. X. Hu, L. Gu, K. Kobayashi, L. Liu, M. Zhang, T. Harada, R. Summers and Y. Zhu, Medical-cxr-vqa dataset: A large-scale llm-enhanced medical dataset for visual question answering on chest x-ray images `https://example.com/medical-cxr-vqa`, (2025), Published January 21, 2025.
8. S. Bae, D. Kyung, J. Ryu, E. Cho, G. Lee, S. Kweon, J. Oh, L. Ji, E. I.-C. Chang, T. Kim and E. Choi, Ehrxqa: A multi-modal question answering dataset for electronic health records with chest x-ray images (2023).
9. X. Hu, L. Gu, Q. An, M. Zhang, L. Liu, K. Kobayashi, T. Harada, R. Summers and Y. Zhu, Medical-diff-vqa: A large-scale medical dataset for difference visual question answering on chest x-ray images `https://example.com/medical-diff-vqa`, (2025), Published February 3, 2025.
10. B. Liu, K. Zou, L. Zhan, Z. Lu, X. Dong, Y. Chen, C. Xie, J. Cao, X.-M. Wu and H. Fu, Gemex: A large-scale, groundable, and explainable medical vqa benchmark for chest x-ray diagnosis (2025).
11. B. Liu, L.-M. Zhan, L. Xu, L. Ma, Y. Yang and X.-M. Wu, Slake: A semantically-labeled knowledge-enhanced dataset for medical visual question answering (2021).
12. J. J. Lau, S. Gayen, A. Ben Abacha and D. Demner-Fushman, A dataset of clinically generated visual questions and answers about radiology images, *Scientific Data* **5** (2018), Published November 20, 2018.
13. O. Banerjee, A. Saenz, K. Wu, W. Clements, A. Zia, D. Buensalido, H. Kavnoudias, A. S. Abi-Ghanem, N. E. Ghawi, C. Luna, P. Castillo, K. Al-Surimi, R. A. Daghistani, Y.-M. Chen, H. sheng Chao, L. Heiliger, M. Kim, J. Haubold, F. Jonske and P. Rajpurkar, Rexamine-global: A framework for uncovering inconsistencies in radiology report generation metrics (2024).
14. F. Yu, M. Endo, R. Krishnan, C. P. Langlotz, V. K. Venugopal and P. Rajpurkar, Evaluating

progress in automatic chest x-ray radiology report generation, *Patterns* **4**, p. 100802 (2023), Published September 8, 2023.
15. A. E. W. Johnson, T. J. Pollard, N. R. Greenbaum, M. P. Lungren, C. ying Deng, Y. Peng, Z. Lu, R. G. Mark, S. J. Berkowitz and S. Horng, Mimic-cxr-jpg, a large publicly available database of labeled chest radiographs (2019).

Leveraging Generative AI for Interpretable Clinical Decision Making Through Causal Graphs

Mehmet Eren Ahsen PhD[1], Rand Kittani[2], Travis Gerke ScD[3], Laya Krishnan[2], Sean Rogan[3], and Erick R. Scott MD MHS[3†]

[1]*Gies College of Business,* [2]*Carle Illinois College of Medicine, University of Illinois Urbana-Champaign, Champaign, IL, 61820, USA*
[3]*cStructure, La Jolla, CA, 92037, USA*
[†]*E-mail: erick@cstructure.io*

Clinical AI systems' lack of interpretability limits their adoption in evidence-based medicine. To address this challenge, we propose a computational framework that harnesses generative AI's medical knowledge to create interpretable structural causal models (SCMs) for clinical decision support, quality improvement evaluation, and population health management. We evaluated our approach through a case study using data from the Midwest Healthcare Conference Causal Diagram Challenge, where we compared transformer-based large language models against human performance on a complex causal reasoning task: estimating COVID-19 treatment effects through target trial emulation. Both groups designed SCMs to evaluate glucocorticoid treatment effects on 28-day mortality using real-world data from more than 2,000 hospitalized patients, benchmarked against published RECOVERY randomized controlled trial results. The best performing SCMs achieved bootstrap coverage rates exceeding 90% for two of three severity strata. Both human and AI models demonstrated equivalent clinical plausibility (n=3 expert reviewers) and similar statistical performance, though both struggled with critical disease severity. Ablation experiments comparing SCM-based approaches against traditional potential outcomes methods revealed SCMs achieved 76-98% coverage versus 1-37% for traditional methods. These results suggest that structural causal models can effectively bridge the interpretability gap in clinical AI by providing essential scaffolding for reliable causal inference and enabling meaningful human-AI collaboration while preserving methodological rigor essential for evidence-based medicine.

Keywords: Causal Inference, Large Language Models, Artificial Intelligence, Clinical Informatics, Structural Causal Models, AI-Supported Interactive Evaluation

1. Introduction

Clinical artificial intelligence poses interpretability and explainability challenges.[1] Although transformer-based large-language models demonstrate impressive performance metrics,[2] their black-box nature delays meaningful and safe integration into clinical decision-making workflows.[3] Regulatory health agencies require explainable AI systems when the device is intended

© 2025 The Authors. Open Access chapter published by World Scientific Publishing Company and distributed under the terms of the Creative Commons Attribution Non-Commercial (CC BY-NC) 4.0 License.

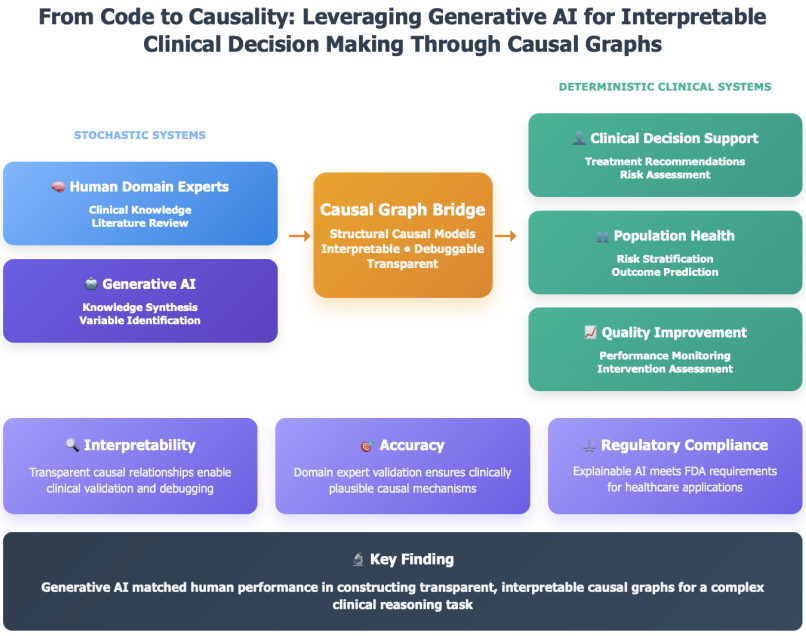

Fig. 1. Graphical Abstract

to diagnose, treat, cure, mitigate, or prevent disease.[4] However, most current AI approaches sacrifice interpretability for accuracy and rely upon post-hoc explanations that fail to reliably provide causal reasoning underlying their recommendations.[5–7]

Generative AI has demonstrated competency solving a limited set of programming tasks by converting probabilistic text generation into deterministic executable systems.[8] The key insight is in converting uncertain outputs into structured and interpretable representations that can be debugged, validated, and iteratively refined by humans.

The same principle can be applied to clinical reasoning. Generative AI's medical domain knowledge can be converted into interpretable structural causal models (SCMs) that provide transparent, debuggable, and quantitative representations of clinical knowledge (**Figure 1**). We evaluate this framework by comparing generative AI and human performance in designing structural causal models. The evaluation uses results from the Midwest Healthcare Conference Causal Diagram Challenge, where human participants without formal causal inference training and with varying levels of domain knowledge designed SCMs to estimate the safety and efficacy of COVID-19 treatment strategies (glucocorticoids in three disease severity contexts) using real-world electronic health record (EHR) data. This study provides empirical evidence for how structural causal models can bridge the gap between model intelligence and human reasoning in clinical medicine.

Collaborative Target Trial Emulation: Framework, Process, and Performance

Causal Roadmap Steps	Challenge Implementation
Step 1: Causal Question, Model, Estimand Define causal question and construct DAG	**Target Trial Emulation** Steroid effects on 28-day survival, stratified by severity
Step 2: Observed Data Assess data quality	**SDY1662 Dataset** 2,074 patients, person-time transformation
Step 3: Identifiability Evaluate assumptions	**cStructure Platform** Automated d-separation analysis
Step 4: Statistical Estimand Translate to statistical quantity	**Risk Ratio** 28-day survival with severity stratification
Step 5: Model Selection Choose statistical methods	**Pooled Logistic Regression** G-formula
Step 6: Sensitivity Analysis Assess robustness	**Bootstrap Validation** 500 samples per severity level
Step 7: Compare Designs Evaluate alternatives	**Human vs. AI** Collaborative comparison

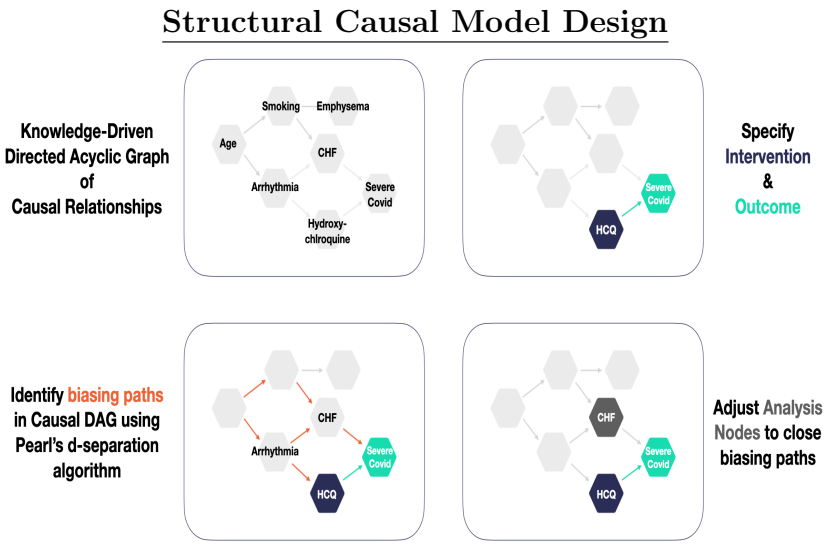

Dimension	Transformer Models	Structural Causal Models
Breadth of Knowledge	+++	N/A
Speed	+++	–
Creativity	++	N/A
Natural Language Processing	++	–
Factual Accuracy	+	+++
Transparency	—	+++
Reproducibility	—	++
Quantitative Reasoning	—	++

While transformer-based LLMs excel in knowledge breadth and speed, SCMs provide superior accuracy, transparency, and reproducibility essential for clinical applications. Complementary strengths suggest hybrid approaches leveraging LLM knowledge within structural causal frameworks.

Fig. 2. **Collaborative Target Trial Emulation Framework and LLM-SCM Integration. Left:** Implementation of the Causal Roadmap framework in the UIUC Challenge demonstrating systematic translation from clinical questions to validated causal models. **Top right:** DAG construction process showing progression from domain knowledge specification to automated validation. **Bottom right:** Comparison of Large Language Models and Structural Causal Models across key dimensions, highlighting complementary strengths that enable hybrid approaches combining AI knowledge generation with rigorous causal inference.

2. Background and Related Work

2.1. *Causal Inference in Clinical Research*

The Causal Roadmap provides a systematic approach for generating high-quality real-world evidence through explicit specification of causal questions, identification assumptions, estimands, and statistical estimators, (**Figure 2, left panel**).[9] Target trial emulation employs this framework to design observational studies that carefully emulate randomized controlled trials (RCTs), enabling rigorous causal inference from real-world data.[10] Despite methodological advances, causal inference remains underutilized in clinical practice. Current tools require extensive statistical programming expertise, creating barriers for clinical researchers who have

essential domain knowledge—precisely those best positioned to identify confounders, evaluate clinical plausibility, and validate causal assumptions.

2.2. *Structural Causal Models as an Interpretable AI Framework*

Structural causal models (SCMs) represent causal relationships as directed acyclic graphs (DAGs) where nodes denote variables and edges encode causal dependencies between them.[11] The construction of SCMs follows a systematic process that transforms clinical knowledge into formal causal structures (**Figure 2, top-right panel**). Domain experts specify variables relevant to the clinical question, define directional causal relationships based on biological mechanisms and temporal precedence, and use Pearl's d-separation algorithm to identify biasing pathways that must be controlled through statistical adjustment to obtain valid causal estimates..[12]

Unlike black-box machine learning models, SCMs make causal assumptions explicit through visual representations that clinical experts can evaluate, modify, and validate against biological knowledge derived from randomized and observational studies.[13] This 'glass-box' approach enables target trial emulation for therapeutic safety and efficacy evaluation, clinical decision support for precision medicine, performance monitoring of quality improvement programs, and outcome prediction for population health management.[14] This causal graph approach addresses fundamental limitations of current clinical AI systems by providing interpretable, debuggable representations of causal reasoning. SCMs enable iterative refinement of causal assumptions, transparent communication of modeling decisions, and systematic evaluation of model validity against established clinical knowledge.[15]

2.3. *Human-AI Collaboration in Clinical Decision Making*

Effective clinical AI requires seamless integration of algorithmic capabilities with human expertise, as purely automated approaches often fail to capture nuanced clinical reasoning while manual approaches cannot scale to complex medical data.[16,17] Current systems typically provide predictions without exposing underlying reasoning processes, limiting meaningful human oversight—a critical gap given regulatory requirements for transparent, interpretable AI outputs that clinicians can evaluate and validate.[4]

Large language models show promise for clinical documentation and treatment planning but lack mechanisms for incorporating causal relationships or clinical knowledge in systematic, verifiable ways.[18] Complex causal reasoning tasks further challenge these models through long context windows and the 'lost-in-the-middle' problem.[19] However, the success of generative AI in programming tasks suggests a pathway: transforming probabilistic language generation into structured, interpretable representations that clinical experts can refine (**Figure 2, bottom-right panel**). We present evidence that structural causal models provide the necessary framework for this transformation, bridging model intelligence with human clinical expertise.

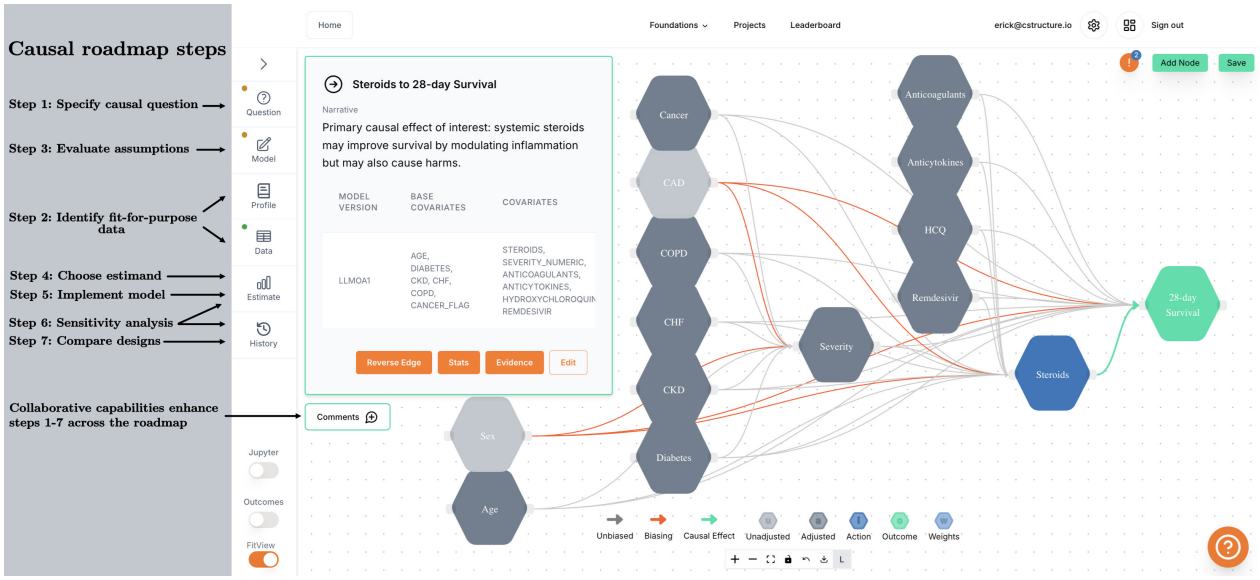

Fig. 3. Building knowledge-based Structural Causal Models in cStructure. Creating Edges: Participants could create directed edges between nodes to represent causal relationships. For example, they might add an edge from "Age" to "28-day Survival" to indicate that age directly affects survival outcomes. Adding Narratives: For each node and edge, users could provide detailed narratives explaining the node and its causal relationship with other nodes. These narratives were crucial for explaining the reasoning behind each causal connection and for evaluation of the model's plausibility. Users were encouraged to organize their graphs logically, typically with a left-to-right flow reflecting temporal precedence, where causes precede effects. This SCM along with the narrative text was generated by o3. User workflows in the cStructure platform are designed to follow the causal roadmap.

3. Methods

3.1. *Study Design and Participants*

We organized the UIUC Midwest Healthcare Conference Challenge to evaluate target trial emulation performance by participants without formal causal inference training. **Conference participants** were recruited without background restrictions and designed structural causal models via a collaborative interface to replicate RECOVERY trial effects of COVID-19 treatment using observational data, with the RECOVERY Trial serving as the gold-standard benchmark due to its randomized controlled design.[20] **Data access:** Participants received comprehensive SDY1662 metadata (data dictionaries, variable definitions, statistical profiles) but no patient-level data, with all analyses occurring via secure API calls through the cStructure interface. **AI comparison:** One year later, we conducted comparative analysis using four state-of-the-art generative AI models (OpenAI o3, DeepSeek R1, Gemini Pro 2.5, Claude Opus).

3.2. *Dataset and Target Trial Framework*

Dataset: We utilized ImmPort's SDY1662 dataset containing >2,000 hospitalized COVID-19 patients from Mount Sinai Health System (March-May 2020), transformed into person-time format (∼65,000 person-day observations) for pooled logistic regression.[21] **Severity classi-**

fication: Disease severity was classified using oxygen support requirements: mild-moderate (room air or low-flow oxygen, $SpO_2 \geq 94\%$ on $\leq$ 4L O_2), severe (high-flow oxygen, non-invasive/mechanical ventilation without vasopressors), and critical (mechanical ventilation with vasopressors or end-organ dysfunction: creatinine clearance < 30 mL/min or ALT $> 5\times$ ULN).[22] Missing data was handled using last observation carried forward; variables >50% missing were excluded. **Mini-cohorts:** To minimize immortal time bias, we created daily mini-cohorts evaluating treatment-eligible patients and assigning them to treatment strategies reflecting observed exposure, with patients appearing multiple times under different assignments and censoring upon strategy deviation.[23,24] For example, a patient receiving steroids on hospital day 2 would be classified as 'never treat' in mini-cohorts 0-1 but '10 days of steroids' in mini-cohort 2. **Target trial:** Participants estimated causal effects of glucocorticoids on 28-day all-cause mortality stratified by severity, applying RECOVERY eligibility criteria: hospitalized patients ≥18 years with COVID-19, no contraindications, sufficient follow-up, comparing glucocorticoid versus standard care. Data available at ImmPort.org under accession SDY1662.

3.3. *Model Construction and Platform Implementation*

cStructure platform: The platform provides a browser-based collaborative environment with interactive DAG editing, real-time d-separation analysis for confounding pathway identification, and JSON model serialization transmitted via REST API to secure analysis servers, with patient data remaining on secure servers while participants constructed models using metadata only (**Figure 3**). Real-time d-separation algorithms (TypeScript) identified open backdoor paths between treatment and outcome, providing automated feedback on confounding control. **Human-generated SCMs:** Participants constructed DAGs specifying nodes from dataset features, directional edges representing causal relationships, scientific rationale documentation, and node classifications (Action/Outcome/Adjusted/Unadjusted), with automated validation including d-separation analysis, temporal ordering checks, and convergence assessment. **Transformer-generated SCMs:** AI models received identical materials as human participants: challenge announcement, SDY1662 data dictionary, cStructure platform description, and GraphML specification format, with standardized prompts requesting causal diagrams evaluating steroid safety/efficacy on 28-day survival (**Supplementary Materials**). **SCM ablation study:** To test whether causal graphs provide unique benefits beyond LLM reasoning, we conducted controlled experiments with multiple models (OpenAI o3, Claude Opus, Gemini Pro 2.5, DeepSeekV1) receiving Potential Outcomes tasks requesting traditional causal inference methods (IPTW, AIPW, g-computation) without graph structure, using identical data dictionaries, bootstrap requirements (n=500), and target trial descriptions, isolating the effect of structured causal reasoning while holding constant statistical objectives, data access, model capabilities, and evaluation framework.

3.4. *Statistical Analysis and Evaluation*

Causal Plausibility: Three independent and blinded clinical reviewers evaluated the causal plausibility of the directed edges from Human (n=36) and Transformer-generated SCMS (n=86) using an ordinal scale (0=no plausible causal pathway, 1=low/weak rationale, 2=mod-

erate/plausible mechanism, 3=high/strong evidence). A Bayesian hierarchical model was used to compare plausibility scores between the two groups. **G-formula estimation:** Causal effects were estimated using the parametric g-formula (PyGFormula v1.1.6) with 500 bootstrap samples per severity stratum (seed=123), selected to overcome convergence issues encountered during the challenge, with bootstrap sampling at patient level to preserve within-patient correlations and risk ratios comparing predicted 28-day survival probabilities under treatment versus standard care. **Coverage analysis:** Bootstrapped confidence interval coverage against RECOVERY trial results using 500 bootstrap samples per severity stratum, ranking models by bootstrap estimates falling outside RECOVERY 95% CIs across all strata (n=1,500 total), with two-way binomial tests comparing each model's coverage against the Age base model. **Sign error analysis:** Directional accuracy where sign error equaled bootstrap estimate with opposite sign of severity-specific RECOVERY point estimate, ranking models by total sign errors across 1,500 iterations, with two-way binomial tests generated using coverage analysis procedures. **Software:** Statistical analysis used Python 3.13.3, Bayesian hierarchical regression (bambi v0.15.0, pymc v5.22.0), two-way binomial tests (scipy v1.15.2) were adjusted for multiple comparisons (n=7) with visualization via Matplotlib/Seaborn

4. Results

We evaluated causal diagrams, constructed by human participants and transformer-based language models, as transparent and interpretable bridges between domain expertise and quantitative clinical reasoning. Human participants from the Midwest Healthcare Conference Challenge (n=3 teams) and four transformer models (OpenAI o3, DeepSeek R1, Gemini Pro 2.5, Claude Opus) independently constructed causal diagrams to estimate COVID-19 glucocorticoid treatment effects on 28-day mortality using real-world data from more than 2,000 hospitalized patients. All models employed target trial emulation methodology with similar data access and challenge specifications. Performance was assessed through bootstrap coverage analysis against published RECOVERY trial benchmarks (n=500 iterations per disease severity stratum), sign error analysis for directional accuracy, and expert review of the causal plausibility of each directed edge.

Table 1: Performance comparison of transformer and human models showing causal plausibility scores, bootstrap outlier counts, and coverage percentages across disease severity strata.

Model	Type	Rank	Nodes	Edges	Adj. Set Final	Plaus. Score	Total Outliers	Coverage (%)
o3	LLM	1	15	35	13	2.25(0.68)	563	62.4
Team 1	Human	2	15	20	5	2.38(0.58)	576	61.6
GeminiPro2.5	LLM	3	13	22	4	2.59(0.36)	580	61.3
Age	Base	4	3	3	1	3	604	59.7
Team 2	Human	5	13	16	5	2.42(0.40)	610	59.3
Team 3	Human	6	6	5	4	2.27(0.86)	612	59.2
DeepSeekR1	LLM	7	5	7	2	2.52(0.42)	612	59.2
ClaudeOpus	LLM	8	19	22	9	2.29(0.74)	640	57.3

Legend: Adj. Set Final = Adjustment Set Final, Plaus. Score = Average Causal Plausibility Score (standard deviation)

4.1. *Comparative Performance of Human and Transformer Models*

4.1.1. *Model Complexity*

Structural complexity varied across human and transformer-generated models, as indicated by node count (5–19), edge count (5–35), and adjustment set node count (2–13) (**Table 1**). A key difference was that the human teams iteratively refined their graph topology and adjustment status to ensure statistical convergence. In contrast, Human-in-the-Loop (HITL) modifications were limited to changing adjustment status and enforcing the one-feature-per-node requirement, with no edges being added or removed. Specifically, the Claude Opus model required: 1) removing one feature from two nodes (ferritin_log2 was removed from Inflammatory Markers leaving CRP_log2, and Asthma was removed from Chronic lung disease node leaving COPD), and 2) unadjusting CAD, Chronic lung disease, Cancer Flag, and Sex. The OpenAI o3 model required unadjusting the CAD and Sex nodes (**Figure 3**), and the DeepSeek R1 model required unadjusting the CRP_log2 node to remove a mediator. Notably, the GeminiPro 2.5 model required no HITL modifications **(Supplementary Materials)**.

4.1.2. *Causal Plausibility*

To evaluate the quality of the causal relationships posited by each structural causal model (SCM), we calculated an average Plausibility Score (0 = implausible to 3 = strong biological basis and clinical evidence) for all directed edges across human-generated (n = 36) and LLM-generated (n = 86) models. These scores were derived from a blinded, expert review by three clinical domain experts, who assessed each edge for biological and clinical plausibility using the 0-3 ordinal scale, **(Table 1)**. Plausibility Scores were nearly identical between Transformer models and human teams, with score distributions differing by 5% at each level (0: 4% vs 6%; 1: 12% vs 12%; 2: 27% vs 22%; 3: 57% vs 60%) and statistically equivalent means (2.37±0.62 vs 2.38±0.56; Cohen's D=0.02). Overall, both human and LLM-derived models demonstrated a similar capacity to construct relationships deemed plausible by a domain expert.

4.1.3. *Sign Error Analysis and Directional Accuracy*

We performed a sign error analysis to assess the directional accuracy of treatment effect estimates compared to RECOVERY trial benchmarks (**Figure 4, Top and Middle Panels**). A sign error was defined as a bootstrap point estimate having the opposite sign of the corresponding severity-specific RECOVERY trial estimate.

Sign error measurement revealed substantial performance variation. Across all severity levels ($n = 1,500$ bootstrap iterations), the two best-performing models were Transformers: Claude Opus (11.1% error rate) and o3 (11.2% error rate), both significantly outperforming the baseline ($p = 2 \times 10^{-8}$). Transformer-generated models generally showed superior directional accu-

racy compared to human models, particularly in the critical disease stratum.

Directional accuracy varied sharply by severity. In mild-moderate disease (Severity 1), o3 achieved the lowest error rate at 9.0%. Severe disease (Severity 2) showed exceptional accuracy, with all models exhibiting minimal error rates (0% – 0.6%). Conversely, critical disease (Severity 3) had the poorest directional accuracy, with all models exceeding a 19% error rate. Performance in this stratum ranged from 19.6% (Claude Opus) to 46.6% (Team 3), suggesting challenges likely due to sample size limitations, unmeasured confounding, and/or true differences in the causal effect of glucocorticoids in this subpopulation.

4.1.4. *Coverage Analysis*

Table 1 presents the comparative performance of structural causal models submitted by the three top-ranked participating teams (Team 1, Team 2, and Team 3), four transformer-based large language models (o3, Gemini Pro 2.5, DeepSeek R1, Claude Opus) one year after the conclusion of the challenge, and a simple base model (Age). The best-performing model overall was generated by OpenAI's o3 transformer, achieving rank 1 with 563 total bootstrap outliers corresponding to 62.4% coverage of RECOVERY trial confidence intervals (unadjusted two-sided binomial p-value = 0.032 compared to Age base model, n=1500) . The second-ranked model was human-generated, achieving similar performance with 576 outliers (61.6% coverage). It is also noteworthy, that the top-performing human team utilized a literature-based approach with a parsimonious adjustment set (n=5 adjusted nodes), whereas the top-performing transformer model generated the most complex causal graph (n=35 edges) with the largest adjustment set (n=13 adjusted nodes).

When comparing coverage performance against the Base model (Age as the only adjustment node), statistical significance varied by severity stratum (**Figure 4, Bottom Panel**). In mild-moderate disease (Severity 1, n=500), only the o3 model outperformed the Base model (p-value = 0.013). For severe disease (Severity 2, n=500), three models showed superior performance: Team 1, o3, and Gemini Pro 2.5 (all p-values < 0.0005), while Claude Opus performed significantly worse than the Base model (p-value < 0.001).

A critical finding was the universal poor performance in the critical disease severity stratum (Severity 3), where all models achieved 0% coverage (500/500 bootstrap outliers). This suggests fundamental challenges in modeling treatment effects with this dataset using the gformula, potentially due to limited sample size and/or unmeasured confounding in this subgroup. In contrast, both mild-moderate and severe disease strata showed reasonable coverage performance, with the best models achieving >97% coverage for severity 1 and 90% coverage for severity 2 disease.

This provides initial evidence that state-of-the-art AI systems can construct models with performance similar to human domain experts without formal causal inference training, though both approaches face limitations in complex clinical scenarios.

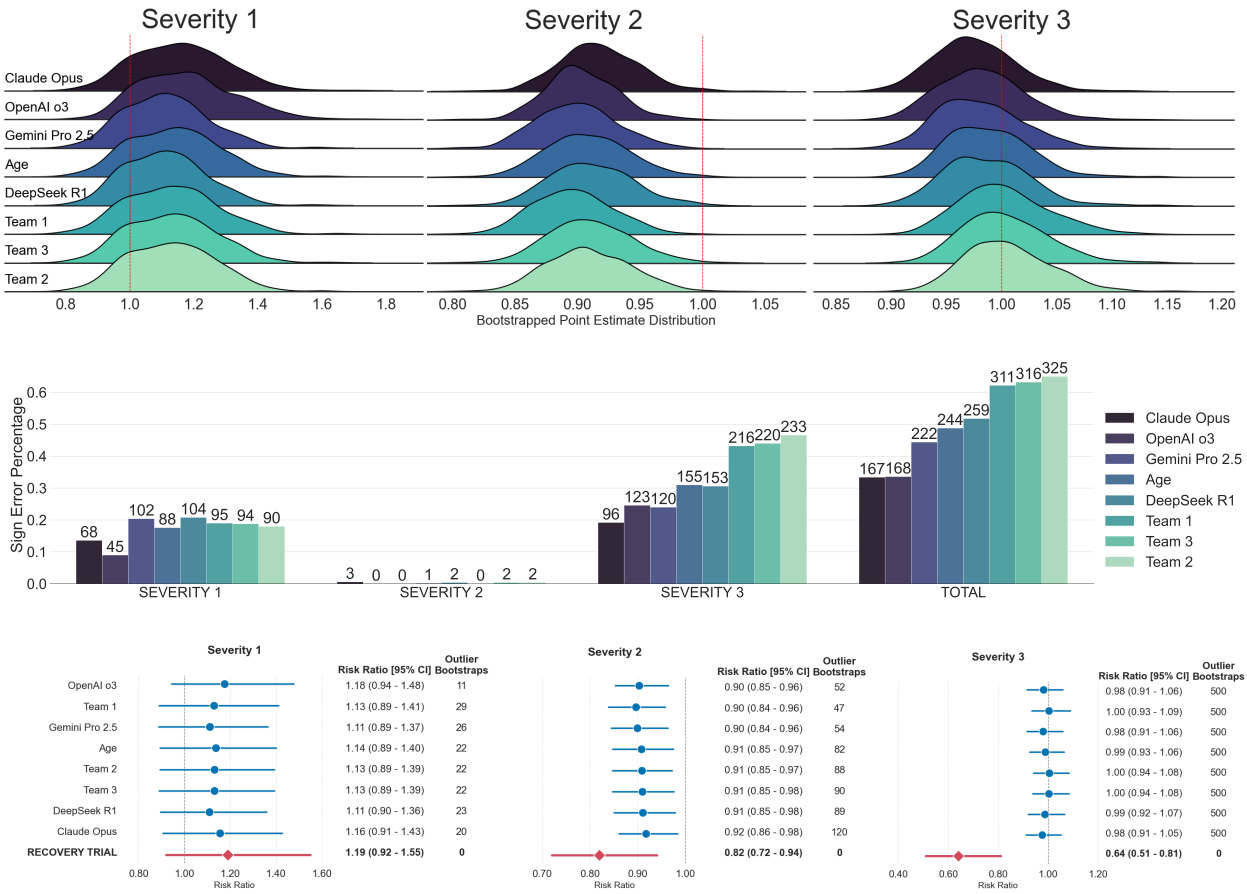

Fig. 4. **Top panel:** Bootstrapped Risk Ratio (RR) distributions across severity levels with ridge plots showing probability densities for each SCM. Red dashed line (RR = 1.0) indicates no effect; distributions right/left suggest increased/decreased 28-day mortality risk. Models ranked by total bootstrap sign errors. **Middle panel:** Sign error distribution by model and severity. Sign errors defined as bootstrap estimates with opposite sign from corresponding RECOVERY trial point estimates (500 iterations per severity, 1,500 total per model). **Bottom panel:** Bootstrap CI coverage versus RECOVERY benchmarks. Forest plot comparing coverage performance between human participants (blue) and AI models (red) across severity strata. Points show proportion of 500 bootstrap estimates within published RECOVERY 95% CIs. Models ranked by total outliers (estimates outside RECOVERY 95% CIs); 500 samples per stratum, 1,500 total. Dashed line indicates RR = 1.

4.1.5. *SCM Ablation using Potential Outcomes*

The SCM ablation results show structural causal models consistently outperformed traditional potential outcomes implementations across all tested models. Traditional PO approaches yielded poor coverage rates of 1-30%, 2-37%, and 1-10% across severities 1-3, with DeepSeekV1 failing to generate any causal estimate despite repeated debugging attempts. The wide PO confidence intervals occasionally produced better sign error rates—notably Claude PO's 0.8% versus SCM's 13.6% in Severity 1—suggesting imprecise estimates sometimes captured correct directionality by chance rather than proper calibration. The PO approaches exhibited

systematic failures regardless of sophistication level, from basic IPTW to advanced cross-fitted ensemble methods, all mishandling the person-time data structure, treatment eligibility, and immortal time bias (see Supplementary Materials). These findings suggest causal graphs provide essential scaffolding for reliable inference in complex longitudinal settings.

Table 2: Performance comparison between Structural Causal Models (SCM) and Potential Outcomes causal inference.

Model	Method	Severity 1	Severity 2	Severity 3
		Inside CI% / Correct Direction%		
OpenAI o3	SCM	97.8% / 91.0%	89.6% / 100.0%	0.0% / 80.8%
	PO	0.8% / 0.2%	1.8% / 63.4%	10.2% / 60.0%
	Δ	**+97.0pp / +90.8pp**	**+87.8pp / +36.6pp**	**-10.2pp / +20.8pp**
Claude	SCM	96.0% / 86.4%	76.0% / 99.4%	0.0% / 66.6%
	PO	19.6% / 99.2%	36.6% / 63.8%	0.6% / 7.4%
	Δ	**+76.4pp / -12.8pp**	**+39.4pp / +35.6pp**	**-0.6pp / +59.2pp**
Gemini 2.5	SCM	94.8% / 82.4%	89.2% / 100.0%	0.0% / 55.6%
	PO	29.6% / 88.6%	10.2% / 100.0%	9.8% / 23.2%
	Δ	**+65.2pp / -6.2pp**	**+79.0pp / 0.0pp**	**-9.8pp / +32.4pp**

RECOVERY Benchmarks: Severity 1: RR=1.19 [0.92, 1.55] (harm) — Severity 2: RR=0.82 [0.72, 0.94] (benefit) — Severity 3: RR=0.64 [0.51, 0.81] (benefit).
Legend: SCM = Structural Causal Model, PO = Potential Outcomes, Δ = Improvement, pp = percentage points

5. Discussion

5.1. *Causal Reasoning Comparative Performance Analysis*

Our evaluation of state-of-the-art transformer models (OpenAI o3, DeepSeek R1, Gemini Pro 2.5, Claude Opus) against human participants from the Midwest Healthcare Conference Challenge revealed nuanced performance differences on a complex causal reasoning task (Target Trial Emulation). All participants successfully constructed causal models and implemented analytical pipelines, though with varying degrees of sophistication in handling the person-time data structure and time-varying confounding inherent in the COVID-19 treatment effect estimation task.

With respect to directional accuracy, transformer-generated models significantly lower rates of sign errors compared to the baseline model. Even in the critical disease stratum (Severity 3) where coverage proved challenging, transformer models maintained better directional consensus. Sign errors are particularly clinically relevant when population health management decisions must be made with limited quality evidence, as was the case during the early days of the Covid-19 pandemic. This superior directional performance suggests transformer models

may better capture underlying biological plausibility even when statistical precision remains elusive.

Coverage analysis revealed a complex performance landscape across severity strata. While the top-performing transformer model (o3) achieved similar overall coverage to the best human team (62.4% vs 61.6% bootstrap coverage against RECOVERY trial benchmarks), performance varied substantially by disease severity. In mild-moderate disease (Severity 1), only o3 significantly outperformed the age baseline ($p = 0.013$), while human teams showed no significant improvement. For severe disease (Severity 2), three models—Team 1, o3, and Gemini Pro 2.5—demonstrated highly significant superior performance (all $p < 0.0005$), while Claude Opus performed significantly worse than baseline ($p < 0.001$). Universal poor performance in the critical disease severity stratum (0% coverage across all models) suggests fundamental challenges in modeling this particular treatment effect that transcend both human and AI approaches, likely reflecting dataset limitations rather than methodological deficiencies. Specifically, we found that sparse confounder patterns paired with missingness observed in this real-world dataset posed convergence challenges and statistical modeling limitations for the participants. While this represents a common impediment to causal inference applications in practice, a larger and more complex dataset may have revealed greater distinctions across human and AI performance.

The SCM ablation experiments suggests that framework choice influences transformer performance on complex causal tasks. SCMs explicitly encode time-oriented causal relationships in their graph structure, while potential outcomes frameworks require practitioners to separately specify these elements when implementing estimators like pooled logistic regression or marginal structural models. The consistent struggles of PO implementations across all transformer models—particularly with person-time data and immortal time bias—hint that translating abstract potential outcomes notation into concrete analytical code demands additional implicit reasoning that current AI systems find challenging. This pattern supports our broader finding that SCMs facilitate human-AI collaboration by providing explicit, visual representations of causal assumptions that both parties can evaluate, rather than leaving critical temporal dynamics implicit in statistical code.

5.2. *Generative AI to Causal Graph Interface*

We developed a novel interface that translates generative AI medical knowledge into regulatory-aligned structural causal models,[14] addressing fundamental limitations in current clinical AI systems. By combining the knowledge generation capabilities of large language models with the transparency and rigor required for target trial emulation, quality improvement monitoring, and clinical decision support, this approach provides an interpretable workflow for healthcare causal inference tasks. The cStructure platform integrates collaborative visual interface design, automated d-separation evaluation, and privacy-preserving statistical analysis to enable rapid systematic validation of AI-generated causal assumptions against established clinical knowledge.

5.3. *Transformer-Based AI for Clinical Causal Reasoning*

While transformer-based generative AI provides rapid access to vast medical domain knowledge with improving accuracy, their probabilistic nature and inscrutable generation processes necessitate structured frameworks that enable human oversight and validation in safety-critical applications. Our results demonstrate that structural causal models can bridge AI capabilities and human expertise by exposing interpretable causal reasoning that can be evaluated, modified, and validated using real-world data. The improved directional accuracy of transformer models suggests complementary strengths to human-generated models, while also serving as accelerators for human-led causal reasoning—particularly for non-experts—when SCMs provide the structured conduit. Practical implementation required extracting LLM domain knowledge into visually accessible representations with explanatory text that enable rapid human-in-the-loop (HITL) evaluation and debugging. This transparent design allowed clinical experts to identify potential biases, verify confounder adjustment, and modify assumptions based on domain knowledge. While transformer models required HITL modifications for statistical convergence—primarily unadjusting nodes causing convergence failures—we deliberately restricted interventions to adjustment status only, preserving AI-generated topology. This constraint simulates realistic rapid review scenarios, contrasting with human teams who iteratively revised both topology and adjustment sets, yet provides a more realistic assessment of how practitioners might use AI-generated causal models in time-constrained clinical settings.

5.4. *Future Directions*

Future research should expand evaluation to diverse causal reasoning tasks across multiple clinical domains, therapeutic areas, and patient populations to establish the generalizability and utility of human-AI equivalence in causal model construction. Additional priorities include developing standardized evaluation frameworks for clinical causal reasoning, investigating hybrid human-AI collaborative approaches that leverage complementary strengths (e.g. Covid Causal Diagram DREAM Challenge), and exploring real-time clinical deployment of AI-generated causal models with appropriate safety monitoring and validation protocols. The framework's potential for regulatory applications warrants investigation through partnerships with health agencies to establish guidelines for AI-assisted causal inference in evidence generation.

Supplement: Supplemental methods, materials, tables, and figures are available at https://github.com/cstructure/interpretable-clinical-scm

Acknowledgements: We would like to thank the participants of the Midwest Healthcare Conference Challenge for their contributions. With a special thanks to: April Wu, Yinglei Wu, Wendy Zheng, Brian Hong, July Chen, Brian Ellis, and Rebecca Shi.

References

1. Gary S Collins, Karel GM Moons, Paula Dhiman, Richard D Riley, Andrew L Beam, Ben Van Calster, Marzyeh Ghassemi, Xiaoxuan Liu, Johannes B Reitsma, Maarten Van Smeden, et al. Tripod+ ai statement: updated guidance for reporting clinical prediction models that use regression or machine learning methods. *bmj*, 385, 2024.
2. Karan Singhal, Tao Tu, Juraj Gottweis, Rory Sayres, Ellery Wulczyn, Mohamed Amin, Le Hou, Kevin Clark, Stephen R Pfohl, Heather Cole-Lewis, et al. Toward expert-level medical question answering with large language models. *Nature Medicine*, 31(3):943–950, 2025.
3. Paul Hager, Friederike Jungmann, Robbie Holland, Kunal Bhagat, Inga Hubrecht, Manuel Knauer, Jakob Vielhauer, Marcus Makowski, Rickmer Braren, Georgios Kaissis, et al. Evaluation and mitigation of the limitations of large language models in clinical decision-making. *Nature medicine*, 30(9):2613–2622, 2024.
4. U.S. Food and Drug Administration and Health Canada and MHRA. Transparency for machine learning-enabled medical devices: Guiding principles. `https://www.fda.gov/medical-devices/software-medical-device-samd/transparency-machine-learning-enabled-medical-devices-guiding-principles`, June 13 2024. Joint publication by FDA, Health Canada MHRA promoting transparency principles for ML medical devices.
5. Scott M Lundberg and Su-In Lee. A unified approach to interpreting model predictions. *Advances in neural information processing systems*, 30, 2017.
6. Marco Tulio Ribeiro, Sameer Singh, and Carlos Guestrin. " why should i trust you?" explaining the predictions of any classifier. In *Proceedings of the 22nd ACM SIGKDD international conference on knowledge discovery and data mining*, pages 1135–1144, 2016.
7. Tom Heskes, Evi Sijben, Ioan Gabriel Bucur, and Tom Claassen. Causal shapley values: Exploiting causal knowledge to explain individual predictions of complex models. *Advances in neural information processing systems*, 33:4778–4789, 2020.
8. Xinyi Hou, Yanjie Zhao, Yue Liu, Zhou Yang, Kailong Wang, Li Li, Xiapu Luo, David Lo, John Grundy, and Haoyu Wang. Large language models for software engineering: A systematic literature review. *ACM Transactions on Software Engineering and Methodology*, 33(8):1–79, 2024.
9. Lauren E Dang, Susan Gruber, Hana Lee, Issa J Dahabreh, Elizabeth A Stuart, Brian D Williamson, Richard Wyss, Iván Díaz, Debashis Ghosh, Emre Kıcıman, et al. A causal roadmap for generating high-quality real-world evidence. *Journal of Clinical and Translational Science*, 7(1):e212, 2023.
10. Miguel A Hernán and James M Robins. Using big data to emulate a target trial when a randomized trial is not available. *American journal of epidemiology*, 183(8):758–764, 2016.
11. Judea Pearl. Causal inference without counterfactuals: Comment. *Journal of the American Statistical Association*, 95(450):428–431, 2000.
12. Judea Pearl and Thomas Verma. The logic of representing dependencies by directed graphs. In *Proceedings of the sixth National conference on Artificial intelligence-Volume 1*, pages 374–379, 1987.
13. MA Hernán and J Robins. Causal inference: What if. boca raton: Chapman & hill/crc.(2020). *Publisher's Note Springer Nature remains neutral with regard to jurisdictional claims in published maps and institutional affiliations*, 2020.
14. U.S. Food and Drug Administration. Real-world evidence: Considerations regarding non-interventional studies for drug and biological products. Draft guidance for industry, U.S. Food and Drug Administration, March 2024. Guidance document, draft issued Mar.2024; docket no. FDA-2023-D-5470.
15. Suhana Bedi, Yutong Liu, Lucy Orr-Ewing, Dev Dash, Sanmi Koyejo, Alison Callahan, Jason A

Fries, Michael Wornow, Akshay Swaminathan, Lisa Soleymani Lehmann, et al. Testing and evaluation of health care applications of large language models: a systematic review. *Jama*, 2025.
16. Ali Soroush, Benjamin S Glicksberg, Eyal Zimlichman, Yiftach Barash, Robert Freeman, Alexander W Charney, Girish N Nadkarni, and Eyal Klang. Large language models are poor medical coders—benchmarking of medical code querying. *NEJM AI*, 1(5):AIdbp2300040, 2024.
17. Maxime Griot, Coralie Hemptinne, Jean Vanderdonckt, and Demet Yuksel. Large language models lack essential metacognition for reliable medical reasoning. *Nature communications*, 16(1):642, 2025.
18. Jeevan Tewari, Benjamin W. Dahl, and Jeffrey J. Saucerman. Benchmarking of signaling networks generated by large language models. *bioRxiv*, 2025.
19. Nelson F. Liu, Kevin Lin, John Hewitt, Ashwin Paranjape, Michele Bevilacqua, Fabio Petroni, and Percy Liang. Lost in the middle: How language models use long contexts, 2023.
20. RECOVERY Collaborative Group. Dexamethasone in hospitalized patients with covid-19. *New England journal of medicine*, 384(8):693–704, 2021.
21. Sanchita Bhattacharya, Patrick Dunn, Cristel G Thomas, Barry Smith, Henry Schaefer, Jieming Chen, Zicheng Hu, Kelly A Zalocusky, Ravi D Shankar, Shai S Shen-Orr, et al. Immport, toward repurposing of open access immunological assay data for translational and clinical research. *Scientific data*, 5(1):1–9, 2018.
22. Diane Marie Del Valle, Seunghee Kim-Schulze, Hsin-Hui Huang, Noam D Beckmann, Sharon Nirenberg, Bo Wang, Yonit Lavin, Talia H Swartz, Deepu Madduri, Aryeh Stock, et al. An inflammatory cytokine signature predicts covid-19 severity and survival. *Nature medicine*, 26(10):1636–1643, 2020.
23. Miguel A Hernán, Brian C Sauer, Sonia Hernández-Díaz, Robert Platt, and Ian Shrier. Specifying a target trial prevents immortal time bias and other self-inflicted injuries in observational analyses. *Journal of clinical epidemiology*, 79:70–75, 2016.
24. Miguel A Hernán, Jonathan AC Sterne, Julian PT Higgins, Ian Shrier, and Sonia Hernández-Díaz. A structural description of biases that generate immortal time. *Epidemiology*, 36(1):107–114, 2025.

Leveraging Large Language Models to Derive Multiple Sclerosis Progression Assessments from Clinical Notes: A Feasibility Study

Sy Hwang[1†], Sunil Thomas[1], Heather Williams[1], Tom Hutchinson[1], Emily Schriver[1], Ashley Batugo[1], Amit Bar-Or[2], Vishakha Sharma[4], Frederik Buijs[3], Christopher Perrone[2], and Danielle Mowery[1]

[1]*Institute for Biomedical Informatics, Perelman School of Medicine University of Pennsylvania, Philadelphia, PA USA*

[2]*Department of Neurology, Perelman School of Medicine, University of Pennsylvania, Philadelphia, PA USA*

[3]*F. Hoffmann-La Roche, Basel, Switzerland*
[4]*Roche Diagnostics, Santa Clara, CA USA*

[†]*Corresponding author e-mail: sy.hwang@pennmedicine.upenn.edu*

Ascertainment of multiple sclerosis (MS) progression is important for informing clinical care decisions and supporting biomedical research. However, the details to infer a patient's MS progression status are locked within clinical notes. In this feasibility study, we assessed the feasibility of developing and validating a large language model (LLM)-based EDSS and FS classifier for ascertaining MS progression from clinical notes.

Keywords: Multiple Sclerosis; Large Language Models; Natural Language Processing.

1. Introduction

Multiple sclerosis (MS), a chronic inflammatory disorder of the brain and spinal cord, is estimated to affect 2.9 million people worldwide and 1 million people in the United States.[1] The condition is characterized by acute episodes of symptoms from which a patient often recovers well, referred to as relapses, and gradual accrual of disability over time, referred to as progression of disability. The presence of these features has formed the basis for the commonly used clinical course descriptors which refer to an individual's clinical phenotype. For instance, patients typically experience relapses early in their clinical referred to as relapsing-remitting multiple sclerosis (RRMS), many of them later manifest with gradual progression of disability that has been referred to as secondary progressive multiple sclerosis (SPMS). Others do not have evident relapses and develop gradual progression of disability from clinical onset, a phenotype referred to as primary progressive multiple sclerosis (PPMS).

While relapses are relatively easy to identify along a patient's disease course due to typically more rapid change in symptoms, MS progression can be more difficult to discern because accrual of disability develops more slowly in subtle ways, often taking many months

© 2025 The Authors. Open Access chapter published by World Scientific Publishing Company and distributed under the terms of the Creative Commons Attribution Non-Commercial (CC BY-NC) 4.0 License.

or years to appreciate. Yet, it is critical to better identify progression as treatment approaches are evolving and can be different. The Expanded Disability Status Scale (EDSS), developed by John Kurtzke in 1983, is a validated clinical assessment tool for measuring disability and its progression in MS.[2] It assigns scores for the degree of neurologic impairment across eight domains called functional systems (FS). These systems include functions in the `visual`, `brainstem`, `pyramidal (strength)`, `cerebellar (coordination)`, `sensory`, `bowel and bladder`, `cerebral (cognitive)`, and `ambulatory (walking)` domains. Each FS contributes to a calculation of overall EDSS score, which ranges from 0 (normal) to 10 (death) with intervals of 0.5. The EDSS is used as a standard outcome measure for clinical trials, and a change of +1.0 for EDSS scores between 0 and 5.5 or a change of +0.5 for EDSS scores between 6 and 10 is deemed evidence of 'clinically significant' progression. The time needed to determine each FS score and the overall EDSS score can pose a challenge for measurement in routine care. There are heuristics that can be used to more easily derive certain EDSS scores (such as the use of a cane resulting in an EDSS of 6.0), but this approach is limited.

Scores can also be retrospectively derived based on the narrative and description of the neurological exam in clinic notes. Natural language processing (NLP) may aid automatic computation of FS and EDSS scores to support both routine clinical care as well as clinical research studies of treatment efficacy. Several studies have explored automated recovery of EDSS from routinely collected data with NLP. Yang et al. compared rule-based, convolutional neural network (CNN), and a combined rule-based+CNN model and found the combined approach performed best for total EDSS (accuracy = 0.90; F1 = 0.83), while FS subscore performance was lower, especially when subscores were not explicitly documented in notes.[3] Alves et al. validated an XGBoost-based estimator on neurologist notes, reporting PPV 0.85 and NPV 0.85[4] . D'Costa et al. introduced MS-BERT and an MS severity classifier, showing transformer-based embeddings substantially improved EDSS macro-F1 of 0.88 and offered gains across subscores vs. Word2Vec and rule-based baselines, yet FS extraction remained the harder task.[5] Beyond note-level NLP, Davis et al. demonstrated early feasibility of rule-driven EDSS extraction from EHR text at scale, motivating subsequent learning-based approaches.[6] Muros-Le Rouzic et al. derived a claims-based proxy for EDSS and validated it against chart EDSS.[7] While granular classification was weak, broader severity groupings, particularly EDSS $\geq$ 6.0, showed much better agreement, underscoring that text-rich notes remain the more precise substrate for fine-grained EDSS. We hypothesize that large language models might improve upon performance for FS in clinical notes because of their ability to reason over heterogeneous phrasing and cross-sentence context, integrating implicit cues with section-aware constraints to map narrative evidence to FS constructs even when explicit subscores are absent.

In the long-term, our objective is to develop a robust and highly accurate, multimodal AI algorithm for determining MS progression of disability over time. For this short-term pilot study, our objective is two-fold: (1) determine the feasibility of automatically deriving MS disability progression from clinical notes leveraging large language models (LLMs) and (2) evaluate how precisely EDSS progression scores can be derived from clinical notes.

2. Methods

This retrospective, feasibility study was approved by the University of Pennsylvania Institutional Review Board.

2.1. *Cohort*

We identified patients with MS from the Penn Neuroimmunology Registry with a diagnosis of MS by a neurologist according to McDonald criteria (revised) treated between calendar years 2024-2025 (n=239 patients with 288 progress notes). The mean number of notes per unique patient encounter was 1.2 ± 0.41.

2.2. *Multiple Sclerosis Progression*

We developed LLM-based classifiers for extracting and encoding two MS-related progression indicators: the standardized and quantified neurological examination and assessment of Kurtzke's `Functional Systems (FS)` and `Expanded Disability Status Scale (EDSS)` from the clinical notes. The complete definitions and logic for computing the EDSS score can be found in Kappos et al.[8] Below, we offer the following more detailed, descriptive summary for FS and EDSS scoring:

(1) **Functional Status (FS)** include subscores based on 8 neurological functions that determine a patient's ability to perform daily activities - basic and complex - necessary for independent living.[9]

   (a) `Visual Functions` include assessments of visual acuity, visual fields, scotoma, and disc pallor with functional system scores ranging from 0=normal to 6=grade 5 plus maximal visual acuity of better eye of 20/60 (0.33) or less,
   (b) `Brainstem Functions` include assessments of extraocular movement impairment, nystagmus, trigeminal damage, facial weakness, hearing loss, dysarthria, dysphagia, and other cranial nerve functions with function system scores ranging from 0=normal to 5=inability to swallow or speak,
   (c) `Pyramidal Functions` include assessments of reflexes, limb strength, functional tests, limb spasticity, gait spasticity, overall motor performance with function system scores ranging from 0=normal to 6=tetraplegia defined as British Medical Research Council (BMRC) grade 0 or 1 in all muscle groups of the upper and lower limbs,
   (d) `Cerebellar Functions` include assessments of head tremor, truncal ataxia, limb ataxia, tandem walking, gait ataxia, Romberg test, other cerebellar tests with function system scores ranging from 0=normal to X=pyramidal weakness BMRC grade 3 or worse in limb strength) or sensory deficits interfere with cerebellar testing,
   (e) `Sensory Functions` include assessments of superficial sensation, vibration sense, position sense, Lhermitte's sign, and paraesthesiae with function system scores ranging from 0=normal to 6=sensation essentially lost below the head,
   (f) `Bowel and Bladder Functions` include assessments of urinary hesitancy and retention, urinary urgency and incontinence, bladder catheterization, bowel dysfunction,

and sexual dysfunction with function system scores ranging from 0=normal to 6=loss of bowel and bladder function,

(g) `Cerebral Functions` include assessments of depression and euphoria, decrease in mentation, and fatigue with function system scores ranging from 0=normal to 5=dementia,

(h) `Ambulation Functions` include assessments of distance and time reported by patient and use of devices with function system scores ranging from 0=unrestricted to 12=essentially restricted to bed or chair or perambulated in wheelchair, but out of bed most of day; retains many self-care functions; generally has effective use of arms (EDSS 8.0).

(2) **Expanded Disability Status Scale (EDSS)** is a standardized assessment tool for determining the degree of disability in patients with MS that is calculated based on the individual FS subscores. The EDSS scores range from 0=normal neurological exam (all FS grade 0) to 10=death due to MS.[9] Because the ambulatory is the largest scaled FS score, it tends to have drive the overall EDSS score. Therefore, the ambulation score can be directly mapped to the EDSS score in a few limited cases illustrated below.

- 0=unrestricted
- 1 = fully ambulatory
- 2 = Walks $\geq$ 300 m, but $<$ 500 m unassisted; mild gait impairment (EDSS 4.5 or 5.0)
- 3 = Walks $\geq$ 200 m, but $<$ 300 m unassisted; noticeable limitation (EDSS 5.0)
- 4 = Walks $\geq$ 100 m, but $<$ 200 m unassisted; may require minimal aid (EDSS 5.5)
- 5 = walking range $< 100m$ w/o assist (EDSS 6.0)
- 6= unilateral assist, $\geq$ 50 m (EDSS 6.0)
- 7= bilateral assist, $\geq$ 120 m (EDSS 6.0)
- 8= unilateral assist, $<$ 50 m (EDSS 6.5)
- 9= bilateral assist, $\geq$ 5 m, but $<$ 120 m (EDSS 6.5)
- 10 = wheelchair w/o help (EDSS 7.0)
- 11 = wheelchair w help (EDSS 7.5)
- 12 = bed or chair bound (EDSS 8.0)

2.3. *Prompts*

We used OpenAI's GPT-4.1 model, which we have historically demonstrated its ability to complete information extraction and patient phenotyping tasks using clinical notes.[10] To reduce the model's stochasticity and improve reproducibility, we set parameters of temperature at 0.1 and top_p at 1. For this feasibility study, we opted to use zero-shot learning after several rounds of curating and making iterative changes to the prompts. We created `system_prompts` and `task_prompts` for executing FS and EDSS processing and classification steps.

```
system_prompt = As a neurologist at a health system, you have been tasked
with reviewing clinical notes for evidence of progression of multiple
sclerosis, an autoimmune disease of the brain and spinal cord. You will be
scoring functional system subscores for patients. For each measure,
analyze the narrative and determine if the type is explicitly and
undeniably present or absent. The clinical note you are assessing can be
lengthy, so focus only on the relevant parts for the task
```

2.3.1. *FS prompt and processing task*

For each functional system, the LLM was instructed carefully review the clinical note and provided more detailed logic to assign a score based on information documented within the narrative. Below, we provide truncated examples for each FS subscore.

FS_task_prompt = For each functional system, carefully review the clinical note and assign a score based on the following criteria:

(1) VISUAL SUBSCORE:

- Score 0: if none of the below are true ...
- Score 5: if there is mention of no light perception (NLP) ...

(2) BRAINSTEM SUBSCORE:

- Score 0: Cranial nerves described as normal or no abnormalities mentioned ...
- Score 5: Unable to speak or swallow, requires enteral nutrition or PEG tube ...

(3) PYRAMIDAL SUBSCORE:

- Score 0: if none of the below are true ...
- Score 6: if there is mention of tetraplegia, all limbs with a grade of 0 or 1 ...

(4) CEREBELLAR SUBSCORE:

- Score 0: if the cerebellar exam is normal or none of the below are true ...
- Score 4: if severe truncal AND limb ataxia is present ...

(5) SENSORY SUBSCORE:

- Score 0: if the sensory exam is described as normal or none of the below are true ...
- Score 6: 6 if complete loss of all sensation in 3-4 limbs (neck down) ...

(6) BOWEL/BLADDER SUBSCORE:

- Score 0: if none of the below are true ...
- Score 6: if complete loss of bladder and bowel control ...

(7) AMBULATION SUBSCORE:

- Score 0: if gait exam is normal or none of the below are true ...
- Score 12: if uses a motorized chair ...

(8) CEREBRAL SUBSCORE:

- Score 0: if none of the below are true, exclude mood related symptoms and also score 0 if there is improvement in a cognitive symptom ...
- Score 5: if there is mention of dementia ...

2.3.2. *EDSS prompt and processing*

For the EDSS task, the LLM was instructed to ascertain the EDSS score from the FS scores using the `EDSS_task_prompt` and provided more detailed post-processing steps that incorporated instructions from Kappos et al.[8]

```
EDSS_task_prompt = You are an expert neurologist specializing in multiple
sclerosis (MS), a chronic autoimmune disease affecting the central nervous
system. One of your key responsibilities is accurately determining a
patient's level of disability using the Expanded Disability Status Scale
(EDSS). The EDSS is the gold standard measure of disability in MS, ranging
from 0 (normal neurological examination) to 10 (death due to MS). This
scale integrates impairments across multiple functional systems into a
single score that reflects overall disability. Your expertise is required
to translate a patient's functional system subscores into an accurate EDSS
rating. These subscores come from a comprehensive neurological examination
and measure impairment in eight key domains: ambulation (walking ability),
vision, brainstem function, pyramidal function (motor strength),
cerebellar function (coordination), sensory function, bowel/bladder control,
and cerebral/mental function. Your goal is to apply the established EDSS
calculation rules consistently and accurately.
```

Using the output from the eight predicted functional system (FS) subscores, an LLM was instructed to deterministically derive an EDSS score (0.0–9.0). Two additional rules must be applied to correctly ascertain clinically-valid EDSS scores. For visual and bowel/bladder FS, scores are adjusted so that these symptoms do not disproportionately contribute to the EDSS score. Use of an assistive device suggests a significant degree of disability and therefore some ambulatory FS scores determine a specific EDSS score regardless of other FS values. The LLM outputs were used to compute the EDSS score using the following steps in order:

(1) Pre-convert `visual` and `bowel/bladder` FS scores to a lower scale
(2) Convert `ambulatory` FS scores directly to EDSS values when possible.

The model was prompted to (i) articulate a concise chain of thought for each of the eight functional-system domains, (ii) assign the corresponding ordinal score, and (iii) return the predictions in a simple, consistently formatted JSON object. Requiring the model to "reason first, a nswer s econd" e nabled i nspection o f i ts i ntermediate r ationale a nd h as b een shown to improve zero-shot classification p erformance i n c linical l anguage t asks.[11,12] H andling one domain at a time limited cross-domain interference and keeps the prompt length manageable for long progress notes. A rigid output schema ensured that the predictions are machine-readable without post-processing, which simplified i ntegration w ith t he e valuation pipeline and downstream analytic workflows.

2.4. *FS Classifier Performance*

We assessed the performance of the FS classifier u sing a ccuracy a s w ell a s p recision, recall, and both weighted and macro F1.

2.5. *EDSS Classifier Performance*

We understand that there is imprecision in classifying EDSS scores from FS scores due to lack of specificity in the measurement and incorrect inference among other reasons. However, not all misclassifications are alike. For example, the documentation of the `ambulatory` FS score may not include distance walked to precisely classify lower scores. Therefore, we devised several lenient match criteria for capturing and assessing performance based on ordinal closeness (adjusts for small numeric differences in documented precision such as off by n) and semantic relatedness (adjusts for similarities in clinical definitions such as use of assistive device).

(1) Exact match: both expert and LLM values match exactly
(2) Lenient match by 1: the LLM value is within 1 point of the expert value
(3) Lenient match by 2: the LLM value is within 2 points of the expert value
(4) Lenient match by category: the LLM value is an exact or falls within a range of values associated with need for assistance. These ranges were as follows: *no assist* ranges from $0 \leq 5.5$, *unilateral assist* is 6, *bilateral assist* is 6.5, and *wheelchair* ranges from $7 \leq 8.5$.

We computed the following agreement and error metrics:

(1) Quadratic Kappa (κ): quantifies agreement by penalizing errors based on order and distance between the true and predicted scores; penalizes larger disagreements more heavily.
(2) Mean Average Error (MAE): measures the average absolute distance between true and predicted scores; interprets error rate by treating all errors linearly.
(3) Root Mean Square Error (RMSE): measures the square root of the mean squared differences between the true and predicted scores; penalizes larger errors more heavily than MAE, making it useful for class imbalance and comparing costly errors and outliers.

3. Results

We developed LLM-based classifiers for extracting and inferring FS and EDSS scores from clinical notes. We report classification performance.

3.1. *FS Classifier Performance*

In **Table 1**, we observed high overall accuracy and weighted recall across FS subtypes ranging from 0.787 (`cerebral`) to 0.971 (`visual`). Weighted F1-scores ranged from moderate at 0.784 (`ambulation`) to high at 0.970 (`visual`); in contrast, macro F1-scores ranged from low at 0.295 (`ambulation`) to moderate at 0.724 (`visual`). The majority class for each FS subscore is 0.

In **Figure 1**, we show the distribution of FS subscores by the generated by the expert and LLM. We observe similar trends within subscore values, e.g., both predict similar prevalence across subscores and the LLM under predicts the majority class of 0 and overpredicts value 1.

In **Figure 2**, we assessed the difference between true, expert-generated FS score values and predicted, LLM-generated FS score values. We observe concordant median score values of 0 for all functional system scores and most exactly match across FS types. Most of the predicted LLM values are off by no more than 2 points from the true value.

Table 1: Performance metrics for FS subtype classification

FS subtype	Accuracy	Precision	Recall	F1-score	Precision	Recall	F1-score
			Weighted			Macro	
`Ambulation`	0.799	0.776	0.799	0.784	0.275	0.362	0.295
`Bowel/Bladder`	0.782	0.876	0.782	0.803	0.476	0.447	0.413
`Brainstem`	0.900	0.930	0.900	0.911	0.495	0.561	0.511
`Cerebellar`	0.879	0.892	0.879	0.878	0.691	0.619	0.631
`Cerebral`	0.787	0.849	0.787	0.801	0.640	0.664	0.641
`Visual`	0.971	0.970	0.971	0.970	0.708	0.744	0.724
`Pyramidal`	0.812	0.815	0.812	0.806	0.456	0.436	0.440
`Sensory`	0.895	0.901	0.895	0.892	0.660	0.638	0.642

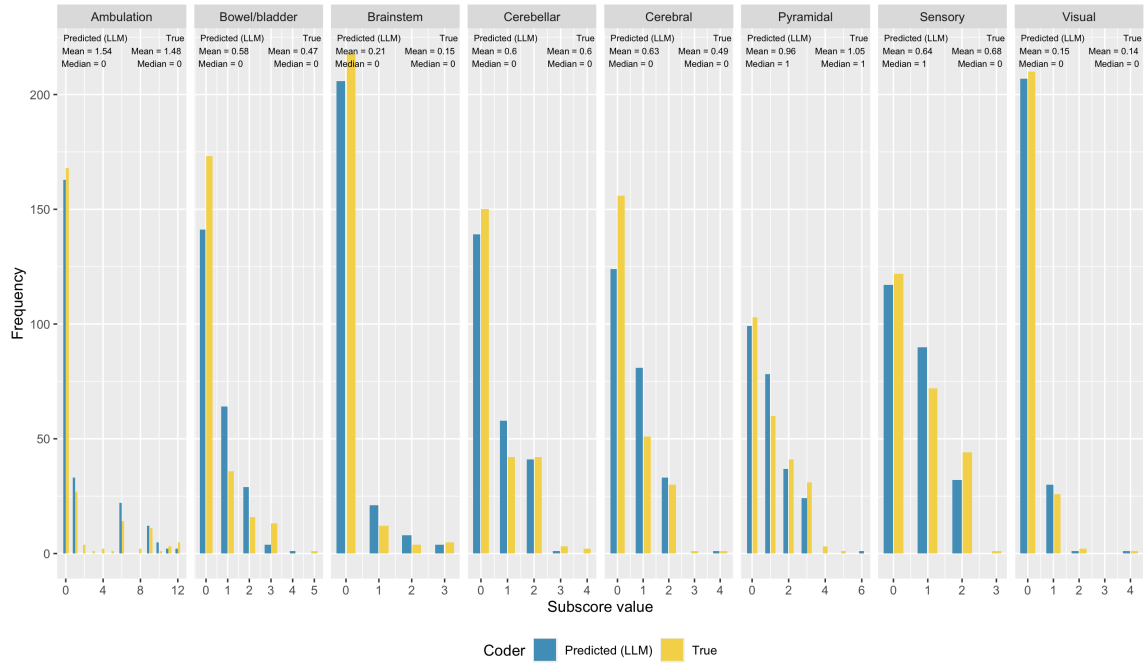

Fig. 1: Distribution of true and predicted FS scores

3.2. *EDSS Classifier Performance*

In **Figure 3**, we performed a sensitivity analysis using exact and lenient match criteria for computing expert-LLM agreement. For exact IAA, EDSS performance ranged from low (score 2.5 at 0.33) to high (score 7 at 1.0). 1 of 16 EDSS subscores achieved 100% agreement. For lenient by 1 IAA, 10 of 16 (62.5%) EDSS subscores achieved 100% agreement; for lenient by 2 IAA, 12 of 16 (75%) EDSS subscores achieved 100% agreement. Match by category produced a high overall of 0.974 and moderate to high IAA: no assist of 0.980, unilateral assist of 0.667, bilateral assist of 0.846, and wheelchair of 1.00.

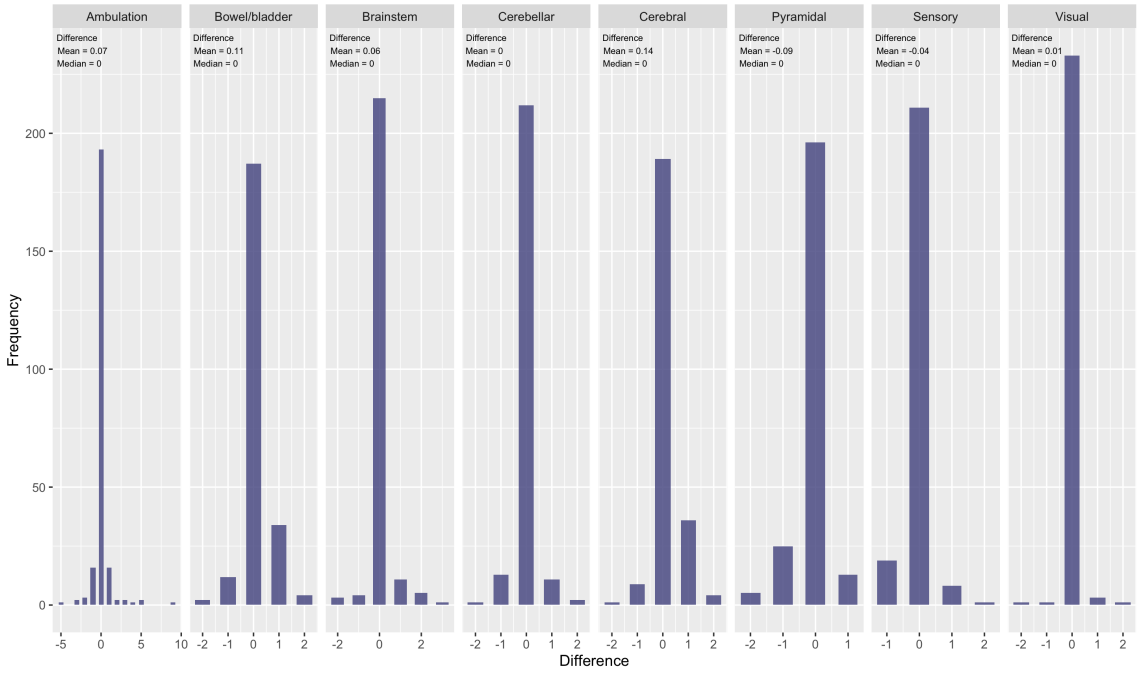

Fig. 2: Differences between true and predicted FS scores

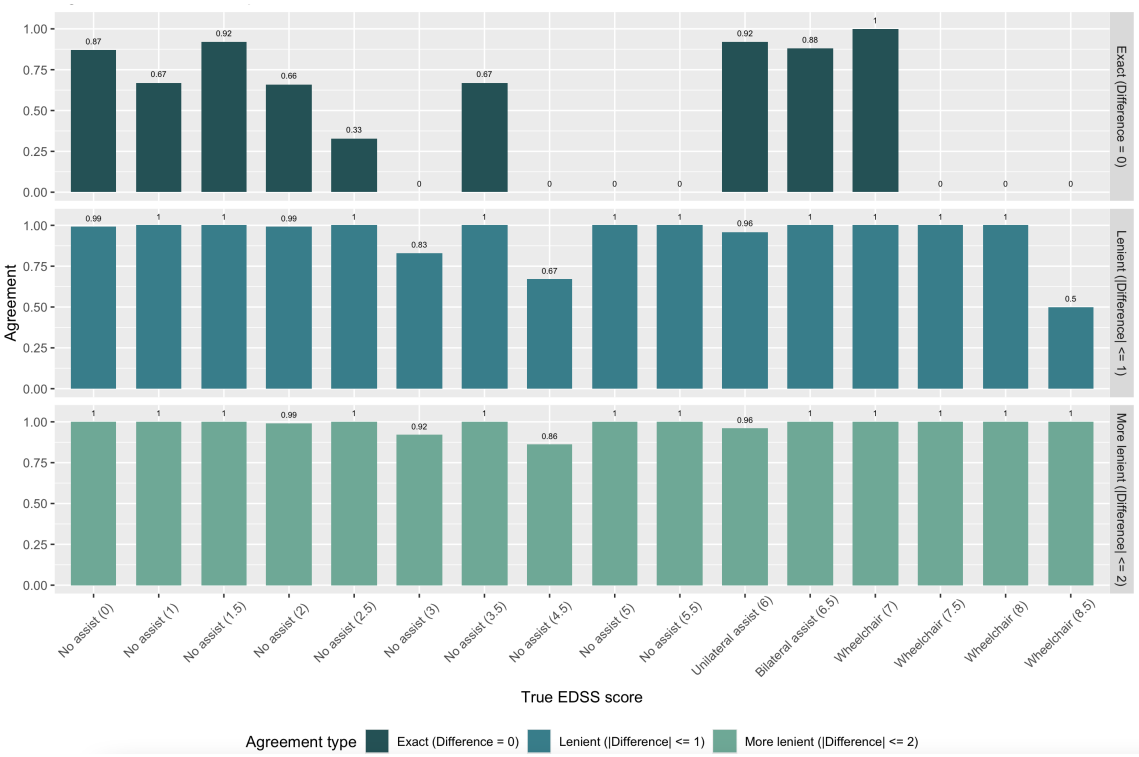

Fig. 3: Agreement between true and predicted EDSS scores varied by match criteria

In **Figures 4 and 5 - Appendix**, we report the confusion matrices with κ, MAE, and RMSE for FS and EDSS scores. κ ranged from moderate (`brainstem` at 0.621) to high

(ambulation at 0.942) for subscores and was high for EDSS at 0.942. MAE ranged from 0.13 for bowel/bladder to 0.34 for ambulation subscores and was 0.34 for EDSS. RMSE ranged from 0.39 for bowel/bladder to 1.04 for ambulation for subscores and was 0.70 for EDSS.

4. Discussion

We conducted a feasibility study leveraging LLMs to encode FS and EDSS scores from clinical notes and an expert-LLM sensitivity analysis to understand imprecise classification of EDSS.

4.1. *FS Classifier Performance*

The language model correctly assigned FS scores in most domains. Five of eight domains exceeded exact accuracy of 0.90. The lower macro-average numbers reflected the class imbalance and the difficulty of long-tailed labels. Visual, sensory, and cerebellar domains achieved macro-F1 above 0.70, whereas ambulation and pyramidal lagged below 0.40. Performance differences follow clinical documentation patterns. Visual loss and cerebellar disorders are usually described with distinct terms such as "optic neuritis" which the model captures reliably. Ambulation scoring depends on walking distance and aid usage, information often omitted or expressed qualitatively. Pyramidal signs occupy a similar gray zone; progress notes may list upper motor neuron findings without quantifying weakness, making precise ordinal mapping challenging.

4.2. *EDSS Classifier Performance*

We observed that most EDSS misclassifications could be captured with more lenient match criteria. Error analysis shows that most residual errors arise at the scale's extremes. In the very mild range (EDSS 0.5–2.5) the model tends to underestimate severity by one half-point, likely because phrases such as "walks independently but tires easily" are interpreted as normal ambulation, demonstrating that underspecified and small variations in ambulation phrasing can lead to whole-point shifts. In the wheelchair-bound range (EDSS $\geq$ 7.0) we observe a few adjacent misclassifications between 7.0, 7.5, and 8.0, but all predictions remain within the acceptable tolerance band.

Because EDSS is an ordinal measure, the clinical impact of a prediction error depends on its magnitude. Misreading a note scored by clinicians as EDSS 6.5, where the patient needs bilateral support to walk, as 2.0, which is indicated only minimal disability, could delay escalation of therapy or understate safety concerns. By contrast, confusing 4.0 with 5.0 seldom changes management. Cognitive error, rather than lack of knowledge, underlies many medical mistakes, and evaluation metrics that ignore the distance between ordinal classes can hide systems that make infrequent yet clinically significant large-magnitude errors. This concern is particularly relevant in the context of bridging AI with human expertise, where misjudgment of disability trends directly distorts decisions about disease progression and treatment response.

4.3. *Related Works*

In comparison to Yang et al.'s highest performing classifiers for FS subscores, our LLM-based solution produced higher F1-scores for `cerebellar`, `cerebral`, `visual`, and `sensory`. However, the LLM-based EDSS classifier performance did not outperform the rules/CNN-based classifier. We hypothesize that poor EDSS classification is partially driven by FS classification as well as insufficient ambulatory score details, e.g., how far a patient can walk in feet documented in the clinical notes.

4.4. *Limitations and Future Work*

This work presents a feasibility evaluation situated alongside prior efforts (Yang et al.), with the primary objective of establishing a clear empirical reference point for automated EDSS and FS extraction from routine notes. Several limitations merit emphasis. Our cohort is modest and drawn from a single institution, which raises the risk of overfitting, particularly given iterative prompt refinement, and limits generalizability. We will mitigate this by expanding the dataset across additional neurologists, encounter types, and less prevalent MS phenotypes; freezing explicit train/dev/test splits with documented seeds and access controls; and employing automated prompt optimization that searches over instruction variants and exemplars to reduce ad-hoc tuning and quantify sensitivity to prompt choices. Labeling in the present study relied in part on a single annotator, which constrains ceiling performance and injects unavoidable uncertainty; the next phase includes multi-rater annotation with adjudication on a stratified subset and reporting of inter-rater agreement.

Methodologically, our zero-shot framing focuses on clinical utility and transparency but remains incremental. Two directions are in progress to strengthen novelty and fit to the task. First, we are conducting targeted error analyses and ablation studies to isolate failure modes and their impact on EDSS and FS outputs. Second, we are exploring a presence-only or maximum-entropy formulation in which the LLM serves as a high recall evidence extractor and a constrained probabilistic layer estimates FS abnormalities and ambulation anchors without treating "no mention" as negative. An ordinal mapping with clinical consistency constraints could then yield EDSS scores. This hybrid approach with LLMs has the potential to improve calibration, reduce silent false negatives, and better respect the ordinal structure of disability scores.

Finally, because EDSS is computed from multiple functional subsystems, errors in any single domain can propagate to the composite score. To curb this, future iterations will incorporate complementary modalities to cross-validate narrative inferences, designate exact-match EDSS as the primary endpoint with tolerance-band results reported as secondary analyses, and extend analyses beyond point estimates to longitudinal trajectories, enabling detection of clinically meaningful changes over time. We emphasize that tolerance bands are not a substitute for exact agreement. They are reported to reflect the known resolution of EDSS assignment in routine practice and to distinguish near-misses from clinically divergent errors. In our error analysis, most disagreements were adjacent and preserved the underlying category, suggesting limited clinical impact. With a larger, more diverse corpus, multi-site validation, multi-rater labels, and principled prompt/model tuning, we aim to deliver a more robust, generalizable

system suitable for prospective evaluation while preserving the practicality and transparency that motivated this feasibility stage.

5. Conclusion

Automating EDSS and FS extraction can lessen clinician documentation burden, unlock historical data for large-scale outcome studies, and provide up-to-date disability estimates to decision support tools. This pilot investigation confirms the technical feasibility of deriving detailed MS disability progression measures from routine neurology notes with a single prompt-based large language model. The model achieved strong FS performance, with accuracy spanning $0.782 – 0.971$ and weighted F1 ranging from 0.784 to 0.970 across the eight neurologic domains. Although overall EDSS exact match agreement was lower, applying clinically-meaningful tolerance bands raised categorical agreement to 0.974, indicating that most disagreements occur within ranges unlikely to alter therapeutic decision making.

6. Acknowledgments

This project was partially funded by a grant from F. Hoffmann-La Roche, Basel, Switzerland.

References

1. L. M. Nelson, M. T. Wallin, R. A. Marrie, W. Culpepper, A. Langer-Gould, J. Campbell, S. Buka, H. Tremlett, G. Cutter, W. Kaye *et al.*, A new way to estimate neurologic disease prevalence in the united states: illustrated with ms, *Neurology* **92**, 469 (2019).
2. J. F. Kurtzke, Rating neurologic impairment in multiple sclerosis: an expanded disability status scale (edss), *Neurology* **33**, 1444 (1983).
3. Z. Yang, C. Pou-Prom, A. Jones, M. Banning, D. Dai, M. Mamdani, J. Oh, T. Antoniou *et al.*, Assessment of natural language processing methods for ascertaining the expanded disability status scale score from the electronic health records of patients with multiple sclerosis: algorithm development and validation study, *JMIR Medical Informatics* **10**, p. e25157 (2022).
4. P. Alves, E. Green, M. Leavy, H. Friedler, G. Curhan, C. Marci and C. Boussios, Validation of a machine learning approach to estimate expanded disability status scale scores for multiple sclerosis, *Multiple sclerosis journal - experimental, translational and clinical* **8**, p. 20552173221108635 (06 2022).
5. A. D'Costa, S. Denkovski, M. Malyska, S. Y. Moon, B. Rufino, Z. Yang, T. Killian and M. Ghassemi, Multiple sclerosis severity classification from clinical text, 7 (November 2020).
6. M. Davis, S. Sriram, W. Bush, J. Denny and J. Haines, Automated extraction of clinical traits of multiple sclerosis in electronic medical records, *Journal of the American Medical Informatics Association : JAMIA* **20** (10 2013).
7. E. Rouzic, M. Ghiani, E. Zhuleku, A. Dillenseger, U. Maywald, T. Wilke, T. Ziemssen and L. Craveiro, Claims-based algorithm to estimate the expanded disability status scale for multiple sclerosis in a german health insurance fund: a validation study using patient medical records, *Frontiers in Neurology* **14** (12 2023).
8. L. Kappos, Neurostatus scoring. slightly modified from jf kurtzke, *Neurology* **1983**, 1444 (2011).
9. J. F. Kurtzke, Historical and clinical perspectives of the expanded disability status scale, *Neuroepidemiology* **31**, 1 (2008).
10. U. Vurcan, S. Hwang, S. Thomas, A. Batugo, A. Acevedo, A. Kaviyarasu, A. BS, O. Mitchell and D. Mowery, Reliability in ai-assisted critical care: Assessing large language model robustness

and instruction following for cardiac arrest identification., in *NeurIPS 2024, the Thirty-Eighth Annual Conference on Neural Information Processing Systems Workshop*, 2024.
11. J. Wei, X. Wang, D. Schuurmans, M. Bosma, B. Ichter, F. Xia, E. Chi, Q. Le and D. Zhou, Chain-of-thought prompting elicits reasoning in large language models (2023).
12. T. Kojima, S. S. Gu, M. Reid, Y. Matsuo and Y. Iwasawa, Large language models are zero-shot reasoners (2023).

7. Appendix

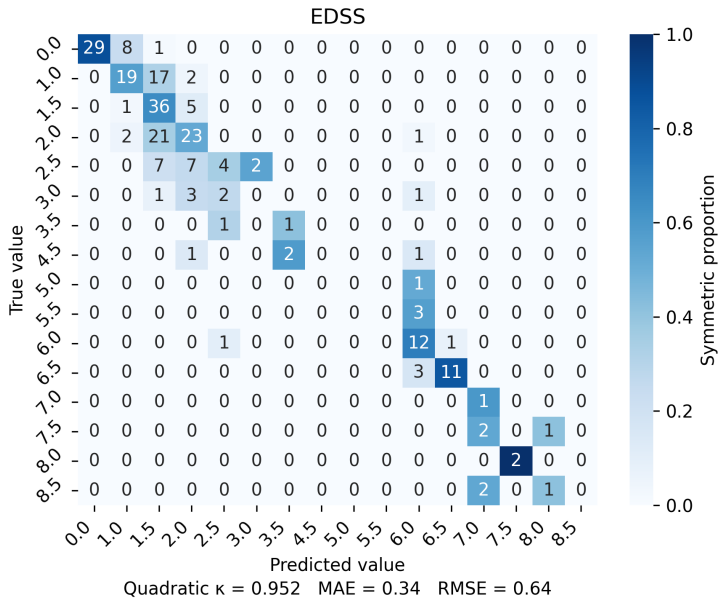

Fig. 4: EDSS confusion matrix

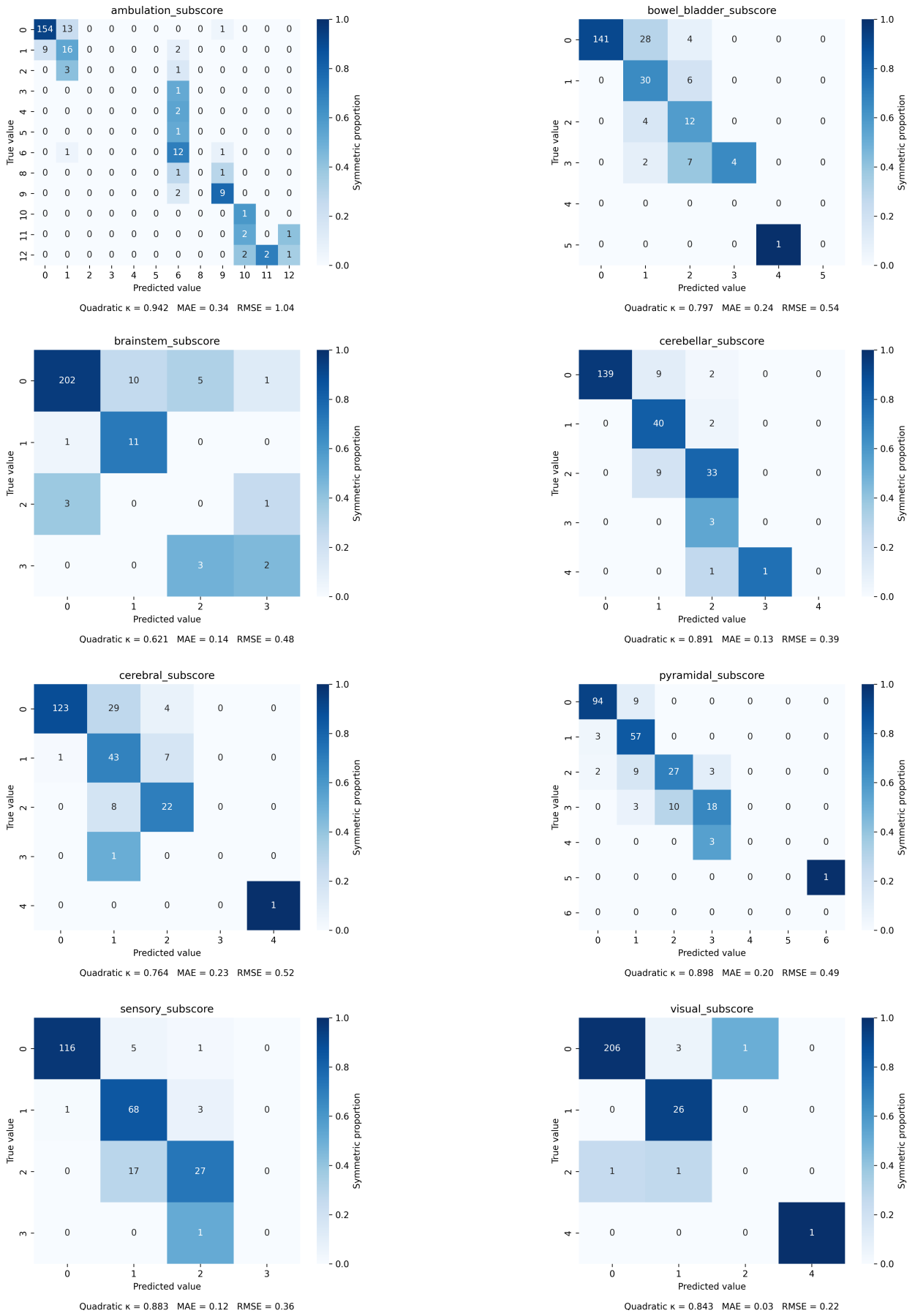

Fig. 5: Functional System (FS) confusion matrices for all subscore categories

WATCH-SS: Developing a Trustworthy and Explainable Modular Framework for Detecting Cognitive Impairment from Spontaneous Speech*

Sydney Pugh, PhD[1†], Matthew Hill[1], Sy Hwang, MS[1], Rachel Wu[1], Kuk Jang, PhD[4], Stacy Iannone, DHSc, MS[2], Karen O'Connor, MS[1], Kyra O'Brien, MD, MSHP[2], Eric Eaton, PhD[3], and Kevin Johnson, MD, MS[1,3]

[1] *Department of Biostatistics, Epidemiology, and Informatics, Perelman School of Medicine, University of Pennsylvania, Philadelphia, PA USA*

[2] *Department of Neurology, Perelman School of Medicine, University of Pennsylvania, Philadelphia, Pennsylvania, USA*

[3] *Department of Computer and Information Science, School of Engineering and Applied Science, University of Pennsylvania, Philadelphia, PA USA*

[4] *Department of Computer Engineering, Hongik University, Seoul, South Korea*

[†] *Corresponding Author E-mail: Sydney.Pugh@PennMedicine.upenn.edu*

Early detection of cognitive impairment (CI) is critical for timely intervention in Alzheimer's disease and AD-related dementias. To address this, we propose the Warning Assessment and Alerting Tool for Cognitive Health from Spontaneous Speech (WATCH-SS), a modular and explainable three-stage framework for detecting CI from a patient's speech sample. The framework uses detectors for five linguistic and acoustic indicators of CI, aggregates their outputs into a set of clinically interpretable summary features, and uses a predictive model for CI classification. We consider multiple approaches to implementing these detectors that range from simple, computationally efficient methods suitable for real-time analysis to strong, resource-intensive methods, better for high accuracy offline analysis. On the DementiaBank ADReSS dataset, WATCH-SS achieved strong predictive performance (AUC = 80% on the test set). This work demonstrates that a modular, feature-based approach can achieve strong performance while providing a transparent diagnostic profile, representing a significant step towards a trustworthy and clinically-usable screening tool for primary care.

Keywords: cognitive impairment, Alzheimer's disease, dementia, natural language processing, large language model, machine learning

*Research reported in this publication was supported by the National Institute On Aging of the National Institutes of Health under Award Number P30AG073105, and by the University of Pennsylvania ASSET Center under the Collaborative Research in Trustworthy AI for Medicine grant. The content is solely the responsibility of the authors and does not necessarily represent the official views of the National Institutes of Health.

© 2025 The Authors. Open Access chapter published by World Scientific Publishing Company and distributed under the terms of the Creative Commons Attribution Non-Commercial (CC BY-NC) 4.0 License.

1. Introduction

As the global population ages, Alzheimer's disease (AD) and AD-related dementias (ADRD) are becoming more prevalent.[1] Yet, more than 50% of persons with AD/ADRD are undiagnosed,[2] delaying crucial interventions that could improve quality of life. The first step in diagnosing AD/ADRD is detecting any degree of cognitive impairment (CI). Ideally, early detection should occur in primary care, where most patients first exhibit subtle signs of CI. Language production is highly sensitive to the neurodegenerative changes characteristic of AD/ADRD. Deficits in core cognitive domains—including semantic memory, executive function, and processing speed—manifest directly in a person's speech patterns.[3–5] Several of these signs manifest in conversations between patients and primary care providers (PCPs) during clinical visits—for example, when a patient repeats themselves several times during the visit or takes a long time to respond to the PCP's questions. However, PCPs often struggle to recognize these clues in real time due to competing priorities, time constraints, and limited expertise.[6]

Speech data can be collected easily and non-invasively, making it an ideal medium for developing accessible tools for early-stage screening of CI. Recent advances in machine learning and natural language processing (NLP) have enabled the development of automated systems for detecting possible CI from speech.[7–9] However, many state-of-the-art approaches rely on "black-box" deep learning models.[10–12] While these systems can achieve high predictive accuracy, their opaque nature makes it impossible to understand the clinical reasoning behind a prediction, hindering trust and adoption in medical settings.

To address this gap, we propose the Warning Assessment and Alerting Tool for Cognitive Health for Spontaneous Speech (WATCH-SS), a modular framework designed to be a trustworthy, interpretable, and extensible tool for detecting CI due to suspected AD/ADRD from a patient's speech sample. The framework leverages several detectors to identify indicators of CI within a speech sample and then aggregates the outputs into a clinically interpretable CI prediction. We demonstrate that our framework achieves strong predictive performance while providing a transparent diagnostic profile that explains the reasoning behind its predictions.

2. Related Work

Spontaneous speech, reliant on cognitive functions like attention and memory, is increasingly used as a non-invasive, cost-effective biomarker for detecting cognitive impairments. Clinically, speech is typically analyzed via structured speech tasks like the *Cookie Theft Picture Description* task from the Boston Diagnostic Aphasia Examination,[13] verbal fluency tasks such as the Semantic Fluency Task (SFT) and Phonemic Fluency Task (PFT),[14] and cognitive tests including the Mini-Mental State Examination (MMSE),[15] the Montreal Cognitive Assessment (MoCA),[16] and the Saint Louis University Mental Status (SLUMS) examination.[17] While these assessments have been rigorously validated, they typically require in-person administration and expert interpretation, making them time-consuming and costly, which can delay diagnosis and treatment of neurodegenerative conditions like AD/ADRD.

Advances in machine learning offer the potential to overcome these limitations by enabling low-cost, remote, and early detection of cognitive decline through speech. They have revealed subtle linguistic and acoustic markers, expanded clinically relevant feature extraction, and

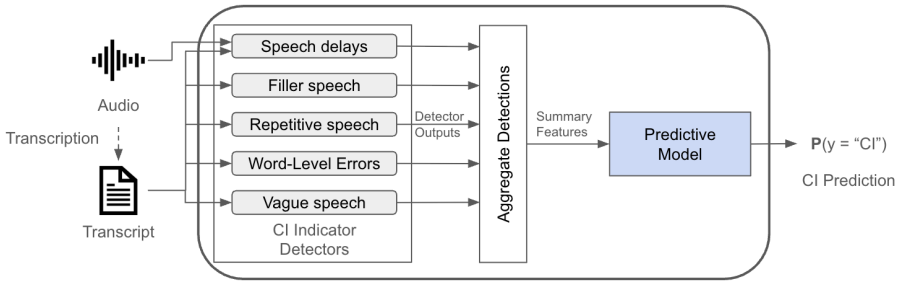

Fig. 1: The WATCH-SS framework is a three-stage pipeline that (1) detects cognitive impairment (CI) indicators from audio and transcripts, (2) aggregates these detections into summary features, and (3) applies a predictive model to the features to generate a final prediction.

enabled scalable, automated speech analysis.

To address these limitations, machine learning has been widely applied to automate the analysis of speech for detecting CI. Early works focused on training traditional models like Support Vector Machines (SVMs) on hand-crafted acoustic features (e.g., pause duration, speech rate)[18] and lexical features (e.g., topic modeling).[19] We refer the reader to Yang et al. [20] for an extensive survey of deep learning-based techniques. More recently, deep learning approaches using models like Convolutional Neural Networks (CNNs) and Long Short-Term Memory networks (LSTMs) have been used to learn patterns directly from audio.[21–23] Transfer learning with large pre-trained models such as BERT, GPT, and wav2vec has also become a common strategy for extracting powerful text and audio embeddings for training various ML learning classifiers.[21,24–26] These methods, often combined in multimodal or ensemble systems,[27,28] have demonstrated high predictive accuracy but low explainability.

While other approaches have also explored training classifiers on interpretable speech features,[8,13,29,30] they often use a mix of clinically interpretable and non-interpretable features. For example, these systems often incorporate acoustic features like GeMAPS or ComParE which are not easily parsed by clinicians. In contrast, WATCH-SS is designed to provide greater interpretability by focusing on high-level, clinician-interpretable features. This approach, coupled with external validation on spontaneous clinical speech, differentiates our work.

3. Methods

3.1. *WATCH-SS*

We propose WATCH-SS, a three-stage framework for detecting cognitive impairment from a patient's speech sample (see Figure 1). The key advantages of our framework are its interpretability and modularity. Unlike "black-box" models, WATCH-SS provides a transparent patient diagnostic profile that breaks down the final CI prediction into the contributions of various indicators of CI, enabling a clinician to understand which specific cognitive deficits are driving the classification. Moreover, the modular architecture of WATCH-SS allows for easy extension or replacement of individual detectors.

WATCH-SS receives as input an audio waveform and the corresponding diarized transcript of a speech sample. First, WATCH-SS runs multiple detectors in parallel to identify five

key indicators of CI: filler speech, repetitive speech, substitution errors, vague speech, and speech delays. In the second stage, the system aggregates the detections into a set of clinically interpretable summary features and feeds them to a model to predict CI in the third stage.

WATCH-SS was implemented in Python (version 3.12.3) using Microsoft Azure Databricks. The code is available at https://github.com/kbjohnson-penn/WATCH-SS.

The remainder of this section describes the data used to develop WATCH-SS (Section 3.2), the detectors for indicators of CI (Section 3.3), the summary features extracted from these detections (Section 3.4), and finally, the predictive model for CI (Section 3.5).

3.2. *Data*

We developed and validated WATCH-SS using two datasets: the ADReSS dataset for detector and predictive model development, and the OBSERVER dataset for external validation.

3.2.1. *DementiaBank ADReSS Challenge Dataset*

The ADReSS dataset[31,32] consists of audio recordings and diarized transcripts of subjects with and without an AD diagnosis describing the Cookie Theft picture from the Boston Diagnostic Aphasia Exam.[33] Transcripts were annotated using the CHAT coding system, a standardized protocol for transcribing conversational interactions and annotating its linguistic features.[34] The training data consists of 108 subjects, while the test data consists of 48 subjects. Each dataset is balanced in age and gender and half of their subjects have an AD diagnosis.

We further partitioned the training data into training and development (dev) datasets using a 70/30 percent split balanced for age, gender, and number of AD subjects. Specifically, we first generated 100 candidate splits stratified by gender and AD label using different random seeds. Then, we selected the split that minimized the absolute difference in mean age across the resulting training and development sets. Table 1 summarizes the resulting datasets.

Data Pre-processing. We processed the CHAT transcripts to produce clean inputs to our detectors by: (1) converting pause annotations to a "[silence]" token, (2) converting event annotations to "[< event >]" tokens, (3) converting inaudible annotations to "[inaudible]" tokens, and (4) removing all other CHAT annotations. Then, we derived ground-truth labels from the original CHAT annotations for all patient utterances. An utterance was labeled positive for a given indicator if it met the following criteria:

- **Filler speech:** The utterance contained any word marked with the filler prefix ("&").
- **Repetitive speech:** The utterance contained the repetition annotation ("[/]").
- **Substitution errors:** The utterance contained the word level error code ("[*]"), including all its subtypes (*e.g.,* "[* s]" for semantic paraphasias or "[* n]" for neologisms).
- **Vague speech:** The utterance contained the annotation for empty speech ("[+ es]") or circumlocution ("[+ cir]").
- **Speech delays:** The utterance contained a pause annotation ("(.)", "(..)", or "(...)").

The prevalence of these labels across the data splits is summarized in Table 2.

Table 1: Characteristics of the ADReSS train, development (dev), and test datasets.

		AD		Control	
Split	Num. Subjects	Pct. Female	Age (mean ± std)	Pct. Female	Age (mean ± std)
train	75	56%	66.5 ± 6.6	55%	66.6 ± 6.8
dev	33	52%	67.4 ± 6.7	56%	65.7 ± 6.0
test	48	54%	66.1 ± 7.4	54%	66.1 ± 7.1

Table 2: Prevalence of cognitive impairment (CI) indicators in the ADReSS train, development (dev), and test datasets. Values are the counts and proportions of positively-labeled utterances.

Split	Num. Utterances	Filler speech	Repetitive speech	Substitution errors	Vague speech	Speech delays
train	991	257 (18.4%)	88 (6.3%)	35 (2.5%)	12 (0.9%)	99 (7.1%)
dev	501	118 (16.6%)	44 (6.2%)	19 (2.7%)	3 (0.4%)	45 (6.3%)
test	590	153 (18.9%)	47 (5.8%)	25 (3.1%)	8 (1.0%)	98 (12.1%)

Table 3: Characteristics of the OBSERVER Repository dataset.

CI			CN		
Num. Visits	Pct. Female	Age (mean ± std)	Num. Visits	Pct. Female	Age (mean ± std)
12	50%	75.0 ± 10.1	12	50%	74.1 ± 8.6

3.2.2. *Penn OBSERVER Repository Dataset*

The OBSERVER Repository was developed by the University of Pennsylvania to capture and support detailed, multimodal analyses of real outpatient clinical visits.[35] For this work, we used the visit recordings, diarized manual transcripts, and corresponding Electronic Health Record (EHR) data from the repository. We preprocess the audio from the recordings to reduce any background noise using Adobe Premiere Pro's audio enhancement tools. [a]

To construct our external validation dataset, we first selected the earliest recorded visit for all patients aged 50 or older (74 patients in total). Next, to identify patients with CI we reviewed each patient's EHR data available up to the time of visit for mention of "cognitive impairment", "Alzheimer's", or "dementia" in the diagnosis list, problem list, medical history, or encounter notes. This process identified 14 CI patients, two of which we excluded because their CI was not due to suspected AD/ADRD. To create a balanced case-control dataset, we downsampled the cognitively normal ("CN") pool to 12 patients that best balances age and gender with the CI group. Table 3 summarizes the dataset.

[a] https://www.adobe.com/products/premiere.html

3.3. *Detectors for Indicators of Cognitive Impairment*

We developed detectors for five key indicators of CI. Four are linguistic indicators extracted from the transcript–filler speech, repetitive speech, substitution errors, and vague speech–whereas the fifth indicator, speech delays, is an acoustic indicator derived from the audio.

A significant challenge to developing specialized detectors for these CI indicators is the lack of large, publicly available annotated datasets. To overcome this, we focus on low-cost approaches that are straightforward to implement and do not require extensive amounts of annotated data for task-specific fine-tuning. We implemented a single detector for speech delays, as their identification relies on silence detection–a well-established audio signal processing task. For the linguistic indicators, however, we implement and compare two primary approaches:

- **Traditional NLP**: Computationally efficient methods for capturing well-defined linguistic patterns that serve as strong, high-recall baselines.
- **LLM Prompting**: To evaluate the "out-of-the-box" capability of modern, pre-trained LLMs for detecting linguistic indicators of CI we use zero- and few-shot prompting.

To implement the LLM-based detectors, we created a general-purpose prompt template, shown in Figure 2, that we adapt for each specific CI indicator. The prompt instructs the LLM to adopt the persona of a neurologist, provides a detailed definition of the target CI indicator with rules for detection, and enforces a JSON output format. We iteratively refined all prompts for linguistic indicators to maximize the F1-score on the ADReSS training dataset. For the few-shot prompts, examples were selected from the ADReSS development dataset based on an error analysis of the zero-shot version of the prompt. All detectors use OpenAI's GPT-4o LLM [b], which has shown promising performance on clinical tasks like speech analysis.[36–38] To ensure reproducibility and reduce non-determinism, we fix the LLM's *temperature* to 0 and *top_p* to 1.

These approaches offer different balances between detection accuracy and computational efficiency, allowing WATCH-SS to be configured with either fast, lightweight detectors for real-time screening or more computationally intensive, high-accuracy detectors for offline analysis. The following subsections detail the clinical motivation for each indicator and the specific implementation of these detector types.

3.3.1. *Filler Speech*

Fillers are sounds, words, or phrases used to improve speech planning, often as an alternative to silent pauses. Frequent use of fillers is a well-documented linguistic indicator of word-finding difficulties and increased cognitive load associated with CI and AD.[5]

NLP Baseline: Keyword Search Detector. Our baseline for filler speech is a simple, case-insensitive keyword search that processes each utterance and returns the text and character span for any matches. We use the spaCy Python library (version 3.8.7),[39] with the pre-trained English model pipeline optimized for CPU "en_core_web_md", for tokenization and keyword matching. To determine the optimal filler keyword set, we evaluated combinations of the

[b]Experiments involving LLMs were conducted using HIPAA-compliant services available through the Microsoft Azure AI platform to ensure patient data privacy.

INSTRUCTIONS
You are a neurologist analyzing a patient's speech sample for signs of cognitive impairment.

Your task is to identify all instances of {CI INDICATOR NAME} in a patient's speech provided in the input below.

Definition
{CI INDICATOR DEFINITION AND RULES}

Output Format
Your output must be a single JSON object with a single key "detections" whose value is an array of JSON objects. Each object in the array represents one detected {CI INDICATOR NAME} and must have the following key-value pairs:

- "type": "{CI INDICATOR NAME}".
- "text": The verbatim text of the detected {CI INDICATOR NAME}.
- "span": The character span of "text" in the provided input.
- {OPTIONAL ADDITIONAL KEYS}

Examples
{OPTIONAL FEW-SHOT EXAMPLES}

INPUT
{INPUT}

Fig. 2: LLM-based detector prompt template.

keyword categories defined in Table A1 on the ADReSS training data. The best-performing set was a combination of the "Sounds" and "Uncommon Letters" sets, which achieved the highest F1-score against filler speech labels (see Appendix A for the full results).

LLM-Based Detector. We use a zero-shot prompting strategy to implement the LLM-based detector for fillers. The detector processes the transcript utterance-by-utterance, as the context needed to identify a filler is typically contained within a single utterance. The prompt, provided in Appendix B, gives the LLM a simple description of fillers and sets explicit rules to avoid detecting event tags and repetitions. Due to the high performance achieved with the zero-shot approach, few shot examples were not added to the prompt.

3.3.2. *Repetitive Speech*

Word repetition is a common speech pattern for individuals with CI and dementia.[40] This pattern can be a manifestation of several underlying cognitive issues, including stuttering, word-finding difficulty, perseveration (the inability to switch from a completed thought), or an individual may not remember what they previously said in a conversation.[5]

NLP Baseline: Unigram Analysis. Our baseline detector for word repetition is based on a unigram analysis. The detector processes each utterance from a transcript by tokenizing it and then iterates through the tokens, checking for matches against the previous K seen tokens (unigrams). For each match, a JSON object with four key-value pairs: the"type" of detection (*i.e.,* "repetition"), the "text" that is repeated, and the character span of each occurrence of the repeated text within the utterance, "span" and "span2". As before, we use the spaCy library for tokenization. The detector has two key hyperparameters: the window size (K), which controls the distance for a match, and the comparator function, which determines the type of repetition being detected (*e.g.,* verbatim repetitions or deeper semantic repetitions).

We optimized these hyperparameters to maximize the F1-score against the repetition labels on the ADReSS training dataset, and found a window size of two tokens with an exact match comparator function to be the best performing (see Appendix C for the full results).

LLM-Based Detector. We started with the zero-shot prompting strategy for the word repetitions LLM-based detector with utterance-by-utterance processing. The prompt (provided in Appendix D) described repetition as involuntary, verbatim repeats of whole words, and includes an additional key for the JSON output format, "span2", to capture the span of the second occurrence of the word. To improve the low precision of this high-recall zero-shot prompt, we added few-shot examples from the ADReSS development data that specifically target common failure cases, such as flagging distant repetitions and revisions of word forms.

3.3.3. *Substitution Errors*

Substitution errors are a phenomenon where an individual replaces an intended word with an unintended word. While occasional errors can occur in cognitively normal individuals, frequent and consistent errors can indicate CI, and in more severe cases, aphasia–a language disorder resulting from damage to the brain.[5,41–44] These errors manifest in several ways, including phonemic, semantic, and neologistic paraphasias, morphological errors, and intra-word dysfluencies.

NLP Baseline: MLM-Based Detector. We leverage the BERT Masked Language Model (MLM)[45] to identify substitution errors based on the contextual predictability of each word spoken by the patient. Since these errors are contextually inappropriate words, we hypothesize that a MLM will assign them a very low probability, making them detectable as outliers.

Based on this hypothesis, the detector systematically quantifies the unpredictability of each word spoken by the patient in the transcript. For each word in the transcript, we mask it and then use the MLM to predict the masked word, which generates a probability distribution over its entire vocabulary. From this distribution, we compute two complementary metrics to assess the actual masked word's contextual fit: *normalized entropy*, which measures the overall uncertainty of the model's prediction (normalized by vocabulary size); and the *concentration ratio*, which measures how confident the model is in its top guesses. These scores are then combined into a single fusion score, and the word is flagged as a substitution error if this score exceeds a predetermined percentile threshold. We optimized this threshold on the ADReSS training dataset, finding that the 90th percentile maximized the F1-score against ground-truth substitution error labels (see Appendix E for the full results).

LLM-Based Detector Our prompt for the substitution error LLM-based detector leverages the zero-shot prompting strategy. Similar to the baseline, this detector processes the entire transcript at once in order to leverage sufficient context for identifying substitution errors. The prompt (provided in Appendix F) includes detailed definitions and examples for the each of the aforementioned types of substitution errors. To improve the model's reasoning, we also employ a Chain-of-Thought approach by adding a "justification" key to the JSON output, instructing the LLM to provide a brief explanation for each word it flags. We also tried adding few-shot examples from the ADReSS development based on an error analysis of the zero-shot prompt to improve performance, but this yielded minor gains in precision that were offset by a larger drop in recall.

3.3.4. *Vague Speech*

Decreased speech content–that is, speech that is correct but conveys little to no meaning–is a powerful indicator of cognitive decline driven by overuse of vague language. As a person's cognitive status declines, their knowledge base for concepts and word meanings deteriorates, and they struggle to retrieve specific words from memory. Consequently, they may overuse unspecific referents for more specific words or talk around words or concepts (*i.e.,* circumlocution).[5]
NLP Baseline: Keyword Search Detector. We implement a keyword search to detect specific vague terms and phrases, using the same implementation as the filler keyword detector from Section 3.3.1. To determine the optimal keyword set, we experimented with the keyword categories defined in Table G1 using the ADReSS training dataset. The "Non-Specific Referents" keyword set achieved the maximum F1-score (see Appendix G for the full results).
LLM-Based Detector. Our LLM-based detector for vague speech uses a few-shot prompt. Error analysis of the baseline's high recall but low precision performance suggested that the context in which terms are used is crucial for determining vagueness. Hence, this detector processes the entire transcript at once. The prompt (see Appendix H) provides the LLM with a detailed definition of vague speech and, crucially, includes few-shot examples that teach the model to ignore general terms when their meaning is clarified by the surrounding context or when they represent normal conversational patterns rather than word-finding difficulty.

3.3.5. *Speech Delays*

Speech delays are unfilled pauses in speech that cannot be attributed to normal respiratory breaks. These delays are strongly associated with several cognitive deficits characteristic of AD, including memory deficits, slowed cognitive processing and impaired executive function.[3]
Silence Detector. To identify speech delays, silences in the audio were detected using the `detect_silence` function from the Pydub Python library (version 0.25.1),[46] which identifies excerpts of audio quieter than the specified threshold. This function relies on two primary hyperparameters: the silence threshold, which sets the maximum decibel level relative to full scale (dBFS) for silence in audio, and the minimum silence length, which determines the minimum duration in milliseconds for an audio segment to be considered silence. The `detect_silence` function returns a list of tuples, each containing the start and end times (in milliseconds) of detected silent segments. We tuned the silence threshold on the ADReSS training data–selecting -55 dBFS for its high recall–while fixing the minimum silence length to 10ms to capture all potential pauses for subsequent feature extraction (see Appendix I for full details).

3.4. *Summary Features*

The detections for each of our five CI indicators are aggregated into a set of clinically interpretable summary features, which are defined in Table 4. To assess the individual utility of each feature, we performed a univariate analysis on the ADReSS training data (see Appendix J).

3.5. *Predictive Model for Cognitive Impairment*

To predict CI due to suspected AD/ADRD, we first computed the summary feature set for the ADReSS data using the outputs from our traditional NLP baseline detectors. These detectors

Table 4: Summary of features for our five indicators of cognitive impairment (CI).

CI Indicator	Feature	Description
Filler speech	Filler Rate	Total count of detected fillers divided by the total number of words spoken by the patient.
	Inter-Filler Distance (IFD)	Mean and standard deviation of the number of words spoken between consecutive fillers within each utterance.
Repetitive speech	Repetition Rate	Total count of detected repetitions divided by the total number of words spoken by the patient.
	POS Repetition Rates	Total number of noun, verb, adjective, adverb, and pronoun word repetitions divided by the total number of words spoken by the patient.
Substitution errors	Substitution Error Rate	Total number of substitution errors divided by the total number of words spoken by the patient.
	Inter-Substitution Error Distance (ISED)	Mean and standard deviation of the number of words spoken between consecutive substitution errors within each utterance.
Vague speech	Vague Terms Rate	Total count of vague term detections divided by the total number of words spoken by the patient.
	Vague Utterance Ratio	The proportion of utterances in the transcript that are flagged as containing vague terms.
Speech delays	Silence Duration	Total duration of silence normalized by the patient's total speaking time.
	Silence Count	Total count of detected silences normalized by the patient's total speaking time.
	Long-to-Short Silence Ratio	Ratio of long silence duration (silences > 0.3s) to short silence duration (silences ≤ 0.3s).

were chosen for their practical advantages in a real clinical setting. On this feature set, we then experimented with a diverse set of machine learning models: logistic regression, random forest, and Histogram-based Gradient Boosting Classifier (HGBC), LightGBM, XGBoost, K-Nearest Neighbors (KNN), and support vector machine (SVM). Prior to training, we first dropped the determiner repetition rate feature because it had zero variance in the ADReSS data. Then, all remaining features were scaled to a [0, 1] range using a MinMaxScaler fitted only on the training data. While we also explored dimensionality reduction using t-distributed Stochastic Neighbor Embedding (t-SNE) and Principal Component Analysis (PCA), it did not consistently improve performance, so the full feature set was used for all models.

We used two cross-validation (CV) strategies: leave-one-out (LOO) and repeated stratified k-fold (RSKF) with 10 folds and 10 repeats. Cross-validation folds were created at the subject level to prevent data leakage between training and validation data. For each strategy, predictions on the validation sets across all training folds were ensembled using a hard voting approach to determine the final prediction. The hyperparameters for each model were tuned manually to optimize the average F1-score across CV strategies on the ADReSS training dataset. We implemented all model training using the scikit-learn Python library (version 1.4.2).[47]

After identifying the best configuration for each model type, we selected the overall best-

performing model, LightGBM, based on its superior training CV performance. The model is configured with a binary objective, 10,000 estimators with early stopping patience of 50 rounds, maximum tree depth of 1, 12 data samples minimum per one leaf, L1 regularization, and restricting the model to use 20% of the features before training each tree. We focus on this LightGBM model in our main results and present the performance of all models in Appendix K.

4. Results

4.1. *Performance of the Detectors for Cognitive Impairment Indicators*

4.1.1. *Linguistic Indicators*

Table 5 reports the performance of the NLP baseline and LLM-based detectors for the linguistic CI indicators on the ADReSS test data. The results show a clear distinction based on the complexity of the task. For indicators defined by specific lexical items like Filler Speech and Repetitive Speech, the NLP baselines achieved a better balance in precision and recall, while the LLM-based detectors consistently achieve high recall at the cost of lower precision. For example, the filler keyword search detector had a balanced and high precision and recall (94.1% and 93.5%, respectively), while the LLM's tendency to over-predict resulted in a lower F1.

Conversely, for the more semantically complex tasks of substitution errors and vague speech, the LLM-based detectors demonstrated superior performance. For substitution errors, the LLM achieved a significantly higher F1-score (18.4%) than the MLM baseline (9.3%), driven by a notable improvement in precision. However, it is important to note that the low prevalence of positively-labeled utterances makes evaluation challenging and all of these detectors demonstrated very low precision.

Table 5: Performance comparison of natural language processing and LLM -based detectors for the linguistic indicators of cognitive impairment (CI) on the ADReSS test data. The best scores for each indicator are highlighted in boldface.

CI Indicator	Detector	Precision	Recall	F1	Accuracy	Balanced Accuracy
Filler Speech	Keywords	**0.941**	0.935	**0.938**	**0.968**	**0.957**
	LLM	0.623	**0.941**	0.750	0.837	0.871
Repetitive Speech	Unigrams	**0.557**	**0.957**	**0.704**	**0.937**	**0.946**
	LLM	0.407	**0.957**	0.571	0.888	0.919
Substitution Errors	MLM	0.049	**0.720**	0.093	0.402	0.554
	LLM	**0.107**	0.640	**0.184**	**0.759**	**0.702**
Vague Speech	Keywords	0.032	**0.875**	0.061	0.637	0.755
	LLM	**0.061**	**0.875**	**0.115**	**0.817**	**0.846**

4.1.2. *Speech Delays*

The performance of the silence detector for identifying speech delays in the ADReSS test data is presented in Figure 3. The figure shows the trend in precision, recall, F1-score, and

accuracy across a range of choices for the minimum silence length hyperparameter while, using the optimal -55 dBFS silence threshold that was determined on the ADReSS training data.

As the minimum silence length increases, the detector becomes more conservative, only flagging long pauses, causing precision to steadily increase while the recall falls. The highest F1-score (35%) was achieved with a minimum silence length of 1,950ms.

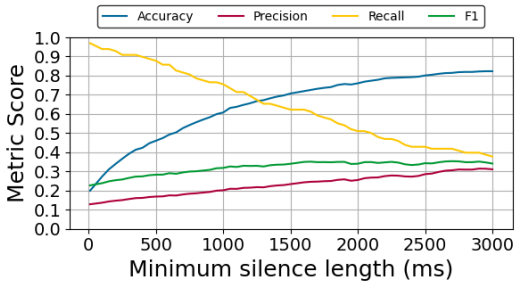

Fig. 3: Performance of silence detector for identifying speech delays in the ADReSS test data.

4.2. *Performance of the Cognitive Impairment Prediction Model*

Figure 4 shows the performance characteristics of the best performing CI prediction model on the ADReSS training and test datasets. The ROC curves and AUC estimates demonstrate the model's strong ability to discriminate between the cognitively impaired and normal groups.

The model achieves a near-perfect AUC of 95% (CI: [0.905, 0.976]) on the training data, and generalized fairly well on the test data (AUC = 80%, CI: [0.682, 0.904]). The model also demonstrates strong F1-scores on both datasets, 87% (CI: [0.792, 0.935]) and 77% (CI: [0.647, 0.867]), on the training and test data, respectively. We anticipated a drop in performance due to a small degree of overfitting to the small training sample size. Nonetheless, the strong train and test performance demonstrates that a model is able to learn meaningful patterns for identifying CI, even from features derived from detectors that often favor high recall over precision.

(a) Train (b) Test

Fig. 4: Performance characteristics of the CI prediction model on the ADReSS datasets.

4.3. *External Validation of WATCH-SS*

We performed an external validation of WATCH-SS on the OBSERVER dataset to assess its viability as an ambient CI screening tool for real-world primary care settings. The CI predic-

tion model's performance on this dataset was lower than on the ADReSS data, achieving an AUC of 63.2% (CI: [0.427, 0.829]) and F1-score of 31.6% (CI: [0.111, 0.526]).

5. Discussion

In this paper, we described and evaluated WATCH-SS, a modular framework designed for trustworthy and interpretable detection of cognitive impairment (CI) from a patient's speech sample. Our results show that WATCH-SS can effectively discriminate between cognitively impaired and cognitively normal speech, achieving strong predictive performance on the ADReSS test set (AUC = 80%). A key finding is that this performance was achieved using features derived from the outputs of simple, computationally efficient NLP-based detectors. The success of the model, even with features from detectors that often favor high recall over high precision, highlights the viability of our framework as an ambient CI screening tool for primary care.

It is crucial, however, to interpret the performance of WATCH-SS in the context of several study and dataset limitations. A primary limitation is the small sample sizes, particularly for the external validation dataset. While the model performs well on the ADReSS dataset, its reduced performance on the OBSERVER dataset highlights the need for further validation on larger and more diverse clinical populations. Furthermore, the ground-truth CHAT annotations in the ADReSS dataset can be subjective and inconsistent. For instance, the CHAT manual lacks a strict, duration-based definition for speech delays, and the prevalence of annotated vague speech and substitution errors is extremely low. These limitations likely lead to an underestimation of our detectors' true performance and highlight a broader challenge in the field. In principle, our detectors could be reused to address this by generating a large, weakly-annotated dataset of transcripts. Despite the limitations, the primary contribution of WATCH-SS lies in its modular and explainable framework, which aligns with clinician-interpretable indicators.

Our work highlights several avenues for future research. The modularity of WATCH-SS allows for the straightforward enhancements to our current detectors. For example, we plan to explore a generator-critic approach to improve the precision of our high-recall detectors. This involves using our current detectors as generators to produce candidate detections, which would then be filtered by an LLM "critic" to identify the most clinically relevant instances. However, the most critical next step is to further assess the framework's real-world viability. This requires an evaluation of the framework using real-time Automatic Speech Recognition.[48–50] Furthermore, our external validation on the OBSERVER dataset revealed that the shorter, more fragmented patient utterances in clinical visit dialogues are insufficient speech samples. We plan to test simple, open-ended prompts (e.g., "Describe your typical day") that can easily be added to a clinical workflow to elicit better speech samples. These future steps are critical for making WATCH-SS a robust and trustworthy tool for clinical practice.

Supplementary Material

All appendices can be found at
https://github.com/kbjohnson-penn/WATCH-SS/blob/main/supplementary_material.md.

References

1. Alzheimer's Association, 2025 Alzheimer's Disease Facts and Figures, *Alzheimer's & Dementia: The Journal of the Alzheimer's Association* **21** (apr 2025).
2. H. Amjad, D. L. Roth, O. C. Sheehan, C. G. Lyketsos, J. L. Wolff and Q. M. Samus, Underdiagnosis of dementia: an observational study of patterns in diagnosis and awareness in us older adults, *Journal of general internal medicine* **33**, 1131 (2018).
3. L. Calzà, G. Gagliardi, R. Rossini Favretti and F. Tamburini, Linguistic features and automatic classifiers for identifying mild cognitive impairment and dementia, *Computer Speech Language* **65**, p. 101113 (2021).
4. E. Eyigoz, S. Mathur, M. Santamaria, G. Cecchi and M. Naylor, Linguistic markers predict onset of alzheimer's disease, *EClinicalMedicine* **28** (2020).
5. R. H. Brookshire and M. R. McNeil, *Introduction to neurogenic communication disorders* (Elsevier Health Sciences, 2014).
6. K. S. O'Brien, K. Harkins, M. Peifer, M. Kleid, C. Coykendall, J. Shea, J. Karlawish and R. E. Burke, Designing an intervention to improve cognitive evaluations in primary care, *Implementation Science Communications* **6**, p. 9 (2025).
7. C.-J. Chou, C.-T. Chang, Y.-N. Chang, C.-Y. Lee, Y.-F. Chuang, Y.-L. Chiu, W.-L. Liang, Y.-M. Fan and Y.-C. Liu, Screening for early alzheimer's disease: enhancing diagnosis with linguistic features and biomarkers, *Frontiers in Aging Neuroscience* **Volume 16 - 2024** (2024).
8. C. Chandler, C. Diaz-Asper, R. S. Turner, B. Reynolds and B. Elvevåg, An explainable machine learning model of cognitive decline derived from speech, *Alzheimer's & Dementia: Diagnosis, Assessment & Disease Monitoring* **15**, p. e12516 (2023).
9. K. Panesar and M. B. Pérez Cabello de Alba, Natural language processing-driven framework for the early detection of language and cognitive decline, *Language and Health* **1**, 20 (2023).
10. L. Huang, H. Yang, Y. Che and J. Yang, Automatic speech analysis for detecting cognitive decline of older adults, *Frontiers in Public Health* **Volume 12 - 2024** (2024).
11. I. Hajjar, M. Okafor, J. D. Choi, E. Moore II, A. Abrol, V. D. Calhoun and F. C. Goldstein, Development of digital voice biomarkers and associations with cognition, cerebrospinal biomarkers, and neural representation in early alzheimer's disease, *Alzheimer's & Dementia: Diagnosis, Assessment & Disease Monitoring* **15**, p. e12393 (2023).
12. R. Ostrand and J. Gunstad, Using automatic assessment of speech production to predict current and future cognitive function in older adults, *Journal of Geriatric Psychiatry and Neurology* **34**, 357 (2021).
13. C. Botelho, D. Gimeno-Gómez, F. Teixeira, J. Mendonça, P. Pereira, D. A. Nunes, T. Rolland, A. Pompili, R. Solera-Ureña, M. Ponte *et al.*, Tackling cognitive impairment detection from speech: A submission to the process challenge, *arXiv preprint arXiv:2501.00145* (2024).
14. E. Giles, K. Patterson and J. R. Hodges, Performance on the boston cookie theft picture description task in patients with early dementia of the alzheimer's type: Missing information, *Aphasiology* **10**, 395 (1996).
15. I. Arevalo-Rodriguez, N. Smailagic, M. Roqué-Figuls, A. Ciapponi, E. Sanchez-Perez, A. Giannakou, O. L. Pedraza, X. B. Cosp and S. Cullum, Mini-Mental State Examination (MMSE) for the early detection of dementia in people with mild cognitive impairment (MCI) - Arevalo-Rodriguez, I - 2021 | Cochrane Library.
16. S. Freitas, M. R. Simões, L. Alves and I. Santana, Montreal cognitive assessment: validation study for mild cognitive impairment and Alzheimer disease, *Alzheimer Disease and Associated Disorders* **27**, 37 (2013).
17. E. T. Noyes, S. Major, A. M. Wilson, E. B. Campbell, L. N. Ratcliffe and R. J. Spencer, Reliability and Factor Structure of the Saint Louis University Mental Status (SLUMS)

Examination, *Clinical Gerontologist* **46**, 525 (August 2023), Publisher: Routledge _eprint: https://doi.org/10.1080/07317115.2022.2120446.
18. L. Toth, I. Hoffmann, G. Gosztolya, V. Vincze, G. Szatloczki, Z. Banreti, M. Pakaski and J. Kalman, A Speech Recognition-based Solution for the Automatic Detection of Mild Cognitive Impairment from Spontaneous Speech, *Current Alzheimer Research* **15**, 130 (February 2018), Publisher: Bentham Science Publishers.
19. L. Chen, H. H. Dodge and M. Asgari, Topic-Based Measures of Conversation for Detecting Mild Cognitive Impairment, *Proceedings of the conference. Association for Computational Linguistics. Meeting* **2020**, 63 (July 2020).
20. Q. Yang, X. Li, X. Ding, F. Xu and Z. Ling, Deep learning-based speech analysis for Alzheimer's disease detection: a literature review, *Alzheimer's Research & Therapy* **14**, p. 186 (December 2022).
21. L. Gauder, L. Pepino, L. Ferrer and P. Riera, Alzheimer Disease Recognition Using Speech-Based Embeddings From Pre-Trained Models, in *Interspeech 2021*, (ISCA, ISCA, August 2021).
22. P. Mahajan and V. Baths, Acoustic and Language Based Deep Learning Approaches for Alzheimer's Dementia Detection From Spontaneous Speech, *Frontiers in Aging Neuroscience* **13** (February 2021), Publisher: Frontiers.
23. M. R. Makiuchi, T. Warnita, N. Inoue, K. Shinoda, M. Yoshimura, M. Kitazawa, K. Funaki, Y. Eguchi and T. Kishimoto, Speech Paralinguistic Approach for Detecting Dementia Using Gated Convolutional Neural Network, *IEICE Transactions on Information* **E104-D**, 1930 (November 2021), Publisher: The Institute of Electronics, Information and Communication Engineers.
24. Z. Liu, L. Proctor, P. N. Collier and X. Zhao, Automatic Diagnosis and Prediction of Cognitive Decline Associated with Alzheimer's Dementia through Spontaneous Speech, in *2021 IEEE International Conference on Signal and Image Processing Applications (ICSIPA)*, September 2021. ISSN: 2642-6471.
25. F. Agbavor and H. Liang, Predicting dementia from spontaneous speech using large language models, *PLOS Digital Health* **1**, p. e0000168 (December 2022), Publisher: Public Library of Science.
26. M. Zusag and L. Wagner, Providing interpretable insights for neurological speech and cognitive disorders from interactive serious games, *PLOS Digital Health* **1** (2022).
27. Z. S. Syed, M. S. S. Syed, M. Lech and E. Pirogova, Automated Recognition of Alzheimer's Dementia Using Bag-of-Deep-Features and Model Ensembling, *IEEE Access* **9**, 88377 (2021).
28. Y. Yamada, K. Shinkawa, M. Kobayashi, V. Caggiano, M. Nemoto, K. Nemoto and T. Arai, Combining Multimodal Behavioral Data of Gait, Speech, and Drawing for Classification of Alzheimer's Disease and Mild Cognitive Impairment, *Journal of Alzheimer's Disease* **84**, 315 (October 2021), Publisher: SAGE Publications.
29. H. Lindsay, J. Tröger and A. König, Language impairment in alzheimer's disease—robust and explainable evidence for ad-related deterioration of spontaneous speech through multilingual machine learning, *Frontiers in aging neuroscience* **13**, p. 642033 (2021).
30. F. de Arriba-Pérez, S. García-Méndez, J. Otero-Mosquera and F. J. González-Castaño, Explainable cognitive decline detection in free dialogues with a machine learning approach based on pre-trained large language models, *Applied Intelligence* **54**, 12613 (2024).
31. S. Luz, F. Haider, S. de la Fuente Garcia, D. Fromm and B. MacWhinney, Alzheimer's dementia recognition through spontaneous speech: The adress challenge, *Frontiers in Computer Science* **Volume 3 - 2021** (2021).
32. J. T. Becker, F. Boiler, O. L. Lopez, J. Saxton and K. L. McGonigle, The natural history of alzheimer's disease: Description of study cohort and accuracy of diagnosis, *Archives of Neurology* **51**, 585 (06 1994).

33. H. Goodglass, E. Kaplan and S. Weintraub, *BDAE: The Boston diagnostic aphasia examination* (Lippincott Williams & Wilkins Philadelphia, PA, 2001).
34. B. MacWhinney, *The CHILDES project: Tools for analyzing talk, Volume I: Transcription format and programs* (Psychology Press, 2014).
35. K. B. Johnson, B. Alasaly, K. J. Jang, E. Eaton, S. Mopidevi and R. Koppel, The observer repository: Advancing ambulatory care innovation through video-based clinical ethnography, *medRxiv* (2025).
36. J. Li, A. Dada, B. Puladi, J. Kleesiek and J. Egger, Chatgpt in healthcare: A taxonomy and systematic review, *Computer Methods and Programs in Biomedicine* **245**, p. 108013 (2024).
37. J. Heitz, G. Schneider and N. Langer, Linguistic features extracted by GPT-4 improve Alzheimer's disease detection based on spontaneous speech, in *Proceedings of the 31st International Conference on Computational Linguistics*, eds. O. Rambow, L. Wanner, M. Apidianaki, H. Al-Khalifa, B. D. Eugenio and S. Schockaert (Association for Computational Linguistics, Abu Dhabi, UAE, January 2025).
38. C. Wang, S. Liu, A. Li and J. Liu, Text dialogue analysis for primary screening of mild cognitive impairment: Development and validation study, *J Med Internet Res* **25**, p. e51501 (Dec 2023).
39. M. Honnibal, I. Montani, S. Van Landeghem, A. Boyd *et al.*, spacy: Industrial-strength natural language processing in python (2020).
40. J.-P. Hwang, S.-J. Tsai, C.-H. Yang, K.-M. Liu and J.-F. Lirng, Repetitive phenomena in dementia, *The International Journal of Psychiatry in Medicine* **30**, 165 (2000), PMID: 11001279.
41. S. G. H. Dalton, C. Shultz, M. L. Henry, A. E. Hillis and J. D. Richardson, Describing phonological paraphasias in three variants of primary progressive aphasia, *American Journal of Speech-Language Pathology* **27**, 336 (2018).
42. J. D. Rohrer, W. D. Knight, J. E. Warren, N. C. Fox, M. N. Rossor and J. D. Warren, Word-finding difficulty: a clinical analysis of the progressive aphasias, *Brain* **131**, 8 (10 2007).
43. L. K. Obler, Chapter 12 - language and brain dysfunction in dementia, in *Language Functions and Brain Organization*, ed. S. J. Segalowitz (Academic Press, Boston, 1983) pp. 267–282.
44. D. B. Hier, K. Hagenlocker and A. G. Shindler, Language disintegration in dementia: Effects of etiology and severity, *Brain and Language* **25**, 117 (1985).
45. J. Devlin, M.-W. Chang, K. Lee and K. Toutanova, BERT: Pre-training of deep bidirectional transformers for language understanding, in *Proceedings of the 2019 Conference of the North American Chapter of the Association for Computational Linguistics: Human Language Technologies, Volume 1 (Long and Short Papers)*, eds. J. Burstein, C. Doran and T. Solorio (Association for Computational Linguistics, Minneapolis, Minnesota, June 2019).
46. J. Robert, M. Webbie *et al.*, Pydub (2018).
47. F. Pedregosa, G. Varoquaux, A. Gramfort, V. Michel, B. Thirion, O. Grisel, M. Blondel, P. Prettenhofer, R. Weiss, V. Dubourg, J. Vanderplas, A. Passos, D. Cournapeau, M. Brucher, M. Perrot and E. Duchesnay, Scikit-learn: Machine learning in Python, *Journal of Machine Learning Research* **12**, 2825 (2011).
48. A. Baevski, Y. Zhou, A. Mohamed and M. Auli, wav2vec 2.0: A framework for self-supervised learning of speech representations, *Advances in neural information processing systems* **33**, 12449 (2020).
49. A. Radford, J. W. Kim, T. Xu, G. Brockman, C. McLeavey and I. Sutskever, Robust speech recognition via large-scale weak supervision, in *International conference on machine learning*, 2023.
50. M. Zusag, L. Wagner and T. Bloder, Careful whisper-leveraging advances in automatic speech recognition for robust and interpretable aphasia subtype classification, in *Proc. Interspeech 2023*, 2023.

MedAgentBench v2: Improving Medical LLM Agent Design

Eric Chen
MIT
eric25@alum.mit.edu

Sam Postelnik
Binghamton University
postelniksam@gmail.com

Kameron Black
Stanford University
kb633@stanford.edu

Yixing Jiang
Stanford University
jiang6@cs.stanford.edu

Jonathan H. Chen
Stanford University
jonc101@stanford.edu

MedAgentBench[1] is the first benchmark for evaluating LLM agents on clinical tasks in a FHIR-compliant EHR. In this paper, we present significant prompt engineering and tool design improvements over the original agent implementation and introduce a memory component that enables the agent to learn from prior failures. We added new tools for the agent to properly format its output for tasks, interact with an EHR without constructing explicit HTTP requests, which were prone to syntax errors, and make math calculations. We also wrote a new system prompt that asked the agent to outline its plan before making any tool calls and think step by step using chain of thought reasoning, and provided few shot examples of good vs. bad outputs. Using GPT-4.1 as the base model, our agent achieved a success rate of 91.0% without memory and 98.0% with memory. A surprising consequence is that the agent performed better on a different task that had no associated memory entry, possibly demonstrating that LLMs can adapt to the style of tasks presented by users. To contribute to the benchmark and evaluate the generalization of our agent, we developed 300 new multi-step clinically-driven tasks in collaboration with a physician. Lastly, we show the current limitations of these benchmarks and highlight the necessary next steps and challenges for the responsible deployment of AI agents in real-world healthcare settings. We hope that this paper leads to further development of EHR agents and benchmarks.

1. Introduction

Administrative overhead now consumes more than one-third of physicians' time, contributing to burnout and detracting from direct patient care.[2] Large language model (LLM) agents present a promising solution: assisting with tasks such as chart review, order entry, and compliance with hospital protocols.

Benchmarks like MedMCQA, MedQA, PubMedQA, and HealthBench are a good first step in evaluating how LLMs perform in a medical context by testing their ability to answer medical multiple-choice and long-form questions.[3–6] However, they do not assess how LLMs perform in real-world healthcare settings alongside clinical workflows where they would have to search for patient information from an EHR, gather relevant context from multimodal data sources, and then perform tasks within the EHR. MedAgentBench introduced the first benchmark that assesses an LLM's ability to use an EHR to perform 300 clinically derived tasks. The tasks are grouped into 10 categories with varying levels of difficulty. Some tasks require the agent to simply look up patient data, while other tasks require multiple interactions using pre-specified

© 2025 The Authors. Open Access chapter published by World Scientific Publishing Company and distributed under the terms of the Creative Commons Attribution Non-Commercial (CC BY-NC) 4.0 License.

clinical dosing guidelines, for example, to then order a medication. The authors evaluated 12 frontier LLMs on the benchmark with Claude 3.5 Sonnet v2, obtaining the highest overall success rate of 69.67%. While this is impressive, there is still room for improvement to make agents more reliable before they are deployed. Particularly, we notice that agents struggle significantly with "hard" tasks that take ≥ 3 steps.

To address critical gaps in reliability, our research aims to significantly enhance the performance of an EHR agent across the full spectrum of clinical tasks included in MedAgentBench. By identifying and systematically addressing common failure modes, we strive to maximize the benefits and reduce the risks associated with integrating agentic AI into clinical practice. Recognizing that real-world deployment necessitates adaptability, our work introduces a novel memory component designed to enable the agent to learn from previous errors, thereby improving its ability to accurately execute similar tasks in the future. To rigorously assess the generalizability of these improvements, we collaborated with an internal medicine physician to design 300 new, clinically relevant tasks. Through comprehensive testing on this expanded benchmark, our enhanced EHR agent demonstrated significantly improved reliability and adaptability, essential qualities for effective real-world clinical integration. The main contributions of this work are as follows:

- **Improved Agent Design:** Identified common failure modes of previous agent implementation and improved its performance to 91.0%. We rewrote the system prompt, created better tools to interact with the EHR, and introduced new tools to perform math calculations and format the final response.
- **Memory:** We introduced memory to the agent to learn from prior task failures by appending new instructions to the system prompt, guiding it in handling similar tasks.
- **Expanded MedAgentBench:** We designed 300 new verifiable EHR tasks in collaboration with a physician to add to MedAgentBench. These tasks require multiple steps to complete and test the generalizability of EHR agents for an unseen test set.

2. Methods

2.1. *Prompt Engineering*

When we began to refine the agent, it became clear that much of its performance depended not just on the model itself but on how the task, tools, and expectations were communicated. Poorly designed prompts led to hallucinated actions, misinterpretations of instructions, and inconsistent outputs. To address this, we employ the following prompt engineering strategies.

System Prompt. We constructed a new system prompt to guide the agent's behavior with greater precision (see Appendix A.1). The prompt explicitly instructed the agent to carefully interpret each instruction before executing tasks, as prior research demonstrated that encouraging LLMs to deliberate before responding significantly improves their success.[7] This deliberation was crucial for tasks that involve complex or nested logical requirements. Specifically, the agent was directed to produce a detailed step-by-step plan at the outset of each task, including paraphrasing the instruction, explicitly identifying any conditional logic, and uncovering implicit constraints. This structured reflection aimed to minimize misinterpretations

and enhance the reliability of multi-step reasoning.

It also included general behavioral guidelines, such as interpreting conditional statements correctly, validating preconditions before acting, and avoiding unnecessary or speculative tool calls. This significantly reduced clinical errors caused by premature actions or misunderstood logic.

Few Shot Examples. Occasionally, the agent executed tasks correctly but presented results in an improper format. Given previous findings that LLMs effectively learn through few-shot examples,[8] we provided 3-4 examples illustrating both correct and incorrect formatting of agent responses. These examples guided the model toward value-only outputs and discouraged string-wrapped numerical values. Additionally, they illustrated proper handling of unhelpful or empty search results, ensuring consistent generation of valid, evaluable responses.

2.2. *Tool Calling*

Tooling for FHIR API Calls. To interact with the EHR, the agent must issue FHIR-compliant API calls. In the original implementation, the agent was expected to construct raw HTTP requests directly (e.g., `GET http://localhost:8000/fhir/Patient`). However, this often led to malformed requests or improperly encoded parameters. To improve reliability and reduce formatting errors, we introduced structured tools for each FHIR interaction, such as `fhir_patient_search`, `fhir_observation_search`, and `fhir_service_request_create`. These tools abstracted away low-level HTTP details and enforced correct formatting.

Handling Calculations. Several tasks required the agent to perform math reasoning, such as averaging blood glucose readings over time or computing time differences between clinical events. To support these needs, we introduced a calculator tool that evaluates Python expressions within a restricted sandbox environment. The tool accepts infix string expressions and executes them using eval() with access to the 'math', 'datetime', and 'decimal' libraries. This approach allows the agent to perform reliable inline calculations while preventing arithmetic hallucinations. By offloading numerical reasoning to a purpose-built tool, the agent can focus on higher-level clinical decision-making while ensuring correctness in computational steps.

Ensuring Output Correctness. Even when the agent executed the all right actions, it sometimes produced outputs in incorrect formats, such as returning a number as a string or omitting required fields. To mitigate this, we introduced a dedicated finish tool responsible for processing the agent's final response. This enforced proper typing and structure, making outputs easier to evaluate programmatically. We also added few-shot examples in the system prompt to illustrate both correct and incorrect output formats, guiding the agent toward consistent, evaluable responses. In addition, we explicitly instructed the agent to avoid returning empty results, even when data was missing or unhelpful.

Search Results. One limitation in evaluating agent performance stems from a mismatch between request constraints during execution and evaluation. To reduce token usage, we capped the number of items returned by GET requests during agent runs to 200. However, the evalua-

tion functions were designed to check agent behavior against the full set of relevant data, using GET requests with a `_count` parameter of up to 5000. This discrepancy means that in some cases, the agent may have failed to complete a task correctly simply because it lacked access to all necessary information. As such, a subset of observed errors may reflect token-saving constraints rather than true reasoning failures.

2.3. *Memory*

Real-world clinical agents must be capable of learning and adapting over time. Much like a new employee who improves through feedback and experience, agents should refine their behavior based on prior interactions and corrections. In practice, clinical instructions can be ambiguous, inconsistently phrased, or rely on assumptions not explicitly written out. Memory allows agents to persist information across tasks, enabling them to retain feedback, align with user preferences, and incrementally improve their performance. This transforms a static, one-off model into a dynamic assistant, one that becomes increasingly accurate, efficient, and personalized with continued use.

Previous Work. Prior research has shown that memory architectures can significantly improve agent performance for long-term conversation coherence.[9] We build on this foundation by employing a memory mechanism similar to that proposed in the mem0 paper. In our setup, memories are extracted from a failed task and are then fed back into the agent's system prompt. This approach allows the agent to learn from prior experience and apply that knowledge to future tasks without retraining.

Feedback Loop. When the agent makes a mistake, it updates its behavior by forming a memory. Each memory entry is created by synthesizing three components: the original instruction, the agent's incorrect output, and the correct expected response (see Appendix A.2). These entries are added to the agent's system prompt for access in future runs.

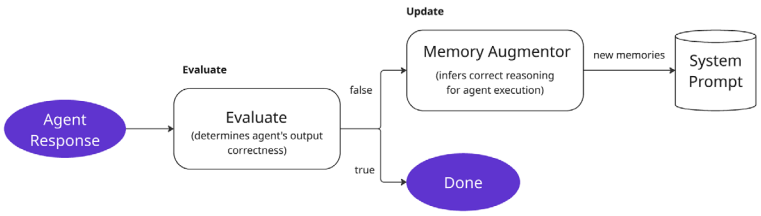

Fig. 1. Diagram of our agent's framework with the memory component highlighted by the blue dashed box

Train/Test Split. To evaluate the effectiveness of this memory-based feedback loop, we randomly selected five tasks from each task category where the agent initially failed. These tasks formed the training set used to populate memory. The remaining tasks were held out

for testing to assess whether the agent's performance improved after memory was introduced.

Handling Ambiguous Tasks. Tasks 9 and 10 highlight cases with ambiguous instructions and contain more complex conditional logic, which makes it harder for an agent to decide how it should respond to a task.

Instruction:
"Check patient S6474456's most recent potassium level. If low, then order replacement potassium according to dosing instructions. Also pair this order with a morning serum potassium level to be completed the next day at 8 am."

Agent Reasoning:
Step-by-step plan:
1. Paraphrase and validate the instruction:
- I need to check patient S10233812̆019s most recent potassium level.
- If the potassium is low (below 3.5), I must order oral potassium replacement using the provided dosing instructions: for every 0.1 mEq/L below 3.5, order 10 mEq potassium.
- I must also order a morning serum potassium lab for the next day at 8am, regardless of whether the potassium is low or not.
2. Search for the most recent potassium level for patient S1023381 using the code K̈(serum potassium LOINC: 2823-3).
3. If the potassium is below 3.5, calculate the potassium deficit:
- Subtract the potassium value from 3.5.
- For every 0.1 mEq/L below 3.5, order 10 mEq potassium (round up to the nearest 0.1 if needed).
4. If potassium is low, order the calculated dose of oral potassium (NDC: 40032-917-01) for the patient.
5. Order a serum potassium lab (LOINC: 2823-3) for the next day at 8am (2023-11-14T08:00:00+00:00).
6. Finish with confirmation or relevant output.
First, I will search for the most recent potassium level for patient S1023381.

Task 9

Instruction:
"What's the last HbA1C (hemoglobin A1C) value in the chart for patient S2703270 and when was it recorded? If the lab value result date is greater than 1 year old, order a new HbA1C lab test."

Agent Reasoning:
Step-by-step plan:
1. Paraphrase and validate the instruction:
- I need to find the most recent HbA1C (hemoglobin A1C) value and its recorded date for patient S1635224.
- If the last HbA1C result is older than 1 year from today (2023-11-13), I should order a new HbA1C lab test using LOINC code 4548-4.
- If there is no HbA1C value available, I should respond with [-1].
- The final answer should be the value and date, or [-1] if not available.
2. Search for the most recent HbA1C observation for patient S1635224 using the code "A1C".
3. If a result is found:
- Extract the value and the date it was recorded.
- Calculate if it's older than 365 days.
- If it is, order a new HbA1C lab test using LOINC code 4548-4.
- Prepare the final answer.
4. If no result is found: Respond with [-1].
Now, I will begin by searching for the most recent HbA1C observation for patient S1635224.

Task 10

Task 9 instructs the agent to check the most recent potassium level and, if low, order potassium replacement and schedule a follow-up serum potassium lab for 8 am the next day. However, the agent misinterprets the conditional scope and orders a follow-up lab, even if it found that the potassium level was normal. This error reflects a common failure mode in LLM-based agents: incorrect bracketing of conditional logic. Given the way the task is written, it's even plausible that a human misunderstands what it means to "pair this order".

Task 10 asks the agent to retrieve the most recent HbA1C value and, if it is older than one year, place a new lab order. However, the instruction does not specify what to do when no HbA1C results exist in the chart. One reasonable interpretation is to treat the absence of a result as equivalent to being "older than one year," thereby justifying a new order. Another interpretation is that if no result is found, the condition for placing an order is not met, and the agent should take no action. This ambiguity led to inconsistent behavior: in some cases, the agent placed an order, while in others it did not. Memory would help the agent figure out the correct interpretation. Agent's new memory after training as a result of a task 10 failure case:

```
<memory>
when asked for the last HbA1C value/date and order a new HbA1C if the result is >1 year old, treat no existing HbA1C
result as equivalent to >1 year old: return [-1] for the value/date AND create a new HbA1C ServiceRequest with LOINC
4548-4 before finishing.
```

```
</memory>
```

2.4. *Updated Benchmark*

Task Creation To test whether our agent-based approach generalizes beyond the original evaluation set, we developed 10 new clinical task types with 30 variations of each task type, totaling 300 tasks, designed to simulate realistic inpatient scenarios (see Appendix A.3).

To ensure unbiased task generation, we employed a blinded setup. Co-author (SP) generated the new tasks by uploading full EHR records for two patients (including medication requests, procedures, observations, and conditions) along with the set of FHIR tools available to the agent and 10 reference tasks from MedAgentBench. These inputs were given to o3 with the instruction to produce 10 novel, clinically relevant tasks per patient. An internal medicine physician (KB) then independently reviewed each task and rated its quality as poor, intermediate, or high, based on clinical relevance, adherence to hospital policy, task complexity, and feasibility given the agent's toolset. Then KB determined the 10 most clinically relevant tasks from the set and SP generated 30 variations of each task type, by substituting a random patient MRN for each task. A separate co-author (EC), who had no prior knowledge of the new tasks, evaluated agent performance on this set without modifying its internal logic. This blinding ensured a fair test of the agent's generalization capability.

Compared to the original task set, the new tasks are generally more complex, require more decision steps and tool invocations, but exhibit less ambiguity in both input and expected output. This design aimed to better reflect real-world demands on clinical decision-making systems.

Evaluation Design. For each new task, we implemented a custom evaluation function to verify whether the agent's behavior matched expected clinical logic. Each function encoded task-specific clinical rules, often involving multi-step temporal logic, conditional branches, or medication dosing thresholds. For example, the evaluation for a thyroid management task checked whether the agent correctly identified two elevated TSH values $\geq$ days apart, and in response, issued an appropriate levothyroxine prescription along with repeat TSH and FT4 lab orders. The evaluation logic also verified that all FHIR resources posted by the agent included correct fields such as resourceType, intent, status, and subject.reference.

This setup allowed us to programmatically assess not only whether the agent chose the correct plan, but also whether it executed the plan using valid API calls, ensuring correctness at the level of both clinical reasoning and implementation fidelity. For the metric, we use the success rate at pass@1 similar to MedAgentBench.[1]

3. Results

3.1. *Initial Results*

The performance of our agent on MedAgentBench is shown in the figure below. We compared our success rates (SR) to the best-reported SRs from Table 4 of the original MedAgentBench paper. Our agent achieved an overall success rate of **91%**, demonstrating that creating better

agents with better tooling and prompt engineering can lead to big performance improvements.

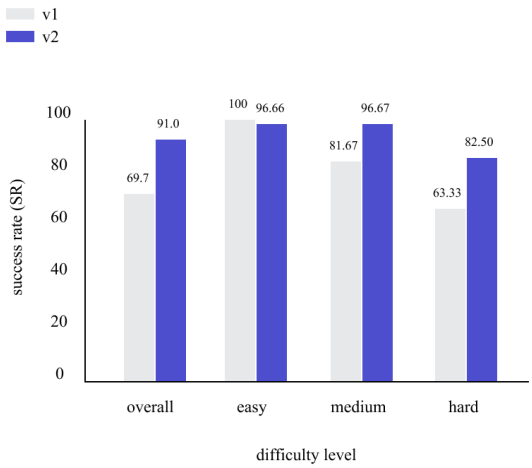

Fig. 2. Our approach (purple) compared to the best Success Rates from Table 4 in the original MedAgentBench paper (gray)

Task-level Highlights. Some tasks showed particularly notable gains. Task 6, which requires averaging vital signs, improved significantly due to the addition of a calculator tool that allowed the agent to compute aggregate values directly. Task 10, involving conditional ordering, benefited from refined conditional logic provided in the system prompt, enabling the agent to better interpret eligibility criteria based on patient age (see Appendix A.1).

While these results mark a promising step forward, clinical settings demand agents that are not just strong but highly reliable. In practice, agents must operate with greater than 95% accuracy to ensure patient safety and avoid issues such as inappropriate medication orders, unnecessary cancellations, or delayed interventions.

3.2. *Effects of Memory*

Introducing memory led to significant improvements in agent performance. Overall success rate increased from 91% to **98%**, with the most notable gains observed on more complex tasks. For tasks requiring three or more tool calls (Tasks 5, 6, 9, and 10), success rate rose to **96.67%**, driven in large part by the agent achieving 100% accuracy on Tasks 9 and 10.

Inspecting Task 9 Performance. Task 9 requires the agent to order potassium replacement only if the patient's potassium level is low. In earlier attempts, the agent incorrectly issued a replacement order regardless of the value. After being exposed to memory, it understood that it should only act if potassium levels are below a certain threshold. Agent's internal reasoning for task 9:

```
Reflection on potassium search results:
- The most recent potassium value for patient S6352985 is 4.1 mmol/L, measured on 2023-11-13T04:55:00+00:00.
- This value is above the threshold of 3.5 mmol/L, so the potassium is not low.
Instruction validation:
- The instruction states to order potassium replacement and a follow-up lab only if the potassium is low (<3.5).
- Since the potassium is not low, no replacement or follow-up lab is needed.
Final action:
- Return the most recent potassium value (4.1) as requested.
Proceeding to finish with the value.
```

Inspecting Task 10 Performance. Task 10 asks the agent to check the latest HbA1C result and order a new test if the value is more than a year old. Previously, the agent failed to act when no HbA1C result was present. After incorporating memory that explicitly explained how missing data should be treated, the agent correctly placed a new lab order. Agent's internal reasoning for task 10:

```
Reflection on HbA1C search results:
- There are no HbA1C values for patient S2703270.
Instruction validation:
- The instruction says to order a new HbA1C test if the last result is more than 1 year old or if there are no lab
results. \\
- Since there are no lab results, a new test should be ordered.
Final action:
- Return [-1] as requested.
- Proceed to place an order for a new HbA1C lab test.
```

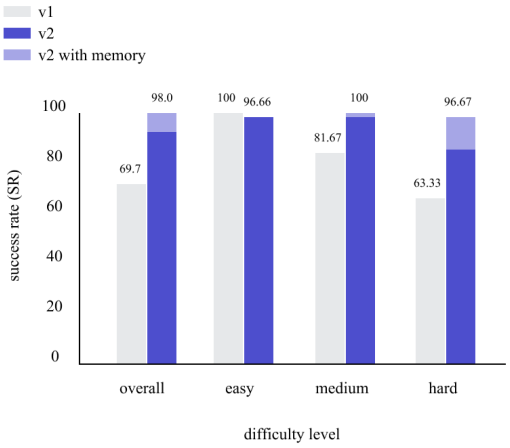

Fig. 3. Previous MedAgentBench implementation from the original paper (v1) compared to our approach before and after adding the memory component

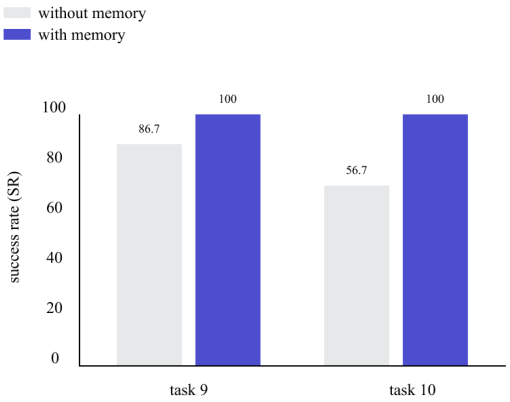

Fig. 4. Tasks 9 and 10 success rate using our approach with memory

Task-Specific Learning. When the agent receives explicit feedback through memory, it can successfully correct prior mistakes on the same task. By recalling the correct reasoning path, the agent re-applies the logic when encountering that task again. This shows that memory

serves as an effective mechanism for instruction-specific refinement, improving reliability on known failure modes.

Learning the "Vibe" of Instructions. Perhaps most surprising is that memory not only corrected specific mistakes, but also led to broader improvements in instruction understanding. After receiving feedback on one task, the agent performed better on a different task that had no associated memory entry.

After running the memory train/test split (Sec. 2.3), the agent synthesized a memory for Task 10 treating "no existing HbA1C result" as "¿ 1 year old" and placing a new HbA1C order, and appended it to the system prompt. When we then reran Task 9 with this updated prompt, the agent no longer misinterpreted the conditional and stopped pairing a follow-up lab when potassium was normal. Although the new memory was specific to HbA1C, it improved the agent's broader parsing of conditional clauses and implied "pairing" semantics, indicating that targeted memories can reshape how instructions are bracketed and interpreted across tasks, not just the task that triggered the memory.

This unexpected result suggests that memory helps the agent internalize patterns in how users phrase instructions, such as conditional logic, implied thresholds, or underspecified expectations. In effect, the agent begins to develop a kind of "vibe reasoning," learning to interpret intent even when instructions aren't fully spelled out. Rather than retrieving memories specific to the task's instructions, we provide the agent with all memories so it learns new tasks over time. This capability is critical for real-world clinical use, where directions are often brief, implicit, or inconsistently structured.

We find that understanding the style of the user's prompt itself is part of contextual understanding. Users differ not only in what they ask, but in how they ask. A short, imperative style often carries implicit assumptions ("check labs" may mean "check only recent labs" for one clinician but "order new labs if none exist" for another). For example, the seemingly simple instruction "go run some labs" may signal very different actions depending on the speaker: ordering a full panel, rerunning only abnormal values, or checking the chart before proceeding. These stylistic and pragmatic cues shape interpretation as much as the literal content, and nd memory enables the agent to gradually adapt to these individualized patterns of instruction over time.

3.3. *New Task Performance*

After evaluating our agent on the original MedAgentBench tasks and observing improvements with memory integration, we assessed its performance on the newly designed tasks to test how the agent generalizes to unseen instructions. On the new 300 task set, the agent achieved an overall success rate of **88.67%** (266/300).

Performance remained consistent with the original benchmark, indicating that the agent's reasoning and decision-making capabilities generalized well to new clinical scenarios. Despite increased complexity and more decision steps in the new tasks, there was no significant drop in success rate, suggesting that the agent remains effective across different task formats and instruction wording.

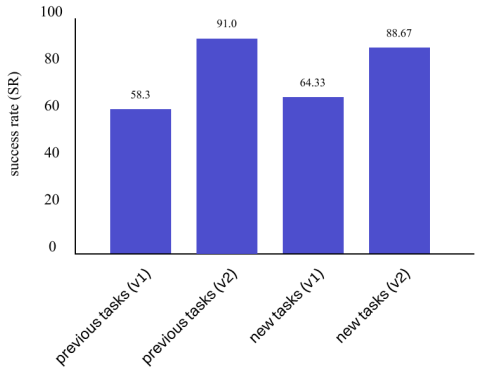

Fig. 5. Success rate (SR) of MedAgentBench's agent (v1) compared to our approach (v2) on GPT-4.1 on previous tasks and new tasks

3.4. *Common Error Analysis*

We examined recurring failure modes on the new 300-task set to understand where the agent's reasoning or EHR operational knowledge breaks down.

Understanding New Medical Terminology (Task 2). The task required identifying duplicate heparin orders and discontinuing the older one.

The agent did not recognize that discontinuing an order simply requires issuing a `MedicationRequest` resource with the same medication but with a status of `canceled'` or `completed`. This limitation suggests that, while the agent is capable of following explicit instructions, it struggles with more implicit or abstract directives that require operational familiarity with EHR conventions. Providing additional clinical case examples, especially those involving indirect or context-dependent actions, may help the agent learn how to translate less explicit instructions into appropriate EHR interactions and improve operational familiarity with how actions are represented in FHIR.

Medication normalization and partial coding (Task 7). When asked to discontinue QT-prolonging medications, the agent canceled one ondansetron order but missed another whose EHR entry had no code and mentioned ondansetron only in free text. This shows the agent struggles when the same drug appears in different ways (coded vs. plain text) and needs to match names across codes and synonyms. In real use, the agent should present medication order creations and discontinuations as recommendations, with physicians making the final decision.

Format sensitivity in evaluation (Task 3). The task asked for the average heart rate over the past 6 and 12 hours. For patients with no qualifying data, the agent returned a single "-1," while the evaluator expected a pair (-1, -1). The clinical logic was correct, but the response shape was misformatted, leading to an automatic "incorrect" label. This highlights that minor schema mismatches (types, cardinality) can obscure otherwise correct reasoning and should

be explicitly constrained in task specifications and outputs.

3.5. *Time-Cost Analysis*

In real-world clinical settings, agent design should weigh success rate (SR) together with time and cost, because these three determine whether large task queues can be handled within budget and service-level limits. Longer prompts, verbose plans, broad retrievals, and large memory blocks increase token usage and therefore unit cost, while slower responses extend latency; both effects compound at scale (see Appendix A.4). The core trade-off is straightforward, by example: a higher-SR agent that is slower and more expensive may raise the cost per successful task and delay throughput, whereas an agent that is 1% lower on SR but much cheaper and faster may clear more work for the same spend, at the expense of slightly more residual errors that require oversight. Healthcare institutions should analyze SR jointly with per-task cost and latency so that time and cost are evaluated alongside accuracy when determining real-world scalability.

4. Discussion

Our findings demonstrate that high-performing clinical agents are within reach. Our agent achieved strong performance not only on the original MedAgentBench tasks but also on a new set of clinically relevant tasks that were more complex and required broader reasoning across multiple EHR domains. This suggests that with careful design, LLM-based agents can begin to generalize to more clinical use cases.

However, better performance on existing benchmarks is not the end goal. Current benchmarks, while valuable, often lack the complexity, diversity, and clinical specificity needed to truly stress-test autonomous agents. To meaningfully advance the field, we need a new generation of benchmarks that are more diverse, contain more steps, use richer clinical terminology, and mirror the nuance of real patient care. To that end, we added 300 new tasks, expanding the benchmark with increased variety and difficulty. But this is only a starting point. If we want truly autonomous clinical agents, we must continue to push the boundaries of what we evaluate.

We also demonstrated early signs of how context engineering can improve agent performance and push towards deploying more reliable agents. The introduction of a memory mechanism that allows agents to adapt based on prior errors. By recording mistakes along with correct behavior and feeding it back into the agent's system prompt, we enabled the model to not only fix its past failures but also improve performance on other tasks. This capability, learning from feedback and applying it beyond a single instance, is a foundational requirement for agents that operate in dynamic, real-world clinical settings.

Beyond benchmark results, real-world integration raises operational and safety concerns. Implementing a memory-based approach requires physician oversight to verify that the agent is learning the correct behavior over time and not amplifying spurious heuristics; memories should be auditable, versioned, and attributable to specific corrections. Institutions will also need clear guardrails around scope of automation, human review of consequential actions (e.g., medication orders), sandboxed and logged EHR interactions, and monitoring for drift or

regressions. Finally, integration must align with institutional risk management and applicable regulatory review processes, including documentation of intended use, validation against representative clinical workflows, post-deployment monitoring, and incident reporting. These practical constraints shape not only whether an agent is accurate, but whether it is deployable in routine care.

4.1. *Limitations*

Task Design. When developing benchmarks to evaluate clinical agents, it is important to analyze how tasks are constructed and whether they realistically reflect the constraints of clinical settings. In the case of MedAgentBench, we observed that ambiguous or under-specified instructions frequently led to agent failures, not necessarily due to reasoning flaws, but due to unclear expectations. Furthermore, the task instructions used in both MedAgentBench and our study were often overly explicit, providing detailed descriptions and well-structured conditional logic.

This does not fully mirror real-world clinical practice, where physicians may issue terse, implicit instructions and expect the system to infer missing context. In practice, clinicians are unlikely to write out full logical conditions or explain task dependencies in natural language; they expect systems to 'just understand.' Developing agents that can reliably interpret such underspecified instructions remains an open challenge and will be critical for enabling real-world deployment. As such, future benchmarks should aim to capture this mismatch and evaluate agents in settings where instruction quality varies and contextual inference is necessary.

Evaluation Design. In some cases, the agent arrived at a correct response, but outputted it in an unexpected format. As a result, the evaluation function, designed for expected response formats, flagged these responses as incorrect. This issue of rigid format matching was also observed in the original MedAgentBench evaluation approach, where correct outputs were marked incorrect due to being incorrect in structure. This highlights the need for more flexible and semantically aware evaluation mechanisms when outputs vary in formatting or expression.

4.2. *Future Work*

Context Engineering. As LLM agents become more capable, the bottleneck is no longer just model performance; it's whether the model has been given the right context to succeed. Our study shows that when provided with well-structured prompts, curated tools, and clear instructions, agents can reliably perform complex clinical tasks. However, in real-world deployments, such ideal inputs are rare. Bridging this gap requires more than prompt engineering; it requires context engineering.

Going forward we see context engineering as the 'last mile' problem in clinical AI: not a model change, but a system design challenge. Done well, context engineering can turn LLMs into trustworthy clinical assistants that learn, adapt, and reason with precision.

Additionally, we would like to see benchmarks that qualitatively assess how an agent performs on tasks with multiple correct answers, such as "get me the patient history". A

possible first step for medical AI's deployment could be getting relevant context for a physician to make diagnoses and aid with clinical decision making.

Code

Code is publicly available at: https://github.com/ericoericochen/medagentbenchv2.

Appendix A.

Appendix A.1. *System Prompt*

System Prompt

You are an expert medical AI agent.

You will be given a clinical task to perform that involves interacting with a FHIR-compliant EHR system.

Everything you need to complete the task is in the EHR. Do not ask any clarifying questions to the user.

Take your time and think through every step. You MUST plan extensively before each function call, and reflect extensively on the outcomes of the previous function calls.

You have access to the following tools:

- fhir_patient_search: search and filter for patients using FHIR search params
- calculator: evaluate mathematical expressions in python
- fhir_observation_search: search for observations for a patient by code
- fhir_vitals_create: file vital signs for all flowsheets
- fhir_vitals_search: search for vital signs
- fhir_procedure_search: search for procedures
- fhir_condition_search: search for conditions
- fhir_medication_request_create: create a medication request
- fhir_medication_request_search: search for medication requests
- fhir_service_request_create: create a service request
- finish: respond with the final answer in the correct data type

ALWAYS use the finish tool to respond with your final answer. The output format will be stated in the instructions or context.

You should always respond with an answer. IT IS IMPORTANT THAT THE TYPE OF ANSWER IS CORRECT. If a value is a number, DO NOT respond with the string version of it. There should not be empty responses like []. Below are good vs. bad examples.

GOOD Examples:

```
finish({ value: [-1] })
finish({ value: ["S6330912"] })
finish({ value: [10] })
finish({ value: [5.5, "2023-11-13T10:15:00+00:00"] })
```

BAD Examples:

```
finish({ value: [] })
finish({ value: ["-1"] })
finish({ value: ["10"] })
```

<guidelines>

- Write a detailed step-by-step plan on how you would execute the task. MAKE SURE TO INTERPRET THE INSTRUCTIONS CORRECTLY.
- Always paraphrase and validate the instruction at the beginning of your plan, including identifying any conditional logic.
- Carefully interpret conditional phrases. For example, if an instruction says "If X, then do Y, and also do Z", treat both Y and Z as conditional unless Z is clearly independent.
- Do not perform any action unless all of its stated preconditions are satisfied.
- Validate every instruction before execution. Avoid assumptions.
- Supply all necessary parameters to search calls; the more specific, the better.
- Always use the calculator tool for math operations (e.g., addition, subtraction, dose).
- In your final response, respond only with the specific value requested. No units.
- Format dates as ISO strings.

</guidelines>

<memory> </memory>

You must be especially cautious about performing actions only when their preconditions are satisfied. Misinterpreting conditional statements can lead to clinically inappropriate or unnecessary actions.

Appendix A.2. *Memory Prompt*

Memory Augmentation Instruction

```
Add memory to the current_prompt. Since the current agent doesn't handle
this task correctly, write instructions for a correct approach to the
agent's memory so that when it sees the task again, it gets it right.
Think about the task description, the agent's previous response, and
what the evaluation function tests to figure out why the agent got the
wrong response.

Use 1--3 sentences to correct its MAIN mistake. Start your response
with:
when asked "...", ...

Example Response: when asked "If low, then order replacement IV
magnesium according to dosing instructions.", low indicates a value
below 1.5 mg/dL.

<task_description> {task_description} </task_description>
<agent_response> {agent_response} </agent_response>
<eval_output> {eval_result} </eval_output>
<current_prompt> {system_prompt} </current_prompt>
```

Appendix A.3. *New Tasks*

Table A1. Broad categories for new tasks

Broad Category	**Example Instruction**	**Example Context**
Imaging surveillance *(Tasks 1 & 5)*	"Confirm patient S6315806 has a malignant neoplasm of left kidney diagnosis. If true and the last CT Abdomen/Pelvis is more than 3 months old, order a new CT and referral to Interventional Radiology."	"The ICD-10 code for malignant neoplasm of left kidney is C64.2. The CPT code for CT Abdomen/Pelvis with IV contrast is 74177 (for oncologic follow-up). The CPT code for Interventional Radiology referral is CON417 with the request: 'Evaluate renal mass for biopsy or ablation.'"
Medication order validation *(Tasks 2 & 8)*	"Verify that every active opioid analgesic order for patient S6474456 has a matching naloxone prescription. If an opioid order is active without naloxone, create a naloxone order."	"Opioid medications to search for include hydromorphone, oxycodone, fentanyl, hydrocodone, morphine. The naloxone order is naloxone nasal spray 4 mg."
Observation data analysis (Task 3)	"Calculate the average heart rate over the past 6 hours and the past 12 hours for patient S6315806."	"The code for heart rate is 'HEARTRATE'. It's 2023-11-07T22:47:00+00:00 now"
Device monitoring *(Task 4)*	"Check if patient S6315806 has a urinary catheter that has been in place for more than 48 hours without a documented removal order. If so, create a service request to remove the catheter."	"The procedure code for urinary catheter is 'NUR1373'. It's 2023-11-16T10:00:00+00:00 now."
Clinical observation monitoring *(Tasks 6 & 7)*	"Retrieve the most recent TSH and free T4 values for patient S6474456. Based on the results, take appropriate action according to the protocol."	"The code for TSH is 'TSH' and for free T4 is 'FT4'. Protocol: If TSH ¿ 10 uIU/mL on two separate instances of lab values (separated by at least one month in date of lab collection), start levothyroxine 25 mcg PO daily and order repeat TSH/FT4 in 6 weeks. If TSH is 4.5–10 uIU/mL and free T4 is normal (0.8–1.8 ng/dL), order repeat TSH/FT4 in 3 months (no medication yet)."
Preventive immunization management *(Tasks 9 & 10)*	"Determine the date of the last influenza vaccine for patient S6474456. If it was administered more than 365 days ago, order a new influenza vaccine for today."	"It's 2024-01-09T00:00:00+00:00 now. The CPT code for influenza vaccine is 90686. The vaccine to order is influenza vaccine (quadrivalent, preservative-free, IM) for today."

Appendix A.4. *Time Cost Analysis*

Table A2. Comparative analysis of token consumption, tool usage, latency, and cost across representative tasks executed with the `gpt-4.1` model. Total Token Usage denotes the average number of tokens consumed per task, capturing both input and output tokens. Tool Calls indicates the average number of tool invocations performed by the agent during a single run; this value varies depending on whether the agent's instructions require additional reasoning or data retrieval. Latency reports the average end-to-end response time in seconds. Total Cost quantifies the average expense per task, calculated using the standard OpenAI pricing model based on input and output token usage.

Task	Total Token Usage	Tool Calls	Latency (sec)	Total Cost ($)
Task 1	6,291	2	7.805	0.0141
Task 2	10,068	3	11.560	0.0222
Task 3	10,791	3	18.254	0.0249
Task 4	14,766	2.2	20.632	0.0237
Task 5	10,937	2.4	20.524	0.0247
Task 6	10,074	2	16.892	0.0232
Task 7	32,415	3	14.470	0.0667
Task 8	6,596	2	12.874	0.0157
Task 9	25,102	2.2	20.324	0.0535
Task 10	8,697	2.4	18.118	0.0206

References

1. Y. Jiang, K. C. Black, G. Geng, D. Park, J. Zou, A. Y. Ng and J. H. Chen, Medagentbench: A realistic virtual ehr environment to benchmark medical llm agents (2025).
2. H. S. Saag, K. Shah, S. A. Jones, P. A. Testa and L. I. Horwitz, Pajama time: Working after work in the electronic health record, *Journal of General Internal Medicine* **34**, 1695 (2019).
3. A. Pal, L. K. Umapathi and M. Sankarasubbu, Medmcqa : A large-scale multi-subject multi-choice dataset for medical domain question answering (2022).
4. D. Jin, E. Pan, N. Oufattole, W.-H. Weng, H. Fang and P. Szolovits, What disease does this patient have? a large-scale open domain question answering dataset from medical exams (2020).
5. Q. Jin, B. Dhingra, Z. Liu, W. W. Cohen and X. Lu, Pubmedqa: A dataset for biomedical research question answering (2019).
6. R. K. Arora, J. Wei, R. S. Hicks, P. Bowman, J. Quiñonero-Candela, F. Tsimpourlas, M. Sharman, M. Shah, A. Vallone, A. Beutel, J. Heidecke and K. Singhal, Healthbench: Evaluating large language models towards improved human health (2025).
7. T. Kojima, S. S. Gu, M. Reid, Y. Matsuo and Y. Iwasawa, Large language models are zero-shot reasoners (2023).
8. T. B. Brown, B. Mann, N. Ryder, M. Subbiah, J. Kaplan, P. Dhariwal, A. Neelakantan, P. Shyam, G. Sastry, A. Askell, S. Agarwal, A. Herbert-Voss, G. Krueger, T. Henighan, R. Child, A. Ramesh, D. M. Ziegler, J. Wu, C. Winter, C. Hesse, M. Chen, E. Sigler, M. Litwin, S. Gray, B. Chess, J. Clark, C. Berner, S. McCandlish, A. Radford, I. Sutskever and D. Amodei, Language models are few-shot learners (2020).
9. P. Chhikara, D. Khant, S. Aryan, T. Singh and D. Yadav, Mem0: Building production-ready ai agents with scalable long-term memory (2025).

Automated Evaluation of Large Language Model Response Concordance with Human Specialist Responses on Physician-to-Physician eConsult Cases

David JH Wu[1*], Fateme Nateghi Haredasht[2*], David Wu[3*], Vishnu Ravi[4,5*], Liam G. McCoy[6,7,8], Yingjie Weng[9], Kanav Chopra[2], Selin S. Everett[5], George Nageeb[5], Wenyuan Chen[2], Stephen P. Ma[10], Saloni Kumar Maharaj[10], Jessica Tran[10], Leah Rosengaus[11], Lena Giang[11], Olivia Jee[12], Ethan Goh[2,13,†,‡] Jonathan H Chen[2,10,13,14,‡]

[1]Department of Radiation Oncology, Stanford Cancer Center, Palo Alto, CA, USA

[2]Stanford Center for Biomedical Informatics Research, Stanford, CA, USA

[3]Department of Dermatology, Mass General Brigham, Harvard Medical School, Boston, USA.

[4]Stanford Mussallem Center for Biodesign, Stanford University, Stanford, CA, USA

[5]Stanford University, School of Medicine, Stanford, CA, USA

[6]Division of Neurology, Faculty of Medicine and Dentistry, University of Alberta, Edmonton, AB, Canada

[7]Department of Medicine, Beth Israel Deaconess Medical Center, Boston, MA, USA

[8]Institute for Medical Engineering and Science, Massachusetts Institute of Technology, Cambridge, MA, USA

[9]Quantitative Sciences Unit, Stanford University, School of Medicine, Stanford, CA, USA

[10]Division of Hospital Medicine, Stanford University, School of Medicine, Stanford, CA, USA

[11]Stanford Health Care, Stanford Medicine, Palo Alto, CA, USA

[12]Division of Primary Care and Population Health, Stanford University School of Medicine, Palo Alto, CA, USA

[13]Clinical Excellence Research Center, Stanford School of Medicine, Stanford, CA, USA

[14]Department of Medicine, Stanford University, Stanford, CA, USA

*These authors contributed equally: David JH Wu, Fateme Nateghi Haredasht, David Wu, Vishnu Ravi

† Email: ethangoh@stanford.edu

‡ These authors jointly supervised this work: Ethan Goh, Jonathan Chen

Specialist consults in primary care and inpatient settings typically address complex clinical questions beyond standard guidelines. eConsults have been developed as a way for specialist physicians to review cases asynchronously and provide clinical answers without a formal patient encounter. Meanwhile, large language models (LLMs) have approached human-level performance on structured clinical tasks, but their real-world effectiveness requires evaluation, which is bottlenecked by time-intensive manual physician review. To address this, we evaluate two automated methods: LLM-as-judge and a decompose-then-verify framework that breaks down AI answers into verifiable claims against human eConsult responses. Using 40 real-world physician-to-physician eConsults, we compared AI-generated responses to human answers using both physician raters and automated tools. LLM-as-judge outperformed decompose-then-verify, achieving human-level concordance assessment with F1-score of 0.89 (95% CI: 0.750, 0.960) and Cohen's kappa of 0.75 (95% CI 0.47,0.90) , comparable to physician inter-rater agreement κ = 0.69-0.90 (95% CI 0.43-1.0).

Keywords: Large Language Models; LLM-as-a-judge; eConsult; Medical Consult Answering; Decompose-then-Verify; Concordance

1. Introduction

Electronic consultations (eConsults) expand specialist access by enabling generalists to asynchronously obtain expert advice without an in-person referral. Real-world studies have demonstrated faster care and clinical quality comparable to face-to-face consults[1,2]. Despite growing adoption, eConsult programs often face workflow bottlenecks for both referring physicians and specialists, as formulating high-quality consults and responses requires retrieving dispersed clinical data, synthesizing relevant context, and drafting clear, actionable recommendations. These challenges have prompted growing interest in AI systems that can streamline and augment key steps in the consultation workflow. Early pilot use cases of large language models (LLMs) reduce inbox burden and documentation time[3–5] and now match or surpass clinicians on standardized medical vignettes[4,6–12] and, when paired with physicians, can boost diagnostic accuracy[13–15].

Stanford Health Care operates a mature multispecialty eConsult program that generates a retrospective corpus of real physician-to-specialist consults. This dataset includes question-and-answer pairs with accompanying clinical context—offering a valuable resource for evaluating AI systems in realistic workflows. As part of ongoing efforts to augment end-to-end eConsult workflows, we have been developing SAGE (Specialist AI Guiding Experts), a system combining vector embeddings, predictive models, and generative AI to route clinical queries to the correct specialty, retrieve relevant chart information, suggest evidence-backed recommendations, and draft specialist-level replies to physician queries.

© 2025 The Authors. Open Access chapter published by World Scientific Publishing Company and distributed under the terms of the Creative Commons Attribution Non-Commercial (CC BY-NC) 4.0 License.

Recent LLM evaluation studies rely on polished vignettes or synthetic benchmarks that sanitize the inherent ambiguity and incompleteness of real-world cases[16,17]. Real-world perturbations, such as changes in geography, patient demographics, idiosyncratic phrasing, or missing context, can swing diagnostic accuracy by 20 percentage points[18], suggesting current benchmarks overestimate clinical readiness. Moreover, human evaluation of LLM outputs is labor-intensive, costly, and difficult to scale. Researchers are responding by developing more comprehensive benchmarks to evaluate their performance[19–23].

In this study, we compare two scalable, LLM-assisted evaluation methods against human specialist ratings on a diverse set of real eConsults: (1) an LLM-as-judge approach directly scores concordance between SAGE drafts and human responses; (2) a decompose-then-verify framework, inspired by and adapted from current existing methods MedScore, VeriFact, which breaks AI outputs into atomic claims for fact-checking[24,25]. We benchmark both approaches against blinded ratings from board-certified specialists to determine whether LLM-assisted grading can reliably and efficiently approximate human judgment when comparing AI versus expert concordance. By assessing robustness across multiple specialties and noisy, unstructured cases, we ask whether these methods provide reliable, low-cost grading that can keep pace with rapid model iterations, ultimately enabling safer, large-scale deployment of LLM-augmented eConsult workflows.

2. Methods:

2.1 Data Collection and Study Population

A random sampling of 50 physician-to-physician eConsult pairs performed from October 2022 to March 2024 was collected from Stanford Health Care's clinical data. The eConsult program was initiated as a way for general physicians to consult advanced specialties such as dermatology and hematology virtually via the EHR. Relevant consult notes were extracted from the EHR using structured metadata (e.g., specialty, consult type, and date ranges) and keyword-matched section headers (e.g., “eConsult Question” and “eConsult Response”). All data were de-identified using the Safe Harbor method according to National Institute of Standards and Technology (NIST) guidelines, and the clinical text was further anonymized using the TiDE algorithm to ensure compliance with privacy regulations. The answering physicians in eConsult provided clinical recommendations based solely on chart review and did not see the patient or perform a physical examination. Based on physician discretion, some patients would be deemed medically appropriate for referral to their respective specialty clinic. The eConsult program did not permit back-and-forth conversation between physicians. If the consulting physician’s question could not be answered satisfactorily, the patient was referred to the specialty clinic for further evaluation, or the consult was declined due to reasons such as the wrong scope of specialty or lack of clarifying details. The eConsult consult-and-answer pairs were then de-identified again using a BERT-based method and manually reviewed by DW, DJW to confirm removal of any identifying information. Duplicate, incomplete, or erroneous consults were excluded from the study. This study was conducted with IRB approval (IRB-47618) to ensure compliance with ethical research standards.

Age Range (years)	
18–34	3 (7.5%)
35–49	13 (32.5%)
50–64	8 (20%)
≥65	16 (40%)
Sex	
Female	27 (67.5%)
Male	12 (32.5%)
Medical Specialties Included (Each containing at least 2 eConsults)	
Cardiology, Endocrinology, Gastroenterology, Immunology, Infectious Diseases, Neurology, Obstetrics/Gynecology, Hematology/Oncology, Psychiatry, Pulmonology.	

Table 1*: Patient eConsult demographics by consult type, age, and sex.*

2.2 AI eConsult Response Generation

AI responses were generated using a secure, HIPAA-compliant large language model instance ("SecureGPT") approved for PHI analysis at Stanford University, utilizing OpenAI GPT-4.1 as the underlying model. A standardized prompt was developed to structure AI responses into Assessment, Recommendations and Rationale, Contingency Plan, and Citations sections. To provide appropriate clinical context, the three most recent clinical Progress Note with length >3,500 characters (we found in initial pilot work that those less than this cut-off were more likely to be clerical notes without meaningful clinical significance), prioritizing the consulted specialty in question, were also provided in the API query, as well as the 20 most recent lab values.

2.3 LLM-assisted Concordance Evaluation

To assess the concordance between AI-generated and human-generated eConsult responses, we developed two LLM-assisted evaluation workflows, with the original specialist consult answer as a "silver-label answer". For our two LLM-assisted concordance evaluation workflows, one was based on using *LLM-as-Judge (LaJ)* and the other using a *Decompose-then-Verify* (*DtV)* approach.

In our *LaJ* approach, we provided a concordant and discordant example case not included in the data set to provide as a reference in the prompt (Supplemental Fig. 2). API calls were made using a secure, HIPAA-compliant, and PHI-safe institution-specific endpoint and automated python script.

In our *DtV* approach, we implemented a two-stage pipeline adapted from and inspired by the MedScore and VeriFact frameworks[22,23]. First, AI responses were decomposed into atomic, independently verifiable medical claims using a specialized LLM query. Second, each atomic claim was verified against the original human specialist response using a separate verification query. Claims with ≥80% support percentage were classified as concordant. The pipeline was implemented in Python. Three of the authors (DJW, DW, LM) not involved in the final physician review reviewed 4 examples of cases decomposed into atomic claims and their corresponding LLM-assisted verification. Consensus determination was that overall performance was satisfactory, and a sampling of these cases was included as examples in both the decomposition and the verification prompt.

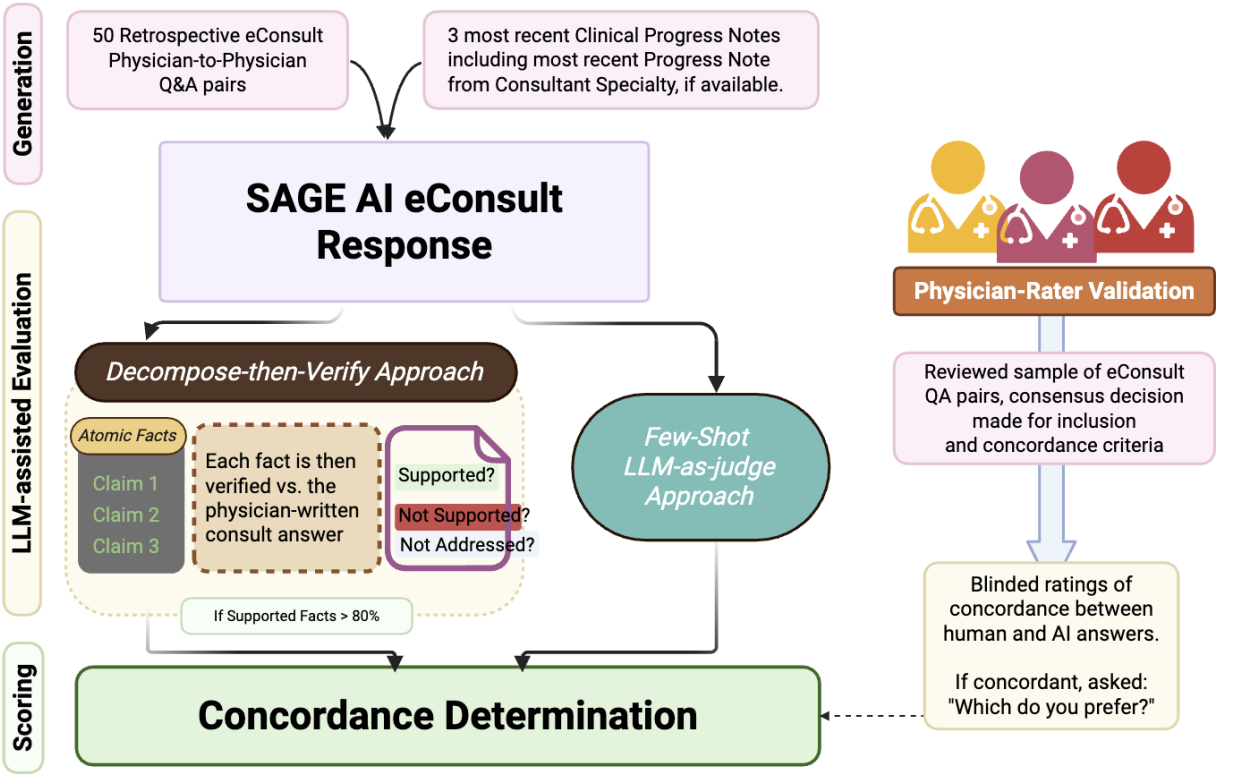

Figure 1: *Schematic of study design. 50 real-world retrospective eConsult cases were collected. We provided the original consult question as well as clinical context consisting of the three most recent clinical progress notes and 20 most recent lab values, generating an AI e-Consult response. We then manually assessed concordance of the AI response to human response and also performed LLM-assisted automated concordance evaluations.*

2.4 Human Physician Evaluation

Forty eConsult question-and-answer pairs were provided to three blinded attending internal medicine attending physicians (VS, SM, JT) for concordance evaluation. Physicians rated concordance between AI-generated and human specialist responses on a binary scale (1 = Concordant, 0 = Discordant). For concordant cases, raters indicated their preference between the

AI and human responses. For equipoise, only cases in which AI and human were rated as concordant were used in Preference rating. Prior to rating, the physician reviewers participated in a calibration session to establish consensus on concordance definitions and rating criteria.

2.5 Statistical Analysis

Aggregate physician concordance ratings were determined by majority vote (best-of-three). Inter-rater agreement among the three physician evaluators was calculated using Fleiss' kappa for multi-rater categorical data. Agreement between physician ratings and LLM-assisted concordance evaluations was assessed using Cohen's kappa for pairwise comparisons. Kappa values were interpreted as: <0.20 (poor), 0.21-0.40 (fair), 0.41-0.60 (moderate), 0.61-0.80 (substantial), and 0.81-1.00 (almost perfect) agreement.

Performance metrics for both LLM evaluation approaches were calculated, including sensitivity, specificity, precision, recall, and F1-score (calculated as harmonic mean of precision and recall) using physician majority vote as the reference standard. Ninety-five percent confidence intervals for all kappa and F1 coefficients were calculated using bias-corrected and accelerated (BCa) bootstrap resampling. The BCa method accounts for both bias and skewness in the bootstrap distribution, providing more accurate coverage than standard percentile methods. All statistical analyses were performed using Python with scikit-learn and statsmodels libraries.

3. Results

3.1 LLM-Assisted Concordance Evaluation Performance

Forty eConsult cases were included in the final analysis after excluding duplicate, incomplete, or erroneous eConsults, with an equal distribution of 20 concordant and 20 discordant cases based on physician majority vote. Both LLM evaluation approaches demonstrated substantial performance in concordance assessment, with LaJ consistently outperforming the DtV approach (Figure 2). The DtV approach achieved moderate performance (F1-score: 0.73 [95% CI: 0.55, 0.86], $\kappa = 0.40$, [95% CI: 0.12, 0.65]), while LaJ methods showed substantial to near-perfect agreement. Among LaJ implementations, DeepSeek R1 achieved the highest performance (F1-score: 0.89 [95% CI: 0.750, 0.960], $\kappa = 0.75$, [95% CI: 0.47, 0.90]), followed by Gemini 2.5 Pro (F1-score: 0.86 [95% CI: 0.44, 0.89], $\kappa = 0.70$, [95% CI: 0.44, 0.89]). All LaJ approaches demonstrated superior concordance evaluation compared to the claim-based DtV method.

The DtV pipeline decomposed AI responses into an average of 24.9 atomic claims per case (range: 17-34 claims). Of these claims, 41.0% were classified as "Supported," 10.1% as "Not Supported," and 48.9% as "Not Addressed" by the reference specialist consult answer, suggesting a significant amount of extra information added in the AI consult answers. ROC analysis of the support percentage threshold revealed an AUC of 0.745.

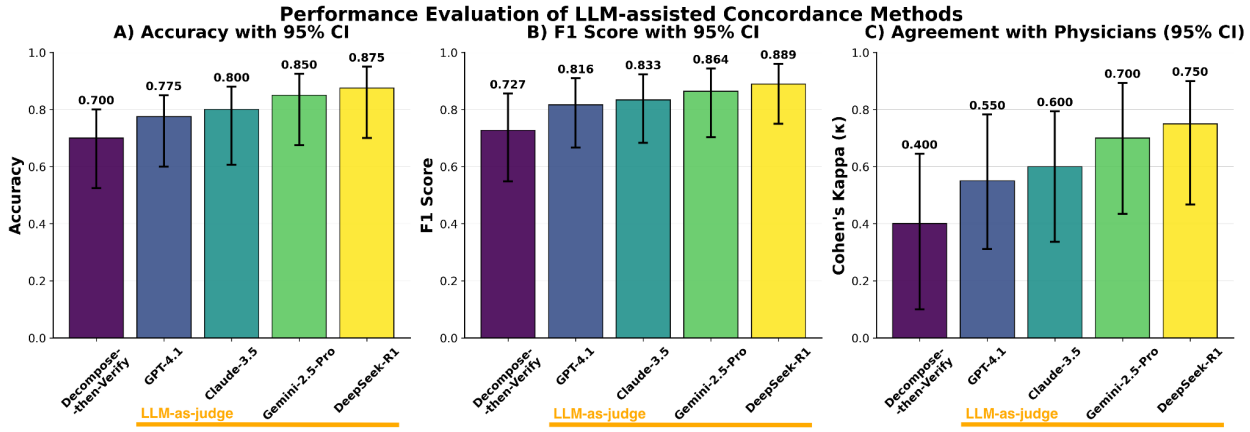

Figure 2: *Three-panel comparison showing (A) Accuracy, (B) F1-score, and (C) Cohen's kappa agreement with physician majority vote for five different approaches. LLM-as-Judge methods (GPT-4.1, Gemini 2.5 Pro, DeepSeek R1, Claude 3.5) consistently outperformed the Decompose-then-Verify approach across all metrics. DeepSeek R1 achieved the highest performance with near-human-level agreement (κ = 0.75,* 95% CI 0.47-0.90*)*

3.2 Physician and LLM Inter-Rater Concordance Agreement

Inter-rater agreement among the three physician evaluators was moderate (Fleiss' κ = 0.456, n=32). Perfect agreement across all three raters occurred in 61.3% of cases, indicating variability in concordance assessment even among experienced clinicians. Individual physician agreement rates with the aggregate majority vote were substantial: Physician 1 (κ = 0.90, 95% CI 0.70-1.0), Physician 2 (κ = 0.69, 95% CI 0.43-0.88), and Physician 3 (κ = 0.69, 95% CI 0.42-0.89), with Physician 1 demonstrating the highest consistency with the consensus rating. Pairwise agreement between individual physicians showed moderate agreement: Physician 1 vs Physician 2 (κ = 0.57), Physician 1 vs Physician 3 (κ = 0.59), and Physician 2 vs Physician 3 (κ = 0.34). When comparing LLM-assisted methods to individual physician raters, several patterns emerged (Figure 3). DeepSeek R1 achieved substantial agreement with all three physicians (κ = 0.65, 0.61, 0.55), while Gemini 2.5 Pro demonstrated strong agreement with Physicians 1 and 2 (κ = 0.70, 0.61) but more moderate agreement with Physician 3 (κ = 0.44). The Decompose-then-Verify approach showed consistently moderate agreement across all physician raters (κ = 0.40, 0.30, 0.42). Notably, the best-performing LLM methods achieved agreement levels with individual physicians that were comparable to inter-physician agreement

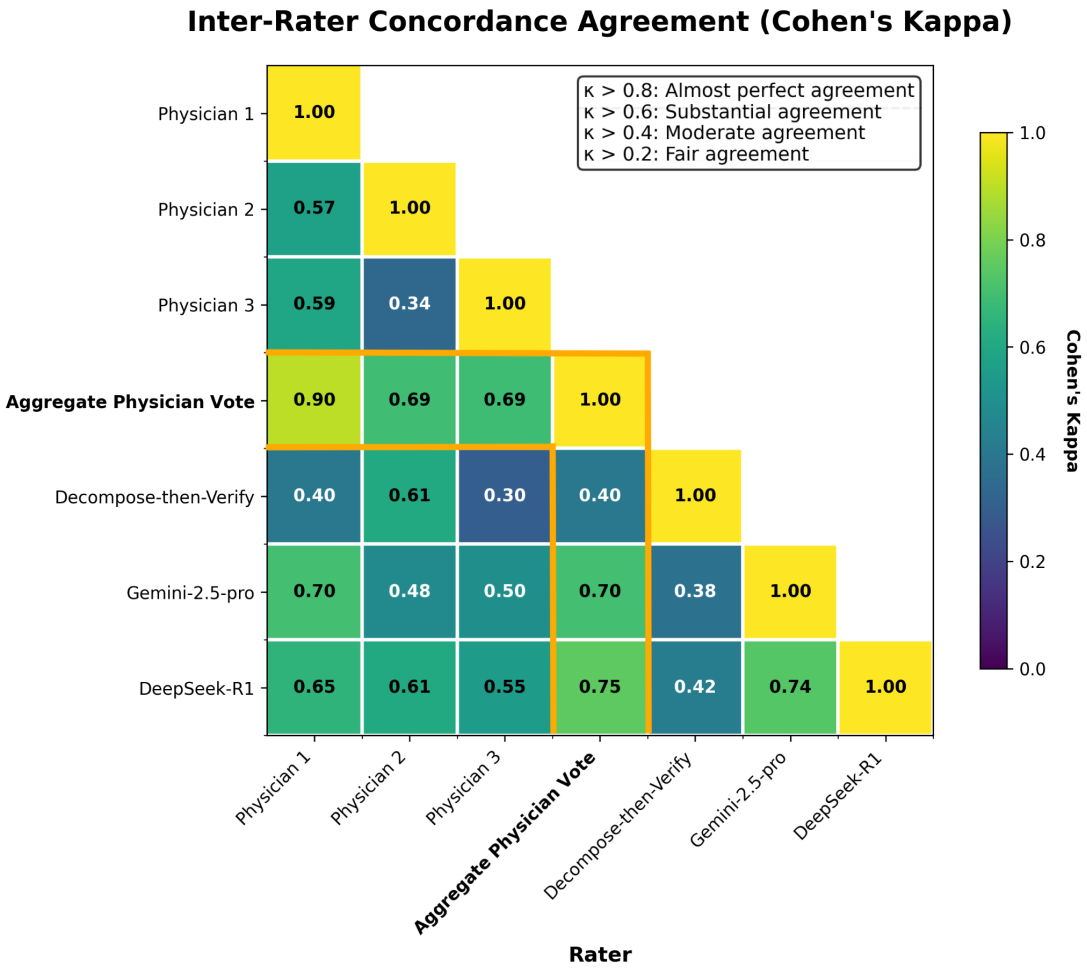

Figure. 3: **Inter-rater Agreement Heatmap for Concordance Evaluation.** *Cohen's kappa coefficients between all rater pairs, displayed as a lower-triangular heatmap. Values range from 0 (no agreement) to 1 (perfect agreement), with darker colors indicating higher agreement. The aggregate physician vote represents majority consensus among the three physician raters. LLM-assisted methods (DeepSeek R1, Gemini 2.5 Pro) achieved substantial agreement with physician raters, comparable to inter-physician agreement levels.*

3.3 Physician Preference Analysis

Among the 20 cases rated as concordant by majority vote, physician preferences between AI and human responses showed substantial heterogeneity (Figure 4). Individual preference patterns varied dramatically: Physician 1 preferred AI responses in 33.3% of concordant cases, Physician 3 in 12.5%, and Physician 2 in 81.8% of cases. This divergence in preferences highlights the subjective nature of response quality assessment, even when both AI and human responses are deemed clinically appropriate. Inter-rater agreement on preferences was poor (Fleiss' $\kappa = -0.12$, n=11), with pairwise agreements ranging from $\kappa = -0.23$ (Physician 1 vs Physician 3) to $\kappa = 0.19$ (Physician 1 vs Physician 2). The negative kappa values indicate systematic disagreement beyond what would be expected by chance, suggesting that physicians may have intrinsic differences in preference and criteria for those preferences, even when responses are clinically concordant.

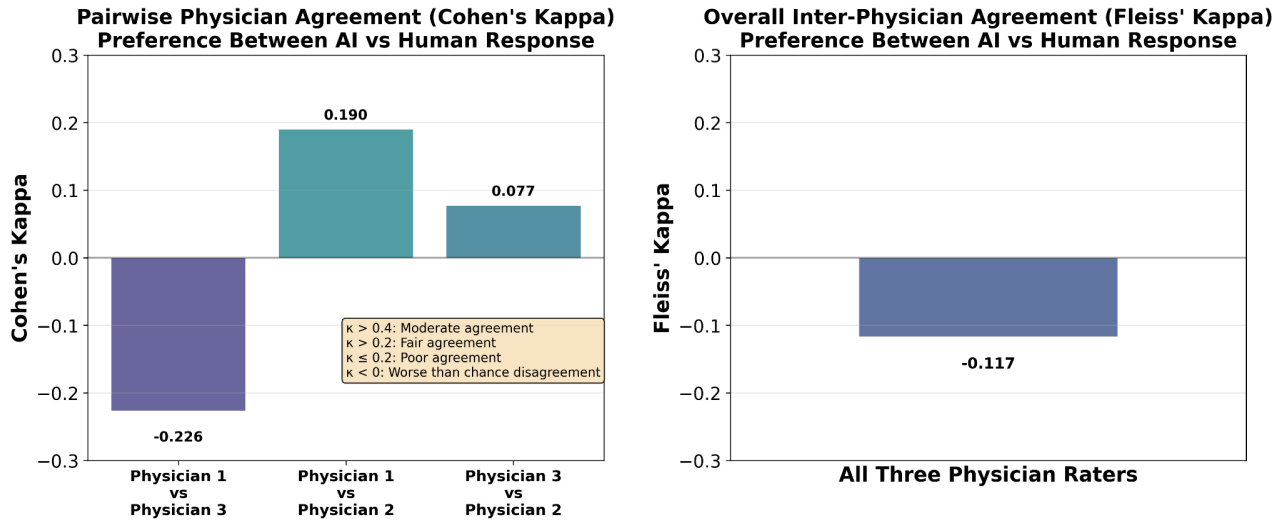

Figure 4: *(A) Pairwise Cohen's kappa coefficients between physicians for preference assessment (AI vs human responses), showing poor agreement with negative values indicating systematic disagreement. (B) Overall, Fleiss' kappa (κ = -0.12) demonstrates poor multi-rater agreement on preferences. Analysis limited to the 20 cases where all three physicians agreed responses were clinically concordant, highlighting that clinical acceptability does not predict preference uniformity*

4. Discussion

This study demonstrates that LLM-assisted evaluation of concordance between AI-generated and human specialist eConsult responses achieves substantial performance comparable to inter-physician agreement. The LLM-as-Judge approach consistently outperformed the Decompose-then-Verify method, with the best-performing model (DeepSeek R1) achieving an F1-score of 0.89 (95% CI: 0.75, 0.96) and Cohen's κ of 0.75 (95% CI: 0.47, 0.90)—approaching the range of inter-physician agreement (κ = 0.69-0.90, 95% CI: 0.43, 1.0) observed in clinical settings. This represents the first validation of automated concordance evaluation in real-world physician-to-physician eConsultations, addressing a critical bottleneck in scalable LLM evaluation for clinical applications.

Our findings address a key challenge in clinical AI evaluation: the labor-intensive nature of expert review that limits scalable assessment of LLM performance in real-world settings. Traditional evaluations rely heavily on standardized clinical vignettes, which may overestimate performance in practice due to their structured nature and absence of real-world ambiguity. By demonstrating that LLM-assisted evaluation can reliably assess concordance in unstructured eConsult cases, this work provides a pathway for large-scale retrospective benchmarking of clinical LLMs prior to deployment that can be tailored to each institution.

Interestingly, we noted substantial heterogeneity in physician preferences (Fleiss' κ = -0.12) even among concordant cases, highlighting an important distinction between clinical acceptability and physician preference: while responses may be equally acceptable from a clinical standpoint,

individual physicians maintain distinct preferences regarding communication style, comprehensiveness, and presentation format (Fig. 5). One physician rater noted that the human responses took into account factors such as insurance or even manually reviewed EKG findings themselves to provide their own insight, which is beyond the capabilities of the current AI eConsult system. Another physician favored the AI responses because they were more well-structured and readable. The substantial preference heterogeneity suggests that AI integration in clinical practice may benefit from personalization approaches and further iterative improvement that accommodate individual physician preferences while maintaining clinical appropriateness.

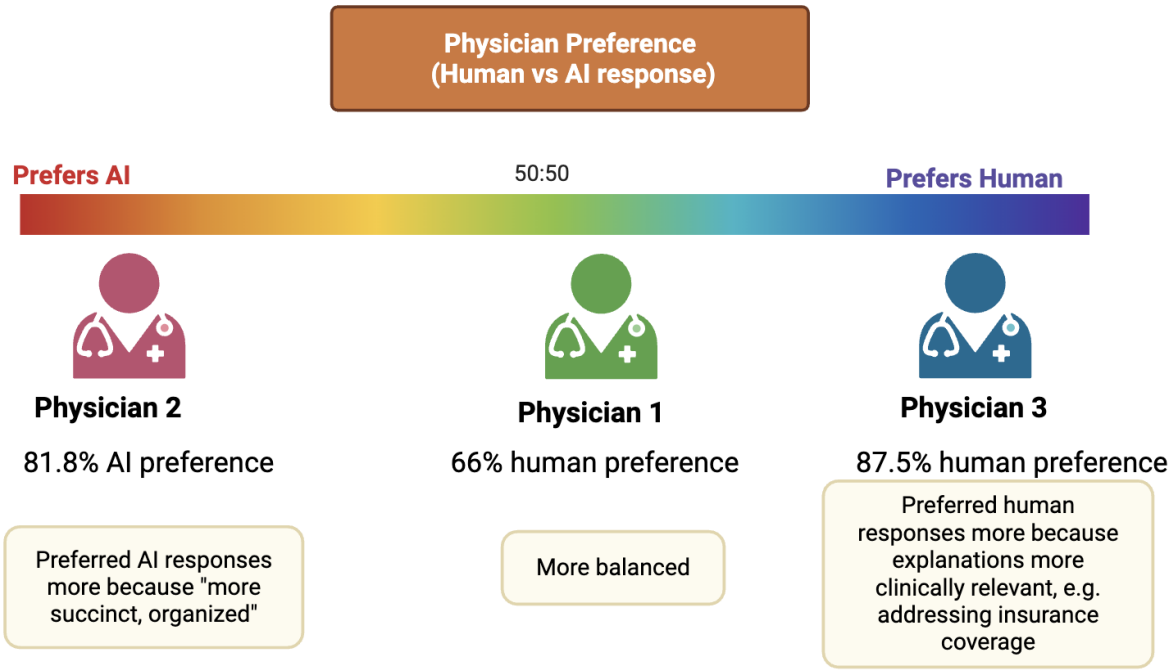

Figure 5: Physician Preference Distribution of Clinically Concordant Human vs AI responses.
Significant differences in patterns of preference were observed between our physician raters, calculated by total average preference rating per physician in clinically concordant cases.

The superior performance of LaJ over DtV approaches likely reflects the complexity of medical reasoning that is not entirely captured by simple decomposition and verification of atomic claims. Clinical decision-making often involves nuanced integration of multiple factors, contextual considerations, and implicit medical knowledge that may be lost when responses are parsed into discrete verifiable statements. The DtV approach's moderate performance suggests utility for systematic claim verification but indicates limitations for holistic clinical assessment. Interestingly, 48.9% of all claims generated were classified as ‘Not Addressed’ by the reference material, suggesting that AI responses often included extra details that the human physician did not. In discussion with the physician raters, it was usually only one or two key “atomic claims” in each case, such as the decision to start a new drug or not, that pushed them to decide whether a

case was concordant or discordant, whereas in the DtV approach each claim is weighted equally relative to the other claims.

Several limitations warrant consideration. The sample of 40 cases evaluated is not intended to generalize across specialties and clinical scenarios, but was sufficiently powered to confirm the potential for this methodology to systematically evaluate a volume of cases that would be impractical for manual review. Human specialist responses are used here as a comparison standard for comparison, but this should NOT be used to assume that actual care delivered represents optimal care decisions. Existing evidence and standards of care establish a high correlation between actual and preferred clinical decision-making, while also acknowledging legitimate and acceptable variations in clinical approaches. Our evaluation focused on concordance rather than clinical outcomes, leaving questions about whether concordant responses lead to better patient care. Concordance with human experts is thus not the only critical measure of medical advice, but an important one, especially in complex clinical scenarios where "correct" answers are often poorly defined with limited definitive evidence. It is indeed often the case where limited evidence or guidelines are available that physicians reach for specialist consultation.

During the process of analysis, we also found in discussion with our physician reviewers that concordance is difficult to rate in a binary fashion, there is often a spectrum of concordance, with some cases being definitely concordant while others fall in a gray zone; sometimes answers are concordant in their recommended intervention but differ in their contingency plans. This complexity in concordance rating likely explains the moderate inter-rater agreement among physicians, highlighting the nuances of medical reasoning and decision making that complicates concrete ground truth for clinical evaluations. We originally anticipated that the systematic decomposition and then claim-by-claim verification of the DtV method would better capture these nuances but were ultimately surprised by the superior and human-level performance of the LaJ approach, hinting at the rapid improvement of these models' innate clinical reasoning abilities on a clinical concordance determination task that is difficult even for licensed physicians.

Conclusion

This study demonstrates that large language models can be evaluated on real-world physician-to-physician eConsults using automated concordance methods, with LLM-as-Judge (LaJ) approaches achieving performance comparable to human physician raters. Compared to decomposition-based verification methods, LaJ more reliably captured overall clinical concordance between AI- and human-generated responses. These findings suggest that automated, LLM-based clinical evaluation methods can benchmark the performance of AI in clinical practice in a scalable fashion, especially in the eConsult setting, promising to ultimately expand patient access to specialty care through broader adoption of AI-augmented care and contribute to physician wellness by reducing the cognitive burden of conducting these consults.

Supplemental Fig. 1 – Example Case: Hematologic eConsult

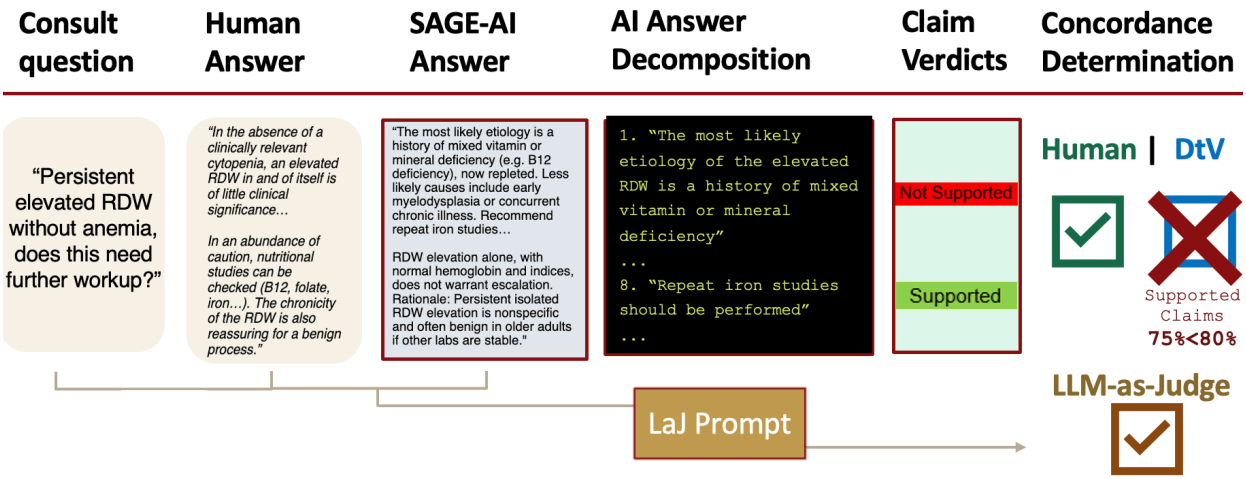

Supplemental Figure 1: An example case consisting of human consult question, human answer, SAGE-AI answer, the decomposition of the AI answer into atomic claim, LLM-determined claim verdicts, and final concordance determination of human physician composite rating, DtV rating, and LLM-As-Judge.

Supplemental Fig. 2 – LLM-as-judge Concordance Prompt

PROMPT = """You are a medical expert evaluating concordance between two clinical answers. Your task is to determine if both answers are medically consistent and aligned in their core recommendations.

CONCORDANCE DEFINITION:

- Concordant (1): Both answers provide medically consistent recommendations, diagnoses, or treatment approaches that do not contradict each other, even if they differ in detail level or phrasing

- Discordant (0): The answers contain medically contradictory information, conflicting recommendations, or fundamentally different clinical approaches

EVALUATION CRITERIA:

Focus on medical substance over style differences:

- Do both answers reach similar clinical conclusions?
- Are the treatment recommendations compatible?
- Do they identify the same key medical issues?
- IMPORTANT: If the AI recommends a medication or intervention that the human doesn't recommend, or contradicts what the human recommends, mark as discordant
- Ignore differences in: formatting, verbosity, organization, or minor procedural details

RESPONSE FORMAT: Respond ONLY with valid JSON:

{{"concordant": 1, "explanation": "Brief 1-2 sentence explanation focusing on key medical alignment or contradiction"}}

EXAMPLES:

CONCORDANT EXAMPLE:

Question: 68 yo F with history of rheumatoid arthritis, with Tchol 201 and LDL 149. Is statin indicated?

Answer A (Human): Based on 10-year ASCVD risk of 10.5-13.6%, moderate intensity statin is indicated.

Answer B (AI): Start moderate-intensity statin therapy (e.g., atorvastatin 20 mg daily) for primary prevention, as RA is considered a risk-enhancing factor.

Evaluation: {{"concordant": 1, "explanation": "Both answers agree on starting moderate-intensity statin therapy based on elevated ASCVD risk factors."}}

DISCORDANT EXAMPLE:

Question: Patient with hypothyroidism, TSH 33.03, on levothyroxine 100mcg daily. Please help manage/adjust.

Answer A (Human): Check TSH and Free T4 now. Dose will have to be adjusted based on repeat labs.

Answer B (AI): Increase levothyroxine to 125 mcg daily, repeat TSH and free T4 in 4-6 weeks to assess response.

Evaluation: {{"concordant": 0, "explanation": "Human recommends checking labs first before dose adjustment, while AI recommends immediate dose increase - contradictory management approaches."}}

Now evaluate the following:

Question: {question}.
Answer A (Human): {answer}.
Answer B (AI): {ai_output}:"""

Bibliography

1. Palen TE, Price D, Shetterly S, Wallace KB. Comparing virtual consults to traditional consults using an electronic health record: an observational case–control study. *BMC Medical Informatics and Decision Making*. 2012;12(1):65. doi:10.1186/1472-6947-12-65

2. Peeters KMM, Reichel LAM, Muris DMJ, Cals JWL. Family Physician–to–Hospital Specialist Electronic Consultation and Access to Hospital Care: A Systematic Review. *JAMA Network Open*. 2024;7(1):e2351623. doi:10.1001/jamanetworkopen.2023.51623

3. Garcia P, Ma SP, Shah S, et al. Artificial Intelligence-Generated Draft Replies to Patient Inbox Messages. *JAMA Netw Open*. 2024;7(3):e243201. doi:10.1001/jamanetworkopen.2024.3201

4. Hirosawa T, Kawamura R, Harada Y, et al. ChatGPT-Generated Differential Diagnosis Lists for Complex Case-Derived Clinical Vignettes: Diagnostic Accuracy Evaluation. *JMIR Med Inform*. 2023;11:e48808. doi:10.2196/48808

5. Wu DJ, Bibault JE. Pilot applications of GPT-4 in radiation oncology: Summarizing patient symptom intake and targeted chatbot applications. *Radiotherapy and Oncology*. 2024;190. doi:10.1016/j.radonc.2023.109978

6. Rutledge GW. Diagnostic accuracy of GPT-4 on common clinical scenarios and challenging cases. *Learn Health Syst*. 2024;8(3):e10438. doi:10.1002/lrh2.10438

7. Rao A, Pang M, Kim J, et al. Assessing the Utility of ChatGPT Throughout the Entire Clinical Workflow: Development and Usability Study. *Journal of Medical Internet Research*. 2023;25(1):e48659. doi:10.2196/48659

8. Yavuz YE, Kahraman F. Evaluation of the prediagnosis and management of ChatGPT-4.0 in clinical cases in cardiology. *Future Cardiol*. 20(4):197-207. doi:10.1080/14796678.2024.2348898

9. Greif C, Mpunga N, Koopman IV, Pye A, Hivnor CM, Owen JL. Evaluating the effectiveness of ChatGPT4 in the diagnosis and workup of dermatologic conditions. *Dermatol Online J*. 2024;30(4). doi:10.5070/D330464104

10. Mikhail D, Milad D, Antaki F, et al. Multimodal Performance of GPT-4 in Complex Ophthalmology Cases. *J Pers Med*. 2025;15(4):160. doi:10.3390/jpm15040160

11. Galetta K, Meltzer E. Does GPT-4 have neurophobia? Localization and diagnostic accuracy of an artificial intelligence-powered chatbot in clinical vignettes. *Journal of the Neurological Sciences*. 2023;453:120804. doi:10.1016/j.jns.2023.120804

12. Brodeur PG, Buckley TA, Kanjee Z, et al. Superhuman performance of a large language model on the reasoning tasks of a physician. Published online June 2, 2025. doi:10.48550/arXiv.2412.10849

13. Goh E, Gallo RJ, Strong E, et al. GPT-4 assistance for improvement of physician performance on patient care tasks: a randomized controlled trial. *Nat Med*. 2025;31(4):1233-1238. doi:10.1038/s41591-024-03456-y

14. Goh E, Gallo R, Hom J, et al. Large Language Model Influence on Diagnostic Reasoning: A Randomized Clinical Trial. *JAMA Network Open*. 2024;7(10):e2440969. doi:10.1001/jamanetworkopen.2024.40969

15. Jabbour S, Fouhey D, Shepard S, et al. Measuring the Impact of AI in the Diagnosis of Hospitalized Patients: A Randomized Clinical Vignette Survey Study. *JAMA*. 2023;330(23):2275-2284. doi:10.1001/jama.2023.22295

16. Bedi S, Liu Y, Orr-Ewing L, et al. Testing and Evaluation of Health Care Applications of Large Language Models: A Systematic Review. *JAMA*. 2025;333(4):319-328. doi:10.1001/jama.2024.21700

17. Evaluation and mitigation of the limitations of large language models in clinical decision-making | Nature Medicine. Accessed July 31, 2025. https://www.nature.com/articles/s41591-024-03097-1

18. Asiedu M, Tomasev N, Ghate C, et al. Contextual Evaluation of Large Language Models for Classifying Tropical and Infectious Diseases. Published online January 15, 2025. doi:10.48550/arXiv.2409.09201

19. Bedi S, Cui H, Fuentes M, et al. MedHELM: Holistic Evaluation of Large Language Models for Medical Tasks. Published online June 2, 2025. doi:10.48550/arXiv.2505.23802

20. Ma MD, Ye C, Yan Y, et al. CliBench: A Multifaceted and Multigranular Evaluation of Large Language Models for Clinical Decision Making. Published online October 11, 2024. doi:10.48550/arXiv.2406.09923

21. Wu C, Qiu P, Liu J, et al. Towards evaluating and building versatile large language models for medicine. *npj Digit Med*. 2025;8(1):1-13. doi:10.1038/s41746-024-01390-4

22. Arora RK, Wei J, Hicks RS, et al. HealthBench: Evaluating Large Language Models Towards Improved Human Health.

23. McCoy LG, Swamy R, Sagar N, et al. Do Language Models Think Like Doctors? Published online February 12, 2025:2025.02.11.25321822. doi:10.1101/2025.02.11.25321822

24. Chung P, Swaminathan A, Goodell AJ, et al. VeriFact: Verifying Facts in LLM-Generated Clinical Text with Electronic Health Records. Published online January 28, 2025. doi:10.48550/arXiv.2501.16672

25. Huang H, DeLucia A, Tiyyala VM, Dredze M. MedScore: Factuality Evaluation of Free-Form Medical Answers. Published online May 24, 2025. doi:10.48550/arXiv.2505.18452

MedFactEval and MedAgentBrief: A Framework and Workflow for Generating and Evaluating Factual Clinical Summaries

François Grolleau MD, PhD[1,⋆], Emily Alsentzer PhD[2], Timothy Keyes PhD[3], Philip Chung MD, MS[4], Akshay Swaminathan BA[2], Asad Aali MS[5], Jason Hom MD[7], Tridu Huynh MD[7], Thomas Lew MD[7], April Liang MD[7], Weihan Chu MD[7], Natasha Steele MD[7], Christina Lin MD[7], Jingkun Yang MD[7], Kameron Black MD[7], Stephen Ma MD, PhD[7], Fateme N. Haredasht PhD[1], Nigam H. Shah MBBS, PhD[1,2,7], Kevin Schulman MD, MBA[6,7], Jonathan H. Chen MD, PhD[1,6,7]

[1] *Center for Biomedical Informatics Research, Stanford University, Stanford, CA, USA*
[2] *Department of Biomedical Data Science, Stanford University, Stanford, CA, USA*
[3] *Stanford Health Care, Palo Alto, CA, USA.*
[4] *Department of Anesthesiology and Pain Medicine, Stanford Medicine, Stanford, CA, USA*
[5] *Department of Radiology, Stanford University, Stanford, CA, USA*
[6] *Stanford Clinical Excellence Research Center, Stanford University, Stanford, CA, USA*
[7] *Department of Medicine, Stanford University, Stanford, CA, USA*
[⋆] *To whom correspondence should be addressed: grolleau@stanford.edu*

Evaluating factual accuracy in Large Language Model (LLM)-generated clinical text is a critical barrier to adoption, as expert review is unscalable for the continuous quality assurance these systems require. We address this challenge with two complementary contributions. First, we introduce **MedFactEval**, a framework for scalable, fact-grounded evaluation where clinicians define high-salience key facts and an "LLM Jury"—a multi-LLM majority vote—assesses their inclusion in generated summaries. Second, we present **MedAgentBrief**, a model-agnostic, multi-step workflow designed to generate high-quality, factual discharge summaries. To validate our evaluation framework, we established a gold-standard reference using a seven-physician majority vote on clinician-defined key facts from inpatient cases. The MedFactEval LLM Jury achieved almost perfect agreement with this panel (Cohen's $\kappa = 81\%$), a performance statistically non-inferior to that of a single human expert ($\kappa = 67\%, P < 0.001$). Our work provides both a robust evaluation framework (MedFactEval) and a high-performing generation workflow (MedAgentBrief), offering a comprehensive approach to advance the responsible deployment of generative AI in clinical workflows.

1. Introduction

Large Language Models (LLMs) offer substantial potential for automating clinical documentation, a primary driver of physician burnout.[1] By generating draft discharge summaries, LLMs can perform critical information synthesis, freeing time for clinicians to focus on patient care.[2,3] However, the risk of factual errors impedes their adoption.[4] These errors manifest as both errors of *omission*, where clinically vital information is excluded, and errors of *commission* (or "hallucinations"), where generated text contradicts source data or fabricates information.[5,6]

The gold standard for identifying such errors—expert human review—is prohibitively slow and expensive for the routine, iterative quality assurance these systems require. This creates a critical evaluation bottleneck, as current automated metrics (e.g., BLEU, ROUGE-L, BERT-Score) often fail to capture clinical nuance. Consequently, there is an urgent need for

© 2025 The Authors. Open Access chapter published by World Scientific Publishing Company and distributed under the terms of the Creative Commons Attribution Non-Commercial (CC BY-NC) 4.0 License.

an evaluation framework that is both scalable and replicates the clinical validity of expert judgment.

To address this challenge, this paper makes two complementary contributions. First, we introduce and validate **MedFactEval**, a framework designed to enable the fact-grounded, iterative improvement of AI systems for clinical information synthesis. Second, we introduce **MedAgentBrief**, a novel, model-agnostic LLM workflow for generating high-quality, factual discharge summaries. We then demonstrate the utility of MedFactEval by using it to benchmark the performance-cost tradeoffs of these different generation strategies.

Our specific contributions are:

1. We define the **MedFactEval** framework, which grounds evaluation in clinician-defined key facts and uses an LLM Jury for robust, scalable assessment to drive iterative model improvement.
2. We introduce and evaluate **MedAgentBrief**, a multi-step, model-agnostic workflow for generating high-fidelity clinical summaries.
3. We conduct a rigorous meta-evaluation of MedFactEval, demonstrating that our LLM Jury achieves almost perfect agreement with a seven-physician panel (Cohen's $\kappa = 81\%$) and is statistically non-inferior to a single human expert ($\kappa = 67\%, P < 0.001$).
4. We demonstrate MedFactEval's utility by benchmarking the factual performance of MedAgentBrief against a baseline single-prompt strategy.

Our primary contribution is the validation of the MedFactEval framework, establishing that an LLM Jury can serve as a reliable and scalable proxy for expert human evaluation. We then demonstrate the framework's utility by applying it to benchmark generation strategies, providing a foundational component for the safety monitoring of generative AI in clinical medicine.

2. Related Work

The evaluation of LLM-generated medical text is a rapidly evolving field. Early approaches relied on comparing AI-generated summaries against human-written references using global quality ratings from physician experts.[2,3,7] While these foundational studies established that LLMs can produce summaries of comparable quality to humans, they also highlighted a persistent risk of factual errors, including both omissions and commissions. However, such global ratings are inherently subjective and often demonstrate low inter-rater reliability. This makes them a noisy signal, insufficient for the granular, fact-based feedback required to systematically improve model factuality and ensure patient safety.

To address the need for more objective evaluation, automated fact-checking has emerged as a key area of research.[8,9] For instance, "VeriFact" is a system that retrospectively verifies claims in generated text by decomposing them into atomic facts and checking them against the entire electronic health record (EHR) using retrieval-augmented generation.[9] While powerful, this approach faces challenges: the EHR itself can be noisy or contain outdated information, and the system does not inherently know which facts are most clinically salient for a specific care context. Other work has confirmed that LLMs can struggle with fact decomposition, for example, the FactEHR effort showed that different LLMs generate up to 2.6x different number

of facts per sentence.[10] In addition, standard natural language processing metrics often fail to correlate with human judgments of factuality.[11]

Our MedFactEval framework is distinct from prior work in three key ways. First, it is designed for **ongoing evaluation of an in-use workflow** rather than for one-off, retrospective analysis, providing a mechanism for continuous quality assurance. Second, it shifts the source of ground truth from the entire, potentially noisy EHR to a small set of **clinician-defined, key facts**. This strategically reframes the ambiguous task of "is this summary good?" into a series of concrete, verifiable questions (e.g., "Does the summary include Fact X?"). This ensures the evaluation is focused on what matters most for a given patient context. Finally, it introduces an **LLM Jury** to automate this assessment, enhancing robustness and reliability over single-model judgments.[12] These design choices position MedFactEval as a pragmatic tool for both real-time quality assurance and the iterative improvement of AI systems in clinical practice.

3. Methods

3.1. *Study Setting and Data Source*

We conducted a retrospective study using a cohort of adult inpatients to validate MedFactEval, our framework for the ongoing evaluation of in-use clinical AI workflows. The cohort was drawn from patients admitted to the Division of Hospital Medicine at Stanford Health Care between January 1, 2023, and June 1, 2024. To ensure representative cases of sufficient clinical complexity, we included only patients with a hospital length of stay between 2 and 14 days. From this eligible cohort, we randomly sampled 30 patients. For each patient, we extracted the complete set of de-identified, unstructured clinical notes from the Electronic Health Record (EHR), including the History & Physical, all progress notes, and the physician-authored discharge summary.

3.2. *Generation of AI Discharge Summaries for Evaluation*

For each of the 30 cases, the collected clinical notes served as source material to generate a diverse set of draft discharge summaries. We employed two distinct AI synthesis strategies to produce summaries for evaluation.

Strategy 1: Single-Prompt Summarization. In this baseline approach, all source notes for a given patient were concatenated and provided within the context window of a foundation model. The model was then prompted to generate a complete discharge summary in a single step.

Strategy 2: MedAgentBrief Workflow. We developed MedAgentBrief, a model-agnostic, multi-step workflow designed to enhance factual accuracy through an iterative process:

(i) **Initial Draft Generation:** A foundation model produced a first-pass summary using only the History & Physical and the final progress note as source documents.

(ii) **Iterative Refinement:** The initial draft was then iteratively refined by processing the remaining progress notes in chronological order. For each note, a prompt instructed the

model to identify salient medical information, integrate it into the evolving summary, and simultaneously embed a corresponding provenance tag (e.g., <PROG_NOTE_7>) with each new statement.

(iii) **Hallucination Reduction & Citation:** A concluding step first performed a verification pass, reviewing the summary to identify and mitigate unsupported factual claims. Following this check, the embedded provenance tags were resolved, linking each tag to its full source note to enable downstream citation generation.

An anonymized sample of a MedAgentBrief output is available as Supplementary Data 1.

Foundation Models and Output Structure. These two strategies were implemented using various foundation models, such as GPT-4o and DeepSeek-R1 (see Supplementary Table S1 for a complete list), all accessed via a secure, HIPAA-compliant Application Programming Interface (API) infrastructure to ensure data privacy.[13] The scope of our generation task focused on the narrative synthesis of a patient's stay. All models were prompted to produce a consistent, structured output containing: (1) a one-line summary, (2) a brief narrative of the hospital course, and (3) a problem-focused summary. This task was explicitly scoped to synthesizing information already present in the source notes. The generation of boilerplate text (e.g., standard patient instructions) and novel medical recommendations not found in the provided documentation was considered out of scope.

3.3. *The MedFactEval Framework*

The MedFactEval framework consists of three main steps: benchmark creation, LLM Jury evaluation, and automated reporting.

Step 1: Benchmark Creation—Key Fact Extraction. For each patient case, one or more senior attending physicians reviewed the original, human-written discharge summary to identify three high-salience clinical facts. These "key facts" represent critical information that a high-quality summary must not omit. Examples of such key facts include: (i) a new critical diagnosis, (ii) a key change in management, or (iii) an essential follow-up action.

To streamline this process, annotators were optionally provided with candidate key facts suggested by a Task-Assisting LLM (based on models such as GPT-4o and Gemini 2.0 Flash), which they could then review, edit, or discard. This process yields a benchmark of clinician-validated facts, creating a trusted reference for evaluating AI summaries on their ability to capture clinically critical information.

Step 2: LLM Jury Evaluation. To evaluate a generated summary, our framework employs an "LLM Jury" of ten distinct LLM judges. For each key fact, the jury is prompted to assess whether the summary includes that fact. Each judge provides a binary verdict and a brief justification, with the final decision determined by a majority vote. A parallel process is used to assess for contradictions, where the jury determines if the summary contains information inconsistent with the key fact.

Step 3: Automated Evaluation Report. To synthesize the evaluation results into an actionable format, the framework generates an automated report for each evaluated AI system. This report uses a language model to distill qualitative themes from the LLM Jury's explanations for omitted or contradicted facts. The final output programmatically aggregates these insights with quantitative performance scores into a structured HTML document. An anonymized sample of a complete HTML report is available as Supplementary Data 2.

3.4. *Meta-Evaluation of the MedFactEval Framework*

The validity of MedFactEval hinges on whether its automated scores correspond with expert human judgment. We therefore conducted a meta-evaluation to assess this correspondence.

Gold Standard Creation. We created a gold standard reference using a subset of the generated summaries. Specifically, summaries generated for all 30 cases by two MedAgentBrief systems (one using GPT-4o, the other DeepSeek-R1) were selected, resulting in 60 unique summaries for evaluation. A panel of seven attending physicians independently evaluated each summary, providing a binary judgment (present/absent) for each of the three corresponding key facts. The gold standard for fact presence was then defined as the majority vote of this seven-physician panel.

Human Expert Baseline. To establish a performance baseline for a single human expert, we calculated the agreement for each of the seven physicians against the majority vote of the other six (a leave-one-out approach). The final human expert baseline is then reported as the average of these seven individual agreement scores.

Statistical Analysis. Our primary outcome was the inter-rater agreement between an evaluator (MedFactEval LLM Jury or a single human expert) and the seven-physician gold standard. We measured agreement using Cohen's kappa coefficient (κ) and used a one-sided test to assess for non-inferiority against a pre-specified margin of 10% for the kappa coefficient.[14] Ninety-five percent confidence intervals (95% CI) were calculated by bootstrapping (9999 iterations).

4. Results

4.1. *An Instantiated Benchmark for Discharge Summaries*

Applying the first step of the MedFactEval framework—Key Fact Extraction—we developed a benchmark for the task of discharge summary generation. This benchmark comprises three core components: First, it specifies the **task** as the synthesis of a patient's hospital course into a structured discharge summary. Second, it provides the **source data**: the complete set of unstructured clinical notes for each of 30 patients, including the History & Physical and all progress notes from both physician (attending and consultant) and allied health services (e.g., clinical nutrition, occupational therapy, speech language pathology). Finally, it establishes the **evaluation standard**: a set of 90 clinician-defined "key facts" (three per case), which provide the concrete criteria for assessing the factual integrity of a generated summary.

Examples of such key facts include new critical diagnoses (e.g., "admitted for recurrent malignant biliary obstruction with hyperbilirubinemia requiring percutaneous transhepatic drainage"), key changes in management (e.g., "discharged with deep vein thrombosis prophylaxis, with anemia at hemoglobin 9g/dL"), and essential follow-up actions (e.g., "will return next week to have the small skin cancer on the right cheek removed"). The specific characteristics of this benchmark are detailed in Table 1.

Table 1. **Benchmark Characteristics.** SD: Standard Deviation, IQR: InterQuartile Range.

Characteristic	**Value**
Patient Demographics	
Number of patients	30
Age, mean (SD), years	60 (16)
Sex, n (%)	
Female	17 (57)
Male	13 (43)
Length of stay, median (IQR), days	5 (4–8)
Source Documents (per case)	
Total progress notes, median (IQR)	12 (10–16)
Physician notes, median (IQR)	9 (7–11)
Allied health notes, median (IQR)	3 (2–6)
Key Fact Categorization	
Total Key Facts	90
Diagnosis-related, n (%)	46 (51)
Management Change, n (%)	36 (40)
Follow-up Action, n (%)	5 (6)
Other, n (%)	3 (3)

4.2. *Benchmarking Generation Strategies with MedFactEval*

We applied MedFactEval to compare our two generation strategies—the baseline Single-Prompt approach and the MedAgentBrief workflow—across various foundation models.

Fact Presence vs. Inference Cost. As illustrated in Figure 1, the MedAgentBrief workflow consistently improved factual presence scores over the Single-Prompt baseline for every foundation model tested. This performance gain, however, came at an increased inference cost, highlighting a clear trade-off between factuality and expense. A parallel trade-off between performance and generation time (latency) was also observed (see Supplementary Figure S1). While the models designated as "Reasoning models" in our benchmark (e.g., DeepSeek-R1, Gemini-2.5-Pro) occupied the high-performance quadrant, other powerful models also benefited significantly. For instance, the factual presence score of GPT-4o improved by 17 percentage points (from 48% to 65%) when using the MedAgentBrief workflow.

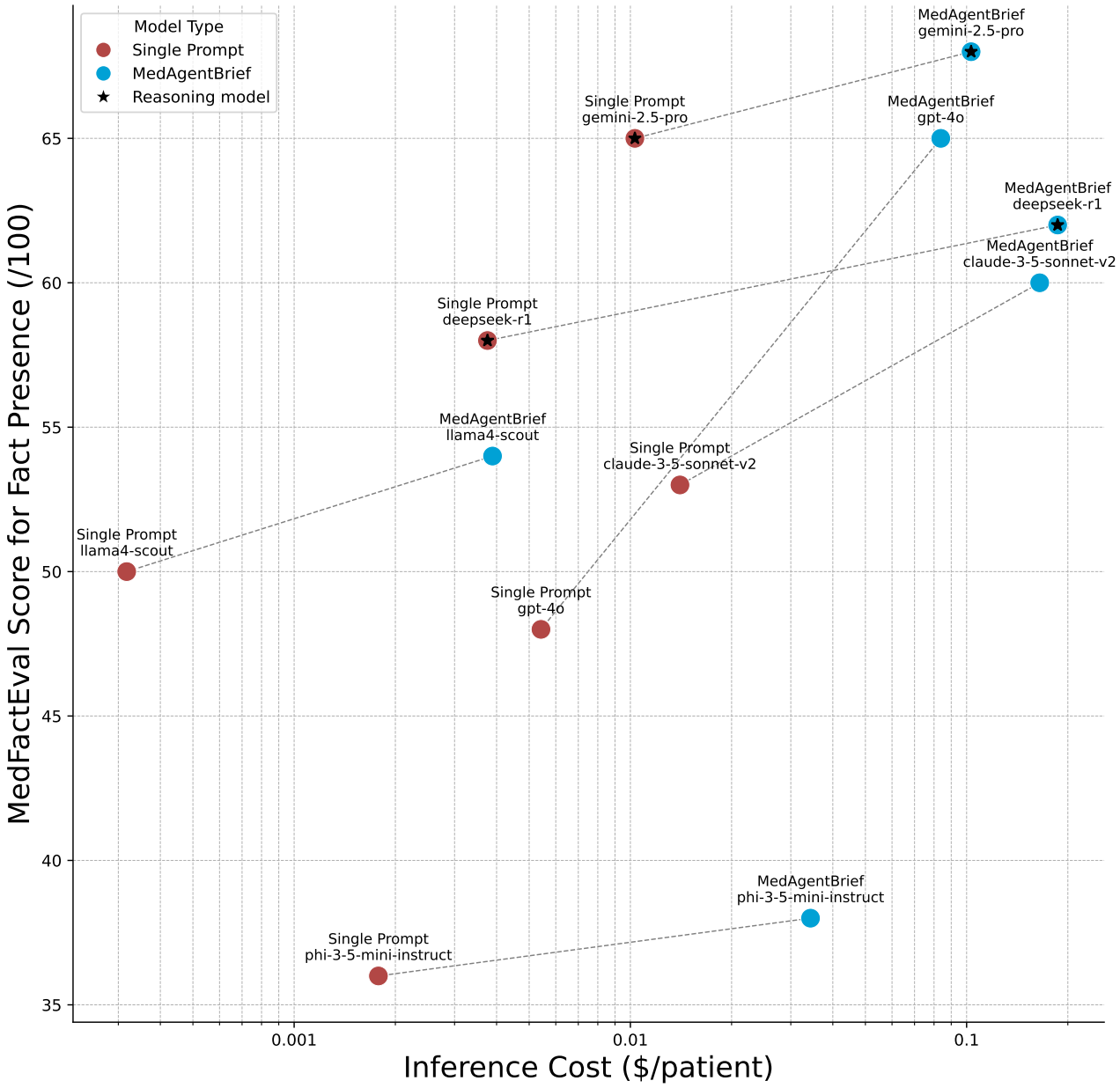

Fig. 1. **Performance-Cost Trade-off of AI Summary Generation, Measured by MedFactEval.** The y-axis represents the MedFactEval score for factual presence (higher is better), while the x-axis shows inference cost per patient on a logarithmic scale. For each foundation model, the MedAgentBrief workflow (cyan) consistently yields a higher factuality score than the baseline Single Prompt approach (brown), demonstrating its effectiveness at the expense of increased cost. Models designated as "Reasoning models" (starred) generally occupy the high-performance, high-cost quadrant.

Analysis of Factual Errors. MedFactEval identified contradiction rates ranging from 10% to 25% across the different systems, with performance varying by both foundation model and generation strategy (see Supplementary Figure S2). A manual review revealed that this rate is attributable to MedFactEval LLM Jury's high sensitivity in detecting subtle yet clinically

significant inconsistencies. For instance, the jury correctly flagged a summary that misrepresented a complex fondaparinux-to-apixaban transition as a simple initiation. This distinction is critical, as it obscures the patient's prior anticoagulation history and the clinical reasoning for the change (e.g., treatment failure or convenience), information vital for future care decisions. While notable, these contradiction rates were consistently lower than errors of omission, making fact presence the primary differentiator between systems.

4.3. *Meta-Evaluation: Validating MedFactEval LLM Jury*

Our primary goal was to validate whether the MedFactEval LLM Jury could serve as a reliable proxy for human expert evaluation.

LLM Jury Agreement with Gold Standard. As shown in Figure 2, the 10-member LLM Jury demonstrated almost perfect agreement with the seven-physician majority vote gold standard for determining fact presence. This strong performance was observed across both systems evaluated: for summaries from the GPT-4o-based MedAgentBrief, the jury achieved a Cohen's kappa of $\kappa = 81\%$ (95% CI: 66%–92%), while for the DeepSeek R1-based MedAgentBrief system, the agreement was $\kappa = 75\%$ (95% CI: 59%–88%). This level of agreement was substantially higher than that achieved by any individual LLM judges, underscoring the value of the jury ensemble approach.

Non-Inferiority to a Single Human Expert. Our analysis confirmed that the MedFactEval LLM Jury is statistically non-inferior to a single human expert for evaluating factual presence (Figure 3). When evaluating summaries from the GPT-4o-based MedAgentBrief, the full LLM Jury's agreement ($\kappa = 81\%$) was substantially higher than the single-physician baseline ($\kappa = 67\%$, 95% CI: 49%–83%). This resulted in a kappa difference of 15% (95% CI: -1%–29%), satisfying our non-inferiority criteria ($P < 0.001$). This finding of non-inferiority also held when evaluating the Deepseek R1-based system, which showed a kappa difference of 2% (95% CI: -11%–15%; $P < 0.001$) (see Supplementary Figure S3). Furthermore, as shown in Figure 3, the cost-effective "Small LLM Jury" (comprising Claude 3.5, Llama-4-Scout, and DeepSeek-R1) also met the non-inferiority threshold, suggesting that practical, lower-cost versions of the jury are viable for real-world application.

5. Discussion

In this work, we introduced and validated MedFactEval, a scalable framework for fact-grounded evaluation, and presented MedAgentBrief, a high-performing workflow for generating clinical summaries. Our primary finding is that an LLM Jury, guided by clinician-defined key facts, can evaluate the factual accuracy of AI-generated text with a reliability non-inferior to that of a single human physician expert. While we focused on discharge summaries, the MedFactEval methodology is intentionally generalizable and can be applied to other clinical information synthesis tasks by defining a new set of relevant key facts.

This result is significant because it offers a path to overcoming the critical evaluation bottleneck in clinical AI. Manual, expert-led review is unsustainable for the continuous mon-

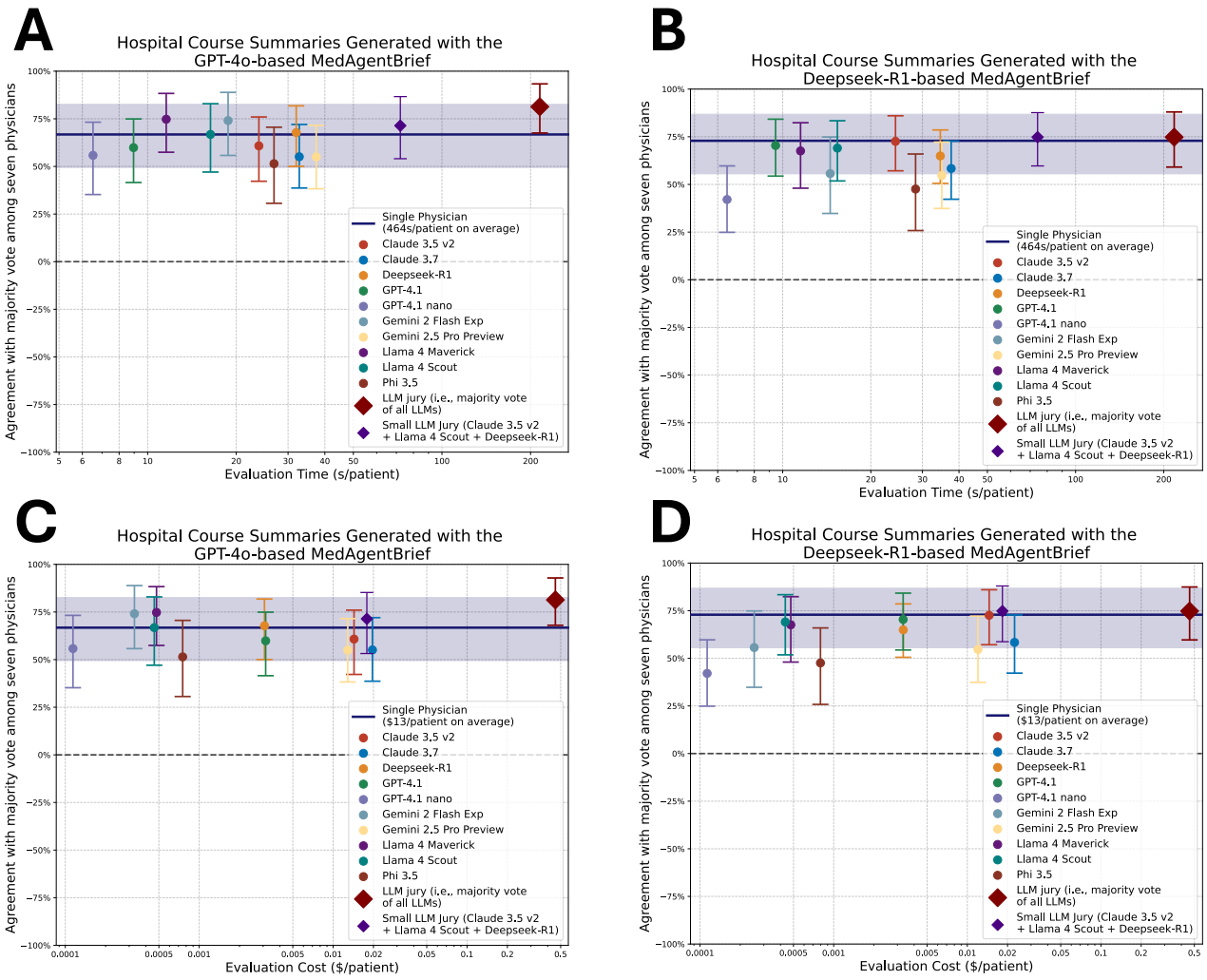

Fig. 2. **Agreement of LLM Judges and Juries with the Physician Gold Standard.** Each point represents the Cohen's kappa agreement for an evaluator against the seven-physician majority vote. **(A, C)** Agreement versus evaluation time for summaries from the GPT-4o and Deepseek-R1 workflows, respectively. **(B, D)** Agreement versus evaluation cost for the same summaries. The full 10-member LLM Jury (red diamond) consistently achieves higher agreement than most individual judges. The Small LLM Jury (purple diamond) offers a faster, lower-cost alternative while maintaining performance comparable to the single physician reference (blue shaded area, representing the 95% CI for a single physician's agreement).

itoring required for safe deployment. By demonstrating that an LLM Jury can serve as a reliable and scalable proxy, MedFactEval provides a practical tool for real-time quality assurance and iterative model improvement. This moves evaluation from a retrospective academic exercise toward a dynamic, automated process suitable for live clinical environments.

Furthermore, our benchmarking results highlight the utility of MedFactEval for concrete development tasks. The clear performance-cost trade-off revealed in Figure 1 can guide decisions about model and strategy selection. The framework's ability to systematically identify errors of omission—which our analysis confirmed is the predominant failure mode—provides

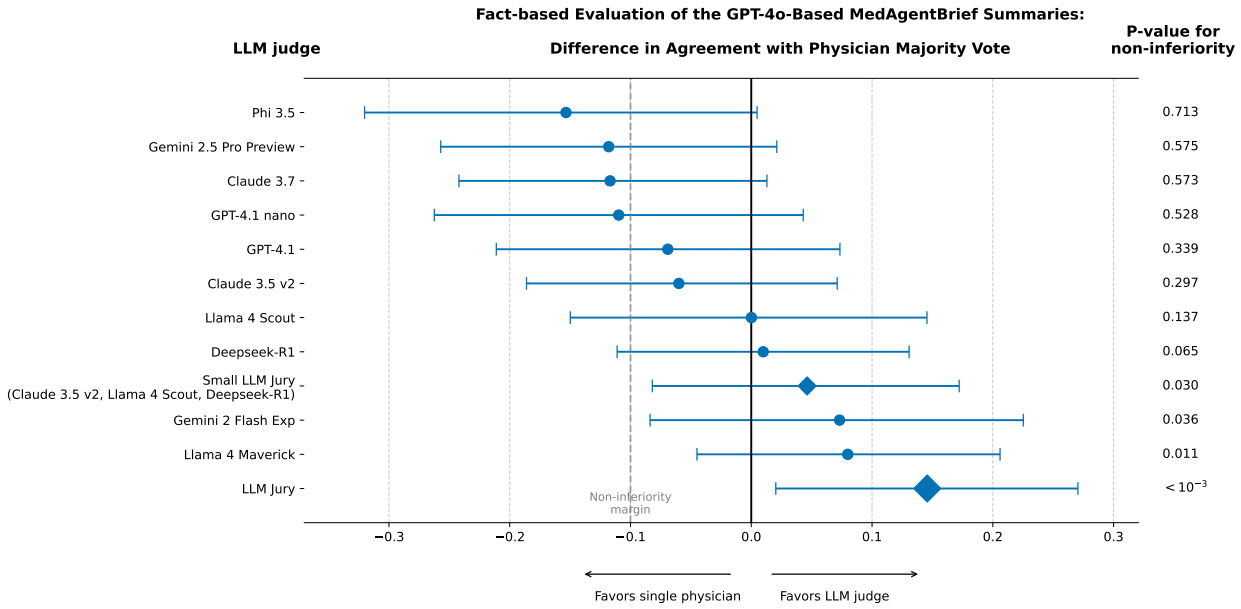

Fig. 3. **Non-Inferiority of LLM Judges Compared to a Single Physician Expert.** The plot shows the difference in Cohen's kappa between each LLM judge and the average single physician, for summaries generated by the GPT-4o-based MedAgentBrief. Points to the right of the vertical line favor the LLM judge. The dashed line indicates the pre-specified non-inferiority margin. The full LLM Jury (bottom diamond) and the Small LLM Jury both surpassed the single physician baseline and met the criteria for non-inferiority ($P < 0.001$). Error bars represent 90% confidence intervals, consistent with the one-sided nature of the non-inferiority test.

developers with the granular, actionable feedback needed to improve the safety and reliability of their systems.

Limitations and Future Directions

Our study has several limitations. The validation was conducted on a cohort from a single service-line (general inpatient medicine) from a single academic medical center. While we demonstrated that even a small, locally-created benchmark can provide a powerful signal for model selection and improvement, larger-scale validation across diverse settings is warranted. Second, our framework intentionally focuses on a small number of clinician-defined, high-salience facts (three per case in our study), a constraint chosen to mirror the low cognitive burden required for practical integration into a busy clinical workflow. This ensures clinical relevance but does not assess other quality dimensions like fluency or conciseness, nor does it detect the omission of facts not pre-specified by the clinician. MedFactEval is therefore intended as a targeted fact-checking tool to be used alongside other holistic evaluation methods. Integrating our framework into comprehensive platforms like MedHELM[15] would support this goal by enabling multi-dimensional assessment. Finally, the process of selecting key facts is inherently subjective. This was a deliberate design choice, meant to empower physicians to direct the evaluation toward what they deem clinically critical. However, future work could explore methods to further standardize or automate this selection process.

Looking forward, our immediate goal is to deploy MedAgentBrief in a pilot study, using MedFactEval to provide real-time safety monitoring. In this prospective workflow, a clinician would define a small number of critical facts for their patient's summary. The MedFactEval jury would then assess the AI-generated draft against these facts, providing immediate feedback on whether the facts were correctly included or contradicted. This real-time loop would empower clinicians to identify AI failure modes as they occur. Furthermore, this process would generate a prospectively collected, real-world dataset of clinical notes paired with expert-defined key facts, providing an invaluable resource for future model training and evaluation.

6. Conclusion

This work advances the safe and effective use of AI in clinical documentation by providing two key contributions: a robust evaluation framework, MedFactEval, and a high-performing generation workflow, MedAgentBrief. By demonstrating that an LLM Jury can reliably and scalably replicate expert judgment for fact-checking, we offer a practical solution for the continuous safety monitoring required for the responsible deployment of AI systems for clinical information synthesis.

Supplementary Materials

Supplementary materials associated with this article can be found at:
https://fcgrolleau.github.io/medfacteval/supplementary_materials.pdf
This includes Supplementary Table S1 and Supplementary Figures S1-S3.

Code Availability

The complete source code for the MedFactEval framework, the MedAgentBrief workflow, and all experiments presented in this paper is open-source and publicly available on GitHub at: https://github.com/fcgrolleau/medfacteval.

Data Availability

The validation benchmark used in this study contains detailed clinical notes of recently admitted patients at Stanford Health Care. Due to the sensitive nature of this data and the risk of direct re-identification, it cannot be publicly shared. The following supplementary data are available with this article:

- **Supplementary Data 1:** Anonymized sample of a MedAgentBrief-generated summary (HTML format). Available at:
  https://fcgrolleau.github.io/medfacteval/samples/anonymized_medagentbrief_sumary.html
- **Supplementary Data 2:** Anonymized sample of an automated MedFactEval evaluation report (HTML format). Available at:
  https://fcgrolleau.github.io/medfacteval/samples/anonymized_medfacteval_report.html

References

1. A. J. Moy, J. M. Schwartz, R. Chen, S. Sadri, E. Lucas, K. D. Cato and S. C. Rossetti, Measurement of clinical documentation burden among physicians and nurses using electronic health records: a scoping review, *Journal of the American Medical Informatics Association* **28**, 998 (2021).
2. D. Van Veen, C. Van Uden, L. Blankemeier, J.-B. Delbrouck, A. Aali, C. Bluethgen, A. Pareek, M. Polacin, E. P. Reis, A. Seehofnerová *et al.*, Adapted large language models can outperform medical experts in clinical text summarization, *Nature Medicine* **30**, 1134 (2024).
3. C. Y. Williams, C. R. Subramanian, S. S. Ali *et al.*, Physician-and large language model-generated hospital discharge summaries, *JAMA Internal Medicine* (May 2025).
4. B. Meskó and E. J. Topol, The imperative for regulatory oversight of large language models (or generative AI) in healthcare, *NPJ Digital Medicine* **6**, p. 120 (2023).
5. D. J. Morgan, W. Branch-Elliman and K. E. Goodman, Time to study implementation of AI-generated discharge summaries, *JAMA Internal Medicine* (2025).
6. C. Hong, A. Chowdhury, A. D. Sorrentino, H. Wang, M. Agrawal, A. Bedoya, S. Bessias, N. J. Economou-Zavlanos, I. Wong, C. Pean *et al.*, Application of unified health large language model evaluation framework to in-basket message replies: bridging qualitative and quantitative assessments, *Journal of the American Medical Informatics Association* **32**, 626 (2025).
7. E. Asgari, N. Montaña-Brown, M. Dubois, S. Khalil, J. Balloch, J. A. Yeung and D. Pimenta, A framework to assess clinical safety and hallucination rates of LLMs for medical text summarisation, *NPJ Digital Medicine* **8**, p. 274 (2025).
8. K. Zuo and Y. Jiang, MedHallBench: A new benchmark for assessing hallucination in medical large language models, *arXiv preprint arXiv:2412.18947* (2024).
9. P. Chung, A. Swaminathan, A. J. Goodell, Y. Kim, S. M. Reincke, L. Han, B. Deverett, M. A. Sadeghi, A.-B. Ariss, M. Ghanem *et al.*, Verifact: Verifying facts in LLM-generated clinical text with electronic health records, *arXiv preprint arXiv:2501.16672* (2025).
10. M. Munnangi, A. Swaminathan, J. A. Fries, J. Jindal, S. Narayanan, I. Lopez, L. Tu, P. Chung, J. A. Omiye, M. Kashyap *et al.*, Assessing the limitations of large language models in clinical fact decomposition, *arXiv preprint arXiv:2412.12422* (2024).
11. L. Tang, Z. Sun, B. Idnay, J. G. Nestor, A. Soroush, P. A. Elias, Z. Xu, Y. Ding, G. Durrett, J. F. Rousseau *et al.*, Evaluating large language models on medical evidence summarization, *NPJ Digital Medicine* **6**, p. 158 (2023).
12. L. Zheng, W.-L. Chiang, Y. Sheng, S. Zhuang, Z. Wu, Y. Zhuang, Z. Lin, Z. Li, D. Li, E. Xing *et al.*, Judging LLM-as-a-judge with MT-bench and chatbot arena, *Advances in Neural Information Processing Systems* **36**, 46595 (2023).
13. M. Y. Ng, J. Helzer, M. A. Pfeffer, T. Seto and T. Hernandez-Boussard, Development of secure infrastructure for advancing generative artificial intelligence research in healthcare at an academic medical center, *Journal of the American Medical Informatics Association* **32**, 586 (2025).
14. J. R. Landis and G. G. Koch, The measurement of observer agreement for categorical data, *Biometrics* , 159 (1977).
15. S. Bedi, H. Cui, M. Fuentes, A. Unell, M. Wornow, J. M. Banda, N. Kotecha, T. Keyes, Y. Mai, M. Oez *et al.*, MedHELM: Holistic evaluation of large language models for medical tasks, *arXiv preprint arXiv:2505.23802* (2025).

Asking the Right Questions: Benchmarking Large Language Models in the Development of Clinical Consultation Templates

Liam G. McCoy†
Division of Neurology, Faculty of Medicine and Dentistry, University of Alberta, Edmonton, AB, Canada; Department of Medicine, Beth Israel Deaconess Medical Center, Boston, MA, USA;
Email: lmccoy@ualberta.ca

Fateme Nateghi Haredasht† and Kanav Chopra
Stanford Center for Biomedical Informatics Research Stanford, CA, USA
Email: fnateghi@stanford.edu; kanav@stanford.edu

David Wu
Department of Dermatology, Mass General Brigham, Harvard Medical School, Boston, MA, USA
Email: dwu@mgh.harvard.edu

David JH Wu and Abass Conteh
Department of Radiation Oncology, Stanford Cancer Center, Palo Alto, CA, USA
Email: davidjwu@stanford.edu; aconteh@stanford.edu

Sarita Khemani and Saloni Kumar Maharaj
Division of Hospital Medicine, Stanford University School of Medicine, Stanford, CA, USA
Email: skhemani@stanford.edu; salonikumar@stanford.edu

Vishnu Ravi
Stanford Mussallem Center for Biodesign, Stanford University; Stanford University School of Medicine, Stanford, CA, USA
Email: vishnur@stanford.edu

Arth Pahwa
Division of Neurology, Faculty of Medicine and Dentistry, University of Alberta, Edmonton, AB, Canada
Email: apahwa@ualberta.ca

Yingjie Weng
Quantitative Sciences Unit, Stanford University School of Medicine, Stanford, CA, USA
Email: yweng7@stanford.edu

Leah Rosengaus and Lena Giang
Stanford Health Care, Stanford Medicine, Palo Alto, CA, USA
Email: LRosengaus@stanfordhealthcare.org; LGiang@stanfordhealthcare.org

Kelvin Zhenghao Li
Department of Ophthalmology, Stanford Byers Eye Institute; Department of Ophthalmology, Tan Tock Seng Hospital; Centre of AI in Medicine, Lee Kong Chian School of Medicine, Nanyang Technological University Palo Alto, CA, USA; Singapore, Singapore
Email: kelvinli@stanford.edu

Olivia Jee
Division of Primary Care and Population Health, Stanford University School of Medicine, Palo Alto, CA, USA
Email: ojee@stanford.edu

Daniel Shirvani
Faculty of Medicine, University of British Columbia, Vancouver, BC, Canada
Email: dshirv@student.ubc.ca

Ethan Goh*
Stanford Center for Biomedical Informatics Research Clinical Excellence Research Center, Stanford School of Medicine, Stanford, CA, USA
Email: ethangoh@stanford.edu

Jonathan H. Chen*
Stanford Center for Biomedical Informatics Research Division of Hospital Medicine, Stanford School of Medicine; Clinical Excellence Research Center, Stanford School of Medicine; Department of Medicine, Stanford University, Stanford, CA, USA
Email: jonc101@stanford.edu

†Authors contributed equally. *Authors jointly supervised this work. Corresponding: Ethan Goh

© 2025 The Authors. Open Access chapter published by World Scientific Publishing Company and distributed under the terms of the Creative Commons Attribution Non-Commercial (CC BY-NC) 4.0 License.

This study evaluates the capacity of large language models (LLMs) to generate structured clinical consultation templates for electronic consultation. Using 145 expert-crafted templates developed and routinely used by Stanford's eConsult team, we assess frontier models—including o3, GPT-4o, Kimi K2, Claude 4 Sonnet, Llama 3 70B, and Gemini 2.5 Pro—for their ability to produce clinically coherent, concise, and prioritized clinical question schemas. Through a multi-agent pipeline combining prompt optimization, semantic autograding, and prioritization analysis, we show that while models like o3 achieve high comprehensiveness (up to 92.2%), they consistently generate excessively long templates and fail to correctly prioritize the most clinically important questions under length constraints. Performance varies across specialties, with significant degradation in narrative-driven fields such as psychiatry and pain medicine. Our findings demonstrate that LLMs can enhance structured clinical information exchange between physicians, while highlighting the need for more robust evaluation methods that capture a model's ability to prioritize clinically salient information within the time constraints of real-world physician communication. Limitations include reliance on Stanford-specific templates and concordance-based grading, which may not capture all clinically reasonable outputs.

Keywords: Large Language Models (LLMs); Clinical Communication; Consultation Templates; Medical NLP; Prompt Optimization; Autograding; Prioritization; Physician-to-Physician Communication; E-consults; Healthcare AI Evaluation

1. Introduction

Medicine is fundamentally a knowledge processing and collaborative discipline[1]. High-quality consultation between generalist clinicians and specialists ensures accurate, timely, and efficient patient care. Communication breakdowns contribute frequently to medical errors[2], leading to death and preventable harm[3–5]. Improving the structure and quality of specialist–generalist consultation templates offers a direct opportunity to reduce diagnostic delays, treatment errors, and unnecessary testing[6]. Effective specialist consultations hinge on a subtle cognitive balance—comprehensively capturing clinical details, while anticipating and selectively prioritizing the specialist's informational needs[7,8]. Traditional synchronous consultations, such as those conducted over the phone, enable specialists to ask targeted follow-up questions, dynamically acquiring necessary details to inform their clinical decision.

Asynchronous e-consultation systems offer a structured workflow to streamline primary care physician (PCP)-specialist interactions but place greater reliance on the initial information provided by the consulting physician[9–12]. Stanford's SAGE eConsult product (Specialist AI Guiding Experts) utilizes specialist-generated consultation templates (*Supplementary Figure S1*) developed by Stanford's eConsult team to guide primary care physicians in submitting structured, high-yield clinical consults[13]. Each template outlines both required and optional elements—such as key history, medications, labs, and comorbidities—that enable specialists to provide more actionable recommendations. However, maintaining a library of expert-crafted templates is resource-intensive, requiring continuous updates to reflect evolving guidelines, specialist expectations, and health system workflows. Static templates also fail to capture the breadth of clinical variability and edge cases[14,15]. Given the wide variability of possible conditions and relevant questions, novel AI template generation is important to fully scale this workflow.

We evaluate the ability of contemporary large language models (LLMs) to generate clinically useful consultation templates that can contextually adapt to individual consults, expanding coverage beyond common scenarios while preserving clinical rigor and relevance. Beyond its practical value, template generation represents a unique cognitive challenge rarely examined in medical natural language processing (NLP): models must anticipate what another clinician needs to know, not simply recall facts or summarize text. Evaluating this capability required developing new approaches that measure performance under the competing demands of comprehensiveness and conciseness, challenges absent from traditional benchmarks. Through this work, we aim to highlight both the practical clinical potential and the technical challenges in deploying LLMs for nuanced clinical communication tasks.

2. Methods

2.1. *Data*

The Stanford eConsult Templates dataset consists of 173 expert-generated templates for inbound specialist consultations generated from 2019 to 2025. These templates are based on frequently received consults and consist of mandatory and recommended information for the consulting physician to include. Templates were screened for inclusion based on clinical relevance and specificity. Exclusion criteria included: (i) templates that consisted primarily of redirection to other services, (ii) templates that consisted exclusively of links to educational resources or instructions for photo submission (most notably in dermatology), and (iii) "other" templates that did not specify a condition. After applying these criteria, the final dataset consisted of 145 templates across 20 specialties (allergy, cardiology, hematology, chemical dependency, endocrinology, otolaryngology, gastroenterology, gynecology, infectious disease, interventional pulmonology, LGBTQ+ medicine, nephrology, neurology, orthopedics, pain medicine, psychiatry, pulmonology, rheumatology, sleep medicine, and urology). These templates are highly variable in content, containing 1601 unique fields, with 99.3% of these fields present in <10% of templates, and an average Jaccard similarity of 23.7% within specialties. An example template can be found in *Supplementary Figure S1*.

2.2. *Response Autograder*

LLM-generated template items rarely match the expert templates verbatim. Therefore, we deployed a semantic autograder that judges clinical equivalence at the item level (*Figure 1)*. The grader is an OpenAI o3[16] instance prompted to decide, for every pair of strings, whether the LLM-generated item satisfies the information request of the expert template item. For example, a generation of "TSH" is accepted as equivalent to the expert template item of "thyroid function tests". Concordance analysis was performed on a per-item basis, assessing whether the item in the original template has an equivalent in the generated template (Figure 3A). Conciseness was evaluated by comparing the total number of novel generated template items to the total number of items in the original template.

The autograder was first calibrated by assessment of a random sample of 40 templates graded by either GPT-4.1[17] or o3. Three blinded US board-certified internal medicine physicians (SK, VR, SM) reviewed the accuracy of the autograder's matches, rating them (i) a full match, if the generated item was clinically equivalent to the original item or fully contained its contents (ii) a partial match, if the generated item included the original item but with a clinically significant difference, and (iii) a disagreement, if the autograder erred in matching the two items. To assess whether the autograder was excessively conservative in its matching, items from the original templates that were rated as 'unmatched' by the model were manually reviewed against all generated items. Final autograder validation was performed, with an iteratively updated prompt, on a set of 20 additional templates evaluated by the same criteria.

Krippendorff's α[18,19] (multi-rater, nominal, tolerant of missingness) and Gwet's AC1[20] (chance-corrected agreement, less sensitive than Cohen's κ to prevalence/marginal imbalance[21]) were used to compare the three clinicians and the autograder. For Krippendorff's α, values ≥ 0.80 generally indicate strong agreement, whereas ~0.67–0.80 support tentative conclusions[19,22], whereas Gwet's AC1 does not have standard interpretive bands.

2.3. *Prompt Optimization*

In our study, Declarative Self-Improving Python (DSPy)[23] was used to generate model-specific prompts for each candidate LLM, refining examples, formatting, and instructions to maximize both clinical quality and structural adherence. DSPy is an open-source framework that treats prompt engineering as a learnable, declarative pipeline. Rather than manually crafting prompts, the user specifies an objective—such as "maximize fidelity to the SAGE template schema under a length constraint"—and DSPy automatically explores variations in prompt structure to optimize performance against this target. Each model was trained on 20 specialty-specific templates, with its outputs evaluated by an o3-based autograder that penalized both omissions of key elements and excessive verbosity. DSPy used this feedback in an iterative loop to adapt the prompt over successive rounds, allowing model performance itself to guide the evolution of the prompt until improvements plateaued. Full prompt details, including examples, may be found at https://github.com/liamgmccoy/stanfordtemplatepublic.

2.4. *Template Generation*

Following DSPy-based few-shot prompt optimization using 20 templates, the finalized prompt was applied to the remaining 125 conditions. For each, the model was provided only the specialty and condition and tasked with generating a complete consultation template (*Supplementary Figure S1*)

2.5. *Template Prioritization Analysis*

In order to assess for conciseness as well as comprehensiveness, a secondary prioritizer agent (using the same underlying model, e.g., an o3 prioritizer for o3-generated templates, or a K2 prioritizer for K2 templates) (*Figure 1*) was used to rank the generated template items in order of clinical importance. From this ranked list, truncated sets of the original generated template were produced

based on a "top-*n*" format where *n* equals the number of elements in the original template (that is, for an original template with 6 items, top-*n* would take the top 6 elements from the original template, top-*n*+3 would take the top 9 elements, etc). This enables a degree of normalization for the length and complexity of the original templates. These truncated templates were placed through the standard autograder evaluation process, with their relative performance assessed using both standard recall values (recall@k[24], as a percentage of the original template items present within the truncated subset) and normalized discounted cumulative gain at k (NDCG@k)[25], calculated by assigning a value of 2 to items labelled "required" in the initial templates, and 1 to those labelled "optional".

2.6. *Model Benchmarking*

The performance of multiple frontier models on the template generation task was assessed, including OpenAI's GPT-4o[26] and o3[16] models, Google's Gemini 2.5 Pro[27], Anthropic's Claude 4 Sonnet[28], and leading open-source models Kimi K2[29] and Llama 3 70B[30]. Models were compared for both overall template generation performance as well as their performance on the prioritization task

2.7. *Novel Template Generation*

In order to assess the generalization of template generation, novel cases were generated in the specialties of infectious disease, neurology, ophthalmology, and radiation oncology based on five novel topics per specialty suggested by a board-certified (KL) or senior resident physician (DW, AP, AC) co-author in each specialty. All templates were generated by o3 with the DSPy-optimized final prompt. These cases were reviewed item by item for the clinical relevance and importance of each suggested item, with the additional ability for the authors to add additional important items.

3. Results

3.1. *Novel Template Generation*

Novel templates were generated for 20 expert-selected topics across the specialties of neurology, dermatology, radiation oncology, and ophthalmology (*Figure 2)*. Across our novel template experiments, the generated templates demonstrated a high degree of clinical validity, with 96.2% of required components (475 of 494) deemed clinically appropriate. Moreover, the templates proved highly complete, with our human experts adding on average only 1.2 items per template (24 additions across 20 templates) to achieve full coverage. The templates were not as concise as they could be, with only 73.1% of items (361 of 494) rated by human experts as necessary to include. On average, 18 items per template were rated as necessary, compared to the 8.0 items included in the original templates (for neurology specifically, 23.6 necessary items on average in the generated templates vs 11.6 in the original neurology templates for different conditions).

3.2. *Autograder Validation*

Initial human evaluation of the o3 and GPT-4.1 autograders in a randomized fashion demonstrated a clear superiority for the former model (77.1% vs 71.7% perfect matches, and 1.2% vs 7% complete disagreement). Iterative evaluation of the final o3 autograder with an optimized prompt *(Figure 3*) demonstrated a high degree of concordance across three independent clinical reviewers in rating items as appropriately matched (94.1% full agreement, 4.6% partial agreement, and only 1.3% disagreement), as well as in correctly rating items as unmatched (98.2% accuracy with only 1 false negative among 56 missed elements). Inter-rater reliability analysis revealed substantial agreement among human reviewers by exact agreement and Gwet's AC1, but less substantial agreement by Krippendorff's α (86.9% exact agreement, AC1 = 0.904, α = 0.612). When treating partial matches as acceptable, the autograder achieved 98.7% concordance with human experts; when requiring perfect matches only, concordance ranged from 91-98% across reviewers. Partial disagreements tended to relate to the comprehensiveness and specificity of results (for example, asking for "all imaging results" when a specialist specifically requested "MRI").

3.3. *Overall Model Performance*

When evaluating for comprehensiveness across the full generated template (*Figure 4)*, o3 demonstrates clearly superior performance with 92.2% overall comprehensiveness, followed by Claude 4 Sonnet and Gemini 2.5 Pro tied at 82.0%, then Kimi K2 at 78.2%. GPT-4o and Llama-3-70B trail at 76.0% and 71.2% respectively. However, this superior performance came at the cost of conciseness, with o3 producing 2.58x as many template items as were present in the initial template, followed by 2.07x for Claude, 1.56x for Gemini, 1.50x for Kimi, 1.47x for 4o, and 1.27x for Llama.

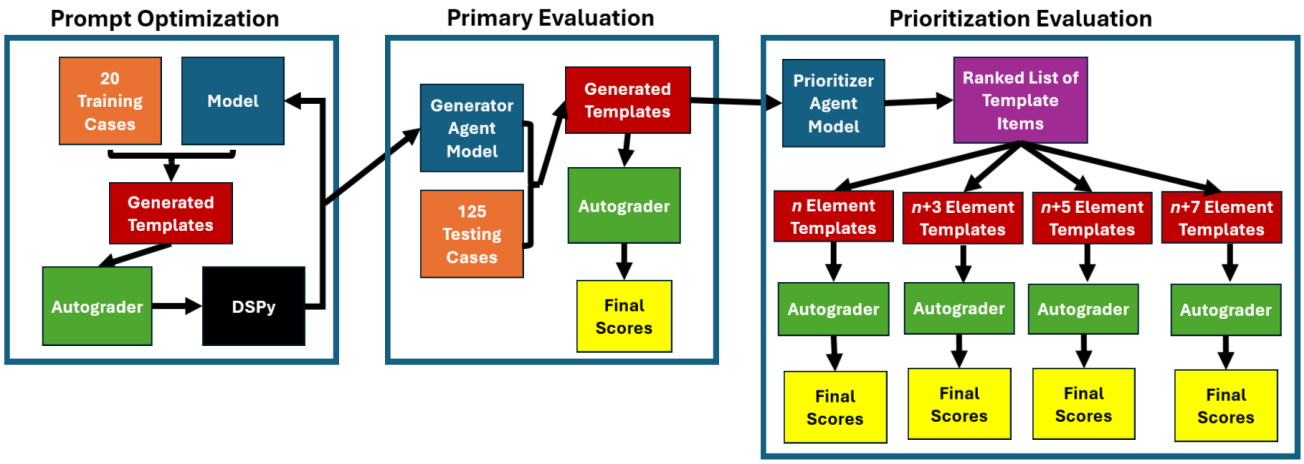

Figure 1. Overview of Multi-Agent Structure for Template Generation and Evaluation. Our pipeline comprises three stages: (1) Prompt Optimization, where DSPy iteratively refines a few-shot prompt on a small training set of 20 cases by generating templates, scoring them with an o3 autograder for missing elements or verbosity, and adjusting the prompt until scores converge; (2) Primary Evaluation, in which the finalized prompt is applied to 125 held-out cases and autograded to produce quality and schema-adherence metrics; and (3) Prioritization Evaluation, where a prioritizer agent ranks schema elements and subsets (based on the top-n elements where n equals the number of elements within the original expert template) are assembled and scored to assess the model's ability to surface the most critical items

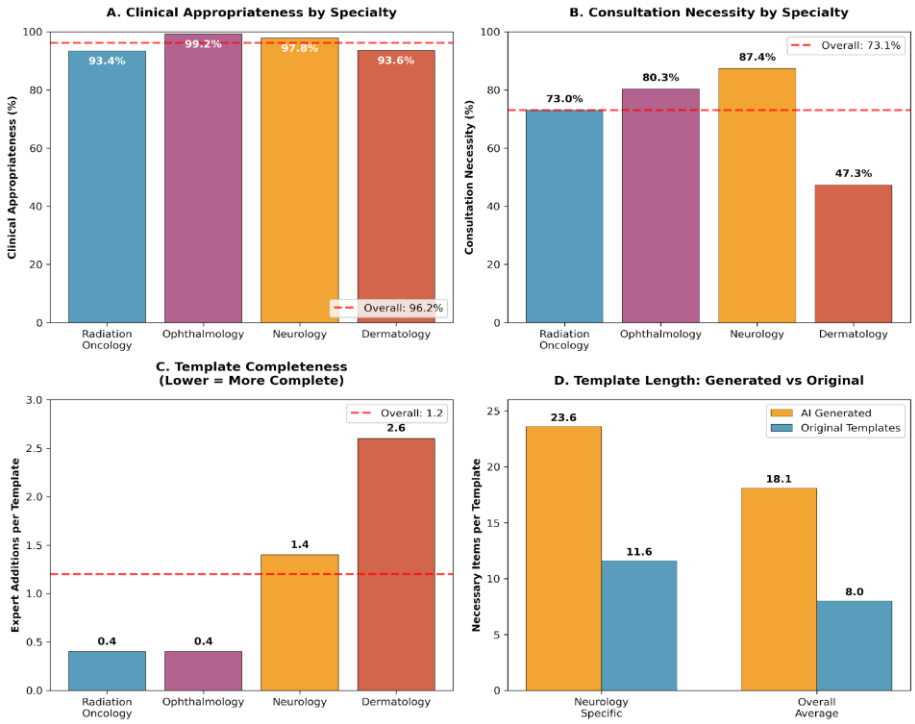

Figure 2. Expert Clinical Validation of Novel AI-Generated Medical Templates. All templates generated by o3 with DSPy optimized prompt (A) Clinical appropriateness by specialty showing percentage of template components deemed clinically reasonable by expert reviewers. (B) Consultation necessity by specialty, showing the percentage of components considered essential for specialist consultation. (C) Template completeness is measured by expert additions per template. (D) Template length comparison between AI-generated templates and original Stanford templates, showing necessary items per template for neurology specifically (as there are neuro templates in the original dataset) and the overall average, compared to all specialties.

3.4. *Prioritization Performance*

While OpenAI's reasoning model o3 had the highest score at full length (92.2% coverage), it demonstrated poor prioritization with only 60.4% coverage when confined to the top-*n* items (where n equals the number of items in the original template) (*Figure 5)*. Kimi K2, a recent large-parameter non-reasoning LLM, demonstrated clearly superior performance in this conciseness evaluation, achieving 69.5% coverage at top-n and 77.7% coverage at top-n+3, despite top results of only 78.2%, representing the best retention of performance when forced to prioritize.

3.5. *Specialty-Specific Performance*

Across the full-length evaluation (*Figure 4C*), coverage spanned nearly 35 percentage points: nephrology (97.4%), endocrinology (95.4%), infectious disease (93.9%) and cardiology (93.1%) sat at the top of the heat-map, whereas psychiatry (61.5%), pain medicine (68.2%), sleep medicine (73.1%), and LGBTQ+ medicine (61.4%) clustered at the low end. When the same outputs were truncated to the top-n items (*Figure 5C*), the ordering persisted but the gaps widened: high-performing specialties still retained approximately 70% of reference items, while psychiatry and pain medicine fell below 45%. o3 particularly underperformed relative to its robust performance

elsewhere with 14% for LGBTQ+ and 36% for psychiatry. Assessment of the novel templates (*Figure 2B*) demonstrated notably worse conciseness and completeness for the dermatology templates, although the included information was highly appropriate.

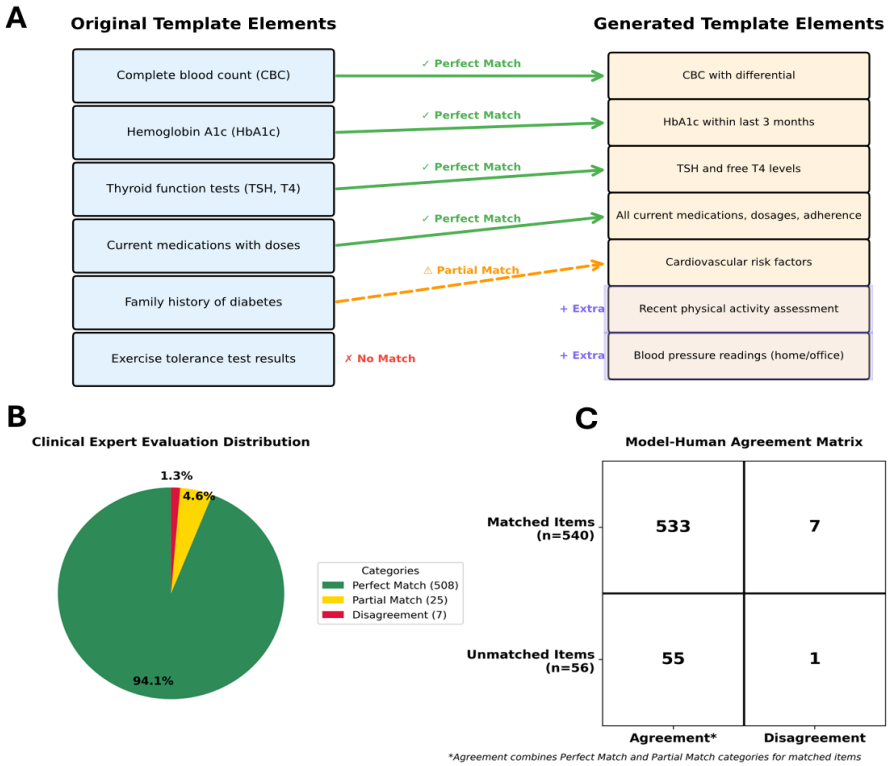

Figure 3. Structure and Validation of Template Matching Autograder (A) Example alignment of expert-template elements to a model-generated template, for diabetes mellitus. Arrows represent autograder matches, with color representing human rater assessment of full vs partial match. (B) Distribution of clinician ratings for matched items. (C) Agreement matrix comparing the autograder with human reviewers for both matched and unmatched elements; "agreement" collapses perfect and partial matches

4. *Discussion*

Our study demonstrates that LLMs can generate clinically comprehensive consultation templates that closely approximate expert-created schemas but remain limited in their ability to prioritize high-yield information under real-world constraints. The top-performing model, o3 (a reasoning model from OpenAI), achieved 92.2% coverage of expert template items when unconstrained, but retained only 60.4% coverage when forced to prioritize to the original template length. In contrast, Kimi K2 (a large, open-source non-reasoning model) demonstrated lower full-length comprehensiveness (78.2%) but stronger prioritization retention (69.5%). Across specialties, performance varied substantially: structured domains like nephrology and infectious disease maintained high coverage, while narrative-heavy fields such as psychiatry and pain medicine exhibited significant performance degradation—particularly under length constraints. These findings underscore a central limitation of current LLMs: while they are increasingly capable of enumerating relevant clinical content, they struggle with the task of effective curation.

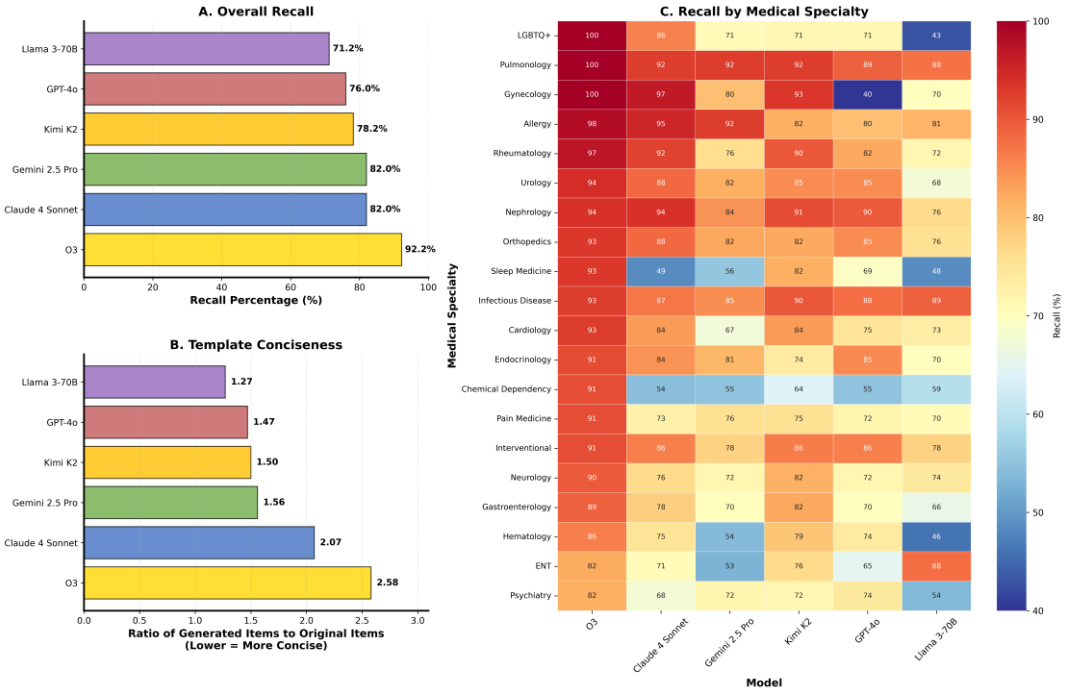

Figure 4. Multi-Model Performance on Structured Consultation Template Generation. (A) Overall template item coverage (Recall, in % of reference items matched in generated templates). (B) Conciseness as the excess ratio (generated items ÷ expert template items; lower is more concise). (C) Per-specialty coverage heatmap showing heterogeneity across domains. The central number indicates comprehensiveness scores as a percentage.

While many recent studies have focused on evaluating AI performance within physician-patient interactions and clinical decision making[31–35], the role of LLMs in physician–physician communication remains comparatively underexamined with only limited work on AI-generated handoffs[36] and discharge communications[37,38]. Yet this is precisely where precision, parsimony, and contextual judgment are most acutely required[39]. Unlike patient-facing interactions, which often emphasize rapport, accessibility, or empathic scaffolding[8], physician–physician communication is optimized for signal density and clinical relevance[9]. Where models have been assessed on these tasks, such as in emergency medicine handoffs, similar failures of curation and conciseness have already been observed[36].

The cognitive demands of physician-physician communication are not well-captured by benchmarks oriented around clinical question answering[32], document summarization[40], or patient interaction[41–43]. Moreover, while healthcare AI benchmark studies rely primarily on simulated data and vignettes[41], the templates used in this study reflect real-world specialist information needs and are both actively updated and used in patient care, making them effective for assessing whether LLMs can match expert judgment in structuring clinical communication. Although recent work shows that language models can now identify their own knowledge gaps—either by steering retrieval toward the missing fact[44] or by posing sharper follow-up questions that narrow diagnostic uncertainty[45] —these advances typically occur in closed-loop settings, where the model both detects and benefits from the additional context. A consultation note, by contrast, is written for another clinician, whose

attention span, cognitive load, and clinical priorities—not the model's context window—set the real limits on relevance. The ability to recognize what else is needed is, therefore, necessary but not sufficient: models must also curate and compress information in ways that align with the recipient's constraints. For these reasons, our study offers not only a novel task but a clinically grounded benchmark for evaluating language model performance in real-world medical communication.

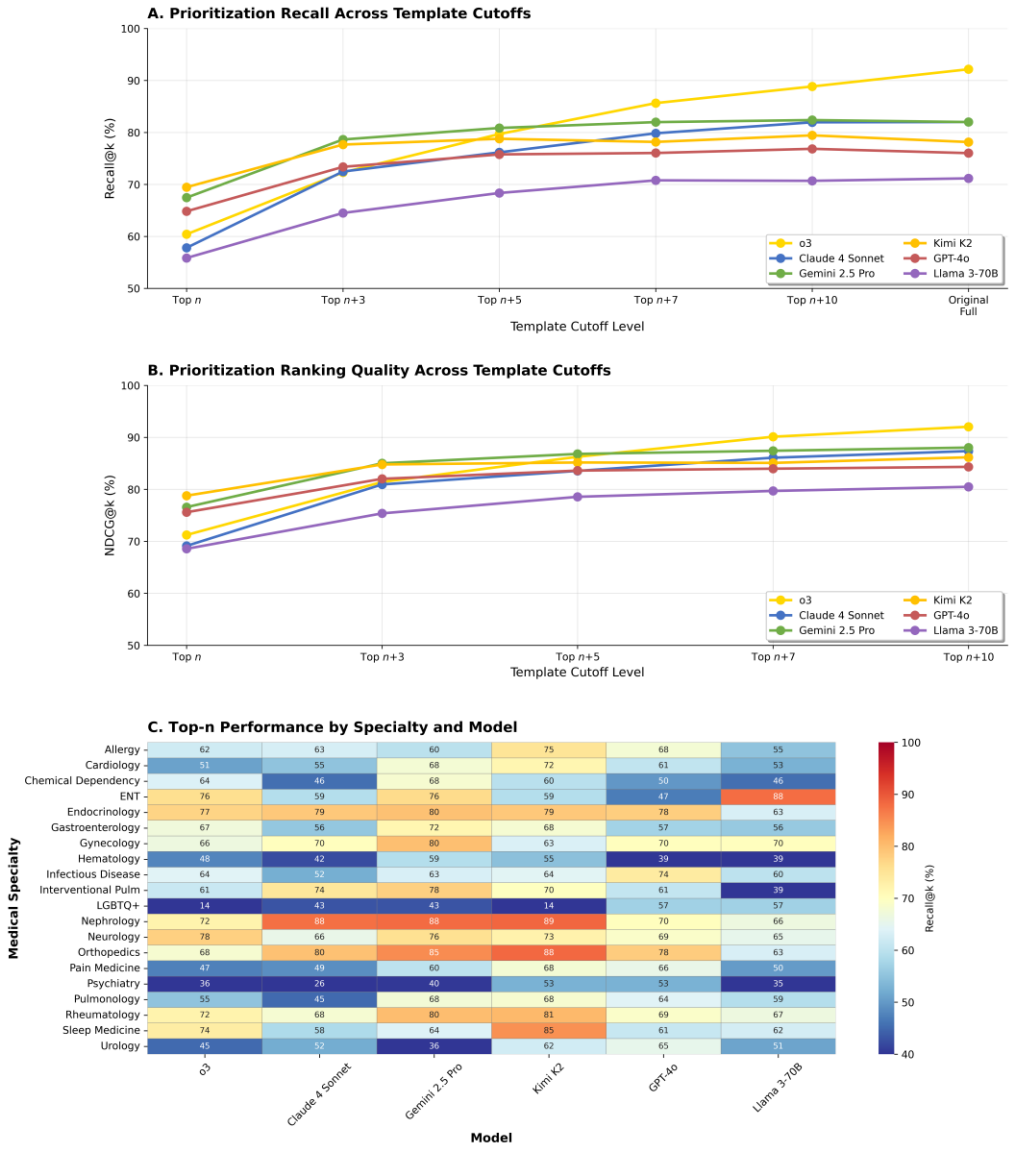

Figure 5. Prioritization Performance Across Template Cutoffs (A) Model performance at various cutoffs for template size, based on the prioritizer agent's ranking (using the same underlying model) of template items (n = number of items in the original template, recall@k = the number of original items matched at a given threshold) (B). Analysis of Normalized Discounted Cumulative Gain (NDCG) at a given position in the list, with "required" items valued at 2, and "optional" items valued at 1 (C) Specialty-by-specialty analysis of model performance at top-n cutoff. The central number indicates recall scores.

Even at low prioritization levels, the longest o3-generated templates continued to surface clinically relevant information, with performance improving beyond the top-n+10 items—unlike other

models, which plateaued by n+5. These differences reveal deeper epistemological fault lines. Structured, laboratory-anchored specialties like nephrology and infectious disease, which rely on codified data, align well with LLM recall and show minimal degradation under truncation. In contrast, narrative-heavy fields such as psychiatry, pain medicine, and sleep medicine depend on contextual nuance and psychosocial insight. These features are not only harder for models to generate but are also the first to be discarded under compression. That these specialties exhibit both the lowest baseline performance and the steepest prioritization drop-off highlights a core weakness: current LLMs still struggle to assign salience to soft-signal clinical features, even when they can enumerate them in an unconstrained setting.

Expert evaluation of the novel AI-generated templates revealed a consistent pattern: specialists rated a greater number of items as necessary compared to those included in the original human-generated templates. Yet those original templates were themselves authored by specialists, explicitly instructed to balance informational value with the cognitive and workflow constraints of generalist users, and the cognitive load of the receiving specialist. The discrepancy highlights a key issue: in the absence of such constraint, both models and human specialist reviewers tend to favor comprehensiveness over conciseness[7], even though this may be operationally burdensome for generalists in practice[46]. Solutions such as length-aware prompting, structured prioritization, progressive disclosure through expandable sections[47], and integration of routinely available EHR data[15] may thus better align models with real-world clinician workflows. Ultimately, conciseness should not be seen as compromising clinical rigor but rather as essential to avoiding the upstream transfer of documentation burdens to generalist providers.

These tensions are directly analogous to the classical precision–recall trade-offs in information retrieval and detection—tightening decision thresholds typically raises precision at the expense of recall—and are well characterized in methodological work on PR vs. ROC analysis and cost-sensitive decision-making[24,48,49]. While our autograder was calibrated to align closely with expert judgment, it ultimately reflects a single, schema-bound notion of alignment. As generative clinical AI systems grow more capable, the field will require evaluation frameworks that can account for ambiguity, tolerate diversity in clinically reasonable output, and move beyond rigid concordance toward assessments grounded in pragmatic utility.

Beyond generation, ongoing work within the SAGE Consult ecosystem aims to operationalize these templates by auto-populating them with relevant data from the medical record and evaluating how their structure shapes downstream specialist response quality. While automation may reduce the cognitive burden of verbose templates, it cannot fully resolve issues of prioritization or signal-to-noise. A central objective is to assess not just whether templates are clinically coherent, but whether they measurably improve communication efficiency, diagnostic precision, and decision-making accuracy. Parallel efforts focus on empowering generalist clinicians to formulate higher-quality consultation questions—scaffolding the initial request to elicit more targeted and actionable input. We also aim to examine the broader impact of these automations—on workflow, satisfaction, and perceived utility—for both consultants and referring clinicians. Taken together, these initiatives reflect a broader ambition: to move beyond passive documentation toward interactive, intelligence-augmented clinical dialogue, in which both ends of the consultation are meaningfully enhanced by LLM-mediated structure.

This work also has several limitations which are important to acknowledge. These templates are Stanford-specific and may not fully generalize to other healthcare contexts. Further, they are the product of a small number of specialists and may reflect individualized idiosyncrasies in the absence of a universally defined "gold standard". This task also reflects the inherent limitations of concordance-based assessment: just because a model output does not align with the original template does not necessarily mean it is incorrect. In some cases, a divergent response may be clinically reasonable—or even preferable—depending on context, specialty norms, or emerging practices. Alignment, as measured here, is a pragmatic proxy for quality, not a definitive judgment, and is difficult to reduce to binary metrics in complex clinical circumstances. As such, this benchmark should be viewed as a first-layer filter, useful for surfacing patterns and relative model performance, but insufficient on its own to determine the optimal or most expert-like consultation schema.

Deeper evaluation (through prospective trials and ultimate clinical implementation) will be necessary to fully understand which outputs best serve the needs of generalist-specialist communication. Further technical analyses would strengthen best-practice guidance for template generation. In particular, useful analyses would include (i) ablations with and without DSPy on a model-by-model basis to assess incremental benefit, (ii) a comparison of post-hoc prioritization versus constrained generation at fixed budgets (e.g., n, n+3, n+5), and (iii) detailed prompt tuning to enable a range of comprehensiveness/conciseness equilibria. Techniques for further improving grader robustness, such as multi-LLM ensembling and targeted red-teaming with semantically similar but clinically distinct items, may be beneficial. Further implementation of this work could itself improve salience: by tracking which template elements are emphasized or ignored by both consultants and consultors in real time, systems could learn what information is most valuable. Coupled with EHR auto-population of routine data, this feedback loop may better align model outputs with the practical priorities of daily clinical workflows. Owing to compute and human-review bandwidth limits, we defer these to a follow-on study and to pre-deployment hardening.

In many ways, the consultation template embodies a traditional medical informatics philosophy[50]: structured and deliberately constrained to minimize ambiguity. This approach offers clear advantages in terms of accuracy, interpretability, and interoperability[51]. Yet it also imposes limits, both on expressiveness and on adaptability to novel cases[51]. Large language models, by contrast, offer the promise of flexibility: they can process unstructured input, accommodate a wide range of clinical styles, and synthesize across disparate data. But this flexibility can come at the cost of precision, especially when reasoning implicitly or generating without clear grounding. Effective clinical AI may require combining approaches: leveraging LLMs' broad medical knowledge while imposing external structure through traditional informatics methods[52], grounding tool use[53], or human oversight. Template generation thus illustrates a broader challenge in clinical informatics—determining when to rely on models' flexibility versus when to enforce rigid schemas. The path forward likely involves systems where human expertise defines the structure and constraints, while LLMs help populate and adapt content within those boundaries.

5. Conclusion

This study finds that contemporary large language models can generate comprehensive clinical consultation templates, but struggle with the selective prioritization essential for efficient physician-

to-physician communication. Using Stanford's expert-created, actively deployed clinical consultation templates as a benchmark, and employing a physician-calibrated autograder that achieved high concordance with clinical judgment, we reveal that while frontier models successfully capture most clinically relevant information, they produce substantially longer outputs than expert-crafted templates. Moreover, this difficulty with prioritization varies markedly across specialties, with models performing particularly poorly in domains requiring nuanced contextual judgment and communication like psychiatry and pain medicine. Effective integration of LLMs into physician communication will require models that can not only recall relevant information but also recognize what matters most—within the time, attention, and workflow constraints of clinical practice.

Original Template	***O3-Generated Template***
### My Clinical Question **My Clinical Question (condition: diabetes mellitus):** *** ### My most current assessment **My most current assessment of this problem can be found in the note dated:** {Today/***} ### In your clinical question, or current note, please include information on: #### Assessments - Required **Is the patient currently taking medication to treat diabetes?** If yes, please describe. **Is this a new diagnosis of diabetes mellitus?** If not, when was the patient diagnosed with diabetes? **What type of diabetes mellitus does the patient have?** (Type I or Type II) **Insulin (including pump) or non-insulin dependent** #### Assessments - Optional **Diabetic complications** (e.g., CKD, CHF, CAD) **Glucose logs** (if available) #### Diagnostics - Required **Hemoglobin A1c (HbA1c)** **Fasting Lipid Profile** **Fasting Glucose** **Liver Function Tests** **Basic Metabolic Panel** #### Diagnostics - Optional **GAD antibodies** **C-peptide level**	### My Clinical Question **My Clinical Question (condition: diabetes mellitus):** *** ### My most current assessment **My most current assessment of this problem can be found in the note dated:** {Today/***} ### In your clinical question, or current note, please include information on: #### Assessments - Required **Type, duration, age at diagnosis** **All current medications, doses, frequency, adherence, recent changes** **Self-monitoring or CGM data:** fasting, post-prandial, patterns **Severe or symptomatic hypoglycemia episodes** (frequency, triggers, treatment) **DKA or hyperosmolar events within past year** **Dietary pattern and carbohydrate counting or exchanges** **Physical activity:** type, minutes/week, barriers; **Weight, BMI, recent change, waist circumference**; **Blood pressure readings, home and clinic** **Microvascular status:** nephropathy, retinopathy, neuropathy findings **Macrovascular disease:** CAD, cerebrovascular, peripheral arterial **Foot exam findings:** pulses, sensation, skin, ulcers **Psychosocial factors:** depression, health literacy, support, financial barriers **Family history of diabetes or cardiovascular disease** #### Assessments - Optional **Pregnancy plans or current pregnancy status**; **Sleep quality, suspected/diagnosed obstructive sleep apnea**; **Alcohol, tobacco, recreational drug use** #### Diagnostics - Required **Hemoglobin A1c** (within last 3 months) **Complete Metabolic Panel (CMP,** within last 6 months) **Urine Albumin-to-Creatinine Ratio** (within last year) **Lipid Panel** (within last year) #### Diagnostics - Optional **C-Peptide or islet antibodies** if type unclear **TSH and thyroid antibodies** (Type 1 or symptoms) **Vitamin B12 level** if on metformin >4 years **Retinal imaging report** (within past year) **12-lead ECG** (if cardiovascular risk factors)

Supplementary Figure S1. Example Templates for Endocrinology Diabetes Mellitus Consults

References

1. Kohane IS, Beam AL, Manrai AK. Why Medicine Must Become a Knowledge-Processing Discipline. *NEJM AI*. 2024;1(7):AIp2400582. doi:10.1056/AIp2400582

2. Humphrey KE, Sundberg M, Milliren CE, Graham DA, Landrigan CP. Frequency and Nature of Communication and Handoff Failures in Medical Malpractice Claims. *J Patient Saf*. 2022;18(2):130-137. doi:10.1097/PTS.0000000000000937

3. Starmer AJ, Spector ND, Srivastava R, et al. Changes in Medical Errors after Implementation of a Handoff Program. *N Engl J Med*. 2014;371(19):1803-1812. doi:10.1056/NEJMsa1405556

4. Starmer AJ, Sectish TC, Simon DW, et al. Rates of medical errors and preventable adverse events among hospitalized children following implementation of a resident handoff bundle. *JAMA*. 2013;310(21):2262-2270. doi:10.1001/jama.2013.281961

5. Umberfield E, Ghaferi AA, Krein SL, Manojlovich M. Using Incident Reports to Assess Communication Failures and Patient Outcomes. *Jt Comm J Qual Patient Saf*. 2019;45(6):406-413. doi:10.1016/j.jcjq.2019.02.006

6. Wåhlberg H, Valle PC, Malm S, Broderstad AR. Impact of referral templates on the quality of referrals from primary to secondary care: a cluster randomised trial. *BMC Health Serv Res*. 2015;15:353. doi:10.1186/s12913-015-1017-7

7. Tobin-Schnittger P, O'Doherty J, O'Connor R, O'Regan A. Improving quality of referral letters from primary to secondary care: a literature review and discussion paper. *Prim Health Care Res Dev*. 2018;19(3):211-222. doi:10.1017/S1463423617000755

8. Burden M, Sarcone E, Keniston A, et al. Prospective comparison of curbside versus formal consultations. *J Hosp Med*. 2013;8(1):31-35. doi:10.1002/jhm.1983

9. Lee MS, Ray KN, Mehrotra A, Giboney P, Yee HF Jr, Barnett ML. Primary Care Practitioners' Perceptions of Electronic Consult Systems: A Qualitative Analysis. *JAMA Intern Med*. 2018;178(6):782-789. doi:10.1001/jamainternmed.2018.0738

10. Liddy C, Drosinis P, Fogel A, Keely E. Prevention of delayed referrals through the Champlain BASE eConsult service. *Can Fam Physician*. 2017;63(8):e381-e386.

11. Peeters KMM, Reichel LAM, Muris DMJ, Cals JWL. Family Physician–to–Hospital Specialist Electronic Consultation and Access to Hospital Care: A Systematic Review. *JAMA Netw Open*. 2024;7(1):e2351623. doi:10.1001/jamanetworkopen.2023.51623

12. Arora A, Fekieta R, Spatz E, et al. Implementation and evaluation of an electronic consult program at a large academic health system. *PLOS ONE*. 2024;19(9):e0310122. doi:10.1371/journal.pone.0310122

13. New Frontiers in Team Science: Empowering Patients With AI-Driven E-Consults | DoM Annual Reports. Accessed August 1, 2025. https://domannualreports.stanford.edu/new-frontiers-in-team-science-empowering-patients-with-ai-driven-e-consults/

14. Vimalananda VG, Gupte G, Seraj SM, et al. Electronic consultations (e-consults) to improve access to specialty care: A systematic review and narrative synthesis. *J Telemed Telecare*. 2015;21(6):323-330. doi:10.1177/1357633X15582108

15. Laing S, Jarmain S, Elliott J, et al. Codesigned standardised referral form: simplifying the complexity. *BMJ Health Care Inform*. 2024;31(1):e100926. doi:10.1136/bmjhci-2023-100926

16. OpenAI o3 and o4-mini System Card. Accessed August 1, 2025. https://openai.com/index/o3-o4-mini-system-card/

17. Introducing GPT-4.1 in the API. Accessed August 1, 2025. https://openai.com/index/gpt-4-1/

18. Zapf A, Castell S, Morawietz L, Karch A. Measuring inter-rater reliability for nominal data – which coefficients and confidence intervals are appropriate? *BMC Med Res Methodol*. 2016;16:93. doi:10.1186/s12874-016-0200-9

19. Hayes AF, Krippendorff K. Answering the Call for a Standard Reliability Measure for Coding Data. *Commun Methods Meas*. 2007;1(1):77-89. doi:10.1080/19312450709336664

20. Gwet K. *Handbook of Inter-Rater Reliability: How to Estimate the Level of Agreement Between Two or Multiple Raters*. STATAXIS Publishing Company; 2001.

21. Wongpakaran N, Wongpakaran T, Wedding D, Gwet KL. A comparison of Cohen's Kappa and Gwet's AC1 when calculating inter-rater reliability coefficients: a study conducted with personality disorder samples. *BMC Med Res Methodol*. 2013;13:61. doi:10.1186/1471-2288-13-61

22. Krippendorff K. *Content Analysis: An Introduction to Its Methodology*. Fourth Edition. SAGE Publications, Inc.; 2025. doi:10.4135/9781071878781

23. Khattab O, Singhvi A, Maheshwari P, et al. DSPy: Compiling Declarative Language Model Calls into Self-Improving Pipelines. *arXiv*. Preprint posted online October 5, 2023. doi:10.48550/arXiv.2310.03714

24. Shani G, Gunawardana A. Evaluating Recommendation Systems. In: Ricci F, Rokach L, Shapira B, Kantor PB, eds. *Recommender Systems Handbook*. Springer US; 2011:257-297. doi:10.1007/978-0-387-85820-3_8

25. Järvelin K, Kekäläinen J. Cumulated gain-based evaluation of IR techniques. *ACM Trans Inf Syst*. 2002;20(4):422-446. doi:10.1145/582415.582418

26. OpenAI, Hurst A, Lerer A, et al. GPT-4o System Card. *arXiv*. Preprint posted online October 25, 2024. doi:10.48550/arXiv.2410.21276

27. Gemini 2.5: Our most intelligent AI model. Google. March 25, 2025. Accessed August 1, 2025. https://blog.google/technology/google-deepmind/gemini-model-thinking-updates-march-2025/

28. Introducing Claude 4. Accessed August 1, 2025. https://www.anthropic.com/news/claude-4

29. Kimi K2: Open Agentic Intelligence. Accessed August 1, 2025. https://moonshotai.github.io/Kimi-K2/

30. Introducing Meta Llama 3: The most capable openly available LLM to date. Accessed August 1, 2025. https://ai.meta.com/blog/meta-llama-3/

31. Brodeur PG, Buckley TA, Kanjee Z, et al. Superhuman performance of a large language model on the reasoning tasks of a physician. *arXiv*. Preprint posted online June 2, 2025. doi:10.48550/arXiv.2412.10849

32. Singhal K, Tu T, Gottweis J, et al. Toward expert-level medical question answering with large language models. *Nat Med*. 2025;31(3):943-950. doi:10.1038/s41591-024-03423-7

33. Tu T, Palepu A, Schaekermann M, et al. Towards Conversational Diagnostic AI. *arXiv*. Preprint posted online January 11, 2024. doi:10.48550/arXiv.2401.05654

34. Goh E, Gallo R, Hom J, et al. Large Language Model Influence on Diagnostic Reasoning. *JAMA Netw Open*. 2024;7(10):e2440969. doi:10.1001/jamanetworkopen.2024.40969

35. Busch F, Hoffmann L, Rueger C, et al. Current applications and challenges in large language models for patient care: a systematic review. *Commun Med*. 2025;5:26. doi:10.1038/s43856-024-00717-2

36. Hartman V, Zhang X, Poddar R, et al. Developing and Evaluating Large Language Model–Generated Emergency Medicine Handoff Notes. *JAMA Netw Open*. 2024;7(12):e2448723. doi:10.1001/jamanetworkopen.2024.48723

37. Williams CYK, Subramanian CR, Ali SS, et al. Physician- and Large Language Model-Generated Hospital Discharge Summaries. *JAMA Intern Med*. 2025;185(7):818-825. doi:10.1001/jamainternmed.2025.0821

38. Landman AB, Tilak SS, Walker GA. Artificial Intelligence–Generated Emergency Department Summaries and Hospital Handoffs. *JAMA Netw Open*. 2024;7(12):e2448729. doi:10.1001/jamanetworkopen.2024.48729

39. McCoy LG, Manrai AK, Rodman A. Large Language Models and the Degradation of the Medical Record. *N Engl J Med*. Published online October 31, 2024. doi:10.1056/NEJMp2405999

40. Ntinopoulos V, Rodriguez Cetina Biefer H, Tudorache I, et al. Large language models for data extraction from unstructured and semi-structured electronic health records: a multiple model performance evaluation. *BMJ Health Care Inform*. 2025;32(1):e101139. doi:10.1136/bmjhci-2024-101139

41. Bedi S, Liu Y, Orr-Ewing L, et al. Testing and Evaluation of Health Care Applications of Large Language Models. *JAMA*. 2025;333(4):319-328. doi:10.1001/jama.2024.21700

42. Hager P, Jungmann F, Holland R, et al. Evaluation and mitigation of the limitations of large language models in clinical decision-making. *Nat Med*. 2024;30(9):2613-2622. doi:10.1038/s41591-024-03097-1

43. McCoy LG, Swamy R, Sagar N, et al. Do Language Models Think Like Doctors? *medRxiv*. Preprint posted online February 12, 2025:2025.02.11.25321822. doi:10.1101/2025.02.11.25321822

44. Wang K, Duan F, Li P, Wang S, Cai X. LLMs Know What They Need: Leveraging a Missing Information Guided Framework to Empower Retrieval-Augmented Generation. *arXiv*. Preprint posted online April 22, 2024. doi:10.48550/arXiv.2404.14043

45. Li SS, Mun J, Brahman F, Ilgen JS, Tsvetkov Y, Sap M. Aligning LLMs to Ask Good Questions A Case Study in Clinical Reasoning. *arXiv*. Preprint posted online February 20, 2025. doi:10.48550/arXiv.2502.14860

46. Baines R, Tredinnick-Rowe J, Jones R, Chatterjee A. Barriers and Enablers in Implementing Electronic Consultations in Primary Care: Scoping Review. *J Med Internet Res*. 2020;22(11):e19375. doi:10.2196/19375

47. Panigutti C, Beretta A, Fadda D, et al. Co-design of Human-centered, Explainable AI for Clinical Decision Support. *ACM Trans Interact Intell Syst*. 2023;13(4):21:1-21:35. doi:10.1145/3587271

48. Davis J, Goadrich M. The relationship between Precision-Recall and ROC curves. In: *Proceedings of the 23rd International Conference on Machine Learning*. ICML '06. Association for Computing Machinery; 2006:233-240. doi:10.1145/1143844.1143874

49. Elkan C. The foundations of cost-sensitive learning. In: *Proceedings of the 17th International Joint Conference on Artificial Intelligence - Volume 2*. IJCAI'01. Morgan Kaufmann Publishers Inc.; 2001:973-978.

50. Bates DW, Kuperman GJ, Wang S, et al. Ten commandments for effective clinical decision support: making the practice of evidence-based medicine a reality. *J Am Med Inform Assoc JAMIA*. 2003;10(6):523-530. doi:10.1197/jamia.M1370

51. Rosenbloom ST, Denny JC, Xu H, Lorenzi N, Stead WW, Johnson KB. Data from clinical notes: a perspective on the tension between structure and flexible documentation. *J Am Med Inform Assoc JAMIA*. 2011;18(2):181-186. doi:10.1136/jamia.2010.007237

52. Geng S, Cooper H, Moskal M, et al. JSONSchemaBench: A Rigorous Benchmark of Structured Outputs for Language Models. *arXiv*. Preprint posted online February 27, 2025. doi:10.48550/arXiv.2501.10868

53. Goodell AJ, Chu SN, Rouholiman D, Chu LF. Large language model agents can use tools to perform clinical calculations. *Npj Digit Med*. 2025;8(1):163. doi:10.1038/s41746-025-01475-8

Biological molecular function: methods and benchmarks for finding function in biological dark matter

Jason E. McDermott
Computational Biology Group, Pacific Northwest National Laboratory
Richland, Washington 99352, USA
Department of Molecular Microbiology and Immunology, Oregon Health & Science University
Portland, Oregon 97239, USA
Email: Jason.McDemott@pnnl.gov

Yana Bromberg
Departments of Computer Science and Biology, Emory University
Atlanta, Georgia 30322, USA
Email: yana.bromberg@emory.edu

Hannah Carter
Division of Genomics and Precision Medicine, University of California, San Diego
San Diego, California 92093, USA
Email: hkcarter@ucsd.edu

Travis Wheeler
College of Pharmacy, University of Arizona
Tucson, Arizona 85721, USA
Email: twheeler@arizona.edu

The accurate determination of biological molecular function remains one of the most significant challenges in computational biology, with vast areas of biological "dark matter" persisting in microbiomes, viruses, and unexplored sequence space. To meet this challenge, we developed at PSB session to address the limitations of traditional sequence similarity-based functional annotation methods and explores how recent advances in AI/ML and high-throughput data generation are transforming the field. We highlight four innovative contributions presented in this session: a geometric framework using signed distance functions for modeling protein surfaces; a reinforcement learning-based approach for steering protein generative models to design functional sequences; an ensemble framework combining sequence, structural, and network features for subcellular localization prediction; and a scalable factorization method integrating gene-gene interaction data for analyzing high-dimensional genetic perturbation profiles. Together, these methodologies showcase the potential for computational and AI-driven tools to address the complex and multiscale nature of molecular function prediction, paving the way for new discoveries in understanding and engineering biological systems.

Keywords: function, machine learning, artificial intelligence, sequence.

© 2025 The Authors. Open Access chapter published by World Scientific Publishing Company and distributed under the terms of the Creative Commons Attribution Non-Commercial (CC BY-NC) 4.0 License.

1. Introduction

What is biological molecular function? We doubt you'd be able to get two experts on the subject to agree on what precisely this entails. By relying on textbook definitions, the term can be interpreted to mean the specific biochemical activity performed by any molecule. Within a cell this is typically a protein or RNA. Activity includes enzymatic activities, binding interactions, and structural roles among an infinity of other functions. Here, however, the ease of definitions ends. Can function be described without consideration of molecular, cellular, organismal, and even community/ecosystem context? Are parts of the same pathway considered to be interacting even if they are never in the same location? Does the human ortholog of a yeast enzyme have the same function? In spite of these issues with definition, the field has been developing methods for years aimed at prediction and characterization of gene and protein function (Zhou, Jiang et al. 2019).

Even for well-characterized organisms, the number of genes and proteins with unknown or poorly defined functional annotations is substantial (Rocha, Jayaram et al. 2023), with particular blind spots for non-canonical isoforms. And in microbial communities and viruses, existing methods frequently leave more than half of the proteins with unannotated functions often failing to find even putative homologs. RNA sequences, metabolites and other small molecules are even less well-characterized, with only a fraction of identified species having any kind of known functional role. Furthermore, even the existing functional labels are limited, with many describing only aspects of function or lacking specificity to accurately describe the role of the molecule in the system.

Function depends on the context in which it takes place, as molecules participate in systems and structures at differing levels of scale and abstraction. High-throughput data generation methods, along with automated platforms for experimental investigation, offer ways to provide contextual information by measuring many thousands of molecular species in biological samples under different environmental conditions that cause changes in system interactions. Until now, however, the potential of these data streams to inform learning models for functional annotation has remained largely untapped.

The recent revolution in AI/ML methods represents a significant opportunity to make in-roads into the problem of unknown functions. Especially relevant are advances in protein structure prediction, which can now be accomplished with high fidelity from just protein sequence alone. These approaches have opened new avenues for computational function determination. However, these approaches have not solved the function annotation problem; significant limitations and dark areas of function for many molecules still remain.

This session is focused on bringing to light new thinking about the following questions: How can we define a function of a particular molecule? How can this functional label be propagated to other molecules? What is the relationship of these labels? How can labeling systems describe context at different levels of detail, and how do they link to phenotypic outcomes?

2. Overview of the functional annotation problem

Functional characterization of individual genes and proteins has a long history in science, with years of research leading to specific enzymatic, signaling, and/or systems-level functions being

determined for individual molecules. In the era of high-throughput biological data acquisition, our ability to gather novel genetic material and thus protein sequences has vastly outpaced our ability to determine functions experimentally for those molecules. In part, this is because experimental function determination is not easily possible in unculturable organisms, such as those from environmental sources, or for many viruses where experimental systems do not exist and/or genetic manipulation is challenging (Schloss and Handelsman 2005, Mahler, Costa et al. 2023).

To address this gap, databases that capture experimental functional knowledge have been developed and, concomitantly, bioinformatic methods for determining sequence similarity. Sequence similarity is the primary method used to infer evolutionary relationships between sequences and can be used to associate a novel sequence with a sequence or sequence family that has an experimentally determined function allowing transference of annotations computationally to a large number of sequences (Hamp, Kassner et al. 2013). However, it is estimated that in many organisms, 20-40% of the proteins encoded cannot be assigned a specific function (Lobb, Tremblay et al. 2020). This problem is more pronounced in sequences derived from microbiomes and viromes, where the majority of proteins can't be annotated in this way (Wang, Ma et al. 2017).

Traditional methods rely on sequence similarity to infer evolutionary (and therefore functional) relationships between genes and proteins. The BLAST (Altschul, Gish et al. 1990) software suite provides relatively rapid methods for searching large sequence databases, while modern alternatives like MMSeqs2 (Steinegger and Soding 2017) and DIAMOND (Buchfink, Reuter and Drost 2021) introduce greater speed, and profile hidden Markov models (Eddy 2011, Roddy, Rich and Wheeler 2024) can increase sensitivity particularly when provided with organized sequence families (Mistry, Chuguransky et al. 2021).

3. Use of structure for prediction of function

Recent advances in structure prediction have opened new possibilities for determining structure-based similarity from known or predicted structures, which can identify relationships not evident from sequence alone. Tools like FoldSEEK leverage structure predictions to enable rapid searching for structurally similar proteins (Pan, Wu et al. 2024, van Kempen, Kim et al. 2024). Because protein structure determines function these approaches allow transference of annotations using structural similarity. Some methods exist which aim to characterize structural properties or motifs to more directly predict function, for example, predicting binding sites and substrates directly from structure (Krivak and Hoksza 2018, Fang, Jiang et al. 2023). These are particularly exciting as they do not directly depend on the existence of well-characterized orthologs for function determination. Additionally, related methods are being developed that allow prediction of functional context via structure, to predict protein localization and interactions with cellular systems context.

For example, the paper by Scott et al., 'Implicitly and Differentiably Representing Protein Surfaces and Interfaces' presents an innovative method for computationally representing protein shapes,

emphasizing the use of signed distance functions (SDFs) to model solvent-accessible surfaces. By integrating SDFs with constructive solid geometry operations, the authors demonstrate potential advancements in predicting protein conformation with potential impact on estimates of binding potential and structure-aware design predictions. The work sets the stage for leveraging machine learning techniques, such as pretrained protein transformers, to enhance these representations and better understand protein behavior.

The paper by Viggiano et al., 'Steering Protein Generative Models at Test-Time for Guided AAV2 Capsid Design' does not attempt to predict protein function. Instead it explores methods for guiding pretrained generative models to design protein sequences with specific functional properties. Their method, ProVADA+, utilizes reinforcement learning-based adaptive masking and advanced sequence evaluation metrics to efficiently explore sequence space to generate optimized variants. The method demonstrates success in designing viable Adeno-Associated Virus (AAV2) capsids, overcoming challenges posed by rugged fitness landscapes. This approach highlights the potential for computational techniques to accelerate the rational design of proteins with complex, user-defined functionalities.

4. Protein language models for predicting function

New protein language models trained on large sets of sequence data such as ESM (Rives, Meier et al. 2021) and ProteinBERT (Brandes, Ofer et al. 2022) allow searching sequence space for contextual patterns, and may provide insight into underlying biology and thus function of those sequences. These models build on numerous advances in machine learning and deep learning in the past few decades, with many methods being developed to target specific functional prediction problems for classes of proteins, address limitations in standard sequence similarity methods, or predict specific functional properties for proteins like localization or tissue specificity. In our session, the paper by Ahmed, et al. 'HALO: Hybrid Attention Model for Subcellular Localization' integrates structural and sequence-based approaches to predict subcellular localization for proteins, an important component of functional context. It emphasizes the use of large-scale language models like ESM and ProtT5, fine-tuned on subcellular localization datasets, to generate rich protein representations. By combining sequence embeddings, structural features, and graph neural networks within an ensemble framework, the approach achieves enhanced predictive accuracy and robustness. The work underscores the transformative potential of combining structural biology and deep learning to better understand protein function.

5. Analysis of high-throughput functional assays for function prediction

The ability to assay thousands of molecules at once provides rich sources of data for a diverse range of systems. These datasets have been used extensively to provide functional information for many genes and proteins at varying levels of scale and for different purposes (McDermott, Arshad et al. 2020, Kustatscher, Collins et al. 2022). They have been also used to determine relationships between molecules, and thus inform about their function through grouping similar functions (Wolfe, Kohane

and Butte 2005) or through associating molecular profiles with phenotypes of disease outcomes or genetic features. Similarly, the ability to genetically manipulate hundreds or thousands of genes in cells provides a powerful way of examining the effects of individual genes on the system function, as well as examining interactions between genes. In our session, the paper by Chang et al., 'PertSpectra: Interpretable Matrix Factorization for Genetic Perturbations' presents a scalable approach for analyzing high-dimensional genetic perturbation datasets to uncover biologically relevant gene interactions. The method combines matrix factorization with biologically informed inductive biases, integrating gene-gene interaction graphs to improve the interpretability of learned embeddings. PertSpectra demonstrates improved computational efficiency and scalability compared to other models, making it well-suited for large-scale genetic screens. The framework offers a powerful tool for predicting cellular responses to complex perturbations and advancing our understanding of gene function and regulation.

6. Large Language Models (LLMs) in protein function prediction

The development of large language models (LLMs) has transformed computational biology by enabling sophisticated analyses of protein sequences and functions. Trained on vast quantities of text from many domains, they provide a great deal of context and can be used to help predict function. However, their ability to generalize and to predict function for proteins and systems that have not been well studied are likely limited. The comprehensiveness and accuracy of training data raises concerns about biases and generalization to understudied proteins, microbiomes, and viromes.

The paper by, Shringapure et al. demonstrate the powerful and scalable application of LLMs for causal gene prioritization in genome-wide association studies (GWAS). By synthesizing complex scientific literature, LLMs helped identify high-probability candidate genes, successfully outperforming current methods across benchmark datasets. The paper highlights the potential of LLMs to fill critical gaps in understanding functional impacts of genetic loci while underscoring the need for refined methodologies to enhance transparency and mitigate biases in their predictions.

The study by Wang et al. introduces Gene-R1, a specialized open-source LLM framework aimed at improving gene set analysis tasks. By incorporating domain-specific knowledge and reinforced fine-tuning methodologies, Gene-R1 narrows the performance gap between open models and proprietary systems. While it exhibits significant advancements in reasoning and task-specific accuracy, this study also acknowledges existing challenges, such as hallucinations outside of training domains and transferability to other ontologies, emphasizing future directions for development.

Zhapa-Camacho et al. explore the emerging potential of agent-based LLM systems, such as LangChain and CAMEL-AI, for protein function prediction. These systems enhance traditional LLM capabilities by introducing multi-step reasoning processes that integrate structured biological datasets and experimental evidence on-the-fly. This approach allows predictions to be iteratively refined, combining computational outputs with curated biological constraints. Such frameworks significantly improve both the interpretability and accuracy of protein function determination,

positioning LLM-agent systems as a powerful tool for addressing the complexity of biological datasets.

These contributions demonstrate both the progress and the persistent challenges for LLMs in protein function prediction. By addressing core issues such as limited interpretability, data bias, and the integration of curated biological knowledge, these studies push the boundaries of applying LLMs to one of computational biology's most enduring challenges.

7. Conclusions

Computational prediction of molecular function is critical to our ability to understand, utilize, and control biological systems. Our session highlights a number of advances in this area, from new approaches to using protein structure to methods for making sense of large-scale genetic perturbations. Advances in AI and systems modeling, coupled with the explosive growth of various forms of biological data from different systems is likely to drive a transformation of this problem in the near future.

8. Acknowledgments

The session organizers would like to thank Dr. Martin Steinegger for giving an invited talk at the session and the anonymous reviewers who reviewed the submitted papers for the session. Funding to support this work was provided to JEM from Pacific Northwest National Laboratory's Predictive Phenomics Initiative conducted under the Laboratory Directed Research and Development Program. PNNL is a multiprogram national laboratory operated by Battelle for the U.S. Department of Energy under Contract No. DE-AC05-76RL01830. Funding to support JEM and TJW was provided under NIH/NIDCR U01DE034176-01.

References

Altschul, S. F., W. Gish, W. Miller, E. W. Myers and D. J. Lipman (1990). "Basic local alignment search tool." J Mol Biol **215**(3): 403-410.

Brandes, N., D. Ofer, Y. Peleg, N. Rappoport and M. Linial (2022). "ProteinBERT: a universal deep-learning model of protein sequence and function." Bioinformatics **38**(8): 2102-2110.

Buchfink, B., K. Reuter and H. G. Drost (2021). "Sensitive protein alignments at tree-of-life scale using DIAMOND." Nat Methods **18**(4): 366-368.

Eddy, S. R. (2011). "Accelerated Profile HMM Searches." PLoS Comput Biol **7**(10): e1002195.

Fang, Y., Y. Jiang, L. Wei, Q. Ma, Z. Ren, Q. Yuan and D. Q. Wei (2023). "DeepProSite: structure-aware protein binding site prediction using ESMFold and pretrained language model." Bioinformatics **39**(12).

Hamp, T., R. Kassner, S. Seemayer, E. Vicedo, C. Schaefer, D. Achten, F. Auer, A. Boehm, T. Braun, M. Hecht, M. Heron, P. Honigschmid, T. A. Hopf, S. Kaufmann, M. Kiening, D. Krompass, C. Landerer, Y. Mahlich, M. Roos and B. Rost (2013). "Homology-based inference sets the bar high for protein function prediction." BMC Bioinformatics **14 Suppl 3**(Suppl 3): S7.

Krivak, R. and D. Hoksza (2018). "P2Rank: machine learning based tool for rapid and accurate prediction of ligand binding sites from protein structure." J Cheminform **10**(1): 39.

Kustatscher, G., T. Collins, A. C. Gingras, T. Guo, H. Hermjakob, T. Ideker, K. S. Lilley, E. Lundberg, E. M. Marcotte, M. Ralser and J. Rappsilber (2022). "Understudied proteins: opportunities and challenges for functional proteomics." Nat Methods **19**(7): 774-779.

Lobb, B., B. J. Tremblay, G. Moreno-Hagelsieb and A. C. Doxey (2020). "An assessment of genome annotation coverage across the bacterial tree of life." Microb Genom **6**(3).

Mahler, M., A. R. Costa, S. P. B. van Beljouw, P. C. Fineran and S. J. J. Brouns (2023). "Approaches for bacteriophage genome engineering." Trends Biotechnol **41**(5): 669-685.

McDermott, J. E., O. A. Arshad, V. A. Petyuk, Y. Fu, M. A. Gritsenko, T. R. Clauss, R. J. Moore, A. A. Schepmoes, R. Zhao, M. E. Monroe, M. Schnaubelt, C. F. Tsai, S. H. Payne, C. Huang, L. B. Wang, S. Foltz, M. Wyczalkowski, Y. Wu, E. Song, M. A. Brewer, M. Thiagarajan, C. R. Kinsinger, A. I. Robles, E. S. Boja, H. Rodriguez, D. W. Chan, B. Zhang, Z. Zhang, L. Ding, R. D. Smith, T. Liu, K. D. Rodland and C. Clinical Tumor Analysis (2020). "Proteogenomic Characterization of Ovarian HGSC Implicates Mitotic Kinases, Replication Stress in Observed Chromosomal Instability." Cell Rep Med **1**(1).

Mistry, J., S. Chuguransky, L. Williams, M. Qureshi, G. A. Salazar, E. L. L. Sonnhammer, S. C. E. Tosatto, L. Paladin, S. Raj, L. J. Richardson, R. D. Finn and A. Bateman (2021). "Pfam: The protein families database in 2021." Nucleic Acids Res **49**(D1): D412-D419.

Pan, H., Z. Wu, W. Liu and G. Zhang (2024). "AlphaFun: Structural-Alignment-Based Proteome Annotation Reveals why the Functionally Unknown Proteins (uPE1) Are So Understudied." J Proteome Res **23**(5): 1593-1602.

Rives, A., J. Meier, T. Sercu, S. Goyal, Z. Lin, J. Liu, D. Guo, M. Ott, C. L. Zitnick, J. Ma and R. Fergus (2021). "Biological structure and function emerge from scaling unsupervised learning to 250 million protein sequences." Proc Natl Acad Sci U S A **118**(15).

Rocha, J. J., S. A. Jayaram, T. J. Stevens, N. Muschalik, R. D. Shah, S. Emran, C. Robles, M. Freeman and S. Munro (2023). "Functional unknomics: Systematic screening of conserved genes of unknown function." PLoS Biol **21**(8): e3002222.

Roddy, J. W., D. H. Rich and T. J. Wheeler (2024). "nail: software for high-speed, high-sensitivity protein sequence annotation." bioRxiv.

Schloss, P. D. and J. Handelsman (2005). "Metagenomics for studying unculturable microorganisms: cutting the Gordian knot." Genome Biol **6**(8): 229.

Steinegger, M. and J. Soding (2017). "MMseqs2 enables sensitive protein sequence searching for the analysis of massive data sets." Nat Biotechnol **35**(11): 1026-1028.

van Kempen, M., S. S. Kim, C. Tumescheit, M. Mirdita, J. Lee, C. L. M. Gilchrist, J. Soding and M. Steinegger (2024). "Fast and accurate protein structure search with Foldseek." Nat Biotechnol **42**(2): 243-246.

Wang, J., Z. Ma, S. A. Carr, P. Mertins, H. Zhang, Z. Zhang, D. W. Chan, M. J. Ellis, R. R. Townsend, R. D. Smith, J. E. McDermott, X. Chen, A. G. Paulovich, E. S. Boja, M. Mesri, C. R. Kinsinger, H. Rodriguez, K. D. Rodland, D. C. Liebler and B. Zhang (2017). "Proteome Profiling Outperforms Transcriptome Profiling for Coexpression Based Gene Function Prediction." Mol Cell Proteomics **16**(1): 121-134.

Wolfe, C. J., I. S. Kohane and A. J. Butte (2005). "Systematic survey reveals general applicability of "guilt-by-association" within gene coexpression networks." BMC Bioinformatics **6**: 227.

Zhou, N., Y. Jiang, T. R. Bergquist, A. J. Lee, B. Z. Kacsoh, A. W. Crocker, K. A. Lewis, G. Georghiou, H. N. Nguyen, M. N. Hamid, L. Davis, T. Dogan, V. Atalay, A. S. Rifaioglu, A. Dalkıran, R. Cetin Atalay, C. Zhang, R. L. Hurto, P. L. Freddolino, Y. Zhang, P. Bhat, F. Supek, J. M. Fernández, B. Gemovic, V. R. Perovic, R. S. Davidović, N. Sumonja, N. Veljkovic, E. Asgari, M. R. K. Mofrad, G. Profiti, C. Savojardo, P. L. Martelli, R. Casadio, F. Boecker, H. Schoof, I. Kahanda, N. Thurlby, A. C. McHardy, A. Renaux, R. Saidi, J. Gough, A. A. Freitas, M. Antczak, F. Fabris, M. N. Wass, J. Hou, J. Cheng, Z. Wang, A. E. Romero, A. Paccanaro, H. Yang, T. Goldberg, C. Zhao, L. Holm, P. Törönen, A. J. Medlar, E. Zosa, I. Borukhov, I. Novikov, A. Wilkins, O. Lichtarge, P. H. Chi, W. C. Tseng, M. Linial, P. W. Rose, C. Dessimoz, V. Vidulin, S. Dzeroski, I. Sillitoe, S. Das, J. G. Lees, D. T. Jones, C. Wan, D. Cozzetto, R. Fa, M. Torres, A. Warwick Vesztrocy, J. M. Rodriguez, M. L. Tress, M. Frasca, M. Notaro, G. Grossi, A. Petrini, M. Re, G. Valentini, M. Mesiti, D. B. Roche, J. Reeb, D. W. Ritchie, S. Aridhi, S. Z. Alborzi, M. D. Devignes, D. C. E. Koo, R. Bonneau, V. Gligorijević, M. Barot, H. Fang, S. Toppo, E. Lavezzo, M. Falda, M. Berselli, S. C. E. Tosatto, M. Carraro, D. Piovesan, H. Ur Rehman, Q. Mao, S. Zhang, S. Vucetic, G. S. Black, D. Jo, E. Suh, J. B. Dayton, D. J. Larsen, A. R. Omdahl, L. J. McGuffin, D. A. Brackenridge, P. C. Babbitt, J. M. Yunes, P. Fontana, F. Zhang, S. Zhu, R. You, Z. Zhang, S. Dai, S. Yao, W. Tian, R. Cao, C. Chandler, M. Amezola, D. Johnson, J. M. Chang, W. H. Liao, Y. W. Liu, S. Pascarelli, Y. Frank, R. Hoehndorf, M. Kulmanov, I. Boudellioua, G. Politano, S. Di Carlo, A. Benso, K. Hakala, F. Ginter, F. Mehryary, S. Kaewphan, J. Björne, H. Moen, M. E. E. Tolvanen, T. Salakoski, D. Kihara, A. Jain, T. Šmuc, A. Altenhoff, A. Ben-Hur, B. Rost, S. E. Brenner, C. A. Orengo, C. J. Jeffery, G. Bosco, D. A. Hogan, M. J. Martin, C. O'Donovan, S. D. Mooney, C. S. Greene, P. Radivojac and I. Friedberg (2019). "The CAFA challenge reports improved protein function prediction and new functional annotations for hundreds of genes through experimental screens." Genome Biol **20**(1): 244.

Implicitly and Differentiably Representing Protein Surfaces and Interfaces

Cory B. Scott†, Charlie Rothschild, and Benjamin E. Nye
Department of Mathematics and Computer Science, Colorado College, Colorado Springs, CO 80909, USA
†*E-mail: cbs@coloradocollege.edu*
https://sites.coloradocollege.edu/cbs/

We introduce a pipeline for implicitly representing a protein, or protein complex, as the union of signed distance functions (SDFs) by representing each atom as a sphere with the appropriate van der Waals radius. While this idea has been used previously as a way to render images of proteins, it has not, to our knowledge, been widely adopted in a machine learning setting. Mirroring recent successful work applying SDFs to represent 3D geometry, we present a proof of concept that this representation of proteins could be useful in several biologically relevant applications. We also propose further experiments that are necessary to validate the proposed approach.

Keywords: Signed Distance Function; Differentiability; Protein Structure; Solvent Accessible Surface

1. Introduction

Modeling the three-dimensional shape of proteins is crucially important for understanding how they interact with other molecules. Advances in representations of protein structure have lead to corresponding advances in the ability for machine learning (ML) methods to predict biologically relevant properties of proteins, such as: binding affinity with bioactive molecules; prediction of protein conformation; and simulation of protein behavior under a variety of external conditions. One common representation of proteins that has received much attention is the *protein surface*,[1] also sometimes called the *solvent accessible surface* (SAS), which is a 2D manifold that represents the portion of the protein's surface that is physically accessible to a solvent. Classical methods[2] for computing the SAS involve rolling an imaginary probe (with the radius of a solvent molecule, typically water) over the surface of the protein and storing the points of contact between the probe and the surface.

In contrast, in this work, we propose an alternate protein surface representation: an isosurface of a signed distance function (SDF), produced by smoothing the boolean union of individual spherical SDFs for each of the protein's component atoms. This approach naturally produces the same biologically relevant notion of a protein's solvent-accessible surface, but represented as an alternative object that naturally integrates with current ML methods and tooling. Historically, changes in the way an object is represented can significantly affect the tractability of modeling it for ML tasks. We present a proof-of-concept demonstration of

© 2025 The Authors. Open Access chapter published by World Scientific Publishing Company and distributed under the terms of the Creative Commons Attribution Non-Commercial (CC BY-NC) 4.0 License.

how this representation can be applied to predict protein-protein interactions; further work is needed to quantify the benefits of the proposed approach. The main contributions of this work are as follows: 1) we discuss prior work training machine learning models on protein surface geometry; 2) we demonstrate a way to represent this surface as the zero-level set of a signed distance function, constructed with boolean operations; 3) we investigate using acceleration structures to query a protein SDF more efficiently; 4) we produce a dataset of protein-protein interface meshes, and provide code to reproduce our results; 5) we illustrate two potential applications to analyzing proteins in motion as well as binding sites.

1.1. *Mathematical and Biological Background*

We first introduce some necessary background in protein biology, geometry, and geometric machine learning. Throughout this paper, variables with an arrow ($\vec{x}$) represent points in nD Euclidean space, lowercase letters represent constants, and $||\cdot||$ is the nD Euclidean norm.

Signed Distance Functions (SDFs) Let $\Omega \subset \mathbb{R}^n$ be a compact subset of Euclidean space, and let $\partial\Omega$ represent its boundary. For any point $\vec{x} \in \mathbb{R}^n$, the signed distance $d_\Omega(\vec{x})$ is defined as:

$$d_\Omega(\vec{x}) = \begin{cases} 0 & x \in \partial\Omega \\ -||\vec{x} - \vec{y}|| & \vec{x} \in \Omega \quad \text{where} \quad \vec{y} = \arg\min_{\vec{y} \in \partial\Omega} ||\vec{x} - \vec{y}|| \\ ||\vec{x} - \vec{y}|| & \vec{x} \notin \Omega \end{cases} \tag{1}$$

In other words, the signed distance measures the distance between any point and the boundary of Ω, with the sign indicating whether a point is inside the shape or not (some authors take the opposite sign as convention, i.e. positive values denote an object's interior). Signed distance functions have many properties that make them useful in a machine learning context: 1) they have unit gradient everywhere the gradient is defined; 2) analytic formulae have been found for a wide variety of SDFs for specfic shapes;[3] and most significantly for this work, 3) simple SDFs can be combined into SDFs for more complex shapes using basic boolean operations. We will specifically make use of the exponential *smooth-min* operation, one of a family of SDF blending operations originally proposed by Quilez.[4] If $d_1(x), d_2(x), \ldots d_n(x)$ are a set of SDFs, then their smooth-min $\mathbf{d}$ is given by

$$\mathbf{d}(\vec{x}) = -k \log \left(\sum_{i=1}^{n} e^{-\frac{1}{k} d_i(\vec{x})} \right) \text{ where } k \text{ determines the smoothing radius.} \tag{2}$$

As a relevant example of a specific closed-form analytic SDF, the SDF d for a n-dimensional sphere of radius r centered at $\vec{y}$ is given by $d(\vec{x}) = ||\vec{x} - \vec{y}|| - r$.

When SDFs are combined with boolean operations, the resulting function may not be a true SDF, in the sense that it may not strictly satisfy Equation 1, but in practice the resulting distance fields are approximate enough for typical applications including training ML models.

Protein Surfaces Protein surfaces[5] are a common way to represent the parts of a protein that are available to react/bind with other proteins or small molecules. A protein surface is typically calculated by representing each atom as a hard-shell sphere of a given radius, and

rolling a simulated spherical probe (typically taken to have the radius of a single hydrogen atom, 1Å) over the collection of atoms. The final mesh representing the protein is produced by discretizing the surface traced by the probe. If we trace the center of the probe sphere, we get the Solvent Accessible Surface (SAS) of the protein. Tracing instead all the contact points between the probe and the atoms of our molecule produces the Solvent Excluded Surface. See Figure 1 for examples of protein solvent excluded surfaces.

1.2. *ML Analysis of Protein Surfaces*

Protein design and analysis is a rapidly evolving application area of machine learning.[6,7] For a more thorough review of ML for protein design and concepts in geometric machine learning, we refer the reader to Cheng et al.[8] and Bronstein et. al[9] respectively. Protein surfaces have been widely adopted as a representation of proteins that facilitates training machine learning models to identify possible protein-protein and protein-ligand interactions.[10–15] While much of the prior work on protein surfaces has focused on meshes as an intermediate representation, there is a complimentary vein of work that uses signed distance functions to represent proteins. SDFs have been thoroughly examined in the context of rendering 2D and 3D images of proteins.[16–18] Much of this prior work uses machine learning or an SDF representation of proteins, but not both. A notable exception is Sverrisson et al.[19] which uses a similar atomic union SDF to the one we propose. However, that work mainly examines the definition of a convolution-like operation on implicitly defined protein surfaces, and does not consider combinations of such surfaces with constructive solid geometry operations as we do in the present work.

2. Method

2.1. *Protein Representation*

We propose representing a protein as the union of spherical SDFs of each of its component atoms, where each atom is a sphere sized according to its van der Waals radius (as reported by Bondi[20]). These spherical SDFs are combined using the smooth-min operation, which we and others have observed in practice[19,21] to closely resemble SAS and SES computed via other means. See Figure 1 for several examples of protein SDFs computed according to this method. We implement these SDFs in Pytorch,[22] enabling backpropagation of error through loss functions composed of protein SDF queries, and provide the code for operationalizing ML tasks using SDF protein surface representations.

2.1.1. *Possible Issues*

As noted above, boolean operations on SDFs are not guaranteed to produce a function that satisfies Equation 1. The effect of this on our proposed protein SDF can be seen in Figure 2. The overlapping SDFs in the protein interior produce a lower bound instead of the true SDF value. However, for the union operation, the resulting SDF has the correct $d = 0$ isosurface and exterior distance values. We expect that this limitation should have little impact on downstream applications, since protein-protein and protein-ligand interactions occur exclusively on the exterior.

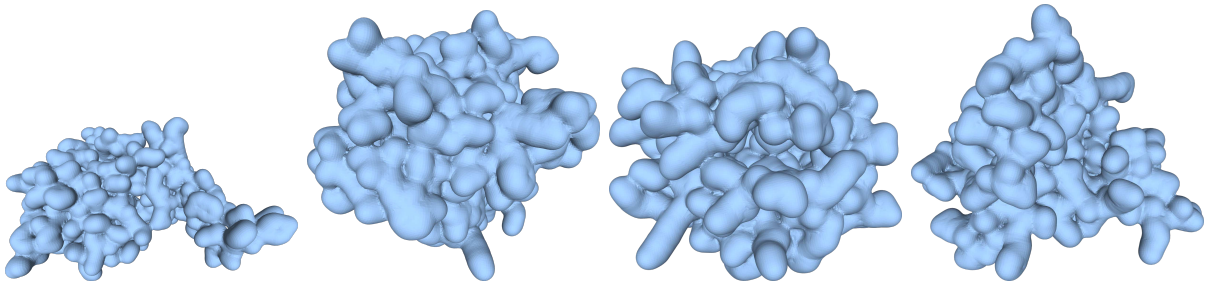

(a) 2I9B (b) 1JK9 (c) 1WEJ (d) 1PXV

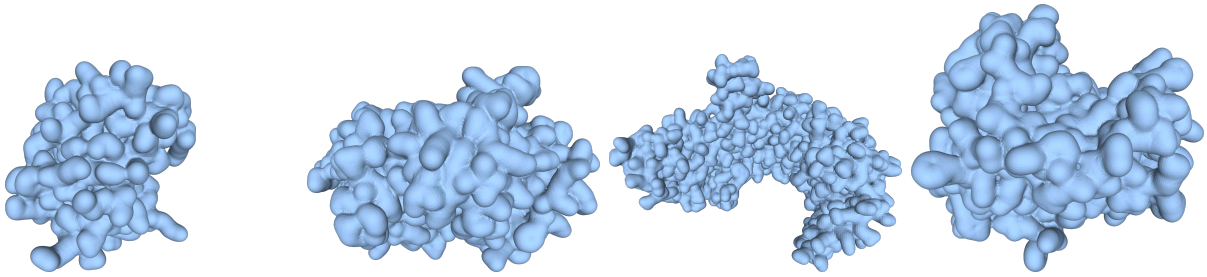

(e) 7CEI (f) 2GAF (g) 1IBR (h) 1A2K

Fig. 1: $d = 0$-level set meshes of multiple proteins from the DB5 dataset. Each protein imaged here is the "left" chain of the protein complex, in its bound confirmation. See Table 1 for a detailed explanation of these proteins.

2.2. *Intersection of Protein Chains*

In this section, we use properties of SDFs to produce an implicit function that represents the shared interface between two protein chains. In addition to the smooth min defined in Equation 2, we make use of three operations on SDFs: 1) the rounding operation $d^{(r)}(\vec{x}) = d(\vec{x}) - r$, which expands the zero level set of an SDF by r in the positive direction; 2) the intersection operation, where the intersection of two SDFs d_1 and d_2 is given by $d_{d_1 \cap d_2}(\vec{x}) = \max(d_1(\vec{x}), d_2(\vec{x}))$, and finally 3) the union operation, where the union of two SDFs d_1 and d_2 is given by $d_{d_1 \cup d_2}(\vec{x}) = \min(d_1(\vec{x}), d_2(\vec{x}))$. Let d_1 and d_2 be the SDFs for two protein chains. Then we calculate an interface SDF as:

$$d_{\text{INTER}} = \min\big(\max\left(d_1\left(\vec{x}\right) - r, d_2\left(\vec{x}\right)\right), \max\left(d_1\left(\vec{x}\right), d_2\left(\vec{x}\right) - r\right)\big) \tag{3}$$

This produces an SDF that represents the area that is within r of both protein surfaces, i.e. the space between the two chains. See Figures 3 and 5 for examples of these interface meshes with an intersection radius of $r = 4$Å.

2.3. *Accelerating Queries*

We investigate the use of two data structures for accelerating spatial queries of protein SDFs: Bounding Volume Hierarchies (BVHs) and K-D Trees. For further details about these data

Table 1: PDB ID, atom count, and short description for each of the proteins used in figures in this paper. For more information, we refer the reader to the individual PDB entries, or to the description pages for the DB5[23] or PLINDER[24] datasets.

Source	PDB ID	# Atoms	Description
DB5	2I9B	11696	ATF-urokinase receptor complex
DB5	1JK9	5954	Heterodimer between H48F-ySOD1 and yCCS
DB5	1WEJ	4166	IGG1 fragment with horse cytochrome
DB5	1PXV	4816	Staphostatin-staphopain complex
DB5	7CEI	1724	Colicin E7 in complex with inhibitor
DB5	2GAF	6011	Vaccinia polyadenylate polymerase
DB5	1IBR	9739	RAN with Beta
DB5	1A2k	6732	NTF2:RanGDP complex
DB5	1WDW	29252	Tryptophan synthase a2b2 complex
PLINDER	1GOL	2901	Rat MAP kinaser ERK2
PLINDER	2CJM	8856	CDK2 Y15p T160p in complex with cyclin
PLINDER	2PY7	4133	E. coli phosphoenolpyruvate carboxykinase
PLINDER	3DAW	4056	Actin-depolymerizing factor
PLINDER	4EOM	8710	Human cyclin A3 complex with ATP
PLINDER	4EOQ	8717	Human cyclin A3 complex with ATP
PLINDER	6AEC	2579	Human DNA Polymerase Mu with MnATP
PLINDER	8AEC	2748	Compound 17 bound to CK2alpha
Fan et al.[25]	2QF1	4410	Zinc transporter YiiP

structures, we refer the reader to several surveys on data structures.[26–28] BVHs in particular have been previously explored as a technique to accelerate SDF queries.[29] Both of these data structures use spatial subdivision to accelerate finding the k nearest points to a given query point. See Figure 4 for an illustration of the BVH approach. Both of these data structures yield an approximation (see Figure 6) of the original signed distance function, but with a substantially lower memory footprint, which we analyze in Section 3.4. We also note here that the object-oriented implementation of a protein as a Torch module may add overhead in comparison to computing the all-pairs distance between a query point and all of a protein's atoms. A further potential benefit of the object-oriented approach, which we hope to explore in future work, is the ability to represent protein subunits like residues and secondary structure.

2.4. *Implementation Details*

Code used to build the SDFs described in this paper is available at `https://github.com/cory-b-scott/protein_sdfs`. Our code is built on top of the `torch_sdf` package, which is available at `https://github.com/cory-b-scott/torch_sdf`. For visualizing SDFs, we first convert each to a mesh using the Marching Cubes algorithm[30] as implemented in SciKit-Image.[31] We render images of each mesh using the `meshplot` package. The final meshes for each interface in the DB5 dataset may be downloaded from `https://osf.io/xzgyc/?view_only=6634b1aa0bf6401990ac2f217cef068b`.

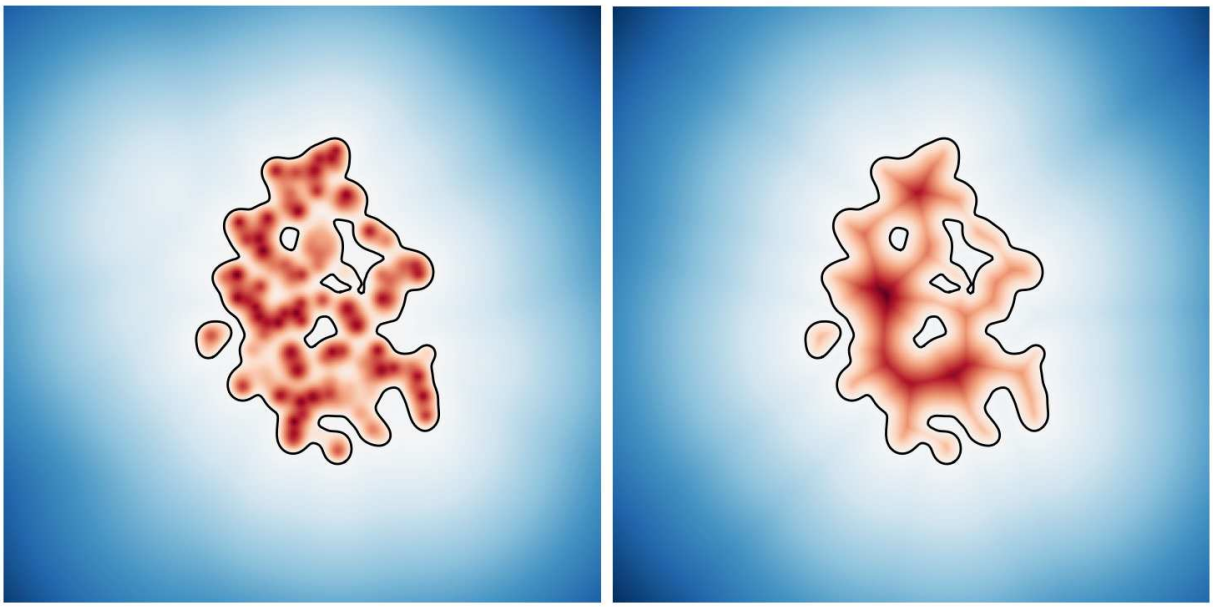

Fig. 2: An illustration of one possible issue when representing a protein as a collection of spherical SDFs. The left shows the union SDF, while the right shows the true distance to the $d = 0$ isosurface. The union SDF is incorrect in the protein's interior.

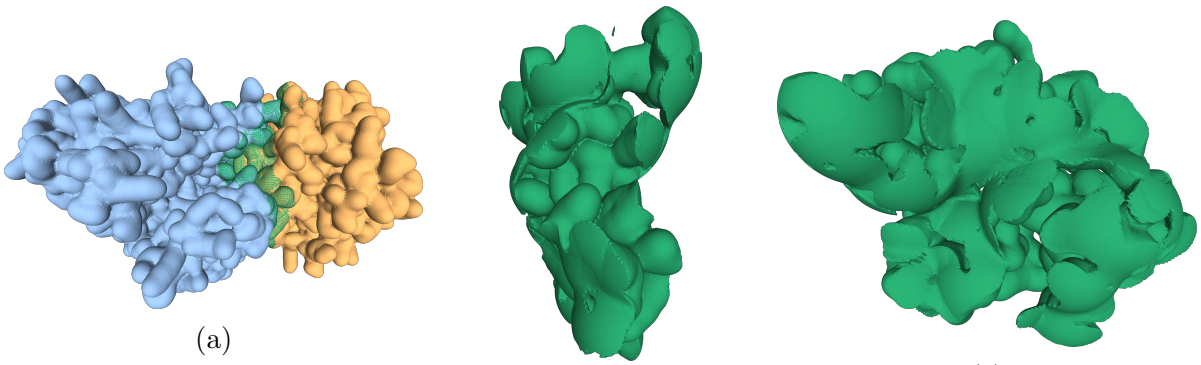

(a) (b) (c)

Fig. 3: An example of the $d(\mathbf{x}) = 0$ isosurface generated by our method for the protein 1WDW from the DB5 dataset. Left: The intersection isosurface rendered alongside both chains of the protein complex (color denotes chain ID). Nodes in the intersection region have been highlighted in green. Right: two views of the isolated intersection mesh.

3. Results and Applications

For this paper, we evaluate our model on the Docking Benchmark 5 (DB5)[23] and PLINDER[24] datasets. DB5 consists of protein complexes, where each complex includes two chains. Each chain is represented with PDB files[32] with atom coordinates for both its undocked pose (i.e.

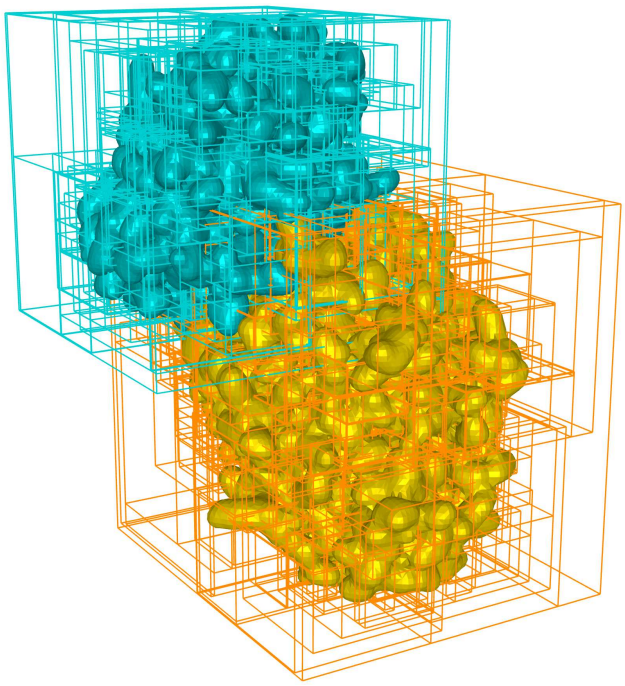

Fig. 4: A visualization of the bounding volume hierarchy built by our method for the protein 1WDW.

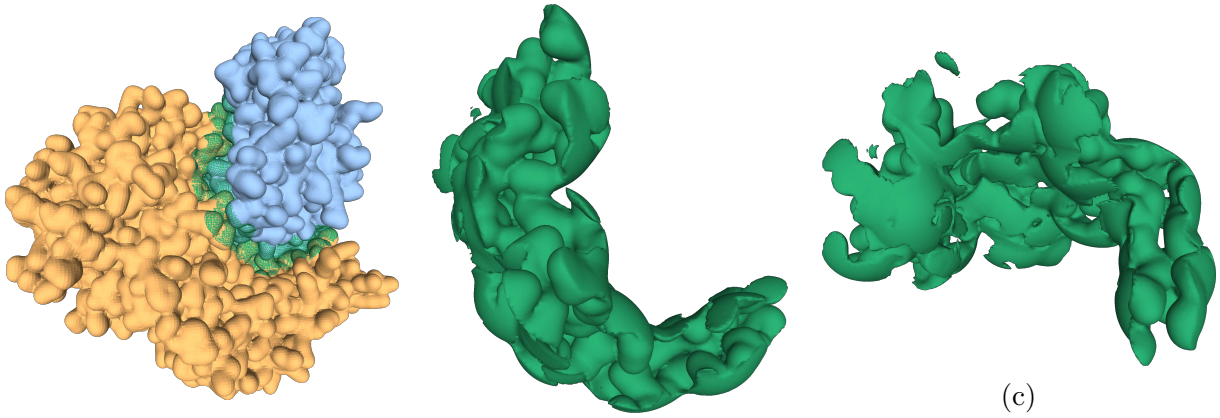

Fig. 5: As in Figure 3, but for protein 2GAF.

Table 2: Comparison of time/memory usage by two acceleration structures.

	Avg time (ms)	Peak memory
Basic	48.01	1.91MB
KDTree	77.43	11.15 kB
BVH	45.77	7.06 kB

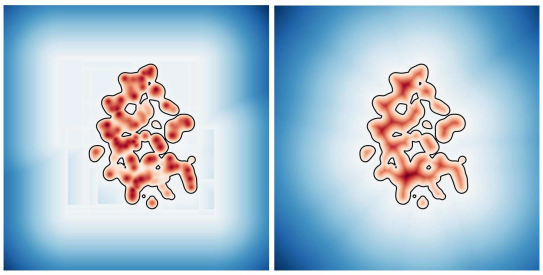

(a) 1A2K, BVH rendering.

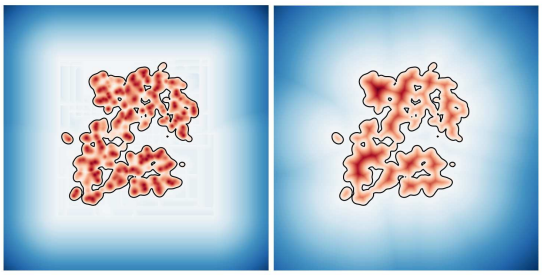

(b) 1WDW, BVH rendering.

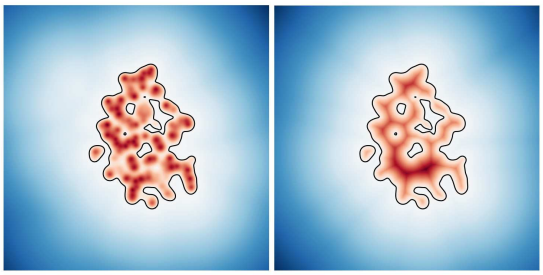

(c) 1A2K, kd-tree rendering.

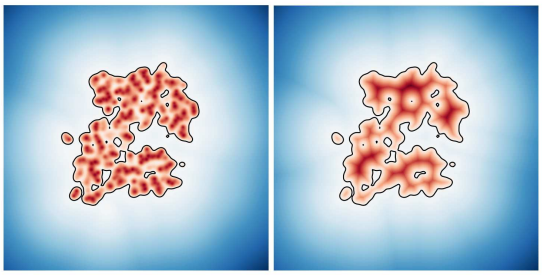

(d) 1WDW, kd-tree rendering.

Fig. 6: Illustration of SDFs produced by the two acceleration structures we examine in this paper. Each picture shows a 2D slice through the signed distance field at $z = 0$. We see that both accelerated SDFs are only approximations of the SDFs in Figure 2. In particular, the BVH approach leads to rectilinear artifacts on the exterior of the SDF; this could likely be ameliorated by using a different shape as the bounding volume (as opposed to axis-aligned rectangular prisms).

the pose it folds into naturally) and its docked pose with the other protein in the complex. We use the "bound" version of each chain in the complex. PLINDER is a searchable catalogue of protein-ligand complexes which can be filtered by protein/ligand/complex properties. We use the holo conformation of several proteins bound to ATP for the SDFs we render in Figure 8.

3.1. *Calculation of Protein Interaction Surfaces Using Smooth-Min SDFs*

We use the SDF defined in Equation 3 to compute signed distance functions for all of the protein complexes in the DB5 dataset, as well as SDFs and meshes for their interfaces. We use an interaction radius of 4.0Å in line with previous work on protein-protein interaction.[33,34] This data supports ML tasks using SDF representations, as well as explicit modeling of the biologically active surfaces. See Figures 3 and 5 for example protein interface meshes.

3.2. *Visualizing Molecular Dynamics Trajectories*

In this section, we demonstrate using protein SDFs to visualize a protein's shape over time during a molecular dynamics (MD) simulation. We generate an SDF for an entire protein trajectory as follows: first, we generate an SDF $f_t(\vec{x})$ for the protein at each timestep using

the approach introduced in Section 2.1. Then we take the smooth-min of all of these SDFs over t: $F(\vec{x}) = \text{smin}_t f_t(\vec{x})$. This produces an outer envelope showing the shape of the protein over the course of the entire simulation. Visualizing a protein in this way can tell us which structural features of the protein are persistent over time. To illustrate this technique we use a 9ns trajectory of the YiiP membrane protein[25] (See Figure 7). This illustrates that this SDF representation extends naturally to time-series protein data.

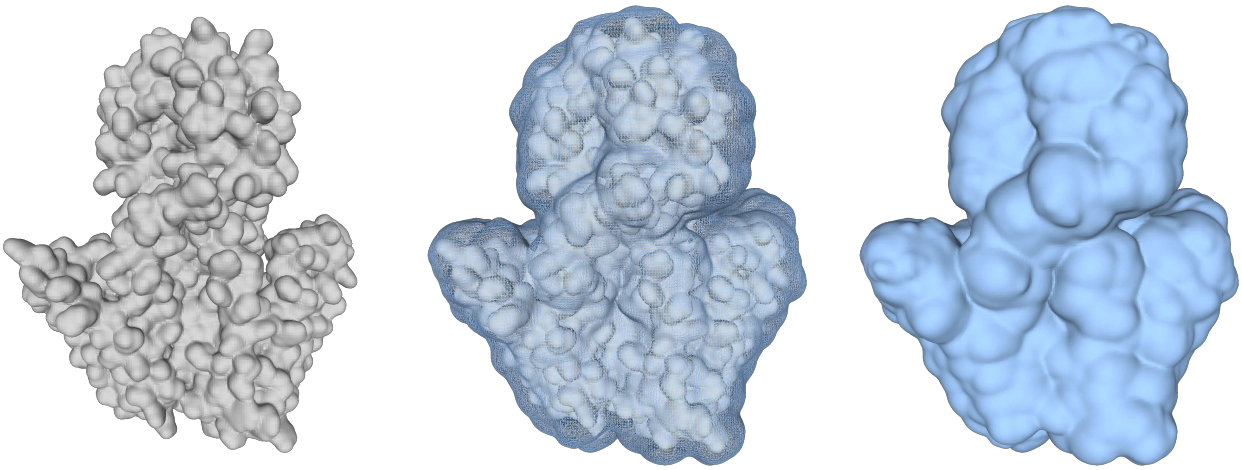

Fig. 7: An SDF computed over all timesteps of a MD simulation of the YiiP membrane protein in water. Left: the protein SDF for the first timestep only. Right: the SDF computed by taking the smooth-min blend of all timesteps. Center: left and right views overlaid.

3.3. *Visualizing Ligand Pockets*

We use the method described in Section 3 to generate visualizations of ligands and their associated binding sites. We download a subset of arbitrarily chosen protein-ligand complexes from the PLINDER training dataset,[24] filtering for complexes which consist of a single protein bound to ATP. We extract an SDF representing the binding site by building the smooth-min SDF for the protein, and then taking the intersection of that SDF with that of a 10Åsphere centered on the ATP molecule. We visualize these binding site SDFs in Figure 8, both with and without the ATP molecule visualized. Because each of these SDFs is constructed in a fully differentiable way, we could train a neural net to memorize and reproduce these pocket shapes, in the manner of a DeepSDF[35] model.

3.4. *Comparison of Acceleration Structures*

We compare the performance of the two acceleration structures described in Section 2.3. For each protein complex in the DB5 dataset, we benchmark the time and GPU memory needed to evaluate all grid points in a 256^3 grid laid over the bounding box of the complex. In Figure 9, we compare the accelerated version of each protein structure to the time and memory required to query all of the atomic SDFs for a given complex. We see that the BVH

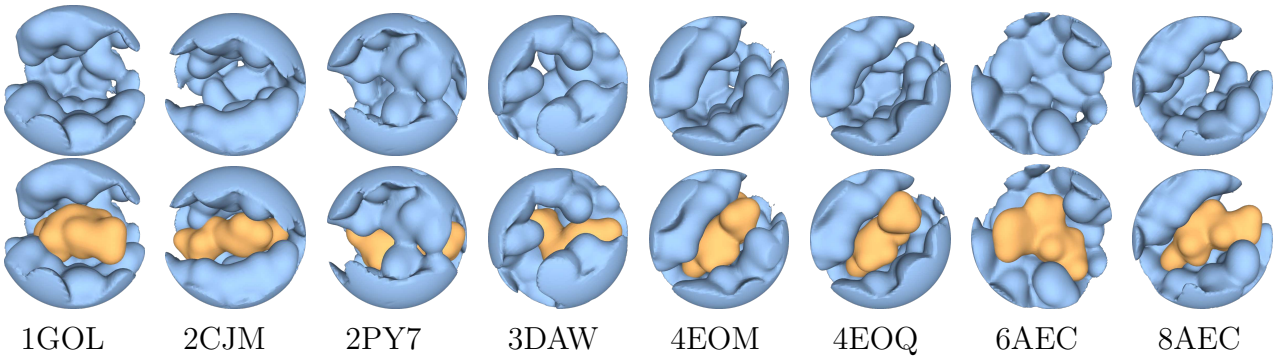

Fig. 8: Visualization of binding pockets for ATP for several proteins. Top row shows the pocket only; bottom row shows the pocket occupied by the ATP molecule (orange). See Table 1 for a description of each protein.

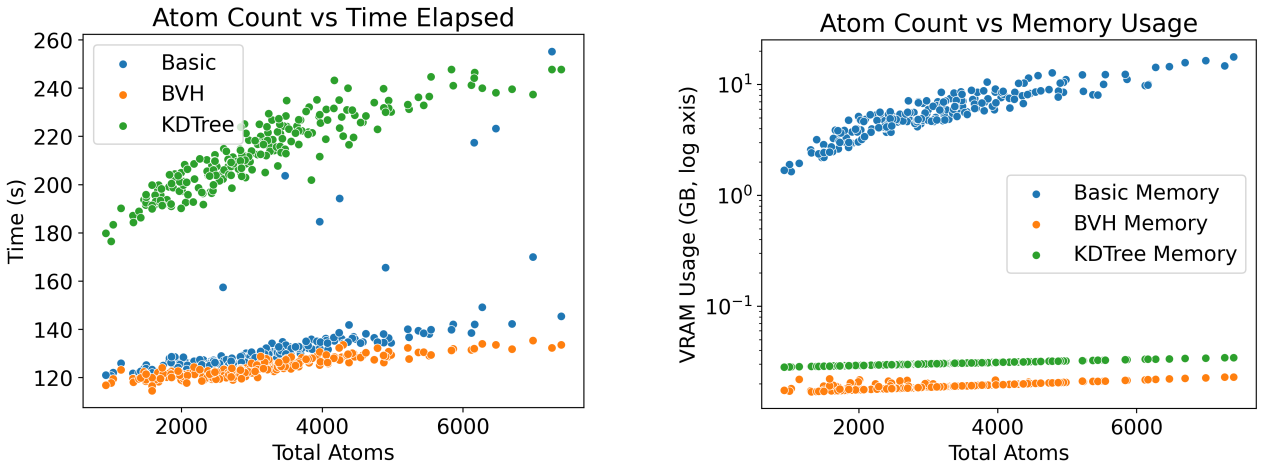

Fig. 9: Time/memory benchmarking of acceleration structures for querying protein SDFs.

approach is slightly faster than the naive approach, but the KDTree is much slower, likely due to CPU-GPU latency (at time of writing, there was no functional Torch+CUDA KDTree implementation, so the KDTree approach necessitates copying data back to the CPU. We hope to ameliorate this inefficiency in future work). All timings were collected on a consumer NVIDIA RTX A6000 GPU. Both the KDTree and BVH approaches offer significant memory savings (see Table 2). However, this approximation does incur some rectangular artifacts in the BVH tree approach; this could likely be resolved by using a different shape primitive in the volume hierarchy (e.g. bounding spheres instead of axis-aligned rectangles).

4. Conclusion and Future Work

This paper demonstrates the utility of representing a protein using the signed distance to its solvent-accessible surface (as approximated by the smooth-min function to the protein's component atoms). We also show how this can facilitate constructive solid geometry operations on protein interfaces. While this technique is promising, further work is needed to validate

the proposed approach. One of the major advantages of building our protein representation in PyTorch[22] is the ability to optimize over parts of the protein representation. In future work, we hope to use our framework to optimize protein shape, conformation, and position according to SDF-based loss functions.

Recent work[35] has used neural networks as maps between vectors of latent states and signed distance functions, producing a single model that is able to predict SDF values for a dataset of multiple 3D shapes. We hope to investigate a combination of this approach and our SDF construction, perhaps by utilizing embedding vectors from a pretrained protein transformer architecture.[36] We also hope to incorporate atomic characteristics as features of the generated surfaces. Finally, the literature includes examples of data structures like the ChainTree[37] which have been specifically developed for fast querying of energy potentials of proteins. It is likely that our proposed approach could be further enhanced by one of these protein-specific acceleration structures.

Finally, we note that constructing an SDF that implicitly stores the SAS shape is only the first step. We anticipate that this approach could be useful in any case where a machine learning model operates on the solvent accessible surface (AKA, where differentiability is needed). An example could include optimizing the position and pose of amino acids to produce an SAS that fits some other structural motif; or to provide some other machine learning model with a training signal that takes protein shape into account. We hope to use our SAS representation in one or more of these applications.

Acknowledgements

This work was supported in part by the Euclid Fund of the Department of Mathematics and Computer Science at Colorado College, and in part by the Dean of the Faculty at Colorado College's Mrachek Research Grant.

References

1. M. L. Connolly, Solvent-accessible surfaces of proteins and nucleic acids, *Science* **221**, 709 (1983).
2. M. L. Connolly, Analytical molecular surface calculation, *Applied Crystallography* **16**, 548 (1983).
3. I. Quilez, Modeling with distance functions. `http://iquilezles.org/www/articles/distfunctions/distfunctions.htm`, (2008).
4. I. Quilez, Smooth minimum. `https://iquilezles.org/articles/smin/`, (2013).
5. A. Shrake and J. A. Rupley, Environment and exposure to solvent of protein atoms. lysozyme and insulin, *Journal of Molecular Biology* **79**, 351 (1973).
6. R. Casadio, P. L. Martelli and C. Savojardo, Machine learning solutions for predicting protein–protein interactions, *Wiley Interdisciplinary Reviews: Computational Molecular Science* **12**, p. e1618 (2022).
7. P. Notin, N. Rollins, Y. Gal, C. Sander and D. Marks, Machine learning for functional protein design, *Nature biotechnology* **42**, 216 (2024).
8. J. Cheng, A. N. Tegge and P. Baldi, Machine learning methods for protein structure prediction, *IEEE reviews in biomedical engineering* **1**, 41 (2008).
9. M. M. Bronstein, J. Bruna, Y. LeCun, A. Szlam and P. Vandergheynst, Geometric deep learning: going beyond Euclidean data, *IEEE Signal Processing Magazine* **34**, 18 (2017).
10. A. J. Bordner and A. A. Gorin, Protein docking using surface matching and supervised machine learning, *Proteins: Structure, Function, and Bioinformatics* **68**, 488 (2007).
11. P. Gainza, F. Sverrisson, F. Monti, E. Rodolà, D. Boscaini, M. Bronstein and B. Correia, Deciphering interaction fingerprints from protein molecular surfaces using geometric deep learning, *Nature Methods* **17**, 184 (2020).
12. K. Atz, F. Grisoni and G. Schneider, Geometric deep learning on molecular representations, *Nature Machine Intelligence* **3**, 1023 (2021).
13. O. Méndez-Lucio, M. Ahmad, E. A. del Rio-Chanona and J. K. Wegner, A geometric deep learning approach to predict binding conformations of bioactive molecules, *Nature Machine Intelligence* **3**, 1033 (2021).
14. S. K. Mylonas, A. Axenopoulos and P. Daras, DeepSurf: a surface-based deep learning approach for the prediction of ligand binding sites on proteins, *Bioinformatics* **37**, 1681 (2021).
15. V. Mallet, Y. Miao, S. Attaiki, B. Correia and M. Ovsjanikov, AtomSurf: Surface representation for learning on protein structures, in *The Thirteenth International Conference on Learning Representations*,
16. J. Parulek and I. Viola, Implicit representation of molecular surfaces, **1**, 217 (2012).
17. J. Parulek and A. Brambilla, Fast blending scheme for molecular surface representation, *IEEE Transactions on Visualization and Computer Graphics* **19**, 2653 (2013).
18. D. Klepáč, Rendering molecular surfaces using signed distance functions [online] (2023 [cit. 2024-09-16]), SUPERVISOR : Jan Byška.
19. F. Sverrisson, J. Feydy, B. E. Correia and M. M. Bronstein, Fast end-to-end learning on protein surfaces, 15272 (2021).
20. A. v. Bondi, van der Waals volumes and radii, *The Journal of Physical Chemistry* **68**, 441 (1964).
21. G. Patané and M. Spagnuolo, State-of-the-art and perspectives of geometric and implicit modeling for molecular surfaces, *Computational Electrostatics for Biological Applications: Geometric and Numerical Approaches to the Description of Electrostatic Interaction Between Macromolecules* , 157 (2015).
22. A. Paszke, S. Gross, S. Chintala, G. Chanan, E. Yang, Z. DeVito, Z. Lin, A. Desmaison, L. Antiga and A. Lerer, Automatic differentiation in PyTorch (2017).
23. T. Vreven, I. H. Moal, A. Vangone, B. G. Pierce, P. L. Kastritis, M. Torchala, R. Chaleil, B. Jiménez-García, P. A. Bates, J. Fernandez-Recio *et al.*, Updates to the integrated protein–

protein interaction benchmarks: docking benchmark version 5 and affinity benchmark version 2, *Journal of Molecular Biology* **427**, 3031 (2015).
24. J. Durairaj, Y. Adeshina, Z. Cao, X. Zhang, V. Oleinikovas, T. Duignan, Z. McClure, X. Robin, G. Studer, D. Kovtun *et al.*, PLINDER: The protein-ligand interactions dataset and evaluation resource, *bioRxiv* , 2024 (2024).
25. S. Fan and O. Beckstein, Molecular Dynamics trajectories of membrane protein YiiP (5 2019).
26. E. Reinhard, B. Smits and C. Hansen, Dynamic acceleration structures for interactive ray tracing, 299 (2000).
27. T. Foley and J. Sugerman, Kd-tree acceleration structures for a GPU raytracer, 15 (2005).
28. D. Meister, S. Ogaki, C. Benthin, M. J. Doyle, M. Guthe and J. Bittner, A survey on bounding volume hierarchies for ray tracing, **40**, 683 (2021).
29. F. Liu and Y. J. Kim, Exact and adaptive signed distance fieldscomputation for rigid and deformable models on gpus, *IEEE transactions on visualization and computer graphics* **20**, 714 (2013).
30. T. Lewiner, H. Lopes, A. W. Vieira and G. Tavares, Efficient implementation of marching cubes' cases with topological guarantees, *Journal of graphics tools* **8**, 1 (2003).
31. S. Van der Walt, J. L. Schönberger, J. Nunez-Iglesias, F. Boulogne, J. D. Warner, N. Yager, E. Gouillart and T. Yu, scikit-image: image processing in Python, *PeerJ* **2**, p. e453 (2014).
32. H. M. Berman, J. Westbrook, Z. Feng, G. Gilliland, T. N. Bhat, H. Weissig, I. N. Shindyalov and P. E. Bourne, The protein data bank, *Nucleic acids research* **28**, 235 (2000).
33. J. Salamanca Viloria, M. F. Allega, M. Lambrughi and E. Papaleo, An optimal distance cutoff for contact-based protein structure networks using side-chain centers of mass, *Scientific reports* **7**, p. 2838 (2017).
34. R. A. Laskowski, J. Jabłońska, L. Pravda, R. S. Vařeková and J. M. Thornton, PDBsum: structural summaries of PDB entries, *Protein science* **27**, 129 (2018).
35. J. J. Park, P. Florence, J. Straub, R. Newcombe and S. Lovegrove, DeepSDF: Learning continuous signed distance functions for shape representation, 165 (2019).
36. C. Dallago, K. Schütze, M. Heinzinger, T. Olenyi, M. Littmann, A. X. Lu, K. K. Yang, S. Min, S. Yoon, J. T. Morton and B. Rost, Learned embeddings from deep learning to visualize and predict protein sets, *Current Protocols* **1**, p. e113 (2021).
37. I. Lotan, F. Schwarzer and J.-C. Latombe, Efficient energy computation for monte carlo simulation of proteins, 354 (2003).

Steering Protein Generative Models at Test-Time for Guided AAV2 Capsid Design

Ben Viggiano[†1], Wenhui Sophia Lu[†2], Xiaowei Zhang[†3,4], Luis S. Mille-Fragoso[3,4,5], Xiaojing J. Gao[5,8], Euan Ashley[1,6,7], Wing Hung Wong[1,2,5]

[1]*Department of Biomedical Data Science, Stanford University, Stanford, CA, USA*
[2]*Department of Statistics, Stanford University, Stanford, CA, USA*
[3]*Department of Bioengineering, Stanford University, Stanford, CA, USA*
[4] *Sarafan ChEM-H, Stanford University, Stanford, CA, USA*
[5]*Stanford Bio-X, Stanford University, Stanford, CA, USA*
[6]*Department of Medicine, Stanford University, Stanford, CA, USA*
[7]*Center for Undiagnosed Diseases, Stanford University, Stanford, CA, USA*
[8]*Department of Chemical Engineering, Stanford University, Stanford, CA, USA*
[†] *Equal Contribution*

Recent advances in protein generative models have created new opportunities for protein engineering. However, a significant challenge remains in effectively steering these models to generate sequences with specific, desired functionalities, especially when these properties are defined by "black-box" or non-differentiable fitness functions. To address this, we present ProVADA+, a model-agnostic framework that guides pretrained generative models at test-time without costly retraining. Our approach introduces a reinforcement learning-based adaptive masking technique (MADA-DUCB) that significantly accelerates convergence. We demonstrate this framework on the challenging task of designing novel Adeno-Associated Virus 2 (AAV2) capsids. By coupling a ProteinMPNN generative prior with a fine-tuned AAV viability oracle, our method successfully navigates the rugged fitness landscape where unguided random mutagenesis is ineffective—with prior experiments showing as few as 0.3% of variants with six or more mutations are viable. In its final iterations, ProVADA generated a pool of novel candidates with a mean viral selection score of 2.72, consistently scoring highly viable variants while maintaining a diverse range of sequence similarity to the wild-type sequence. Our results show that ProVADA provides a powerful and efficient framework for accelerating the design of proteins with complex, user-defined properties.

Keywords: Protein Engineering, Conditional Adaptation, Generative Guidance, Test-time Steering, Adeno-Associated Virus

1. Introduction

Protein engineering is the process of developing useful or novel proteins by modifying the amino acid sequences to improve existing structural and functional properties or confer new activities. Traditionally, one of the primary techniques available to researchers is directed evolution, an iterative laboratory process in which large libraries of protein variants are generated—typically through random mutagenesis of wild-type sequences—and then screened

© 2025 The Authors. Open Access chapter published by World Scientific Publishing Company and distributed under the terms of the Creative Commons Attribution Non-Commercial (CC BY-NC) 4.0 License.

using functional assays.[1] While this approach has demonstrated success in many applications,[2] it remains a resource-intensive and time-consuming process, particularly when dealing with intricate sequence-fitness landscapes or when mechanistic insights into protein function are limited.[3]

In the past several years, advances in machine learning have led to the development of powerful new approaches that demonstrate significant potential to accelerate protein engineering methodology. Structure prediction and downstream inverse-folding models have enabled a new way to condition sequence generation that preserves target structural folds in the final protein.[4–6] Large-scale protein language models (pLMs) trained on billions of biological sequences using simple pretraining objectives enable state-of-the-art performance on protein property prediction tasks.[7,8] Together, these tools accelerate candidate prioritization and substantially reduce the need for exhaustive experimental screening.

Researchers are increasingly looking to use a combination of these models to conditionally guide the generative process toward variants with desired functional properties. Most techniques revolve around classifier-guided plug-and-play approaches to steer sequence generation by backpropagating through a differentiable surrogate objective.[9–11] During generation, gradients from this reward bias a pretrained generative model toward specific properties. However, these methods depend on differentiable surrogate models and are thus incompatible with non-differentiable scoring functions. In contrast, fine-tuning and preference-learning approaches, such as classifier-free guidance[12] or reinforcement-learning-based fine-tuning,[13] adapt the model parameters directly to optimize for downstream rewards. While often effective, these techniques typically demand significant computational resources and large labeled datasets.

To address these limitations, we recently introduced ProVADA, a model-agnostic framework that steers any generative model using black-box fitness oracles without requiring costly retraining or gradients.[14] At the core of this framework is Mixture-Adaptation Directed Annealing (MADA), a novel sampling algorithm designed to efficiently navigate high-dimensional sequence landscapes. In this work, we propose several key enhancements to the ProVADA framework (ProVADA+) that substantially improve its biological relevance and algorithmic efficiency. Our primary contribution is an informed and adaptive mutation site selection strategy that employs reinforcement learning (MADA-DUCB) to accelerate convergence by intelligently identifying optimal mutation positions (Figure 1). Additionally, we introduce sequence constraints, including the ability to preserve specific residue positions crucial for protein function, and incorporate a biologically-informed distance metric based on the BLOSUM62 substitution matrix. This metric penalizes biochemically unfavorable mutations while permitting conservative substitutions, thereby generating variants with enhanced biological plausibility.

We demonstrate the power of this enhanced framework by applying it to a challenging protein design task: conditionally engineering Adeno-Associated Virus 2 (AAV2) capsids for improved viability. Our *in silico* results demonstrate that ProVADA+ effectively navigates the rugged fitness landscape to generate a diverse pool of novel candidates with high predicted viral selection scores, substantially outperforming unguided *in silico* selection from random mutagenesis approaches which fail to efficiently identify viable variants.

1.1. *AAV Capsid Design*

AAVs are small, non-pathogenic, single-stranded DNA viruses that rely on co-infection with helper viruses, typically adenoviruses, for replication.[15] Due to their favorable biological properties, engineered AAV capsids have become a leading platform for next-generation *in vivo* gene therapy vector development.[16] For example, the 13 commonly studied AAV serotypes exhibit distinct tissue tropisms, enabling selective transduction of specific cell types. This cell-type specificity is a major objective in vector engineering, as it can significantly reduce off-target effects from delivered therapeutic payloads.[16]

Within the full 60-mer capsid protein complex, sequence and structural variations found in small surfaced exposed *hyper-variable* regions have been shown to have out-sized impact on capsid functional properties.[17,18] For these reasons, AAV genetic modification in vector engineering research has commonly focused on the screening and directed evolution of these regions.[19,20] In this work, we explore utilizing ProVADA+ to engineer novel AAV capsid proteins for *in silico* predicted capsid viability, which characterizes whether a particular capsid is able to form. Moving forward, such predictive sampling could be combined with high-throughput experimental screens to guide selection for desirable functional traits beyond viability, such as transduction efficiency, low immunogenicity, and tissue tropism.

2. Methods

2.1. *ProVADA: Gradient-Free Guidance for Conditional Protein Adaptation at Test-Time*

We begin with a brief overview of the ProVADA framework for gradient-free steering of protein generation at test time. ProVADA comprises two core components: a fitness oracle to provide targeted guidance, and the Mixture-Adaptation Directed Annealing (MADA) sampler to efficiently navigate the intricate topology of sequence-fitness landscapes. To formalize our framework, we first define the key notations and definitions for the problem setup.

Let $\ell \in \mathbb{N}$ be the fixed sequence length, which defines the discrete sequence space $\mathcal{X} = \{1, \ldots, 20\}^\ell$. Our objective is to engineer a given wild-type reference sequence, $x_{wt} \in \mathcal{X}$, to improve its functional properties, which are quantified by a fitness oracle $F : \mathcal{X} \to [0, 1]$, where higher values indicate superior fitness. Additionally, we require a generative model capable of proposing mutations through efficient in-painting of masked sequence regions, thereby producing complete sequences that preserve fundamental properties such as structural integrity. The implicit sampling distribution of this generative model with parameters ϕ—whether autoregressive, diffusion-based, or alternative architectures—is denoted p_ϕ and henceforth referred to as the generative prior. Let $\mathbf{C}$ be an amino acid substitution matrix, where $\mathbf{C}(x_i, x_j)$ represents the score of substituting amino acid x_i with amino acid x_j.

Biochemically-Informed Sequence Divergence Penalty

To maintain proximity to the reference sequence and thus facilitate *conditional engineering* rather than *de novo* generation, we employ a composite fitness objective. This objective penalizes deviations from the wild-type sequence, x_{wt}, using a biologically-informed distance metric

$d(x, x_{wt})$ that respects amino acid properties while penalizing excessive substitutions. This metric is consisted of two terms: First, a *Hamming distance* (d_H), which penalizes the total number of mutations regardless of their biochemical properties. Second, we also include a *substitution cost* (d_C), which employs a penalty based on the BLOSUM62 substitution matrix.[21] Widely utilized in sequence alignment tools such as BLAST,[22] BLOSUM62 provides log-odds scores that reflect the evolutionary likelihood of amino acid substitutions. Positive scores indicate conservative substitutions that frequently occur in nature, while negative scores suggest less favorable, potentially deleterious changes. Under this framework, substitutions with positive BLOSUM62 scores incur no penalty, yielding a more informative and better evolutionarily aligned metric than the Hamming distance alone.

Ensemble-guided Composite Fitness Objective

The composite objective function, $H_\lambda(x)$, balances fitness enhancement with sequence conservation through tunable coefficients ($\lambda = (\lambda_H, \lambda_C)$):

$$d_H(x, x_{wt}) = 1/\ell \sum_{i=1}^{\ell} \mathbb{1}_{\{x_i \neq (x_{wt})_i\}}, \quad d_C(x, x_{wt}) = \sum_{i: x_i \neq (x_{wt})_i} \mathbf{C}(x_i, (x_{wt})_i) \in [0, 1],$$

$$H_\lambda(x) = F(x) - \big(\underbrace{\lambda_H d_H(x, x_{wt})}_{\substack{\text{Hamming} \\ \text{penalty}}} + \underbrace{\lambda_C d_C(x, x_{wt})}_{\substack{\text{Substitution} \\ \text{cost}}} \big),$$

where $\lambda_H, \lambda_C \geq 0$ are tunable regularization parameters that control the strength of the divergence penalties. To this end, we construct an ensemble target distribution proportional to the generative prior exponentially tilted by the tempered composite fitness $\pi_{\phi,H,\tau}(x) \propto p_\phi(x) \exp(H_\lambda(x)/\tau)$, where τ is a temperature parameter that governs how sharply sampling concentrates on high-fitness regions. As τ decreases, the sampler becomes increasingly concentrated on top-scoring sequences, whereas higher τ values encourage broader exploration of the sequence space.

2.2. *Constructing the Fitness Oracle*

ProVADA employs a user-defined black-box fitness oracle to guide its generative process. This oracle, trained on experimentally characterized protein sequences, predicts a numerical score quantifying the desired properties for each input sequence. The implementation of such an oracle is flexible, ranging from simple biophysical calculators to complex machine learning architectures. A particularly effective approach for creating high-performance oracles involves fine-tuning large, pre-trained protein language models (pLMs). Typically, this is achieved by appending a regression head, such as a multi-layer perceptron (MLP), to the pLM's final layer. The resulting model is then trained on task-specific datasets to accurately predict properties of interest from the model's sequence embeddings. In our experiments, we construct an oracle to predict AAV viability based on the ESM-Cambrian model; we provide more details in Section 3.2.

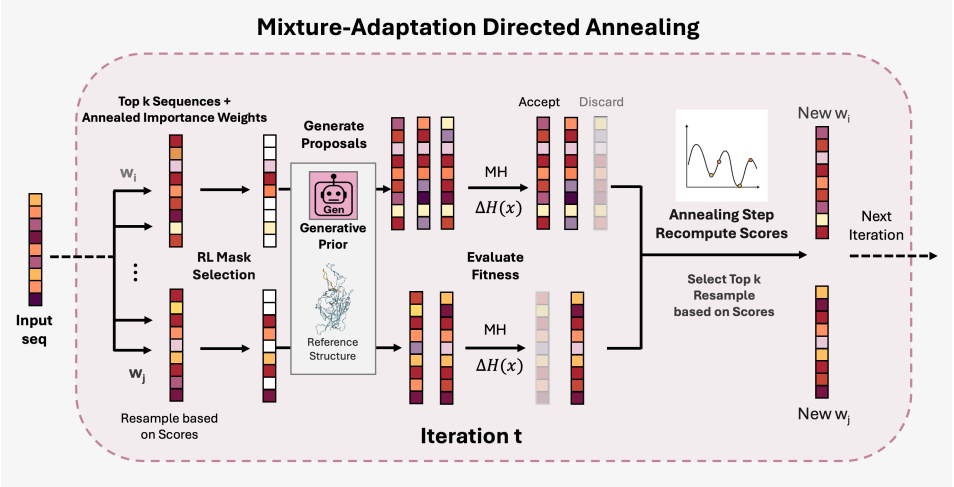

Fig. 1. Schematic overview of the *Mixture-Adaptation Directed Annealing* (MADA) sampling workflow. This iterative process integrates Sequential Monte Carlo population dynamics with adaptive simulated annealing to efficiently explore the protein sequence-fitness landscape.

2.3. *Mixture-Adaptation Directed Annealing with Informed Position Masking (MADA-DUCB)*

To simultaneously navigate the complex fitness landscapes and high-dimensional protein sequence space, ProVADA employs Mixture-Adaptation Directed Annealing (MADA). This novel sampling algorithm integrates Sequential Monte Carlo population dynamics with adaptive simulated annealing, iterating through cycles of *selection*, *mutation*, and *stabilization*. At each iteration, MADA maintains a diverse ensemble of promising candidate sequences, thereby balancing population diversity with focused exploration. Subsequently, offspring are generated through annealed importance sampling and partial rejection control, then refined using Metropolis-Hastings steps with fitness-guided local generative mutation kernels. Throughout the iterations, a gradually decaying temperature schedule transitions the sampler from broad exploration in the early stages to targeted exploitation as the search progresses. This adaptive approach enables MADA to efficiently traverse the vast protein sequence space while concentrating computational efforts on promising regions.

We introduce additional notation required for the MADA sequence manipulation procedure. Let $T \geq 1$ denote the number of iterations for which MADA is executed. Recall that the sequence length is ℓ, and define $I = \{1, 2, \ldots, \ell\}$ as the set of all sequence positions. We denote by $I_{\text{fixed}} \subset I$ the subset of positions that remain fixed throughout the optimization process, with cardinality $|I_{\text{fixed}}| = \ell_{\text{fixed}}$. The corresponding set of all viable positions for mutation is then defined as $I_{\text{mut}} = I \setminus I_{\text{fixed}}$. The masking rate $p_S \in (0, 1]$ controls the proportion of variable positions that are masked at each iteration. Let N denote the population size maintained throughout the sampling process.

Starting from the wild-type sequence x_{wt}, MADA proceeds through the following iterative procedure. At each iteration, we stochastically determine the number of positions M to mask by sampling $M = \max\left\{1, \text{Binomial}\left(|I_{\text{mut}}|, p_S\right)\right\}$, where the maximum operation ensures at least one position is masked. Building upon the work of Lu et al., who select mask locations

uniformly at random from the entire sequence (as the authors do not consider hard-fix constraints), we propose MADA-DUCB, which extends MADA with *informed* and *adaptive* position selection using reinforcement learning.[14] This approach, detailed in Section 2.4, enhances the mutation strategy by introducing targeted position selection. For the current discussion, we assume a set of mask positions $S \subseteq I_{\text{mut}}$ has been identified for mutation.

Mutation and Stabilization

Let the current iteration be $t \in \{1, \ldots, T\}$. Given a pool of N candidate sequences, which contains duplicates, we generate a set of M unique mask positions $S \subseteq I_{\text{mut}}$ for each *unique* candidate. For these identified unique sequences, we employ a generative prior to propose mutations at the masked sites, effectively filling these positions with new amino acids. Notably, this operation leaves the hard-fix positions I_{fixed} and the unmasked positions *unchanged*. Our transition kernel from the sequence before mutation x to the sequence after mutation x' is $q(x' \mid x) = p(S \mid x)p_\phi(x'_S \mid x_{S^c})$, where x_{S^c} represents the unmasked residues. However, not all mutations will necessarily enhance fitness. Thus, we perform a single Metropolis-Hastings step to stabilize the transition from x to x'. The acceptance ratio for this move is given by $a(x, x') = \min\left(1, \frac{p(S|x')}{p(S|x)} \cdot \frac{\exp(H_\lambda(x')/\tau_t)}{\exp(H_\lambda(x)/\tau_t)}\right)$, where we accept the proposed sequence x' if $U \sim \text{Uniform}[0, 1] < a(x, x')$; otherwise, we retain the original sequence x. This process results in an updated pool of N sequences, each having undergone mutation and stabilization.

Selection and Annealed Importance Resampling

After mutation and stabilization, we apply an MH rejuvenation kernel that leaves π_{ϕ,H,τ_t} invariant and then transition the population to $\pi_{\phi,H,\tau_{t+1}}$ via annealed importance resampling. The annealed importance weight for each sequence is given by $w_i^{(t+1)} \propto \exp\left(\left(\frac{1}{\tau_{t+1}} - \frac{1}{\tau_t}\right) H_\lambda(x_i)\right)$.

To focus the particle population on high-potential candidates and amortize the cost of generative prior calls, we employ a two-phase resampling strategy where a small set of K *prototypes* is selected and then used to regenerate the full population. First, we select a subset of K representative sequences, denoted as $\{x_j^*\}_{j=1}^K$, from the original N candidates $\{x_i\}_{i=1}^N$. This selection process uses weighted sampling with replacement, where weights $w_i^{(t+1)}$ reflect each sequence's importance. Then from these K prototypes, we reconstruct a full ensemble of N sequences, $\{\tilde{x}_i^{(t+1)}\}_{i=1}^N$, through uniform random sampling with replacement. The ensemble encapsulates $\leq K$ distinct sequence prototypes primed for the subsequent mutation phase.

Alternatively, instead of stochastic resampling, particles can be selected greedily by their importance weights. Although this top-K selection procedure introduces a small bias through the permanent elimination of low-weight particles, empirically, it often results in accelerated convergence to high-fitness regions.

2.4. *Informed Mutation Strategy via Reinforcement Learning-Based Adaptive Mask Selection*

In this section, we introduce a novel strategy to construct an informed proposal distribution for selecting mutation sites based on reinforcement learning. This adaptive approach enhances the

efficacy of the mutation process within the MADA sampling procedure. We frame the selection of mask positions as a sequential decision problem aimed at maximizing cumulative reward. This framework embodies the classic exploration-exploitation dilemma: balancing the selection of positions that have historically yielded beneficial mutations against exploring positions that may reveal unexpected improvements.

At each mutation step $t_m = 1, \ldots, T_m$, where $T_m = K \times T$, the action involves choosing a mask set $S_{t_m} \subseteq I_{\text{mut}}$ of size M. This is equivalent to simultaneously pulling M arms in a multi-armed bandit setting, constituting a combinatorial bandit problem. Following a mutation based on mask S_{t_m}, proposed by the generative prior $p_\phi(\cdot)$ and subjected to the Metropolis-Hastings step, we observe a reward $r_{t_m} = (H_\lambda(x') - H_\lambda(x))/M$. We employ a key simplifying heuristic by attributing the observed reward equally to each of the M chosen positions within the mask $S_{t_m} = \{S_{t_m,j}\}_{j=1}^{M}$. This approach assesses the impact of individual positions, even though they are selected and mutated in combination. Over many diverse trials, it allows the estimated value of a single mutation site to approximate its current marginal contribution across various contexts. Although this simplification does not capture interaction effects, it provides a computationally tractable approach to an otherwise intractable search space of $\binom{\ell-\ell_{\text{fixed}}}{M}$ possible mask configurations.

For additional computational efficiency, our bandit algorithm is *context-free*, meaning we do not provide the sequence context when making decisions. This makes our masking probability identical for all particles, i.e., $p(S \mid x) = p(S \mid x')$ for all x, x'. Consequently, the acceptance ratio simplifies to $a(x, x') = \min\left(1, \frac{\exp(H_\lambda(x')/\tau_t)}{\exp(H_\lambda(x)/\tau_t)}\right)$. As our particle population evolves through the MADA procedure, this creates a non-stationary reward distribution with the underlying reward for each position constantly shifting as the sequence context changes. To address the non-stationarity inherent in this setting, we employ the discounted Upper-Confidence Bound (D-UCB) algorithm.[23] This approach utilizes a discounted empirical average,

$$N_{j,t_m}(\gamma) = \sum_{o=1}^{t_m-1} \gamma^{t_m-1-o} \mathbb{1}_{\{j \in S_o\}}, \quad \hat{\mu}_{j,t_m} = \frac{\sum_{o=1}^{t_m-1} \gamma^{t_m-1-o} r_o \mathbb{1}_{\{j \in S_o\}}}{N_{j,t_m}(\gamma)},$$

where $\gamma \in (0, 1)$ is the discount factor. The choice of γ creates a bias-variance trade-off: $\gamma \to 1$ yields low bias but slow adaptation to changes, while $\gamma \to 0$ offers fast adaptation but high variance in estimates. In practice, we use $\gamma \approx 0.95$ to balance adaptation speed with estimation stability. The upper-confidence bound is then updated as

$$\text{UCB}_{j,t_m} = \underbrace{\hat{\mu}_{j,t_m}}_{\text{exploitation}} + \alpha \underbrace{\sqrt{\frac{\log \sum_{i=1}^{\ell-\ell_{\text{fixed}}} N_{i,t_m}(\gamma)}{N_{j,t_m}(\gamma)}}}_{\text{exploration}},$$

where $\alpha > 0$ is the exploration constant, balancing exploitation of known high-reward positions with exploration of less certain options. We implement these discounted summations using a recursive update scheme. Subsequently, we select the M positions with the highest upper-confidence bounds to form our mask set for the current iteration.

3. Experiments

3.1. *Dataset*

To evaluate the effectiveness of ProVADA+ in AAV capsid design, we leveraged a large-scale publicly available dataset of experimentally characterized AAV2 variants originally reported by Bryant et al.[3] The dataset comprises 293,574 variants derived through targeted random mutagenesis of a 28-residue hyper-variable region in the VP3 capsid protein (positions 359-387) found to play a critical role in capsid assembly, heparin binding, and immune recognition. Its functional importance has made it a focal point for previous protein engineering efforts.[24]

To quantify capsid viability, each variant in the dataset was evaluated using a high-throughput production assay that measures the efficiency with which it assembles into a capsid and encapsidates a viral genome. This was operationalized by comparing the relative abundance of each variant in two distinct experimental libraries: a plasmid DNA input library representing the initial pool of designed sequences, and a viral library composed of genomes extracted from successfully assembled capsids.

For a given variant i, the viability was summarized by a "viral selection score," defined as the log-ratio between its normalized read count in the viral library ($n_{i,\text{viral}}$) and the corresponding count in the DNA library ($n_{i,\text{DNA}}$), $\text{score}_i = \log\left(\frac{n_{i,\text{viral}}}{n_{i,\text{DNA}}}\right)$. This score serves as a quantitative proxy for packaging fitness: Higher values indicate that a variant is preferentially enriched in the viral output pool relative to its starting frequency, reflecting successful capsid assembly and genome packaging. Notably, this enrichment-based metric captures both structural integrity and functional assembly capacity of the AAV2 capsid, and was validated through replicate experiments showing high reproducibility.[3]

Prior to use, we applied several preprocessing steps to the original dataset to ensure consistency and validity. All variants containing premature stop codons or non-finite viral selection scores were excluded. To resolve conflicting measurements, we removed duplicate sequences that had inconsistent viral selection values across records. In addition, each sequence in the dataset was annotated with its corresponding full-length VP1, VP2, and VP3 isoform sequences. After cleaning, our final dataset comprised 289,736 variants, with a distribution of viral selection scores shown in Figure 2. We include a link to the processed version of this dataset in Section 6.

3.2. *AAV Viability Oracle*

To support generative steering with a black-box oracle, we trained a predictive model to estimate viral selection scores directly from AAV2 hyper-variable region sequences. As our base architecture, we used ESM-Cambrian (ESMC), a 600-million parameter transformer from the ESM family optimized for protein representation learning and sequence-level prediction tasks.[25] A five-layer MLP regression head was added on top of the final layer, which takes the mean-pooled token embeddings to produce a final continuous score prediction. The model was fine-tuned using mean squared error (MSE) loss on the processed dataset, which was randomly split into three parts: training (60%), validation (20%), and test (20%) sets. On the held-out test set, the model achieved strong performance, with an MSE of 1.4262, root

mean squared error (RMSE) of 1.1942, mean absolute error (MAE) of 0.8761, and coefficient of determination (R^2) of 0.8738. We refer to this fine-tuned model as the ESMC oracle, and use it in all subsequent experiments to both guide sequence generation and evaluate generated sequences through *in silico* viability score prediction.

3.3. *Structure-Conditioned AAV2 Capsid Design with ProVADA+*

To generate novel AAV2 capsid variants with high predicted viability, we implemented an AAV2-focused version of ProVADA+ that integrates a structure-based generative model with our black-box viability oracle. This approach allows us to enforce a structural prior on the generated sequences while simultaneously steering the design process toward our desired functional objective.

We used ProteinMPNN—an inverse folding model that designs amino acid sequences conditioned on a fixed protein structure—as our generative prior. Given a backbone with masked residues, ProteinMPNN proposes plausible amino acid substitutions. As a starting point, we first predicted the structure of the wild-type AAV2 VP3 protein using Boltz-2.[5] This predicted structure was then used as a fixed backbone scaffold for ProteinMPNN throughout all subsequent generations. For the fitness oracle ($F(x)$), we utilize the ESMC oracle (Section 3.2) to provide the predicted viral selection score for any given sequence variant. The search was guided by the composite objective ($H_\lambda(x)$) defined in Section 2.1, which balances the predicted viability score with a BLOSUM62-based sequence similarity penalty to maintain proximity to the wild-type sequence. The design process focused on the 28-residue hyper-variable region (positions 359-387). All positions outside this region were held constant, and only positions within the hyper-variable region were masked for redesign. We ran the design trajectories with three different seeds for both the MADA and MADA-DUCB sampling variants.

4. Results

4.1. *Baseline Analysis: In Silico Selection of Random Mutagenesis*

To establish a performance baseline and contextualize the difficulty of the AAV2 capsid design task, we first evaluated a "generate-and-filter" strategy. This approach is analogous to the 'model-selected' approach used in Bryant et al., where a machine learning model is used to screen a large pool of randomly generated sequences,[3] and corresponds to the rejection sampling baseline presented in Lu et al.[14] A workflow without ProVADA+ could similarly use our ESMC oracle to rank random mutants and select the highest-scoring candidates *in silico*. We generated 30,000 random variants at each mutational distance (k) for $k = 1, 3, 5, 7$ from the wild-type AAV2 hyper-variable sequence and used the ESMC oracle to obtain predicted viral selection scores. We then selected the top 2% (600 variants) from each mutational distance. (Note: for $k = 1$, there are only $19 \times 28 = 532$ possible variants, so all were included).

The results, summarized in Figure 3A, demonstrate that this undirected random mutagenesis approach is an inefficient strategy for improving capsid viability. As the number of mutations increases, the distribution of predicted scores shifts progressively toward lower, more deleterious values. Notably, while some variants with three mutations ($k = 3$) achieve high predicted scores, the population exhibits very little sequence diversity, clustering tightly

near the wild-type sequence. This *in silico* finding directly corroborates the experimental results of Bryant et al., who reported that only 10% of randomly chosen variants with 2 to 10 mutations were viable—a figure that plummeted to just 0.3% for variants with six or more mutations.[3] Our baseline analysis similarly underscores the ruggedness of the AAV2 fitness landscape and confirms that a naive, undirected search is highly unlikely to yield improved variants. This motivates the need for more sophisticated, oracle-guided generation strategies like ProVADA+.

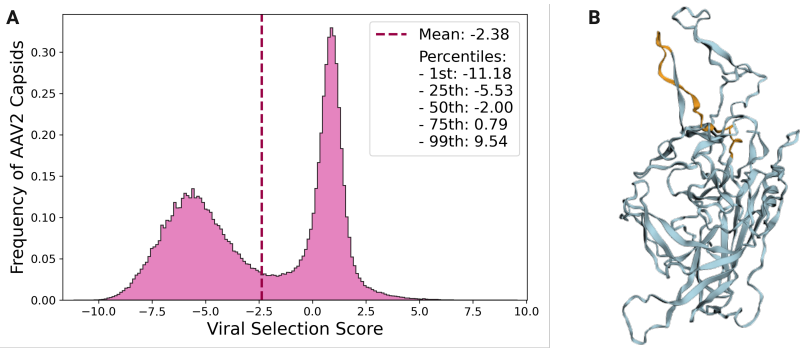

Fig. 2. A) Underlying bimodal distribution of viral selection scores in the processed version of the Bryant et al. dataset. B) Predicted structure of the wild-type VP3 protein containing the 359-387 hyper-variable region, which is highlighted orange in the structure.

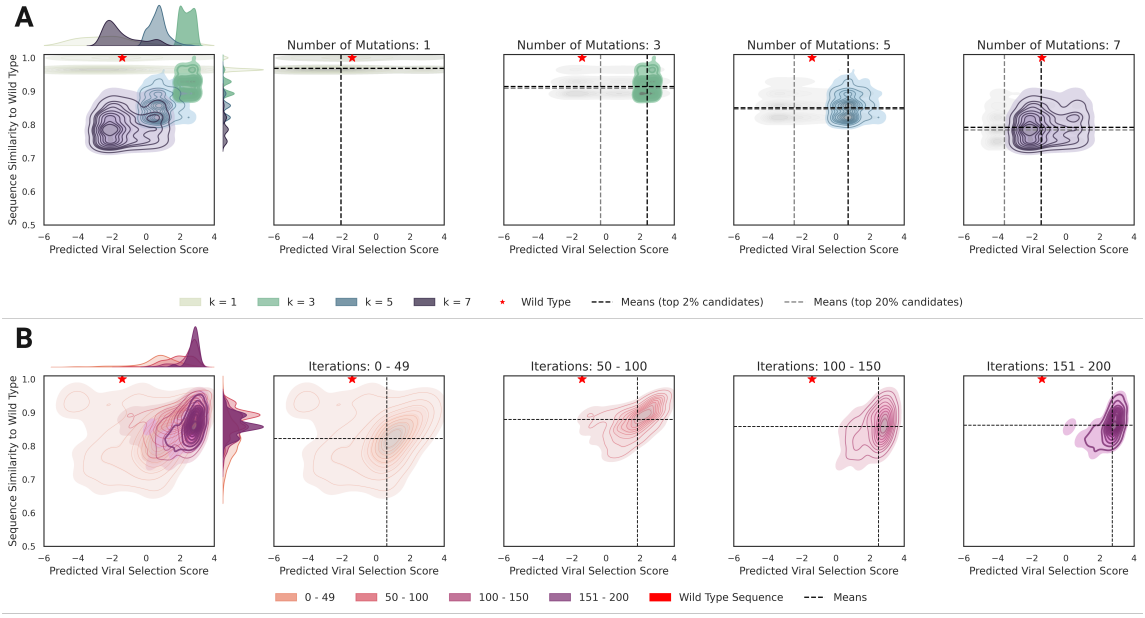

Fig. 3. Joint distributions of predicted viral selection score and similarity to wild-type of the sequences generated through A) *In silico* selected variants from random mutagenesis; B) ProVADA-guided design. Variants generated via ProVADA+ consistently exhibit high viral selection scores while maintaining adequate diversity.

4.2. *MADA and MADA-DUCB Convergence*

To assess the impact of our informed mutation strategy, we compared the convergence performance of the standard Mixture-Adaptation Directed Annealing (MADA) algorithm against our enhanced variant, MADA-DUCB, which employs a reinforcement learning approach for adaptive mask selection. We tracked the average combined fitness objective, $H_\lambda(x)$, for the population of sequences over 200 design iterations. The experiment was conducted using three independent seeds for each method to ensure the robustness of our findings.

The results are summarized in Figure 4. Both sampling methods successfully guide the design process toward sequences with significantly improved fitness scores, demonstrating the overall effectiveness of the ProVADA framework. However, the MADA-DUCB variant exhibits superior sampling efficiency. As shown by the steeper initial slope of its convergence curve, MADA-DUCB achieves higher fitness values much earlier in the trajectory compared to the standard MADA sampler, which relies on uniform random masking. This accelerated convergence highlights the benefit of intelligently targeting mutation sites that are more likely to yield high-reward outcomes. While both methods eventually approach a similar fitness plateau, the adaptive strategy of MADA-DUCB enables a more rapid and efficient exploration of the high-dimensional sequence landscape to identify optimal candidates.

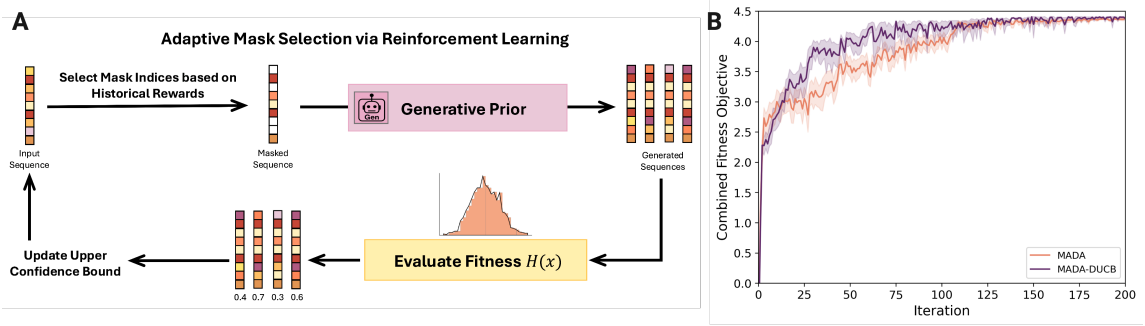

Fig. 4. A) Schematic overview of the informed mutation position selection procedure (D-UCB). B) Comparison of trajectory plots between MADA and MADA-DUCB. The plot shows the mean composite fitness objective $H_\lambda(x)$ with error bands over 200 design iterations. Lines represent the mean across three independent runs for both sampling methods.

4.3. *ProVADA+ Steers Generation Towards High-Viability Sequences*

To better understand the trajectory of the guided design process, we plot the sequence populations at four different stages throughout a MADA-DUCB sampler run. Figure 3B shows the joint distribution of predicted viral selection score and sequence similarity (BLOSUM62-informed Hamming distance divided by the hyper-variable region length) to the wild-type at different stages of the design trajectory. The process begins with a broad exploration phase (Iterations 0-49), where the sampler generates a diverse set of sequences centered around the wild-type reference. In this initial stage, most variants have low predicted viral selection scores, many of which are predicted to be less viable than the wild-type. As the trajectory progresses (Iterations 50-150), the population distribution systematically shifts toward the right, indicat-

ing a steady increase in predicted viability scores. In the final iterations (151-200), the sampler converges on a concentrated population of high-quality sequences. These final candidates exhibit significantly improved predicted viral selection scores, while maintaining an adequately diverse range of sequence similarity (0.8-0.95) to the wild-type.

5. Discussion

In this work, we introduce ProVADA+, an enhanced framework that provides substantial improvements in flexibility, biological relevance, and algorithmic efficiency to ProVADA. First, we incorporate fixed residue constraints to preserve important functional sites and augment the original Hamming distance with a biologically-informed BLOSUM62-based sequence divergence penalty, thereby generating variants with improved biochemical plausibility. Second, we propose an informed and adaptive strategy for selecting which residue positions to mutate. This approach leverages the discounted Upper-Confidence Bound (D-UCB) algorithm to facilitate a more efficient and targeted exploration of the sequence space. Collectively, these methodological advances yield a more powerful and flexible framework for generating optimized protein sequences, with the potential to accelerate the rational design of novel proteins for biotechnological and therapeutic applications. We demonstrate the superiority of ProVADA+ on *in silico* adaptation of AAV capsids for viability over the widely-used targeted random mutagenesis.

This work opens several directions for future investigation. For example, alternative algorithms could be employed to identify high-viability reference sequences that differ substantially from the wild-type AAV sequence, serving as improved initialization points for the MADA algorithm to explore more distant regions of the sequence space. Furthermore, the modularity of the ProVADA+ framework is particularly well-suited for multi-objective optimization through composable guidance. The composite objective function, $H_\lambda(x)$, could be readily extended to incorporate a weighted combination of multiple, independent fitness oracles. Each oracle could be trained on data from a distinct experimental assay, representing a different desired functional property—such as transduction efficiency, tissue tropism, or low immunogenicity. For instance, in AAV engineering, one could simultaneously steer the generative process with the current viability oracle, a second oracle trained on an *in vivo* screen for heart-specific tropism, and a third designed to minimize predicted T-cell epitopes. In future work, we plan to integrate additional stability-related scoring functions and incorporate uncertainty metrics into oracle predictions to prioritize variants for wet laboratory validation to enable more complex designs. This approach would allow researchers to create a bespoke fitness landscape tailored to a complex set of design criteria and thus enable the generation of highly specialized variants that jointly satisfy multiple functional constraints.

6. Code and Data Availability

The implementation of ProVADA+ is publicly available at the following GitHub repository: https://github.com/SUwonglab/ProVADA. In addition, the preprocessed version of the AAV2 capsid viability fitness dataset, originally reported in Bryant et al.,[3] is available at the following Hugging Face link: https://huggingface.co/datasets/bviggiano/aav2_capsid_viability.

References

1. L. Sellés Vidal, M. Isalan, J. T. Heap and R. Ledesma-Amaro, A primer to directed evolution: current methodologies and future directions, *RSC Chem. Biol.* **4**, 271 (April 2023).
2. J. T. Koerber, J.-H. Jang and D. V. Schaffer, DNA shuffling of adeno-associated virus yields functionally diverse viral progeny, *Mol. Ther.* **16**, 1703 (October 2008).
3. D. H. Bryant, A. Bashir, S. Sinai, N. K. Jain, P. J. Ogden, P. F. Riley, G. M. Church, L. J. Colwell and E. D. Kelsic, Deep diversification of an AAV capsid protein by machine learning, *Nat. Biotechnol.* **39**, 691 (June 2021).
4. J. Jumper, R. Evans, A. Pritzel, T. Green, M. Figurnov, O. Ronneberger, K. Tunyasuvunakool, R. Bates, A. Žídek, A. Potapenko, A. Bridgland, C. Meyer, S. A. A. Kohl, A. J. Ballard, A. Cowie, B. Romera-Paredes, S. Nikolov, R. Jain, J. Adler, T. Back, S. Petersen, D. Reiman, E. Clancy, M. Zielinski, M. Steinegger, M. Pacholska, T. Berghammer, S. Bodenstein, D. Silver, O. Vinyals, A. W. Senior, K. Kavukcuoglu, P. Kohli and D. Hassabis, Highly accurate protein structure prediction with AlphaFold, *Nature* **596**, 583 (August 2021).
5. S. Passaro, G. Corso, J. Wohlwend, M. Reveiz, S. Thaler, V. R. Somnath, N. Getz, T. Portnoi, J. Roy, H. Stark, D. Kwabi-Addo, D. Beaini, T. Jaakkola and R. Barzilay, Boltz-2: Towards accurate and efficient binding affinity prediction, *bioRxiv* , p. 2025.06.14.659707 (June 2025).
6. J. Dauparas, I. Anishchenko, N. Bennett, H. Bai, R. J. Ragotte, L. F. Milles, B. I. M. Wicky, A. Courbet, R. J. de Haas, N. Bethel, P. J. Y. Leung, T. F. Huddy, S. Pellock, D. Tischer, F. Chan, B. Koepnick, H. Nguyen, A. Kang, B. Sankaran, A. K. Bera, N. P. King and D. Baker, Robust deep learning-based protein sequence design using ProteinMPNN, *Science* **378**, 49 (October 2022).
7. A. Madani, B. Krause, E. R. Greene, S. Subramanian, B. P. Mohr, J. M. Holton, J. L. Olmos, Jr, C. Xiong, Z. Z. Sun, R. Socher, J. S. Fraser and N. Naik, Large language models generate functional protein sequences across diverse families, *Nat. Biotechnol.* **41**, 1099 (August 2023).
8. T. Hayes, R. Rao, H. Akin, N. J. Sofroniew, D. Oktay, Z. Lin, R. Verkuil, V. Q. Tran, J. Deaton, M. Wiggert, R. Badkundri, I. Shafkat, J. Gong, A. Derry, R. S. Molina, N. Thomas, Y. Khan, C. Mishra, C. Kim, L. J. Bartie, M. Nemeth, P. D. Hsu, T. Sercu, S. Candido and A. Rives, Simulating 500 million years of evolution with a language model, *bioRxiv* , p. 2024.07.01.600583 (July 2024).
9. A. Bansal, H.-M. Chu, A. Schwarzschild, S. Sengupta, M. Goldblum, J. Geiping and T. Goldstein, Universal guidance for diffusion models, *arXiv [cs.CV]* (February 2023).
10. H. Chung, J. Kim, M. T. Mccann, M. L. Klasky and J. C. Ye, Diffusion posterior sampling for general noisy inverse problems, *arXiv [stat.ML]* (September 2022).
11. P. Emami, A. Perreault, J. Law, D. Biagioni and P. C. S. John, Plug & play directed evolution of proteins with gradient-based discrete MCMC, *arXiv [cs.LG]* (December 2022).
12. J. Ho and T. Salimans, Classifier-free diffusion guidance, *arXiv [cs.LG]* (July 2022).
13. N. Blalock, S. Seshadri, A. Babbar, S. A. Fahlberg, A. Kulkarni and P. A. Romero, Functional alignment of protein language models via reinforcement learning, *bioRxiv* , p. 2025.05.02.651993 (May 2025).
14. W. S. Lu, X. Zhang, L. S. Mille-Fragoso, H. Dai, X. J. Gao and W. H. Wong, ProVADA: Generation of subcellular protein variants via ensemble-guided test-time steering, *bioRxiv* , p. 2025.07.11.664238 (July 2025).
15. M. F. Naso, B. Tomkowicz, W. L. Perry, 3rd and W. R. Strohl, Adeno-associated virus (AAV) as a vector for gene therapy, *BioDrugs* **31**, 317 (August 2017).
16. D. Wang, P. W. L. Tai and G. Gao, Adeno-associated virus vector as a platform for gene therapy delivery, *Nat. Rev. Drug Discov.* **18**, 358 (May 2019).
17. M. B. Demircan, L. J. Zinser, A. Michels, M. Guaza-Lasheras, F. John, J. M. Gorol, S. A.

Theuerkauf, D. M. Günther, D. Grimm, F. R. Greten, P. Chlanda, F. B. Thalheimer and C. J. Buchholz, T-cell specific in vivo gene delivery with DART-AAVs targeted to CD8, *Mol. Ther.* **32**, 3470 (October 2024).
18. L. E. Mays, L. Wang, R. Tenney, P. Bell, H.-J. Nam, J. Lin, B. Gurda, K. Van Vliet, K. Mikals, M. Agbandje-McKenna and J. M. Wilson, Mapping the structural determinants responsible for enhanced T cell activation to the immunogenic adeno-associated virus capsid from isolate rhesus 32.33, *J. Virol.* **87**, 9473 (September 2013).
19. K. Börner, E. Kienle, L.-Y. Huang, J. Weinmann, A. Sacher, P. Bayer, C. Stüllein, J. Fakhiri, L. Zimmermann, A. Westhaus, J. Beneke, N. Beil, E. Wiedtke, C. Schmelas, D. Miltner, A. Rau, H. Erfle, H.-G. Kräusslich, M. Müller, M. Agbandje-McKenna and D. Grimm, Pre-arrayed pan-AAV peptide display libraries for rapid single-round screening, *Mol. Ther.* **28**, 1016 (April 2020).
20. M. Tabebordbar, K. A. Lagerborg, A. Stanton, E. M. King, S. Ye, L. Tellez, A. Krunnfusz, S. Tavakoli, J. J. Widrick, K. A. Messemer, E. C. Troiano, B. Moghadaszadeh, B. L. Peacker, K. A. Leacock, N. Horwitz, A. H. Beggs, A. J. Wagers and P. C. Sabeti, Directed evolution of a family of AAV capsid variants enabling potent muscle-directed gene delivery across species, *Cell* **184**, 4919 (September 2021).
21. S. Henikoff and J. G. Henikoff, Amino acid substitution matrices from protein blocks, *Proc. Natl. Acad. Sci. U. S. A.* **89**, 10915 (November 1992).
22. S. F. Altschul, W. Gish, W. Miller, E. W. Myers and D. J. Lipman, Basic local alignment search tool, *J. Mol. Biol.* **215**, 403 (October 1990).
23. A. Garivier and E. Moulines, On upper-confidence bound policies for non-stationary bandit problems, *arXiv preprint arXiv:0805.3415* (2008).
24. Y.-S. Tseng and M. Agbandje-McKenna, Mapping the AAV capsid host antibody response toward the development of second generation gene delivery vectors, *Front. Immunol.* **5**, p. 9 (January 2014).
25. ESM cambrian: Revealing the mysteries of proteins with unsupervised learning Accessed: 2025-5-23.

HALO: Hybrid Attention Model for Subcellular Localization

Shafayat Ahmed, Nazifa Ahmed Moumi, and Liqing Zhang
Virginia Tech,
Blacksburg, VA, USA
E-mail: shafayatpiyal@vt.edu, moumi@vt.edu, lqzhang@vt.edu

Subcellular localization prediction is critical for understanding protein functions and interactions, providing insights into cellular mechanisms and potential therapeutic targets. We propose HALO (Hybrid Attention model for subcellular LOcalization), a framework that integrates semantic embeddings from fine-tuned protein language models (e.g., ESM) with structural information derived from AlphaFold. HALO uses a graph attention network (GAT) to incorporate biochemical, structural, and sequence-derived features into a unified representation, while dynamically balancing their contributions. Crucially, the design allows HALO to operate in two modes: (i) a sequence-only mode, where predictions are made from the fine-tuned protein language model (PLM) when structural data are unavailable, and (ii) a hybrid mode, where structural adjacency and biochemical features complement PLM predictions, especially in low-confidence regions. We evaluate HALO on multiple datasets with minimal homology between training and test sets, where it achieves competitive performance across key metrics. By flexibly combining sequence-based and structure-informed predictions, HALO addresses the limitations of relying on a single modality and offers an adaptable framework for accurate and generalizable subcellular localization.

Keywords: Subcellular Localization, LLM, ESM, AlphaFold, Protein Structure, Graph Attention Network

1. Introduction

The localization of proteins within a cell is an essential aspect of their biological roles and interactions within the cell environment.[1] The ability to predict subcellular localization could provide benefits for functional annotation, drug discovery, and understanding disease mechanisms.[2,3] Traditionally, subcellular localization prediction has relied on alignment-based methods, such as BLAST,[4] that use sequence similarity to homologous proteins to infer localization. Although effective for well-annotated databases, these methods are not generalizable for novel or poorly characterized proteins. Increasingly, machine learning models have been developed to predict the subcellular location of a given protein. For example, CELLO[5] and WoLF PSORT[6] use features such as amino acid composition and physicochemical properties to predict subcellular localization. However, the features used in these models do not necessarily capture the intricate relationships between the amino acids within the protein sequences. To address this problem, DeepLoc[7] was developed, integrating convolutional and recurrent neural networks to capture the spatial relationships of amino acids for subcellular localization

© 2025 The Authors. Open Access chapter published by World Scientific Publishing Company and distributed under the terms of the Creative Commons Attribution Non-Commercial (CC BY-NC) 4.0 License.

prediction. While DeepLoc is generally effective due to its ability to model sequence-based spatial patterns, it relies solely on sequence information and does not incorporate protein structural data, which is critical for improving subcellular localization predictions.[8,9] The advent of protein language models, such as ESM (Evolutionary Scale Modeling)[10] and ProtT5,[11] has further revolutionized the field. Luo et al.[12] showed how to maximize the efficacy of ESM-2 embeddings for subcellular localization tasks. These models, trained on large-scale protein databases, extract rich, context-aware embeddings that capture evolutionary and functional information. Furthermore, fine-tuning these language models has proven to improve the accuracy even further.[13] Similarly, AlphaFold[9] and ESM-fold[14] have transformed structural biology by providing accurate predictions of protein 3D structures, offering opportunities to integrate structural information into predictive models. The utilization of protein structures for downstream function annotation has proven to be effective for subcellular localization prediction tasks.[15] GPSFun[16] employs large language models to predict 3D conformations of protein sequences and extract informative sequence embeddings. These embeddings, combined with structural features processed by a geometric featurizer, are used in a graph neural network for subcellular localization prediction tasks. The AlphaFold structure database, known for its extensive repository of 3D protein structures, is widely regarded as more reliable than ESMFold due to its superior accuracy and validation against experimentally resolved structures, as demonstrated in studies like Lin et al. (2021).[17] AlphaFold's reliance on evolutionary covariation and sequence alignments provides robust structural predictions, particularly for highly conserved proteins, making it a gold standard in structural bioinformatics. In contrast, ESMFold, while faster and alignment-free, may exhibit lower accuracy for proteins with less sequence conservation or sparse evolutionary information. Fine-tuning large language models like ESM or ProtT5 on task-specific datasets further enhances their ability to capture nuanced functional and localization signals, as shown by Schmirler et al. (2024).[13] Integrating these fine-tuned models into an ensemble framework, which combines predictions from sequence embeddings, structural features, and graph neural networks, offers an unprecedented opportunity to improve predictive accuracy. Such an approach not only leverages the complementary strengths of language models and structural information but also mitigates individual model biases, providing a unified and robust solution for subcellular localization prediction.

In this study, we introduce HALO, a novel framework that combines sequence embeddings from a fine-tuned ESM model with structural features derived from AlphaFold-predicted 3D structures. Unlike existing methods, HALO leverages a Graph Attention Network (GAT)[18] to integrate these diverse feature modalities. By constructing a graph representation of proteins, where residues are nodes enriched with sequence, structural, and biochemical features, HALO captures both local and global dependencies within the protein. Additionally, using learnable weights for different feature types ensures adaptive prioritization of relevant information. Our framework bridges the gap between sequence- and structure-based predictions, addressing the limitations of previous methods that rely on either modality alone. By incorporating multimodal data and leveraging graph-based learning, HALO offers a significant advance in the ability to predict subcellular localization, paving the way for improved functional annotation of proteins, particularly in datasets with limited prior annotations.

2. Methods

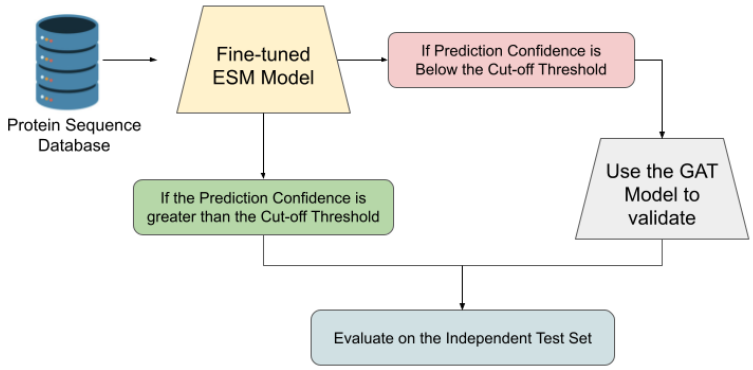

Fig. 1. A hybrid model leveraging Fine-tuned ESM and AlphaFold structure-based GAT attention model for subcellular localization.

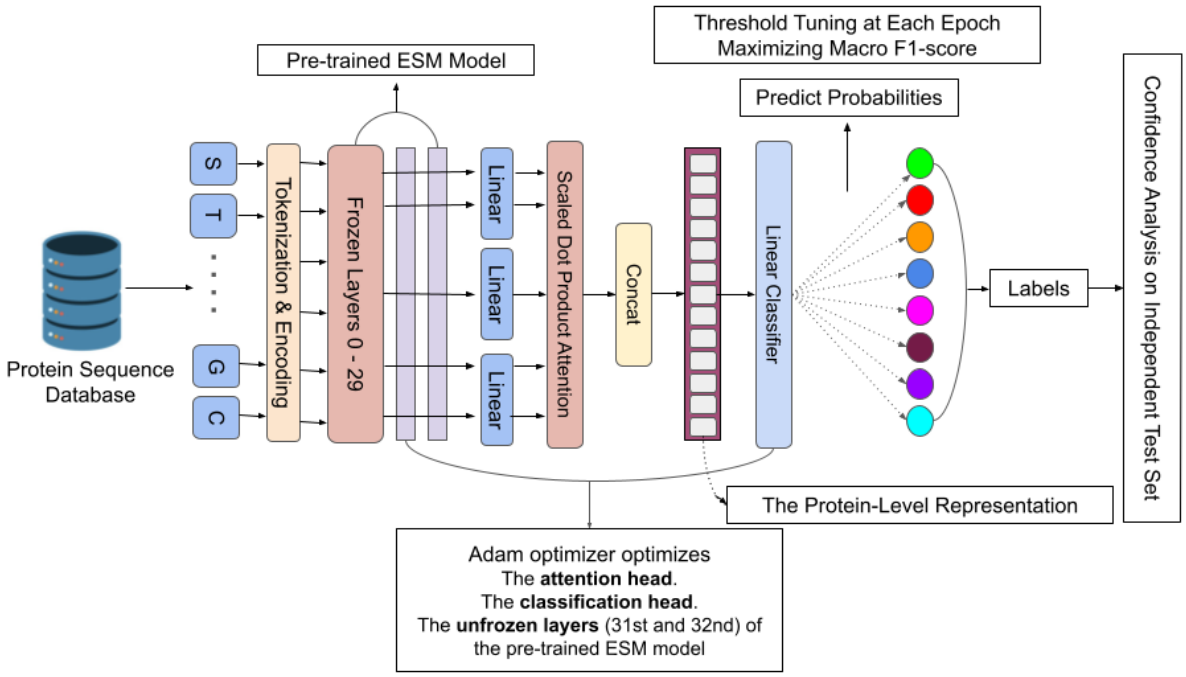

Fig. 2. Fine-tuned pre-trained ESM model for subcellular localization prediction.

Overview

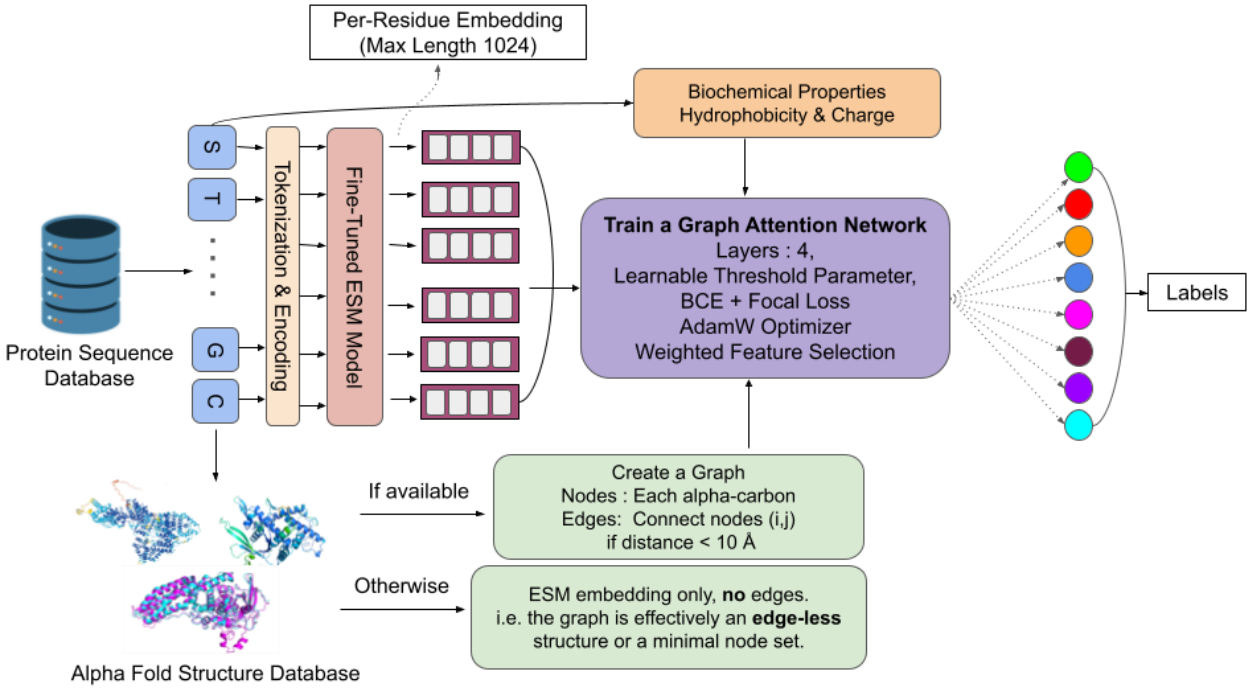

Fig. 3. Leveraging the Fine-Tuned ESM with AlphaFold Structures and Biochemical Properties for training a weighted graph attention model.

We developed HALO, a hybrid framework that integrates features derived from fine-tuned ESM embeddings with those extracted through a Graph Attention Network (GAT) model utilizing AlphaFold-predicted structural data. Below, we detail the individual components of these models and the novel pipeline used to ensemble them.

2.1. *Fine-Tuning ESM Model*

This model (Figure 2) is designed for multi-label protein subcellular localization. It uses the Hugging Face ESM2 backbone to generate embeddings, which are then processed by an attention-based aggregator to highlight important features. Finally, a linear classifier predicts the localization labels. Each protein's sequence is at first tokenized via the ESMTokenizer (up to length 1024 to align with the ESM2 capacity). Batches of sequences are forwarded into the ESM2 base model. Rather than directly using the final classifier layer, we introduce an attention head. Within this head, it learns a soft weight (softmax over positions) to highlight important tokens, producing a single aggregated embedding by summing each token's hidden state scaled by its attention score. On top of that aggregated embedding, a fully connected layer (the classifier) outputs multi-label logits (one dimension per subcellular class). Because the ESM2 base is large, most of its layers are frozen (except the last two encoder blocks and the classifier) to reduce computational cost and risk of overfitting. This design keeps the core ESM2 features intact while still providing some fine-tuning capability on the final layers.

Training proceeds with batches fetched from PyTorch DataLoaders, guided by a focal loss (a variant of binary cross-entropy that upweights hard-to-classify instances). During each

training epoch, only the unfrozen ESM2 layers, the attention-based aggregation, and the classification heads are updated, with a checkpoint saved at the end of each iteration. After training, the code performs threshold tuning: it systematically tests thresholds from 0.1 to 0.95 in small increments, computing macro F1 at each threshold and logging the results. The best threshold is chosen by maximum macro F1, which is then used for the final evaluation. In parallel, the script groups each prediction's confidence into bins (e.g., 95–100%, 90–95%, etc.), tracking how often the model is correct vs. incorrect in each bin to analyze calibration. Early stopping is driven by a plateau in the learning rate scheduler (ReduceLROnPlateau). Based on the threshold analysis, 0.45 yielded the maximum F1 score on the validation set.

2.2. *The GAT Model Training*

The GAT model (Figure 3) is trained by generating fine-tuned ESM embeddings for each protein sequence. Sequences are truncated to 1,024 tokens to fit ESM2's maximum input length extracting the final hidden layer on a per-residue basis. For three-dimensional structural information, we utilize AlphaFold-predicted Protein Data Bank (PDB) files obtained from the AlphaFold structure database. We choose AlphaFold structures over, for example, ESMFold predictions because AlphaFold's large-scale, standardized dataset offers broader coverage and consistency. If the file is absent, that is, no structural information is available, we will use only fine-tuned ESM embeddings (no structural coordinates or edges). As a result, proteins lacking structural information are still included in training and inference, represented solely by node features. This approach avoids discarding valuable sequence-level data simply because an AlphaFold structure is unavailable. For each protein, we build a graph where each residue's alpha-carbon is a node and these nodes are connected with edges if the distance is less than 10 Å. We rely on learned attention coefficients within the GAT to model residue-residue interactions. Each node's feature vector comprises scaled three-dimensional coordinates (coord_weight), fine-tuned ESM embedding (esm_weight), and biochemical properties (bio_weight). A multi-layer GAT with global mean pooling transforms these features into graph-level embeddings, which undergo a focal loss that uses a learnable threshold for multi-label predictions. Early stopping is triggered if macro F1 on the validation set ceases to improve. We varied weights on coordinates, ESM embeddings, and biochemical properties to balance structural and sequence information, tested combinations, and selected the one that maximized validation accuracy within our computational limits.

2.3. *HALO*

We introduce HALO, a hybrid architecture that harnesses the complementary strengths of two separate models: a fine-tuned ESM (sequence-based) model and a GAT (structure-based) model. Our empirical comparisons revealed that the fine-tuned ESM model delivers higher overall accuracy and often outperforms the GAT model on a per-class basis. However, a detailed confidence analysis (see Figure 4) indicates that the ESM model's predictive reliability decreases substantially (Accuracy drops below 60%) for the DeepLoc dataset below a 55% confidence threshold. In other words, for predictions labeled with less than 55% confidence, the fine-tuned ESM model is more prone to misclassification. This shortcoming motivated us

to incorporate the GAT model's alternative perspective, particularly its ability to leverage 3D structural adjacency through residue-residue edges, to boost performance on those uncertain predictions.

Hence, HALO operates by initially relying on the fine-tuned ESM model's logits to classify each protein sample. When the ESM model's confidence for a label is above 55%, the label is taken as the final prediction. When confidence dips below 55%, the GAT model's prediction is considered as well and if both models predict the same label, we incorporate it in the final multi-label output, otherwise, we discard that prediction. This cross-checking mechanism effectively rescues uncertain predictions, mitigating the ESM model's confidence drop. Figure 1, provides an overview of HALO's pipeline: sequences flow first into ESM for classification; afterward, low-confidence candidates are passed to the GAT for structural verification, leading to robust synergy in multi-label subcellular localization tasks. By combining sequence-derived semantics (ESM) with structural adjacency insights (GAT), HALO achieves higher overall precision across different confidence levels than either model alone.

2.4. *Implementation Details*

The framework was implemented in Python, leveraging PyTorch and PyTorch Geometric libraries. All computations were performed on an NVIDIA RTX 4090 GPU to handle the computational demands of graph-based learning and large protein embeddings. Detailed logging of training and evaluation metrics was maintained for reproducibility, and the model dynamically adjusted weights for each feature type during training to optimize the contribution of sequence, structural, and biochemical information. The complete code, data, and, results are included in the repository - https://github.com/Shafayat115/HALO.

3. Experiments & Results

3.1. *Evaluation Metrics*

We split the data into training, validation, and test sets with minimal inter-set homology to increase predictive difficulty. We used the validation set for hyperparameter tuning and the test set for final evaluation. Our evaluation employed a broad suite of metrics, including accuracy, macro and micro-averaged F1-scores, Jaccard Index, precision, recall, and Matthews Correlation Coefficient (MCC). To further assess the contribution of each model component, we conducted an extensive comparative analysis of the sub-models. Additionally, we benchmarked our hybrid approach against state-of-the-art methods across two distinct datasets, emphasizing its performance under challenging conditions.

3.2. *Performance Analysis for Component Models*

Table 1, compares the performance of three GAT models on the DeepLoc test set: one using the pre-trained ESM embeddings (ESM), one with the fine-tuned ESM embeddings (F-ESM), and the last version is with a weighted combination of the fine-tuned ESM embeddings, biochemical features, and structural coordinates (WF-ESM). The WF-ESM model demonstrates the best performance across most metrics, showcasing the benefits of incorporating additional

Table 1. Performance comparison of three GAT models on the DeepLoc test set.

Metric	**ESM**	**F-ESM**	**WF -ESM**
macro F1	0.5420	0.55	0.5942
micro F1	0.6023	0.61	0.6803
Accuracy	0.2671	0.24	0.3819
Jaccard Index	0.5375	0.5375	0.6164
Precision	0.4706	0.48	0.5771
Recall	0.8361	0.85	0.8283
ROC AUC	0.9293	0.93	0.9399
Label-wise MCC			
Cytoplasm	0.4608	0.38	0.4798
Nucleus	0.6806	0.67	0.5731
Extracellular	0.8209	0.84	0.8389
Cell Membrane	0.4516	0.47	0.5401
Mitochondrion	0.6973	0.74	0.7371
Plastid	0.7935	0.83	0.8456
Endoplasmic Reticulum	0.4088	0.4	0.5314
Lysosome/Vacuole	0.2798	0.25	0.2674
Golgi Apparatus	0.2043	0.22	0.3214
Peroxisome	0.2259	0.25	0.3112

structural and biochemical information. It achieves the highest macro F1-Score (0.5942), micro F1-Score (0.6803), and Jaccard Index (0.6164), reflecting a better balance and accuracy in multi-label classification compared to the other models. The ROC AUC of WF-ESM (0.9399) is also slightly higher than the other two models, highlighting its robust ability to distinguish between classes. Furthermore, the WF-ESM model shows notable improvements in Precision (0.5771), indicating a reduction in false positives, while maintaining a strong Recall (0.8283).

The F-ESM model improves over the baseline ESM model in terms of Recall (0.85 vs. 0.8361) and maintains competitive performance for most metrics. However, its macro F1-Score (0.55) and micro F1-Score (0.61) are only slightly better than the ESM model, indicating that fine-tuning alone provides moderate improvements without incorporating additional features.

The ESM model shows relatively weaker performance, with lower macro F1 (0.5420), micro F1 (0.6023), and precision (0.4706). Despite these shortcomings, it demonstrates strong recall (0.8361) and robust performance in high-confidence predictions, as indicated by its ROC AUC (0.9293).

Regarding label-wise MCC, the WF-ESM model consistently outperforms the other two models for most subcellular localization labels. Notably, it achieves the highest MCC for Cell Membrane (0.5401), Endoplasmic Reticulum (0.5314), and Golgi Apparatus (0.3214), demonstrating its ability to accurately predict labels that are typically more challenging due to their sparse representation. All models perform competitively for well-represented labels such as Plastid and Extracellular, with MCC values above 0.8 for both labels across all three models. However, the WF-ESM model still leads among them with marginal improvements in

these categories.

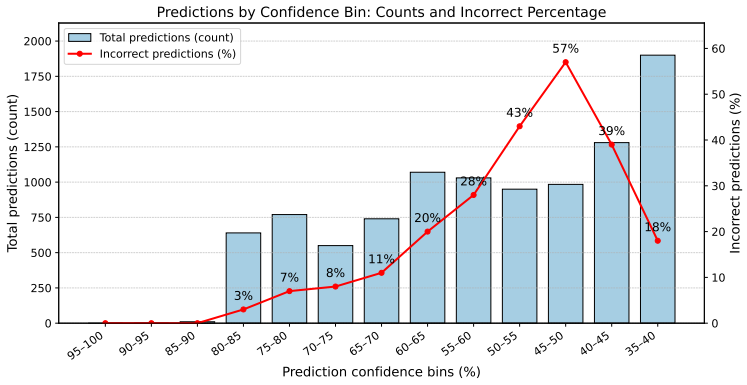

Fig. 4. Confidence distribution of the fine-tuned ESM model on the evaluation set, with total predictions and misclassifications per confidence range. Errors concentrate at lower confidence ranges, indicating that confidence is informative about reliability.

Figure 4, illustrates the distribution of total and incorrect predictions across varying confidence ranges for the fine-tuned ESM model, highlighting the relationship between prediction confidence and model accuracy. Predictions with high confidence (70-100%) demonstrate remarkable reliability, with negligible incorrect predictions, underscoring the robustness of the model in these intervals. However, as confidence decreases, the proportion of incorrect predictions increases significantly, particularly in the 55-65% range, marking a critical threshold for model reliability. In the lowest confidence ranges (55-45% and 45-40%), nearly half of the predictions are incorrect, indicating a substantial decline in model performance. These results emphasize the importance of using confidence thresholds to assess prediction reliability, suggesting that predictions below 55% confidence should be subjected to additional validation. This analysis provides critical insights into the strengths and limitations of the model across confidence levels, guiding its effective application in practical scenarios.

Table 2, highlights the comparative performance of HALO, fine-tuned ESM, and GAT models on the DeepLoc test set, showcasing HALO's ability to bridge the strengths of both sequence and structure-focused approaches. HALO achieves a macro F1 of 0.6782 and a micro F1 of 0.7364, indicating robust performance that effectively balances the complementary modalities of sequence and structural information. Notably, HALO surpasses the fine-tuned ESM model in key metrics such as Jaccard Index (0.7187 vs. 0.7075) and ROC AUC (0.9412 vs. 0.9254), while also demonstrating strong precision (0.7098) and overall MCC (0.7131), reflecting its capacity for multi-label classification across diverse localization labels.

The fine-tuned ESM model, while slightly ahead in metrics like macro F1 (0.6688) and micro F1 (0.7471), emphasizes nuanced sequence-level features, benefiting from attention-based aggregation. On the other hand, the GAT model leverages structural adjacency and 3D relationships to deliver strong MCC values for Extracellular (0.8389) and Plastid (0.8456), although it falls behind in overall metrics like accuracy (0.3819) and macro F1 (0.5942).

HALO's hybrid approach integrates high-confidence predictions from the fine-tuned ESM

Table 2. Comparison of overall performance metrics and MCC per subcellular localization label across HALO, fine-tuned ESM, and GAT models on the DeepLoc test set.

Metric	HALO	Fine-tuned ESM	GAT
macro F1	0.6782	0.6688	0.5942
micro F1	0.7364	0.7471	0.6803
Accuracy	0.5756	0.5621	0.3819
Jaccard Index	0.7187	0.7075	0.6164
Precision	0.7098	0.6996	0.5771
Recall	0.6511	0.6537	0.8283
ROC AUC	0.9412	0.9254	0.9399
Matthews Correlation Coefficient (MCC) per Label			
Cytoplasm	0.6125	0.6162	0.4798
Nucleus	0.6819	0.6821	0.5731
Extracellular	0.8559	0.8554	0.8389
Cell Membrane	0.6752	0.6660	0.5401
Mitochondrion	0.7921	0.7999	0.7371
Plastid	0.8918	0.8758	0.8456
Endoplasmic Reticulum	0.5735	0.5864	0.5314
Lysosome/Vacuole	0.2621	0.2982	0.2674
Golgi Apparatus	0.3349	0.3283	0.3214
Peroxisome	0.5835	0.5991	0.3112

model with structural insights from the GAT model, particularly excelling in cases where sequence- or structure-only models face limitations. This synergy allows HALO to enhance robustness and maintain precision across challenging labels, such as Extracellular (MCC: 0.8559) and Plastid (MCC: 0.8918). However, the model shows room for improvement in complex localizations such as Lysosome/Vacuole (MCC: 0.2621) and Golgi Apparatus (MCC: 0.3349), suggesting that further optimization in the ensemble mechanism could enhance performance for these challenging categories. HALO's ability to integrate sequence and structure-derived features establishes it as a versatile and adaptable framework for subcellular localization prediction.

3.3. *Comparison with other tools*

We compared our model's performance with two of the state-of-the-art tools for subcellular localization prediction using two different datasets curated by them. Here is a detailed comparison of our tool in these datasets -

3.3.1. *DeepLoc*

Table 3, showcases the comparative performance of HALO, DeepLoc 1.0, DeepLoc 2.0 (ESM1b and ProtT5), and other models on the DeepLoc test set, underscoring HALO's strong performance relative to state-of-the-art methods. HALO achieves a macro F1 score of 0.6782 and a micro F1 score of 0.7364, significantly outperforming DeepLoc 1.0 (0.47 and 0.58, respectively)

Table 3. Comparison of Performance Metrics and Matthews Correlation Coefficient (MCC) per Subcellular Localization Label across All Models

Metric	DeepLoc 1.0	DeepLoc 2.0 (ESM1b)	DeepLoc 2.0 (ProtT5)	HALO	Fine-tuned ESM	GAT
Accuracy	0.48	0.53	0.55	0.5756	0.5621	0.3819
Jaccard Index	0.56	0.68	0.69	0.7187	0.7075	0.6164
micro F1	0.58	0.72	0.73	0.7364	0.7471	0.6803
macro F1	0.47	0.64	0.66	0.6782	0.6688	0.5942
Precision	–	–	–	0.7098	0.6996	0.5771
Recall	–	–	–	0.6511	0.6537	0.8283
ROC AUC	–	–	–	0.9412	0.9254	0.9399
Matthews Correlation Coefficient (MCC) per Label						
Cytoplasm	0.45	0.61	0.62	0.6125	0.6162	0.4798
Nucleus	0.46	0.66	0.69	0.6819	0.6821	0.5731
Extracellular	0.78	0.85	0.85	0.8559	0.8554	0.8389
Cell Membrane	0.53	0.64	0.66	0.6752	0.6660	0.5401
Mitochondrion	0.58	0.73	0.76	0.7921	0.7999	0.7371
Plastid	0.69	0.88	0.90	0.8918	0.8758	0.8456
Endoplasmic Reticulum	0.32	0.52	0.56	0.5735	0.5864	0.5314
Lysosome/Vacuole	0.06	0.24	0.28	0.2621	0.2982	0.2674
Golgi Apparatus	0.20	0.36	0.34	0.3349	0.3283	0.3214
Peroxisome	0.15	0.48	0.56	0.5835	0.5991	0.3112

and closely approaching DeepLoc 2.0 (ProtT5), which achieves a macro F1 of 0.66 and a micro F1 of 0.73. HALO's Jaccard Index (0.7187) and accuracy (0.5756) also exceed DeepLoc 1.0 (0.56 and 0.48, respectively) and closely align with ProtT5's performance (0.69 and 0.55).

HALO demonstrates consistent improvement over DeepLoc 1.0 in several subcellular localization labels, such as Cytoplasm (0.6125 MCC), Nucleus (0.6819 MCC), and Cell Membrane (0.6752 MCC). For complex localizations like Extracellular (0.8559 MCC) and Plastid (0.8918 MCC), HALO performs on par with DeepLoc 2.0 models, maintaining robust predictions. However, HALO shows a slight performance gap in more challenging labels like Lysosome/Vacuole (0.2621 MCC) and Golgi Apparatus (0.3349 MCC), where it lags behind ProtT5 (0.28 and 0.34, respectively).

Overall, HALO bridges the gap between DeepLoc 1.0 and the more advanced DeepLoc 2.0 models by effectively integrating sequence and structural insights through its hybrid approach. While it does not universally surpass DeepLoc 2.0 (ProtT5) in every metric, HALO offers a balanced and versatile framework for subcellular localization prediction, with the potential for further optimization to improve predictions in complex localization categories.

3.3.2. *Single-Label Swissprot Dataset*

We also compared our model with the work of Luo et. al.[12] They proposed different ESM2 representation feature extraction strategies, considering both the character type and position within the ESM2 input sequence. They benchmarked their models curated from the SwissProt section of the UniProt database,[19] focusing on entries with a "Reviewed" status and confirmed protein existence at the protein level (updated as of April 15, 2023). Proteins selected for their study had amino acid sequence lengths ranging from 15 to 4000 and were associated with a single classification label. The dataset was randomly shuffled and split into two subsets: a training set (60% of the total) and a test set (40%). Additionally, protein localization data were obtained from the TrEMBL section of the UniProt database, serving as independent

test datasets. De-homology datasets were subsequently generated by excluding proteins that showed homology with those in SwissProt. We performed using the exact train and test set for HALO and compared it with the results they put up in their paper. We added some additional metrics to better represent our model's performance in that data split, which are represented as a gap for their methodologies.

Table 4. Performance comparison across the three datasets S (Swiss-Prot), T (TrEMBL Independent), and N (non-homology TrEMBL Independent) for our HALO model and the interpretable LLM models.[12]

Metric	**HALO_S**	**RF_S**	**MLP_S**	**HALO_T**	**RF_T**	**MLP_T**	**HALO_N**	**RF_N**	**MLP_N**
Macro Precision	0.9178	0.722	0.644	0.8712	–	–	0.7860	–	–
Macro Recall	0.5319	0.563	0.606	0.4426	–	–	0.3364	–	–
macro F1	0.5722	0.596	0.621	0.4900	–	–	0.3827	–	–
micro F1	0.8358	–	–	0.7182	–	–	0.5672	–	–
Jaccard Index	0.7940	–	–	0.6503	–	–	0.4912	–	–
Accuracy	0.7924	0.9555	0.963	0.6468	–	–	0.4880	–	–
ROC AUC	0.9284	0.766	0.792	0.9072	–	–	0.8242	–	–
Overall MCC	0.8198	–	–	0.6943	–	–	0.5338	–	–
MCC Per Label									
Cell Junction	0	0.377	0.187	0	0.06	0.07	0	0	0
Cell Membrane	0.83	0.780	0.824	0.72	0.62	0.67	0.50	0.21	0.26
Cell Projection	0	0.069	0.151	0	0.21	0.12	0	0	0
Cytoplasm	0.66	0.558	0.620	0.44	0.40	0.43	0.26	0.19	0.19
ER	0.71	0.618	0.699	0.74	0.65	0.71	0.58	0.19	0.18
Golgi Apparatus	0.62	0.605	0.612	0.43	0.51	0.48	0.34	0.41	0.25
Lysosome	0.24	0.380	0.314	0.14	0.68	0.63	0	0	0
Mitochondrion	0.89	0.878	0.865	0.77	0.73	0.64	0.67	0.47	0.23
Nucleus	0.87	0.730	0.836	0.76	0.61	0.68	0.55	0.26	0.30
Secreted	0.91	0.866	0.896	0.81	0.69	0.72	0.60	0.53	0.52

Table 4, represents the performance comparison across the three datasets SwissProt (S), TrEMBL Independent (T), and Non-Homology TrEMBL Independent (N). It highlights the effectiveness of different models, including HALO, and the interpretable LLM's,[12] two final models comprising all their features with Random Forest (RF), and Multi-Layer Perceptron (MLP) model. HALO consistently demonstrates superior performance in most metrics across the datasets, particularly excelling in Macro Precision, Macro Recall, and ROC AUC, with scores of 0.9178, 0.5319, and 0.9284, respectively, on the SwissProt dataset. This indicates its ability to make highly confident and accurate predictions while capturing class-specific variability. In contrast, RF and MLP models show comparable but slightly lower performance, particularly in Precision and F1 Score for the SwissProt dataset, with MLP slightly outperforming RF in macro Recall and macro F1. On the TrEMBL Independent dataset, HALO maintains its lead with a Macro Precision of 0.8712 and an ROC AUC of 0.9072, indicating its robustness in generalizing to independent datasets. However, RF and MLP performance metrics for this dataset were not fully available, suggesting potential limitations in model generalizability or dataset-specific challenges.

For the Non-Homology TrEMBL Independent dataset, which presents the most challeng-

ing scenario due to the elimination of homologous proteins, HALO still performs reasonably well, achieving a macro F1 of 0.3827 and an ROC AUC of 0.8242. These results underscore HALO's ability to make accurate predictions in scenarios with reduced homology information. In comparison, RF and MLP show worse performance across most metrics, particularly for complex labels like Cell Membrane and Mitochondrion, highlighting their limitations in handling non-homologous data.

Overall, HALO's superior performance, particularly in ROC AUC and Macro Precision, indicates its strength in capturing complex patterns within protein localization data. While RF and MLP provide competitive results, especially for simpler datasets, their performance declines in independent and non-homologous datasets, emphasizing the importance of advanced modeling techniques like HALO.

4. Conclusion

HALO represents a novel hybrid approach that integrates sequence and structural information to enhance subcellular localization prediction. By combining fine-tuned protein language model (PLM) embeddings, biochemical properties such as residue charge and hydrophobicity, and AlphaFold-predicted structural information, HALO delivers competitive performance across multiple datasets with minimal homology between train and test splits. Importantly, HALO demonstrates that structural information, even in a relatively simple representation, can play a critical role in rescuing low-confidence sequence-based predictions, highlighting the value of complementary modalities for functional annotation. These findings underscore the importance of flexible frameworks that can operate effectively in both sequence-only and hybrid sequence–structure modes.

Future work will focus on several directions. First, more sophisticated structural encodings, such as contact maps, torsion angles, and geometric message-passing layers, could capture richer spatial dependencies and further improve predictive accuracy, especially for challenging compartments like Lysosome/Vacuole and Golgi Apparatus. Second, systematic benchmarking of different fine-tuning strategies for PLMs and alternative graph neural network architectures will be pursued as resources permit, extending beyond our current constraint of fine-tuning only the final two ESM layers. Third, sensitivity analyses of design parameters such as the 55% gating threshold and the 10 Å distance cutoff will provide a more comprehensive justification of these choices. Finally, future work will explore feature attribution and modality importance analyses to improve the biological interpretability of HALO, clarifying which inputs contribute most to accurate predictions. Collectively, these enhancements will improve robustness, scalability, and interpretability, expanding HALO's utility to broader protein functional annotation tasks and advancing the integration of multi-modal data in bioinformatics.

Acknowledgments and Appendices

This work was partly funded by the National Science Foundation (NSF grants #2319522, #2125798, and #2004751).

References

1. B. Alberts, D. Bray, J. Lewis, M. Raff, K. Roberts, J. D. Watson *et al.*, *Molecular biology of the cell* (Garland New York, 1994).
2. H. Yin and A. D. Flynn, Drugging membrane protein interactions, *Annual review of biomedical engineering* **18**, 51 (2016).
3. J. P. Overington, B. Al-Lazikani and A. L. Hopkins, How many drug targets are there?, *Nature reviews Drug discovery* **5**, 993 (2006).
4. S. F. Altschul, T. L. Madden, A. A. Schäffer, J. Zhang, Z. Zhang, W. Miller and D. J. Lipman, Gapped blast and psi-blast: a new generation of protein database search programs, *Nucleic acids research* **25**, 3389 (1997).
5. C.-S. Yu, Y.-C. Chen, C.-H. Lu and J.-K. Hwang, Prediction of protein subcellular localization, *Proteins: Structure, Function, and Bioinformatics* **64**, 643 (2006).
6. P. Horton, K.-J. Park, T. Obayashi, N. Fujita, H. Harada, C. Adams-Collier and K. Nakai, Wolf psort: protein localization predictor, *Nucleic acids research* **35**, W585 (2007).
7. J. J. Almagro Armenteros, C. K. Sønderby, S. K. Sønderby, H. Nielsen and O. Winther, Deeploc: prediction of protein subcellular localization using deep learning, *Bioinformatics* **33**, 3387 (2017).
8. G. Wang, Y.-J. Zhai, Z.-Z. Xue and Y.-Y. Xu, Improving protein subcellular location classification by incorporating three-dimensional structure information, *Biomolecules* **11**, p. 1607 (2021).
9. J. Jumper, R. Evans, A. Pritzel, T. Green, M. Figurnov, O. Ronneberger, K. Tunyasuvunakool, R. Bates, A. Žídek, A. Potapenko *et al.*, Highly accurate protein structure prediction with alphafold, *nature* **596**, 583 (2021).
10. D. J. Beal, Esm 2.0: State of the art and future potential of experience sampling methods in organizational research, *Annu. Rev. Organ. Psychol. Organ. Behav.* **2**, 383 (2015).
11. A. Elnaggar, M. Heinzinger, C. Dallago, G. Rehawi, Y. Wang, L. Jones, T. Gibbs, T. Feher, C. Angerer, M. Steinegger *et al.*, Prottrans: Toward understanding the language of life through self-supervised learning, *IEEE transactions on pattern analysis and machine intelligence* **44**, 7112 (2021).
12. Z. Luo, R. Wang, Y. Sun, J. Liu, Z. Chen and Y.-J. Zhang, Interpretable feature extraction and dimensionality reduction in esm2 for protein localization prediction, *Briefings in Bioinformatics* **25**, p. bbad534 (2024).
13. R. Schmirler, M. Heinzinger and B. Rost, Fine-tuning protein language models boosts predictions across diverse tasks, *Nature Communications* **15**, p. 7407 (2024).
14. Z. Lin, H. Akin, R. Rao, B. Hie, Z. Zhu, W. Lu, N. Smetanin, A. dos Santos Costa, M. Fazel-Zarandi, T. Sercu, S. Candido *et al.*, Language models of protein sequences at the scale of evolution enable accurate structure prediction, *bioRxiv* (2022).
15. G. Dubourg-Felonneau, A. Abbasi, E. Akiva and L. Lee, Improving protein subcellular localization prediction with structural prediction & graph neural networks, *bioRxiv* , 2022 (2022).
16. Q. Yuan, C. Tian, Y. Song, P. Ou, M. Zhu, H. Zhao and Y. Yang, Gpsfun: geometry-aware protein sequence function predictions with language models, *Nucleic Acids Research* , p. gkae381 (2024).
17. Z. Lin, H. Akin, R. Rao, B. Hie, Z. Zhu, W. Lu, N. Smetanin, R. Verkuil, O. Kabeli, Y. Shmueli *et al.*, Evolutionary-scale prediction of atomic-level protein structure with a language model, *Science* **379**, 1123 (2023).
18. P. Veličković, G. Cucurull, A. Casanova, A. Romero, P. Lio and Y. Bengio, Graph attention networks, *arXiv preprint arXiv:1710.10903* (2017).
19. U. Consortium, Uniprot: a hub for protein information, *Nucleic acids research* **43**, D204 (2015).

PertSpectra: Interpretable Matrix Factorization for Predicting Functional Impact of Genetic Perturbation Experiments

Seowon Chang[1], Anna Shcherbina[2], Tal Ashuach[2], Shahin Mohammadi[2], Stephanie See[2], Ninad Ranadive[2], Emily Fox[2], Navpreet Ranu[2]

1. Center for Computational and Molecular Biology, Brown University, Providence, Rhode Island, 02912, USA

2. Insitro, South San Francisco, California, 94080, USA

E-mail: seowon_chang@brown.edu, annashch@insitro.com, tal.ashuach@insitro.com

In drug discovery, measuring the effects of genetic perturbations is a powerful tool for studying unknown disease mechanisms, but biological interpretation of these effects, especially with the advent of screens involving combinatorial perturbations, remains challenging. To address limitations in current methodology we introduce PertSpectra, a guided triple matrix factorization that incorporates perturbation information and regularizes the model using a known gene-gene interaction graph prior to generate sparse, biologically relevant latent factors that capture perturbational effects. We evaluate PertSpectra on three single-cell RNA-seq datasets with both single and combinatorial genetic perturbations, measuring latent space interpretability, predictive ability on unseen combinations of observed perturbations, and stratification of functionally similar perturbations. We show that PertSpectra provides an integrated modeling approach to understanding combinatorial perturbation data in the context of drug discovery.

Keywords: Machine learning; perturb-seq; single cell RNA-seq; matrix factorization; combinatorial perturbations; functional impact; gene ontology

© 2025 The Authors. Open Access chapter published by World Scientific Publishing Company and distributed under the terms of the Creative Commons Attribution Non-Commercial (CC BY-NC) 4.0 License.

1. Introduction

Perturb-seq,[1] single-cell RNA sequencing performed on genetic perturbation screens, has emerged in recent years as a powerful tool in drug discovery for studying how targeted perturbations of individual genes affect cellular phenotype, providing insights into disease mechanisms. However, analyzing these experiments presents significant challenges, since the impact of each perturbation is often relatively small in comparison to the noise and sparsity in the data.[2] Furthermore, recent studies include multiple perturbations introduced into the same cells,[3] but few models attempt to untangle the effect of multiple perturbations. A variety of approaches have been proposed to tackle these challenges and assist in downstream tasks, such as interpreting perturbational effects, prediction of unseen combinations of perturbations, and predicting the cellular effects of unseen perturbations.

Autoencoder frameworks such as CPA[4] and GEARS[5] focus on capturing confounding variables such as cell type and batch effects to make predictions on unseen perturbations. sVAE+[6] and SAMS-VAE[7] are generative frameworks that incorporates a sparse shift mechanism, which capture interventions' sparse effects as explicit latent variables, improving the perturbation effect prediction. These models focus on predicting the transcriptional effects induced by perturbations, but quantifying the contributions of each gene to the latent dimensions remains difficult, making the latent spaces produced by these models challenging to interpret without extensive prior knowledge or expert annotations.

Other models prioritize learning an interpretable latent space, often by employing matrix factorization techniques,[8,9] which decomposes the observed cell-by-gene matrix into cell-by-factor and factor-by-gene matrices. This factor-by-gene matrix, denoted the gene loading matrix, captures the contribution of each individual gene to each learned factor in the latent space, thereby enabling biological interpretation of these factors. However, matrix factorization has several limitations in the context of interpreting perturb-seq data: (1) these models are largely designed for observational data, and need to be modified to support perturbational assays; (2) there are many ways of decomposing a matrix, and many models lack a biologically-informed inductive bias that would bias the decomposition towards biologically coherent factors, so these models often produce factors that remain difficult to interpret.

There are recent matrix factorization models that attempt to address some of these limitations. GSFA[10] is a Bayesian factorization method that incorporates perturbation information in a triple matrix factorization. Perturbation labels are encoded in a binary cell-by-perturbation design matrix, and the observed cell-by-gene matrix is decomposed into this cell-by-perturbation matrix and learned perturbation-by-factor and factor-by-gene matrices. Thereby GSFA learns an embedding space for perturbations, as opposed to individual cells. However, GSFA uses uninformative priors on the gene loading matrix that do not incorporate prior biological knowledge, so learned factors might not align with the underlying biology in the data. Additionally, GSFA is optimized with Gibbs-sampling, a computationally expensive algorithm that struggles with large-scale perturb-seq datasets.

Another recent development in this direction is Spectra,[9] a matrix factorization model designed for observational RNA-seq data that incorporates biologically informed inductive bias into the optimization procedure. Spectra maps the learned gene loading matrix to a gene-gene interaction graph, which is regularized by a known gene-gene interaction graph prior. In doing so, Spectra balances biological domain knowledge with data-driven relationships captured in the latent factors. However, Spectra does not support perturbation labels and was not designed for genetic screens.

Inspired by these contributions and motivated by the complementary limitations of existing approaches, here we introduce PertSpectra, a scalable guided triple matrix factorization method designed for genetic perturbation experiments, which leverages prior biological knowledge. We incorporate perturbational information as a fixed binary design matrix as in GFSA, and employ graph regularization on the gene loading matrix to guide the latent factors in a biologically-meaningful direction as in Spectra. Notably, this construction naturally supports additive combinatorial perturbations, as the perturbation design matrix can simply have multiple perturbations encoded for a given cell. PertSpectra is designed to (1) correctly predict both single and combinatorial perturbed cell expression profiles and (2) yield interpretable latent factors that yield insights into the functional impact of perturbations. Our main contributions can be summarized as:

- A triple matrix factorization formulation incorporating perturbation information as a fixed binary matrix.
- A functional protein graph[11] prior used during optimization to incorporate functional information into the learned latent factors.
- A set of qualitative and quantitative evaluations against baseline methods on three real-world perturb-seq datasets, one of which was generated in-house, to demonstrate state-of-the-art performance. We introduce an interpretability analysis as a part of these benchmarks.

We evaluate PertSpectra on three perturb-seq datasets including single and combinatorial perturbations, and demonstrate that Spectra produces biologically coherent, highly interpretable latent factors, while maintaining or improving performance on predictive tasks, compared with similar models. We benchmark PertSpectra against scETM, a single cell topic model, and GSFA, a perturbation-focused matrix factorization, to show the benefits of both incorporating perturbation information and inductive bias to model genetic perturbation experiments.

2. Background and Problem Setting

2.1. *Data and Preprocessing*

Three perturb-seq datasets were analyzed: Norman[3] (growth-pathway specific combinatorial knockouts in the K562 cell line), Replogle[2] (genome wide, CRISPRi in the K562 cell line), and an in-house dataset (combinatorial knockouts in the A549 cell line along the TNFa and IL1B mediated signaling along the NFκB pathway). The gene-by-sample matrices for each

individual dataset were filtered to remove cells with low counts and genes with expressed in few cells and then log-normalized with scanpy[12] (full details in appendix A). The top 5000 highly variable genes across all samples were then selected. The identity of the perturbation for each cell was encoded in a binary matrix $\boldsymbol{H}$, where $\boldsymbol{H}_{ij} = 1 \iff$ gene j was perturbed in cell i. PertSpectra also incorporates prior knowledge from the StringDB[11] knowledge graph of known protein-protein interactions. We filtered to high-confidence, validated interactions and subset the graph to genes measured in the perturb-seq experiments (full details in appendix A).

Table 1. Evaluation datasets

Dataset	Type	# Cells	# Perts
In-house	Combinatorial	65648	182
Norman	Combinatorial	101484	235
Replogle	Single	105943	517

2.2. *Training Setup*

For the combinatorial perturbation datasets (in-house and Norman), we evaluated model performance on unseen combinations of observed singleton perturbations. Therefore, we held out 30% of combinatorial perturbations and reserved all cells that received those combinatorial perturbations for the test set. We then further divided the rest of the cells into 80-20 train/validation sets, proportionally to the perturbations received.

For the single perturbation datasets (Replogle), we wanted to evaluate model performance on unseen cells for seen perturbations. Therefore, data was divided into a 80-20 train/test split by cell, and the training split was further divided into a 80-20 train/validation split.

2.3. *Spectra*

As PertSpectra utilizes several components of Spectra, it stands to give a brief overview of the Spectra model.

A perturb-seq experiment yields an expression matrix $\mathbf{X}$ of dimensions $n \times g$, where n is the number of cells and g is the number of genes. Spectra learns a gene loading matrix $\boldsymbol{\theta}$ with dimensions $z \times g$, and cell loading matrix $\boldsymbol{\alpha}$ with dimensions $n \times z$ where z is the number of latent factors. The cell loading matrix $\boldsymbol{\alpha}$ is restricted to be strictly positive, under the assumption that a transcriptional profile of a cell is the sum of a set of active pathways, and negative pathway activation is difficult to interpret in a biological setting. This gives the decomposition

$$\mathbb{E}[\mathbf{X_{ij}}] = \boldsymbol{\alpha}_i^\intercal \boldsymbol{\theta}_j, \tag{1}$$

where $\mathbf{X_{ij}}$ is the expression of gene j in cell i, $\boldsymbol{\alpha}_i \in \mathbb{R}_+^z$ is the cell loading for cell i, and $\boldsymbol{\theta}_j \in \Delta^z$ (where Δ^z is the set of positive z-vectors that sum to 1) is the gene loading for gene j.

Spectra also addresses technical variation that may be present in the data. Certain genes that are involved in basic cellular functions are often highly expressed, while other important genes, such as transcription factors, may be lowly expressed. Matrix factorization methods may give higher weight to genes in the former group and less weight on the latter group, leading to poor latent factors. Spectra corrects for this by introducing a learned parameter ν_j as a gene-specific scaling factor, bounded from below by a hyperparameter δ. This allows the model to capture high expression and variability of specific genes, without increasing the weights of gene factors and giving too much or too little importance to specific genes. Thus, the base model of Spectra is given as

$$\mathbb{E}[\mathbf{X_{ij}}] = (\nu_j + \delta)\boldsymbol{\alpha}_i^\intercal \boldsymbol{\theta}_j, \tag{2}$$

The objective function to learn Spectra's parameters $\boldsymbol{\Theta} = \{\alpha, \theta, \nu\}$ is given by

$$\mathcal{L}(\boldsymbol{\Theta}) = \lambda \mathcal{L}_{recon}(\boldsymbol{\Theta}) + \mathcal{L}_{graph}(\boldsymbol{\Theta}), \tag{3}$$

where $\mathcal{L}_{recon}$ is the reconstruction loss, $\mathcal{L}_{graph}$ is the penalty term on the gene loading matrix $\boldsymbol{\theta}$, and λ a hyperparameter controlling the balance between the two loss terms. We give a brief overview of the intuition and formulation of the components of the loss function.

For $\mathcal{L}_{recon}$, Spectra uses the Poisson log likelihood

$$\mathcal{L}_{recon}(\boldsymbol{\Theta}) = -\mathbf{X}\log(\hat{\mathbf{X}}(\boldsymbol{\Theta})) + \hat{\mathbf{X}}(\boldsymbol{\Theta}), \tag{4}$$

where $\hat{\mathbf{X}}$ is Spectra's estimated gene expression from its learned parameters $\boldsymbol{\Theta}$. Spectra chooses this loss term as this function derived from the Poisson distribution has been widely used for modeling single cell RNA-seq counts.[8,13] Furthermore, it does not overly weight highly expressed or lowly expressed genes, as the loss scales according to the expression values of $\mathbf{X}$. Thus, this serves as a reasonable objective function for reconstructing the gene expression.

For $\mathcal{L}_{graph}$, we are first given a prior knowledge adjacency matrix $\mathbf{A}$, where edge $\mathbf{A}_{ij} = 1$ if there is a direct biological relationship between genes i and j. Spectra generatively defines its own gene-by-gene adjacency matrix as a weighted inner product of $\boldsymbol{\theta}$ with itself, with parameters that allow for random edge generation/deletion:

$$\mathbb{P}[\mathbf{A}_{ij} = 1] := (1-\kappa)(1-\rho)\langle \boldsymbol{\theta}_i, \boldsymbol{B}\boldsymbol{\theta}_j \rangle + \kappa(1-\rho), \tag{5}$$

where $\boldsymbol{B}$ is a learned scaling factor, κ is an edge creation rate, and ρ is an edge deletion rate. Spectra lets $\mathbb{P}[\mathbf{A}_{ij} = 1]$, or the the probability of an edge between genes i and j, be correlated to similarity of the factor distribution between the two genes captured by $\boldsymbol{\theta}_i$ and $\boldsymbol{\theta}_j$. $\boldsymbol{B}$ is a scaling factor that prevents the regularization from discouraging discovery of new gene-gene relationships. If genes i and j show clear relationship from the data but not in the prior information, a simple inner product $\langle \boldsymbol{\theta}_i, \boldsymbol{B}\boldsymbol{\theta}_j \rangle$ would discourage the model from learning this new discovery. Thus, $\boldsymbol{B}$ prevents heavy bias towards the prior information graph. Furthermore, parameters κ and ρ allow for the model to add or delete edges if the expression data that drives $\boldsymbol{\theta}$ deviates from the relationships in the prior graph. Therefore, cliques and communities within this generated graph, that represent gene groups with shared latent factors, should reflect

functional groupings of genes. By regularizing this factor-dependent gene-gene graph against a prior graph derived from experiments, Spectra constrains the learned $\boldsymbol{\theta}$ to yield biologically interpretable factors. Therefore, the graph regularization loss is the negative log likelihood:

$$\mathcal{L}_{graph}(\boldsymbol{\Theta}) = -\mathbf{A}_{ij} \log(\mathbb{P}[\mathbf{A}_{ij} = 1]) - (1 - \mathbf{A}_{ij}) \log(1 - \mathbb{P}[\mathbf{A}_{ij} = 1]), \tag{6}$$

Spectra optimizes $\mathcal{L}(\boldsymbol{\Theta})$ using the Adam optimizer, with a learning rate schedule of [1.0, 0.5, 0.1, 0.01, 0.001, 0.0001] and maximum number of epochs set at 10,000.

3. Methods

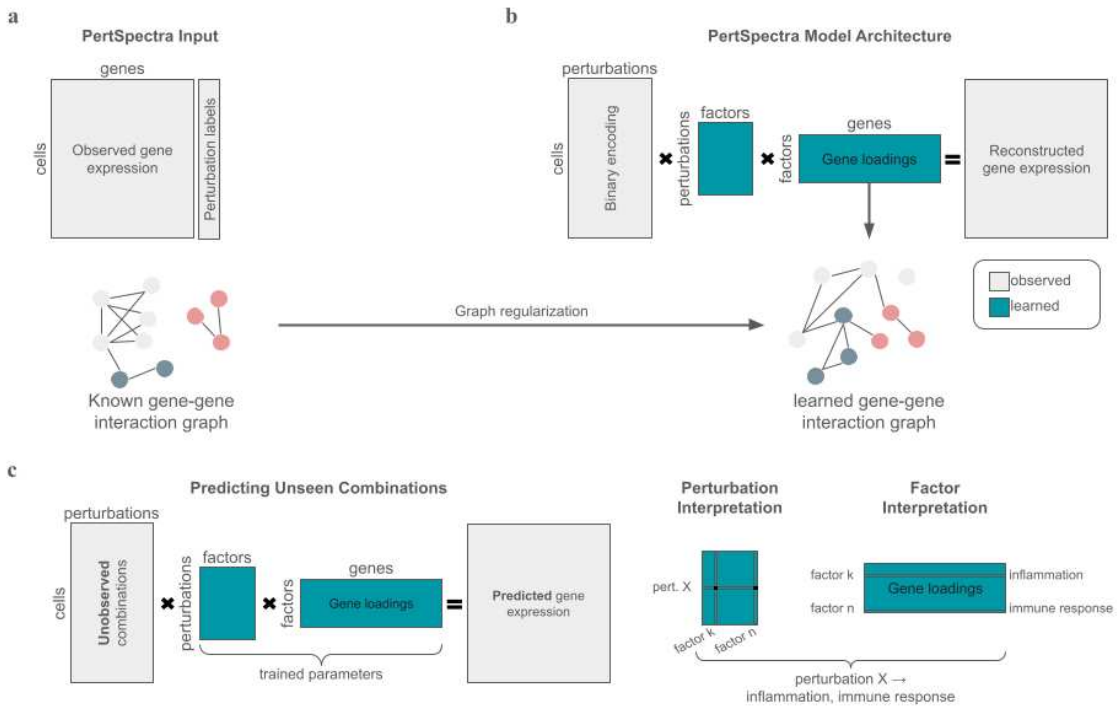

Fig. 1. a. Input for PertSpectra, b. Illustration of PertSpectra model, c. Downstream applications of a trained PertSpectra model

3.1. *PertSpectra Architecture and Training Procedure*

PertSpectra is a guided triplet matrix factorization model that incorporates both perturbation information from the experiment as well as biological knowledge graphs. Specifically, we modified Spectra, a single-cell matrix factorization method, to account for perturbation information. A perturbation sequencing experiment outputs a gene expression matrix $\mathbf{X}$ with dimensions $n \times g$ and perturbation labels vector $\boldsymbol{h}$ of length n, where n is the number of cells and g is the number of genes. We can transform h into a binary matrix $\boldsymbol{H}$ of dimensions $n \times p$, where p is the number of unique perturbations, such that $\boldsymbol{H}_{i,j} = 1 \iff \boldsymbol{h}_i = j$. Unlike

Spectra, which decomposes the gene expression matrix into two matrices, PertSpectra has the following factorization:

$$\mathbb{E}[\mathbf{X_{ij}}] = (\nu_j + \delta)\boldsymbol{H}_i^\intercal \boldsymbol{P}\boldsymbol{W}_j \tag{7}$$

where $\boldsymbol{H}_i \in \{0,1\}^p$ is the binary encoding of the known perturbation design vector for cell i, $\boldsymbol{P}_i$ is a $p \times z$ perturbation loading matrix, and $\boldsymbol{W}_j \in \Delta^z$ (where Δ^z is the set of positive z-vectors that sum to 1) is the gene loading vector for gene j, and z is the latent dimension.

Since the $\boldsymbol{H}$ matrix is fixed, PertSpectra learns estimates of the $\boldsymbol{P}$ and $\boldsymbol{W}$ matrices. We can then treat $\boldsymbol{W}$ as a loading matrix (analogous to Principal Components Analysis), which provides the ability to study each factor based on the loadings of the genes in $\boldsymbol{W}$. The graph regularization biases these loadings towards capturing known gene-gene relationships, further increasing the ability to interpret the results. Since the $\boldsymbol{P}$ matrix has dimensions $p \times z$, or factors per perturbation, this provides a per-perturbation relation to each factor. Therefore, this factorization gives us (1) biologically interpretable gene loadings and (2) an association of the latent factors to perturbations, rather than individual cells.

To optimize this factorization, we consider a reconstruction loss term between the predicted and observed normalized expression and a graph regularization penalty on $\boldsymbol{W}$. Formally, the objective function for learning PertSpectra's parameters $\boldsymbol{\Theta}$ is

$$\mathcal{L}(\boldsymbol{\Theta}) = \lambda \mathcal{L}_{recon}(\boldsymbol{\Theta}) + \mathcal{L}_{graph}(\boldsymbol{\Theta}). \tag{8}$$

As in the original Spectra model, we use Poisson log likelihood for the reconstruction loss:

$$\mathcal{L}_{recon} = -\mathbf{X}\log(\hat{\mathbf{X}}) + \hat{\mathbf{X}}, \tag{9}$$

where $\hat{\mathbf{X}}$ is PertSpectra's estimated gene expression from its learned parameters. To account for imbalance in the number of cells receiving a certain perturbation in the training set, we weight the reconstruction loss in the following manner: For cell i receiving perturbation $\boldsymbol{h}_i$, we weight its reconstruction loss by the reciprocal of the number of cells that received perturbation $\boldsymbol{h}_i$:

$$\boldsymbol{\eta}_i = \frac{1}{|C_i|}, \tag{10}$$

where $C_i = \{k : \boldsymbol{h}_k = \boldsymbol{h}_i, 1 \le k \le n\}$. Thus, the reconstruction loss $\mathcal{L}_{recon}(\boldsymbol{\Theta})$ becomes

$$\mathcal{L}_{recon}(\boldsymbol{\Theta}) = \boldsymbol{\eta}\big[-\mathbf{X}\log(\hat{\mathbf{X}}(\boldsymbol{\Theta})) + \hat{\mathbf{X}}(\boldsymbol{\Theta})\big], \tag{11}$$

where $\boldsymbol{\eta} \in \mathbb{R}_+^n$ is a vector of the cell weights as described above.

For the graph penalty loss, we use the graph regularization term used by Spectra. Given an input prior graph $\mathbf{A}$, we generatively defined PertSpectra's adjacency matrix as

$$\mathbb{P}[\mathbf{A}_{ij} = 1] := (1-\kappa)(1-\rho)\langle \boldsymbol{W}_i, B\boldsymbol{W}_j\rangle + \kappa(1-\rho), \tag{12}$$

with κ and ρ representing the same learned edge creation/deletion parameters as described in Spectra. Then, we define the graph penalty function as

$$\mathcal{L}_{graph}(\boldsymbol{\Theta}) = -\mathbf{A}_{ij}\log(\mathbb{P}[\mathbf{A}_{ij} = 1]) - (1-\mathbf{A}_{ij})\log(1-\mathbb{P}[\mathbf{A}_{ij} = 1]), \tag{13}$$

We optimize PertSpectra's objective function using AdamW, with a learning rate schedule of [1.0, 0.5, 0.1, 0.01, 0.001, 0.0001] and maximum number of epochs set at 10,000.

3.2. *Benchmark Model Training Procedure*

We benchmarked PertSpectra against two models designed specifically for interpretability of gene expression data: scETM and GSFA. scETM[14] is a topic model designed for learning a triplet factorization of cell-by-topic, topic-by-embedding, and embedding-by-gene matrices. The learned topics should be biologically relevant, and the matrix factorization yields interpretability for analyzing the learned topic and gene embeddings. While designed for observational single cell RNA-seq datasets, scETM's topics should provide similar interpretability analysis and biologically-relevant latent embeddings.

GSFA[10] is a Bayesian factorization model that, similarly to PertSpectra, factorizes the gene count matrix into cell-by-perturbation, perturbation-by-embedding, and embedding-by-gene matrices, where the first matrix is given from a perturb-seq experiment and the latter two matrices are learned. Unlike PertSpectra, GSFA imposes mixture priors on the loading matrices rather than a graph regularization, and parameter optimization is achieved via Gibbs Sampling.

We chose these models as benchmarks as a form of ablation for different aspects of our proposed model. scETM does not leverage perturbation information in learning the loading matrices, so improvement over this model would demonstrate the benefits of explicitly incorporating perturbation information in learning interpretable latent factors. GSFA is a similar guided factorization model, but does not incorporate prior knowledge in regularizing the learned factors; thus, improvement over GSFA would demonstrate the importance of leveraging prior information to yield more interpretable factors.

To train scETM, we used the gene by sample count matrix as input, as scETM does not account for perturbation information. The expression matrix was filtered with the same steps as mentioned above, and the counts were normalized as described by the scETM paper (raw count of the gene divided by the total counts in each cell). The train-test splits as described above for PertSpectra were used to split the data for scETM. To train GSFA, the expression matrix was normalized as described in their methodology. Because of memory constraints of the Gibbs Sampling algorithm, GSFA was trained on subsets of the in-house and Norman datasets. We downsampled the train-test splits used for PertSpectra, proportionally to the perturbation labels. GSFA was not able to train on the Replogle dataset, and we encountered persistent out-of-memory issues when training on more than 20,000 cells on an EC2 instance with 128 Gb of RAM and 32 vCPUs.

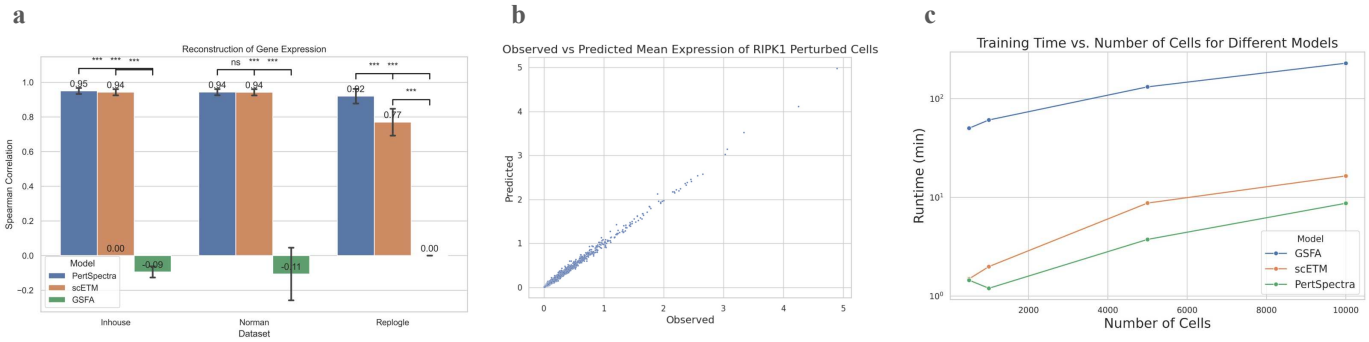

Fig. 2. a. Spearman correlation between predicted and observed mean gene expression by perturbation, b. Predicted vs observed mean expression for the perturbation RIPK1 (inhouse), c. Training runtime vs. number of cells across different models

4. Evaluation

4.1. *Predicting Unseen Combinations of Perturbations*

We first evaluated the models' ability to reconstruct gene expression levels for unseen cells or unseen combinations of perturbations. We computed Spearman correlation on the observed vs. predicted mean normalized gene expression for each perturbation or combination. This measures the ability of the model to correctly predict the gene expression profile of cells with unseen combinations of seen perturbations for the combinatorial datasets (in-house and Norman), and the ability of the model to correctly predict the gene expression profiles of unseen cells with seen perturbations for the single perturbation datasets (Replogle). We see that PertSpectra and scETM perform comparably across the in-house and Norman datasets (mean correlations of 0.95 and 0.94 for in-house, 0.94 for Norman for both methods), and PertSpectra achieves better performance than scETM on the Replogle dataset (0.92 and 0.77, respectively), with the error bars representing the standard deviation of the distribution of correlations and significance shown with ***: $p < 0.001$, **: $p < 0.01$, *: $p < 0.05$, and ns: no significance (Figure 2). GSFA's poor performance may be attributed either to the model's focus on interpretability rather than reconstruction, or due to the down-sampling procedure we used to avoid out-of-memory issues.

We also evaluated the training runtime of these models, as they varied drastically. We found that PertSpectra scaled best as experiment size (number of cells sequenced) increased, as it uses a gradient-based optimization with GPU capabilities. GSFA performed poorly in this metric, due to its use of Gibbs Sampling to optimize its parameters and lack of GPU integration.

4.2. *Biological Structure in the Perturbation Embedding*

Next, to evaluate how well the perturbation latent factors $\boldsymbol{P}$ capture the underlying biology in the data, we reasoned that perturbations that target functionally related genes would have similar latent factors. Importantly, the model does not receive information on which gene

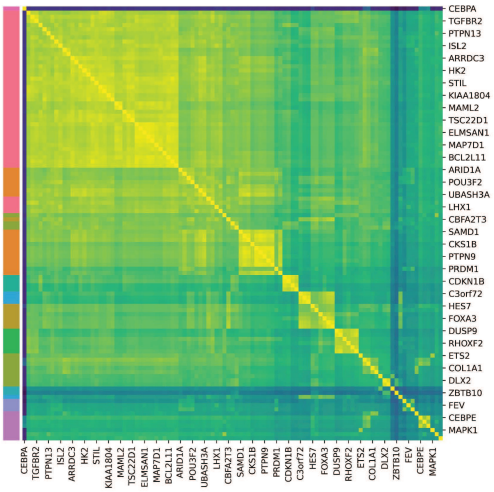

Cluster ID	Description
1	Developmental processes, kinase activity
2	Tyrosine phosphate activity
3	Transcription factor activity, DNA binding
4	Embryonic development
5	No significant gProfiler hits
6	Kinase inhibitor activity
7	No significant gProfiler hits
8	Embryonic morphogenesis
9	DNA-binding transcription activator
10	RNA polymerase II transcription regulation
11	C/EBP complex

Fig. 3. Hierarchical clustering on distance matrix computed on PertSpectra's perturbation loading matrix shows meaningful biological structure

is targeted by each perturbation, and therefore cannot leverage the graph prior provided to influence the embedding space, ensuring that distances in the perturbation embedding are reflecting signals gleaned from the data, and not from the prior graph. As an initial exploratory task, we first qualitatively analyzed the $\boldsymbol{P}$ matrix from the Norman dataset. To do so, computed the pairwise Euclidean distance matrix, performed hierarchical clustering, and tested the resulting clusters for enrichment of genes that share a biological pathway, using Gene Ontology (GO) annotations and a software package gprofiler.[15] We then filter significant GO terms (p-values ¡ 0.05) and picked out the top 1 or 2 most common GO terms that show up for each cluster to indicate the prevalent biological functions assigned to that cluster. We see that biological functions clustered together, indicating that information about the perturbations' biological impacts were captured in the perturbation loading matrix structure.

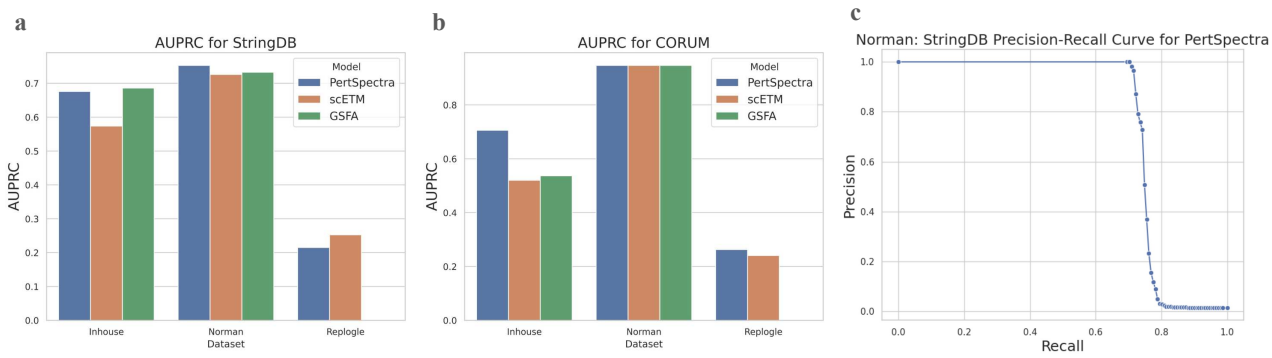

Fig. 4. a. Area under the Precision-recall curve (AUPRC) for StringDB known relationships, b. AUPRC for CORUM known relationships, c. Precision-recall curve for PertSpectra on the Norman dataset

Having established that our model is capturing biological information, we then conducted

a quantitative analysis comparing against scETM and GSFA. We used StringDB[11] and CORUM[16] as the true labels, where the pair of genes A and B have a label of 1 if that relationship exists in the database, and 0 otherwise. To generate pairwise similarity between perturbations from the models, we compute pairwise euclidean distance and normalize it to the range $[0, 1]$ using the learned perturbation loading matrices, either learned directly in the case of PertSpectra and GSFA ($\boldsymbol{P}$ and $\boldsymbol{\alpha}$, respectively), or for scETM the aggregated perturbation loading matrix. We take $(1 -$ distance matrix) to generate pairwise similarity. Finally, we computed the AUPRC between pairwise similarity of perturbations in the learned latent space and prior gene-gene relationship labels from knowledge bases. We find that PertSpectra performs competitively across the three datasets, suggesting that the learned factors across the three models capture similar levels of biological relationships between the perturbations (Figure 4).
One limitation of this analysis is that because of the use of a similarity metric, rather than a classifier, to identify gene-gene relationship labels, we found that the distribution of the labels may not be well calibrated. For example, as seen in Figure 4c., the precision-recall curve is not well calibrated, indicating that this recall metric may be flawed. Therefore, analyzing the interpretability of the learned latent substructure required the following more in-depth analysis.

4.3. *Interpretability of Loading Matrices*

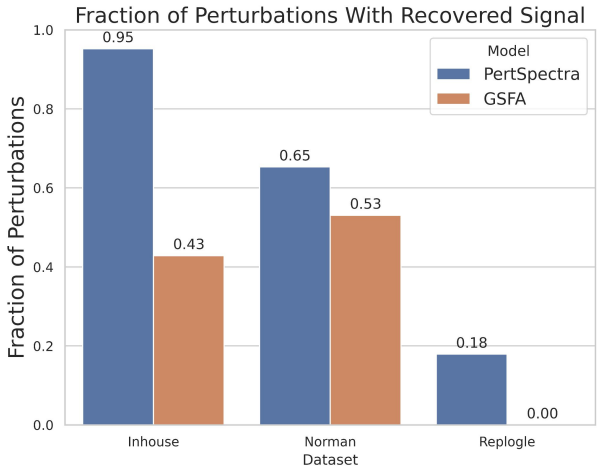

Fig. 5. Recovery of known biological functions from hypergeometric test interpretability analysis

We evaluated the interpretability of the loading matrices $\boldsymbol{P}$ and $\boldsymbol{W}$ with the following analysis. We reason that the matrix factorization learned "good" latent factors if 1) the gene loading weights indicate latent variables represent different biological functions and 2) the perturbation loadings associate perturbations to those biologically representative latent variables. From the $z \times g$ loading matrix $\boldsymbol{W}$, we can extract the biological functions represented by each latent factor by applying Gene Set Enrichment Analysis (GSEA)[17] on each loading vector $\boldsymbol{W}_i$ for $i \in 1, 2, ..., z$. GSEA is a statistical analysis that identifies over-represented sets

of genes that correspond to biological phenotypes. Thus, since the loading weights $\boldsymbol{W}$ indicate the contribution of each gene to each loading vector, GSEA performed on the $\boldsymbol{W}_i$ captures the biological functions represented by each latent factor. We can then observe the $\boldsymbol{P}$ matrix, and for each perturbation retrieve the top k factors associated with each perturbation. Thus, we can observe the biological functions assigned by the model to each perturbation. To quantify the quality of recall of these biological functions, we can observe the overlap with a known, annotated set of gene sets that contain the perturbed gene. We then perform a hypergeometric test on the overlap of the model's biological functions and the known biological functions, with significance (p-value < 0.001) indicating that the model can recall the correct biological functions non-randomly. The hypergeometric test accounts for the sizes of the model's GO term set and the known GO term set, which controls for a naive model assigning arbitrary number of GO terms to a perturbation to get a good recall. For each perturbation, we can perform this hypergeometric test and calculate the fraction of perturbations in which a model can confidently recall gene sets. Full details of the analysis available in Appendix C.

In the first step of this analysis, scETM did not yield statistically significant GO terms for its factors, suggesting that scETM's gene loading matrix did not sufficiently capture known biological patterns. Thus, scETM could not be included in this analysis. In comparing PertSpectra to GSFA, we find significant improvement in perturbation recovery via the learned loading matrices (Figure 5). The fraction of perturbations that have significant p-values from the hypergeometric test is much higher for PertSpectra in both the in-house (0.95 vs 0.43) and Norman (0.65 vs 0.53) datasets. This gives further confidence to PertSpectra's ability to capture biological function in its latent factors.

5. Discussion and Future Work

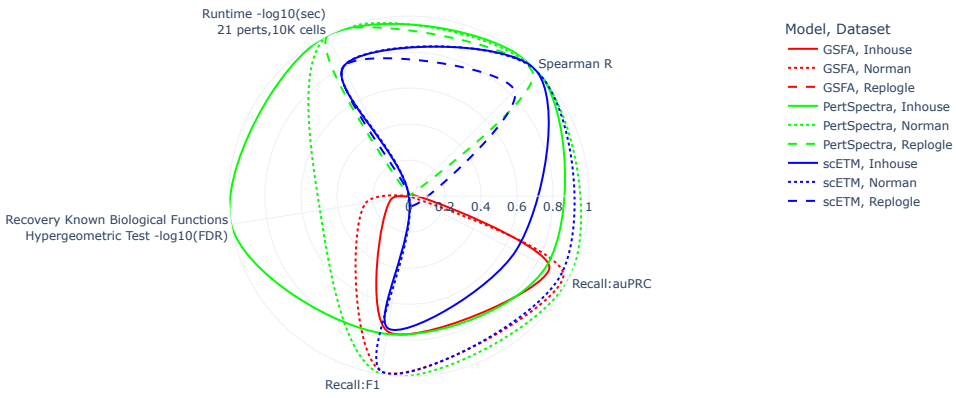

Fig. 6. Radar plot summarizing model performance across metrics/downstream analyses

In this paper, we introduce PertSpectra, a guided matrix factorization framework designed

for perturb-seq data that incorporates biological domain knowledge to learn interpretable, biologically coherent representations of cellular response to perturbations. PertSpectra regularizes the gene loading matrix with a known gene-gene interaction graph prior, introducing crucial inductive bias to guide the factorization towards biologically coherent latent factors, thereby increasing the interpretability of the measure responses. Furthermore, PertSpectra's factorization incorporates a binary design matrix to encode the perturbation labels, a construction which naturally extends beyond single perturbations to capture additive effects of seen or unseen combinatorial perturbations. Overall, PertSpectra generates highly interpretable latent factors, accurately predicts associations between perturbations and biological processes, and scales seamlessly into larger datasets. In addition to interpretability, we demonstrate that PertSpectra is competitive with or outperforms other methods across a variety of datasets and tasks, including on held-out cells and unseen combinations of perturbations (Figure 6). Genetic perturbation experiments hold the potential for discovering key biological mechanisms driving cellular phenotypes - we hope that PertSpectra will aid in the computational analysis of these experiments to gain deeper insights into novel biology.

We note that while PertSpectra can associate perturbations with biological functions in the form of gene-set signatures, this relationship does not indicate a causal relationship and should not be construed as such. There is extensive work in learning causal mechanisms from perturb-seq data,[18–20] which is a separate effort from interpretability frameworks for identifying associations from perturbations to functional processes. Furthermore, due to the linear nature of matrix factorization, PertSpectra is limited to interpreting effects of single perturbations or additive effects of combinatorial perturbations. Further research is required for interpretation of non-additive synergistic combinations of perturbations, and would be important in several applications, including target discovery of combinatorial therapeutics.

6. Code Availability

The code for implementations, analysis, and figures are available at https://github.com/insitro/PertSpectra.

7. Data Availability

The model weights, precomputed metrics, the inhouse dataset, and reference datasets used in downstream analyses are available at s3://pert-spectra/ and on zenodo https://zenodo.org/records/14740509.

Acknowledgements

We thank Angela Pisco for discussions throughout the duration of this project which greatly improved this work. We also thank members of the Data Science and Machine Learning department at Insitro for providing constructive feedback on the results presented in this work. Disclosures: This work was performed while Seowon Chang was an intern at Insitro. Anna Shcherbina, Tal Ashuach, Shahin Mohammadi, Stephanie See, Ninad Ranadive, Emily Fox, and Navpreet Ranu are employees of Insitro.

References

1. A. Dixit *et al.*, Perturb-seq: Dissecting molecular circuits with scalable single-cell rna profiling of pooled genetic screens, *Cell* **167**, 1853 (2016).
2. J. Replogle *et al.*, Mapping information-rich genotype-phenotype landscapes with genome-scale perturb-seq, *Cell* **85**, 2559 (2022).
3. T. Norman *et al.*, Exploring genetic interaction manifolds constructed from rich single-cell phenotypes, *Science* **365**, 786 (2019).
4. M. Lotfollahi, A. Klimovskaia Susmelj, C. De Donno, L. Hetzel, Y. Ji, I. L. Ibarra, S. R. Srivatsan, M. Naghipourfar, R. M. Daza, B. Martin *et al.*, Predicting cellular responses to complex perturbations in high-throughput screens, *Molecular Systems Biology* , p. e11517 (2023).
5. Y. Roohani, K. Huang and J. Leskovec, Predicting transcriptional outcomes of novel multigene perturbations with gears, *Nature Biotechnology* (2023).
6. R. Lopez, N. Tagasovska, S. Ra, K. Cho, J. K. Pritchard and A. Regev, Learning causal representations of single cells via sparse mechanism shift modeling, *Conference on Causal Learning and Reasoning* (2023).
7. M. Bereket and T. Karaletsos, Modelling cellular perturbations with the sparse additive mechanism shift variational autoencoder, in *Advances in Neural Information Processing Systems*, 2023.
8. H. M. Levitin, J. Yuan, Y. L. Cheng, F. J. Ruiz, E. C. Bush, J. N. Bruce, P. Canoll, A. Iavarone, A. Lasorella, D. M. Blei and P. A. Sims, De novo gene signature identification from single-cell rna-seq with hierarchical poisson factorization, *Molecular Systems Biology* **15**, p. e8557 (2019).
9. R. Kunes *et al.*, Supervised discovery of interpretable gene programs from single-cell data, *Nature Biotechnology* **42**, 1084– (2024).
10. Y. Zhao, K. Luo, L. Liang, M. Chen and X. He, A new bayesian factor analysis method improves detection of genes and biological processes affected by perturbations in single-cell crispr screening, *Nature Methods* **20**, 1693– (2023).
11. D. Szklarczyk, R. Kirsch, M. Koutrouli, K. Nastou, F. Mehryary, R. Hachilif, A. L. Gable, T. Fang, N. T. Doncheva, S. Pyysalo, P. Bork, L. J. Jensen and C. von Mering, The STRING database in 2023: protein-protein association networks and functional enrichment analyses for any sequenced genome of interest, *Nucleic Acids Res.* **51**, D638 (January 2023).
12. F. A. Wolf, P. Angerer and F. J. Theis, SCANPY: large-scale single-cell gene expression data analysis, *Genome Biol.* **19** (December 2018).
13. E. Dann, N. C. Henderson, S. A. Teichmann, M. D. Morgan and J. C. Marioni, Differential abundance testing on single-cell data using k-nearest neighbor graphs, *Nature Biotechnology* **40**, p. 245–253 (September 2021).
14. Y. Zhao, H. Cai, Z. Zhang and Y. Li, Learning interpretable cellular and gene signature embeddings from single-cell transcriptomic data, *Nature Communications* **12** (2021).
15. U. Raudvere, L. Kolberg, I. Kuzmin, T. Arak, P. Adler, H. Peterson and J. Vilo, g:profiler: a web server for functional enrichment analysis and conversions of gene lists, *Nucleic Acids Research* **47**, p. W191–W198 (2019).
16. A. Ruepp, B. Brauner, I. Dunger-Kaltenbach, G. Frishman, C. Montrone, M. Stransky, B. Waegele, T. Schmidt, O. N. Doudieu, V. Stumpflen and H. W. Mewes, Corum: the comprehensive resource of mammalian protein complexes, *Nucleic Acids Research* **36**, p. D646–D650 (December 2007).
17. A. Subramanian *et al.*, Gene set enrichment analysis: A knowledge-based approach for interpreting genome-wide expression profiles, *Proceedings of the National Academy of Sciences of the United States of America* **102**, 15545 (2005).
18. P. Brouillard, S. Lachapelle, A. Lacoste, S. Lacoste-Julien and A. Drouin, Differentiable causal

discovery from interventional data, in *Advances in Neural Information Processing Systems*, 2020.
19. R. Lopez, J.-C. Hütter, J. K. Pritchard and A. Regev, Large-scale differentiable causal discovery of factor graphs, in *Advances in Neural Information Processing Systems*, 2022.
20. A. Nazaret, J. Hong, E. Azizi and D. Blei, Stable differentiable causal discovery, *arXiv preprint arXiv:2311.10263* (2023).

Large language models identify causal genes in complex trait GWAS

Suyash S. Shringarpure[1], Wei Wang[1], Sotiris Karagounis[1], Xin Wang[1], Anna C. Reisetter[1], Adam Auton[1], and Aly A. Khan[1,2]

[1] *23andMe Inc., Palo Alto, CA, USA*
[2] *Departments of Family Medicine, and Pathology, and Institute for Population and Precision Health, University of Chicago, Chicago, IL, USA*
E-mail: suyashss@gmail.com; aakhan@uchicago.edu

Pinpointing causal genes at genome-wide association study (GWAS) loci remains a major bottleneck. Existing literature-mining approaches are often limited in accuracy and scalability. We show that large language models (LLMs) can accurately prioritize likely causal genes at GWAS loci. We systematically evaluated several widely available general-purpose LLMs against benchmark datasets of high-confidence causal genes, including a unique set from 23 unpublished GWAS. Our results demonstrate that LLMs outperform or match current state-of-the-art methods and, crucially, exhibit robust performance on novel loci not previously linked to traits, underscoring their generalizability. Moreover, when integrated with existing methods, LLMs substantially enhance overall performance. This work establishes LLMs as an accurate, scalable, and broadly generalizable approach to accelerate causal gene identification in complex traits.

Keywords: Large Language Models; GWAS; Causal Gene Identification; Gene Prioritization.

1. Introduction

Genome-wide association studies (GWAS) have identified numerous genomic regions associated with complex traits, enhancing our understanding of trait biology. However, pinpointing the exact causal genes within these regions remains a major hurdle. Approaches to causal gene identification from GWAS loci utilize a broad range of information including functional annotation, colocalization with quantitative trait loci (QTL) datasets, biological insights, and literature evidence. Literature mining for the co-occurrence of a (disease, gene) pair in a publication can provide evidence for the causal role of the gene, recapitulating knowledge an expert biologist might use. However, current literature mining approaches[1,2] have been evaluated in limited settings or through indirect tasks, and their generalizability to diverse phenotypes remains unclear.

Large language models (LLMs) are deep learning models trained on large text corpora for tasks including text generation, summarization, and question-answering. Recent studies have demonstrated their capability to perform biomedical tasks,[3] including summarizing gene function,[4] medical question answering,[5] cell-type annotation,[6] predicting CRISPR screening

© 2025 The Authors. Open Access chapter published by World Scientific Publishing Company and distributed under the terms of the Creative Commons Attribution Non-Commercial (CC BY-NC) 4.0 License.

results,[7] and identifying causal genetic factors from murine experimental data.[8] We hypothesize that LLMs like GPT-4[9] and Claude 3.5,[10] with extensive training on scientific publications, provide a systematic and scalable approach to identify likely causal genes at GWAS loci, potentially overcoming the limitations of manual expert annotation.

We systematically evaluated several general-purpose LLMs, comparing their performance to state-of-the-art methods (Supplementary Figure S1, available online). We assembled three distinct evaluation sets with different ground-truth criteria (Supplementary Table S1, available online). The first set comprises recently published GWAS loci (after April 2023) (the "GWAS Catalog"). The second set contains loci from a benchmark not publicly available online[11] ("Weeks et al."). Finally, we created a new dataset from 23 previously unpublished GWAS from a 23andMe cohort to test performance on novel loci. Our results demonstrate that LLM-based predictions surpass existing methods, including the polygenic priority score (PoPS)[11] and the 'nearest gene' method,[12] in precision, recall, and F-score (Supplementary Figure S2 and Supplementary Table S2, available online). Furthermore, we show that integrating LLM predictions with existing methods can lead to substantial performance improvements.

2. Methods

2.1. *Evaluation Datasets*

We assembled three datasets to benchmark LLMs for causal gene prioritization. A key challenge in evaluating performance is potential data contamination, where evaluation data may have been part of the LLM training corpora. To mitigate this, our datasets were chosen for their varying levels of public availability and recency. Additionally, we tested for direct inclusion of these datasets in the LLMs via prompting and found no evidence of contamination (Supplementary Table S20, available online). For all datasets, we defined a standard locus window of 500 kbp on either side of the lead variant to generate candidate gene lists, a common distance used in causal gene prioritization methods.[11,12,21] We restricted our gene lists to only include protein-coding genes. Our evaluation framework assumes a single causal gene per locus for each prediction.

2.1.1. *Weeks et al. Dataset*

The Weeks et al. benchmark dataset[11] contains 1,348 causal gene-phenotype pairs, with ground truth established through genetic interpretation. The authors identified non-coding credible sets from UK Biobank GWAS that were located within 500 kbp of a high-confidence (Posterior Inclusion Probability > 0.5) fine-mapped coding variant from the same GWAS. The gene containing the coding variant was designated the causal gene. As this dataset is not publicly available online and was obtained directly from the authors via email, it serves as a strong control against LLM training data contamination.

2.1.2. *GWAS Catalog Dataset*

To evaluate performance on recent discoveries, we created a dataset from the GWAS Catalog (v1.0.2, associations_e111_r2024-03-11, downloaded March 19, 2024). To minimize the

possibility of these loci being included in the benchmark LLMs trainings, we selected only associations from manuscripts published after April 30, 2023. A causal gene was assigned using a methodology similar to the Weeks et al. dataset: if a non-coding lead variant was within 500 kbp of a coding lead variant in the same study, the gene corresponding to the coding variant was considered causal. This process resulted in a dataset of 641 loci. Candidate genes for each locus were identified using GENCODE release 43.

2.1.3. *Unpublished 23andMe Novel Loci Dataset*

To test the generalizability of LLMs to novel unseen data, we utilized unpublished GWAS data from 23andMe for 23 phenotypes (Supplementary Table S13, available online). We first performed fine-mapping using SuSiE to identify credible sets containing a protein-coding variant (PIP > 0.5). We then identified independent non-coding credible sets within 500 kbp of these. A locus was defined as "novel" if its lead variant had a linkage disequilibrium (LD) $r^2 < 0.5$ with any variant in the entire GWAS catalog. This process resulted in a test set of 403 loci to assess performance on genetic associations not previously documented in the GWAS catalog.

2.2. *LLM Execution and Prompting Strategy*

2.2.1. *Models and Prompting*

We evaluated version-controlled models from major developers: OpenAI (gpt-3.5-turbo-0125, gpt-4-0613, gpt-4o-2024-08-06), Anthropic (Claude 3.5 Sonnet), Google (Gemini 1.5 Pro), and Meta (Llama 3.1-405b). To ensure more consistent behavior, all models were queried with temperature set to 0. OpenAI and Google models were queried via their native APIs, while Anthropic and Meta models were accessed via AWS Bedrock using the LangChain[23] framework. To prevent any potential for positional bias, all gene lists provided to the models were lexicographically sorted.

We used a two-part prompt structure: a general system prompt outlining the task, and a locus-specific user prompt providing the data. As a sanity check, we confirmed that model performance degraded considerably when provided with randomly shuffled phenotypes instead of the correct ones, validating that the models were using the phenotype information for their predictions (Supplementary Table S21, available online).

System Prompt: LLM Instructions

```
You are an expert in biology and genetics.
Your task is to identify likely causal genes within a locus for a
given GWAS phenotype based on literature evidence.
From the list, provide the likely causal gene (matching one of the
given genes), confidence (0: very unsure to 1: very confident),
and a brief reason (50 words or less) for your choice.
Return your response in JSON format, excluding the GWAS phenotype
name and gene list in the locus. JSON keys should be
'causal_gene','confidence','reason'.
```

```
Your response must start with '{' and end with '}'.
```

User Prompt: Locus-Specific Data

```
Identify the causal gene.
GWAS phenotype: {Morning person}
Genes in locus: {A},{B},{C},{D}
```

2.3. *Benchmark Methods for Comparison*

2.3.1. *Nearest Gene Method*

This baseline method assigns causality to the gene whose body (defined by GENCODE release 43 on the hg38 reference genome) has the smallest physical distance to the lead GWAS variant. For the Weeks et al. dataset, we used the nearest gene predictions provided directly by the authors. In the approximately 4% of cases where a lead variant was located within the bodies of multiple genes, one gene was chosen at random to simplify the evaluation.

2.3.2. *Polygenic Priority Score (PoPS)*

PoPS is a state-of-the-art gene prioritization method that integrates gene-level features with polygenic enrichments to generate a prioritization score for a given phenotype.[11] We obtained pre-computed PoPS scores for the 1,348 loci in the Weeks et al. dataset directly from the original authors. For each locus, the gene with the highest PoPS score was selected as the predicted causal gene.

We did not include other methods, such as ones that leverage expression quantitative trait loci (eQTLs) in our comparison, since previous work has shown that they are outperformed by the nearest gene and PoPS approaches.[11]

2.4. *Performance Evaluation and Statistical Analysis*

Model performance was quantified using standard metrics: Precision (the proportion of correct predictions among all predictions made), Recall (the proportion of true causal genes correctly identified), and the F-score (the harmonic mean of precision and recall). We computed 95% confidence intervals for all metrics using bootstrapping with 1,000 samples. Statistical significance for performance differences between methods was assessed using a Wilcoxon signed-rank test.

To understand factors influencing performance, we analyzed the impact of locus complexity (measured as the number of genes in the locus) and publication bias (measured by the publication count per gene from NCBI's gene2pubmed database) using Spearman correlation. To assess the impact of multiple independent signals at the same locus, which can complicate evaluation, we also analyzed performance on deduplicated datasets where only one signal per unique gene window was retained for each phenotype (Supplementary Figure S4 and Supplementary Table S5, available online).

2.5. *Analysis of Model Behavior and Robustness*

We conducted several analyses to probe the behavior of the LLMs. A prediction was classified as a "hallucination" if the predicted gene was not present in the input list provided to the model; these were penalized as incorrect predictions in our evaluation. We assessed the calibration of the LLM-provided confidence scores by comparing them to the empirical precision at different score levels.

Robustness was tested through multiple experiments. We tested sensitivity to the input gene list by removing the true causal gene and observing the change in prediction confidence. We also randomly shuffled the gene order to check for sensitivity to input structure. To understand if a more complex prompting strategy would improve results, we tested minimal "ablation" prompts and "chain-of-thought" prompting, neither of which improved performance (Supplementary Figure S6, S10 and Supplementary Table S9, available online). Finally, to probe the models' internal representations of biological concepts, we generated gene and phenotype descriptions with GPT-3.5, embedded these descriptions into a high-dimensional space using OpenAI's text-embedding-3-large model,[19] and calculated their cosine similarity.

2.6. *Ensemble Modeling Framework*

To explore whether combining the distinct information captured by LLMs and traditional methods could yield superior performance, we developed an ensemble learning framework. The problem was framed as a classification task to predict which method (e.g., LLM or nearest gene) would be correct for a given locus. We trained a decision tree classifier using the scikit-learn[25] library with two primary features: (1) a binary indicator of whether the LLM and a non-LLM method agreed on the prediction, and (2) the confidence score provided by the LLM. To prevent data leakage during training, we employed a nested, chromosome-based cross-validation scheme, where all loci from a given chromosome were held out for the test set while the model was trained on the remaining chromosomes. Model features are listed in Supplementary Table S19 (available online).

3. Results

Our study systematically evaluated the ability of LLMs to identify causal genes at GWAS loci. We compared their performance against established methods, analyzed their robustness and reasoning, and developed an ensemble framework to enhance prediction accuracy. The overall methodology is depicted in Figure 1.

3.1. *LLMs Significantly Outperform Existing Methods on Public Benchmarks*

To establish a performance baseline, we first compared a suite of LLMs against established methods on two public benchmark datasets. Our evaluation revealed that recent LLMs, particularly Claude 3.5 Sonnet[10] and OpenAI's GPT-4o,[14] deliver a substantial performance improvement. On the GWAS Catalog dataset, Claude 3.5 Sonnet achieved an F-score of 0.66, representing a 49% improvement over the "nearest gene" method (F-score = 0.44).[12] Similarly, on the Weeks et al. dataset, Claude 3.5 Sonnet (F-score = 0.60) and GPT-4o (F-score

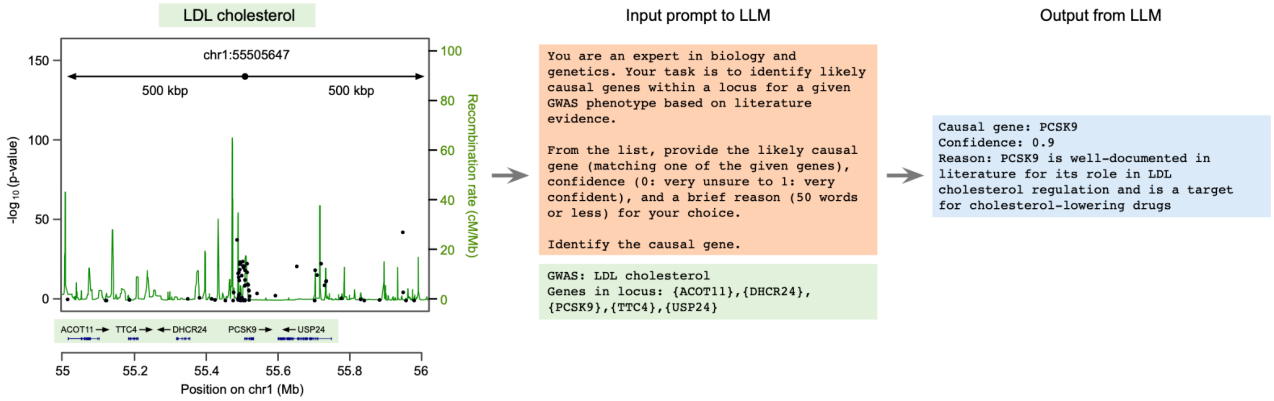

Fig. 1. Schematic of the LLM-based approach for identifying causal genes at GWAS loci. For a given locus, a 500 kbp window around the lead variant defines the candidate gene set. The LLM receives the phenotype name and an alphabetical list of candidate genes. The model is instructed to return the most likely causal gene, a confidence score, and a brief justification. The orange-colored text in the prompt is fixed, while the green-colored text is locus-specific. The example shows a locus for LDL cholesterol containing the well-established causal gene PCSK9.

= 0.58) showed a marked improvement over PoPS, the best non-LLM method (F-score = 0.50)[11] (Figure 2a-b). The performance difference between Claude 3.5 Sonnet and GPT-4o was not statistically significant, establishing these two models as a clear top tier for this task (Supplementary Table S3, available online).

To understand the drivers of this performance advantage, we examined how performance varied with locus complexity and the extent of existing literature. While all methods performed worse in loci with a higher number of candidate genes, this performance drop was less pronounced for LLMs. This amplified their advantage in gene-dense regions, where LLMs achieved up to a 67% improvement on the GWAS catalog dataset and a 38% improvement on the Weeks et al. dataset relative to the next-best method (Figure 2c; Supplementary Figure S3 and Supplementary Table S4, available online). Furthermore, LLM accuracy positively correlated with the number of publications for the causal gene, indicating these models effectively leverage the scientific literature to inform their predictions (Figure 2d; Supplementary Table S2, available online).

3.2. *LLM Predictions are Robust, Calibrated, and Reasoned*

Beyond raw accuracy, a critical aspect of any predictive model is reliability. We therefore conducted a series of experiments to assess the robustness, calibration, and reasoning capabilities of the top-performing LLMs. We found that LLM-generated confidence scores were well-calibrated at high levels (≥ 0.9) but tended toward overconfidence at lower scores (0.6 to 0.8) (Supplementary Figure S5 and Supplementary Table S6, available online). Importantly, these confidence scores were highly reproducible, with identical inputs yielding identical scores in 96% of test cases (Supplementary Table S7, available online). An examination of the justifications for correct predictions revealed that the models frequently provided valid rationales based on gene function (e.g., "is involved in," "key regulator of") or established phenotype

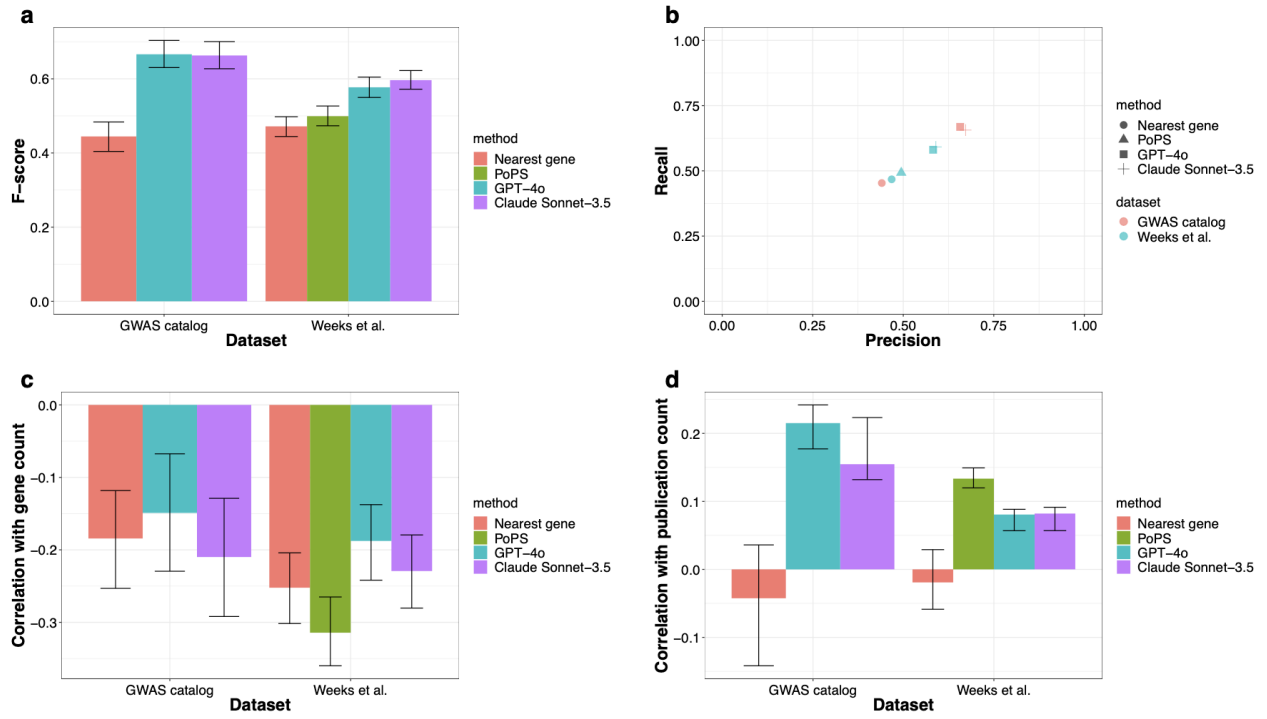

Fig. 2. Performance comparison of leading LLMs and benchmark methods. (a) F-scores show that Claude 3.5 Sonnet and GPT-4o outperform Nearest Gene and PoPS on both evaluation datasets. (b) The precision-recall plot highlights the superior balance of LLM performance. (c) Prediction accuracy for all methods negatively correlates with the number of genes at a locus. (d) LLM and PoPS accuracy positively correlates with the number of publications for the causal gene, unlike the nearest gene method.

associations (Supplementary Table S8, available online).

Robustness of the model was further confirmed through perturbation experiments.[18] Removing the true causal gene from the input list not only caused a significant drop in confidence but also led to a 77% reduction in high-confidence predictions, demonstrating that the model relies on the correct gene's presence (Supplementary Table S11, available online). Conversely, shuffling the input gene order had a minimal impact, resulting in a prediction match 87% of the time, with mismatches concentrated in lower-confidence predictions (Supplementary Table S12, available online). Finally, obvious hallucinations (predicting a gene not provided in the input) were rare, occurring in fewer than 4% of loci for Claude 3.5 Sonnet (Supplementary Table S15, available online).

3.3. *Impact of deduplication on performance*

To assess potential performance inflation due to multiple signals within the same locus, we deduplicated loci with overlapping gene windows. Dataset sizes were reduced (Weeks: 1,348 to 965 loci; GWAS Catalog: 641 to 336 loci), and performance dropped by 10–20% across all methods. However, Claude 3.5 Sonnet and GPT-4o continued to outperform non-LLM methods (Supplementary Figure S4 and Table S5). We therefore retained the original datasets

for subsequent analyses to mirror typical GWAS post-processing pipelines.

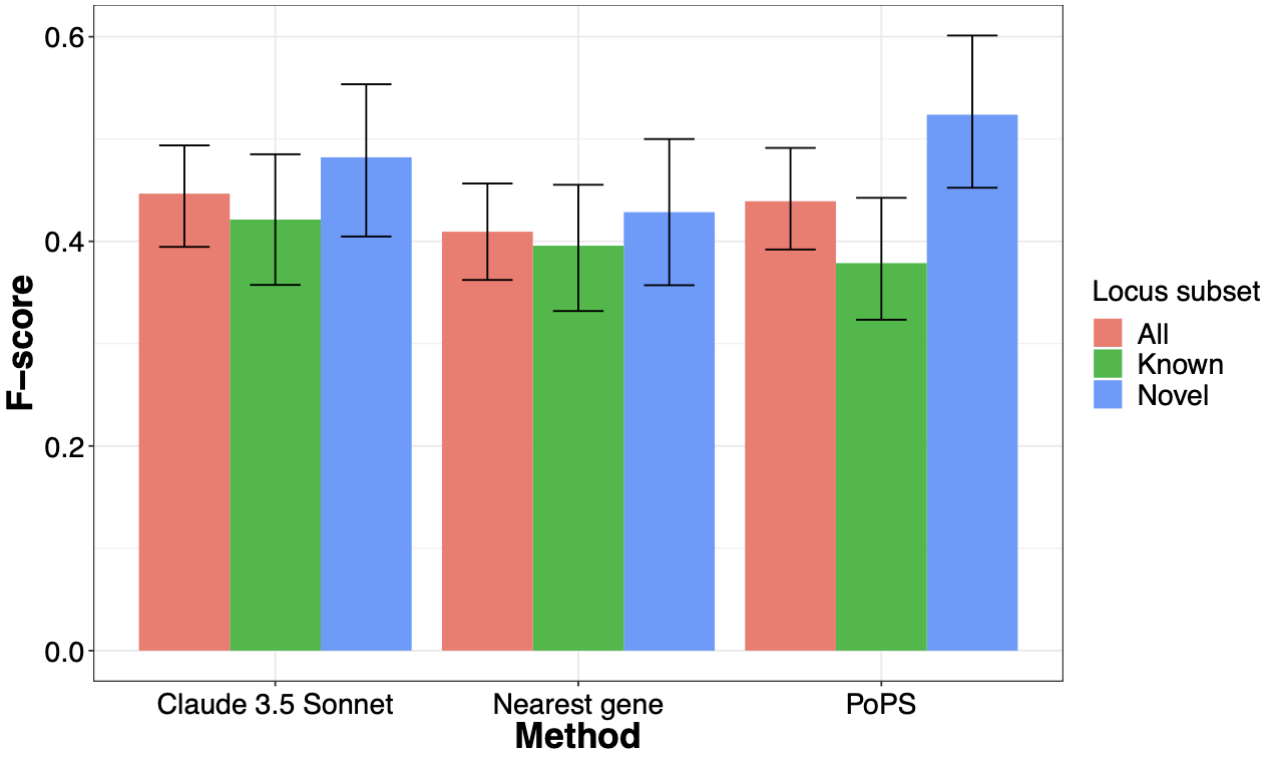

Fig. 3. Performance on the unpublished 23andMe dataset containing novel loci. F-scores are shown for the full dataset (All), the subset of known loci, and the subset of novel loci. Novel loci are defined as having an index variant with LD r-squared < 0.5 with any variant in the GWAS catalog. LLM performance remains stable on novel loci.

3.4. *LLMs Generalize to Novel Loci and Leverage Semantic Similarity*

A key question is whether LLMs simply retrieve known associations or can generalize to novel biological inferences. To test this, we evaluated their performance on an unpublished 23andMe dataset containing loci absent from the GWAS catalog. On this dataset, Claude 3.5 Sonnet again performed best (F-score = 0.45), slightly ahead of PoPS (0.44) and 'nearest gene' (0.41). Crucially, LLM performance did not degrade on these novel loci compared to known loci (F-score 0.48 on novel vs. 0.42 on known). In contrast, the performance of PoPS was significantly better on novel loci (F-score 0.52 vs. 0.38), suggesting LLMs may generalize more consistently across varying levels of prior evidence (Figure 4; Supplementary Table S14, available online). A logistic regression model confirmed that locus complexity (number of genes) was a much stronger predictor of LLM accuracy (McFadden's pseudo-R-squared = 3.6%) than novelty status (pseudo-R-squared = 0.26%).

This generalization capability appears to be driven by a semantic understanding of biology, a concept foundational to modern language models.[20] An approach based solely on the cosine similarity of gene and phenotype text embeddings (generated using the 'text-embedding-3-

large‘ model[19]) achieved 58-68% of the performance of Claude 3.5 Sonnet (Supplementary Figure S7, available online). For a locus associated with LDL cholesterol, the causal gene PCSK9 is closest to the phenotype in the embedding space (Figure 4a; Supplementary Figure S8, available online). Across our datasets, the true causal gene was among the top 5 most semantically similar genes to the corresponding phenotype for 75-93% of loci. This observation indicates that while semantic similarity is a key driver, LLMs utilize additional context from the prompt to refine predictions (Figure 4b; Supplementary Figure S9, available online).

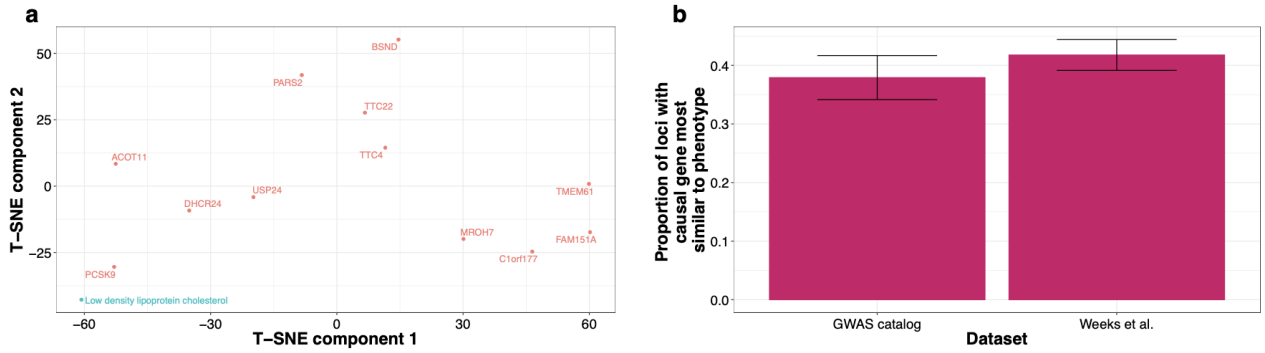

Fig. 4. Text embeddings of genes and phenotypes partially explain LLM performance. (a) A t-SNE plot visualizing text embeddings for a locus associated with LDL cholesterol shows the causal gene PCSK9 is closest to the phenotype in the embedding space. (b) Across both datasets, the causal gene is the most semantically similar to the phenotype in over 35% of cases.

3.5. *Failure Modes of LLMs*

LLMs occasionally struggled with ambiguous phenotype descriptions or overly broad trait interpretation. For example, gpt-4-0613 achieved only 0.08 precision on the “Total protein” phenotype, likely due to misinterpreting the term as general protein synthesis rather than serum protein levels. Providing more specific phenotype descriptions improved performance, and newer models such as Claude 3.5 Sonnet and GPT-4o did not show this issue (precision = 0.52). Another failure mode occurred when highly studied genes dominated predictions. For “Neonatal circulating Complement Component 4 (C4) protein concentration,” Claude 3.5 Sonnet always predicted C4A as causal (precision = 0.0), despite coding variant evidence pointing to other genes. This suggests that LLMs over-rely on well-known gene–phenotype associations, underscoring the need to combine LLMs with functional annotations for improved causal gene prioritization. Precision and recall values for all phenotypes are provided in Supplementary Table S10 (available online).

3.6. *Ensemble Framework Boosts Performance by Integrating Methods*

We sought to investigate whether LLMs provide orthogonal information to existing gene prioritization methods and whether combining them would enhance causal gene prediction. Previous work has shown that combining multiple gene prioritization methods improves performance.[11,12,21] We hypothesized this would also apply to LLM-based approaches. We began by

examining the concordance of predictions across different methods. We found that LLM-based methods showed the highest agreement with other LLM-based methods, but only moderate agreement with the polygenic priority score (PoPS) and the 'nearest gene' methods (Supplementary Figure S12 and Supplementary Table S16, available online). These findings suggest that LLMs and existing methods capture distinct aspects of the data, implying a potential for improved performance through combined approaches.

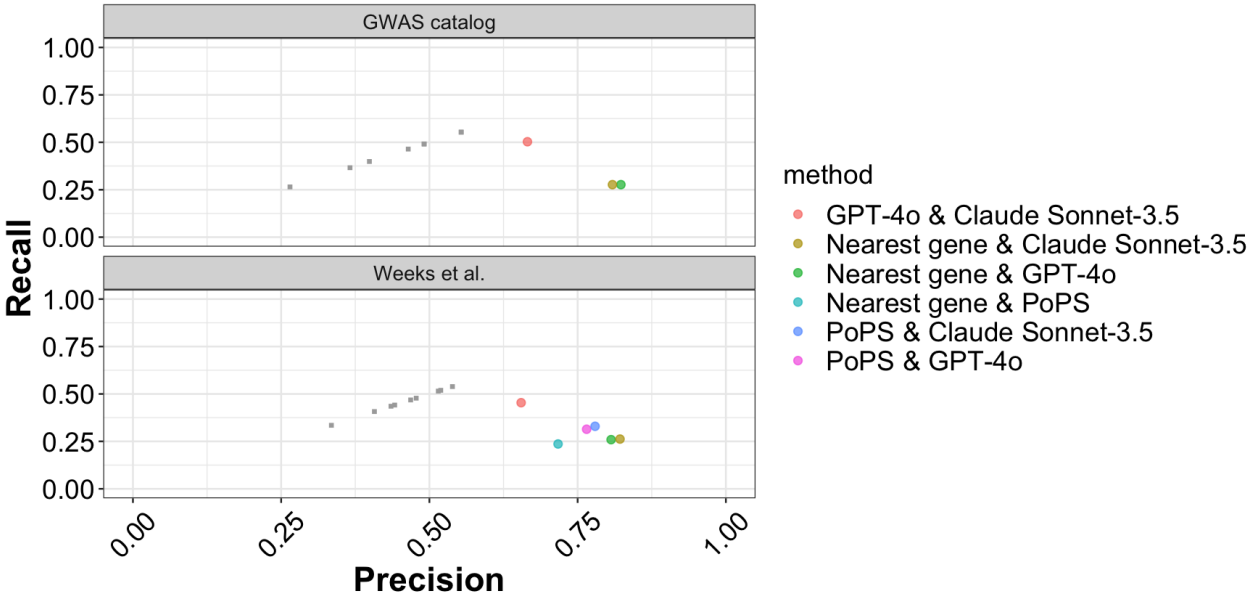

Fig. 5. Performance of consensus prediction methods. Gray squares represent the performance of individual methods. Consensus methods, which only make a prediction when two methods agree, consistently achieve higher precision but lower recall.

To leverage this, we first tested a simple consensus approach, which improved precision to 0.86-0.89 but did so at a significant cost to recall (0.33-0.36), as this approach discards all discordant predictions (Figure 5). To overcome this trade-off, we developed a trained ensemble decision tree framework to intelligently arbitrate between methods. This ensemble approach significantly enhanced overall performance. By combining Claude 3.5 Sonnet with the 'nearest gene' method, the F-score on the GWAS catalog dataset improved by 48% (from 0.45 to 0.67) (Supplementary Table S17, available online). A similar integration with PoPS on the Weeks et al. dataset increased the F-score by 17% (from 0.50 to 0.59) (Supplementary Table S18, available online). These results demonstrate that integrating the unique, literature-based intelligence of LLMs with traditional methods offers a powerful and robust strategy to advance causal gene prediction (Figure 6).

4. Discussion

This work establishes that LLMs are a powerful, scalable, and cost-effective new tool for causal gene prioritization. We show that LLMs can accurately synthesize vast scientific literature to

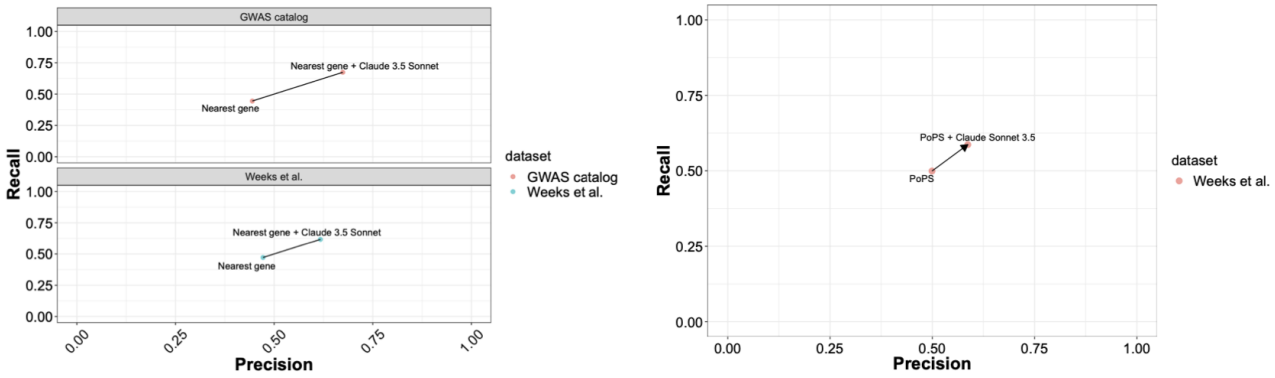

Fig. 6. Performance of the ensemble framework compared to individual methods. The ensemble classifier (red points), which combines predictions from Claude Sonnet-3.5 and the Nearest Gene method, significantly outperforms the individual methods on both datasets.

identify high-probability candidate genes. To address the critical issue of data circularity in AI benchmarking, we introduce a rigorous evaluation framework that includes a novel benchmark built from 23 unpublished GWAS and systematic comparisons with state-of-the-art methods. This framework provides a transparent and unbiased assessment of LLM performance, setting a foundation for best practices in the field.

Our results reveal two key insights. First, on public datasets, advanced LLMs such as Claude 3.5 Sonnet and GPT-4o substantially outperform established methods, with the largest gains observed in gene-dense regions, underscoring their ability to exploit the existing knowledge base. Second, on truly novel loci, including the unpublished 23andMe GWAS dataset, LLMs perform comparably to state-of-the-art tools, confirming their capacity for generalization rather than memorization. Finally, our ensemble approach, which integrates LLM predictions with established methods, significantly improves causal gene identification, positioning LLMs as a complementary and transformative component of next-generation gene prioritization pipelines.

Broader Implications and Potential Applications

The LLM-based framework has broad implications for genomics research. It enables rapid annotation and prioritization of genes from any GWAS, even when full summary statistics are unavailable, a common limitation of approaches like PoPS. This capability can accelerate hypothesis generation by highlighting likely causal genes for functional follow-up. In drug discovery, it could help identify new therapeutic targets by linking disease-associated loci to druggable genes. Overall, this work provides a blueprint for leveraging the exponential growth of scientific literature, transforming unstructured text into structured, actionable biological insights.

A practical advantage of our approach is its scalability and cost-effectiveness. The LLMs used are accessible via paid APIs with costs determined by the number of processed tokens. For example, the average per-locus cost for Claude 3.5 Sonnet was approximately $0.0022 USD, meaning that annotating a GWAS with 300 significant loci can be completed for less than $1 USD. This cost profile makes LLM-based prioritization feasible for routine, large-scale

analyses.

Limitations and Future Directions

This study provides a foundational baseline for applying LLMs to causal gene prioritization. Recognizing the risk of data contamination from public training corpora, we employed a robust evaluation design, testing across multiple datasets, including recent publications and unpublished GWAS, to provide a reliable assessment of model generalization.

Several challenges remain before LLMs can be fully integrated into scientific workflows. The "black box" nature of current LLMs limits the ability to trace predictions to specific sources. A clear next step is the development of Retrieval-Augmented Generation (RAG) frameworks that cite verifiable references from curated corpora like PubMed, improving both trust and interpretability.

It is also important to note that LLMs learn statistical associations from text rather than performing formal causal inference. The "causal" labels in our benchmarks are proxies derived from genetic evidence rather than functional validation. Future work should incorporate experimentally validated datasets to further refine these models. Moreover, our evaluation primarily focused on data from individuals of European ancestry. Expanding benchmarks to include diverse populations is essential to ensure equitable and generalizable applications. In the benchmark creation, we focused only on examples where the causal gene is a protein-coding gene. For some published loci, noncoding RNAs have been implicated as causal. The performance of our approach at such loci remains to be explored.

In conclusion, this work demonstrates that LLMs are powerful and scalable tools for causal gene prioritization. By synthesizing the scientific literature, they dramatically improve candidate gene identification for well-documented associations and perform comparably to state-of-the-art methods on truly novel loci. The future of this field lies in improving transparency and mitigating data circularity, likely through RAG-based systems and more robust, prospective benchmarks. By integrating the reasoning capabilities of LLMs with other data modalities, we can accelerate the translation of GWAS discoveries into deeper biological understanding.

Acknowledgments

The authors thank the employees and research participants of 23andMe for making this work possible. We acknowledge Elle Weeks, Hilary Finucane, and Jacob Ulirsch for sharing the evaluation dataset from their publication. We also thank our colleagues at 23andMe for their helpful comments on the manuscript. The authors gratefully acknowledge support from AWS for GPU computing and credits.

Data and Supplementary Materials Availability

Processed datasets, prediction results, and intermediate outputs are available via Zenodo (doi: 10.5281/zenodo.15594712). All supplementary materials, figures, and tables are publicly available online: `https://github.com/akds/llm-gwas-causal-genes`.

References

1. Kafkas, S., Dunham, I. & McEntyre, J. Literature evidence in open targets - a target validation platform. *J. Biomed. Semant.* **8**, 20 (2017).
2. Tirunagari, S. et al. Lit-OTAR Framework for Extracting Biological Evidences from Literature. Preprint at https://doi.org/10.1101/2024.03.06.583722 (2024).
3. Sarwal, V. et al. BioLLMBench: A Comprehensive Benchmarking of Large Language Models in Bioinformatics. Preprint at https://doi.org/10.1101/2023.12.19.572483 (2023).
4. Chen, Y. & Zou, J. GenePT: A Simple But Effective Foundation Model for Genes and Cells Built From ChatGPT. Preprint at https://doi.org/10.1101/2023.10.16.562533 (2024).
5. Singhal, K. et al. Large language models encode clinical knowledge. *Nature* **620**, 172–180 (2023).
6. Hou, W. & Ji, Z. Assessing GPT-4 for cell type annotation in single-cell RNA-seq analysis. *Nat. Methods* 1–4 (2024) doi:10.1038/s41592-024-02235-4.
7. Song, S. et al. Virtual CRISPR: Can LLMs Predict CRISPR Screen Results? *Proc. 24th Workshop on Biomedical Language Processing*, 354–364 (Association for Computational Linguistics, 2025). https://aclanthology.org/2025.bionlp-1.30/
8. Tu, T. et al. Genetic Discovery Enabled by A Large Language Model. Preprint at https://doi.org/10.1101/2023.11.09.566468 (2023).
9. OpenAI et al. GPT-4 Technical Report. Preprint at https://doi.org/10.48550/arXiv.2303.08774 (2024).
10. Anthropic. The Claude 3 Model Family: Opus, Sonnet, Haiku. Preprint at https://www-cdn.anthropic.com/de8ba9b01c9ab7cbabf5c33b80b7bbc618857627/Model_Card_Claude_3.pdf (2024).
11. Weeks, E. M. et al. Leveraging polygenic enrichments of gene features to predict genes underlying complex traits and diseases. *Nat. Genet.* **55**, 1267–1276 (2023).
12. Stacey, D. et al. ProGeM: a framework for the prioritization of candidate causal genes at molecular quantitative trait loci. *Nucleic Acids Res.* **47**, e3–e3 (2019).
13. Brown, T. B. et al. Language Models are Few-Shot Learners. Preprint at https://doi.org/10.48550/arXiv.2005.14165 (2020).
14. OpenAI et al. GPT-4o System Card. Preprint at https://doi.org/10.48550/arXiv.2410.21276 (2024).
15. OpenAI et al. OpenAI o1 System Card. Preprint at https://doi.org/10.48550/arXiv.2412.16720 (2024).
16. Team, G. et al. Gemini 1.5: Unlocking multimodal understanding across millions of tokens of context. Preprint at https://doi.org/10.48550/arXiv.2403.05530 (2024).
17. Grattafiori, A. et al. The Llama 3 Herd of Models. Preprint at https://doi.org/10.48550/arXiv.2407.21783 (2024).
18. Sclar, M., Choi, Y., Tsvetkov, Y. & Suhr, A. Quantifying Language Models' Sensitivity to Spurious Features in Prompt Design or: How I learned to start worrying about prompt formatting. Preprint at https://doi.org/10.48550/arXiv.2310.11324 (2024).
19. OpenAI. New embedding models and API updates. New embedding models and API updates https://openai.com/index/new-embedding-models-and-api-updates/ (2024).
20. Mikolov, T., Chen, K., Corrado, G. & Dean, J. Efficient Estimation of Word Representations in Vector Space. Preprint at http://arxiv.org/abs/1301.3781 (2013).
21. Mountjoy, E. et al. An open approach to systematically prioritize causal variants and genes at all published human GWAS trait-associated loci. *Nat. Genet.* **53**, 1527–1533 (2021).
22. Bordt, S., Nori, H., Rodrigues, V., Nushi, B. & Caruana, R. Elephants Never Forget: Memorization and Learning of Tabular Data in Large Language Models. Preprint at

https://doi.org/10.48550/arXiv.2404.06209 (2024).
23. Chase, H. LangChain. (2022).
24. Khattab, O. et al. DSPy: Compiling Declarative Language Model Calls into Self-Improving Pipelines. Preprint at https://doi.org/10.48550/arXiv.2310.03714 (2023).
25. Pedregosa, F. et al. Scikit-learn: Machine Learning in Python. *J. Mach. Learn. Res.* **12**, 2825-2830 (2011).

Gene-R1: Reasoning with Data-Augmented Lightweight LLMs for Gene Set Analysis*

Zhizheng Wang†, Yifan Yang†, Qiao Jin, Zhiyong Lu‡
Division of Intramural Research (DIR), National Library of Medicine (NLM),
National Institutes of Health (NIH), Bethesda, MD 20894, USA
Email: {zhizheng.wang; yifan.yang3; qiao.jin; zhiyong.lu}@nih.gov

The gene set analysis (GSA) is a foundational approach for uncovering the molecular functions associated with a group of genes. Recently, LLM-powered methods have emerged to annotate gene sets with biological functions together with coherent explanatory insights. However, existing studies primarily focus on proprietary models, which have been shown to outperform their open-source counterparts despite concerns over cost and data privacy. Furthermore, no research has investigated the application of advanced reasoning strategies to the GSA task. To address this gap, we introduce **Gene-R1**, a data-augmented learning framework that equips lightweight and open-source LLMs with step-by-step reasoning capabilities tailored to GSA. Experiments on 1,508 in-distribution gene sets demonstrate that Gene-R1 achieves substantial performance gains, matching commercial LLMs. On 106 out-of-distribution gene sets, Gene-R1 performs comparably to both commercial and large-scale LLMs, exhibiting robust generalizability across diverse gene sources.

Keywords: Gene Set Analysis; Data Augmentation; Fine-tuning; Reasoning; LLM

1. Introduction

Gene set analysis (GSA) is a foundational approach for revealing the molecular functions associated with groups of genes involved in physiological processes, healthcare, and disease[1,2]. By identifying the biological functions enriched in gene sets, GSA provides critical insights for elucidating disease mechanisms and discovering therapeutic targets[3,4]. Such mechanistic insights would greatly advance our understanding of functional genomics.

Over its development, GSA has progressed through two notable methodological paradigms: classical functional enrichment analysis and emerging solutions based on large language models (LLMs). The traditional methods[5,6] typically compare gene sets against predefined categories in manually curated databases such as Gene Ontology (GO)[7] and Molecular Signatures Database (MSigDB)[8] to identify functions that are statistically significantly enriched. The LLM-powered approaches aim to generate biological functional annotations and coherent explanatory narratives for gene sets through instruction learning[2,9] and language agents[10].

Recently, advanced LLMs incorporating reasoning processes have shown superior performance across various tasks[11,12]. However, most of these reasoning models are commercial and subscription-based services. In addition to cost considerations, the handling of highly sensitive data such as pre-clinical differentially expressed genes and private gene sequences raises concerns about uploading to commercial platforms where users have limited control over data governance[13]. Consequently, to reduce the cost and address data privacy concerns, recent studies[14,15] have turned to fine-tuning the open-source LLMs using reinforcement learning policies like online direct preference optimization

* This research is supported by the NIH Intramural Research Program, National Library of Medicine (NLM)
† These authors contributed equally to this work
‡ The corresponding author

© 2025 The Authors. Open Access chapter published by World Scientific Publishing Company and distributed under the terms of the Creative Commons Attribution Non-Commercial (CC BY-NC) 4.0 License.

(DPO)[16] and group relative policy optimization (GRPO)[17], so that these systems can be deployed locally. Nevertheless, no studies have yet explored reasoning-based solutions specifically for the GSA task. In addition, despite evidence that domain-specific knowledge is crucial for the effective LLM fine-tuning[18,19], most of current fine-tuned LLMs is trained on general-domain data collected from the internet, which limits their effectiveness in specialty applications such as biomedicine.

To address this shortcoming, we propose **Gene-R1**, a data-augmented fine-tuning framework that endows lightweight, open-source LLMs with step-by-step reasoning capabilities tailored to the GSA task, aiming to close the performance gap with commercial reasoning LLMs. As illustrated in **Fig.1**, Gene-R1 comprises three modules: knowledge warm-up (KW), reasoning activation (RA), and task alignment (TA). The KW module augments the backbone model with curated knowledge via the pre-training strategy. Using this warmed-up model as the student model, the RA module instills step-by-step inference capabilities by fine-tuning on supervised reasoning examples distilled from the teacher model. Finally, the TA module employs GRPO as the reinforcement learning policy to ensure robust performance in both accuracy and output preferences, with rewards reflecting soft matching to gold-standard function names and strict alignment of outputs and reasoning processes.

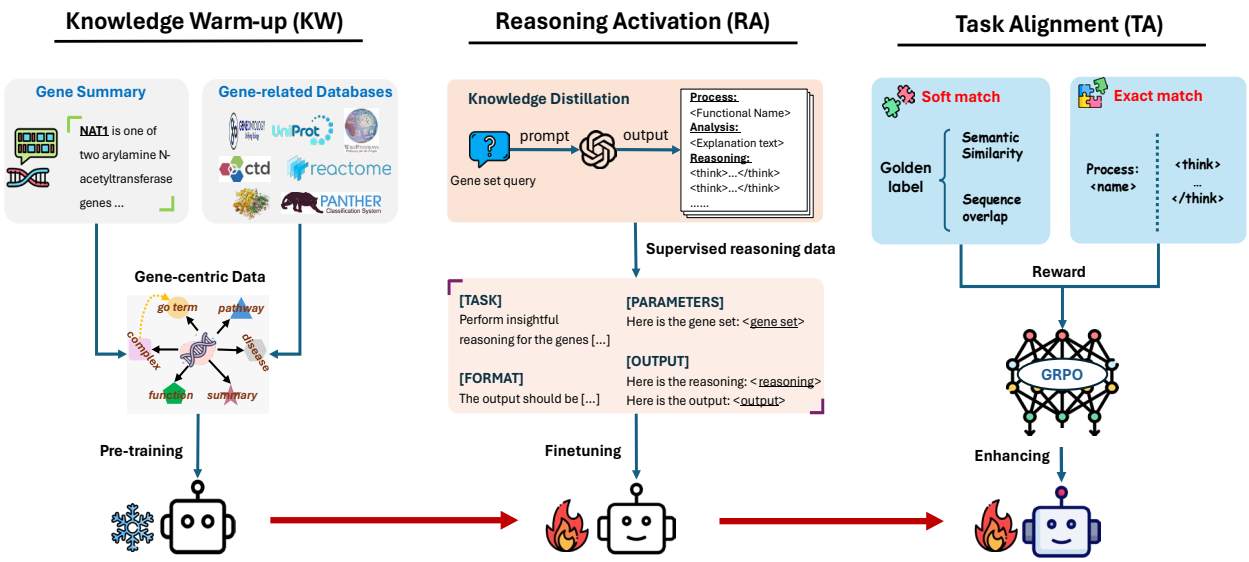

Fig. 1. The overall framework of Gene-R1, which consists of three modules designed to fine-tune lightweight Llama models for the GSA task. These modules are knowledge warm-up, reasoning activation, and task alignment. These modules play a systematic role for incorporating curated knowledge, enhancing reasoning capabilities, and refining the output format of the fine-tuned model, respectively.

We evaluate Gene-R1 in two scenarios: on gene sets whose functional name distributions match those of the fine-tuning data in the RA module (*in-distribution*); on gene sets drawn from different distributions (*out-of-distribution*). In in-distribution evaluation, Gene-R1 outperforms all baselines, demonstrating the effectiveness of the proposed training strategy in instilling step-by-step reasoning capabilities into lightweight LLMs. Meanwhile, in out-of-distribution evaluation, Gene-R1 matches the performance of both commercial LLMs and large-scale models, underscoring its robust generalizability across diverse gene-set sources while requiring fewer computational resources.

Overall, our contributions are summarized as follows: (1) We introduce Gene-R1, the first attempt to empower lightweight LLMs with step-by-step reasoning capabilities for the gene set analysis task through data-augmented fine-tuning, which closes the performance gap between open-source and best-performing commercial LLMs. (2) We demonstrate the benefit of priming backbone LLMs with curated domain-specific knowledge for gene set analysis. (3) We validate the robust generalization of Gene-R1 by evaluating it on gene sets from multiple biological sources and across different lightweight LLM variants.

2. Related Works

Our study primarily intersects gene set analysis and the fine-tuning of large language models.

Gene set analysis is a foundational computational approach in bioinformatics that interprets gene expression data by identifying coordinated changes within the predefined groups of genes. Classical methods, most notably Gene Set Enrichment Analysis (GSEA)[5], compare the expression levels of gene sets against curated biological functions documented in the specialized databases. Various tools have been developed for GSEA: g:Profiler[6] performs functional profiling by mapping genes to curated functional resources and detecting statistically significant enrichments, while Enrichr[20] provides a search engine and extensive libraries of annotated gene sets.

Recently, large language models have become valuable tools for GSA, owing to their powerful ability to capture biological context and generate detailed explanations. Jin *et al*.[21] introduced GeneGPT to tackle genomic-related question-answering tasks by augmenting LLMs with external bioinformatics tools. Wu *et al*.[22] presented AutoGen that allows users to build LLM applications like genomic question-answering by composing multiple agents. Hu *et al*.[2] benchmarked five LLMs using instruction and few-shot learning for GSA. Wang *et al*.[10] developed the first-of-its-kind AI agent for the same task, which employs multiple domain-specific databases to self-verify the raw outputs of an LLM. Additionally, SPINDOCTOR[9] exploits the summarization capabilities of LLMs to extract biologically plausible processes from gene-function narratives.

Fine-tuning LLMs has been a promising way to boost the performance of LLMs on specialized tasks, overcoming the generalization limits of off-the-shelf models. Two efficient approaches are widely used: supervised fine-tuning (SFT) and reinforcement learning (RL). In SFT, approaches such as MedAlpaca[23] show that modest amounts of curated biomedical question-answering pairs can align general LLMs with domain-specific tasks, improving factual grounding and response style. ClinicalCamel[24] scales this paradigm to more than 1M instructions annotated by clinicians, achieving competitive results on multiple biomedical question-answering datasets. Meanwhile, the RL strategies can further refine LLMs by optimizing generation quality to match domain-expert preferences. For instance, Med-PaLM 2[25] combines instruction tuning with physician-provided reward models, surpassing 85% answer accuracy on USMLE-style exams. DeepSeek[11] employs the GRPO policy to finetune the LLMs and obtain the state-of-the-art performance across multiple tasks. In the biomedical domain, UltraMedical[26] collections facilitate the fine-tuning of several advanced medical LLMs based on the Llama-3 series. Recently, cell-o1[27] trained a 7B-parameter LLM for the CellPuzzles task by equipping the RL with batch-level rewards.

3. Methodology

As illustrated in **Fig. 1**, Gene-R1 comprises three steps: knowledge warm-up, reasoning activation, and task alignment. The components are designed to incorporate prior gene-relevant knowledge, learn biological reasoning patterns, and align with format-specific output preferences, respectively.

The KW module aims to equip the model with a foundational understanding of gene symbols and pre-defined biological terminology. Most existing open-source LLMs are fine-tuned on general-domain corpora so that they are rarely exposed to domain-specific knowledge such as gene annotations. As a result, without prior exposure or contextual grounding, gene symbols are typically treated as meaningless strings by these LLMs and are likely to induce hallucination. In our study, we hypothesize that LLMs can significantly benefit from early-stage exposure to gene-relevant knowledge, and therefore, we collect gene summaries and their topological associations with other biological terminology from several databases (*e.g.*, CTD[28], UniProtKB[29], *etc*.). These data are consolidated into a gene-centric relational dataset $\{d_i\}_{i=1}^{N}$ as shown in **Tab.1**, enabling the model to learn meaningful associations between gene symbols and their biological contexts.

Based on this dataset, we leverage **pre-training** to incorporate domain-specific knowledge. Each instance d_i is considered as a declarative sentence to optimize the parameter set of backbone LLMs by minimizing the token-level likelihood probabilities. After pre-training, the model is better able to recognize the gene symbol rather than hallucinating a factually incorrect definition. For example, the base model (Llama-3) recognizes GHRHR as "*a receptor that regulates the expression of ERAD-related genes*", whereas the pre-trained model can correctly recall gene knowledges and output "*The gene GHRHR is involved in growth hormone signaling and growth regulation.*"

Table 1. Statistics of data using for the Gene-R1 training.

	# Source	# Instance	Description
KW via model pre-training	8	244,754	Gene-centric relational data from GO, UniProtKB, CTD, Reactome[30], Wikipathway[31], Panther[32], COURM[33], and NCBI[34]
RA via model fine-tuning	3	9,873	Gene sets with reasoning process generated by GPT-o1. These gene sets are sampled from GO:BP, GO:MF, and GO:CC.
TA via reinforcement learning	5	13,327	Gene sets with ground-truth labels from source databases: GO, Omics analysis platform[35], PubMed, Reactome, and MSigDB

Building upon the pre-trained model, the RA module further enables the model to perform reasoning with the step-by-step investigations for gene utilities and associations.

Due to the lack of existing reasoning annotations and the impracticality of manually curating step-by-step reasoning processes for gene sets, we employ the o1 model (GPT) to automatically generate reasoning chains for gene sets derived from the three major branches of the GO database. Specifically, we build a supervised reasoning corpus $\{q_i, r_i, f_i\}_{i=1}^{K}$ for model **fine-tuning** as shown in **Tab.1**, where each instance includes a gene-set query (q), a step-by-step reasoning process (r), and the biological function (f) generated from reasoning process. The prompt template used for GPT-o1 to generate such instances is provided in **Tab.2**. Importantly, to ensure high-quality supervised data, we only retain those instances in which the generated function achieves a similar score greater than 0.7 with the ground-truth label. The resulting dataset is then used to fine-tune the pre-trained model, enabling it to learn biologically grounded reasoning patterns between gene sets

and their corresponding biological functions. After fine-tuning the model on the supervised reasoning corpus, the model could make biological inference steps for the input gene set such as "*the CRY2 gene functions in the regulation of gene expression in response to cellular stress, which impacts the regulation of phosphate homeostasis.*"

After fine-tuning, the model is capable of generating functional names for given gene sets based on step-by-step reasoning. However, the generated names may differ significantly from expert-curated ground-truth labels, and the reasoning process may also be presented in a fragmented or disorganized manner. To address these limitations, we introduce the TA module, equipped with the GRPO policy, with the goal of enhancing both prediction accuracy and output coherence.

Specifically, to improve prediction accuracy, we construct a benchmark dataset $\{g_i, a_i\}|_{i=1}^{M}$, where each g_i represents a gene set and a_i denotes its ground-truth annotation, as shown in **Tab.1**. This dataset is used to train a **reinforcement learning** algorithm that guides the function name $f(g_i)$, generated by the fine-tuned model, toward the correct annotation a_i. To capture nuanced alignment between predicted and reference annotations, we defined a soft-match reward function-within the GRPO framework, accounting for both similarity and lexical overlap between $f(g_i)$ and a_i. The soft-match function integrates the MedCPT[36] score for semantic similarity and the longest common subsequence (LSC)[37] score for lexical alignment. In parallel, to ensure the output adheres to the expert-preference format that includes a "*Process*" identifier for the prominent biological function and uses a "*<think></think>*" tag pair to separate different reasoning steps, we retain the exact-match reward function used in the original GRPO framework. This dual-reward strategy can be defined as follows, allowing the model to optimize both the semantic correctness and structural compliance.

$$R_Score = \alpha * medcpt(f(g_i), a_i) + \beta * lsc(f(g_i), a_i) + (\mathbb{P}(\mathrm{f}(g_i)) + \mathbb{T}(f(g_i)))$$

where $\alpha$and β are two hyperparameters controlling weights of the two rewards. $\mathbb{P}$ outputs 1 if the model output contains the correct answer format, and $\mathbb{T}$ outputs 1 if the model output follows the step-by-step reasoning format.

Table 2. The template for the GPT-o1 model to generate reasoning corpora for gene sets.

System: You are an efficient and insightful assistant to a molecular biologist.
User: Perform insightful reasoning for the interacting proteins and write a critical analysis of the biological functions based on your reasoning.
Propose a brief name for the prominent biological functions performed by the system, such as biological process, molecular function, cellular component, and so on.
The proposed name and critical analysis should:
Be concise; avoid unnecessary words.
Be textual; do not use format symbols such as "*", "-", or other tokens.
Be specific; avoid overly general statements such as "the proteins are involved in various cellular processes."
Be factual; do not editorialize.
For each reasoning point and the critical analysis, describe the supporting information. They should:
Be comprehensive; collect various gene functions from different aspects, including gene summaries, enrichment analysis, gene complexes, gene domains, pathway analysis, and more.
Be complete; ensure no necessary or helpful genes in the given gene set are missed.
Be convincing; do not generate ambiguous statements for any genes.
Be ample; provide long, high-quality, and credible evidence for the proposed process name.
Here is the gene set: ***{genes}***
The analysis must include the following format:
1. Put the name at the top of the analysis as ***"Process: <name>"***.
2. The reasoning process must be placed at the bottom of the analysis, starting with the message: "Reasoning: ".
3. Each reasoning step should be organized within the ***"<think></think>"*** tags.

4. Experiments

Our experiments are designed to answer the following questions:

Q1. How does the Gene-R1 perform compared with both the state-of-the-art open-source and commercial LLMs?

Q2. How well does Gene-R1 generalize across different gene sets (in-distribution *vs*. out-of-distribution evaluation)?

Q3. What are the contributions of each individual module within Gene-R1?

4.1. *Datasets*

For model evaluation, we curated five independent datasets from the GO database, proteomics analysis, and a molecular function database repository. We made sure none of the test data was previously used during the development phase of Gene-R1. As shown in **Tab.3**, all GO datasets are employed for in-distribution evaluation, while the other two datasets are reserved for out-of-distribution assessment.

Table 3. Statistics of data used for the Gene-R1 evaluation.

	# Sets	#Genes in a Set	Avg. #Genes	Source
GO:BP	1,000	3 to 456	48.3	Literature curation
GO:MF	340	1 to 5,973	78.2	Literature curation
GO:CC	168	2 to 13,075	249.5	Literature curation
NeST	50	5 to 323	2.2	Proteomics analysis
MsigDB	56	4 to 200	3.0	Molecular function

4.2. *Experimental Setting*

Task definition: Given a gene set ($\mathcal{S} = \{g_i|_{i=1}^{k}\}$), our goal is applying the fine-tuned LLM ($\mathcal{L}$) on $\mathcal{S}$ to generate the function ($\mathcal{F}$) and explanatory context ($\mathbb{C}$) through a step-by-step reasoning.

Evaluation metrics: To comprehensively evaluate Gene-R1, we employed two complementary metrics: **ROUGE** (Recall-Oriented Understudy for Gisting Evaluation)[37] to measure the lexical overlap and **Similarity Score** to quantify the semantic relevance. To mitigate potential bias inherent to a single semantic encoder, we calculated semantic similarity using three biomedical encoders—MedCPT[36], SentenceBERT[38], and SapBERT[39]—and reported the average scores.

Implementations: All training and evaluation are implemented with python 3.13.5 and torch 2.7.1 on the AWS (Amazon Web Services) services (8 GPU cards). Other required software packages are transformers (4.53.2), trl (0.19.0), accelerate (1.8.1), deepspeed (0.17.2).

4.3. *Backbone and comparison LLMs*

After investigating criteria involving accessibility, fine-tuning cost, performance, and general usability, we select the Meta Llama[40] as the backbone LLMs for Gene-R1. Specifically, we use Llama3.1 (8B parameters) and Llama3.2 (1B and 3B parameters) to demonstrate the flexibility of proposed fine-tuning pipeline. Furthermore, we compare Gene-R1 with the aligned Llama models and widely used commercial GPT models: GPT-4, GPT-4o, o1, and o3-mini. All Llama models are accessed from the hugging-face community, while the GPT models are provided by the Azure API.

5. Results

5.1. *In-distribution Evaluation*

To address Q1 that is related to the accuracy of Gene-R1, we evaluate a range of LLMs on 1,508 gene sets whose label distributions matched those of the fine-tuning data used in the RA module.

Table 4. Performance of Gene-R1 on gene sets derived from three branches of the GO database (In-distribution Evaluation). **R.-(*)** denotes the ROUGE score under different metrics. **Score (avg.)** represents the semantic similarity score averaged across MedCPT, SentenceBERT, and SapBERT. The best results for each dataset are highlighted in **bold**. Δ denotes the relative improvement calculated as $(\mathbf{bold} - x)/x * 100\%$. The improvements are significant (p-value < 0.05) according to a two-tailed paired t-test at a 95% confidence interval.

	Models	R.-L	Δ	R.-1	Δ	R.-2	Δ	Score (avg.)	Δ
GO: BP	Llama3-1B	0.107	158.9%	0.109	165.1%	0.049	122.4%	0.468	38.2%
	Llama3-3B	0.083	233.7%	0.087	232.2%	0.011	890.9%	0.505	28.1%
	Llama3-8B	0.133	108.3%	0.146	97.9%	0.025	336.0%	0.562	15.1%
	Llama3-70B	0.196	41.3%	0.212	36.3%	0.062	75.8%	0.611	5.9%
	GPT-4	0.184	50.5%	0.201	43.8%	0.049	122.4%	0.614	5.4%
	GPT-4o	0.184	50.5%	0.207	39.6%	0.036	202.8%	0.629	2.9%
	o1	0.164	68.9%	0.178	62.4%	0.040	172.5%	0.626	3.4%
	o3-mini	0.154	79.9%	0.167	73.1%	0.033	230.3%	0.614	5.4%
	Gene-R1(1B)	0.225	23.1%	0.232	24.6%	0.075	45.3%	0.617	4.9%
	Gene-R1(3B)	0.229	21.0%	0.238	21.4%	0.080	36.3%	0.623	3.9%
	Gene-R1(8B)	**0.277**	/	**0.289**	/	**0.109**	/	**0.647**	/
GO: MF	Llama3-1B	0.028	1057.1%	0.028	1067.9%	0.002	7900.0%	0.470	45.7%
	Llama3-3B	0.095	241.1%	0.095	244.2%	0.022	627.3%	0.538	27.3%
	Llama3-8B	0.099	227.3%	0.102	220.6%	0.027	492.6%	0.564	21.5%
	Llama3-70B	0.114	184.2%	0.114	186.8%	0.024	566.7%	0.586	16.9%
	GPT-4	0.100	224.0%	0.101	223.8%	0.023	595.7%	0.588	16.5%
	GPT-4o	0.096	237.5%	0.097	237.1%	0.020	700.0%	0.584	17.3%
	o1	0.147	120.4%	0.150	118.0%	0.037	332.4%	0.632	8.4%
	o3-mini	0.119	172.3%	0.120	172.5%	0.029	451.7%	0.611	12.1%
	Gene-R1(1B)	0.315	2.9%	0.318	2.8%	0.122	31.1%	0.661	3.6%
	Gene-R1(3B)	0.316	2.5%	0.319	2.5%	0.122	31.1%	0.661	3.6%
	Gene-R1(8B)	**0.324**	/	**0.327**	/	**0.160**	/	**0.685**	/
GO: CC	Llama3-1B	0.039	546.2%	0.039	564.1%	0.008	962.5%	0.449	43.9%
	Llama3-3B	0.075	236.0%	0.076	240.8%	0.013	553.8%	0.497	30.0%
	Llama3-8B	0.092	173.9%	0.093	178.5%	0.028	203.6%	0.536	20.5%
	Llama3-70B	0.091	176.9%	0.091	184.6%	0.022	286.4%	0.546	18.3%
	GPT-4	0.093	171.0%	0.092	181.5%	0.016	431.3%	0.562	14.9%
	GPT-4o	0.105	140.0%	0.105	146.7%	0.020	325.0%	0.573	12.7%
	o1	0.144	75.0%	0.148	75.0%	0.038	123.7%	0.609	6.1%
	o3-mini	0.139	81.3%	0.142	82.4%	0.031	174.2%	0.598	8.0%
	Gene-R1(1B)	0.222	13.5%	0.226	14.6%	0.054	57.4%	0.618	4.5%
	Gene-R1(3B)	0.143	76.2%	0.143	81.1%	0.035	142.9%	0.578	11.8%
	Gene-R1(8B)	**0.252**	/	**0.259**	/	**0.085**	/	**0.646**	/

As shown in **Tab.4**, Gene-R1 consistently outperforms all baselines on both ROUGE and semantic-similarity metrics. Specifically, compared to Llama3 models, Gene-R1 increased ROUGE scores by 133.1%, 133.9%, and 257.3% in average, respectively. Compared to the GPT series reasoning models, it improved these metrics by 82.0%, 77.5%, and 192.8% in average. The marked

gain in ROUGE-2 indicates that the biological function names predicted by Gene-R1 exhibit substantially longer n-gram overlaps with the gold-standard labels, demonstrating that our fine-tuning workflow effectively captures distributional patterns for precise sequence generation. This high ROUGE performance also translates into superior semantic alignment. By averaging similarity scores from MedCPT, SentenceBERT, and SapBERT, we found that Gene-R1 achieved gains of 5.9%, 16.9%, and 18.3% respectively over Llama-based models and 2.9%, 8.4%, and 6.1% respectively over GPT-based models across the three evaluation datasets. These results confirm that Gene-R1 closes the performance gap with commercial LLMs.

Additionally, the paired comparisons between the backbone models and Gene-R1 at the 1B, 3B, and 8B parameter scales show that our fine-tuning workflow preserves strong performance across Llama variants of different sizes. Specifically, Gene-R1 consistently delivers over 15% gains in terms of the semantic similarity scores on every evaluation dataset, underscoring its robustness. This reliability opens new avenues for applying Gene-R1 to a wide range of tunable and open-source LLMs for the specificized downstream task, thereby being able to shorten development cycles.

5.2. *Out-of-distribution Evaluation*

To address Q2, which concerns the generalization of Gene-R1, we evaluated on 106 gene sets curated by Hu *et al*.[2] and filtered by Wang *et al*.[10] These gene sets are annotated with labels that exhibit distributions distinct from those used during the RA module.

Table 5. Performance comparison between Gene-R1 and other LLMs on out-of-distribution datasets. The best results in different datasets are **bold**. "**n.s.**" denotes no significant difference (p-value > 0.05) according to a two-tailed paired t-test at the 95 % confidence level. Note that we only compute the p-value for the comparable results.

Datasets	Models	ROUGE-L	ROUGE-1	ROUGE-2	Similarity Score (avg.)
NeST	Llama3-1B	0.149	0.154	0.056	0.522
	Llama3-3B	0.152	0.162	0.033	0.570
	Llama3-8B	0.197	0.210	0.073	0.610
	Llama3-70B	0.220	0.234	0.071	0.633 (n.s.)
	GPT-4	0.239	0.252	0.082	**0.638 (n.s.)**
	GPT-4o	0.185	0.200	0.065	0.611
	o1	0.153	0.156	0.028	0.618
	o3-mini	0.179	0.190	0.035	0.625
	Gene-R1 (1B)	**0.249**	**0.252**	0.071	0.630
	Gene-R1 (3B)	0.238	0.243	**0.091**	0.635
	Gene-R1 (8B)	0.216	0.223	0.089	0.616
MsigDB	Llama3-1B	0.033	0.033	0.005	0.463
	Llama3-3B	0.164	0.164	0.030	0.563
	Llama3-8B	0.177	0.177	0.037	0.596
	Llama3-70B	0.195	0.195	0.070	0.611
	GPT-4	**0.239**	**0.239**	0.074	0.628 (n.s.)
	GPT-4o	0.220	0.220	0.046	**0.632 (n.s.)**
	o1	0.167	0.167	0.031	0.625
	o3-mini	0.165	0.165	0.011	0.605
	Gene-R1 (1B)	0.177	0.177	0.041	0.605
	Gene-R1 (3B)	0.214	0.218	**0.077**	0.622
	Gene-R1 (8B)	0.203	0.203	0.068	0.625

As shown in **Tab.5**, although Gene-R1 does not outperform all comparison methods on every evaluation metric, it is consistently comparable to the best baselines across both datasets. Notably, significance tests on similarity scores between Gene-R1 and the top-performing LLMs reveal no significant differences, indicating that Gene-R1 achieves performance on par with both commercial LLMs such as GPT-4 and large-scale models like Llama3.3-70B. It is also worth mentioning that Gene-R1 consistently surpasses the o1 and o3-mini, demonstrating that the task-specific reasoning generated by Gene-R1 better aligns with biological functions than general-purpose reasoning LLMs. These findings highlight the strong generalization capability of Gene-R1 for diverse gene sets.

5.3. *Ablation Experiments*

Additional ablation experiments were conducted to address Q3 by investigating the individual contributions of each module within Gene-R1.

We designed an incremental fine-tuning setup in which modules are introduced one at a time, enabling us to quantify their independent effects on model performance. Specifically, we produced two intermediate variants of Gene-R1: one using only the gene-centric relational data from the knowledge warm-up module (i.e., w/ KW) and another with both realtional data and the supervised reasoning data from the reasoning activation modue (i.e., w/ KW&RA). To ensure robust evaluation, we applied different variants acorss multiple backbone models (Llama 1B, 3B, and 8B) and datasets (in-distribution and out-of-distribution). The results are summarized in **Fig.2**.

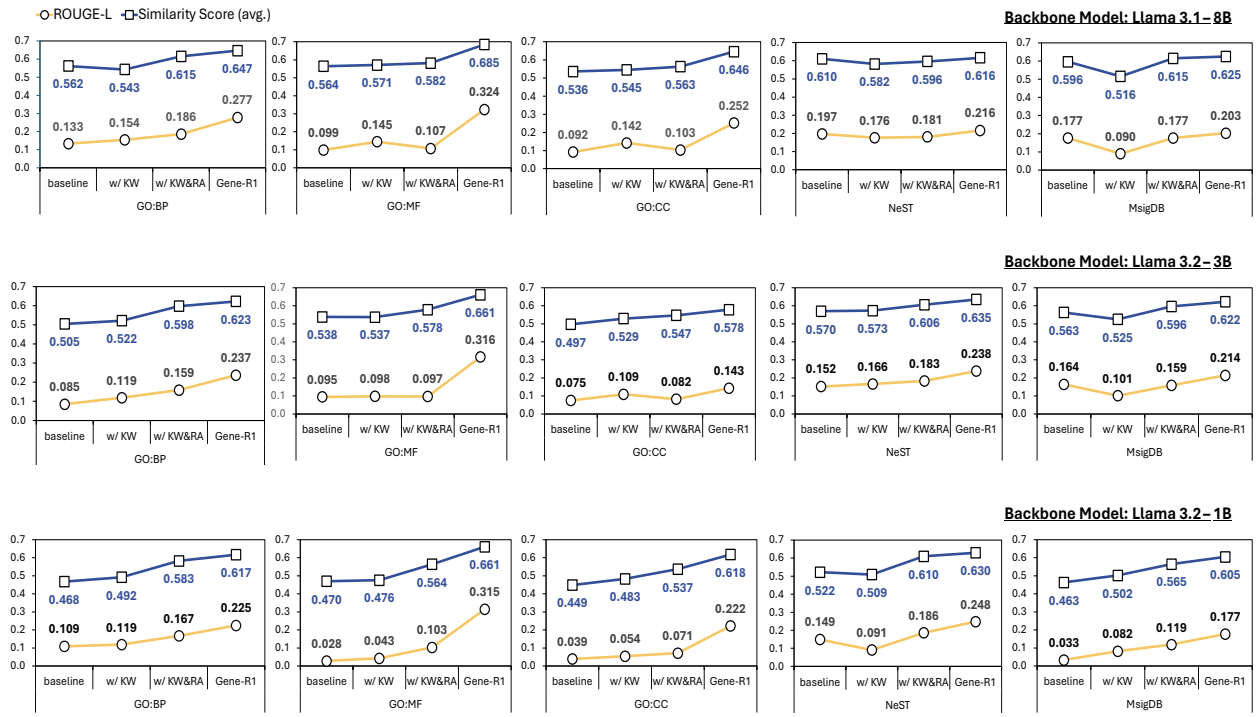

Fig. 2. Performance comparison of the individual module contributes to Gene-R1. The experiments were conducted using Llama with 1B, 3B, and 8B parameters, respectively. The y-axis represents the performance score, while the x-axis indicates the sequential addition of modules to the baseline backbone model.

On the in-distribution datasets (i.e., GO:BP, GO:MF, and GO:CC), each module demonstrated a clear and consistent positive contribution to the performance of Gene-R1 compared to the baseline model. In constract, the results on the out-of-distribution datasets (i.e., NeST and MsigDB) revealed that no individual module consistency improved performance in solation. Instead, the combination of all three modules (i.e., w/ KW&RA&TA) provided systematic improvement. Notably, the most significant performance gain was observed when the TA module was incorporated, underscoring the critical role of reinforcement learning in enhancing the effectiveness of Gene-R1. For example, on the GO:MF benchmark, the model using Llama3.1-8B backbone achieveed a 10.3 percentage point increase in semantic similarity and a 0.217 absolute gain in ROUGE-L.

6. Discussion

Advantages of data augmentation for lightweight LLM fine-tuning. In this work, we present Gene-R1, an effective pipeline that enables open-source LLMs with fewer parameters to achieve performance comparable to larger models, including popular commercial alternatives. The high cost and opaque nature of commercial LLMs raise concerns including budget and data privacy, which hinder their deployment in real world settings. Although recent fine-tuned LLMs have shown promise in domain-specific tasks, they often generate fabricated content such as incorrect definitions of technical terms, due to limited exposure to specialized knowledge. In contrast, Gene-R1 incorporates domain knowledge to its fine-tuning workflow that uses accessible lightweight open-source LLMs. This allows local deployment with limited computational resources and can reduce domain-specific hallucinations and inference expenditure.

Different reward functions for reinforcement learning. Reinforcement learning is crucial for Gene-R1's performance. To further investigate this component, we examined how the choice of reward modeling and reward function design impacts the performance of Gene-R1.

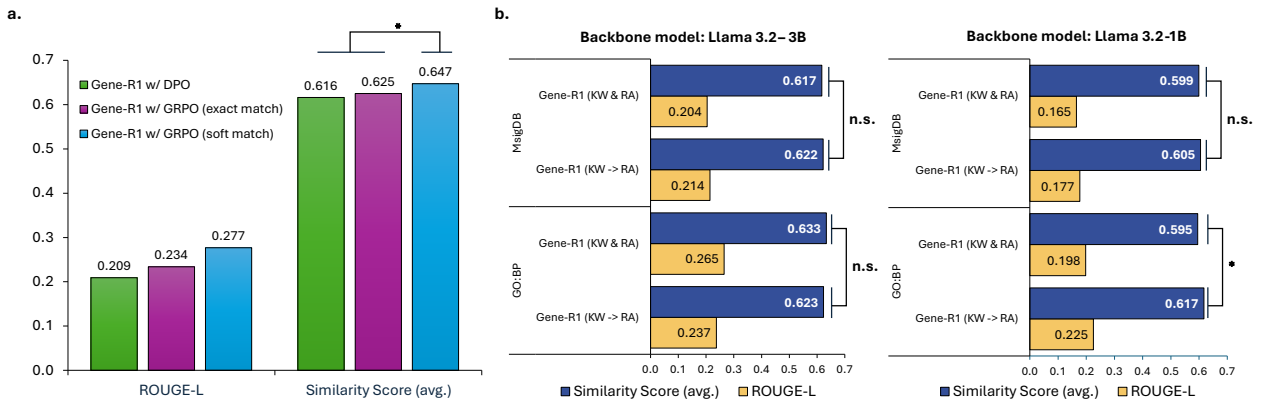

Fig. 3. Alation experiments for Gene-R1. (a) The comparison for Gene-R1 with different reinforcement learning settings. (b) The results of different approaches for the incorporation of gene-centric relational data. "KW & RA" denotes merged strategy, while "KW -> RA" denote the cascade strategy. "*" indicates the significant improvement (p-value < 0.05) according to a two-tailed paired t-test at a 95% confidence interval, while "**n.s.**" indicates there is not significant.

We first compare the GRPO with standard online DPO, where the reward model is trained on pre-generated responses[a]. Then, we relax the reward formulation by introducing a "soft-match" component that assigns partial credit for outputs that are semantically related to the gold-standard labels. For this evaluation, we use the most stable model (Llama 8B) and the GO:BP bechmark as shown in Fig.2. As summarized in **Fig.3 (a)**, the GRPO with soft-match rewards consistently outperforms both the online DPO and GRPO with only exact-match rewards.

Different strategies to incorporate domain-specific knowledge. This work has shown that domain-specific knowledge provides the foundational biological context necessary for Gene-R1's step-by-step reasoning. To explore the optimal strategy for injecting the gene-centric relational knowledge into model training, we investigated two separate approaches: the *Cascade* strategy (employed in Gene-R1) and a *Merged* strategy.

In the alternative merged approach, relational data are appended directly to the reasoning exemplars and introduced solely during the RA stage. This allows the model to learn structural knowledge and reasoning patterns simultaneously, without a dedicated pre-training phase. We evaluate them on two representative benchmarks containing the largest number of gene sets: GO:BP (in-distribution) and MsigDB (out-of-distribution). The results shown in **Fig.3 (b)**, demonstrating that the cascade strategy yields only modest improvements over the merged approach in terms of both similarity score; however, most of these differences are not statistically significant.

Error analysis. In addition to being constrained by the inherent limitations of the Llama model for the gene set analysis task, the primary source of errors in Gene-R1 comes from its informal reasoning processes. As shown in **Tab.6**, the models fail to consistently achieve 100% accuracy in output formatting. Some outputs either lack a clearly defined biological function name or fail to adhere to a valid step-by-step reasoning structure, ultimately resulting in incorrect predictions. A promising solution to this shortcoming is to manually create a subset of high-quality reasoning annotations to guide the teacher policy (e.g., the GPT-o1 model) in generating better supervised data. Alternatively, customized reward functions can be introduced to encourage the production of longer and more coherent reasoning chains.

Table 6. The proportion of correct output format generated by Gene-R1

	Gene-R1 (1B)	**Gene-R1 (3B)**	**Gene-R1 (8B)**
GO:BP	95.6% (956/1000)	42.4% (424/1000)	93.8% (938/1000)
GO:MF	94.4% (321/340)	94.4% (321/340)	85.0% (289/340)
GO:CC	91.7% (154/168)	42.9% (72/168)	88.1% (148/168)
NeST	96.0% (48/50)	100% (50/50)	100% (50/50)
MsigDB	91.1% (51/56)	100% (56/56)	100% (56/56)

[a] In Online DPO, a reward function is used to determine the chosen and rejected response during training. In our work, we train the reward function using pre-generated model responses from GPT. Specifically, for each gene set query, we generate four types of responses in preference order: 1. Response with correct answer and contains reasoning; 2. Response with correct answer and does not contain reasoning; 3. Response with incorrect answer and contains reasoning; 4. Response with incorrect answer and does not contain reasoning. These responses are then used to create a pair-wise dataset consisting of chosen-rejected pairs. Given two responses, the reward model is trained to distinguish and select the better response following the preference order.

Limitaions. Despite these advancements achieved by Gene-R1, it currently relies on manual data collection for the training workflow, which limits the flexibility when applied to novel or underrepresented genes. Moreover, Gene-R1 may still hallucinate plausible-sounding but incorrect functions when operating on unseen genes which are outside its training domain. Furthermore, our evaluation primarily focuses on biological function annotation, leaving the model's transferability to other ontologies (e.g., disease ontology, phenotype ontology) as open questions.

7. Conclusions

In this study, we present Gene-R1 to equip lightweight, open-source LLMs with strong reasoning capabilities specifized for the gene set analysis task, effectively narrowing the performance gap with proprietary, large-scale models. The effectiveness of Gene-R1 is shown by both the in-distribution and out-of-distribution evaluations on five datasets containing 1604 gene sets. LLMs trained with general domain data are highly capable of linguistic tasks, knowledge recalling and reasoning, but they often fail in domain specific tasks. We believe one best way to fully utilize the power of the LLMs is through incoporating domain knowledges, and methods like our Gene-R1 can enable powerful AIs for wider and more diffuclt tasks.

8. Data Availability

The GitHub repository (https://github.com/ncbi-nlp/Gene-R1) containing code to reproduce this work. Supplementary materials, including the training data and case studies, are also provided in the same repository. The fully fine-tuned model is available on the Hugging Face platform (https://huggingface.co/ncbi/Gene-R1).

References

1. de Leeuw, C., Neale, B., Heskes, T. *et al.* The statistical properties of gene-set analysis. *Nat Rev Genet* **17**, 353–364 (2016).
2. Hu, M., Alkhairy, S., Lee, I. *et al.* Evaluation of large language models for discovery of gene set function. *Nat Methods* **22**, 82–91 (2025).
3. Ma, K., Huang, S., Ng, K.K. *et al*. Saturation mutagenesis-re-inforced functional assays for disease-related genes. Cell **187**, 6707–6724.e22 (2024).
4. Tachmazidou, I., Hatzikotoulas, K., Southam, L. *et al.* Identification of new therapeutic targets for osteoarthritis through genome-wide analyses of UK Biobank data. *Nat Genet* **51**, 230–236 (2019).
5. Subramanian, A., Tamayo, P., Mootha, V.K. *et al*. Gene set enrichment analysis: a knowledge-based approach for interpreting genome-wide expression profiles. *Proceedings of the National Academy of Sciences* **102**, 15545-15550 (2005).
6. Raudvere, U., Kolberg, L., Kuzmin, I. *et al*. g: Profiler: a web server for functional enrichment analysis and conversions of gene lists (2019 update). *Nucleic acids research* **47**, W191-W198 (2019).

7. Ashburner, M., Ball, C., Blake, J. *et al.* Gene Ontology: tool for the unification of biology. *Nat Genet* **25**, 25–29 (2000).
8. Liberzon, A., Birger, C., Thorvaldsdóttir, H. *et al*. The molecular signatures database hallmark gene set collection. *Cell systems* **1**, 417-425 (2015).
9. Joachimiak, M.P., Caufield, J.H., Harris, N.L. *et al*. Gene set summarization using large language models. *ArXiv*, arXiv-**2305** (2024).
10. Wang, Z., Jin, Q., Wei, CH. *et al.* GeneAgent: self-verification language agent for gene-set analysis using domain databases. *Nat Methods* **22**, 1677–1685 (2025).
11. Liu, A., Feng, B., Xue, B. *et al*. Deepseek-v3 technical report. *arXiv*:**2412**.19437 (2024).
12. Jaech, A., Kalai, A., Lerer, A. *et al*. Openai o1 system card. *arXiv*:**2412**.16720 (2024).
13. Yang, Y., Jin, Q., Leaman, R. *et al*. Ensuring safety and trust: Analyzing the risks of large language models in medicine. *arXiv* preprint arXiv:**2411**.14487 (2024).
14. Wang, Z., Du, Y., Sun, Z. *et al*. Re2llm: reflective reinforcement large language model for session-based recommendation. *Proceedings of the AAAI Conference on Artificial Intelligence* **39**, 12827-12835 (2025).
15. Trung, L., Zhang, X., Jie, Z. *et al*. Reft: Reasoning with reinforced fine-tuning. *Proceedings of the 62nd Annual Meeting of the Association for Computational Linguistics* **1**, 7601-7614 (2024).
16. Qi, B., Li, P., Li, F. *et al*. Online dpo: Online direct preference optimization with fast-slow chasing. *arXiv* preprint arXiv:**2406**.05534 (2024).
17. Shao, Z., Wang, P., Zhu, Q. *et al*. Deepseekmath: Pushing the limits of mathematical reasoning in open language models. *arXiv* preprint arXiv:**2402**.03300 (2024).
18. Xue, Z., Li, L., Tian, S. *et al*. Domain knowledge is all you need: A field deployment of llm-powered test case generation in fintech domain. *Proceedings of the 2024 IEEE/ACM 46th International Conference on Software Engineering: Companion Proceedings* 314-315 (2024).
19. Song, Z., Yan, B., Liu, Y. *et al*. Injecting domain-specific knowledge into large language models: a comprehensive survey. *arXiv* preprint arXiv:**2502**.10708 (2025).
20. Kuleshov, M. V., Jones, M. R., Rouillard, A. D. *et al*. Enrichr: a comprehensive gene set enrichment analysis web server 2016 update. *Nucleic acids research* **44**, W90-W97 (2016)
21. Jin, Q., Yang, Y., Chen, Q., & Lu, Z. Genegpt: Augmenting large language models with domain tools for improved access to biomedical information. *Bioinformatics* **40**, btae075 (2024).
22. Wu, Q., Bansal, G., Zhang, J. *et al*. Autogen: Enabling next-gen LLM applications via multi-agent conversations. *First Conference on Language Modeling* (2024).
23. Han, T., Adams, L.C., Papaioannou, J.M. *et al*. MedAlpaca--an open-source collection of medical conversational AI models and training data. *arXiv* preprint arXiv:**2304**.08247 (2023).
24. Toma, A., Lawler, P.R., Ba, J. *et al*. Clinical camel: An open expert-level medical language model with dialogue-based knowledge encoding. *arXiv* preprint arXiv:**2305**.12031 (2023).
25. Singhal, K., Tu, T., Gottweis, J. *et al.* Toward expert-level medical question answering with large language models. *Nat Med* **31**, 943–950 (2025).
26. Zhang, K., Zeng, S., Hua, E. *et al*. Ultramedical: Building specialized generalists in biomedicine. *Advances in Neural Information Processing Systems* **37**, 26045-26081 (2024).
27. Fang, Y., Jin, Q., Xiong, G. *et al*. Cell-o1: Training LLMs to Solve Single-Cell Reasoning Puzzles with Reinforcement Learning. *arXiv* preprint arXiv:**2506**.02911 (2025).

28. Davis, A.P., Grondin, C.J., Johnson, R.J. *et al*. Comparative toxicogenomics database (CTD): update 2021. *Nucleic acids research* **49**, D1138-D1143 (2021).
29. Coudert, E., Gehant, S., De Castro *et al*. Annotation of biologically relevant ligands in UniProtKB using ChEBI. *Bioinformatics* **39**, btac793 (2023).
30. Fabregat, A., Jupe, S., Matthews, L. et al. The reactome pathway knowledgebase. Nucleic acids research 46, D649-D655 (2018).
31. Agrawal, A., Balcı, H., Hanspers, K. *et al*. WikiPathways 2024: next generation pathway database. *Nucleic acids research* **52**, D679-D689 (2024).
32. Thomas, P.D., Ebert, D., Muruganujan, A. *et al*. PANTHER: Making genome - scale phylogenetics accessible to all. *Protein Science* **31**, 8-22 (2022).
33. Giurgiu, M., Reinhard, J., Brauner, B. *et al*. CORUM: the comprehensive resource of mammalian protein complexes—2019. *Nucleic acids research* **47**, D559-D563 (2019).
34. Geer, L.Y., Marchler-Bauer, A., Geer, R.C. *et al*. The NCBI biosystems database. *Nucleic acids research* **38**, D492-D496 (2010).
35. Zheng, F., Kelly, M.R., Ramms, D.J. *et al*. Interpretation of cancer mutations using a multiscale map of protein systems. *Science* **374**, eabf3067 (2021).
36. Jin, Q., Kim, W., Chen, Q. *et al*. Medcpt: Contrastive pre-trained transformers with large-scale pubmed search logs for zero-shot biomedical information retrieval. *Bioinformatics* **39**, btad651 (2023).
37. Lin, C.Y. Rouge: A package for automatic evaluation of summaries. In Text summarization branches out, 74-81 (2004).
38. Reimers, N., & Gurevych, I. Sentence-BERT: Sentence Embeddings using Siamese BERT-Networks. *Proceedings of the 2019 Conference on Empirical Methods in Natural Language Processing and the 9th International Joint Conference on Natural Language Processing (EMNLP-IJCNLP)*, 3982-3992 (2019).
39. Liu, F., Shareghi, E., Meng, Z. *et al*. Self-alignment pretraining for biomedical entity representations. *North American Association for Computational Linguistics 2021*, *Association for Computational Linguistics* (*ACL*), 4228-4238 (2021).
40. Touvron, H., Lavril, T., Izacard, G. *et al*. Llama: Open and efficient foundation language models. *arXiv* preprint arXiv:**2302**.13971 (2023).

LLM Agent Based Protein Function Prediction

Fernando Zhapa-Camacho, Olga Mashkova, Robert Hoehndorf†, and Maxat Kulmanov
Computer, Electrical and Mathematical Sciences and Engineering, King Abdullah University of Science and Technology,
Thuwal, Makkah Region, Saudi Arabia
†*E-mail: robert.hoehndorf@kaust.edu.sa*
www.kaust.edu.sa

Protein function prediction remains a fundamental challenge in computational biology. Here, we present a Large Language Model (LLM) agent-based system that improves protein function prediction performance using knowledge-augmented reasoning and multi-source evidence synthesis.

Our approach integrates computational predictions with structured protein metadata, scientific literature, and ontological knowledge through a multi-stage reasoning process. An LLM agent equipped with specialized tools progressively refines functional predictions by querying constraints, cross-referencing evidence, and ensuring biological plausibility. Furthermore, the system provides detailed explanations for each prediction update, documenting the reasoning process and evidence sources.

We evaluate our approach against established baseline methods across three Gene Ontology sub-ontologies using four complementary metrics, achieving superior performance in threshold-dependent measures, attaining the lowest $S_{\min}$ scores across all ontologies and the best $F_{\max}$ for Molecular Function and Cellular Component ontologies. We make our code publicly available at `https://github.com/bio-ontology-research-group/go-agent`.

Keywords: Gene Ontology; Protein Function Prediction; Large Language Models; Agents.

1. Introduction

Protein function prediction is one of the key challenges in modern biology and bioinformatics as it enables better understanding of the roles and interactions of proteins within living systems. Accurate functional descriptions of proteins are necessary for tasks such as identification of drug targets, understanding disease mechanisms, and improving biotechnological applications in industry. While predicting protein structures has become increasingly accurate in recent years,[1] predicting protein function remains challenging due to the small number of known functions combined with their complexity and interactions.

Functions of proteins are described using the Gene Ontology (GO).[2] GO includes three sub-ontologies for describing molecular functions (MFO) of a single protein, biological processes (BPO) to which proteins can contribute, and cellular components (CCO) where proteins are active. Researchers identify protein functions based on both targeted experiments and high-throughput experimental approaches, generating scientific reports which are then

© 2025 The Authors. Open Access chapter published by World Scientific Publishing Company and distributed under the terms of the Creative Commons Attribution Non-Commercial (CC BY-NC) 4.0 License.

taken by database curators and added to knowledge bases. Currently, the UniProtKB/Swiss-Prot database[3] contains reviewed GO annotations for thousands of organisms and more than 570,000 proteins.

Protein function prediction methods can rely on different sources of information such as sequence, interactions, protein tertiary structure, literature, or the information provided in GO.[4–16] The methods may use sequence domain annotations,[5,6,8,11,17] directly apply deep convolutional neural networks (CNN)[13] or language models such as LSTMs[9] and transformers,[14] or use pretrained protein language models[10,15] to represent amino acid sequences. Models may also incorporate protein–protein interactions through knowledge graph embeddings,[12,16] approaches using k-nearest neighbors,[17] and graph convolutional neural networks.[6] Also, natural language models applied to scientific literature have been successful in automated function prediction.[8]

Despite these advances, current protein function prediction methods face several limitations. Most approaches treat prediction as a static classification problem without incorporating the rapidly growing nature of biological literature or providing multi-step reasoning explanations for their predictions. While some methods offer interpretability through attention mechanisms[14] or graph-based explanations in GNNs[18] or LLMs[19] they typically highlight important features rather than providing structured reasoning that traces through multiple evidence sources and biological constraints. Traditional methods, although capable of integrating multiple data types as demonstrated by approaches like GOLabeler,[5] often rely on fixed integration schemes that cannot re-evaluate evidence based on context-specific biological knowledge. These methods cannot easily incorporate new biological insights without retraining or adapt their integration strategy based on the reliability of different evidence sources for specific protein families or functional categories. Furthermore, while these methods provide confidence scores, they lack the ability to generate natural language explanations that trace the logical steps from evidence to conclusion, making it difficult for biologists to assess the reliability of predictions or understand the biological reasoning supporting specific functional assignments.

The emergence of large language models (LLMs) has introduced new capabilities for integrating heterogeneous information sources and performing evidence-based reasoning in computational biology. Traditional machine learning approaches for protein function prediction rely on fixed feature representations and statistical patterns learned from training data, limiting their ability to incorporate new biological knowledge or provide explanations for their predictions. In contrast, LLM agent-based systems, exemplified by frameworks such as LangChain[a] and multi- agent systems like CAMEL-AI,[20] can access external knowledge bases on-demand, synthesize information from scientific literature, and apply domain-specific constraints through specialized tools. The key advantage of LLM agents over standalone LLMs lies in their ability to perform multi-step reasoning processes, where intermediate results can be validated against external knowledge sources and refined through iterative consultation of different information repositories. This agent-based approach enables the combination of computational predictions

[a]https://github.com/langchain-ai/langchain

with structured biological knowledge and experimental evidence from literature, potentially improving both the accuracy and interpretability of protein function predictions.

In this work, we propose an LLM agent-based system that addresses these limitations by combining computational predictions with LLM-generated reasoning and evidence synthesis. Our approach integrates multiple information sources including supervised predictions from a multi-layer perception (MLP) network trained on SwissProt annotations, homology-based predictions from DiamondScore methods, structured protein metadata from UniProtKB, relevant scientific literature from PubMed[b], and ontological knowledge from the Gene Ontology database. The system employs a multi-stage reasoning process where an LLM agent equipped with specialized tools progressively refines functional predictions through evaluation of available evidence and ontological consistency checking. Unlike traditional black-box approaches, our method provides detailed explanations for each prediction update, tracing the reasoning process and evidence sources that influenced the final annotations. We evaluate our approach against established baseline methods and demonstrate improved performance in semantic accuracy and optimal threshold-dependent metrics, while providing interpretable insights that support biological hypothesis generation and validation.

2. Materials and Methods

2.1. *Gene Ontology and Dataset*

We obtained all proteins that were manually curated and reviewed from the UniProtKB/Swiss-Prot Knowledgebase. We generated a time-based test set by following the CAFA[21] challenge time-based approach. For training, we took all proteins from release v2023_05 (08-Nov-2023).[3] For validation, we took the proteins that collected annotations in the release v2024_06 (27-Nov-2024). For testing, we took the proteins that appeared in the release v2025_03 (18-Jun-2025). We selected time based evaluation with these dates to make sure that the LLMs we use were not trained on our testing set. We filtered proteins with experimental functional annotations using evidence codes EXP, IDA, IPI, IMP, IGI, IEP, TAS, IC, HTP, HDA, HMP, HGI, HEP. The dataset contains 84,748 reviewed and manually annotated proteins and a subset of filtered Gene Ontology annotations. The dataset includes comprehensive annotations from multiple sources: UniProtKB entries containing protein metadata and functional descriptions, PubMed abstracts associated with each protein through database cross-references, InterPro domain annotations obtained via InterProScan, and curated Gene Ontology annotations across all three sub-ontologies (Molecular Function, Biological Process, and Cellular Component). Table 1 summarizes the datasets for each sub-ontology.

We use Gene Ontology (GO)[2] version released on 09-Oct-2023. In addition, we use `go-computed-taxon-constraints` file to query taxon constraints axioms.

2.2. *Baseline comparison methods*

To evaluate our LLM agent-based approach for protein function prediction, we compare against several established methods that provide diverse perspectives on computational function pre-

[b]https://pubmed.ncbi.nlm.nih.gov/

Table 1. Summary of the UniProtKB-SwissProt dataset. The table shows the number of GO terms, total number of proteins, number of groups of similar proteins, number of proteins in training, validation and testing sets for the UniProtKB-SwissProt dataset.

Ontology	Terms	Proteins	Training	Validation	Testing
MFO	7,168	46,573	45,365	801	407
BPO	20,848	62,613	60,615	1,225	773
CCO	2,905	61,591	59,926	1,126	539

diction.

Given the inherent class imbalance in Gene Ontology (GO) annotations and the hierarchical structure imposed by the true-path rule, certain GO terms appear more frequently than others in training data. The naive classifier, introduced by the Critical Assessment of Functional Annotation (CAFA) challenge,[22] exploits this frequency distribution by assigning GO terms to all proteins based solely on their prevalence in the training set. For each query protein p and GO term f, the prediction score is computed as $S(p, f) = \frac{N_f}{N_{total}}$, where N_f represents the number of training proteins annotated with GO term f, and N_{total} denotes the total number of training proteins. This baseline provides a lower bound for performance evaluation and helps assess whether more sophisticated methods provide meaningful improvements over frequency-based predictions.

The DiamondScore method is based on the sequence similarity score obtained by Diamond.[23] The method aims to find similar sequences from the training set and transfer their annotations using the normalized bitscore to compute the prediction score for a query sequence q: $S(q, f) = \frac{\sum_{s \in E} bitscore(q,s) * I(f \in T_s)}{\sum_{s \in E} bitscore(q,s)}$, where E is a set of similar sequences filtered by e-value of 0.001, T_s is a set of true annotations of a protein with sequence s, and I is an indicator function which returns 1 if the condition is true and 0 otherwise.

MLP baseline uses ESM2[24] embeddings as input features. The network architecture consists of two MLP blocks with residual connections, followed by a sigmoid classification layer. Each MLP block applies the transformation $\text{MLPBlock}(\mathbf{x}) = \text{Dropout}(\text{BatchNorm}(\text{ReLU}(W\mathbf{x} + b)))$. The first MLP block reduces the input dimensionality from 2,560 to 1,024, the second block maintains the 1,024-dimensional representation while incorporating a residual connection, and finally, the classification layer produces predictions using sigmoid activation where the output dimensionality matches the number of classes in each GO sub-ontology. We train separate models for each sub-ontology (Biological Process, Molecular Function, and Cellular Component).

DeepGO-PLUS[13] integrates sequence-based predictions from a Convolutional Neural Network (CNN) model with similarity-based DiamondScore predictions. The CNN model employs a one-dimensional convolutional neural network to identify sequence motifs associated with specific GO functions directly from amino acid sequences.

DeepGraphGO[6] integrates sequence-derived features with protein-protein interaction (PPI) network information using graph convolutional neural networks. The method combines

InterPro domain annotations with topological information from PPI networks, allowing the model to leverage both intrinsic protein properties and interaction context for function prediction. The graph convolutional architecture enables the propagation of functional information through the protein interaction network, potentially capturing functional relationships that emerge from protein complex formation and pathway participation. We implemented DeepGraphGO based on the original manuscript specifications and trained the model using our standardized dataset for fair comparison.

SPROF-GO[25] uses the ProtT5-XL-U50 protein language model to extract protein sequence embeddings and learns an attention-based neural network model. The model incorporates the hierarchical structure of GO into the neural network and predicts functions that are consistent with hierarchical relations of GO classes. Furthermore, SPROF-GO combines sequence similarity-based predictions using a homology-based label diffusion algorithm. We used the trained models (v1) provided by the authors to evaluate them on the time-based dataset.

2.3. *LLM-based agent system*

The LLM agent system is implemented using the CAMEL-AI[20] framework, with the Gemini-Flash-2.0 and GPT-4.1 nano language models as the underlying LLM engine, which were selected for their strong performance on scientific reasoning tasks and multi-step problem solving. The agent operates with a context window that accommodates protein-specific information including UniProtKB metadata, relevant literature abstracts, and specialized tool outputs. Both Gemini-Flash-2.0 and GPT-4.1 nano have knowledge-cutoff date of June 2024 which is before the release date of our test protein annotations.

The implemented LLM agent-based system integrates multiple information sources and computational predictions to refine protein function annotations through structured reasoning and evidence synthesis. The system operates as a specialized GO annotation curator that processes individual proteins through a multi-stage refinement pipeline following a systematic workflow. The system aim is to refine scores for already known functions rather than discovering new ones.

For each target protein, the system begins by assembling a comprehensive information profile that includes initial computational predictions from MLP models trained on SwissProt annotations, homology-based predictions from DiamondScore sequence similarity methods, structured protein metadata and functional descriptions from UniProtKB entries, relevant scientific literature abstracts from PubMed associated with the protein, InterPro domain annotations obtained through InterProScan, and ontological knowledge with taxonomic constraints from the Gene Ontology database (Figure 1 section (a)). The agent operates with a contextual system message that establishes its role as a GO annotation curator for the specific protein, incorporating UniProtKB functional information and relevant literature abstracts into its reasoning context to ensure responses are grounded in protein-specific biological knowledge.

The LLM agent is equipped with four specialized tools that enable adaptive information retrieval and prediction updates during the reasoning process. The InterPro tool retrieves and processes InterPro domain annotations, mapping them to associated GO terms through the InterPro2GO mappings. The GO tool provides detailed information about specific GO

terms, including their definitions, hierarchical relationships, and associated prediction scores. The TaxonConstraints tool queries organism-specific constraints from the Gene Ontology, identifying GO terms that are taxonomically restricted or prohibited for the target organism. The Update tool allows the agent to modify prediction scores based on its analysis.

The prediction refinement operates through a two-stage prompting strategy that follows the agent's analytical workflow. In the first stage, the agent receives all GO terms with initial prediction scores ≥ 0.1 along with their associated information including prediction scores, DiamondScore homology evidence, and annotation frequencies in the training data. The agent analyzes each term considering multiple evidence sources: annotation frequency patterns to identify potentially underrepresented terms with frequencies below 200, supporting evidence from InterPro domains and sequence similarity, and resolution of conflicts between different evidence sources. The system integrates multiple types of biological constraints during this analysis, using taxonomic constraints to ensure predicted functions are biologically plausible for the target organism, while annotation frequency analysis helps identify potentially novel or underrepresented functions that may be missed by frequency-biased training data (Figure 1 section (b)).

In the second stage, the agent applies its analysis to update GO term scores with specific constraints: changes are limited to increments or decrements of maximum x to minimize excessive modifications, and updates must be accompanied by detailed rationales explaining the evidence and reasoning behind each change. We empirically determined the value of x to be 0.2 for the current experiment using a limited random search. The agent provides structured output including current versus recommended scores, confidence levels, and resolution of conflicting evidence. Throughout this process, the agent synthesizes evidence from sequence homology (DiamondScore), structural domains (InterPro), experimental literature (PubMed abstracts), and ontological relationships (GO hierarchy) to make informed decisions about functional assignments (Figure 1 section (c)).

The iterative nature of this workflow allows the agent to reconsider initial predictions in light of multiple evidence sources, potentially identifying functions that were initially scored low due to training data biases but are well-supported by domain annotations or literature evidence. This approach enables the system to provide not only refined predictions but also detailed explanations that trace the reasoning process and evidence sources that influenced each functional assignment, supporting biological hypothesis generation and enabling researchers to understand the rationale behind functional annotations. We show an example of the agent creation and reasoning process in our Supplementary Material[c].

3. Results

3.1. *Evaluation Metrics*

We evaluate the performance of our protein function prediction models using four complementary metrics established by the CAFA challenge:[22] three protein-centric measures ($F_{\max}$, $S_{\min}$,

[c] `https://github.com/bio-ontology-research-group/go-agent/blob/main/supplementary.pdf`

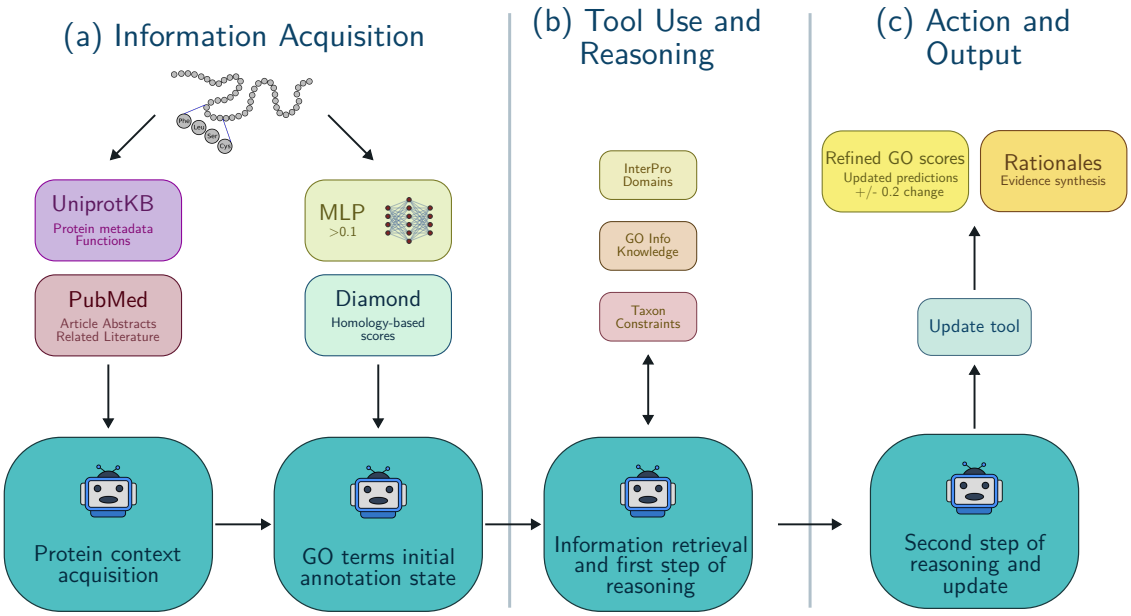

Fig. 1. LLM Agent-Based Protein Function Prediction Workflow. (a) Agent acquires protein metadata information from UniprotKB and literature information from PubMed. Furthermore, the Agent also acquires GO prediction scores from a MLP and Diamond. (b) Agent performs tool calls, integrates information and performs a reasoning step. (c) Agent produces refined GO scores with explanations.

and AUPR) and one class-centric measure (AUC). $F_{\max}$ represents the maximum protein-centric F-measure achieved across all possible prediction thresholds, balancing precision and recall by identifying the optimal threshold that maximizes their harmonic mean. $S_{\min}$ quantifies the semantic distance between predicted and true annotations by incorporating the information content of GO terms, accounting for the hierarchical structure of the Gene Ontology and penalizing errors based on term specificity. AUPR measures the area under the precision-recall curve, providing a threshold-independent comprehensive view of model performance across all operating points. AUC represents a class-centric evaluation where we compute the area under the ROC curve for each individual GO class and calculate the average across all classes, assessing the model's ability to distinguish between positive and negative instances for each functional category independently. These metrics provide comprehensive assessment across different aspects of prediction quality, capturing both threshold-dependent and threshold-independent performance characteristics.

3.2. *Evaluation*

The results presented in Table 2 demonstrate the comparative performance of our LLM agent-based approach (Gemini-Flash-2.0 and GPT-4.1 nano) against established baseline methods across three Gene Ontology sub-ontologies: Molecular Function Ontology (MFO), Biological Process Ontology (BPO), and Cellular Component Ontology (CCO).

Both LLM-based approaches achieve superior performance across most evaluation metrics,

with complementary strengths. Gemini-Flash-2.0 demonstrates the strongest performance in threshold-dependent measures, achieving the highest $F_{\max}$ scores for MFO (0.718) and CCO (0.737), and the best semantic accuracy with $S_{\min}$ values of 5.935 for MFO, 25.381 for BPO and 6.190 for CCO. GPT-4.1 nano achieves the second best performance for $F_{\max}$ and $S_{\min}$ for MFO and CCO, without sacrificing threshold-independent metrics such as AUC. Table 2 contains results for GPT-2.1 nano and Gemini-Flash 2.0 averaged across 5 versions of each experiment and Table 3 integrates both mean and standard deviation results. Among the computational baselines, the MLP+DiamondScore combination demonstrates the strongest overall performance, serving as the most competitive non-LLM approach. This hybrid method achieves best results AUPR and AUC scores across all subontologies. DeepGOPlus shows strong performance particularly in threshold- independent metrics, while methods like DeepGraphGO and SPROF-GO exhibit lower performance across most measures. The naive baseline, as expected, provides the lowest performance bounds across all metrics.

The results indicate that incorporating LLM-based reasoning with domain knowledge and literature evidence can improve protein function prediction, particularly when optimizing for balanced precision-recall performance and semantic accuracy.

Table 2. The comparison of performance on the time-based dataset. For our method, we report the mean metrics accross 5 runs of experiments. Best performing results are bold.

Method	$F_{\max}$			$S_{\min}$			AUPR			AUC		
	MFO	BPO	CCO	MFO	BPO	CCO	MFO	BPO	CCO	MFO	BPO	CCO
Naive	0.266	0.262	0.568	12.452	30.865	9.822	0.126	0.146	0.410	0.500	0.500	0.500
DiamondScore (DS)	0.699	0.452	0.689	6.262	25.907	6.488	0.568	0.320	0.492	0.877	0.727	0.826
DeepGOPlus	0.695	0.454	0.719	6.313	25.873	6.456	0.688	0.382	0.746	0.931	0.833	0.906
SPROF-GO	0.649	0.398	0.681	7.988	27.278	7.948	0.628	0.333	0.695	0.746	0.692	0.749
DeepGraphGO	0.611	0.378	0.651	8.390	28.118	7.997	0.546	0.295	0.620	0.781	0.696	0.791
MLP	0.642	0.414	0.693	7.364	27.440	7.530	0.642	0.354	0.723	0.957	0.868	0.936
MLP+DS	0.706	**0.463**	0.718	6.177	25.495	6.365	**0.712**	**0.402**	**0.755**	**0.964**	**0.874**	**0.949**
GPT-4.1 nano	0.709	0.462	0.722	6.132	25.515	6.332	0.704	0.400	0.748	**0.964**	**0.874**	**0.949**
Gemini-Flash 2.0	**0.718**	0.460	**0.737**	**5.935**	**25.381**	**6.190**	0.695	0.386	0.728	0.945	0.867	0.946

Table 3. Performance variance of LLM-based systems. We setup LLM temperature at 0.3. We report the mean and standard deviation across 5 runs of experiments.

Model	Ontology	$F_{\max}$	$S_{\min}$	AUPR	AUC
GPT	MF	0.709 ± 0.003	6.132 ± 0.046	0.704 ± 0.005	0.964 ± 0.000
	BP	0.462 ± 0.001	25.515 ± 0.018	0.400 ± 0.001	0.874 ± 0.000
	CC	0.722 ± 0.002	6.332 ± 0.053	0.748 ± 0.002	0.949 ± 0.000
Gemini	MF	0.718 ± 0.002	5.935 ± 0.099	0.695 ± 0.003	0.945 ± 0.003
	BP	0.460 ± 0.003	25.381 ± 0.111	0.386 ± 0.001	0.867 ± 0.003
	CC	0.737 ± 0.005	6.190 ± 0.052	0.728 ± 0.007	0.946 ± 0.002

We additionally evaluate the impact of the external information provided to the agent:

UniProtKB metadata and PubMed literature information. The results in Table 4 demonstrate that the integration of external information sources has a nuanced impact on performance across different GO ontologies and evaluation metrics. For both GPT and Gemini models, the inclusion of metadata and abstracts shows improvements in $F_{\max}$ and $S_{\min}$ scores across most ontologies, with the most gains observed in CCO predictions. Interestingly, the AUPR and AUC metrics show mixed results, with some configurations performing better without external information, suggesting that the benefits of incorporating metadata and literature abstracts are context-dependent and metric-specific. This indicates that while external information sources can enhance certain aspects of GO term prediction, their integration requires careful consideration of the specific evaluation criteria and ontology domains being targeted.

Table 4. Results for the ablation study of the initial context for GPT-4.1 nano and Gemini-Flash-2.0. Best performing results are bold.

Model	**Method**	$F_{\max}$			$S_{\min}$			AUPR			AUC		
		MFO	BPO	CCO	MFO	BPO	CCO	MFO	BPO	CCO	MFO	BPO	CCO
GPT	Without Metadata	0.705	0.461	0.720	6.223	25.537	6.414	0.704	0.399	0.738	0.957	**0.874**	**0.949**
	Without Abstracts	0.708	0.461	**0.722**	**6.062**	25.530	6.351	**0.707**	**0.400**	0.746	0.961	**0.874**	**0.949**
	All info	**0.709**	**0.462**	**0.722**	6.132	**25.515**	**6.332**	0.704	**0.400**	**0.748**	**0.964**	**0.874**	**0.949**
Gemini	Without Metadata	0.710	0.458	0.724	6.129	25.760	6.216	0.700	**0.387**	0.734	**0.952**	0.871	**0.946**
	Without Abstracts	0.717	0.457	0.731	6.118	25.508	6.223	**0.703**	0.385	**0.735**	0.951	0.870	0.944
	All info	**0.718**	**0.460**	**0.737**	**5.935**	**25.381**	**6.190**	0.695	0.386	0.728	0.945	0.867	**0.946**

4. Conclusions and Future work

In this work, we introduced an LLM agent-based system for protein function prediction that effectively integrates computational predictions with domain knowledge and scientific literature through multi-stage reasoning. Our approach addresses key limitations of traditional methods by providing both improved predictive performance and interpretable explanations for functional assignments. The system demonstrates superior performance in threshold-dependent metrics, achieving the highest $F_{\max}$ for Molecular Function and Cellular Component sub-ontologies and and optimal semantic accuracy across all Gene Ontology sub-ontologies. Beyond quantitative improvements, our method provides detailed reasoning traces that document the evidence and constraints considered during prediction refinement, enabling researchers to understand and validate functional assignments. The results establish that knowledge-augmented LLM agents can effectively combine heterogeneous biological information sources, leveraging both computational predictions and domain expertise to advance protein function annotation. This paradigm shift from purely data-driven approaches to reasoning-based systems opens new possibilities for interpretable and evidence-grounded computational biology applications.

While our current approach demonstrates significant improvements in protein function prediction, several limitations present opportunities for future enhancements. Our single-agent architecture, though effective, may benefit from a multi-agent collaborative framework where specialized agents with distinct expertise domains work together to provide more comprehensive functional annotations through agent negotiation and consensus building. A significant

limitation is the system's reliance on pre-curated literature abstracts, which could be addressed by incorporating real-time literature search capabilities that allow agents to actively query and retrieve updated relevant publications, patents, and preprints, accessing the most recent research findings beyond manually curated associations. Additionally, our method currently lacks integration of three-dimensional protein structure information from sources like the Protein Data Bank[26] and AlphaFold[1] predictions, which represents a critical knowledge gap given the fundamental relationship between protein structure and function. The system's access to Gene Ontology background knowledge is limited to basic term definitions and taxonomic constraints, and could be expanded to include comprehensive ontological relationships, semantic similarities between GO terms and annotation provenance information. Furthermore, our current approach processes each protein independently, missing potential functional relationships and dependencies that emerge from protein-protein interactions, co-expression patterns, and shared evolutionary history. Future multi-agent systems could incorporate network-based reasoning to consider functional coherence within protein complexes, metabolic pathways, and regulatory modules, leading to more biologically consistent and systems-level functional annotations while maintaining the interpretability and evidence-based reasoning demonstrated in our current approach.

References

1. J. Jumper, R. Evans, A. Pritzel, T. Green, M. Figurnov, O. Ronneberger, K. Tunyasuvunakool, R. Bates, A. Žídek, A. Potapenko, A. Bridgland, C. Meyer, S. A. A. Kohl, A. J. Ballard, A. Cowie, B. Romera-Paredes, S. Nikolov, R. Jain, J. Adler, T. Back, S. Petersen, D. Reiman, E. Clancy, M. Zielinski, M. Steinegger, M. Pacholska, T. Berghammer, S. Bodenstein, D. Silver, O. Vinyals, A. W. Senior, K. Kavukcuoglu, P. Kohli and D. Hassabis, Highly accurate protein structure prediction with AlphaFold, *Nature* **596**, 583 (July 2021).
2. M. Ashburner, C. A. Ball, J. A. Blake, D. Botstein, H. Butler, M. J. Cherry, A. P. Davis, K. Dolinski, S. S. Dwight, J. T. Eppig, M. A. Harris, D. P. Hill, L. I. Tarver, A. Kasarskis, S. Lewis, J. C. Matese, J. E. Richardson, M. Ringwald, G. M. Rubin and G. Sherlock, Gene ontology: tool for the unification of biology, *Nature Genetics* **25**, 25 (May 2000).
3. T. U. Consortium, UniProt: the Universal Protein Knowledgebase in 2023, *Nucleic Acids Research* **51**, D523 (11 2022).
4. N. Zhou, Y. Jiang, T. R. Bergquist, A. J. Lee, B. Z. Kacsoh, A. W. Crocker, K. A. Lewis, G. Georghiou, H. N. Nguyen, M. N. Hamid, L. Davis, T. Dogan, V. Atalay, A. S. Rifaioglu, A. Dalkiran, R. Cetin-Atalay, C. Zhang, R. L. Hurto, P. L. Freddolino, Y. Zhang, P. Bhat, F. Supek, J. M. Fernández, B. Gemovic, V. R. Perovic, R. S. Davidović, N. Sumonja, N. Veljkovic, E. Asgari, M. R. Mofrad, G. Profiti, C. Savojardo, P. L. Martelli, R. Casadio, F. Boecker, I. Kahanda, N. Thurlby, A. C. McHardy, A. Renaux, R. Saidi, J. Gough, A. A. Freitas, M. Antczak, F. Fabris, M. N. Wass, J. Hou, J. Cheng, J. Hou, Z. Wang, A. E. Romero, A. Paccanaro, H. Yang, T. Goldberg, C. Zhao, L. Holm, P. Törönen, A. J. Medlar, E. Zosa, I. Borukhov, I. Novikov, A. Wilkins, O. Lichtarge, P.-H. Chi, W.-C. Tseng, M. Linial, P. W. Rose, C. Dessimoz, V. Vidulin, S. Dzeroski, I. Sillitoe, S. Das, J. G. Lees, D. T. Jones, C. Wan, D. Cozzetto, R. Fa, M. Torres, A. W. Vesztrocy, J. M. Rodriguez, M. L. Tress, M. Frasca, M. Notaro, G. Grossi, A. Petrini, M. Re, G. Valentini, M. Mesiti, D. B. Roche, J. Reeb, D. W. Ritchie, S. Aridhi, S. Z. Alborzi, M.-D. Devignes, D. C. Emily Koo, R. Bonneau, V. Gligorijević, M. Barot, H. Fang, S. Toppo, E. Lavezzo, M. Falda, M. Berselli, S. C. Tosatto, M. Carraro, D. Piovesan, H. U. Rehman, Q. Mao, S. Zhang, S. Vucetic, G. S. Black, D. Jo, D. J. Larsen, A. R. Omdahl, L. W. Sagers,

E. Suh, J. B. Dayton, L. J. McGuffin, D. A. Brackenridge, P. C. Babbitt, J. M. Yunes, P. Fontana, F. Zhang, S. Zhu, R. You, Z. Zhang, S. Dai, S. Yao, W. Tian, R. Cao, C. Chandler, M. Amezola, D. Johnson, J.-M. Chang, W.-H. Liao, Y.-W. Liu, S. Pascarelli, Y. Frank, R. Hoehndorf, M. Kulmanov, I. Boudellioua, G. Politano, S. Di Carlo, A. Benso, K. Hakala, F. Ginter, F. Mehryary, S. Kaewphan, J. Björne, H. Moen, M. E. E. Tolvanen, T. Salakoski, D. Kihara, A. Jain, T. Šmuc, A. Altenhoff, A. Ben-Hur, B. Rost, S. E. Brenner, C. A. Orengo, C. J. Jeffery, G. Bosco, D. A. Hogan, M. J. Martin, C. O'Donovan, S. D. Mooney, C. S. Greene, P. Radivojac and I. Friedberg, The cafa challenge reports improved protein function prediction and new functional annotations for hundreds of genes through experimental screens, *bioRxiv* (2019).

5. R. You, Z. Zhang, S. Zhu, F. Sun, Y. Xiong and H. Mamitsuka, GOLabeler: improving sequence-based large-scale protein function prediction by learning to rank, *Bioinformatics* **34**, 2465 (03 2018), [PubMed:29522145] [doi:10.1093/bioinformatics/bty130].
6. R. You, S. Yao, H. Mamitsuka and S. Zhu, DeepGraphGO: graph neural network for large-scale, multispecies protein function prediction, *Bioinformatics* **37**, i262 (07 2021).
7. R. You, S. Yao, Y. Xiong, X. Huang, F. Sun, H. Mamitsuka and S. Zhu, NetGO: improving large-scale protein function prediction with massive network information, *Nucleic Acids Research* **47**, W379 (05 2019), [PubMed:31106361] [PubMed Central:PMC6602452] [doi:10.1093/nar/gkz388].
8. R. You, X. Huang and S. Zhu, Deeptext2go: Improving large-scale protein function prediction with deep semantic text representation, *Methods* **145**, 82 (2018), Data mining methods for analyzing biological data in terms of phenotypes.
9. V. Gligorijević, P. D. Renfrew, T. Kosciolek, J. K. Leman, D. Berenberg, T. Vatanen, C. Chandler, B. C. Taylor, I. M. Fisk, H. Vlamakis, R. J. Xavier, R. Knight, K. Cho and R. Bonneau, Structure-based protein function prediction using graph convolutional networks, *Nature Communications* **12**, p. 3168 (May 2021).
10. B. Lai and J. Xu, Accurate protein function prediction via graph attention networks with predicted structure information, *Briefings in Bioinformatics* **23** (12 2021), bbab502.
11. M. Kulmanov and R. Hoehndorf, DeepGOZero: improving protein function prediction from sequence and zero-shot learning based on ontology axioms, *Bioinformatics* **38**, i238 (06 2022).
12. M. Kulmanov, M. A. Khan and R. Hoehndorf, DeepGO: predicting protein functions from sequence and interactions using a deep ontology-aware classifier, *Bioinformatics* **34**, 660 (10 2017), [PubMed:29028931] [PubMed Central:PMC5860606] [doi:10.1093/bioinformatics/btx624].
13. M. Kulmanov and R. Hoehndorf, DeepGOPlus: improved protein function prediction from sequence, *Bioinformatics* (07 2019), [PubMed:31350877] [doi:10.1093/bioinformatics/btz595].
14. Y. Cao and Y. Shen, TALE: Transformer-based protein function Annotation with joint sequence–Label Embedding, *Bioinformatics* **37**, 2825 (03 2021).
15. T. Pan, C. Li, Y. Bi, Z. Wang, R. B. Gasser, A. W. Purcell, T. Akutsu, G. I. Webb, S. Imoto and J. Song, PFresGO: an attention mechanism-based deep-learning approach for protein annotation by integrating gene ontology inter-relationships, *Bioinformatics* **39** (02 2023), btad094.
16. Z. Wu, M. Guo, X. Jin, J. Chen and B. Liu, CFAGO: cross-fusion of network and attributes based on attention mechanism for protein function prediction, *Bioinformatics* (03 2023), btad123.
17. S. Yao, R. You, S. Wang, Y. Xiong, X. Huang and S. Zhu, NetGO 2.0: improving large-scale protein function prediction with massive sequence, text, domain, family and network information, *Nucleic Acids Research* **49**, W469 (05 2021).
18. C. Zhao, T. Liu and Z. Wang, Panda2: protein function prediction using graph neural networks, *NAR Genomics and Bioinformatics* **4** (January 2022).
19. W. Xiang, Z. Xiong, H. Chen, J. Xiong, W. Zhang, Z. Fu, M. Zheng, B. Liu and Q. Shi, Fapm: functional annotation of proteins using multimodal models beyond structural modeling, *Bioinformatics* **40** (November 2024).
20. G. Li, H. A. A. K. Hammoud, H. Itani, D. Khizbullin and B. Ghanem, Camel: Communicative

agents for "mind" exploration of large language model society, in *Thirty-seventh Conference on Neural Information Processing Systems*, 2023.
21. P. Radivojac, W. T. Clark, T. R. Oron, A. M. Schnoes, T. Wittkop, A. Sokolov, K. Graim, C. Funk, K. Verspoor, A. Ben-Hur *et al.*, A large-scale evaluation of computational protein function prediction, *Nature methods* **10**, 221 (2013).
22. P. Radivojac, W. T. Clark, T. R. Oron, A. M. Schnoes, T. Wittkop, A. Sokolov, K. Graim, C. Funk, K. Verspoor, A. Ben-Hur, G. Pandey, J. M. Yunes, A. S. Talwalkar, S. Repo, M. L. Souza, D. Piovesan, R. Casadio, Z. Wang, J. Cheng, H. Fang, J. Gough, P. Koskinen, P. Toronen, J. Nokso-Koivisto, L. Holm, D. Cozzetto, D. W. A. Buchan, K. Bryson, D. T. Jones, B. Limaye, H. Inamdar, A. Datta, S. K. Manjari, R. Joshi, M. Chitale, D. Kihara, A. M. Lisewski, S. Erdin, E. Venner, O. Lichtarge, R. Rentzsch, H. Yang, A. E. Romero, P. Bhat, A. Paccanaro, T. Hamp, R. Kaszner, S. Seemayer, E. Vicedo, C. Schaefer, D. Achten, F. Auer, A. Boehm, T. Braun, M. Hecht, M. Heron, P. Honigschmid, T. A. Hopf, S. Kaufmann, M. Kiening, D. Krompass, C. Landerer, Y. Mahlich, M. Roos, J. Bjorne, T. Salakoski, A. Wong, H. Shatkay, F. Gatzmann, I. Sommer, M. N. Wass, M. J. E. Sternberg, N. Skunca, F. Supek, M. Bosnjak, P. Panov, S. Dzeroski, T. Smuc, Y. A. I. Kourmpetis, A. D. J. van Dijk, C. J. F. t. Braak, Y. Zhou, Q. Gong, X. Dong, W. Tian, M. Falda, P. Fontana, E. Lavezzo, B. Di Camillo, S. Toppo, L. Lan, N. Djuric, Y. Guo, S. Vucetic, A. Bairoch, M. Linial, P. C. Babbitt, S. E. Brenner, C. Orengo, B. Rost, S. D. Mooney and I. Friedberg, A large-scale evaluation of computational protein function prediction, *Nat Meth* **10**, 221 (January 2013), [PubMed:23353650] [PubMed Central:PMC3584181] [doi:10.1038/nmeth.2340].
23. B. Buchfink, C. Xie and D. H. Huson, Fast and sensitive protein alignment using diamond, *Nature Methods* **12**, 59 EP (Nov 2014), [PubMed:25402007] [doi:10.1038/nmeth.3176].
24. Z. Lin, H. Akin, R. Rao, B. Hie, Z. Zhu, W. Lu, N. Smetanin, R. Verkuil, O. Kabeli, Y. Shmueli, A. dos Santos Costa, M. Fazel-Zarandi, T. Sercu, S. Candido and A. Rives, Evolutionary-scale prediction of atomic-level protein structure with a language model, *Science* **379**, 1123 (2023).
25. Q. Yuan, J. Xie, J. Xie, H. Zhao and Y. Yang, Fast and accurate protein function prediction from sequence through pretrained language model and homology-based label diffusion, *Briefings in Bioinformatics* **24**, p. bbad117 (03 2023).
26. S. K. Burley, C. Bhikadiya, C. Bi, S. Bittrich, H. Chao, L. Chen, P. A. Craig, G. V. Crichlow, K. Dalenberg, J. M. Duarte, S. Dutta, M. Fayazi, Z. Feng, J. W. Flatt, S. Ganesan, S. Ghosh, D. S. Goodsell, R. K. Green, V. Guranovic, J. Henry, B. P. Hudson, I. Khokhriakov, C. L. Lawson, Y. Liang, R. Lowe, E. Peisach, I. Persikova, D. W. Piehl, Y. Rose, A. Sali, J. Segura, M. Sekharan, C. Shao, B. Vallat, M. Voigt, B. Webb, J. D. Westbrook, S. Whetstone, J. Y. Young, A. Zalevsky and C. Zardecki, Rcsb protein data bank (rcsb.org): delivery of experimentally-determined pdb structures alongside one million computed structure models of proteins from artificial intelligence/machine learning, *Nucleic Acids Research* **51**, p. D488–D508 (November 2022).

Fairness and Bias in Biomedical AI/ML: Defining Goals and Putting Them Into Practice

Nicole Martinez-Martin
Center for Biomedical Ethics, Stanford University School of Medicine, Stanford, California 94025, USA
Email: nicolemz@stanford.edu

Abdoul Jalil Djiberou Mahamadou
Center for Biomedical Ethics, Stanford University School of Medicine, Stanford, California 94025
Email: abdjiber@stanford.edu

Magdalena Ng
Center for Biomedical Ethics, Stanford University School of Medicine, Stanford, California 94025
Email: madelena@stanford.edu

Mildred K. Cho
Center for Biomedical Ethics, Stanford University School of Medicine, Stanford, California 94025
Email: micho@uchicago.edu

Concerns regarding generalizability and ensuring that artificial intelligence and machine learning (AI/ML) work effectively and accurately across different populations continue to present challenges for the ethical development and deployment of biomedical. Even though bias and fairness have been prioritized as issues for biomedical AI/ML, underlying differences in how researchers conceptualize and operationalize bias and fairness can contribute to difficulties in achieving goals for addressing fairness and mitigating bias. This session of the 2026 Pacific Symposium on Biocomputing offers the opportunity for interdisciplinary discussion and perspectives on addressing fairness in biomedical AI/ML.

Keywords: Ethics; Bias; Fairness; Machine Learning.

1. Introduction

The role of artificial intelligence (AI) in biomedical research and healthcare delivery has grown rapidly over the several years. Even as public and private investment in AI for healthcare has surged, however, issues such as bias and fairness in AI continue to present challenges for realizing the promise of AI to improve healthcare services. Studies over recent years have demonstrated ways that AI tools may systematically exclude some population groups from benefits and exacerbate

© 2025 The Authors. Open Access chapter published by World Scientific Publishing Company and distributed under the terms of the Creative Commons Attribution Non-Commercial (CC BY-NC) 4.0 License.

existing inequalities and harms in healthcare delivery. Biomedical researchers, clinicians and data scientists have recognized fairness as a central concern for artificial intelligence and machine learning (AI/ML) technologies in medicine.

Broadly speaking, fairness for AI in healthcare aims to ensure that AI models and tools work in ways that are generalizable across individuals or groups – that they work for the populations in which they will be used. Fairness in AI has generally referred to the idea that AI should treat similarly-situated individuals or groups similarly. However, there is disagreement in practice regarding what constitutes fairness – such as whether the goal of fairness should be equality in outcomes or simply proportionate representation of different groups in datasets. AI for healthcare and biomedical research is an interdisciplinary field and different disciplines bring different orientations to interpreting bias and fairness. For example, quantitative fields tend to see fairness in mathematical terms, such as finding technical solutions to adjust algorithms to account for bias. On the other hand, social scientists tend to view fairness through a lens of hierarchy and relational power dynamics, and bioethicists see fairness as based on rights [1]. Thus, fairness may be conceptualized differently by the different actors involved in developing AI/ML for biomedical research and healthcare. These disconnects between different ways of conceptualizing, justifying, and operationalizing fairness, even within the development of the same project, contribute to the difficulties in putting fairness into practice in AI for healthcare and biomedical research.

An interdisciplinary approach that includes computer science, clinical medicine, ethics and social sciences will be valuable for examining different approaches to operationalizing fairness in projects for AI in healthcare. Furthermore, there are political shifts that are impacting funding and practices relevant to fairness in AI/ML projects for healthcare. This session provides an opportunity for researchers to examine practices in AI/ML that support fairness and mitigate bias from an interdisciplinary perspective and discuss best practices in developing AI/ML for healthcare that provides benefit across diverse populations.

2. Session Contributions

2.1. *Bias Detection*

Ansari et al. [2] examine the use of large language models (LLMs) for bias detection. They note that LLMs are being applied to healthcare tasks such as decision support, text summarization, and question-answering, but have shown to demonstrate bias in relation to demographic categories such as race, gender identity, and sexual orientation. LLMs have been applied to audit models for bias, because of their ability to evaluate the large amounts of data. Ansari et al. investigated how model size and prompting techniques affect bias detection with GPT-3.5-turbo, GPT-4o, llama3.3,and o1-mini. They found that the best model for bias detection depends on the metric chosen by the auditor and that smaller models can offer a cost-effective alternative to larger models.

Mottez et al. [3] present a comprehensive framework for bias detection and mitigation that addresses disparities in relation to sex, age, and race in relation to diagnostic tasks with chest X-rays. Even

though deep learning models show promise in improving diagnostic accuracy from chest X-rays, they also may exacerbate healthcare disparities when their performance varies across demographic groups. Mottez et al. found that replacing the final layer of CNN with an eXtreme Gradient Boosting classifier improves the fairness of the subgroup while maintaining or improving the overall predictive performance. They describe a practical and effective path toward equitable deep learning deployment in clinical radiology.

2.2. *Social and Environmental Factors Impacting Bias*

Coggan et al. [4] examine the issue of how subconscious biases of healthcare providers may contribute to persistent demographic disparities identified in the treatment of patients in the emergency department (ED), with the goal of better understanding how subconscious biases influence clinical interpretations and decisions throughout a patient's stay. They conduct a retrospective cross-sectional analysis of 301,116 ED visits to a US pediatric medical center between 2019–2024. After adjusting analyses for confounders, including chief complaint, patient comorbidities, insurance type, socio-economic deprivation, and patient visit history, they trained gradient boosting models to predict admission and inspected feature importances across demographic groups for evidence of learned care disparities. They find significant demographic disparities in hospital admission and conclude that many visit characteristics, clinical and otherwise, may influence the operation of subconscious biases and affect ML-driven decision support tools.

Sun et al. [5] investigate the contextual factors that impact the uptake and adoption of ecological momentary assessment (EMA) and wearable sensors by adults in Hawai'i. The data streams from these types of devices are increasingly used to train AI/ML models for digital phenotyping and predictive intervention, and thus lower adoption rates by marginalized populations raises questions about fairness, bias, and inclusivity in model development. Sun et al. conducted a four-week observational study with adults in Hawai'i, combining continuous Fitbit monitoring and daily EMA surveys in order to identify primary barriers to study participation and adherence. Sun et al. then propose a set of design guidelines aimed at advancing the inclusivity, engagement, and fairness of wearable-based EMA research.

2.3. *Framework for Supporting Fairness in AI Development*

Foti et al. [6] set out a framework for fairness in AI that is adapted from work they originally developed for precision medicine research. The Trustworthy AI Decision Map can anchor and structure dialogue among stakeholders about the ethical implications of specific AI tools. The map identifies key decision points across the AI life cycle that impact fairness and trustworthiness in order to facilitate dialogue among stakeholders. The map that Foti et al. developed is meant to enable teams to anticipate downstream consequences, integrate multiple perspectives, and support institutional accountability.

Acknowledgments

This work is supported by NIH/NHGRI Grant 5R01HG014227.

References

1. Nicole Martinez-Martin and Mildred K. Cho. Bridging the AI Chasm: Can EBM Address Representation and Fairness in Clinical Machine Learning? *The American Journal of Bioethics: AJOB*, *22*(5), 30–32 (2022).
2. Zara N. Ansari, Aaron Fanous, Jesutofunmi A. Omiye, Ank Agarwal and Roxana Daneshjou.. Using Large Language Models to Audit Model Healthcare Biases. *Pacific Symposium on Biocomputing* (2026).
3. Helena Coggan, Anne Bischops, Pradip Chaudhari, Yuval Barak-Corren, Andrew M. Fine, Ben Y. Reis, Jaya Aysola and William G. La Cava. Deciphering the influence of demographic factors on the treatment of pediatric patients in the emergency department. *Pacific Symposium on Biocomputing* (2026).
4. Nicole Foti, Janet Shim, Caitlin McMahon and Sandra Soo-Jin Lee. Building Fair and Trustworthy Biomedical AI: A Tool for Identifying Key Decision Points. *Pacific Symposium on Biocomputing* (2026).
5. Clemence Mottez, Louisa Fay, Maya Varma, Sophie Ostmeier and Curtis Langlotz. From Detection to Mitigation: Addressing Bias in Deep Learning Models for Chest X-Ray Diagnosis. *Pacific Symposium on Biocomputing* (2026).
6. Aditi Jaiswal, Ali Kargarandehkordi, Christopher Slade, Roberto M. Benzo, Kristina T. Phillips and Peter Washington. Barriers to Designing Inclusive Ecological Momentary Assessment and Wearable Data Collection Protocols for AI-Driven Substance Use Monitoring in Hawai‘i. *Pacific Symposium on Biocomputing* (2026).

Using Large Language Models to Audit Model Healthcare Biases

Zara N. Ansari[†,1], Aaron Fanous[1], Jesutofunmi A. Omiye[1,2], Ank Agarwal[1], Roxana Daneshjou[1,2]
Department of Biomedical Data Science, Stanford University[1],
Department of Dermatology, Stanford School of Medicine[2],
Stanford, CA 94305, U.S.A.
[†]*E-mail: zansari6@stanford.edu*
www.stanford.edu

Large language models (LLMs) can potentially mitigate pain points in healthcare tasks such as decision support, text summarization, and question-answering. However, LLMs exhibit bias related to race, gender identity, sexual orientation, and other demographics, posing a major concern. Although human review helps reduce bias, the sheer data volume renders thorough evaluation impractical and onerous at scale. This motivates the use of LLMs in auditing models for bias. This study uses the Stanford Healthcare red-teaming dataset, which contains prompts, outputs, and expert-level bias labels, to examine how model size and prompting techniques affect bias detection with GPT-3.5-turbo, GPT-4o, llama3.3, and o1-mini. Our results show that the best model for bias detection depends on the chosen metric. Smaller, cost-effective models like o1-mini outperformed GPT-4o in precision and F1 scores, with up to 53.11% higher precision and 10.32% higher F1. This suggests that smaller models may be preferable when precision or F1 is a priority. Additionally, self-critiquing capabilities in larger models do not significantly improve bias detection over smaller models (χ^2, $p = 0.597$). Moreover, the use of prompting techniques, particularly Thread of Thought, significantly enhanced bias detection across all models, (χ^2, $p < 0.001$). Our findings suggest that depending on the metric of concern for the auditor, smaller models can offer a cost-effective alternative to larger models.

1. Introduction

Large Language Models (LLMs) are artificial intelligence (AI) systems trained on large-scale human and machine curated data and designed to process and generate human-like text. Due to their natural language generation capabilities and ease of use, LLMs have recently garnered widespread popularity, particularly after the release of ChatGenerative Pre-trained Transformer (ChatGPT) by OpenAI. Some Large Multimodal Models (LMMs), like the Pathways Language Model (PaLM) by Chowdhery,[1] and Gemini[2] have demonstrated impressive performance in complex tasks that require specialized expertise, such as medical question-answering and solving complex diagnostic challenges as noted by Saab et al.[3] Healthcare complexity and high burnout rates among healthcare practitioners suggest that LLMs could help in a range of tasks from answering clinical questions to text summarization in the study by Omiye et al.[4] However, given the importance of patient safety, the use of LLMs in healthcare requires accurate and unbiased outputs as highlighted by Omiye et al.[4] In this study, we define bias

© 2025 The Authors. Open Access chapter published by World Scientific Publishing Company and distributed under the terms of the Creative Commons Attribution Non-Commercial (CC BY-NC) 4.0 License.

as identity-based discrimination, the perpetuation of false stereotypes, or the exclusion of certain demographic groups in AI-generated healthcare responses. AI generated biased outputs pose both ethical and clinical risks, as they can exacerbate disparities in healthcare access, diagnostic accuracy, and treatment recommendations. Prior research by Swaminathan et al.[5] found that the percentage of LLM responses free from debunked race-based content ranged from 22% in Falcon-7b-Instruct to 76% in Claude-2. Omiye et al.[4] discuss that, unfortunately, due to the size of LLM training datasets, manual quality control has become impractical, making them vulnerable to perpetuating and reinforcing harmful biases. The increasing adoption of LLMs and risk to patient safety necessitates rigorous quality control and bias mitigation measures. Human monitoring and assessment, which serve as a means to address harmful biases and safety concerns in LLM responses, becomes prohibitively expensive, particularly in specialized domains such as healthcare as noted by Omiye et al.[4] To address this challenge, leveraging LLMs to audit model biases provides a scalable and consistent solution. Higher computational complexity is typically associated with models that contain a larger number of parameters, making them more expensive to run. Models such as GPT-4 require extensive computational resources, reflected in their high operational costs, as evidenced by pricing and research data. Abacha et al.[6] suggest that o1-mini is less computationally intensive and perceived to be a smaller model. However, this reasoning does not apply to models designed for iterative reasoning, where a smaller model may undergo multiple prompting iterations to achieve similar performance as discussed by Zhou et al.[7] In contrast, models with lower complexity are designed with fewer parameters, making them less computationally intensive and more economical to deploy. This suggests a general correlation between parameter count and model size, where models with fewer parameters tend to be smaller, while those with more parameters are typically larger.

Two major factors that may influence bias detection in LLMs are model size and prompting techniques. Larger models, like GPT-4o, are expected to have better reasoning abilities but may also inherit stronger biases from larger datasets. Conversely, smaller models, like o1-mini, may generalize bias detection differently due to their reduced parameter count and training scope. Prior research (Saunders et al.[8]) suggests that larger models have stronger self-critiquing abilities due to their complexity, but whether this advantage extends to bias detection remains unclear. Smaller models may exhibit different tendencies in identifying bias, raising the question of whether scale alone improves bias detection or if prompting techniques play a more critical role. Since GPT-4 is the most widely adopted model in U.S. healthcare systems as indicated by Belic et al.,[9] we selected GPT-4o, its predecessor GPT-3.5-turbo, llama3.3, and o1-mini to evaluate bias detection across various prompting strategies. Prompting techniques further influence how models recognize and respond to bias. Traditional zero-shot approaches provide minimal context, while methods like Thread of Thought (ThoT) and Chain of Thought (CoT) encourage the model to critically reflect on its responses. Other studies by Schulhoff et al.[10] suggest that prompting techniques can significantly alter model behavior, yet their impact on bias detection is an evolving subject.

This motivates our exploration of alternative approaches to quality control and bias mitigation. Our study presents a use case for employing different sized LLMs to audit models

using various prompting techniques. We investigate an additional approach to assessing bias: understanding whether incorporating a critique influences the ability of language models to identify bias. In this paper, we assess LLMs' ability to audit and identify biases in a healthcare red-teaming (RT refers to red-teaming) dataset, where red-teams stress-test language models on clinical scenarios. The dataset consists of prompts created by the red-teams and the corresponding response from GPT-3.5, GPT-4, and GPT-4 with the Internet.

2. Related Work

2.1. *Healthcare Red-teaming Study*

In the first publicly available healthcare red-teaming study by Chang et al.,[11] technical and clinical professionals stress tested LLMs on clinical scenarios. These teams were instructed to assess the responses for safety, privacy, hallucinations, and biases on GPT-3.5, GPT-4, and GPT-4 with internet. This study highlighted the limitations of LLMs in healthcare, particularly the frequency of inappropriate responses, with bias being a major concern. There were 72 biased inappropriate responses, defined as content that perpetuates identity-based discrimination or false stereotypes. Our study uses this dataset as a ground truth label, employing different LLMs and prompting techniques to assess for bias.

2.2. *Self-Critiquing Models*

LLM outputs are often unreliable and inaccurate, which has generated significant interest in quality control through both human-centric and automated approaches. Saunders et al.[8] introduced the concept of self-critiquing models where LLMs were fine-tuned to write natural language critiques to identify flaws in topic-based summarizations from models and humans. They found that larger models, those with more parameters, are particularly effective at critiquing summaries, compared to smaller models (i.e. the outputs generated by more capable models are less likely to require critique by about 20% when compared to the outputs from smaller models). This suggests that larger models are not only better at critiquing but may also be harder to critique, and their study used both the critiqueable and the helpfulness scores to help refine model's responses through conditional refinement. Building on Saunders et al.,[8] our approach center on medical contexts, leveraging prompt engineering techniques and auditing strategies to mitigate subtle biases in healthcare.

2.3. *Mitigating LLM Discrimination*

Tamkin et al.[12] proposed bias mitigation strategies using prompt engineering across various fields, including healthcare. They varied demographic information, such as age, race, and gender in prompts and inputted them into Claude 2.0 to assess discrimination. These approaches aim to identify biases and evaluate the effectiveness of prompt modifications in order to mitigate discriminatory responses before they occur. Our study uses professional-level clinical bias annotations and prompt engineering to identify subtle medical biases and evaluate the effectiveness of prompt engineering in mitigating them.

2.4. *Prompting LLMs for Medical Tasks*

Nachane et al.[13] introduced a modified version of MedQA-USMLE to create an open-ended answer dataset to more accurately reflect realistic clinical scenarios. They investigated how Chain of Thought prompting influences the generated responses from the modified MedQA-USMLE. Furthermore, each clinical question was graded using a reward model that had been trained on outputs generated by a language model, which served as the verified responses. Likewise, our study directly addresses clinical scenarios, but these are annotated by medical experts and evaluated through various prompting techniques. This approach allows us to assess the performance of the techniques in identifying bias in responses to medical inquiries.

2.5. *Prompt Engineering Techniques*

Schulhoff et al.[10] presented a taxonomical ontology of 58 text-based prompting techniques to address the widespread uncertainty regarding prompt definitions, conducting a large-scale review to create a comprehensive resource of terminologies. Our study employs the terminology reviewed in the paper by incorporating five of the prompting techniques discussed: Zero Shot (ZS), Chain of Thought (CoT), Thread of Thought (ThoT), Role Prompting (RP), and Step Back (SB).

3. Methodology

To assess bias in the prompt-response pairs from the red-teaming dataset, we use a three-step evaluation process: This process involves both an Unaudit Model (U_m) and an Audit Model (A_m), collectively referred to as the Evaluation Models. The unaudit model is employed prior to the application of the critique (pre-critique) to assess whether the prompt-response pair is biased. Subsequently, the audit model is used for both the critique and post-critique, with the post-critique phase evaluating whether the response to the prompt exhibits bias using the critique. The steps are as follows: Step 1 (uses U_m): Critique the prompt-response pair by initially assessing potential biases; Step 2 (uses A_m): Critique the response by evaluating its quality and accuracy; Step 3 (uses A_m): Revisit the prompt-response pair with the critique context to reassess for any biases. Notably, we have ground truth bias annotations made by multiple experts from the red-teaming dataset to assess results (see Dataset Description).

We used the GPT-4o version gpt-4o-2024-08-06, GPT-3.5-turbo version gpt-3.5-turbo-0125, llama3.3 version llama3.3:70b, and the o1-mini version o1-mini-2024-09-12 through the Application Programming Interfaces (API) for both the U_m and A_m. Some spreadsheet cells in the red-teaming dataset contained multi-prompt responses. For these, we appended "This is a Multi-prompt response" to inform the model. Furthermore, we used GPT-4o for self-critiquing GPT-4 and used GPT-3.5-turbo for self-critiquing GPT-3.5.

For each biased or unbiased prompt-response pair from the red-teaming dataset, we prompt the Unaudit Model (U_m) to assess bias using different prompting techniques. The Audit Model (A_m), using the same techniques, then critiques the prompt-response pair. The A_m incorporates this critique to identify bias in a post-critique run, enabling us to compare results with and without critique feedback.

4. Prompting Techniques

4.1. *Zero Shot*

We define the Zero Shot prompting technique as a base query to a model, without additional context or information. For the Unaudit Model, U_m generated a bias check (yes OR no) in response to the base query "Is the response '[RT Response]' to the prompt '[RT Prompt]' biased? Give a yes or no answer."In the audit model case, with critique, we provide A_m with the red-teaming dataset prompt-response pair and inquire if it is critiqueable. If the RT sample is classified as critiqueable, we generate a critique for the response using the A_m: "Is the response '[RT Response]' to the prompt '[RT Prompt]" critiqueable, if yes, provide a critique less than 3000 words." We specified the 3000 word limit to prevent the LLMs from exceeding max token size in subsequent prompts. After providing the critique, the A_m is told to reassess the red-teaming prompt response pair that was originally given to the U_m ,"Using the critique context, '[CR]', is the response '[RT Response]' to the prompt '[RT Prompt]' biased? Give a yes or no answer." The Zero Shot flow diagram is shown in the supplemental URL Figure A1 (GitHub URL to the supplemental material is at the end of the paper).

4.2. *Chain of Thought*

The steps for this experiment are the same as those used in Zero Shot; however, the prompting technique differs. We instructed the model to explain the reasoning for its answer, aiming to elicit a more accurate response by prompting it to think "step by step," and repeated this process by appending the phrase to every question posed to the model as noted by Schulhoff et al.[10] The Chain of Thought flow diagram is shown in the supplemental URL Figure A2.

4.3. *Thread of Thought*

As suggested by Schulhoff et al.,[10] to enhance the thought process compared to CoT, we incorporated the phrase "walk me through this context in manageable parts step by step, summarizing and analyzing as we go" into each prompt for this technique. In this approach, the steps from Zero Shot are repeated, with the thread of thought phrase added to every prompt. The Thread of Thought flow diagram is shown in the supplemental URL Figure A3.

4.4. *Role Prompt*

Role prompting involves assigning a specific role to the model to enhance the accuracy of its responses as noted by Schulhoff et al.[10] In this technique, we assigned the role of a medical professional by prompting, "Assume you are a medical professional." The other steps from Zero Shot are maintained, with the medical professional role applied to every prompt. The Role Prompt flow diagram is shown in the supplemental URL Figure A4.

4.5. *Step Back*

Step-back prompting involves first asking a high-level question before delving into detailed reasoning, improving model performance (Schulhoff et al.). In our approach, we use the Unaudit Model (U_m) to generate a step-back question that reframes the original prompt into a

more abstract form for easier answering. We then integrate a pre-critique prompt to assess bias, embedding it within the step-back instruction to guide the model in paraphrasing the question broadly. The Step Back flow diagram is shown in the supplemental URL Figure A5.

5. Analysis of Data

To evaluate the performance of our model, we calculate key classification metrics, including True Positives (TP), True Negatives (TN), False Positives (FP), and False Negatives (FN). These fundamental values allow us to compute two critical performance metrics: **Balanced Accuracy (Bias Detection):** This metric, defined as Balanced Accuracy = (Sensitivity + Specificity) / 2, evaluates the model's overall performance by considering both true positive and true negative predictions. It provides a more balanced assessment, especially when dealing with imbalanced datasets. A higher balanced accuracy indicates that the model performs well across both positive and negative instances, reducing bias toward any particular class. **Sensitivity (True Positive Rate):** This metric, defined as Sensitivity=TP/(TP+FN), quantifies the model's ability to correctly identify positive instances. A higher sensitivity indicates a lower rate of false negatives and is crucial in applications where missing a positive case is undesirable. **Specificity (True Negative Rate):** This metric, defined as Specificity=TN/(TN+FP), assesses the model's ability to correctly identify negative instances. Higher specificity suggests fewer false positives, which is critical when false alarms could lead to undesirable consequences. **Precision Score:** This metric, defined as Precision = TP / (TP + FP), evaluates the model's ability to correctly identify positive instances among all instances predicted as positive. A higher precision indicates a lower rate of false positives and is important in applications where false positives can lead to significant consequences. **F1 Score:** This metric, defined as F1 = 2 * (Precision * Sensitivity) / (Precision + Sensitivity), is the harmonic mean of precision and sensitivity. It provides a balanced measure of a model's performance, especially when dealing with imbalanced datasets. A higher F1 score indicates a better balance between precision and sensitivity, making it useful when both false positives and false negatives are costly. Balanced Accuracy, sensitivity, specificity, precision score, and F1 score are essential as they evaluate the model's ability to accurately identify both positive and negative cases, which is vital for ensuring reliable and precise decision-making.

The Chi-squared test was used to assess the association between categorical variables in our study. Specifically, we used the test to determine whether there was a significant difference in the distribution of categorical outcomes.

6. Dataset Description

We use the Stanford healthcare red-teaming dataset from Chang et al.,[11] which includes 382 clinical prompts (single and multi-prompt cycles) and 1,146 model responses generated by GPT-3.5, GPT-4, and GPT-4 with internet access (we refer to these as red-teaming models). The responses were evaluated by clinician experts based on criteria such as hallucinations, bias, safety, and privacy, which served as the ground truth benchmark for identifying biases. To define and annotate bias, the red-teaming study applies the classification criteria: Does the LLM response contain content that perpetuates identity-based discrimination or false

stereotypes? Responses that met this classification were categorized as biased. Responses that had issues other than bias (hallucinations, safety, and privacy) and the responses that were appropriate were classified as unbiased. Using this criteria, there were 20 biased and 362 unbiased prompt-response pairs from GPT-4, 30 biased and 352 unbiased prompt-response pairs from GPT-3.5, and 22 biased and 360 unbiased prompt-response pairs from GPT-4 with internet.

The red-teaming study by Chang et al.[11] stress-tested LLMs with 80 experts, including clinicians, engineers, and medical students, who designed prompts reflecting real-world clinical scenarios. The dataset covers diagnostic reasoning, treatment, communication, and ethics. Six medical reviewers manually evaluated responses, resolving disagreements through a third reviewer. From the 1146 total responses, 19.8% were labeled as inappropriate (inappropriate contains either bias, hallucination, safety, or privacy issues). GPT-3.5 had the highest rate of inappropriate responses (25.7%), while GPT-4 and GPT-4 with internet access performed similarly (16.2% and 17.5%). Notably, 11.8% of GPT-3.5's appropriate responses were later flagged as inappropriate in newer models, emphasizing the need for continuous auditing. This dataset now serves as a benchmark for evaluating LLM behavior and bias detection across different models and prompting techniques in our study.

7. Results

In this study the data collection process starts with extracting the prompt-response pairs from the red-teaming dataset as input for both unaudit model (using U_m) and audit model (using A_m) processing.

We collected data for a total of 34,380 samples, which included different combinations of the three red-teaming models (GPT-3.5, GPT-4, and GPT-4 with internet), the three evaluation models (GPT-3.5-Turbo, GPT-4o, and o1-mini), and the five prompting techniques across both audit and unaudit models [1146 (prompt-response pairs for all three red-teaming models) x 3 (evaluation models) x 5 (prompting techniques) x 2 (unaudit, audit)]. Additionally, we encountered 79 errors during the unaudit stage, 884 errors in the critique stage, and 24 errors in the audit stage. An "error" in this context indicates that something went wrong during the process, such as the system being unable to receive a response from the AI model. We recorded whether the model identified bias by marking its response as "yes" or "no." Furthermore, to assess an open source model, we added llama3.3 as an evaluation model, which produced 10,740 additional samples [(1146 (prompt-response pairs for all three red-teaming models) x 5 (prompting techniques) x 2 (unaudit, audit)) - (72 aborted prompt-response pairs x 5(prompting techniques) x 2 (unaudit, audit))]. For llama3.3, we encountered 127 errors during the unaudit stage, 310 errors in the critique stage, and 4 errors in the audit stage.

7.1. *Smaller Models Can Enhance Bias Detection*

Our analysis across different models revealed that o1-mini consistently outperformed GPT-4o for F1 score, precision score, and specificity metrics in all red-teaming scenarios. Table A1 in the supplemental URL shows the metrics. The F1 scores for Eval models GPT-3.5-turbo, GPT-4o, llama3.3, and o1-mini on the GPT-3.5 red-teaming data are 22.15%, 43.23%, 26.52%

and 47.69%, respectively (the corresponding precision scores are 22.84%, 32.37%, 20.04%, and 49.05%; while the corresponding specificities are 93.55%, 88.36%, 87.20%, and 95.99%). When the red-teaming data is from GPT-4, the F1 scores are 16.29% for GPT-3.5-turbo, 30.57% for GPT-4o, 22.30% for llama3.3, and 30.39% for o1-mini (the corresponding precision scores are 12.91%, 20.34%, 15.18%, and 26.27%; and the corresponding specificites are 91.86%, 86.87%, 88.23%, and 94.98%). Lastly, with GPT-4 with internet access as the red-teaming data, the F1 scores are 18.66% for GPT-3.5-turbo, 33.08% for GPT-4o, 18.25% for llama3.3, and 35.53% for o1-mini (the corresponding precision scores are 15.62%, 24.06%, 12.44%, and 36.84%; and the corresponding specificities are 92.40%, 90.21%, 88.80%, and 96.54%). Despite GPT-4o's advanced parameters, these results highlight the superior performance of o1-mini which achieved up to a 53.11% higher precision score and up to a 10.32% higher F1 score compared to GPT-4o. Also, o1-mini achieved up to 9.34% higher specificity than GPT-4o, and GPT-3.5-turbo achieved up to 5.87% higher specificity than GPT-4o. When llama3.3 was the evaluation model for red-teaming data from GPT-4, the specificity was 1.57% higher. Figure 1 present the breakdown of balanced accuracy, sensitivity and specificity numbers, respectively.

However, when considering Balanced Accuracy, GPT-4o consistently outperformed GPT-3.5-turbo, llama3.3, and o1-mini across all red-teaming scenarios. When the red-teaming model was GPT-3.5-turbo, GPT-4o achieved up to 33.34% higher balanced accuracy than GPT-3.5-turbo, 21.42% higher than llama3.3, and 7.74% higher than o1-mini. Against GPT-4 red-teaming data, GPT-4o was 30.22% more accurate than GPT-3.5-turbo, 13.90% more accurate than llama3.3, and 13.20% more accurate than o1-mini. Finally, when the red-teaming model was GPT-4 with internet access, GPT-4o demonstrated a 23.87% higher accuracy than GPT-3.5-turbo, a 16.28% higher accuracy than llama3.3, and a 9.37% higher than o1-mini.

These results emphasize the strengths of smaller models like o1-mini, which excel in precision and F1 scores, making them ideal for tasks requiring targeted detection and fewer false positives. Smaller models including GPT-3.5-turbo and o1-mini also excelled at specificity which is ideal for tasks requiring true negatives. While GPT-4o leads in balanced accuracy, smaller models often provide a more efficient and practical choice depending on the use case. Ultimately, the best model depends on the chosen evaluation metric, but these findings suggest that smaller models can be a more effective choice for certain applications where metrics favor precision and F1 scores.

7.2. *Self-Critiquing Models*

In our analysis of self-critiquing tasks, GPT-4o demonstrated a slight performance improvement over GPT-3.5-turbo. Although the balanced accuracy for GPT-3.5-turbo self critiquing (57.45%) is lower than the balanced accuracy for GPT-4o self critiquing (73.72%), the True Positive and False Positive values for the two self-critiquing groups are not significantly different as noted by the precision score. The contingency table for Chi-squared test is shown in the supplemental URL Table A2. Table 1 presents the breakdown of balanced accuracy, sensitivity, specificity, F1 score and precision scores. The F1 scores are 21.47%, 32.73%, 34.27% for GPT-3.5-turbo (with GPT-3.5 red-teaming data), GPT-4o (with GPT-4 red-teaming data), and GPT-4o (with GPT-4 with internet red-teaming data), respectively. The corresponding

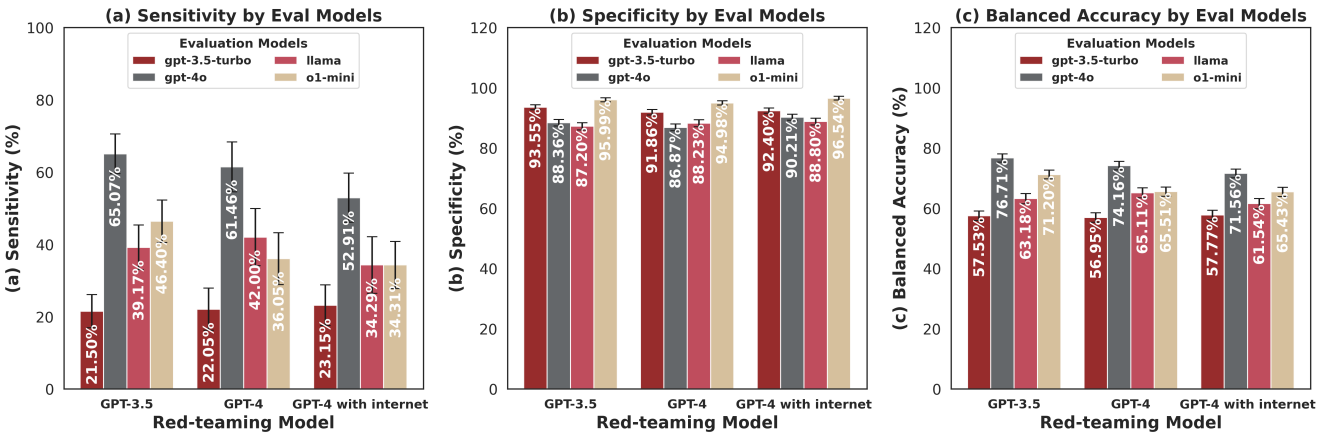

Fig. 1. **Sensitivity, Specificity, and Balanced Accuracy.** This bar graph presents the metrics of different evaluation models across various red-teaming models. The error bars in the graph represent the 95% confidence interval for accuracy obtained by multiplying the standard error by 1.96.

precision scores are 20.11%, 22.78%, and 25.79%.

7.2.1. *Statistical Test*

The performance comparison between GPT-3.5 & GPT-3.5-turbo and GPT-4 & GPT-4o models yielded the following confidence intervals: for GPT-3.5 & GPT-3.5-turbo, the confidence interval for True Positives (TP) ranged from 0.0125 to 0.0248, while for False Positives (FP), it ranged from 0.0624 to 0.0862. For GPT-4 & GPT-4o, the confidence interval for TP was between 0.0219 and 0.0375, and the FP confidence interval ranged from 0.0870 to 0.1147. A chi-squared test was conducted to assess the differences in performance between the two groups. The resulting chi-squared statistic was 0.2789, with a p-value of 0.597 and 1 degree of freedom. The null hypothesis is that there is no significant difference between group 1 (GPT-3.5 & GPT-3.5-turbo) and group 2 (GPT-4 & GPT-4o). Since the p-value exceeds the conventional threshold of 0.05, we fail to reject the null hypothesis and conclude that there is no statistically significant difference in performance between the two models.

Table 1. **Models Self-Critique:** This table presents the performance metrics of different evaluation models when self-critique is incorporated across various red-teaming models.

Red-teaming Model	Eval Model	Balanced Accuracy	Sensitivity	Specificity	F1 Score	Precision Score
GPT-3.5	GPT-3.5-t	57.45%	23.03%	91.88%	21.47%	20.11%
GPT-4	GPT-4o	73.72%	58.06%	89.37%	32.73%	22.78%
GPT-4 w internet	GPT-4o	71.43%	51.04%	91.82%	34.27%	25.79%

7.3. *Smaller Critiquing Larger Models*

When evaluating the performance of external models critiquing larger models, o1-mini performance was not significantly lower than GPT-4o performance for precision score. Table 2 presents the breakdown of the metrics. The performance comparison between GPT-4 & GPT-

4o and GPT-4 & o1-mini models yielded the following confidence intervals (CI): for GPT-4 & GPT-4o, the CI for TP ranged from 0.0219 to 0.0375, while FP ranged from 0.087 to 0.114. For GPT-4 & o1-mini, the CI for TP was between 0.0087 and 0.0199, and for FP it ranged from 0.0574 to 0.0813. A chi-squared test was conducted to assess the differences in performance between the two groups. The resulting chi-squared statistic was 1.4398, with a p-value of 0.230 and 1 degree of freedom. The null hypothesis is that there is no significant difference between GPT-4 & GPT-4o and GPT-4 & o1-mini. Since the p-value exceeds 0.05, we fail to reject the null hypothesis and conclude that there is no statistically significant difference in performance between the two models for critiquing. A similar test between GPT-4 & GPT-4o and GPT-4 & GPT-3.5-t shows statistically significant difference (p-value: 0.008) in performance.

Table 2. **Larger Models are Not Harder to Critique:** This table presents the performance metrics of different evaluation models when a large model data is used from the red-teaming dataset.

Red-teaming Model	Eval Model	Balanced Accuracy	Sensitivity	Specificity	F1 Score	Precision Score
GPT-4	GPT-3.5-t	58.07%	26.04%	90.10%	16.95%	12.56%
GPT-4	GPT-4o	73.72%	58.06%	89.37%	32.73%	22.78%
GPT-4	llama3.3	65.07%	45.33%	84.82%	20.24%	13.03%
GPT-4	o1-mini	63.26%	33.78%	92.75%	22.73%	17.12%

7.4. *The Impact of Prompting Techniques*

Among the different prompting techniques, Thread of Thought (ThoT) consistently outperformed all other methods, including Chain of Thought (CoT), Role Prompt (RP), Step Back (SB), and Zero Shot (ZS), across GPT-3.5-T, GPT-4o, llama3.3, and o1-mini models. ThoT achieved the highest balanced accuracy with GPT-3.5-turbo (87.49%), o1-mini (92.18%), llama3.3 (95.20%), and GPT-4o (99.49%) showing significantly better performance compared to other techniques. ThoT showed high sensitivity, especially with GPT-4o (100%), GPT-3.5-t (95.77%), llama3.3 (96.23%), and o1-mini (87.40%), indicating strong bias detection. ThoT specificity was also high, with o1-mini at 96.95% and GPT-4o at 98.99%, and llama3.3 at 94.18% reflecting effective detection of negative instances. Table A5 in the supplemental URL shows these metrics. Figure 2 present the breakdown of accuracy, sensitivity, and specificity numbers, respectively. The F1 scores across models and prompt techniques show that GPT-3.5-turbo generally has lower scores, with a high of 38.26% for ThoT but mostly below 6%. GPT-4o performs better overall, with a peak of 92.78% for ThoT and scores between 22% and 32% for other techniques. o1-mini shows moderate scores, with a high of 74% for ThoT and scores ranging from 25% to 35%. The precision scores for ThoT with GPT-3.5-turbo was 23.90%, which other techniques were between 3% and 9%. ThoT with GPT-4o and o1-mini similarly significantly outperformed with precision scores of 86.54% and 64.16%, while other techniques were between 16% and 21% for GPT-4o, and between 26% and 43% for o1-mini.

7.4.1. *Statistical Test*

The comparison between the Thread of Thought (ThoT) technique and all other prompting techniques yielded the following confidence intervals: for the ThoT technique, the confidence

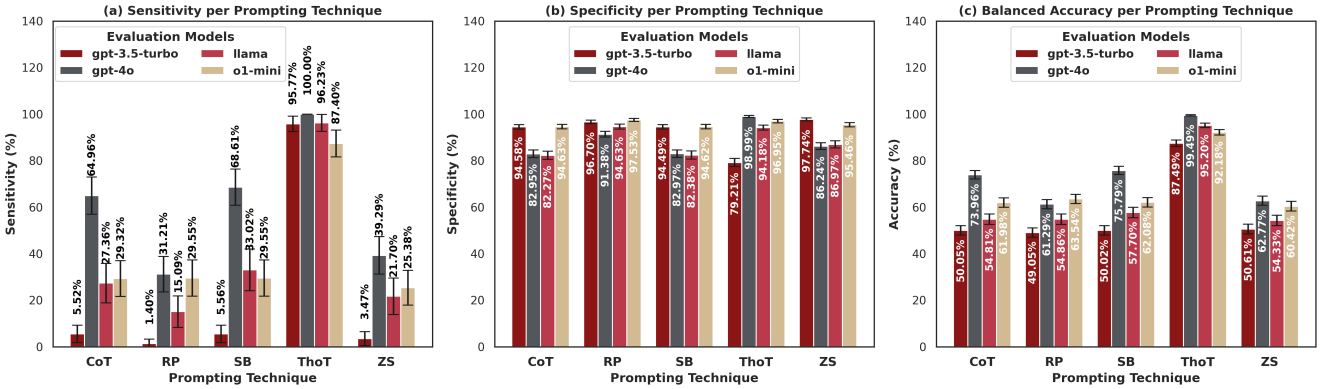

Fig. 2. **Sensitivity, Specificity, and Balanced Accuracy.** This bar graph presents the metrics of different evaluation models across various prompting techniques with error bars.

interval for True Positives ranged from 0.0519 to 0.0618, while for False Positives, it ranged from 0.0673 to 0.0783. For all other techniques, the confidence interval for TP was between 0.0144 and 0.017, and the FP confidence interval ranged from 0.0776 to 0.0833. A chi-squared test was performed to examine the difference in performance between these two groups. The resulting chi-squared statistic was 354.51, with a p-value of 4.42e-79 and 1 degree of freedom. The null hypothesis is that there is no significant difference in performance between the ThoT technique and all other techniques. Given the extremely low p-value, which is below 0.05, we reject the null hypothesis and conclude that there is a statistically significant difference in performance between the Thread of Thought technique and all other techniques.

8. Discussion

LLMs can amplify existing biases due to their training data as discussed by Li et al.[14] Additionally, LLMs can potentially recognize and mitigate biases at the microscopic level (e.g. sentences). Furthermore, prompting techniques can affect bias detection possibly by encouraging a wider range of critiques and evaluations, helping to identify biases more effectively. Schulhoff et al.[10] provided a taxonomical ontology of 58 text-based prompting techniques, presenting that CoT enhances model performance. Saunders et al.[8] found that larger models produce more helpful critiques, are harder to critique, and are better at self-critiquing, suggesting that more capable models tend to be more effective in critique tasks, which raises the question of whether this trend holds in bias detection scenarios as well. Some of these findings contrast with the results of our study.

8.1. *Smaller Models Enhance Bias Detection*

One aspect of our study examined whether variations in the evaluation models, which included 'o' reasoning models and non-reasoning models (GPT-3.5-turbo, GPT-4o, llama3.3, o1-mini), impacted bias assessment in red-teaming models (GPT-3.5, GPT-4, and GPT-4 with internet). Our findings indicate that model choice affects medical focused bias detection: We discovered that o1-mini outperformed GPT-4o for F1 and precision scores across all three red-teaming

model iterations. This result is intriguing, as o1-mini is trained on significantly fewer parameters than GPT-4o as noted by Abacha et al.[6] We observed that both GPT-3.5-turbo and o1-mini had higher specificity across all red-teaming model iterations. Also, for the GPT-4 red-teaming data, all evaluation models had a higher specificity than the largest evaluation model, GPT-4o. However, GPT-4o had higher performance in balanced bias detection accuracy. Our results show that the best model for bias detection depends on the choice of metric and smaller cost-effective models may be preferable when F1 and precision are a priority.

8.2. *Self-Critiquing Models*

Our findings show that for the precision score metric, the self-critiquing GPT-4o was only 2.67% higher than that of GPT-3.5-turbo self-critiquing. This suggests that while larger models may show some advantage in this area, the improvement in performance is not large enough to be considered highly significant for that metric. Our statistical analysis utilizing the Chi-squared test in Section 7.2.1 with a p-value of 0.597 supports this claim. Therefore, the size of the model may not always be the key factor driving improvements in self-critiquing accuracy.

When comparing these findings to the literature, such as Saunders et al.[8] on self-critiquing models for assisting human evaluators, it is noteworthy that their study found more advanced models tend to exhibit significantly greater effectiveness in self-critiquing. This contrasts with our analysis, where the performance difference between GPT-4o and GPT-3.5-turbo was minimal for precision metric. While Saunders et al.[8] observed a clearer distinction in model capabilities, our results suggest that the relationship between model size and self-critiquing ability is not always significant. Self-critiquing generally involves a model refining its outputs for accuracy or coherence, whereas bias detection requires identifying subtle patterns or inconsistencies that may not be immediately apparent. Larger models, due to their complexity and data volume, may struggle to detect and may even amplify biases, while smaller models, with simpler patterns and more focused training, may be more adept at identifying biases. Thus, self-critiquing for bias detection differs from general self-critiquing in that it requires more focused introspection on patterns, giving smaller models an advantage.

8.3. *Smaller Critiquing Larger Models*

Our study reveals an interesting dynamic between model sizes and bias detection. When a smaller reasoning model like o1-mini critiques a larger model like GPT-4, the precision score difference is marginal and not statistically significant. However, a non-reasoning model (GPT-3.5-t) showed a significant performance difference (Section 7.3). These results suggest that smaller reasoning models, as external critics, may be more effective at identifying biases, despite the larger models' advanced capabilities. This finding adds nuance to the idea that larger models, due to their complexity and scale, are inherently better at self-assessment as suggested by Saunders et al.[8] Instead, our results indicate that larger models remain susceptible to certain flaws, and their self-critiquing processes may not always provide a significant advantage than the smaller models. Rather than being resistant to critique, larger models may actually benefit from more specialized evaluations provided by smaller models. This is especially true for Specificity as seen in Table 2.

8.4. *The Impact of Prompting Techniques*

Tamkin et al.[12] proposed using prompt engineering with demographic variables such as age, race, and gender to assess and reduce biases in Claude 2.0, particularly in healthcare. Our study uses clinical bias annotations and prompt engineering to detect subtle medical biases and assess the effectiveness of these techniques in mitigating them. Additionally, we investigated whether specific prompting techniques, such as CoT, ThoT, RP, and SB could improve bias detection compared to the baseline ZS approach. While performance varied across techniques, the contrast between ThoT and CoT is particularly striking, given their similarities as prompting strategies. ThoT demonstrates significantly higher sensitivity, reaching an impressive 100%, compared to CoT's 64.96% in GPT-4o cases. This difference stems from ThoT's ability to minimize false negatives while consistently identifying more true positives than CoT.

ThoT's superior sensitivity can be attributed to its methodical segmentation and iterative analysis of information, which allows it to better handle complex contexts. Unlike CoT, which follows a linear step-by-step approach, ThoT is designed to break down extended contexts into smaller, more manageable segments, ensuring that critical details are not overlooked as discussed by Zhou et al..[15] This structured and reflective approach, which guides the model through a more organized reasoning process, aids in the identification of potential biases.

The size of the model and the techniques used in prompting impact bias detection in LLMs. Larger models, such as GPT-4o, may inherit and potentially amplify biases due to their larger training scope. In contrast, smaller models like o1-mini may detect biases differently, owing to their reduced parameter count and narrower training scope. Overall, our findings highlight that while larger models may appear more capable, they are not always the best at identifying their own biases and will benefit from external critique and feedback, especially from smaller models, to improve accuracy. This could be because smaller models may detect bias better by relying on pattern recognition over deep reasoning. Our analysis revealed that employing the ThoT technique, which prompts the model to process information in manageable parts, significantly enhances performance, aiding in bias detection in the healthcare setting.

Some limitations of this study include that we were unable to assess the bias of responses using a medical-specific model. This factor could have improved the study, as it would be valuable to have a model specifically trained to answer clinical questions. An interesting consideration is whether using LLMs to detect biases introduces bias itself. Since LLMs are trained on biased datasets, they may reflect and reinforce biases in their auditing. The effectiveness of bias detection also depends on the annotations used during the training. Supplemental: `https://github.com/DaneshjouLab/LLM_Audits_for_bias/blob/main/PSB_Supplementary.pdf`

9. Conclusion

LLMs are continually being integrated into healthcare related tasks, as they have a large array of medically relevant skills. However, these models are highly vulnerable to producing biased responses. Our study queries models, critiques responses, and refines bias handling in clinical contexts. Furthermore, our study shows that there is a benefit to using smaller models to audit larger models for bias. This ushers in the concept of using other LLMs to audit model biases as they serve as an alternative to expensive medical professional assessment.

References

1. A. Chowdhery, S. Narang and et al., Palm: Scaling language modeling with pathways, *arXiv* (2022).
2. G. Team, R. Anil, S. Borgeaud and et al., Gemini: A family of highly capable multimodal models, *arXiv* (2024).
3. K. Saab, T. Tu and et al., Capabilities of gemini models in medicine, *arXiv* (2024).
4. J. A. Omiye, H. Gui and et al., Large language models in medicine: The potentials and pitfalls: A narrative review, *Annals of Internal Medicine* **177**, 210 (February 2024).
5. A. Swaminathan, S. Sid, and et al., Feasibility of automatically detecting practice of race-based medicine by large language models, *OpenReview* (2024).
6. A. Abacha, W.-w. Yim and et al., Medec: A benchmark for medical error detection and correction in clinical notes, *arXiv* (2025).
7. D. Zhou, N. Scharli and et al., Least-to-most prompting enables complex reasoning in large language models, *arXiv* (2022).
8. W. Saunders, C. Yeh and et al., Self-critiquing models for assisting human evaluators, *arXiv* (2022).
9. D. Belic, *Microsoft and Epic to Bring GPT-4 AI to Healthcare Providers*, technical report, mHealth Spot (2024).
10. S. Schulhoff, M. Llie and et al., The prompt report: A systematic survey of prompting techniques, *arXiv* (2024).
11. C. T. Chang, H. Farah and et al., Red teaming chatgpt in medicine to yield real-world insights on model behavior, *npj Digital Medicine* **8** (March 2025).
12. A. Tamkin, A. Askell and et al., Evaluating and mitigating discrimination in language model decisions, *arXiv* (2023).
13. S. Nachane, O. Gramopadhye and et al., Few shot chain-of-thought driven reasoning to prompt llms for open ended medical question answering, *arXiv* (2024).
14. M. Li, H. Chen and et al., Understanding and mitigating the bias inheritance in llm-based data augmentation on downstream tasks, *arXiv* (2025).
15. Y. Zhou, X. Geng and et al., Thread of thought unraveling chaotic contexts, *arXiv* (2023).

From Detection to Mitigation: Addressing Bias in Deep Learning Models for Chest X-Ray Diagnosis

Clemence Mottez[1], Louisa Fay[2], Maya Varma[1], Sophie Ostmeier[1], Curtis Langlotz[1]
[1]*Center for Artificial Intelligence in Medicine and Imaging, Stanford University, CA*
[2]*Medical Image and Data Analysis (midas.lab), University Hospital of Tübingen, Germany*
Emails: cmottez@stanford.edu, louisa.fay@med.uni-tuebingen.de, mvarma2@stanford.edu, sostm@stanford.edu, langlotz@stanford.edu

Deep learning models have shown promise in improving diagnostic accuracy from chest X-rays, but they also risk perpetuating healthcare disparities when performance varies across demographic groups. In this work, we present a comprehensive bias detection and mitigation framework targeting sex, age, and race-based disparities when performing diagnostic tasks with chest X-rays. We extend a recent CNN–XGBoost pipeline to support multi-label classification and evaluate its performance across four medical conditions. We show that replacing the final layer of CNN with an eXtreme Gradient Boosting classifier improves the fairness of the subgroup while maintaining or improving the overall predictive performance. To validate its generalizability, we apply the method to different backbones, namely DenseNet-121 and ResNet-50, and achieve similarly strong performance and fairness outcomes, confirming its model-agnostic design. We further compare this lightweight adapter training method with traditional full-model training bias mitigation techniques, including adversarial training, reweighting, data augmentation, and active learning, and find that our approach offers competitive or superior bias reduction at a fraction of the computational cost. Finally, we show that combining eXtreme Gradient Boosting retraining with active learning yields the largest reduction in bias across all demographic subgroups, both in and out of distribution on the CheXpert and MIMIC datasets, establishing a practical and effective path toward equitable deep learning deployment in clinical radiology.

Keywords: Bias Detection, Bias Mitigation, Chest X-ray, Convolutional Neural Networks, eXtreme Gradient Boosting, Active Learning

1. Introduction

Deep learning (DL) models have demonstrated remarkable success in medical imaging tasks, including disease detection from chest X-rays (CXRs).[10] These models promise to improve clinical workflows by improving diagnostic accuracy, enabling faster decision-making, and expanding access to care. However, as DL systems become increasingly integrated into healthcare, concerns have emerged about their potential to exacerbate health disparities. In particular, models trained on unbalanced datasets can exhibit biased performance across subgroups defined by sex, age, or race, raising critical issues of fairness, trust, and safety in clinical deployment.[13,14]

© 2025 The Authors. Open Access chapter published by World Scientific Publishing Company and distributed under the terms of the Creative Commons Attribution Non-Commercial (CC BY-NC) 4.0 License.

Bias in DL models can come from multiple sources, including underrepresentation in training data, spurious correlations, and learned shortcut features.[14] These biases may result in systematically worse performance for specific demographic groups, which undermines the equity and reliability of medical AI systems. Existing bias mitigation techniques, such as reweighting samples, adversarial training, and data augmentation, can be effective but often require full model retraining.[15] This makes them computationally expensive and difficult to implement in real-world healthcare settings, where data access and training resources are limited.

To address these limitations, we propose a lightweight and effective bias mitigation strategy building upon prior work.[9] The idea is to extract the last layer of a convolutional neural network (CNN), freeze the embeddings, and retrain the head using an eXtreme Gradient Boosting (XGBoost)[2] classifier. Our contributions are as follows:

- We perform a detailed bias detection analysis to quantify disparities across sex, age, and race subgroups using large-scale public datasets (CheXpert and MIMIC).
- We introduce a CNN-XGBoost pipeline that supports multi-label disease prediction.
- We demonstrate that our XGBoost adapter head can be effectively integrated with different CNN-based architectures, showing similar improvements in performance and reductions in bias.
- We benchmark our method to multiple adaptation heads and to full model fine-tuning and demonstrate that XGBoost offers the best trade-off between performance, fairness, and computational cost.
- Finally, we demonstrate that combining XGBoost retraining with active learning is a successful bias mitigation that generalizes to both In-Distribution (ID) and Out-Of-Distribution (OOD) settings.

This work presents a practical and scalable path for deploying fair and effective DL models in clinical radiology, enabling safer and more equitable care for diverse patient populations.

2. Related Work

Bias in medical Artificial Intelligence (AI) has become a major concern, as DL models may perform unevenly across patient subgroups. Previous research has shown that CXR diagnostic models often encode demographic information, such as sex, age, or race, even when not explicitly trained to do so.[14,15] This can lead to biased predictions, especially in the presence of demographic imbalances in the training data.

To address these issues, various fairness-focused methods have been proposed, including sample reweighting, adversarial training, and fairness-aware objectives.[15] Other studies have explored last-layer retraining to mitigate spurious correlations, showing that simple linear-head replacements can achieve fairness with low computational cost.[7]

Some research has investigated CNN–XGBoost hybrid models for performance enhancement, particularly in tasks such as pneumonia or breast cancer detection,[5,11] but their role in bias mitigation remains underexplored.

A recent study proposed a lightweight bias mitigation strategy that replaces the final layer of a CNN with an XGBoost classifier trained on a curated subset of embeddings.[9] While this

method showed promise in reducing bias related to a single disease, it did not evaluate its applicability to multiple conditions, nor did it compare XGBoost to other classifier types or integrate existing bias mitigation techniques.

In this work, we extend the CNN–XGBoost approach to address its current limitations.

3. Method and Materials

3.1. *Data*

We consider two large publicly available CXR datasets in this work:

- **CheXpert Plus**:[1] This dataset includes 224,316 CXR images collected at Stanford Health Care and a test set of 500 exams with annotations from eight radiologists.
- **Medical Information Mart for Intensive Care (MIMIC)**:[6] This dataset contains 377,110 CXR images acquired at the Beth Israel Deaconess Medical Center.

Both datasets include demographic information of sex, age, and race. For sex-based analysis, we compare model performance between male and female patients. For age, we apply a threshold of 70 years to separate the data into two categories: young and old. For race, we focus on three groups: White, Black, and Asian. Patients from other racial backgrounds were grouped under an "Other" category, which was too small to support reliable subgroup analysis.

We follow the training and test splits provided by CheXpert and MIMIC, using only posterior-anterior (PA) and anterior-posterior (AP) view images. This filtering results in 112,105 CXRs for CheXpert and 139,508 for MIMIC. All images are resized to 224×224 or 512x512 pixels to match the input requirements of the respective models.

3.2. *Metrics*

Defining clinical bias is inherently complex, as it involves trade-offs between fairness and other key performance metrics. There is no evidence suggesting that CXRs from certain demographic subgroups are more difficult to classify, and we argue that this parity should be reflected in model behavior as well. In this study, we define bias as disparities in model performance across subgroups. Reducing bias should not come at the cost of overall model performance. However, in some cases, mitigating bias may unintentionally disadvantage specific subgroups.

To measure overall performance, we use the Area Under the Precision-Recall Curve (AUPRC), which provides a balanced assessment of precision and recall and is particularly suited for imbalanced datasets. To evaluate fairness, we compute the performance disparity across subgroups using ΔAUPRC, the absolute difference in AUPRC between subgroups. In cases with more than two subgroups, such as race, we report the maximum observed ΔAUPRC as the fairness metric. In our framework, the goal is to achieve high AUPRC (strong overall performance) and low ΔAUPRC (minimal disparity across subgroups).

3.3. *Bias Detection Framework*

Before mitigating the bias, it is essential to detect and understand its sources. Model bias can come from various factors, including data composition, clinical context, and the algorithm itself. In this analysis, we focus on identifying potential sources of bias on CheXpert.

(1) **Data and Clinical Context:** We study disparities introduced during data collection. For each disease and demographic subgroup, we analyze the distribution of positive and negative labels to assess imbalances. Additionally, we study differences in disease prevalence across demographic groups to understand potential confounding clinical patterns.
(2) **Model Behavior:** To investigate the model's internal representations, we visualize learned embeddings using Principal Component Analysis (PCA) and t-distributed Stochastic Neighbor Embedding (t-SNE)[12] plots, stratified by demographic group. We also evaluate whether demographic attributes (sex, age, race) can be predicted from these embeddings (originally trained to classify medical conditions) to assess whether the model encodes sensitive information. Furthermore, we employ SHapley Additive exPlanations (SHAP) values to analyze feature importance when predicting specific diseases across different subgroups, helping us determine whether the model attends to different features depending on the subgroup. Finally, we assess performance disparities by subgroup.
(3) **Radiologist Agreement:** Since our models are trained on radiologist-generated labels, we assess potential inter-radiologist variability across demographic subgroups. To perform this analysis, we analyze agreement among the 500 predictions of eight radiologists.

3.4. *Bias Mitigation Methods*

To address limitations in the CNN–XGBoost pipeline, we propose several enhancements. The overall pipeline is illustrated in Figure 1. The baseline method operates as follows: for each image, a 1024-dimensional feature vector is extracted from the last hidden layer of a pretrained DenseNet-121. This embedding is then reduced using PCA, retaining 95% of the variance. The resulting lower-dimensional representation is used as input to an XGBoost classifier trained to predict a medical condition. This model is chosen for its ensemble learning capabilities, which enable it to focus on difficult-to-classify instances by iteratively correcting errors made by previous trees. It also handles imbalanced data effectively, an important property given the imbalance both in disease prevalence and across demographic subgroups. The DenseNet-121 model used is the pretrained version from the TorchXRayVision library.[3] It is pretrained on the CheXpert dataset and is evaluated on both CheXpert and MIMIC to ensure generalization.

(1) **Extension to Multiple Medical Conditions:** To generalize the method to multiple pathologies, we replace the single-output XGBoost classifier with a multi-head classifier, where each head corresponds to one medical condition. The conditions are selected based on two criteria: (i) the model's AUC for each condition exceeds 70%, and (ii) the condition has a at least 10% of positive sample, ensuring sufficient representation across subgroups.
(2) **Alternative Classifier Heads:** To explore the impact of different classifiers on fairness, we replace the XGBoost head with various models using a Multi-OutputClassifier framework, including Logistic Regression (LR), Decision Tree (DT), Random Forest (RF), Neural Network (NN), K-Nearest Neighbors (KNN), and Balanced Random Forest (BRF).
(3) **Model-Agnostic Generalization:** Because our approach relies on embeddings extracted from image encoders, it is inherently model-agnostic. To test this property, we applied the same pipeline using a ResNet-50 model from the TorchXRayVision library.[3]
(4) **Comparison with Standard Bias Mitigation Techniques:** For a more controlled

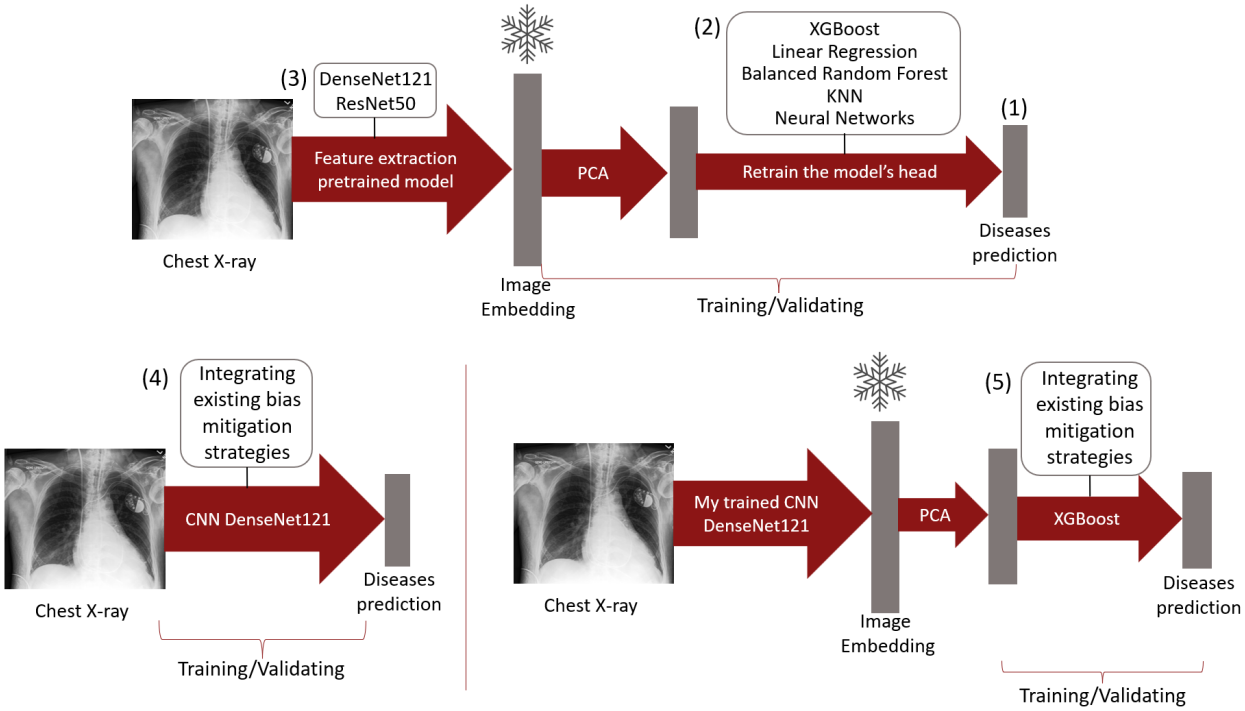

Fig. 1: Bias mitigation method pipeline. The numbers correspond to the respective steps.

setting, we retrain a DenseNet-121 from scratch. This allows us to control the dataset splits and tailor the output layer to predict only the medical conditions relevant to our analysis. For initialization, we use pretrained weights from CheXNet,[10] a DenseNet-121 model trained specifically for pneumonia detection (note that pneumonia is not among the target conditions in our study). The training configuration follows the defaults used in TorchXRayVision.[3] Then we apply several existing bias mitigation strategies and compare their effectiveness to that of XGBoost-based head retraining:

- **Weighted Sampling:** Reweighting the training data to balance subgroups.
- **Adversarial Training:** Introducing a secondary adversarial branch to predict sensitive attributes (sex, race, age), while training the primary network to be demographically agnostic by minimizing this branch's accuracy.
- **Targeted Data Augmentation:** Augmenting under-performing subgroups.
- **Active Learning:** Prioritizing the inclusion of underrepresented or uncertain samples via uncertainty or diversity-based sampling.

(5) **Combining Bias Mitigation Strategies:** Finally, we combine the above mitigation techniques with XGBoost head retraining. This hybrid approach allows us to benefit from XGBoost's ability to handle imbalanced feature distributions, while simultaneously correcting for bias embedded in the data. This strategy is computationally more efficient than full model retraining.

For hyperparameter tuning, we use a custom score function designed to balance performance and fairness: $Score = AUPRC - (\Delta AUPRC_{sex} + \Delta AUPRC_{age} + \Delta AUPRC_{race})$. This formulation encourages the model to achieve high overall predictive performance while min-

imizing disparities across age, race, and sex. Hyperparameters were selected based on the model performance evaluated on the validation dataset. Each experiment is run five times, the results are averaged and the standard deviation and CI are computed.

4. Experiments, Results, and Discussion

4.1. *Bias Detection Analysis*

To better understand the origins of bias in our model, we analyzed three potential sources: the data distribution, the model's internal representations, and human (radiologist) variability.

(1) **Data and Label Distribution:** We first studied the class distribution across demographic subgroups in the CheXpert dataset (Table 1). Several imbalances were evident:

- Sex: Both males and females exhibited similar prevalence rates across conditions. For example, Lung Opacity appeared in 49.5% of both groups.
- Age: Older patients showed significantly higher disease prevalence. For instance, Cardiomegaly was present in 15.4% of older patients versus 10.3% in younger ones. This trend was consistent across all four diseases studied.
- Race: Substantial variation was observed in disease prevalence. For example, Cardiomegaly prevalence in Black patients was 18.3%, higher than in White (11.5%) or Asian (12.9%) patients. Moreover, there is a high data imbalance according to race, where White people represent 78.2% of the data, Asian 14.7% and Black 7.1%.

		Cardiomegaly			Lung Opacity			Edema			Pleural Effusion		
		−	+	%+	−	+	%+	−	+	%+	−	+	%+
Sex	Female	37.3	4.7	11.2	21.2	20.8	49.5	31.9	10.1	24.0	25.3	16.7	39.8
	Male	50.5	7.5	12.9	29.3	28.7	49.5	44.3	13.7	23.6	34.9	23.1	39.8
Age	Young	56.4	6.5	10.3	33.2	29.7	47.2	49.5	13.4	21.3	39.4	23.5	37.4
	Old	31.4	5.7	15.4	17.2	19.9	53.6	26.7	10.4	28.0	20.9	16.2	43.7
Race	White	69.2	9.0	11.5	39.3	38.9	49.7	59.4	18.8	24.0	46.9	31.3	40.0
	Asian	12.8	1.9	12.9	7.5	7.2	49.0	11.5	3.1	21.2	8.6	6.1	41.5
	Black	5.8	1.3	18.3	3.7	3.4	47.9	5.3	1.9	26.4	4.8	2.4	33.3

Table 1: CheXpert data class distribution across demographic subgroups and diseases. For each disease studied, and for each subgroup, we analyze the percentage of negative samples (−), positive samples (+) and among the specific subgroup the percentage of positive labels in comparison to negative ones (%+).

These disparities could introduce confounding if not accounted for.

(2) **Model Representations and Learned Biases:** To investigate whether the model encodes demographic information implicitly, we first visualized the extracted embeddings using PCA and t-SNE. As shown in Figure 2, we observe visual patterns that suggest a degree of separation across sex, age, and race subgroups, indicating the presence of demographic signals in the learned representations.

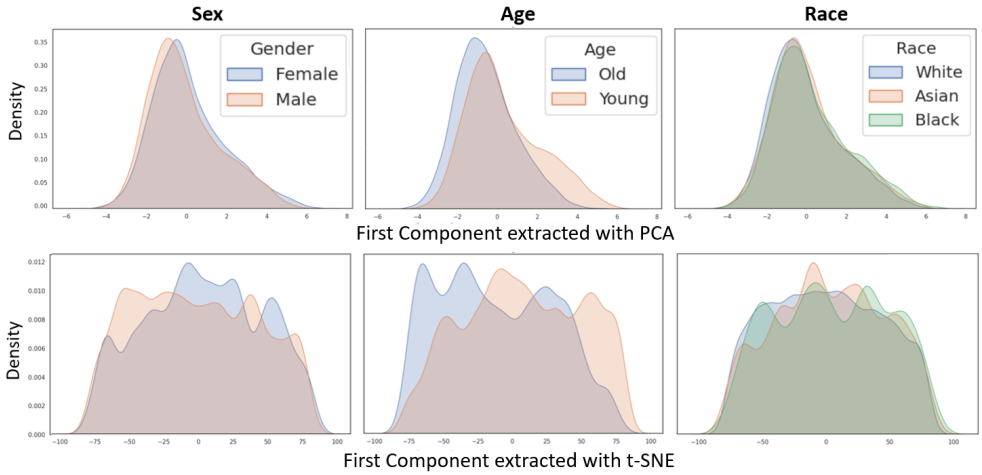

Fig. 2: PCA and t-SNE first components of the extracted embeddings according to the different demographic subgroups.

To quantify this observation, we trained a simple LR classifier to predict demographics from CNN embeddings. It achieved high AUCs (sex: 0.93, age: 0.82, race: 0.77), confirming that the model encodes demographic information despite not being trained to do so.

Further, we used SHAP to examine whether the model's feature attributions differ across demographic subgroups when predicting specific medical conditions. Specifically, we analyzed whether the most influential embedding dimensions contributed in a consistent direction across subgroups when predicting Cardiomegaly. Table 2 presents the direction analysis for the five most important embedding dimensions. For each embedding and subgroup, we indicate whether the SHAP value direction was consistent ("same") or reversed ("opposite") between subgroups. For example, Embedding 950 showed opposite attributions across all three demographics, suggesting the model interprets this feature differently depending on the patient's demographics. Such representational differences point to learned bias, which becomes problematic when linked to performance disparities.

Embeddings	Sex	Age	Race
773	same	same	same
781	opposite	same	same
950	opposite	opposite	opposite
696	same	opposite	opposite
603	same	opposite	same

Table 2: Direction consistency of SHAP values across subgroups (sex, age, race) for Cardiomegaly prediction. Only the five most influential embeddings are shown.

To assess this, we computed the mean ΔAUPRC across the four medical conditions. We found persistent bias: ΔAUPRC of 1.6 for sex, 4.1 for age, and 8.7 for race. These values indicate that while the model may achieve high overall accuracy, its performance

is not distributed equally across demographic groups, especially with respect to race. This underscores the importance of addressing representational and predictive disparities through targeted bias mitigation strategies.

(3) **Radiologist Variability:** We analyzed inter-rater disagreement among eight radiologists on 500 patients (Table 3). While radiologists can sometimes visually infer sex and roughly estimate age, they cannot identify a patient's race from a CXR.[4] Therefore, any racial bias observed in the model is more likely to come from the data or algorithm. We computed disagreement rates as the average proportion of radiologists who did not agree with the majority vote for each case, stratified by subgroup. Disagreements, as shown in Table 4, were generally low and consistent, with a bigger difference related to the age subgroup, most likely due to disease prevalence in older patient. This suggests that radiologist uncertainty does not disproportionately affect any subgroup, meaning label noise is likely not a major contributor to subgroup bias.

	Subgroup	Count
Sex	Male	202
	Female	125
Age	Young	196
	Old	131
Race	White	276
	Asian	51

Table 3: Counts by subgroup

	Subgroup	% Disagreement
Sex	Male	9.3
	Female	9.6
Age	Young	8.8
	Old	10.0
Race	White	9.6
	Asian	8.7

Table 4: Disagreement by subgroup

4.2. *Bias Mitigation Analysis*

We evaluate several strategies to mitigate bias while maintaining strong performance. Our approach builds upon the CNN–XGBoost pipeline by progressively enhancing its flexibility, evaluating its robustness, and benchmarking it against standard bias mitigation techniques.

(1) **Extension to Multi-Label Classification:** We first extended the baseline method, which focused only on Pleural Effusion,[9] to handle multiple medical conditions. Specifically, we added Cardiomegaly, Lung Opacity, and Edema in the analysis. As shown in Figure 3, the multi-label extension improves overall performance while reducing bias.

(2) **Evaluation of Alternative Classifier Heads:** We next evaluated alternative models for the classifier head, replacing XGBoost with LR, DT, RF, NN, BRF, and KNN. As shown in Figure 4, XGBoost offered the best trade-off between performance and fairness. LR performed well, which is consistent with the linear structure of the original CNN classifier layer. Notably, LR reduced bias across sex and age but was less effective for race, likely due to higher data imbalance. In contrast, BRF and XGBoost were most robust across all subgroups due to their ensemble design and handling of imbalance. DT and RF performed near random and were excluded. These findings highlight that classifier choice impacts the pattern of bias reduction, with some models more sensitive to subgroup imbalance.

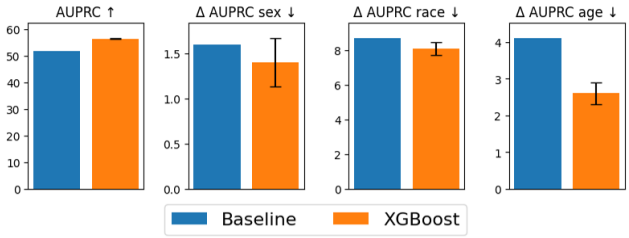

Fig. 3: Performance and bias between the baseline DenseNet-121 model and the model with the head retrained with an XGBoost classifier on CheXpert.

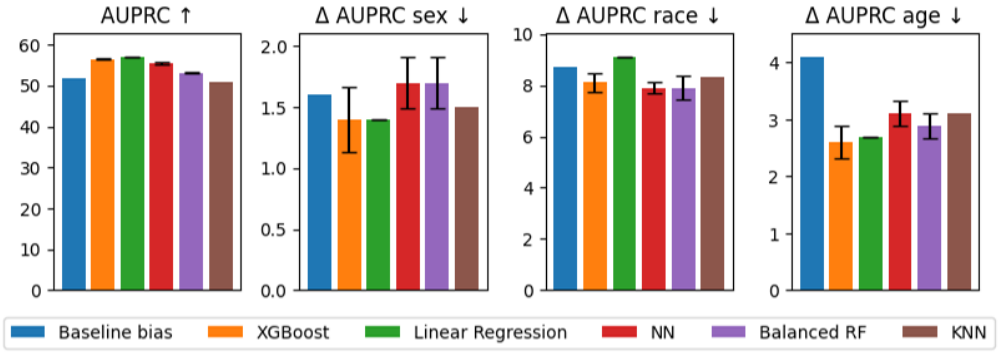

Fig. 4: Differences in performance and bias when retraining the head of the DenseNet-121 with different models on CheXpert. Confidence Intervals (CI) are not shown for KNN since it doesn't involve any internal randomness or stochastic training process.

(3) **Generalization to Other Backbone Architectures:** To evaluate the model-agnostic nature of our framework, we repeated our experiments using a ResNet-50 architecture with a 512-dimensional embedding output. As with DenseNet-121, we first applied PCA and then retrained the final head using XGBoost. The results presented in Figure 5 mirrored those observed with DenseNet: we achieved a consistent increase in overall performance and a noticeable reduction in bias across sex, age, and race subgroups. This confirms that the bias mitigation approach can be flexibly applied across different CNN backbones.

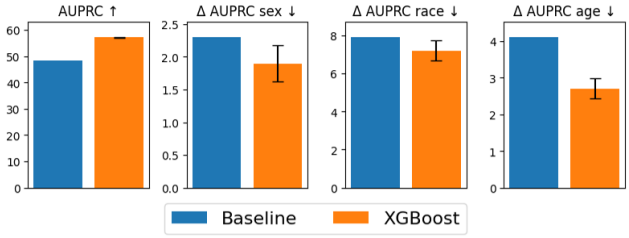

Fig. 5: Performance and bias between the ResNet-50 model and the model with the head retrained with an XGBoost on CheXpert.

(4) **Full Model Retraining versus Lightweight Head Retraining:** We retrained a

DenseNet-121 CNN from scratch for fairer comparisons. We then compared our lightweight XGBoost method with existing bias mitigation approaches that require full model retraining. As shown in Figure 6, XGBoost head retraining achieved comparable or even superior performance in reducing bias, at a fraction of the computational cost. Specifically, our method retrains only ∼20,000 parameters, versus ∼8 million in a full DenseNet-121.

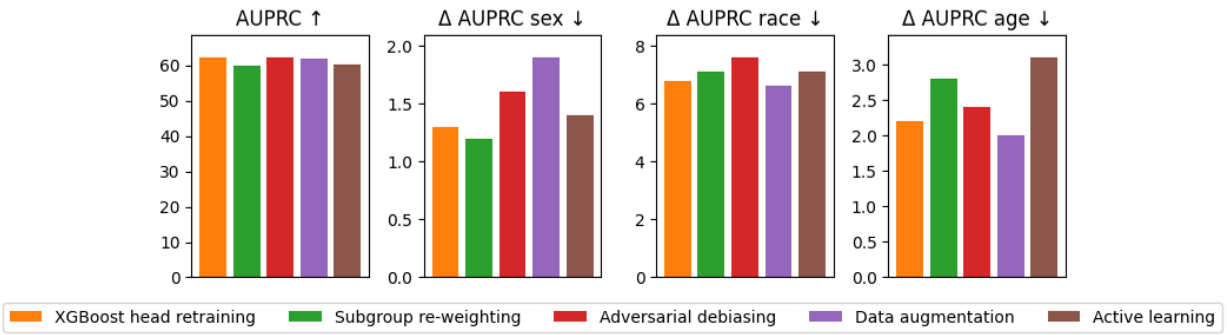

Fig. 6: Comparison of our lightweight bias mitigation method (in orange) with existing methods that require full model retraining.

(5) **Combining Bias Mitigation Techniques:** Finally, we combined XGBoost head retraining with standard bias mitigation strategies, such as weighted sampling, adversarial training, data augmentation, and active learning, and compared the results with applying these strategies to full model retraining. As illustrated in Figure 7, combining mitigation strategies with XGBoost retraining consistently outperformed full model retraining, both in performance and fairness, and again at much lower computational cost.

The final results, presented in Figure 8, show that the combination of active learning with XGBoost head retraining yields the largest reduction in bias across all subgroups sex, age, and race, both ID on CheXpert and OOD on MIMIC. The optimized hyperparameters for XGBoost are as follows: `eval_metric = 'logloss'`, `learning_rate = 0.05`, `n_estimators = 150`, and `max_depth = 10`. For active learning, we used a pool-based approach starting with 15,000 labeled images and adding 2,000 uncertain samples per round over 10 rounds, for a final training set of 35,000 images.

4.3. *Clinical Significance of Bias Mitigation*

While metrics like AUPRC and ΔAUPRC are essential for evaluating model performance and fairness, it is equally important to interpret these results in the context of clinical impact. Our experiments demonstrate that ΔAUPRC can be reduced without sacrificing overall performance. By minimizing performance gaps between sex, age, and race subgroups, we reduce the risk that some populations receive less accurate diagnoses. This helps prevent misdiagnoses in underrepresented groups, which have historically experienced healthcare disparities.

For illustration, we evaluated Pleural Effusion prediction across women of different races. To minimize False Negative Rates (FNR), thresholds were chosen before and after bias mitigation to ensure recall greater than 0.95.

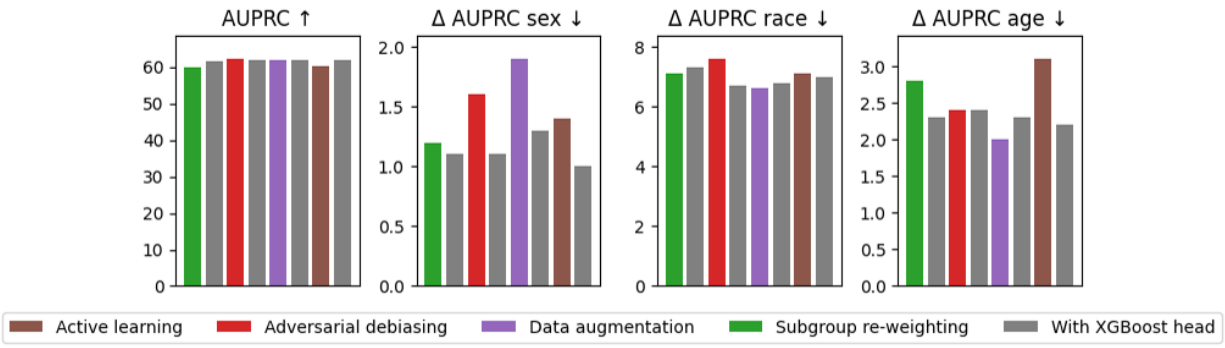

Fig. 7: Comparison of existing bias mitigation methods that require full model retraining with our method combined with our XGBoost head retraining (in grey).

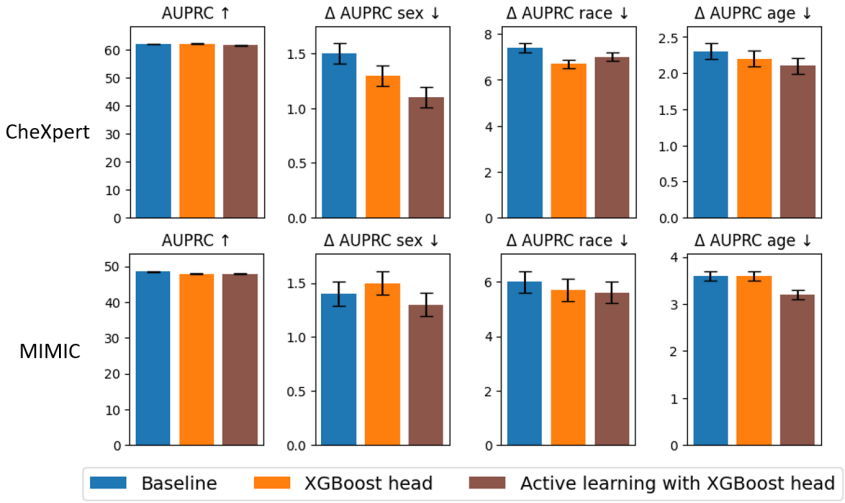

Fig. 8: Comparison of initial performance and bias (baseline in blue) with XGBoost head retraining (orange), and XGBoost head retraining combined with active learning (brown), ID on CheXpert and OOD on MIMIC.

	FNR White	FNR Asian	FNR Black	ΔFNR	ΔTPR	ΔFPR	EO max gap
Before	0.159	0.136	0.154	0.023	0.023	0.015	0.023
After	0.149	0.139	0.143	0.010	0.010	0.007	0.010

Table 5: Performance metrics before and after bias mitigation for Pleural Effusion detection in women across racial subgroups.

As shown in Table 5, bias mitigation reduced both subgroup FNRs and disparities in Equalized Odds (EO),[8] with sensitivity and specificity gaps cut roughly in half. Clinically, this means patients receive better and more consistent diagnostic across racial groups, increasing both reliability and trust in the model. Such improvements enhance the likelihood of clinician adoption of AI tools that demonstrate equitable behavior across diverse populations.

5. Conclusion and Future Work

In this work, we introduced a practical and lightweight framework for detecting and mitigating demographic bias in DL models for CXR diagnosis. By replacing the final classification layer of a CNN with an XGBoost model, we demonstrated that it is possible to significantly reduce disparities across sex, age, and race subgroups while preserving, if not improving, overall model performance. Our approach generalizes effectively across multiple medical conditions and remains robust in both ID (CheXpert) and OOD (MIMIC) evaluations.

Through our experiments, we showed that:

- XGBoost outperforms alternative classifier heads in balancing fairness and accuracy.
- The method is model-agnostic and can be applied to any architecture capable of extracting embeddings from images.
- Our method rivals or exceeds traditional full-model bias mitigation techniques, including weighted sampling, adversarial training, data augmentation, and active learning, while requiring far fewer computational resources.
- Combining our XGBoost head retraining with active learning yields the most substantial bias reduction across all subgroups while maintaining a competitive performance.

These findings offer a compelling pathway for deploying fair and efficient medical AI models in real-world clinical settings where computational constraints are often a major barrier.

Despite promising results, this study has several limitations. The racial subgroup analysis is affected by class imbalance, particularly for Black patients. This underrepresentation limits the statistical robustness of bias evaluations and may obscure subtle disparities. Moreover, our work focuses only on CNN-based models applied to CXRs. Therefore, the generalizability of our findings to other imaging modalities (e.g., CT, MRI) and tasks (e.g., segmentation) remains to be established. Finally, our approach relies on last-layer retraining. While efficient, it may be insufficient to fully mitigate spurious correlations compared with approaches leveraging representations from all network layers.

Future work include extending the framework to other architectures such as Vision Transformers (ViTs) and applying and validating this approach on other imaging modalities and in tasks beyond classification.

Code Availability

Our code is publicly available on our GitHub. The repository includes documentation and scripts to adapt our bias detection and mitigation framework to new datasets and tasks.

Acknowledgment

This work was supported in part by the Medical Imaging and Data Resource Center, which is funded by the National Institute of Biomedical Imaging and Bioengineering under contract 75N92020C00021 and through the Advanced Research Projects Agency for Health.

References

1. Jean-Benoit Delbrouck Chambon, Thomas Sounack, Shih-Cheng Huang, Zhihong Chen, Maya Varma, Steven Q. H. Truong, Chu The Chuong, and Curtis P. Langlotz. Chexpert plus: Augmenting a large chest x-ray dataset with text radiology reports, patient demographics and additional image formats. ArXiv, 2024.
2. Tianqi Chen and Carlos Guestrin. Xgboost: A scalable tree boosting system. In *Proceedings of the 22nd ACM SIGKDD International Conference on Knowledge Discovery and Data Mining*, pages 785–794. ACM, August 2016.
3. Joseph Cohen, Joseph Viviano, Paul Bertin, Paul Morrison, Parsa Torabian, Matteo Guarrera, Matthew Lungren, Akshay Chaudhari, Rupert Brooks, Mohammad Hashir, and Hadrien Bertrand. Torchxrayvision: A library of chest x-ray datasets and models, 10 2021.
4. Judy Wawira Gichoya, Imon Banerjee, Ananth Reddy Bhimireddy, John L. Burns, Leo Anthony Celi, and Li-Ching Chen. Ai recognition of patient race in medical imaging: a modelling study, 2022.
5. Yousra Hedhoud, Tahar Mekhaznia, and Mohamed Amroune. An improvement of the cnn-xgboost model for pneumonia disease classification. *Polish Journal of Radiology*, 88:483–493, 2023.
6. A. E. W. Johnson, T. J. Pollard, S. J. Berkowitz, and et al. Mimic-cxr, a de-identified publicly available database of chest radiographs with free-text reports. Sci Data, 2019.
7. Polina Kirichenko, Pavel Izmailov, and Andrew Gordon Wilson. Last layer re-training is sufficient for robustness to spurious correlations, 2023.
8. Nathan Srebro Moritz Hardt, Eric Price. Equality of opportunity in supervised learning. 2016.
9. Clemence Mottez, Louisa Fay, Jean-Benoit Delbrouck, and Curtis Langlotz. Lightweight model adaptation for mitigating bias in deep learning models for chest x-ray analysis. *Medical Imaging with Deep Learning*, 2025.
10. Pranav Rajpurkar, Jeremy Irvin, Kaylie Zhu, Brandon Yang, Hershel Mehta, Tony Duan, Daisy Ding, Aarti Bagul, Curtis Langlotz, Katie Shpanskaya, Matthew P. Lungren, and Andrew Y. Ng. Chexnet: Radiologist-level pneumonia detection on chest x-rays with deep learning, 2017.
11. Endang Sugiharti, Riza Arifudin, Dian Wiyanti, and Arief Susilo. Integration of convolutional neural network and extreme gradient boosting for breast cancer detection. *Bulletin of Electrical Engineering and Informatics*, 11:803–813, 04 2022.
12. Hinton Van der Maaten. Visualizing data using t-sne. 2008.
13. Saria S. Wiens, M. Sendak, and et al. Do no harm: a roadmap for responsible machine learning for health care. *Nature Medicine*, 2019.
14. Yuzhe Yang, Haoran Zhang, Judy Wawira Gichoya, and et al. The limits of fair medical imaging ai in real-world generalization. *Nature Medicine*, 2024.
15. Yuzhe Yang, Haoran Zhang, Dina Katabi, and Marzyeh Ghassemi. On mitigating shortcut learning for fair chest x-ray classification under distribution shift. In *NeurIPS 2023 Workshop on Distribution Shifts: New Frontiers with Foundation Models*, 2024.

Deciphering the influence of demographic factors on the treatment of pediatric patients in the emergency department

Helena Coggan[1,2], Anne Bischops[1,2], Pradip Chaudhari[3], Yuval Barak-Corren[4], Andrew M. Fine[2,5], Ben Y. Reis[1,2], Jaya Aysola[6] and William G. La Cava[1,2]

[1]*Computational Health Informatics Program, Boston Children's Hospital, Boston, MA, USA*

[2]*Harvard Medical School, Boston, MA, USA*

[3]*Division of Emergency and Transport Medicine, Children's Hospital Los Angeles and Department of Pediatrics, Keck School of Medicine of the University of Southern California, Los Angeles, CA, USA*

[4]*Department of Pediatric Cardiology, Schneider Children's Medical Center, Affiliated to Tel Aviv University Faculty of Medical and Health Sciences, Petach Tikvah, Israel*

[5]*Division of Emergency Medicine, Boston Children's Hospital, Boston, MA, USA*

[6]*Leonard Davis Institute of Health Economics, University of Pennsylvania; Department of Medicine, Perelman School of Medicine, University of Pennsylvania; and Penn Medicine Center for Health Equity Advancement, Philadelphia, Pennsylvania*

Persistent demographic disparities have been identified in the treatment of patients seeking care in the emergency department (ED). These may be driven in part by subconscious biases, which providers themselves may struggle to identify. To better understand the operation of these biases, we performed a retrospective cross-sectional analysis using electronic health records describing 339,400 visits to the ED of a single US pediatric medical center between 2019-2024. Odds ratios were calculated using propensity-score matching. Analyses were adjusted for confounding variables, including chief complaint, insurance type, socioeconomic deprivation, and patient comorbidities. We also trained a machine learning [ML] model on this dataset to identify predictors of admission. We found significant demographic disparities in admission (Non-Hispanic Black [NHB] relative to Non-Hispanic White [NHW]: OR 0.77, 95% CI 0.73-0.81; Hispanic relative to NHW: OR 0.80, 95% CI 0.76-0.83). We also identified disparities in individual decisions taken during the ED stay. For example, NHB patients were significantly less likely than NHW patients to be assigned an 'emergent' triage acuity score of (OR 0.70, 95% CI 0.67-0.72), but emergent NHB patients were also significantly less likely to be admitted than NHW patients with the same triage acuity (OR 0.86, 95% CI 0.80-0.93). Demographic disparities were particularly acute wherever patients had normal vital signs, public insurance, moderate socio-economic deprivation, or a home address distant from the hospital. An ML model assigned higher importance to triage score for NHB than NHW patients when predicting admission, reflecting these disparities in assignment. We conclude that many visit characteristics, clinical and otherwise, may influence the operation of subconscious biases and affect ML-driven decision support tools.

Keywords: epidemiology; emergency medicine; algorithmic fairness; disparities.

© 2025 The Authors. Open Access chapter published by World Scientific Publishing Company and distributed under the terms of the Creative Commons Attribution Non-Commercial (CC BY-NC) 4.0 License.

1. Background

Demographic disparities in emergency care and outcomes are an ongoing concern.[1,2] Studies of adult patients show that Black patients are assigned lower triage acuity scores (ESI)[3] than White patients, and Black and Hispanic patients with non-urgent triage acuity wait longer to be seen.[4] Black patients admitted to hospital also experience longer ED stays than White patients.[5] These disparities appear in the treatment of specific conditions,[6,7] and in outcomes beyond admission, such as lower likelihood of receiving opioids for pain-related visits.[8] Gender-based differences are also evident: women more often report difficulty obtaining timely ED care.[9]

These disparities extend to the pediatric emergency care setting. Pediatric patients face racial differences in triage assessments, both overall[10] and for specific complaints such as fever.[11] Black, Hispanic, Asian and Native American pediatric patients are less likely than White patients to receive radiological tests, though gaps narrow for conditions with standardized protocols.[12] Providers are also more likely to interrupt, and less likely to make eye contact with, patients from different racial and ethnic groups,[13] suggesting subconscious bias influences ED care well before admission decisions. Potentially biased upstream decisions include triage acuity scores, test orders, and prioritizing care to one patient before another.[14] Biases may also affect clinical interpretation of vital signs and non-clinical variables such as insurance type and socio-economic status, which in turn affect the output of clinical decision support tools trained to predict admission[15–17] or clinical orders.[18] To reduce sex- and race-based disparities, and to safely deploy predictive algorithms, we need a fuller picture of the mechanisms driving ED decision-making.

In this study we quantified demographic disparities in admission at a large urban pediatric ED in Boston, Massachusetts. We considered two main classes of disparity. First, we examined *upstream disparities*: differences in clinical decisions made before decisions to admit or discharge (e.g. the likelihood of receiving a medication or triage acuity score). Second, we examined *downstream disparities*: differences in outcomes like admission rates between patients with the same medication or score. Finally, we assessed *feature importance disparities*: differences in the predictive importance an ML model assigns to visit characteristics across demographic groups.

Our study provides a more detailed view of disparities within a hospital than is possible using the widely-studied National Hospital Ambulatory Medical Care Survey (NHAMCS),[19] which lacks some key variables. These results can inform clinical education and help developers design fairer clinical support tools.

2. Study Sample and Available Information

We performed a retrospective study of 352,324 visits to a large urban pediatric ED between January 2019 and December 2024. We excluded 3,452 visits (0.98%) which lacked demographic

information; 5,606 (1.6%) which did not result in admission or discharge; and 3,149 (0.9%) which did not have a linked chief complaint. A small number of visits (<0.5%) were further excluded because of recording errors (obviously implausible lengths of stay in months or years, departure or admission request preceding arrival, no recorded sex, or no consistent patient identifier). Where a final disposition was not recorded, we inferred admission from the presence of an admission request, and inferred discharge if vitals were recorded but no admission request was made. Our final dataset contained 339,400 visits (96% of the original dataset) from 179,944 unique patients. The overall composition of these visits is recorded in Table 1.

Our primary exposures of interest were sex (male or female) and race (Asian, Hispanic, Non-Hispanic Black, Hispanic White, Non-Hispanic White, Other, and unknown). Available data included age (categorised into 0-3 months, 3-6 months, 6-12 months, 12-18 months, 18-36 months, 3-5 years, 5-10 years, 10-15 years, and 15+ years[16]), primary language (condensed to English, Spanish or Other), and type of insurance (public or private). We also considered the 'triage acuity score' each patient was assigned shortly after arrival (also known as the Emergency Severity Index or ESI score). A score of 1 indicates that a patient requires immediate and lifesaving intervention, whereas a score of 5 indicates low severity.

From the patient's zip code, we calculated the distance travelled to the ED for the visit (assuming that a patient left from their home address), whether a patient came from out of state, and a socio-economic deprivation index (SDI), using the scores developed by the Robert Graham Center for 2019, the most recent year available[20] (see Table 2).

We also included a patient's history within the thirty days preceding the visit, separated into number of previous admissions and number of previous visits without admission. Other visit-specific variables included mode of transport to the ED; season, time of day, year of arrival, and whether the visit occurred on a weekend; and the number of other patients in the ED at the time a patient arrived (referred to throughout this paper as 'crowdedness'), weighted by severity (so that a patient with an ESI score of 1 was weighted 5 times more than a patient with an ESI score of 5). Chief complaint was recorded as a free text field, which complicated the consistent identification of ailments. To deal with this, we first manually expanded common abbreviations ('s.o.b.' to 'shortness of breath'), and then shortened each word in a patient's complaint to its 'stem' (e.g. 'diabetes' and 'diabetic' to 'diabet') using the R package SnowballC.[21] We then categorised complaints using the Pediatric Emergency Reason for Visit clustering system.[22]

We also had information on a patient's vitals across their ED stay: heart rate (HR), respiration rate (RR), oxygen saturation, blood pressure, and reported pain (on a scale of 0-10, with 0 corresponding to 'no pain'). We recorded the minimum, maximum and mean reading of each vital across a visit as separate variables. HR, RR and weight variables were converted to a score corresponding to the number of standard deviations from the mean of each age group.[16] Blood pressure scores were calculated according to the PALS (Pediatric Advanced Life Support) criterion, which incorporates systolic blood pressure (SBP) and age to determine whether a pediatric patient is hypotensive.

We controlled for a patient's medical history, and for the diagnoses resulting from the ED

visit, by defining two variables for each category of comorbidities in the pediatric comorbidity index (PCI).[23] For each category (e.g. developmental disorders, chromosomal abnormalities,), we recorded the presence of a previous condition if a relevant diagnosis had been noted more than one day but less than one year before the visit, and a 'current condition' if a relevant diagnosis was noted within a day of the visit. (This does not necessarily mean that the diagnosis was *initially made* during the visit, but it does imply that the diagnosis was relevant to that visit).

3. Statistical Analyses

As a majority of visits were from male patients and a plurality from Non-Hispanic White (NHW) patients (see Table 1), male sex and NHW race were taken as reference groups. Our primary outcome of interest was admission to hospital. Secondary outcomes included assignment of ESI score, dispensing of medications, ordering of radiological tests, and length of stay.

We calculated odds ratios using propensity-score matching. Propensity scores were calculated using the R package glmnet.[24,25] If a sociodemographic variable was unknown (e.g. SDI), we recorded this in a separate binary variable (e.g. SDI_unknown) and set the value of the original variable for that visit to the cohort mean (on the basis that nothing could be known about the patient's socioeconomic deprivation beyond what is known about the population served by the ED as a whole).

For each demographic characteristic (e.g. Non-Hispanic Black [NHB] race), we restricted the cohort to this demographic and the reference group (e.g. only visits from NHB and NHW patients) and fitted a logistic regression model to 'predict' NHB race using all relevant variables. Due to the large number of variables available (around 300), we fit propensity scores using LASSO regression. We used five-fold cross-validation and chose the penalty parameter to produce the most regularised model (i.e. to select the fewest variables) whilst remaining within one standard deviation of the minimum possible error.

When the outcome of interest was triage acuity (ESI score), we excluded all variables from the propensity score which we assumed were not known at triage. These included triage acuity score itself, pediatric comorbidity score, and all 'post-triage' vitals. ('Triage vitals' were assumed to be the first set of vitals recorded.) It was not clear when a patient was asked for their insurance type or ZIP code, and so it is possible that some other variables are also unknown at triage (specifically insurance type, miles travelled, SDI, and state of origin). However, we assumed that the triage nurses knew or could guess these variables, and so included them in order to 'err on the side of caution' when attempting to measure the independent effect of race and sex on triage acuity (separately from insurance or socioeconomic class).

We matched visits 1:1 with greedy nearest-neighbour matching on the propensity score, using the R package MatchIt.[26] We set a caliper threshold of 10% of the standard deviation of the propensity score, and recalculated at 20% to check that our results were robust to caliper thresholds. Odds ratios were calculated using McNemar's exact test. Multiple hypothesis correction was conducted using the Bonferroni method. For each set of outcomes (overall

Table 1. Demographic characteristics of the study population in the BCH dataset. Numbers correspond to visits. ESI: Emergency Severity Index. EMS: Emergency medical services (ambulance, helicopter, etc).

Characteristic		Number (%) of visits	Admission rate (%)
Sex	Female	161725 (47.7)	17.4
	Male	177675 (52.3)	18.4
Race	Asian	13260 (3.91)	18.3
	Hispanic	88106 (26)	12.2
	Hispanic White	728 (0.214)	17.9
	Non-Hispanic Black	50853 (15)	12.5
	Non-Hispanic White	116339 (34.3)	25.5
	Other	33639 (9.91)	16.4
	Unknown	36475 (10.7)	16.5
Age	0-3 months	14178 (4.18)	30
	3-6 months	9332 (2.75)	20.3
	6-12 months	20089 (5.92)	15
	12-18 months	18300 (5.39)	14.4
	18-36 months	41084 (12.1)	14
	3-5 years	40078 (11.8)	14.2
	5-10 years	69520 (20.5)	15.8
	10-15 years	58468 (17.2)	19.7
	15 years and older	68351 (20.1)	22.1
Mode of arrival	EMS	27295 (8.04)	31.7
	Transfer	14429 (4.25)	55.1
	Walk in	296449 (87.3)	14.8
	Unknown	1227 (0.362)	24.3
Primary Language	Arabic	4734 (1.39)	22.7
	Cape Verdean	1819 (0.536)	12.2
	Chinese Mandarin	1357 (0.4)	15.1
	English	270314 (79.6)	19
	Haitian Creole	3071 (0.905)	13.4
	Other	13104 (3.86)	15.5
	Portuguese	6648 (1.96)	17.6
	Spanish	38353 (11.3)	11.2
Triage acuity (ESI) score	1	1535 (0.452)	71.9
	2	83163 (24.5)	41.2
	3	159571 (47)	15.4
	4	85969 (25.3)	0.943
	5	8811 (2.6)	0.375
	Unknown	351 (0.103)	20.8
Insurance	Public	167458 (49.3)	21.1
	Private	171942 (50.7)	14.8

admission, upstream decisions, and admission following upstream decisions) we performed Bonferroni correction across all interventions simultaneously.

We also sought to test the effect of downstream disparities on the quality of predictive algorithms trained on these data. To do this, we designed a model using XGBoost[27] to predict

Table 2. Distributions of the features of visits to the BCH ED. Distance travelled to the hospital is calculated as the distance between the patient's zip code and the hospital's (02115). A higher social deprivation score indicates a poorer zip code.

Characteristic	Lower quartile	Median	Upper quartile
Length of stay (minutes)	158	244	372
Distance travelled to hospital (miles)	3.78	7.44	21.69
Social deprivation index	18	57	92

admission on a continuous basis during a patient's stay. Stays were 'sampled' at the start and end of their visit, and then every 60 minutes within the visit itself. At each sampled timepoint, all information known about the patient up to this timepoint was collated, including the ordering of any radiological tests, the dispensing of the top 50 most common medications (including the method of its administration, e.g. intravenous [IV] or oral), and the most recent results of the 50 most common laboratory tests (age-normalised so that each result lies between 0 and 1, with the 1st and 99th percentile set as lower and upper bounds for stability). As the timing of triage assessment could not be reliably determined, we assumed that ESI score and demographic characteristics were available at every timepoint during the patient's stay. We took the first three and a half years of visits as the training data and the next year (roughly May 2023-May 2024) as the test data (removing visits after this point due to difficulties in mapping radiological tests). Although our train/test split was chronological, we included the year of admission as features in the test and training data to allow the model to learn from changes in admission rates during the pandemic. We split before extracting timepoint-samples, to ensure information about the same visit did not appear in both. Hyperparameters were tuned on a dataset comprising one randomly chosen sample from each visit in the training dataset, using randomised search on 100 hyperparameter sets and five-fold cross validation. During both the training and testing process, timepoints were weighted in inverse proportion to visit length (such that the weights of all timepoints associated with the same visit summed to 1).

4. Results

4.1. *Admission to Hospital*

Visits to the ED during this period had an overall admission rate of 17.9% and a median LOS of just over 4 hours. We examined the overall impact of race and sex on a patient's odds of being admitted to hospital. We calculated odds ratios at three levels of adjustment. Firstly, we calculated 'unadjusted' odds ratios (ORs), where (for example) visits from female patients were matched to visits from male patients at random, without accounting for any other factors. Next, 'partially adjusted' ORs were computed using a propensity score which included 'patient-specific factors': age group, primary language, history of previous visits, gender identity, socio-economic deprivation, insurance, distance lived from the hospital, state of origin, previous diagnoses, and weight. Partially adjusted odds ratios also accounted for sex when comparing racial groups, and for race when comparing sexes. Finally, we computed 'fully

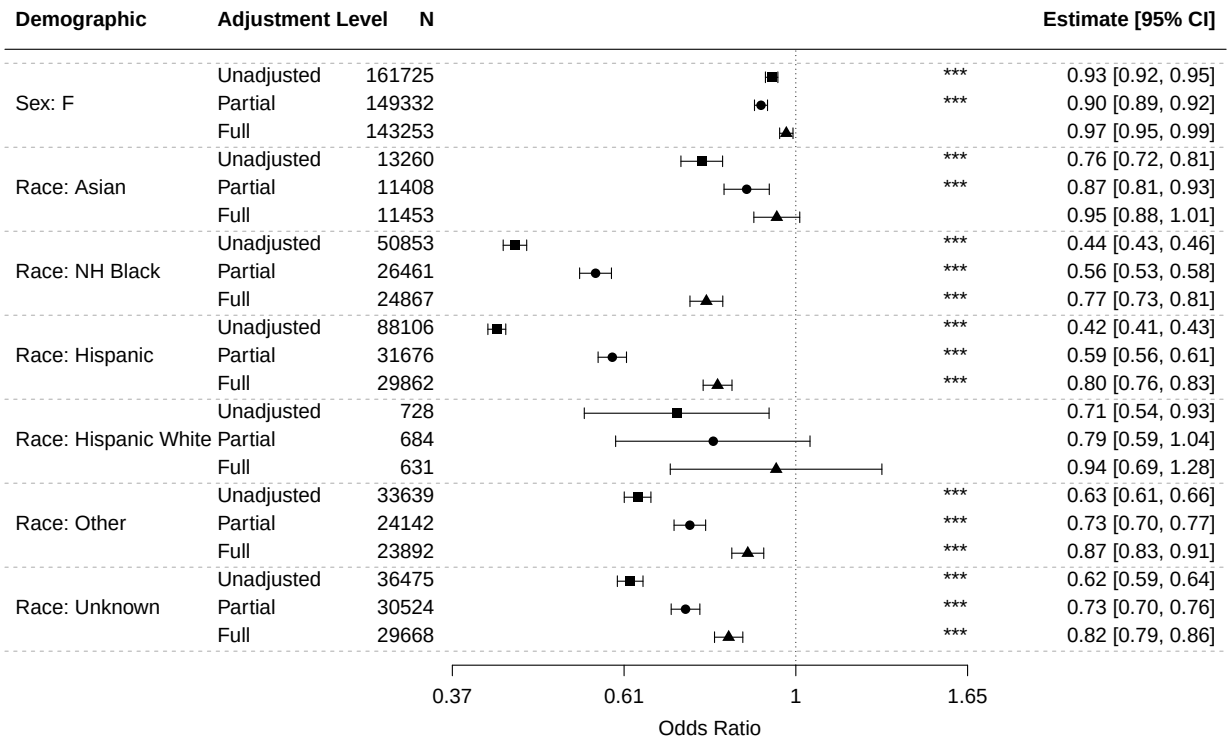

Fig. 1. Adjusted odds ratios describing the likelihood that different demographic groups of patients will be admitted to hospital. Significance is indicated with asterisks, where p-values have been Bonferroni-corrected across all demographic groups and levels of adjustment simultaneously (*** = $p < 0.001$, ** = $p < 0.01$, * = $p < 0.05$). NH=Non-Hispanic. N=number of visits (i.e. N visits from female patients are compared to N visits from male patients). 'Partial' adjustment accounts for all patient-specific factors; full adjustment incorporates visit-specific factors (see text).

adjusted' ORs. In addition to the factors included in the partial adjustment, these accounted visit-specific factors: chief complaint, ESI score, vitals measured across a patient's stay, current diagnoses, mode and time of arrival, and crowdedness.

When performing both partial and full adjustment, covariate balance on the matched cohort was checked using a Love plot. Full balance (standardised mean differences of less than 10% in all covariates[28]) was achieved on all cohorts except when comparing visits from Hispanic White (HW) patients to visits from NHW patients, as groups of a few hundred visits are difficult to balance across many covariates.

Unadjusted odds ratios suggested that sex and race had significant effect on hospital admission (see Figure 1). Before adjustment, visits from all racial groups considered (except HW) were significantly less likely than visits from NHW patients to result in an admission, as were visits from female patients relative to visits from male patients. After full adjustment, significant negative effects could still be observed for all racial groups except HW and Asian. Fully adjusted effects were largest for Hispanic and NHB patients. Racial disparities, and their

significance levels, were robust to a doubling of the caliper threshold used to match patients (Hispanic relative to NHW: OR = 0.78, 95% CI 0.75-0.81; NHB relative to NHW: 0.76[0.73-0.80]). Code used to perform our analyses is available at `https://github.com/hcoggan/BCH-ED`.

4.2. *Triage Acuity and Length of Stay*

We next examined the effect of race on two secondary outcomes: triage acuity and length of stay in the emergency department (LOS). We considered both the odds that a patient would be 'assigned' a certain outcome (e.g. an ESI score of 2, or a lowest-quartile LOS) and the odds that a patient *who had been assigned that outcome* would then be admitted. For simplicity, we focused on the three largest demographic groups (other than the reference groups): female patients, Hispanic patients, and NHB patients. All odds ratios were fully adjusted.

Disparities could be observed across scores other than ESI 1 (see Figure 2), which is reserved for the most severe cases. Female patients were significantly less likely to be assigned a score of 2 than male patients, and more likely to be assigned a score of 3 or 4. Hispanic and NHB patients were less likely than NHW patients to be assigned scores of 2 or 3 and more likely to be assigned a score of 4. We also detected (primarily racial) disparities in the 'operation' of ESI scores: Hispanic and NHB patients who had already been assigned an ESI score of 2 or 3 were significantly less likely than NHW patients *at the same triage score* to be admitted to hospital.

Disparities could also be observed in LOS. Female patients tended to have longer stays than male patients, and were less likely to be admitted *only if* they experienced a long stay in the ED; female patients who experienced short stays were admitted at almost the same rates as male patients. Overall, female patients stayed in the ED 26 minutes longer than matched male patients before admission (95% CI 18-34 min, paired t-test on log-transformed wait times), and 10 minutes longer before discharge (95% CI 8.5-12 min). When comparing NHB to NHW patients, however, we found the opposite pattern. NHB patients tended to experience *shorter* stays than NHW patients overall, but racial disparities in admission rates were only significant for patients who experienced shorter stays (see Figure 2). NHB and Hispanic patients tended to have longer stays before admission than NHW patients (NHB: 40 min., 17-63 min.; H: 26 min., 7.7-44 min.) but were discharged more quickly (NHB: 9.1 min., 4.2-14 min.; H: 8.4 min., 4.0-13 min.)

4.3. *Imaging, Laboratory Tests and Medications*

We also examined differences in the rates at which laboratory tests, radiological tests and medications (hereafter collectively referred to as 'interventions') are ordered for different groups of patients).

Female patients were significantly more likely than male patients to have laboratory tests ordered for them, and to be treated with intravenous (IV) medications, but were significantly less likely to be admitted after receiving those interventions (see Figure 3). Hispanic patients were significantly less likely to receive radiological imaging, and both NHB and Hispanic patients were significantly less likely to receive IV medications. Whilst we found no significant

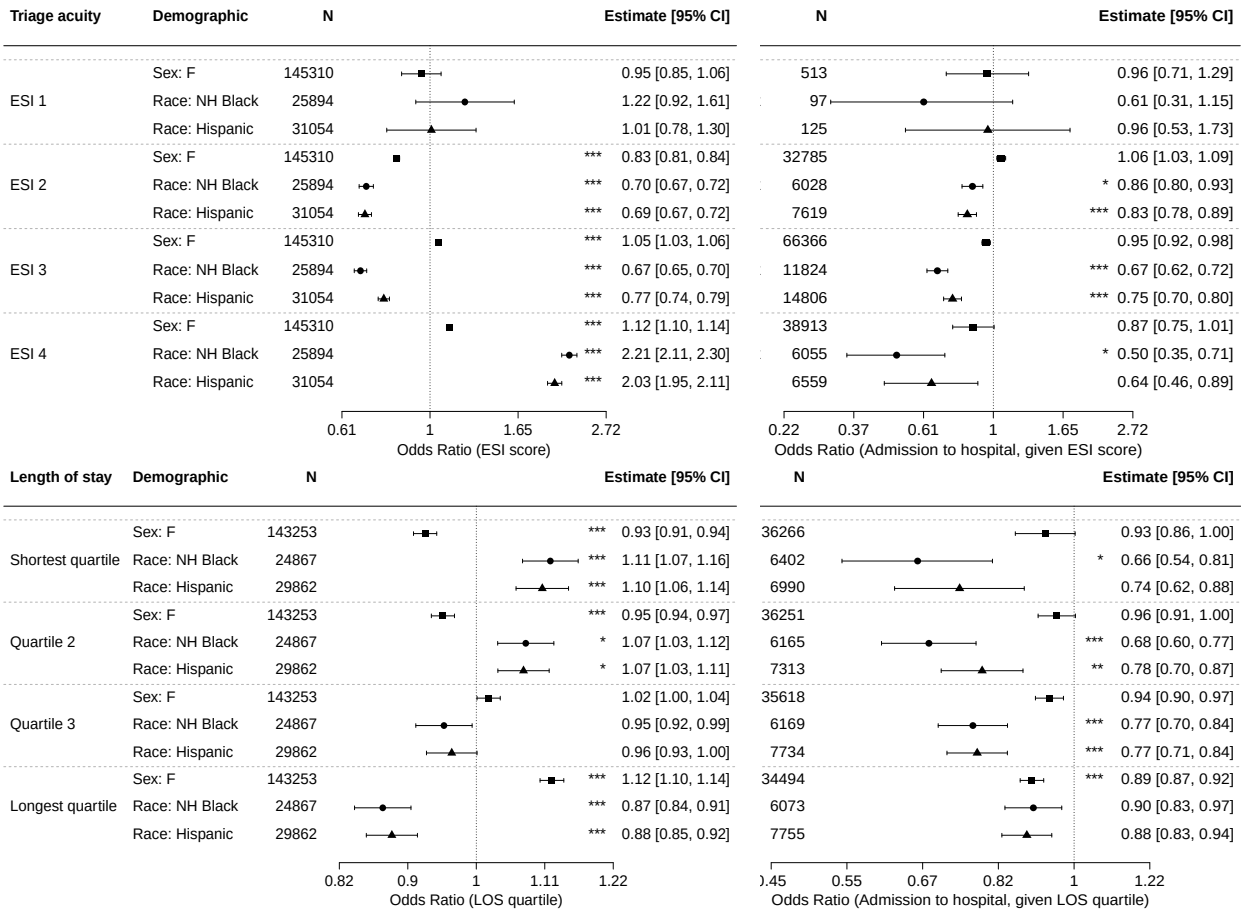

Fig. 2. Top: Fully adjusted odds ratios describing the likelihood that different demographic groups of patients will be: assigned to each triage group (left); admitted to hospital, given they were assigned to that triage group (right). ESI 5, the least urgent, is excluded due to low sample size. Bottom: Fully adjusted odds ratios describing the likelihood that different demographic groups: will experience different lengths of stay, (left, where lower percentiles indicate a shorter stay), and will be admitted to hospital given each length of stay (right). Odds ratios for female patients are measured relative to male patients; odds ratios for NHB and Hispanic patients are measured relative to NHW patients.

disparities in the rates at which laboratory tests were ordered, NHB and Hispanic patients who had tests were significantly less likely to be admitted than tested NHW patients.

4.4. *Vital Signs, Reported Pain, and Crowding*

We next considered whether visit characteristics outside of the clinician's control, such as insurance type and the vitals measured across a patient's stay, affected disparities in admission. We first divided visits into categories based on these characteristics (e.g. public and private insurance), and then tested those subgroups individually for admission disparities (see Figure 4). NHB and Hispanic patients with public insurance were less likely than NHW patients with public insurance to be admitted, but no significant disparities existed between patients with private insurance. Racial disparities were significant in the second and third SDI quartiles, but vanished at the fourth (the most deprived quartile). This suggests that 'moderate deprivation'

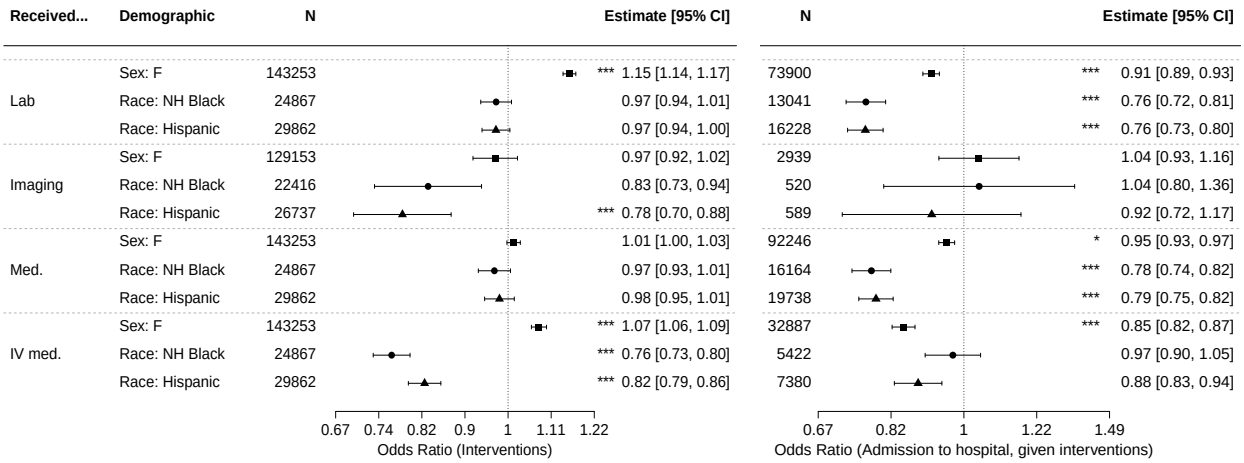

Fig. 3. Fully adjusted odds ratios describing the likelihood that different demographic groups of patients: received any intervention (left); were admitted to hospital, given they received that intervention (right). Information on laboratory tests were only available if their results came back during the ED visit. 'Medications' include IV medications. Imaging refers to radiological tests; we exclude visits after May 2024 for this test, due to difficulties obtaining records. Odds ratios for female patients are measured relative to male patients; odds ratios for NHB and Hispanic patients are measured relative to NHW patients.

tends to increase racial disparities. NHB patients who lived locally to the hospital were *more* likely than similar NHW patients to be admitted, but NHB patients who lived far away were less likely.

We also observed that disparities decreased as a patient's vital readings (HR, RR and oxygen saturation) became more abnormal for their age group. The exception to this rule was weight: sex-based admission disparities were individually significant only for patients with a 'normal' weight, but race-based disparities were *exacerbated* by abnormal weight (see Figure 4).

Other subpopulations in which NHB-NHW and Hispanic-NHW disparities were individually significant included: patients aged 5-10 (NHB: OR=0.68, 95% CI 0.70-0.76, H: 0.79, 0.72-87) and 15+ (NHB: 0.67, 0.61-0.74; H: 0.74, 0.68-0.81); patients brought in by emergency medical services (NHB: 0.73, 0.64-0.83; H: 0.71, 0.63-0.81); walk-in arrivals (NHB: 0.77, 0.73-0.81; H: 0.80, 0.76-0.84); patients with no thirty-day history of admissions (NHB: 0.77, 0.73-0.81; H: 0.76, 0.73-0.80) or visits without admission; (NHB: 0.76, 0.72-0.80; H: 0.77, 0.74-0.80); English-speakers (NHB: 0.75, 0.71-0.78; H: 0.77, 0.74-0.81); patients with previous diagnoses of gastrointestinal conditions (NHB: 0.58, 0.45-0.73; H: 0.53, 0.43-0.65) or nausea (H: 0.71, 0.59-0.83); and patients complaining of fever (NHB: 0.67, 0.56-79), abdominal pain (NHB: 0.48, 0.39-0.60; H: 0.73, 0.62-0.85), vomiting (NHB: 0.46, 0.35-0.61; H: 0.57, 0.45-0.72), or seizures (H: 0.58, 0.45-0.74). Female patients were much less likely than male patients to be admitted with previous diagnoses of nausea (0.80, 0.73-0.86) or when complaining of abdominal pain (0.74, 0.69-0.80), but were much more likely to be admitted for psychiatric complaints (1.37, 1.23-1.53). We found that, after full adjustment, female, NHB and Hispanic patients waited slightly but significantly longer to leave the ED once an admission decision had been

taken (female vs male: 12 min., 95% CI 7.8-17 min.; NHB vs NHW: 20 min., 7.4-33 min.; H vs NHW: 11 min., 1.0-21 min.), suggesting that minoritised patients may be de-prioritised when assigning inpatient beds.

Finally, to properly understand the effect of language on admission decisions, we matched patients of a variety of languages to English speakers of the same race. We found that NHW Portuguese speakers were significantly less likely to be admitted than NHW English speakers (0.67, 0.55-0.82), as were NHW speakers of 'other' languages than the 7 most common specified in Table 1 (0.80, 0.70-0.90). However, NHB speakers of Portuguese were significantly *more* likely to be admitted (2.63, 1.52-1.73) than NHB English speakers, suggesting that the effect of language on a patient's experience in the ED is dependent on their race.

4.5. *Impact on Admission Prediction*

To test whether these disparities would affect the workings of clinical decision support tools, we trained a boosted tree model to predict examined disparities in the features treated as important by our model. Using only timepoints taken at the start of each visit, our model had an overall AUROC of 0.921 (bootstrapped 95% CI 0.918-0.923) and AUPRC of 0.632 (0.620-0.643); at the one-hour mark, an AUROC of 0.928 (0.926-0.930) and AUPRC of 0.700 (0.689-0.708); and at the end of each visit, an AUROC of 0.970 (0.968-0.971) and AUPRC of 0.841 (0.835-0.848). The model relied most heavily on ESI score, the presence of fever, duration of stay, and distance travelled to the hospital (see Figure 5).

To clarify how disparities in patient treatment affect the model's ability to learn from the decisions taken during a patient's stay, we broke out SHAP values by race for key features (see Figure 5). We found that the model 'penalised' NHB and Hispanic patients more heavily for a non-urgent ESI score and 'rewarded' NHW patients more an emergent one. Certain other features, such as oxygen saturation and current length of visit, were more important for NHB than NHW patients. These feature importance disparities highlight that models trained on biased data will apply those biases to future cohorts.

5. Discussion

Our study observed wider demographic disparities where providers had greater discretion, such as where patients had 'normal' vitals, in line with previous studies of radiological testing.[12] This suggests that the subjective judgement of clinicians about the 'look' of a patient may be affecting the treatment of borderline cases and the speed at which admitted patients are prioritised for inpatient beds. Training to address subconscious biases could be effective in reducing racial disparities,[29] especially in the specific clinical subpopulations in which those biases are most acute. These include patients with abnormal weight and from areas of moderate socioeconomic deprivation, as well as speakers of non-English primary languages, whose use of an interpreter may influence a physician's impression of their testimony.

Our results also suggest that female patients may be 'overtreated' with IV medications and 'overtested' in the ED relative to male patients, leading to longer stays and lower eventual admission rates. These effects, along with differences in the interpretation of vital signs, modified the importance assigned by a machine learning model to clinical decisions when trying

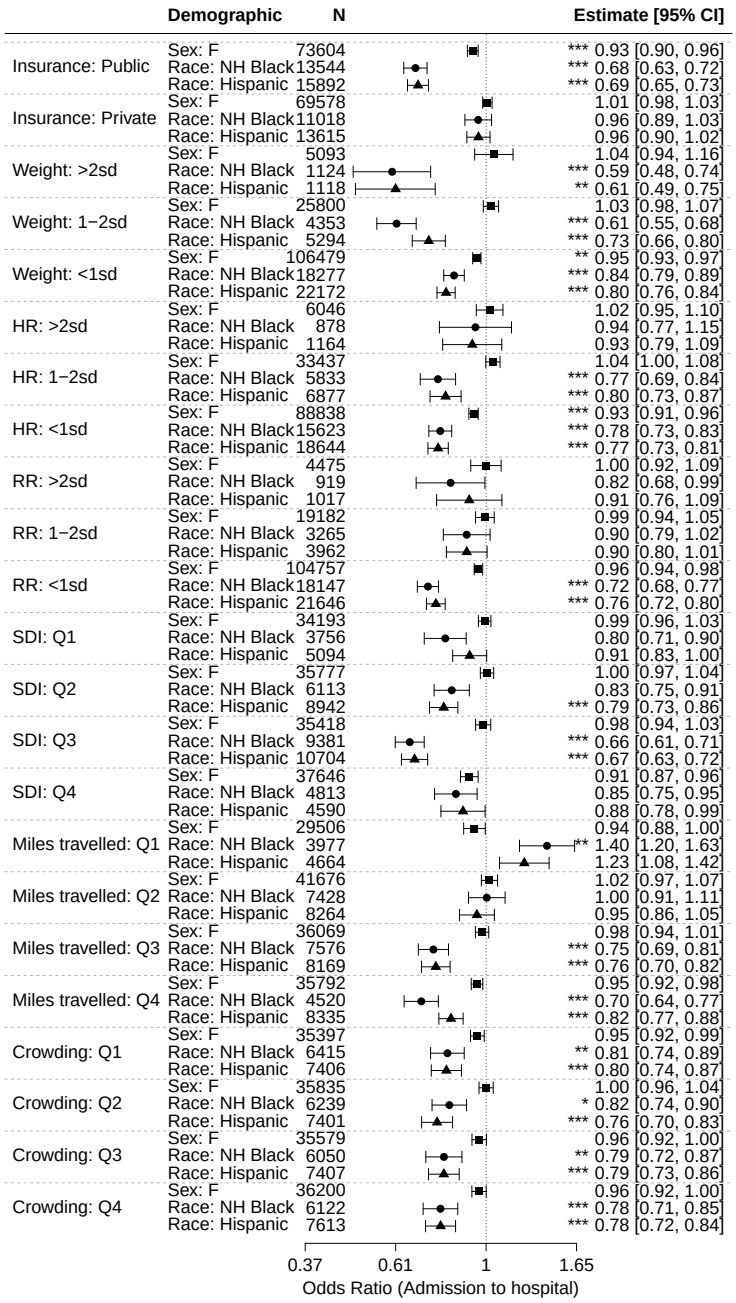

Fig. 4. Fully adjusted odds ratios describing the likelihood that different demographic groups of patients will be admitted to hospital, given various characteristics. HR = heart rate; O2 = oxygen saturation; SDI = social deprivation index. SDI Q4 is most deprived, SDI Q1 is least. RR, HR and weight are measured in numbers of standard deviations (sd) from the age-group mean, so that lower values indicate 'normal' vitals and higher values indicate 'abnormal' vitals.

to predict admission for minoritised groups.

Our dataset came from a single site, and our findings may not extrapolate to other hospitals

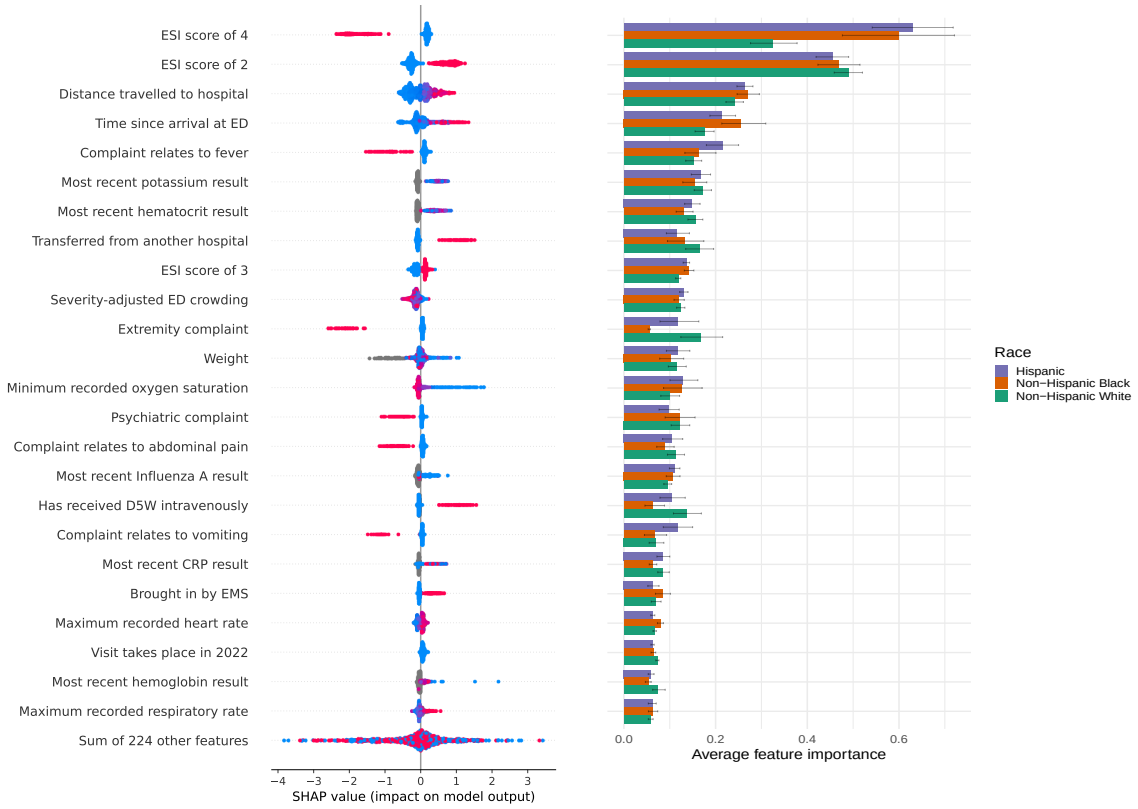

Fig. 5. Left: The top 24 most important features highlighted by our model, which is trained on individual timepoints throughout a patient's visit. Blue dots indicate low feature value, red dots indicate high, and grey indicate that the information is unmeasured (e.g. grey for a laboratory test indicates that, if ordered, its result was unknown at that point in the visit). SHAP values are taken from 1000 random timepoints in the test set. Right: Average feature importance for key features, broken out by patient race. Errorbars indicate bootstrapped 95% confidence intervals.

or beyond the pediatric care setting. We did not account for the specific provider or team of providers which treated a particular patient, and did not have a record of the medications a patient was taking at the time of their admission to the ED. Whilst we used the number and severity of patients waiting in the ED as a measure of 'crowdedness', we lacked information on NEDOCS scores (which take into account the number of beds available within the hospital and the number of clinicians on staff) and so may not have fully account for the pressures on the ED. Nonetheless, our findings illuminate a number of important patterns in the 'mechanisms' of race and sex-based disparities, and should inform both the education of future clinicians and the development of clinical decision support tools.

Acknowledgments

Research reported in this publication was supported by the National Library of Medicine of the National Institutes of Health (NIH) Award R01LM014300. The content is the responsibility of the authors and does not necessarily represent the official views of NIH.

References

1. A. Nelson, Unequal treatment: confronting racial and ethnic disparities in health care., *Journal of the National Medical Association* **94**, 666 (8 2002).
2. K. Hamberg, Gender Bias in Medicine, *Women's Health* **4**, 237 (5 2008).
3. C. D. Schrader and L. M. Lewis, Racial disparity in emergency department triage, *Journal of Emergency Medicine* **44**, 511 (2 2013).
4. F. Q. Lu, A. D. Hanchate and M. K. Paasche-Orlow, Racial/ethnic disparities in emergency department wait times in the united states, 2013–2017, *The American Journal of Emergency Medicine* **47**, 138 (9 2021).
5. J. M. Pines, R. A. Localio and J. E. Hollander, Racial disparities in emergency department length of stay for admitted patients in the united states, *Academic Emergency Medicine* **16**, 403 (5 2009).
6. C. A. Martin, T. Coats, M. Pareek, K. Khunti, R. Abeyratne and N. J. Brunskill, Ethnicity and outcomes for patients with gastrointestinal disorders attending an emergency department serving a multi-ethnic population, *BMC Medicine* **22**, p. 275 (7 2024), non-white patients less likely to have GI disorders investigated in emergency room.
7. J. Longcoy, R. Patwari, S. Hasler, T. Johnson, E. Avery, K. Stefanini, S. Suzuki, D. Ansell and E. Lynch, Racial and ethnic differences in hospital admissions of emergency department covid-19 patients., *Medical care* **60**, 415 (6 2022).
8. H. Kang, P. Zhang, S. Lee, S. Shen and E. Dunham, Racial disparities in opioid administration and prescribing in the emergency department for pain, *American Journal of Emergency Medicine* **55**, 167 (5 2022).
9. P. G. Chen, A. Tolpadi, M. N. Elliott, R. D. Hays, W. G. Lehrman, D. S. Stark and L. Parast, Gender differences in patients' experience of care in the emergency department., *Journal of general internal medicine* **37**, 676 (2 2022).
10. P. Metzger, L. Allum, E. Sullivan, F. Onchiri and M. Jones, Racial and language disparities in pediatric emergency department triage, *Pediatric Emergency Care* • **38** (2022).
11. J. A. Dennis, Racial/ethnic disparities in triage scores among pediatric emergency department fever patients, *Pediatric Emergency Care* • **37** (2021).
12. N. R. Payne and S. E. Puumala, *Racial Disparities in Ordering Laboratory and Radiology Tests for Pediatric Patients in the Emergency Department*, tech. rep. (2009).
13. J. Aysola, J. T. Clapp, P. Sullivan, P. J. Brennan, E. J. Higginbotham, M. D. Kearney, C. Xu, R. Thomas, S. Griggs, M. Abdirisak, A. Hilton, T. Omole, S. Foster and M. Mamtani, Understanding contributors to racial/ethnic disparities in emergency department throughput times: a sequential mixed methods analysis., *Journal of general internal medicine* **37**, 341 (2 2022).
14. R. B. Sangal, H. Su, H. Khidir, V. Parwani, B. Liebhardt, E. J. Pinker, L. Meng, A. K. Venkatesh and A. Ulrich, Sociodemographic Disparities in Queue Jumping for Emergency Department Care, *JAMA Network Open* **6**, p. E2326338 (7 2023).
15. W. G. La Cava, E. Lett and G. Wan, Fair admission risk prediction with proportional multicalibration, in *Proceedings of the Conference on Health, Inference, and Learning*, (PMLR, June 2023).
16. Y. Barak-Corren, A. M. Fine and B. Y. Reis, Early prediction model of patient hospitalization from the pediatric emergency department, *Pediatrics* **139** (5 2017).
17. Y. Barak-Corren, P. Chaudhari, J. Perniciaro, M. Waltzman, A. M. Fine and B. Y. Reis, Prediction across healthcare settings: a case study in predicting emergency department disposition, *npj Digital Medicine* **4** (12 2021).
18. H. S. Hunter-Zinck, J. S. Peck, T. D. Strout and S. A. Gaehde, Predicting emergency department orders with multilabel machine learning techniques and simulating effects on length of stay,

Journal of the American Medical Informatics Association **26**, 1427 (December 2019).
19. National Hospital Ambulatory Medical Care Survey: 2017 Emergency Department Summary Tables, p. 37 (2017).
20. Robert Graham Center - Policy Studies in Family Medicine & Primary Care, Social deprivation index (SDI) (November 2018).
21. M. Bouchet-Valat, *SnowballC: Snowball Stemmers Based on the C 'libstemmer' UTF-8 Library*, (2023). R package version 0.7.1.
22. M. H. Gorelick, E. R. Alpern and E. A. Alessandrini, A system for grouping presenting complaints: The pediatric emergency reason for visit clusters, *Academic Emergency Medicine* **12**, 723 (8 2005).
23. J. W. Sun, F. T. Bourgeois, S. Haneuse, S. Hernández-Díaz, J. E. Landon, B. T. Bateman and K. F. Huybrechts, Development and validation of a pediatric comorbidity index, *American Journal of Epidemiology* **190**, 918 (5 2021).
24. J. Friedman, T. Hastie and R. Tibshirani, Regularization paths for generalized linear models via coordinate descent, *Journal of Statistical Software* **33**, 1 (2010).
25. J. K. Tay, B. Narasimhan and T. Hastie, Elastic net regularization paths for all generalized linear models, *Journal of Statistical Software* **106**, 1 (2023).
26. D. E. Ho, K. Imai, G. King and E. A. Stuart, MatchIt: Nonparametric preprocessing for parametric causal inference, *Journal of Statistical Software* **42**, 1 (2011).
27. T. Chen and C. Guestrin, Xgboost, in *Proceedings of the 22nd ACM SIGKDD International Conference on Knowledge Discovery and Data Mining*, (ACM, 8 2016).
28. P. C. Austin, An introduction to propensity score methods for reducing the effects of confounding in observational studies., *Multivariate behavioral research* **46**, 399 (5 2011).
29. A. J. Zeidan, U. G. Khatri, J. Aysola, F. S. Shofer, M. Mamtani, K. R. Scott, L. W. Conlon and B. L. Lopez, Implicit bias education and emergency medicine training: Step one? awareness., *AEM education and training* **3**, 81 (1 2019).

Barriers to Designing Inclusive Ecological Momentary Assessment and Wearable Data Collection Protocols for AI-Driven Substance Use Monitoring in Hawai‘i

Yinan Sun
The Information Systems and Technology (IST) Department, College of Engineering and Computing, George Mason University, Fairfax, VA 22030, United States; Department of Information and Computer Science, University of Hawaii, Honolulu, HI 96822, United States
E-mail: sunyinan@hawaii.edu

Aditi Jaiswal
Department of Information and Computer Science, University of Hawaii, Honolulu, HI 96822, United States
E-mail: ajaiswal@hawaii.edu

Ali Kargarandehkordi
Department of Information and Computer Science, University of Hawaii, Honolulu, HI 96822, United States
E-mail: kargaran@hawaii.edu

Christopher Slade
Department of Information and Computer Science, University of Hawaii, Honolulu, HI 96822, United States
E-mail: cslade@hawaii.edu

Roberto M. Benzo
Division of Cancer Prevention and Control, Department of Internal Medicine, College of Medicine, The Ohio State University Comprehensive Cancer Center, The Ohio State University Wexner Medical Center, Columbus, OH 43210, United States
E-mail: roberto.benzo@osumc.edu

Kristina T. Phillips
Center for Integrated Health Care Research, Kaiser Permanente Hawaii, Honolulu, HI, United States
E-mail: kristina.t.phillips@kp.org

Peter Washington
Division of Clinical Informatics and Digital Transformation, Department of Medicine, University of California, San Francisco, CA, United States
E-mail: peter.washington@ucsf.edu

Ecological momentary assessment (EMA) and wearable sensors offer unprecedented opportunities to capture the dynamics of substance use through real-time, high-resolution behavioral and physiological data. These data streams are increasingly used to train AI/ML models for digital

© 2025 The Authors. Open Access chapter published by World Scientific Publishing Company and distributed under the terms of the Creative Commons Attribution Non-Commercial (CC BY-NC) 4.0 License.

phenotyping and predictive intervention, raising critical questions about fairness, bias, and inclusivity in model development. However, the adoption of these technologies, or the lack thereof, among diverse and historically marginalized groups raises questions and challenges of equity, cultural relevance, and participant trust. In this study, we conducted a four-week observational study with adults in Hawai‘i where we combined continuous Fitbit monitoring and daily EMA surveys to document substance use patterns and cravings. Through semi-structured interviews and grounded theory analysis, we identified six primary barriers to study participation and adherence: (1) disruptions to daily routines, (2) physical and psychosocial discomfort associated with wearing the Fitbit device, (3) concerns about aesthetic compatibility and professional appearance, (4) phone-related issues, (5) challenges related to substance use and cravings, and (6) socially sensitive contexts. We also highlight participant-identified facilitators, such as the value of participant-driven scheduling, motivational feedback, and contextually adaptive protocols. Drawing on these collective findings, we propose a set of design guidelines aimed at advancing the inclusivity, engagement, and fairness of wearable-based EMA research.

Keywords: Digital Health Equity; Wearable AI; mHealth; mHealth Fairness; Digital Health Fairness; Ecological Momentary Assessment (EMA); Wearables; Human-Centered Design

1. Introduction

1.1 The Rise of EMA and AI/ML in Substance Use Monitoring

Ecological momentary assessment (EMA) and wearable sensing technologies have quickly transitioned from experimental research tools to core data sources in digital health and biomedical AI pipelines[1,2]. EMA involves capturing repeated, in-the-moment self-reports of mood, context, craving, or behavior, reducing recall bias and capturing the dynamic variability that characterizes substance use trajectories[3,4]. Wearables, including smartwatches, activity bands, biosensor patches, and connected mobile peripherals, can complement this approach by providing continuous or high-frequency passive data on physiology (e.g., heart rate variability), sleep, mobility, and biochemical correlates relevant to the outcome of interest[5-7]. When integrated with machine learning (ML) and predictive modeling[8,9], multimodal EMA and sensor data can be used to identify relapse risk windows, tailor just-in-time adaptive interventions (JITAIs), and model individual responses to treatment in close to real-time[10,11].

However, this promise has yet to be fully realized in real-world settings. Datasets powering substance use prediction models are disproportionately drawn from convenience samples that over-represent relatively homogeneous, higher-income, and more digitally connected populations[12,13]. Device design assumptions, such as about wrist circumference, skin tone reflectance, notification literacy, language, and connectivity stability, may encode sociotechnical and cultural biases even before any model is trained[14,15]. Downstream AI/ML systems using these digital health data thus risk amplifying representational gaps and producing performance disparities across groups whose lived experiences differ markedly from those in the training data.

1.2. Fairness in Practice: Wearables, EMA, and Inclusion

Calls for "fair AI" often emphasize algorithmic metrics, such as calibration, error rate parity, or representational balance in training datasets[16,17]. While absolutely necessary, these abstractions are insufficient when digital tools interface with minoritized communities whose experiences of health, surveillance, trust, land, and data sovereignty differ from mainstream clinical populations[18,19]. Operationalizing fairness in practice demands attention to relational, cultural, and material dimensions[14,20]. Wearable and EMA study procedures may inadvertently create barriers to inclusion through usability challenges: straps that do not fit larger wrists; optical sensors that lose accuracy across skin tones; prompts scheduled without considering working schedule, individual lifestyle, social norms, or cultural practice; data dashboards that fail to reflect relational models of wellness (e.g., family, peers, community)[21-24]. These are not merely usability bugs; they are sites where fairness either breaks or is built.

1.3 Study Goals

We sought to understand the experiences of participants living in Hawai‘i interacting with wearable-linked EMA tools through the context of substance use research as a demonstrative example of a digital health application area disproportionately affecting underserved populations. Through community-engaged recruitment, qualitative thematic analysis, and demographic disaggregation, we identified several sociotechnical barriers that hinder sustained and equitable participation in wearable-based EMA studies. Therefore, our study was situated at the intersection of biomedical AI fairness, digital inclusion, and sociotechnical analysis of wearable-based EMA. Specifically, we sought to answer: (1) What sociotechnical and cultural challenges arise when deploying wearable-based EMA tools among a population living in Hawai‘i? (2) How can insights from these challenges inform more equitable and culturally responsive approaches to fairness in biomedical AI and digital health research?

2. Methods

2.1 Study Participants

Our study aimed to explore sociotechnical and cultural challenges in using wearable-linked EMA tools for substance use monitoring in Hawai'i. We recruited participants through three sites: a harm reduction outreach program, a residential treatment center, and the University of Hawai‘i. Inclusion criteria of our study were: (1) at least 18 years of age, (2) current residence on the island of O‘ahu, (3) reliable access to a smartphone with either a data plan or consistent Wi-Fi connectivity, and (4) self-reported active substance use on at least two different days per week involving one or more of the following: methamphetamine, alcohol, cannabis, opioids, cocaine, sedatives/benzodiazepines, nicotine, psilocybin, or gamma-hydroxybutyrate (GHB).

Exclusion criteria included: (1) active homicidal or suicidal ideation, (2) inability to provide informed consent, (3) inability to complete interviews in English, (4) anticipated incarceration or relocation from O‘ahu during the study period, and (5) failure to provide contact information either by email or phone number. Our study was conducted following the Declaration of Helsinki and was

approved by the Institutional Review Board of the University of Hawai‘i (Protocol No. 2022-01030, approved on March 22, 2023).

2.2 Device Deployment and EMA Protocol

At the initial intake meeting, participants were provided with Fitbit Charge 5 devices, which continuously collected physiological and behavioral data for a four-week period. During waking hours, the devices recorded heart rate (HR) and step count; during sleep, they monitored breathing rate (BR), blood oxygen saturation (SpO_2), and sleep quality. Participants were instructed to wear the device continuously, removing it only when necessary (e.g., for showering or water-based activities).

Concurrently, participants completed four EMA surveys per day using a custom mobile application called BanAware (Figure 1), developed for both iOS and Android platforms. The app prompted participants to report substance use events, cravings, and associated emotional states in real time. Specifically, EMA survey reminders were automatically sent four times a day at 9: 00 AM, 1:00 PM, 5:00 PM, and 9:00 PM. Additionally, participants could submit an EMA survey at any time when experiencing substance use or craving events. To reduce stigma and safeguard privacy, participants could opt to use fruit-based code names in place of specific substance names. After completing the four-week monitoring period, participants returned the devices and participated in semi-structured exit interviews to share their experiences. The full study protocol is described in detail by Sun et al.[25].

Fig. 1. User interface of the BanAware mobile app. Participants were asked to complete an EMA 4 times a day at fixed times, asking for self-reported substance use and cravings. Participants had the option of coding substances as fruit names to ensure privacy.

In addition, we developed AI models using a subset of these data by implementing a baseline 1D convolutional neural network (CNN) with traditional supervised learning and an experimental self-supervised learning (SSL) model[10]. We found that the SSL models outperformed equivalent purely supervised models on average and demonstrated the feasibility of using wearable biosignals for personalized substance use prediction.

2.3 Data Collection

We employed a qualitative design to address the research questions through a combination of intake questionnaires and in-depth interviews. At the beginning of the study, all participants completed an intake questionnaire comprising both open- and closed-ended questions. These questions captured sociodemographic characteristics (e.g., "*How do you define your race/ethnic background?*"), substance use patterns, and treatment history.

After the 4-week wearable and EMA monitoring period, participants took part in semi-structured exit interviews, conducted in person by the first and second authors. Each interview lasted between 30 and 60 minutes and was audio-recorded with the participant's consent. Exit interviews explored participants' lived experiences with the Fitbit device and the BanAware application, with a focus on usability, physical comfort, privacy, and sociocultural relevance (e.g., "*How was your experience in this study?", "How comfortable was it to wear the Fitbit all the time?"*). Field notes were recorded during each session to capture non-verbal cues and contextual observations.

2.4 Data Analysis

2.4.1. Conceptual Framework

To guide our analysis and interpretation, we adopted the Social-Ecological Model (SEM), a well-established framework for examining the multiple and interacting influences on health-related behavior. SEM conceptualizes health as shaped by factors operating across four levels: individual, interpersonal, community or organizational, and societal or policy[26]. This model provides a structured lens for identifying and categorizing the sociotechnical and cultural challenges reported by participants in our study.

2.4.2. Analytic Strategy

All audio-recorded interviews were transcribed verbatim and uploaded into Dedoose[27] a qualitative analysis software platform. We employed a grounded theory approach to inductively identify themes and categories relevant to our research questions[28]. The initial round of coding was done line-by-line within transcripts, so that codes stayed close to the data and remained open. Short, descriptive phrases were assigned as codes that outline participants' barriers (e.g., "my phone is really slow," "lost the charger," "forgot to log EMA"). The second round of coding identified the most frequent or significant themes that can respond to the research questions (e.g., "device discomfort," "emotional stress," and "social context is sensitive"). The third round of coding focused on extracting themes for a conceptual understanding and aligning them with the SEM framework (e.g., individual barrier, structural barriers).

To link the emerging codes and themes with the SEM framework, we systematically reviewed and mapped different types of codes onto its four levels during the selective coding phase. The first and second authors independently coded the transcripts and met regularly to review and reconcile coding discrepancies. Divergences were resolved through reflective discussion, iterative memo writing, and cross-validation against the original transcripts and field notes to ensure interpretive rigor and consensus.

3. Results

3.1. *Baseline Characteristics of Participants*

21 participants completed both the 4-week wearable-based EMA protocol and entry and exit interviews. The final analytic sample included participants with diverse sociodemographic backgrounds. Gender identities included male (n = 11), female (n = 8), non-binary (n = 1), and transgender (n = 1). Ages ranged from 23 to 65 years (mean = 39.0 years), with distribution as follows: 20–29 years (n = 6), 30–39 (n = 5), 40–49 (n = 6), 50–59 (n = 3), and 60+ (n = 1).

Participants self-identified as White (n = 6), Native Hawaiian (n = 5), Filipino (n = 3), Hispanic (n = 2), Samoan (n = 3), Japanese (n = 1), and Chinese (n = 1). Educational attainment included high school (n = 10), college (n = 6), master's-level students (n = 2), PhD students (n = 2), and one PhD holder (n = 1). In terms of occupation, 15 participants were employed or actively enrolled as students, while six were not working at the time of the study. Regarding EMA reporting, 15 participants opted to use substance names, and 6 chose fruit code names for privacy. Seven participants, including White (n = 4), Chinese (n = 1), Japanese (n = 1), and Filipino (n = 1), reported prior experience using wearable devices (e.g., Apple Watch, Fitbit, Samsung Galaxy). These baseline characteristics are summarized in Table 1.

Table 1. Demographic characteristics of participants.

ID	Gender	Age	Race	Log Type	Education
5	Male	65	White	Substance	College
9	Male	39	Native Hawaiian	Substance	High School
10	Male	24	Japanese	Fruit	College
12	Male	41	Hispanic	Substance	College
13	Female	24	Samoan	Fruit	Master
14	Male	32	White	Substance	Master
15	Female	28	Filipino	Substance	College
16	Non-binary	27	White	Substance	PhD Student
19	Female	55	White	Fruit	High School
20	Female	42	Native Hawaiian	Fruit	High School
23	Male	24	White	Substance	College
24	Female	25	Filipino	Substance	College
26	Male	42	White	Substance	PhD Student
27	Female	56	Native Hawaiian	Fruit	High School
28	Female	32	Chinese	Substance	PhD
29	Male	51	Filipino	Substance	High School
30	Female	40	Native Hawaiian	Substance	High School
32	Male	41	Samoan	Substance	High School
33	Transgender	34	Hispanic	Fruit	High School
34	Male	41	Native Hawaiian	Substance	High School
35	Male	35	Samoan	Substance	High School

3.2. *Sociotechnical Barriers to Wearable-Based EMA Participation*

We explored the sociotechnical and cultural changes experienced during participation in wearable-based EMA studies. Guided by the SEM framework, we identified six sociotechnical factors that influenced the sustainability and fairness of EMA engagement.

3.2.1. *Individual Factors*

Daily Routine

Participants reported difficulty responding to EMA survey prompts during specific periods of the day, such as early mornings, late evenings, work hours, classes, church services, driving, swimming, or while traveling. For example, participant 9 explained the challenges of responding during work hours, despite having phone access on the job: "*I've been working at Best Buy for two years, so I'm always doing something around 1:00 PM. I might be in the middle of helping a customer, or there's a busy line.*" Notably, timing preferences varied across groups. Some participants indicated that they preferred later EMA survey prompts. For example, participant 25 reported that the EMA survey is too early for them: "*There are sometimes in the morning. I think it was 9:00 AM. If I have class on that day, it will be fine. But on the weekends, I am sorry, I am not waking up at that time*."

In contrast, participants 5 and 26 stated that the EMA survey prompts were too late for them and described themselves as morning people. In some cases, disruptions to daily life further hindered participation. For example, participant 28 described the logistical and physiological challenges of participating in the study while traveling: "*…I was traveling for 2 weeks of the study. I lost the charger. Because it was an unfamiliar environment, I didn't check for all of my belongings before I left.*"

Wearable Device Discomfort

Participants reported skin irritation or physical discomfort from the Fitbit's rubber band, particularly when it was wet. For example, participant 29 stated, *"I was allergic to rubber*." Similarly, participant 10 described a related issue: "*I don't like the rubber band. I tried it for the first day, and I think I had it too tight. … when I go swimming, it would be really uncomfortable*."

In addition to the discomfort caused by the rubber band during the daytime, four participants reported that wearing the devices while sleeping was uncomfortable and intrusive. For example, participant 14 described their experience of wearing the Fitbit when sleeping: "*I did not really like sleeping in it. I prefer not to have. It's just like I will take my earrings out when I sleep. … I could feel it digging into my wrist or cheek.*"

This physical discomfort was exacerbated by psychosocial stress, as participants 14 and 28 preferred to sleep without wearing any digital devices, which they associated with a sense of bodily freedom. Furthermore, participants 5, 13, and 14 mentioned that they did not have the habit of wearing digital devices when sleeping before participating in the study and needed to adjust.

In addition to the discomfort caused by the device or the rubber band, participants 14, 18, and 26 reported experiencing fatigue due to continuous device use, citing a lack of relaxation and reduced bodily autonomy. For example, participant 18 stated that wearing the Fitbit device constantly made them less relaxed: "*I cannot ignore it every time it vibrates, because it's physically on my body. ... It's more open to distractions from people who try to get in touch with me.*"

Additionally, participant 26 stated that repeated EMA surveys can lead to a sense of surveillance: "*The check-in was like I was on probation, and I was constantly contacted by my probation officer.*"

Phone Issues

Participants reported phone-related disruptions, including outdated or slow devices, switching phones during the study, which led to failing to receive EMA survey prompts or disengagement. For example, participant 34 described how phone-related issues prevented them from continuing participation: *"I was on the point in the first week, and my phone stopped working. My phone was super slow, and sometimes I wouldn't receive notifications. ... Then, I got a new phone two weeks ago, but I didn't think about connecting back to the study since I missed so much*."

In addition, participant (ID 29) described a challenge related to not being able to charge the device in a safe environment: *"I don't have my own place yet. I don't have my car. I don't have a job. I don't have my benefits. I lived in a shelter. ... There is a common area I can charge. But I didn't want to leave the charger there. Somebody can grab it."*

Substance Use and Craving

Participants reported that substance use and cravings interfered with their ability to engage with the study, due to reasons such as irregular sleep patterns, active use periods, and experiencing relapse. For example, participant 33 described how substance use disrupted their sleep schedule, resulting in missed EMA survey prompts: "*I use substances to stay up. ... my sleep schedule is crazy. Sometimes when I get up, I have already missed two alerts. ... it feels like I haven't logged in my data for the day, so I'm trying to catch up, sometimes I have a craving, and then I forget [to log]."* Missing EMA survey prompts can further contribute to the stress of catching up, making engagement even more stressful. Beyond these immediate effects, substance use can affect EMA compliance indirectly. For example, participant 30 shared how a relapse, triggered by multiple life stressors, contributed to disengagement from the study: "…*things are stressed, like relationship-wise, and then I lost my car, and then financial issues, and now I am trying to get a new job. So I relapsed, and it caused me to isolate and draw away from people. .... I think it was because of my whole relapse, I guess I just did not want to do it.*"

Aesthetic Compatibility and Professional Appearance

Participants expressed concerns related to the aesthetic compatibility of the wearable device with their daily outfits, particularly in social and professional settings. This concern was raised by three female participants and one male participant. For example, participant ID 25 described removing the Fitbit to comply with the dress code at a nightclub: "*We would go out to the clubs, but they did not allow specific things, such as a Fitbit. If I wore it, they would ask me to throw it away. ... you have to dress up nicely because it is a club, so it doesn't fit.*" Similarly, participant 14 noted that they would not wear their bracelets and Fitbit together since the two did not look aesthetically compatible. Beyond informal general aesthetic and specific dress code concerns, the professional image was also a source of tension. Specifically, participant 28 expressed hesitation

about wearing a Fitbit in professional environments: "*I like the rainbow band. However, since I'm often in a professional setting, that kind of material and color is not the most professional. That makes me a little self-conscious.*"

3.2.2. *Community and Organizational Factors*

Social Context

Participants reported that social environments can be a barrier to EMA compliance. Specifically, they expressed the fear of being judged if others became aware of their substance use or study participation. For instance, participant ID 35 shared their experience of being questioned by their coworkers: "*There is a guy at work. He always asked me about the Fitbit. For a moment, I didn't want to tell him what it was, but probably by the second week, I had to tell him because I grew tired of him asking. I told him what Fitbit is for and the study, … and he gave me one look, and I didn't like it.*" Similarly, participant ID 18 explained how they failed to comply when receiving the EMA survey during the class: "*I get a reminder at 1:00 PM to log in. I wouldn't log because I'm in class, and there was a little tiny thought like, what if somebody looks over [my phone]? I chose to use the substance name.*"

3.2.3. *Explicit Participant Suggestions*

Four participants expressed confusion about how and when to log substance cravings, which hindered accurate and consistent EMA compliance. For example, participant 10 emphasized the lack of a clear time anchor for reporting cravings: "*It was kind of confusing. …If I had cravings, there's no time that I can associate with putting on the craving*." In addition to this confusion, participants 14 and 15 reported that they typically recorded substance use rather than craving, as the craving and subsequent use often occurred in close succession.

Participants 13, 20, and 26 suggested more frequent reminders. For example, participant 26 stated that they preferred a text-based reminder to sync the Fitbit data: "*I would like to get an update about refreshing the Fitbit data, because I've got updates regularly from BanAware, but I wasn't getting any updates about the Fitbit. And I'd have to remember at some points, but I wouldn't remember every day.*" Similarly, participants 13 and 20 echoed this preference, noting that text-based reminders would help them stay on track with syncing the device.

Additionally, three participants (ID 18, ID 28, ID 33) proposed visual summaries of personal data, such as craving and usage trends, to enhance user engagement and self-awareness. Two participants (ID14, ID20) recommended incorporating gamified features to strengthen motivation. Two participants (ID 18, ID 28) expressed interest in learning more about the data they provided.

4. Discussion

4.1. *Lesson Learned and Design Recommendations for Culturally Responsive and Participant-Centered EMA Implementation*

Drawing on our qualitative findings and participant feedback, we identify design considerations for improving the feasibility, equity, and sustainability of wearable-based EMA studies.

Participant-controlled scheduling and context-aware notifications reduce disruption and fatigue. Poorly timed notifications, which were reported by 13 out of the 21 participants, emerged

as a major reason for missed EMA entries. Participants requested the ability to schedule prompts around their daily routines and temporarily "snooze" reminders during rest, work, or other socially and culturally significant events. When possible, study protocols should prioritize participant autonomy in notification timing and context-sensitivity to protect daily rhythms and increase adherence.

Comfort, customization, and device compatibility are essential for long-term engagement. Our findings highlight that physical comfort and device aesthetics, reported by eight and four participants, respectively, are central determinants of sustained use. Future studies can invest in a range of device and accessory options, offer education on optimal fit, and actively address concerns around social visibility to foster consistent engagement.

Digital equity, social adaptability, and cultural relevance can broaden participation and reduce exclusion. Practical barriers, such as unreliable device/charging access and concerns about being questioned in public, reported by five and four participants, respectively, threatened inclusion for some participants, who were co-affected by socioeconomic and cultural factors. Privacy concerns and fear of stigmatization also shaped willingness to log sensitive events, especially in socially sensitive environments. Protocols that offer alternative data collection methods, portable chargers, and flexible grace periods for non-compliance can enable higher compliance. Equally important are features that empower autonomy and confidentiality: discreet notification options, anonymous user interfaces, and the ability for participants to withhold or delay entries when privacy cannot be assured. Allowing generic branding or dual-purpose device presentation and supplying participants with neutral explanations for their wearable use (e.g., "It's for a wellness challenge") can reduce both stigma and unwanted attention in real-world settings.

Supportive, nonjudgmental re-engagement pathways are critical after life disruptions. Emotional distress and life events, reported by five participants, can interrupt participation. Study protocols should anticipate these disruptions by offering friendly, judgment-free check-ins, supportive re-engagement features, and explicit permission to "restart" or recalibrate their engagement after lapses. Framing all data as valuable, regardless of lapses, can help participants return to the study when ready.

Clear definitions and flexible temporal anchoring are essential for accurate event logging. Ambiguity about when and how to log cravings versus substance use events was a consistent source of confusion, reported by four participants, leading to under-reporting or misclassification, reported by four participants. EMA platforms should provide clearer distinctions between event types, as well as the ability to retrospectively log events. EMA tools can also make temporal context explicit, through visual summaries, reminders of event definitions, and support for logging, to ensure reliable data and participant confidence in reporting.

Motivational feedback and tangible progress can sustain engagement beyond initial curiosity. Sustained participation depended on meaningful feedback and motivation. Features such as congratulatory messages, visual progress charts, and milestone rewards, reported by four participants, could have helped participants perceive their contributions as valuable and encouraged continued logging, making them feel more "motivated". Designers should integrate ongoing feedback mechanisms, goal-setting, and positive reinforcement to maintain momentum, especially as novelty wanes. Taken together, these qualitative insights demonstrate how fairness can be enhanced not only through algorithms but also by making human-centered design choices that reduce digital inequalities, offer scheduling flexibility, and support culturally sensitive device use.

4.2. *Limitations*

Our study has several limitations. First, our inclusion criteria required participants to have access to a smartphone with either a data plan or consistent Wi-Fi connectivity, which may have excluded individuals with limited digital access or unstable living conditions, factors especially relevant in substance use and underserved populations who often overlap. Second, our study relied on a relatively small sample size, which limits statistical generalizability and reduces our ability to capture subgroup-specific barriers, particularly among Native Hawaiian and Pacific Islander (NHPI) communities, which were reported by prior studies[29,30]. Third, our findings did not identify significant sociotechnical barriers at the interpersonal (e.g., social support) or societal/policy levels (e.g., stable housing), as noted in prior studies[31,32]. Fourth, while our findings highlight several sociotechnical barriers to EMA compliance, these factors were often deeply intertwined, making it difficult to isolate their specific impacts. Moreover, these sociotechnical factors can be linked to broader social and cultural norms. For example, concerns about aesthetic compatibility and professional appearance may be influenced by gender norms, peer pressure, or expectations from senior colleagues, factors that are often associated with youth culture or hierarchical social settings[33,34]. Yet, participants internalized these concerns as personal preferences, suggesting how broader social and cultural norms can subtly shape EMA compliance in ways that both participants and researchers may overlook, which were not fully explored in our study. Fifth, the four-week observation period may not reflect long-term patterns of engagement or the sustainability of EMA and wearable use. Sixth, the sample was broad and heterogeneous, with participants varying in both substance use severity and the type of substances used. Not all substances carry the same risks or patterns of use, and as a result, participants experiences were likely quite different. Lastly, it is noteworthy that all NHPI participants in this study reported lower educational attainment compared to participants from other racial or ethnic groups. This disparity may affect the generalizability of the findings to broader or more diverse populations.

4.3. *Opportunities for Future Work*

In future work, we aim to include larger, demographically disaggregated samples, especially within NHPI populations, to identify sociotechnical and culturally specific barriers and to ensure that Indigenous perspectives are meaningfully incorporated into fairness frameworks. Qualitative approaches will be essential for surfacing nuanced challenges to digital health engagement in NHPI and other underserved communities[35,36]. Second, we aim to leverage the design insights described here to develop new EMA systems that prioritize comfort, offer customizable, socially adaptable, and culturally responsive designs, and incorporate data visualization and motivational feedback to support diverse user needs and encourage sustained engagement. Third, we plan to implement more restrictive eligibility criteria or substance-specific subgroups to enable clearer interpretation of outcomes and ensure that differences related to substance type and severity are appropriately captured. We also intend to examine differences in participant context, such as housing status, age group, or educational attainment, to better understand how situational factors shape substance use experiences and to improve generalizability. Finally, we would like to include longer-term deployments to evaluate how life events, daily routines, and the presence or absence of support mechanisms influence the effectiveness of EMA health research over time.

5. References

1. Battaglia, B., Lee, L., Jia, S. S., Partridge, S. R., & Allman-Farinelli, M. (2022). The Use of Mobile-Based Ecological Momentary Assessment (mEMA) Methodology to Assess Dietary Intake, Food Consumption Behaviours and Context in Young People: A Systematic Review. *Healthcare (Basel, Switzerland)*, *10*(7), 1329. https://doi.org/10.3390/healthcare10071329
2. Lampreia, F., Madeira, C., & Dores, H. (2024). Digital health technologies and artificial intelligence in cardiovascular clinical trials: A landscape of the European space. *Digital health*, *10*, 20552076241277703. https://doi.org/10.1177/20552076241277703
3. Stinson, L., Liu, Y., & Dallery, J. (2022). Ecological Momentary Assessment: A Systematic Review of Validity Research. *Perspectives on behavior science*, *45*(2), 469–493. https://doi.org/10.1007/s40614-022-00339-w
4. Stone, A. A., & Shiffman, S. (1994). Ecological momentary assessment (EMA) in behavorial medicine. *Annals of Behavioral Medicine, 16*(3), 199–202. https://doi.org/10.1093/abm/16.3.199
5. Lee, J. S., Browning, E., Hokayem, J., Albrechta, H., Goodman, G. R., Venkatasubramanian, K., Dumas, A., Carreiro, S. P., O'Cleirigh, C., & Chai, P. R. (2024). Smartphone and Wearable Device-Based Digital Phenotyping to Understand Substance use and its Syndemics. *Journal of medical toxicology : official journal of the American College of Medical Toxicology*, *20*(2), 205–214. https://doi.org/10.1007/s13181-024-01000-5
6. Dian, F.J., Vahidnia, R. and Rahmati, A. (2020) Wearables and the Internet of Things (IoT), Applications, Opportunities, and Challenges: A Survey. IEEE Access, 8, 69200-69211. https://doi.org/10.1109/ACCESS.2020.2986329
7. Kang, M., & Chai, K. (2022). Wearable Sensing Systems for Monitoring Mental Health. *Sensors (Basel, Switzerland)*, *22*(3), 994. https://doi.org/10.3390/s22030994
8. Kargarandehkordi, A., Li, S., Lin, K., Phillips, K. T., Benzo, R. M., & Washington, P. (2025). Fusing Wearable Biosensors with Artificial Intelligence for Mental Health Monitoring: A Systematic Review. *Biosensors*, *15*(4), 202. https://doi.org/10.3390/bios15040202
9. Islam, T., & Washington, P. (2024). Non-Invasive Biosensing for Healthcare Using Artificial Intelligence: A Semi-Systematic Review. *Biosensors*, *14*(4), 183. https://doi.org/10.3390/bios14040183
10. Li, S., Fan, C., Kargarandehkordi, A., Sun, Y., Slade, C., Jaiswal, A., Benzo, R. M., Phillips, K. T., & Washington, P. (2024). Monitoring Substance Use with Fitbit Biosignals: A Case Study on Training Deep Learning Models Using Ecological Momentary Assessments and Passive Sensing. *AI (Basel, Switzerland)*, *5*(4), 2725–2738. https://doi.org/10.3390/ai5040131
11. Slade, C., Sun, Y., Chao, W. C., Chen, C. C., Benzo, R. M., & Washington, P. (2025). Current challenges and opportunities in active and passive data collection for mobile health sensing: a scoping review. *JAMIA open*, *8*(4), ooaf025. https://doi.org/10.1093/jamiaopen/ooaf025
12. Celi, L. A., Cellini, J., Charpignon, M. L., Dee, E. C., Dernoncourt, F., Eber, R., Mitchell, W. G., Moukheiber, L., Schirmer, J., Situ, J., Paguio, J., Park, J., Wawira, J. G., Yao, S., & for MIT Critical Data (2022). Sources of bias in artificial intelligence that perpetuate healthcare disparities-A global review. *PLOS digital health*, *1*(3), e0000022. https://doi.org/10.1371/journal.pdig.0000022
13. Nordling L. (2019). A fairer way forward for AI in health care. *Nature*, *573*(7775), S103–S105. https://doi.org/10.1038/d41586-019-02872-2
14. Dolata, M., Feuerriegel, S., & Schwabe, G. (2022). A sociotechnical view of algorithmic fairness. *Information Systems Journal*, 32(4), 754–818. https://doi.org/10.1111/isj.12370
15. Mergen, A., Çetin-Kılıç, N., & Özbilgin, M. F. (2025). Artificial intelligence and bias towards marginalised groups: Theoretical roots and challenges. In AI and Diversity in a Datafied World of Work: Will the Future of Work be Inclusive? (Vol. 12, pp. 17-38). Emerald Publishing Limited.

16. Chen, R. J., Wang, J. J., Williamson, D. F. K., Chen, T. Y., Lipkova, J., Lu, M. Y., Sahai, S., & Mahmood, F. (2023). Algorithmic fairness in artificial intelligence for medicine and healthcare. *Nature biomedical engineering*, *7*(6), 719–742. https://doi.org/10.1038/s41551-023-01056-8
17. Huerta, E. A., Blaiszik, B., Brinson, L. C., Bouchard, K. E., Diaz, D., Doglioni, C., Duarte, J. M., Emani, M., Foster, I., Fox, G., Harris, P., Heinrich, L., Jha, S., Katz, D. S., Kindratenko, V., Kirkpatrick, C. R., Lassila-Perini, K., Madduri, R. K., Neubauer, M. S., Psomopoulos, F. E., … Zhu, R. (2023). FAIR for AI: An interdisciplinary and international community building perspective. *Scientific data*, *10*(1), 487. https://doi.org/10.1038/s41597-023-02298-6
18. Kaur, J. S., & Burhansstipanov, L. (2024). From Insufficient Data to New Models of Healthcare in the USA. In Indigenous and Tribal Peoples and Cancer (pp. 77-80). Cham: Springer Nature Switzerland.
19. Kong, Y. (2022). Are "Intersectionally Fair" AI Algorithms Really Fair to Women of Color? A Philosophical Analysis. In Proceedings of the 2022 ACM conference on fairness, accountability, and transparency (pp. 485-494). https://doi.org/10.1145/3531146.3533114
20. Giovanola, B., & Tiribelli, S. (2023). Beyond bias and discrimination: redefining the AI ethics principle of fairness in healthcare machine-learning algorithms. *AI & society*, *38*(2), 549–563. https://doi.org/10.1007/s00146-022-01455-6
21. Bell, B. M., Alam, R., Mondol, A. S., Ma, M., Emi, I. A., Preum, S. M., de la Haye, K., Stankovic, J. A., Lach, J., & Spruijt-Metz, D. (2022). Validity and Feasibility of the Monitoring and Modeling Family Eating Dynamics System to Automatically Detect In-field Family Eating Behavior: Observational Study. *JMIR mHealth and uHealth*, *10*(2), e30211. https://doi.org/10.2196/30211
22. Fabbrizio, A., Fucarino, A., Cantoia, M., De Giorgio, A., Garrido, N. D., Iuliano, E., Reis, V. M., Sausa, M., Vilaça-Alves, J., Zimatore, G., Baldari, C., & Macaluso, F. (2023). Smart Devices for Health and Wellness Applied to Tele-Exercise: An Overview of New Trends and Technologies Such as IoT and AI. *Healthcare (Basel, Switzerland)*, *11*(12), 1805. https://doi.org/10.3390/healthcare11121805
23. Ferguson, K., Gunthert, K., Kaidbey, J. H., Parr, M., Visek, A. J., Sacheck, J. M., & Sylvetsky, A. C. (2023). Behavioral Patterns of Sugary Drink Consumption among African American Adolescents: A Pilot and Feasibility Study Using Ecological Momentary Assessment. *Nutrients*, *15*(9), 2171. https://doi.org/10.3390/nu15092171
24. Lei, C., Qu, D., Liu, K., & Chen, R. (2023). Ecological momentary assessment and machine learning for predicting suicidal ideation among sexual and gender minority individuals. *JAMA Netw Open.* 2023;6(9):e2333164. https://doi.org/10.1001/jamanetworkopen.2023.33164
25. Sun, Y., Kargarandehkordi, A., Slade, C., Jaiswal, A., Busch, G., Guerrero, A., Phillips, K. T., & Washington, P. (2024). Personalized Deep Learning for Substance Use in Hawaii: Protocol for a Passive Sensing and Ecological Momentary Assessment Study. *JMIR research protocols*, *13*, e46493. https://doi.org/10.2196/46493
26. McLeroy, K. R., Bibeau, D., Steckler, A., & Glanz, K. (1988). An ecological perspective on health promotion programs. *Health education quarterly*, *15*(4), 351–377. https://doi.org/10.1177/109019818801500401
27. Salmona, M., Lieber, E., & Kaczynski, D. (2019). Qualitative and mixed methods data analysis using Dedoose: A practical approach for research across the social sciences. Sage Publications.
28. Charmaz, K. (2008). Grounded theory as an emergent method. Handbook of emergent methods, 155, 172.
29. Pike, J. R., Xie, B., Tan, N., Sabado-Liwag, M. D., Orne, A., Toilolo, T., Cen, S., May, V., Lee, C., Pang, V. K., Rainer, M. A., Vaivao, D. E., Lepule, J. T., Tanjasiri, S. P., & Palmer, P. H. (2016). Developing an Internet- and Mobile-Based System to Measure Cigarette Use Among Pacific Islanders: An Ecological Momentary Assessment Study. *JMIR mHealth and uHealth*, *4*(1), e2. https://doi.org/10.2196/mhealth.4437

30. Kaholokula, J. K. A., Okamoto, S. K., & Yee, B. W. (2019). Special issue introduction: Advancing Native Hawaiian and other Pacific Islander health. Asian American Journal of Psychology, 10(3), 197.
31. Fortuna, K. L., Wright, A. C., Mois, G., Myers, A. L., Kadakia, A., & Collins-Pisano, C. (2022). Feasibility, Acceptability, and Potential Utility of Peer-supported Ecological Momentary Assessment Among People with Serious Mental Illness: a Pilot Study. *The Psychiatric quarterly*, *93*(3), 717–735. https://doi.org/10.1007/s11126-022-09986-3
32. Turner, C. M., Arayasirikul, S., Trujillo, D., Lê, V., & Wilson, E. C. (2019). Social Inequity and Structural Barriers to Completion of Ecological Momentary Assessments for Young Men Who Have Sex With Men and Trans Women Living With HIV in San Francisco. *JMIR mHealth and uHealth*, *7*(5), e13241. https://doi.org/10.2196/13241
33. Sun, Y., & Suthers, D. (2022, January). Examining cultural and technological change: A study of cultural affordances on WeChat. In Proceedings of the 55th Hawaii International Conference on System Sciences.
34. Urien, J., & Urien, P. (2025). Psychological Effects of Professional Dress Code of Students on their Studies and Behaviour at Delta State University, Abraka. *African Journal of Sociology, Psychology and Rural Studies*, *5*(1), 175-199.
35. Kawakami, K. L., Muneoka, S., Burrage, R. L., Tanoue, L., Haitsuka, K., & Braun, K. L. (2022). The Lives of Native Hawaiian Elders and Their Experiences With Healthcare: A Qualitative Analysis. *Frontiers in public health*, *10*, 787215. https://doi.org/10.3389/fpubh.2022.787215
36. Masuda, A., Nakamura, L., Preston-Pita, H., Hermosura, S., Morgan, L., Stueber, K., Spencer, S. D., Qina‘au, J., & Austin-Seabury, A. A. (2024). Native Hawaiians' Views on Depression and Preferred Behavioral Health Treatments: a Preliminary Qualitative Investigation. *The journal of behavioral health services & research*, *51*(2), 203–218. https://doi.org/10.1007/s11414-023-09874-z

Building Fair and Trustworthy Biomedical AI: A Tool for Identifying Key Decision Points

Nicole Foti
Stanford Center for Biomedical Ethics, Stanford University
Stanford, CA, USA
Email: nfoti@stanford.edu

Janet K. Shim
Department of Social and Behavioral Sciences, University of California San Francisco
San Francisco, CA, USA

Caitlin McMahon
Division of Ethics, Columbia University
New York, NY, USA

Sandra Soo-Jin Lee
Division of Ethics, Columbia University
New York, NY, USA

Recent advancements in artificial intelligence (AI) have transformed biomedicine, offering tools for improved diagnostics, drug discovery, and patient care. Yet these innovations raise pressing ethical concerns, including bias, inequitable outcomes, and privacy risks, which highlight the need for deliberate attention to fairness, trust, and trustworthiness in AI development. In this paper, we argue that ethical responsibility should be embedded at both institutional and individual levels, and that multi-stakeholder engagement, especially with underrepresented groups, is essential to ensure AI tools meet diverse needs. Building on a framework originally developed for precision medicine research, we present an adapted decision-mapping tool—the Trustworthy AI Decision Map—that can anchor and structure dialogue about the ethical implications of specific AI tools. The map identifies key decision points across the AI life cycle that impact fairness and trustworthiness and facilitates dialogue among stakeholders. In making these decisions visible, the map seeks to enable teams to anticipate downstream consequences, integrate multiple perspectives, and support institutional accountability. We illustrate its potential through a case involving the deployment of AI in rural healthcare settings. Moving forward, we suggest that empirical testing with stakeholders is needed to validate and refine the map's utility in biomedical AI contexts to promote fair and trustworthy AI practices.

Keywords: Biomedical AI, Fairness, Trust, Trustworthiness, Stakeholder engagement

© 2025 The Authors. Open Access article published by World Scientific Publishing Company and distributed under the terms of the Creative Commons Attribution Non-Commercial (CC BY-NC) 4.0 License.

1. Introduction

Artificial intelligence is transforming biomedicine. From improving diagnostic accuracy to accelerating drug discovery, AI offers powerful tools for advancing research and clinical care. Yet this potential is entangled with a range of ethical concerns, including biased training data that can exacerbate health disparities, threats to privacy, and the risk of unintended harms when algorithms are used in ways not originally intended. These concerns raise critical questions about responsibility and process: At what points in the development cycle are ethical issues identified, and through what mechanisms? Who bears responsibility for addressing them? And how can interventions be structured to anticipate downstream consequences rather than reacting only once problems emerge?

For many working in biomedical AI, responsibility for ethical outcomes is either unclear or assumed to lie elsewhere. Some developers believe their products are unlikely to cause harm, while others may recognize the risks but feel ill-equipped to address them. A recent study on software startup environments found that ethical concerns are often deferred or displaced—framed as someone else's problem, or something to be handled "later," if at all.[1] Even when researchers or developers want to build more fair and trustworthy systems, they may lack the structures, support, or tools to identify where their decisions have ethical consequences.

This ambiguity reflects a deeper issue, in which the burden of ethical AI is often placed on individuals when it should be understood as a shared, institutional responsibility. Our work responds to this challenge. Building on a framework originally developed for use in precision medicine research (PMR), we offer a tool for identifying key decision points across the life cycle of biomedical AI/ML development that shape fairness and trustworthiness. By making these decision points visible, the tool can support both individual reflection and institutional accountability by facilitating dialogue about when and where to intervene.

1.1. *Fairness, trust, and trustworthiness in AI*

In recent years, there has been a surge of interest in "fair" and "trustworthy" AI.[2,3] Yet these terms are often invoked without careful definition, or treated in ways that gloss over their complexity. Even less attention is paid to the fact that fairness, trust, and trustworthiness can have very different meanings depending on social, cultural, and institutional context. What one group views as fair or trustworthy may be contested by another. For instance, a widely cited study of fairness in AI shows how applying different fairness metrics to the same case can yield opposing conclusions, with some assessing the case as fair and others as unfair.[4]

For the purpose of this paper, we follow a sociological perspective that treats trust as a *relational* process.[5] In this view, trust exists when one party believes another has incentives to act in their best interest.[6] This perspective distinguishes trust from trustworthiness. Trust refers to the belief or expectation held by one party that the other will act in their best interest, while

trustworthiness encompasses the actual practices and qualities that justify that belief. Kraft and colleagues emphasize this distinction in precision medicine, arguing that *building trust* and *being trustworthy* are two distinct actions.[7] Institutions may cultivate trust through strategic outreach or branding, but this does not guarantee trustworthiness. To be trustworthy requires substantive commitments: maintaining transparency, ensuring accountability, minimizing conflicts of interest, addressing systemic inequities, and engaging meaningfully with participants' lived experiences and histories.

Fairness is related but distinct, focusing attention on how the benefits and harms of AI are distributed and, importantly, on the broader systems of inequality in which technologies take shape. Fair AI is defined in some frameworks as tools and models that are impartial, do not introduce bias, and are applied equitably to produce equitable outcomes across populations.[8] Other frameworks go beyond these somewhat more technical dimensions to also include principles of transparency (comprised of qualities of interpretability, explainability, accountability) and inclusion (including completeness of information to detect bias and responsible collection of data, patient and family engagement) into proposed definitions of fairness in AI.[9] In this latter, more fulsome definition of fairness, there is substantial alignment with notions of trustworthiness.

Together, fairness and trustworthiness are integral in the evaluation of ethical AI. But because these concepts are situated and contested, principle-driven approaches can be limited. To ensure fair and trustworthy AI, it is essential to bring in perspectives from patients, members of the public, and especially individuals from marginalized communities.[10,11] Thus, we need tools that can help elicit, compare, and negotiate diverse stakeholder understandings of what fair and trustworthy AI requires in particular contexts, such as in clinical care.

1.1.1. *Multi-stakeholder perspectives*

Engagement with AI developers, patients, researchers, healthcare professionals, policymakers, and marginalized groups is crucial for understanding the varied and context-specific meanings of trust, fairness, and trustworthiness in the development and deployment of AI in health and biomedicine. As noted, these concepts are not universal; they are shaped by local conditions, histories, and relationships, and their interpretations can differ significantly across multiple stakeholder groups. Such differences directly influence whether, and under what circumstances, communities are willing to adopt AI technologies and how these technologies might affect them. Assumptions about shared values, potential benefits, or possible harms may overlook important concerns and priorities. Instead, these must be surfaced through meaningful engagement.

Effective engagement extends beyond one-way collection or dissemination of information to forms of collaboration in which communities and stakeholders have genuine influence and power over decisions. Community and stakeholder engagement can take many forms, from focus groups

and participatory workshops to long-term advisory boards, community-based participatory research, or co-design processes that embed stakeholders throughout every stage of a project.[12] Importantly, engagement should not be viewed as a box-checking exercise—it requires time, resources, and careful planning.[13] When done haphazardly, it can erode trust, especially if participants perceive the process as performative or if they do not see their contributions as leading to meaningful outcomes; however, strong engagement practices can often strengthen trust and trustworthiness.[14,15] Thus, our mapping tool offers one pathway and a set of procedures toward this goal. Unlike principles-based frameworks that rely on predefined ethical standards, our map is designed to facilitate dialogue among diverse stakeholders about their own definitions of fairness, trust, and trustworthiness.

1.2. *Current tools for ethical AI in biomedicine*

Several tools have been proposed to address ethical considerations in biomedical AI. Ng and colleagues adopt a lens related to ours, focusing on the AI life cycle to systematically identify ethical concerns across each stage.[16] Importantly, they emphasize the interdependence of these stages, arguing that ethical implications should be assessed holistically rather than in isolation. A team at Stanford Health Care developed an assessment to identify Fair, Useful, and Reliable AI Models (FURMs), a framework used "to routinely estimate the achievable benefits of AI model-guided workflows before deployment."[17] In addition to technical, infrastructural, and impact considerations, each FURM assessment includes a component to assess ethical considerations, including responsibility, equity, traceability, reliability, governance, nonmaleficence, and autonomy. Trotsyuk and colleagues offer yet another approach, focusing on preventing and mitigating misuse of AI in biomedicine.[18] Their framework identifies current guidance and regulations, recommends existing "off-the-shelf" mitigation strategies, and considers design-specific interventions to address potential harms.

Given that most of these tools focus on identifying specific ethical issues to guide the development of fair and trustworthy AI, in this paper, we explore the possibility of adapting a tool we created for a different domain—supporting cross-stakeholder dialogue and collaboration in precision medicine research (PMR)—to the context of AI development and deployment in biomedicine. Our Diversity Decision Map (DDM) was designed to provide a platform to elicit and compare multiple stakeholders' understandings of diversity and equity, and to examine how these values are integrated into research decisions. We believe this approach has potential utility for structuring multi-stakeholder discussions around the concepts of fairness, trust, and trustworthiness in biomedical AI, and for integrating these values into governance practices.

Below, we first describe the development of the DDM—how it was created, how it can be applied in PMR, and an illustrative example emphasizing community engagement. Building on this foundation, we introduce a new, adapted map for AI development that highlights key decision points affecting fairness, trust, and trustworthiness. Although this AI-focused map has not been reviewed

by stakeholders for feedback like the DDM, we show how it could be used in practice, using a real-world example of AI that again underscores the importance of diverse stakeholder engagement throughout the development life cycle—from problem identification and team formation through model maintenance and monitoring.

2. The Diversity Decision Map

From 2018 to 2023, our research team conducted the Ethics of Inclusion (EOI) Study,[19–22] where our goal was to determine how definitions of diversity impact precision medicine research practices such as retention, engagement, and return of results. We assessed how approaches towards diversity and inclusion are managed in tandem with other research goals, and the implications of specific trade-offs that result. As part of our effort to create data-informed guidance for PMR, we developed an empirically derived draft dialogical tool, the Diversity Decision Map (DDM), to support multi- and cross-stakeholder conversations and more collaborative, deliberate decision-making around how to achieve goals of diversity, inclusion, and equity in PMR.[23]

2.1. *Methods and development of DDM*

The methods for the development of the DDM are described fully elsewhere.[23] Briefly, we analyzed our EOI Study data to identify and create a visual display of key decision-making nodes that influenced and/or impacted goals of diversity and equity. We took inspiration from the burgeoning literature on designing biomedical research for diversity and equity[24–31] but sought to offer something distinct from the existing literature, motivated by the decision-making support needs expressed by our participants. They indicated needing ways to help anticipate the future consequences of research choices and tradeoffs for diversity, inclusion, and equity; a platform and opportunities for greater multi-stakeholder dialogue; and tools to retrospectively reflect on different study choices—paths taken and not taken—that ended up impacting the inclusivity of their research practices and diversity of participant samples in unanticipated ways. To assess the potential utility of the DDM, we conducted three engagement sessions with regulatory and ethics staff at an academic medical center, precision medicine investigators who are part of a genetic research consortium, and community partners with experience advising a clinical translational science institute. Results indicated that the DDM would catalyze the kinds of discussions and raise the kinds of questions we hoped it would, and supported the proof of principle for the DDM.

2.2. *Orientation to the DDM*

In Figure 1, we show our current draft of the DDM. It represents our EOI Study findings that PMR studies often engaged in different research stages at the same time, as investigators iterated on study procedures after encountering issues or new conditions. Significantly, we found that multiple

seemingly minor research decisions made upstream incrementally shaped and constrained consequences for participant diversity, the kinds of data collected, relations with participants or community advisors, and the potential to aggregate data with those of other studies. Similarly, choices made at one time about one study activity often looped back to shape other activities and options available in the future. Thus, we constructed the DDM to indicate how research activities (in boxes) across the research life course (related but different from the research life cycle[23]) connect to and influence one another, through double-headed arrows that represent the potential mutual influence of different study stages and research activities. Not all possible arrows are depicted, and the study stages described in the boxes in the DDM are not intended to be exhaustive, but rather highlight common domains of research identified in our EOI data that were impacted by and influenced goals of diversity.

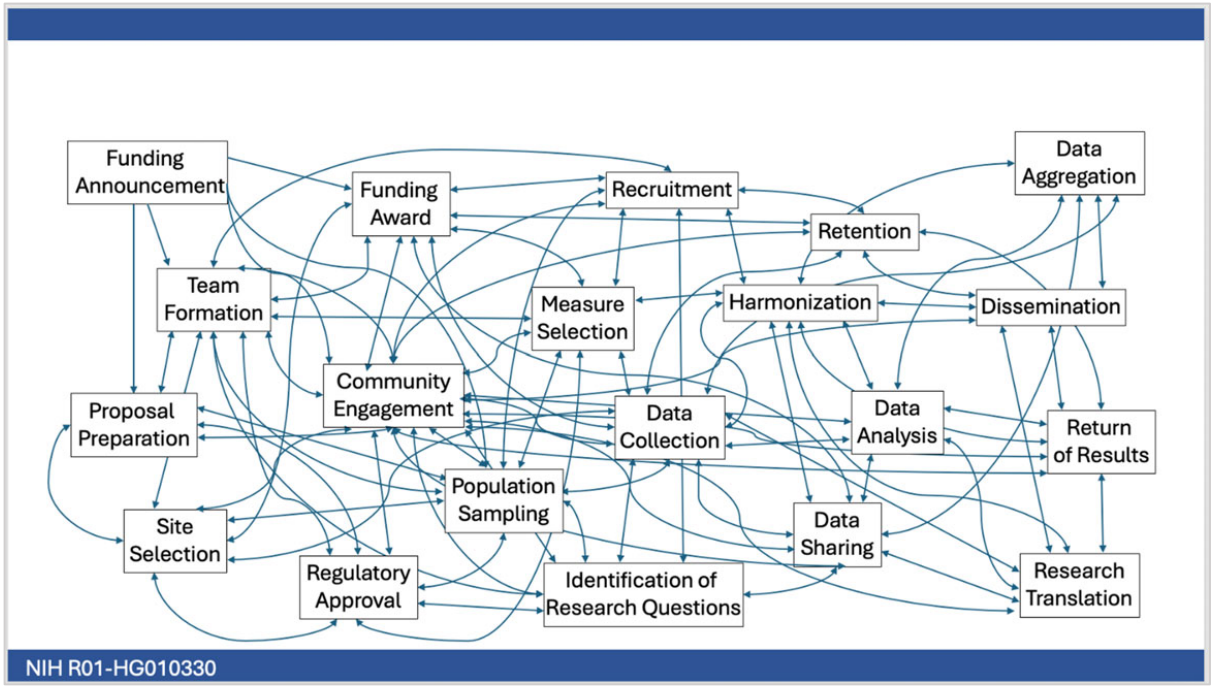

Fig. 1. Diversity decisions across the research life course

The DDM is not meant as a prescriptive, normative guide for what specific research decisions can and should be made to optimize equity. Instead, we developed the DDM to serve as a useful heuristic and tool to enable stakeholders to identify tradeoffs and facilitate stakeholder dialogue about those tradeoffs, at multiple stages of a study and even when the research is well underway (see our DDM User Guide[32]). To do so, we found that the DDM allowed stakeholders to locate where they are in the research process (much like a map reader who must pinpoint where they are before navigating their way). Stakeholders then could weigh competing interests, consider methodological and resource tradeoffs, anticipate the future consequences of different choices for

inclusion and equity, and seek to make informed decisions. The DDM thus helped guide the systematic consideration of the potential effects of study decisions about one set of research activities on others, by attending to how boxes are and might be connected to and influence others.

As a brief example of how PMR teams might use the DDM, we illustrate this by focusing on community engagement, located in the center-left of the DDM. Examining potential arrows between Community Engagement and other boxes leads to posing questions about whether, when, and how community engagement is or is not incorporated into the governance of the study throughout the research life course. The degree of commitment to Community Engagement affected choices about Team Formation, as represented in the arrow between those two boxes (see Figure 2): our EOI findings suggest that strong commitments to an engaged approach led to community partners needing to be part of study leadership, whereas understandings of community input as advisory meant that community engagement could happen more separately.[13] The relative integration of community input often affected who enrolled in PMR studies, as seen by arrows connected to Recruitment and Retention (both in top middle) and Population Sampling (bottom middle). Community Engagement could also be linked to other research stages such as Identification of Research Questions (bottom center): empirically, we found that decisions about who to engage, when, and how shaped whether community advisors provided input on what sorts of research questions were pursued, and therefore what data were collected and how.

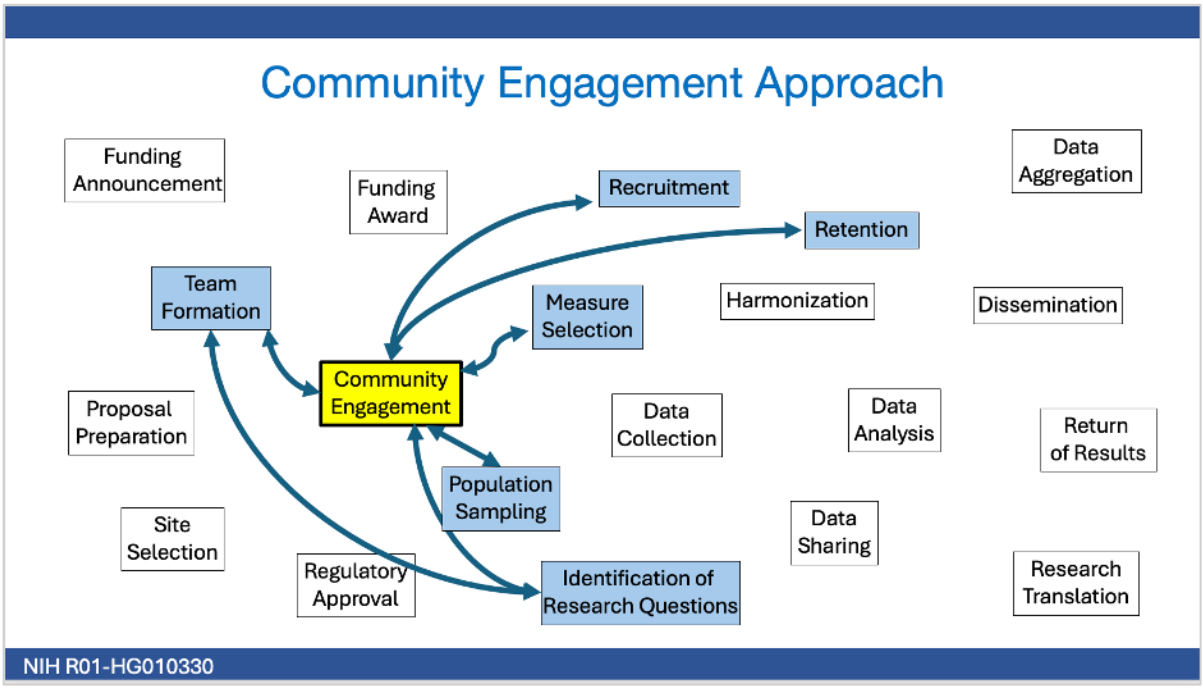

Fig. 2. Example of the DDM to analyze whether, when, and how community engagement is integrated into PMR studies

3. Mapping Key Decision Points in AI Development for Fair and Trustworthy AI

We believe that many of the same contexts, constraints, and issues that we observed in our EOI Study, with respect to values and practices related to diversity and equity in PMR, also play out in the development and deployment of AI tools in biomedicine. This domain is similarly marked by the competing interests and priorities of innovation and those of communities. Yet despite the growing influence of AI in health and medicine, there remain few formal mechanisms to ensure that considerations of fairness and trustworthiness, and their meanings by multiple stakeholders, are consistently integrated into decision-making.

3.1. *Applying the decision map to AI*

To support reflection and deliberation in this space, we adapted the original DDM into a new tool we call the *Trustworthy AI Decision Map,* or AI-DM for short (Figure 3). While several other frameworks exist for guiding ethical AI development—most notably those organized around high-level phases of the AI life cycle and principle-based ethical analysis—our approach differs in important ways. Rather than treating the stages of AI development as discrete or linear, the AI-DM emphasizes the dense network of *micro-decisions* that occur within and across those stages. Drawing from our prior findings, we argue that decisions impacting fairness and trustworthiness are not resolved at singular points or stages of the life cycle, but are continually shaped through seemingly routine or technical choices: how a problem or need is identified and defined, how a dataset is created, how missing data is handled, or how a model is implemented in a specific context. The AI-DM is designed to make these granular choices more visible and open to scrutiny, enabling teams to better anticipate downstream consequences and identify opportunities for intervention.

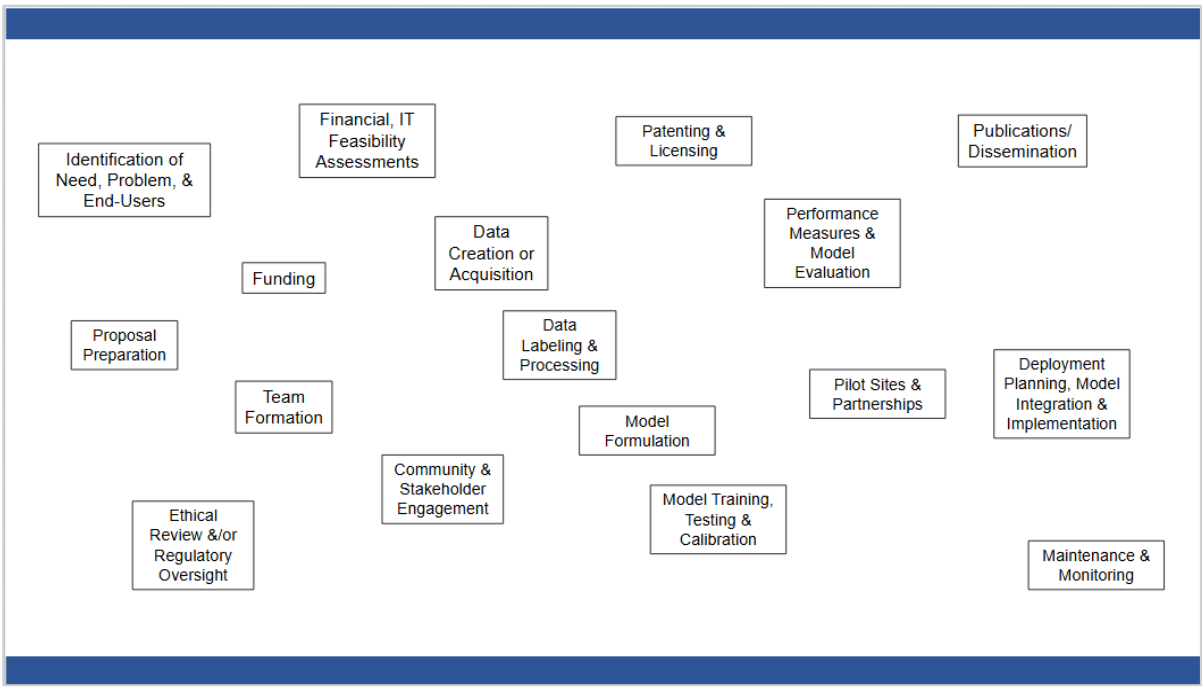

Fig. 3. Map of decision points impacting fairness and trustworthiness in biomedical AI development

The AI-DM is intended to help structure reflections on and dialogue about where and how issues around fairness and trustworthiness arise and where outcomes that impact these qualities are being shaped. While retrospection is always important, the key intervention we hope the AI-DM can have is to elicit conversations in proactive and anticipatory ways among multiple stakeholders. To do so, the AI-DM may be used by academic medical centers, health systems, research and other institutions to convene and conduct discussions focused on the fair and responsible development and deployment of an AI tool.

Data scientists, AI developers, researchers and/or clinicians, regulatory staff, and patient and community representatives, among others, can participate in facilitator-led discussions that are anchored by and oriented to the AI-DM. Advance prep work and review of accompanying resources would familiarize participants with the AI-DM, its purpose, and the charge or agenda for the discussion. A facilitated session would then further introduce and explain the AI-DM and demonstrate its use. Participants would then discuss (in breakout groups depending on size) such prompts as:

- What stage is the AI tool in right now, and how does this impact perceptions of its fairness and trustworthiness?

  Sub-questions: Have different stakeholder groups' definitions of fairness and trustworthiness been elicited, and how might these definitions differ? Are tradeoffs or

conflicts between fairness and trustworthiness explicitly acknowledged (e.g., an approach that appears "fair" across groups may still lack accountability or responsiveness, and thus be seen as untrustworthy)? What decisions, in what other boxes on the AI-DM, have already been made? Who has been involved in these decisions, whose input has been meaningfully considered, and to what extent has there been transparency around the reasoning for these decisions? What impacts do these previous decisions have on the current stage for fairness (e.g., new biases, representativeness) and trustworthiness (e.g., clarity of documentation, perceived responsiveness to concerns)? What options remain open at the current stage, and what have been closed off due to previous decisions? How do these open and closed options affect how the AI tool is seen as fair and trustworthy, by whom, and for whom? What additional ethical implications, such as equity and inclusion, are potentially at play at this decision point?

- After choosing (or being assigned) a decision-making point to discuss, consider at least two different options or pathways.
  Sub-questions: By locating and considering different boxes on the AI-DM, what are the potential downstream consequences related to fairness and trustworthiness that the different pathways might impact? For example, which stakeholder groups are most affected by this decision point and the different pathways? Are there processes in place to ensure these groups are aware of these potential effects, and to what extent will they be engaged in shaping future decisions about what paths will be pursued? To what extent do stakeholders see clear reasoning and accountability in how choices were made? How might each pathway differently affect trust-building with various communities? What fairness concerns might emerge from each option (e.g., are benefits and harms equitably distributed)? What perspectives on fairness and trustworthiness from affected stakeholders might be missing from this analysis? By tracing pathways between the current stage and other boxes, systematically walk through how a specific decision at the current stage could impact options at future stages. Generate explicit discussion about potential unintended ethical consequences by tracing pathways from the current stage to boxes that appear to be indirectly connected or located farther downstream.
- Synthesize and think iteratively and systematically:
  Sub-questions: Look back upstream: Could earlier decisions be modified or redirected in ways that might change the downstream pathways available, and their effects for fairness and trustworthiness? What different pathways forward have been identified, and what are their potential tradeoffs and consequences? What has not been considered on the AI-DM? Are there boxes or pathways that have not been explored or discussed that could impact fairness and trustworthiness?

The facilitated session would then end with reflections and strategizing next steps based on the discussion.

3.2. *Example of applying the AI-DM: Thinking through the consequences of stakeholder engagement on ethical AI*

To illustrate the potential utility of the AI-DM, we consider a real-world example (anonymized here for confidentiality) in which a developer created an AI-enabled chatbot assistant for doctors, designed specifically to support rural clinicians. The chatbot was designed to be trained on institution-specific content to assist with clinical questions about diagnoses and treatments, clinical guidelines, drug information, and more. Keeping clinicians up to date on rapidly evolving medical knowledge is a persistent challenge, especially in rural contexts, and such a tool could help rural doctors provide higher-quality care for their patients. Yet, realizing this potential requires careful consideration of how rural medical practices can differ from urban settings. Underresourced clinics and hospitals often face serious constraints in infrastructure and staffing, which means that questions of fairness and trustworthiness may emerge differently than in better-resourced settings. We see this not as a reason to exclude rural clinics from AI deployment; if AI implementation occurs only in well-resourced institutions, it risks compounding inequities in access to the benefits of AI. Instead, we suggest that our tool may provide a mechanism to surface and consider how AI development can be responsive to local conditions.

The AI-DM (Figure 4) can help make potential ethical and technical issues that impact fairness and trustworthiness visible by drawing out important connections between different decision points in the AI development life cycle. Community and stakeholder engagement is especially critical as it connects with upstream stages such as identifying needs and end-users, and with downstream areas like deployment, evaluation, and maintenance. By involving rural clinicians, patients, and administrators early, developers can surface potential mismatches between what the tool is designed to deliver and what is actually feasible in underresourced contexts. For example, presumptions about access to certain technologies (e.g., stable Wi-Fi), or requirements that place added burdens on patients—such as traveling long distances for follow-up tests—can be identified and addressed before the tool is deployed. Similarly, engagement can clarify whether rural clinics have the infrastructure and staff to test, integrate, and sustain a tool of this kind.

The *Community and Stakeholder Engagement* box is positioned as a point of connection, not an isolated stage, and links to multiple other decision points in the life cycle. At the stage of *Identifying Need, Problem, and End-users*, rural clinicians and patients, as well as other case managers and providers of social services, for example, can clarify what kinds of assistance would be most useful or practical, and flag and modify advice from the chatbot that might be unrealistic in underresourced contexts. With respect to *Data Acquisition* and *Model Training*, stakeholder

engagement with experienced rural physicians and providers, perhaps even epidemiologists and other experts in rural health, could help ensure that conditions more prevalent in rural populations are represented, and/or assessing whether the tool might inadvertently be optimized for urban patient populations, given that clinical research is predominantly conducted by academic medical centers located in urban areas. In *Deployment Planning and Model Integration*, stakeholders with diverse perspectives and deep experiences in rural healthcare can surface infrastructural barriers that can introduce inequities such as bandwidth limitations or IT support needs, or inappropriate assumptions about clinic workflow and operations, that may otherwise derail uptake. In *Performance Measures and Evaluation*, they can shape definitions of success that extend beyond accuracy (e.g., correct diagnosis) to those identified by affected stakeholders, such as whether the tool eases clinical burdens or improves healthcare encounters from the perspective of patients. Even downstream areas such as *Maintenance and Monitoring* could benefit from multi-stakeholder dialogue, such as who is responsible for adapting the chatbot to local hospital protocols, keeping it up to date, and ensuring that the tool remains sustainable if internal systems shift, and where will *Funding* and other resources come from to support these key tasks?

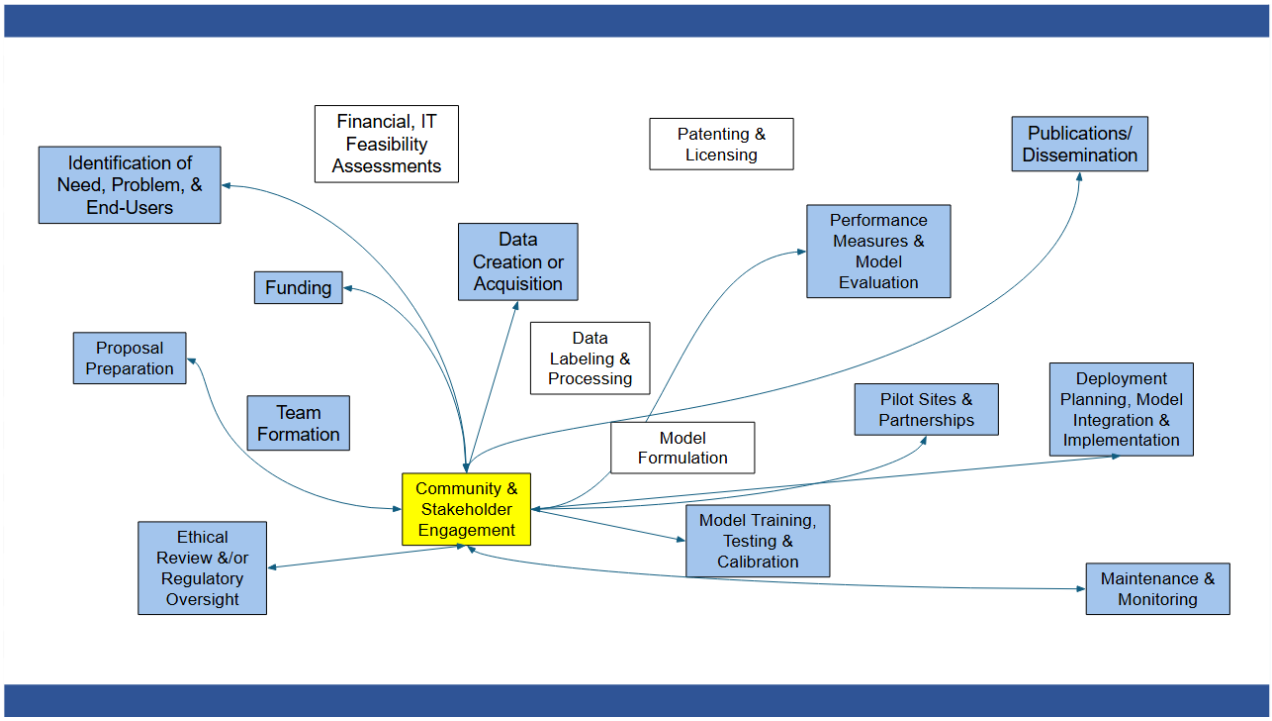

Fig. 4. Example of the Trustworthy AI Decision Map focusing on community and stakeholder engagement

In this way, the AI-DM helps identify where ethical and practical challenges may arise that impact fairness and trustworthiness, while also structuring cross-stakeholder engagement so that these issues can be surfaced early and revisited as they evolve. It prompts developers, health system

administrators, and other leaders in decision-making positions to work with diverse and multiple groups of stakeholders to identify, consider, and keep sight of downstream consequences and future implications of present choices, fostering more intentional and forward-looking decision-making across the AI development life cycle.

4. Conclusion

This paper has shown that fairness, trust, and trustworthiness in biomedical AI are situated concepts that require dialogue rather than fixed definitions. By adapting our Diversity Decision Map, we propose a tool to elicit diverse perspectives, support multi-stakeholder engagement, and guide decision-making throughout the AI life cycle that promotes fairness and trustworthiness. We argue that responsibility rests at the institutional level, and leaders and researchers need tools and support to carry this work forward. Future testing of the AI-DM with stakeholders will be key to evaluating its value for fostering accountability and shared responsibility in biomedical AI in order to promote fair and trustworthy AI.

5. Acknowledgments

Funding for “The Ethics of Inclusion: Diversity in Precision Medicine Research” study and development of the original Diversity Decision Map came from the National Human Genome Research Institute/NIH [Grant # R01HG010330].

References

1. Vakkuri V, Kemell KK, Jantunen M, Abrahamsson P. “This is Just a Prototype”: How Ethics Are Ignored in Software Startup-Like Environments. *Agile Processes in Software Engineering and Extreme Programming*. 2020;383:195-210. doi:10.1007/978-3-030-49392-9_13

2. Richardson B, Gilbert JE. A Framework for Fairness: A Systematic Review of Existing Fair AI Solutions. *arXiv*. Preprint posted online December 10, 2021. doi:10.48550/arXiv.2112.05700

3. Zhang J, Zhang Z ming. Ethics and governance of trustworthy medical artificial intelligence. *BMC Medical Informatics and Decision Making*. 2023;23(1):7. doi:10.1186/s12911-023-02103-9

4. Verma S, Rubin J. Fairness definitions explained. In: *Proceedings of the International Workshop on Software Fairness*. ACM; 2018:1-7. doi:10.1145/3194770.3194776

5. Cook KS, Santana JJ. Trust: Perspectives in Sociology. In: Simon J, ed. *The Routledge Handbook of Trust and Philosophy*. Routledge; 2020.

6. Cook KS, Hardin R, Levi M. *Cooperation Without Trust?* Russell Sage Foundation; 2005. Accessed August 30, 2025. https://www.jstor.org/stable/10.7758/9781610441353

7. Kraft SA, Cho MK, Gillespie K, et al. Trustworthiness in Untrustworthy Times: Response to Open Peer Commentaries on Beyond Consent. *The American Journal of Bioethics*. 2018;18(5):W6-W8. doi:10.1080/15265161.2018.1461953

8. U.S. Department of Human Services. *Trustworthy AI (TAI) Playbook*.; 2021. https://digitalgovernmenthub.org/wp-content/uploads/2023/08/hhs-trustworthy-ai-playbook.pdf

9. Sikstrom L, Maslej MM, Hui K, Findlay Z, Buchman DZ, Hill SL. Conceptualising fairness: three pillars for medical algorithms and health equity. *BMJ Health Care Inform*. 2022;29(1):e100459. doi:10.1136/bmjhci-2021-100459

10. Parthasarathy S, Katzman J. Bringing Communities In, Achieving AI for All. *Issues in Science and Technology*. 2024;XL(4):41-44.

11. Banerjee S, Alsop P, Jones L, Cardinal RN. Patient and public involvement to build trust in artificial intelligence: A framework, tools, and case studies. *Patterns*. 2022;3(6):100506. doi:10.1016/j.patter.2022.100506

12. Domecq JP, Prutsky G, Elraiyah T, et al. Patient engagement in research: a systematic review. *BMC Health Serv Res*. 2014;14(1):89. doi:10.1186/1472-6963-14-89

13. Shim JK, Foti N, Vasquez E, et al. Community Engagement in Precision Medicine Research: Organizational Practices and Their Impacts for Equity. *AJOB Empirical Bioethics*. 2023;14(4):185-196. doi:10.1080/23294515.2023.2201478

14. Holzer JK, Ellis L, Merritt MW. Why We Need Community Engagement in Medical Research. *Journal of Investigative Medicine*. 2014;62(6):851-855. doi:10.1097/JIM.0000000000000097

15. Pratt B, Cheah PY, Marsh V. Solidarity and community engagement in global health research. *The American Journal of Bioethics*. 2020;20(5):43-56. doi:10.1080/15265161.2020.1745930

16. Ng MY, Kapur S, Blizinsky KD, Hernandez-Boussard T. The AI life cycle: a holistic approach to creating ethical AI for health decisions. *Nat Med*. 2022;28(11):2247-2249. doi:10.1038/s41591-022-01993-y

17. Callahan A, McElfresh D, Banda JM, et al. Standing on FURM Ground: A Framework for Evaluating Fair, Useful, and Reliable AI Models in Health Care Systems. *NEJM Catalyst*. 2024;5(10). doi:10.1056/CAT.24.0131

18. Trotsyuk AA, Waeiss Q, Bhatia RT, et al. Toward a framework for risk mitigation of potential misuse of artificial intelligence in biomedical research. *Nat Mach Intell*. 2024;6(12):1435-1442. doi:10.1038/s42256-024-00926-3

19. Lee SSJ, Fullerton SM, McMahon CE, et al. Targeting Representation: Interpreting Calls for Diversity in Precision Medicine Research. *Yale J Biol Med*. 2022;95(3):317-326.

20. Jeske M, Vasquez E, Fullerton SM, et al. Beyond inclusion: Enacting team equity in precision medicine research. *PLOS ONE*. 2022;17(2):e0263750. doi:10.1371/journal.pone.0263750

21. Shim JK, Bentz M, Vasquez E, et al. Strategies of inclusion: The tradeoffs of pursuing "baked in" diversity through place-based recruitment. *Social Science & Medicine*. 2022;306:115132. doi:10.1016/j.socscimed.2022.115132

22. McMahon CE, Foti N, Jeske M, et al. Interrogating the Value of Return of Results for Diverse Populations: Perspectives from Precision Medicine Researchers. *AJOB Empirical Bioethics*. 2024;15(2):108-119. doi:10.1080/23294515.2023.2279965

23. Shim JK, McMahon CE, Saco L, Bentz M, Foti N, Lee SSJ. A qualitative study of diversity in precision medicine research: The development and stakeholder assessment of a Diversity Decision Map. *Journal of Clinical and Translational Science*. 2025;9(1):e78. doi:10.1017/cts.2025.45

24. Claw KG, Anderson MZ, Begay RL, Tsosie KS, Fox K, Garrison NA. A framework for enhancing ethical genomic research with Indigenous communities. *Nat Commun*. 2018;9(2957):1-7. doi:10.1038/s41467-018-05188-3

25. Rebbeck TR, Bridges JFP, Mack JW, et al. A Framework for Promoting Diversity, Equity, and Inclusion in Genetics and Genomics Research. *JAMA Health Forum*. 2022;3(4):e220603. doi:10.1001/jamahealthforum.2022.0603

26. Watson KS, Cohn EG, Fair A, et al. Adapting a conceptual framework to engage diverse stakeholders in genomic/precision medicine research. *Health Expectations*. 2022;25(4):1478-1485. doi:10.1111/hex.13486

27. Hudson M, Beaton A, Milne M, et al. *Te Mata Ira: Guidelines for Genomic Research with Māori*. Te Mata Hautū Taketake - Māori & Indigenous Governance Centre, University of Waikato; 2016.

28. Tindana P, Yakubu A, Staunton C, et al. Engaging research ethics committees to develop an ethics and governance framework for best practices in genomic research and biobanking in Africa: the H3Africa model. *BMC Medical Ethics*. 2019;20(1):69. doi:10.1186/s12910-019-0398-2

29. Blanchard J, Hiratsuka V, Beans JA, et al. Power sharing, capacity building, and evolving roles in elsi: the center for the ethics of indigenous genomic research. *Collaborations: A Journal of Community-Based Research and Practice*. 2020;3(1):18. doi:10.33596/coll.71

30. Joosten YA, Israel TL, Williams NA, et al. Community Engagement Studios: A Structured Approach to Obtaining Meaningful Input From Stakeholders to Inform Research. *Academic Medicine*. 2015;90(12):1646-1650. doi:10.1097/ACM.0000000000000794

31. Tuttle KR, Knight R, Appelbaum PS, et al. Integrating Patient Priorities with Science by Community Engagement in the Kidney Precision Medicine Project. *CJASN*. 2021;16(4):660-668. doi:10.2215/CJN.10270620

32. The Ethics of Inclusion: Diversity in Precision Medicine Research. Department of Medical Humanities and Ethics. July 25, 2023. Accessed August 30, 2025. https://www.mhe.cuimc.columbia.edu/ethics/research/research-projects/ethics-inclusion-diversity-precision-medicine-research

Precision Medicine: Integrating Large-Scale Data and Intermediate Phenotypes for Understanding Health and Treating Disease

Steven E. Brenner
University of California, Berkeley
Email: brenner@compbio.berkeley.edu

Nilah M. Ioannidis
University of California, Berkeley; University of California, Santa Cruz
Email: nilah@berkeley.edu

Tayo Obafemi-Ajayi
Missouri State University
Email: tayoobafemiajayi@missouristate.edu

Anne O'Donnell-Luria
Boston Children's Hospital; Harvard Medical School; Broad Institute of MIT and Harvard
Email: odonnell@broadinstitute.org

The field of precision medicine has undergone rapid development over the past three decades, driven by advances in high-throughput molecular profiling, large-scale electronic health data, and computational modeling. The central objective is to refine disease risk prediction, diagnosis, and treatment strategies by incorporating genetic, molecular, environmental, and clinical information into individualized care. However, the effective integration of these heterogeneous data sources presents substantial analytical challenges. The 2026 Precision Medicine session of the Pacific Symposium on Biocomputing (PSB) highlights computational methods that bridge large-scale biological data and intermediate phenotypes, emphasizing approaches that advance mechanistic understanding, risk prediction, and clinical utility. The contributions span multi-modal risk modeling, biomarker discovery, and causal inference frameworks, demonstrating the breadth and depth of research in computational precision medicine.

Keywords: Precision medicine; Multi-modal analysis; Biomarker discovery; Machine learning.

1. Introduction

Precision medicine seeks to tailor prevention, diagnosis, and treatment to individual patients by integrating biological and clinical information beyond traditional risk factors. Early progress emerged from the application of genomics to targeted therapy, most notably in oncology. More recently, the scope has expanded to include diverse high-throughput data modalities, including transcriptomics, proteomics, metabolomics, spatial omics, and single-cell technologies, combined with electronic health records (EHRs) and lifestyle data. The proliferation of these data provides an

© 2025 The Authors. Open Access chapter published by World Scientific Publishing Company and distributed under the terms of the Creative Commons Attribution Non-Commercial (CC BY-NC) 4.0 License.

unprecedented opportunity to identify intermediate phenotypes—molecular, cellular, or physiological traits that mediate between genotype and disease outcome—and to use them for predictive and mechanistic modeling. At the same time, the scale and complexity of such datasets introduce challenges in data harmonization, statistical power, and interpretability. Machine learning (ML) and deep learning (DL) methods have emerged as powerful strategies for extracting meaningful signals from heterogeneous data. Yet clinical translation requires models that are interpretable, mechanistically grounded, and generalizable across diverse populations.

The PSB has long provided a forum for the precision medicine community, and the 2026 session emphasizes computational and methodological innovations for integrating large-scale data and intermediate phenotypes to advance individualized healthcare. The accepted papers cover several broad themes: (i) integrating multi-modal data to improve disease risk prediction, (ii) modeling heterogeneity and disease subtypes, (iii) biomarker discovery, and (iv) modeling mechanism and causality. The papers in this session collectively advance the practice of precision medicine by integrating diverse data types to improve prediction, diagnosis, and mechanistic understanding. From generative transformers trained on millions of longitudinal health trajectories to multi-modal imaging-proteomics-genomics models and causal inference frameworks, the research highlights the power of computational biomedicine to uncover heterogeneity in disease processes and inform individualized care.

2. Session Contributions

2.1. *Multi-modal data integration for personalized risk prediction*

German et al. [1] introduce the Next Health Event (NHE) model, a generative transformer trained on the longitudinal health records of more than seven million participants. By incorporating demographic information, polygenic risk scores for nearly 300 traits, and longitudinal BMI into sequential health trajectories, the model can forecast disease progression at the individual level. Their ablation studies underscore the unique contributions of both genetic risk and longitudinal BMI, demonstrating the potential of integrated generative models for predictive health.

Venkatesh et al. [2] develop a multi-modal framework for coronary microvascular disease risk prediction. They integrate PET imaging-derived endotypes, plasma proteomics, and polygenic risk scores to classify patients more effectively. This approach captures disease heterogeneity, offering the first demonstration of imaging-based endotyping combined with genomic and proteomic data for this condition.

Cardone et al. [3] present an integrative framework that combines polygenic scores with clinical, lifestyle, and social determinants of health to predict heart failure. Their results show that combined predictors significantly outperform individual components, highlighting the clinical value of multi-domain integration for early detection and intervention.

2.2. *Modeling biological heterogeneity and disease subtypes*

Rifat et al. [4] present BioLM-NET, an interpretable deep learning framework that combines prior biological knowledge—including protein–protein and protein–DNA interactions and pathway

information—with large language model–derived gene embeddings to interpret gene expression and DNA methylation data. Applied to colorectal and breast cancer, glioblastoma, colon cancer, and Alzheimer's disease datasets, BioLM-NET improves prediction of subtype, progression and metastasis while enhancing interpretability.

Seagle et al. [5] explore the biological heterogeneity of apparent treatment-resistant hypertension by clustering associated variants into distinct cardiometabolic profiles, which may reflect underlying mechanisms such as metabolic dysregulation, inflammation, and vascular reactivity. This approach provides a route to disentangling heterogeneous mechanisms of complex traits and stratifying patients for tailored interventions.

2.3. *Diagnostics and biomarker discovery from digital data*

Sethi et al. [6] use ProtoECGNet, a prototype-based neural network trained for multi-label ECG classification, to learn physiologically meaningful prototypes that serve as interpretable digital biomarkers. Their results show that these prototypes correlate with clinical outcomes for both cardiovascular and systemic conditions, providing clinically meaningful and transferable intermediate phenotypes.

Choi et al. [7] develop a deep learning approach for diagnosing Postural Orthostatic Tachycardia Syndrome using continuously collected wearable ECG and accelerometer data. Their method captures physiological variability in daily life, offering a less burdensome alternative to traditional tilt-table tests and demonstrating the potential of wearable devices in digital phenotyping.

Tamura et al. [8] propose an approach for identifying sparse phenotype embeddings from histopathological images using weakly supervised neuron selection and sparse autoencoders applied to dense representations generated by pathology foundation models. Their approach results in interpretable phenotypes with strong performance on tumor patch identification.

2.4. *Causality and mechanistic modeling*

Sriram et al. [9] introduce DeepDiff-SHAP, an interpretable deep learning framework for subgroup-specific causal inference. Using conditional SHAP values, their method uncovers nonlinear and subgroup-specific causal changes in relationships that are obscured in population-averaged analyses. Applications to diabetes and sepsis datasets reveal clinically meaningful, comorbidity-specific mechanisms.

Jiang et al. [10] generate causal networks connecting genetic variants to biological processes and disease phenotypes based on mechanistic statements extracted from the literature. Their model reconstructs causal molecular mechanisms and predicts consequences for variants lacking prior annotation, enabling mechanistic interpretation of genomic variation.

References

1. C. German, S. Shringarpure, P. Dibaeinia, J. Ashenhurst, B. L. Koelsch, A. Auton, A. A. Khan. Integrating Polygenic Risk Improves Generative Forecasting of Disease Trajectories. *Pacific Symposium on Biocomputing* (2026).
2. R. Venkatesh, T. Cherlin, Penn Medicine BioBank, M. D. Ritchie, M. A. Guerraty, S. S. Verma. Integrating Imaging-Derived Clinical Endotypes with Plasma Proteomics and External Polygenic Risk Scores Enhances Coronary Microvascular Disease Risk Prediction. *Pacific Symposium on Biocomputing* (2026).
3. K. M. Cardone, D. Kim, M. D. Ritchie. Integrating Polygenic Scores with Clinical, Lifestyle, and Social Risk Factors to Improve Heart Failure Risk Prediction. *Pacific Symposium on Biocomputing* (2026).
4. J. I. M. Rifat, T. Tabashum, M. M. Rahman, M. F. Mokter, S. Engala, S. Bozdag. BioLM-NET: an interpretable deep learning model combining prior biological knowledge and contextual LLM gene embeddings on multi-omics data to predict disease. *Pacific Symposium on Biocomputing* (2026).
5. H. M. Seagle, J. Kim, A. T. Akerele, VA Million Veteran Program, A. Hung, J. N. Hellwege, T. L. Edwards. Polygenic partitioning of apparent treatment resistant hypertension implicates distinct biological processes in pathogenesis. *Pacific Symposium on Biocomputing* (2026).
6. S. Sethi, D. Chen, M. C. Burkhart, N. Bhandari, B. Ramadan, B. Beaulieu-Jones. Prototype Learning to Create Refined Interpretable Digital Phenotypes from ECGs. *Pacific Symposium on Biocomputing* (2026).
7. H. Choi, N. Matsumoto, X. Li, D. Teodorescu, A. Kote, M.-J. Yang, X. Liu, M. E. Hernandez, J. H. Moore, G. G. Hernandez, P.-S. Chen. Deep Learning-based Classification of Patients with Postural Orthostatic Tachycardia Syndrome using Wearable ECG and Accelerometer Data. *Pacific Symposium on Biocomputing* (2026).
8. K. Tamura, Y.-z. Zhang, Y. Okubo, S. Imoto. Patch-level phenotype identification via weakly supervised neuron selection in sparse autoencoders for CLIP-derived pathology embeddings. *Pacific Symposium on Biocomputing* (2026).
9. A. Sriram, S. Kim, J. A. Carcillo, H. J. Park. DeepDiff-SHAP: Interpretable deep learning for subgroup-specific causal hypothesis generation using conditional SHAP. *Pacific Symposium on Biocomputing* (2026).
10. J. Jiang, P. Radivojac, B. M. Gyori. Literature-driven extraction and computational prediction of causal statements linking genetic variants to biological processes, pathways and phenotypes. *Pacific Symposium on Biocomputing* (2026).

Integrating Polygenic Risk Improves Generative Forecasting of Disease Trajectories

Chris German[1], Suyash Shringarpure[1], Payam Dibaeinia[1], James Ashenhurst[1], Bertram L. Koelsch[1], Adam Auton[1], and Aly A. Khan[1,2]

[1] *23andMe, Inc., Palo Alto, CA, USA*
[2] *Departments of Family Medicine, and Pathology, and Institute for Population and Precision Health, University of Chicago, Chicago, IL, USA*
E-mail: chrisg@23andme.com; aakhan@uchicago.edu

Predicting the longitudinal sequence of diseases an individual will develop over their lifetime is a central challenge in medicine. While recent AI models can process health histories, they have been limited by cohort size and the omission of genetic data. Here we introduce the Next Health Event (NHE) model, a generative transformer trained on the health trajectories of 7.1 million research participants. By using a transformer architecture to integrate demographic data, longitudinal BMI, and polygenic risk scores (PRS) for 297 traits with sequential health history, NHE significantly outperforms baseline models, including XGBoost with the same inputs, in predicting the next diagnosis across 129 conditions (Top-1 accuracy 25.5% vs. 22.3%). Systematic ablation studies reveal that both PRS and longitudinal BMI provide substantial, non-redundant predictive power, whereas self-reported lifestyle information offers limited additional value. The model's predictive accuracy is the same when forecasting prospectively reported incident outcomes vs. combined prospectively and retrospectively reported outcomes (AUROC 0.917), demonstrating its utility for real-world risk assessment. By uniting large-scale health histories with genetics, our work establishes a new framework for predictive health and demonstrates that generative models can effectively forecast individual disease pathways.

Keywords: Disease Prediction, Polygenic Risk Score, Longitudinal Data, BMI.

1. Introduction

Predicting an individual's lifetime health trajectory is a central goal of personalized medicine. These trajectories can be represented as ordered sequences of clinical events, characterized by complex temporal dependencies and patterns of comorbidity. While traditional machine learning can predict risk for single diseases, it often fails to capture this rich longitudinal structure. Recent advances in natural language processing, particularly transformer-based large language models (LLMs), provide a powerful framework for overcoming this limitation by treating health histories as sequences of clinical events, and integrating multimodal context such as genetic information.

The application of LLMs to health data is rapidly maturing, with distinct methodological

© 2025 The Authors. Open Access chapter published by World Scientific Publishing Company and distributed under the terms of the Creative Commons Attribution Non-Commercial (CC BY-NC) 4.0 License.

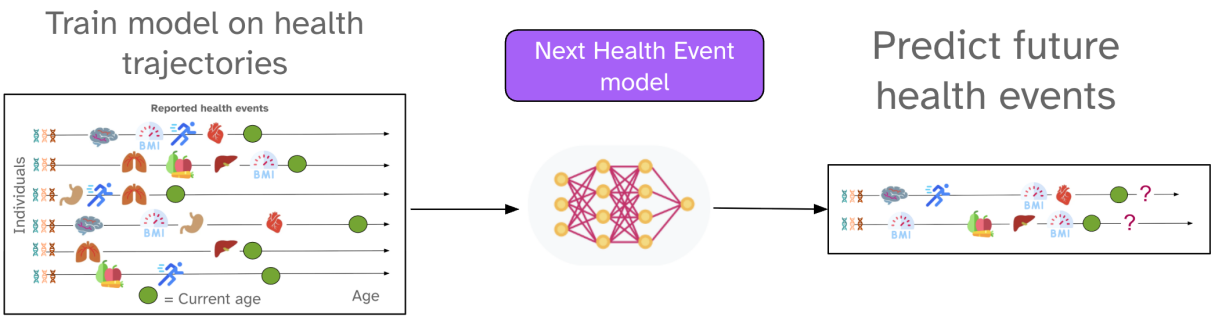

Fig. 1. The Next Health Event (NHE) model framework for forecasting disease trajectories. The model trains on multi-modal health histories (diagnoses, genetics, BMI) from over 7 million individuals (left) using a generative transformer (center) to predict an individual's future health events based on their current history (right).

approaches demonstrating success. Some models focus on multimodal data integration; for instance, HeLM combines structured clinical data with high-dimensional inputs like spirograms, while PH-LLM leverages time-series data from wearables to generate personalized health insights.[1,2] Another class of models learns deep representations from medical terminologies themselves. For example, GRASP utilizes a masked language modeling approach on structured Electronic Health Record (EHR) data to create robust embeddings of medical codes, and life2vec models an individual's entire life course, including health, social, and economic events, to predict outcomes like mortality.[3,4]

Most recently, generative pre-trained transformer (GPT) architectures have been adapted to directly forecast future health events. Foresight models clinical histories from structured data and clinical notes to predict subsequent medical outcomes, while Delphi-2M, a GPT-inspired model trained on the UK Biobank cohort, has shown strong performance in predicting over 1,000 distinct diagnoses.[5,6] Notably, the superior accuracy of a domain-specific model like Delphi-2M compared to zero-shot predictions from a general-purpose LLM underscores the necessity of specialized training on health records.

Despite this rapid progress, two critical gaps limit the current state-of-the-art. First, and most critically, existing models have not integrated an individual's innate genetic risk, a fundamental determinant of health, as a core input. Prior work has shown accounting for genetic risk improves prediction beyond clinical factors alone.[7–9] Second, these generative models have mostly been trained on datasets of fewer than one million individuals, which restricts their power to model rare diseases and to accurately dissect the complex interplay between genetic predispositions and environmental factors.

To bridge these gaps, we introduce the Next Health Event (NHE) model, a generative transformer trained and evaluated on a large cohort of over 7 million research participants from the 23andMe Research Cohort (Figure 1).[10] 23andMe, Inc. is a consumer genetics and research company where customers are offered the opportunity to consent to participate in research studies via online surveys. The key innovation of NHE is its ability to create a unified

representation of an individual by integrating their unique sequence of diagnosed health conditions with demographics, polygenic risk scores (PRS) for 297 traits, longitudinal body mass index (BMI) measurements, and lifestyle survey data. This scale and multimodal approach provide a critical testbed directly relevant to major population-scale health initiatives, such as Our Future Health and All of Us, which are building cohorts of over one million people.

We demonstrate through comprehensive ablation studies and analyses of prospectively collected data that the NHE model establishes a new state-of-the-art in health forecasting. Our analyses show that: (1) the generative sequence model significantly outperforms strong non-sequential baselines (e.g., XGBoost); (2) integrating genetic risk and longitudinal BMI provides substantial and non-redundant contributions to predictive accuracy across a wide range of diseases; and (3) the model generalizes effectively, maintaining high performance when predicting prospectively collected, incident health outcomes. By successfully fusing deep genetic and longitudinal phenotypic data at population scale, NHE provides a powerful and validated blueprint for the next generation of personalized health models.

2. Methods

2.1. *Study cohort*

Research participants from 23andMe, Inc., a consumer genetics and research company, were used to train and evaluate the Next Health Event model. These participants were genotyped as part of the 23andMe Personal Genome Service. All participants included in the analysis provided informed consent and volunteered to participate in online research under a protocol approved by Ethical & Independent (E&I) Review Services, an external AAHRPP-accredited IRB. As of 2022, E&I Review Services is part of Salus IRB (https://www.versiticlinicaltrials.org/salusirb).

2.2. *Data details*

Data were collected via self-reported online surveys. A baseline "Health Profile" survey captured each participant's health history, including diagnosed conditions and age of onset. Age of onset information was collected on 129 conditions. The 129 conditions were selected based on a combination of factors, including their prevalence within the research cohort, their clinical significance, and the availability of reliable age-of-onset data

Since 2016, a longitudinal"Health Update" survey was administered every 1-2 years to capture incident diagnoses. Information on incident diseases from follow-up surveys was available for 65 of the 129 conditions. Individuals were included in the analysis if they reported at least one diagnosed condition. The model integrated the following data modalities:

- **Health History:** Sequences of diagnosed conditions and their corresponding ages of onset were constructed for 129 conditions. If multiple conditions were reported during the same age, the ordering was randomly assigned so the model did not learn any specific ordering.
- **Demographics:** Self-reported birth year, sex, and genetically determined ancestry.
- **Longitudinal BMI:** Body mass index (BMI) was measured at multiple time points, discretized into deciles, and integrated into the health sequence.

- **Genetic Risk:** 297 polygenic risk scores (PRS) were calculated for traits related to the modeled conditions. Individuals were classified as high-risk (top 5%) or low-risk (bottom 5%) relative to a genetic ancestry-matched distribution. Individuals that fell within the middle 90% of the distribution for any single PRS had no classification represented in the model for that specific PRS. 36/297 PRSs were trained using data from the 23andMe research cohort as detailed below. The remaining PRSs were taken from the PGSCatalog.
- **Lifestyle:** Responses from a lifestyle survey (e.g., diet, sleep, activity) were encoded as tokens and assigned to the participant's age at the time of survey completion. The lifestyle survey is only surfaced to participants after the Health Profile survey is completed.

BMI was discretized into deciles of the age-and-sex-matched distribution to provide a non-parametric, normalized representation of weight status that is robust to population-level shifts over time. This approach was chosen for its simplicity and effectiveness in preliminary experiments. Simialrly, PRS were encoded as binary high-risk (top 5%) and low-risk (bottom 5%) indicators to create distinct, high-impact tokens that the model could easily differentiate. While this approach simplifies the continuous nature of genetic risk, it effectively captures individuals at the extremes of the genetic liability spectrum where risk is most pronounced, and reduces model complexity.

The 23andMe PRSs were trained excluding the individuals in the NHE validation and test sets. We used a cross-validation approach to train these PRSs where we split all European individuals in the training cohort into 5 folds. PRSs were estimated for each fold by performing GWAS on the other 4 folds and running LDPred2[11] to estimate the PRS on the left out fold. This approach was done to reduce overfitting to the training set. After PRSs were estimated, we standardized each PRS within each fold with mean 0 and variance 1 to transform them the same scale. The remaining 261 PRSs were taken from the PGSCatalog.[12,13] In total, data from 7,184,380 individuals were used, split into a training set (5,747,786), a validation set (718,041), and a held-out test set (718,553).

2.3. *Model details and training*

We adapted the generative pretrained transformer (GPT-2) architecture for the NHE model.[14] We selected a GPT-2 architecture due to its autoregressive nature, which enables the model to learn conditional dependencies over time and predict future health events by sequentially conditioning on an individual's prior history. Each age, condition, PRS, BMI decile, unique value of demographic variables, and lifestyle response included in the model prompt was encoded into the model vocabulary as distinct tokens. It has an embedding size of 288, 12 attention heads, 12 layers, and a maximum sequence length of 1024. The total number of parameters in the model including the language modeling head is 13,071,744. It was trained from scratch on 8 NVIDIA A100 GPUs for up to 50 epochs, using early stopping based on validation set performance. With this setup the model training time is under 3 days. This relatively compact architecture was chosen to ensure computational efficiency and facilitate reproducibility, demonstrating that powerful predictive performance can be achieved without requiring massive-scale computational resources.

2.4. *Model evaluations*

2.4.1. *Comparison with baselines*

We compared the NHE model to several baselines in a held-out test set to investigate whether we gain additional prediction accuracy by (1) including personalized health information as inputs (i.e., PRS and health history) and (2) using a language modeling framework. To assess (1), we compared the NHE model to a naive prevalence based estimator that predicts the top condition(s) in the training data as well as an age and sex-specific prevalence estimator that uses sex-matched condition rates in the training data ±2 years from the target prediction age. To assess (2) we compared the NHE model trained without BMI and lifestyle data (trained on demographic, PRS, and health history data) to an XGBoost model that has the same features. XGBoost was selected as a baseline due to its strong empirical performance in a variety of structured prediction tasks and its ability to capture non-linear interactions and handle missing data, making it a strong benchmark for assessing the value of a generative, sequence-based approach. Training of all baseline models took under an hour. The primary evaluation metric was the top-1 and top-5 accuracy in predicting the most recent health condition in an individual's history. Top-k accuracy measures how often the correct answer is among the top k predictions a model makes.

For the NHE model, we prompted the model with each person's health history in the test set omitting their last condition (and any following BMI values/lifestyle responses) to generate top candidates for the held-out condition. We also compared macro-/micro-AUROC estimates, per-condition AUROC, precision, and recall between the NHE and XGBoost models. We quantify discrimination with the micro-averaged area under the receiver-operating characteristic curve (micro-AUROC). Unless noted otherwise, 'AUROC' refers to this micro-averaged value, computed by pooling true-positive, false-positive, and false-negative counts across all conditions before drawing the ROC curve.

2.4.2. *Ablation studies*

To assess the contribution of different data modalities to the predictive performance of our model, we conducted ablation studies. In these experiments, we systematically removed one or more types of data from the model's training input and evaluated the resulting impact on its accuracy and other relevant metrics. The data modalities we investigated included polygenic risk scores (PRS), body mass index (BMI), lifestyle data (such as smoking status, physical activity levels, and dietary habits), and demographic information (including birth year, sex, and genetic ancestry). By comparing the model performance trained on the complete set of modalities to its performance after the exclusion of each individual modality, as well as combinations, we aimed to quantify the relative importance and potential redundancy of these different data sources in predicting the health events. This systematic removal and evaluation process allowed us to gain a deeper understanding of which types of information were most critical for achieving optimal model performance and to identify potential areas for future model refinement and data collection efforts.

Since BMI and lifestyle may be indirectly captured by other signals via health history (e.g.,

BMI is correlated with many metabolic conditions), we conducted a subanalysis on individuals without prior health conditions, examining model performance when specific data types were available. By examining model performance within this specific subset of individuals, we can better understand each modality's unique contributions.

We further investigated the impact that PRSs have on the model by comparing the full model to the model trained without PRS information, restricting to individuals whose held-out trait is one that had a direct match with a PRS in the model and who were either at elevated or decreased genetic risk for that trait (they were in the top or bottom 5% of the PRS distribution). No individuals in the NHE validation or test sets were included in the GWAS or PRS training datasets used to develop the 23andMe PRSs incorporated into the model. Because they are directly related to a trait of interest, the PRSs capture relevant risk information for the phenotypes, and these comparisons can highlight the importance of including genetic risk information into the model.

2.4.3. *Incident data prediction*

The majority of the data being trained on is retrospective in nature - research participants fill out a health profile survey that asks them questions about prior conditions they have been diagnosed with since birth. Some participants have completed follow-up longitudinal health update surveys that collect incident data, asking about recent diagnoses. The model is trained on the combination of these data types. We tested the model's ability to specifically predict incident data, which is available on 65 out of 129 phenotypes.

In one evaluation, we used the previous task of holding out the last condition and having the model predict it. We stratified by if the condition was coming from a retrospective survey or a prospective survey, and compared top-1 and top-5 accuracies.

In the other evaluation we used the individual's prompt prior to any incident data as input into the model, and estimated approximate probabilities of each condition occurring over 5 years since completion of the health profile survey. The approximate probability is defined as:

$$\hat{P}_c^{(k)} := \sum_{i=1}^{k} P(a = \alpha + i|\pi) \cdot P(c|\pi, a = \alpha + i)$$

where:

- $\hat{P}_c^{(k)}$ is the estimated probability of condition c occurring within k years
- α is the age of the individual and π is the prompt (e.g., demographic and PRS information, BMI, lifestyle, and health history prior to the follow-up survey)
- $P(a = \alpha + i|\pi)$ is the model's predicted probability that the next age is $\alpha + i$ given prompt π
- $P(c|\pi, a = \alpha + i)$ is the model's predicted probability of condition c given prompt π and the next age is $\alpha + i$

We used these probabilities to calculate AUROC across the 65 incident phenotypes, and compared it to the AUROC coming from the held-out last token task from the combined data (retrospective and prospective) restricted to the 65 phenotypes. Individuals who reported no new conditions in the health update surveys were kept in this analysis, as it more accurately

reflects the target population.

3. Results

3.1. *NHE Model Outperforms Baselines in Disease Prediction*

The NHE model significantly outperformed all baselines, including population-based prevalence estimators and a powerful XGBoost classifier. In a held-out test set, the NHE model achieved a top-1 accuracy of 25.5% for predicting the next diagnosis, compared to 22.3% for the strongest baseline, XGBoost (Figure 2a). This performance advantage extended to top-5 accuracy (56.1% vs. 52.2%). The generative model also demonstrated superior discriminative ability, yielding a higher micro-averaged AUROC of 0.938 compared to 0.926 for XGBoost (Figure 2b). Macro-averaged AUROC, and per-condition AUROC, precision, and recall were also consistently higher for the NHE model (Figures 2c–f). Overall, across the 129 conditions in the model, the NHE model had significantly higher accuracy compared to all baselines.

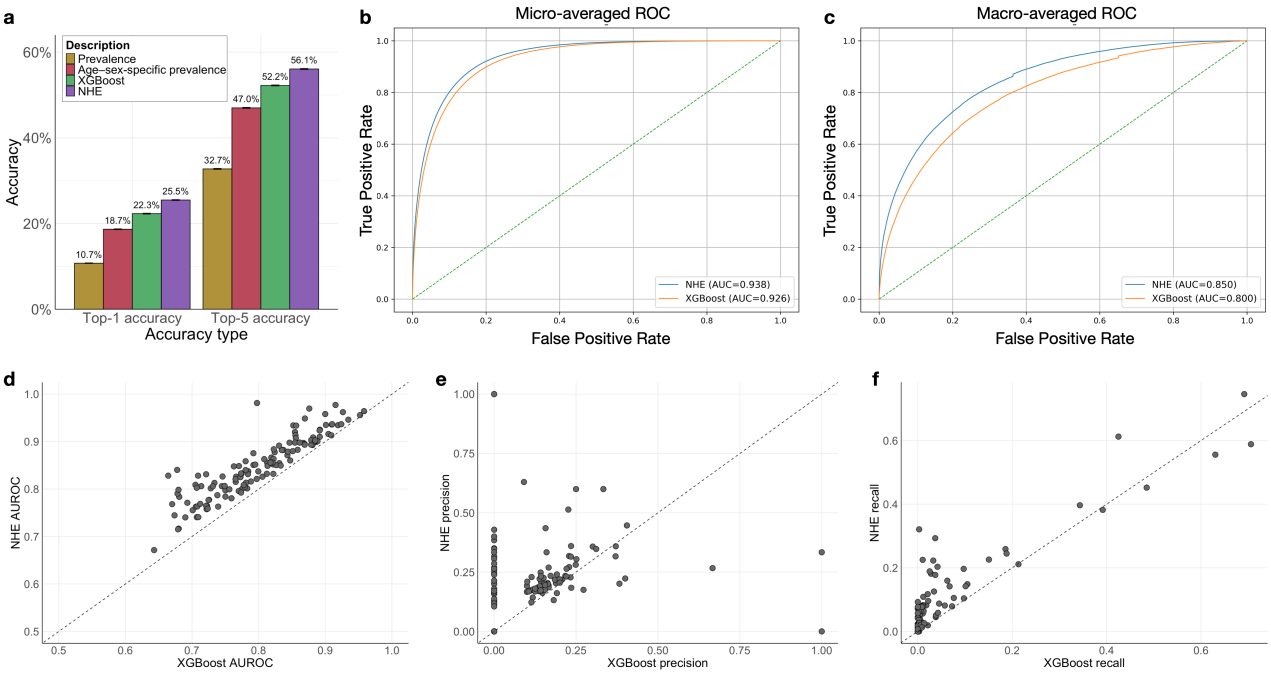

Fig. 2. The NHE model significantly outperforms baselines in next-disease prediction. Performance on a held-out test set (N=718,553) comparing NHE to XGBoost and prevalence estimators. (a) NHE achieves the highest Top-1 and Top-5 accuracy. (b-f) The model also demonstrates superior discriminative ability, with consistently higher AUROC, precision, and recall over XGBoost, highlighting the value of its sequence-aware architecture. Error bars indicate 95% confidence intervals.

3.2. *Genetic Risk and Longitudinal BMI Provide Non-Redundant Predictive Power*

To evaluate the contribution of each data modality, we performed ablation studies in which specific input types were systematically removed from the model. The NHE model incorpo-

rating all information and the model with lifestyle data removed achieved the highest top-1 and top-5 prediction accuracies. There was no significant difference between the model with all information and the one with lifestyle data removed, suggesting lifestyle data does not offer additional predictive accuracy when accounting for BMI, PRS, and demographic information. Accuracy decreased upon the removal of any of the other single data modalities or combinations thereof, indicating that each of those data types provide non-redundant contributions to the model's predictive performance (Figure 3a). The model using only health history information, "No demographics, PRS, BMI, lifestyle" had the lowest performance.

In our stratified analyses of individuals with only a single reported condition (i.e., no prior health conditions in the prompt), we found that excluding BMI and lifestyle data from training significantly reduced performance compared to the full model (top-1 accuracy: 21.1% vs 19.4%, $P < 0.01$; Figure 3b). However, when comparing the full model to a version trained only without lifestyle data (while retaining BMI), there was no significant difference in performance among individuals who had lifestyle data available ($P = 0.62$).

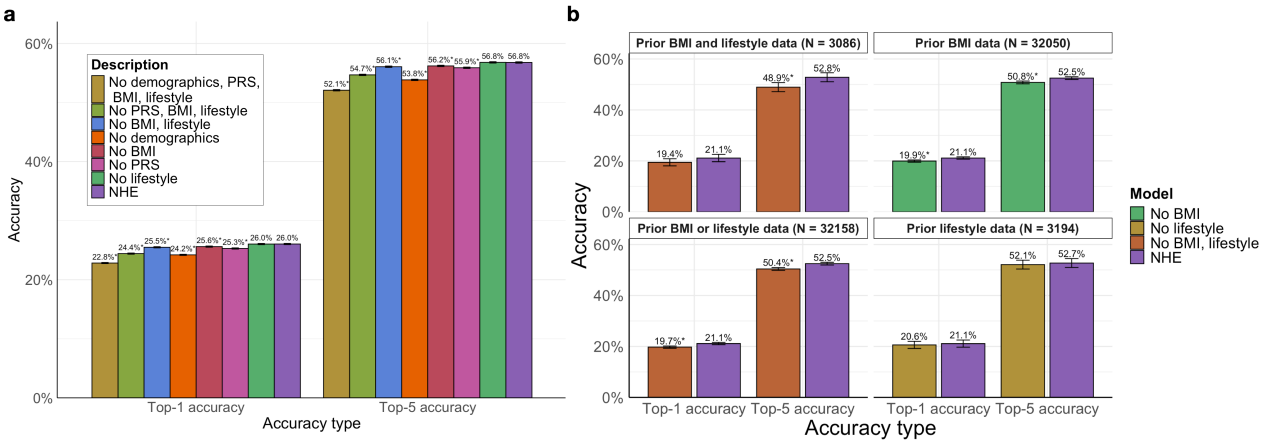

Fig. 3. Genetic risk (PRS) and longitudinal BMI provide non-redundant predictive power. Ablation studies on the test set (N=718,553) quantify the contribution of each data modality. (a) Removing PRS or BMI significantly degrades model accuracy, while removing lifestyle data does not. (b) In a stratified analysis of individuals with no prior health conditions, BMI and PRS are shown to be critical for an initial diagnosis. Asterisks (*) denote a significant ($P < 0.05$) accuracy drop compared to the full model.

For individuals with a held-out trait that matched one of the included PRSs and who were at either elevated or reduced genetic risk for that same trait, the full NHE model outperformed the version trained without PRS with higher top-1 accuracy (34.2% vs 28.2%, $P <$ 2e-16) and top-5 accuracy (65.5% vs 59.0%, $P <$ 2e-16), showing that genetic risk information meaningfully improves the model's predictive ability (Figure 4).

The ablation studies demonstrate that demographics, PRS, and BMI contribute to the NHE model's overall performance. The importance of each modality varies depending on an individual's health history and the specific condition being predicted. Incorporating PRS data improves prediction accuracy for traits with available PRS data. These findings underscore

the value of leveraging diverse data modalities for developing comprehensive and accurate health prediction models.

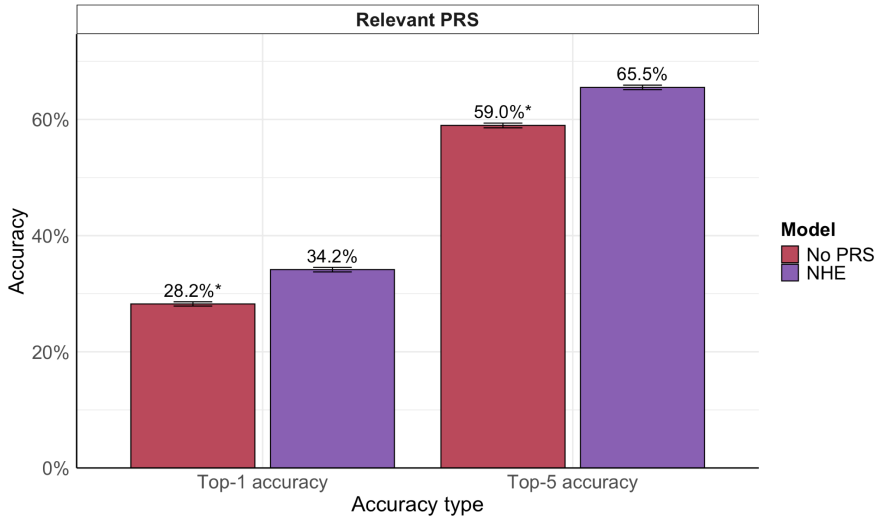

Fig. 4. Integrating Polygenic Risk Scores provides a dramatic boost in predictive accuracy for relevant traits. Analysis of individuals (N=56,519) with a condition matching their high/low genetic risk profile. The full NHE model (with PRS) substantially outperforms a model without PRS in both Top-1 (34.2% vs 28.2%) and Top-5 (65.5% vs 59.0%) accuracy, demonstrating the critical value of genetic data. Error bars indicate 95% confidence intervals.

3.3. *Model Generalizes to Prospectively Reported Incident Outcomes*

To assess real-world utility, we tested the model's ability to predict prospectively reported diagnoses. We evaluated its performance on incident outcomes – conditions newly reported by participants in follow-up health update surveys, surfaced every 1-2 years after the initial health profile survey. The NHE model had strong generalization to prospective outcomes. In predicting the held-out last condition task, the accuracy was similar regardless of whether the condition was coming from the retrospective health profile survey or the prospective health update survey, with only slightly decreased accuracy (top-1 accuracy 24.1% vs 26.1%, top-5 accuracy 57.3% vs 58.9%).

In the separate evaluation using the 5-year probability estimates derived from model outputs prior to any incident data, performance, measured by AUROC, was comparable when restricted to the 65 phenotypes with available incident data and evaluated on either prospective outcomes alone or on the combined dataset (0.917 for both). These findings indicate that the model is able to learn patterns from a mix of retrospective and prospective data and effectively generalize to future risk prediction.

4. Discussion

By integrating genetics with longitudinal health records at population scale, the Next Health Event (NHE) model establishes a new framework for predicting individual disease trajecto-

ries. Trained on a dataset of over 7 million individuals, our generative model learns complex patterns of comorbidity and age of onset to outperform strong baselines. More importantly, our work quantifies the distinct contributions of multiple data modalities, providing critical insights for the development of future predictive health tools.

Our findings confirm the power of transformer architectures for modeling sequential health data, aligning with previous work such as Delphi-2M and Foresight. However, NHE addresses a critical gap in the field by being the first, to our knowledge, to integrate an individual's innate genetic risk via polygenic risk scores (PRS) as a core input. The resulting enhancement in predictive accuracy, particularly for genetically-linked conditions, underscores the necessity of unifying genetics and health histories to create truly personalized predictive models.

A key finding from our work is the quantification of the non-redundant predictive power of both genetic risk and longitudinal BMI. Through systematic ablation, we demonstrated that each modality provides unique, valuable information. Conversely, self-reported lifestyle data offered minimal additional benefit, suggesting its predictive signal is likely captured by more proximal biological measures like BMI and the presence of related diagnoses in the health history. Our stratified analyses further refined these insights: BMI proved critical for risk assessment in individuals with sparse health histories, while PRS substantially improved predictions for those with known genetic predispositions. This reaffirms the value of multimodal data for creating robust and personalized clinical and preventive strategies.

A significant strength of our study is the demonstration of the model's prospective validity. The NHE model's high performance on incident outcomes, reported years after the initial data collection, shows that it learns generalizable patterns rather than simply memorizing historical sequences. This robust generalization to future events is a crucial step toward establishing real-world clinical utility for short-term risk forecasting.

Broader Implications and Potential Applications

Beyond its technical advancements, the NHE framework has significant implications for both clinical practice and biomedical research. For instance, the model could be used to inform personalized screening schedules, suggesting earlier or more frequent monitoring for individuals forecast to be at high risk for specific conditions like breast cancer or heart disease. It could also accelerate therapeutic development by enriching clinical trial cohorts, identifying individuals with a high prospective risk for a disease of interest more efficiently than traditional criteria. Perhaps most importantly, NHE serves as a validated blueprint for large-scale population health initiatives like the All of Us Research Program and the UK's Our Future Health, demonstrating a clear path to translate these massive data collection efforts into tangible predictive health tools.

Limitations and Future Directions

Despite its strong performance, the current NHE architecture has several limitations that represent clear avenues for future work. First, and most critically, our binary encoding of PRS as high/low-risk indicators, while effective, discards the majority of the continuous risk signal for 90% of individuals. Future work should prioritize the development of modality-specific

encoders to integrate the full, continuous PRS values, which could unlock a more nuanced understanding of genetic liability. Second, the 23andMe PRSs included were trained only on individuals of European genetic ancestry, reflecting the limited sample sizes available for running the cross-validation GWAS/PRS construction pipeline in other groups. To partially address this, we applied ancestry-matched thresholds (top and bottom 5%) to define high and low genetic risk within each group. Developing more robust PRSs that integrate information across ancestries will be essential to capture both shared and population-specific genetic architecture. Third, the model's current temporal encoding does not explicitly handle co-occurring diagnoses at the same age. Adopting a more flexible positional encoding strategy could better represent the complex structure of multimorbidity.

The model also faces limitations related to its data source. The reliance on self-reported data introduces the possibility of recall bias and healthy volunteer bias. While our prospective validation mitigates some of these concerns, a critical next step is to validate the model's predictions against structured clinical records (e.g., EHRs) to quantify any potential bias and its impact. Additionally, while the model incorporated PRS developed for multiple ancestries where available, many were derived from European-ancestry GWAS. Expanding the inclusion of well-powered, diverse-ancestry PRS is essential for improving predictive equity and generalizability across all populations. Finally, it is crucial to emphasize that NHE is a predictive, not a causal, model. While it can forecast what might happen next, it does not explain the underlying biological mechanisms.

In conclusion, the NHE model provides a powerful and validated blueprint for the next generation of predictive health tools. By successfully fusing deep genetic and longitudinal phenotypic data at population scale, our work highlights a clear path toward more accurate and comprehensive health forecasting. Continued refinement and validation of these methods will be essential for realizing a future where medicine can shift from a reactive to a proactive and deeply personalized paradigm.

Acknowledgements

We would like to thank the research participants and employees of 23andMe for making this work possible. We also thank David Hinds, Steve Pitts, Bertram Michael Holmes, Stella Aslibekyan, and Nick Eriksson for their comments on the manuscript. The authors gratefully acknowledge support from AWS for GPU computing and credits.

References

1. A. Belyaeva, A. Belyaeva, A. Shmatko, I. Ushinin, A. Avramov, N. Egorov, K. Sargsyan, M. Kartashev, R. Shalaby, T. Rocktäschel *et al.*, Multimodal llms for health grounded in individual-specific data, *arXiv preprint arXiv:2307.09018* (2023).
2. J. Cosentino, O. Shaik, A. Nag, T.-C. Liu, H. Adam, A. Adithyan, J. Agnes, B. Al-Banna, M. Al-Hajj, V. Anand *et al.*, Towards a personal health large language model, *arXiv preprint arXiv:2406.06474* (2024).
3. M. Kirchler, M. Ferro, V. Lorenzini, FinnGen, C. Lippert and A. Ganna, Large language models improve transferability of electronic health record-based predictions across countries and coding systems, *Health Informatics* (2025).

4. G. Savcisens, T. Eliassi-Rad, L. K. Hansen, L. H. Mortensen, L. Lilleholt, A. Rogers, I. Zettler and S. Lehmann, Using sequences of life-events to predict human lives, *Nat. Comput. Sci.* **4**, 43 (2023).
5. Z. Kraljevic, C. Tomlinson, R. Bendayan, T. Searle, L. Roguski, K. Noor, D. Bean, A. Mascio, J. T. Teo, R. J. Dobson *et al.*, Foresight—a generative pretrained transformer for modelling of patient timelines using electronic health records: a retrospective modelling study, *Lancet Digit. Health* **6**, e281 (2024).
6. A. Shmatko, A. Belyaeva, I. Ushinin, A. Avramov, N. Egorov, K. Sargsyan, M. Kartashev, R. Shalaby, T. Rocktäschel, S. Bach *et al.*, Learning the natural history of human disease with generative transformers, *Epidemiology* (2024).
7. A. King, L. Wu, H.-W. Deng, H. Shen and C. Wu, Polygenic risk score improves the accuracy of a clinical risk score for coronary artery disease, *BMC medicine* **20**, p. 385 (2022).
8. L. Li, S. Pang, F. Starnecker, B. Mueller-Myhsok and H. Schunkert, Integration of a polygenic score into guideline-recommended prediction of cardiovascular disease, *European heart journal* **45**, 1843 (2024).
9. G. R. Zirpoli, R. M. Pfeiffer, K. A. Bertrand, D. Huo, K. L. Lunetta and J. R. Palmer, Addition of polygenic risk score to a risk calculator for prediction of breast cancer in US black women, *Breast Cancer Research* **26**, p. 2 (2024).
10. J. Y. Tung, C. B. Do, D. A. Hinds, A. K. Kiefer and N. Eriksson, Efficient replication of over 180 genetic associations with self-reported medical data, *PLoS ONE* **6**, p. e23473 (2011).
11. F. Privé, J. Arbel and B. J. Vilhjálmsson, Ldpred2: better, faster, stronger, *Bioinformatics* **36**, 5424 (2021).
12. S. A. Lambert, L. Gil, S. Jupp, S. C. Ritchie, Y. Xu, A. Buniello, A. McMahon, G. Abraham, M. Akiyama, A. Al-Chalabi *et al.*, The polygenic score catalog as an open database for reproducibility and systematic evaluation, *Nat. Genet.* **53**, 420 (2021).
13. S. A. Lambert, L. Gil, S. C. Ritchie, M. Inouye, P. Würtz, S. Jupp, A. Buniello and J. A. MacArthur, Enhancing the polygenic score catalog with tools for score calculation and ancestry normalization, *Nat. Genet.* **56**, 1989 (2024).
14. A. Radford, J. Wu, R. Child, D. Luan, D. Amodei and I. Sutskever, Language models are unsupervised multitask learners, *OpenAI Blog* **1**, p. 9 (2019).

Integrating Imaging-Derived Clinical Endotypes with Plasma Proteomics and External Polygenic Risk Scores Enhances Coronary Microvascular Disease Risk Prediction†

Rasika Venkatesh[1], Tess Cherlin[2], Penn Medicine BioBank[3], Marylyn D. Ritchie[4], Marie A. Guerraty[5], Shefali S. Verma[2,*]

[1]*Genomics and Computational Biology Graduate Group,* [2]*Department of Pathology and Laboratory Medicine, University of Pennsylvania, Philadelphia, PA, USA*

[3]*Penn Medicine Biobank, University of Pennsylvania, Philadelphia, PA, USA*

[4]*Department of Genetics,* [5]*Department of Medicine, University of Pennsylvania, Philadelphia, PA, USA*

**Corresponding author, Email: Shefali.SetiaVerma@pennmedicine.upenn.edu*

Coronary microvascular disease (CMVD) is an underdiagnosed but significant contributor to the burden of ischemic heart disease, characterized by angina and myocardial infarction. The development of risk prediction models such as polygenic risk scores (PRS) for CMVD has been limited by a lack of large-scale genome-wide association studies (GWAS). However, there is significant overlap between CMVD and enrollment criteria for coronary artery disease (CAD) GWAS. In this study, we developed CMVD PRS models by selecting variants identified in a CMVD GWAS and applying weights from an external CAD GWAS, using CMVD-associated loci as proxies for the genetic risk. We integrated plasma proteomics, clinical measures from perfusion PET imaging, and PRS to evaluate their contributions to CMVD risk prediction in comprehensive machine and deep learning models. We then developed a novel unsupervised endotyping framework for CMVD from perfusion PET-derived myocardial blood flow data, revealing distinct patient subgroups beyond traditional case-control definitions. This imaging-based stratification substantially improved classification performance alongside plasma proteomics and PRS, achieving AUROCs between 0.65 and 0.73 per class, significantly outperforming binary classifiers and existing clinical models, highlighting the potential of this stratification approach to enable more precise and personalized diagnosis by capturing the underlying heterogeneity of CMVD. This work represents the first application of imaging-based endotyping and the integration of genetic and proteomic data for CMVD risk prediction, establishing a framework for multimodal modeling in complex diseases.

Keywords: Cardiovascular Disease; Multi-omics; Proteomics; Polygenic Risk Scores, Risk Prediction, Endotyping

1. Introduction

1.1. *CMVD contributes to the large burden of ischemic heart disease.*

Coronary microvascular disease (CMVD) is increasingly recognized as a major contributor to the global burden of ischemic heart disease (IHD)[1–3]. Unlike obstructive coronary artery disease (CAD),

† This work was supported by Alpha Phi Heart to Heart (MG, SSV), NHLBI R01HL175485 and BWF CAMS (MG), NIA AG066833 (MDR), and NHLBI HL169458 (MDR).

© 2025 The Authors. Open Access chapter published by World Scientific Publishing Company and distributed under the terms of the Creative Commons Attribution Non-Commercial (CC BY-NC) 4.0 License.

which involves large-vessel atherosclerosis, CMVD affects the smaller vessels of the heart and can present clinically in patients as angina, ischemia, myocardial infarction with no obstructed coronary arteries, or increased major adverse cardiovascular events[4]. Studies estimate that CMVD may account for 30–50% of cases of angina in patients without obstructive CAD, underscoring its critical role in IHD[1,3]. CMVD is often undetected through standard cardiac imaging methods, leading to underdiagnosis; advanced techniques such as perfusion positron emission tomography (PET) currently represent the non-invasive gold standard for diagnosis[5]. Despite its high prevalence, no targeted therapies for CMVD currently exist, and its diagnosis relies on specialized testing that limits routine clinical use[5,6]. The diagnostic challenges and lack of targeted treatment for CMVD reflect a limited understanding of its pathophysiology[7]. CMVD involves both structural and functional changes to microvasculature, driven by cardiovascular comorbidities[1,5]. The genetic and molecular underpinnings of the condition remain poorly understood, resulting in underdiagnosis and insufficient treatment. Improved molecular characterization incorporating advanced imaging, genetics, and proteomics holds promise for better risk stratification, improved diagnostic approaches, and eventual therapeutic development for this condition.

1.2. *Pathophysiological variation in CMVD supports the presence of endotypes.*

CMVD is a highly heterogeneous disease with variable clinical presentation[7]. Existing clinical studies rely on measurements of coronary microvascular function, using invasive and non-invasive imaging tools to measure myocardial blood flow and flow reserve (MBFR). Reduced MBFR suggests impaired microvascular function and has been associated with increased mortality[2,8]. Clinical studies using cardiac perfusion PET imaging have shown that impaired MBFR can result from either increased resting flow or blunting of stress flow, indicating that multiple pathophysiologic pathways may exist, reflecting biologically distinct disease subtypes[8,9]. These disparate clinical mechanisms suggest the presence of different endotypes of CMVD manifesting with distinct flow patterns. A one-size-fits-all approach to modeling CMVD is insufficient for precise diagnosis and management. We stratified patients into endotypes in this study based on image-derived flow parameters. This approach enables more nuanced modeling of intermediate and heterogeneous cases, laying the groundwork for precision medicine in CMVD.

1.3. *Existing early risk prediction methods for CMVD are limited.*

Current diagnostic approaches for CMVD rely on clinical measurements derived from perfusion PET imaging, alongside tracking of clinical risk factors like cholesterol levels and comorbidities such as diabetes as they emerge. As a result, the condition is often underdiagnosed, and patients can be misclassified. Biomarker-based risk prediction incorporating genetic and proteomic features could provide an alternative for identifying individuals at risk for CMVD prior to the emergence of clinical risk factors. However, the development of predictive models for CMVD has been limited by the lack of large-scale genome-wide association studies (GWAS), and to date, no polygenic risk scores (PRS) have been developed for the disease. The clinical model developed by Prescott *et al.* is the only existing risk prediction model for CMVD. This prior study incorporated integrated

proteomics and achieved relatively strong performance (AUROC = 0.61-0.66) but still relies on lab measurements and clinical variables that develop over time, such as diabetes and hypertension[10].

CAD GWAS have historically enrolled heterogeneous IHD populations that include both obstructive CAD and CMVD, making CAD GWAS effectively IHD GWAS[3]. Despite their clinical differences, CMVD and obstructive CAD may arise from overlapping genetic mechanisms, including those involved in inflammation and microvascular remodeling[3]. While many CAD-associated loci are relevant to CMVD, our previous work has shown that CMVD also involves distinct loci not captured by CAD studies[11]. This overlap and divergence indicate that CMVD shares components of the broader IHD genetic architecture while maintaining unique molecular underpinnings[3,6,11]. In this study, we evaluate the utility of an externally derived PRS for coronary artery disease (CAD), a related phenotype with overlapping enrollment criteria, to assess the potential for cross-phenotype genetic risk modeling. We present the first machine learning framework for CMVD risk prediction that integrates genomic and proteomic data without the need for clinical input. By incorporating endotype-based stratification from imaging, we also demonstrate improved classification performance. We demonstrate the ability to predict risk earlier than clinical features emerge across traditional and intermediate groups, thereby greatly enhancing the clinical utility of the model for patient prioritization and potential for new diagnostic approaches.

2. Methods

2.1. *PennMedicine BioBank Study Population*

The Penn Medicine BioBank (PMBB) represents a diverse population of 57,170 participants who have been genotyped and imputed using the TOPMed reference panel (Version r2 2020)[12,13]. Each participant's genetic data is linked with their Electronic Health Record (EHR), which includes perfusion PET stress testing data. We identified 4,007 patients who underwent Rubidium-82 perfusion PET stress testing at the Hospital of the University of Pennsylvania as part of routine

Table 1. Demographic and clinical information for the study population. P-values calculated using Pearson's Chi-Squared Test (Sex, Ancestry) and Welch's T-Test (Age, Imaging)

Variable	Cases (n = 428)	Controls (n = 401)	P-Value
Sex			0.0056
Male	183 (43%)	211 (53%)	
Female	245 (57%)	190 (47%)	
Ancestry			0.0178
African (AFR)	218 (50.9%)	249 (62.1%)	
Admixed American (AMR)	1 (0.2%)	1 (0.2%)	
European (EUR)	208 (48.7%)	149 (37.2%)	
South Asian (SAS)	1 (0.2%)	1 (0.2%)	
NA	0 (0%)	1 (0.2%)	
Enrollment Age	59.1 $\pm$ 12	56.3 $\pm$ 11.5	0.0037
Flow Reserve	1.5 $\pm$ 0.3	2.6 $\pm$ 0.5	< 0.001
Stress Flow	1.7 $\pm$ 0.6	2.3 $\pm$ 0.7	< 0.001
Rest Flow	1.1 $\pm$ 0.3	0.9 $\pm$ 0.3	< 0.001

clinical care and enrolled in PMBB. As shown in **Table 1**, 829 of these participants had high-quality perfusion PET imaging, genetic, and proteomics data (92 proteins from OLINK Cardiovascular II panel) available and were included in the final analysis. This comprises one of the largest multi-omics datasets for CMVD, with integrated imaging, genetics, and proteomics data.

All patients received dipyridamole or regadenoson for coronary vasodilation, and the imaging data was analyzed using Siemens Syngo MBF or Invia Corridor 4DM. Patients with incomplete or poor-quality myocardial blood flow reserve (MBFR) or proteomic data were excluded from the analysis during quality control, resulting in the final cohort size of 829 participants. The proteomics data for these patients were normalized using intensity normalization and subsequently $\log_2$ transformed. CMVD case-control status was defined by MBFR, with cases exhibiting MBFR < 2, indicative of impaired coronary microvascular function, and controls having MBFR ≥ 2, indicative of normal function[8]. Demographic covariates of age, sex, and principal components (PCs) accounting for population stratification based on genetic ancestry (determined in Verma *et al.*[12]) were selected based on statistical significance to CMVD case-control status (**Table 1)**.

2.2. *Polygenic Risk Score Calculation*

To investigate the genetic contribution to CMVD risk, we calculated external PRS using the --score function in PLINK, based on previously published GWAS summary statistics from Aragam *et al*., a large-scale study of CAD conducted on 1,165,690 participants[14–16]. This PRS aggregates the effects of genetic variants associated with CAD risk and applies them to our samples to estimate each individual's inherited predisposition to vascular disease[16,17]. The variants identified in CAD GWAS, particularly those relevant to CMVD, provide a biologically informed basis for constructing PRS to assess shared susceptibility.

We constructed 3 PRS models: 1) CAD PRS: using 235 genome-wide significant SNPs identified in the CAD GWAS that also had genotypes in our PMBB participants, 2) CMVD Targeted PRS: 15 SNPs previously reported as significantly associated with CMVD in a targeted association study from CAD GWAS summary statistics[11] and 3) CMVD Targeted + GWAS PRS: combining the 15 SNPs with 5 SNPs, rs6700366, rs115240131, rs11573191, rs1969348, and rs839696, identified as significant in prior CMVD-focused GWAS, fine-mapping, and TWAS analyses[11]. The list of SNPs included in each PRS is presented in **Supplemental Table S1**. This modeling approach compared the predictive utility of broad CAD-related SNPs in creating CMVD-focused genetic risk profiles in our cohort. The PRS was fitted with a LASSO regression, using case/control status after splitting the dataset into a 80% training and 20% testing split across 100 random iterations, balanced by the case/control ratio[18–20]. Model performance was evaluated across metrics, including the area under the receiving operator characteristic (AUROC), precision-recall curve (AUPRC), F1-score, balanced accuracy (BA), and R^2 calculated using the Matthews Correlation Coefficient (MCC)[21,22].

2.3. *CMVD Disease State Endotyping*

We applied unsupervised k-means clustering to an independent cohort of 3,130 PMBB individuals with recorded global reserve, rest, and stress myocardial blood flow values to identify distinct

physiological endotypes associated with CMVD[8,23]. The distribution of these imaging measurements is shown in **Supplemental Figure S1**. Prior to clustering, all variables were standardized and outliers removed to ensure comparability. The optimal number of clusters was determined using the silhouette score and the elbow method[24]. After defining CMVD endotypes in this cohort, we projected our independent cohort of 829 individuals with OLINK proteomics data onto the identified clusters by calculating the Euclidean distance between each proteomics individual's reserve, rest, and stress values and the centroids of the defined clusters, assigning each individual to the closest endotype[8,24].

2.4. *Risk Modeling*

2.4.1. *Model Architectures and Feature Sets*

To investigate the predictive value of genetic and proteomic data for CMVD risk prediction, we developed several machine learning models across a range of feature inputs. We trained 4 distinct linear and nonlinear model types using Scikit-learn and Pytorch: logistic regression with elastic net regularization (EN), eXtreme gradient boosting (XGBoost), deep autoencoders, and fully connected feedforward neural networks (FNN)[25,26]. All modeling approaches were applied to a standardized set of 8 input feature sets (**Table 2**), to systematically assess performance and interpretability.

Table 2. Model feature inputs and total number of features.

Feature Set	Feature Inputs	Total Number of Features
1	age, sex	2
2	age, sex, PCs 1-5	7
3	proteomics (92)	92
4	age, sex, PCs 1-5, proteomics (92)	99
5	age, sex, PCs 1-5, CAD PRS	8
6	age, sex, PCs 1-5, CMVD Targeted PRS	8
7	age, sex, PCs 1-5, CMVD Targeted + GWAS PRS	8
8	age, sex, PCs 1-5, Best PRS, proteomics (92)	100

Feature set 1 used only age at enrollment and biological sex extracted from EHR as demographic features. Set 2 accounted for population structure by including the top 5 PCs as well as age and sex. Sets 3 and 4 incorporated 92 plasma proteins, resulting in 92 and 99 features, respectively. Feature sets 5-7 incorporated the 3 different PRS, each using 8 features with age, sex, and PCs 1-5. Feature set 8 combined the best-performing PRS with proteomics (100 features) and was extended to a multiclass prediction task based on CMVD subtype clustering results. All models underwent hyperparameter tuning and top feature were assessed. We employed this modeling design to assess model performance and biologically-informed feature contributions comprehensively.

2.4.2. *Elastic-Net Logistic Regression (EN)*

To classify CMVD risk status, we implemented a logistic regression model with Elastic Net regularization (EN) to handle high-dimensional and potentially correlated input features[27]. After

separating the data into 80% training and 20% test splits, the EN model was trained with nested cross-validation for hyperparameter tuning. We tested a range of inverse regularization strengths (Cs=10) across multiple parameters (L1 ratios from 0.1 to 1.0), using 5-fold cross-validation and AUROC as the optimization metric[27]. To ensure robustness, the entire training and evaluation process was repeated across 100 stratified and Z-score normalized training and testing splits. Models were evaluated using AUROC, AUPRC, F1-score, BA, precision, recall, and Brier score[28,29]. Feature importance was assessed using SHapley Additive exPlanations (SHAP) values for local additive explanations of the model output from a LinearExplainer[30].

2.4.3. *eXtreme Gradient Boosted Trees (XGBoost)*

To capture nonlinear interactions among the features, we implemented a gradient boosting framework using XGBoost for binary classification of CMVD status[31]. For each of 10 independent iterations, the data were stratified by CMVD status and split into training (80%) and test (20%) sets, with a further 20% validation set split from the training data. Hyperparameter tuning was performed on the validation set using Optuna with 10 trials per iteration, leveraging a tree-structured Parzen estimator (TPE) sampler[32]. Tuned parameters included tree depth, learning rate, subsample, and column sampling ratios, L1/L2 regularization (alpha, lambda), minimum loss reduction (gamma), and scaled positive weight for class imbalance. Each model was trained with the binary logistic objective and early stopping based on validation AUROC, with a patience of 20 rounds[33,34]. The best model per iteration was selected and evaluated on the held-out test set. Model performance was assessed across metrics including AUROC, AUPRC, F1-score, precision, recall, BA, and Brier score[28,29]. Feature importance was evaluated SHAP values from TreeExplainer for the best-performing model to interpret the contributions of top features[30,35].

2.4.4. *Autoencoder*

A deep autoencoder architecture was also employed to attempt to analyze the high-dimensional protein expression profiles for CMVD detection[36]. In each iteration, the dataset was randomly divided into training and testing sets with an 80% and 20% split, stratified by CMVD. The training set was further split into 20% validation subsets for nested hyperparameter optimization. The encoder consists of multiple fully connected layers, with the number of layers and the number of units per layer optimized via hyperparameter tuning. Each encoder layer applied a linear transformation followed by batch normalization, ReLU activation, and dropout to prevent overfitting[37]. The decoder then reconstructed the original input from the compressed latent representation. A classification head was attached to the final layer to predict CMVD using a sigmoid activation function[37]. This architecture enabled simultaneous learning of a compressed representation and a classification output from the same latent features. The autoencoder was trained using the Adam optimizer, with the learning rate selected from a log-uniform distribution between 1E-04 and 1E-02[38].

The model minimized a combined loss comprising mean squared error (MSE) for input reconstruction and binary cross-entropy (BCE) for classification, ensuring the encoded features

were representative of the protein profiles and predictive of CMVD status[39]. We employed early stopping with a patience of 5 epochs, based on the combined validation loss, and monitored it over a maximum of 300 epochs[36]. A batch size of 64 was used and poorly performing trials were pruned during hyperparameter tuning. Model performance was assessed through repeated stratified splits and evaluation over 10 iterations. Performance metrics were calculated on the independent test sets and averaged across iterations to ensure robustness. Metrics included the AUROC, AUPRC, precision, recall, F1-score, BA, and Brier score. SHAP values were computed using DeepExplainer on the best model to interpret feature contributions to the CMVD classification[30].

2.4.5. *Feedforward Neural Network (FNN)*

A feedforward neural network (FNN) was developed to model binary classification for CMVD risk[40]. In each iteration, the dataset was randomly divided into training and testing sets with an 80% and 20% split, stratified by CMVD status to maintain class balance. The training set was further split into 20% validation subsets for hyperparameter optimization. Input features were standardized using z-score normalization. The network architecture consisted of 2 or 3 fully connected hidden layers, selected based on hyperparameter tuning per iteration, followed by batch normalization, ReLU activation, and dropout regularization to enhance convergence stability and reduce overfitting. The size of each layer, dropout rates, and learning rate were also optimized using Optuna with a randomized search[41]. The final output layer used a single sigmoid-activation function, producing probabilistic outputs for CMVD risk. BCE was used as the loss function, and training was performed with the Adam optimizer. Early stopping was applied based on validation loss with a fixed patience threshold of 5 epochs to minimize overfitting[38,40].

To ensure robustness and generalizability, the training pipeline was repeated across 10 random stratified splits. For each iteration, the model was retrained using the best hyperparameters identified via nested optimization. Performance metrics—including AUROC, AUPRC, F1-score, BA, precision, recall, and Brier score—were calculated on held-out test data and summarized using means and standard deviations. Model explainability was assessed using SHAP, applied to the best-performing iteration to identify the most influential features driving CMVD risk prediction. SHAP values were computed using KernelExplainer on a reduced background set, and results were visualized through summary plots and ranked feature importance[30].

2.4.6. *Multi-Class Classification*

To predict CMVD endotypes identified through unsupervised clustering of perfusion PET imaging data, we implemented a supervised multiclass classification framework using both XGBoost and multinomial logistic regression (MLR)[42]. The input data consisted of integrated transcriptomic and proteomic features, with clustering-derived labels representing distinct CMVD endotypes. For model training and evaluation, the dataset was randomly split into 80% training and 20% testing subsets in each iteration, with stratification by endotype label to preserve class distributions. The training set was further divided into 80% training and 20% validation subsets.

We performed 10 independent iterations of model training for both XGBoost and MLR to evaluate performance stability across data splits. For XGBoost, Optuna optimization was employed

within each iteration to tune hyperparameters over 10 trials, aiming to minimize multiclass log-loss on the validation set. Parameters included tree depth, learning rate, number of estimators, L1/L2 regularization, and feature and sample subsampling rates[31]. For MLR, we optimized regularization strength, penalty type, solver, maximum iterations, tolerance, and L1 ratio (for EN)[27]. Final models in each iteration were trained with early stopping and evaluated on the held-out test set. Metrics collected per iteration included macro-averaged precision, recall, F1-score, AUROC, AUPRC (one-vs-rest), and BA. Model interpretability was assessed using SHAP values from TreeExplainer to identify the most influential features contributing to each endotype classification[43].

3. Results

3.1. *PRS Performance*

PRS models were evaluated for their ability to predict binary CMVD case-control status using different sets of SNPs, as seen in **Table 3.** Across all SNP sets, model performance improved with the inclusion of age, sex, and genetic ancestry covariates (PCs 1–5), as reflected in higher AUROC, AUPRC, and R^2 values. The CMVD-targeted PRS, using 15 CMVD-related SNPs, demonstrated improved predictive performance compared to the CAD PRS. Incorporating the additional 5 SNPs from CMVD GWAS also showed improvement over the CAD PRS, achieving similar performance to the targeted approach. When combined with covariates, the CMVD-targeted SNP models

Table 3: PRS model performance in CMVD risk prediction. Metrics reported as mean (standard deviation).

PRS Model	Feature Inputs	AUROC	AUPRC	BA	F1-Score	R^2
CAD	PRS	0.569 (0.033)	0.590 (0.040)	0.543 (0.030)	0.544 (0.068)	0.086 (0.060)
CAD	PRS, age, sex, PCs	0.587 (0.031)	0.595 (0.040)	0.554 (0.027)	0.552 (0.035)	0.108 (0.054)
CMVD Targeted	PRS	0.572 (0.029)	0.570 (0.035)	0.546 (0.025)	**0.624 (0.035)**	0.106 (0.058)
CMVD Targeted	PRS, age, sex, PCs	**0.601 (0.028)**	**0.598 (0.036)**	**0.571 (0.024)**	0.569 (0.031)	**0.142 (0.048)**
CMVD Targeted + GWAS	PRS	0.543 (0.025)	0.555 (0.035)	0.521 (0.021)	0.540 (0.033)	0.042 (0.033)
CMVD Targeted + GWAS	PRS, age, sex, PCs	0.595 (0.028)	0.597 (0.035)	0.570 (0.025)	0.588 (0.032)	0.141 (0.050)

achieved the highest AUROC (0.601) and R^2 (0.142), indicating that focusing on CMVD-relevant genetic variants when using weights from a related phenotype enhances performance. These findings highlight the utility of targeted PRS approaches in improving genetic risk prediction.

3.2. *Binary Risk Prediction Model Performance*

We evaluated the performance of 8 predictive models incorporating demographic variables (age, sex), genetic ancestry (PCs), PRS, and plasma proteomics using multiple performance metrics, including the AUROC, AUPRC, BA, and F1-score. **Figure 1** summarizes the comparative performance across models. Full results across all metrics are provided in **Supplemental Table S2**. EN and XGBoost consistently outperformed other models across evaluation metrics, particularly when proteomic features were included alongside demographic and genetic variables. With only age and sex as inputs, model discrimination was modest (AUROC = 0.57), but when proteomics data were added in Feature sets 3, 4, and 8, AUROC values rose substantially. The EN improved

Fig. 1. Model performance (AUROC, AUPRC, BA, F1-score) across all feature sets for EN, XGBoost, Autoencoder, and FNN models.

from 0.577 to 0.675 in Set 3, and XGBoost from 0.573 to 0.659. These trends held when including PCs and PRS, further reinforcing the additive predictive value of proteomic data. EN achieved the best overall performance across AUROC (0.676), AUPRC (0.683), and Brier Score (0.229) when using the feature set of age, sex, proteomics, and PCs (Feature set 4). XGBoost excelled in recall, reaching a high of 0.966 with the CMVD Targeted PRS and 0.907 with the full proteomic panel, indicating that it is particularly effective in identifying true positives. While the autoencoder and feedforward neural network (FNN) models performed more modestly, they still benefited from proteomic inclusion, demonstrating significant increases in performance. SHAP feature importances for all models are reported in **Supplemental Table S3** and SHAP summary plots for the top models (Feature sets 3, 4, and 8) are available in **Supplemental Figures S2-4**. Overall, these results underscore the added value of proteomics in capturing biological signals relevant to CMVD and highlight the strengths of EN and XGBoost in classification performance.

3.3. *CMVD Endotype Clustering and Multiclass Prediction*

The k-means clustering analysis identified distinct endotypes based on global reserve, rest, and stress values, with an overall inertia of 1035.87, indicating meaningful separation between clusters. The elbow plot for determining the optimal number of clusters is shown in **Supplemental Figure S5**; the data are best represented by 4 clusters, as shown in **Figure 2**[24]**.** Class 0 (n = 290) represented the classic CMVD cases, characterized by reduced flow reserve and low stress flow values, consistent with impaired microvascular function. In contrast, Class 2 (n = 110) comprised the classic control group, with the highest reserve values. Class 1 (n = 233) and Class 3 (n = 192) reflect intermediate groups, with Class 3 characterized by low or borderline reserve due to elevated resting flow.

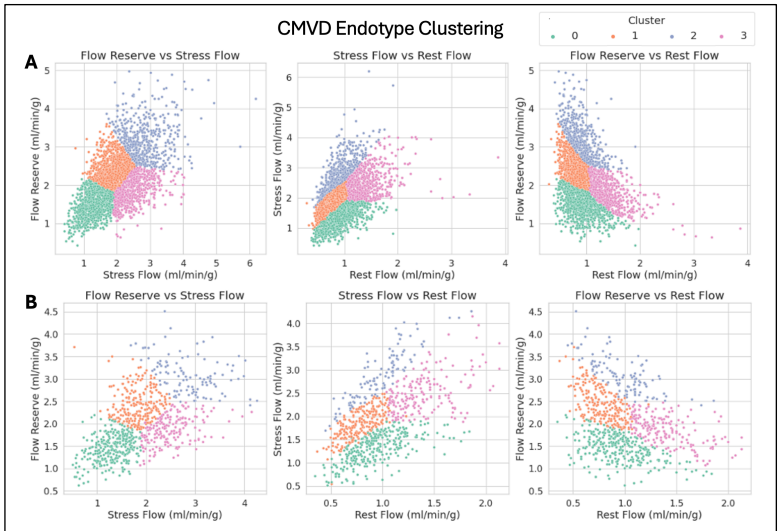

Fig. 2. CMVD endotype clustering by flow stress, rest, and reserve. A) Unsupervised clustering of PMBB individuals not in OLINK. B) Projection of 829 OLINK individuals onto defined clusters.

Together, these clusters define a spectrum of microvascular phenotypes ranging from healthy controls to individuals with CMVD and intermediate physiological profiles[8].

To further characterize these endotypes, we trained XGBoost and MLR multiclass classifiers using PRS and proteomics, with model interpretation performed using SHAP analysis. The XGBoost multiclass model showed substantial improvement in performance relative to the binary classification approaches, as shown in **Table 4.**

Table 4: Performance metrics for multiclass model (mean, standard deviation) reported for each class and overall performance.

Class	AUROC	AUPRC	Precision	Recall	BA	F1-Score	Brier Score
Class 0	0.723 (0.036)	0.584 (0.065)	0.491 (0.033)	0.712 (0.053)	0.580 (0.030)	0.656 (0.030)	0.197 (0.009)
Class 1	0.648 (0.048)	0.434 (0.056)	0.419 (0.067)	0.389 (0.072)	0.402 (0.063)	0.587 (0.042)	0.192 (0.006)
Class 2	0.721 (0.054)	0.345 (0.084)	0.389 (0.173)	0.145 (0.067)	0.206 (0.094)	0.553 (0.038)	0.107 (0.005)
Class 3	0.669 (0.028)	0.389 (0.047)	0.394 (0.045)	0.295 (0.094)	0.333 (0.075)	0.580 (0.037)	0.168 (0.005)
All Classes	0.690 (0.024)	0.438 (0.030)	0.434 (0.041)	0.447 (0.031)	0.422 (0.039)	0.447 (0.031)	0.166 (0.004)

While the binary models achieved AUROCs around 0.66, comparable with previously published studies, the multiclass framework reached a macro- averaged AUROC of 0.690, with balanced accuracies for individual classes approaching or exceeding the binary models. The strongest performance was observed for Class 0 (AUROC = 0.723, BA = 0.580), the classic case presentation of CMVD. For Class 2, the classic control group, the model performed similarly (AUROC = 0.721), indicating that the model strongly predicted classical case/control presentations. Performance remained robust in less prevalent classes, despite expected class imbalance and reduced sample sizes. Class 1 and Class 3, which represent smaller subsets of the cohort, achieved AUROCs of 0.648 and 0.669, respectively, demonstrating that the model was able to generalize its predictive capacity beyond dominant classes. Multiclass models consistently yielded lower (better) Brier scores than binary models. Results for the MLR model are reported in **Supplemental Table S4**.

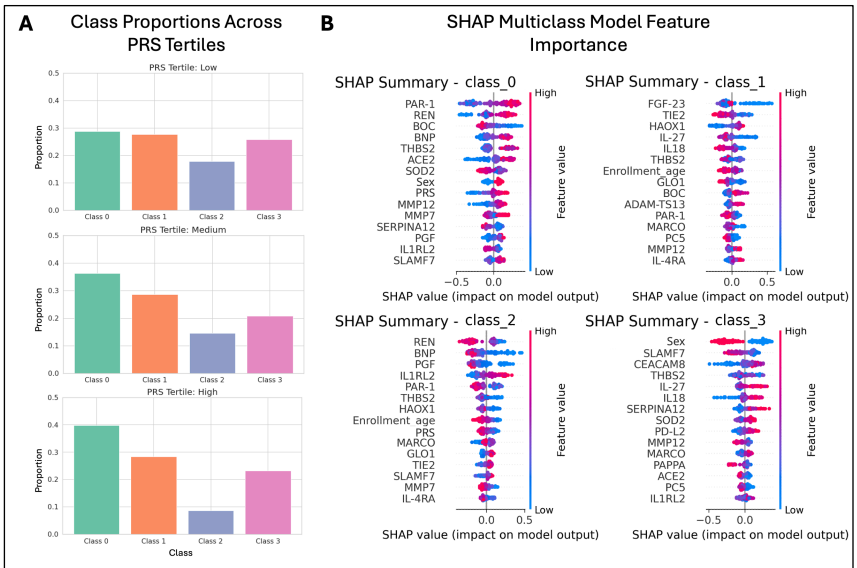

Fig. 3. Multiclass model performance. A) Class stratification across PRS tertiles. B) SHAP multiclass feature importance.

Measuring the class proportions across stratified PRS risk tertiles, shown in **Figure 3A**, revealed patterns supporting the clinical relevance of the endotypes. Class 0 showed a clear positive association with high PRS, suggesting that individuals with higher genetic risk are more likely to have the most pathologically consistent endotype. In contrast, Class 2 demonstrated a decline in frequency with higher PRS, consistent with its characterization as a low-risk

phenotype. Class 1 and Class 3 remained relatively stable across PRS tertiles. These patterns underscore how integrating endotyping with genetic risk stratification can reveal nuanced and biologically grounded subphenotypes that would be obscured in binary classifications. Based on SHAP analysis, shown in **Figure 3B**, each endotype displayed unique proteomic drivers as key features. Class 0, representing the traditional CMVD case phenotype, was distinguished by proteins PAR-1, REN, BOC, and BNP, among others. In Class 2, representing the traditional control group, REN, BNP, and IL1RL2 contributed the most to the classification. Both cases and controls included the PRS as an essential feature, consistent with **Figure 3A**. Class 1 and Class 3 represented the intermediate groups but prioritized different features. Class 1 prioritized FGF-23 and TIE2 and included enrollment age as a key feature. Class 3, in contrast, had biological sex as the most important SHAP feature, followed by SLAMF7, CEACAM8, THBS2, IL-27, and other proteins.

4. Discussion

4.1. *Information Gain from Imaging and Proteomics Data*

This study represents a novel and comprehensive effort to predict CMVD using multi-modal imaging, proteomics, and genetic data, integrated through machine learning approaches. Unlike existing clinical models, our models were specifically designed to predict risk in earlier, potentially asymptomatic stages[10]. This shift toward earlier identification is critical for a condition like CMVD, which often goes undetected until significant vascular damage has occurred[5,7]. By excluding disease-driven clinical comorbidities, we demonstrated that genetic and proteomic features can drive predictive accuracy. Our models, particularly EN and XGBoost, achieved strong performance across all metrics when incorporating proteomics, surpassing demographic and genetic models alone, and existing clinical models. These improvements are especially meaningful for risk stratification in clinical populations where overt signs of disease have not yet emerged, offering the potential for earlier intervention and monitoring. The relatively poorer performance of the autoencoders and FNNs likely reflects the limited feature space and relatively small sample size in this dataset[36,41]. Parameter complexity of these models is relatively high; the limited data available may have been insufficient to fully train them. As sample sizes increase, performance of these methods may improve; however, our results underscore the robustness of linear and tree-based methods for proteomics-guided risk prediction in CMVD.

In addition to predictive gains in modeling, our findings provide biological insights into CMVD pathogenesis. Previously known markers of cardiac stress such as age, BNP, and REN were top contributors to model performance, in line with the previous model in Prescott *et al*. ACE2, another mediator art of the renin-angiotensin-aldosterone system (RAAS), not seen in other clinical models, was significant in our models[10,44–46]. These findings support expert consensus that targeting RAAS may be helpful for CMVD, despite not being fully captured by prior risk models. Additional proteomic signals of interest from top models included ADM, THBS2, and PTX3, among others. ADM is a vasodilatory peptide that helps maintain vascular integrity, while THBS2 and PTX3 have been implicated in vascular inflammation[47–49]. These findings suggest that proteomic profiling may enhance risk stratification and improve our understanding of CMVD pathophysiology.

4.2. *Image-Derived Endotyping Significantly Improves Risk Prediction*

CMVD is a multifactorial disease with several underlying mechanisms. While a MBFR threshold of 2 for PET is often used for binary classifications clinically, this may obscure important heterogeneity in pathophysiology and patient trajectory. By applying multiclass modeling and endotyping approaches, we demonstrate that stratifying patients into biologically-informed subgroups improves risk prediction and reveals distinct associations with genetic and proteomic features. Our results identified four major endotypes, each with unique proteomic signatures and potential clinical implications. The PRS demonstrated stronger risk stratification capabilities across the standard case/control classes, with weaker resolution in the intermediate classes. Class 0 represents the classic CMVD case group, characterized by severely impaired flow and a strong signal of vascular injury and remodeling. Top SHAP features for this group included PAR-1, BNP, BOC, REN, ACE2, and SOD, all of which are implicated in endothelial dysfunction, neurohormonal activation, and oxidative stress[44,46,50,51]. These findings are consistent with known pathophysiological mechanisms of microvascular ischemia and validate Class 0 as the most prototypical disease phenotype[1,8,11]. In contrast, Class 2 represents the classic control group, characterized by preserved MBFR and a biomarker profile indicative of vascular homeostasis. Essential proteins in this group included REN, BNP, PGF, IL1RL2, PAR-1, and THBS2, which, despite some overlap with Class 0, appear with inverse directionality. This group likely reflects a more regulated state, with expression patterns consistent with effective vascular signaling and less inflammation[44,46,49,50,52]. Class 1 is an intermediate phenotype with largely preserved flow but early indications of vascular stress. The top features in this group, FGF-23, TIE2, IL-27, and PRSS27, are linked to dysregulation in vascular tone, angiogenesis, and immune signaling[53–56]. These patients may be at higher risk of progression and warrant closer monitoring. Class 3 presented with notable sex-specific influences, with sex emerging as a top SHAP feature and showing a wide, polarized distribution, indicating strong and variable effects. This is consistent with findings of sex-specific modulation in stress and rest flow[8,57]. The key proteins driving this endotype included SLAMF7, CEACAM8, and SERPINA12, suggesting an immunomodulatory signature potentially influenced by sex hormones or variations in the immune system[58–60]. These patients may represent a CMVD phenotype that is not easily captured by traditional perfusion metrics.

This multiclass endotyping framework outperformed binary models in uncovering distinct biological patterns and enhancing associations with both PRS and proteomic profiles. The AUROC scores across all classes were high, suggesting that the model effectively distinguished between patients at varying levels of CMVD risk. Class 0 and Class 2 achieved AUROCs of 0.723 and 0.721, respectively, while the overall multiclass AUROC reached 0.690, indicating robust ranking capability. However, metrics such as precision and recall were generally lower, particularly for minority classes (Class 2 had a recall of 0.145), largely due to class imbalance introduced by the clustering strategy. Importantly, F1-scores remained relatively high and Brier scores remained low across all classes (0.107-0.197 per class, 0.166 overall), suggesting that while exact class predictions may have been imperfect, predicted probabilities were well-calibrated[61,62]. The results underscore the value of redefining disease states using clinical data and machine learning tools. This approach

enables a more nuanced and interpretable understanding of CMVD heterogeneity, with potential implications for risk stratification, biomarker discovery, and therapeutic targeting.

4.3. *Future Approaches and Limitations*

This study has some limitations and opportunities for improvement. The patient cohort was drawn from a single center, the Hospital of the University of Pennsylvania, and includes only patients referred for perfusion PET imaging as part of routine clinical care. This population thus represents a higher-risk clinical group, which may not be generalizable to the broader population. However, this enrichment for disease enhances the ability to detect biological signals associated with CMVD. Additionally, the proteomic analysis was restricted to angiogenesis-related proteins from the OLINK Cardiovascular II panel, which may not capture other potential mechanisms, such as immune or metabolic pathways. The effect sizes for the PRS were derived from a CAD GWAS, rather than a CMVD-specific GWAS. This was necessary due to the lack of sufficiently powered GWAS on CMVD, but the genetic risk captured may not fully represent the genetic architecture unique to microvascular dysfunction. Future availability of large-scale CMVD GWAS will be critical to improve PRS relevance and specificity for this condition.

This is the first study integrating imaging-derived measurements with genetics and proteomics to characterize risk and define CMVD endotypes in an unsupervised manner. Furthermore, our use of a multiclass classifier and SHAP-based interpretation provides novel insights into the clinical and molecular distinctions across CMVD subtypes. Future work will expand proteomic coverage and incorporate additional clinical data, such as comorbidities and laboratory measurements to improve prediction. We will assess if genetic and proteomic predictors perform consistently across different ancestral backgrounds. Another key direction is further investigation of biological sex differences within CMVD endotypes, particularly in the intermediate group (Class 3), which exhibits early vascular signaling patterns that may present differently across sexes. Overall, this work highlights the potential of integrating multi-omics and endotyping approaches to advance personalized risk assessment and enable earlier diagnosis and targeted prevention for CMVD.

5. Acknowledgements

We acknowledge the Penn Medicine BioBank and Regeneron Genetics Center for providing data and thank the patient-participants of Penn Medicine who consented to participate in this research program. The PMBB is approved under IRB protocol# 813913 and supported by the Perelman School of Medicine at the University of Pennsylvania, a gift from the Smilow family, and the National Center for Advancing Translational Sciences of the National Institutes of Health under CTSA award number UL1TR001878.

6. Appendix

Supplemental figures and tables are available at:
https://ritchielab.org/publications/supplementary-data/psb-2026/cmvdriskpred
All modeling and analysis code are available at:
https://github.com/rvenkatesh99/Proteomics_Modeling

References

1. Crea, F., Camici, P. G. & Bairey Merz, C. N. Coronary microvascular dysfunction: an update. *European Heart Journal* **35**, 1101–1111 (2014).
2. Duncker, D. J., Koller, A., Merkus, D. & Canty, J. M. Regulation of Coronary Blood Flow in Health and Ischemic Heart Disease. *Progress in Cardiovascular Diseases* **57**, 409–422 (2015).
3. Wayne, N. *et al.* Genetic Insights Into Coronary Microvascular Disease. *Microcirculation* **32**, e12896 (2025).
4. Ischemia and No Obstructive Coronary Artery Disease (INOCA) | Circulation. https://www.ahajournals.org/doi/full/10.1161/CIRCULATIONAHA.116.024534.
5. Tonet, E. *et al.* Coronary Microvascular Dysfunction: PET, CMR and CT Assessment. *J Clin Med* **10**, 1848 (2021).
6. Masi, S. *et al.* Assessment and pathophysiology of microvascular disease: recent progress and clinical implications. *European Heart Journal* **42**, 2590–2604 (2021).
7. Spione, F., Arevalos, V., Gabani, R., Sabaté, M. & Brugaletta, S. Coronary Microvascular Angina: A State-of-the-Art Review. *Front. Cardiovasc. Med.* **9**, (2022).
8. Guerraty, M. A. *et al.* The role of resting myocardial blood flow and myocardial blood flow reserve as a predictor of major adverse cardiovascular outcomes. *PLOS ONE* **15**, e0228931 (2020).
9. van de Wouw, J. *et al.* Perturbations in myocardial perfusion and oxygen balance in swine with multiple risk factors: a novel model of ischemia and no obstructive coronary artery disease. *Basic Res Cardiol* **115**, 21 (2020).
10. Prescott, E. *et al.* Biomarkers and Coronary Microvascular Dysfunction in Women With Angina and No Obstructive Coronary Artery Disease. *JACC: Advances* **2**, 100264 (2023).
11. Venkatesh, R. *et al.* Genome-Wide Association Study of Coronary Microvascular Disease assessed by cardiac perfusion Positron Emission Tomography converges on NF-κB pathway. *medRxiv* (2025) doi:10.1101/2025.03.20.25324357.
12. Verma, A. *et al.* The Penn Medicine BioBank: Towards a Genomics-Enabled Learning Healthcare System to Accelerate Precision Medicine in a Diverse Population. *Journal of Personalized Medicine* **12**, 1974 (2022).
13. Das, S. *et al.* Next-generation genotype imputation service and methods. *Nat Genet* **48**, 1284–1287 (2016).
14. Aragam, K. G. *et al.* Discovery and systematic characterization of risk variants and genes for coronary artery disease in over a million participants. *Nat Genet* **54**, 1803–1815 (2022).
15. Chang, C. C. *et al.* Second-generation PLINK: rising to the challenge of larger and richer datasets. *GigaScience* **4**, s13742-015-0047–8 (2015).
16. Choi, S. W., Mak, T. S.-H. & O'Reilly, P. F. Tutorial: a guide to performing polygenic risk score analyses. *Nat Protoc* **15**, 2759–2772 (2020).
17. Dudbridge, F. Power and Predictive Accuracy of Polygenic Risk Scores. *PLOS Genetics* **9**, e1003348 (2013).
18. Pain, O. *et al.* Evaluation of polygenic prediction methodology within a reference-standardized framework. *PLOS Genetics* **17**, e1009021 (2021).
19. Jayasinghe, D., Eshetie, S., Beckmann, K., Benyamin, B. & Lee, S. H. Advancements and limitations in polygenic risk score methods for genomic prediction: a scoping review. *Hum. Genet.* **143**, 1401–1431 (2024).

20. Zhao, Z. *et al.* Optimizing and benchmarking polygenic risk scores with GWAS summary statistics. *Genome Biol* **25**, 260 (2024).
21. Chicco, D. & Jurman, G. The Matthews correlation coefficient (MCC) should replace the ROC AUC as the standard metric for assessing binary classification. *BioData Mining* **16**, 4 (2023).
22. Powers, D. M. W. Evaluation: from precision, recall and F-measure to ROC, informedness, markedness and correlation. Preprint at https://doi.org/10.48550/arXiv.2010.16061 (2020).
23. Sinaga, K. P. & Yang, M.-S. Unsupervised K-Means Clustering Algorithm. *IEEE Access* **8**, 80716–80727 (2020).
24. Saputra, D. M., Saputra, D. & Oswari, L. D. Effect of Distance Metrics in Determining K-Value in K-Means Clustering Using Elbow and Silhouette Method. in 341–346 (Atlantis Press, 2020). doi:10.2991/aisr.k.200424.051.
25. Paszke, A. *et al.* PyTorch: An Imperative Style, High-Performance Deep Learning Library. Preprint at https://doi.org/10.48550/arXiv.1912.01703 (2019).
26. Pedregosa, F. *et al.* Scikit-learn: Machine Learning in Python. *Journal of Machine Learning Research* **12**, 2825–2830 (2011).
27. Park, H. & Konishi, S. Robust logistic regression modelling via the elastic net-type regularization and tuning parameter selection. *Journal of Statistical Computation and Simulation* (2016).
28. Steyerberg, E. W. *et al.* Assessing the performance of prediction models: a framework for some traditional and novel measures. *Epidemiology* **21**, 128–138 (2010).
29. Gerds, T. A., Cai, T. & Schumacher, M. The Performance of Risk Prediction Models. *Biometrical Journal* **50**, 457–479 (2008).
30. Lundberg, S. M. & Lee, S.-I. A Unified Approach to Interpreting Model Predictions. in *Advances in Neural Information Processing Systems* vol. 30 (Curran Associates, Inc., 2017).
31. Chen, T. & Guestrin, C. XGBoost: A Scalable Tree Boosting System. in *Proceedings of the 22nd ACM SIGKDD International Conference on Knowledge Discovery and Data Mining* 785–794 (ACM, San Francisco California USA, 2016). doi:10.1145/2939672.2939785.
32. Akiba, T., Sano, S., Yanase, T., Ohta, T. & Koyama, M. Optuna: A Next-generation Hyperparameter Optimization Framework. in *Proceedings of the 25th ACM SIGKDD International Conference on Knowledge Discovery & Data Mining* 2623–2631 (Association for Computing Machinery, New York, NY, USA, 2019). doi:10.1145/3292500.3330701.
33. Efendi, A., Fitri, I. & Nurcahyo, G. W. Improvement of Machine Learning Algorithms with Hyperparameter Tuning on Various Datasets. in *2024 International Conference on Future Technologies for Smart Society (ICFTSS)* 75–79 (2024). doi:10.1109/ICFTSS61109.2024.10691354.
34. Dalal, S., Onyema, E. M. & Malik, A. Hybrid XGBoost model with hyperparameter tuning for prediction of liver disease with better accuracy. *World J Gastroenterol* **28**, 6551–6563 (2022).
35. Lundberg, S. M., Erion, G. G. & Lee, S.-I. Consistent Individualized Feature Attribution for Tree Ensembles. Preprint at https://doi.org/10.48550/arXiv.1802.03888 (2019).
36. Li, P., Pei, Y. & Li, J. A comprehensive survey on design and application of autoencoder in deep learning. *Applied Soft Computing* **138**, 110176 (2023).
37. Tomescu, V.-I., Czibula, G. & Niţică, Ş. A study on using deep autoencoders for imbalanced binary classification. *Procedia Computer Science* **192**, 119–128 (2021).

38. Kingma, D. P. & Ba, J. Adam: A Method for Stochastic Optimization. Preprint at https://doi.org/10.48550/arXiv.1412.6980 (2017).
39. Hira, M. T. *et al.* Integrated multi-omics analysis of ovarian cancer using variational autoencoders. *Sci Rep* **11**, 6265 (2021).
40. Geetha, R. *et al.* Analysing Osteoporosis Detection: A Comparative Study of CNN and FNN. in *2024 7th International Conference on Signal Processing and Information Security (ICSPIS)* 1–6 (2024). doi:10.1109/ICSPIS63676.2024.10812652.
41. Xu, C., Coen-Pirani, P. & Jiang, X. Empirical Study of Overfitting in Deep FNN Prediction Models for Breast Cancer Metastasis. Preprint at https://doi.org/10.48550/arXiv.2208.02150 (2022).
42. Otieno, J. A., Häggström, J., Darehed, D. & Eriksson, M. Developing machine learning models to predict multi-class functional outcomes and death three months after stroke in Sweden. *PLOS ONE* **19**, e0303287 (2024).
43. Lundberg, S. M. *et al.* From local explanations to global understanding with explainable AI for trees. *Nat Mach Intell* **2**, 56–67 (2020).
44. Hirakawa, K. *et al.* Correlation between microvascular dysfunction and B-type natriuretic peptide levels in non-ischemic heart failure patients with cardiac fibrosis. *International Journal of Cardiology* **228**, 881–885 (2017).
45. Heusch, G. Coronary microvascular obstruction: the new frontier in cardioprotection. *Basic Res Cardiol* **114**, 45 (2019).
46. Wu, C.-H. *et al.* Renin-Angiotensin System and Cardiovascular Functions. *Arteriosclerosis, Thrombosis, and Vascular Biology* **38**, e108–e116 (2018).
47. Terata, K., Miura, H., Liu, Y., Loberiza, F. & Gutterman, D. D. Human coronary arteriolar dilation to adrenomedullin: role of nitric oxide and K+ channels. *American Journal of Physiology-Heart and Circulatory Physiology* **279**, H2620–H2626 (2000).
48. Presta, M., Camozzi, M., Salvatori, G. & Rusnati, M. Role of the soluble pattern recognition receptor PTX3 in vascular biology. *Journal of Cellular and Molecular Medicine* **11**, 723–738 (2007).
49. Zhang, X.-J. *et al.* Association between single nucleotide polymorphisms in thrombospondins genes and coronary artery disease: A meta-analysis. *Thrombosis Research* **136**, 45–51 (2015).
50. Bae, J.-S., Kim, Y., Park, M.-K. & Rezaie, A. R. Concentration dependent dual effect of thrombin in endothelial cells via Par-1 and Pi3 Kinase. *Journal of Cellular Physiology* **219**, 744–751 (2009).
51. Dubois-Deruy, E., Peugnet, V., Turkieh, A. & Pinet, F. Oxidative Stress in Cardiovascular Diseases. *Antioxidants* **9**, 864 (2020).
52. Mazidi, M. *et al.* Plasma Proteomics to Identify Drug Targets for Ischemic Heart Disease. *JACC* **82**, 1906–1920 (2023).
53. Higgins, S. J. *et al.* Tie2 protects the vasculature against thrombus formation in systemic inflammation. *J Clin Invest* **128**, 1471–1484 (2018).
54. Fitzpatrick, E. A., Han, X., Xiao, Z. & Quarles, L. D. Role of Fibroblast Growth Factor-23 in Innate Immune Responses. *Front. Endocrinol.* **9**, (2018).
55. Zhang, B. *et al.* The cross talk between cervical carcinoma cells and vascular endothelial cells mediated by IL-27 restrains angiogenesis. *American Journal of Reproductive Immunology* **78**, e12706 (2017).

56. Plaza-Florido, A., Rodriguez-Ayllon, M., Altmäe, S., Ortega, F. B. & Esteban-Cornejo, I. Cardiorespiratory fitness and targeted proteomics involved in brain and cardiovascular health in children with overweight/obesity. *European Journal of Sport Science* **23**, 2076–2085 (2023).
57. Murthy, V. L. *et al.* Effects of Sex on Coronary Microvascular Dysfunction and Cardiac Outcomes. *Circulation* **129**, 2518–2527 (2014).
58. Zhang, Z., Zhang, Y., Chen, Z. & Xia, L. Emerging roles of SLAMF7 in immune cells and related diseases. *Innate Immun* **31**, 17534259251326700 (2025).
59. Singer, B. B. *et al.* Soluble CEACAM8 Interacts with CEACAM1 Inhibiting TLR2-Triggered Immune Responses. *PLOS ONE* **9**, e94106 (2014).
60. Heiker, J. T. Vaspin (serpinA12) in obesity, insulin resistance, and inflammation. *Journal of Peptide Science* **20**, 299–306 (2014).
61. Redelmeier, D. A., Bloch, D. A. & Hickam, D. H. Assessing predictive accuracy: How to compare brier scores. *Journal of Clinical Epidemiology* **44**, 1141–1146 (1991).
62. Alakus, T. B. & Turkoglu, I. Comparison of deep learning approaches to predict COVID-19 infection. *Chaos, Solitons & Fractals* **140**, 110120 (2020).

Integrating Polygenic Scores with Clinical, Lifestyle, and Social Risk Factors to Improve Heart Failure Risk Prediction

Katie M. Cardone[1], Dokyoon Kim[2,3], Marylyn D. Ritchie[1,2,3]
[1]*Department of Genetics,* [2]*Institute for Biomedical Informatics,* [3]*Division of Informatics, Department of Biostatistics, Epidemiology, and Informatics*
University of Pennsylvania Perelman School of Medicine, Philadelphia, PA, USA
Email: marylyn@pennmedicine.upenn.edu

Heart failure (HF) is highly prevalent, high-burden disorder with its prevalence expected to increase. Early detection of HF can reduce morbidity and mortality; therefore, novel early detection methods are needed. Polygenic scores (PGS) can combine common variants across the genome and provide phenotype-specific risk scores. However, there are also many well-known, non-genomic risk factors of HF, in the clinical, lifestyle, and social determinant of health (SDOH) domains, and it is not clear how genetic and non-genetic risk factors collectively contribute to HF risk. To address this question, we assessed whether combining HF PGS with clinical, lifestyle, and SDOH risk factors improves risk prediction. Leveraging data from the *All of Us* Research Program (n = 22,275), clinical risk factors were aggregated into a clinical risk score (CRS) while lifestyle and SDOH risk factors were aggregated into a polyexposure score (PXS). Feature selection was conducted with LASSO regression and statistical significance thresholding from logistic regression models ($p < 0.05$). Features were included in the model if they were statistically significant and important in ≥ 95% of 1000 iterations. To assess model performance, logistic regressions with HF case/control status were conducted with each risk score individually, as well as integrated models. The integrated model (PGS + CRS + PXS) performed better than individual risk scores (AUROC = 0.763, AUPRC = 0.047, F1 score = 0.062, balanced accuracy = 0.683). To assess the validity of the CRS and PXS, an integrated model with the PGS along with clinical and exposure risk factors as independent features was also evaluated. Based on AUPRC and F1 score, this integrated risk model (PGS + CRS risk factors + PXS risk factors) performed better than the combining the PGS with the CRS and PXS (AUROC = 0.738, AUPRC = 0.047, F1 score = 0.066, balanced accuracy = 0.657). These findings demonstrate that integration of risk factors across multiple domains can improve HF prediction. Knowing that PGS combined with clinical, lifestyle, and SDOH risk factors is predictive of HF risk provides greater opportunity for the identification of individuals at risk of HF prior to disease onset with the goal of prevention or early intervention.

Keywords: Heart Failure; Polygenic Score; Clinical Risk Score; Polyexposure Score; Integrated Risk Model

1. Introduction

1.1. *Heart Failure Risk Factors*

Heart failure (HF) is a significant burden on the population, as 6.7 million individuals in the United States over age twenty are affected. Due to an aging population and increased survival rates after

© 2025 The Authors. Open Access chapter published by World Scientific Publishing Company and distributed under the terms of the Creative Commons Attribution Non-Commercial (CC BY-NC) 4.0 License.

diagnosis, prevalence is expected to rise by millions each decade[1]. In addition, HF mortality rates have been increasing since 2012[1]. Early detection of HF may decrease morbidity and mortality, through early implementation of guideline-directed medical therapy, the gold-standard treatment for HF[1–3]. Major cardiovascular disease (CVD) events can be prevented with early detection, so, novel methods must be developed to improve early detection of HF[4].

To date, the leading risk factors for HF include older age, smoking, atrial fibrillation (AF), hypertension, ischemic heart disease, obesity, and diabetes mellitus[1]. Cardiovascular conditions are interrelated and share many clinical, environmental, lifestyle, and social determinant of health (SDOH) risk factors[4]. Hypercholesterolemia and hyperlipidemia can lead to atherosclerosis and development of CVD, so many CVD treatments aim to lower lipid levels[4]. These risk factors are assessed in clinical settings with lipid panels that measure high-density lipoprotein (HDL) cholesterol, low-density lipoprotein (LDL) cholesterol, and triglycerides[4]. Other medications aim to lower blood pressure, as high blood pressure is also a major risk factor for CVD[4]. Another clinical risk factor for CVD is diabetes (type I and type II), which is measured by elevated glucose and hemoglobin A1c (HbA1c) levels[1,4].

In addition to clinical risk factors, there are many lifestyle-related risk factors for CVD, including smoking, lack of physical activity, and poor diet[4]. Modifying lifestyle has a major impact on CVD as it is known to slow or reverse progression[4]. Sedentary lifestyle and unhealthy diet can lead to obesity, which is measured by body mass index (BMI)[4]. Lifestyle and SDOH risk factors are often interconnected[4,5]. For example, low income and education level are associated with nutrition status[4,5]. In addition, neighborhood factors such as grocery store availability, park and sidewalk access, poorly kept up housing, vandalism, and graffiti can influence diet and physical activity[4]. Other SDOH factors that are associated with CVD are single-living status, neighborhood deprivation, social isolation, employment status, food insecurity, childhood adversity, living alone, social deprivation index, and census-based income[4–8]. There are also environmental risk factors for CVD, such as air pollution and ambient temperatures[1,5,9,10].

Genomics also play a role in HF development. HF has a heritability of 34% when excluding cardiomyopathies, suggesting some genomic contribution[11]. Familial/Mendelian traits that are caused by variants in single genes such as cardiomyopathies and hypercholesterolemia significantly increase the risk of HF[12–14]. Besides these Mendelian genetic risk factors, many common and rare genetic variants have also been associated with non-Mendelian HF[15].

1.2. *Heart Failure Risk Prediction*

Known risk factors can be leveraged to predict HF risk. For example, genetic testing of variants in single genes that contribute to familial cardiomyopathies and hypercholesterolemia is used for early detection[12–14]. However, not all HF is Mendelian; therefore polygenic scores (PGS) offer an opportunity to aggregate common variants across the genome and provide phenotype-specific risk scores[16]. PGS are the cumulative, mathematical aggregation of risk derived from the total contribution of variants across the genome[16]. PGS have been shown to be predictive at the population-level for complex traits such as CAD, AF, type II diabetes (T2D), breast cancer, schizophrenia, bipolar disorder, among other traits[17–26]. Additionally, recent studies have found that

PGS is predictive of HF[15,27–29]. The clinical utility of PGS is an active area of investigation and discussion in the field, with important considerations such as interpretability, integration with existing clinical risk models, cost-effectiveness, equitable access across diverse populations, and the need for clinician education and infrastructure to support its implementation[26,30–36]

Other risk scores, such as clinical risk scores (CRS) and polyexposure scores (PXS), can be used to integrate non-genomic risk factors, such as clinical, lifestyle, environmental, and SDOH variables into predictive risk models[6,37,38]. CRS is the linear combination of clinical risk factors associated with a disease of interest[38]. Many CRS have been developed and validated to predict HF, utilizing known HF predictor variables including clinical conditions, lifestyle factors, medications, and other risk factors[38]. These models have been shown to be predictive of HF (highest area under the receiver operating curve (AUROC) = 0.87)[38]. Conversely, PXS linearly integrates lifestyle, environmental, and SDOH risk factors into a singular score[37]. A PXS in one recent study was shown to be predictive of T2D status (C-index = 0.762)[37].

These risk scores have been shown to be individually predictive for various CVDs. Integration of PGS with non-genomic risk factors has previously improved predictive ability for CAD, T2D, and aortic stenosis[39,40]. Another study found that combining PGS, CRS, and PXS together improved T2D classification accuracy[37]. Leveraging genomic, electronic health record (EHR), and survey data, this study aims to identify whether integration risk factors across multiple domains can improve prediction of HF risk.

2. Methods

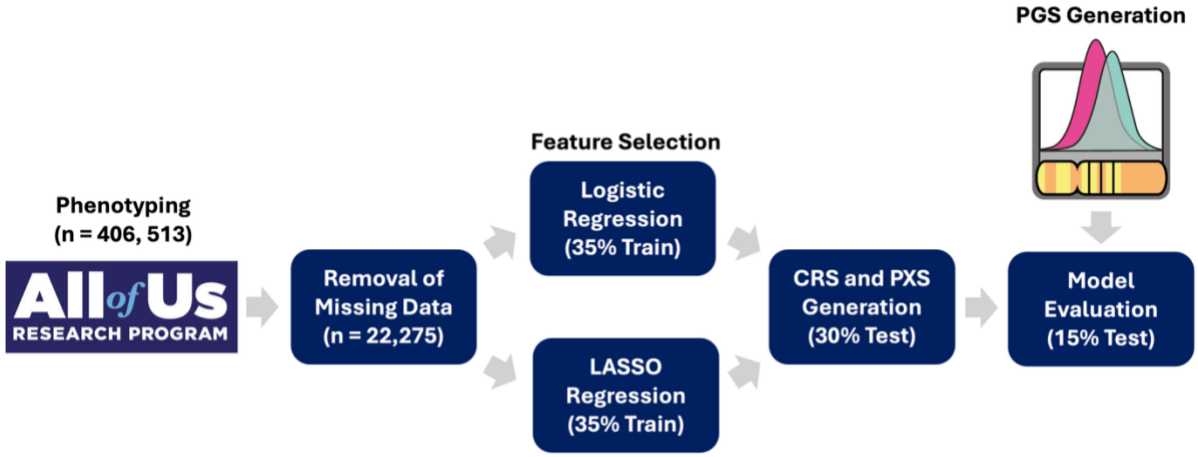

Figure 1: Overview of methodology

2.1. *Data and Study Participants*

The *All of Us* Research Program (AOU) is a longitudinal, cohort study based in the United States[41]. Participants provided informed consent for optional data collection, including blood sample collection for whole genome sequencing (WGS), access to electronic health records (EHR) and wearables, and completion of health-related surveys and physical measurements at the time of enrollment[41]. Data from version 8 (v8) was utilized in this study[41].

2.2. *Genotyping and Quality Control*

AOU genome centers extracted DNA from blood samples, which were genotyped with an Illumina NovaSeq 6000 instrument and processed on the Illumina DRAGEN platform[41]. Following processing, samples were included with mean coverage ≥ 30x, genome coverage ≥ 90% at 20x, coverage of hereditary disease risk genes ≥ 95% at 20x, aligned Q30 bases ≥ 8 x 10^{10}, cross-individual contamination < 3%, concordance with independently processed genotype array, and concordance between sex call and self-reported sex at birth[41]. During joint calling, additional sample-level quality control (QC) was conducted, including sample hard threshold flagging (number of single nucleotide polymorphisms (SNPs) < 2.4 million and > 5.0 million, number of variants not present in gnomAD 3.1 > 100K, and heterozygous to homozygous ratio (Het/Hom) > 3.3 (for SNPs and insertions and deletions (INDELs) separately)), and sample population outlier flagging (eight median absolute deviations (MAD) away from the median residual in deletion count, insertion count, SNP count, number of variants not in gnomAD 3.1, insertion to deletion ratio, transition to transversion ratio, or SNP or INDEL Het/Hom). Variant-level quality control was also conducted, excluding variants with no high-quality genotype (genotype quality (GQ) ≥ 20, depth of coverage (DP) ≥ 10, and allele balance (AB) ≥ 0.02 for heterozygotes), excess heterozygosity < 54.69, SNP quality (QUAL) score < 60, INDEL QUAL score < 69, > 100 alternate alleles, and variants that are likely artifacts (using the Variant Extract-Train-Score Filtering (VETS) algorithm)[41]. Finally, eight well-characterized control samples were included to validate the QC pipeline by calculating sensitivity and precision[41].

2.3. *Polygenic Score Calculation*

PGS weights were generated using the largest HF genome-wide association study (GWAS) to date (n-individuals = 2,322,691, n-variants = 1,274,692)[15]. Weights were extracted from the PGS catalog (PGS005097) and applied to the AOU cohort using the PGSC-CALC pipeline, which adjusts for the confounding effects of genetically inferred ancestry by normalizing based on differences in population means and standard deviations[42–44].

2.4. *Phenotyping*

Individuals were categorized as cases and controls for ICD-based phenotypes based on ICD-9 and ICD-10 mappings to PhecodeX, which represent meaningful phenotypes in statistical genetics[45]. The outcome, HF status, was defined by PhecodeX CV_424. T2D status, a predictor included in the CRS, was defined by PhecodeX EM_202.2 (**Table 1**). For both phenotypes, individuals had to have at least two instances of mapped ICD codes to be a case (rule of two), and zero instances to be a control[46]. Age at first diagnosis, represented by age at first HF ICD code, was computed for HF cases, while age at last data release (October 1st, 2023) was computed for HF controls. Reported sex at birth was encoded numerically, including only males and females.

Lab values were derived from the electronic health record (EHR) and were obtained from serum or plasma. Triglycerides, HDL cholesterol, LDL cholesterol, non-fasting glucose, HbA1c, systolic blood pressure (SBP), and diastolic blood pressure (DBP) were included in the CRS while BMI was included in the PXS (**Table 1**). Values were first filtered by measurement name. Many values were

extremely abnormal so values ≥ 5 MAD away from the median were excluded, as well as values ≤ 0. Many individuals had multiple measurements, so the closest value before their calculated age (age at first diagnosis for cases, age at data release for controls) was retained. Individuals who did not have lab measurements before their coded age were excluded.

Lifestyle risk factors (smoking status, physical activity, and nutrition status), as well as SDOH risk factors (income level, highest achieved education level, neighborhood, and single-living status), were extracted to be included in the PXS (**Table 1**). This data was derived from surveys, which were taken once at recruitment. Income, education level, and physical activity were derived from one question. Conversely, twenty-four neighborhood questions were extracted and kept as separate features. Smoking status was derived from nine questions which were integrated into one variable, classifying individuals as nonsmokers (0), former smokers (1), or current smokers (2)[47]. Individuals had to respond as a non-smoker in all questions to be classified as a non-smoker. Individuals were classified as former smokers if they identified as a former smoker or the age they completely quit smoking was less than their coded age. Individuals who responded as a smoker in any question were classified as a current smoker. Answers for all questions were coded numerically, such that each variable reflected a positive association with HF. The questions, answers, and answer encodings for each variable are described in the supplementary material (**Supplementary Table 1**). Census-based income and social deprivation index (SDI) were also included in the PXS, which were calculated by AOU based on three-digit zip codes (**Table 1**). Physical activity may change after a HF diagnosis, so the closest value prior to computed age was utilized. Individuals who did not have a physical activity variable prior to their coded age were excluded.

All continuous variables in the CRS and PXS, including labs, measurements, census-based income, and SDI were normalized with inverse-normal transformation. Prior to integration, all variables were put on the same scale. Variables were downscaled to match the variable with the lowest number of categories in their risk score group. CRS variables were scaled to 0-1 to align with T2D status and PXS variables were scaled to 0-2 to align with smoking status. Individuals with missing data in any variable were removed.

2.5. *Clinical Risk Score and Polyexposure Score Construction*

Data was split into 70% train and 30% test splits. The training portion was used for feature selection and weight generation. It was split in half, so 35% of the dataset was used for logistic regressions and 35% was used for LASSO regression. Logistic regression was used to identify risk factors that were significantly associated with HF ($p < 0.05$), while LASSO regression was used to identify important risk factors in HF prediction. In these training splits, SMOTE was used to combat case/control imbalance and increase sample size[48]. In both regression models, the outcome was HF case/control status, and age and sex were used as covariates in the logistic regression. 1000 iterations of these splits were conducted (for both 70/30 training/testing split and 35/35 training split), using a different random seed each time. Sampling was conducted without replacement. Only risk factors that were significant and important ≥ 95% of iterations (95% confidence) were included in CRS and PXS generation. In the testing set, risk factors were combined into cohesive scores using a

weighted sum, using effect sizes (betas) from logistic regressions as the weights. As a comparison, unweighted sum was assessed as well.

2.6. *Model Evaluation*

Model evaluation was conducted in the testing split using logistic regressions. The testing set was split in half, so 15% of the dataset was used for model training and 15% was used for model testing. Like before, 1000 iterations of these splits were conducted. SMOTE was again used in the training set[48]. Each risk score was tested individually as well as every possible grouping of scores. Models with individual risk factors were tested as a comparison to the CRS and PXS. This resulted in seventeen distinct models (**Table 3**). In each model, age and sex were utilized as covariates. Performance metrics used were AUROC, area under the precision-recall curve (AUPRC), F1 score, and balanced accuracy. Mean metrics across the 1000 iterations were computed.

3. Results

Eighteen risk factors were initially selected for inclusion in the study (**Table 1**). Eight clinical risk factors were selected for the CRS, while four lifestyle risk factors and six SDOH risk factors were selected the PXS (**Table 1, Supplementary Table 1**). Nutrition and single-living status were excluded due to high data missingness (**Table 1**). DBP, SBP, and seven neighborhood variables were excluded because they were not significant in ≥ 95% of logistic regression iterations (**Table 1, Table 2, Supplementary Table 1**). Glucose and HbA1c were excluded because they were not important in ≥ 95% of LASSO regression iterations (**Table 1, Table 2**). Additionally, triglyceride levels were excluded because they were neither significant nor important (**Table 1, Table 2**). After filtering, ten risk factors remained, including three clinical risk factors (HDL cholesterol, LDL cholesterol, and T2D) in the CRS, and three lifestyle risk factors (physical activity, smoking status and BMI) and four SDOH risk factors (income level, education level, neighborhood, and census-based income) in the PXS, including seventeen neighborhood variables (**Table 1, Table 2, Supplementary Table 1**).

Prevalence of HF was ~5.1% in AOU. Removing missing data decreased the sample size substantially. The sample size decreased from 406,513 (n-controls = 386,518, n-cases = 19,995) to 22,594 (n-controls = 22,275, n-cases = 319). Lab values and neighborhood variables had the lowest percentage of non-missingness, which contributed the most to the sample size decrease (**Supplementary Table 2**). The case count in particular dropped because individuals had to have lab values and physical activity survey answers before their first HF diagnosis to be included. However, SMOTE was used to increase the case count to match the number of controls in all splits except the final testing set.

Clinical Risk Score	**Polyexposure Score**	
Clinical Risk Factors	**Lifestyle Risk Factors**	**Social Determinant of Health Risk Factors**
Diastolic Blood Pressure[†]	BMI	Census-based income
Glucose[‡]	Nutrition status[*]	Education level
HbA1c[‡]	Physical activity	Income level

HDL cholesterol LDL cholesterol Systolic Blood Pressure† T2D status Triglycerides†‡	Smoking status	Neighborhood† Single-level status* Deprivation index†‡

Table 1: Known risk factors for HF to be included in integrated risk scores. *Risk factors excluded due to low data availability. †Risk factors excluded because they were not significant in ≥ 95% of logistic regression iterations. ‡Risk factors excluded because they were not important in ≥ 95% of LASSO regression iterations. Some, but not all, neighborhood questions were excluded.

Category (Risk Score)	Risk Factor	Mean P-Value	Percent Significant	Mean Absolute Coefficient	Percent Important
Clinical (CRS)	Diastolic Blood Pressure	0.048	88.30%	1.322	96.30%
Clinical (CRS)	Glucose	0.007	97.80%	0.819	93.80%
Clinical (CRS)	HbA1c	0.001	99.70%	0.914	91.90%
Clinical (CRS)	HDL cholesterol	0.008	98.00%	2.014	97.70%
Clinical (CRS)	LDL cholesterol	0.000	99.90%	1.403	95.00%
Clinical (CRS)	Systolic Blood Pressure	0.112	73.50%	0.946	92.60%
Clinical (CRS)	T2D	9.50E-81	100.00%	0.980	100.00%
Clinical (CRS)	Triglycerides	0.120	71.40%	0.924	92.60%
Lifestyle (PXS)	BMI	3.82E-20	100.00%	2.511	100.00%
Lifestyle (PXS)	Everyday Physical Activity	4.40E-48	100.00%	0.847	100.00%
Lifestyle (PXS)	Smoking	0.004	99.10%	0.242	99.70%
SDOH (PXS)	Annual Income	1.16E-54	100.00%	0.397	99.40%
SDOH (PXS)	Census Median Income	3.40E-18	100.00%	0.914	96.90%
SDOH (PXS)	Highest Education	6.23E-08	100.00%	0.385	97.30%
SDOH (PXS)	Neighborhood- Abandoned Buildings	0.002	99.40%	0.293	97.10%
SDOH (PXS)	Neighborhood- Alcohol Use	0.023	94.30%	0.667	99.40%
SDOH (PXS)	Neighborhood- A lot of Crime	0.005	99.00%	0.365	98.00%
SDOH (PXS)	Neighborhood- Cleanliness	0.016	95.30%	0.288	97.90%
SDOH (PXS)	Neighborhood-Crime Rate Makes It Unsafe to Walk at Night	0.001	99.90%	0.343	99.00%
SDOH (PXS)	Neighborhood- Crime Rate Makes It Unsafe to Walk During the Day	1.95E-13	100.00%	0.544	99.00%
SDOH (PXS)	Neighborhood- Drug Use	0.003	99.40%	0.484	97.20%
SDOH (PXS)	Neighborhood- Facilities to Bike	2.47E-07	100.00%	0.324	99.40%
SDOH (PXS)	Neighborhood- Free/Low-Cost Recreation Facilities	0.001	99.20%	0.243	99.30%

SDOH (PXS)	Neighborhood- Get Along with Neighbors	0.113	73.00%	0.835	99.20%
SDOH (PXS)	Neighborhood- Graffiti	0.014	96.20%	0.301	97.90%
SDOH (PXS)	Neighborhood-Main Type of Housing	0.075	80.80%	0.256	98.30%
SDOH (PXS)	Neighborhood- Neighbors Can Be Trusted	0.001	99.90%	0.451	96.70%
SDOH (PXS)	Neighborhood- Neighbors Take Good Care of Their Homes	0.006	98.80%	0.256	97.80%
SDOH (PXS)	Neighborhood- Neighbors Watch Out for Each Other	0.046	88.00%	0.289	98.40%
SDOH (PXS)	Neighborhood- Noise	0.099	77.40%	0.255	97.70%
SDOH (PXS)	Neighborhood- People Share the Same Values	0.046	88.30%	0.293	97.90%
SDOH (PXS)	Neighborhood- Safe from Crime	0.002	99.40%	0.303	97.80%
SDOH (PXS)	Neighborhood- Shops, Stores, Markets or Other Places to Buy Things are Within Walking Distance	0.000	99.90%	0.309	99.40%
SDOH (PXS)	Neighborhood- Sidewalks on Most Streets	0.008	97.90%	0.159	98.70%
SDOH (PXS)	Neighborhood- Too Many People Hanging Around on the Streets Near Home	0.014	96.40%	0.345	96.60%
SDOH (PXS)	Neighborhood- Transit Stop Within Walking Distance	0.019	95.20%	0.152	98.70%
SDOH (PXS)	Neighborhood- Trouble with Neighbors	0.002	99.50%	0.347	97.70%
SDOH (PXS)	Neighborhood- Vandalism	0.006	98.50%	0.304	97.20%
SDOH (PXS)	Social Deprivation Index	0.090	77.60%	0.697	93.40%

Table 2: Significance and importance of variables across 1000 iterations. Mean beta, mean p-value and percent significant columns were calculated from logistic regressions, while mean absolute coefficient and percent important columns were calculated from LASSO regressions.

Model 13 (PGS + weighted CRS + weighted PXS) performed best based on AUROC and balanced accuracy, while model 17 (PGS + CRS risk factors + PXS risk factors) performed best based on AUPRC and F1 score (**Table 3, Table 4, Figure 2**). Based on AUROC and balanced accuracy, the next best performing model was model 11 (weighted CRS + weighted PXS) (**Table 3, Table 4, Figure 2**). Based on F1 score and AUPRC, the next best performing models were model 13 (PGS + weighted CRS + weighted PXS) and model 16 (CRS risk factors + PXS risk factors) (**Table 3, Table 4, Figure 2**). After this, the performance ranking of the models varied by metric (**Table 3, Table 4, Figure 2**). However, based on AUROC, F1 score, and balanced accuracy, the

worst performing models were model 4 (unweighted PXS), model 6 (PGS + unweighted CRS), model 2 (unweighted CRS), and model 1 (PGS) (**Table 3, Table 4, Figure 2**). Model 4 (unweighted PXS), model 2 (unweighted CRS), and model 1 (PGS) were among the worst performing models based on balanced accuracy, with the addition of model 5 (weighted PXS) (**Table 3, Table 4, Figure 2**).

Model Number	Model	Number of Features
1	PGS	3
2	CRS_SUM	3
3	CRS_WEIGHTED_SUM	3
4	PXS_SUM	3
5	PXS_WEIGHTED_SUM	3
6	PGS + CRS_SUM	4
7	PGS + CRS_WEIGHTED_SUM	4
8	PGS + PXS_SUM	4
9	PGS + PXS_WEIGHTED_SUM	4
10	CRS_SUM + PXS_SUM	4
11	CRS_WEIGHTED_SUM + PXS_WEIGHTED_SUM	4
12	PGS + CRS_SUM + PXS_SUM	5
13	PGS + CRS_WEIGHTED_SUM + PXS_WEIGHTED_SUM	5
14	CRS Risk Factors	7
15	PXS Risk Factors	12
16	CRS Risk Factors + PXS Risk Factors	17
17	PGS + CRS Risk Factors + PXS Risk Factors	18

Table 3: Overview of evaluation models. Features included each risk score, as well as age and sex as covariates.

Model Number	Risk Factor	AUROC	AUPRC	F1 Score	Balanced Accuracy
1	PGS	0.669	0.034	0.044	0.607
2	CRS_SUM	0.676	0.033	0.042	0.598
3	CRS_WEIGHTED_SUM	0.736	0.042	0.055	0.655
4	PXS_SUM	0.709	0.032	0.052	0.646
5	PXS_WEIGHTED_SUM	0.730	0.034	0.056	0.660
6	PGS + CRS_SUM	0.678	0.036	0.043	0.603
7	PGS + CRS_WEIGHTED_SUM	0.737	0.046	0.057	0.662
8	PGS + PXS_SUM	0.715	0.036	0.054	0.652
9	PGS + PXS_WEIGHTED_SUM	0.734	0.038	0.057	0.665
10	CRS_SUM + PXS_SUM	0.732	0.039	0.055	0.652
11	CRS_WEIGHTED_SUM + PXS_WEIGHTED_SUM	0.762	0.043	0.061	0.678
12	PGS + CRS_SUM + PXS_SUM	0.734	0.041	0.057	0.658

13	PGS + CRS_WEIGHTED_SUM + PXS_WEIGHTED_SUM	0.763	0.047	0.062	0.682
14	CRS Risk Factors	0.729	0.040	0.055	0.655
15	PXS Risk Factors	0.723	0.041	0.060	0.647
16	CRS Risk Factors + PXS Risk Factors	0.738	0.046	0.065	0.658
17	PGS + CRS risk factors + PXS risk factors	0.738	0.047	0.065	0.657

Table 4: Model evaluation metrics.

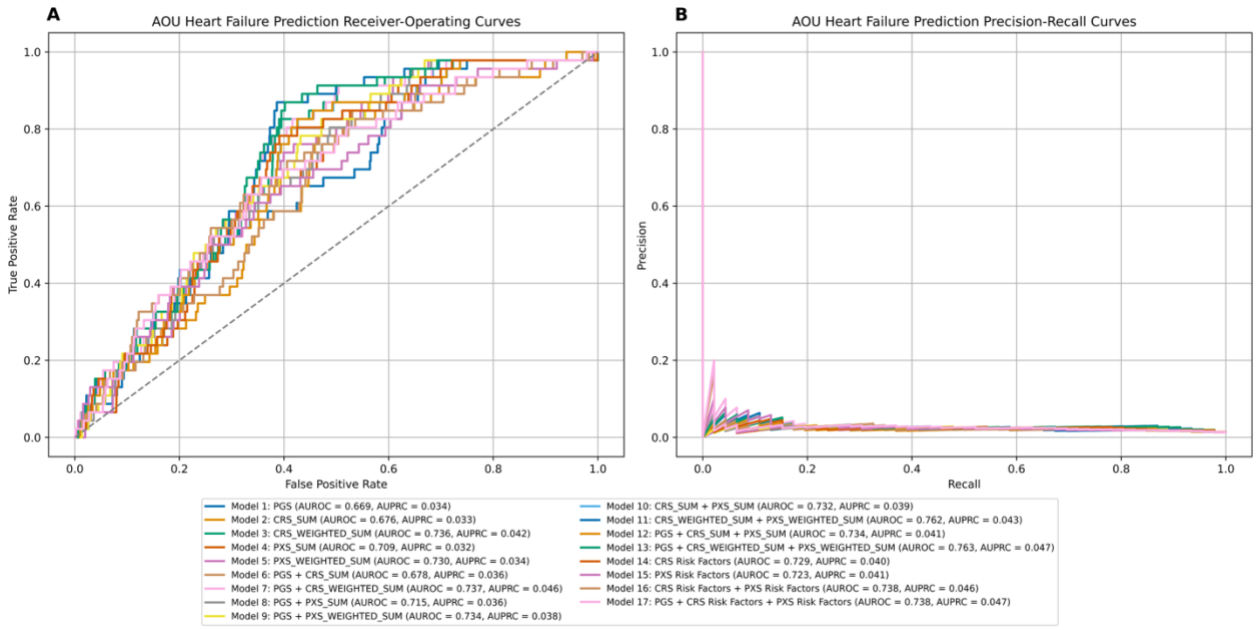

Figure 2: AOU Receiver-operator (ROC) curves (**Panel A**) and precision-recall (PRC) curves (**Panel B**).

4. Discussion

This study exhibited that integration of genetic, clinical, lifestyle, and SDOH risk factors improved predictive performance of heart failure risk in comparison to the separate risk scores alone. Based on all metrics, the integrated risk models containing risk factors across all domains (model 13, PGS + weighted CRS and PXS, and model 17, PGS + CRS and PXS risk factors) were the top performing models (**Table 3, Table 4, Figure 2**). Based on AUPRC and F1 score, model 17 (PGS + CRS and PXS risk factors) performed best but model 13 (PGS + weighted CRS and PXS) performed best based on AUROC and balanced accuracy (**Table 3, Table 4, Figure 2**). Thus, it is unclear which integration metric is best, but models containing risk factors across multiple domains were always the top performing model. This finding is consistent with previous literature[37,39,40].

The PGS seemed to contribute the least to model performance, as model 1 (PGS) performed worse than model 3 (weighted CRS), model 14 (CRS risk factors), model 5 (weighted PXS), and model 15 (PXS risk factors) based on all metrics, which is consistent with previous literature (**Table 3, Table 4, Figure 2**)[37]. Additionally, model 11 (weighted CRS + weighted PXS) and model 16 (CRS risk factors + PXS risk factors) were among the top performing models. It is unclear whether clinical risk factors or lifestyle and SDOH risk factors contributed more, as performance ranking

varied by metric, and quantitative differences were very small (**Table 3, Table 4, Figure 2**). In addition, models 3 (weighted CRS) and 5 (weighted PXS) performed better than models 2 (unweighted CRS) and 4 (unweighted PXS), demonstrating that integrating risk factor effect sizes enhances predictive performance.

Model 1 (PGS) yielded a lower AUROC compared to the study in which the weights were derived, possibly due to differences in the test dataset, sample size, or outcome phenotyping (**Table 3, Table 4, Figure 2**)[15]. Additionally, the PGSC-CALC pipeline normalized the PGS based on differences in population means and standard deviations, while the previous study did not normalize the PGS and instead scaled/centered the PGS within individual ancestry groups and utilized principal components as covariates in the regression models[15,42–44]. Models 2 (unweighted CRS) and 3 (weighted CRS) also had a lower AUROC than seen in previous literature (**Table 3, Table 4, Figure 2**)[38]. However, these studies included other clinical variables such as various clinical conditions, lab measurements, and medications, so it is possible that these variables in addition to different sample sizes, datasets, or combination methods, may have led to AUROC differences[38]. Model 5 (weighted PXS) has only been evaluated in one prior study, which did not use the same performance metrics, preventing direct pairwise comparison[37].

Model training yielded variables that were considered most predictive. Based on logistic regressions, the ten risk factors with the lowest mean p-values were T2D, income, physical activity, BMI, census-based income, education, four neighborhood variables, and LDL cholesterol (**Table 2**). T2D, LDL, BMI, physical activity, and census-based income overlapped with the ten risk factors with the highest mean absolute coefficients based on LASSO regressions (**Table 2**). Other variables deemed more important by LASSO regressions were HDL cholesterol, DBP, SBP, triglycerides, and HbA1c (**Table 2**). SDOH risk factors appeared more significant in logistic regressions, while clinical risk factors appeared more important in LASSO regressions (**Table 2**). Thus, there is some variability based on the feature selection method.

This study had several limitations. Sample size was low due to removal of missing values, and performance may have improved if it was higher, particularly in the training sets. It is also possible that more predictors may have appeared significant and important in $\geq 95\%$ of iterations, which could have changed performance. This study also did not include a validation dataset, and replication would have strengthened these findings. However, these findings are replicated by similar studies in the literature[37,38,40]. Several other factors may have improved performance. For example, performance may have improved with the inclusion more clinical, lifestyle, and SDOH risk factors associated with heart failure, as not all known HF/CVD risk factors were included in this study. CVDs have some overlapping genetic architecture, so correcting for this may have improved performance[49]. PGS performance was worse than risk factors in other domains, and it is possible that stratifying the sample to high-risk individuals classified by other CVD risk factors may improve its performance[26]. In addition, performance may have been enhanced with ancestry-stratified analyses, but the sample size was too low to further subset the cohort. As AOU continues to grow, we anticipate that sample sizes will increase and much of these risk factors will become populated in these datasets in the future. There are also some limitations regarding the phenotyping strategy. Rule of two phenotyping accounts for some error in ICD-based phenotyping, but it is possible that there may be some present errors as ICD codes are used for billing purposes and not

diagnosis documentation[46]. In addition, many of the lifestyle and SDOH risk factors were based on self-reported survey data, which is susceptible to bias[50]. Last, prevalence of HF in the general population is estimated to be 1.9 - 2.8%, which is lower than prevalence in these datasets[1]. This, in addition to participation bias of individuals who opt in to biobank studies, may impact the generalizability of this study's findings to the general population[51].

Despite these limitations, this study demonstrated that integrating risk factors across multiple domains improves predictive performance of HF risk, highlighting the need to consider these risk factors in clinical settings. Integrating polygenic scores with clinical, lifestyle, and SDOH risk factors may be used to improve early detection of HF, and therefore its adverse consequences. Such multi-domain risk models may facilitate more precise risk stratification in clinical settings, enabling earlier interventions and improved management for individuals at risk for HF.

5. Acknowledgements

We gratefully acknowledge *All of Us* participants for their contributions, without whom this research would not have been possible. We also thank the National Institutes of Health's *All of Us* Research Program for making available the participant data examined in this study. Funding was provided by HL169458.

6. Supplementary Material

All supplemental material can be found at: https://ritchielab.org/publications/supplementary-data/psb-2026/hf-irm. All code can be found at: https://github.com/RitchieLab/HF_IRM.git

References

1. Bozkurt, B. *et al.* HF STATS 2024: Heart Failure Epidemiology and Outcomes Statistics An Updated 2024 Report from the Heart Failure Society of America. *J. Card. Fail.* **31**, 66–116 (2025).
2. Wang, H. *et al.* Importance of early diagnosis and treatment of heart failure across the spectrum of ejection fraction. *Eur. Heart J.* **44**, ehad655.892 (2023).
3. Kittleson, M. M. *et al.* 2024 Update to the 2020 ACC/AHA Clinical Performance and Quality Measures for Adults With Heart Failure: A Report of the American Heart Association/American College of Cardiology Joint Committee on Performance Measures. *Circ. Cardiovasc. Qual. Outcomes* **17**, e000132 (2024).
4. 2025 Heart Disease and Stroke Statistics: A Report of US and Global Data From the American Heart Association | Circulation. https://www.ahajournals.org/doi/10.1161/CIR.0000000000001303.
5. Bazoukis, G. *et al.* Impact of Social Determinants of Health on Cardiovascular Disease. *J. Am. Heart Assoc.* **14**, e039031 (2025).
6. Ana Palacio, M. D. *et al.* Social Determinants of Health Score: Does It Help Identify Those at Higher Cardiovascular Risk? **26**, (2020).
7. Jilani, M. H. *et al.* Social Determinants of Health and Cardiovascular Disease: Current State and Future Directions Towards Healthcare Equity. *Curr. Atheroscler. Rep.* **23**, 55 (2021).
8. Bevan, G. H., Nasir, K., Rajagopalan, S. & Al-Kindi, S. Socioeconomic Deprivation and Premature Cardiovascular Mortality in the United States. *Mayo Clin. Proc.* **97**, 1108–1113 (2022).
9. Jia, Y. *et al.* Effect of Air Pollution on Heart Failure: Systematic Review and Meta-Analysis. *Environ. Health Perspect.* **131**, 76001 (2023).
10. Feng, J., Zhang, Y. & Zhang, J. Epidemiology and Burden of Heart Failure in Asia. *JACC Asia* **4**, 249–264 (2024).
11. Lindgren, M. P. *et al.* A Swedish Nationwide Adoption Study of the Heritability of Heart Failure. *JAMA Cardiol.* **3**, 703–710 (2018).
12. Miller, D. T. *et al.* ACMG SF v3.2 list for reporting of secondary findings in clinical exome and genome sequencing: A policy statement of the American College of Medical Genetics and Genomics (ACMG). *Genet. Med. Off. J. Am. Coll. Med. Genet.* **25**, 100866 (2023).
13. Brownrigg, J. R. *et al.* Epidemiology of cardiomyopathies and incident heart failure in a population-based cohort study. *Heart Br. Card. Soc.* **108**, 1383–1391 (2022).
14. Tada, H. *et al.* Familial hypercholesterolemia is related to cardiovascular disease, heart failure and atrial fibrillation. Results from a population-based study. *Eur. J. Clin. Invest.* **54**, e14119 (2024).
15. Lee, D. S. M. *et al.* Common-variant and rare-variant genetic architecture of heart failure across the allele-frequency spectrum. *Nat. Genet.* **57**, 829–838 (2025).
16. Choi, S. W., Mak, T. S.-H. & O'Reilly, P. F. Tutorial: a guide to performing polygenic risk score analyses. *Nat. Protoc.* **15**, 2759–2772 (2020).

17. Ratman, D. *et al.* Polygenic risk scores improve CAD risk prediction in individuals at borderline and intermediate clinical risk. *Npj Cardiovasc. Health* **2**, 13 (2025).
18. Patel, A. P. *et al.* A multi-ancestry polygenic risk score improves risk prediction for coronary artery disease. *Nat. Med.* **29**, 1793–1803 (2023).
19. Gibson, J. T. & Rudd, J. H. F. Polygenic risk scores in atrial fibrillation: Associations and clinical utility in disease prediction. *Heart Rhythm* **21**, 913–918 (2024).
20. Khera, A. V. *et al.* Genome-wide polygenic scores for common diseases identify individuals with risk equivalent to monogenic mutations. *Nat. Genet.* **50**, 1219–1224 (2018).
21. Ge, T. *et al.* Development and validation of a trans-ancestry polygenic risk score for type 2 diabetes in diverse populations. *Genome Med.* **14**, 70 (2022).
22. Roberts, E., Howell, S. & Evans, D. G. Polygenic risk scores and breast cancer risk prediction. *Breast Edinb. Scotl.* **67**, 71–77 (2023).
23. Mars, N. *et al.* Polygenic and clinical risk scores and their impact on age at onset and prediction of cardiometabolic diseases and common cancers. *Nat. Med.* **26**, 549–557 (2020).
24. Duncan, L. *et al.* Polygenic scores for psychiatric disorders in a diverse postmortem brain tissue cohort. *Neuropsychopharmacology* **48**, 764–772 (2023).
25. Liu, H., Wang, L., Yu, H., Chen, J. & Sun, P. Polygenic Risk Scores for Bipolar Disorder: Progress and Perspectives. *Neuropsychiatr. Dis. Treat.* **19**, 2617–2626 (2023).
26. O'Sullivan, J. W. *et al.* Polygenic Risk Scores for Cardiovascular Disease: A Scientific Statement From the American Heart Association. *Circulation* **146**, e93–e118 (2022).
27. Soh, C. H., Xiang, R., Takeuchi, F. & Marwick, T. H. Use of Polygenic Risk Score for Prediction of Heart Failure in Cancer Survivors. *JACC CardioOncology* **6**, 714–727 (2024).
28. Han, Y. *et al.* A novel polygenic risk score improves prognostic prediction of heart failure with preserved ejection fraction in the Chinese Han population. *Eur. J. Prev. Cardiol.* **30**, 1382–1390 (2023).
29. Ahn, H.-J. *et al.* Polygenic risk-based prediction of heart failure in young patients with atrial fibrillation: an analysis from UK Biobank. *EP Eur.* **27**, euaf104 (2025).
30. Martin, A. R. *et al.* Clinical use of current polygenic risk scores may exacerbate health disparities. *Nat. Genet.* **51**, 584–591 (2019).
31. Abramowitz, S. A. *et al.* Evaluating Performance and Agreement of Coronary Heart Disease Polygenic Risk Scores. *JAMA* **333**, 60–70 (2025).
32. Kumuthini, J. *et al.* The clinical utility of polygenic risk scores in genomic medicine practices: a systematic review. *Hum. Genet.* **141**, 1697–1704 (2022).
33. Xiang, R. *et al.* Recent advances in polygenic scores: translation, equitability, methods and FAIR tools. *Genome Med.* **16**, 33 (2024).
34. Lewis, C. M. & Vassos, E. Prospects for using risk scores in polygenic medicine. *Genome Med.* **9**, 96 (2017).
35. Torkamani, A., Wineinger, N. E. & Topol, E. J. The personal and clinical utility of polygenic risk scores. *Nat. Rev. Genet.* **19**, 581–590 (2018).
36. Lennon, N. J. *et al.* Selection, optimization and validation of ten chronic disease polygenic risk scores for clinical implementation in diverse US populations. *Nat. Med.* **30**, 480–487 (2024).

37. He, Y. *et al.* Comparisons of Polyexposure, Polygenic, and Clinical Risk Scores in Risk Prediction of Type 2 Diabetes. *Diabetes Care* **44**, 935–943 (2021).
38. Sinha, A. *et al.* Risk-Based Approach for the Prediction and Prevention of Heart Failure. *Circ. Heart Fail.* **14**, e007761 (2021).
39. Small, A. M. *et al.* Novel Polygenic Risk Score and Established Clinical Risk Factors for Risk Estimation of Aortic Stenosis. *JAMA Cardiol.* **9**, 357–366 (2024).
40. van Dam, S. *et al.* The necessity of incorporating non-genetic risk factors into polygenic risk score models. *Sci. Rep.* **13**, 1351 (2023).
41. Bick, A. G. *et al.* Genomic data in the All of Us Research Program. *Nature* **627**, 340–346 (2024).
42. Lambert, S. A. *et al.* Enhancing the Polygenic Score Catalog with tools for score calculation and ancestry normalization. *Nat. Genet.* **56**, 1989–1994 (2024).
43. Khera, A. V. *et al.* Whole-Genome Sequencing to Characterize Monogenic and Polygenic Contributions in Patients Hospitalized With Early-Onset Myocardial Infarction. *Circulation* **139**, 1593–1602 (2019).
44. Khan, A. *et al.* Genome-wide polygenic score to predict chronic kidney disease across ancestries. *Nat. Med.* **28**, 1412–1420 (2022).
45. Shuey, M. M. *et al.* Next-generation phenotyping: introducing phecodeX for enhanced discovery research in medical phenomics. *Bioinformatics* **39**, btad655 (2023).
46. Schrodi, S. J. The Impact of Diagnostic Code Misclassification on Optimizing the Experimental Design of Genetic Association Studies. *J. Healthc. Eng.* **2017**, 7653071 (2017).
47. Tindle, H. A. *et al.* Lifetime Smoking History and Risk of Lung Cancer: Results From the Framingham Heart Study. *J. Natl. Cancer Inst.* **110**, 1201–1207 (2018).
48. Chawla, N. V., Bowyer, K. W., Hall, L. O. & Kegelmeyer, W. P. SMOTE: synthetic minority over-sampling technique. *J Artif Int Res* **16**, 321–357 (2002).
49. Qiao, J. *et al.* Shared genetic architecture contributes to risk of major cardiovascular diseases. *Nat. Commun.* **16**, 8368 (2025).
50. Choi, B. C. K. & Pak, A. W. P. A Catalog of Biases in Questionnaires. *Prev. Chronic. Dis.* **2**, A13 (2004).
51. Ridgeway, J. L. *et al.* Potential Bias in the Bank: What Distinguishes Refusers, Non-responders and Participants in a Clinic-based Biobank? *Public Health Genomics* **16**, 10.1159/000349924 (2013).

BioLM-NET: an interpretable deep learning model combining prior biological knowledge and contextual LLM gene embeddings on multi-omics data to predict disease

Jubair Ibn Malik Rifat, Thasina Tabashum, Md Marufi Rahman, Md Farhad Mokter, Sarthak Engala

Department of computer Science & Engineering, University of North Texas,
Denton, Texas, 76203, USA
Email: jubairibnmalikrifat@my.unt.edu; thasinatabashum@my.unt.edu; mdmarufirahman@my.unt.edu; mdfarhadmokter@my.unt.edu; sarthakengala@my.unt.edu

Serdar Bozdag

Department of Computer Science & Engineering, Department of Mathematics, Center for Computational Life Sciences, University of North Texas,
Denton, Texas, 76203, USA
Email: serdar.bozdag@.unt.edu

Biologically informed deep neural networks, which connect input layer to hidden layers based on gene-pathway relationship have gained popularity in recent years. However, most existing methods do not incorporate protein-protein interactions (PPI) and protein-DNA interactions (PDI) in their designs. In this study, we introduce BioLM-NET, a deep learning-based framework that fuses single cell or bulk gene expression data and DNA methylation data with prior biological knowledge including Protein-Protein Interactions (PPI), Protein-DNA Interactions (PDI). BioLM-NET also aggregates latent representation of omics signals at pathway-level through an attention-based pathway layer where a pre-trained large language model (LLM) was incorporated to generate context-specific gene embeddings. We evaluated BioLM-NET on single cell colorectal cancer data from scTrioseq2 platform to predict primary and metastatic cancer cells, on TCGA-BRCA, TCGA-GBM, TCGA-COAD to predict cancer subtypes and ROSMAP data to predict Alzheimer's disease patient. Our results showed that BioLM-NET outperformed baseline and state-of-the-art (SOTA) methods, P-NET and PASNet with statistical significance on scTrioseq2 data, TCGA-COAD and ROSMAP data and ties with SVM and Dense neural network on TCGA-BRCA data. Our ablation studies demonstrated the importance of incorporating PPI, PDI data and attention-based pathway layer. We also interpret our models and found out that our important input features are significantly enriched in GO terms and KEGG pathways and can serve as potential biomarkers or therapeutic targets for the corresponding disease.

Keywords: Biologically Informed Neural Network, Large Language Model, scTrioseq2, Alzheimer's disease.

© 2025 The Authors. Open Access chapter published by World Scientific Publishing Company and distributed under the terms of the Creative Commons Attribution Non-Commercial (CC BY-NC) 4.0 License.

1. Introduction

The integration of multi-omics data—including genomics, transcriptomics, epigenomics, and proteomics—holds significant promise for enhancing the accuracy of disease prediction and classification. Several machine learning (ML) and deep learning (DL) models have been developed to integrate multi-omics datasets. However, most existing approaches lack interpretability reducing their practical usability.

To address this issue, recently biologically informed deep neural networks have been developed. For instance, Elmarakeby et al. introduced P-NET, a biologically informed deep neural network initially developed to classify prostate cancer patients into treatment-resistant or primary groups[1]. P-NET demonstrated not only superior prediction performance compared to conventional methods but also provided critical insights into novel therapeutic targets through its interpretable architecture. Although the model is easy to interpret, it relies on existing pathway databases, thereby might miss new or unknown interactions not yet captured in those resources. Other biologically informed neural network architectures such as DrugCell[2] and DCell[3] have demonstrated capability in modeling biological processes and predicting therapeutic responses. However, because DCell was validated in yeast, its direct translation to human diseases may fail to capture the complexity of human biology.

Fortelny and Bock et al. proposed Knowledge-Primed Neural Networks (KPNNs) by incorporating biological network priors into models analyzing single-cell RNA-seq data[4]. While KPNNs showed good interpretability and accuracy, they did not utilize multi-omics data and depended heavily on the quality of the input biological networks. Wang et al. developed BioNet for analyzing tumor heterogeneity from imaging data, but its accuracy may vary with image quality and clinical settings[5]. Another interpretable model, PASNet incorporated sparse coding and pathway-level representations to predict prognosis from high-throughput gene expression data[6]. While PASNet demonstrated robust performance and clear interpretability through pathway hierarchies, it did not utilize multi-omics inputs and was tested only on bulk transcriptomic data from glioblastoma.

Most of the current models use either pathway or Protein-Protein Interaction (PPI) and Protein-DNA Interaction (PDI) networks but none combine all three. These models may be interpretable but are not context-specific, and most of them work on single omics type from bulk tissue rather than single-cell and multi-omics data.

To address these gaps, we introduce BioLM-NET, a novel PPI, PDI, and pathway aware neural network framework that fuses single-cell gene expression, DNA methylation, and pretrained Large Language Model (LLM) based gene embeddings. We conducted comprehensive benchmarking across five datasets, namely scTrio-seq2 data for colorectal cancer[7], TCGA-BRCA[8] for breast cancer, TCGA-GBM[9] for glioblastoma, TCGA-COAD[10] for colon cancer, and ROSMAP[11] for Alzheimer's disease (AD) and achieved state-of-the-art (SOTA) performance in most cases. Our results demonstrated enhanced biological interpretability showing how pathway-level attention and LLM-derived embeddings uncover key molecular features of cancer progression and metastasis, cancer subtyping, and enable stratification of AD patients. The source code and datasets for BioLM-NET is available at

https://github.com/bozdaglab/BioLM-NET under Creative Commons Attribution-Noncommercial 4.0 International Public License.

2. Materials and Methods

2.1 *Dataset*

In this study, we utilized gene expression and DNA methylation data from five datasets: Single Cell Trio-seq2 (scTrio-seq2), TCGA-BRCA, TCGA-GBM, TCGA-COAD, and ROSMAP. We downloaded scTrio-seq2 data from the Gene Expression Omnibus (GEO) under accession number GSE97693[7]. Processed TCGA-BRCA and ROSMAP datasets were obtained from Wang et al.[12], while processed TCGA-GBM and TCGA-COAD datasets were obtained from Yang et al.[13]. We utilized the top 500 features from both TCGA-GBM and TCGA-COAD datasets. Biological prior information was obtained from three sources: protein-protein interactions (PPI) from STRING[14] database, protein-DNA interactions (PDI) from the DoRothEA[15] database, and pathway information from KEGG database[16,17]. We also utilized LLM embedding for genes from GenePT [18]. A summary of the five datasets is provided in Table 1.

Table 1: Overview of the five datasets:. GE: Gene expression, DM: DNA methylation, PPI: Protein-protein interaction, PDI: Protein-DNA interaction

Dataset	# samples	# features (GE)	# features (DM)	# PDI (GE)	# PDI (DM)	# PPI (GE)	# PPI (DM)	# Pathways (GE)	# Pathways (DM)
scTrioseq2	609	1,673	1,712	2,459	2,293	21,968	6,690	161	173
BRCA	875	999	999	1,922	1,704	6,280	3,088	133	142
GBM	244	500	500	682	602	2,276	2,358	140	102
COAD	256	500	500	866	874	2,796	2,182	103	97
ROSMAP	351	200	200	497	380	432	620	134	134

2.2 *scTrio-seq2 gene expression data preprocessing*

The gene expression data had two units: FPKM (510 samples, 25,373 genes) and TPM (688 samples, 23,457 genes). We converted all values to TPM to standardize the data. We only kept genes that are common in both units. The final dataset contained 1,198 samples across five classes: Primary Tumor (PT, n=616), Lymph Node Metastasis (LN, n=224), Liver Metastasis (ML, n=226), Post-Treatment Liver Metastasis (MP, n=102), and Normal Colon (NC, n=20). We excluded NC from further analysis to mitigate class imbalance due to its small sample size. We performed differential expression (DE) with MAST[19] (adj. $p < 0.05$, log2FC > 2) and identified 1,673 unique genes across four comparisons. DE analysis details and figures are provided in Supplemental Note 1 and Supplemental Figures 1-2.

2.3 *scTrio-seq2 DNA methylation data preprocessing*

Single-base DNA methylation data were aggregated to the gene-level by averaging promoter signals. From 1,295 samples and 22,910 genes, we retained 17,123 after filtering and selected the top 10% highly variable genes. The details of DNA methylation preprocessing are provided in Supplemental Note 1.

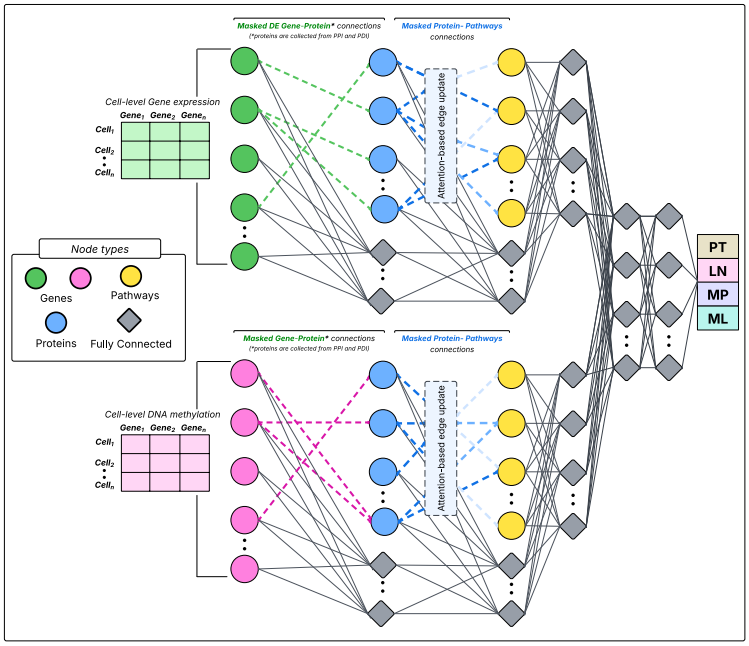

Fig. 1. The architecture of BioLM-NET. (Here, model outputs are four classes: PT = Primary Tumor, LN = Lymph Node Metastasis, MP= Post-Treatment Liver Metastasis, ML= Liver Metastasis)

2.4 *Protein–DNA interaction (PDI) data*

PDI data were obtained from the DoRothEA[15] database. It categorizes TF–target interactions into five confidence levels: A (highest) to E (lowest). For this study, we used only levels A, B, and C. The raw dataset included 32,443 interactions between 430 unique TFs and 9,290 unique target genes. We filtered out target genes that were not DE (gene expression) or not highly variable (DNA methylation)..

2.5 *Protein–protein interaction (PPI) data*

Human PPI data were downloaded from the STRING[14] database. Each PPI interaction has a *combined score* derived from multiple evidence sources. We selected interactions with a combined score > 0.7 to represent high-confidence associations. This filtering resulted in 504,062 high-confidence PPIs. Next, we retained the top 10% of interactions by score to preserve the highest-confidence associations. We further filtered interactions so that at least one of the proteins corresponded to a differentially expressed gene (gene expression data branch) or highly variable gene (DNA methylation data branch).

2.6 *Pathway data*

To compute pathways associated with the genes in PDI and PPI, we utilized the R package clusterProfiler[20] to perform pathway enrichment and kept only the significantly enriched pathways (Benjamini–Hochberg adjusted p-value < 0.05).

2.7 *LLM embedding*

GenePT[18] is an LLM framework that uses OpenAI's text embedding APIs to convert gene-centric descriptions into embeddings. These embeddings capture gene specific context such as aging, drug interactions, and pathway membership. We extracted GenePT embeddings from Hugging Face and kept only embeddings for genes with KEGG pathways identified in our analysis. These gene embeddings were then used to implement an attention mechanism between genes and pathways that allows the model to assign greater importance to genes with higher attention scores so that it enhances model performance and interpretability.

2.8 *Framework architecture*

Our framework uses a dual branch design that processed gene expression and DNA methylation data in parallel. In each branch, PDI and PPI priors are connected via a custom masked dense layer, and gene level activations are aggregated into pathway level embeddings by a custom attention pathway layer. The two pathway embeddings are then concatenated and passed through an MLP to generate the final prediction. The framework architecture is shown in Figure 1.

2.8.1. *Biological mask matrices*

We constructed two biologically informed mask matrices and then merged them. First, the PDI mask matrix, $M_{PDI} \in \{0,1\}^{n \times m}$ (Eq. 1) captures transcriptional regulation, where n is the number of DE genes or highly variable genes and m is the number of unique target genes.

$$M_{PDI}[i,j] = \begin{cases} 1 & if\ gene\ i\ is\ a\ TF\ regulating\ gene\ j \\ 0 & otherwise, \end{cases} \quad (1)$$

Second, the PPI Mask matrix, $M_{PPI} \in \mathbb{R}^{p_1 \times p_2}$ (Eq. 2) encodes interaction strengths between proteins, where p_1 is the number of DE genes or highly variable genes and p_2 is the number of unique proteins.

$$M_{PPI}[i,j] = \begin{cases} \text{combined score}\ between\ protein\ i\ and\ j \\ 0 & otherwise, \end{cases} \quad (2)$$

Finally, we horizontally concatenated those matrices to get a PDI-PPI mask matrix (Eq. 3).

$$M_{PDI-PPI} = [M_{PDI} | M_{PPI}] \quad (3)$$

2.8.2. *Pathway mask matrix*

The pathway mask matrix, $M_{Path} \in \{0,1\}^{r \times s}$ (Eq. 4) is a binary matrix, similar to the M_{PDI}. Here, r is size of the union between target genes from PDI and proteins from PPI data and s is the number of unique KEGG pathways.

$$M_{Path}[i,q] = \begin{cases} 1 & if\ gene\ i\ is\ annotated\ to\ pathway\ q \\ 0 & otherwise, \end{cases} \quad (4)$$

2.8.3. *Masked layer*

A custom masked layer was implemented to pass information from genes to their corresponding genes in the hidden layer based on PDI and PPI. This layer operates by performing element-wise multiplication of the mask matrix with the weight matrix, $W \in \mathbb{R}^{d_{in} \times d_{out}}$ of the dense layer. (Eq. 5)

$$W_{masked} = W \odot M \quad (5)$$

2.8.4. *Attention-based pathway layer*

From PDI-PPI genes, we extracted KEGG pathways and organized them into a pathway layer. Each node i in this layer represents one pathway and is associated with a trainable query vector $w_q^{(i)} \in \mathbb{R}^d$. We stack these k vectors into a matrix $W_q \in \mathbb{R}^{k \times d}$. To pass information from genes to pathways, we employ an attention mechanism. To calculate attention, we begin with fixed, pretrained GenePT embeddings $G \in \mathbb{R}^{r \times d}$ and the previous layer's output $X^{PDI-PPI} \in \mathbb{R}^{b \times r}$, where b is batch size. Rather than linking every gene equally to its pathways, we compute raw attention scores using Eq. 6. After masking out gene-pathway links (Eq. 7), we compute attention weights using Eq. 8. Finally, we aggregate gene signals per pathway using Eq. 9.

$$S = W_q G^T \in \mathbb{R}^{k \times r} \quad (6)$$

$$S_{mask} = S^T \odot M_{path} \quad (7)$$

$$\alpha_{i,k} = \frac{\exp(S_{mask}, i, k)}{\sum_{i'=1}^{r} \exp(S_{mask}, i', k)} \in \mathbb{R}^{r \times k} \quad (8)$$

$$Z_{path} = X^{PDI-PPI} \alpha \in \mathbb{R}^{b \times k} \quad (9)$$

This step gives us pathway-level representations where each pathway combines information from related genes based on learned attention scores. Then we pass pathway-level representation to a dense layer named projection layer to reduce the high dimensional pathway representations. We apply this for both gene expression and DNA methylation branches, obtaining Z_{GE} and Z_{DNA}, respectively.

2.8.5. *Fusion layer*

We fuse the two pathway outputs and pass them through two fully connected layers before the final output (Eq. 10-13).

$$Z_{fused} = [Z_{GE} \,||\, Z_{DNA}] \in \mathbb{R}^{b\times 2k} \tag{10}$$

$$H^1 = \sigma\left(Z_{fused}W^1 + \beta^1\right) \in \mathbb{R}^{b\times d_1} \tag{11}$$

$$H^2 = \sigma(H^1W^2 + \beta^2) \in \mathbb{R}^{b\times d_2} \tag{12}$$

$$\hat{y} = Softmax(H^2W^{out} + \beta^{out}) \in \mathbb{R}^{b\times c} \tag{13}$$

In Eq. 10-13, σ is the activation function, d_1, d_2 are hidden layer dimensions, W^1, W^2, W^{out} are weights, $\beta^1, \beta^2, \beta^{out}$ are biases, and c is the number of classes.

2.8.6. *Customized loss function*

To mitigate class imbalance, we used a customized sparse categorical cross-entropy loss by assigning higher weights to underrepresented classes. The loss for a sample i with true label y_i and predicted probability $\hat{y}_i$ is defined in Eq. 14

$$L_i = -w_i.\log(\hat{y}_i) \tag{14}$$

where w_i is the class weight. The total loss over a batch of N samples is defined in Eq. 15

$$L = \frac{1}{N}\sum_{i=1}^{N} L_i \tag{15}$$

Class weights are computed as $w_c = \frac{n}{C.n_c}$, where n_c is the number of samples in class c, C is the number of classes, and n is the total number of samples.

3. Results

To evaluate BioLM-NET, we tested it using five datasets: scTrioseq2, TCGA-BRCA, TCGA-GBM, TCGA-COAD, and ROSMAP and compared with other tools. The dataset splitting and model evaluation procedures are described in Supplemental Note 2. We also interpreted the model outputs and performed an ablation study to identify the key components of BioLM-NET.

3.1. *Comparing BioLM-NET with baseline and SOTA models*

We compared BioLM-NET to three traditional machine learning classifiers (i.e., Support Vector Machine (SVM), Random Forest (RF), and XGBoost), a fully dense neural network, and two SOTA methods (i.e., P-NET and PASNet). Since SVM, RF, and XGBoost cannot directly incorporate prior

pathway knowledge or LLM derived embeddings, we concatenated the gene expression and DNA methylation data to train these models. For the Dense NN, we preserved BioLM-NET's overall architecture but replaced its sparse connections with dense layers and excluded the attention-pathway module. For both P-NET and PASNet, we concatenated gene expression and DNA methylation data into a single input. P-NET dynamically selects relevant pathways during training, while PASNet relies on user-provided pathways.

Figure 2a summarizes F1 score performance for seven methods across five datasets. BioLM-NET attained the highest F1 score on scTrioSeq2, COAD and ROSMAP, and was on par with Dense NN and SVM on BRCA (0.82). Wilcoxon rank-sum tests confirmed that these improvements over both baseline and state-of-the-art models were statistically significant. Results for precision, recall, and accuracy are provided in Supplemental Figures 3–5. BioLM-NET achieved the highest precision on scTrioSeq2 (0.95), and ROSMAP (0.83) datasets and second highest precision on BRCA dataset. For recall, BioLM-NET attained the top values on scTrioSeq2 (0.96), COAD (0.80) and ROSMAP (0.83) and second highest recall on BRCA dataset. BioLM-NET consistently achieved the highest accuracy on scTrioSeq2 (0.95), COAD (0.87) and ROSMAP (0.83). BioLM-NET, along with other deep learning methods performed comparatively lower on GBM dataset due to significant class imbalance (30.3%, 25.0%, 18.8%, 17.6%, and 8.3%) and limited sample size (195 training and 49 testing). In these settings, traditional machine learning models often outperform deep learning models.

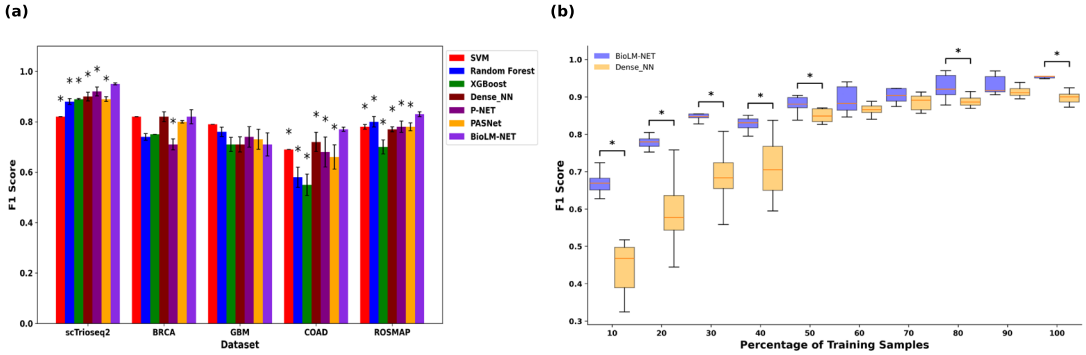

Fig. 2. (a) F1 score comparison of BioLM-NET with baseline and SOTA models. (b) Boxplots of F1 score for BioLM-NET (blue) and Dense_NN (orange) across 10 independent runs at each percentage of training samples. Wilcoxon rank sum test was performed by comparing BioLM-NET with other models (p-value < 0.05 is denoted by *)

3.2. *Predictive performance of BioLM-NET under limited data*

To assess robustness with limited training data, we compared BioLM-NET against a fully dense neural network across smaller training sets. We first split our data into training (80%) and test (20%). We kept the test set constant while subsampling the training data at 10%, 20%, 30%, 40%, 50%, 60%, 70%, 80%, and 90% of its original size. We tested each model trained using a subsample training data on the same test set. We observed that the performance of models improved with more training data. BioLM-

NET outperformed the Dense NN at every fraction (Figure 2b), which shows that it remains robust even when trained on substantially fewer samples. We performed a similar analysis using ROSMAP data (Supplemental Figure 6). In this case, Dense NN outperformed BioLM-NET when using 10–50% of the training data; however, BioLM-NET surpassed Dense NN beyond 50%. This result is possibly due to the limited sample size of the ROSMAP dataset, where BioLM-NET requires more data to learn effectively.

3.3. *Ablation study*

To assess the performance of each data modality with or without sparse connections, we conducted an ablation study using scTrioseq2 dataset. We trained a dense neural network using only gene expression data, which had a F1 score of 0.89 (Table 2). When we incorporated sparse connections based on PDI, the F1 score increased by 3%, whereas adding PPI caused a 1% drop (Table 2). When both PDI and PPI were utilized for sparse connections, the F1 score fell by 5%, which could be due to the extra sparsity introduced by combining PPI with PDI connections.

Table 2. Effect of adding Prior biological knowledge and multi omics data in scTrioseq2 data. GE: Gene Expression data, DM: DNA Methylation data, PPI: Protein-Protein Interaction data, PDI: Protein-DNA Interaction data. The result values are shown as mean ± standard deviation of 10 individual runs.

Model	Precision	Recall	F1 score	Accuracy
GE_Dense	0.90 ± 0.0135	0.90 ± 0.0116	0.89 ± 0.0140	0.89 ± 0.0136
GE_PDI	0.93 ± 0.0113	0.92 ± 0.0104	0.92 ± 0.0105	0.92 ± 0.0096
GE_PPI	0.89 ± 0.0658	0.89 ± 0.0600	0.88 ± 0.0792	0.88 ± 0.0647
GE_PDI_PPI	0.86 ± 0.0896	0.86 ± 0.0605	0.84 ± 0.0783	0.84 ± 0.0580
DM_Dense	0.92 ± 0.0043	0.92 ± 0.002	0.92 ± 0.0035	0.92 ± 0.0040
DM_PDI	0.93 ± 0.0087	0.92 ± 0.0098	0.92 ± 0.0095	0.93 ± 0.0075
DM_PPI	0.91 ± 0.0059	0.91 ± 0.0089	0.91 ± 0.0079	0.92 ± 0.0074
DM_PDI_PPI	0.93 ± 0.0161	0.93 ± 0.0243	0.92 ± 0.0206	0.94 ± 0.0151
GE_DM_Dense	0.92 ± 0.0428	0.89 ± 0.0997	0.88 ± 0.0997	0.89 ± 0.0761
GE_DM_PDI	0.91 ± 0.0134	0.91 ± 0.0096	0.90 ± 0.0124	0.90 ± 0.0120
GE_DM_PPI	0.92 ± 0.0240	0.91 ± 0.0316	0.91 ± 0.0319	0.92 ± 0.0267
GE_DM_PDI_PPI	0.94 ± 0.0153	0.94 ± 0.0113	0.94 ± 0.0126	0.94 ± 0.0111
BioLM-NET	**0.95 ± 0.0062**	**0.96 ± 0.0022**	**0.95 ± 0.0039**	**0.95 ± 0.0039**

We observed that a dense neural network model trained with only DNA methylation data achieved a higher performance (0.92) than the model trained using only gene expression data (Table 2) indicating that DNA methylation data plays a stronger role for distinguishing primary tumors from metastatic sites. Adding sparse connections based on PPI to the DNA methylation-based model reduced the F1 score by

1%, whereas we did not observe any change in the performance when PDI data was utilized with or without PPI.

A dense neural network trained using both gene expression and DNA methylation achieved a slightly lower performance (0.88) than either single-modality model. However, adding sparse connections boosted its performance. Incorporating PDI and PPI individually increased the F1 score by 2% and 3%, respectively. When both PDI and PPI were integrated, the F1 score increased by 6%. The best performance was achieved with BioLM-NET, which adds a pathway attention layer to this framework.

We also evaluated the impact of the attention layer in BioLM-NET. When attention scores were removed or replaced with scores from random embeddings, the F1 score dropped by 2% (Table 3) indicating the importance of attention scores. These results collectively confirm that genuine pathway structure and LLM-derived embeddings both contribute to classifying primary tumors and metastatic regions.

Table 3. Effect of adding Pathway Attention Layer in scTrioseq2 data

Model	Precision	Recall	F1 score	Accuracy
BioLM-NET (Without LLM Embedding)	0.94 ± 0.0079	0.93 ± 0.0103	0.93 ± 0.0082	0.94 ± 0.0079
BioLM-NET (Random LLM embedding)	0.93 ± 0.0168	0.94 ± 0.0250	0.93 ± 0.0215	0.93 ± 0.0204
BioLM-NET	**0.95 ± 0.0062**	**0.96 ± 0.0022**	**0.95 ± 0.0039**	**0.95 ± 0.0039**

To assess the biologically informed connections through PDI, PPI, and pathway associations, for each model with sparse connection, we trained a model with randomized connections while preserving the number of sparse connections (Supplemental Table 1).We observed that GE_PDI, DM_PDI, DM_PPI, GE_DM_PPI models outperformed their random counterparts by 5%, 2%, 6%, and 15% in F1 score, respectively which shows the impact of authentic PDI and PPI connections. In GE_PPI model, performance was unchanged compared to randomized version, suggesting that PPI alone adds no additional signal in this context. However, the random version of GE_DM_PDI model outperformed the true model by 1% underscoring the need of more curated TF-target interactions. When all PDI and PPI connections were randomized while leaving other component of BioLM-NET unchanged, performance dropped by 40% in F1 score relative to BioLM-NET. Randomizing pathway connections and LLM embeddings (while preserving shape) further reduced performance by 7%. Altogether, this ablation study demonstrates that incorporating authentic PPI, PDI, and pathway priors, and LLM embedding is essential for BioLM-NET to achieve superior predictive performance.

3.4. *Interpretability of BioLM-NET*

To understand how multimodal features, genes, and pathways contribute BioLM-NET's performance, we first applied SHAP analysis to rank the top 50 most important input features from gene expression and DNA methylation data. We then performed Gene Ontology (GO) and KEGG pathway enrichment to evaluate their biological relevance.

In the ROSMAP dataset, we identified 32 significantly enriched GO terms from the top 50 SHAP-ranked genes in the gene expression data (Supplemental Table 2). Focusing on the ten most significant terms and taking their associated genes from our gene list, we highlight eight candidates: *KIF1C, NPNT, CCDC69, GPER1, KIF5A, KIF5B, FOXO4, MAP4K4.* Genetic fine-mapping implicates *KIF1C* as an AD risk locus and highlights a role for faulty kinesin mediated vesicular transport in disease susceptibility across ancestries[21]. *NPNT* is consistently upregulated in AD brain transcriptomes across diverse populations[22]. *CCDC69* has emerged as a novel genetic locus associated with AD, pointing to unexpected roles for spindle-assembly proteins in neurodegeneration[23]. Elevated *GPER1* expression correlates with increased tau tangle burden, implicating estrogen-receptor signaling in the modulation of tau pathology[24]. In AD, amyloid-β damages *KIF5A* so mitochondria cannot travel down axons, causing energy shortages that lead to synapse loss[25]. *KIF5B* regulates tau protein dynamics, and its dysregulation may drive tau pathology in AD[26]. As a stress response transcription factor, *FOXO4* governs oxidative-stress and insulin-signaling pathways that are disrupted in AD[27]; and upregulation of *MAP4K4* in Alzheimer's microglia drives neuroinflammatory signaling, marking it as a promising therapeutic target to modulate inflammation in AD[28].

Table 4. Significant survival related genes from top 50 SHAP features in GBM, BRCA, and COAD

Dataset	Branch of BioLM-NET	Significant survival related genes
GBM	Gene Expression	*CBX7*[32], *CENPJ*[33], *DACH1*[34], *NUDT22, PM20D2, RALGAPA1P1, TBX3, WDPCP*
	DNA Methylation	CPS1[35], *C16orf89, CANT1, CDKN2D, ELSPBP1, GON4L, LDLRAP1*
BRCA	Gene Expression	*BCL2*[36], *CXCL1*[37], *EIF2S2*[38], *FGD3*[39], *KDM4B*[40], *NXNL2*[41], *SOX11*[42], *SPARCL1*[43], *SUSD3*[44]
	DNA Methylation	*IGFALS, IGFBP4*, *SCUBE2*[45], *SERPINA12*
COAD	Gene Expression	*ASPHD2, COX11, NMNAT1*[46]
	DNA Methylation	*ARRDC1, CAMTA1, CDC14A, DNAJC17, FABP4*[47], *FGF22*

In the ROSMAP dataset, the top 50 DNA methylation probe-associated genes were enriched in the KEGG pathway hsa00010 (Glycolysis/Gluconeogenesis). Recent evidence indicates that dysregulated glycolytic metabolism plays a critical role in AD development[29]. Qiu et al. further demonstrated that the glycolysis index is markedly lower in AD patients than in controls across four distinct brain regions[30]. Among our top DNA methylation features were three hsa00010 genes: *GAPDHS, LDHC*, and *ALDH3B1*. Consistent with these findings, Wang et al. identified *GAPDHS* via SHAP-based feature

selection and reported its significant differential methylation in an AD prediction model, and also highlighted *LDHC* among eight glycolysis genes with altered methylation profiles in AD versus control subjects[31]. In our DNA methylation dataset, two-sample t-tests comparing AD and control groups yielded significant differences for *GAPDHS* ($t = -2.995$, $p = 2.945 \times 10^{-3}$), *LDHC* ($t = 3.889$, $p = 1.212 \times 10^{-4}$), and *ALDH3B1* ($t = 3.122$, $p = 1.948 \times 10^{-3}$). Density plots of these distributions are presented in Supplemental Figure 7.

From our top 50 SHAP features derived from DNA methylation data in the GBM dataset, we identified three significantly enriched GO terms: GO:0009112 (nucleobase metabolic process), GO:0006206 (pyrimidine nucleobase metabolic process), and GO:0046112 (nucleobase biosynthetic process). Jiang et al. reported that GBM relies on nucleotide metabolism to fuel rapid growth and invasion that leads to poor clinical outcomes[48]. Wang et al. demonstrated that pyrimidine metabolic pathways are consistently upregulated in TCGA-GBM tumors relative to normal brain tissue[49]. Zhou et al. showed that elevated activity of nucleobase biosynthetic enzymes correlates with poor prognosis in GBM[50]. We performed Kaplan–Meier survival analysis in GBM, BRCA, and COAD datasets using the top 50 SHAP-ranked genes from both gene expression and DNA methylation branches. Several genes showed significant associations with patient survival, and their relevance is supported by multiple studies. The gene lists are provided in Table 4, with survival plots shown in Supplemental Figures 8–13. These findings highlight BioLM-NET's ability to uncover biologically meaningful features with potential as biomarkers and therapeutic targets in cancer and AD.

To interpret BioLM-NET using an alternative approach, we applied LIME[51], a model agnostic explainability framework, to identify the most important features contributing to our predictions and asses potential feature biases in comparison with SHAP. We applied LIME on the ROSMAP and GBM datasets and selected the top 50 important features from both the gene expression and DNA methylation branches. We then examined the overlap between LIME and SHAP derived features using a one-sided hypergeometric test. In ROSMAP, we identified 47 common genes ($p = 2.384 \times 10^{-38}$) and 43 common DNA methylation features ($p = 9.565 \times 10^{-30}$). In TCGA-GBM, we found 24 common genes ($p = 6.409 \times 10^{-14}$) and 21 common DNA methylation features ($p = 1.261 \times 10^{-10}$). GO and KEGG analysis of these features further confirmed their disease relevance (Supplemental Note 3).

To assess the key nodes in BioLM-NET layers, we examined per sample activation scores at every layer of BioLM-NET trained on the scTrio-seq2 data for colorectal cancer and selected the ten nodes with the highest mean activation score (Supplemental Figure 14). Early in the network, the class specific density curves overlap almost completely, indicating minimal separability. As data propagate through the fusion layer, the distributions begin to separate, and by the final (output) layer, each class's activation density is distinctly isolated. This illustrates how the model transforms mixed features into clear, class-specific patterns.

Based on the activation scores of the attention-based pathway layer, we selected the top 20 pathways and evaluated their relevance to colorectal cancer and their metastasis. In the gene-expression branch, five KEGG pathways were significant (adjusted p-value <0.05): hsa04151 (PI3K–Akt signaling

pathway), hsa04140 (Autophagy), hsa04144 (Endocytosis), hsa03050 (Proteasome), and hsa00190 (Oxidative phosphorylation). In the DNA methylation branch, three pathways reached significance (adjusted p-value <0.05): hsa05206 (MicroRNAs in cancer), hsa03050 (Proteasome), and hsa00190 (Oxidative phosphorylation). Duan et al. showed that PIK3CA mutations activate the PI3K/Akt cascade to drive colorectal tumor growth and metastasis[52]. Manzoor et al. described how autophagy supports metastatic colorectal cancer cell survival under stress[53]. Qin et al. demonstrated that dysregulated endocytosis facilitates immune escape and metastatic dissemination in colon cancer[54]. Li et al. reported that proteasome-mediated degradation of HIF-1α impairs angiogenesis and migration, thereby restraining CRC metastatic progression[55]. Liu et al. revealed that enhanced oxidative phosphorylation in colorectal cancer stem cells increases ATP production to fuel invasion and metastatic colonization[56]. Together, these findings confirm the relevance of these pathways to colorectal cancer metastasis and demonstrate that the pathway attention layer can identify potential therapeutic targets.

4. Conclusion

In this study, we developed BioLM-NET, a deep learning–based model that integrates prior biological knowledge and LLM embeddings with multi-omics data to improve predictive performance and interpretability. We evaluated BioLM-NET on five datasets spanning various prediction tasks, including cancer subtype classification, AD patient detection, and identification of metastatic regions in colorectal cancer. BioLM-NET achieved the highest performance on three datasets outperforming state-of-the-art models such as P-NET, PASNet, and traditional machine learning and deep learning models and tied on one dataset. Furthermore, model interpretation revealed that the most important input features identified by BioLM-NET were significantly enriched in Gene Ontology (GO) terms and KEGG pathways, suggesting potential as biomarkers or therapeutic targets for the respective diseases. However, BioLM-NET is currently limited to bulk and single-cell omics data and cannot yet handle spatial omics or longitudinal data. Its dual-branch design also restricts integration to only two modalities. Future work will focus on extending the framework to incorporate additional omics types, spatial information, and temporal dynamics to broaden its applicability and biological insight. Supplemental materials are available at https://github.com/bozdaglab/BioLM-NET/blob/main/Supplemental_Material.pdf .

References

1. Elmarakeby, H. A. *et al.* Biologically informed deep neural network for prostate cancer discovery. *Nature* **598**, 348–352 (2021).

2. Kuenzi, B. M. *et al.* Predicting Drug Response and Synergy Using a Deep Learning Model of Human Cancer Cells. *Cancer Cell* **38**, 672-684.e6 (2020).
3. Ma, J. *et al.* Using deep learning to model the hierarchical structure and function of a cell. *Nat Methods* **15**, 290–298 (2018).
4. Fortelny, N. & Bock, C. Knowledge-primed neural networks enable biologically interpretable deep learning on single-cell sequencing data. *Genome Biology* **21**, 190 (2020).
5. Wang, H. *et al.* Biologically-informed deep neural networks provide quantitative assessment of intratumoral heterogeneity in post-treatment glioblastoma. *Res Sq* rs.3.rs-3891425 (2024) doi:10.21203/rs.3.rs-3891425/v1.
6. Hao, J., Kim, Y., Kim, T.-K. & Kang, M. PASNet: pathway-associated sparse deep neural network for prognosis prediction from high-throughput data. *BMC Bioinformatics* **19**, 510 (2018).
7. Bian, S. *et al.* Single-cell multiomics sequencing and analyses of human colorectal cancer. *Science* **362**, 1060–1063 (2018).
8. Comprehensive molecular portraits of human breast tumors. *Nature* **490**, 61–70 (2012).
9. Cancer Genome Atlas Research Network. Comprehensive genomic characterization defines human glioblastoma genes and core pathways. *Nature* **455**, 1061–1068 (2008).
10. The Cancer Genome Atlas Network. Comprehensive molecular characterization of human colon and rectal cancer. *Nature* **487**, 330–337 (2012).

11. Bennett, D. A. *et al.* Religious Orders Study and Rush Memory and Aging Project. *J Alzheimers Dis* **64**, S161–S189 (2018).
12. Wang, T. *et al.* MOGONET integrates multi-omics data using graph convolutional networks allowing patient classification and biomarker identification. *Nat Commun* **12**, 3445 (2021).
13. Yang, Z. *et al.* MLOmics: Cancer Multi-Omics Database for Machine Learning. *Sci Data* **12**, 913 (2025).
14. Szklarczyk, D. *et al.* The STRING database in 2023: protein-protein association networks and functional enrichment analyses for any sequenced genome of interest. *Nucleic Acids Res* **51**, D638–D646 (2023).
15. Garcia-Alonso, L., Holland, C. H., Ibrahim, M. M., Turei, D. & Saez-Rodriguez, J. Benchmark and integration of resources for the estimation of human transcription factor activities. *Genome Res* **29**, 1363–1375 (2019).
16. Kanehisa, M. KEGG: Kyoto Encyclopedia of Genes and Genomes. *Nucleic Acids Research* **28**, 27–30 (2000).
17. Kanehisa, M., Furumichi, M., Sato, Y., Matsuura, Y. & Ishiguro-Watanabe, M. KEGG: biological systems database as a model of the real world. *Nucleic Acids Research* **53**, D672–D677 (2025).
18. Chen, Y. & Zou, J. GenePT: A Simple But Effective Foundation Model for Genes and Cells Built From ChatGPT. *bioRxiv* 2023.10.16.562533 (2024) doi:10.1101/2023.10.16.562533.

19. Finak, G. *et al.* MAST: a flexible statistical framework for assessing transcriptional changes and characterizing heterogeneity in single-cell RNA sequencing data. *Genome Biology* **16**, 278 (2015).
20. Yu, G., Wang, L.-G., Han, Y. & He, Q.-Y. clusterProfiler: an R Package for Comparing Biological Themes Among Gene Clusters. *OMICS* **16**, 284–287 (2012).
21. Rajabli, F. *et al.* Admixture mapping identifies novel Alzheimer disease risk regions in African Americans. *Alzheimers Dement* **19**, 2538–2548 (2023).
22. Felsky, D. *et al.* The Caribbean-Hispanic Alzheimer's disease brain transcriptome reveals ancestry-specific disease mechanisms. *Neurobiol Dis* **176**, 105938 (2023).
23. Wainberg, M., Andrews, S. J. & Tripathy, S. J. Shared genetic risk loci between Alzheimer's disease and related dementias, Parkinson's disease, and amyotrophic lateral sclerosis. *Alzheimers Res Ther* **15**, 113 (2023).
24. Oveisgharan, S. *et al.* G-protein coupled estrogen receptor 1, amyloid-β, and tau tangles in older adults. *Commun Biol* **7**, 569 (2024).
25. Wang, Q., Tian, J., Chen, H., Du, H. & Guo, L. Amyloid beta-mediated KIF5A deficiency disrupts anterograde axonal mitochondrial movement. *Neurobiol Dis* **127**, 410–418 (2019).
26. Selvarasu, K. *et al.* Reduction of kinesin I heavy chain decreases tau hyperphosphorylation, aggregation, and memory impairment in Alzheimer's disease and tauopathy models. *Front Mol Biosci* **9**, 1050768 (2022).

27. Maiese, K. Targeting the core of neurodegeneration: FoxO, mTOR, and SIRT1. *Neural Regeneration Research* **16**, 448 (2021).
28. Jian, C. *et al.* Microglia Mediate the Occurrence and Development of Alzheimer's Disease Through Ligand-Receptor Axis Communication. *Front. Aging Neurosci.* **13**, (2021).
29. Zhang, X., Alshakhshir, N. & Zhao, L. Glycolytic Metabolism, Brain Resilience, and Alzheimer's Disease. *Front Neurosci* **15**, 662242 (2021).
30. Qiu, Z. *et al.* The significance of glycolysis index and its correlations with immune infiltrates in Alzheimer's disease. *Front Immunol* **13**, 960906 (2022).
31. Wang, F. *et al.* A Glycolysis Gene Methylation Prediction Model Based on Explainable Machine Learning for Alzheimer's Disease. SSRN Scholarly Paper at https://doi.org/10.2139/ssrn.3797592 (2021).
32. Zheng, Z.-Q. *et al.* Chromobox 7/8 serve as independent indicators for glioblastoma via promoting proliferation and invasion of glioma cells. *Front. Neurol.* **13**, (2022).
33. de Freitas, G. P. A. *et al.* Centromere protein J is overexpressed in human glioblastoma and promotes cell proliferation and migration. *J Neurochem* **162**, 501–513 (2022).
34. Wang, J. *et al.* DACH1 inhibits glioma invasion and tumor growth via the Wnt/catenin pathway. *Onco Targets Ther* **11**, 5853–5863 (2018).
35. Wu, G. *et al.* Expression and clinical significance of CPS1 in glioblastoma multiforme. *Curr Res Transl Med* **67**, 123–128 (2019).

36. Hwang, K.-T. *et al.* Prognostic influences of BCL1 and BCL2 expression on disease-free survival in breast cancer. *Sci Rep* **11**, 11942 (2021).
37. Zou, A. *et al.* Elevated CXCL1 expression in breast cancer stroma predicts poor prognosis and is inversely associated with expression of TGF-β signaling proteins. *BMC Cancer* **14**, 781 (2014).
38. Guo, M. *et al.* Eukaryotic Translation Initiation Factor 2 Subunit β as a Prognostic Biomarker Associates With Immune Cell Infiltration in Breast Cancer. *J Surg Res* **295**, 753–762 (2024).
39. Susini, T. *et al.* Immunohistochemical Evaluation of FGD3 Expression: A New Strong Prognostic Factor in Invasive Breast Cancer. *Cancers (Basel)* **13**, 3824 (2021).
40. Peña-Llopis, S., Wan, Y. & Martinez, E. D. Unique epigenetic gene profiles define human breast cancers with poor prognosis. *Oncotarget* **7**, 85819–85831 (2016).
41. Conte, F. *et al.* In silico recognition of a prognostic signature in basal-like breast cancer patients. *PLoS One* **17**, e0264024 (2022).
42. Liu, D.-T. *et al.* Clinical and prognostic significance of SOX11 in breast cancer. *Asian Pac J Cancer Prev* **15**, 5483–5486 (2014).
43. Xu, X.-Y. *et al.* Profile and clinical significance of SPARCL1 and its prognostic significance in breast cancer. *Oncol Lett* **29**, 196 (2025).
44. Dong, Y.-M. & Bao, G.-Q. Characterization of SUSD3 as a novel prognostic biomarker and therapeutic target for breast cancer. *Clin Transl Oncol* **27**, 935–949 (2025).

45. Lin, Y.-C., Lee, Y.-C., Li, L.-H., Cheng, C.-J. & Yang, R.-B. Tumor suppressor SCUBE2 inhibits breast-cancer cell migration and invasion through the reversal of epithelial-mesenchymal transition. *J Cell Sci* **127**, 85–100 (2014).
46. Wen, L. *et al.* Prognostic and Immunological Significance of NMNAT1 in Colorectal and Pan-Cancer Contexts. *Onco Targets Ther* **18**, 389–410 (2025).
47. Wu, D. *et al.* Comprehensive analysis of the immune implication of FABP4 in colon adenocarcinoma. *PLOS ONE* **17**, e0276430 (2022).
48. Jiang, L.-W. *et al.* Investigating the relevance of nucleotide metabolism in the prognosis of glioblastoma through bioinformatics models. *Sci Rep* **15**, 5363 (2025).
49. Wang, X. *et al.* Targeting pyrimidine synthesis accentuates molecular therapy response in glioblastoma stem cells. *Sci Transl Med* **11**, eaau4972 (2019).
50. Zhou, W. *et al.* Purine metabolism regulates DNA repair and therapy resistance in glioblastoma. *Nat Commun* **11**, 3811 (2020).
51. Ribeiro, M. T., Singh, S. & Guestrin, C. 'Why Should I Trust You?': Explaining the Predictions of Any Classifier. in *Proceedings of the 22nd ACM SIGKDD International Conference on Knowledge Discovery and Data Mining* 1135–1144 (Association for Computing Machinery, New York, NY, USA, 2016). doi:10.1145/2939672.2939778.
52. Wang, H., Tang, R., Jiang, L. & Jia, Y. The role of PIK3CA gene mutations in colorectal cancer and the selection of treatment strategies. *Front. Pharmacol.* **15**, (2024).

53. Manzoor, S., Muhammad, J. S., Maghazachi, A. A. & Hamid, Q. Autophagy: A Versatile Player in the Progression of Colorectal Cancer and Drug Resistance. *Front. Oncol.* **12**, (2022).
54. Qin, Y., Mao, Y., Han, Y., Cheng, K. & Shi, J. Immune Escape and Metabolic Reprogramming in Colon Cancer: Insights from Endocytosis-Related Genes. *BIO Web Conf.* **111**, 01019 (2024).
55. Li, J. *et al.* Identification of COX4I2 as a hypoxia-associated gene acting through FGF1 to promote EMT and angiogenesis in CRC. *Cellular & Molecular Biology Letters* **27**, 76 (2022).
56. Liu, S. *et al.* Lactate promotes metastasis of normoxic colorectal cancer stem cells through PGC-1α-mediated oxidative phosphorylation. *Cell Death Dis* **13**, 651 (2022).

Impact of using PRS-CSx and pruning and thresholding for polygenic partitioning of apparent treatment resistant hypertension

Hannah M. Seagle[1-4,9], Jeewoo Kim[1-3,5-7], Alexis T. Akerele[1,5,6,10], VA Million Veteran Program, Adriana Hung[3,8,11], Jacklyn N. Hellwege[1,2,8,11]* and Todd L. Edwards[3,4,11]*

[1]Vanderbilt Genetics Institute, [2]Division of Genetic Medicine, [3]Department of Medicine, [4]Division of Epidemiology, [5]Division of Quantitative Science, [6]Department of Obstetrics and Gynecology, [7]Vanderbilt Medical Scientist Training Program, [8]Division of Nephrology and Hypertension, Vanderbilt University Medical Center, Nashville, TN, 37203, USA,

[9]Joseph Maxwell Cleland Atlanta VA Medical Center, Atlanta, GA, 37203, USA

[10]School of Graduate Studies, Meharry Medical College, Nashville, TN, 37208, USA

[11]VA Tennessee Valley Healthcare System (626), Nashville, TN, 37203, USA

**Contributed equally as co-senior and co-corresponding authors*

**Emails: jacklyn.hellwege@vumc.org and todd.l.edwards@vumc.org*

Apparent treatment-resistant hypertension (aTRH) is a clinically challenging condition with heterogeneous etiologies. Understanding the biological pathways underlying resistance to antihypertensive treatment could inform targeted therapeutic strategies. To evaluate how methodological choices in SNP selection influence biological inference, we applied two approaches to select aTRH-associated variants for clustering: PRS-CSx and pruning and thresholding (P&T). Using k-means clustering, we grouped aTRH-associated variants based on their association profiles across 91 cardiometabolic-related phenotypes. We then performed pathway and tissue enrichment analyses to evaluate the biological processes represented by each cluster. Both methods identified multiple genetic clusters, but the distribution of variants and biological signals differed. Clustering based on PRS-CSx produced unequally distributed clusters of SNPs and yielded limited tissue enrichment, while P&T-based clustering captured more uniform trends across cardiometabolic traits and broader tissue and pathway enrichment. These results demonstrate that methodological choices in SNP selection influence downstream clustering and biological interpretation. Despite some overlap in identified pathways and tissue enrichment, each approach identified unique biological signals, highlighting the potential of pairing polygenic methods and k-means clustering to elucidate the biological heterogeneity of aTRH and guide future mechanistic studies.

Keywords: Disease subtyping, cardiometabolic traits, polygenic clustering, resistant hypertension

1. Introduction

Elevated blood pressure (BP), or hypertension (HTN), is defined by systolic BP (SBP) ≥ 130 mmHg and/or diastolic BP (DBP) ≥ 80 mmHg. HTN contributes to over 13% of global premature deaths and is implicated in many cardiovascular diseases, including coronary artery disease, stroke, and renal damage.[1] In the United States, 34% and 44% of non-Hispanic White (NHW) and non-Hispanic

© 2025 The Authors. Open Access chapter published by World Scientific Publishing Company and distributed under the terms of the Creative Commons Attribution Non-Commercial (CC BY-NC) 4.0 License.

Black (NHB) adults, respectively, have HTN, which rank among the highest prevalence rates around the world.[2,3] Treatment guidelines include BP-lowering strategies like antihypertensive medications and lifestyle alterations. However, nearly 25% of individuals with HTN do not achieve target blood pressures.[4]

Apparent treatment-resistant HTN (aTRH), defined as failure to achieve BP control on three antihypertensive medications or concurrent prescriptions for four or more medications regardless of achieving control, increases risk for severe health outcomes including coronary heart disease and stroke, particularly in African ancestry populations.[4,5] Due to varying definitions of aTRH and methods of BP assessment, the estimated prevalence of aTRH has a wide range, from 8.4-50%.[6] Individuals with aTRH are at a greater risk for diabetes, chronic kidney disease, cardiovascular disease, and stroke than individuals with controlled HTN.[7]

Despite its clinical significance, the biological mechanisms underlying aTRH remain poorly understood. aTRH is a heterogeneous condition – patients may reach treatment resistance through different biological routes, such as altered renal sodium handling[8], impaired vascular tone regulation[9], or neurohormonal dysregulation.[10] Additionally, compared to NHW individuals, those who identify as Hispanic, Asian, and NHB have 10-12% lower rates of BP control[11], with some antihypertensive medications having lower efficacy in these populations as well.[12] These differences likely reflect multiple genetic and environmental conditions, underscoring the need for more nuanced classification of aTRH beyond conventional clinical definitions.

To begin addressing this complexity, we sought to apply a k-means clustering approach to identify distinct, non-overlapping clusters of genetic variants associated with aTRH. Previous studies[13] have utilized this approach for well-characterized phenotypes, such as type 2 diabetes mellitus, by clustering based on genome-wide significant ($P < 5x10^{-8}$) independent loci. Given the complexities in phenotyping for aTRH, leading to limited sample sizes and power, this strategy may fail to capture the breadth of relevant genetic variation. To address this limitation, we evaluated alternative approaches to SNP selection that capture a broader spectrum of polygenic effects: linkage disequilibrium (LD) pruning and thresholding (P&T[14]) and PRS-CSx[15], a Bayesian shrinkage method that integrates LD information across populations. We then performed k-means clustering using SNPs selected by each method, grouping variants based on their association patterns across 91 cardiometabolic phenotypes.

These clusters, which varied by SNP selection method, may represent candidate mechanistic pathways underlying treatment resistance that can be personalized. For example, one individual may have strong genetic loading for sodium handling mechanisms, while another may have elevated risk through vascular reactivity mechanisms. By performing pathway and tissue enrichment analyses, we can compare how PRS-CSx- and P&T-selected SNPs result in differences in both cluster assignment and the biological processes implicated. This framework allowed us to assess not only the biological heterogeneity of aTRH, but also how methodological choices in SNP selection influence downstream interpretation.

This study evaluates analytic approaches that provide opportunities to further understand the underlying mechanisms of treatment resistance, with the long-term goal of identifying more targeted, biology-informed therapeutic strategies. Further, these approaches may be utilized for SNP selection for other phenotypes where large numbers of genome-wide significant independent loci may be unavailable, allowing for opportunities to further understand biological mechanisms of disease that may not be possible otherwise.

2. Methods

2.1. *Study Population and Phenotype Definition*

2.1.1. *The Million Veteran Program (MVP)*

We used MVP cross-population summary statistics from an aTRH genome-wide association study (GWAS) in this analysis to select aTRH-associated loci.[16] The MVP cohort is comprised of Veteran Health Administration users, 35% of whom identify as a racial or ethnic minority, making it one of the most heterogeneous research cohorts. Genotypes for approximately 750,000 genetic markers have been measured with the Affymetrix Axiom Biobank array. Genetic variants not covered by the array were imputed using the Trans-Omics for Precision Medicine (TOPMed) reference panel.[17] The case definition for this analysis has been previously described.[18] Briefly, aTRH cases were defined using a previously validated algorithm[6], based on failure to achieve controlled BP on three antihypertensive medications, one of which must be a thiazide diuretic, or prescribed four or more medications regardless of achieving control, excluding patients with chronic kidney disease (stages 4 and 5) as well as causes of secondary HTN. Controls were defined as individuals who achieved control (<140/90 mmHg) on 1 or 2 medication classes. The total number of samples included 16,833 cases (11,762 NHW and 5,071 NHB) and 53,931 controls (42,850 NHW and 11,091 NHB). The GWAS was performed race-stratified and then meta-analyzed.

2.1.2. *Vanderbilt University Medical Center's (VUMC) BioVU*

BioVU is an institutional resource that supports large-scale genomic research at VUMC. A description of human subjects' protection employed for BioVU has been previously described.[19] BioVU genotype data of NHW and NHB adults was used for polygenic score (PS) development and p-value thresholding (described in 2.2).[20] BioVU participant DNA samples were genotyped on a custom Illumina Multi-Ethnic Genotyping Array (MEGA-ex; Illumina Inc., San Diego, CA, USA). Phenotyping of BioVU participants used the same algorithm for defining aTRH cases and controls as above. The total number of samples included 4,286 cases (3,541 NHW and 745 NHB) and 39,356 controls (33,552 NHW and 5,804 NHB).

2.2. *Defining aTRH Loci with PS Development and P-Value Thresholding*

An overview of the methods can be found in Figure 1. Due to the small number of independent genome-wide Bonferroni-corrected significant SNPs ($P < 5x10^{-8}$) from the MVP aTRH GWAS meta-analysis, we compared two methods which could be used to identify the best threshold reflecting genetic contribution to phenotypic variation, prior to clustering. The first method combined PS development with PRS-CSx[15] followed by optimal p-value thresholding.[21] The optimal p-value threshold determined by this step was then used as a p-value cutoff for SNPs that would be used downstream in the clustering analysis (described in 2.3).

PS weights were generated using the MVP NHW and NHB summary statistics with PRS-CSx[15] software and --meta flag. Using those weights, PSs at variable p-value thresholds were built using BioVU genotype data with PLINK2[22], followed by p-value thresholding (range: P=1 to $5x10^{-8}$, 16 thresholds), as described previously.[21] We then performed logistic regression analyses of the PSs

and aTRH, adjusted for age, age^2, sex, body mass index (BMI), and the first ten principal components, and determined which p-value threshold resulted in the maximal variance explained by the PS. Optimal p-value thresholds were P < 1 in the NHW population and P < 0.01 in the NHB population, as determined by maximal variance explained (0.05% and 0.14%, respectively). After filtering to SNPs with P < 0.01 in the MVP cross-population meta-analysis, we had 17,361 SNPs (aTRH SNPs) that were used for the PRS-CSx-based clustering analysis.

The second method utilized the pruning and thresholding approach (P&T[14]). We performed linkage disequilibrium (LD) pruning of SNPs at the same 16-variable p-value thresholds, using an r^2 threshold of 0.1 within a 250 kb window. Independent SNPs at each of the 16-variable p-value thresholds were used to construct PSs as described above. Logistic regression and testing for maximal variance explained were performed as above. The optimal p-value threshold was P < 0.01 for the NHW and NHB populations (maximal variance explained: 0.58% and 3.30%, respectively). We then extracted the 5,479 independent SNPs with P < 0.01 from the MVP aTRH GWAS meta-analysis summary statistics to be used for the P&T-based clustering analysis.

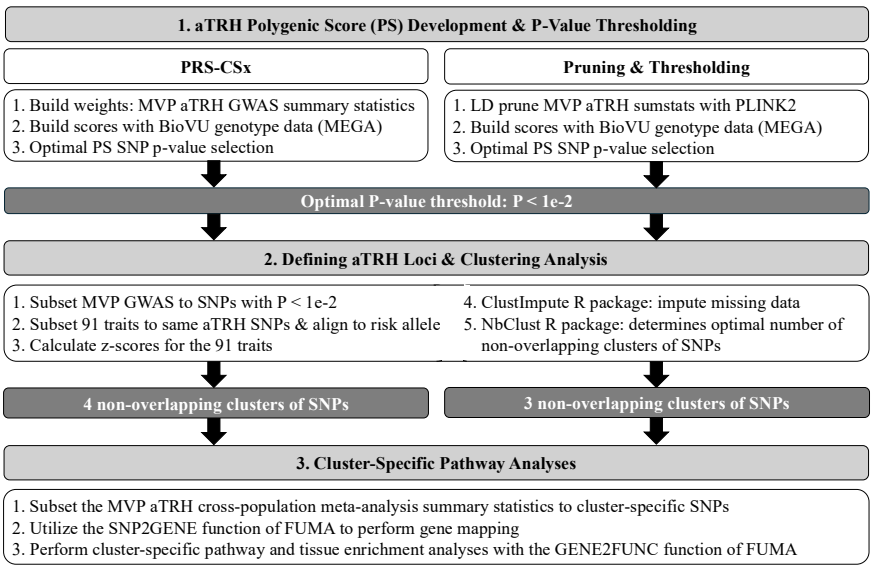

Fig. 1. Schematic overview of methods. MVP GWAS refers to the cross-population meta-analysis of aTRH. BioVU data refers to the genotype data from BioVU (MEGA). PS: Polygenic scores. LD: Linkage disequilibrium.

2.3. *Defining Clusters of aTRH SNPs with Distinct Cardiometabolic Profiles*

We adapted our approach based on a previously published unsupervised "hard clustering" method with imputation of missing traits.[13] Briefly, we identified 91 cardiometabolic-related traits[23-50] that are associated with aTRH, HTN, or BP. Publicly available summary statistics were obtained and the effect estimates were aligned to the aTRH risk allele from the cross-population MVP meta-analysis. Z-scores were then calculated for each trait. K-means clustering of the aTRH SNPs and 91 traits was performed using the ClustImpute[51] and NbClust[52] R packages. The ClustImpute package imputes missing data and the NbClust package determines the optimal number of clusters. ClustImpute was performed with three clusters (minimum). NbClust parameters were based on those used previously[13] which included a minimum of three and maximum of 15 clusters, distance was set to Euclidean, all indices were used, and the significance value for Beale's index was set to 0.1. Clustering parameters were identical for both the PRS-CSx and P&T approaches.

2.4. *Cluster-Specific Pathway Analyses*

To investigate the biological pathways and tissue-specific expression patterns associated with each cluster, we used the SNP2GENE and GENE2FUNC functions of FUMA[53] (Functional Mapping and Annotation of GWAS). We input cluster-specific subsets of the aTRH MVP cross-population meta-analysis summary statistics into the SNP2GENE function of FUMA to perform gene mapping and then used the GENE2FUNC function for functional enrichment analyses, including pathway and tissue enrichment based on Genotype-Tissue Expression (GTEx) version 8 profiles. Parameters for FUMA analyses were identical for both SNP selection methods.

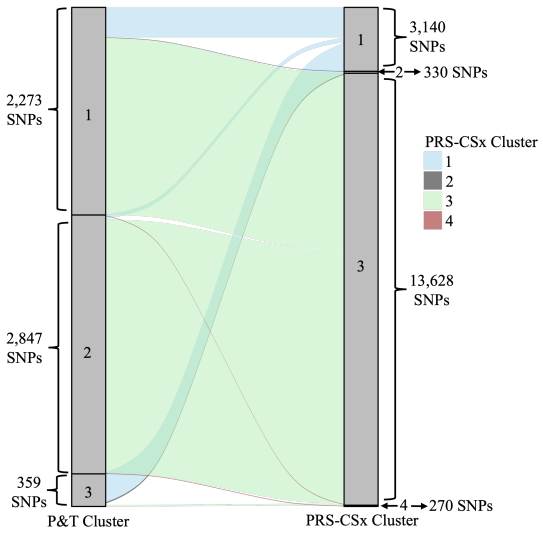

Fig. 2. Alluvial plot showing the differences in distribution of SNPs between P&T Clusters and PRS-CSx Clusters. The number of SNPs per cluster is shown next to each bracket. SNPs that were not shared between both methods were excluded for plotting.

3. Results

We compared the PRS-CSx and P&T methods as two different SNP selection approaches to k-means clustering for phenotypes with limited numbers of independent genome-wide significant loci, with the overarching goal of determining the genetic underpinnings of phenotypic heterogeneity in aTRH. For PRS-CSx, the optimal p-value thresholds were $P < 1$ in the NHW population and $P < 0.01$ in the NHB population (maximal variance explained: 0.05% and 0.14%, respectively). For P&T, the optimal threshold was $P < 0.01$ for the NHW and NHB populations (maximal variance explained: 0.58% and 3.30%, respectively). We then performed two sets of clustering analyses, using the 17,367 SNPs selected from PRS-CSx and 5,479 from P&T (SNPs with $P < 0.01$), aligned to the aTRH risk allele, across 91 cardiometabolic traits. The optimal number of clusters was determined to be four for the PRS-CSx-based method and three for P&T-based method, which represented non-overlapping subsets of SNPs with similar cardiometabolic profiles through application of an unsupervised "hard clustering" method with imputation of missing trait associations.[13] The distribution of SNPs by cluster and method is shown in Figure 2. Clustering based on P&T resulted in two near-equally proportioned clusters out of a total of three, whereas PRS-CSx-based clustering resulted in four clusters, with one including over four times as many SNPs than the next largest cluster (Figure 2). Most SNPs in P&T-based Clusters 1 and 2 were captured in the PRS-CSx-based Cluster 3, where P&T Cluster 3 mostly overlapped with PRS-CSx Cluster 1 (Figure 2).

3.1. *Identifying Biologically Meaningful Clusters of aTRH SNPs*

Each of the non-overlapping SNP clusters derived from both PRS-CSx and P&T showed a unique pattern of association across the 91 cardiometabolic traits (Figure 3), reflecting the genetic and mechanistic heterogeneity of aTRH.

PRS-CSx Cluster 1 showed mixed positive and negative associations across traits, with strong positive associations for SBP, DBP, and pulse pressure, as well as traits related to metabolic health, including fasting glucose, two-hour glucose, and most of the anthropometric and central adipose tissue volume traits. Moderately negative associations were observed for certain cardiac structural/functional traits and some blood cell traits, including hematocrit, hemoglobin concentration, mean corpuscular hemoglobin, and mean corpuscular volume (Figure 2A). PRS-CSx Cluster 2 was characterized by increased associations of all the anthropometric measures, all but one liver-related trait, and many of the lifestyle, sleep and BP traits, as well as cardiac structural/functional phenotypes (Figure 2A). Negative associations appeared for multiple blood cell traits, circulating plasma lipids, women's health and endocrine traits, including age at menarche, sex hormone binding globulin, and plasma renin. PRS-CSx Cluster 3 showed consistently weak or near-zero associations across most traits, except for strong negative associations with BP traits. Cluster 4 displayed nearly inverse patterns of Cluster 2, with negative associations with anthropometric, liver, lifestyle, BP, and cardiac traits, but strong positive associations with blood cell traits and moderate positive associations with women's health and lipid traits (Figure 2A).

P&T Cluster 1 displayed broadly increased associations across nearly all glycemic, anthropometric, adiposity, BP and heart rate, liver, blood cell, lifestyle and women's health traits, with only a few exceptions: decreased associations for HDL, select blood cell traits, testosterone, and sex hormone binding globulin (Figure 2B). P&T Cluster 2 showed the opposite pattern, with negative associations across nearly all glycemic, adiposity, lipid, BP, heart rate, and blood cell traits, while cardiac structural/functional traits remained weakly associated (Figure 2B). Cluster 3 was characterized by strong associations with cardiac structural/functional traits, largely in the negative direction, coupled with positive associations for BP traits and negative associations for adiposity, lipid, and blood cell traits.

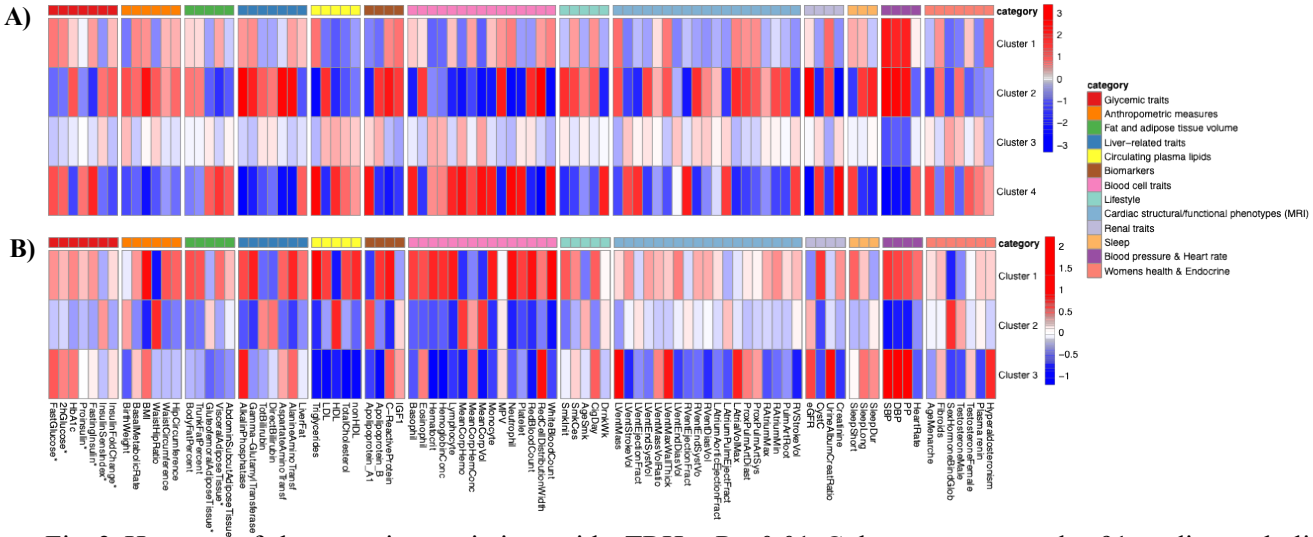

Fig. 3. Heatmap of cluster-trait associations with aTRH at $P < 0.01$. Columns correspond to 91 cardiometabolic traits, grouped by category. Rows correspond to the clusters. Color intensity reflects the direction and magnitude of association (z-score aligned to the aTRH risk allele), with blue indicating negative and red indicating positive associations. Breaks for the color scale were calculated using a quantile-based method. *Traits adjusted for BMI. **A)** PRS-CSx-based results. **B)** P&T-based results.

Overall, both methods produced clusters with nearly inverse association patterns. Compared to PRS-CSx-derived clusters, P&T clusters tended to capture broader and more uniformly positive or

negative trends. These differences indicate that SNP selection strategy can shape both cluster composition and the biological pathways implicated, with PRS-CSx highlighting more subtle contrasts between variant groups and P&T emphasizing broader cardiometabolic signatures.

3.2. *Cluster-Specific Pathways*

The GENE2FUNC tissue specificity analyses revealed significant enrichment ($P_{Bonferroni} < 0.05$) for both PRS-CSx- and P&T-based Clusters, though the patterns differed between methods (Table 1). PRS-CSx Cluster 1 showed enrichment in the bladder, adrenal gland, and heart (left ventricle), while Cluster 3 was enriched for the bladder and adrenal gland (Table 1). P&T Clusters revealed tissue enrichment for more total tissues, including whole blood for Cluster 1 and the bladder, colon, uterus, prostate, and kidney for Cluster 2.

Table 1. Cluster-specific FUMA GENE2FUNC results for tissue specificity. Only significantly ($P_{Bonferroni} < 0.05$) enriched tissues are shown.

Method	Cluster	Tissue	$P_{Bonferroni}$
PRS-CSx	1	Bladder	5.15×10^{-7}
		Adrenal gland	7.82×10^{-7}
		Heart left ventricle	2.20×10^{-4}
	3	Bladder	5.90×10^{-5}
		Adrenal gland	1.10×10^{-3}
P&T	1	Whole blood	2.46×10^{-3}
	2	Bladder	4.98×10^{-9}
		Colon	2.92×10^{-7}
		Uterus	8.94×10^{-4}
		Prostate	4.66×10^{-2}
		Kidney	4.70×10^{-2}

Table 2. Cluster-specific GENE2FUNC results for significantly enriched gene sets ($P_{FDR} < 0.05$). The top 4 of over 20 significant pathways are presented for PRS-CSx Cluster 1 and P&T Cluster 2.

Method	Cluster	Gene Ontology Biological Process	P_{FDR}
PRS-CSx	1	Anterior-posterior pattern specification	7.33×10^{-3}
		Glucocorticoid biosynthetic process	1.87×10^{-2}
		Embryonic skeletal system development	1.87×10^{-2}
		Membrane repolarization during cardiac muscle cell action potential	3.61×10^{-2}
	3	Homophilic cell adhesion via plasma membrane adhesion molecules	1.32×10^{-3}
		Embryonic skeletal system development	3.08×10^{-2}
		Glucocorticoid biosynthetic process	4.33×10^{-2}
P&T	1	Ubiquitin dependent endoplasmic reticulum-associated degradation	2.91×10^{-2}
		Endoplasmic reticulum-associated degradation	3.40×10^{-2}
	2	Embryonic skeletal system development	3.92×10^{-8}
		Embryonic skeletal system morphogenesis	2.41×10^{-7}
		Skeletal system development	2.41×10^{-7}
		Anterior-posterior pattern specification	3.50×10^{-7}

The GENE2FUNC analysis also revealed both convergences and divergences between methods for significant enrichment ($P_{FDR} < 0.05$) of gene ontology biological pathways (Table 2). The top four PRS-CSx-based Cluster 1 pathways were enriched for developmental and regulatory processes, including anterior-posterior pattern specification ($P=7.33 \times 10^{-3}$), glucocorticoid biosynthetic process ($P=1.87 \times 10^{-2}$), embryonic skeletal system development ($P=1.87 \times 10^{-2}$), and membrane repolarization during cardiac muscle cell action potential ($P=3.61 \times 10^{-2}$). PRS-CSx Cluster 3 was enriched for homophilic cell adhesion via plasma membrane adhesion molecules ($P=1.32 \times 10^{-3}$),

embryonic skeletal system development ($P=3.08x10^{-2}$), and glucocorticoid biosynthetic process ($P=4.33x10^{-2}$). In contrast, P&T-based Cluster 1 was enriched for endoplasmic reticulum-associated degradation pathways ($P=2.91x10^{-2}$ and $P=3.40x10^{-2}$), while the top four significant pathways for P&T Cluster 2 were strongly enriched for a broader set of developmental processes, including embryonic skeletal system development and morphogenesis ($P=3.92x10^{-8}$ and $P=2.41x10^{-7}$), skeletal system development ($P=2.41x10^{-7}$), and anterior-posterior pattern specification ($P=3.50x10^{-7}$).

4. Discussion

This study provides insights into the biological heterogeneity of aTRH by applying a clustering framework to genetic variants using two different SNP selection strategies: PRS-CSx and P&T. Each approach identified distinct, non-overlapping clusters of variants with unique cardiometabolic association profiles, supporting the hypothesis that aTRH is a disorder influenced by multiple pathophysiological processes.

Despite differences in SNP selection, both methods revealed clusters enriched for multiple groups of cardiometabolic traits. However, notable divergences were observed. PRS-CSx selected approximately five times the number of SNPs selected by P&T and yielded four clusters with more nuanced traits profiles, whereas P&T produced three clusters characterized by broader and more interpretable trends. These methodological differences highlight how SNP selection strategy can influence both the composition of clusters and downstream biological interpretations.

Across methods, clusters enriched for adiposity and glycemic traits (PRS-CSx Cluster 1 and P&T Cluster 1) suggest a metabolic energy-driven pathway to treatment resistance. These findings are supported by the results of another study that reported a gradual increase in the prevalence of resistant HTN with BMI in overweight patients.[54] Increased adipose tissue is related to increased activity of the renin-angiotensin-aldosterone system (RAAS), which is crucial in BP regulation. In particular, increased adiposity can lead to increased expression of angiotensin type 1 and 2 receptors, elevated circulating angiotensin II, angiotensin-converting enzyme, and aldosterone levels.[55] In obesity specifically, the increased activity of the RAAS can increase sodium retention, leading to volume expansion and HTN.[56]

Positive associations between multiple biomarkers and aTRH are well supported by current literature. One study reported increased risk of aTRH with biomarkers such as interleukin-6 (IL-6), tumor necrosis factor-α (TNF-α), and transforming growth factor-β (TGF-β).[57] These results align with the strong positive association of multiple biomarkers observed in PRS-CSx Cluster 2 and P&T Cluster 3. Other positive associations shared between these clusters include sleep-related traits. Sleep disturbances, obstructive sleep apnea in particular, are highly prevalent (60-71%) among individuals with aTRH.[58] In particular, one study found sleep apnea was significantly more common in individuals with resistant HTN compared to individuals with controlled HTN.[59]

Lastly, positive associations with blood cell traits (PRS-CSx Cluster 4 and P&T Cluster 1) may indicate a vascular-reactivity related mechanism. In a large Japanese cohort over a 40-year follow-up period, absolute neutrophil and white blood cell count have been shown to predict new onset HTN.[60] Further, one study found that compared to both normotensive and controlled hypertensive patients, individuals with aTRH had a significantly higher neutrophil count and neutrophil/lymphocyte ratio.[61] Positive associations with white blood cell, neutrophil and lymphocyte count for both clusters support these findings.

Pathway and tissue enrichment analyses reinforced the unique biological profiles of clusters identified by each method. For PRS-CSx, Cluster 1 was significantly enriched in gene sets related to anterior-posterior pattern specification, glucocorticoid biosynthesis, and embryonic skeletal system development, suggesting early development and hormonal regulation pathways. Glucocorticoid receptor signaling has been implicated in HTN, particularly through sodium and potassium handling and BP regulation.[62] One study reported 51% of patients who carried a heterozygous or homozygous glucocorticoid receptor mutation had HTN.[62] Tissue specificity analysis of PRS-CSx Cluster 1 further revealed enrichment in the adrenal gland, heart, and bladder, aligning with traits tied to volume regulation and hormonal control. PRS-CSx Cluster 3 was enriched for biological processes related to homophilic cell adhesion, embryonic development, and glucocorticoid biosynthesis. One study[63] examined the relationship between adhesion molecules and aTRH and found that endothelial-selectin was a significant indicator of aTRH.

In contrast, P&T identified clusters enriched in a broader range of tissues, including whole blood, bladder, colon, uterus, prostate, and kidney. Functionally, P&T Cluster 1 was linked to protein quality-control pathways including ubiquitin-dependent and endoplasmic reticulum-associated degradation. P&T Cluster 2 was highly significantly enriched for skeletal system development and morphogenesis pathways, overlapping partially with the PRS-CSx findings, but with stronger statistical support, and implicated bladder tissue as well. Together, these enrichment patterns indicate that while both methods highlight developmental and hormonal pathways, PRS-CSx emphasized neurohormonal and cardiac regulation, whereas P&T uncovered stronger signals in developmental and protein homeostasis processes, as well as a broader set of tissues, including reproductive and gastrointestinal systems.

These results demonstrate that both methods recover biologically meaningful clusters but may emphasize different aspects of underlying biology. In this analysis, PRS-CSx tended to highlight pathways related to developmental, endocrine, and cardiac processes, whereas P&T captured a wider range of tissue and pathway enrichments, including immune, reproductive, and protein degradation pathways. The partial overlap between enriched skeletal-related processes across both methods suggests stronger biological themes, but each approach also identified distinct biological signals. These results reinforce that the choice of SNP selection method influences both cluster composition and downstream enrichment analyses. Despite the differences, the overlap in developmental and hormonal pathways across methods provides converging evidence for their role in aTRH, while method-specific findings may reflect complementary aspects of the underlying biology. Taken together, the findings of this study underscore the biological heterogeneity underlying aTRH, suggesting that distinct clusters of genetic variants act through different cardiometabolic routes to contribute to HTN that is refractory to standard treatments.

The identification of mechanistically distinct genetic clusters has implications for precision therapeutics in aTRH. By understanding the unique pathway through which a patient becomes resistant, for example, metabolic overload vs. vascular stiffness vs. hematologic dysfunction, clinicians may be able to tailor interventions to target the underlying biology. Stratification by genetic cluster could test whether pathway-informed interventions improve BP control, which may have potential to overcome the limitations of current treatment guidelines and address population differences in HTN control and efficacy of antihypertensives.

While promising, this work has some limitations. First, the analyses were performed in NHW and NHB cohorts, limiting generalizability to other populations. Given known differences in HTN prevalence and treatment response, population-specific clustering approaches should be further

explored. Additionally, the clustering approach is based solely on genetic association profiles. Future studies including transcriptomic or proteomic data may provide additional biologically relevant information. Finally, SNP selection methods clearly influenced results, underscoring the need for continued methodological evaluation in clustering-based approaches. The difference in number of SNPs along with the SNPs selected could both contribute to these influences.

Together, our findings underscore the potential of genetic clustering to disentangle the biological and mechanistic heterogeneity underlying aTRH and demonstrate that SNP clustering provides a powerful framework to identify distinct mechanistic pathways. Both PRS-CSx and P&T produced biologically interpretable clusters but emphasized different aspects of the genetic architecture. In this analysis, P&T demonstrated clearer interpretability and stronger tissue and pathway signals, indicating that it may be a preferred SNP selection strategy. This work also lays the foundation for use of clustering methods for phenotypes with a limited number of independent genome-wide significant variants. This study represents a step toward precision medicine in aTRH by linking genetic architecture to putative mechanistic pathways, and ultimately, a shift from broad, population-level HTN treatment strategies toward more tailored interventions.

5. Acknowledgements

Vanderbilt University Medical Center's BioVU is supported by institutional funding and by the Vanderbilt CTSA grant UL1 TR000445 from NCATS/NIH. HMS and JK were funded by TL1TR002244. HMS was also funded by T32GM145734-01. ATA was funded by T32HL007737. We thank the Veterans who participated in the Million Veteran Program and the participants of Vanderbilt University Medical Center's BioVU. This research is based on data from the Million Veteran Program, Office of Research and Development, and Veterans Health Administration (MVP000 and MVP001/002). This publication does not represent the views of the Department of Veterans Affairs or the United States Government.

VA Million Veteran Program
Core Acknowledgements for Publications
June 2025

MVP Program Office

- Sumitra Muralidhar, Ph.D., Program Director
  US Department of Veterans, 810 Vermont Avenue NW, Washington, DC 20420
- Jennifer Moser, Ph.D., Associate Director, Scientific Programs
  US Department of Veterans Affairs, 810 Vermont Avenue NW, Washington, DC 20420
- Jennifer E. Deen, B.S., Associate Director, Cohort & Public Relations
  US Department of Veterans Affairs, 810 Vermont Avenue NW, Washington, DC 20420

MVP Executive Committee

- Co-Chair: Philip S. Tsao, Ph.D., Program Director
  VA Palo Alto Health Care System, 3801 Miranda Avenue, Palo Alto, CA 94304
- Co-Chair: Sumitra Muralidhar, Ph.D.
  US Department of Veterans Affairs, 810 Vermont Avenue NW, Washington, DC 20420
- J. Michael Gaziano, M.D., M.P.H
  VA Boston Healthcare System, 105 S. Huntington Avenue, Boston, MA 02130
- Elizabeth Hauser, Ph.D.

Durham VA Medical Center, 508 Fulton Street, Durham, NC 27705
- Amy Kilbourne, Ph.D., M.P.H.
  VA HSR&D, 2215 Fuller Road, Ann Arbor, MI 48105
- Michael Matheny, M.D., M.S., M.P.H
  VA Tennessee Valley Healthcare System, 1310 24th Ave. South, Nashville, TN 37212
- Dave Oslin, M.D
  Philadelphia VA Medical Center, 3900 Woodland Avenue, Philadelphia, PA 19104
- Deepak Voora, M.D.
  Durham VA Medical Center, 508 Fulton Street, Durham, NC 27705

MVP Co-Principal Investigators
- J. Michael Gaziano, M.D., M.P.H
  VA Boston Healthcare System, 105 S. Huntington Avenue, Boston, MA 02130
- Philip S. Tsao, Ph.D.
  VA Palo Alto Health Care System, 3801 Miranda Avenue, Palo Alto, CA 94304

MVP Core Operations
- Jessica V. Brewer, M.P.H., Director, MVP Cohort Operations
  VA Boston Healthcare System, 105 S. Huntington Avenue, Boston, MA 02130
- Mary T. Brophy M.D., M.P.H., Director, VA Central Biorepository
  VA Boston Healthcare System, 105 S. Huntington Avenue, Boston, MA 02130
- Kelly Cho, M.P.H., Ph.D., Director, MVP Phenomics
  VA Boston Healthcare System, 105 S. Huntington Avenue, Boston, MA 02130
- Lori Churby, B.S., Director, MVP Regulatory Affairs
  VA Palo Alto Health Care System, 3801 Miranda Avenue, Palo Alto, CA 94304
- Scott L. DuVall, Ph.D., Director, VA Informatics and Computing Infrastructure (VINCI)
  VA Salt Lake City Health Care System, 500 Foothill Drive, Salt Lake City, UT 84148
- Saiju Pyarajan, Ph.D., Director, Data and Computational Sciences
  VA Boston Healthcare System, 105 S. Huntington Avenue, Boston, MA 02130
- Robert Ringer, Pharm.D., Director, VA Albuquerque Central Biorepository
  New Mexico VA Health Care System, 1501 San Pedro Drive SE, Albuquerque, NM 87108
- Luis E. Selva, Ph.D., Director, MVP Biorepository Coordination
  VA Boston Healthcare System, 105 S. Huntington Avenue, Boston, MA 02130
- Shapoor (Alex) Shayan, M.S., Director, MVP PRE Informatics
  VA Boston Healthcare System, 105 S. Huntington Avenue, Boston, MA 02130
- Brady Stephens, M.S., Principal Investigator, MVP Cohort Development and Management
  VA Boston Healthcare System, 105 S. Huntington Avenue, Boston, MA 02130
- Stacey B. Whitbourne, Ph.D., Director, MVP Cohort Development and Management
  VA Boston Healthcare System, 105 S. Huntington Avenue, Boston, MA 02130

References

1 Lawes, C. M., Vander Hoorn, S., Rodgers, A. & International Society of, H. Global burden of blood-pressure-related disease, 2001. *Lancet* **371**, 1513-1518 (2008). https://doi.org:10.1016/S0140-6736(08)60655-8

2 Roger, V. L. *et al.* Executive summary: heart disease and stroke statistics--2012 update: a report from the American Heart Association. *Circulation* **125**, 188-197 (2012). https://doi.org:10.1161/CIR.0b013e3182456d46

3 Whelton, P. K. *et al.* 2017 ACC/AHA/AAPA/ABC/ACPM/AGS/APhA/ASH/ASPC/NMA/PCNA Guideline for the Prevention, Detection, Evaluation, and Management of High Blood Pressure in Adults: Executive Summary: A Report of the American College of Cardiology/American Heart Association Task Force on Clinical Practice Guidelines. *Hypertension* **71**, 1269-1324 (2018). https://doi.org:10.1161/HYP.0000000000000066

4 Muntner, P. *et al.* Potential U.S. Population Impact of the 2017 ACC/AHA High Blood Pressure Guideline. *J Am Coll Cardiol* **71**, 109-118 (2018). https://doi.org:10.1016/j.jacc.2017.10.073

5 Noubiap, J. J. *et al.* Global prevalence of resistant hypertension: a meta-analysis of data from 3.2 million patients. *Heart* **105**, 98-105 (2019). https://doi.org:10.1136/heartjnl-2018-313599

6 Shuey, M. M. *et al.* Characteristics and treatment of African-American and European-American patients with resistant hypertension identified using the electronic health record in an academic health centre: a case-control study. *BMJ Open* **8**, e021640 (2018). https://doi.org:10.1136/bmjopen-2018-021640

7 Irvin, M. R. *et al.* Apparent treatment-resistant hypertension and risk for stroke, coronary heart disease, and all-cause mortality. *J Am Soc Hypertens* **8**, 405-413 (2014). https://doi.org:10.1016/j.jash.2014.03.003

8 Khawaja, Z. & Wilcox, C. S. Role of the kidneys in resistant hypertension. *Int J Hypertens* **2011**, 143471 (2011). https://doi.org:10.4061/2011/143471

9 Ma, J. *et al.* Signaling pathways in vascular function and hypertension: molecular mechanisms and therapeutic interventions. *Signal Transduct Target Ther* **8**, 168 (2023). https://doi.org:10.1038/s41392-023-01430-7

10 Tsioufis, C. *et al.* Pathophysiology of resistant hypertension: the role of sympathetic nervous system. *Int J Hypertens* **2011**, 642416 (2011). https://doi.org:10.4061/2011/642416

11 Abrahamowicz, A. A., Ebinger, J., Whelton, S. P., Commodore-Mensah, Y. & Yang, E. Racial and Ethnic Disparities in Hypertension: Barriers and Opportunities to Improve Blood Pressure Control. *Curr Cardiol Rep* **25**, 17-27 (2023). https://doi.org:10.1007/s11886-022-01826-x

12 Jamerson, K. & DeQuattro, V. The impact of ethnicity on response to antihypertensive therapy. *Am J Med* **101**, 22S-32S (1996). https://doi.org:10.1016/s0002-9343(96)00265-3

13 Suzuki, K. *et al.* Genetic drivers of heterogeneity in type 2 diabetes pathophysiology. *Nature* **627**, 347-357 (2024). https://doi.org:10.1038/s41586-024-07019-6

14 Prive, F., Vilhjalmsson, B. J., Aschard, H. & Blum, M. G. B. Making the Most of Clumping and Thresholding for Polygenic Scores. *Am J Hum Genet* **105**, 1213-1221 (2019). https://doi.org:10.1016/j.ajhg.2019.11.001

15 Ruan, Y. *et al.* Improving polygenic prediction in ancestrally diverse populations. *Nat Genet* **54**, 573-580 (2022). https://doi.org:10.1038/s41588-022-01054-7

16 Irvin, M. R. *et al.* Genome-Wide Association Study of Apparent Treatment-Resistant Hypertension in the CHARGE Consortium: The CHARGE Pharmacogenetics Working Group. *Am J Hypertens* **32**, 1146-1153 (2019). https://doi.org:10.1093/ajh/hpz150

17 Gaziano, J. M. *et al.* Million Veteran Program: A mega-biobank to study genetic influences on health and disease. *J Clin Epidemiol* **70**, 214-223 (2016). https://doi.org:10.1016/j.jclinepi.2015.09.016

18 Breeyear, J. H., Shuey, M. M., Edwards, T. L. & Hellwege, J. N. Blood Pressure Polygenic Scores Are Associated With Apparent Treatment-Resistant Hypertension. *Circ Genom Precis Med* **15**, e003554 (2022). https://doi.org:10.1161/CIRCGEN.121.003554

19 Pulley, J., Clayton, E., Bernard, G. R., Roden, D. M. & Masys, D. R. Principles of human subjects protections applied in an opt-out, de-identified biobank. *Clin Transl Sci* **3**, 42-48 (2010). https://doi.org:10.1111/j.1752-8062.2010.00175.x

20 Armstrong, N. D. *et al.* Whole genome sequence analysis of apparent treatment resistant hypertension status in participants from the Trans-Omics for Precision Medicine program. *Front Genet* **14**, 1278215 (2023). https://doi.org:10.3389/fgene.2023.1278215

21 Hellwege, J. N. *et al.* Predictive models for abdominal aortic aneurysms using polygenic scores and PheWAS-derived risk factors. *Pac Symp Biocomput* **28**, 425-436 (2023).

22 Chang, C. C. *et al.* Second-generation PLINK: rising to the challenge of larger and richer datasets. *Gigascience* **4**, 7 (2015). https://doi.org:10.1186/s13742-015-0047-8

23 Chen, J. *et al.* The trans-ancestral genomic architecture of glycemic traits. *Nat Genet* **53**, 840-860 (2021). https://doi.org:10.1038/s41588-021-00852-9

24 Broadaway, K. A. *et al.* Loci for insulin processing and secretion provide insight into type 2 diabetes risk. *Am J Hum Genet* **110**, 284-299 (2023). https://doi.org:10.1016/j.ajhg.2023.01.002

25 Williamson, A. *et al.* Genome-wide association study and functional characterization identifies candidate genes for insulin-stimulated glucose uptake. *Nat Genet* **55**, 973-983 (2023). https://doi.org:10.1038/s41588-023-01408-9

26 Warrington, N. M. *et al.* Maternal and fetal genetic effects on birth weight and their relevance to cardio-metabolic risk factors. *Nat Genet* **51**, 804-814 (2019). https://doi.org:10.1038/s41588-019-0403-1

27 Sudlow, C. *et al.* UK biobank: an open access resource for identifying the causes of a wide range of complex diseases of middle and old age. *PLoS Med* **12**, e1001779 (2015). https://doi.org:10.1371/journal.pmed.1001779

28 Sakaue, S. *et al.* A cross-population atlas of genetic associations for 220 human phenotypes. *Nat Genet* **53**, 1415-1424 (2021). https://doi.org:10.1038/s41588-021-00931-x

29 Sinnott-Armstrong, N. *et al.* Genetics of 35 blood and urine biomarkers in the UK Biobank. *Nat Genet* **53**, 185-194 (2021). https://doi.org:10.1038/s41588-020-00757-z

30 Liu, Y. *et al.* Genetic architecture of 11 organ traits derived from abdominal MRI using deep learning. *Elife* **10** (2021). https://doi.org:10.7554/eLife.65554

31 Graham, S. E. *et al.* The power of genetic diversity in genome-wide association studies of lipids. *Nature* **600**, 675-679 (2021). https://doi.org:10.1038/s41586-021-04064-3

32 Keaton, J. M. *et al.* Genome-wide analysis in over 1 million individuals of European ancestry yields improved polygenic risk scores for blood pressure traits. *Nat Genet* **56**, 778-791 (2024). https://doi.org:10.1038/s41588-024-01714-w

33 Chen, M. H. *et al.* Trans-ethnic and Ancestry-Specific Blood-Cell Genetics in 746,667 Individuals from 5 Global Populations. *Cell* **182**, 1198-1213 e1114 (2020). https://doi.org:10.1016/j.cell.2020.06.045

34 Saunders, G. R. B. *et al.* Genetic diversity fuels gene discovery for tobacco and alcohol use. *Nature* **612**, 720-724 (2022). https://doi.org:10.1038/s41586-022-05477-4

35 Khurshid, S. *et al.* Clinical and genetic associations of deep learning-derived cardiac magnetic resonance-based left ventricular mass. *Nat Commun* **14**, 1558 (2023). https://doi.org:10.1038/s41467-023-37173-w

36 Pirruccello, J. P. *et al.* Analysis of cardiac magnetic resonance imaging in 36,000 individuals yields genetic insights into dilated cardiomyopathy. *Nat Commun* **11**, 2254 (2020). https://doi.org:10.1038/s41467-020-15823-7

37 Schmidt, A. F. *et al.* Druggable proteins influencing cardiac structure and function: Implications for heart failure therapies and cancer cardiotoxicity. *Sci Adv* **9**, eadd4984 (2023). https://doi.org:10.1126/sciadv.add4984

38 Aung, N. *et al.* Genome-Wide Analysis of Left Ventricular Maximum Wall Thickness in the UK Biobank Cohort Reveals a Shared Genetic Background With Hypertrophic Cardiomyopathy. *Circ Genom Precis Med* **16**, e003716 (2023). https://doi.org:10.1161/CIRCGEN.122.003716

39 Pirruccello, J. P. *et al.* Genetic analysis of right heart structure and function in 40,000 people. *Nat Genet* **54**, 792-803 (2022). https://doi.org:10.1038/s41588-022-01090-3

40 Ahlberg, G. *et al.* Genome-wide association study identifies 18 novel loci associated with left atrial volume and function. *Eur Heart J* **42**, 4523-4534 (2021). https://doi.org:10.1093/eurheartj/ehab466

41 Liu, H. *et al.* Epigenomic and transcriptomic analyses define core cell types, genes and targetable mechanisms for kidney disease. *Nat Genet* **54**, 950-962 (2022). https://doi.org:10.1038/s41588-022-01097-w

42 Agrawal, S. *et al.* Inherited basis of visceral, abdominal subcutaneous and gluteofemoral fat depots. *Nat Commun* **13**, 3771 (2022). https://doi.org:10.1038/s41467-022-30931-2

43 Teumer, A. *et al.* Genome-wide association meta-analyses and fine-mapping elucidate pathways influencing albuminuria. *Nat Commun* **10**, 4130 (2019). https://doi.org:10.1038/s41467-019-11576-0

44 Dashti, H. S. *et al.* Genome-wide association study identifies genetic loci for self-reported habitual sleep duration supported by accelerometer-derived estimates. *Nat Commun* **10**, 1100 (2019). https://doi.org:10.1038/s41467-019-08917-4

45 van de Vegte, Y. J. *et al.* Genetic insights into resting heart rate and its role in cardiovascular disease. *Nat Commun* **14**, 4646 (2023). https://doi.org:10.1038/s41467-023-39521-2

46 Day, F. R. *et al.* Genomic analyses identify hundreds of variants associated with age at menarche and support a role for puberty timing in cancer risk. *Nat Genet* **49**, 834-841 (2017). https://doi.org:10.1038/ng.3841

47 Kim, J. *et al.* Genome-wide meta-analysis identifies novel risk loci for uterine fibroids within and across multiple ancestry groups. *Nat Commun* **16**, 2273 (2025). https://doi.org:10.1038/s41467-025-57483-5

48 Leinonen, J. T. *et al.* Genetic analyses implicate complex links between adult testosterone levels and health and disease. *Commun Med (Lond)* **3**, 4 (2023). https://doi.org:10.1038/s43856-022-00226-0

49 Folkersen, L. *et al.* Genomic and drug target evaluation of 90 cardiovascular proteins in 30,931 individuals. *Nat Metab* **2**, 1135-1148 (2020). https://doi.org:10.1038/s42255-020-00287-2

50 Loh, P. R., Kichaev, G., Gazal, S., Schoech, A. P. & Price, A. L. Mixed-model association for biobank-scale datasets. *Nat Genet* **50**, 906-908 (2018). https://doi.org:10.1038/s41588-018-0144-6

51 Pfaffel, O. CLUSTIMPUTE: AN R PACKAGE FOR K-MEANS CLUSTERING WITHBUILD-IN MISSING DATA IMPUTATION. *Preprint* (2020). https://doi.org:10.13140/RG.2.2.20143.36007

52 Charrah, M., Ghazzali N., Boiteau, V., Niknafs A. NbClust: An R Package for Determining the Relevant Number of Clusters in a Data Set. *Journal of Statistical Software* **61**, 1-36 (2014). https://doi.org:https://doi.org/10.18637/jss.v061.i06

53 Watanabe, K., Taskesen, E., van Bochoven, A. & Posthuma, D. Functional mapping and annotation of genetic associations with FUMA. *Nat Commun* **8**, 1826 (2017). https://doi.org:10.1038/s41467-017-01261-5

54 Haddadin, F. *et al.* The prevalence and predictors of resistant hypertension in high-risk overweight and obese patients: A cross-sectional study based on the 2017 ACC/AHA guidelines. *J Clin Hypertens (Greenwich)* **21**, 1507-1515 (2019). https://doi.org:10.1111/jch.13666

55 Hall, J. E., do Carmo, J. M., da Silva, A. A., Wang, Z. & Hall, M. E. Obesity-induced hypertension: interaction of neurohumoral and renal mechanisms. *Circ Res* **116**, 991-1006 (2015). https://doi.org:10.1161/CIRCRESAHA.116.305697

56 Lohmeier, T. E. & Iliescu, R. The sympathetic nervous system in obesity hypertension. *Curr Hypertens Rep* **15**, 409-416 (2013). https://doi.org:10.1007/s11906-013-0356-1

57 Chen, J. *et al.* Inflammation and Apparent Treatment-Resistant Hypertension in Patients With Chronic Kidney Disease. *Hypertension* **73**, 785-793 (2019). https://doi.org:10.1161/HYPERTENSIONAHA.118.12358

58 Carnethon, M. R. & Johnson, D. A. Sleep and Resistant Hypertension. *Curr Hypertens Rep* **21**, 34 (2019). https://doi.org:10.1007/s11906-019-0941-z

59 Bhandari, S. K. *et al.* Comparisons of sleep apnoea rate and outcomes among patients with resistant and non-resistant hypertension. *Respirology* **21**, 1486-1492 (2016). https://doi.org:10.1111/resp.12840

60 Tian, N., Penman, A. D., Mawson, A. R., Manning, R. D., Jr. & Flessner, M. F. Association between circulating specific leukocyte types and blood pressure: the atherosclerosis risk in communities (ARIC) study. *J Am Soc Hypertens* **4**, 272-283 (2010). https://doi.org:10.1016/j.jash.2010.09.005

61 Belen, E., Sungur, A., Sungur, M. A. & Erdogan, G. Increased Neutrophil to Lymphocyte Ratio in Patients With Resistant Hypertension. *J Clin Hypertens (Greenwich)* **17**, 532-537 (2015). https://doi.org:10.1111/jch.12533

62 Verouti, S., Hummler, E. & Vanderriele, P. E. Role of glucocorticoid receptor mutations in hypertension and adrenal gland hyperplasia. *Pflugers Arch* **474**, 829-840 (2022). https://doi.org:10.1007/s00424-022-02715-6

63 de Faria, A. P. *et al.* Deregulation of Soluble Adhesion Molecules in Resistant Hypertension and Its Role in Cardiovascular Remodeling. *Circ J* **80**, 1196-1201 (2016). https://doi.org:10.1253/circj.CJ-16-0058

Prototype Learning to Create Refined Interpretable Digital Phenotypes from ECGs

Sahil Sethi[1,2,*], David Chen[2,*], Michael C. Burkhart[2] , Nipun Bhandari[3] , Bashar Ramadan[4], and Brett Beaulieu-Jones[2,†]

[1]*Pritzker School of Medicine, University of Chicago, IL, USA*

[2]*Center for Computational Medicine & Clinical AI, Section of Biomedical Data Science, Department of Medicine, University of Chicago, IL, USA*

[3]*Division of Cardiovascular Medicine, Department of Internal Medicine, University of California Davis, CA, USA*

[4]*Section of Hospital Medicine, Department of Medicine, University of Chicago, IL, USA*

[†]E-mail: beaulieujones@uchicago.edu, ** authors contributed equally*

Prototype-based neural networks offer interpretable predictions by comparing inputs to learned, representative signal patterns anchored in training data. While such models have shown promise in the classification of physiological data, it remains unclear whether their prototypes capture an underlying structure that aligns with broader clinical phenotypes. We use a prototype-based deep learning model trained for multi-label ECG classification using the PTB-XL dataset. Then without modification we performed inference on the MIMIC-IV clinical database. We assess whether individual prototypes, trained solely for classification, are associated with hospital discharge diagnoses in the form of phecodes in this external population. Individual prototypes demonstrate significantly stronger and more specific associations with clinical outcomes compared to the classifier's class predictions, NLP-extracted concepts, or broader prototype classes across all phecode categories. Prototype classes with mixed significance patterns exhibit significantly greater intra-class distances ($p < 0.0001$), indicating the model learned to differentiate clinically meaningful variations within diagnostic categories. The prototypes achieve strong predictive performance across diverse conditions, with AUCs ranging as high as 0.89 for atrial fibrillation to 0.91 for heart failure, while also showing substantial signal for non-cardiac conditions such as sepsis and renal disease. These findings suggest that prototype-based models can support interpretable digital phenotyping from physiologic time-series data, providing transferable intermediate phenotypes that capture clinically meaningful physiologic signatures beyond their original training objectives.

Keywords: electrocardiography (ECG), prototype learning, interpretable artificial intelligence, digital phenotyping, precision medicine.

© 2025 The Authors. Open Access chapter published by World Scientific Publishing Company and distributed under the terms of the Creative Commons Attribution Non-Commercial (CC BY-NC) 4.0 License.

1. Introduction

Modern healthcare systems generate vast quantities of physiologic time-series data, yet our ability to extract clinically meaningful structure from these signals remains limited. Electrocardiograms (ECGs), in particular, encode rich information about cardiac and systemic physiology. While deep learning models have demonstrated impressive accuracy in ECG-based diagnosis,[1,2] their opaque representations offer little insight into how physiologic patterns relate to broader patient phenotypes. Recently, Hughes et al.[3] demonstrated that ECGs can detect a surprisingly broad spectrum of 1,243 different cardiac and non-cardiac conditions, including previously unknown phenotypes such as neutropenia and menstrual disorders, while revealing that many non-cardiac conditions share similar ECG signatures.

As precision medicine aims to stratify patients based on biologically meaningful traits, there is growing interest in models that not only predict, but also explain and discover. Prototype-based neural networks offer an interpretable alternative to black-box classifiers by grounding predictions in similarity to representative signal patterns.[4–7] Recent work has shown that such models can yield clinically coherent explanations in ECG classification tasks,[7] suggesting a promising foundation for data-driven phenotyping.

In this work, we explore whether the latent structure learned by a prototype-based ECG model can reveal informative associations with real-world clinical phenotypes. Rather than training a model for diagnostic prediction, we use a prototype-based model to perform inference on ECGs from the MIMIC-IV database,[8] and assess whether specific waveform prototypes correspond to structured phenotypes such as discharge diagnoses. *Our central hypothesis is that learned ECG prototypes—despite being trained for a different task—may capture transferable physiologic signatures linked to disease.*

This study bridges physiologic modeling and clinical phenotyping by demonstrating how interpretable, prototype-based representations learned for the classification of raw ECGs can be associated with both cardiac and unrelated phenotypes. This reframes the potential of prototype-based models not just as diagnostic tools, but as interpretable instruments with the potential to reveal clinically meaningful structure in physiologic signals.

2. Related Work

2.1. *Prototype-Based Learning for Interpretability*

Prototype-based neural networks offer a transparent alternative to black-box deep learning and post-hoc methods by grounding predictions in similarity to a learned set of representative patterns.[4] Originally developed for image classification, these models have been extended to time-series domains such as electroencephalography (EEG) and ECG, where each prototype is anchored to a localized segment of the input signal.[6,7] Recent work has demonstrated that prototype-based ECG models can produce clinically meaningful explanations and achieve competitive performance on multi-label tasks.[7] However, prior applications focus on supervised classification, and to our knowledge, none have explored whether learned prototypes are associated with structured clinical outcomes.

2.2. *Phenotyping from Physiologic Signals*

Computational phenotyping plays a central role in precision medicine by enabling data-driven identification of patient subgroups that cut across conventional diagnostic boundaries. Existing phenotyping frameworks often rely on structured electronic health record (EHR) data such as ICD codes, lab results, and medication history,[9,10] with limited incorporation of raw physiologic signals. However, with recent advances in deep learning, there has been a growing interest in using electrocardiograms (ECGs) beyond conventional cardiac classification tasks for phenotype discovery. Recent large-scale studies have demonstrated that ECGs encode features associated with a wide range of cardiac and non-cardiac phenotypes, including heart failure, chronic kidney disease, and sepsis.[3,11] Friedman et al. used unsupervised ECG autoencoders to derive latent representations linked to structured outcomes through phenome-wide association studies (PheWAS) across multiple cohorts.[11] Similarly, PheWASNet demonstrated that supervised deep learning models trained on raw ECGs can predict over 1000 phenotypes mapped from EHRs—though without interpretability.[3] An important difference is that their approach set out specifically to map ECGs to phenotypes. While these models highlight the utility of ECG signals, their latent embeddings are difficult to interpret and offer limited insight into which waveform characteristics contribute to prediction. This work learns interpretable features from ECGs by performing a different task and then examines whether these features are associated and predictive of both related and unrelated phenotypes.

3. Methods

3.1. *Data*

3.1.1. *PTB-XL Dataset*

The publicly available PTB-XL dataset[12] was used for model training. PTB-XL contains 21,837 12-lead ECG recordings from 18,885 patients, each sampled at 100 Hz over 10 seconds. Each ECG is annotated with one or more diagnostic statements, mapped to the SCP coding scheme, spanning rhythm disturbances, morphological abnormalities, and conduction disorders. We adopted the 100 Hz version of the signals and followed a multi-label classification setup with all 71 labeled classes. The original stratified 8:1:1 split from the dataset was used for training, validation, and test sets.

3.1.2. *MIMIC-IV ECG Subset*

For downstream phenotyping, we used 12-lead ECG recordings from the MIMIC-IV database.[8] ECGs were resampled to 100 Hz. MIMIC-IV does not contain expert ECG annotations, so structured metadata on hospital discharge diagnoses (ICD-9 and ICD-10) was used for the downstream association analyses. Diagnoses codes were converted to phenotype codes (Phecodes) based on the PheWAS catalog.[13] ECGs with missing metadata were excluded. When a patient had multiple ECGs during a single admission, we used only the first ECG of their admission.

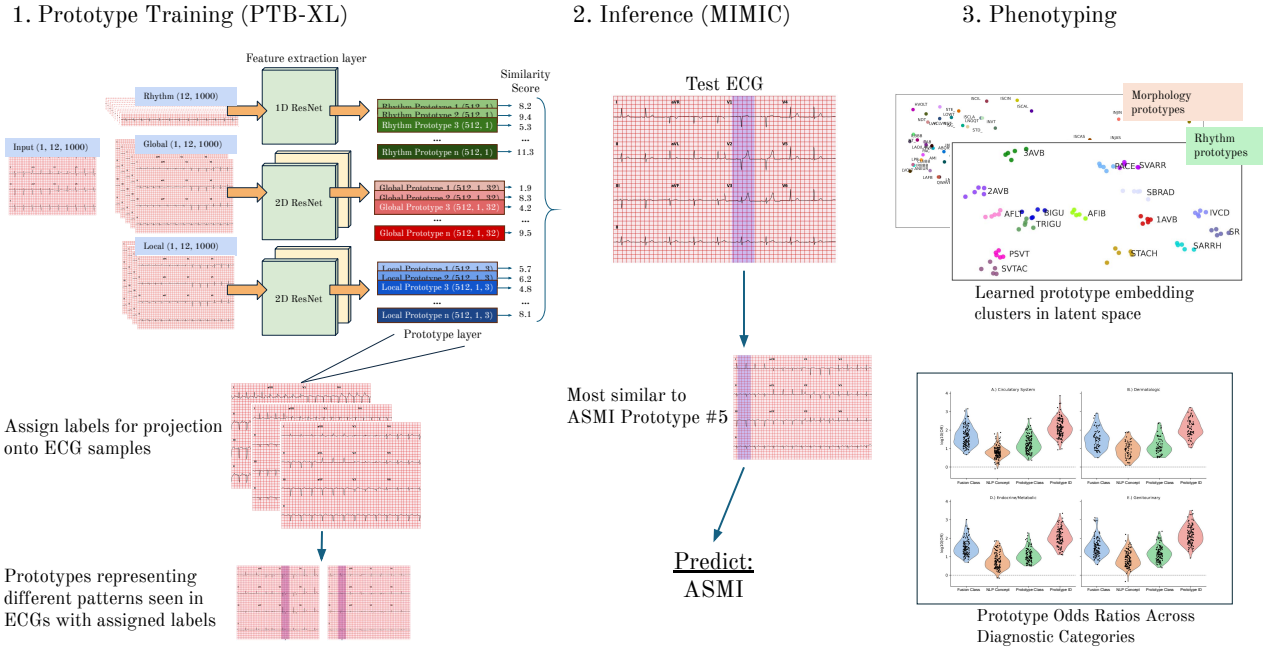

Fig. 1: Overview of study approach. 1.) Prototype training: ProtoECGNet[7] was trained on the PTB-XL dataset for multi-label ECG classification, with three branches (1D rhythm, 2D local morphology, 2D global) that each learned representative waveform prototypes. 2.) Inference: The pretrained model was applied without retraining to MIMIC-IV ECGs, computing similarity scores to identify the most representative prototypes for each recording. 3.) Phenotyping: Prototype activations and branch-level classes were associated with hospital discharge diagnoses (phecodes) and compared with NLP-extracted concepts, enabling statistical testing of whether prototypes capture clinically meaningful, transferable physiologic signatures.

3.2. *Model and Prototype Inference*

See Figure 1 for an overview of our study approach. We used a prototype-based neural network architecture for multi-label ECG classification trained using methods previously described in the literature (code: `https://github.com/bbj-lab/protoecgnet`).[7] In brief, the model architecture consisted of three parallel branches: a one-dimensional convolutional neural network (CNN) with global prototypes for rhythm detection, a two-dimensional CNN with local time-based prototypes for morphology recognition, and a two-dimensional CNN with global prototypes for whole-ECG patterns. Each branch was trained independently using binary cross-entropy loss and a prototype-based loss that promoted both clustering of within-class examples and separation of dissimilar ones. After training the prototype and feature extractor layers, each prototype was projected onto the latent space region most similar to it among training samples with its assigned label. Then, a final fully connected classifier was trained using the similarity scores from all prototypes across branches. During inference, the model was applied to both the PTB-XL test set and all eligible ECGs from MIMIC-IV. For each input ECG, we extracted the similarity score to each prototype and the most activated proto-

types. No retraining or adaptation was performed on the MIMIC-IV data. As in Sethi et al.,[7] the final model used five 1D rhythm prototypes, eighteen 2D partial prototypes, and seven 2D global prototypes per class.

3.3. *Prototype Grouping and Association Analysis*

3.3.1. *Prototype Analysis*

To discover higher-level phenotypic structure and reduce redundancy, we grouped prototypes based on similarity in the latent space. For each model branch, we computed pairwise cosine similarities between the final projected prototype vectors.[7] This analysis visualized prototype embeddings across three ECG feature extraction approaches using principal component analysis (PCA). Prototype vectors were extracted from 1D rhythm branch features, 2D global features, and 2D morphology features, with each prototype assigned to a label held by its associated training ECG from PTB-XL. As described by Chen et al.,[4] some prototypes may project onto the same training patch in the latent space and therefore be identical, but this is not an issue for classification tasks as the weights of the linear layer are tuned to accounted for this. Here, however, redundant prototypes were collapsed to facilitate analysis of independent prototypes. PCA dimensionality reduction was applied to transform high-dimensional prototype vectors into 2D coordinates for visualization. The resulting scatter plots displayed prototype distributions colored by clinical class, with centroid-based labeling used for the morphology features due to high density. This visualization approach enabled assessment of prototype clustering patterns and class separability across different feature extraction methodologies.

3.3.2. *Extraction and Filtering of UMLS Concepts from ECG Reports*

To identify structured clinical concepts within unstructured electrocardiogram (ECG) reports, we used a natural language processing (NLP) pipeline based on the spaCy framework, augmented with biomedical extensions from SciSpaCy.[14] Specifically, we employed the `en_core_sci_scibert` language model, which is pretrained on large-scale biomedical corpora and optimized for clinical and scientific text. We augmented the pipeline with two components: (1) the `scispacy_linker`, which performs entity linking to the Unified Medical Language System (UMLS),[15] and (2) the `negex` component[16] from `negspacy`, which detects negated clinical concepts.

The `scispacy_linker` was configured to resolve abbreviations and to prioritize entity mentions linked to definitions in UMLS, enhancing both precision and interpretability. For each report, the pipeline extracted named entities, resolved them to candidate UMLS concepts, and returned their concept unique identifiers (CUIs), canonical names, and linkage scores. Detected entities were also annotated for negation status based on syntactic context. Each report was processed individually, and the resulting concept-level annotations were aggregated into a structured list of UMLS concepts per report, including the original mention, concept metadata, and negation label.

To facilitate downstream analysis, we computed the frequency distribution of all extracted UMLS concepts across the corpus. Concepts which appeared at least 100 times were then

manually reviewed and filtered to retain only those relevant to ECG interpretation—such as cardiac diagnoses (e.g., atrial fibrillation, myocardial infarction), waveform findings (e.g., ST elevation, QT prolongation), and procedural terminology (e.g., echocardiography references, pacemaker placement). This filtering step ensured that subsequent analyses focused on clinically meaningful ECG content rather than incidental mentions or non-cardiac concepts.

3.3.3. *Statistical Association with Clinical Diagnoses*

We performed association testing between the ECG-derived features and phenotypic outcomes using Fisher's exact tests on the full set of ECGs (using only the first ECG of an admission where multiple ECGs were performed). The categorical variables examined included ECG classification outcomes ("fusion"), prototype-based groupings across the three branches (1D, 2D partial, and 2D global prototypes), as well as the extracted binary medical concept indicators derived from UMLS CUIs. Phenotypic outcomes were represented by phecodes derived from the discharge diagnoses. Phecodes and CUIs present in at least 0.1% of patients were included. For each phecode, 2×2 contingency tables were constructed comparing the presence/absence of each categorical feature value or CUI against phecode status. Multiple testing correction was applied using the Benjamini-Hochberg false discovery rate (FDR) method,[17] with statistical significance defined as $q < 0.05$.

3.4. *Prediction of Phecodes*

ECG data were preprocessed by parsing fusion class predictions and extracting best-matching prototypes for each of the 1D, 2D partial, and 2D global feature spaces using similarity scores to the patient's first ECG of their admission. Phecode outcomes were constructed as binary matrices from diagnostic codes, with prevalence filtering applied to retain phenotypes occurring in ≥0.1% of patients. Four feature sets were evaluated: fusion classes, prototype classes, NLP-derived concepts (CUIs), and the combination of prototype embeddings and fusion classes (Prototype Combination). Logistic regression models were trained using subject-level train/test splits to prevent data leakage. Date shifting in MIMIC prevents temporal stratification of the dataset split. However, given the input features are an ECG rather than structured or clinically initiated data, there is unlikely to be significant dataset shift. Model performance assessed via area under the ROC curve (AUC) and 95% confidence intervals computed through bootstrap resampling (n=1000). This framework enabled systematic comparison of different ECG feature representations for phenotype prediction across multiple cardiovascular and systemic conditions. The conditions of interest were chosen directly based on the Phecodes examined in Hughes et al.[3]

3.5. *Software*

All data processing and statistical analyses were conducted using Python (NumPy, SciPy, scikit-learn) and PostgreSQL for database querying. ECG visualization and clustering analyses were performed using matplotlib and seaborn. ProtoECGNet[7] was trained using a Nvidia A100 (40GB PCIe) GPU with 3.0 GHz AMD Milan processors in a HIPAA-compliant environment.

Computation for this work used AMD Milan processors and took less than 24 hours to run inference on the MIMIC-IV dataset and perform association testing.

4. Results

This work evaluates whether the interpretable prototypes learned in Sethi et al.[7] are potentially useful intermediate or digital biomarkers. To do this, we took the ProtoECGNet model trained on the labeled PTB-XL dataset and performed inference on ECGs from MIMIC-IV-ECG.[8] Within MIMIC there are computer generated reports, but the cardiologists' interpretations are not available—discharge summaries are the only available notes. This means there are no gold-standard labels for ECG class prediction. Thus, in Figure 2, we show ProtoECGNet's predicted classes using PTB-XL and MIMIC to compare the populations. While many labels are predicted at near equal ratios between the two datasets, there are several predicted substantially less frequently in MIMIC, particularly NORM (normal ECG) and SR (sinus rhythm)—likely reflecting the higher patient acuity in the MIMIC cohort, which consists solely of patients admitted to the hospital.

Our prior work found advantages to learning prototypes across three branches, reflecting the way a human clinician might read an ECG: a 1D CNN with global prototypes for rhythm classification, a 2D CNN with time-localized prototypes for morphology-based reasoning, and a 2D CNN with global prototypes for diffuse abnormalities.[7] To better understand the label space, we performed principal component analysis (PCA) to the vectors of the learned prototypes from ProtoECGNet within each class (Figure 3).

In the rhythm branch, the two principal components aligned with core interpretive axes used by clinicians: the vertical axis appeared to reflect heart rate, separating bradyarrhythmias (e.g., third-degree AV block) from tachyarrhythmias (e.g., supraventricular tachycardia), while the horizontal axis partially separated sinus from non-sinus rhythms. Sinus rhythms (SR [sinus rhythm], SARRH [sinus arrhythmia], STACH [sinus tachycardia], SBRAD [sinus bradycardia]) formed a compact cluster, with 1AVB (first-degree atrioventricular block) positioned slightly superior to SR, consistent with its more frequent occurrence in low heart rate contexts. Atrial arrhythmias (AFIB [atrial fibrillation], AFLT [atrial flutter]) appeared near one another despite differing morphology. Bigeminy (BIGU) and trigeminy (TRIGU) appropriately clustered tightly, as did the supraventricular tachycardias SVTAC (supraventricular tachycardia) and PSVT (paroxysmal supraventricular tachycardia). One anomaly was SVARR (supraventricular arrythmia), which clustered with pacemaker rhythms—potentially reflecting latent similarity to atrially paced morphologies.

In the 2D morphology branch, PCA revealed structure consistent with anatomical and electrical localization. Posterior myocardial infarctions (PMI [posterior myocardial infarction], IPLMI [inferoposterolateral myocardial infarction], IPMI [inferoposterior myocardial infarction]) clustered with right-sided conduction abnormalities (CRBBB [complete right bundle branch block], LPFB [left posterior fascicular block], RVH [right ventricular hypertrophy]), reflecting shared manifestations in right precordial leads. In contrast, anterior (AMI) and inferior (IMI) myocardial infarctions clustered separately. Ischemic syndromes (ISC [nonspecific ischemia], ISCLA [ischemia in lateral leads], ISCIN [ischemia in inferior leads], ISCAL

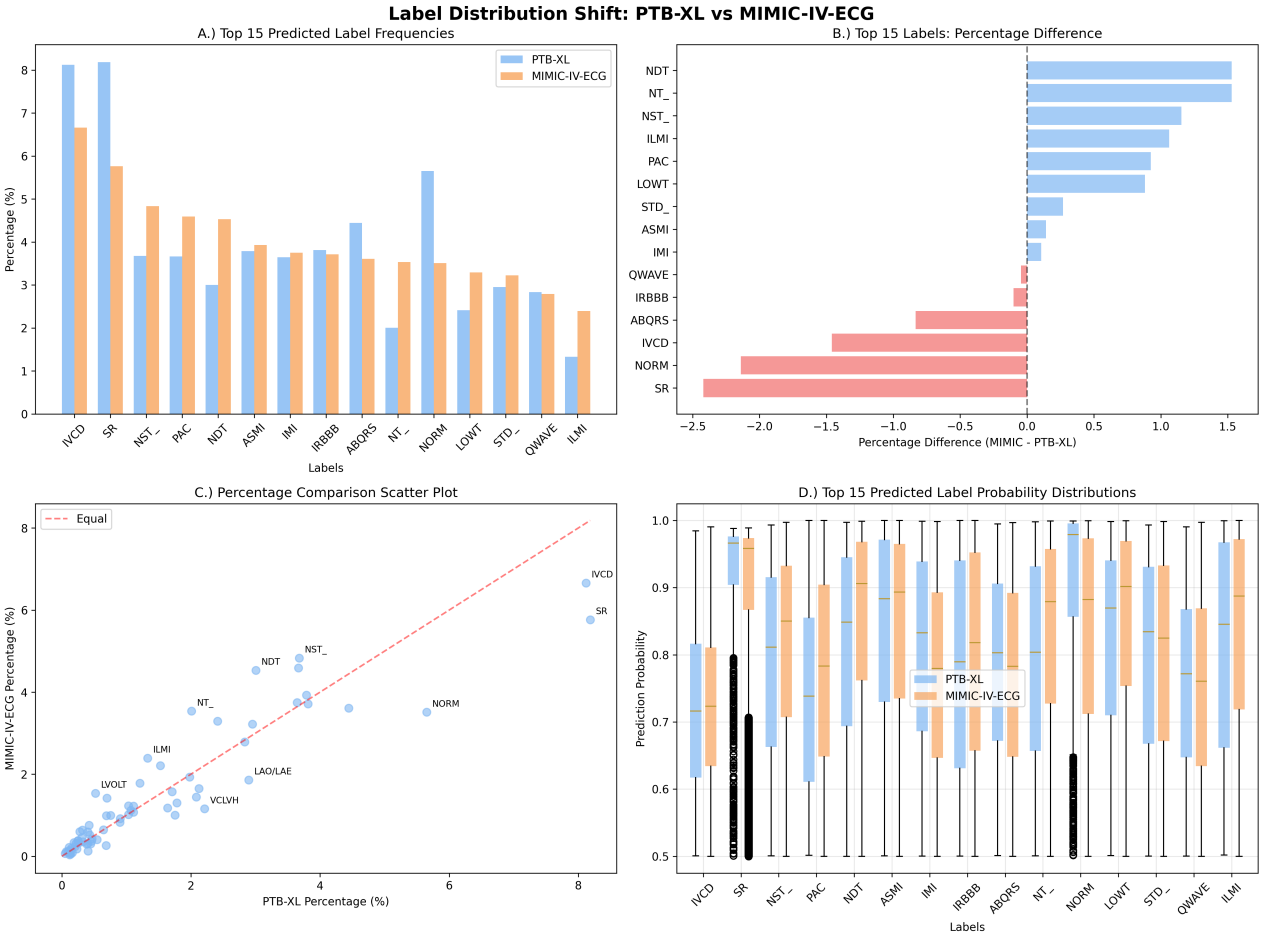

Fig. 2: Comparison of predicted label distributions between PTB-XL and MIMIC-IV-ECG. **A.)** Frequencies (percentage of samples with predicted probability ≥ 0.5) of the 15 most prevalent predicted labels in MIMIC-IV-ECG, compared across both datasets. **B.)** Percentage difference in predicted label prevalence between MIMIC-IV-ECG and PTB-XL. Positive differences indicate higher predicted prevalence in MIMIC-IV-ECG; negative differences indicate lower prevalence compared to PTB-XL. **C.)** Scatterplot comparing label frequencies in PTB-XL and MIMIC-IV-ECG, illustrating broad agreement in prevalence patterns despite dataset differences (e.g., ICU setting in MIMIC). Labels with an absolute percentage difference greater than 1.0% are annotated. The dashed line indicates equal prevalence across datasets. **D.)** Distribution of predicted probabilities for the 15 most prevalent labels in MIMIC-IV-ECG, shown for both PTB-XL and MIMIC-IV-ECG among samples where that label was predicted with probability ≥ 0.5.

[ischemia in anterolateral leads], ISCIL [ischemia in inferolateral leads]) formed a cohesive group, along with ST depressions (STD) and inverted T waves (INVT), which are often diagnostic features of ischemia. Hypertrophy patterns were more dispersed but showed partial alignment with other ECG patterns: RVH (right ventricular hypertrophy) was near right-sided conduction abnormalities, while LVH (left ventricular hypertrophy) appeared near left-sided

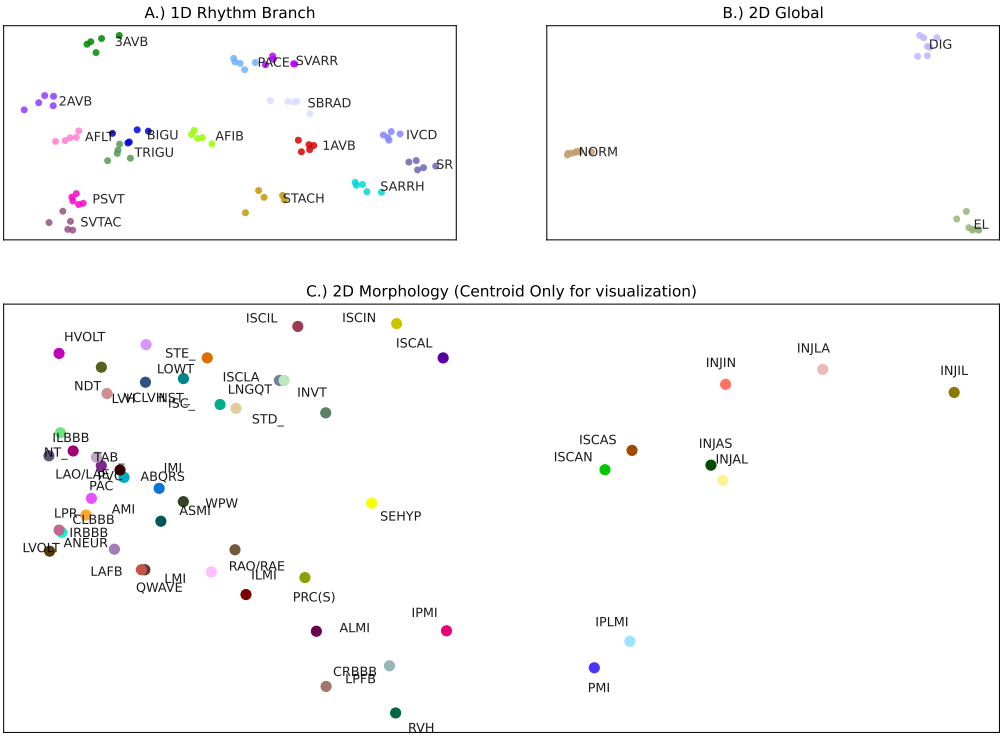

Fig. 3: Principal Component Analysis of the prototype vector embeddings for each class within the 3 branches. A.) Shows each of the 5 prototypes for the 1D rhythm branch, B.) the 7 prototypes for each class in the 2D global branch, and C.) centroids for the 18 prototypes per class in the 2D morphology branch. Only centroids are shown to reduce over-plotting and to allow for visualization. See Sethi et al. for the full list of class abbreviation definitions.[7]

conduction abnormalities, HVOLT (high QRS voltage), and nonspecific T-wave abnormalities. Wide QRS diagnoses (e.g., ILBBB [incomplete left bundle branch block], CLBBB [complete left bundle branch block], ABQRS [abnormal QRS]) partially grouped, but not uniformly. The global 2D branch included only three labels (NORM [normal ECG], EL [electrolyte disturbance or drug effect], DIG [digitalis effect]), which were clearly separated in PCA space.

Performing inference using the pretrained ProtoECGNet model produces labels at three potential levels: a.) fusion class labels are the final predicted classes based on all three branches, b.) prototype class labels are the class predictions within a single branch, and c.) prototype ID labels are the most representative prototypes for an example within the prototype class. An additional source of labels are the UMLS concepts which were extracted from the automated ECG interpretation currently in clinical use. We performed association testing via a PheWAS analysis using each of these four label groupings (Figure 4). We observed both across all Phecodes (Figure 4) and within major systems (Figure 5) that performing the association at the individual prototype level yields stronger associations than any of the other modalities. This was even true within Phecodes categorized within the Circulatory System where there may be a tautological process between the computer-generated report and the discharge diagnoses.

As an additional verification of the learned prototypes, we compared the intra-class dis-

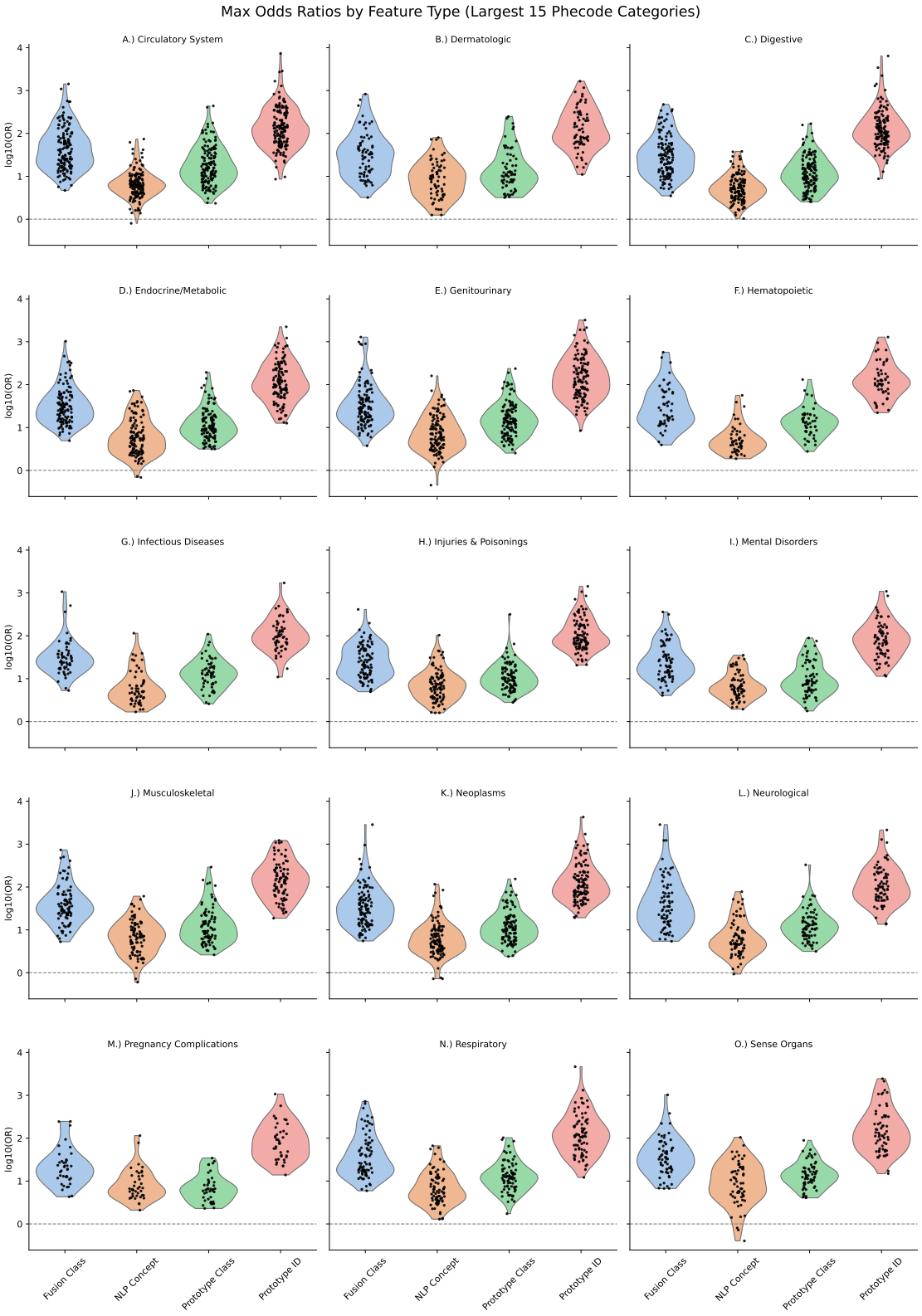

Fig. 5: Comparison of odds ratio magnitude based on each set of available labels broken down across the 15 largest Phecode categories.

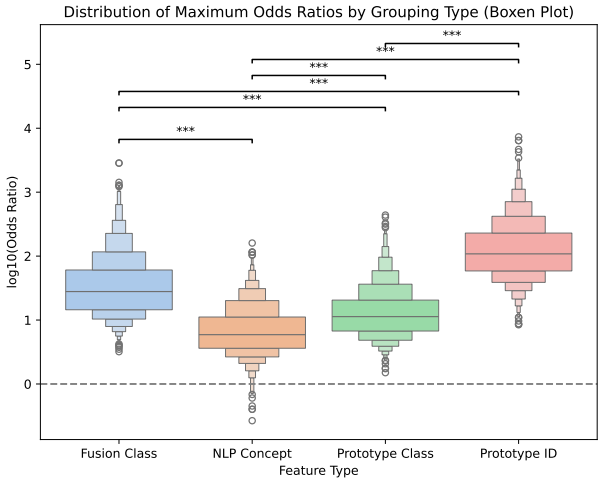

Table 1: Mean intra-class cosine distances for prototype classes with mixed or uniform significance status. A Mann–Whitney U test[18] showed a significant difference ($p < 0.0001$), and Spearman correlation between odds ratio and intra-class distance was $\rho = 0.14$, $p < 0.0001$.

Status	N	Mean	Std	95% CI
Mixed	870	0.245	0.047	[0.242, 0.248]
Uniform	73750	0.228	0.056	[0.228, 0.228]

Fig. 4: (Left.) Comparison of odds ratios based on each class of available labels. Fusion Labels: ProtoECGNet final predictions, NLP Concept: extracted diagnosis related concepts from computer generated ECG reports, Prototype Class: Branch-level class predictions within ProtoECGNet, and Prototype ID: branch-level individual prototypes most similar to a particular ECG. All pairwise comparisons are significant (*** = p-value < 0.001). Prototype ID provides the cleanest groupings for associations to phenotypes.

tances in the learned prototype embedding space (Table 1). We separated branch-level classes into groups: a.) Uniform: where all prototypes within a branch-level class were either significant or all were not significant based on the multiple testing corrected p-value, and b.) Mixed: where some of the prototypes were significant and others were not within the same branch-level class. We observe that the distance between the prototypes is significantly longer in classes where association significance was mixed (which indicates a more heterogeneous class).

Finally, we evaluated whether the prototypes could be useful for the prediction of Phecodes at discharge in a similar manner to Hughes et al[3] in Table 2. However, this cannot be a direct comparison due to two major differences. First, the models in Hughes et al. were explicitly trained to predict the outcome of interest from the raw ECG, and second, the sample size in MIMIC is substantially smaller. In contrast, ProtoECGNet was trained only to predict ECG labels. Despite these handicaps, we observed that using both the fusion classes and the representative prototypes (Prototype Combined) provided substantial signal and predicted many of the outcomes examined by Hughes et al. Intuitively, performance was especially strong for ECG-related diagnoses (e.g., atrial fibrillation), but we also observed similar trends to Hughes et al. for many of the other outcomes. This indicates that the prototypes learned by ProtoECGNet are potentially generalizable intermediate phenotypes or digital biomarkers which may be useful tools in disease specific and broader biological understanding.

5. Discussion

We have demonstrated that prototype-based neural networks trained for ECG classification can capture clinically meaningful physiologic signatures or intermediate phenotypes that ex-

Table 2: Performance of Phecode predictors based on input features (logistic regression).

Phecode	Description	Training Cases	Fusion	Class	CUI	Prototype Combined
38.0	Septicemia	3125	0.69 [0.68, 0.71]	0.69 [0.67, 0.71]	0.67 [0.65, 0.68]	0.77 [0.76, 0.79]
38.1	Gram negative septicemia	1050	0.67 [0.64, 0.70]	0.67 [0.63, 0.70]	0.61 [0.58, 0.65]	0.68 [0.65, 0.72]
260.0	Protein-calorie malnutrition	2215	0.61 [0.59, 0.63]	0.58 [0.56, 0.61]	0.58 [0.55, 0.60]	0.67 [0.65, 0.70]
260.2	severe protein-calorie malnutrition	1055	0.60 [0.57, 0.64]	0.60 [0.57, 0.64]	0.61 [0.58, 0.65]	0.71 [0.68, 0.75]
275.53	Disorders of phosphorus metabolism	1525	0.58 [0.55, 0.61]	0.57 [0.54, 0.60]	0.57 [0.53, 0.60]	0.64 [0.60, 0.67]
276.11	Hyperosmolality and/or hypernatremia	2462	0.67 [0.65, 0.70]	0.66 [0.64, 0.68]	0.64 [0.62, 0.67]	0.72 [0.70, 0.74]
276.6	Fluid overload	1328	0.62 [0.59, 0.65]	0.62 [0.59, 0.65]	0.56 [0.53, 0.59]	0.67 [0.64, 0.70]
284.1	Pancytopenia	1217	0.54 [0.51, 0.58]	0.54 [0.50, 0.57]	0.57 [0.53, 0.60]	0.59 [0.56, 0.62]
286.7	Other and unspecified coagulation defects	1112	0.65 [0.62, 0.69]	0.65 [0.62, 0.68]	0.63 [0.60, 0.66]	0.73 [0.69, 0.76]
290.2	Delirium due to conditions classified elsewhere	2646	0.64 [0.62, 0.66]	0.62 [0.60, 0.64]	0.61 [0.59, 0.63]	0.70 [0.68, 0.72]
317.11	Alcoholic liver damage	1747	0.64 [0.62, 0.67]	0.64 [0.61, 0.67]	0.64 [0.61, 0.67]	0.70 [0.67, 0.73]
395.2	Nonrheumatic aortic valve disorders	3025	0.74 [0.72, 0.76]	0.73 [0.72, 0.75]	0.68 [0.66, 0.70]	0.78 [0.76, 0.80]
395.6	Heart valve replaced	1792	0.77 [0.75, 0.79]	0.78 [0.76, 0.80]	0.74 [0.72, 0.76]	0.86 [0.84, 0.88]
411.2	Myocardial infarction	9581	0.73 [0.72, 0.74]	0.72 [0.70, 0.73]	0.71 [0.70, 0.72]	0.81 [0.79, 0.82]
411.8	Other chronic ischemic heart disease, unspecified	1360	0.83 [0.81, 0.85]	0.81 [0.79, 0.83]	0.79 [0.77, 0.82]	0.90 [0.88, 0.92]
415.2	Chronic pulmonary heart disease	3250	0.72 [0.71, 0.74]	0.71 [0.69, 0.73]	0.70 [0.68, 0.72]	0.80 [0.78, 0.82]
425.1	Primary/intrinsic cardiomyopathies	2034	0.79 [0.77, 0.81]	0.77 [0.75, 0.80]	0.77 [0.75, 0.79]	0.88 [0.86, 0.90]
427.12	Paroxysmal ventricular tachycardia	1486	0.73 [0.70, 0.75]	0.72 [0.69, 0.74]	0.73 [0.70, 0.76]	0.79 [0.76, 0.81]
427.21	Atrial fibrillation	15712	0.81 [0.80, 0.81]	0.81 [0.80, 0.82]	0.80 [0.79, 0.80]	0.89 [0.88, 0.89]
427.22	Atrial flutter	1926	0.74 [0.72, 0.76]	0.75 [0.72, 0.77]	0.73 [0.70, 0.75]	0.85 [0.83, 0.87]
427.42	Cardiac arrest	1212	0.71 [0.68, 0.74]	0.69 [0.66, 0.72]	0.70 [0.67, 0.73]	0.73 [0.71, 0.76]
428.1	Congestive heart failure (CHF) NOS	8327	0.81 [0.80, 0.81]	0.80 [0.79, 0.81]	0.80 [0.79, 0.81]	0.91 [0.90, 0.92]
428.3	Heart failure with reduced EF [Systolic or combined heart failure]	5807	0.83 [0.82, 0.84]	0.82 [0.81, 0.84]	0.80 [0.79, 0.81]	0.88 [0.87, 0.89]
428.4	Heart failure with preserved EF [Diastolic heart failure]	5842	0.73 [0.72, 0.75]	0.73 [0.72, 0.74]	0.70 [0.69, 0.72]	0.82 [0.80, 0.83]
501.0	Pneumonitis due to inhalation of food or vomitus	2325	0.67 [0.65, 0.69]	0.65 [0.63, 0.67]	0.64 [0.62, 0.66]	0.72 [0.70, 0.74]
507.0	Pleurisy; pleural effusion	2746	0.65 [0.64, 0.68]	0.63 [0.61, 0.66]	0.62 [0.60, 0.64]	0.72 [0.70, 0.74]
509.1	Respiratory failure	6355	0.67 [0.66, 0.69]	0.67 [0.66, 0.68]	0.65 [0.63, 0.66]	0.77 [0.75, 0.78]
572.0	Ascites (non malignant)	1416	0.64 [0.61, 0.67]	0.63 [0.60, 0.67]	0.57 [0.54, 0.60]	0.69 [0.66, 0.72]
585.32	End stage renal disease	2242	0.70 [0.68, 0.72]	0.68 [0.66, 0.70]	0.63 [0.60, 0.65]	0.78 [0.76, 0.80]
994.2	Sepsis	4291	0.69 [0.68, 0.71]	0.69 [0.68, 0.71]	0.66 [0.65, 0.68]	0.77 [0.76, 0.79]

tend beyond their original training objectives. Our ProtoECGNet model, trained solely on the PTB-XL dataset for multi-label ECG classification, successfully transferred to the MIMIC-IV clinical database and revealed interpretable associations with a broad spectrum of clinical phenotypes, including both cardiac and non-cardiac conditions.

Individual prototypes consistently showed stronger and more specific associations with clinical outcomes compared to fusion class predictions, NLP-extracted concepts, or broader prototype classes. This granular specificity suggests that the learned prototypes capture physiologically relevant waveform patterns that align with distinct pathophysiologic processes. Our analysis also revealed that prototype classes with mixed significance patterns (where some prototypes within a class were significantly associated with outcomes while others were not) exhibited significantly greater intra-class distances, indicating that the model learned to differentiate subtle but clinically meaningful variations within broader diagnostic categories. The prototypes also demonstrated substantial predictive utility across diverse conditions, achieving strong performance not only for cardiovascular phenotypes like atrial fibrillation (AUC

0.89) and heart failure (AUC 0.91), but also for conditions such as sepsis and renal disease, echoing the broad phenotypic associations previously observed in large-scale ECG studies.

Visualizing the learned prototype vectors revealed that the model's latent space structure mirrors key dimensions of clinical reasoning. In the rhythm branch, principal components aligned with heart rate and rhythm type—two foundational axes of ECG interpretation. Prototypes for sinus bradycardia, supraventricular tachycardia, atrial fibrillation, and paced rhythms were arranged along these axes in a manner that reflected their expected physiological and clinical relationships. Similarly, in the 2D morphology branch, prototypes for posterior myocardial infarctions clustered with right-sided conduction abnormalities, while ischemic syndromes grouped with ST depressions and T-wave inversions. These patterns suggest that, even without explicit supervision for phenotypic structure, the model organizes its internal representations to reflect established axes of clinical reasoning used in ECG interpretation.

Future work should focus on developing systematic approaches for optimal prototype selection and grouping,[19,20] potentially incorporating clinical expertise to ensure the most interpretable representations. Additionally, user studies involving cardiologists and trainees could evaluate how prototypes affect diagnostic accuracy and learning efficiency, potentially informing educational tools. Expanding this framework to incorporate temporal dynamics and multimodal physiologic signals could also enhance the utility of learned phenotypes. Prospective validation would be essential to establish their generalizability and real-world utility.

A limitation of our analysis is that its retrospective nature limits causal inference about the relationships between ECG prototypes and clinical outcomes. Additionally, the absence of expert ECG annotations in MIMIC-IV prevented direct validation of our prototype interpretations against gold-standard clinical assessments. The smaller sample size in MIMIC-IV compared to previous large-scale ECG phenotyping studies may have also limited our power to detect associations with rarer conditions. Furthermore, potential dataset shift between the training (PTB-XL) and inference (MIMIC-IV) populations, including differences in patient acuity and clinical settings, may affect the generalizability of our findings. Finally, while our approach demonstrates the potential for interpretable digital phenotyping, the clinical implementation of such models would require careful consideration of regulatory requirements, workflow integration, and ongoing real-world clinical validation. Despite these limitations, this work demonstrates a promising direction to better incorporate physiological data into phenotyping pipelines even where task-specific gold-standard labels are not available.

6. Acknowledgments

This work was funded in part by the National Institutes of Health, specifically grant number R00NS114850 to BKB. Additionally, we would like to thank the University of Chicago Center for Research Informatics (CRI) High-Performance Computing team. The CRI is funded by the Biological Sciences Division at the University of Chicago with additional funding provided by the Institute for Translational Medicine, CTSA grant number UL1 TR000430 from the NIH.

References

1. A. Y. Hannun, P. Rajpurkar, M. Haghpanahi, G. H. Tison, C. Bourn, M. P. Turakhia and A. Y. Ng, Cardiologist-level arrhythmia detection and classification in ambulatory electrocardiograms using a deep neural network, *Nature Medicine* **25**, 65 (January 2019), Publisher: Nature Publishing Group.
2. P. Elias, T. J. Poterucha, V. Rajaram, L. M. Moller, V. Rodriguez, S. Bhave, R. T. Hahn, G. Tison, S. A. Abreau, J. Barrios, J. N. Torres, J. W. Hughes, M. V. Perez, J. Finer, S. Kodali, O. Khalique, N. Hamid, A. Schwartz, S. Homma, D. Kumaraiah, D. J. Cohen, M. S. Maurer, A. J. Einstein, T. Nazif, M. B. Leon and A. J. Perotte, Deep Learning Electrocardiographic Analysis for Detection of Left-Sided Valvular Heart Disease, *JACC* **80**, 613 (August 2022), Publisher: American College of Cardiology Foundation.
3. J. W. Hughes, J. Theurer, M. Vukadinovic, A. J. Rogers, S. Somani, G. Kang, Z. Ghazizadeh, J. W. O'Sullivan, S. S. Jain, B. Gomes, M. Salerno, E. Ashley, J. Y. Zou, M. V. Perez and D. Ouyang, A deep learning phenome wide association study of the electrocardiogram, *European Heart Journal. Digital Health* **6**, 595 (May 2025).
4. C. Chen, O. Li, D. Tao, A. Barnett, C. Rudin and J. K. Su, This Looks Like That: Deep Learning for Interpretable Image Recognition, in *Advances in Neural Information Processing Systems*, (Curran Associates, Inc., 2019).
5. A. J. Barnett, F. R. Schwartz, C. Tao, C. Chen, Y. Ren, J. Y. Lo and C. Rudin, A case-based interpretable deep learning model for classification of mass lesions in digital mammography, *Nature Machine Intelligence* **3**, 1061 (December 2021), Publisher: Nature Publishing Group.
6. A. J. Barnett, Z. Guo, J. Jing, W. Ge, P. W. Kaplan, W. Y. Kong, I. Karakis, A. Herlopian, L. A. Jayagopal, O. Taraschenko, O. Selioutski, G. Osman, D. Goldenholz, C. Rudin and M. B. Westover, Improving Clinician Performance in Classifying EEG Patterns on the Ictal–Interictal Injury Continuum Using Interpretable Machine Learning, *NEJM AI* **1**, p. AIoa2300331 (May 2024), Publisher: Massachusetts Medical Society.
7. S. Sethi, D. Chen, T. Statchen, M. C. Burkhart, N. Bhandari, B. Ramadan and B. Beaulieu-Jones, ProtoECGNet: Case-Based Interpretable Deep Learning for Multi-Label ECG Classification with Contrastive Learning (May 2025), arXiv:2504.08713 [cs].
8. A. E. W. Johnson, L. Bulgarelli, L. Shen, A. Gayles, A. Shammout, S. Horng, T. J. Pollard, S. Hao, B. Moody, B. Gow, L.-w. H. Lehman, L. A. Celi and R. G. Mark, MIMIC-IV, a freely accessible electronic health record dataset, *Scientific Data* **10**, p. 1 (January 2023), Publisher: Nature Publishing Group.
9. G. Hripcsak and D. J. Albers, Next-generation phenotyping of electronic health records, *Journal of the American Medical Informatics Association: JAMIA* **20**, 117 (January 2013).
10. J. C. Denny, L. Bastarache, M. D. Ritchie, R. J. Carroll, R. Zink, J. D. Mosley, J. R. Field, J. M. Pulley, A. H. Ramirez, E. Bowton, M. A. Basford, D. S. Carrell, P. L. Peissig, A. N. Kho, J. A. Pacheco, L. V. Rasmussen, D. R. Crosslin, P. K. Crane, J. Pathak, S. J. Bielinski, S. A. Pendergrass, H. Xu, L. A. Hindorff, R. Li, T. A. Manolio, C. G. Chute, R. L. Chisholm, E. B. Larson, G. P. Jarvik, M. H. Brilliant, C. A. McCarty, I. J. Kullo, J. L. Haines, D. C. Crawford, D. R. Masys and D. M. Roden, Systematic comparison of phenome-wide association study of electronic medical record data and genome-wide association study data, *Nature Biotechnology* **31**, 1102 (December 2013), Publisher: Nature Publishing Group.
11. S. F. Friedman, S. Khurshid, R. A. Venn, X. Wang, N. Diamant, P. Di Achille, L.-C. Weng, S. H. Choi, C. Reeder, J. P. Pirruccello, P. Singh, E. S. Lau, A. Philippakis, C. D. Anderson, M. Maddah, P. Batra, P. T. Ellinor, J. E. Ho and S. A. Lubitz, Unsupervised deep learning of electrocardiograms enables scalable human disease profiling, *npj Digital Medicine* **8**, p. 23 (January 2025), Publisher: Nature Publishing Group.

12. P. Wagner, N. Strodthoff, R.-D. Bousseljot, D. Kreiseler, F. I. Lunze, W. Samek and T. Schaeffter, PTB-XL, a large publicly available electrocardiography dataset, *Scientific Data* **7**, p. 154 (May 2020), Publisher: Nature Publishing Group.
13. J. C. Denny, L. Bastarache, M. D. Ritchie, R. J. Carroll, R. Zink, J. D. Mosley, J. R. Field, J. M. Pulley, A. H. Ramirez, E. Bowton, M. A. Basford, D. S. Carrell, P. L. Peissig, A. N. Kho, J. A. Pacheco, L. V. Rasmussen, D. R. Crosslin, P. K. Crane, J. Pathak, S. J. Bielinski, S. A. Pendergrass, H. Xu, L. A. Hindorff, R. Li, T. A. Manolio, C. G. Chute, R. L. Chisholm, E. B. Larson, G. P. Jarvik, M. H. Brilliant, C. A. McCarty, I. J. Kullo, J. L. Haines, D. C. Crawford, D. R. Masys and D. M. Roden, Systematic comparison of phenome-wide association study of electronic medical record data and genome-wide association study data, *Nat. Biotechnol.* **31**, 1102 (2013).
14. M. Neumann, D. King, I. Beltagy and W. Ammar, ScispaCy: Fast and robust models for biomedical natural language processing, in *Proceedings of the 18th BioNLP Workshop and Shared Task*, (Association for Computational Linguistics, 2019).
15. O. Bodenreider, The Unified Medical Language System (UMLS): integrating biomedical terminology, *Nucleic Acids Res.* **32** (2004).
16. W. W. Chapman, W. Bridewell, P. Hanbury, G. F. Cooper and B. G. Buchanan, A simple algorithm for identifying negated findings and diseases in discharge summaries, *J. Biomed. Inform.* **34**, 301 (2001).
17. Y. Benjamini and Y. Hochberg, Controlling the false discovery rate: A practical and powerful approach to multiple testing, *J. R. Stat. Soc. Ser. B. Stat. Methodol.* **57**, 289 (1995).
18. H. B. Mann and D. R. Whitney, On a test of whether one of two random variables is stochastically larger than the other, *Ann. Math. Statistics* **18**, 50 (1947).
19. J. Bien and R. Tibshirani, Prototype selection for interpretable classification, *Ann. Appl. Stat.* **5**, 2403 (2011).
20. S. Garcia, J. Derrac, J. Cano and F. Herrera, Prototype selection for nearest neighbor classification: Taxonomy and empirical study, *IEEE Trans. Pattern Anal. Mach. Intell.* **34**, 417 (2012).

Deep Learning-based Classification of Patients with Postural Orthostatic Tachycardia Syndrome using Wearable ECG and Accelerometer Data

Hyunjun Choi[1,†], Nicholas Matsumoto[1,†], Xi Li[1], Debbie Teodorescu[2], Anxhela Kote[2], Min-Jing Yang[2], Xiao Liu[2], Miguel E. Hernandez[1,†], Jason H. Moore[1*], Graciela Gonzalez Hernandez[1*], Peng-Sheng Chen[2*]

[1]*Department of Computational Biomedicine, Center for Artificial Intelligence Research and Education, Cedars Sinai Medical Center,*
700 N. San Vicente Blvd., Pacific Design Center, Suite G-541H, West Hollywood, USA
[2]*Department of Cardiology, Smidt Heart Institute, Cedars-Sinai Medical Center,*
8700 Beverly Blvd., Davis 1016, Los Angeles CA 90048
[†]*E-mail: AISupport@csmc.edu*
www.cedars-sinai.org

Postural Orthostatic Tachycardia Syndrome (POTS) is a chronic autonomic disorder characterized by chronic ($>$ 3 months) orthostatic intolerance and an increase in heart rate (HR) of $\geq$ 30 beats per minute (bpm) without orthostatic hypotension. Traditional diagnostic approaches, such as the active standing or tilt-table test, are typically conducted under controlled clinical conditions, limiting their ability to capture the natural variability of symptoms and the intricate physiological responses occurring in daily life. These tests may cause patient discomfort, dizziness, nausea, or syncope. Furthermore, they are time-consuming and cannot be used as a screening tool for POTS. To address these limitations, this study explored wearable devices that continuously collect physiological data-specifically, electrocardiogram (ECG) and accelerometer (ACC)-derived metrics-from POTS patients and healthy controls during routine daily activities. Physiological features around posture-change events identified in the data were processed and used to train and test a baseline deep learning model. The model demonstrated promising performance in accurately differentiating POTS patients from healthy controls in a relatively small cohort (66 from POTS patients and 20 from controls), indicating its potential as a feasibility study for clinical decision support. Future studies involving larger and more diverse samples under varying clinical conditions would be necessary to enhance the robustness and viability of our diagnostic model.

.

Keywords: Postural Orthostatic Tachycardia Syndrome, POTS, Wearable devices, Diagnostic devices, Deep learning, Ambulatory monitoring, Real-world data, Daily activities, Autonomic dysfunction

1. Introduction

Postural Orthostatic Tachycardia Syndrome (POTS) is a chronic autonomic disorder characterized by chronic ($>$ 3 months) orthostatic intolerance and an increase in heart rate (HR) of

*Co-senior authors

© 2025 The Authors. Open Access chapter published by World Scientific Publishing Company and distributed under the terms of the Creative Commons Attribution Non-Commercial (CC BY-NC) 4.0 License.

≥30 beats per minute (bpm) without orthostatic hypotension during orthostatic tests.[1] It is frequently associated with dizziness, fatigue, palpitations, syncope, presyncope, and multiple other symptoms. POTS was estimated to have a prevalence of 0.2%,[1] but its incidence dramatically increased during the COVID-19 pandemic[2,3] and persists to this date. It is estimated that 2% to 14% of COVID-19 survivors develop POTS, and 9% to 61% experience POTS-like symptoms.[3] POTS can also occur after receiving mRNA vaccines for COVID-19.[4,5] The combined effects of COVID-19 infection and vaccination exposures have substantially broadened the at-risk population. Currently, the diagnosis of POTS primarily relies on clinical evaluations like the tilt-table test or active standing tests, conducted in controlled laboratory or clinical settings.[6] However, these traditional methods have notable limitations, as they are typically performed under artificial testing conditions, often failing to accurately represent the genuine variability of symptoms and the complex physiological responses patients experience daily.[7,8] The abrupt postural changes and prolonged upright positioning required during the tilt-table test may cause considerable patient discomfort, including dizziness, nausea, headache, and in some cases, temporary loss of consciousness. These tests are time-consuming and cannot be used as a screening tool in the general population. It is therefore highly desirable to develop alternative diagnostic approaches that are less burdensome and more comfortable for patients.[9,10]

To overcome these diagnostic constraints, the present study aims to evaluate the diagnostic potential of data derived from wearable technology. This technology collects physiological data from patients while they are engaged in their routine daily activities. This data serves as the foundation for developing and evaluating deep learning models intended to aid clinical decision support in POTS by detecting physiological changes occurring naturally in daily life with wearable technology.

This study introduces a novel approach that automatically identifies posture-change points and leverages ECG- and ACC-derived features from these event windows in combination with deep learning architectures to classify POTS.

2. Methods

The study includes 66 POTS patient measurements and 20 control measurements. Participants were provided with wearable monitoring devices, specifically the Faros 180 ECG monitor, capable of continuously collecting ECG and ACC data.[6] Based on ECG and ACC data, we extracted features that identify posture-change events (referred to as *changepoints* or *CPs*) that reflect physiological characteristics —including Heart Rate Change (HRC), Skin Sympathetic Nerve Activity (SKNA), and movement intensity. These features were organized into longitudinal datasets reflecting physiological state changes of each participant over time, and were used as input data for artificial intelligence (AI) models. Fig. 1 provides an overview of the proposed data-driven diagnostic framework, highlighting key stages: accelerometer-based orientation-invariant transformation (OIT)[11,12] feature extraction, changepoint detection, ECG and ACC feature extraction, sequential data preparation, and model-based classification and visualization.

2.1. *Study Population and Data Collection*

This study analyzed data from 66 POTS and 20 control measurements and was conducted with approval of the Institutional Review Board (IRB) at Cedars-Sinai Medical Center. All participants provided informed written consent prior to participation. Physiological data were recorded using a wearable biosignal monitor (Faros 180, Bittium Corp., Finland), placed on the participants' chest.[13] This device continuously captured ECG signals sampled at 1 kHz and triaxial ACC data sampled at 25 Hz along three perpendicular axes (X, Y, Z), enabling the assessment of body posture and movement over at least 24 hours. Participants were advised to perform their usual daily activities without any restrictions to ensure that the collected physiological data accurately reflected their typical daily routines.

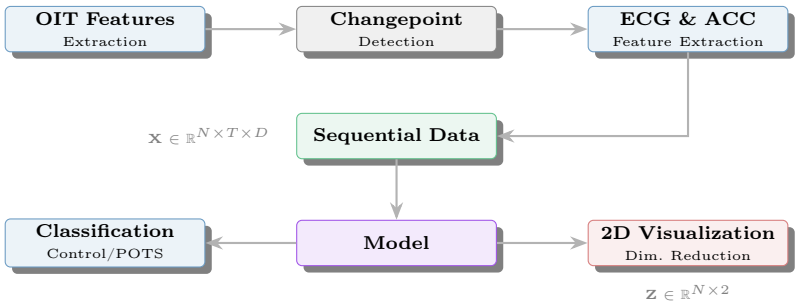

Fig. 1. Overview of our diagnostic framework. **N**: total number of subjects, **T**: sequence length, **D**: dimensionality of combined ECG and ACC features, **X**: input data representing sequential ECG and ACC features, and **Z**: 2D visualization coordinates after dimensionality reduction. The model performs end-to-end learning for both classification and representation learning.

2.2. *Data Preprocessing and Feature Extraction*

The data processing pipeline in this study can be divided into four stages: (1) noise reduction of ECG and accelerometer signals, (2) orientation-invariant transformation of accelerometer signals, (3) detection of posture-change events, and (4) extraction of ECG and ACC features around detected events.

The data collected from wearable sensors was preprocessed using already established algorithms[6,11,12,14,15] to extract features from physiological signals and to reduce noise and enhance signal quality. ECG- and ACC-based features were extracted after preprocessing, as summarized in Table 1.

For accelerometer signals, preprocessing involved applying a moving average filter with a 31-sample window to remove high-frequency noise. Subsequently, orientation-invariant ACC features were derived using the heuristic orientation-invariant transformation (Heuristic OIT).[11,12] The Heuristic OIT transforms raw three-dimensional accelerometer data into nine orientation-robust descriptors, including vector magnitudes, temporal difference norms (first- and second-order), angles between successive vectors, and angular changes computed from vector cross products. This transformation ensures robustness against variations in sensor orientation. Thus, employing Heuristic OIT features as input to the PELT (Pruned Exact Linear

Time) algorithm,[14] which identifies changepoints based on statistical shifts within time-series data, facilitates a more reliable detection of movement-related changepoints by minimizing interference from sensor orientation changes or arbitrary rotations. For ECG signals, noise reduction involved applying a 0.5–150 Hz bandpass filter to mitigate both low-frequency baseline drift and high-frequency artifacts, following the method described by Lee et al. (2022).[6]

Feature Category	Key Characteristics
ECG-based Features	
Statistical	Amplitude statistics, autocorrelation, trend analysis, Hjorth parameters
Spectral	Power spectrum, frequency entropy, wavelet decomposition
Morphological	Zero crossings, peak-trough metrics, waveform shape
Physiological	Heart rate change, SKNA burst
ACC-based Features	
Movement Intensity	Magnitude, jerk, SMA, RMS, energy metrics
Postural	Stability measures, dynamic acceleration, OIT statistics
Spatial	Rotation vector, trajectory curvature, movement patterns
Temporal	Decay time, spectral entropy, windowed analysis

Table 1: Summary of Feature Categories

Based on these Heuristic OIT features, postural transition-related changepoints were identified using the PELT algorithm.[14] This method detects changepoints by optimizing a predefined cost function that balances segmental statistical fidelity with model complexity through a penalty term. Analysis windows, varying from tens of seconds to several minutes, were subsequently defined around each detected changepoint, and physiological response characteristics were extracted from segments meeting established signal quality standards. The comprehensive methodological process employed for changepoint detection is outlined in Algorithm 1.

Measure	**Formula**	**Description**
SNR	$10 \log_{10}(P_{\text{signal}}/P_{\text{noise}})$	Signal-to-noise ratio (power ratio in dB)
TM	$\frac{\sum(x_i-\bar{x})(y_i-\bar{y})}{\sqrt{\sum(x_i-\bar{x})^2 \sum(y_i-\bar{y})^2}}$	Morphological similarity (template x_i, beat y_i)
RMSSD	$\sqrt{\frac{1}{N-1}\sum_{i=1}^{N-1}(RR_{i+1}-RR_i)^2}$	RR variability (successive RR intervals)
SDNN	$\sqrt{\frac{1}{N-1}\sum_{i=1}^{N}(RR_i-\overline{RR})^2}$	RR variability (standard deviation)
PE	$-\sum_i p_i \ln(p_i)$	Complexity entropy (p_i: ordinal probability)

Table 2: ECG Signal Quality and Variability Metrics

Orphanidou et al. (2014)[15] introduced a signal quality index (SQI) designed to quantitatively evaluate ECG signals obtained from wearable sensors, aiming to ensure the reliable extraction of heart rates. Their approach combined physiological plausibility assessments with template matching techniques to determine the reliability of ECG signal segments. Inspired by this method, our study evaluated ECG segments within patient-specific datasets using signal quality metrics commonly employed in ECG research, including signal-to-noise ratio (SNR),[16] template matching (TM),[15] and permutation entropy (PE).[17] Additionally, the root

mean square of successive differences (RMSSD)[18,19] and the standard deviation of NN intervals (SDNN)[18,19] were also utilized. The ECG signal quality and physiological metrics used for evaluating ECG segments in this study are summarized in Table 2 and were calculated following the procedure outlined in Algorithm 2. Algorithm 2 filters dataset D of ECG segments $s_{j,k}$ from subjects P_j using threshold Θ to produce D_{filtered}.

Algorithm 1 Change Point Detection via OIT[11]-PELT[14]

Require: $\boldsymbol{A} \in \mathbb{R}^{3\times M}$ ▷ Triaxial ACC data
Require: W ▷ Moving average window size
Ensure: $\mathcal{C} = \{\tau_1, \ldots, \tau_K\}$ ▷ Change points
I: $\tilde{\boldsymbol{A}} = \mathcal{F}_{\text{MA}}(\boldsymbol{A}, W)$ ▷ Smoothing with window W
II: $\boldsymbol{F}_{\text{OIT}} = f_{\text{OIT}}(\tilde{\boldsymbol{A}})$ ▷ OIT feature extraction
III: $\mathcal{C} = f_{\text{PELT}}(\boldsymbol{F}_{\text{OIT}})$ ▷ PELT detection
return $\mathcal{C}$

For these selected ECG segments, statistical metrics, Hjorth parameters, autocorrelation, linear trends, spectral characteristics, wavelet-based features, and heart rate changes were subsequently extracted. Additionally, features related to SKNA derived from ECG signals[6] were calculated. These included metrics such as burst frequency, amplitude, duration, mean area, threshold, maximum burst amplitude, and baseline statistics.

Algorithm 2 Multi-Criteria ECG Quality Assessment

Require: $\mathcal{D} = \{P_j\}_{j=1}^{N}$, $P_j = \{s_{j,k}\}_{k=1}^{M_j} \subset \mathbb{R}^T$
Require: $\Theta = \{\theta_{\text{SNR}}, \theta_{\text{corr}}, \theta^{\min}_{\text{RMSSD}}, \theta^{\max}_{\text{RMSSD}}, \theta^{\min}_{\text{SDNN}}, \theta^{\max}_{\text{SDNN}}, \theta_{\text{PE}}\}$
Ensure: $\mathcal{D}_{\text{filtered}} = \{P_j^{\text{filtered}}\}_{j=1}^{N}$
for all $P_j \in \mathcal{D}$ **do**
  $P_j^{\text{filtered}} \leftarrow \emptyset$
  for all $s_{j,k} \in P_j$ **do**
    $\pi_1(s_{j,k}) := \mathbb{I}[\text{SNR}(s_{j,k}) > \theta_{\text{SNR}}]$
    $\pi_2(s_{j,k}) := \mathbb{I}[\rho_{\text{template}}(s_{j,k}) > \theta_{\text{corr}}]$
    $\pi_{3a}(s_{j,k}) := \mathbb{I}[\text{RMSSD}(s_{j,k}) \in [\theta^{\min}_{\text{RMSSD}}, \theta^{\max}_{\text{RMSSD}}]]$
    $\pi_{3b}(s_{j,k}) := \mathbb{I}[\text{SDNN}(s_{j,k}) \in [\theta^{\min}_{\text{SDNN}}, \theta^{\max}_{\text{SDNN}}]]$
    $\pi_3(s_{j,k}) := \pi_{3a}(s_{j,k}) \wedge \pi_{3b}(s_{j,k})$ ▷ Both HRV metrics valid
    $\pi_4(s_{j,k}) := \mathbb{I}[H_{\text{perm}}(s_{j,k}) < \theta_{\text{PE}}]$
    if $\prod_{i=1}^{4} \pi_i(s_{j,k}) = 0$ **then**
      $P_j^{\text{filtered}} \leftarrow P_j^{\text{filtered}} \cup \{s_{j,k}\}$
    end if
  end for
end for
return $\mathcal{D}_{\text{filtered}}$

ACC-derived features were extracted, encompassing movement intensity, motion metrics, movement patterns, acceleration magnitude, jerk magnitude, signal magnitude area (SMA), zero-crossing rate (ZCR), energy, decay time, spectral entropy, rotation vector, wavelet-

based descriptors, maximum movement intensity, and overall statistics derived from Heuristic OIT.[11,12] Algorithm 3 performs multimodal feature extraction around change points $\mathcal{C} = \{\tau_i\}_{i=1}^{N}$ using multiple window sizes $\mathcal{W} = \{w_1, w_2, ..., w_K\}$. For each change point τ_i, it creates pre-change ($W^- = [\tau_i - w, \tau_i)$) and post-change ($W^+ = [\tau_i, \tau_i + w]$) windows from 3-axis accelerometer data $\tilde{\boldsymbol{A}} \in \mathbb{R}^{3\times T}$, OIT features $\boldsymbol{F}_{\text{OIT}} \in \mathbb{R}^{9\times T}$, and ECG signals $\boldsymbol{e} \in \mathbb{R}^{T}$. The algorithm applies the feature extraction functions Φ_{ACC}, Φ_{OIT}, and Φ_{ECG} to extract respective features, and then combines these features into comprehensive feature vectors $\mathcal{F}$.

Algorithm 3 ECG & ACC Feature Extraction

Require: $\tilde{\boldsymbol{A}} \in \mathbb{R}^{3\times T}$, $\boldsymbol{F}_{\text{OIT}} \in \mathbb{R}^{9\times T}$, $\boldsymbol{e} \in \mathbb{R}^{T}$ ▷ ACC, OIT, ECG signals
Require: $\mathcal{C} = \{\tau_i\}_{i=1}^{N}$, $\mathcal{W} = \{w_1, w_2, ..., w_K\}$ ▷ Change points, window sizes
Ensure: $\mathcal{F} = \{\boldsymbol{f}_{i,w}^{-}, \boldsymbol{f}_{i,w}^{+}\}_{i,w}$ ▷ Multimodal features

for all $(\tau_i, w) \in \mathcal{C} \times \mathcal{W}$ **do**
  $W^- = [\tau_i - w, \tau_i)$, $W^+ = [\tau_i, \tau_i + w]$
  for all $W \in \{W^-, W^+\}$ **do**
    ACC features: $\boldsymbol{f}_{\text{ACC}} = \Phi_{\text{ACC}}(\tilde{\boldsymbol{A}}|_W)$
    OIT features: $\boldsymbol{f}_{\text{OIT}} = \Phi_{\text{OIT}}(\boldsymbol{F}_{\text{OIT}}|_W)$
    ECG features: $\boldsymbol{f}_{\text{ECG}} = \Phi_{\text{ECG}}(\boldsymbol{e}|_W)$
    $\boldsymbol{f}_W = [\boldsymbol{f}_{\text{ACC}}, \boldsymbol{f}_{\text{OIT}}, \boldsymbol{f}_{\text{ECG}}]$ ▷ Concatenate all features
  end for
end for
return $\mathcal{F}$

2.3. *Model Development and Training*

Recent studies have investigated the application of various artificial intelligence methodologies to ACC and ECG data across multiple tasks. These approaches have demonstrated their utility for anomaly detection and activity classification.[11,12,20–28] In line with these advancements, this study implemented and evaluated two baseline deep learning models to classify patients with POTS from healthy controls using wearable-derived ECG and accelerometer (ACC) features.

The first model was a Transformer-based classifier[29] employing the Attention with Linear Biases (ALiBi) mechanism.[30] This model consisted of six transformer layers, each layer having a hidden dimension of 128, eight attention heads, and a dropout rate of 0.3. Gradient checkpointing was applied for memory optimization.

The second model was a hybrid architecture combining Convolutional Neural Networks (CNN), Bidirectional Long Short-Term Memory (BiLSTM), and self-attention mechanisms (CNN-BiLSTM-Attention).[31,32] The CNN layer contained 64 filters with kernel size 3, followed by two layers of Bidirectional LSTM units, each with a hidden size of 128. A self-attention layer was included to emphasize important temporal segments. The packed sequence method was employed to handle variable sequence lengths.

All models were optimized using Adam with a learning rate of 1×10^{-4}, weight decay of 1×10^{-4}, and coefficients set as $\beta_1 = 0.9$, $\beta_2 = 0.999$. To mitigate issues related to class imbalance, Focal Loss was applied with parameters $\gamma = 2.0$ and $\alpha = 0.25$. Training proceeded

using batches of size 8 for up to 100 epochs.

Data augmentation strategies—including jittering (σ=0.01), scaling (σ=0.1), and permutation (n=4 segments)—were applied to improve model generalization. Additionally, gradient clipping with a threshold of 1.0 and a ReduceLROnPlateau learning rate scheduler were employed to ensure stable model training.

To evaluate model performance, a 10-fold stratified cross-validation was performed. The ratio of POTS patients and control subjects was kept consistent within each fold.

During training in each fold, outliers were identified and handled. Criteria for handling outliers were determined exclusively from each fold's training data and consistently applied to validation data. The standardization process followed the same method.

Performance metrics, including balanced accuracy, sensitivity, specificity, precision, recall, F1-score, and AUC, were recorded at each training epoch. Confusion matrices for the best-performing model in each fold were saved. Results from all folds were summarized using means and standard deviations.

In the holdout evaluation, the model was trained using approximately 70% of the total dataset, which included data from both POTS patients and control subjects. Additionally, around 10% of the dataset was separately allocated for validation purposes. Finally, model performance was assessed using a test dataset comprising roughly 20% of the total data, which was not utilized at any stage during training or validation. All data splits were performed at the session level.

Preprocessing parameters, including standardization and criteria for outlier handling determined during training, were consistently applied to the test dataset.

The trained models classified each sample in the test set as either POTS or control. Additionally, learned feature representations were visualized using dimensionality reduction techniques, enabling comparison between the distributions of test set and those of the training and validation sets.

3. Results

3.1. *Comparative Feature Analysis*

Physiological data collected from wearable sensors were analyzed to investigate potential differences between individuals diagnosed with POTS and healthy control participants. The analyzed features included the previously described ECG and accelerometer-derived metrics, comprising statistical, spectral, morphological, physiological, movement intensity, postural, spatial, and temporal characteristics.

Welch's t-tests revealed that a total of 1169 features showed statistically significant differences between groups after applying the Benjamini-Hochberg false discovery rate correction (FDR, $q < 0.05$). Notably significant features with an FDR-adjusted q-value less than 0.001 included SKNA burst duration, heart rate changes, logarithmic-scale complexity measures, SMA computed both 10 minutes before events and within 10-minute intervals, ECG amplitude maxima over 1-minute intervals, and variance-based principal component characteristics measured around event intervals ($\pm$10 minutes). Detailed statistical results for these significant features—including exact q-values and 95% confidence intervals—are summarized in Table 3.

Boxplots of these significant features listed in Table 3 are presented in Figure 2.

Overall, the analysis demonstrated that physiological features extracted within specific temporal windows around each detected changepoint exhibited statistically significant differences between POTS patients and healthy control participants. The visualization and statistical assessments further suggested that these features could have potential utility in distinguishing between the two groups. These analytical findings provided valuable direction for selecting meaningful features and designing input features for the development of AI-based classification models.

Feature	**FDR q-value**	**95% CI**
ECG max (1 min)	<0.001	[0.253, 0.284]
SMA (10 min)	<0.001	[0.329, 0.361]
EVR PC2 (10 min)	<0.001	[0.371, 0.403]
SKNA burst dur. (5 min)	<0.001	[0.231, 0.262]
SKNA burst dur. (10 min)	<0.001	[0.226, 0.257]
log Hjorth compl. (10 min)	<0.001	[0.198, 0.229]
log Hjorth compl. (5 min)	<0.001	[0.192, 0.224]
log Hjorth compl. (1 min)	<0.001	[0.181, 0.212]
log Hjorth compl. (30 sec)	<0.001	[0.168, 0.199]
HR change (10 min)	<0.001	[0.113, 0.144]
HR change (5 min)	<0.001	[0.098, 0.130]
HR change (1 min)	<0.001	[0.080, 0.112]

Table 3: Detailed Statistical Results for All Features (CP = Changepoint; EVR = Explained Variance Ratio; dur. = duration; compl. = complexity; HR = Heart Rate)

Note: Welch's t-test was used for all comparisons. FDR = False Discovery Rate adjusted q-value; CI = 95% Confidence Interval for effect sizes calculated using Hedges' g. All listed features are significant at FDR-adjusted $q < 0.001$.

3.2. *Classification Performance*

The generalization performance of each model was evaluated using 10-fold stratified cross-validation, and the results are summarized in Table 4.

The Transformer model achieved a balanced accuracy of 0.825 ± 0.116, sensitivity of 0.800 ± 0.135, and precision of 0.940 ± 0.079. This model also demonstrated specificity of 0.850 ± 0.198, an F1-score of 0.841 ± 0.093, and an AUC of 0.813 ± 0.181.

The CNN-BiLSTM-Attention (CNN-BiLSTM) model exhibited higher scores compared to the Transformer across all reported metrics, except for precision. Specifically, the model achieved a balanced accuracy of 0.900 ± 0.084 and sensitivity of 0.950 ± 0.062, indicating a reduced likelihood of false negatives. Furthermore, this model had specificity of 0.850 ± 0.142 and precision of 0.935 ± 0.062. Additionally, the CNN-BiLSTM-Attention model recorded an F1-score of 0.939 ± 0.052 and an AUC of 0.900 ± 0.103.

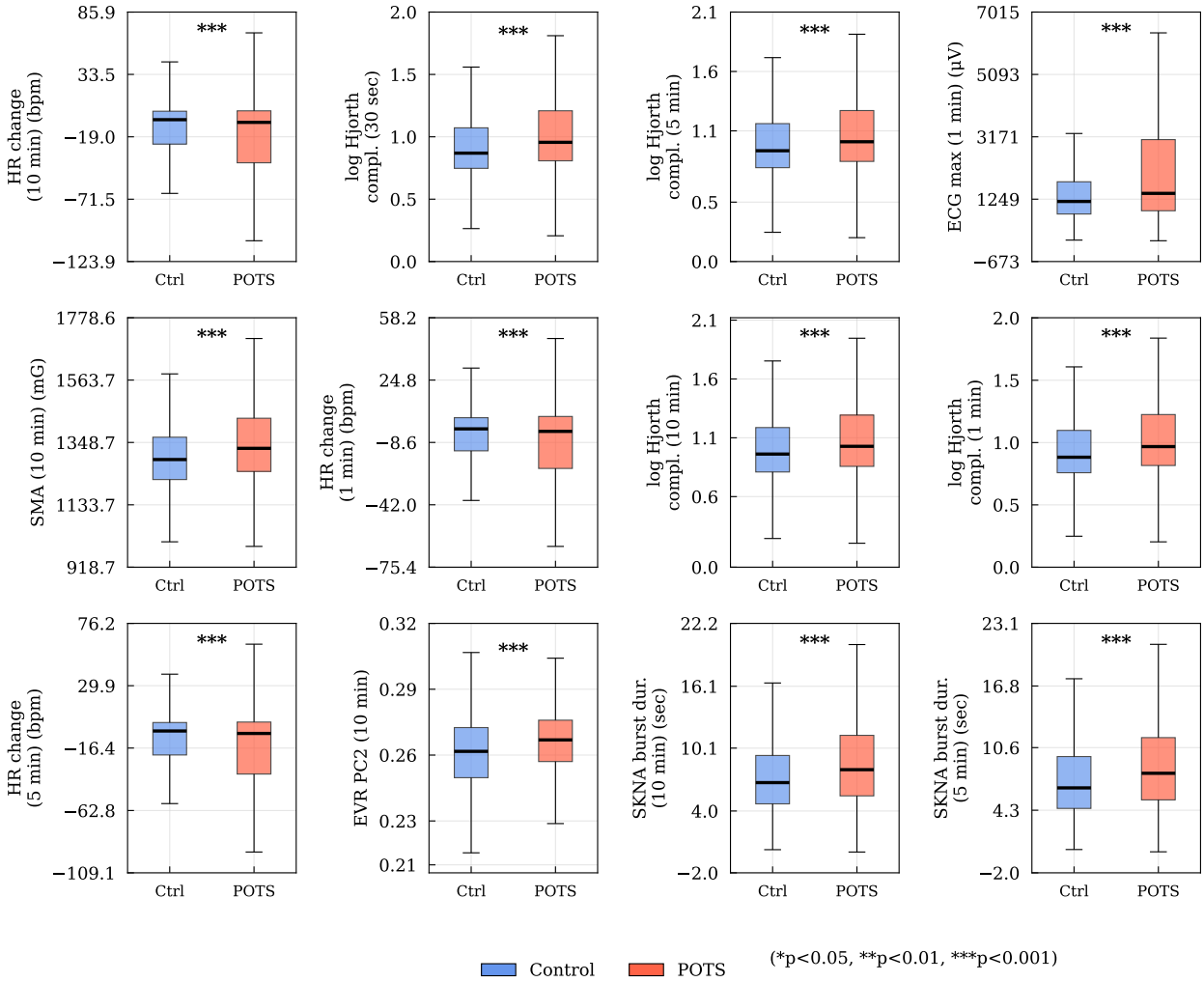

Fig. 2. Comparison of physiological variables between Control and POTS groups

Metric	**Model Architecture**	
	Transformer	CNN-BiLSTM
Balanced Accuracy	0.825 ± 0.116	**0.900 ± 0.084**
Sensitivity	0.800 ± 0.135	**0.950 ± 0.062**
Specificity	0.850 ± 0.198	**0.850 ± 0.142**
Precision	**0.940 ± 0.079**	0.935 ± 0.062
F1 Score	0.841 ± 0.093	**0.939 ± 0.052**
AUC-ROC	0.813 ± 0.181	**0.900 ± 0.103**

Table 4: 10-Fold Cross-validation performance metrics (mean ± 95% confidence interval).

To evaluate the practical performance of the final models trained on the complete dataset, validation was performed using a holdout test set.

The CNN-BiLSTM model exhibited superior overall validation performance compared to

the Transformer model, achieving higher balanced accuracy (86.77% vs. 85.01%), sensitivity (93.55% vs. 90.32%), specificity (96.67% vs. 94.93%), and F1-score (95.08% vs. 93.33%), except for specificity, which was equal (80% vs. 80%). The complete comparison of these validation metrics is provided in Table 5, indicating that the CNN-BiLSTM model may be more effective for classifying this particular dataset than the Transformer model.

Metric	Transformer	CNN-BiLSTM
Balanced Accuracy	85.01%	**86.77%**
Sensitivity	90.32%	**93.55%**
Specificity	80.00%	80.00%
Precision	94.93%	**96.67%**
F1 Score	93.33%	**95.08%**

Table 5: Validation performance metrics

Feature space visualization (Fig. 4) further illustrates the capability of the CNN-BiLSTM-Attention model in distinguishing between POTS patients and healthy controls. Dimensionality reduction techniques, including PCA, t-SNE, and UMAP, applied to the high-dimensional latent representations transformed by this model, revealed separation between the two groups in the two-dimensional feature space, indicating effective discrimination. Additionally, the test set data from POTS patients closely align with the distribution of the existing POTS group, suggesting the model's robustness and potential to generalize effectively to new patient data.

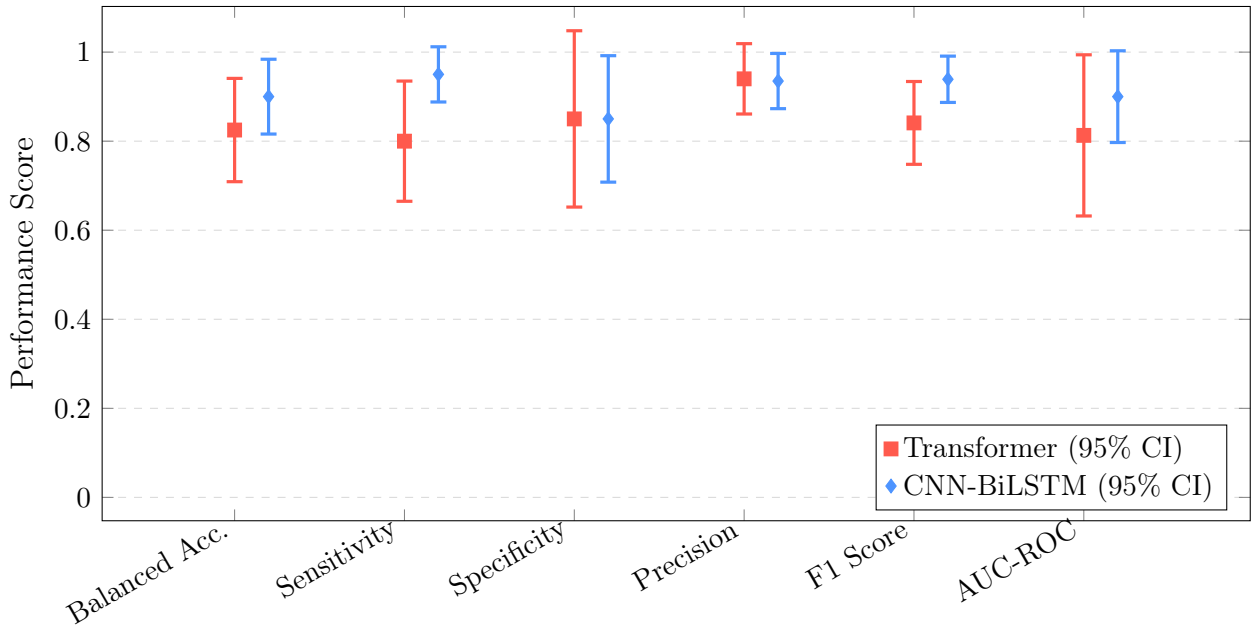

Fig. 3. 10-Fold Cross Validation Results with 95% Confidence Intervals: Model performance comparison with mean values and confidence intervals.

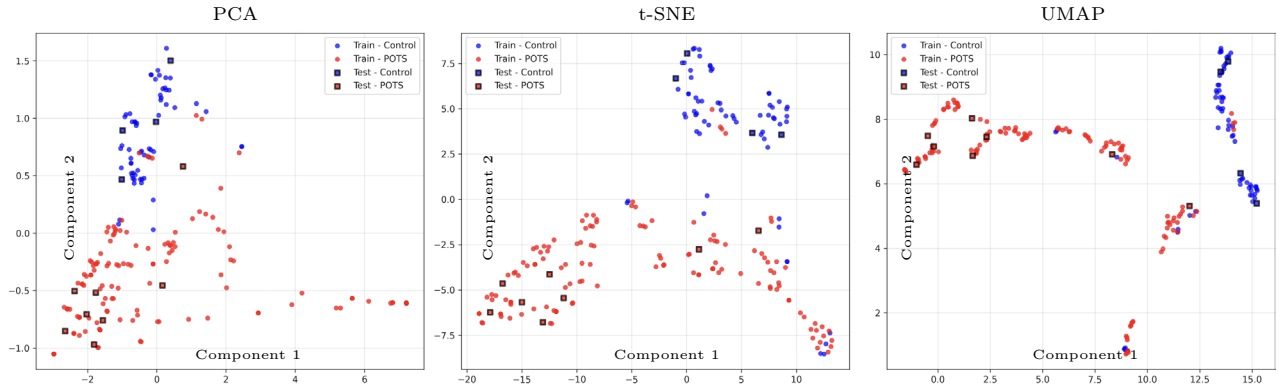

Fig. 4. Feature Space Visualization - CNN-BiLSTM-Attention Model

4. Discussion

The findings of this study suggest potential clinical implications for enhancing the diagnostic approach to POTS. In contrast, the wearable-based methodology employed in this study facilitates continuous and unobtrusive monitoring of subtle yet potentially clinically relevant changes in physiological signals, including ECG and accelerometer-derived features, as they occur naturally in real-world settings. The deep learning models trained on wearable sensor data demonstrated promising performance in differentiating between POTS patients and healthy controls. Nonetheless, to establish the robustness of these findings and evaluate their clinical applicability, it is essential to perform additional validation studies that include expanded patient cohorts, varied clinical settings, and more comprehensive control-group datasets.

Despite the promising results, several considerations must be acknowledged regarding this study. First, the dataset used in this research may not fully represent the broad diversity of clinical conditions and patient populations, suggesting that further validation with larger and more representative samples is required to enhance the generalizability and clinical applicability of the diagnostic models. Second, this study focused primarily on specific physiological signals; therefore, integrating additional physiological parameters or external environmental factors in future research may further improve model generalizability and practical clinical applicability. In addition, the POTS cohort included both patients taking treatment medications and those who were not. Therefore, it remains necessary in future research to clarify explicitly whether the developed classifier is detecting disease-specific signals or instead patterns driven by medication use or other confounding factors.

Additionally, the physiological parameters analyzed in this research—including features derived from ECG and ACC data—may hold diagnostic promise for conditions beyond POTS, indicating potential utility across multiple clinical scenarios. Prior studies have shown ECG and HRV parameters to be valuable in evaluating autonomic dysfunction related to heart failure, cardiac arrhythmias, and diabetes mellitus.[33,34] Likewise, accelerometry-derived metrics have been successfully utilized in assessing motor abnormalities in neurological diseases such as Parkinson's disease and in assessing fall risk among older adults.[35,36] Future research may focus on investigating the potential of these physiological metrics in additional disease contexts, thereby supporting the creation of broadly applicable diagnostic technologies targeting diverse neurological and autonomic conditions.

5. Conclusion

This study investigated the feasibility of using deep learning techniques with features extracted from wearable-derived ECG and ACC data to differentiate patients diagnosed with POTS from healthy controls. The proposed wearable-based approach effectively captured subtle yet clinically significant physiological variations and symptom patterns occurring naturally in daily life. It demonstrates its potential to address key limitations of conventional diagnostic tests such as the tilt-table test. Two deep learning architectures, specifically the Transformer and hybrid CNN-BiLSTM models, demonstrate promising performance that suggests potential applicability in real-world clinical scenarios. The proposed integration of wearable-derived physiological signal analysis and deep learning techniques holds promise for future patient-centered diagnostics and improved clinical management for individuals with POTS.

6. Acknowledgments

This study was supported in part by institutional funds from the Cedars-Sinai Center for AI Research and Education (CAIRE), the American Heart Association grant 23IPA1052289, the United States National Institutes of Health grants R01 HL139829 and OT2OD028190, and the Burns & Allen Chair in Cardiology Research of the Cedars-Sinai Medical Center. In addition, Graciela Gonzalez-Hernandez was funded in part by the National Institute of Allergy and Infectious Diseases (NIAID), National Institutes of Health, under Award Number R01AI164481.

References

1. R. S. Sheldon, B. P. Grubb II, B. Olshansky, W.-K. Shen, H. Calkins, M. Brignole, S. R. Raj, A. D. Krahn, C. A. Morillo, J. M. Stewart et al., 2015 heart rhythm society expert consensus statement on the diagnosis and treatment of postural tachycardia syndrome, inappropriate sinus tachycardia, and vasovagal syncope, Heart rhythm **12**, e41 (2015).
2. D. Dulal, A. Maraey, H. Elsharnoby, P. Chacko and B. Grubb, Impact of covid-19 pandemic on the incidence and prevalence of postural orthostatic tachycardia syndrome, European Heart Journal-Quality of Care and Clinical Outcomes , p. qcae111 (2025).
3. C. K. Ormiston, I. Świątkiewicz and P. R. Taub, Postural orthostatic tachycardia syndrome as a sequela of covid-19, Heart rhythm **19**, 1880 (2022).
4. A. C. Kwan, J. E. Ebinger, J. Wei, C. N. Le, J. R. Oft, R. Zabner, D. Teodorescu, P. G. Botting, J. Navarrette, D. Ouyang et al., Apparent risks of postural orthostatic tachycardia syndrome diagnoses after covid-19 vaccination and sars-cov-2 infection, Nature cardiovascular research **1**, 1187 (2022).
5. D. L. Teodorescu, A. Kote, J. N. Reaso, C. Rosenberg, X. Liu, A. C. Kwan, S. Cheng and P.-S. Chen, Postural orthostatic tachycardia syndrome after covid-19 vaccination, Heart Rhythm **21**, 74 (2024).
6. A. Lee, X. Liu, C. Rosenberg, S. Borle, D. Hwang, L. S. Chen, X. Li, N. B. Merz and P.-S. Chen, Skin sympathetic nerve activity in patients with chronic orthostatic intolerance, Heart Rhythm **19**, 1141 (2022).
7. W. B. Plash, A. Diedrich, I. Biaggioni, E. M. Garland, S. Y. Paranjape, B. K. Black, W. D. Dupont and S. R. Raj, Diagnosing postural tachycardia syndrome: comparison of tilt testing compared with standing haemodynamics, Clinical science **124**, 109 (2013).

8. H. Lee, P. A. Low and H. A. Kim, Patients with orthostatic intolerance: relationship to autonomic function tests results and reproducibility of symptoms on tilt, Scientific reports **7**, p. 5706 (2017).
9. L. Xu, X. Cao, R. Wang, Y. Duan, Y. Yang, J. Hou, J. Wang, B. Chen, X. Xue, B. Zhang et al., Clinical features of patients undergoing the head-up tilt test and its safety and efficacy in diagnosing vasovagal syncope in 4,873 patients, Frontiers in Cardiovascular Medicine **8**, p. 781157 (2022).
10. T. Furukawa, Role of head-up tilt table testing in patients with syncope or transient loss of consciousness, Journal of arrhythmia **33**, 568 (2017).
11. A. Yurtman and B. Barshan, Activity recognition invariant to sensor orientation with wearable motion sensors, Sensors **17**, p. 1838 (2017).
12. A. Yurtman, Activity recognition invariant to position and orientation of wearable motion sensor units, PhD thesis, Bilkent Universitesi (Turkey)2019.
13. X. Liu, C. Rosenberg, J. Ricafrente, M. E. Leier, H. Dinh, T. H. Everett and P.-S. Chen, Using an ambulatory electrocardiogram monitor to record skin sympathetic nerve activity, Heart rhythm **19**, 330 (2022).
14. R. Killick, P. Fearnhead and I. A. Eckley, Optimal detection of changepoints with a linear computational cost, Journal of the American Statistical Association **107**, 1590 (2012).
15. C. Orphanidou, T. Bonnici, P. Charlton, D. Clifton, D. Vallance and L. Tarassenko, Signal-quality indices for the electrocardiogram and photoplethysmogram: Derivation and applications to wireless monitoring, IEEE journal of biomedical and health informatics **19**, 832 (2014).
16. M. Elgendi, Optimal signal quality index for photoplethysmogram signals, Bioengineering **3**, p. 21 (2016).
17. M. Henry and G. Judge, Permutation entropy and information recovery in nonlinear dynamic economic time series, Econometrics **7**, p. 10 (2019).
18. T. Pham, Z. J. Lau, S. A. Chen and D. Makowski, Heart rate variability in psychology: A review of hrv indices and an analysis tutorial, Sensors **21**, p. 3998 (2021).
19. M. G. Frasch, Comprehensive hrv estimation pipeline in python using neurokit2: Application to sleep physiology, MethodsX **9**, p. 101782 (2022).
20. Y. Zheng, Z. Liu, R. Mo, Z. Chen, W.-s. Zheng and R. Wang, Task-oriented self-supervised learning for anomaly detection in electroencephalography, in International Conference on Medical Image Computing and Computer-Assisted Intervention, 2022.
21. A. Jiang, C. Huang, Q. Cao, Y. Xu, Z. Zeng, K. Chen, Y. Zhang and Y. Wang, Anomaly detection in electrocardiograms: Advancing clinical diagnosis through self-supervised learning, arXiv preprint arXiv:2404.04935 (2024).
22. R. Hribar and D. Torkar, Explainable anomaly detection of 12-lead ecg signals using denoising autoencoder, in Intelligent Secure Trustable Things, (Springer, 2024) pp. 127–140.
23. R. Liu, A. A. Ramli, H. Zhang, E. Henricson and X. Liu, An overview of human activity recognition using wearable sensors: Healthcare and artificial intelligence, in International Conference on Internet of Things, 2021.
24. A. R. Javed, M. U. Sarwar, S. Khan, C. Iwendi, M. Mittal and N. Kumar, Analyzing the effectiveness and contribution of each axis of tri-axial accelerometer sensor for accurate activity recognition, Sensors **20**, p. 2216 (2020).
25. J. Park, D.-W. Kim and J. Lee, Calanet: Cheap all-layer aggregation for human activity recognition, Advances in Neural Information Processing Systems **37**, 69419 (2024).
26. E. J. Huang and J.-P. Onnela, Augmented movelet method for activity classification using smartphone gyroscope and accelerometer data, Sensors **20**, p. 3706 (2020).
27. M. Kos, M. Bogdan, N. W. Glynn and J. Harezlak, Classification of human physical activity based on raw accelerometry data via spherical coordinate transformation, Statistics in medicine **39**, 2901 (2020).

28. M. A. Alsheikh, A. Selim, D. Niyato, L. Doyle, S. Lin and H.-P. Tan, Deep activity recognition models with triaxial accelerometers., in AAAI workshop: artificial intelligence applied to assistive technologies and smart environments, 2016.
29. A. Vaswani, N. Shazeer, N. Parmar, J. Uszkoreit, L. Jones, A. N. Gomez, Ł. Kaiser and I. Polosukhin, Attention is all you need, Advances in neural information processing systems **30** (2017).
30. O. Press, N. A. Smith and M. Lewis, Train short, test long: Attention with linear biases enables input length extrapolation, arXiv preprint arXiv:2108.12409 (2021).
31. J. P. Chiu and E. Nichols, Named entity recognition with bidirectional lstm-cnns, Transactions of the association for computational linguistics **4**, 357 (2016).
32. X. Yin, Z. Liu, D. Liu and X. Ren, A novel cnn-based bi-lstm parallel model with attention mechanism for human activity recognition with noisy data, Scientific Reports **12**, p. 7878 (2022).
33. U. Acharya, L. Min and P. Joseph, Hrv analysis using correlation dimension and dfa innovations technol, Biol. Med.(ITBM-RBM) **23**, 333 (2002).
34. F. Shaffer and J. P. Ginsberg, An overview of heart rate variability metrics and norms, Frontiers in public health **5**, p. 258 (2017).
35. S. Patel, K. Lorincz, R. Hughes, N. Huggins, J. Growdon, D. Standaert, M. Akay, J. Dy, M. Welsh and P. Bonato, Monitoring motor fluctuations in patients with parkinson's disease using wearable sensors, IEEE transactions on information technology in biomedicine **13**, 864 (2009).
36. A. Weiss, T. Herman, N. Giladi and J. M. Hausdorff, Objective assessment of fall risk in parkinson's disease using a body-fixed sensor worn for 3 days, PloS one **9**, p. e96675 (2014).

Patch-level phenotype identification via weakly supervised neuron selection in sparse autoencoders for CLIP-derived pathology embeddings

Keita Tamura[1,†], Yao-zhong Zhang[2,†,*], Yohei Okubo[2] and Seiya Imoto[2,*]

1. School of Medicine, Hiroshima University, Hiroshima, 734-8553, Japan

2. Division of Health Medical Intelligence, Human Genome Center, The Institute of Medical Science, The University of Tokyo, Tokyo, 108-8639, Japan

[*] *Corresponding E-mail: yaozhong@ims.u-tokyo.ac.jp and imoto@hgc.jp*

[†] *Equal contribution*

Computer-aided analysis of whole slide images (WSIs) has advanced rapidly with the emergence of multi-modal pathology foundation models. In this study, we propose a weakly supervised neuron selection approach to extract disentangled representations from CLIP-derived pathology foundation models, leveraging the interpretability of sparse autoencoders. Specifically, neurons are ordered and selected using whole-slide level labels within a multiple instance learning (MIL) framework. We investigate the impact of different pre-trained image embeddings derived from general and pathology images and demonstrate that a selected single neuron can effectively enable patch-level phenotype identification. Experiments on the Camelyon16 and PANDA datasets demonstrate both the effectiveness and explainability of the proposed method, as well as its generalization ability for tumor patch identification.

Keywords: Whole-slide image; Sparse autoencoder; Explainable AI

1. Introduction

Whole-slide images (WSIs)—gigapixel digital scans of histopathological slides—have become central to the digitization of diagnostic pathology. They are now routinely used to assist pathologists with tumor grading, biomarker quantification, and prognostic risk stratification. Owing to their cellular-level resolution, WSIs have the potential to reduce inter-observer variability and reveal subtle spatial patterns that are difficult to discern by eye. However, these advantages come with significant technical challenges. A single WSI can exceed 100,000 × 100,000 pixels, making naïve end-to-end model training computationally infeasible. Additionally, tissue appearance varies widely across scanners, laboratories, and staining protocols, while diagnostically relevant structures are often sparse and heterogeneous. Although slide-level labels (e.g., "tumor present") are relatively easy to acquire, generating detailed patch-wise or pixel-wise annotations is labor-intensive and costly, resulting in a severe supervision bottleneck.

To address the challenges of weak supervision and extreme resolution, most modern computational pathology pipelines adopt a multiple-instance learning (MIL)[1] framework. In this paradigm, each slide is divided into hundreds or thousands of tiles (also referred to as patches

© 2025 The Authors. Open Access chapter published by World Scientific Publishing Company and distributed under the terms of the Creative Commons Attribution Non-Commercial (CC BY-NC) 4.0 License.

throughout the text). Each tile is encoded into a feature vector using a representation network, and the resulting embeddings are aggregated via a pooling operator to produce a slide-level prediction trained using only global labels. For tile-level representation, early MIL approaches used generic convolutional neural networks pretrained on natural image datasets such as ImageNet[2,3] (e.g., ResNet[4]). More recent methods have shifted toward domain-specific pathology foundation models, such as UNI,[5] a self-supervised vision transformer trained on over 100 million tiles from more than 100,000 WSIs, and GigaPath,[6] which scales pretraining to over one billion tiles to capture gigapixel context. In parallel, CLIP-based vision-language models (e.g., CONCH[7]) align pathology images with textual descriptions to produce semantically rich embeddings that support zero-shot phenotype querying via natural language. For bag-level aggregation, a variety of strategies have been developed, each influencing slide-level performance differently. These include simple pooling methods (e.g., max, mean), attention-based pooling, gated attention mechanisms, and more expressive set-based functions such as Deep Sets or Transformer-style pooling. Both the choice of representation and the method of aggregation play critical roles in the effectiveness and generalizability of MIL-based WSI models.

While these methods have demonstrated strong slide-level performance, patch-level interpretability is increasingly important for clinical translation. MIL inherently provides coarse localization of discriminative regions by associating predictions with patch-level features. Among existing approaches, the type of method using attention-based aggregator with MIL, such as ABMIL[8] and CLAM,[9] has become a popular method due to its ability to assign learnable weights to individual tiles, highlighting regions most influential to the final prediction. This enables the generation of attention heatmaps without requiring dense annotations. However, a key limitation of attention-based aggregator is that attention weights are normalized within each slide, making them non-comparable across different WSIs. This restricts their utility in standardized patch-level phenotype identification and limits population-scale interpretability. Moreover, the attention mechanism typically operates over entangled high-dimensional representations, which are difficult to interpret biologically.

To overcome these limitations, we draw inspiration from recent advances in model interpretability using sparse autoencoders (SAEs).[10] Recently introduced for dissecting representations in large language models (LLMs)[11] and protein language models (PLMs),[12] SAEs project dense embeddings into sparse, overcomplete spaces by enforcing sparsity constraints during training. Remarkably, many individual neurons in the SAE bottleneck correspond to monosemantic units, each selectively activating for specific, semantically coherent concepts—such as a functional motif in a protein sequence or a syntactic role in text. These properties make SAEs powerful tools for understanding and manipulating the internal representations of large foundation models.

Building on SAE for embeddings of the pathology foundation model, we propose a novel framework for patch-level phenotype identification via weakly supervised neuron selection. Specifically, we train an SAE on CLIP-like pathology embeddings and identify single neurons whose activation patterns correlate with slide-level labels within the MIL paradigm. These neurons represent disentangled, semantically meaningful features that are both predictive of slide-level outcomes and spatially localizable at the patch level, thus enabling interpretable

phenotype annotation without requiring dense supervision. We conducted experiments on the Camelyon16 and PANDA datasets, and the results demonstrate that the proposed approach achieves competitive performance in tumor patch identification while offering interpretable and generalizable spatial phenotyping.

2. Methods

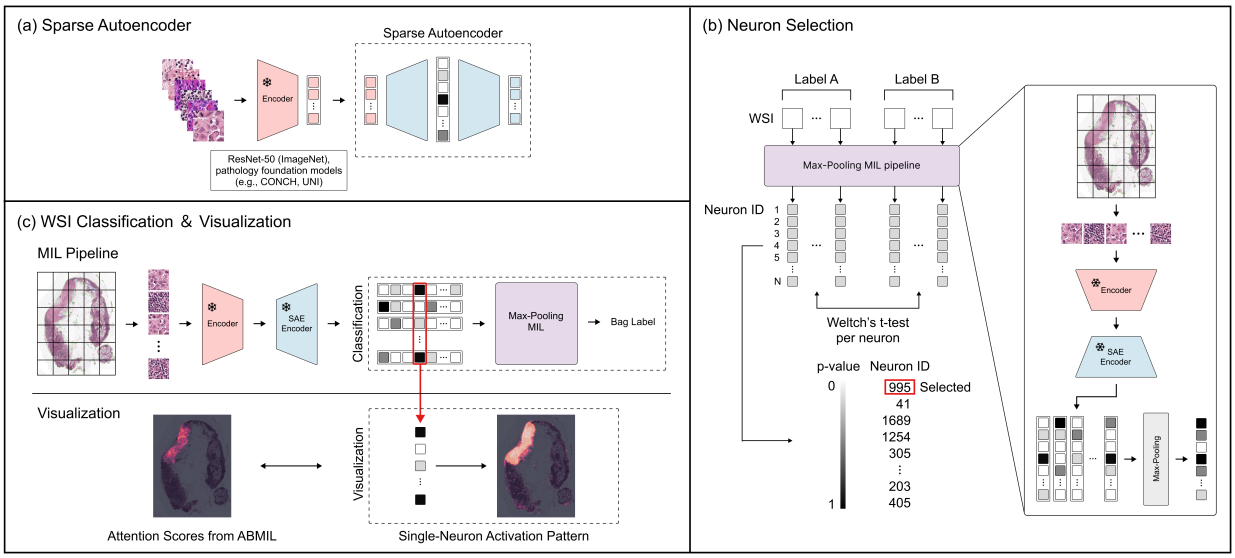

Fig. 1. Overall pipeline of the proposed SAE-1N method. (a) SAE applied for different embeddings of patch images. (b) Neuron selection method for SAE disentangled neurons with weak supervision from the whole-slide labels. (c) MIL pipelines for the whole-slide level classification and patch-level classification with a selected neuron.

An overview of our proposed method SAE-1N is illustrated in Figure 1. SAE-1N denotes the single-neuron selection strategy based on disentangled neurons derived from a sparse autoencoder (SAE). We begin by applying an SAE to disentangle latent representations from patch-level embeddings extracted using a pretrained pathology foundation model. Each latent neuron is then evaluated for its capacity to support whole-slide phenotype classification within a multiple instance learning (MIL) framework. To identify the most informative neurons, we assess their discriminative power between phenotype classes using statistical testing, enabling principled neuron ranking and selection. The top-ranked neurons are subsequently employed for downstream tasks, such as slide- and patch-level phenotype prediction.

2.1. *Sparse Autoencoder for Disentangled Representation*

Sparse autoencoders (SAEs) have emerged as a powerful framework for disentangling superposed representations in high-dimensional neural embeddings. By learning sparse and overcomplete latent codes, SAEs promote the emergence of monosemantic units—individual neurons that consistently correspond to human-interpretable concepts. This property has been

successfully leveraged in mechanistic interpretability studies of large language models,[11] protein language models,[12] and structure–function models such as Evo2,[13] where SAEs have been shown to recover latent dimensions aligned with semantic, biochemical, or structural factors from otherwise entangled activations.

The model architecture of SAE follows the conventional encoder–decoder design of autoencoders but employs an overcomplete latent space, where the number of latent units substantially exceeds the input dimensionality. For learning sparse and overcomplete latent codes, we adopt the BatchTopK Sparse Autoencoder (SAE-BatchTopK),[14] an extension of SAE-TopK.[15] SAE-TopK constrains each input to activate exactly k latent units, which improves interpretability but imposes a fixed sparsity level per sample. SAE-BatchTopK generalizes this idea by enforcing the sparsity constraint across a mini-batch, thereby encouraging feature reuse, allowing per-sample variability, and maintaining consistent average sparsity during training. In practice, this enables simpler inputs to be represented with fewer active neurons, while more complex inputs naturally recruit a larger subset, yielding more flexible and efficient representations.

SAE-BatchTopK was trained to minimize a loss consisting of a reconstruction term and an auxiliary penalty that discourages persistent neuron inactivity. Given a batch of B inputs $\{x_i\}_{i=1}^{B}$ of size D, the total loss is defined as $\mathcal{L} = L_{\text{recon}} + L_{\text{aux}}$, where $L_{\text{recon}} = \frac{1}{BD}\sum_{i=1}^{B} \|x_i - \hat{x}_i\|_2^2$ is the reconstruction loss, and $L_{\text{aux}} = \frac{\lambda_{\text{aux}}}{BD}\sum_{i=1}^{B} \| \sum_{j\in\mathcal{D}} w_j h_{i,j} - (x_i - \hat{x}_i)\|_2^2$ is the auxiliary loss to avoid dead latents. Here, $h_i = W_{\text{enc}} x_i + b_{\text{enc}}$ is the latent activation, $\tilde{h}_i = \text{BatchTopK}(h_i)$ the sparsified vector, $\hat{x}_i = W_{\text{dec}}\tilde{h}_i + b_{\text{dec}}$ the reconstruction, w_j the j-th column from the decoding weights W_{dec}, and $\mathcal{D}$ indexes latent units inactive for $n_{\text{inactive}} = 5$ consecutive batches. As the default setting, training was conducted per dataset for 100 epochs using the Adam optimizer ($\text{lr} = 10^{-3}, \beta_1 = 0.9, \beta_2 = 0.99$), with a batch size of 4096 and gradient norm clipping at 10^5. Decoder weights were re-normalized after each update, and the checkpoint with the lowest validation loss was selected for downstream analysis. Complete configuration details are available in the supplementary material. In the following sections, SAE and SAE-BatchTopK are used interchangeably.

2.2. *Pretrained Pathology Models for Patch Embedding*

The emergence of large-scale foundation models has significantly reshaped the landscape of computational pathology. Early approaches commonly relied on convolutional neural networks (CNNs) pretrained on natural image datasets such as ImageNet,[2] with architectures like ResNet-50[4] serving as generic feature extractors for histopathology patches. While these models provided a strong starting point for weakly supervised learning frameworks such as multiple-instance learning (MIL), their limited domain specificity constrained performance on complex pathology tasks. Recent advances, such as CONCH (CONtrastive learning from Captions for Histopathology)[7] and UNI,[16] have demonstrated that representations learned directly from large-scale pathology data can generalize more effectively across diverse diagnostic settings. These models, typically built upon Vision Transformer backbones and trained using multimodal contrastive or self-supervised objectives, yield domain-specialized embeddings that substantially improve downstream WSI-level classification. However, the result-

ing feature spaces are increasingly high-dimensional and entangled. Despite their predictive strength, these embeddings remain difficult to interpret, presenting a growing performance–interpretability trade-off that limits clinical transparency.

To explore the internal structure and interpretability of high-dimensional embeddings from pathology foundation models, we analyze patch-level features extracted from three representative pretrained encoders. Whole-slide images (WSIs) are first segmented into non-overlapping patches of size 256×256 at a resolution of $0.5\,\mu$m/pixel using the CLAM framework.[9] The following models are used to generate patch-level embeddings: (1) ResNet-50,[4] pretrained on ImageNet,[2] as a conventional convolutional baseline, producing 1024-dimensional features; (2) UNI,[16] a self-supervised Vision Transformer trained on over 100 million image patches from diagnostic slides using a DINOv2-style distillation framework,[17] yielding 1024-dimensional embeddings optimized for general-purpose tissue representation; and (3) CONCH,[7] a CLIP-style foundation model built on a CoCa architecture,[18] trained on 1.17 million image–caption pairs to align histopathology patches with free-text descriptions, producing 512-dimensional semantically enriched embeddings. These diverse encoders reflect the spectrum of representation learning strategies in computational pathology, ranging from natural image transfer learning to large-scale self-supervised and multimodal pretraining. We applied SAE-BatchTopK to each set of patch embeddings to assess whether sparse, monosemantic structure could be recovered from these dense representations. We paid particular attention to CONCH, as its multimodal alignment provides a compelling test case for evaluating interpretability through disentanglement.

2.3. *Disentangled Neuron Explainability and Neuron-phenotype Association*

For identifying the potential meaning of the neurons disentangled by SAEs, prior work has explored various strategies across domains such as language modeling and computational pathology. In the context of large language models (LLMs), mechanistic interpretability studies utilize sparse autoencoders in combination with prompt-based querying to associate individual neurons with semantic functions, often by inspecting example activations.[11] In pathology, ProtoMIL[19] introduces an end-to-end explainable multiple-instance learning (MIL) framework that first trains a sparse autoencoder to extract high-level, human-interpretable concepts from patch-level embeddings. These concepts are then used for slide-level classification. Crucially, ProtoMIL supports *human-in-the-loop* interpretability by enabling domain experts to manually inspect and disable irrelevant or spurious concepts, thereby aligning model predictions more closely with clinical reasoning.

In this work, we propose a weakly supervised strategy to associate whole-slide phenotype labels with individual patch-level neurons disentangled by the sparse autoencoder. Analogous to how neuron activations are profiled in large language models (LLMs) to capture shared input semantics, our approach treats the slide-level supervision as an indirect indicator of neuron selectivity. However, unlike LLM-based methods that rely on coarse approximations of neuron meaning or manual annotation, our method directly links each neuron to a specific whole-slide label. This precise supervision enables the identification of neurons that are both

semantically aligned and highly discriminative, supporting downstream applications such as patch-level phenotype annotation with improved interpretability.

We develop a neuron selection framework that identifies SAE neurons associated with whole-slide phenotype labels. Taking Camelyon16 as an example, where WSIs are labeled as tumor-positive or tumor-negative at the whole-slide level, we leverage patch-level embeddings from pretrained encoders and link them to slide-level signals through statistical inference. This enables explanation at the neuron level without requiring dense annotations or human-in-the-loop labeling. After training SAE-BatchTopK, we compute each neuron's slide-level activations by max-pooling across all patches P_i from slide i: $a_{i,j} = \max_{p \in P_i} h_{p,j}$, where $h_{p,j}$ is the activation of neuron j for patch p. Slides are grouped by phenotype into tumor-positive ($\mathcal{P}^+$) and tumor-negative ($\mathcal{P}^-$) sets based on slide-level labels. To assess neuron–phenotype association, we apply Welch's t-test to compare activation distributions:

$$t_j = \frac{\bar{a}_j^+ - \bar{a}_j^-}{\sqrt{\frac{s_{+,j}^2}{|\mathcal{P}^+|} + \frac{s_{-,j}^2}{|\mathcal{P}^-|}}}, \tag{1}$$

where $\bar{a}_j^{\pm}$ and $s_{\pm,j}^2$ denote the mean and variance of slide-level activations across slides in each phenotype. Neurons are then ranked by statistical significance (i.e., p-values), and top-ranked units are selected as interpretable detectors for downstream patch-level phenotype identification. In SAE-1N, only the top-1 neuron is selected for use.

This approach links sparse neuron activations to weak supervisory signals, aligning tumor-associated neurons with localized high-activation patterns. By isolating individual units associated with disease states, this method provides a transparent mechanism for tracing WSI-level predictions back to single, interpretable features, thereby enhancing explainability while incurring only a reduced compromise in predictive performance.

3. Results

We evaluated the proposed method on two benchmark whole-slide image datasets: Camelyon16 and PANDA. The Camelyon16 dataset is a widely used benchmark for evaluating algorithms in the automated detection of breast cancer metastases in lymph node whole-slide images. It comprises a total of 399 WSIs, including 270 training slides sourced from two pathology centers and 129 test slides. The dataset provides both slide-level labels and detailed pixel-level annotations of tumor regions. During training, only whole-slide labels were used in a weakly supervised manner. For evaluation, however, we additionally incorporated patch-level and pixel-level annotations to assess model performance. We conducted five-fold stratified cross-validation on the Camelyon16 dataset for slide-level metastasis classification.

The PANDA (Prostate cANcer graDe Assessment) dataset is a large-scale benchmark comprising more than 10,000 prostate WSIs collected from two institutions: Radboud University Medical Center (Radboud) and Karolinska Institutet (Karolinska). The Radboud data contain fine-grained, gland-centric annotations that distinguish stroma from epithelium, whereas the Karolinska data provide region-level masks in which both benign and cancer regions include stromal and epithelial tissue. For slide-level cancer detection, we reformulated the ISUP grades such that Grade Group 0 was considered normal, whereas Grade Groups 1–5 were considered

tumors. For the patch-level segmentation task, categories 3–5 in Radboud data and category 2 in Karolinska data were treated as tumor, while categories 0–2 in Radboud data and categories 0–1 in Karolinska data were treated as non-tumor. Owing to its larger scale relative to Camelyon16, we performed experiments under both mixed-institution and independent-institution splits. In each setting, the data were randomly partitioned into training, validation, and test sets following an 80/10/10 ratio.

3.1. *SAE enables disentanglement of superposed features in neural representations*

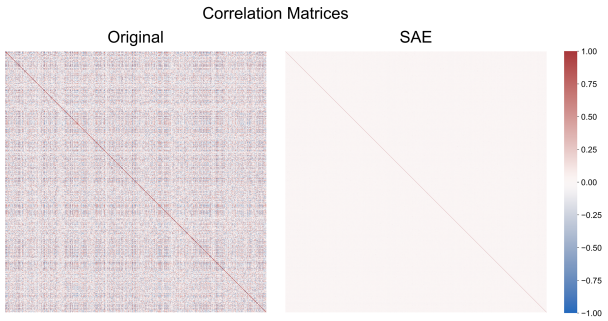

Fig. 2. Correlation matrices of latent neuron activations before and after applying the SAE to CONCH embeddings on the Camelyon16 validation set. The left panel shows the correlation matrix (512×512) of the individual units in the original CONCH embeddings. The right panel displays the correlation matrix (2048×2048) of the neurons in the SAE-transformed representations of the same embeddings.

Figure 2 presents the Pearson correlation matrices of neuron activations before and after applying the SAE to CONCH embeddings on the Camelyon16 validation set. (In the left panel, each unit in the original CONCH embedding is treated as a neuron.) Each neuron is represented by its activation values across all samples. After applying the SAE, the correlation values at off-diagonal positions generally decrease, indicating the effectiveness of the disentanglement achieved by the SAE.

3.2. *Benchmarking Multiple Instance Learning Models with Diverse Embeddings and Aggregation Methods*

To benchmark performance, we evaluated multiple MIL models using various pretrained embeddings and aggregation strategies on the Camelyon16 data, including MaxMIL, MeanMIL, ABMIL,[8] CLAM,[9] TransMIL,[20] and MambaMIL.[21] MaxMIL and MeanMIL are used as baselines. ABMIL introduces a trainable soft attention mechanism that assigns adaptive weights to individual instances, enabling the model to focus on diverse discriminative regions while maintaining interpretability. CLAM (single- or multi-branch) extends ABMIL with class-specific attention and feature-space clustering regularization.TransMIL incorporates transformers to model long-range spatial dependencies among patches, and MambaMIL leverages a state-

space sequence model to efficiently capture global context across large bags of instances. For patch-level image embeddings, we evaluate three widely used pretrained encoders: ResNet-50, trained on natural images from ImageNet; CONCH, a CLIP-style model pretrained on paired pathology images and text captions; and UNI, a self-supervised Vision Transformer trained on a large-scale corpus of diagnostic whole-slide pathology images.

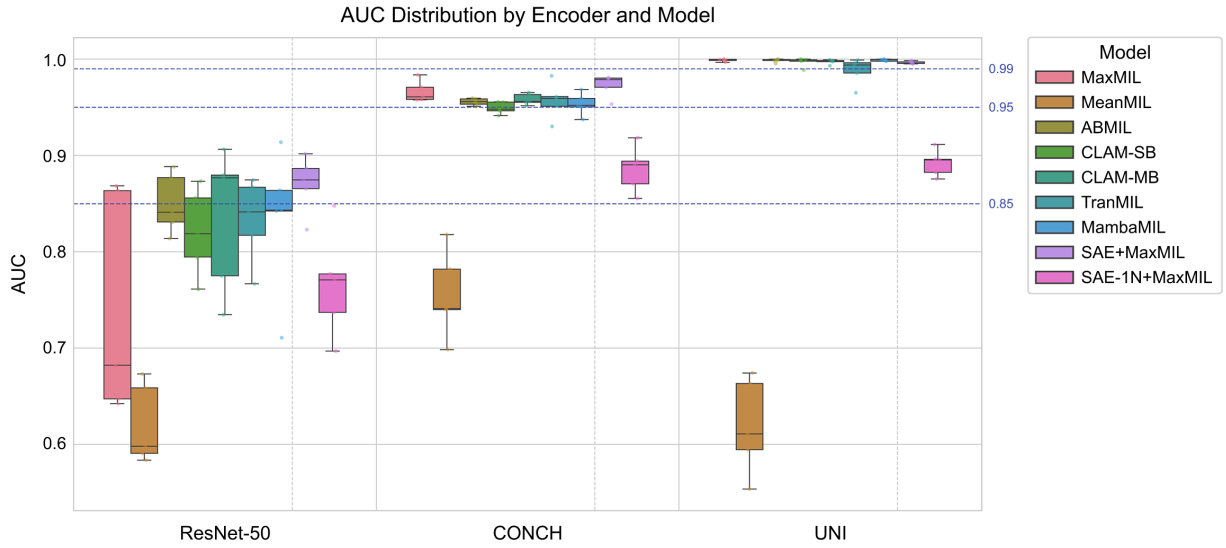

Fig. 3. Whole-slide level performance of different MIL models using various pretrained embeddings (ResNet-50, CONCH, and UNI) on the Camelyon16 dataset. Area Under the Curve (AUC) scores are reported as the primary performance metric. Accuracy results are provided in the supplementary material.

As illustrated in Figure 3, pathology-specific pretrained encoders (CONCH and UNI) consistently outperform the general-purpose ResNet-50 encoder across all multiple instance learning (MIL) models on the Camelyon16 dataset. For instance, using ABMIL, the UNI encoder achieves the highest mean AUC, followed closely by CONCH. In contrast, ResNet-50 yields the lowest performance with the widest interquartile ranges, indicating greater variability and less robust feature extraction. These results underscore the necessity of domain-specific pretraining: encoders trained on large-scale histopathology datasets capture tissue-relevant cues that are absent in models pretrained on natural images like ImageNet. This observation also aligns with findings reported for pathology-based embeddings in survival analysis.[22]

Across all three encoders, MeanMIL consistently produced the weakest performance. This limitation is particularly pronounced in the Camelyon16 dataset, where tumor regions occupy only a small fraction of each WSI—causing average pooling to dilute the discriminative signal from informative patches. In contrast, MaxMIL emerges as a strong baseline, particularly when paired with a high-quality encoder. For example, the UNI encoder combined with MaxMIL achieved median AUC and accuracy scores of 0.9988 and 0.9752, respectively. Attention-based models such as ABMIL, CLAM-SB, and CLAM-MB, as well as transformer-based models like

TransMIL and MambaMIL, generally matched or slightly outperformed MaxMIL approaches. Among them, MambaMIL exhibited the most consistent performance across encoders, suggesting that global sequence modeling further enhances feature aggregation. Therefore, the quality of pretrained embeddings is a dominant factor in WSI-level classification performance, and while architectural innovations in MIL can offer marginal gains, better encoders can elevate simple pooling strategies to near-optimal performance.

3.3. *Phenotype Discrimination with SAE-1N on different Embeddings*

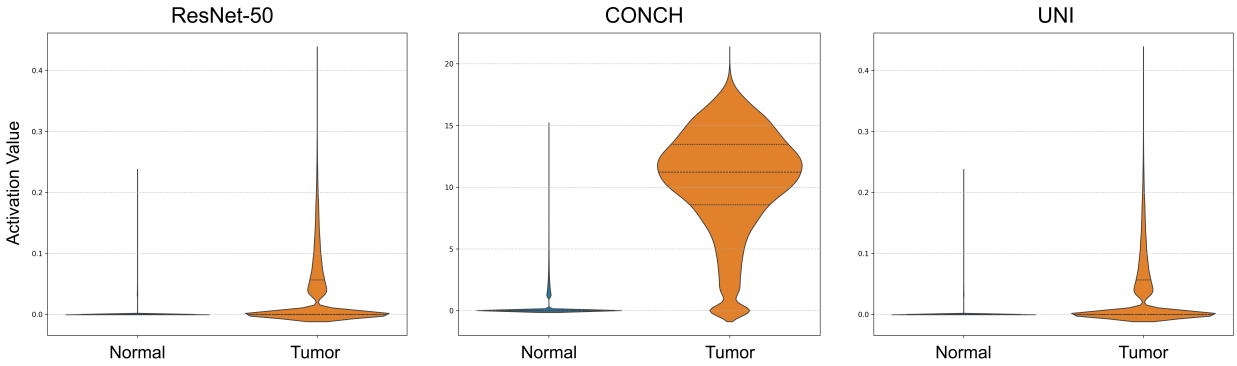

Fig. 4. Violin plots depicting activation distributions of the top-selected SAE neurons for each encoder (ResNet-50, CONCH, and UNI). Activations are grouped according to patch-labels ("Normal" and "Tumor"), derived from pixel-level annotations in Camelyon16, where patches containing $\geq 20\%$ annotated tumor regions are labeled as "Tumor".

We evaluated the effectiveness of the proposed method across different embedding types using pixel-level annotations. Patch-level labels ("Normal" and "Tumor") were derived from the Camelyon16 training set, where patches containing $\geq 20\%$ annotated tumor regions were labeled as "Tumor". To assess the discriminative power of the selected neuron, we grouped patches by their assigned labels and examined the activation values of the selected neuron within each group. As shown in Figure 4, SAE-1N using the CONCH embedding exhibits a clear distinction between tumor and normal patches, whereas SAE-1N applied to ResNet-50 and UNI embeddings does not demonstrate such separation. Since UNI embeddings are also pre-trained on pathology images, one possible explanation for the stronger discriminative capacity of CONCH embeddings is their use of contrastive learning between pathology images and textual descriptions. This cross-modal alignment may coarsely encode phenotype-relevant information into the embeddings, enabling SAE-1N to isolate disentangled neurons that are more effective for phenotype discrimination.

3.4. *Comparison of SAE-1N and Attention-Based Methods for Patch-Level Phenotype Identification*

We further compared the performance of SAE-1N with attention-based MIL models, including ABMIL, CLAM-SB, CLAM-MB, and TransMIL, where attention scores were used empirically

to infer patch-level predictions. For the original CONCH embeddings, we leveraged the model's zero-shot capability within a contrastive learning framework. Text embeddings were generated using CONCH's text encoder with the prompt "An image of metastatic breast carcinoma in a lymph node" for Camelyon16 and "An image of prostate cancer" for the PANDA dataset. Cosine similarity between this text embedding and each patch image embedding was then computed to produce a heatmap. Following prior work,[23] prediction thresholds for the above methods were determined using the validation set, guided by patch-level annotations to optimize classification performance.

Table 1. Comparison of spatial overlap performance on the Camelyon16 and PANDA datasets. For Camelyon16, results are reported as mean Dice coefficients with standard deviations obtained from five-fold cross-validation. For PANDA, Dice coefficients are provided for the combined Radboud and Karolinska (R&K) set, as well as for the Radboud and Karolinska subsets individually.

Method	**Camelyon16**	**PANDA**		
		R&K	**Radboud**	**Karolinska**
Zero-shot (CONCH)	0.1612 (± 0.0107)	0.5361	0.5969	0.4990
ABMIL	0.5146 (± 0.0482)	0.5606	0.6198	0.5017
CLAM-SB	0.4785 (± 0.0630)	0.5563	0.5822	0.4767
CLAM-MB	0.5551 (± 0.0208)	0.5781	0.5596	0.4945
TransMIL	0.0950 (± 0.0269)	0.4566	0.4443	0.4549
SAE-1N	0.6135 (± 0.0309)	0.5705	0.6375	0.5129

The performance results are presented in Table 1. On Camelyon16, SAE-1N achieves the mean Dice score (0.6135), outperforming attention-based MIL methods such as ABMIL (0.5146), CLAM-SB (0.4785), and CLAM-MB (0.5551). On the PANDA dataset, SAE-1N also performs competitively: it achieves 0.5705 on the combined Radboud & Karolinska (R&K) split, surpassing ABMIL (0.5606) and CLAM-SB (0.5563), and achieves the best score on Radboud (0.6375), while obtaining 0.5129 on Karolinska. The zero-shot method exhibits strong sensitivity to text prompt design. Its performance is relatively lower on Camelyon16, and it further decreases to 0.0942 when the prompt is changed to "An image of tumor". Overall, SAE-1N demonstrates the effectiveness of leveraging a single selected neuron to target epithelial regions in WSIs for patch-level phenotype identification.

3.5. *Interpretable Phenotype Visualization Using SAE-1N*

We visualized the activation values of the selected neuron from SAE-1N to highlight phenotype-relevant regions. Three representative whole-slide images from the Camelyon16 test set were selected, each containing tumors of different sizes (small, medium, and large). For the PANDA dataset, one example was randomly selected from Radboud and one from Karolinska. The activation maps from SAE-1N were compared with the attention scores produced by the ABMIL model.

As shown in Figure 5, attention-based methods such as ABMIL often highlight only a subset of the tumor region, even in slides where the tumor occupies a large area. This limitation

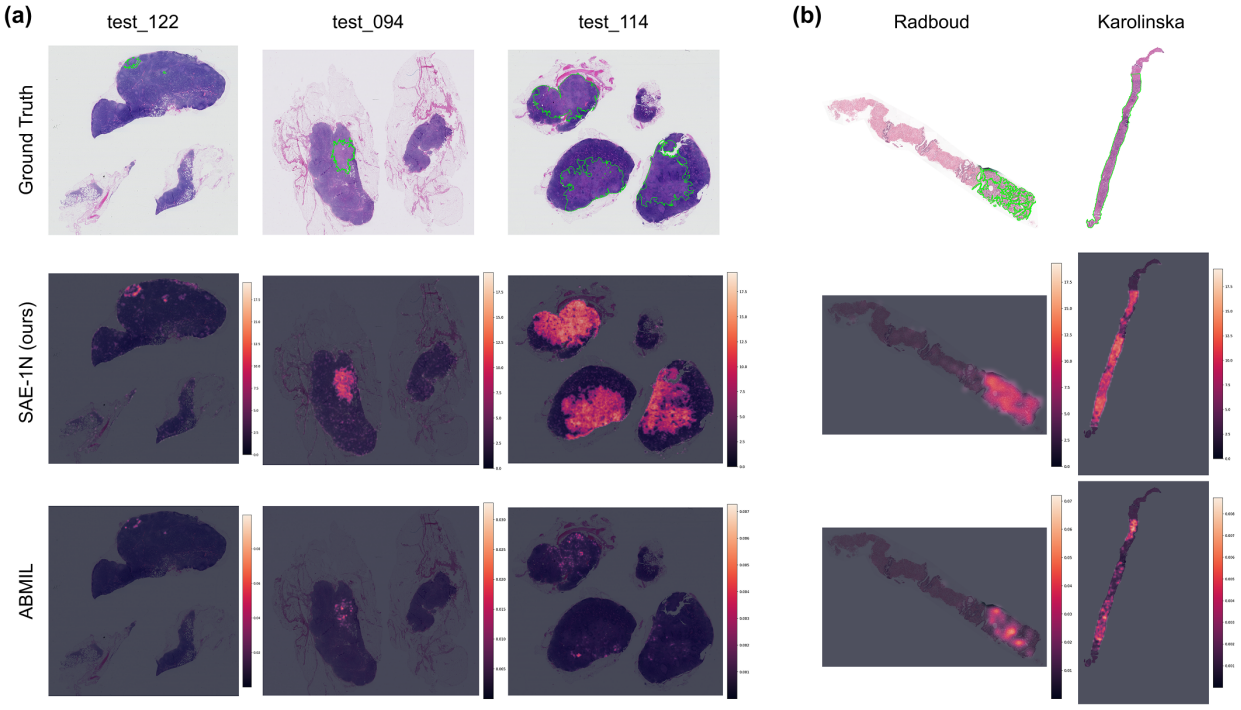

Fig. 5. Visualization results from SAE-1N and ABMIL. From top to bottom: the ground-truth annotation, the activation heatmap of the selected SAE neuron (SAE-1N), and the attention map generated by ABMIL. (a) Camelyon16: From left to right, three cases with different tumor sizes (small: test_122, medium: test_094, and large: test_114). (b) PANDA: From left to right, two cases from the PANDA dataset (Radboud: 3424fa4daa40e0bb944a1f579ca895ca, and Karolinska: 4fc84c3c665c970865284b352e2134e3). The SAE-1N visualizations for PANDA were obtained from the model trained on the combined Radboud and Karolinska (R&K) splits.

arises because, in slide-level classification tasks, a small number of high-attention patches is often sufficient for accurate prediction, even if these patches do not comprehensively represent the entire tumor area. Consequently, conventional MIL classification metrics may overlook such incomplete tumor coverage. Moreover, attention scores reflect regions that contribute most to the model's prediction but do not necessarily correspond to the actual presence of tumor tissue. In contrast, SAE-1N activations show a direct and statistically validated association with tumor regions, achieved through the weakly supervised selection of a neuron linked to the whole-slide–level phenotype.

Unlike attention scores computed via Softmax, which are relative within each slide, the activation value of the selected SAE neuron is defined on an absolute scale based on the training set. This enables consistent evaluation across samples and supports a more accessible visualization strategy for whole-slide image analysis. By relying on a single neuron, SAE-1N offers a simple yet transparent approach for tumor localization in computational pathology.

4. Discussion

Our work diverges from both Le et al.[24] and ProtoMIL[19] in three key respects: supervision, interpretability granularity, and the usage of sparse autoencoders (SAEs). Le et al. demonstrated that unsupervised SAE training on pathology embeddings can uncover monosemantic latent units correlated with cell types. However, their work does not connect latent features to explicit diagnostic tasks. In contrast, our method introduces weak slide-level phenotype supervision within an MIL framework to select individual SAE neurons that are directly predictive of tumor presence. This links each neuron to tile-level phenotype localization, moving beyond unsupervised discovery into task-specific interpretability. ProtoMIL applies SAE to extract human-interpretable "concepts" from embeddings, which are then used in an inherently interpretable MIL classification pipeline. It further allows pathologists to intervene by disabling spurious concepts. While similar in its use of SAE-derived concepts, our work focuses on interpretable neuron selection rather than prototype aggregation, and critically evaluates performance across different pretrained embeddings—especially CLIP-style models like CONCH. We target single-neuron explainability and patch-level phenotype detection, rather than slide-level prototype-based interpretability. Thus, our method complements these works by emphasizing neuron-level transparency, enabling more precise, localized explanations tied to clinical phenotypes.

The advantage of using a single-neuron sparse autoencoder (SAE) as the input feature lies in its high interpretability: a single neuron is directly linked to the final prediction. For instance, in the Camelyon16 classification task that distinguishes tumor from normal tissue, the selected neuron can be clearly attributed to either tumor or normal regions. This makes it a highly intuitive and interpretable marker for visualization. Although this study primarily evaluates the proposed method using the Camelyon16 and PANDA datasets, the approach is not limited to phenotypes such as tumor versus normal. The proposed method can be extended to other phenotype types as well. On the other hand, the current method has primarily been developed for identifying two phenotypes. For multiple phenotypes, the neuron selection strategy based on whole-slide supervision could be extended, for example, by employing Welch's ANOVA. We plan to explore these extensions as part of future work.

5. Conclusion

In this work, we propose a novel approach that leverages a sparse autoencoder to learn disentangled representations from CLIP-based pathology foundation models. We further introduce a statistically grounded weakly supervised method for selecting phenotype-associated neurons for downstream tasks. Our results demonstrate that the proposed method serves as a simple and interpretable indicator for identifying patch-level phenotypes. Experiments on the Camelyon16 and PANDA datasets also show that the proposed SAE-1N model achieves competitive performance on the patch-level annotation task.

Competing interests

The authors declare no competing interests.

Acknowledgment

This work was carried out as a part of the Genome research in CAncers and Rare Diseases(G-CARD) project, supported by the Japan Agency for Medical Research and Development (AMED) under Grant Number 23ck0106873h0002, 23ck0106873h0002, 24ck0106873h0003 and 25ck0106873h0004. The computing resources in this work were provided by Human Genome Center, the Institute of Medical Science, the University of Tokyo.

Code availability

The source code is available at `https://github.com/tamukei/sae-1n`

References

1. T. G. Dietterich, R. H. Lathrop and T. Lozano-Pérez, Solving the multiple instance problem with axis-parallel rectangles, *Artificial Intelligence* **89**, 31–71 (1997).
2. J. Deng, W. Dong, R. Socher, L.-J. Li, K. Li and L. Fei-Fei, Imagenet: A large-scale hierarchical image database, *2009 IEEE Conference on Computer Vision and Pattern Recognition*, 2009.
3. M. Talo, Convolutional neural networks for multi-class histopathology image classification, *arXiv preprint arXiv:1903.10035* (2019).
4. K. He, X. Zhang, S. Ren and J. Sun, Deep residual learning for image recognition, *2016 IEEE Conference on Computer Vision and Pattern Recognition*, 2016.
5. R. J. Chen, T. Ding, M. Y. Lu, D. F. K. Williamson, G. Jaume, B. Chen, A. Zhang, D. Shao, A. H. Song, M. Shaban *et al.*, Towards a general-purpose foundation model for computational pathology, *Nature Medicine* **30**, 850–862 (2024).
6. H. Xu, N. Usuyama, J. Bagga, S. Zhang, R. Rao, T. Naumann, C. Wong, Z. Gero, J. González, Y. Gu *et al.*, A whole-slide foundation model for digital pathology from real-world data, *Nature* **630**, 181–188 (2024).
7. M. Y. Lu, B. Chen, D. F. Williamson, R. J. Chen, I. Liang, T. Ding, G. Jaume, I. Odintsov, L. P. Le, G. Gerber *et al.*, A visual-language foundation model for computational pathology, *Nature Medicine* **30**, 863–874 (2024).
8. M. Ilse, J. M. Tomczak and M. Welling, Attention-based deep multiple instance learning, *International Conference on Machine Learning (ICML)*, 2018.
9. M. Y. Lu, D. F. Williamson, T. Y. Chen, R. J. Chen, M. Barbieri and F. Mahmood, Data-efficient and weakly supervised computational pathology on whole-slide images, *Nature Biomedical Engineering* **5**, 555–570 (2021).
10. A. Makhzani and B. Frey, k-sparse autoencoders, *arXiv preprint arXiv:1312.5663* (2013).
11. R. Huben, H. Cunningham, L. R. Smith, A. Ewart and L. Sharkey, Sparse autoencoders find highly interpretable features in language models, *International Conference on Learning Representations (ICLR) 2024* , 2024.
12. E. Simon and J. Zou, Interplm: discovering interpretable features in protein language models via sparse autoencoders, *Nature Methods* (2025).
13. G. Brixi, M. G. Durrant, J. Ku, M. Poli, G. Brockman, D. Chang, G. A. Gonzalez, S. H. King, D. B. Li, A. T. Merchant *et al.*, Genome modeling and design across all domains of life with evo 2, *bioRxiv* (2025).
14. B. Bussmann, P. Leask and N. Nanda, Batchtopk sparse autoencoders, *arXiv preprint arXiv:2412.06410* (2024).
15. L. Gao, T. D. la Tour, H. Tillman, G. Goh, R. Troll, A. Radford, I. Sutskever, J. Leike and J. Wu, Scaling and evaluating sparse autoencoders, *arXiv preprint arXiv:2406.04093* (2024).

16. R. J. Chen, T. Ding, M. Y. Lu, D. F. Williamson, G. Jaume, A. H. Song, B. Chen, A. Zhang, D. Shao, M. Shaban *et al.*, Towards a general-purpose foundation model for computational pathology, *Nature Medicine* **30**, 850–862 (2024).
17. M. Oquab, T. Darcet, T. Moutakanni, H. Vo, M. Szafraniec, V. Khalidov, P. Fernandez, D. Haziza, F. Massa, A. El-Nouby *et al.*, Dinov2: Learning robust visual features without supervision, *arXiv preprint arXiv:2304.07193* (2023).
18. J. Yu, Z. Wang, V. Vasudevan, L. Yeung, M. Seyedhosseini and Y. Wu, Coca: Contrastive captioners are image-text foundation models, *arXiv preprint arXiv:2205.01917* (2022).
19. S. Sun, D. van Midden, G. Litjens and C. F. Baumgartner, Prototype-based multiple instance learning for gigapixel whole slide image classification, *arXiv preprint arXiv:2503.08384* (2025).
20. Z. Shao, H. Bian, Y. Chen, Y. Wang, J. Zhang, X. Ji *et al.*, Transmil: Transformer based correlated multiple instance learning for whole slide image classification, *Advances in Neural Information Processing Systems* **34**, 2136–2147 (2021).
21. S. Yang, Y. Wang and H. Chen, Mambamil: Enhancing long sequence modeling with sequence reordering in computational pathology, *International Conference on Medical Image Computing and Computer-Assisted Intervention*, 2024.
22. K. M. Papadopoulos and T. Stathaki, Comparing imagenet pre-training with digital pathology foundation models for whole slide image-based survival analysis, *arXiv preprint arXiv:2405.17446* (2024).
23. W. Zhang, J. Chen and C. Kanan, Insight: Explainable weakly-supervised medical image analysis, *arXiv preprint arXiv:2412.02012* (2024).
24. N. M. Le, C. Shen, N. Patel, C. Shah, D. Sanghavi, B. Martin, ... and D. Juyal, Learning biologically relevant features in a pathology foundation model using sparse autoencoders, *arXiv preprint arXiv:2407.10785* (2024).

DeepDiff-SHAP: Interpretable deep learning for subgroup-specific causal hypothesis generation using conditional SHAP

Aditya Sriram[1], Soyeon Kim[2], Joseph A Carcillo[2], Hyun Jung Park[1,*]

[1]*Department of Human Genetics, University of Pittsburgh, Pittsburgh, PA, USA*
[2]*Department of Pediatrics, University of Pittsburgh, Pittsburgh, PA, USA*
[*]*E-mail: hyp15@pitt.edu*

Precision medicine aims to tailor healthcare strategies to individual differences in genetic, clinical, and environmental factors. However, identifying subgroup-specific causal relationships in complex biomedical data remains a major challenge, especially when standard causal inference methods average over population heterogeneity. We introduce DeepDiff-SHAP, a novel framework that combines regression-based and deep learning-based differential causal inference to detect changes in causal relationships across patient subgroups. DeepDiff-SHAP integrates conditional SHapley Additive exPlanations (SHAP) to estimate conditional dependencies and perform nonlinear differential causal inference in a principled, interpretable manner. Applying DeepDiff-SHAP to two population-scale datasets, the CDC Diabetes Health Indicators Dataset and a UK Biobank sepsis cohort stratified by hypertension status, we identified clinically meaningful and subgroup-specific causal changes in relationships between features across the datasets including age, general health, alkaline phosphatase, and cholesterol. Our results reinforce the idea that deep learning enhances sensitivity to complex interaction patterns overlooked by linear models, providing new biological insights into disease progression and comorbidity-specific risk mechanisms. DeepDiff-SHAP offers a scalable and interpretable solution to uncover individualized causal pathways, advancing the goal of truly personalized medicine.

Keywords: Differential Causal Inference; Deep Learning; Precision Medicine; Shapley Additive exPlanations (SHAP).

1. Introduction

Precision medicine is transforming biomedical research and clinical care by shifting the focus from one-size-fits-all treatments to strategies tailored to individual differences in genetic, environmental, and lifestyle factors. As precision medicine continues to gain traction, there is a growing need for analytical methods that can identify subgroup-specific risk factors that either influence disease risk or therapeutic responses differently across distinct populations, or differently across multiple states within the same population. Examples include genetic variants such as *rs11673407* in the fucosyltransferase 3 gene (*FUT3*) elevating cardiovascular risk in men but not in women[1], or nine potentially protective and 25 harmful metabolic biomarkers predicting future incidence of type 2 diabetes[2]. Traditional causal inference frameworks, however, typically estimate average treatment or exposure effects across a global population grouping[3-5]. As an example, CausalMGM is a well-established mixed graphical model method for inferring causal relationships from observational data that may include multiple data types[6]. However, since it runs on a single aggregated cohort, it can obscure possible nuanced, group-specific mechanisms and lead to ineffective or even harmful interventions in underrepresented subgroups within the larger data group.

© 2025 The Authors. Open Access chapter published by World Scientific Publishing Company and distributed under the terms of the Creative Commons Attribution Non-Commercial (CC BY-NC) 4.0 License.

Recently, a method proposed by Belyaeva et al. called Differential Causal Inference (DCI), established a principled approach to detect differences in causal effects across groups by directly comparing the strength of variable-outcome relationships in one subgroup versus another[7]. DCI is methodologically distinct from simply performing causal inference separately in two groups and comparing the results. In a standard two-group approach, causal models are estimated independently for each group (e.g., diseased and healthy), and differences in effect estimates are compared post hoc. However, this approach does not account for estimation variance or the statistical significance of the differences, potentially leading to spurious findings or uncertainty in drawing conclusions. In contrast, DCI directly models and tests the difference in causal effects between groups as the primary quantity of interest within a unified framework that allows for more robust inference. This enables the identification of subgroup-specific causal mechanisms while controlling for variability and potential biases. Furthermore, the naive approach of fitting models separately in subgroups, especially in high-dimensional settings, can lead to unstable estimates due to small sample sizes or overfitting. DCI's framework borrows strength across groups through joint modeling or shared representations, improving estimation accuracy and interpretability. This enables researchers and clinicians to uncover risk factors that are uniquely relevant to particular population subgroups, such as non-responders to immunotherapy[8] or patients with treatment-resistant depression[9], and in turn advance the development of more precise and targeted interventions.

Despite its advantage as being the only current differential causal inference method, DCI is based on regression-based framework and thus limited in its ability to capture the sophisticated mechanisms underlying disease heterogeneity. Disease heterogeneity arises from complex, multilayered biological processes that involve nonlinear interactions among genetic, epigenetic, and environmental factors. Regression models, which rely on additive and linear assumptions, are insufficient in capturing these involved dependencies, potentially overlooking key disease-driving mechanisms.

To model complex biological and clinical systems, which are governed by intricate, nonlinear interactions among molecular signals (e.g., gene expression, DNA methylation)[10,11], environmental

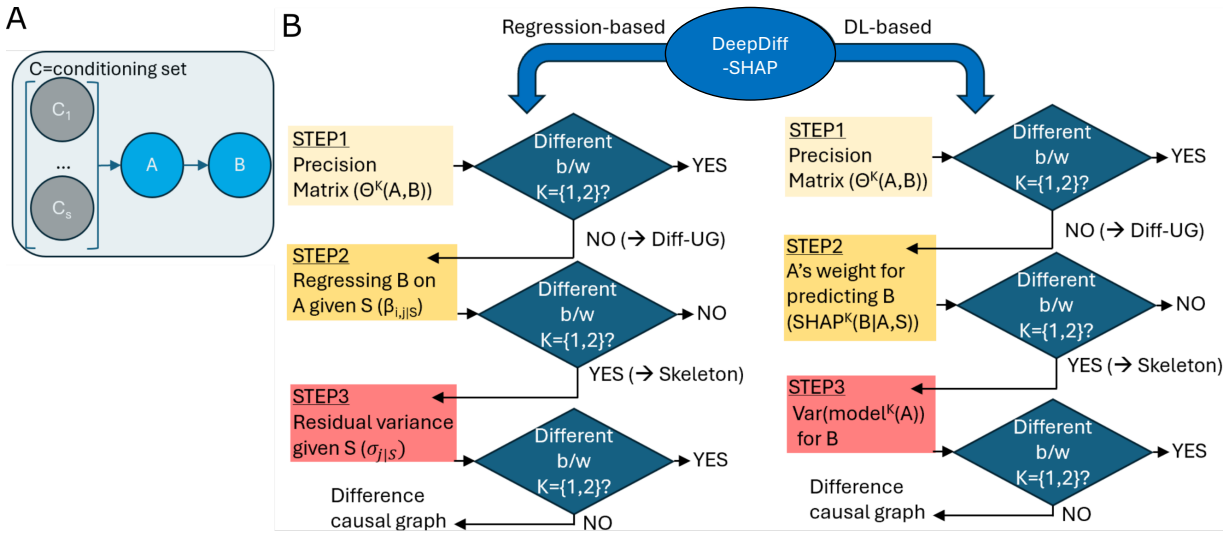

Figure 1. (A) Causal relationship from A to B to test for the difference based on the conditioning set expressed as $C = \{C1, \ldots, Cs\}$. (B) Algorithm of DeepDiff-SHAP with the regression and the deep learning components.

exposures (e.g., smoking, pollution)[12,13], and clinical variables (e.g., comorbidities, treatment history)[14,15], we will extend regression-based DCI using deep learning (DL). With its multilayered architecture and nonlinear activation functions, DL can effectively learn hierarchical feature representations that capture subtle, high-order dependencies between inputs. It has already demonstrated success in a variety of biomedical tasks including disease risk prediction[16,17] and image-based diagnostics[18,19]. This makes deep learning particularly well-suited for extending DCI for contexts in which causal effects are likely to vary not just in magnitude, but in functional form, across subgroups.

Specifically, for a framework outlining a causal association from input feature A to outcome B with conditioning on set C (**Fig. 1A**), we will extend the established regression-based three step approach of DCI[7] (**Fig. 1B**) by using DL architecture. While this approach evaluates model parameters for the conditional probability of each variable pair between conditions, performing these steps requires conditional probabilities, e.g., $P(A|B,C)$, where C is a set of conditioning nodes. In the regression setting, such conditional distributions have closed-form expressions based on covariances and are thus tractable. However, in DL settings, these conditional distributions become complex and high-dimensional. To address this, we propose a novel deep learning framework, **DeepDiff-SHAP**, that incorporates advanced SHapley Additive exPlanations (SHAP)[20] to quantify differential conditional dependence between variables (**Fig. 1C**). SHAP has been adapted to estimate conditional expectations in supervised learning[21], but its use for computing conditional dependencies between input variables, as required for formal causal inference, remains limited and underexplored. By adapting SHAP to contrast feature contributions of certain variables, while conditioning on the shared, high-dimensional covariate space that exists in most biomedical data, our method enables robust and interpretable identification of variables whose causal effects differ across groups. This approach directly targets the core objective of DCI and offers a scalable, principled solution for uncovering subgroup-specific causal mechanisms in complex biomedical data. Below, we will first formalize the three-step workflow of DeepDiff-SHAP: (1) screen for causal edges that change between two states by contrasting precision matrices; (2) prune edges that may appear variant but do not actually differ, using a SHAP-based test of whether one variable's influence on another still differs after conditioning on nearby variables; and (3) orient the remaining edges by checking which putative parent sets keep prediction residuals stable across states using lightweight neural networks. We apply DeepDiff-SHAP to two case studies: (1) CDC Diabetes survey data, and (2) a UK Biobank cohort of sepsis patients stratified by hypertension status, both representing disease groups with distinct etiologies and risk structures for which we discuss key empirical findings. Finally, we provide practical guidance on aligning comparison groups with the intended causal effect modifiers and conclude with a transparent discussion of limitations and planned methodological improvements.

2. Introduction

We introduce DeepDiff-SHAP as a principled, statistically sound three-algorithm approach rooted in regression and DL frameworks for causal structure changes between two states (**Fig. 1B**). DeepDiff-SHAP works without having to fully reconstruct each underlying network in a dataset. Step 1 involves identifying candidate nodes and edges where the dependency structure differs between states, based on changes in the precision matrix; in this case, the precision matrix is the pseudoinverse of the empirical covariance matrix. Since structural changes in a causal graph often result in shifts in the precision matrix, this step ensures a stable, high recall starting point for further

evaluation and refinement. In Step 2, we test whether the strength of variable dependency relationships (i.e., how much one variable predicts another after conditioning on a third variable in the undirected graph) remains stable across the two states. If a relationship does not change, it is pruned from the candidate set, thus removing possible false positives identified by Step 1. Finally, in Step 3, we compute differences in residual (unexplained) variances calculated via deep neural networks (DNNs) to infer directionality between nodes; if there is statistical evidence of DNN residual invariance when conditioning on a set of nodes, it suggests that the node set contains the true causal parents related to the outcome.

2.1. *Estimation of the difference undirected graph*

To identify pairwise changes in conditional dependence structure between two states, we begin by estimating a **difference undirected graph (Δ-UG)** that aims to identify statistically significant evidence of interactions that vary between the two state-separated data groups. Let $X^{(1)} \in \mathbb{R}^{n_1 \times p}$ and $X^{(2)} \in \mathbb{R}^{n_2 \times p}$ denote independent data groups from states 1 and 2, respectively. Each dataset is denoted by state-specific precision matrices $\Theta^{(1)} = \Sigma^{(1)^{-1}}$ and $\Theta^{(2)} = \Sigma^{(2)^{-1}}$, where $\Sigma^{(k)}$ is the covariance matrix of state k.

We implement a constraint-based approach that computes an edge-specific test statistic for each pair of variables (i, j) based on their estimated precision matrix entries. This step is adapted from the framework first formalized by Belyaeva et al[22]. Specifically, we estimate $\widehat{\Theta}^{(1)}$ and $\widehat{\Theta}^{(2)}$ using the Moore–Penrose pseudoinverse of the empirical covariance matrices computed from $X^{(1)}$ and $X^{(2)}$, respectively. The test statistic for each pair (i, j) is defined as:

$$\widehat{Q}_{ij} \coloneqq \frac{\left(\widehat{\Theta}_{ij}^{(1)} - \widehat{\Theta}_{ij}^{(2)}\right)^2}{\left(\frac{\widehat{\Theta}_{ii}^{(1)}\widehat{\Theta}_{jj}^{(1)} + (\widehat{\Theta}_{ij}^{(1)})^2}{n_1} + \frac{\widehat{\Theta}_{ii}^{(2)}\widehat{\Theta}_{jj}^{(2)} + (\widehat{\Theta}_{ij}^{(2)})^2}{n_2}\right)}.$$

This statistic quantifies the squared difference in partial correlations between the two states, scaled by their estimated variances. Under the null hypothesis $H_0: \Theta_{ij}^{(1)} = \Theta_{ij}^{(2)}$, the statistic $\widehat{Q}_{ij}$ asymptotically follows a noncentral F-distribution[23,24]:

$$\widehat{Q}_{ij} \sim F(1, \nu), \quad \text{where} \quad \nu = n_1 + n_2 - 2p + 2.$$

We compute p-values from this distribution using the cumulative noncentral F distribution function and define a significance threshold $\alpha \in [0,1]$. The difference undirected graph Δ is then constructed as:

$$\mathcal{E}_\Delta \coloneqq \left\{\{i, j\} \;\middle|\; p_{ij} \leq \alpha\right\},$$

where p_{ij} is the p-value corresponding to $\widehat{Q}_{ij}$. To reduce the downstream hypothesis testing burden in skeleton discovery and edge orientation, we define the set of conditioning nodes as:

$$\mathcal{C} \coloneqq \{i \mid \exists j \text{ such that } \{i, j\} \in \mathcal{E}_\Delta\}.$$

We limit the nodes included in the conditioning set to the nodes involved in the edges of the difference undirected graph, Δ-UG. We block the inclusion of any additional nodes (i.e. marginal or conditional distributions differing across states) leading to node inclusion in the conditioning set, ensuring a very strict and regulated edge inclusion step.

2.2. *Skeleton discovery via SHAP-based conditional invariance testing*

In the second step of our method, we further prune the initial undirected difference graph by testing for conditional invariance of cross-state feature dependencies. Specifically, for each edge (i, j) in the initial undirected difference graph, we assess whether the importance of feature i for predicting feature j remains invariant across states, and vice versa, after conditioning on subsets of features part of the conditioning set S.

We model each feature i as a function of its potential parent j and a conditioning set $S \subseteq \mathcal{C}\{i, j\}$, where $\mathcal{C}$ denotes the set of conditioning nodes obtained from Step 1. For each direction, we train two multilayer perceptron regressors $f_i^{(1)}$ and $f_i^{(2)}$ on the two datasets $X^{(1)}$ and $X^{(2)}$ to predict X_i using X_j and S.

To assess the contribution of X_j to the prediction of X_i in each state, we compute conditional SHAP values using KernelSHAP with a fixed background distribution that isolates the effect of X_j given S[25]. Specifically, we calculate:

$$\phi_{j|S}^{(k)} = \text{SHAP}\left(X_j \mid S; f_i^{(k)}, X^{(k)}\right),$$

where $k \in \{1,2\}$ and $\phi_{j|S}^{(k)}$ denotes the absolute SHAP values across test samples. These values are then compared between states using a normalized squared difference statistic:

$$T_{ij|S} := \frac{(\mu_1 - \mu_2)^2}{\frac{\sigma_1^2}{n_1} + \frac{\sigma_2^2}{n_2}},$$

where μ_k and σ_k^2 are the mean and variance of the SHAP values in state k, and n_k is the number of SHAP samples. A two-sided p-value is derived from the noncentral F-distribution with degrees of freedom $\nu = n_1 + n_2 - 2 - 2|S|$.

For each ordered pair ($i \leftarrow j$ and $j \leftarrow i$) we test for SHAP heterogeneity across states conditional on the set of conditioning nodes. When $p > \alpha$, we fail to reject the null hypothesis of conditional invariance across states and remove the corresponding edge from the undirected difference graph. When $p < \alpha$, we reject the null hypothesis of conditional invariance, and we include the edge. This process is repeated across all conditioning sets up to a specified maximum size $r_{\max}$. The remaining edges after this pruning step make up the edge difference skeleton used in the subsequent direction-orientation step for the leftover edges.

This SHAP-based invariance testing allows for nonlinear, model-flexible detection of asymmetric changes in feature relationships, extending the regression-based conditional independence tests to deep neural network models with a more structurally sound framework.

2.3. *Edge orientation via invariance testing*

In step 3, we orient edges obtained in step 2 (the pruned edge difference skeleton) to end up with a directed graph that captures differences in functional dependencies across the two states. We assume that for any node j, if the conditional variance of X_j given a set of likely parents S is invariant across states, then S represents a valid set of parents for j. This principle is rooted in the theory that the functional form of the conditional distribution $P(X_j \mid X_S)$ should remain stable under invariance[26].

For each node j in the graph, we test candidate parent sets $S \subseteq \mathcal{C}\{j\}$ of size $k = 1$, where $\mathcal{C}$ is the set of conditioning nodes identified from the pruned edge difference skeleton from algorithm 2. We train DNNs to regress X_j on X_S separately in each state using a two-layer multilayer perceptron (MLP). The residual variance is estimated as:

$$\hat{\sigma}_{j|S}^{2}{}^{(k)} \coloneqq \mathrm{Var}\left(X_j^{(k)} - f_j^{(k)}\left(X_S^{(k)}\right)\right),$$

where $f_j^{(k)}$ denotes the fitted DNN regressor in state $k \in \{1,2\}$, and $\hat{\sigma}^2$ is computed on the training data. To assess whether the conditional variance differs significantly between states, we compute a two-sided test statistic based on the ratio of residual variances:

$$T_{j|S} \coloneqq \frac{\hat{\sigma}_{j|S}^{2}{}^{(1)}}{\hat{\sigma}_{j|S}^{2}{}^{(2)}},$$

with a p-value computed using the noncentral F-distribution with degrees of freedom $(n_1 - |S|, n_2 - |S|)$:

$$p = 2 \cdot \min\left(F_{\mathrm{cdf}}(T_{j|S}), 1 - F_{\mathrm{cdf}}(T_{j|S})\right).$$

If the p-value exceeds a specified threshold α, we fail to reject the null hypothesis and conclude that the conditional variance is invariant, therefore accepting S as the parent set for j. The directed edges $i \rightarrow j$ for all $i \in S$ are added to the graph. We perform additional cycle and contradiction checks using transitive closure on the directed graph to prevent invalid orientations.

For any edges that remain unoriented after this test, we apply graph traversal rules to resolve directionality wherever a consistent path structure allows. For example, for any set of nodes in which $i \rightarrow node_1 \rightarrow node_x \rightarrow j$, we orient $i \rightarrow j$. This rationale is formalized by Meek and reviewed by Colombo et al[27,28]. The final output is a directed adjacency matrix, a log of all the orientation decisions, and the set of edges that could not be oriented by algorithm 3's invariance testing.

This DNN-based residual variance orientation strategy expands on the original DCI steps defined for regression-based models and leverages DL via a DNN framework to capture potentially nonlinear predictive structure, and tests whether this structure is preserved across states; this allows for stronger performance of causal inference in a model-independent way[22]. Our model eliminates the assumption of linear-Gaussian data by utilizing DNN-based predictions for variable dependencies.

For results mentioned in this paper, DeepDiff-SHAP was initialized with the following parameters: $\alpha_{ug} = 0.005, \alpha_{skeleton} = 0.3, \alpha_{orient} = 0.001$ corresponding to the threshold levels for each of the three steps of the algorithm. Conditioning set size was set to 1 (maximum set size is 2, range from 0 to 2; a higher conditioning set size leads to sparser causal network graphs).

2.4. Computational feasibility of conditional-based SHAP

While standard KernelSHAP is known to suffer from high computational cost, it is important to note that conditional SHAP can reduce computational cost significantly. In the cost calculation, computational expense in KernelSHAP scales as $2^{(p)}$ model evaluations, where p is the number of features. On the other hand, instead of evaluating all subsets of non-target features, conditional SHAP computes the contribution of a predictor j given a limited conditioning set S, integrating over the distribution of the remaining features via $p(X_{S\setminus\{j\}} \mid X_S)$. As a result, the model evaluation space collapses from size 2^p to $2^{|S|}$ (the subsets of $\{j\} \cup S$). Since our algorithm restricts $| S | \leq r_{\max}$, we can significantly reduce the number of model evaluations. Reusing a shared conditional background distribution across all test instances further reduces per-sample computational load.

3. Results

3.1. *DeepDiff-SHAP reveals nonlinear subgroup-specific causal structures in diabetes populations*

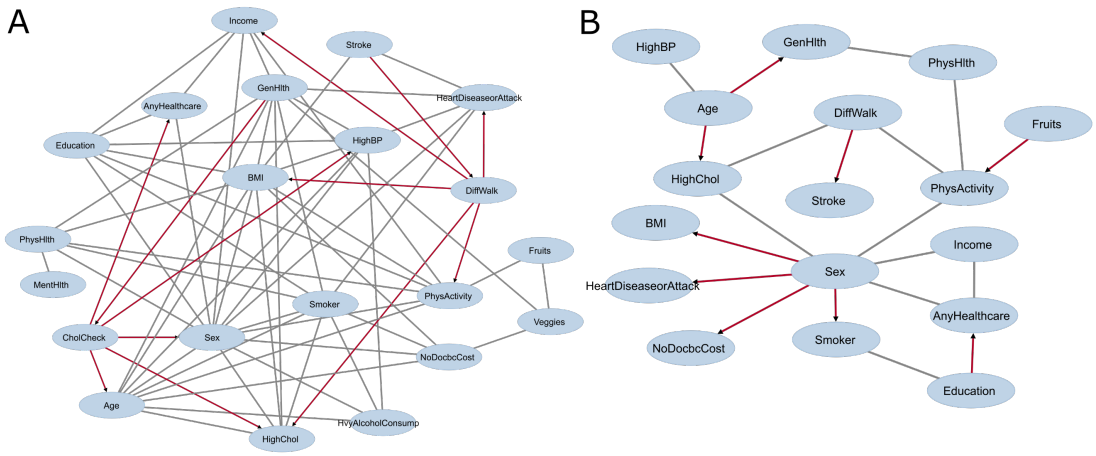

Figure 2. DCI graph on the diabetes data as identified by (A) the regression-based and (B) deep-learning-based DeepDiff-SHAP. Gray lines represent the association changes that are not attributed as differential causal relationship and red lines represent the differential causal relationships.

To investigate changes in causal relationships associated with chronic disease, we ran the regression-based DCI and DL-based DeepDiff-SHAP on the 2014 Centers for Disease Control and Prevention (CDC) Diabetes Health Indicators Dataset[29]. This dataset includes health status, behavioral, and access-to-care survey data for 253,680 individuals, among whom 39,977 were diagnosed as diabetic or prediabetic and 213,703 were not diagnosed with diabetes. Using the regression-based module of DeepDiff-SHAP, which follows the original DCI framework, we detected 68 feature pairs with differential associations between the diabetic and non-diabetic groups. Many of these association changes involved well-known demographic confounders such as age and sex, which influence a wide range of lifestyle and health indicators. For instance, age was differentially associated with features like general health (labeled "GenHlth"), stroke, smoking status (labeled "Smoker"), and access to health care (labeled "AnyHealthcare"), while sex was

associated with differences in income, smoking status, and BMI (**Fig. 2A**). 12 of the 68 differential associations (17.64%) were attributed to underlying causal relationship changes by the regression-based model. Notably, among participants categorized as diabetic or prediabetic, worse general health exerted a stronger causal effect on obtaining a cholesterol check within 5 years (labeled "CholCheck"), and, in turn, the check had a causal link with individuals who had high-cholesterol (labeled "HighChol") and high-blood pressure (HighBP); these relationships were not observed in the non-diabetic patient group. However, only 2 (16.66%) of the 12 findings involved age or sex as causal variables, despite their central role in shaping health outcomes. While it is clinically plausible that age impacts general health status differently in people with and without diabetes, this causal difference was not detected by the regression model. In contrast, the deep learning module of DeepDiff-SHAP (**Fig. 2B**) identified this expected causal difference[30] from age to general health, as well as a differential causal effect of age on high cholesterol. Similarly, while the regression-based model did not attribute any of the sex-related association changes, such as those from sex to heart disease or heart attack (labeled "HeartDiseaseAttack"), smoking status, and BMI, to changes in causal relationships, the DL-based approach successfully identified all these as differential causal effects between the diabetic/pre-diabetic and non-diabetic groups.

We note the importance of these particular causal relationships in the DeepDiff-SHAP network graph, age to high cholesterol and sex to coronary heart disease or myocardial infarction, both which have been previously mentioned in the context of type 2 diabetes being associated with women having a greater risk of cardiovascular disease, as well as studies implicating earlier cardiovascular disease events in women with T2D compared to men[31-33]. These findings suggest that deep learning-based causal inference can uncover subtle and nonlinear changes in causal structure that may be missed by linear models. Notably, the regression-based DCI model identified some relationships that appear potentially misleading. As an example, regression-based DCI attributed a directional causal difference in the relationship from stroke to difficulty walking, which is more plausibly explained in the reverse direction or mediated by baseline functional impairments in diabetic individuals. Altogether, these results both highlight the limitations of traditional regression-based causal inference in detecting meaningful shifts in causal mechanisms between disease subpopulations as well as showcase how our deep learning framework enables more nuanced detection of differential causal structures, supporting its utility in understanding the biological and behavioral heterogeneity of chronic diseases such as diabetes.

3.2. *Uncovering comorbidity-specific mechanisms in sepsis through causal inference*

To investigate how chronic comorbidities modulate causal relationships in sepsis, we applied DeepDiff-SHAP (**Fig. 1B**) to a subset of the UK Biobank patient database comprising 3,181 individuals diagnosed with sepsis, stratified by hypertension status (hypertension: n = 2,669; no hypertension: n = 512). Sepsis remains a leading cause of morbidity and mortality in adults and children, yet its clinical progression is strongly influenced by pre-existing conditions such as hypertension, a factor often overlooked in risk modeling[34]. We identified sepsis cases using ICD-10 codes (e.g., A40, A41, B37.7, O85), capturing a range of septicemia and related conditions. From the UK Biobank, we selected 42 variables spanning domains of cardiometabolic health, renal and liver function, inflammation, hormones, blood pressure, and pulmonary status. Using DeepDiff-SHAP's regression-based module, we identified 18 associations that differed between hypertensive and non-hypertensive sepsis patients, of which 8 (44.44%) were attributed to shifts in causal relationships (**Fig. 3A**). Notably, these included altered causal links including from urate to SHBG

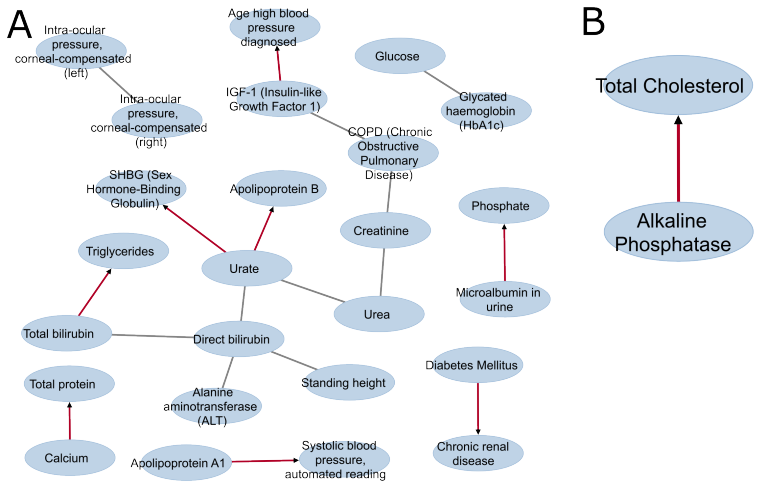

Figure 3. Differential causal graphs on UK Biobank sepsis data as identified by (A) the regression-based and (B) deep-learning-based DeepDiff-SHAP. Gray lines represent the association changes that are not attributed as differential causal relationship and red lines represent the differential causal relationships.

and apolipoprotein B, total bilirubin to triglycerides, calcium to total protein, apolipoprotein A1 to systolic blood pressure, and IGF-1 to age at hypertension diagnosis, suggesting distinct physiological pathways influenced by vascular stress. Importantly, the deep learning component of DeepDiff-SHAP uncovered an additional causal shift from alkaline phosphatase to total cholesterol that was not detectable via the regression-based model (**Fig. 3B**), highlighting the added value of incorporating nonlinear modeling.

Together, these findings demonstrate that DeepDiff-SHAP enables a comprehensive discovery of subgroup-specific causal mechanisms in sepsis by building on regression-driven DCI with a deep learning framework.

3.3. *Benchmarking DeepDiff-SHAP*

3.3.1. *Benchmarking DeepDiff-SHAP against regression-based DCI: enhanced sensitivity to nonlinear causal differences*

To benchmark performance, we compared DeepDiff-SHAP against DCI, the only existing differential causal inference method currently available. Importantly, the regression-based component of DeepDiff-SHAP is mathematically equivalent to this original DCI method, as both frameworks follow the same three-step procedure: identifying structural differences, testing conditional invariance, and estimating directionality based on residual variance. Therefore, any observed differences in results between DeepDiff-SHAP's deep learning (DL) module and the regression-based DCI can be attributed to the modeling framework itself, rather than the procedural design. To assess relative sensitivity to causal structure changes, we compared the number of association differences that were ultimately attributed to changes in causal strength (i.e., differential causal degrees). Since the comparison holds the inference pipeline constant while varying only the functional form (linear vs. nonlinear approach), this metric offers a controlled and clear evaluation of how effectively each approach detects meaningful causal differences. Between the diabetes (pre-

diabetic and diabetic diagnosis) and healthy population groups in the CDC Diabetes dataset, the original DCI method identified 68 association changes, but only 12 (17.6%) were attributed to differences in causal degree. In contrast, DeepDiff-SHAP detected 19 association changes, with 9 (47.3%) resolved as true causal degree differences, demonstrating a significantly higher sensitivity in uncovering meaningful causal changes (P-value = 0.02). A similar pattern emerged in the sepsis dataset: DeepDiff-SHAP resolved 1 causal degree difference out of 1 association change, whereas the original DCI resolved 8 out of 18 association changes (P-value = 0.2). Although the weaker significance in the sepsis dataset may reflect the presence of only a single nonlinear association difference, these findings nonetheless underscore the improved sensitivity of DeepDiff-SHAP, particularly for detecting complex, nonlinear causal relationships.

3.3.2. *Benchmarking DeepDiff-SHAP against CausalMGM: comparing objectives and outputs with an existing causal inference method*

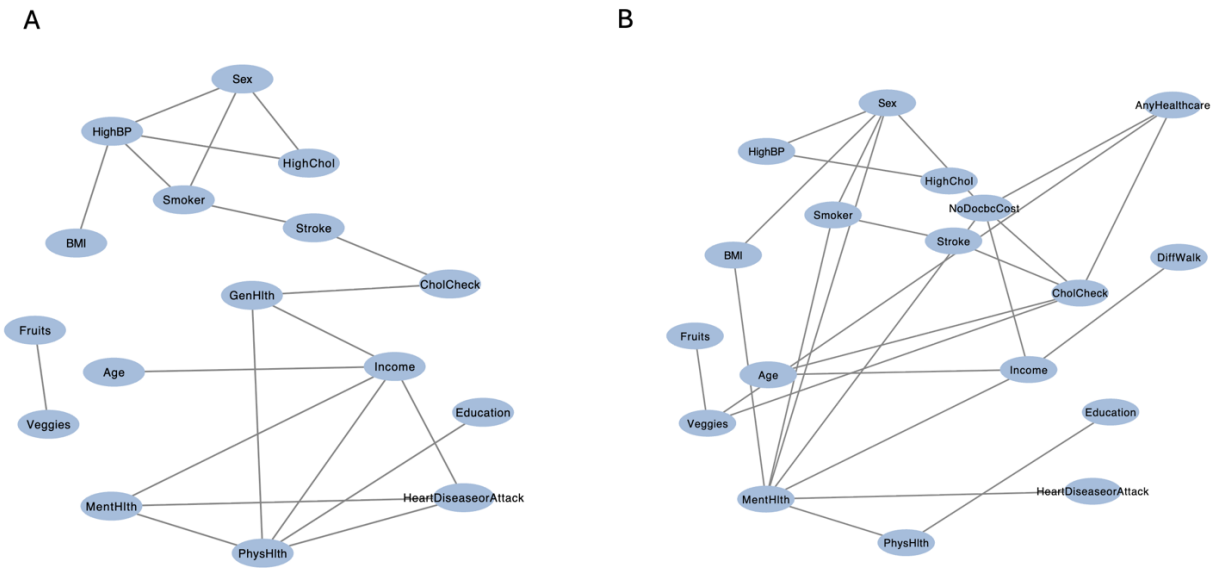

Figure 4. Differential causal graphs on CDC Diabetes data as identified by CausalMGM. (A) non-diabetic group (B) diabetic and prediabetic group.

We benchmarked DeepDiff-SHAP against CausalMGM[6] by running CausalMGM separately on the diabetic/prediabetic and non-diabetic subgroups (**Fig. 4**). CausalMGM learns which features are associated via regression and then attempts to assign a causal direction to those associations using the Peter-Clark (PC) algorithm[35]. Importantly, PC does not determine causal directions when the data does not have enough empirical evidence to do so. In our CDC Diabetes dataset, neither subgroup produced any oriented edges, suggesting that PC as part of CausalMGM has limited power to infer causal directions in this context. By extension, it would be even more difficult to compare causal differences between the two groups using CausalMGM. Despite the absence of oriented edges, CausalMGM did recover several undirected associations. Many were shared across groups and likely reflect background co-variation rather than diabetes-specific biology (e.g., high blood

pressure and high cholesterol, labeled “HighBP” and HighChol”; history of stroke and lifetime cigarette consumption, labeled “Stroke” and “Smoker”; how many days in the last 30 days were an individual’s physical and mental health considered “not good”, respectively labeled “PhysHealth” and “MentHlth”). CausalMGM also reported group-specific patterns; in the diabetic and prediabetic subgroup, associations centered on having any kind of healthcare, labeled “AnyHealthcare”, with links to CholCheck, NoDocbcCost (doctor visit skipped due to high cost), and vegetable consumption once or more per day, labeled “Veggies”, whereas in the non-diabetes subgroup, associations primarily involved general health condition, labeled “GenHlth” (e.g., connections to CholCheck, Income, PhysHlth). These findings are suggestive but remain undirected under CausalMGM. DeepDiff-SHAP advances this framework in two ways. First, DeepDiff-SHAP could determine causal directions on two diabetes-specific edges that CausalMGM only flagged as undirected: CholCheck to Age and CholCheck to AnyHealthcare. The CholCheck to Age direction is not causally plausible (a test cannot cause age) and likely reflects latent confounding or reverse causation. However, CholCheck to AnyHealthcare is consistent with a plausible behavioral pathway (i.e. lipid screening may lead to more health-care engagement). In both cases, DeepDiff-SHAP provides specified causal directions that can serve as hypotheses for relevant further investigation and work. Additionally, DeepDiff-SHAP determined the causal direction of nonlinear associations, some of which are known to be associated with diabetes[31,36]. Altogether, these results (1) validate several DeepDiff-SHAP findings against an established graphical-model baseline, (2) demonstrate greater power to orient effects where CausalMGM remains agnostic, and (3) show enhanced interpretability through subgroup-specific direction estimates and detection of nonlinear structure relevant to diabetes biology.

4. Discussion

We introduce DeepDiff-SHAP as a method that builds on regression-based DCI with a deep learning-based differential causal inference framework (**Fig. 1B**). Our method’s modular design, split into three steps with flexible parameter initialization settings, allows researchers to systematically evaluate subgroup-specific differences in feature importance and directional relationships, creating a highly customizable approach to evaluating causal data structure. Additionally, the results observed from our comparative analysis across two unique patient datasets, the CDC Diabetes Health Indicators Dataset and a UK Biobank cohort of sepsis patients stratified by hypertension, demonstrate DeepDiff-SHAP’s ability to identify biologically meaningful and study-supported causal relationships that regression-only DCI may overlook.

DeepDiff-SHAP’s performance in the analysis of the CDC Diabetes dataset offers novel insights into the differential roles of classical foundational variables such as age and sex. These variables act as upstream regulators, often influencing many downstream pathways at once. They can moderate, mediate, or interact with other risks, rather than affecting only a single chain of events. DeepDiff-SHAP models these nonlinear, interactive, and layered relationships through a unified DL-based framework. This framework helps uncover how different factors can influence multiple pathways at once, highlighting regulatory patterns that may vary across subgroups. By capturing these effects without having to specify every possible mediator or interaction in advance, it offers a practical way to study the complexity of chronic diseases like diabetes. Diabetes is a persistent metabolic disease that compounds over time; individuals with diabetes are more likely to experience a steeper deterioration in general health as they age, compared to individuals without diabetes. Additionally, aging itself brings about general decline in metabolic efficiency, immune function, and tissue repair,

all of which can be exacerbated by the presence of diabetes. By leveraging DL's multilayer modeling capacities, we reveal a synergistic effect between age and diabetes, where the impact of aging on general health is causally differential. In contrast, individuals without diabetes may experience a more gradual, less pronounced decline in general health with aging. Similarly, regarding the unique causal difference result between sepsis patients with and without hypertension, several studies have made the link between serum alkaline phosphatase (ALP) and coronary artery disease, with hypertension recognized as a well-known contributor to the development of coronary artery disease[37,38]. Additional studies in humans and mice have linked ALP with elevated cholesterol levels, particularly in those with dyslipidemia, and observe that high ALP in dyslipidemia patients leads to hypertension and coronary heart disease[39,40].

An important design consideration in DCI is deciding which variable defines the groups being compared. For the CDC diabetes dataset analysis, we looked at differences between individuals with and without diabetes, using diabetes status as the grouping variable. In this construct, the key question becomes whether the relationship between an exposure (X) and an outcome (Y) differs by diabetes status. If, instead, the question of interest centered around sex-specific differences, then the grouping variable would have to be defined as sex. Misspecification of the grouping variable with the intended modifier can lead to estimating a completely different causal relationship than originally intended and, in some cases, introduce collider bias if the outcome itself is used to define groups. For this reason, we recommend that the grouping variable of interest be specified a priori and that steps be taken to ensure balance across groups, such as through reweighting or matching.

In practice, DeepDiff-SHAP is designed to produce two outputs that are functionally relevant to clinical settings. First, it produces subgroup-specific causal networks that diagram how exposures influence outcomes differently across a chosen modifier. Second, it translates the identified subgroup-level effects into targeted risk predictions using SHAP-based effect size estimation. By structuring the analysis around the modifier of interest, but still reinforcing the defined disease as the *outcome*, this approach avoids common pitfalls like collider bias and ensures that causal results are in line with the question of interest. In conjunction, DeepDiff-SHAP's outputs support clearer communication of subgroup-specific risks and help prioritize the most important risk factors for patient care.

Despite the promise of DeepDiff-SHAP in identifying subgroup-specific differences in causal structure, our current framework has some limitations. First, like other computational approaches to causal discovery, DeepDiff-SHAP faces fundamental limits, particularly when reverse causality or feedback loops are present. Most algorithms based on directed acyclic graphs (DAGs) assume acyclicity, faithfulness, and often causal sufficiency. These assumptions prevent them from representing feedback processes and make it challenging to orient causal directions when multiple graphs are observationally indistinguishable. In practice, claiming and assigning directionality to edges typically warrants additional sources of information, such as interventions, time ordering, or invariance across environments. However, our results remain vulnerable to hidden confounding, measurement error, or selection bias. Established methods such as the PC[35] algorithm, the Fast Causal Inference (FCI)[41] algorithm, and the Greedy Equivalence Search (GES)[42,43] algorithm formalize some of this, but often lose rigor with higher dimensional data structures such as -omics data. Differential causal inference (DCI) methods that compare two conditions inherit these same identification constraints from their base graphs and can misattribute distributional shifts as causal edge differences when assumptions fail. Thus, reverse causality and hidden common causes remain crucial obstacles to solve concerning causal discovery from observational data. Second, the

computational efficiency of the SHAP-based conditional invariance testing step remains a major challenge. Specifically, estimating conditional SHAP values for each candidate variable pair across multiple conditioning subsets is computationally expensive, particularly for large-scale datasets with many variables and complex feature interactions. Third, our current approach uses an ad hoc restriction on the conditioning set to reduce complexity: we limit candidate conditioning variables to those involved in edges identified in the difference undirected graph (Δ-UG). While this helps avoid an exponential increase in the number of SHAP computations, it may miss subtler or higher-order conditional dependencies. This limitation can inherently bias results towards more prominent signal changes while underestimating other nuanced shifts in conditional structure. To address this, future iterations of DeepDiff-SHAP could benefit from dimensionality reduction techniques such as variable screening, supervised embedding, or attention-based feature selection before applying conditional SHAP. Finally, we will also investigate adaptive strategies for selecting conditioning sets that leverage measures such as mutual information or latent feature representations. The goal is to balance out computational feasibility and the capacity to capture potentially hidden dependencies. Methods such as autoencoder-based dimensionality reduction, graph neural network–derived embeddings, or Bayesian network–informed priors may help us develop principled ways to limit the conditioning set space while still retaining the most relevant differential dependency structures in data sources of interest.

As medicine increasingly moves toward personalized interventions, understanding how risk factors or biological pathways operate differently across patient subpopulations, such as those with or without comorbidities like diabetes or hypertension, is essential to avoid generalized solutions that can be ineffective or even harmful. Traditional regression-based methods average over heterogeneity, preventing subtle but important biological differences from being uncovered. Our approach, which integrates the theoretical rigor of differential causal inference with the interpretable power of deep learning and SHAP, allows researchers to discover changes in causal structure that vary with disease state, comorbidity, or population subgroup. These insights can directly inform the design of more precise diagnostic criteria, risk prediction tools, and treatment strategies, ultimately improving clinical outcomes by ensuring the appropriate interventions are delivered to the appropriate patients.

5. Acknowledgments

The CDC Diabetes Health Indicators dataset comes from the University of California, Irvine Machine Learning Repository and the CDC 2014 Annual Data report. UK Biobank data comes from the UK Biobank Resource under Application Number 83829. This research was supported in part by the University of Pittsburgh Center for Research Computing, RRID:SCR_022735, through the resources provided. Specifically, this work used the HTC cluster, which is supported by NIH award number S10OD028483.

6. Code and Data Availability

DeepDiff-SHAP code and examples can be accessed at: https://github.com/ads303/DeepDiff-SHAP. UK Biobank data is not permitted for public dispensing. CDC Diabetes survey data can be accessed at: https://archive.ics.uci.edu/dataset/891/ for immediate download.

References

1 Silander, K. *et al.* Gender Differences in Genetic Risk Profiles for Cardiovascular Disease. *PLOS ONE* **3**, e3615 (2008).

2 Peddinti, G. *et al.* Early metabolic markers identify potential targets for the prevention of type 2 diabetes. *Diabetologia* **60**, 1740-1750 (2017).

3 Sedgewick, A. J. *et al.* in *Bioinformatics* Vol. 35 1204-1212 (2019).

4 Zheng, X., Aragam, B., Ravikumar, P. K. & Xing, E. P. in *Advances in Neural Information Processing Systems* Vol. 31 (eds S Bengio *et al.*) (Curran Associates, Inc., 2018).

5 Moccia, C. *et al.* Machine learning in causal inference for epidemiology. *European Journal of Epidemiology* **39**, 1097-1108 (2024).

6 Ge, X., Raghu, V. K., Chrysanthis, P. K. & Benos, P. V. CausalMGM: an interactive web-based causal discovery tool. *Nucleic Acids Res* **48**, W597-W602 (2020).

7 Belyaeva, A., Squires, C. & Uhler, C. in *Bioinformatics* Vol. 37 3067-3069 (2021).

8 Davar, D. *et al.* Neoadjuvant vidutolimod and nivolumab in high-risk resectable melanoma: A prospective phase II trial. *Cancer Cell* **42**, 1898-1918.e1812 (2024).

9 Ruberto, V. L., Jha, M. K. & Murrough, J. W. Pharmacological Treatments for Patients with Treatment-Resistant Depression. *Pharmaceuticals* **13**, 116 (2020).

10 Olecka, M. *et al.* Nonlinear DNA methylation trajectories in aging male mice. *Nature Communications* **15**, 3074 (2024).

11 Zablotskii, V., Gorobets, O., Gorobets, S. & Polyakova, T. Effects of Static and Low-Frequency Magnetic Fields on Gene Expression. *Journal of Magnetic Resonance Imaging* (2025).

12 Cheng, W.-C. *et al.* Non-linear association between long-term air pollution exposure and risk of metabolic dysfunction-associated steatotic liver disease. *Environmental health and preventive medicine* **29**, 7-7 (2024).

13 Demateis, D., Keller, K. P., Rojas-Rueda, D., Kioumourtzoglou, M. A. & Wilson, A. Penalized distributed lag interaction model: Air pollution, birth weight, and neighborhood vulnerability. *Environmetrics* **35**, e2843 (2024).

14 Chesnaye, N. C. *et al.* Non-linear relationships in clinical research. *Nephrology Dialysis Transplantation* **40**, 244-254 (2025).

15 Zhang, Y. *et al.* Analysis of the nonlinear relationships between insulin resistance indicators such as LAP and TyG and depression, and population characteristics: a cross-sectional study. *European Journal of Medical Research* **30**, 513 (2025).

16 Oh, T. R. Integrating predictive modeling and causal inference for advancing medical science. *Childhood Kidney Diseases* **28**, 93-98 (2024).

17 Nkoy, F. L., Stone, B. L., Zhang, Y. & Luo, G. A roadmap for using causal inference and machine learning to personalize asthma medication selection. *JMIR Medical Informatics* **12**, e56572 (2024).

18 Deshpande, S., Li, Z. & Kuleshov, V. Multi-Modal Causal Inference with Deep Structural Equation Models. *arXiv preprint arXiv:2203.09672* (2022).

19 Zang, C., Wang, H., Pei, M. & Liang, W. in *Proceedings of the IEEE/CVF Conference on Computer Vision and Pattern Recognition.* 19027-19036.

20 Lundberg, S. M. & Lee, S.-I. Vol. 30 (eds I. Guyon *et al.*) (2017).

21 Sundararajan, M. & Najmi, A. in *International conference on machine learning.* 9269-9278 (PMLR).

22 Belyaeva, A., Squires, C. & Uhler, C. DCI: learning causal differences between gene regulatory networks. *Bioinformatics* **37**, 3067-3069 (2021).

23 Lütkepohl, H. *New introduction to multiple time series analysis*. (New York : Springer, 2005).

24 Yuhao Wang, C. S., Anastasiya Belyaeva, Caroline Uhler. in *NeurIPS 2018* Vol. 31 (Advances in Neural information Processing Systems, Montreal, 2018).

25 Scott M Lundberg, S.-I. L. in *International Conference on Neural Information Processing Systems* Vol. 30 (Advances in Neural Information Processing Systems, Long Beach, CA, 2017).

26 Peters, J., Bühlmann, P. & Meinshausen, N. Causal Inference by using Invariant Prediction: Identification and Confidence Intervals. *Journal of the Royal Statistical Society Series B: Statistical Methodology* **78**, 947-1012 (2016).

27 Meek, C. in *Proceedings of the Eleventh conference on Uncertainty in artificial intelligence* 403–410 (Morgan Kaufmann Publishers Inc., Montréal, Qué, Canada, 1995).

28 Diego Colombo, M. H. M. Order-Independent Constraint-Based Causal Structure Learning. *Journal of Machine Learning Research* **15**, 3921—3962 (2014).

29 Burrows, N. R., Hora, I., Geiss, L. S., Gregg, E. W. & Albright, A. Incidence of End-Stage Renal Disease Attributed to Diabetes Among Persons with Diagnosed Diabetes - United States and Puerto Rico, 2000-2014. *MMWR Morb Mortal Wkly Rep* **66**, 1165-1170 (2017).

30 Guo, J. *et al.* Aging and aging-related diseases: from molecular mechanisms to interventions and treatments. *Signal Transduct Target Ther* **7**, 391 (2022).

31 Madonna, R. *et al.* Impact of Sex Differences and Diabetes on Coronary Atherosclerosis and Ischemic Heart Disease. *J Clin Med* **8** (2019).

32 Yoshida, Y., Chen, Z., Fonseca, V. A. & Mauvais-Jarvis, F. Sex Differences in Cardiovascular Risk Associated With Prediabetes and Undiagnosed Diabetes. *Am J Prev Med* **65**, 854-862 (2023).

33 Ballotari, P., Venturelli, F., Greci, M., Giorgi Rossi, P. & Manicardi, V. Sex Differences in the Effect of Type 2 Diabetes on Major Cardiovascular Diseases: Results from a Population-Based Study in Italy. *Int J Endocrinol* **2017**, 6039356 (2017).

34 Ahlberg, C. D. *et al.* Linking Sepsis with chronic arterial hypertension, diabetes mellitus, and socioeconomic factors in the United States: A scoping review. *Journal of Critical Care* **77**, 154324 (2023).

35 Pearl, J. (Cambridge University Press, Cambridge, 2009).

36 Tramunt, B. *et al.* Smoking and Diabetes: Sex and Gender Aspects and Their Effect on Vascular Diseases. *Can J Cardiol* **39**, 681-692 (2023).

37 Chen, Y. *et al.* Patients with comorbid coronary artery disease and hypertension: a cross-sectional study with data from the NHANES. *Ann Transl Med* **10**, 745 (2022).

38 Weber, T. *et al.* Hypertension and coronary artery disease: epidemiology, physiology, effects of treatment, and recommendations : A joint scientific statement from the Austrian Society of Cardiology and the Austrian Society of Hypertension. *Wien Klin Wochenschr* **128**, 467-479 (2016).

39 Adamidis, P. S. *et al.* Association of Alkaline Phosphatase with Cardiovascular Disease in Patients with Dyslipidemia: A 6-Year Retrospective Study. *J Cardiovasc Dev Dis* **11** (2024).

40 Bessueille, L. *et al.* Inhibition of alkaline phosphatase impairs dyslipidemia and protects mice from atherosclerosis. *Transl Res* **251**, 2-13 (2023).

41 Zhang, J. in *Artificial Intelligence* Vol. 172 1873-1896 (2008).
42 Ramsey, J., Glymour, M., Sanchez-Romero, R. & Glymour, C. in *International Journal of Data Science and Analytics* Vol. 3 121-129 (2017).
43 Ge, E., Li, Y., Wu, S., Candido, E. & Wei, X. Association of pre-existing comorbidities with mortality and disease severity among 167,500 individuals with COVID-19 in Canada: A population-based cohort study. *PLoS One* **16**, e0258154 (2021).

Literature-driven extraction and computational prediction of causal statements linking genetic variants to biological processes, pathways and phenotypes

Jici Jiang, Predrag Radivojac†, Benjamin M. Gyori†
Northeastern University
Boston, MA 02115, United States
†*E-mail: predrag@northeastern.edu; b.gyori@northeastern.edu*

Understanding the mechanistic basis of pathogenic genetic variants requires reconstructing the molecular pathways connecting the variant, via a chain of molecular intermediates, to a disease-causing biological process and phenotype. However, a literature-wide assembly of causal networks connecting variants, molecular pathways, biological processes and phenotypes has not been previously available. To create such a resource, we developed an automated pathway reconstruction approach building on the Integrated Network and Dynamical Reasoning Assembler (INDRA) system which extracts causal mechanistic statements (positive regulation, phosphorylation, complex formation, etc.) by combining structured databases and literature mining. We traversed INDRA statements extracted from publications to identify those describing a genetic variant resulting in a protein point mutation. We then reconstructed directed paths (consisting of one or more linked INDRA statements) connecting this variant to a term representing a biological process, phenotype or disease within the same publication. This resulted in a directed multigraph obtained from 25,862 paths for variants in 2,561 proteins. Each node in this graph corresponds to an ontology-grounded molecular or process term and each edge is explicitly linked to supporting literature evidence, enabling full auditability of inferred mechanisms. To leverage the assembled networks, we trained a classification model to predict likely downstream biological processes or specific disease associations for protein variants. As features to the model, we integrated molecular annotations (including protein sequence features, ClinVar pathogenicity labels, and UniProt domain mappings) in combination with representations from the ESM2 transformer-based protein language model. The performance achieved by this model shows promise for reconstructing causal mechanistic statements associated with function of genetic variants, a framing of the variant effect prediction task that goes significantly beyond simple assessment of pathogenicity. This integrative framework enables the mechanistic interpretation of known variants and prediction of functional relevance for variants lacking prior phenotypic annotation.

Keywords: text mining, machine learning, variant interpretation

1. Introduction

Advances in genomic sequencing have greatly increased the number of genetic variants observed in human populations; however, understanding how these variants affect biological processes and lead to disease remains an ongoing challenge.[1] Current computational approaches

© 2025 The Authors. Open Access chapter published by World Scientific Publishing Company and distributed under the terms of the Creative Commons Attribution Non-Commercial (CC BY-NC) 4.0 License.

for variant impact prediction are powerful.[2–4] They rely predominantly on sequence information, evolutionary conservation, and structural features, and are trained to predict specific functional alterations (e.g., impact on protein stability) or some form of variant viability, often using pathogenicity information from clinical databases.[5,6] While these methods have achieved widespread adoption in genomic pipelines,[7,8] they continue to exhibit fundamental limitations in deciphering the molecular mechanisms that lead to disease.[9] Specifically, these methods, along with recent studies that aim to establish genotype-phenotype causal relationships,[10] generally cannot reconstruct causal paths from individual variants, through specific molecular events, to downstream biological and disease processes. Moreover, current variant interpretation tools lack the ability to trace predictions back to supporting literature evidence, limiting their explainability and clinical applicability.

To address these challenges, we developed an integrated framework that combines automated path reconstruction with transformer-based machine learning for mechanistic variant interpretation. Building on the Integrated Network and Dynamical Reasoning Assembler (INDRA) system,[11,12] which extracts and assembles causal mechanistic statements from scientific literature and structured databases, we reconstructed mechanistic paths connecting protein variants to biological processes and disease phenotypes. This approach yielded a comprehensive network covering 6,268 variants and 25,862 causal paths across 2,561 proteins, where each causal path (chain of events) is explicitly linked to supporting literature evidence, enabling full auditability of predicted mechanisms. We then trained an attention-based model that integrates protein sequence features, domain annotations, pathogenicity scores, and pathway representations to predict chains of events that lead to both broad functional categories and specific biological process associations.

We proposed two prediction strategies for associating protein variants with biological processes and disease causal paths: a fine-grained model that directly scores all target labels, and a hierarchical model that incorporates intermediate broad functional categories to guide prediction. While both strategies achieve comparable overall performance, the hierarchical model provides a structured framework for organizing outputs and supports more interpretable classification. Incorporating mechanistic paths extracted from the literature substantially improves prediction quality, highlighting the importance of biological context in variant interpretation. Combined with domain and pathogenicity information, these features enable functionally explainable predictions and systematic exploration of variant impact across biological networks. We deployed an interactive web portal for exploring literature-derived mechanistic networks, which enables researchers to investigate the network-level propagation of variant effects. This approach advances mechanistic interpretation of variant effects and supports downstream applications in target prioritization, biomarker discovery, and precision medicine.

2. Methods

2.1. *Extracting causal paths from the literature*

To reconstruct causal paths connecting genetic variants to biological processes, we leveraged the INDRA Database (`https://db.indra.bio`). The INDRA Database contains mechanistic *Statements* extracted from PubMed abstracts and PubMed Central full text articles using

multiple natural language processing systems combined with the content of curated pathway databases, assembled using INDRA.[12] Each INDRA Statement represents an assertion about a causal relationship between biological *Agents* (genes, proteins, small molecules, biological processes, etc.), where an Agent may represent additional states such as mutations and post-translational modifications.[11] Statements can express, for instance that "CDK12 phosphorylates POLR2A on S1896" or "EGFR-G796D activates cell proliferation", with each statement linked to specific supporting evidence sentences and source publications.

From the INDRA Database we extracted all Statements in which an Agent representing the mutated form of a protein (corresponding to a genetic variant) was involved. Our path extraction process identified the shortest directed paths connecting genetic variants to biological process terms through chains of molecular intermediates within individual publications. The extracted paths form a directed graph connecting variants, via molecular intermediates, to disease-causing biological processes or phenotypes, with edges representing causal relationships. An example causal path for the A53T variant in *SNCA* is shown in Fig. 1. Each complete path was constrained to originate from a single publication (rather than drawing on statements from multiple publications) ensuring coherence of context in which the genetic variant and its effects are described.

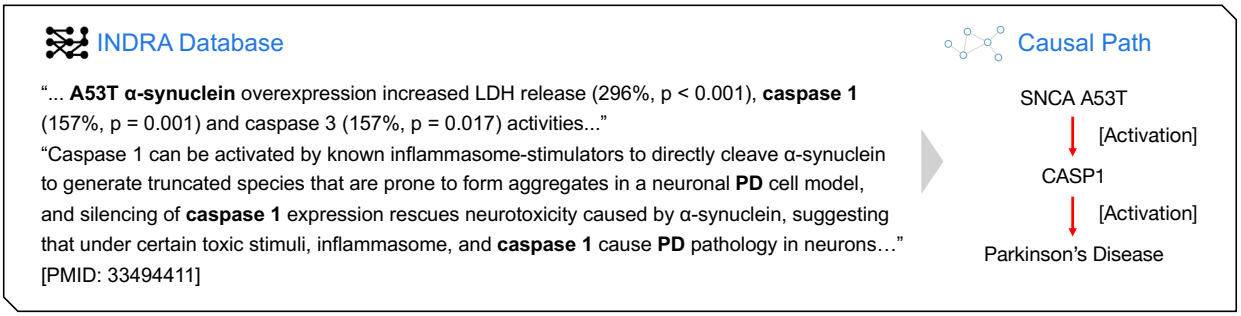

Fig. 1. An example of constructing a causal path for *SNCA* A53T based on literature evidence extracted from INDRA Database, with the cited publication supporting a mechanistic link from variant to Parkinson's disease via *CASP1*.

Through this extraction, we identified 19 types of relations capturing mechanistic interactions between molecular entities (Table 1). The "Identity" relation (ID 0) connects genetic variants to their corresponding proteins to facilitate graph neural network training. We treat the "Complex" (ID 3) relation as undirected, to describe mutual binding rather than directional causality. All other relations are directed, thus reflecting their inherent causal nature.

This approach yielded 25,862 causal records covering 2,561 proteins. The entities and the relations between them form a comprehensive network of causal relationships that serves as the foundation for our knowledge graph construction and subsequent analyses.

2.2. *Variant feature construction*

To ensure effective utilization of sequence information in model training, we validate position-to-amino acid correctness using UniProt Swiss-Prot canonical sequences and splice variant

Table 1. Mechanistic relation types between molecular entities in the knowledge graph

ID	Type	ID	Type	ID	Type	ID	Type
0	Identity	5	DecreaseAmount	10	Glycosylation	15	Palmitoylation
1	Acetylation	6	Deglycosylation	11	Hydroxylation	16	Phosphorylation
2	Activation	7	Demethylation	12	IncreaseAmount	17	Sumoylation
3	Complex	8	Dephosphorylation	13	Inhibition	18	Ubiquitination
4	Deacetylation	9	Deubiquitination	14	Methylation		

isoforms. The validation process filters for human proteins (OX = 9606) with canonical sequences taking precedence when isoform information was imprecise. This approach corrects potential text mining errors in variant position and amino acid assignment, generating protein sequence mappings for accurate variant feature construction, with 20,442 records successfully matching protein sequences across 1,989 proteins to yield 4,511 unique protein-variant pairs.

Next, we incorporate embedding from Evolutionary-Scale Modeling 2 (ESM2),[13] a pretrained protein language model developed for capturing evolutionary and structural information of proteins. Domain features provide binary encoding of the domain types where the variant is located. Amino acid features capture reference and alternative amino acid properties through concatenated embeddings. Position features represent the normalized position within the protein sequence. ClinVar annotations contribute two clinically curated features: pathogenicity scores and review star ratings. Categorical values are mapped to continuous scores as described in Table 2.

Table 2. Mapping of ClinVar pathogenicity and review star annotations to feature values

Value	Pathogenicity	Value	Review star rating
0.99	pathogenic	4	practice guideline
0.90	likely pathogenic	3	expert panel
0.50	uncertain significance/missing	2	multiple submitters, no conflicts
0.10	likely benign	1	single submitter
0.01	benign	0	no review/missing

The final variant feature vector x_v for variant v combines ESM2 embeddings, domain type features, ClinVar annotations, amino acid features, and position features as shown in Fig. 2.

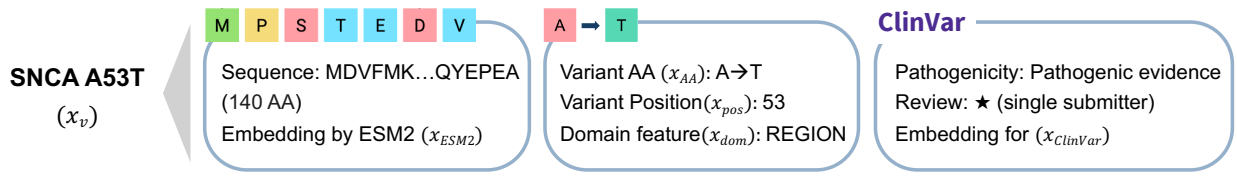

Fig. 2. Constructed feature representation for *SNCA* A53T, incorporating sequence embedding (via ESM2), variant annotations (substitution, domain type), ClinVar annotations.

2.3. *Dataset*

We constructed a hierarchical multi-label dataset to evaluate variant functional predictions across biological processes and diseases. The dataset (Fig. 3A) comprises 4,511 unique protein variants with experimentally validated functional annotations, organized into a two-level hierarchy: 1,085 fine-grained biological process and disease labels were manually mapped to 30 broader categories such as cancer and neoplasms, clinical symptoms, cellular transport, immune response, and cardiovascular diseases.

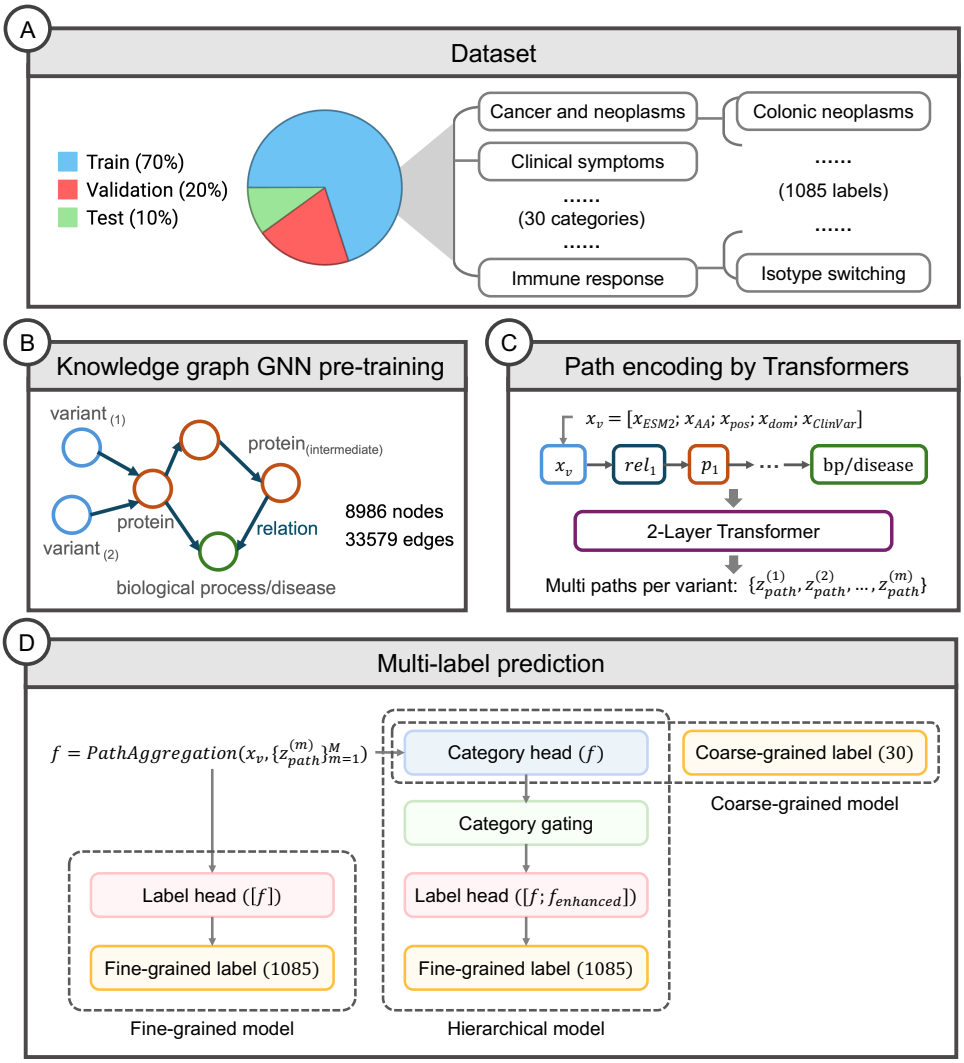

Fig. 3. Prediction framework. (A) Dataset construction with 1,085 fine-grained labels across 30 biological categories; variants are split into training, validation, and test sets. (B) Knowledge graph pre-training comprising 8,986 nodes (molecular entities) and 33,579 edges (mechanistic relations). (C) Causal paths are encoded using a 2-layer transformer. (D) Multi-label prediction: a fine-grained model (left) directly predicts all fine-grained labels; a hierarchical model (right) scores the categories first, then predicts fine-grained labels through the category-guided gating mechanism.

To prevent overfitting to specific proteins or categories, we adopted a stratified data splitting strategy repeated over 30 independent runs. In each run, variants were partitioned into training (70%), validation (20%), and test (10%) subsets. Across the 30 runs, the split sizes were highly consistent (mean ± std): 3,158.4 ± 59.8 for training, 889.5 ± 55.5 for validation, and 463.1 ± 29.3 for testing. To quantify the stability of variant allocation, we computed the Jensen–Shannon (JS) divergence between each variant's observed split distribution and the expected uniform distribution. The average JS divergence was 0.084 ± 0.046. All 30 categories were represented in every training and validation split on average, while the test set maintained 99.3% category coverage, with only occasional omissions in a few runs.

2.4. *Pre-training GNN model for knowledge graph construction*

Using validated sequences as described in Section 2.2, we constructed a knowledge graph $G = (V, E, R)$ comprising $|V| = 8986$ unique nodes representing variants, proteins, biological processes, and phenotypes. These nodes are connected by $|E| = 33579$ edges representing $|R| = 19$ distinct relation types, as shown in Table 1 and Fig. 3B.

We employed a 2-layer Relational Graph Convolutional Network (R-GCN)[14] to learn node embeddings, where the embedding dimensionality is chosen as 256. The initial node embeddings are randomly initialized from a standard normal distribution:

$$\mathbf{H}^{(0)} \in \mathbb{R}^{8986\times 256}, \quad \mathbf{h}_i^{(0)} \sim \mathcal{N}(0,1)$$

The R-GCN forward propagation is performed according to the following update rule:

$$\mathbf{h}_i^{(l+1)} = \sigma\left(\sum_{r\in\mathcal{R}}\sum_{j\in\mathcal{N}_i^r}\frac{1}{c_{i,r}}\mathbf{W}_r^{(l)}\mathbf{h}_j^{(l)}\right)$$

where $\mathbf{h}_i^{(l)}$ is the embedding of node i at layer l, $\mathcal{N}_i^r$ represents the set of neighbors of node i connected by relation r, $\mathbf{W}_r^{(l)}$ is the learnable weight matrix for relation r at layer l, $c_{i,r} = |\mathcal{N}_i^r|$ is the normalization constant, and σ denotes the ReLU activation function.

For knowledge graph completion, we employ the DistMult scoring function[15] $f(s,t,o)$ to evaluate the plausibility of triples:

$$f(s,t,o) = \langle \mathbf{h}_s, \mathbf{r}_t, \mathbf{h}_o\rangle = \sum_{d=1}^{256} h_{s,d}^{(2)} \cdot r_{t,d} \cdot h_{o,d}^{(2)}$$

where s is the subject node index, t is the relation type index, o is the object node index, and d denotes the dimension index of the embedding vectors.

The model parameters are optimized using a softplus margin ranking loss:

$$\mathcal{L}_{link} = \frac{1}{|E|}\sum_{(s,t,o)\in E}\left[\log(1+e^{-f(s,t,o)}) + \frac{1}{k}\sum_{i=1}^{k}\log(1+e^{f(s,t,o_i')})\right]$$

where $k = 2$ is the number of negative samples and o_i' denotes the i-th randomly sampled negative[16] object node.

Upon completion of training, the model produces node embeddings $\mathbb{E}_{node} \in \mathbb{R}^{8986\times 256}$ and relation embeddings $\mathbb{E}_{rel} \in \mathbb{R}^{19\times 256}$.

2.5. *Path encoding by transformers*

To encode causal paths from variants to biological processes or diseases, each path is represented as a sequential token sequence as illustrated in Fig. 3C. The path token $p^{(i)}$ is constructed as:

$$p^{(i)} = [x_v^{(proj)}, e_{r_1}, e_{n_1}, e_{r_2}, e_{n_2}, ..., e_{r_k}, e_{BP}]$$

where i denotes the path index, node embeddings $\mathbb{E}_{node}[n_i]$ are projected to e_{n_i} for each intermediate node n_i, relation embeddings $\mathbb{E}_{rel}[r_i]$ are projected to e_{r_i} for each relation r_i, and e_{BP} represents the final biological process or disease term. Each path $p^{(i)}$ is processed through a 2-layer transformer[17] to obtain the path encoding $z_{path}^{(i)}$.

2.6. *Category-guided multi-label prediction*

For a variant v with m encoded paths $\{z_{path}^{(1)}, z_{path}^{(2)}, ..., z_{path}^{(m)}\}$, an attention mechanism aggregates the path information by computing importance weights. The variant representation queries all paths to focus on the most relevant causal connections, giving the aggregated representation f_v. The prediction process follows a hierarchical approach. First, category-level predictions are generated through a classification head, producing probability distributions $p_{cat} \in [0,1]^{30}$ over 30 broader categories. Category information is then incorporated through a gated mechanism to enhance variant representations. The weighted category representation c_{weight} is computed using learned category embeddings weighted by predicted probabilities:

$$c_{weight} = p_{cat}^T C$$

where $C \in \mathbb{R}^{30\times512}$ contains learned embeddings for each category.

A variant-specific gate $g \in [0,1]^{512}$ determines which dimensions should incorporate category information,[18] which enhances the original variant representation f_v into $f_{enhanced}$ as:

$$f_{enhanced} = f_v + g \odot c_{weight}$$

where $\odot$ denotes element-wise multiplication.

Finally, fine-grained label predictions are generated using both original and enhanced representations to predict across 1,085 specific biological processes and diseases. To address the inherent class imbalance in multi-label biological process prediction, we employ asymmetric loss[19] which applies different focusing parameters for positive and negative samples, emphasizing learning from underrepresented positive classes. This hierarchical framework leverages category-level guidance for accurate fine-grained predictions while handling class imbalance through specialized loss functions.

3. Results

3.1. *Protein variant network*

We constructed a comprehensive protein variant network integrating 25,862 variant-to-disease paths across 2,561 proteins. Each causal edge is fully auditable with explicit links to supporting literature evidence, enabling researchers to trace any variant-disease association to its original experimental sources. We created an interactive web portal (http://variants.indra.bio) that

provides community access for browsing causal paths, visualizing network connections, and accessing supporting evidence. Table 3 summarizes the genes most frequently linked to causal paths in our network.

Table 3. Summary statistics for the top 20 genes ranked by the count of causal paths

Gene	Paths	Variants	BPs/diseases	PMIDs	Gene	Paths	Variants	BPs/diseases	PMIDs
TP53	1298	87	110	261	PIK3CA	180	9	47	55
BRAF	1218	30	130	562	EGFR	179	29	38	78
KRAS	1152	27	162	365	SNCA	178	10	45	52
TARDBP	909	35	54	30	NRAS	173	14	47	63
LRRK2	398	17	77	166	CTNNB1	156	20	36	59
SOD1	305	16	53	141	DNM1L	156	16	41	48
JAK2	231	16	50	125	RAC1	151	16	51	54
HRAS	225	14	56	89	MDM2	136	22	41	37
MAPT	187	19	77	55	GSK3B	128	15	39	40
RPS6KB1	183	4	58	100	PTEN	127	23	39	40

Figure 4 demonstrates a variant-centric mechanistic network derived for *SNCA*, a gene strongly associated with Parkinson's Disease. The visualization integrates multiple *SNCA* variants (e.g., A30P, E46K, G51D, A53E) and their downstream effects through molecular intermediates. Highlighted biological processes include unfolded protein response, autophagy, oxidative stress, and neuroinflammation. Key proteins such as *LRRK2*, *PRKN*, and *TNF* mediate diverse regulatory interactions including activation, inhibition, and post-translational modifications, ultimately converging on phenotypes such as cell death and Parkinson's Disease.

3.2. *Hierarchical model for prediction performance*

We compared three prediction strategies: (i) a fine-grained model that directly predicts all 1,085 biological process and disease labels; (ii) a coarse-grained model that predicts the 30 categories, which collectively cover all 1,085 fine-grained labels; (iii) a hierarchical model that first scores the categories and then uses those scores to guide fine-grained label predictions through a category-guided gating mechanism. Each strategy was trained and evaluated over 30 data splits using the same architecture and training protocol. Table 4 reports mean test performance over the 30 runs.

Table 4. Average test performance across 30 data splits for the three prediction strategies

Model	Micro-P	Micro-R	Micro-F_1	AUROC	AUPRC
fine-grained	**0.684**	0.622	**0.647**	0.913	0.286
coarse-grained	0.959	0.863	0.908	0.959	0.751
hierarchical	0.520	**0.644**	0.573	**0.919**	**0.307**

Bold values indicate the best performance between fine-grained and hierarchical models.

As expected, the coarse-grained model exhibited the strongest performance, achieving a

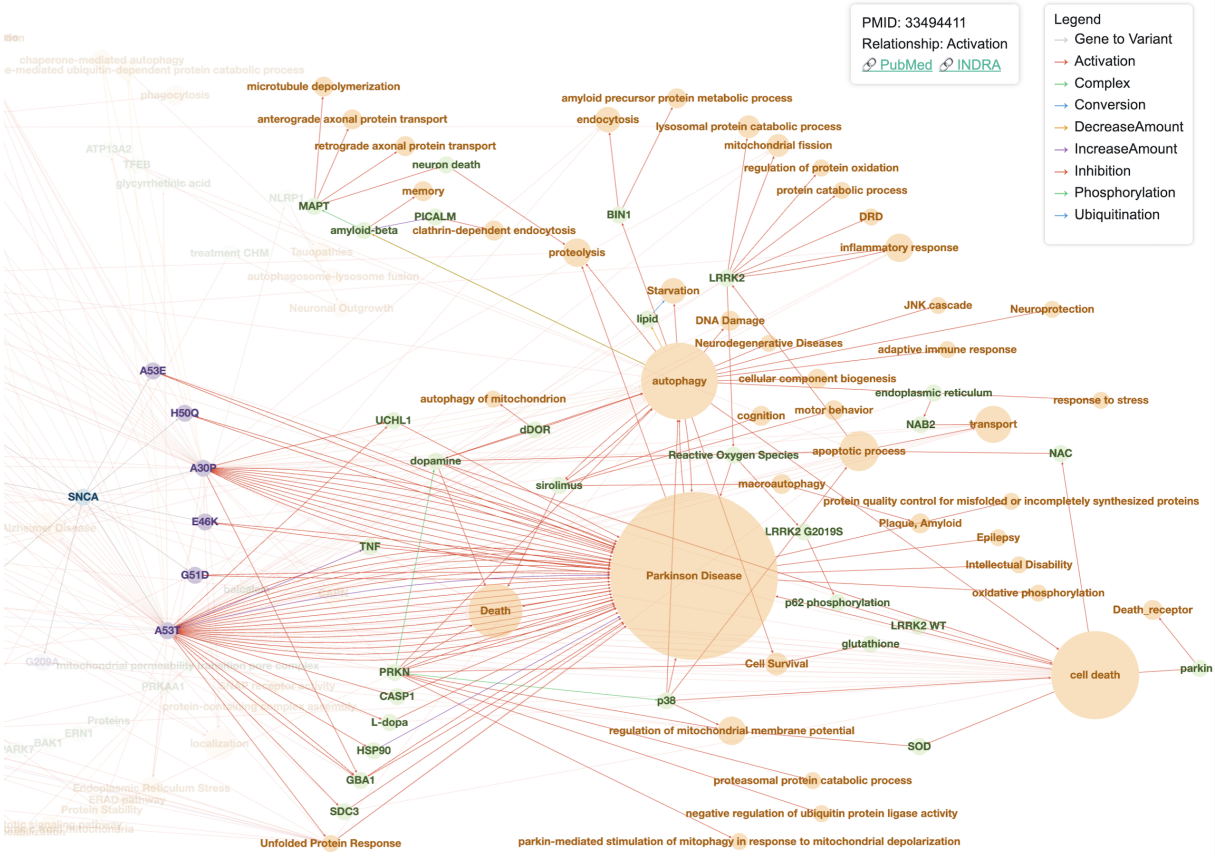

Fig. 4. Interactive visualization of *SNCA* variant network showing path to Parkinson's Disease. Blue nodes represent proteins, purple nodes indicate variants, green nodes denote intermediate processes, and orange nodes mark biological process or disease endpoints.

Micro-F_1 of 0.908. This result reflects the relative ease and reliability of coarse-grained classification, which benefits from stronger label signals and reduced sparsity. A more informative comparison concerns the two models that address the full 1,085-label space. The fine-grained model, which assigns probabilities to every label in a single step, achieves higher precision and an F_1 score, indicating stronger threshold-based classification on the frequent labels. By contrast, the hierarchical model achieves higher recall and slightly better AUROC and AUPRC. Because AUROC and especially AUPRC are less biased toward majority classes, these gains suggest that hierarchical supervision slightly helps find rare but relevant variant-label associations. Training all three models across the 30 random splits (100 epochs each) required approximately 12-14 hours using 4 H100 GPUs.

3.3. *Ablation study to assess feature contributions*

To evaluate the contribution of different features (Fig. 2), we conducted an ablation study in one of the 30 splits combining UniProt domain, ClinVar, and path-based inputs under three prediction strategies. The results are shown in Table 5. Among single-feature inputs, the path-only setting consistently outperformed domain or ClinVar in every prediction mode. With path

features alone, the coarse-grained model reaches an $F_1 = 0.922$, while hierarchical and fine-grained models attain 0.595 and 0.414, respectively. In contrast, using only domain or ClinVar information yields F_1 values below 0.3 across all modes, underscoring the comparatively weak signal carried by these annotations.

Table 5. Ablation results for different feature combinations and prediction strategies

Feature	Model	Micro-P	Micro-R	Micro-F_1	ACC	AUROC	AUPRC
Domain	fine-grained	0.201	0.196	0.199	0.016	0.564	0.056
	coarse-grained	0.462	0.117	0.187	0.059	0.596	0.160
	hierarchical	0.233	0.205	0.218	0.012	0.587	0.059
ClinVar	fine-grained	0.216	0.198	0.207	0.018	0.592	0.056
	coarse-grained	0.416	0.221	0.288	0.065	0.617	0.166
	hierarchical	0.219	0.253	0.235	0.008	0.574	0.059
Path	fine-grained	0.459	0.377	0.414	0.089	0.872	0.130
	coarse-grained	0.960	0.886	0.922	0.811	0.961	0.782
	hierarchical	0.527	0.683	0.595	0.175	0.925	0.279
Domain+ClinVar	fine-grained	0.263	0.205	0.230	0.008	0.594	0.061
	coarse-grained	0.522	0.124	0.200	0.075	0.611	0.172
	hierarchical	0.267	0.240	0.253	0.010	0.593	0.062
Domain+Path	fine-grained	0.501	0.482	0.491	0.142	0.890	0.177
	coarse-grained	0.969	0.895	0.931	0.815	0.974	0.791
	hierarchical	0.529	0.685	0.597	0.181	0.927	0.300
ClinVar+Path	fine-grained	0.563	0.545	0.554	0.258	0.900	0.182
	coarse-grained	0.961	0.911	0.936	0.823	0.964	0.779
	hierarchical	0.521	0.693	0.595	0.199	**0.929**	0.314
Domain+ClinVar+Path	fine-grained	**0.578**	0.562	0.570	**0.268**	0.902	0.200
	coarse-grained	0.968	0.908	0.937	0.827	0.969	0.783
	hierarchical	0.545	**0.695**	**0.611**	0.215	0.926	**0.317**

Bold values indicate the best performance between fine-grained and hierarchical models.

Adding path features to domain type or ClinVar inputs produces substantial gains, especially for fine-grained and hierarchical prediction. For example, adding path features to domain feature raises fine-grained F_1 from 0.198 to 0.491 and hierarchical F_1 from 0.218 to 0.597. A similar trend is observed for the ClinVar + path combination, where hierarchical F_1 goes to 0.595 and AUROC exceeds 0.928.

When all three feature types are combined, the hierarchical model achieves the best overall balance (Micro-$F_1 = 0.611$; AUPRC = 0.317), while the fine-grained model records its highest precision (0.578) and accuracy (0.268). These results confirm that path-derived context provides the dominant functional signal, while ClinVar pathogenicity annotation and UniProt domain type features add some complementary evidence that can further enhance precision and broaden label coverage when integrated with path information.

3.4. *De novo variant impact prediction*

To demonstrate the practical utility of our trained hierarchical model, we developed a prediction tool that annotates protein variants with biological process and disease associations. During inference, the model queries external databases to construct feature vectors, with missing features imputed using appropriate default values, as summarized in Fig. 2 and Table 2. The prediction tool outputs sigmoid-normalized probability scores (0-1) for each label and category, with predictions ranked by confidence to facilitate experimental prioritization.

Figure 5 illustrates a representative prediction for two variants, *VPS35* R524W and *PSEN1* L435F. *VPS35* encodes a retromer complex component involved in endosomal trafficking,[20] and the R524W substitution was not present in our training data. Our model predicts high-confidence associations with translation (62.9%), DNA damage processes (49.7%), and Parkinson's Disease (49.0%). These predictions align with *VPS35* known trafficking functions and established links between variants and neurodegeneration. Similarly, for *PSEN1* L435F, the model highlights associations with localization (74.1%), translation (62.5%), and apoptotic signaling (51.0%), consistent with *PSEN1* role in γ-secretase complex activity and its involvement in Alzheimer's Disease pathology. These examples demonstrate the predictor ability to capture both direct molecular consequences and downstream pathological processes.

Variant	VPS35_R524W		PSEN1_L435F	
Query	Sequence	MPTTQQSP...PIYEGLIL (796 AA)	Sequence	MTELPAPLSYF... QLAFHQFYI (467 AA)
	Domain	REGION	Domain	REGION, MOTIF
	ClinVar	Pathogenicity: not provided Review: 0	ClinVar	Pathogenicity: not provided Review: 0
Predict	biological process/disease	probability	biological process/disease	probability
	translation (protein synthesis degradation)	62.9%	localization (cellular transport)	74.1%
	DNA damage (DNA chromatin processes)	49.7%	translation (protein synthesis degradation)	62.5%
	Parkinson disease (neurological disorders)	49.0%	apoptotic process (cell death survival)	51.0%
	……		……	

Fig. 5. Predicted process and disease for novel variants *VPS35* R524W and *PSEN1* L435F; predictor queries external databases for sequences, domain types, and ClinVar annotations based on the input variant, outputs probability scores.

4. Discussion

The mechanistic paths reconstructed by our framework address a gap in variant interpretation in that it is able to generate specific, experimentally tractable hypotheses about variant function. Unlike pathogenicity scores that classify variants as "pathogenic" or "benign", our predictions identify particular molecular mechanisms that could facilitate targeted experimental validation and therapeutic design. This mechanistic understanding is valuable for interpreting variants of uncertain significance (VUS), where clinical care teams need biological context beyond pathogenicity scores to guide treatment decisions and experimental follow-up.

It is important to mention that this is not the first approach that attempts to predict molecular mechanisms of disease upon mutation. Prediction of disruption of protein stability

has been a long-standing problem in the community.[21,22] The MutPred[23–27] suite of tools has used unsupervised and supervised approaches to predict loss and gain of more than fifty different types of structural and functional disruption (e.g., loss of metal binding, gain of post-translational modification sites). Most recently, predictors capable of predicting disruption of specific protein-protein interactions have also emerged.[28] However, none of these approaches go beyond the effect of the variant on the protein's structure and function. They therefore do not identify a causal path from the variant to a broad biological process disrupted by the variant and ultimately a specific disease phenotype.

The network we constructed illustrates the power of automated literature synthesis for biological knowledge integration. It organizes mechanistic knowledge previously scattered across publications, with each path reconstructed from individual studies describing complete causal chains from variant to phenotype. Since they are constructed from the same publications, these paths provide internal consistency and minimize potential confounding effects from unrelated variants in the same protein. Such network-level analysis provides insights into complex diseases where multiple molecular pathways contribute to pathogenesis. Thus, our framework offers a distinct perspective on variant interpretation that prior pathogenicity predictors that focus on binary classification or local molecular effects do not capture, in particular, how these effects propagate through biological networks to influence disease outcomes.

The mechanistic insights provided by our framework have direct implications for precision medicine applications.[29] By identifying specific biological pathways disrupted by variants observed in patients, clinicians could select targeted therapies that address underlying molecular mechanisms rather than relying solely on pathogenicity scores. For instance, variants predicted to affect DNA repair pathways might guide the selection of PARP inhibitors, while those affecting metabolic processes could inform dietary or pharmacological interventions. The resolution of predictions can be adapted to specific use cases: 1085 fine-grained mechanistic labels support detailed experimental design for lab-based molecular studies, while broader 30 biological categories may suffice for initial clinical assessment and disease area identification.

While our literature-derived networks capture the latest findings and can identify novel mechanistic relationships not yet represented in curated databases, they are subject to inherent biases in the scientific literature. Well-studied proteins and diseases tend to have richer path coverage, while emerging areas of biology may be underrepresented until sufficient experimental evidence accumulates. The reliance on literature-curated pathways may limit prediction for novel variants lacking prior experimental characterization. Future developments should integrate multiple knowledge sources, including structural predictions and functional genomics data, to provide more complete mechanistic characterization of variant effects.

Availability

Code and data are available at `https://github.com/gyorilab/indra_variants`.

Acknowledgements

This work was funded by the DARPA ASKEM and ARPA-H BDF programs HR00112220036 (BMG), and the NIH award U01HG012022 (PR).

References

1. M. Arnaudi, M. Utichi, M. Tiberti and E. Papaleo, Predicting the structure-altering mechanisms of disease variants, *Curr Opin Struct Biol* **91**, 102994 (2025).
2. T. A. Peterson, E. Doughty and M. G. Kann, Towards precision medicine: advances in computational approaches for the analysis of human variants, *J Mol Biol* **425**, 4047 (2013).
3. P. Katsonis, K. Wilhelm, A. Williams and O. Lichtarge, Genome interpretation using in silico predictors of variant impact, *Hum Genet* **141**, 1549 (2022).
4. Y. J. Lin, A. S. Menon, Z. Hu and S. E. Brenner, Variant Impact Predictor database (VIPdb), version 2: trends from three decades of genetic variant impact predictors, *Hum Genomics* **18**, 90 (2024).
5. M. J. Landrum, J. M. Lee, M. Benson, G. Brown, C. Chao, S. Chitipiralla, B. Gu, J. Hart, D. Hoffman, J. Hoover, W. Jang, K. Katz, M. Ovetsky, G. Riley, A. Sethi, R. Tully, R. Villamarin-Salomon, W. Rubinstein and D. R. Maglott, ClinVar: public archive of interpretations of clinically relevant variants, *Nucleic Acids Res* **44**, D862 (2016).
6. P. D. Stenson, M. Mort, E. V. Ball, M. Chapman, K. Evans, L. Azevedo, M. Hayden, S. Heywood, D. S. Millar, A. D. Phillips and D. N. Cooper, The Human Gene Mutation Database (HGMD®): optimizing its use in a clinical diagnostic or research setting, *Hum Genet* **139**, 1197 (2020).
7. S. Richards, N. Aziz, S. Bale, D. Bick, S. Das, J. Gastier-Foster, W. W. Grody, M. Hegde, E. Lyon, E. Spector, K. Voelkerding and H. L. Rehm, Standards and guidelines for the interpretation of sequence variants: a joint consensus recommendation of the american college of medical genetics and genomics and the association for molecular pathology, *Genet Med* **17**, 405 (2015).
8. V. Pejaver, A. B. Byrne, B. J. Feng, K. A. Pagel, S. D. Mooney, R. Karchin, A. O'Donnell-Luria, S. M. Harrison, S. V. Tavtigian, M. S. Greenblatt, L. G. Biesecker, P. Radivojac, S. E. Brenner and ClinGen Sequence Variant Interpretation Working Group, Calibration of computational tools for missense variant pathogenicity classification and ClinGen recommendations for PP3/BP4 criteria, *Am J Hum Genet* **109**, 2163 (2022).
9. IGVF Consortium, Deciphering the impact of genomic variation on function, *Nature* **633**, 47 (2024).
10. K.-S. Benjamin, K. O. Buduka, P. W. Thomas and E. M. Adilson, Generative prediction of causal gene sets responsible for complex traits, *Proceedings of the National Academy of Sciences* **122**, p. e2415071122 (2025).
11. B. M. Gyori, J. A. Bachman, K. Subramanian, J. L. Muhlich, L. Galescu and P. K. Sorger, From word models to executable models of signaling networks using automated assembly, *Mol Syst Biol* **13**, 954 (2017).
12. J. A. Bachman, B. M. Gyori and P. K. Sorger, Automated assembly of molecular mechanisms at scale from text mining and curated databases, *Mol Syst Biol* **19**, e11325 (2023).
13. Z. Lin, H. Akin, R. Rao, B. Hie, Z. Zhu, W. Lu, N. Smetanin, R. Verkuil, O. Kabeli, Y. Shmueli, A. dos Santos Costa, M. Fazel-Zarandi, T. Sercu, S. Candido and A. Rives, Evolutionary-scale prediction of atomic-level protein structure with a language model, *Science* **379**, 1123 (2023).
14. M. Schlichtkrull, T. N. Kipf, P. Bloem, R. van den Berg, I. Titov and M. Welling, Modeling relational data with graph convolutional networks, *arXiv preprint arXiv:1703.06103* (2017).
15. B. Yang, W. tau Yih, X. He, J. Gao and L. Deng, Embedding entities and relations for learning and inference in knowledge bases, *arXiv preprint arXiv:1412.6575* (2015).
16. A. Bordes, N. Usunier, A. Garcia-Durń, J. Weston and O. Yakhnenko, Translating embeddings for modeling multi-relational data, *Advances in Neural Information Processing Systems* **26**, p. 2787–2795 (2013).
17. A. Vaswani, N. Shazeer, N. Parmar, J. Uszkoreit, L. Jones, A. N. Gomez, L. Kaiser and I. Polosukhin, Attention is all you need, *Advances in Neural Information Processing Systems* **30**, p.

6000–6010 (2017).
18. J. Hu, L. Shen and G. Sun, Squeeze-and-excitation networks, in *2018 IEEE/CVF Conference on Computer Vision and Pattern Recognition*, 2018.
19. E. Ben-Baruch, T. Ridnik, N. Zamir, A. Noy, I. Friedman, M. Protter and L. Zelnik-Manor, Asymmetric loss for multi-label classification, *arXiv preprint arXiv:2009.14119* (2020).
20. D. Hu, Z. Liu and X. Qi, Mitochondrial quality control strategies: Potential therapeutic targets for neurodegenerative diseases?, *Front Neurosci* **15**, 746873 (2021).
21. E. Capriotti, P. Fariselli and R. Casadio, I-Mutant2.0: predicting stability changes upon mutation from the protein sequence or structure, *Nucleic Acids Res* **33**, W306 (2005).
22. J. Schymkowitz, J. Borg, F. Stricher, R. Nys, F. Rousseau and L. Serrano, The FoldX web server: an online force field, *Nucleic Acids Res* **33**, W382 (2005).
23. B. Li, V. G. Krishnan, M. E. Mort, F. Xin, K. K. Kamati, D. N. Cooper, S. D. Mooney and P. Radivojac, Automated inference of molecular mechanisms of disease from amino acid substitutions, *Bioinformatics* **25**, 2744 (2009).
24. M. Mort, U. S. Evani, V. G. Krishnan, K. K. Kamati, P. H. Baenziger, A. Bagchi, B. J. Peters, R. Sathyesh, B. Li, Y. Sun, B. Xue, N. H. Shah, M. G. Kann, D. N. Cooper, P. Radivojac and S. D. Mooney, In silico functional profiling of human disease-associated and polymorphic amino acid substitutions, *Hum Mutat* **31**, 335 (2010).
25. K. A. Pagel, V. Pejaver, G. N. Lin, H. J. Nam, M. Mort, D. N. Cooper, J. Sebat, L. M. Iakoucheva, S. D. Mooney and P. Radivojac, When loss-of-function is loss of function: assessing mutational signatures and impact of loss-of-function genetic variants, *Bioinformatics* **33**, i389 (2017).
26. K. A. Pagel, D. Antaki, A. Lian, M. Mort, D. N. Cooper, J. Sebat, L. M. Iakoucheva, S. D. Mooney and P. Radivojac, Pathogenicity and functional impact of non-frameshifting insertion/deletion variation in the human genome, *PLoS Comput Biol* **15**, e1007112 (2019).
27. V. Pejaver, J. Urresti, J. Lugo-Martinez, K. A. Pagel, G. N. Lin, H.-J. Nam, M. Mort, D. N. Cooper, J. Sebat, L. M. Iakoucheva, S. D. Mooney and P. Radivojac, Inferring the molecular and phenotypic impact of amino acid variants with MutPred2, *Nat Commun* **11**, 5918 (2020).
28. J. C. Siwek, A. A. Omelchenko, P. Chhibbar, S. Arshad, A. Rosengart, I. Nazarali, A. Patel, K. Nazarali, J. Rahimikollu, J. S. Tilstra, M. J. Shlomchik, D. R. Koes, A. V. Joglekar and J. Das, Sliding window interaction grammar (SWING): a generalized interaction language model for peptide and protein interactions, *Nat Methods* **22**, 1707 (2025).
29. B. Rost, P. Radivojac and Y. Bromberg, Protein function in precision medicine: deep understanding with machine learning, *FEBS Lett* **590**, 2327 (2016).

Systems Biology and Network Analysis: From Multi-omics Integration to Biological Mechanisms

Gurkan Bebek
Center for Proteomics and Bioinformatics, Case Western Reserve University, Cleveland, OH 44106, USA
E-mail: gurkan@case.edu

Onur Mutlu
Information Technology and Electrical Engineering Department, ETH Zürich, Zurich, 8092, Switzerland
E-mail: aonur.mutlu@inf.ethz.ch

Iman Hajirasouliha
Department of Systems and Computational Biomedicine Weill Cornell Medicine, New York City, NY 10021, USA
E-mail: imh2003@med.cornell.edu

Joshua Welch
Computational Medicine and Bioinformatics, University of Michigan, Ann Arbor, MI 48109, USA
E-mail: welch@umich.edu

Serguei Pakhomov
Department of Pharmaceutical Care & Health Systems, University of Minnesota, Minneapolis, MN 55455, USA
E-mail: pakh0002@umn.edu

1. Session Introduction: Systems Biology and Network Analysis

Recent advances in multi-omics technologies have generated unprecedented volumes of data, offering new opportunities to decode the complex interplay between molecular components and biological mechanisms. This session, *Systems Biology and Network Analysis: From Multi-omics Integration to Biological Mechanisms*, brings together innovative computational approaches that span transcriptomics, proteomics, metabolic modeling, and network biology. The selected papers exemplify how systems-level analysis can reveal interpretable, mechanistically grounded insights into disease processes, therapeutic strategies, and biological regulation.

The session is anchored in the belief that bridging molecular interactions with cellular and tissue-level phenomena is essential for understanding disease mechanisms and developing personalized interventions. The contributions in this session reflect the growing synergy between network biology and machine learning, particularly in areas such as dynamic network inference, drug repurposing, and multi-modal data integration.

© 2025 The Authors. Open Access chapter published by World Scientific Publishing Company and distributed under the terms of the Creative Commons Attribution Non-Commercial (CC BY-NC) 4.0 License.

2. Session Summary

This session includes an invited talk, five peer-reviewed papers selected for oral presentation by the session chairs, and one poster presentation selected by the conference organizers. The studies featured in this session focus on the development of computational methods that leverage multi-omics data—including transcriptomics, proteomics, and network biology—to investigate complex biological mechanisms. These contributions exemplify the session's emphasis on systems-level modeling, mechanistic interpretation, and translational relevance.

2.1. *Session Papers*

The following papers will be presented at the Systems Biology and Networks Session:

Tasnina et al. address a critical gap in network biology by introducing a path-based provenance tracing framework for diffusion algorithms. Their metrics—path-based effective diffusion and diffusion betweenness—quantify how scores propagate through biological networks, revealing the global structure exploited by diffusion algorithms. Applied to SARS-CoV-2 interactors and human protein networks, their work provides a new lens for interpreting network-based predictions, directly supporting the session's goal of mechanistic transparency in AI-driven models.

Zhou et al. present REPEL, a graph augmentation method that improves protein function prediction by introducing random repelling forces in network embeddings. Evaluated on yeast and E. coli networks, REPEL outperforms existing methods such as Mashup, deepNF, and BIONIC. This contribution illustrates how uniform perturbation can denoise embeddings and enhance robustness, aligning with the session's interest in scalable, generalizable methods for functional annotation across biological networks.

Blair et al. introduce NORSP, a novel algorithm for identifying sparse perturbation sets capable of transitioning biological systems between steady states. By combining network propagation with supervised learning, NORSP enables biologically feasible control strategies across transcriptomic and metabolic models. This contribution aligns with the session's focus on systems-level modeling and experimental design, offering a scalable framework for hypothesis generation and therapeutic prioritization.

Chen and Wang introduce a transcriptomic signature-based framework built on the GenoMAS system, designed to analyze over 1,300 disease–condition pairs. Their work constructs a disease similarity network that successfully recovers known comorbidities while revealing unexpected cross-category relationships. By combining gene-level and pathway-level similarities, the study underscores the value of interpretable multi-omics integration for generating mechanistic hypotheses. Their focus on rare diseases, including autism spectrum disorder, highlights the promise of network-based methodologies in advancing precision medicine.

Orlenko et al. present a random-walk-based learning framework aimed at drug repurposing for Alzheimer's disease. Leveraging Hetionet and AlzKB, they generate network-informed gene embeddings and apply a multi-objective AutoML strategy to rank candidate genes. Their approach illustrates how integrating knowledge graphs with network-derived metrics can reveal both established and previously unrecognized biological connections—reflecting the session's broader emphasis on data-driven strategies for drug discovery and the importance of

transparent, interpretable modeling.

The poster presentation by Rajagopalan et al. introduces DRIVE-KG, a heterogeneous knowledge graph framework designed to integrate multi-omics data for variant–phenotype association discovery in complex and understudied diseases such as endometriosis. By combining biological knowledge from diverse sources and applying graph-based machine learning, the authors uncover novel SNP–phenotype associations and demonstrate improved patient classification performance compared to traditional genetic risk scores. This work exemplifies the session's goals by showing how graph-based integration of multi-modal data can advance precision medicine, particularly in historically underdiagnosed conditions.

Together, these papers reflect the session's commitment to advancing systems biology through computational innovation. They demonstrate how network-based methods can integrate multi-omics data, generate testable hypotheses, and provide mechanistic insights into disease and biology. By bridging molecular and cellular scales, and combining network biology with machine learning, this session contributes to the broader goals of precision medicine, translational research, and biological discovery.

3. Acknowledgments

Gurkan Bebek is supproted by an NIH NIA grant (1R21AG074287). Iman Hajirasouliha is supported by an NIH NIGMS grant (R35GM138152) and an Irma T. Hirschl/Monique Weill-Caulier Trust Research Award.

Provenance Tracing in Network Diffusion Algorithms

Nure Tasnina
Dept. of Computer Science, Virginia Tech, Blacksburg, VA 24061, USA
E-mail: tasnina@vt.edu

Mark Crovella
Dept. of Computer Science, Boston University, Boston, MA 02215, USA

Simon Kasif
Dept. of Biomedical Engineering, Dept. of Computer Science, Graduate Program in Bioinformatics, Boston University, Boston, MA 02215, USA

T. M. Murali
Dept. of Computer Science, Virginia Tech, Blacksburg, VA 24061, USA
E-mail: murali@cs.vt.edu

We propose a novel strategy for provenance tracing in random walk-based network diffusion algorithms, a problem that has been surprisingly overlooked in spite of the widespread use of diffusion algorithms in biological applications. Our path-based approach enables ranking paths by the magnitude of their contribution to each node's score, offering insight into how information propagates through a network. Building on this capability, we introduce two quantitative measures: (i) *path-based effective diffusion*, which evaluates how well a diffusion algorithm leverages the full topology of a network, and (ii) *diffusion betweenness*, which quantifies a node's importance in propagating scores. We applied our framework to SARS-CoV-2 protein interactors and human PPI networks. Provenance tracing of the Regularized Laplacian and Random Walk with Restart algorithms revealed that a substantial amount of a node's score is contributed via multi-edge paths, demonstrating that diffusion algorithms exploit the non-local structure of the network. Analysis of diffusion betweenness identified proteins playing a critical role in score propagation; proteins with high diffusion betweenness are enriched with essential human genes and interactors of other viruses, supporting the biological interpretability of the metric. Finally, in a signaling network composed of causal interactions between human proteins, the top contributing paths showed strong overlap with COVID-19-related pathways. These results suggest that our path-based framework offers valuable insight into diffusion algorithms and can serve as a powerful tool for interpreting diffusion scores in a biologically meaningful context, complementing existing module- or node-centric approaches in systems biology. The code is publicly available at `https://github.com/n-tasnina/provenance-tracing.git` under the GNU General Public License v3.0.

Keywords: protein-protein interaction, network diffusion, molecular mechanism

© 2025 The Authors. Open Access chapter published by World Scientific Publishing Company and distributed under the terms of the Creative Commons Attribution Non-Commercial (CC BY-NC) 4.0 License.

1. Introduction

Protein-protein interaction networks[1,2] have emerged as invaluable resources for studying the complex workings of living cells.[3,4] Within such a network, each node represents a protein, while each edge corresponds to an interaction between two proteins, e.g., physical or genetic. Diffusion algorithms are widely used to analyze such networks, enabling a variety of applications such as protein function prediction,[5,6] disease module discovery,[7] disease characterization,[8,9] and drug target prediction.[10] In recent years, they have also driven momentum in *in silico* drug repositioning[11,12]. The principle underlying these algorithms is that proteins with similar functions tend to interact with each other.[13,14] Typical network diffusion algorithms assign specific scores or labels to a set of experimentally determined nodes or seed nodes, e.g., proteins known to perform a particular function, and iteratively propagate this information through the network's edges to nearby nodes. This process continues for a fixed number of steps or until convergence. The final score of each node, which reflects its proximity to seed nodes, can be used as a surrogate for the node's association with the function of interest.

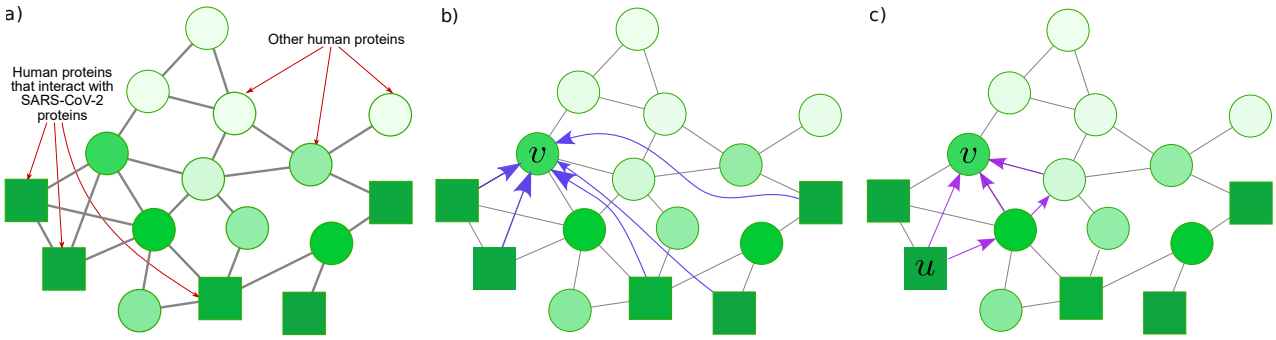

Fig. 1. **Illustration of provenance tracing**. a) A pictorial depiction of diffusion of score in a human protein-protein interaction network where nodes are the proteins and edges represent any interaction between proteins. Here, circular nodes depict all human proteins except those with experimental evidence of interaction with SARS-CoV-2 proteins. The SARS-CoV-2 protein interactors (seed nodes) are represented by square-shaped nodes. A network diffusion algorithm propagates scores from the seed nodes to all other human proteins in the network. The green hue of the nodes corresponds to the computed likelihood (score) of interaction with SARS-CoV-2, with a higher intensity indicating a greater likelihood. b) Node based algorithms of provenance tracing allow computing the contribution from each of the five seed nodes to the final score of the node v. c) Path-based algorithms of provenance tracing compute contributions coming along individual paths from seed nodes to other nodes, e.g., u to node v.

The last 10 years of research in AI has emphasized the importance of interpretability, explainability, and transparency of predictions independent of the specific prediction methodology used.[15] This is particularly important in scientific or medical application of network diffusion. In this context, "provenance" is defined as a trace from a predicted activity associated with a node (e.g., protein) to the factual (experimentally determined) evidence associated with seed nodes that were most informative in computing the predicted score.[16] Provenance tracing is the process of determining the origin of a predicted score back to the seed nodes.

While network diffusion algorithms have been deployed for more than 20 years, the question of provenance tracing is understudied.[16] Law *et al.*[17] explored a node-oriented method for provenance tracing in the important context of random walk based diffusion algorithms. For every node v, Law *et al.* computed how much each seed node contributed to the score of v. They defined "node-based effective diffusion" (NED) as the fraction of a node's score contributed by seed nodes that are not direct neighbors. Using SARS-CoV-2 interactors of humans as seed nodes,[18] they found that for each top-ranking prediction (i.e., a node with a high score), the largest contribution came from a seed node that was a direct neighbor. They also varied the algorithm's parameters to allow the random walker to travel longer paths in the network, with the expectation that this change would diffuse high scores beyond the direct neighborhood of the seed nodes. However, the outcome of these experiments only confirmed their earlier findings. This observation prompted us to delve deeper into the widely accepted belief that diffusion algorithms utilize the non-local neighborhood of the network.[14]

We developed a novel path-based strategy for provenance tracing in random walk-based algorithms by leveraging our ability to compute the magnitude of the contribution made to a node's score by each path starting at a seed node and ending at the corresponding node (Section 2.3). In this work, we focused on two well-known network diffusion algorithms: Regularized Laplacian (RL)[19] and Random Walk with Restart (RWR).[20] In these algorithms, the predicted score s_v of a node v is the linear sum of the 'contribution' made by each seed node to s_v (Section 2.2). In our path-based approach, we show for every u–v path (where u is a seed node and v is a node), how to compute its contribution to s_v (Section 2.3). We further proposed two new measures: 1) path-based effective diffusion (PED) (Section 2.3.1) and 2) diffusion betweenness (Section 2.3.3). PED measures the fraction of a node's score contributed by multi-edge paths. Diffusion betweenness measures a node's importance in score propagation by quantifying the total contribution transmitted along paths passing through that node.

We implemented RL and RWR on human protein-protein interaction (PPI)[1,2] networks with SARS-CoV-2 human protein interactors as seed nodes.[18] Analysis of PED demonstrated that a substantial amount of a node's score was contributed via paths with more than one edge. Moreover, the vast majority of the nodes in the network were involved in paths carrying non-zero contributions to the top-scoring nodes. We concluded that diffusion algorithms do exploit the non-local structure of a network. Our analysis of diffusion betweenness further revealed the biological relevance of the proteins playing a critical role in score propagation across the network, as they were enriched with essential human genes and interactors of other viruses. Finally, as a case study, we applied our path-based approach to a signaling network containing causal interactions between human proteins.[21] We observed that the edges in the paths that contributed most to the scores of top-scoring nodes had a high degree of overlap with COVID-19-related pathways. Our new path-based analysis may produce novel insights in systems biology.

2. Methods

In this section, we provided a detailed description of two network diffusion algorithms: Regularized Laplacian (RL) and Random Walk with Restart (RWR). Next, we outlined both the

node-based and path-based approaches to provenance tracing. Finally, we defined the diffusion betweenness score and presented the formula used for its computation.

2.1. *Network diffusion algorithms*

Let $G = (V, E, w)$ be a weighted network where each node $v \in V$ is a human protein, and each edge $(u, v) \in E$ represents either an interaction between proteins u and v when G is an undirected PPI network or causal effect of u on v when G is a directed signaling network, and w_{vu} specifies the weight of edge (u, v). Given G and a set $P \subset V$ of seed nodes, e.g., human proteins that interact with SARS-CoV-2 proteins, we seek to compute a score s_v for each node v indicating our confidence that it either physically interacts with or is functionally linked to the virus. In this avenue, we employ RL and RWR algorithm on the undirected PPI networks and RWR on the directed signaling network.

Regularized Laplacian (RL).

(1) Define a label vector $\vec{y}$ over the nodes in G where $y_u = 1$ if node $u \in P$ and $y_u = 0$, otherwise.
(2) Define $W \in \mathbb{R}^{n \times n}$ as the adjacency matrix of G with edge weights, i.e., W_{vu}, the entry in row v and column u of W equals w_{vu} if (u, v) is an edge in G and 0, otherwise.
(3) Define D as a diagonal matrix with $D_{uu} = d_u = \sum_v W_{vu}$. Here, D contains the degree of every node u in G.
(4) Compute $\tilde{W} = D^{-1/2} W D^{-1/2}$, which denotes the normalized network.
(5) Compute the Laplacian of G as $\tilde{L} = \tilde{D} - \tilde{W}$, where we define $\tilde{D}$ to be a diagonal matrix with $\tilde{D}_{uu} = \sum_v \tilde{W}_{vu}$.
(6) Given a parameter $\alpha > 0$ and the goal to minimize the loss function:

$$\sum_{u \in V} (s_u - y_u)^2 + \alpha \sum_{(u,v) \in E} \tilde{W}_{vu} (s_u - s_v)^2 \tag{1}$$

where s_v is the computed score of node v, we obtain the score vector from the unique, global optimization of Equation (1) as follows:

$$\vec{s} = (I + \alpha \tilde{L})^{-1} \vec{y} \tag{2}$$

Here, $\tilde{L}$ is symmetric and positive semidefinite. Hence, $(I + \alpha \tilde{L})$ is symmetric, positive definite, and invertible.

Random walk with restart (RWR).

(1) Define $\vec{y}$, W, D as defined in RL.
(2) Compute the normalized network matrix $\tilde{W} = W D^{-1}$.
(3) Given a parameter $0 < \alpha < 1$, where α is the restart probability, and the goal to minimize the loss function:

$$\alpha \sum_{u \in V} \frac{(s_u - y_u)^2}{d_u} + (1 - \alpha) \sum_{(u,v) \in E} W_{vu} \left(\frac{s_u}{d_u} - \frac{s_v}{d_v} \right)^2 \tag{3}$$

we obtain the score vector from the unique, global optimization of Equation (3) as follows:

$$\vec{s} = \frac{\alpha}{|P|}(I - (1-\alpha)\tilde{W})^{-1}\vec{y} \tag{4}$$

Here, $\tilde{W}$ is column-stochastic (every column sums to 1 and all entries are nonnegative). By the Perron-Frobenius theorem, every eigenvalue for $(I-(1-\alpha)\tilde{W})$ is strictly positive, making $(I-(1-\alpha)\tilde{W})$ invertible.

We chose a value of α in RL (and RWR) such that it balances out the two terms in the quadratic loss function in Equation (1) (and Equation (3)). We did a binary search to find out the exact value for which the two loss terms are equal. For RL, α ranged between 0.94 and 1.33 and for RWR, α was 0.49 across all networks.

2.2. *Node-based provenance tracing*

For RL, let K denote the matrix $(I+\alpha\tilde{L})^{-1}$. According to Equation (2), s_v is the sum of K_{vu} over all nodes $u \in P$ (i.e., seed nodes); $s_v = \sum_{u\in P} K_{vu}$. Hence, K_{vu} denotes the contribution of seed node u to node v's score s_v. For RWR, let K denote the matrix $\alpha/|P|(I-(1-\alpha)\tilde{W})^{-1}$ (Equation (4))

Node-based effective diffusion (NED). Law *et al.*[17] summarized node-based provenance tracing with a score, namely, *node-based effective diffusion (NED)* where NED(v) is defined as the fraction of v's score contributed from seed nodes that are not direct neighbors. Following is the corresponding formula:

$$\text{NED}(v) = 1 - \frac{\sum_{u\in P\cap N(v)} K_{vu}}{s_v}, N(v) \text{ is the set of neighbors of node } v.$$

2.3. *Path-based provenance tracing*

In this section, we show how to express the score s_v of node v as the sum of weighted 'contributions' along paths that start at some seed node and end at v. First, we describe a matrix M that captures the contribution along an edge. Then we extend the formula to compute the contribution along longer paths.

***M* for RL.** We consider diffusion by the RL algorithm as a fluid flow model where no node contains any fluid initially and then a hypothetical fluid is pumped into every seed node at a constant rate of 1.[22] The fluid diffuses from one node to another at a first-order rate of $\alpha\tilde{D}$ and fluid *leaves* the network at a first-order rate of 1. M_{ji} is the rate of incoming flow at node j from node i via edge (i,j). Applying the fluid flow model we formulated M as follows: $M = \alpha\tilde{W}(I+\alpha\tilde{D})^{-1}$

***M* for RWR.** For RWR, M_{ji} denotes the probability that a random walker moves from node i to node j in a single time step. Hence, we formulated M as follows: $M = (1-\alpha)\tilde{W}$

Having established how to compute the contribution along a single edge using M, we now extend this to longer paths involving multiple edges. Given a u and any node v in V, for a

u–v path in G, the contribution made by this path to s_v is the product of the edge weights along the path, where the edge weights are from M. For instance, via a path $u \to t \to x \to v$ containing three edges: $(u,t),(t,x),(x,v)$, u's contribution to s_v is $M_{tu}M_{xt}M_{vx}$. More generally, M^n_{vu} is the contribution from a u to a node v via all paths of length n.

2.3.1. *Path-based effective diffusion*

We define *path-based effective diffusion* (PED) of a node v as the fraction of its score, s_v contributed by paths that start at some seed node, end at v, and contain more than one edge. We formulate $PED(v)$ as follows:

$$\text{PED}(v) = 1 - \frac{c(v)\sum_{u\in P} M_{vu}}{s_v},$$

where $\sum_{u\in P} M_{vu}$ denotes the incoming contribution to s_v along paths with one edge from any seed node and $c(v)$ denotes a weight. For RL, $c(v) = (1+\alpha\tilde{D}_{vv})^{-1}$ while for RWR, $c(v) = \frac{\alpha}{|P|}$ is a constant. Note that $M_{vu} = 0$ if u is not a neighbor of v.

2.3.2. *Find top m contributing paths*

The path-based provenance tracing, more precisely the derived matrix M provided us with the ability to compute contribution coming along any path starting at a seed node to any node in the network. Though there can be infinite paths between a seed node and any other node (considering paths with cycles in them), the most interesting paths are the ones that carry substantial contributions to nodes' scores. In this avenue, from all the paths starting at any seed node carrying contribution to any of the top k (in this experiment $k = |P|$) predicted nodes, we find m most contributing paths.

Suppose, M' is the weighted adjacency matrix of a graph where $M'_{ji} = -\log_{10}(M_{ji})$. In this graph, the m-shortest paths from a seed node u to a node v are the most *contributing* m paths from u to s_v. To compute the m-shortest paths between any seed node and the top-k predicted proteins (based on their scores), we augmented the network with two dummy nodes: (1) a super-source, connected to all seed nodes, and (2) a super-sink, connected from the top-k predicted nodes. We then computed the m-shortest paths from the super-source to the super-sink using Eppstein's k-shortest paths algorithm that considers looped paths.

2.3.3. *Computing diffusion betweenness*

The diffusion betweenness score of a node aims to capture the total amount of score propagating along paths on which the corresponding node lies. For a node t, we define its *diffusion betweenness* score $b(t)$ as the sum of the contribution made to s_v along *all* π_{u-t-v} paths in which u ranges over all seed nodes, t is an internal node, and v ranges over all nodes in V.

In practice, while computing diffusion betweenness, we use a heuristic where we consider only paths with at most four edges, since a negligible fraction of the score propagates via paths with more edges.[23,24] To formulate $b(t)$, we introduce another matrix Q where Q_{vt} is the

contribution from any seed node to s_v along *all* paths (length ≤ 4) ending at v having t as an intermediate node. We formulate $b(t)$ as follows: $b(t) = \sum_{v \in V} c(v) Q_{vt}$

Computation of Q. We define X^{lm} where X^{lm}_{vt} holds the contribution to s_v along all paths of length $(l+m)$ with t being the lth intermediate node. We compute $Q_{vt} = \sum_{(l+m) \leq 4} X^{lm}_{vt}$.

Computation of X^{lm}. Let us divide any π_{u-t-v} path into two segments: (1) from the seed node to the intermediate node, i.e., u–t, and (2) from the intermediate node to the endpoint, i.e., t–v. As the contribution along a path is only the product of the edge weights (from M) along that path, the contribution of π to s_v equals the product of: (1) contribution along u–t, (2) contribution along t–v. We can extend this two-component-product concept to compute X^{lm}_{vt} as follows:

$$X^{lm}_{vt} = M^m_{vt}.(M^l \vec{y})_t,$$

Here, $(M^l \vec{y})_t$ is the sum of the contribution to s_t along *all* u–t paths of length l and M^m_{vt} is the sum of the contribution to s_v along *all* t–v paths of length m.

3. Datasets

3.1. *Experimentally determined nodes*

We considered 332 human proteins that interact with SARS-CoV-2[18] as seed nodes. We included the ACE2 receptor in this set.

3.2. *Human protein-protein interaction networks*

We considered three human protein-protein interaction (PPI) networks: STRING,[1] BioGRID-Phy,[2] and BioGRID-Y2H.[2] In STRING, an edge may represent physical binding or indirect functional interaction. While BioGRID-Y2H contains direct physical interactions only, BioGRID-Phy can additionally contain interactions denoted by the co-existence of two proteins in a stable complex. After mapping the proteins in a PPI network to their corresponding UniProt IDs and considering only the largest connected component, STRING contained $16,315$ nodes and $246,086$ edges whereas BioGRID-Phy had $17,758$ nodes and $723,772$ edges, and BioGRID-Y2H had $13,185$ nodes and $94,427$ edges.

3.3. *Causal interaction network for human*

We considered a directed signaling network from SIGNOR 3.0[21] database that contains manually curated causal interactions between biological entities such as proteins, protein complexes, and chemicals. The causal interaction denotes an up or down-regulation effect with a mechanism such as binding, phosphorylation, and transcriptional activation associated with it. After removing chemical and protein complexes and mapping the proteins to their corresponding UniProt, we retained $4,853$ nodes and $11,866$ edges.

3.4. *SARS-CoV-2 hallmark pathways and COVID-19 causal network*

We extracted causal interaction data organized in nine network modules or pathways, i.e., the hallmark pathways, representing the impact of SARS-CoV-2 proteins on cellular functions[21] of humans. To address the lack of evidence regarding SARS-CoV-2, these hallmark pathways contain manually annotated and validated causal interactions with SARS-CoV-2 as well as SARS-CoV-1, Middle East Respiratory Syndrome (MERS) proteins, and the human host from the literature.[25] We also considered a single network combining these nine hallmark pathways, i.e., COVID-19 causal network, available in SIGNOR 3.0.[21]

3.5. *Essential genes*

We extracted the essential genes for humans from the Database of Essential Genes.[26] It contained $2,452$ essential genes for humans from Liao *et al.*[27] and Georgei *et al.*,[28] where Georgei *et al.* considered human orthologs of mouse essential genes as putative essential genes for humans. This database also contained human essential proteins from exome sequencing-based experiments. We retained $4,807$ essential genes after mapping them to their UniProt IDs.

3.6. *Viral interactors*

We compiled a set of viral interactors, i.e., human proteins that physically interact with viruses from three databases of host-pathogen interactions.[29–31] After mapping these human proteins to their corresponding UniProt IDs and removing the SARS-CoV-2 interactors the final dataset contained $7,808$ proteins.

4. Results

In this section, first, we described how the path-based approach to provenance tracing confirmed that random walk based diffusion algorithms utilize the non-local network structure to propagate scores from seed nodes (Section 4.1). Next, we demonstrated that nodes with high diffusion betweenness scores are biologically significant (Section 4.2). Finally, by extending our analysis to directed networks, we showed that the paths with high contributions to top-scoring nodes (Section 2.3.2) often contain biologically relevant causal edges (Section 4.3).

For the first two experiments, using human interactors of SARS-CoV-2[18] as seed nodes, we ran both RL and RWR on three undirected human PPI networks, namely, STRING,[1] BioGRID-Physical,[2] and BioGRID-Y2H.[2] STRING consists of edges representing physical binding or indirect functional interaction. While BioGRID-Y2H contains only direct physical interactions, BioGRID-Phy also includes indirect interactions defined by the presence of two proteins in a stable complex. For our final analysis, we ran RWR on directed network SIGNOR[21] that contains directed causal interaction between proteins in human.

4.1. *Path-based provenance tracing confirms the ability of diffusion algorithms to capture non-local network structure*

We ran each diffusion algorithm to predict the score of each node in a network. We ranked the nodes that were not seed nodes based on their scores. We computed the path-based effective

diffusion (PED) and node-based effective diffusion (NED) scores for each of the top k proteins in this ranked list, setting k to be the number of seed nodes in the network.

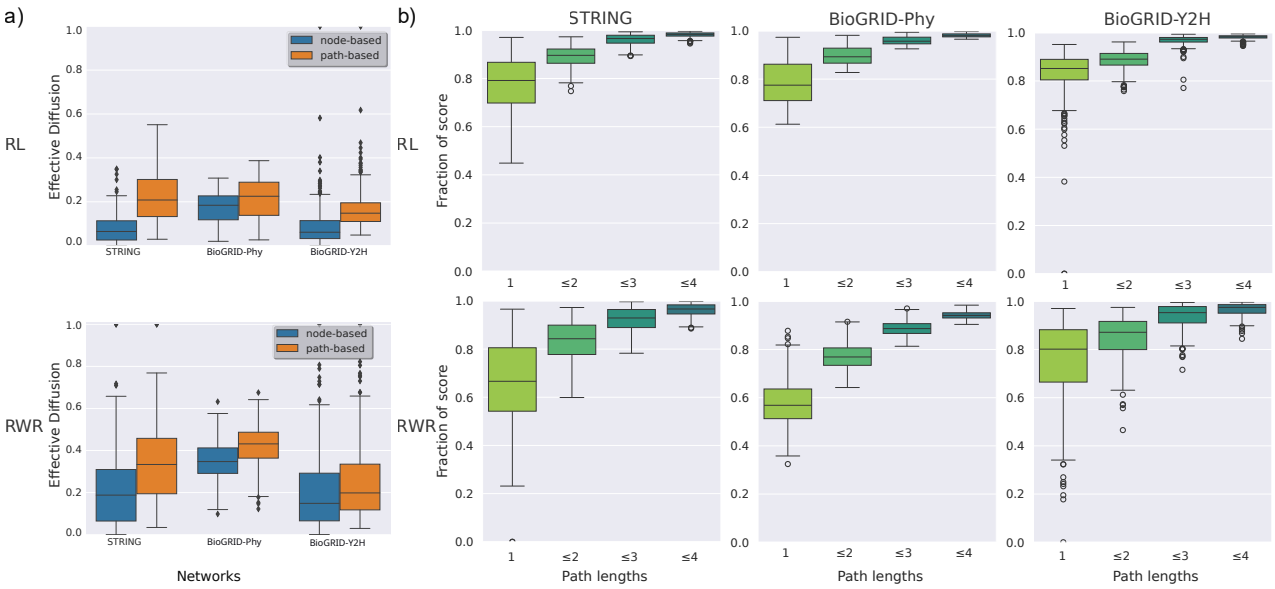

Fig. 2. **Path-based approach for provenance tracing.** a) Comparison of node-based and path-based effective diffusion. Effective diffusion score for top k predictions for three PPI networks: STRING, BioGRID-Phy, BioGRID-Y2H. Here, k is equal to the number of seed nodes in the network. b) Contribution along paths of different lengths. The x-axis shows the maximum allowed path length (e.g., ≤ 2, ≤ 3), and the y-axis shows the fraction of the score contributed by paths whose maximum length falls within that range.

We observed that for RL and RWR on all three PPI networks, a substantial amount of a node's score was contributed via paths with multiple edges (Figure 2a). For example, for RL in the STRING network, we observed that the median PED was 0.2, i.e., paths of length more than one contributed at least 20% of the score for at least half the nodes (Figure 2a). We also noted that PED was significantly higher than NED (Figure 2a, p-values $< 8.08 \times 10^{-10}$, one-sided Mann Whitney U test) across all the algorithm-network pairs. Note that PED considers any contribution from the seed nodes as long as it arises from paths of length > 1 (irrespective of whether the seed node is a direct neighbor or not), whereas NED disregards any contributions from direct neighboring seed nodes. The larger values of PED in comparison to NED scores highlight that diffusion from even a direct neighbor can and does traverse paths of length > 1, leveraging the non-local neighborhood of the network. To further investigate the algorithms' ability to leverage the network's topology, we computed the precise contribution coming along paths of length ≤ 2, ≤ 3, and ≤ 4. We observed that a substantial fraction of the diffusion scores arose from paths with more than two edges (Figure 2b).

We computed the diffusion betweenness score for each node to evaluate whether the diffusion algorithm is confined to interactions between seed nodes and top-scoring nodes or engages other nodes in score propagation. We observed that 73% to 99% of the nodes are intermediate nodes in paths carrying non-zero contributions to top-scoring k nodes with 17%–42% nodes

lying on paths carrying at least 0.1% of the score of any top-scoring node.

In summary, node-based effective diffusion collapsed contributions from all paths between two nodes into a single quantity, creating a misleading impression that network diffusion algorithms are "local" in practice. In contrast, path-based effective diffusion in combination with diffusion betweenness provided a better way to capture the diffusion algorithms' ability to exploit the non-local structure of a network.

4.2. *Proteins with high diffusion betweenness are enriched with viral interactors and essential genes*

We sought to investigate the biological relevance of the nodes that are critical for score propagation in diffusion algorithms, i.e., the nodes with high diffusion betweenness scores. Accordingly, we analyzed the overlap between these nodes and two specific categories: known human interactors of viral proteins and essential genes.

Overlap with viral interactors. Viruses from diverse families exploit shared molecular mechanisms in their interactions with host cells throughout key stages of their life cycles.[32] Hence, we investigated whether nodes with high diffusion betweenness are enriched in human proteins interacting with other viruses. To this end, we computed the overlap between viral interactors (Section 3.6) and the k ($k \in \{200, 400, 600, 800, 1{,}000, 2{,}000, 5{,}000, 10{,}000\}$) proteins with the highest diffusion betweenness scores (excluding seed nodes and top predictions). Using SARS-CoV-2 interactors as seed nodes, we observed statistically significant overlaps for both RL and RWR across all values of k in STRING and BioGRID networks (adjusted p-value < 0.01, one-sided Fisher's exact test with Benjamini-Hochberg correction for multiple hypothesis testing, Figure 3a). For instance, in the STRING network, 76% and 69% of the top 200 proteins (ranked by diffusion betweenness) were viral interactors for RL and RWR, respectively, compared to only 38% across the entire network.

To test whether these findings depended on the specific choice of seed nodes, we repeated the analysis with a set of random seed nodes of the same size as the set of SARS-CoV-2 interactors. We generated random seeds in two ways: (i) preserving the degree sequence of the original seed nodes (i.e., SARS-CoV-2 interactors),[17] and (ii) selecting nodes uniformly at random from the entire network. In both cases, the overlap between viral interactors and proteins with high diffusion betweenness remained statistically significant (adjusted p-value < 0.01). We interpreted this result to suggest that viral interactors were important in mediating diffusion even from randomly-selected seed nodes.

Overlap with essential genes. Essential genes govern the fundamental functions necessary for cell survival.[33] We hypothesized that essential genes critical for disseminating biological information in a cell might also be crucial to network diffusion algorithms in propagating scores. To test our hypothesis, we computed the overlap between the k ($k \in \{200, 400, 600, 800, 1{,}000, 2{,}000, 5{,}000, 10{,}000\}$) proteins with the highest diffusion betweenness scores (excluding seed nodes and top predicted proteins) and essential human genes (Section 3.5). using SARS-CoV-2 interactors as seed nodes, we observed statistically significant overlap (adjusted p-value < 0.01, one-sided Fisher's exact test with Benjamini-Hochberg correction for multiple

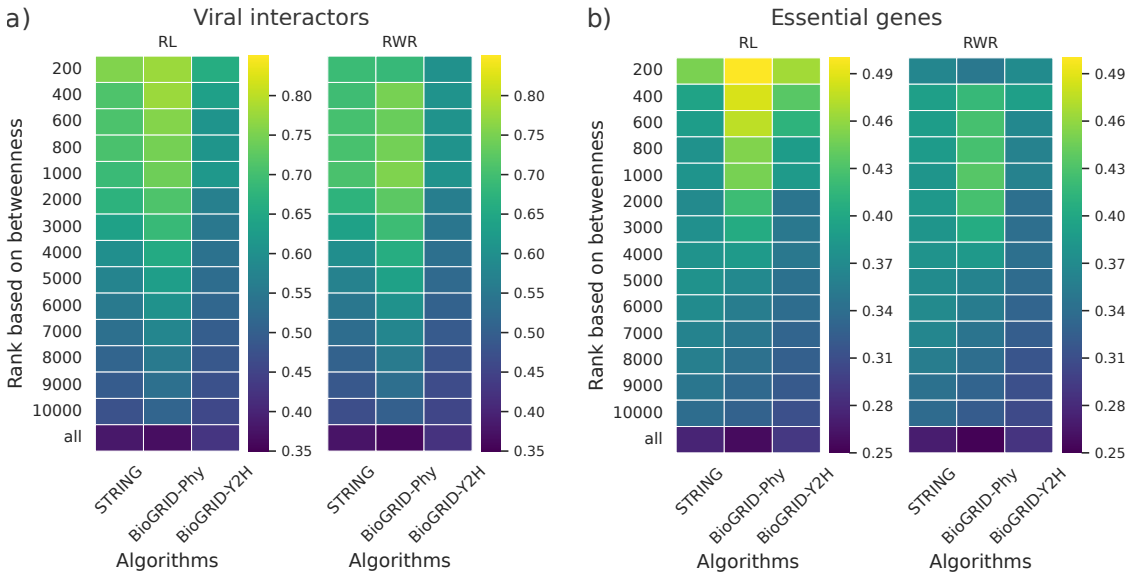

Fig. 3. **Overlap between proteins with high diffusion betweenness and the proteins of interest (i.e., viral interactors and essential genes).** Each column corresponds to a network and each row corresponds to k, protein rank based on diffusion betweenness. **a)** Each cell in the heatmap indicates the fraction of **viral interactors** in top-ranked k proteins. The row 'all' contains the fraction of viral interactors among all nodes in the corresponding network. **b)** Each cell in the heatmap indicates the fraction of **essential genes in humans** in the top-ranked k proteins. The row 'all' contains the fraction of essential genes among all nodes in the corresponding network.

hypothesis testing, Figure 3b) for each algorithm-network pair. For instance, in the STRING network, 45% and 37% of the top 200 proteins (ranked by diffusion betweenness) were essential genes for RL and RWR, respectively, compared to only 27% across the entire network. Repeating this analysis with random seed sets yielded a similar pattern of significant overlaps (adjusted p-value < 0.01), further highlighting the seed-node–agnostic importance of essential genes in network diffusion.

4.3. *Top contributing paths show significant overlap with COVID causal network and hallmark SARS-CoV pathways*

To demonstrate an application of our path-based approach in identifying biologically relevant pathways, we extended our analysis to a directed signaling network containing causal interactions between pairs of human proteins.[21] We considered all the paths in this network that started at a seed node and ended at any one of the top-k proteins (based on prediction score). We applied Eppstein's k-shortest paths algorithm to compute paths with the m highest contributions in this set (Section 2.3.2).

For $m = 1,000$, we found a significantly high overlap (Fisher's exact test p-value $= 1.76 \times 10^{-23}$) between the edges in the m most contributing paths and edges appearing in the COVID-19 casual network[25] (Section 3.4). We concluded that the RWR algorithm propagates scores from known SARS-CoV-2 interactors to other proteins in the network using causal interactions that are known to be modulated by viral infection.

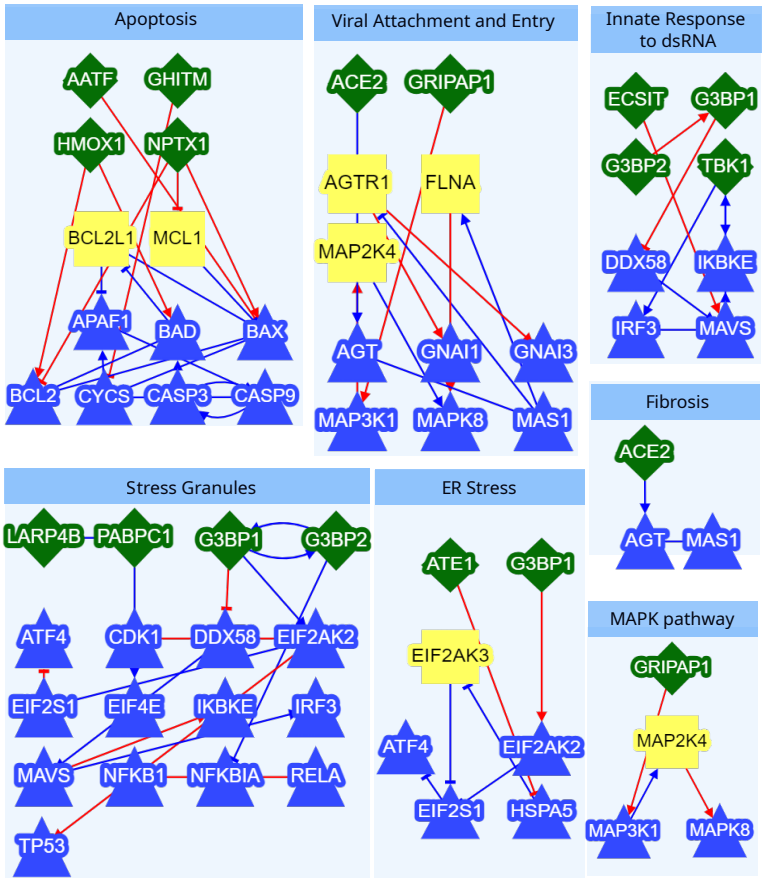

Fig. 4. **Top contributing paths assigned to hallmark SARS-CoV-2 pathways.** Each block here is for one SARS-CoV-2 causal pathway containing the top contributing paths assigned to it where we assigned a path to the pathway with the most overlap. A green diamond denotes a seed node (i.e., known SARS-CoV-2 interactors) and a blue triangle indicates protein appearing in top k predictions. Yellow rectangles denote the rest of the proteins. A blue edge indicates an edge common between a top contributing path and the corresponding SARS-CoV-2 pathway and a red edge denotes otherwise. An edge with a triangular arrow and tee denote up-regulation and down-regulation effect, respectively.

Next, we analyzed each of the top contributing paths separately. Among the $m = 1,000$ most contributing paths, we considered those with at least two edges and at most one edge missing from the COVID-19 causal network. These criteria yielded 55 paths with two to five edges. To discern the specific SARS-CoV-2 hallmark pathways[21,25] in which the top-contributing paths were involved, we assigned each path to the pathway with the most overlapping edges. We discovered that these paths appeared (either entirely or with one non-overlapping edge) in seven hallmark pathways (Section 4.3), namely, apoptosis, attachment and entry, stress granules, innate response to dsRNA, ER stress, MAPK-pathway, and fibrosis.

We further investigated the non-overlapping causal interactions. There were seven such edges across all the paths assigned to the apoptosis pathway. The source nodes in all these edges were experimentally determined SARS-CoV-2 interactors[18] with evidence of a regulatory effect on apoptosis: NPTX1,[34] AATF,[35] HMOX1,[36] and GHITM.[37] Additionally, the non-overlapping causal interaction (ATE1, HSPA5) in the ER stress pathway is crucial to the

human stress response. ATE1 facilitates the degradation of damaged proteins through arginylation,[38] while HSPA prevents apoptosis by assisting in the proper folding of nascent proteins and the refolding of misfolded protein under stress conditions.[39] Another missing signaling edge (G3BP1, DDX58) in the stress granule contains G3BP1, a known SARS-CoV-2 interactor[18] with evidence of involvement in the corresponding pathway.[40] From these observations, we concluded that non-overlapping interactions in top-contributing paths may result from incomplete annotation of COVID-19 causal pathways. These interactions could potentially be experimentally validated as being exploited by SARS-CoV-2 during viral infection.

5. Computational Setup and Runtime

We multiplied (dense) matrices using the `matmul` function in the NumPy package. We inverted matrices using SciPy's `linalg.inv` function, which computes the exact inverse up to floating-point precision. Both operations have a time complexity of $O(n^3)$. We conducted all experiments on a server equipped with an Intel 13th Gen Core i9-13900K CPU (24 cores, 32 threads, base frequency 3.0 GHz, turbo frequency up to 5.8 GHz). We observed the highest matrix multiplication runtime of 39 seconds and matrix inversion runtime of 24 seconds for BioGRID-Phy, which has the largest number of nodes among the three networks.

Acknowledgments

National Science Foundation grants 2233967 and 1759858 to TMM supported this research.

References

1. D. Szklarczyk, A. L. Gable, K. C. Nastou, D. Lyon, R. Kirsch, S. Pyysalo, N. T. Doncheva, M. Legeay, T. Fang, P. Bork *et al.*, The STRING database in 2021: customizable protein-protein networks, and functional characterization of user-uploaded gene/measurement sets, *Nucleic Acids Research* **49**, D605 (2021).
2. R. Oughtred, J. Rust, C. Chang, B.-J. Breitkreutz, C. Stark, A. Willems, L. Boucher, G. Leung, N. Kolas, F. Zhang *et al.*, The BioGRID database: A comprehensive biomedical resource of curated protein, genetic, and chemical interactions, *Protein Science* **30**, 187 (2021).
3. T. Wang, W. Shao, Z. Huang, H. Tang, J. Zhang, Z. Ding and K. Huang, MOGONET integrates multi-omics data using graph convolutional networks allowing patient classification and biomarker identification, *Nature Communications* **12**, p. 3445 (2021).
4. H. Göös, M. Kinnunen, K. Salokas, Z. Tan, X. Liu, L. Yadav, Q. Zhang, G.-H. Wei and M. Varjosalo, Human transcription factor protein interaction networks, *Nature Communications* **13**, p. 766 (2022).
5. R. Sharan, I. Ulitsky and R. Shamir, Network-based prediction of protein function, *Molecular Systems Biology* **3**, p. 88 (2007).
6. W. S. Noble, R. Kuang, C. Leslie and J. Weston, Identifying remote protein homologs by network propagation, *The FEBS Journal* **272**, 5119 (2005).
7. K. Mitra, A.-R. Carvunis, S. K. Ramesh and T. Ideker, Integrative approaches for finding modular structure in biological networks, *Nature Reviews Genetics* **14**, 719 (2013).
8. T. Ideker and R. Sharan, Protein networks in disease, *Genome Research* **18**, 644 (2008).
9. D.-Y. Cho, Y.-A. Kim and T. M. Przytycka, Chapter 5: Network biology approach to complex diseases, *PLoS Computational Biology* **8**, p. e1002820 (2012).

10. P. Csermely, T. Korcsmáros, H. J. Kiss, G. London and R. Nussinov, Structure and dynamics of molecular networks: a novel paradigm of drug discovery: a comprehensive review, *Pharmacology & Therapeutics* **138**, 333 (2013).
11. Y. Luo, X. Zhao, J. Zhou, J. Yang, Y. Zhang, W. Kuang, J. Peng, L. Chen and J. Zeng, A network integration approach for drug-target interaction prediction and computational drug repositioning from heterogeneous information, *Nature Communications* **8**, p. 573 (2017).
12. D. Morselli Gysi, Í. Do Valle, M. Zitnik, A. Ameli, X. Gan, O. Varol, S. D. Ghiassian, J. Patten, R. A. Davey, J. Loscalzo *et al.*, Network medicine framework for identifying drug-repurposing opportunities for COVID-19, *Proceedings of the National Academy of Sciences* **118**, p. e2025581118 (2021).
13. J. Menche, A. Sharma, M. Kitsak, S. D. Ghiassian, M. Vidal, J. Loscalzo and A.-L. Barabási, Uncovering disease-disease relationships through the incomplete interactome, *Science* **347**, p. 1257601 (2015).
14. L. Cowen, T. Ideker, B. J. Raphael and R. Sharan, Network propagation: a universal amplifier of genetic associations, *Nature Reviews Genetics* **18**, 551 (2017).
15. M. R. Karim, T. Islam, M. Shajalal, O. Beyan, C. Lange, M. Cochez, D. Rebholz-Schuhmann and S. Decker, Explainable AI for bioinformatics: methods, tools and applications, *Briefings in Bioinformatics* **24**, p. bbad236 (2023).
16. S. Kasif and R. J. Roberts, We need to keep a reproducible trace of facts, predictions, and hypotheses from gene to function in the era of big data, *PLoS Biology* **18**, p. e3000999 (2020).
17. J. N. Law, K. Akers, N. Tasnina, C. M. D. Santina, S. Deutsch, M. Kshirsagar, J. Klein-Seetharaman, M. Crovella, P. Rajagopalan, S. Kasif *et al.*, Interpretable network propagation with application to expanding the repertoire of human proteins that interact with SARS-CoV-2, *GigaScience* **10**, p. giab082 (2021).
18. D. E. Gordon, G. M. Jang, M. Bouhaddou, J. Xu, K. Obernier, K. M. White, M. J. O'Meara, V. V. Rezelj, J. Z. Guo, D. L. Swaney *et al.*, A SARS-CoV-2 protein interaction map reveals targets for drug repurposing, *Nature* **583**, 459 (2020).
19. F. Fouss, K. Francoisse, L. Yen, A. Pirotte and M. Saerens, An experimental investigation of kernels on graphs for collaborative recommendation and semisupervised classification, *Neural Networks* **31**, 53 (2012).
20. L. Page, S. Brin, R. Motwani and T. Winograd, *The PageRank citation ranking: Bringing order to the web.*, tech. rep., Stanford Infolab (1999).
21. P. Lo Surdo, M. Iannuccelli, S. Contino, L. Castagnoli, L. Licata, G. Cesareni and L. Perfetto, Signor 3.0, the signaling network open resource 3.0: 2022 update, *Nucleic Acids Research* **51**, D631 (2023).
22. Y. Qi, Y. Suhail, Y.-y. Lin, J. D. Boeke and J. S. Bader, Finding friends and enemies in an enemies-only network: a graph diffusion kernel for predicting novel genetic interactions and co-complex membership from yeast genetic interactions, *Genome Research* **18**, 1991 (2008).
23. S. Mostafavi, A. Goldenberg and Q. Morris, Labeling nodes using three degrees of propagation, *PloS One* **7**, p. e51947 (2012).
24. W. Ba-Alawi, O. Soufan, M. Essack, P. Kalnis and V. B. Bajic, DASPfind: new efficient method to predict drug-target interactions, *Journal of Cheminformatics* **8**, 1 (2016).
25. L. Perfetto, E. Micarelli, M. Iannuccelli, P. Lo Surdo, G. Giuliani, S. Latini, G. M. Pugliese, G. Massacci, S. Vumbaca, F. Riccio *et al.*, A resource for the network representation of cell perturbations caused by SARS-CoV-2 infection, *Genes* **12**, p. 450 (2021).
26. H. Luo, Y. Lin, T. Liu, F.-L. Lai, C.-T. Zhang, F. Gao and R. Zhang, DEG 15, an update of the Database of Essential Genes that includes built-in analysis tools, *Nucleic Acids Research* **49**, D677 (2021).
27. B.-Y. Liao and J. Zhang, Null mutations in human and mouse orthologs frequently result in

different phenotypes, *Proceedings of the National Academy of Sciences* **105**, 6987 (2008).
28. B. Georgi, B. F. Voight and M. Bućan, From mouse to human: evolutionary genomics analysis of human orthologs of essential genes, *PLoS Genetics* **9**, p. e1003484 (2013).
29. S. Durmuş Tekir, T. Çakır, E. Ardıç, A. S. Sayılırbaş, G. Konuk, M. Konuk, H. Sarıyer, A. Uğurlu, İ. Karadeniz, A. Özgür *et al.*, PHISTO: pathogen-host interaction search tool, *Bioinformatics* **29**, 1357 (2013).
30. M. G. Ammari, C. R. Gresham, F. M. McCarthy and B. Nanduri, HPIDB 2.0: a curated database for host-pathogen interactions, *Database* **2016**, p. baw103 (2016).
31. X. Yang, X. Lian, C. Fu, S. Wuchty, S. Yang and Z. Zhang, HVIDB: a comprehensive database for human-virus protein-protein interactions, *Briefings in Bioinformatics* **22**, 832 (2021).
32. M. S. Ravindran, P. Bagchi, C. N. Cunningham and B. Tsai, Opportunistic intruders: how viruses orchestrate ER functions to infect cells, *Nature Reviews Microbiology* **14**, 407 (2016).
33. L. Funk, K.-C. Su, J. Ly, D. Feldman, A. Singh, B. Moodie, P. C. Blainey and I. M. Cheeseman, The phenotypic landscape of essential human genes, *Cell* **185**, 4634 (2022).
34. Y. Zhao, Y. Yu, W. Zhao, S. You, M. Feng, C. Xie, X. Chi, Y. Zhang and X. Wang, As a downstream target of the AKT pathway, NPTX1 inhibits proliferation and promotes apoptosis in hepatocellular carcinoma, *Bioscience Reports* **39**, p. BSR20181662 (2019).
35. D. Welcker, M. Jain, S. Khurshid, M. Jokić, M. Höhne, A. Schmitt, P. Frommolt, C. M. Niessen, J. Spiro, T. Persigehl *et al.*, AATF suppresses apoptosis, promotes proliferation and is critical for Kras-driven lung cancer, *Oncogene* **37**, 1503 (2018).
36. Y. S. Basmaeil, D. Algudiri, R. Alenzi, A. Al Subayyil, A. Alaiya and T. Khatlani, HMOX1 is partly responsible for phenotypic and functional abnormalities in mesenchymal stem cells/stromal cells from placenta of preeclampsia (PE) patients, *Stem Cell Research & Therapy* **11**, 1 (2020).
37. S. Li, L. Wang, M. Berman, Y.-Y. Kong and M. E. Dorf, Mapping a dynamic innate immunity protein interaction network regulating type I interferon production, *Immunity* **35**, 426 (2011).
38. K. Deka, A. Singh, S. Chakraborty, R. Mukhopadhyay and S. Saha, Protein arginylation regulates cellular stress response by stabilizing HSP70 and HSP40 transcripts, *Cell Death Discovery* **2**, 1 (2016).
39. G. Jego, A. Hazoumé, R. Seigneuric and C. Garrido, Targeting heat shock proteins in cancer, *Cancer Letters* **332**, 275 (2013).
40. V. Iadevaia, J. M. Burke, L. Eke, C. Moller-Levet, R. Parker and N. Locker, Novel stress granule-like structures are induced via a paracrine mechanism during viral infection, *Journal of Cell Science* **135**, p. jcs259194 (2022).

REPEL - Random Embedding Perturbation for Enhanced Learning of Protein Function

Di Zhou[1], Lenore J. Cowen[1,2], Kaiyi Wu[2], Xiaozhe Hu[2], Donna K. Slonim[1]

[1] *Department of Computer Science, Tufts University, Medford, MA 02155, USA*
[2] *Department of Mathematics, Tufts University, Medford, MA 02155, USA*
Email: di.zhou@tufts.edu, cowen@cs.tufts.edu, kaiyiwu0124@gmail.com, xiaozhe.hu@tufts.edu, slonim@cs.tufts.edu

Protein function prediction from multiplex protein-protein association networks is a crucial approach to extending functional annotation. Current methods use embeddings of the heterogeneous network data that aim to place related proteins near each other in embedding space. However, such embeddings suffer from spurious protein proximity as well, reducing function prediction accuracy. Because heterogeneous input networks often have very different structures, it is hard to confidently declare proteins to be dissimilar using the network structure or the resulting embeddings. Here we address this problem with REPEL, a function prediction tool using a random graph augmentation method that applies a uniform weak force to push nodes apart. We assess this method on simulated networks with planted overlapping communities, as well as on real multiplex yeast and *E.coli* protein association networks. Surprisingly, we find that this method consistently improves protein function prediction over competing methods Mashup, deepNF, and BIONIC. The random repelling nature of the augmented graphs has a denoising effect on the learning process, distancing node pairs with spurious proximity while preserving true functional connections, thus increasing robustness. This graph augmentation principle may generalize to denoising and improving robustness in other graph-based learning algorithms.

Keywords: Protein Function Prediction; Protein-Protein Interaction, Denoising, Noise Injection for Regularization, Embedding, Multiplex Networks, Robustness

Code and data availability: http://bcb.cs.tufts.edu/REPEL
https://github.com/TuftsBCB/REPEL.git
Supplementary material: https://bcb.cs.tufts.edu/REPEL/repelsupplement.pdf

1. Introduction

Determining the functional roles of genes and proteins is crucial for better understanding biological processes and developing focused medical interventions. Given the cost and complexity of experimental assays of gene function in different cellular contexts, computational prediction of function is an important problem. Data from large-scale protein-protein interaction (PPI) networks has often been used for such purposes.[1]

Most early results in this area relied on the principle of "guilt by association," which assumes that protein functions are likely similar to those of other proteins with which they

© 2025 The Authors. Open Access chapter published by World Scientific Publishing Company and distributed under the terms of the Creative Commons Attribution Non-Commercial (CC BY-NC) 4.0 License.

interact.[2] Subsequent efforts grouped functions within highly connected graph communities or minimized interactions linking proteins with different functional annotations.[3–5] Improvements in predictive accuracy came from new measures of graph proximity that reflected random walk[6,7] or diffusion distances,[8] characterizing information flow in the local graph structures.

In 2016, Cho et al.[9] introduced the Mashup algorithm, integrating information across multiple biological networks reflecting heterogeneous sources of protein-protein interactions. Mashup consists of three main steps. First, Random Walk with Restart (RWR)[7] is run separately for each node for each network. Next, a low-dimensional embedding is constructed to minimize the distance to all the individual network-specific vectors. Finally, these global low-dimensional feature vectors are passed to classifiers such as k-nearest neighbors[8] or support vector machines[10] to predict functional labels. The aim of this low dimensional embedding is to induce proximity between nodes linked by network edges.

In this paper, we characterize the effects of extending the Mashup embedding paradigm by adding *negative* weight edges that push nodes further apart. Specifically, we augment the network with new artificial nodes and connect each original protein node uniformly, with negative weight "repelling" edges, to a *random* artificial node. The result of this random augmentation is to stretch out the integrated PPI network. Original protein nodes are still pulled closer together by the source network edges. However, the the new augmented nodes simultaneously are uniformly repelling, pushing everything further apart.

Surprisingly, we find that the resulting stretched network is far better for functional label prediction. We believe this improvement shows that the repelling process from the augmentation, though not strong enough to separate well-connected communities of truly related nodes, has sufficient strength to pull apart nodes placed in proximity just by chance. Accordingly, this repelling approach effectively regularizes the embedding, improving its utility for protein function prediction. We believe this represents another example of random perturbations effectively denoising and improving machine learning algorithms.[11–13]

2. Algorithms

2.1. *Preliminaries and Notation*

Let $G^i = (V, E^i)$ with $i \in \{1, \cdots, M\}$ be a multiplex network which shares a set of nodes V, with $|V| = n$. Each individual network i has its own set of edges E^i corresponding to different types of pairwise associations. The weighted adjacency matrix $A^i \in [0, 1]^{n \times n}$ contains the confidence scores of the association edge of type i between the node pairs being correct.

Let $L^{l \times n}$ denote a function annotation matrix with l functional labels and n proteins. We let $L_{ij} = 1$ if protein i has label j, otherwise $L_{ij} = 0$.

2.2. *The REPEL Algorithm*

REPEL de-noises the learned protein embeddings by augmenting the network before the embedding and function prediction phases. Figure 1 gives an overview of the procedure; details of the algorithm follow.

Augmentation. For the proteins with known labels, we randomly split them into 5 folds, and use 4 folds as function voting proteins and 1 fold as testing proteins. We further randomly split

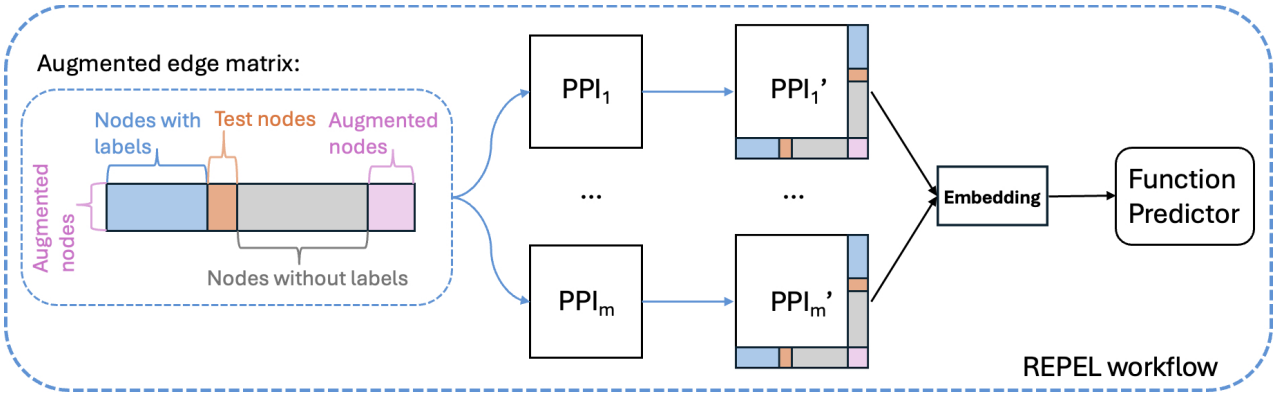

Fig. 1. REPEL Workflow. The blue arrows illustrate how we augment auxiliary nodes and edges. The blue rectangle area represents the augmented edge matrices for proteins with functional labels. The orange and gray rectangles represent the all edge 0 matrix between test proteins (orange) and unlabeled proteins (gray). The pink square illustrates the repelling negative weight matrix. Using these augmented networks, REPEL follows the feature representation learning procedures of Mashup to learn a protein embedding and predict functions.

the function voting proteins into x *equal sized* non-overlapping groups, to achieve a uniformly "repelling" power. For each group, we create one auxiliary node, and connect each protein that belongs to that group to the auxiliary node with an edge with weight 1. We augment all networks with the same set of edges between the auxiliary nodes and proteins. Then we add a "repel" edge with weight -1 between each pair of the auxiliary nodes to push them apart. We denote the augmented graph as $\overline{G}^i$. The resulting symmetrical weighted signed adjacency matrix $\overline{A}^i \in [-1,1]^{(n+x)\times(n+x)}$ is defined as:

$$\overline{A}^i_{uv} = \begin{cases} A^i_{uv} & \text{if } u,v \in V, \\ 1 & \text{if } edge(u,v) \in E_{aug}, \\ -1 & \text{if } u,v \in V_{aug}, u \neq v, \\ 0 & \text{otherwise,} \end{cases}$$

where V_{aug} is the augmented node set with $|V_{aug}| = x$, and E_{aug} is the augmented edge set. In addition, due to how we augment the graph, we ensure

$$\sum_v \overline{A}^i_{uv} = c \quad \text{for all } u \in V_{aug} \text{ and } v \in V, \ \sum_u \overline{A}^i_{uv} = 1 \quad \text{for all } u \in V_{aug} \text{ and } v \in V.$$

The constant c is the closest integer to the number of voting proteins divided by x, the total number of groups. Each group contains c proteins, except the last one which may contain more or fewer to account for the remainder.

Diffusion. On each augmented graph $\overline{G}^i$, a diffusion process using RWR on the signed graph is run which creates a matrix representation denoted as $\overline{\boldsymbol{W}}^i$ of the augmented network. Since we augment the links with negative weights to the graph, the original RWR won't work, because it requires positive transition probabilities. Thus, we need to generalize the diffusion state matrix $\boldsymbol{W}^i$ to signed graphs.

A natural generalization to a signed graph is obtained by replacing the weighted degree

matrix $\boldsymbol{D}$ in the normal RWR diffusion state equation with the signed weighted degree matrix $\overline{\boldsymbol{D}}$. Letting α represent the restart rate, the diffusion state matrix for signed graphs is defined:

$$\overline{\boldsymbol{W}} = \alpha\overline{\boldsymbol{D}}\left(\overline{\boldsymbol{D}} - (1-\alpha)\overline{\boldsymbol{A}}\right)^{-1}$$

Embedding. A shared low-dimensional embedding $\boldsymbol{X} \in \mathbb{R}^{d\times n}$ is created using the matrix representation $\overline{\boldsymbol{W}}^i$ where $i \in \{1, \cdots, M\}$. This is achieved via a singular value decomposition (SVD). Ultimately this results in a d-dimensional vector representation of every node in the dataset. We adopted Mashup's approach to combine these matrix representations to obtain a low-dimensional embedding.

Once each set of M networks has been represented by its RWR matrix $\overline{\boldsymbol{W}}^i$, the low-dimensional embedding $\boldsymbol{X}$ is formed by the scaled largest d left singular vectors of the concatenated matrix $\log(\boldsymbol{S})$ where $\boldsymbol{S} = [(\overline{\boldsymbol{W}}^1)^T, \cdots, (\overline{\boldsymbol{W}}^M)^T]^T$ and $\log(\cdot)$ denotes the element-wise logarithm. As suggested in the Mashup paper,[9] to optimize the implementation, the SVD-based embedding can be computed by the eigenvalue decomposition of the $n \times n$ matrix $\boldsymbol{R}$,

$$\boldsymbol{R} = \sum_{i=1}^{M} \log(\overline{\boldsymbol{W}}^i)^T \log(\overline{\boldsymbol{W}}^i).$$

A small constant is added to $\overline{\boldsymbol{W}}^i$ to avoid taking the logarithm of zero. Taking the top d eigenvalues $\boldsymbol{\Lambda} = \mathrm{diag}(\lambda_1, \cdots, \lambda_d)$ and eigenvectors $\boldsymbol{U} = (\boldsymbol{u}_1, \cdots, \boldsymbol{u}_d) \in \mathbb{R}^{n\times d}$, the low-dimensional embedding is $\boldsymbol{X} = \boldsymbol{\Lambda}^{1/4}\boldsymbol{U}^T$.

Learning. Once the embedding $\boldsymbol{X}$ for every node in the dataset is learned, any classical function prediction method can be applied. We adopted a weighted majority voting classifier by k-nearest neighbors (kNN) (similar to that used by Cao, *et al.*[8]) to predict functional labels using the embedding and the available annotations.

2.3. *Prior Work and Review of Comparator Algorithms*

In the experiments in this paper, we compare REPEL to Mashup; DeepNF, which uses a multimodal deep autoencoder; and BIONIC, which integrates biological networks using a Graph Convolutional Network based model. Each of these is reviewed briefly below.

2.3.1. *Mashup*

The original Mashup procedure consists of three core steps. First a **Diffusion** step that creates a RWR matrix representation $\boldsymbol{W}^i \in \mathbb{R}^{n\times n}$ for each input of the network G^i, followed by an **Embedding** step where a shared embedding is created using the matrix representations generated in the diffusion step. This is achieved via singular value decomposition or dictionary learning techniques. Ultimately, this gives a d-dimensional vector representation of every node in the dataset. Finally the **Learning** step: once every node in the dataset is represented by a vector, the existing function prediction methods can be applied using the embedding and available annotations. The original Mashup used a support vector machine (SVM) for the final learning step. However, it also carefully filtered the set of GO labels that it considered to discard GO labels whose set of labeled genes overlapped (with a Jaccard threshold greater than 0.1), advantaging methods such as SVM that search for a separating hyperplane. Since

we are mainly interested in the functional enrichment of the embedding itself and in the more realistic setting where GO labels are allowed to overlap, we instead use kNN as the classifier to compare the different embedding methods in this paper.

2.3.2. *deepNF*

DeepNF[14] tries to learn a useful low-dimensional embedding of proteins with a multimodal deep autoencoder (MDA)[15] that preserves non-linear network structure across multiple networks characterized by diverse connectivity patterns.[14] It is shown to preserve the non-linear network structure with its deep neural network (DNN) architecture in an efficient and scalable manner, and at the same time it denoises the links in the networks.

It first utilizes RWR to create its matrix representation $\boldsymbol{W}^i \in \mathbb{R}^{n \times n}$ for each input network G^i. Then each RWR matrix is converted into a Positive Pointwise Mutual Information (PPMI) matrix $\boldsymbol{Q}^i \in \mathbb{R}^{n \times n}$ that captures the structural information of the network. Then an MDA is trained that takes the PPMI matrices as input. A canonical d-dimensional feature representation across the networks is extracted from the middle layer of the MDA, which will be fed into the downstream function predictors.

2.3.3. *BIONIC*

BIONIC[16] is a Graph Convolutional Network[17] based deep learning model to learn a unified, combined gene feature representation using multiple biological networks. It reflects the underlying network topologies while capturing the gene functional information.

BIONIC first encodes each biological networks through a 3-layer GAT[18] model, then aggregates the learned features through a weighted, stochastically masked summation. It has both unsupervised and semi-supervised learning modes depending on availability of the gene functional information. For the unsupervised learning mode, the model will be trained with network reconstruction loss as the objective. For the semi-supervised learning mode, an additional label classification loss term, introduced by incorporating the known label information, will be added along with the reconstruction loss as the training objective. Here, to match the learning modes of REPEL, Mashup, and deepNF, and to make as fair a comparison as possible, we adopted the unsupervised approach and retrieved the learned gene embeddings using the recommended parameters.

2.3.4. *Other methods*

In addition to the methods discussed here and in the Introduction, there have been other efforts to predict function from heterogeneous networks using modern neural network approaches. However, because most also require other input data, these could not be directly compared on the data used by Mashup and REPEL. For example, NetGO[19] and its subsequent incarnations integrate data across multiple species and predict cross-species interactions, a separate and challenging problem. GTPLM-GO[20] and SEGT-GO[21] are related graph transformer methods that both require additional protein sequence data. It would, however, also be interesting to test REPEL against DropEdge[22] variants of DeepNF or BIONIC, or other GCN augmenta-

tion strategies for BIONIC that, like REPEL, are intended to prevent over-squashing of the embedding space.[23]

3. Materials and Methods

3.1. *Biological Interaction Data*

3.1.1. *Protein-protein Interaction Networks*

Yeast Networks The set of yeast (*Saccharomyces cerevisiae*) networks we consider in this paper are the ones used in the original Mashup paper[9] and are also described in detail there. They come from the STRING database v9.1,[24] excluding links derived from text-mining. In particular, we consider six heterogeneous networks featuring neighborhood, fusion, co-occurrence, co-expression, experimental, and database interaction types with edge counts ranging from $1,361$ to $314,013$ over the same set of $6,400$ genes (see Table S1 in the Supplement).

***E. coli* Networks** We downloaded analogous *E. coli* (*Escherichia coli*) networks from STRING database v12.0.[25] We use the same interaction types as in yeast, with edge counts ranging from $9,152$ to $219,483$ on the same set of $4,140$ genes (see Table S1 in the Supplement).

3.1.2. *Protein annotation*

We use functional annotation from the Gene Ontology (GO)[26] for yeast and *E. coli*; functional labels are separated according to their three distinct hierarchies: Biological Process (BP), Molecular Function (MF), and Cellular Component (CC). As in the Mashup paper, we filter the GO terms to only retain functional labels of intermediate specificity, terms labeling more than 10 and fewer than 301 protein nodes. This label set is further divided into levels of varying specificity, each containing labels that annotate either 11-30, 31-100, or 101-300 proteins, respectively.[27] Thus for each organism we perform 9 different function prediction experiments, parameterized by one of the three hierarchies (BP, MF, or CC) and one of the three levels of GO-term specificity (11-30, 31-100, and 101-300). Number of GO labels in each bin appear in Table S2 in the Supplement.

3.2. *Synthetic Data*

To clarify the role of negative weight edges, we generate synthetic data that we use to specifically compare Mashup to REPEL in cases where there are known, correct annotations.

To create synthetic datasets with a realistic multi-network structure, we begin by randomly generating one graph referred to as the ***base graph***, denoted $\mathcal{G}_{\mathcal{B}}$. The graph $\mathcal{G}_{\mathcal{B}}$ contains multiple communities, characterized by a higher density of intra-community edges and a lower density of inter-community edges; these communities are each assigned a different label that is considered to be the ground truth. Each node is assigned to exactly one community.

We create $\mathcal{G}_{\mathcal{B}}$ with 1,000 nodes using the LFR_benchmark_graph function[28] from the NetworkX library.[29] This function produces a simulated graph in which both the node degrees and community sizes follow power-law distributions, where we set the power-law exponent to 2.5 and 1.5, respectively, resembling the real-world biological networks we study. The mixing

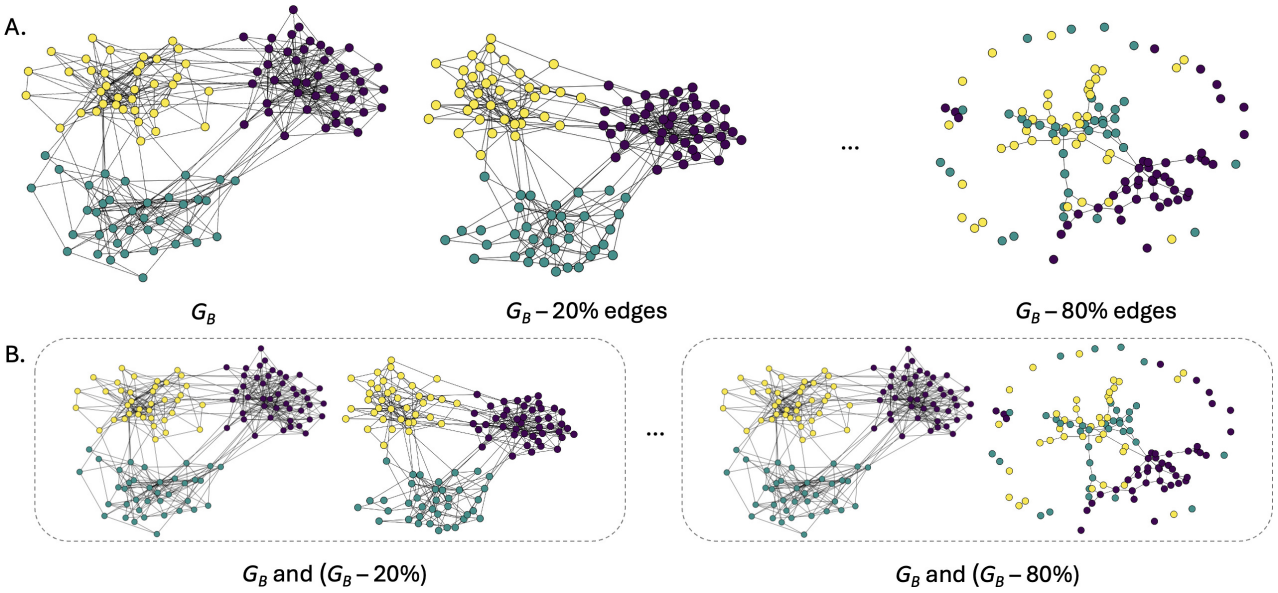

Fig. 2. Illustration of sparsity robustness analysis experiment settings. (A.) An example of $\mathcal{G}_\mathcal{B}$ generated with the LFR algorithm but with just 120 nodes to improve visualization. $\mathcal{G}_\mathcal{B}$ is shown on the left. The next two graphs illustrate $\mathcal{G}_\mathcal{B}$ with a random 20% and 80% of the edges removed, respectively. For the first round of sparsity experiments, we input each individual graph alone to both Mashup and REPEL. (B.) In the second experimental setting, both the Mashup and REPEL algorithms receive as input a pair of graphs: $\mathcal{G}_\mathcal{B}$ plus one of the graphs with edges randomly removed.

parameter μ, which controls the fraction of each node's edges that connect to nodes outside its own community, is set to 0.15, reflecting relatively well-separated communities. We set the average node degree to 20 and the maximum degree to 100, while constraining community sizes to range from 15 to 100 nodes.

From $\mathcal{G}_\mathcal{B}$ we then generate multiple graphs, each of which captures different (yet consistent and overlapping) parts of this base graph community structure. To mimic the noisy, incomplete, and biased nature of our real input networks, we create these simulated networks such that the communities among multiple networks have some overlap, but we allow different levels of sparsity and noise.

Sparsity Available PPI network data are typically sparse,[30] motivating an investigation of how sparsity impacts model performance. To introduce varying levels of sparsity, we randomly remove 20%, 40%, 60% and 80% of the edges from $\mathcal{G}_\mathcal{B}$ to generate increasingly sparse versions. We then evaluate model performance under two input settings: first, using only the sparse graph, and second, using both the sparse graph and $\mathcal{G}_\mathcal{B}$ as input, as shown in Figure 2. We note that although these methods are all designed to learn from *multiple* networks, in some simulations, we assess performance when learning from just a single network as a control.

Noise Similar to the sparsity analysis, and motivated by the fact that PPI networks are often noisy and biased,[30] we also conducted a noise robustness analysis. To simulate variation and introduce noise while preserving the community information, we construct a new empty graph with the same set of nodes as $\mathcal{G}_\mathcal{B}$ and add its edges as follows: for each community, we randomly select a subset comprising p percent of its nodes. Within this subset, we add intra-

community edges with higher probabilities to ensure cluster formation. Also, we randomly add edges between these selected nodes and nodes outside their community (inter-community) with lower probabilities, thereby introducing a degree of noise. This process yields a noisy graph derived from $\mathcal{G}_{\mathcal{B}}$ that maintains at least some of its core community structure.

Table 1. Configurations for Noisy Graph Generation

Configurations	num graph	$G_{gen}1$ param set	$G_{gen}2$ param set	$G_{gen}3$ param set
Config 1	3	[0.8, 0.2, 0.005]	[0.8, 0.2, 0.005]	[0.8, 0.2, 0.005]
Config 2	3	[0.8, 0.2, 0.005]	[0.6, 0.2, 0.005]	[0.4, 0.2, 0.005]
Config 3	3	[0.2, 0.005, 0.005]	[0.2, 0.005, 0.005]	[0.2, 0.005, 0.005]
Config 4	1	[0.2, 0.005, 0.005]	NA	NA

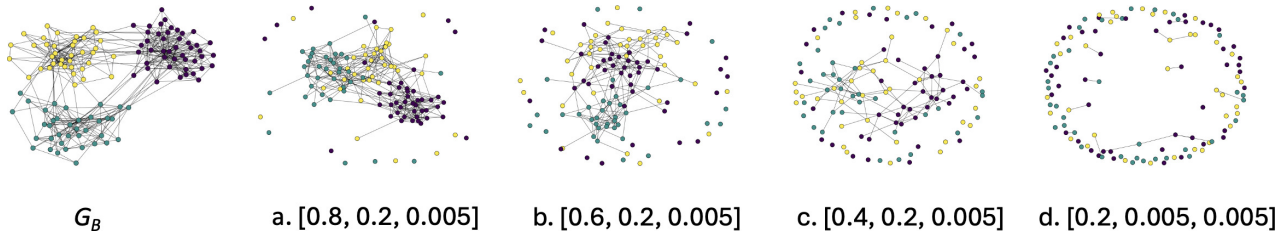

Fig. 3. Illustration of noise robustness analysis experiment settings. The base graph $\mathcal{G}_{\mathcal{B}}$ shown is generated using the LFR algorithm with 120 nodes for clarity of visualization. Noisy graphs *a.* to *d.* are randomly generated using the methods in Section 3.2 under different sets of parameters (Table 1). Each parameter list denotes the percentage of preserved cluster core nodes, the probability of edges existing intra-cluster, and the probability of edges existing inter-cluster. From graph *a.* to *d.*, the structure of $\mathcal{G}_{\mathcal{B}}$ becomes more disrupted.

We construct multiple noisy graphs under varying configurations to simulate different noise scenarios and assess model robustness. The parameters for the four chosen configurations are shown in Table 1, where the parameters for each of three simulated graphs are listed in order: percent of preserved cluster core nodes, probability of within-cluster edges, and probability of between cluster edges.

In Configuration 1, we generate three random graphs with similar structural characteristics to $\mathcal{G}_{\mathcal{B}}$. In these graphs, the core structure of each cluster is largely preserved and remains connected, while inter-cluster edges are kept sparse. In Configuration 2, we also generate three random graphs with the same overall probability of intra-cluster and inter-cluster edges as in Configuration 1. However, in this case, the core structures within the clusters are gradually disrupted, simulating a scenario where community integrity is degraded. In Configuration 3, we generate three graphs in which the cluster cores are deliberately disrupted and the clusters are only loosely connected. In Configuration 4, we follow the same procedure as in Configuration 3 but generate only a single corrupted graph.

Thus, Configurations 3 and 4 together serve as a negative control, providing a baseline for evaluating model performance in the absence of a meaningful community structure. In each case, we evaluate the performance by providing the algorithms either with only the simulated

graphs, or with the simulated graphs derived graphs together with $\mathcal{G}_{\mathcal{B}}$.

3.3. *Evaluation Methods*

We evaluate the performance of Mashup, deepNF, BIONIC and our REPEL approaches for predicting GO functional labels across the three GO hierarchies, BP, MF, and CC, using the yeast and *E. coli* multi-network collections. On the simulated networks, we evaluate the performance using only Mashup and REPEL, to directly analyze how the augmented uniform repel strength denoises the learned embeddings. Evaluation is conducted via five-fold cross-validation, by randomly splitting the nodes into five folds. In each iteration, the labels from one fold are withheld and treated as test data.

For each test fold, after obtaining the low-dimensional embedding of each node, we identify its k nearest neighbors based on the pairwise Euclidean distance in the embedding space. A weighted majority vote is then performed, where each neighbor's vote is weighted by the reciprocal of its distance to the test node. The GO terms receiving the highest total votes are assigned as the predicted functions.

In each simulation setting, following the evaluation protocol described in the Mashup paper,[9] we report the performance as accuracy, measured as the proportion of correctly annotated nodes. We conduct 10 independent runs of five-fold cross-validation. The averaged prediction accuracy and the standard deviation of that accuracy across the 10 runs are reported.

In experiments on real data, we conduct 5 independent runs of five-fold cross-validation and report the accuracy, F1 score, and area under the precision–recall curve (AUPRC), again following the definitions in the Mashup paper.[9]

3.4. *Algorithm Parameters*

For all experiments, REPEL was run with default parameters (summarized also in Tables S3 and S4) as follows. We set the dimensionality of the embeddings to 400, consistent with the recommendation of Cho et al[9] for yeast and *E.coli*, which suggests retaining the dimensionality of $5\% - 10\%$ of the original number of nodes. We also adopt the restart rate α of 0.5 from the Mashup implementation. For label prediction, we only consider the nodes with labels within the nearest 10 neighbors. Positive and negative edge weights are set to 1 and -1. The number of auxiliary nodes was set to 15 based on a hyperparameter search, in which we observed that when the number of augmented nodes is below 5, the results are noisy. The performance becomes and remains stable with 10 to 20 augmented nodes, then starts to drop very gradually as more augmented nodes are added (see Figure S1 in the Supplement).

4. Results and Discussion

4.1. *REPEL is Robust on Synthetic Networks*

In our synthetic data experiments, we generated "ground-truth" base graphs consisting of $1,000$ nodes. Using the procedures described in Section 3.2, we constructed several sets of additional sparse and noisy graphs. We evaluated REPEL and Mashup performance based on the accuracy in predicting community labels for the test nodes to directly compare the impact of random graph augmentation in controlled settings.

The results of the sparsity simulations are reported in Table S6 in the Supplement. When provided with only the single network $\mathcal{G}_{\mathcal{B}}$ as input, both Mashup and REPEL perfectly recover the community assignments of all nodes. Removal of up to 40% of edges does not significantly impact prediction accuracy for either method. However, a noticeable decline in accuracy is observed at a 60% edge removal rate. With removal of 80% of the edges, performance deteriorates substantially for both methods, with Mashup being more severely affected than REPEL.

Incorporating $\mathcal{G}_{\mathcal{B}}$ with the sparse graph consistently improves prediction performance as expected. When the edge removal rate is 60% or lower, both methods achieve accuracy above 0.99. Notably, at an 80% edge removal rate, if provided with $\mathcal{G}_{\mathcal{B}}$, REPEL's accuracy rebounds to above 0.99, while Mashup's performance only returns to 0.92. These results indicate that Mashup is robust to some degree of sparsity, but becomes more sensitive as sparsity increases. In contrast, REPEL not only achieves comparable performance when more community information is available, but also demonstrates greater robustness under high levels of sparsity.

Performance in the noise robustness simulations is reported in Table S7 in the Supplement. Here, the results of Configuration 1 indicate that Mashup is more sensitive to noise, while REPEL demonstrates greater robustness. Moreover, when $\mathcal{G}_{\mathcal{B}}$ is incorporated as additional input, REPEL shows a larger performance gain compared to Mashup, suggesting its better ability in leveraging the underlying structures. As more noise is introduced in Configuration 2, both Mashup and REPEL experience a decline in performance. However, REPEL consistently demonstrates greater robustness, maintaining higher accuracy. While incorporating $\mathcal{G}_{\mathcal{B}}$ as a fourth input network leads to improved performance for Mashup, it remains substantially affected by the noise. In contrast, REPEL is able to more effectively incorporate the structural information provided by $\mathcal{G}_{\mathcal{B}}$, restoring its accuracy to over 0.95.

The results from Configurations 3 and 4 further support the above observations. When only severely corrupted graphs are provided as input, both Mashup and REPEL perform poorly as expected, with similarly low accuracy. When $\mathcal{G}_{\mathcal{B}}$ is included, Mashup performs more variably given different numbers of degraded graphs. Specifically, additional corrupted graphs more strongly degrade Mashup's performance, suggesting it struggles to distinguish noise from real graph structure. This highlights a limitation in Mashup's ability to filter out spurious information. In contrast, although the addition of more corrupted graphs also leads to a decrease in REPEL's performance, the impact is smaller. This suggests that REPEL is better equipped to extract and preserve underlying structure in the presence of noise.

4.2. *Evaluation on Real Networks*

We observed that REPEL outperforms Mashup, deepNF and BIONIC on accuracy, F1 score and AUPRC in all experiments on the yeast networks (Figures 4 and 5, Tables S5A and S5B). On the *E.coli* networks, REPEL also outperforms other methods in all BP and MF experiment settings. The methods show similar performance in CC settings on terms labeling at least 31 nodes, because there are very few (≤ 30) terms in these categories, so the numbers of labels and test genes are too low to reliably distinguish the methods.

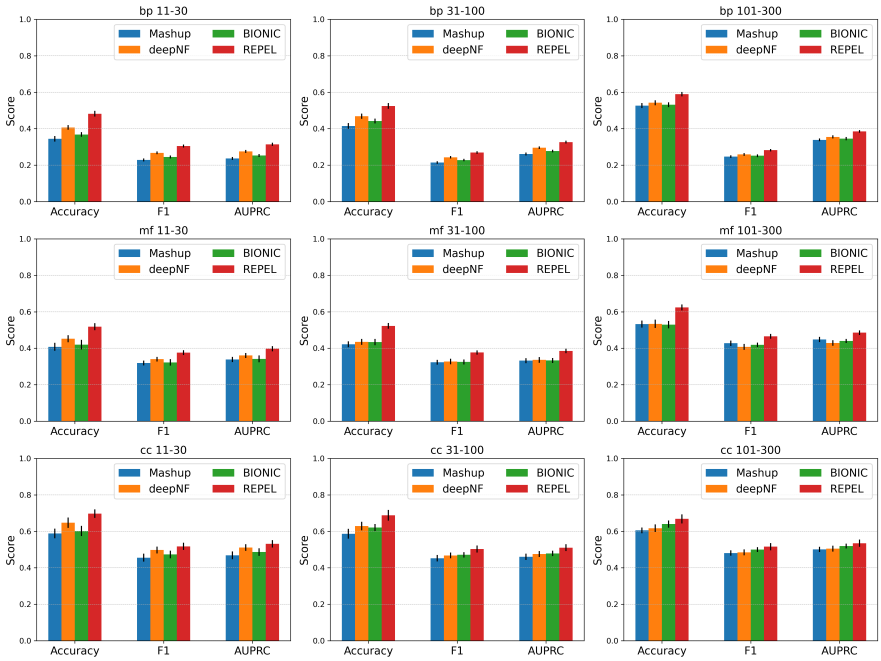

Fig. 4. Cross-validation performance on **yeast** protein networks with GO functional labels for BP, MF, and CC hierarchies compared to Mashup, deepNF and BIONIC. Performance measured by accuracy, F1 score and AUPRC, averaged across 5 independent runs of 5-fold cross-validation. The black lines denote the averaged standard deviation. Full numerical results in Table S5A.

4.3. *REPEL Finds Better Functional Clusters*

We analyzed the learned embeddings for both REPEL and Mashup. Given a protein, we find its nearest 10 neighbor proteins using L2 distance according to the learned protein feature vectors. Then we queried the protein along with its neighbors in the STRING v12.[25] database. We filter out the text mining interactions, and only keep the interactions with combined confidence scores higher than 0.9. Figure 6 shows the interactions among some example proteins and their neighbors, with line thickness indicating the strength of data support. We observe more consistent and more functionally closely connected proteins using REPEL.

For example, OLI1 is a mitochondrial ATP synthase. Mashup is able to find some functionally related genes, including ATP1, ATP2, COX4 and CYT1, however, the rest of its neighbor genes are not obviously functionally closely related. REPEL is able to find more ATP related genes including ATP1, ATP2, ATP3, ATP5, ATP6, ATP8, ATP16, and ATP17.

For another example protein, COB, both Mashup and REPEL find overlapping sets of close functionally related genes. However, the protein set found by REPEL shows slightly higher connectivity, with an average local clustering coefficient of 0.952, versus 0.846 for the neighbors according to Mashup.

5. Discussion

We have introduced the simple but effective REPEL algorithm for protein function prediction. Our experiments on both synthetic data and biological data demonstrate the power of

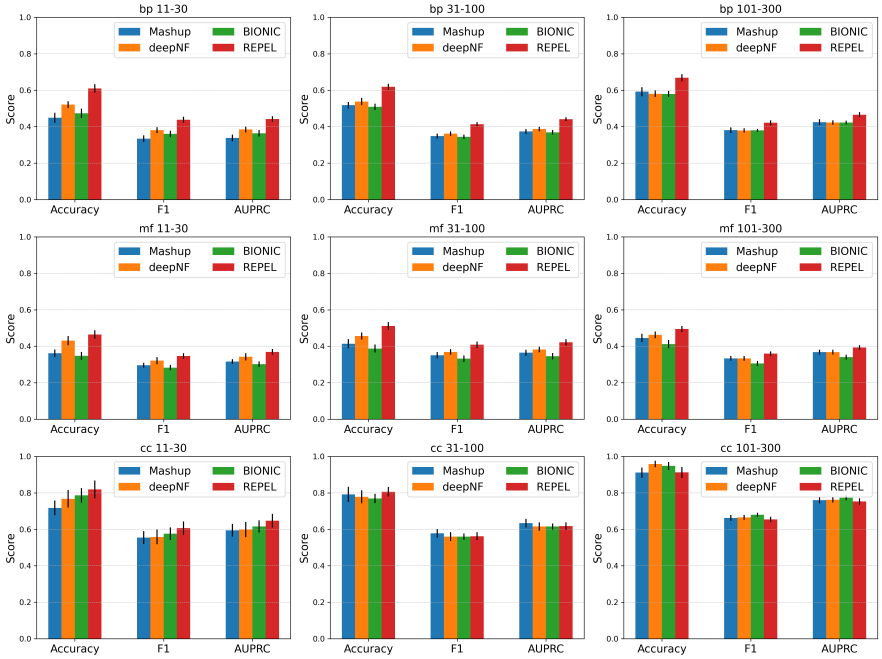

Fig. 5. Cross-validation performance on ***E. coli*** protein networks with GO functional labels for BP, MF, and CC hierarchies compared to Mashup, deepNF and BIONIC. Performance measured by accuracy, F1 score and AUPRC, averaged across 5 independent runs of 5-fold cross-validation. The black lines denote the averaged standard deviation. Full numerical results in Table S5B.

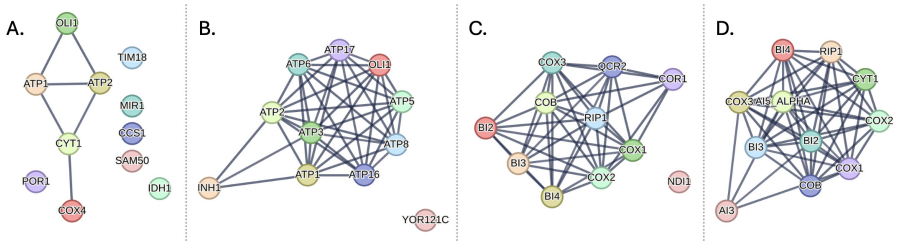

Fig. 6. OLI1, COB proteins and their 10 nearest proteins learned by Mashup and REPEL. A.) Mashup learned neighbors for OLI1. B) REPEL learned neighbors for OLI1. C.) Mashup learned neighbors for COB. D) REPEL learned neighbors for COB

injecting uniform random repelling strength in regularizing protein embeddings across multiplex networks. The simulation experiments highlight that this approach appears to increase robustness, effectively de-noising the learned embeddings. In the current version of REPEL, we apply the node augmentation before embedding, but it would be interesting to see what happens if instead we did it afterwards. Also, we have kept the focus on the information content of the embedding by having the learning module simply perform k-nearest neighbors to predict the functional labels. However, the best way to combine the REPEL embedding with more sophisticated classifiers could be an interesting topic of future work. In addition, we would like to add some degree of uncertainty quantification to the REPEL framework, so that in addition to predicting functions, REPEL gives confidence levels for its predictions.

Funding

Early work in this paper was partially supported by the National Science Foundation under grant CCF-1934553. LC also thanks the National Institute Of General Medical Sciences of the National Institutes of Health under Award Number R01GM163241. The content is solely the responsibility of the authors and does not necessarily represent the official views of the National Institutes of Health.

References

1. B. Schwikowski, P. Uetz and S. Fields, A network of protein-protein interactions in yeast, *Nature Biotechnology* , 1257 (Dec 2000).
2. P. Uetz, L. Giot, G. Cagney, T. A. Mansfield, R. S. Judson, J. R. Knight, D. Lockshon, V. Narayan, M. Srinivasan, P. Pochart *et al.*, A comprehensive analysis of protein–protein interactions in Saccharomyces cerevisiae, *Nature* **403**, 623 (2000).
3. A. Vazquez, A. Flammini, A. Maritan and A. Vespignani, Global protein function prediction from protein-protein interaction networks, *Nature Biotechnology* **21**, 697 (2003).
4. U. Karaoz, T. Murali, S. Letovsky, Y. Zheng, C. Ding, C. R. Cantor and S. Kasif, Whole-genome annotation by using evidence integration in functional-linkage networks, *Proceedings of the National Academy of Sciences* **101**, 2888 (2004).
5. E. Nabieva, K. Jim, A. Agarwal, B. Chazelle and M. Singh, Whole-proteome prediction of protein function via graph-theoretic analysis of interaction maps, *Bioinformatics* **21**, i302 (2005).
6. L. Cowen, T. Ideker, B. J. Raphael and R. Sharan, Network propagation: a universal amplifier of genetic associations, *Nature Reviews Genetics* **18**, 551 (2017).
7. H. Tong, C. Faloutsos and J.-Y. Pan, Fast random walk with restart and its applications, in *Sixth international conference on data mining (ICDM'06)*, 2006.
8. M. Cao, H. Zhang, J. Park, N. M. Daniels, M. E. Crovella, L. J. Cowen and B. Hescott, Going the distance for protein function prediction: a new distance metric for protein interaction networks, *PLOS One* **8**, p. e76339 (2013).
9. H. Cho, B. Berger and J. Peng, Compact integration of multi-network topology for functional analysis of genes, *Cell Systems* **3**, 540 (2016).
10. A. Ben-Hur, C. S. Ong, S. Sonnenburg, B. Schölkopf and G. Rätsch, Support vector machines and kernels for computational biology, *PLOS Computational Biology* **4**, p. e1000173 (2008).
11. G. E. Hinton, N. Srivastava, A. Krizhevsky, I. Sutskever and R. R. Salakhutdinov, Improving neural networks by preventing co-adaptation of feature detectors (2012), arXiv 1207.0580.
12. J. Ho, A. Jain and P. Abbeel, Denoising diffusion probabilistic models, *Advances in Neural Information Processing Systems* **33**, 6840 (2020).
13. P. Vincent, H. Larochelle, Y. Bengio and P.-A. Manzagol, Extracting and composing robust features with denoising autoencoders, in *Proceedings of the 25th International Conference on Machine Learning*, 2008.
14. V. Gligorijević, M. Barot and R. Bonneau, deepNF: deep network fusion for protein function prediction, *Bioinformatics* **34**, 3873 (2018).
15. P. Vincent, H. Larochelle, I. Lajoie, Y. Bengio, P.-A. Manzagol and L. Bottou, Stacked denoising autoencoders: Learning useful representations in a deep network with a local denoising criterion., *Journal of Machine Learning Research* **11** (2010).
16. D. T. Forster, S. C. Li, Y. Yashiroda, M. Yoshimura, Z. Li, L. A. V. Isuhuaylas, K. Itto-Nakama, D. Yamanaka, Y. Ohya, H. Osada, B. Wang, G. D. Bader and C. Boone, BIONIC: Biological network integration using convolutions, *Nature Methods* **19**, p. 1250–1261 (October 2022).
17. T. N. Kipf and M. Welling, Semi-supervised classification with graph convolutional networks

(2016), arXiv:1609.02907.
18. P. Veličković, G. Cucurull, A. Casanova, A. Romero, P. Liò and Y. Bengio, Graph attention networks (2017), arXiv: 1710.10903.
19. R. You, S. Yao, Y. Xiong, X. Huang, F. Sun, H. Mamitsuka and S. Zhu, NetGO: improving large-scale protein function prediction with massive network information, *Nucleic Acids Research* **47**, W379 (2019).
20. H. Zhang, Y. Sun, Y. Wang, X. Luo, Y. Liu, B. Chen, X. Jin and D. Zhu, GTPLM-GO: Enhancing protein function prediction through dual-branch graph transformer and protein language model fusing sequence and local–global PPI information, *International Journal of Molecular Sciences* **26**, p. 4088 (2025).
21. Y. Wang, Y. Sun, B. Lin, H. Zhang, X. Luo, Y. Liu, X. Jin and D. Zhu, SEGT-GO: a graph transformer method based on PPI serialization and explanatory artificial intelligence for protein function prediction, *BMC Bioinformatics* **26**, p. 46 (2025).
22. Y. Rong, W. Huang, T. Xu and J. Huang, Dropedge: Towards deep graph convolutional networks on node classification, *arXiv:1907.10903* (2019).
23. S. Akansha, Over-squashing in graph neural networks: A comprehensive survey, *Neurocomputing* , p. 130389 (2025).
24. A. Franceschini, D. Szklarczyk, S. Frankild, M. Kuhn, M. Simonovic, A. Roth, J. Lin, P. Minguez, P. Bork, C. von Mering and L. J. Jensen, STRING v9.1: protein-protein interaction networks, with increased coverage and integration, *Nucleic Acids Research* **41**, p. D808–D815 (November 2012).
25. D. Szklarczyk, R. Kirsch, M. Koutrouli, K. Nastou, F. Mehryary, R. Hachilif, A. L. Gable, T. Fang, N. T. Doncheva, S. Pyysalo, P. Bork, L. J. Jensen and C. von Mering, The STRING database in 2023: protein–protein association networks and functional enrichment analyses for any sequenced genome of interest, *Nucleic Acids Research* **51**, p. D638–D646 (November 2022).
26. M. Ashburner, C. A. Ball, J. A. Blake, D. Botstein, H. Butler, J. M. Cherry, A. P. Davis, K. Dolinski, S. S. Dwight, J. T. Eppig, M. A. Harris, D. P. Hill, L. Issel-Tarver, A. Kasarskis, S. Lewis, J. C. Matese, J. E. Richardson, M. Ringwald, G. M. Rubin and G. Sherlock, Gene ontology: tool for the unification of biology, *Nature Genetics* **25**, p. 25–29 (May 2000).
27. A. Ruepp, A. Zollner, D. Maier, K. Albermann, J. Hani, M. Mokrejs, I. Tetko, U. Guldener, G. Mannhaupt, M. Munsterkotter and H. W. Mewes, The FunCat, a functional annotation scheme for systematic classification of proteins from whole genomes, *Nucleic Acids Research* **32**, 5529 (2004).
28. A. Lancichinetti, S. Fortunato and F. Radicchi, Benchmark graphs for testing community detection algorithms, *Phys. Rev. E Stat. Nonlin. Soft Matter Phys.* **78**, p. 046110 (October 2008).
29. A. Hagberg, P. Swart and D. S Chult, *Exploring network structure, dynamics, and function using NetworkX*, tech. rep., Los Alamos National Lab.(LANL), Los Alamos, NM (United States) (2008).
30. N. Safari-Alighiarloo, M. Taghizadeh, M. Rezaei-Tavirani, B. Goliaei and A. A. Peyvandi, Protein-protein interaction networks (PPI) and complex diseases, *Gastroenterol. Hepatol. Bed Bench* **7**, 17 (2014).

Network optimal retrieval of sparse perturbations for steady-state control

Krithika Krishnan[1], Tiange Shi[2], Satyam Kumar[1], Han Yu[3] and Rachael Hageman Blair[1,2]

[1]*Institute for Artificial Intelligence and Data Science, University at Buffalo,*
[2]*Department of Biostatistics, University at Buffalo,*
Buffalo, NY 14228, USA
www.buffalo.edu

[3]*Roswell Park Comprehensive Cancer Center*
Buffalo, NY 14263, USA
www.buffalo.edu

Corresponding Author:
Rachael Hageman Blair
E-mail: hageman@buffalo.edu

Prioritizing targeted perturbation experiments remains a central challenge in systems biology, where experimental constraints limit network manipulation. We introduce NORSP (Network Optimal Retrieval of Sparse Perturbations). This novel computational framework integrates network propagation with supervised subset selection to identify minimal perturbation sets that can shift a system from its initial to a desired steady state. NORSP leverages a sensitivity matrix derived solely from network topology, enabling control prediction without requiring full knowledge of system dynamics. Applicable to undirected, directed, and signed networks, NORSP accommodates a broad range of biological models and experimental scenarios. We validate its effectiveness using YBX1 knockdown transcriptomics data and 61 curated metabolic networks from the BioModels repository, demonstrating NORSP's robustness, scalability, and experimental relevance. Even under constraints that obscure true perturbations, the algorithm reliably infers alternative targets that achieve comparable control. Control is confirmed both in graphical approximations and through full dynamical model simulations. Overall, NORSP provides a practical and generalizable solution for steady-state control in complex biological systems, laying the foundation for multi-omics hypothesis generation and systems-level experimental design.

Keywords: Biological networks, systems biology, optimization, propagation

1. Introduction

Network analysis is central to systems biology, enabling the exploration of gene regulation, protein interactions, and metabolic control. Mathematical modeling has transformed this domain, offering powerful frameworks to simulate biological responses and drive hypothesis generation. Computation manipulations of network components, known as *in silico* experiments, allow for systematic investigation of system perturbation, guiding experimental design and

© 2025 The Authors. Open Access chapter published by World Scientific Publishing Company and distributed under the terms of the Creative Commons Attribution Non-Commercial (CC BY-NC) 4.0 License.

accelerating discovery. Despite their utility, computational models face a critical bottleneck: identifying which perturbations are most informative. Network flexibility and high dimensionality introduce uncertainty, while practical considerations such as experimental cost, biological feasibility, and node accessibility constrain the number of feasible interventions. Addressing this challenge requires control strategies that are both tractable and biologically grounded.

Recent advances have accelerated the integration of network modeling, causal inference, and perturbation data for the discovery of therapeutic targets. Integrated regulatory–metabolic frameworks couple probabilistic gene regulatory networks with constraint-based metabolic models to predict cell type–specific responses to interventions and prioritize therapeutic strategies.[1] Causal inference methods such as Causal Differential Networks (CDN) identify intervention targets by comparing causal graphs derived from observational and interventional single-cell data, outperforming existing approaches on Perturb-seq benchmarks.[2] Bayesian frameworks like BaCaDI further address unknown interventions by jointly inferring causal structures and targets.[3] Network-based approaches, including NETPERT, use perturbation theory to prioritize druggable intermediates,[4] while data-driven control methods enable optimal network manipulation without explicit dynamical models.[5] Together, these developments highlight emerging strategies that combine causal modeling, network theory, and data-driven methods to identify minimal and effective intervention sets in complex biological systems.

Beyond causal inference and control frameworks, network propagation provides a complementary strategy for modeling how perturbations diffuse through biological networks. By iteratively updating the state of each node based on its neighbors, propagation estimates the spread of information across a graph, effectively simulating how biological signals disseminate through molecular systems. This approach has been widely applied in systems biology for identifying disease-associated genes,[6,7] uncovering genetic associations,[8] characterizing biological networks,[9] and investigating cancer.[10,11] In this work, we build on the PRINCE (PRIoritizatioN and Complex Elucidation) algorithm,[12] which was originally developed to identify associations between protein complexes and human diseases using network propagation.

Building on propagation concepts, the DYNAMO (DYNamics-Agnostic Network MOdels) framework[13] extended network propagation to approximate perturbation responses in biological systems. DYNAMO introduced the key insight that a sensitivity matrix, derived solely from network topology, can serve as a surrogate for the Jacobian matrix of partial derivatives. This matrix quantifies the local influence of perturbations across the network and enables meaningful predictions when kinetic parameters or reaction mechanisms are unavailable. By leveraging structural information alone, DYNAMO outperformed traditional centrality-based metrics across several biological models.

More recently, the IGPON (Integrated Graph-based Perturbation Optimization using Network propagation) algorithm[14] used the sensitivity matrix to optimize perturbations through Broyden's quasi-Newton method, reframing network reprogramming as an unconstrained optimization problem without requiring explicit system dynamics. As a proof of concept, IGPON showed that propagation-based approximations can guide networks toward desired steady states. However, it assumes perturbations can be applied to all N nodes, which is rarely

feasible experimentally, as only a limited subset of nodes can typically be targeted.

This work introduces NORSP (Network Optimal Retrieval of Sparse Perturbations), a computational framework for identifying minimal, biologically actionable subsets of perturbations capable of steering a system toward a desired steady state. NORSP integrates network propagation with subset selection, reformulating network reprogramming as a tractable supervised learning problem. By using a sensitivity matrix derived solely from network topology to guide a greedy search, the method enables targeted intervention design without requiring detailed dynamical models.

In relation to existing strategies, NORSP fills a distinct methodological gap. Frameworks such as DYNAMO and IGPON prioritize individual nodes based on influence or centrality, whereas this approach identifies the minimal subset of nodes needed to achieve a specified perturbation. Causal inference methods like CDN and BaCaDI focus on inferring targets from perturbation data rather than determining how to intervene to control network states. By contrast, NORSP emphasizes control under experimental constraints, making it well suited for prioritizing limited, biologically feasible interventions.

NORSP is broadly applicable to undirected, directed, and mixed-direction networks. Its performance was evaluated using YBX1 knock-out gene expression data from breast cancer cell lines[15] and 61 curated metabolic models from BioModels.[16] Across these applications, the algorithm identified biologically meaningful targets in Wnt, T-cell receptor, and Jak–Stat signaling pathways, and reliably found minimal perturbation sets capable of shifting metabolic systems to desired steady states. Even when exact perturbations were not recovered, the NORSP identified alternative nodes that achieved comparable control, underscoring its potential as a scalable and practical tool for hypothesis generation in complex biological networks.

2. Materials and Methods

2.1. *Network Optimal Retrieval of Sparse Perturbations*

A network (graph), G, is defined by a set of nodes (vertices), V, and the edges, E, representing the connections between the nodes. Propagation is a process that simulates the flow of information through a network and can be used to estimate a node's influence. Mathematically, we define the graph adjacency matrix, $G = (V, E, w) \in \mathbf{R}^{N \times N}$, where w defines an edge weight. This work assumes that the connections are unweighted ($w_i = 1,\ \forall i$) and that G is a binary adjacency matrix. Undirected graphs are symmetric, whereas directed graphs are binary matrices with $g_{i,j} = 1$ if there is a directed edge between v_i and v_j.

A normalized version of the adjacency matrix that accounts for node degree[17] is defined as: $G' = D_1^{-1/2} G D_2^{-1/2}$, where D_1 and D_2 are the diagonal matrices with entries $d_1(i,i)$ and $d_2(i,i)$ as the sum of the absolute values of the rows and columns, respectively. This normalization creates a smoothing effect over the network.[18] The sensitivity matrix is defined as: $S = (1 - \alpha)(I - \alpha G')^{-1}$, where $\alpha \in [0, 1]$ denotes a tuning parameter for the propagation strength.[13] The sensitivity matrix captures the effect of node perturbations on other nodes in the network, and has been shown to be a good proxy for the Jacobian matrix.[13] Unlike the Jacobian matrix, which relies on partial derivatives of the system, the sensitivity matrix is estimated directly from the network structure (Figure 1A).

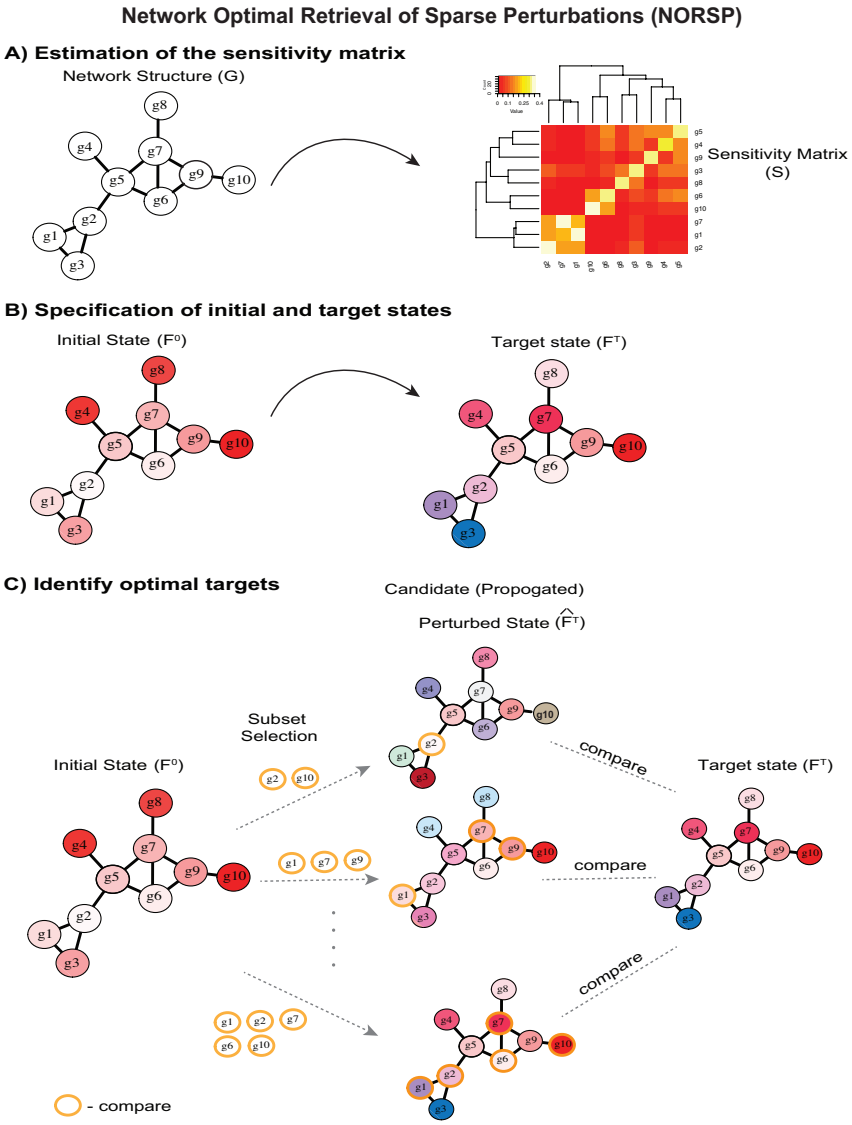

Fig. 1. Schematic of the NORSP framework. **(A)** The graph, G, serves as input and is used to generate a sensitivity matrix, S. **(B)** The optimization problem is to identify the optimal perturbations to drive an initial steady-state, F^0, to a target steady-state, F^T. **(C)** Subset selection generates sets of perturbed candidate states, $\hat{F}^T$, that are compared to the target, F^T, via error calculations. Candidate states are sorted in terms of proximity to the target to identify the optimal perturbation that drives the initial steady-state closest to the target.

This work aims to identify optimal perturbations that drive an observed network, F^0, to a target state, F^T (Figure 1B). This requires the selection of nodes to perturb, and an estimation of the nature of their perturbation. The methodology integrates machine learning via subset selection and network propagation, and we define it as: Network Optimal Retrieval of Sparse Perturbations (NORSP). Mathematically, we want to identify a perturbation vector, $\Delta \in \mathbf{R}^N$, such that:

$$F^T = F^0 + S\Delta. \tag{1}$$

In other words, we want to find a small change $S\Delta$, that will drive F^0 to the target F^T. Rewriting Equation 1, we obtain the following linear model:

$$F^T - F^0 = S\Delta + \epsilon. \tag{2}$$

Let the dependent variable be $y = F^T - F^0$, then the regression model is defined as:

$$y = S\Delta + \epsilon, \tag{3}$$

where $\epsilon \sim N(0, \sigma^2 I)$. The elements of the sensitivity matrix, $S(i, j)$, express the sensitivity of node v_i to small changes in node v_j.

A single or a small number of perturbations are typically possible in experimental systems. Thus, we aim to find a parsimonious solution to this problem that perturbs only a subset of nodes. NORSP uses subset selection to identify the solution that minimizes $\|y - S\Delta\|_2^2$.[19] This feature selection approach will yield the selected nodes for perturbation and the estimated regression coefficient that serves as the perturbation value. Forward subset selection is employed in this work, although alternative methods can be used. NORSP can be understood in Figure 1C, where different sets of nodes are selected for perturbation and propagated to a candidate perturbed state, $\hat{F}^T$. Candidate models arising from subset selection are again contrasted against the target state to identify the optimal solution. Model selection criteria, such as Bayesian Information Criteria (BIC) or adjusted R^2, can be used for selection. Notably, due to the nature of the graph representation, it is not possible to use data splitting or cross-validation without changing the structure.

2.2. *Simulations and Biological Data*

To rigorously assess NORSP's capabilities, we designed a series of simulations that evaluate its accuracy in perturbation recovery, performance across networks from different organisms and biological contexts and robustness to noise and structural misspecification.

Knockdown data: We applied NORSP to mean gene expression data for YBX1, a pro-oncogenic transcription factor, from the KnockTF database (GEO: GSE63565). The dataset includes 24 control and 24 knockdown samples, with expression profiles derived from log-transformed means. Significant KEGG pathways (Wnt, MAPK, and JAK–STAT) were selected to test NORSP's ability to identify perturbations that drive the system from control (F^0) to knockdown (F^T). YBX1 itself is not present in these pathways, reflecting downstream effects of the knockdown. Pathway graphs were imported using `KEGGgraph`, mapped via Entrez Gene IDs and gene symbols (`org.Hs.eg.db`), and trimmed to exclude unmapped nodes.

Evaluation on BioModels Repository: BioModels[16] are previously published peer-reviewed mathematical models of dynamical biochemical and cellular systems. The BioModels repository contained XML files in the Systems Biology Markup Language (SBML) format. BioModels were manually downloaded from the repository and read into Matlab using the `libSBML 5.19.0` API library.[20] The Biomodels include both the dynamical systems and the parameter specifications and initial concentration levels of biochemical species.

Simulations were performed by running each Biomodel to steady-state with the initializations provided in the database. The resulting concentration values represent an initial steady state, F^0. A perturbation was made to F^0, which sets the biochemical species with

the highest concentration to zero (a knock-out). The system was run to a new steady-state, F^T, representing the target state. The Jacobian matrices were estimated for each BioModel using finite differences. Following Santolini *et al.*,[13] the Jacobian estimates were used to construct the influence diagram that depicts the network representation we use with NORSP. For each Biomodel, three networks were constructed from the Jacobian: undirected, directed, and directed signed. Biomodels with unconnected nodes in the network were not considered. A total of 61 Biomodels, ranging across organisms and processes, were used for simulation. Network sizes ranged from 7 to 77; details are in the Supplementary Table (https://github.com/krithikakrishnan04/norsp). The inputs to NORSP include the network structure along with the initial and target states for each BioModel.

To evaluate the accuracy of node selection, we ranked the list of perturbed nodes identified in the optimal solution based on the order in which they were selected during the forward subset selection process. The first validation criterion assessed whether the actual perturbed node appeared in the optimal solution. The second criterion evaluated whether the perturbed gene was ranked first in the list. These metrics collectively characterize the effectiveness of NORSP's node selection strategy.

To assess control efficacy in BioModels, we evaluated whether NORSP-identified perturbations could drive the dynamical system toward its target steady state. This was done by reintroducing the top-ranked perturbation into each full dynamical model and simulating the system's response. This step mirrors experimental validation by examining how closely the perturbed system approaches the desired target state. If the top-ranked node matches the true perturbed node, F^T is recovered exactly. If not, alternate perturbations must be considered. To quantify control efficacy, we define a control performance metric: $F^{\text{ctr}}_{\text{dyn}} = \frac{\|F^T - \hat{F}^T_{\text{dyn}}\|_2}{\|F^T - F^0\|_2}$, which indicates movement toward the target state when $F^{\text{ctr}}_{\text{dyn}} < 1$, and divergence when $F^{\text{ctr}}_{\text{dyn}} > 1$. We also consider the relative prediction error of the dynamical model prediction, $F^{\text{err}}_{\text{dyn}} = \frac{\|F^T - \hat{F}^T_{\text{dyn}}\|_2}{\|F^T\|_2}$.

Sensitivity to noise and misspecification of the network structure: To assess the robustness of NORSP to observational noise and network misspecification, we generated scale-free networks with $N_n = 30$ nodes using a Barabási–Albert model. Two perturbation regimes were considered: sparse ($N_p = 5$ perturbed nodes) and dense ($N_p = 25$). Target states were generated by propagating ground-truth perturbation vectors through the sensitivity matrix. Additive Gaussian noise with mean zero and varying variance was then introduced either to the initial state (linear model) to mimic measurement error, or to the sensitivity matrix to mimic structural uncertainty. Noise levels ranged from 10^{-7} to 10^{-1}. For each noise level and condition, NORSP was applied to 100 simulated networks. Performance was quantified using the average relative error in recovering the target steady state ($\bar{F}^{\text{err}}$) and the average relative error in estimating the perturbation vector ($\bar{\Delta}^{\text{err}}$).

NORSP will be released to CRAN (https://cran.r-project.org/) as an open-source R package upon publication, providing an accessible platform for researchers and practitioners to apply the method across biological domains. The package will include simulation tools, visualization features, and support for custom network formats. Code for the simulations can be found on github (https://github.com/krithikakrishnan04/norsp).

3. Results

NORSP was evaluated across two main types of datasets: transcriptomic knockdown data and a diverse collection of 61 dynamic models from the BioModels repository. These datasets span a range of biological scales and modeling formalisms, allowing us to assess NORSP's generalizability and robustness. In both contexts, NORSP successfully identified sparse sets of perturbation targets capable of shifting the system from an initial state (F^0) to a target state (F^T), even under constraints typical of real-world experimental scenarios. The results demonstrate NORSP's ability to accommodate networks of varying sizes, topologies, and biological complexity, providing both accurate target approximations and interpretable, minimal intervention strategies.

We investigated pathway-level control using YBX1 knockdown data. Adjusted R^2 values were computed to assess the quality of the F^T approximation across different pathways. Overall, we found that F^T can be accurately approximated, with model fit naturally improving as the number of selected nodes increases. Using a selection threshold of 0.90, we achieved high accuracy across the three pathways while obtaining a parsimonious solution. Figure 2 shows the adjusted R^2 as a function of the selected nodes in the respective pathways. The selected nodes at the 0.90 threshold are indicated in red. Results indicate the relative error (F^{err}) of 0.0008 with 38 nodes selected from 115 in the Wnt signaling pathway (Figure 2A). The T cell receptor signaling pathway yielded a F^{err} of 0.0006 with 39 out of 113 nodes selected (Figure 2B), while the JAK-STAT signaling pathway showed a F^{err} of 0.0003 with 33 of 92 nodes selected (Figure 2C). In addition to model performance, the selected profiles help identify key targets for perturbation. These typically correspond to the earliest genes selected during the subset selection process and are thus prioritized for intervention.

In addition to the error rates, we also examined functions of the top-selected genes. In our application of NORSP, forward subset selection is used; thus, the prioritization is according to the order in which they are selected. In the Wnt signaling pathway, 18 of the 38 selected nodes were differentially expressed genes. The top three—MYC, DKK1, and PRKCA—are well-established components or downstream effectors of the pathway. MYC plays a central role in regulating genes essential for Wnt activation,[21–23] while DKK1 is a known inhibitor of Wnt signaling.[24,25] Notably, MYC has also been shown to suppress DKK1, promoting Wnt activation in breast cancer.[22,26] PRKCA encodes PKCα, which has been implicated in the negative regulation of Wnt signaling.[27] In the T-cell receptor signaling pathway, the top selected perturbation targets were CSF2, JUN, and MAPK9. Of these, CSF2 and JUN were among 10 enriched genes within the 39 selected nodes. In the JAK-STAT signaling pathway, SPRY1, MYC, and JAK1 emerged as top perturbation targets. All three were among 17 enriched genes out of the 33 selected. JAK1, in particular, is known to physically associate with the oncogene v-Abl, a key activator of the JAK-STAT pathway.[28]

NORSP was evaluated using metabolic models in the BioModel repository. To illustrate the methodology, we first present results from a single model before summarizing performance across all 61 systems. The metabolic model of the Calvin cycle (Figure 3A) was used to generate an influence network, serving as input to NORSP. The corresponding influence matrix, derived from the system's Jacobian, is shown in Figure 3B, with the perturbed node

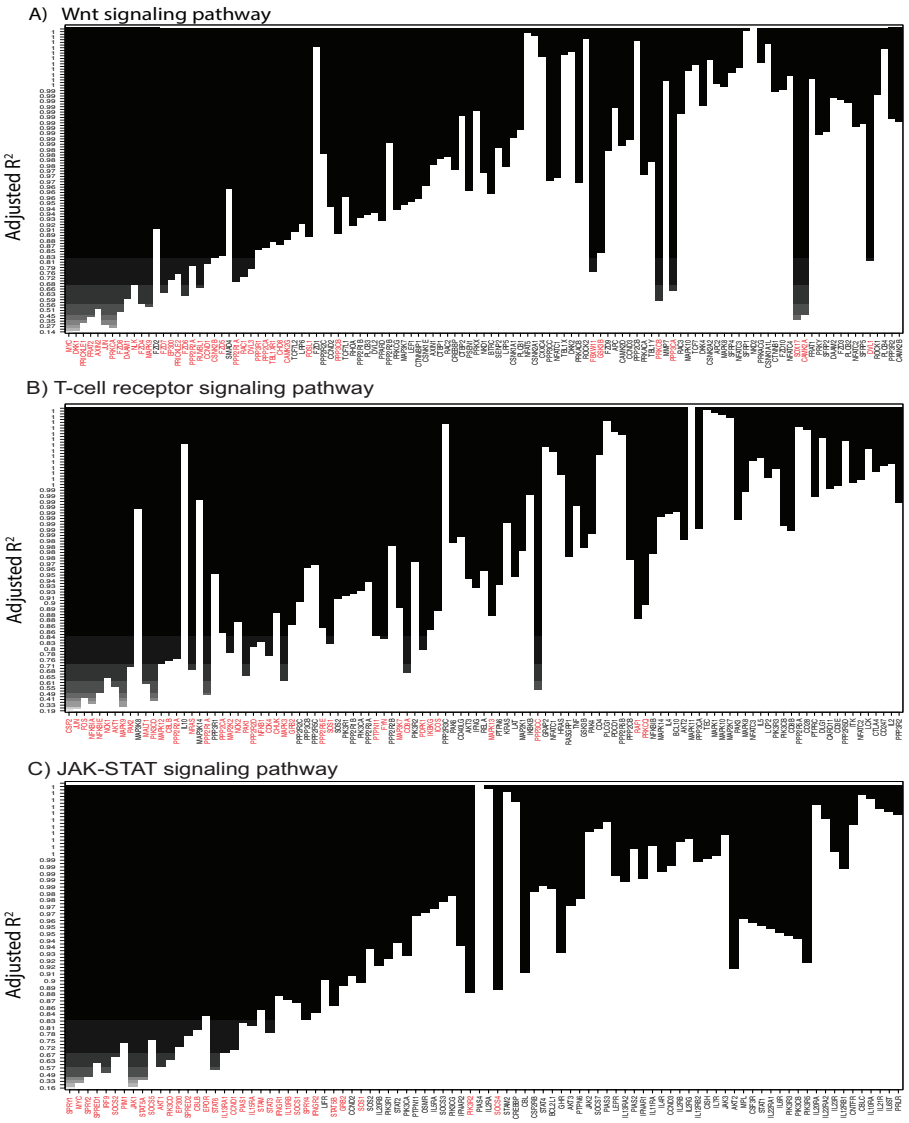

Fig. 2. NORSP results for YBX1 knockdown data, aiming to transition breast cancer cell lines (F^0) toward a healthy cell state (F^T). Subset selection results are shown for the top enriched KEGG pathways: **(A)** Wnt signaling, **(B)** MAPK signaling, and **(C)** JAK-STAT signaling. Adjusted R^2 is plotted as a function of the selected genes. Genes corresponding to the adjusted R^2 threshold are highlighted in red.

G6P, which was fixed at zero, circled in red. Using subset selection based on adjusted R^2, NORSP identified optimal perturbations across three types of influence networks: undirected, directed, and directed signed. In each case, the target node G6P was ranked among the top candidates (Figure 3C, shown in red). To better understand factors influencing network controllability, we examined structural properties of the BioModels under different graph representations—including node count, average degree, and clustering coefficients. However, these features did not consistently predict controllability outcomes (data not shown), suggesting

that control properties may depend on more complex, model-specific interactions.

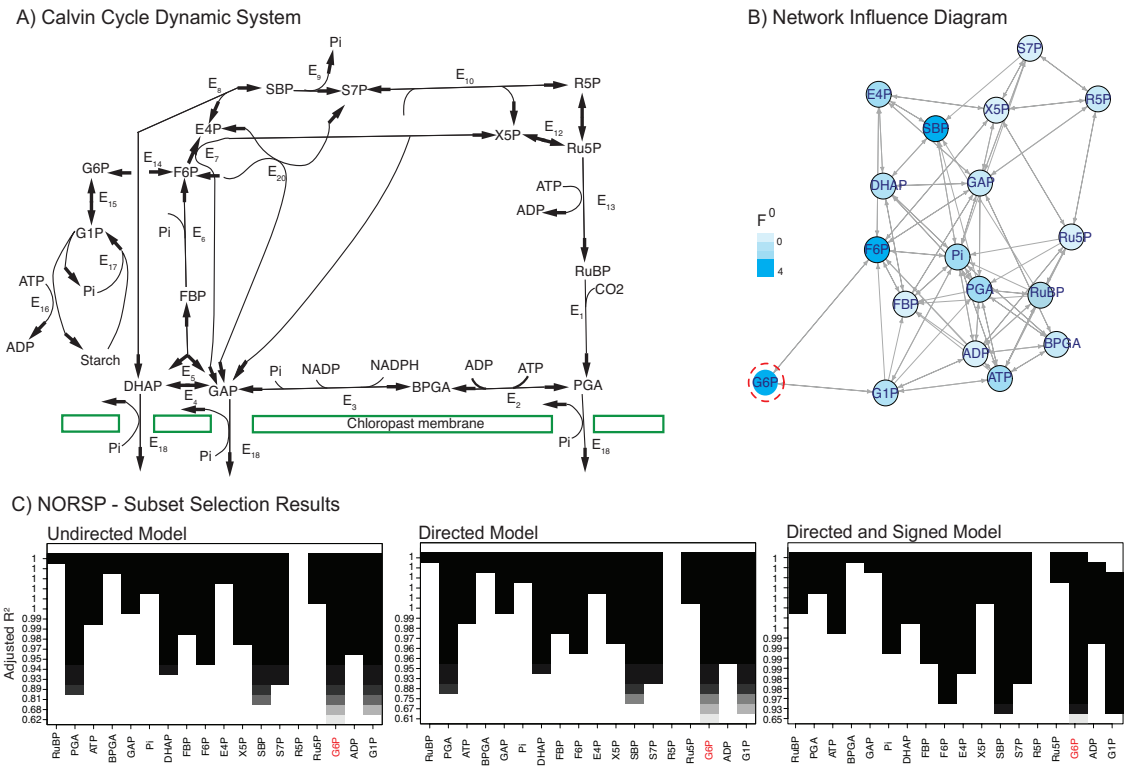

Fig. 3. An overview of NORSP applied to a single BioModel of the Calvin Cycle. **(A)** Schematic of the dynamic model representing the Calvin Cycle metabolism,[29] which is run to steady state and to obtain F^0, and perturbed to obtain a new target steady state, F^T. **(B)** The network influence diagram serves as the structural input to NORSP. The graph is extracted from the Jacobian and can be represented as undirected, directed, and signed. In this example, G6P is the perturbed node. **(C)** NORSP applied to the undirected, directed, and signed networks, and the corresponding model selection results using adjusted R^2 for target state approximation. The highest-ranked perturbation is G6P in all results, indicating that NORSP was able to identify the correct solution.

The results of the 61 BioModel simulations are summarized in Table 1. We evaluated graphical models derived from the influence matrix, which captures the network dynamics of each biological system, using the relative F error ratio. Three network propagation strategies were tested: undirected, directed, and directed signed. Model performance was assessed using two criteria: (1) adjusted R^2, and (2) the successful selection of the perturbed node among the top-ranked features, labeled as "target found." Under the adjusted R^2 criterion, 56, 57, and 55 models (out of 61) were correctly identified for the undirected, directed, and directed signed propagation methods, respectively (Table 1, Columns 1 and 2). This corresponds to 5, 4, and 6 misses, indicating a high success rate in selecting relevant perturbations across all three propagation strategies. We also examined the selected features to assess which models had identified the target as the top-ranked (Table 1, Column 3). We found that 48, 49, and

51 models correctly identified the perturbed node for the undirected, directed, and directed signed approaches, respectively. Finally, we counted the models for which the target was missed altogether, which were low 13, 12, and 10 (Table 1, Columns 4). These results highlight the robustness of the proposed framework in identifying meaningful perturbations across a broad range of biological models.

Table 1: Controllability results for the 61 Biomodels.
The F_{err}^{ctr} ratio is evaluates controllability (< 1) in the graphical (gm) and dynamical models (dyn).

Biomodel graph representation	Target found (# models)	Target ranked #1 (# models)	Target missed (# models)	Top hits in control graph ($F_{\text{gm}}^{\text{ctr}} <1$)	Top hits in control dyn. sys. ($F_{\text{dyn}}^{\text{ctr}} <1$)	Missed target in control dyn. sys. ($F_{\text{dyn}}^{\text{ctr}} <1$)
Undirected	56	48	13	48/48	35/48	9/13
Directed	57	49	12	49/49	33/49	11/12
Directed + Signed	55	51	10	51/51	36/51	10/10

A second mode of evaluation focused on system control, wherein the predicted perturbation was reintroduced into the system. Control was defined as the system's ability to approach the desired target state and was assessed both in the graphical model and the underlying dynamical system. When the target node was ranked as a top-priority candidate, control was consistently achieved across all models, as indicated by $F_{gm}^{ctr} < 1$ in the graphical model (Table 1, Column 5). Importantly, only the top-ranked perturbation of the selected set was introduced into the corresponding dynamical systems. System control was observed in the cases when the actual target was selected as the highest ranking (Table 1, Column 6). Notably, even in cases where the actual target was not ranked highest, the systems frequently remained controllable, especially when perturbations were derived from directed and signed-directed network models. This observation underscores the robustness of NORSP in identifying effective, experimentally actionable perturbations, even in the presence of uncertainty in target ranking.

To further assess NORSP's robustness, we simulated networks and introduced Gaussian noise either in the sensitivity matrix S or in the linear model. Table 2 summarizes the average prediction and perturbation errors across noise levels up to 10^{-1}. NORSP maintained low relative errors across both sparse and dense perturbation regimes when noise was confined to either the linear model or the sensitivity matrix. For small noise levels ($\epsilon \leq 10^{-3}$), both $\bar{F}_{\text{rel.err}}$ and $\bar{\Delta}_{\text{rel.err}}$ remained stable, typically below 0.01 and 0.07, respectively, demonstrating strong numerical stability. As noise increased to 10^{-1}, moderate increases in perturbation error were observed, most notably for the sensitivity matrix in the dense perturbation regime ($N_p = 25$), while target state errors remained low. These results indicate that NORSP is robust to moderate levels of measurement error and network misspecification, accurately recovering target states and perturbation patterns across a wide noise range.

Table 2: Noise added to the initial state of the system. Prediction errors of F_{target} were averaged over 100 simulations for networks with $N_n = 30$ nodes, under two perturbation regimes: sparse ($N_p = 5$) and dense ($N_p = 25$).

Noise-level ϵ	**Linear error**				**Sensitivity matrix error**			
	$N_p = 5$		$N_p = 25$		$N_p = 5$		$N_p = 25$	
	$\bar{F}^{\text{err}}$	$\bar{\Delta}^{\text{err}}$	$\bar{F}^{\text{err}}$	$\bar{\Delta}^{\text{err}}$	$\bar{F}^{\text{err}}$	$\bar{\Delta}^{\text{err}}$	$\bar{F}^{\text{err}}$	$\bar{\Delta}^{\text{err}}$
1e-07	0.007	0.069	0.023	0.171	0.006	0.053	0.023	0.174
1e-06	0.006	0.061	0.022	0.172	0.007	0.061	0.022	0.169
1e-05	0.007	0.060	0.022	0.166	0.006	0.062	0.022	0.168
1e-04	0.006	0.057	0.022	0.169	0.007	0.066	0.022	0.167
1e-03	0.000	0.065	0.022	0.178	0.007	0.065	0.022	0.165
1e-02	0.006	0.062	0.023	0.171	0.006	0.060	0.021	0.162
1e-01	0.006	0.056	0.022	0.164	0.007	0.288	0.024	0.257

4. Discussion

In this study, we introduced NORSP, a novel algorithm designed to identify sparse perturbations capable of guiding a system from an initial to a target steady state. By reframing the problem of network control as a subset selection task informed by network propagation, NORSP brings a practical approach to biological network optimization. It integrates graph-based sensitivity matrices with supervised learning, enabling direct prioritization of candidate perturbations without assuming full access to or manipulability of all network nodes.

A critical challenge in systems biology is to identify effective control strategies that are both interpretable and experimentally feasible. Traditional approaches, such as structural controllability theory,[30] offer important theoretical insights by identifying Minimum Driver Sets (MDSs)-the minimal number of nodes that must be controlled to steer the system. This framework has been widely applied in biological networks to classify nodes as critical, ordinary, or redundant,[31–33] and has informed analysis in domains such as metabolic regulation, disease gene identification, and signaling pathway dynamics.[34–36] Extensions of this theory have further characterized control modes and revealed emergent properties in complex systems.[37]

Despite its contributions, structural controllability also presents limitations. It often requires perturbation of a large proportion of nodes to achieve control, which is not compatible with experimental or clinical constraints.[38,39] It may also lack robustness in nonlinear systems, and typically does not estimate the magnitude or directionality of perturbations. These methods can be computationally expensive and may be less flexible in incorporating biological noise or measurement uncertainty.[40,41] Alternative strategies that involve iterative adjustment of system states, such as gradient-based approaches or local state feedback,[42,43] can also be computationally burdensome and sensitive to parameter initialization. NORSP is distinct from prior approaches that prioritize influential nodes (e.g., DYNAMO,[13] IGPON[14]) or rely on rich perturbation time-series data (e.g., CDN,[3] BaCaDI,[3] NETPERT[4]). Instead, NORSP operates in a realistic setting where only the network structure is available and perturbations must be experimentally actionable. Using gold-standard BioModels, knockdown data, and controlled

noise simulations, we showed that NORSP can recover true perturbations and effectively drive systems toward target states using only top-ranked candidates.

A significant strength of NORSP is the ability to find alternative paths towards perturbation when the true node target is not selected or is inaccessible. Simulation studies demonstrate that even when the actual perturbation is not among the top-ranked candidates, the system can still be driven toward the target state using alternate paths. This flexibility is particularly valuable in experimental contexts where not all network components are druggable or measurable. NORSP was also shown to be robust to misspecifications in the network structure and measurement error, which can be expected in models of biological systems. NORSP also expands the methodological toolkit for network control by using propagation-based sensitivity matrices as surrogates for the Jacobian. This allows the method to generalize across undirected, directed, and signed networks, accommodating the diverse structures found in biological systems. The use of subset selection aligns with a supervised learning framework, providing interpretability and scalability, especially when implemented with greedy forward selection or information criteria.

Nevertheless, several limitations warrant discussion. First, the propagation strength parameter must be manually tuned, as there is currently no theoretical guideline for optimal selection.[12,13] Second, while the subset selection framework simplifies the search space, the combinatorial nature of the optimization introduces heuristic dependencies. Furthermore, a threshold must be selected in subset selection according to model selection criteria. The use of forward subset selection can be viewed as modular, and alternatives could be considered. Future work could explore more sophisticated search strategies or Bayesian model averaging to enhance stability in parameter selection. Finally, an important limitation lies in the propagation assumption itself. Specifically, NORSP approximates the system Jacobian using a static network-derived sensitivity matrix. This simplification enables tractable optimization across large networks but does not capture nonlinear feedback, context-specific regulation, or time-dependent effects inherent to real biological dynamics. Future work could incorporate hybrid models that combine propagation-based inference with local dynamical refinement or explore adaptive sensitivity estimation from data.

Beyond theoretical utility, NORSP's targeted perturbation predictions may assist in prioritizing gene knockdowns or metabolic interventions for experimental validation. In particular, this framework could support early-stage drug screening by identifying mechanistically informative nodes whose control shifts replicate desired therapeutic outcomes. Its integration of sparse feasibility with network topology makes NORSP adaptable to both pathway-centric disease modeling and tissue-specific gene expression studies.

In summary, NORSP provides a principled yet practical framework for driving biological networks to target states using sparse, experimentally tractable interventions. By integrating ideas from network science, machine learning, and systems biology, it offers a new direction for hypothesis generation, experimental design, and therapeutic prioritization in complex biological systems. Its effectiveness across gene regulatory and metabolic networks highlights its versatility and potential as a tool for discovery.

References

1. T. Shi, H. Yu and R. H. Blair, Integrated regulatory and metabolic networks of the tumor microenvironment for therapeutic target prioritization, *Statistical Applications in Genetics and Molecular Biology* **22**, p. 20220054 (2023).
2. M. Wu, U. Padia, S. H. Murphy, R. Barzilay and T. Jaakkola, Identifying biological perturbation targets through causal differential networks, *arXiv preprint arXiv:2410.03380* (2024).
3. A. Hägele, J. Rothfuss, L. Lorch, V. R. Somnath, B. Schölkopf and A. Krause, Bacadi: Bayesian causal discovery with unknown interventions, in *International Conference on Artificial Intelligence and Statistics*, 2023.
4. M. C. Perrone, M. G. Lerner, M. Dunworth, A. J. Ewald and J. S. Bader, Prioritizing drug targets by perturbing biological network response functions, *PLoS Computational Biology* **20**, p. e1012195 (2024).
5. G. Baggio, D. S. Bassett and F. Pasqualetti, Data-driven control of complex networks, *Nature Communications* **12**, p. 1429 (2021).
6. S. Köhler, S. Bauer, D. Horn and P. N. Robinson, Walking the interactome for prioritization of candidate disease genes, *The American Journal of Human Genetics* **82**, 949 (2008).
7. E. O. Paull, D. E. Carlin, M. Niepel, P. K. Sorger, D. Haussler and J. M. Stuart, Discovering causal pathways linking genomic events to transcriptional states using tied diffusion through interacting events (tiedie), *Bioinformatics* **29**, 2757 (2013).
8. L. Cowen, T. Ideker, B. J. Raphael and R. Sharan, Network propagation: a universal amplifier of genetic associations, *Nature Reviews Genetics* **18**, 551 (2017).
9. G. Barel and R. Herwig, Netcore: a network propagation approach using node coreness, *Nucleic Acids Research* **48**, e98 (2020).
10. F. Vandin, E. Upfal and B. J. Raphael, Algorithms for detecting significantly mutated pathways in cancer, *Journal of Computational Biology* **18**, 507 (2011).
11. M. Hofree, J. P. Shen, H. Carter, A. Gross and T. Ideker, Network-based stratification of tumor mutations, *Nature Methods* **10**, p. 1108 (2013).
12. O. Vanunu, O. Magger, E. Ruppin, T. Shlomi and R. Sharan, Associating genes and protein complexes with disease via network propagation, *PLoS Computational Biology* **6**, p. e1000641 (2010).
13. M. Santolini and A.-L. Barabási, Predicting perturbation patterns from the topology of biological networks, *Proceedings of the National Academy of Sciences* **115**, E6375 (2018).
14. K. Krishnan, T. Shi, H. Yu and R. Blair, Integrated graph propagation and optimization with biological applications, in *Pacific Symposium on Biocomputing*, 2023.
15. C. Feng, C. Song, Y. Liu, F. Qian, Y. Gao, Z. Ning, Q. Wang, Y. Jiang, Y. Li, M. Li, J. Chen, J. Zhang and C. Li, KnockTF: a comprehensive human gene expression profile database with knockdown/knockout of transcription factors, *Nucleic Acids Research* **48**, D93 (2020).
16. M. Glont, T. V. N. Nguyen, M. Graesslin, R. Hälke, R. Ali, J. Schramm, S. M. Wimalaratne, V. B. Kothamachu, N. Rodriguez, M. J. Swat, R. Eils, H. Planatscher, E. Wingender, O. Wolkenhauer, H. Hermjakob, M. Hucka, N. Le Novere and R. S. Malik-Sheriff, Biomodels: expanding horizons to include more modelling approaches and formats, *Nucleic Acids Research* **46**, D1248 (2018).
17. M. Newman, *Networks* (Oxford university press, 2018).
18. O. Vanunu, O. Magger, E. Ruppin, T. Shlomi and R. Sharan, Associating genes and protein complexes with disease via network propagation, *PLoS Computational Biology* **6**, p. e1000641 (2010).
19. A. Miller, *Subset selection in regression* (chapman and hall/CRC, 2002).
20. B. J. Bornstein, S. M. Keating, A. Jouraku and M. Hucka, LibSBML: an API library for SBML, *Bioinformatics* **24**, 880 (2008).

21. Y.-H. Hao, M. C. Lafita-Navarro, L. Zacharias, N. Borenstein-Auerbach, M. Kim, S. Barnes, J. Kim, J. Shay, R. J. DeBerardinis and M. Conacci-Sorrell, Induction of lef1 by myc activates the wnt pathway and maintains cell proliferation, *Cell Communication and Signaling* **17**, 1 (2019).
22. V. H. Cowling and M. D. Cole, Turning the tables: Myc activates wnt in breast cancer, *Cell Cycle* **6**, 2625 (2007).
23. B. Madan, N. Harmston, G. Nallan, A. Montoya, P. Faull, E. Petretto, D. M. Virshup *et al.*, Temporal dynamics of WNT-dependent transcriptome reveal an oncogenic wnt/myc/ribosome axis, *The Journal of Clinical Investigation* **128**, 5620 (2019).
24. A. Niida, T. Hiroko, M. Kasai, Y. Furukawa, Y. Nakamura, Y. Suzuki, S. Sugano and T. Akiyama, Dkk1, a negative regulator of wnt signaling, is a target of the β-catenin/tcf pathway, *Oncogene* **23**, 8520 (2004).
25. V. H. Cowling, C. M. D'Cruz, L. A. Chodosh and M. D. Cole, c-myc transforms human mammary epithelial cells through repression of the Wnt inhibitors DKK1 and SFRP1, *Molecular and Cellular Biology* **27**, 5135 (2007).
26. J. Li, I. Sarosi, R. C. Cattley, J. Pretorius, F. Asuncion, M. Grisanti, S. Morony, S. Adamu, Z. Geng, W. Qiu, P. Kostenuik, D. L. Lacey, W. S. Simonet, B. Bolon, X. Qian, V. Shalhoub, M. S. Ominsky, H. Z. Ke, X. Li and W. G. Richards, Dkk1-mediated inhibition of wnt signaling in bone results in osteopenia, *Bone* **39**, 754 (2006).
27. J. Gwak, M. Cho, S. Gong, J. Won, D. Kim, E. Kim, S. S. Lee, M. Kim, T. K. Kim, J. Shin and S. Oh, Protein-kinase-c-mediated β-catenin phosphorylation negatively regulates the wnt/β-catenin pathway, *Journal of Cell Science* **119**, 4702 (2006).
28. N. N. Danial, A. Pernis and P. B. Rothman, Jak-stat signaling induced by the v-abl oncogene, *Science* **269**, 1875 (1995).
29. M. Poolman, H. Assmus and D. Fell, Applications of metabolic modelling to plant metabolism, *Journal of Experimental Botany* **55**, 1177 (2004).
30. C.-T. Lin, Structural controllability, *IEEE Transactions on Automatic Control* **19**, 201 (1974).
31. Y.-Y. Liu, J.-J. Slotine and A.-L. Barabási, Controllability of complex networks, *Nature* **473**, 167 (2011).
32. S. Nie, X. Wang, H. Zhang, Q. Li and B. Wang, Robustness of controllability for networks based on edge-attack, *PloS One* **9**, p. e89066 (2014).
33. C.-L. Pu, W.-J. Pei and A. Michaelson, Robustness analysis of network controllability, *Physica A: Statistical Mechanics and its Applications* **391**, 4420 (2012).
34. E. Kawakami, V. K. Singh, K. Matsubara, T. Ishii, Y. Matsuoka, T. Hase, P. Kulkarni, K. Siddiqui, J. Kodilkar, N. Danve, I. Subramanian, M. Katoh, Y. Shimizu-Yoshida, S. Ghosh, A. Jere and H. Kitano, Network analyses based on comprehensive molecular interaction maps reveal robust control structures in yeast stress response pathways, *NPJ Systems Biology and Applications* **2**, 1 (2016).
35. A. Vinayagam, T. E. Gibson, H.-J. Lee, B. Yilmazel, C. Roesel, Y. Hu, Y. Kwon, A. Sharma, Y.-Y. Liu, N. Perrimon and A. Barabasi, Controllability analysis of the directed human protein interaction network identifies disease genes and drug targets, *Proceedings of the National Academy of Sciences* **113**, 4976 (2016).
36. V. Ravindran, V. Sunitha and G. Bagler, Identification of critical regulatory genes in cancer signaling network using controllability analysis, *Physica A: Statistical Mechanics and its Applications* **474**, 134 (2017).
37. T. Jia, Y.-Y. Liu, E. Csóka, M. Pósfai, J.-J. Slotine and A.-L. Barabási, Emergence of bimodality in controlling complex networks, *Nature Communications* **4**, 1 (2013).
38. X. Liu and L. Pan, Detection of driver metabolites in the human liver metabolic network using structural controllability analysis, *BMC Systems Biology* **8**, 1 (2014).

39. V. Ravindran, J. C. Nacher, T. Akutsu, M. Ishitsuka, A. Osadcenco, V. Sunitha, G. Bagler, J.-M. Schwartz and D. L. Robertson, Network controllability: Viruses are driver agents in dynamic molecular systems, *bioRxiv* , p. 311746 (2018).
40. M. Li, H. Gao, J. Wang and F.-X. Wu, Control principles for complex biological networks, *Briefings in Bioinformatics* **20**, 2253 (2019).
41. R. M. D'Souza, M. di Bernardo and Y.-Y. Liu, Controlling complex networks with complex nodes, *Nature Reviews Physics* **5**, 250 (2023).
42. S. P. Cornelius, W. L. Kath and A. E. Motter, Realistic control of network dynamics, *Nature Communications* **4**, p. 1942 (2013).
43. M. R. Yousefi and E. R. Dougherty, Intervention in gene regulatory networks with maximal phenotype alteration, *Bioinformatics* **29**, 1758 (2013).

Discovery of Disease Relationships via Transcriptomic Signature Analysis Powered by Agentic AI*

Ke Chen

School of Information Sciences,
University of Illinois Urbana-Champaign,
Urbana, IL, USA
E-mail: kec10@illinois.edu

Haohan Wang

School of Information Sciences,
University of Illinois Urbana-Champaign,
Urbana, IL, USA
E-mail: haohanw@illinois.edu

Modern disease classification often overlooks molecular commonalities hidden beneath divergent clinical presentations. This study introduces a transcriptomics-driven framework for discovering disease relationships by analyzing over 1,300 disease–condition pairs using GenoMAS, a fully automated agentic AI system. Beyond identifying robust gene-level overlaps, we develop a novel pathway-based similarity framework that integrates multi-database enrichment analysis to quantify functional convergence across diseases. The resulting disease similarity network reveals both known comorbidities and previously undocumented cross-category links. By examining shared biological pathways, we explore potential molecular mechanisms underlying these connections—offering functional hypotheses that go beyond symptom-based taxonomies. We further show how background conditions such as obesity and hypertension modulate transcriptomic similarity, and identify therapeutic repurposing opportunities for rare diseases like autism spectrum disorder based on their molecular proximity to better-characterized conditions. In addition, this work demonstrates how biologically grounded agentic AI can scale transcriptomic analysis while enabling mechanistic interpretation across complex disease landscapes. All results are publicly accessible at `github.com/KeeeeChen/Pathway_Similarity_Network`.

Keywords: Disease similarity network; Transcriptomic associations; AI-driven discovery

*This research was supported by the National AI Research Resource (NAIRR) under grant number 240283.

© 2025 The Authors. Open Access chapter published by World Scientific Publishing Company and distributed under the terms of the Creative Commons Attribution Non-Commercial (CC BY-NC) 4.0 License.

1. Introduction

Modern disease classification is predominantly grounded in clinical symptoms, anatomical locations, and observable phenotypes.[1–3] While practical for diagnosis and treatment, this symptom-centric taxonomy often obscures deeper biological relationships between diseases—especially those with divergent clinical manifestations but shared molecular origins.[4,5] In contrast, transcriptomic signatures[6] capture gene expression patterns directly reflective of underlying cellular mechanisms, offering a biologically principled lens to reexamine disease relationships.

Recent studies have shown that transcriptomic profiling not only reveals disease-specific pathways related to susceptibility,[7,8] progression,[9–11] and resilience,[12,13] but also uncovers shared molecular programs[6,14,15] across phenotypically distinct diseases. These shared patterns, often invisible to clinical observation,[16,17] have profound implications for disease reclassification,[18,19] biomarker discover,[20,21] and therapeutic repurposing.[22,23] However, realizing these benefits at scale remains challenging:[24,25] each transcriptomic dataset requires extensive preprocessing, normalization, and analysis—an effort that is labor-intensive and difficult to replicate consistently across diverse biological and demographic contexts. Existing frameworks such as Hetionet[26] and DisGeNET[27] have provided valuable resources for studying disease–disease associations, yet they are largely knowledge-based: relying on curated gene–disease links or heterogeneous databases. As a result, they are limited in capturing transcriptomic mechanisms directly from large-scale molecular data or in accounting for condition-specific variation across diseases.

To address this, we leveraged GenoMAS,[28] a fully automated, agentic AI system that performs large-scale transcriptomic analyses across 1,384 disease–condition pairs drawn from the GenoTEX[29] benchmark dataset. Each *pair* represents a disease under a specific biological or demographic condition (e.g., age, sex, obesity, comorbidity), enabling nuanced profiling across 132 diseases and 911 cohorts. Powered by a team of specialized LLM agents, the agentic system performs end-to-end processing, from data cleaning to statistical inference, to identify the genes associated with the disease status under the conditions. In other words, the agentic system identified the *transcriptomic signatures* for each *pair* of disease and condition.

Building on these results, we construct a disease relation network through transcriptomic signatures, identifying statistically significant transcriptomic overlaps between thousands of disease–condition pairs. We validate this network against ICD-10-CM categories and observe both strong within-category clustering and biologically plausible cross-category links—highlighting hidden disease relationships overlooked by traditional taxonomy.

To further interpret the functional basis of these relationships, we extend our analysis to the pathway level. By conducting multi-database enrichment and introducing a novel pathway-based similarity scoring framework, we identify over 1,000 disease combinations that converge on shared molecular pathways. These shared pathways reveal fundamental biological mechanisms that transcend clinical presentation and reflect the cellular logic underlying diverse disease states.

Our analysis recovers well-established comorbidities (e.g., epilepsy and Canavan disease), confirms mechanistically plausible cross-category relationships (e.g., ankylosing spondylitis

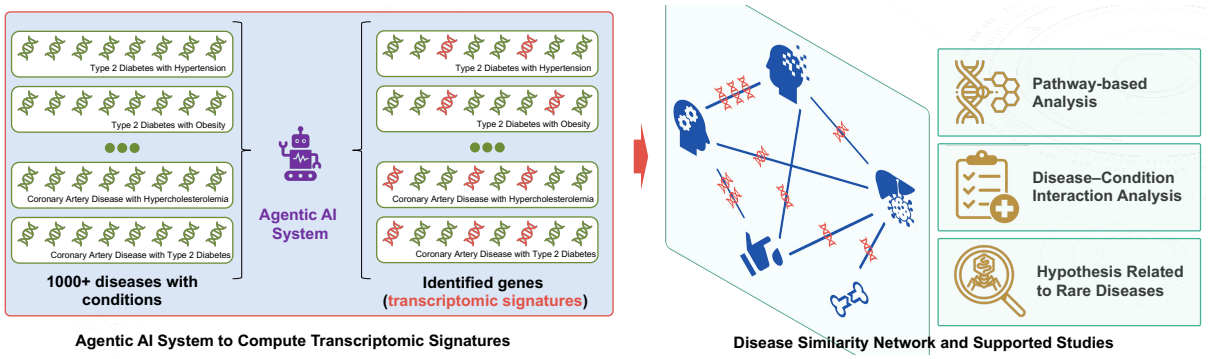

Fig. 1: Agenetic AI analysis of transcriptomic data for transcriptomic signatures and the network of diseases constructed from the signatures.

and osteoporosis), and—most notably—uncovers novel disease links that have not been previously reported in the literature. For these unexpected pairs, we hypothesize potential biological mechanisms supported by shared pathways and gene functions, providing initial interpretive insights to be explored in future studies—for instance, immune and glycosylation-related convergence between Gaucher disease and kidney cancer, or shared metabolic signaling and oxidative stress patterns observed in neurodegenerative diseases and `Ocular Melanoma`.

Finally, we explore how background conditions like obesity and hypertension modulate disease–disease transcriptomic similarity and highlight rare disease cases, such as autism spectrum disorder, where shared molecular signatures with more common diseases may inform drug repurposing opportunities.

To encourage broader exploration of hidden disease relationships, we have made our full results publicly available at `github.com/KeeeeChen/Pathway_Similarity_Network`. Additionally, an initial biological plausibility assessment was conducted using GPT-4o to highlight approximately 200 disease-combinations that exhibit interpretable functional convergence. We hope this resource can inspire new hypotheses and offer alternative perspectives for understanding disease mechanisms beyond established taxonomies.

In summary, the contributions of this paper are illustrated in Figure 1 and as follows:

- We perform large-scale transcriptomic signature analysis across 1,384 disease-condition pairs using an agentic AI system (GenoMAS).
- We construct a gene-level transcriptomic similarity network based on transcriptomic signatures, revealing both strong within-category and cross-category connections.
- We introduce a pathway-level similarity framework based on multi-database enrichment and joint pathway scoring, identifying over 1,000 disease-condition combinations that converge on interpretable molecular mechanisms.
- We highlight examples of transcriptomic convergence in both well-established and unexpected disease pairings, including several cases with no previously documented clinical or molecular connection.
- We study how background conditions such as obesity and hypertension modulate transcriptomic similarity between diseases, and identify rare diseases whose molecular profiles suggest potential therapeutic strategies based on cross-disease alignment.

2. Results

Before presenting our main findings, we first clarify several key terms used throughout the analysis. Our study involves multiple levels of comparison across diseases, biological conditions, and their combinations. Table 1 summarizes the terminology used.

Table 1: Terminology used in this study

Term	Definition / Example
Disease	A clinical diagnosis or condition label. *e.g., Liver Cancer*
Condition	A biological or demographic modifier that contextualizes the disease. *e.g., Obesity, Sex, Age, Hypertension*
Pair	A disease combined with a specific condition. *e.g., Liver Cancer–Obesity*
Combination	A pairwise comparison between two disease–condition pairs. *e.g., (Liver Cancer–Obesity) vs. (Schizophrenia–Gender)*

2.1. *Gene-Based Similarity Network*

To investigate inter-disease relationships at the transcriptomic level, we preliminarily analyzed the statistical significance of overlap of transcriptomic signatures between every *combination* of the 1,384 disease–condition pairs (hereafter, *"combinations"*).

Based on these shared gene relationships, we constructed a graph in which each node represents a disease–condition pair, and each edge connects two pairs that significantly share a set of genes (see Section 3.2 for details). To validate the biological plausibility of the resulting network, we compared our result with the ICD-10-CM classification system.[1] Specifically, we prompted GPT-4o to assign an ICD category to each disease, and constructed a heatmap of average pairwise gene similarity scores for both pairs within the same ICD category and cross-category pairs. (Figure 2)

As expected, many chapters show the strongest similarity within their own category—e.g., Chapter 6, 13, and 9 all display elevated diagonal values. However, the heatmap also reveals that several chapters exhibit their highest similarity scores with other categories rather than their own. For instance, certain subtypes within Chapter 2 and 3 share stronger transcriptomic profiles with Chapter 13 than within their own chapters, suggesting biologically meaningful cross-category overlap. While some of these connections may arise from annotation bias or shared tissue origin, others may reflect previously overlooked biological commonalities.

Together, these findings suggest that while disease taxonomy based on anatomy or symptoms often aligns with molecular signatures, gene-level similarity can also uncover latent biological relationships that transcend clinical classifications. This motivated our subsequent pathway-level analysis to probe deeper into shared mechanisms.

2.2. *Pathway-Based Disease Similarity*

While these combinations significantly shared some genes, their biological relevance remained unclear without understanding what molecular processes these genes are involved in. To better

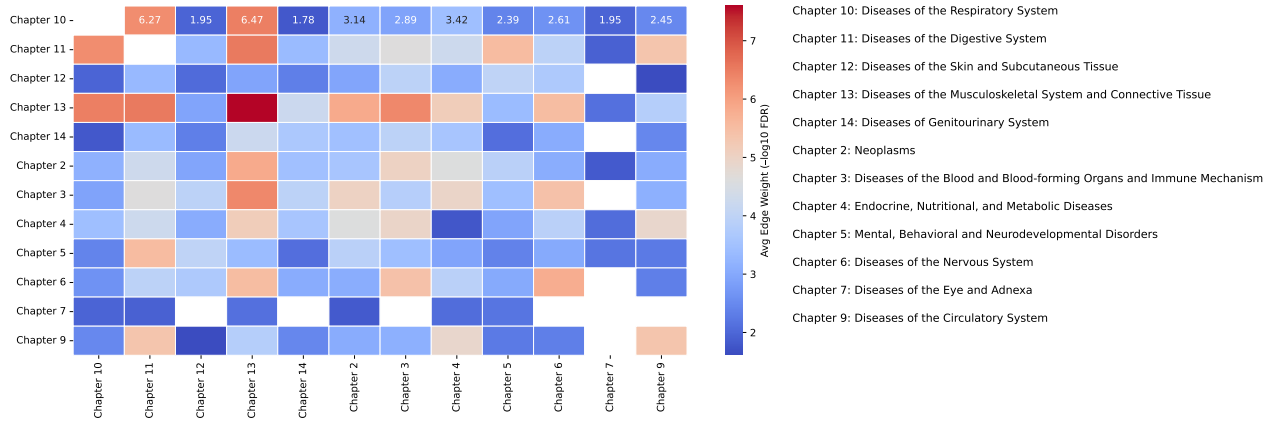

Fig. 2: Heatmap of average gene-based similarity between ICD-10-CM chapters. Diagonal blocks (e.g., Chapters 6, 9, 13) show strong within-category similarity, while several off-diagonal blocks indicate cross-category transcriptomic convergence. Notably, chapter 2, 3, 10, and 11 show higher similarity to other categories than within their own, suggesting latent biological overlap.

interpret the functional basis of disease similarity, we examined pathway-level overlap among the 1,293 significant disease–condition combinations identified by our gene-based analysis (see Section 3.3 for details). Among these combinations, 1,060 were found to share at least one enriched pathway. To visualize these relationships, we constructed a weighted undirected graph (see Figure 3) to provide a systems-level view of transcriptomic convergence across diseases.

This network reveals a clear tendency for nodes of the same ICD-10-CM category to cluster together, which suggests that our pathway-based analysis, while agnostic to clinical labels, nonetheless recapitulates key elements of traditional disease taxonomy. At the same time, many edges span across categories, hinting at molecular commonalities that transcend existing clinical boundaries.

Subsequent analyses in this study are grounded in this network representation. Specifically, we focus on interpretable subgraphs extracted from the full network—such as highly connected modules, cross-category clusters, and rare disease neighborhoods—to uncover novel patterns of comorbidity, shared vulnerability, and potential therapeutic convergence. This pathway network thus serves as the functional scaffold for the biological insights that follow.

2.2.1. *Transcriptomic Similarity Reflects Symptom-Based Taxonomy*

Many high-scoring combinations correspond closely to well-established disease relationships. For example, `Canavan Disease` and `Epilepsy`—both neurological disorders—significantly shared pathways such as **detection of chemical stimulus**, **sensory perception**, and **G protein-coupled receptor signaling pathway**. These pathways are central to neuronal communication and signal transduction, especially in sensory and stimulus-related neural activity. This is consistent with clinical consensus.

There are also other top-scoring combinations aligned with known biological and clinical groupings, including: - `Stomach Cancer` and `Peptic Ulcer Disease`, both involving the gas-

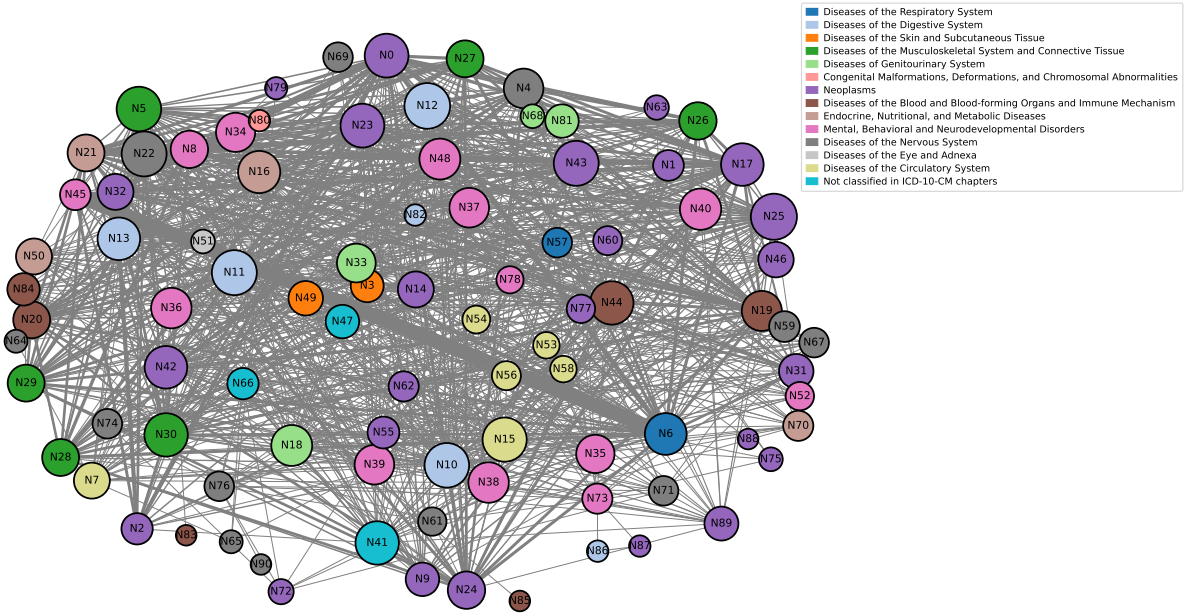

Fig. 3: Pathway-level similarity network. Each node represents a disease–condition pair, colored by ICD-10-CM category. Edges indicate statistically significant overlap in enriched pathways. Both the thickness and the length of each edge reflect the strength of similarity—stronger pathway-level similarity results in shorter and thicker edges. Node size reflects degree centrality. While many nodes are connected, this visualization is designed to emphasize the strength of similarity rather than the presence of connection.

Table 2: P-values of pathological-related shared Pathways in Canavan Disease and Epilepsy

Pathway	**Canavan_Disease–None**	**Epilepsy–None**
detection of chemical stimulus	2.04×10^{-22}	3.72×10^{-26}
sensory perception	6.01×10^{-16}	1.50×10^{-22}
G protein-coupled receptor signaling pathway	1.17×10^{-13}	2.43×10^{-17}

trointestinal system; - `Depression` and `Schizophrenia`, both major psychiatric disorders; - `Bladder Cancer` and `Endometrioid Cancer`, which share hormonal and tissue-level commonalities.

2.2.2. *Cross-Category Transcriptomic Similarity with Empirical Support*

Beyond well-established within-category associations, our pathway-based analysis also revealed biologically meaningful links across some phenotypically unrelated disease categories.

One example is `Ankylosing Spondylitis (AS)` and `Osteoporosis`, two conditions traditionally categorized under musculoskeletal and metabolic disorders, respectively. They significantly share genes such as *AAMDC*, *ABCB1*, and *ABCA5*, along with enriched pathways

related to lipid metabolism, cholesterol regulation, ABC transporters, steroid biosynthesis, and xenobiotic response.

These functions jointly regulate inflammation, immune activity, and bone remodeling—suggesting a shared biological axis linking chronic inflammation, lipid dysregulation, and bone loss. This supports the hypothesis that inflammatory mechanisms in AS may drive osteoporosis risk through disrupted metabolic signaling. Our findings are consistent with recent empirical studies confirming an elevated osteoporosis risk in AS patients,[30,31] and with transcriptomic evidence highlighting immune-driven bone density reduction.[32] Our results further clarify potential shared molecular mechanisms underlying this comorbidity.

We also observed high pathway-based similarity between `Hemochromatosis` and `Liver Cancer`, supported by significantly shared genes such as *AADAT*, *A1BG*, *A4GNT*, and *AARS2*. These genes participate in pathways related to amino acid metabolism, mitochondrial function, immune regulation, and glycoprotein processing.

These shared pathways converge on several key processes: iron overload in Hemochromatosis promotes oxidative stress and chronic inflammation in the liver—an organ central to both conditions. Pathways such as *Tryptophan metabolism*, *immune response signaling*, and *protein glycosylation* highlight a potential mechanistic chain involving metabolic disruption, immune imbalance, and epithelial cell proliferation—all of which may facilitate hepatocarcinogenesis.

These findings align with prior epidemiological studies confirming elevated liver cancer risk in patients with HFE-related Hemochromatosis,[33] and extend beyond prior expression analyses by identifying a broader set of molecular mediators.[34]

These examples illustrate how pathway-level similarity can provide complementary context to gene-level overlap, offering candidate functional processes that may help interpret co-occurrence patterns between diseases.

2.2.3. *Transcriptomic Similarities That Are Potentially Unexpected from Conventional View*

One interesting outcome of our transcriptomic similarity analysis is the resemblance observed between several phenotypically and clinically unrelated conditions. One example is `Gaucher Disease` and `Kidney Chromophobe`. Although `Gaucher Disease` is a lysosomal storage disorder and `Kidney Chromophobe` is a renal carcinoma subtype, they share significant expression of genes such as *A1BG*, *A4GNT*, and *A2M*, alongside co-enrichment in pathways involving immune signaling, extracellular matrix (ECM) remodeling, and protein glycosylation.

These overlapping genes suggest a common functional landscape shaped by immune regulation, protein processing, and inflammation. *A1BG* has been linked to tumor-associated immune modulation;[35,36] *A4GNT* influences glycosylation—a process central to immune escape and cellular signaling;[37] and *A2M* is involved in ECM maintenance and inflammatory control.[38] Pathway-level analysis further reveals enrichment in immune response, ECM organization, glycoprotein biosynthesis, and cellular stress adaptation. Together, these findings point to a shared cellular environment marked by chronic inflammation and metabolic stress—hallmarks of both lysosomal disorders and tumorigenesis. While no direct clinical relationship has been reported between `Gaucher Disease` and `Kidney Cancer`, our results suggest

a potentially overlooked biological intersection that warrants further investigation.

A second example involves an unexpected transcriptomic connection between `Alzheimer's Disease & Parkinson's Disease`, and `Ocular Melanoma`. These conditions share significant expression of *AADAT* and *AASDH*, genes involved in lysine[39,40] and tryptophan metabolism,[39] which regulate NAD^+ biosynthesis, glutamate balance, oxidative stress response, and immune modulation.[41–43] Though these processes diverge in pathological outcomes, they are central to both neurodegeneration and cancer.

As shown in Figure 4, we observed shared enrichment in pathways related to amino acid catabolism, β-oxidation, and cellular response to oxidative stress. In neurodegenerative diseases, these pathways are often impaired,[44] leading to energy failure and excitotoxicity. In contrast, `Ocular Melanoma` exhibits enhanced β-oxidation,[45] supporting tumor proliferation and immune evasion. This inverse utilization of the same metabolic axis may reflect a mechanistic fork, shaped by the shared neural crest origin of retinal and neural tissues.[46] AADAT's dual role in neural excitotoxicity and tumor immune regulation further supports this.

Although no clinical relationship has been established between neurodegenerative disorders and `Ocular Melanoma`, the observed transcriptomic similarities may reflect a shared developmental or metabolic context. These findings raise the possibility of underlying molecular features that span traditionally unrelated disease categories, which may merit further investigation through functional or mechanistic studies.

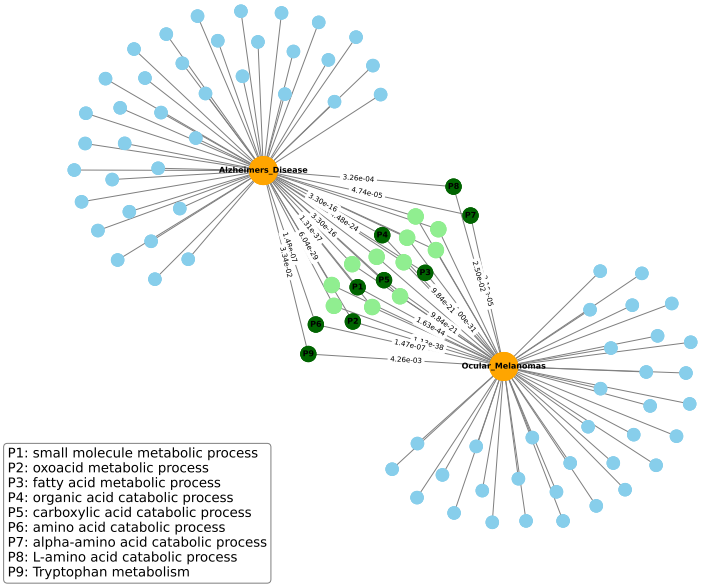

Fig. 4: Shared transcriptomic pathways between Alzheimer's Disease and Ocular Melanoma. The graph displays the top 50 most significant enriched pathways in each disease. Blue nodes represent highly enriched but not shared pathways. Green nodes indicate pathways shared by both diseases, with darker green highlighting the pathways discussed in 2.2.3, which are potentially relevant to the comorbidity. Edge labels reflect pathway significance (p-values), and edge lengths scale with significance.

2.3. *Disease–Condition Interaction Analysis: Triggers of Comorbidity*

While disease–disease similarities often reflect shared genetic programs or pathological mechanisms, the presence of specific physiological or environmental conditions can further modulate the expression of such relationships. In our analysis, we explored disease–condition pairs to understand how background factors—such as obesity or hypertension—may shape transcriptomic overlaps and increase the risk of co-occurrence.

One interesting case involves the co-occurrence of `Celiac Disease` and `Uterine Carcinosarcoma` in obese individuals. Though one is an autoimmune enteropathy and the other a rare uterine malignancy, they share dysregulation of genes such as *A1CF*, *AACS*, and *ABCB1*, which point to altered mRNA editing, amino acid metabolism, and xenobiotic transport. These genes are enriched in pathways that are particularly sensitive to metabolic dysregulation in obesity, including glycosphingolipid biosynthesis, bile secretion, and branched-chain amino acid degradation. In obese individuals, chronic inflammation, disrupted metabolic homeostasis, and impaired detoxification mechanisms may jointly promote both autoimmune activation and tumorigenesis, thus creating a fertile biological landscape for comorbidity.

Another example is the comorbidity of `Acute Myeloid Leukemia` and `Osteoarthritis` in individuals with hypertension. These diseases converge on genes such as *A2ML1* and *A2M*, which regulate extracellular matrix homeostasis and inflammation, as well as *A1CF*, which modulates immune signaling through RNA editing. The two diseases also share enrichment in immune and complement pathways, ECM degradation, and glucocorticoid response—features that are frequently exacerbated in hypertensive individuals. Hypertension, by promoting systemic inflammation, endothelial dysfunction, and hormonal imbalance, may amplify shared transcriptomic vulnerabilities in both hematologic and joint tissues.

This is not an isolated observation. In fact, 11 of the top 20 highest-scoring disease–condition pairs in our transcriptomic similarity analysis involve hypertension, including connections with `Acute Myeloid Leukemia, Adrenocortical Cancer, Gaucher Disease`, and `Osteoarthritis`. These findings underscore the wide-reaching systemic impact of hypertension—not just as a cardiovascular risk factor, but as a molecular amplifier of disease vulnerability across diverse biological systems. Given its high prevalence and silent progression, we emphasize the importance of early detection and integrative management of hypertension to mitigate its far-reaching comorbidity burden.

2.4. *Hypotheses Related to Rare Diseases*

In addition to mapping disease–disease similarity, we also examined whether transcriptomic overlaps with well-characterized conditions could highlight underexplored disorders that worth further investigation. For example, we extracted the subgraph centered on `Autism Spectrum Disorder (ASD)`. As shown in Figure 5, this local network reveals close transcriptomic and pathway-level similarity between ASD and other conditions, including `Osteoporosis` and `Type 1 Diabetes`. While these two diseases are typically studied in distinct clinical domains, their established therapeutic pipelines and shared molecular features with ASD raise the possibility of identifying underexamined connections or therapeutic hypotheses, particularly in individuals with overlapping metabolic or immune phenotypes.

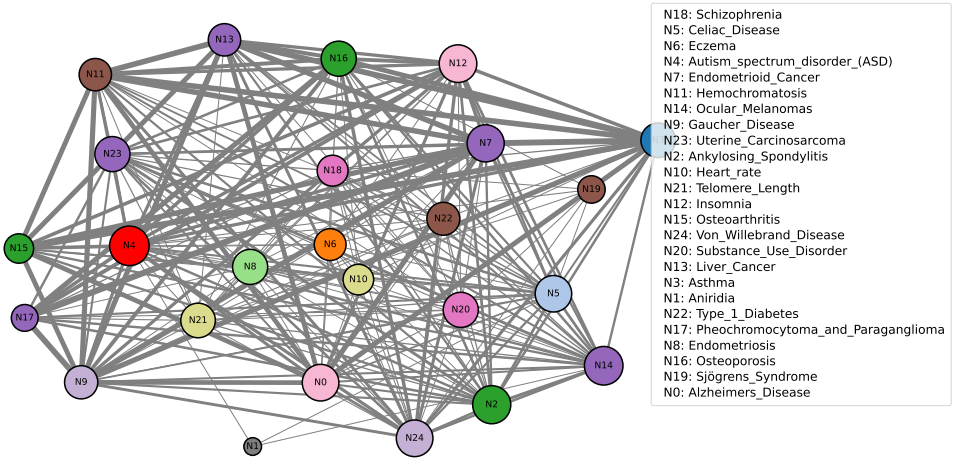

Fig. 5: Subnetwork of diseases showing significant pathway-level similarity to ASD (the red node with index N4). Osteoporosis and Type 1 Diabetes (T1D) emerge as strongly connected conditions, both with established pharmacological pipelines.

In the case of Osteoporosis, ASD shares genes such as *AADAC*, *ABCF3*, and *ABCA7*, which participate in lipid metabolism and ABC transporter pathways. While these genes have not been directly targeted in ASD, several lipid-modulating agents—such as statins, bisphosphonates, and ANGPTL3/APOC3 inhibitors—have demonstrated activity along the same pathways. Their mechanistic action on lipid regulation and inflammatory balance raises the possibility that they could be repurposed for ASD, particularly in individuals with lipid signaling or neuroinflammation phenotypes.

A similar pattern emerges with T1D: shared genes like *AADAT*, *ABCD1*, and *AATF* point to convergence in fatty acid oxidation, mitochondrial stress, and immune dysregulation. Corresponding therapeutic approaches—ranging from anti-inflammatory agents (e.g., α1-antitrypsin, TYK2 inhibitors) to metabolic modulators (e.g., *ABCD1* gene therapy, PPARγ agonists like Leriglitazone)—may offer a foundation for exploratory ASD interventions aimed at metabolic or immune correction.

3. Methodology

3.1. *Large-Scale Gene Analysis via Transcriptomic Agentic AI System*

To explore disease relationships from a transcriptomic perspective, we leveraged the GenoTEX dataset,[29] a large-scale, biologically curated benchmark for automated gene expression analysis. GenoTEX comprises 1,384 gene–disease association problems, spanning 132 distinct human diseases, each analyzed under varying biological or demographic conditions (e.g., age, sex, obesity, hypertension, or comorbidities). For clarity, we refer to the combination of a disease and a condition as a "disease–condition pair", or simply a "pair", throughout this study. The dataset encompasses 911 unique cohorts, totaling over 150,000 biological samples, with each cohort containing more than 18,000 normalized gene features on average.

To process this data at scale, we employed GenoMAS,[28] a multi-agent agentic AI framework

built for code-level automation in genomic analysis. In practice, GenoMAS automates the full workflow of gene expression analysis—from dataset retrieval and preprocessing to regression-based gene–trait association modeling. During preprocessing, the system standardizes heterogeneous data formats (e.g., RNA-seq and microarray), performs gene identifier normalization, and applies corrections for batch effects and population stratification. For statistical inference, it primarily relies on regularized regression (e.g., Lasso) to select trait-associated genes under high-dimensional settings, while incorporating confounder adjustment and imputation strategies to ensure robust signal detection. Using this system, we performed end-to-end gene significance analysis for all 1,384 disease–condition pairs. The results include gene-level effect sizes (regression coefficients), lists of significant genes.

3.2. *Gene-Based Similarity Network*

To quantify transcriptomic similarity, we assessed gene overlap significance for each of the pairwaise combinations of 1384 pairs. For each pair, we retained genes with $|\beta| > 0.05$ from Lasso regression, filtering out weak associations. We then computed shared genes between each combination and performed a bidirectional hypergeometric test, testing enrichment of set A within set B and vice versa, so that significance was not driven solely by large gene sets, while accounting for gene set sizes and the full gene universe (18,000+ genes). Benjamini–Hochberg correction was applied to adjust for multiple testing.

We retained only combinations with false discovery rate (FDR) ≤ 0.05, yielding approximately 65,000 significant pairwise links out of nearly 1 million tested combinations.

To avoid redundancy, we further filtered out overlapping combinations involving generalized condition entries labeled as `None` (i.e., entries not conditioned on any specific biological factor). For example, if a significant link was already identified between `Disease1--None` and `Disease2--Obesity`, then additional links such as `Disease1--Sex` or `Disease1--Age` with `Disease2--Obesity` were considered redundant, as the shared signal likely reflects disease-level rather than condition-specific effects. This de-duplication step prevents generalized associations from inflating or obscuring condition-specific links, reducing the network from over 65,000 initially significant combinations to 1,293 unique links after filtering.

We constructed a gene-level similarity network using `NetworkX`. In this network, each node corresponds to a disease–condition pair, and an edge is drawn between two nodes if their overlap of significant genes passes the bidirectional hypergeometric test after FDR correction. To quantify edge strength, we defined the weight as $-\log_{10}(\text{FDR})$, such that more significant overlaps are assigned larger weights. The resulting weighted graph thus captures both the presence and relative strength of transcriptomic similarity among disease–condition pairs.

For visualization, we employed the `nx.spring_layout()` algorithm to arrange nodes in 2D space. To account for edge strength, we defined the layout weight as the inverse of the edge similarity score ($w_{uv} = 1/(\text{weight}_{uv} + 10^{-5})$), so that stronger similarities correspond to shorter distances. We set the repulsive force parameter to $k = 0.2$ to generate a more compact layout. These settings allow the visualization to reflect both the local clustering and the global structure of the similarity network in a consistent manner.

To annotate the biological identity of each node, we assigned an ICD-10-CM category to

every disease using GPT-4o. These categories were also used as node colors in the visualization for pathway-based similarity network (Figure 3).

3.3. *Pathway-Based Disease Similarity*

To investigate functional overlap among disease–condition pairs, we performed pathway enrichment analysis and similarity scoring for all 1,293 significant combinations identified in the gene-level analysis.

Pathway Enrichment per Pair. For each disease–condition pair, we mapped significantly expressed genes (with $|\beta| > 0.05$) to pathways using six complementary annotation databases: GO:Biological Process (GO:BP),[47] Reactome (REAC), KEGG,[48] transcription factor targets (TF), miRNA targets (MIRNA), and Human Phenotype Ontology (HP).[49] This ensures both biological breadth and low redundancy. We adopted the g:Profiler[50] framework to retrieve enriched terms. g:Profiler selects higher-level, abstracted pathway terms to mitigate semantic variability across databases and maximize interpretability.

Identification of Shared Pathways. For each disease–condition pairwise combination (hereafter, "combination"), we focused only on the genes that were shared between the two pairs. For each such shared gene, we retrieved its pathway annotations in both pairs. A pathway was considered "shared" if it was enriched for the same gene in both pairs.

Similarity Scoring. To quantify the overall strength of pathway-level similarity between two disease–condition pairs, we computed a cumulative score across all shared pathways using the following formula:

$$\text{Similarity Score} = \sum_{k=1}^{N} [\log(1 - p_{1k}) + \log(1 - p_{2k})]$$

Here, N is the number of shared pathways between the two pairs, and p_{1k}, p_{2k} are the enrichment p-values of the k-th pathway in the first and second pair, respectively. For each pathway, this score reduces to $\log((1 - p_{1k}) \times (1 - p_{2k}))$, which reflects the joint probability that both enrichments are non-random. That is, the score becomes more positive when both p_1 and p_2 are small, indicating that the pathway is likely involved in both disease contexts. Summing across all such shared pathways allows us to capture not just the presence of overlap, but the joint confidence in their functional relevance.

Filtering. We retained only combinations where at least one shared pathway had a positive similarity score, indicating non-random co-enrichment. This yielded 1,060 pathway-supported combinations out of the original 1,293 gene-sharing ones.

Pathway-level Graph Construction To visualize cross-disease functional similarity, we constructed an undirected weighted network in which each node represents a disease-condition pair. An edge is drawn between two nodes if the two diseases share at least one enriched pathway. The edge weight corresponds to the pathway-level similarity score. Node size reflects its

degree (i.e., the number of connected neighbors), and node color encodes ICD-10-CM categories. Similar to the gene-level network, we applied a spring-force layout in which edge lengths are inversely proportional to similarity weights. To better illustrate the strength of functional similarity, edge thickness is scaled proportionally to the similarity score—stronger similarities are rendered as thicker connections. In subsequent analyses, we also constructed disease-level subgraphs by collapsing the condition dimension (e.g., Figure 5). In these subgraphs, node size reflects the average degree of each disease across all associated conditions, while edge width and length correspond to the average pathway similarity between the connected diseases.

4. Limitation and Discussion

This work has several limitations. Most importantly, our results are hypothesis-generating rather than experimentally validated. While we provide mechanistic hypotheses for selected examples, these remain speculative until confirmed by biological experiments. For other findings, we performed an initial interpretability assessment using GPT-4o, but these outputs still require expert review and validation to ensure robustness.

We envision several ways in which our resources may support future research. The similarity network may help generate hypotheses on disease etiology, comorbidity, or molecular mimicry. For instance, rare-disease investigators may identify molecular patterns shared with more prevalent conditions, suggesting avenues for drug repurposing or biomarker development. Gene- and pathway-level results may also guide validation studies, especially in evaluating the functional relevance of shared molecular programs. Finally, by providing structured and interpretable outputs from AI-generated analyses, we aim to lower the barrier for translational researchers to engage with complex transcriptomic datasets.

More broadly, we advocate closer integration of AI systems with biomedical research—not just automation, but biologically interpretable and clinically useful output. Agentic AI, when grounded in biological context, can help bridge the gap between large-scale computation and meaningful biological interpretation.

5. Conclusion

This study introduces a transcriptomics-driven framework for rethinking disease relationships beyond traditional clinical boundaries. Leveraging the GenoMAS system, we analyzed over 1,300 disease–condition pairs to construct both gene- and pathway-level similarity networks.

Our multi-layered approach reveals both well-established comorbidities and novel cross-category links, proposing molecular connections across diseases through shared pathways in metabolism, immune response, and cellular stress. We further show that systemic conditions such as obesity and hypertension modulate transcriptomic similarity, while rare diseases like autism spectrum disorder may benefit from therapeutic hypotheses derived from better-characterized conditions.

By publicly sharing our results and network resources, we aim to support hypothesis generation and translational research. More broadly, this work demonstrates how biologically grounded agentic AI can scale transcriptomic analysis while enabling mechanistic interpretation across complex disease landscapes.

References

1. C. for Medicare & Medicaid Services (U.S.) and N. C. for Health Statistics (U.S.), *ICD-10-CM Official Guidelines for Coding and Reporting FY 2024 – UPDATED October 1, 2023 (October 1, 2023 - September 30, 2024)*, tech. rep., Centers for Medicare & Medicaid Services (CMS) (July 2023), Published July 24, 2023.
2. A. S. Fauci, E. Braunwald, D. L. Kasper *et al.*, *Harrison's Principles of Internal Medicine* (McGraw-Hill, 2008).
3. K. I. Goh, M. E. Cusick, D. Valle *et al.*, The human disease network, *Proceedings of the National Academy of Sciences* **104**, 8685 (2007).
4. L. P. Santamaría, E. P. G. del Valle, M. Zanin *et al.*, Classifying diseases by using biological features to identify potential nosological models, *Scientific Reports* **11**, p. 21096 (2021).
5. M. Zanin, J. M. Tuñas and E. Menasalvas, Understanding diseases as increased heterogeneity: A complex network computational framework, *Journal of The Royal Society Interface* **15**, p. 20180405 (2018).
6. N. M. Ferraro *et al.*, Transcriptomic signatures across human tissues identify functional rare genetic variation, *Science* **369**, p. eaaz5900 (2020).
7. F. Q. Wang *et al.*, Unraveling transcriptomic signatures and dysregulated pathways in systemic lupus erythematosus across disease states, *Arthritis Research & Therapy* **26**, p. 99 (2024).
8. L. Shao *et al.*, T-cell transcriptomic signatures in adults with primary untreated immune thrombocytopenia segregate by age, revealing distinct druggable pathways, *Blood* **144**, p. 124 (2024).
9. Z. Poon *et al.*, Transcriptomic signature and functional abnormalities of bone marrow mesenchymal stromal cells mediate disease progression of myelodysplastic/myeloproliferative neoplasms, *Blood* **142**, p. 5618 (2023).
10. Q. Wang *et al.*, Deep learning-based brain transcriptomic signatures associated with the neuropathological and clinical severity of alzheimer's disease, *Brain Communications* **4**, p. fcab293 (2022).
11. S. C. Mendelsohn *et al.*, Transcriptomic signatures of progression to tuberculosis disease among close contacts in brazil, *The Journal of Infectious Diseases* , p. jiae237 (2024).
12. S. Chaudhuri *et al.*, Cell-specific transcriptional signatures of vascular cells in alzheimer's disease: Perspectives, pathways, and therapeutic directions, *Molecular Neurodegeneration* **20**, p. 12 (2025).
13. T. M. Pelaia, M. Shojaei and A. S. McLean, The role of transcriptomics in redefining critical illness, in *Annual Update in Intensive Care and Emergency Medicine 2023*, 2023 pp. 3–14.
14. D. B. Antcliffe *et al.*, Transcriptomic signatures in sepsis and a differential response to steroids: From the vanish randomized trial, *American Journal of Respiratory and Critical Care Medicine* **199**, 980 (2019).
15. J. Bigot *et al.*, Transcriptomic signature of the cd, *American Journal of Transplantation* **16**, 3430 (2016).
16. R. Q. Figueiredo *et al.*, Towards a global investigation of transcriptomic signatures through co-expression networks and pathway knowledge for the identification of disease mechanisms, *Nucleic Acids Research* **49**, 7939 (2021).
17. A. Jha *et al.*, Identifying common transcriptome signatures of cancer by interpreting deep learning models, *Genome Biology* **23**, p. 117 (2022).
18. J. A. Harrill *et al.*, Signature analysis of high-throughput transcriptomics screening data for mechanistic inference and chemical grouping, *Toxicological Sciences* **202**, 103 (2024).
19. M. Kim *et al.*, Refining diagnosis of renal cell carcinoma subtypes through single-cell resolution transcriptomic signatures, *Cancer Research* **84**, 3500 (2024).
20. S. Namba, M. Iwata and Y. Yamanishi, From drug repositioning to target repositioning: Predic-

tion of therapeutic targets using genetically perturbed transcriptomic signatures, *Bioinformatics* **38**, i68 (2022).
21. Z. Zhai *et al.*, Disignatlas: An atlas of human and mouse disease signatures based on bulk and single-cell transcriptomics, *Nucleic Acids Research* **52**, D1236 (2024).
22. S. Lessard *et al.*, Leveraging large-scale multi-omics evidences to identify therapeutic targets from genome-wide association studies, *BMC Genomics* **25**, p. 1111 (2024).
23. F. Wang and C. A. Barrero, Multi-omics analysis identified drug repurposing targets for chronic obstructive pulmonary disease, *International Journal of Molecular Sciences* **25**, p. 11106 (2024).
24. Anaconda, *The State of Data Science 2020: Moving from Hype Toward Maturity*, tech. rep., Anaconda, Inc. (2020).
25. R. BPC, *Navigating the Intersection of Biostatistics, Bioinformatics, and Machine Learning*, tech. rep. (2023), Publication details not fully specified.
26. D. S. Himmelstein, A. Lizee, C. Hessler, L. Brueggeman, S. L. Chen, D. Hadley, A. Green, P. Khankhanian and S. E. Baranzini, Systematic integration of biomedical knowledge prioritizes drugs for repurposing, *eLife* **6**, p. e26726 (2017).
27. J. Piñero, J. M. Ramírez-Anguita, J. Saüch-Pitarch, F. Ronzano, E. Centeno, F. Sanz and L. I. Furlong, The disgenet knowledge platform for disease genomics: 2019 update, *Nucleic Acids Research* **48**, D845 (2020).
28. H. Liu, Y. Li and H. Wang, Genomas: A multi-agent framework for scientific discovery via code-driven gene expression analysis, *arXiv preprint arXiv:2507.21035* (2025).
29. H. Liu, S. Chen, Y. Zhang *et al.*, Genotex: An llm agent benchmark for automated gene expression data analysis, *arXiv preprint arXiv:2406.15341* (2024).
30. K. Sharif, A. M. Tsur, N. Ben-Shabat *et al.*, The risk of osteoporosis in patients with ankylosing spondylitis—a large retrospective matched cohort study, *Medicina Clínica* **160**, 373 (2023).
31. J. Mei, H. Hu, H. Ding *et al.*, Investigating the causal relationship between ankylosing spondylitis and osteoporosis in the european population: A bidirectional mendelian randomization study, *Frontiers in Immunology* **14**, p. 1163258 (2023).
32. D. Zhang, J. Liu, B. Gao *et al.*, Immune mechanism of low bone mineral density caused by ankylosing spondylitis based on bioinformatics and machine learning, *Frontiers in Genetics* **13**, p. 1054035 (2022).
33. J. K. Olynyk and G. A. Ramm, Risk of liver cancer in hfe-hemochromatosis (2021).
34. A. Jayachandran, R. Shrestha, K. R. Bridle *et al.*, Association between hereditary hemochromatosis and hepatocellular carcinoma: A comprehensive review, *Hepatoma Research* **6**, N/A (2020).
35. M. Tian, Y.-Z. Cui, G.-H. Song *et al.*, Proteomic analysis identifies mmp-9, dj-1 and a1bg as overexpressed proteins in pancreatic juice from pancreatic ductal adenocarcinoma patients, *BMC Cancer* **8**, p. 241 (2008).
36. N. Piyaphanee, Q. Ma, O. Kremen *et al.*, Discovery and initial validation of α1-b glycoprotein fragmentation as a differential urinary biomarker in pediatric steroid-resistant nephrotic syndrome, *Proteomics Clinical Applications* (2011).
37. C. Fujii, S. Harumiya, Y. Sato, M. Kawakubo, H. Matoba and J. Nakayama, α1,4-linked n-acetylglucosamine suppresses gastric cancer development by inhibiting mucin-1-mediated signaling, *Cancer Science* **113**, 3852 (2022).
38. C. Sun, C. Cao, T. Zhao *et al.*, A2m inhibits inflammatory mediators of chondrocytes by blocking il-1β/nf-κb pathway, *Journal of Orthopaedic Research* **41**, 241 (2023).
39. E. Okuno, M. Tsujimoto, M. Nakamura and R. Kido, 2-aminoadipate-2-oxoglutarate aminotransferase isoenzymes in human liver: A plausible physiological role in lysine and tryptophan metabolism, *Enzyme and Protein* **47**, 136 (1993).
40. A. Hallen, J. F. Jamie and A. J. L. Cooper, Lysine metabolism in mammalian brain: An update

on the importance of recent discoveries, *Amino Acids* **45**, 1249 (2013).
41. M. M. Essa, S. Subash, N. Braidy *et al.*, Role of nad$^+$, oxidative stress, and tryptophan metabolism in autism spectrum disorders, *International Journal of Tryptophan Research* **6**, p. IJTR.S11355 (2013).
42. L. Yang, Z. Chu, M. Liu *et al.*, Amino acid metabolism in immune cells: Essential regulators of the effector functions, and promising opportunities to enhance cancer immunotherapy, *Journal of Hematology & Oncology* **16**, p. 59 (2023).
43. C. Michaudel, C. Danne, A. Agus *et al.*, Rewiring the altered tryptophan metabolism as a novel therapeutic strategy in inflammatory bowel diseases, *Gut* **72**, 1296 (2023).
44. E. O. Olufunmilayo, M. B. Gerke-Duncan and R. M. D. Holsinger, Oxidative stress and antioxidants in neurodegenerative disorders, *Antioxidants* **12**, p. 517 (2023).
45. D. Lumaquin-Yin, E. Montal, E. Johns, A. Baggiolini, T. H. Huang, Y. Ma, C. LaPlante, S. Suresh, L. Studer and R. M. White, Lipid droplets are a metabolic vulnerability in melanoma, *Nature Communications* **14**, p. 3192 (2023).
46. E. Castro-Pérez, M. Singh, S. Sadangi *et al.*, Connecting the dots: Melanoma cell of origin, tumor cell plasticity, trans-differentiation, and drug resistance, *Pigment Cell & Melanoma Research* **36**, 330 (2023).
47. P. Gaudet, N. Škunca, J. C. Hu *et al.*, Primer on the gene ontology, *Methods in Molecular Biology* **1446**, 25 (2017).
48. M. Kanehisa, The kegg database, in *In Silico Simulation of Biological Processes: Novartis Foundation Symposium 247*, (John Wiley & Sons, Ltd, Chichester, UK, 2002).
49. S. Köhler, L. Carmody, N. Vasilevsky *et al.*, Expansion of the human phenotype ontology (hpo) knowledge base and resources, *Nucleic Acids Research* **47**, D1018 (2019).
50. U. Raudvere, L. Kolberg, I. Kuzmin *et al.*, g:profiler: A web server for functional enrichment analysis and conversions of gene lists (2019 update), *Nucleic Acids Research* **47**, W191 (2019).

A random-walk-based learning framework to uncover novel gene candidates for Alzheimer's disease therapy

Alena Orlenko*[1], Binglan Li[1], Neda Khanjani[1], Mythreye Venkatesan[1], Li Shen[2,3], Marylyn D. Ritchie[2,3,4], Zhiping Paul Wang[1], Tayo Obafemi-Ajayi[5], Jason H. Moore[1]

[1]*Department of Computational Biomedicine*
Cedars-Sinai Medical Center, Los Angeles, CA, USA

[2]*Division of Informatics, Department of Biostatistics, Epidemiology, and Informatics*
[3]*Institute for Biomedical Informatics*
[4]*Department of Genetics*
Perelman School of Medicine, University of Pennsylvania, Philadelphia, PA, USA

[5]*Engineering Program*
Missouri State University, Springfield, Missouri, USA

Identifying repurposable therapeutic targets for Alzheimer's disease (AD) remains challenging due to various clinical and biological factors. This study aimed to identify candidate genes for AD therapy. We hypothesize that gene and disease-specific network properties—learnable from these large-scale biomedical knowledge graphs—can inform implicit gene-AD connections and prioritize repurposable AD drug targets. To evaluate the hypothesis, we focused on druggable genes curated from Drug-Gene Interaction Database and Alzheimer's Knowledge Base (AlzKB). We applied scalable random walk methods to Hetionet to learn unbiased gene and disease embeddings, representative of their topological and semantic network properties. The embeddings were then used to compute gene-AD similarity and derive network-based scores for each gene. To validate the scores, using Alzheimer's Disease Sequencing Project (ADSP) data, we constructed AD classifier models with Tree-based pipeline optimizer 2 (TPOT2), an automated machine learning framework. Models were optimized for performance, model complexity, and high aggregate network-based scores. Network-based scores successfully prioritized diverse feature sets—many not previously associated with AD—that are enriched in biologically meaningful body parts such as brain, and pathways including neuronal signaling, potassium channels, and creatine metabolism. The results suggested that knowledge graphs and network-informed embeddings can capture both known and novel insights into AD mechanisms. Additionally, integrating network-based scores with feature-set-guided TPOT2 offers a scalable and biologically interpretable framework for AD drug repurposing and discovery.

Keywords: genomics; Alzheimer's disease; random walks; knowledge graph; network analysis

*This work was supported by National Institutes of Health (USA) grants U01 AG066833, P30 AG094848 and R01 LM010098.

© 2025 The Authors. Open Access chapter published by World Scientific Publishing Company and distributed under the terms of the Creative Commons Attribution Non-Commercial (CC BY-NC) 4.0 License.

1. Introduction

Therapeutic intervention for Alzheimer's disease (AD) remains a significant challenge, largely due to pronounced clinical and etiological heterogeneity as well as a limited understanding of the genetic mechanisms underlying its pathogenesis.[1–3] Over 80 genetic loci have been associated with AD, including well-known risk factors such as common gene polymorphisms in *APOE* as well as rare mutations in *APP*, *PSEN1*, and *PSEN2*.[4] Despite advances in AD genotypic characterization, these variations explain only a limited fraction of the overall disease risk and offer few actionable insights for therapeutic development.

To address this gap, computational drug discovery methods provide a cost-efficient, systematic approach to identifying novel therapeutic targets.[5,6] These include methods such as computational molecular docking, pathway or network mapping, retrospective clinical analysis of electronic health records, and genetic associations. In addition, the utility of knowledge graphs (e.g., Hetionet,[7] PrimeKG,[8] and AlzKB[9]) can facilitate the drug discovery process by providing a framework to systematically integrate structured, relational information (e.g., gene–drug interactions) across diverse biomedical entities into disease-specific network contexts. For example, prior work identified AD therapy candidates using the AlzKB network mining of AD genes and their first neighbors, reflecting nonspecific gene-gene interactions.[10] Knowledge graphs also enable the inference of indirect relationships among domain-specific entities, such as predicting latent associations between drugs and diseases. Drug repurposing is sometimes modeled as a link prediction task in a knowledge graph to infer novel associations between drugs and diseases.[11]

The overall aim of this study is to identify novel, biologically relevant gene candidates for AD therapy by systematically leveraging insights derived from the knowledge graphs by using network learning models. We hypothesize that network properties learnable from these large-scale biomedical knowledge graphs can inform implicit gene-AD connections to prioritize repurposable, druggable gene targets. Note that druggability is based on an evidence-based interaction score derived from the Drug–Gene Interaction Database (DGIdb).[12] DGIdb is a knowledge repository built from expert curation and text mining of over 40 curated biological resources, with a specific focus on confirmed and potential drug–gene interactions.

A variety of computational approaches have been developed to exploit the topological and semantic structures of knowledge graphs for the link prediction task, including graph neural networks (GNNs),[13] random walk-based techniques (e.g., node2vec,[14] edge2vec[15]), and rotation-based embedding models (e.g., RotatE[16]). Collectively, these methods are capable of learning continuous vector representations that capture the complex relational patterns embedded within the knowledge graph. In this study, we applied random-walk-based approaches on Hetionet to learn gene and disease embeddings that could potentially encode useful topological and semantic properties. The walk-based approaches are scalable and can preserve both local connectivity and global network structural features. Given that Hetionet comprises relational information among heterogeneous biomedical entities beyond AD, extracting gene and disease embeddings from the network should mitigate biases towards AD and overfitting in downstream analysis. The learned embeddings are subsequently used to compute the similarity between a druggable gene node and the disease (AD) node. These similarities are

applied to derive network-based scores for each gene, under the hypothesis that such scores approximate the likelihood of a gene as an AD drug target by integrating network topology and biological relevance.

To evaluate the efficacy of network-based learning approaches in uncovering novel drug targets, we constructed AD predictive models informed by network-derived scores using an automated machine learning framework, Tree-based Pipeline Optimizer 2 (TPOT2). TPOT2 incorporates both multi-objective optimization and a feature set selector, enabling the model selection process to be guided by both predictive performance and the relevance of predefined feature groups. By exploring two feature sets derived from pathways and drug–gene interactions, we identified a pareto front of optimal machine learning pipelines that produced AD-relevant solutions that were high-performing and minimally complex. Enrichment analysis of the top-performing models revealed functionally diverse gene sets, highlighting promising candidates for future investigation.

2. Methods

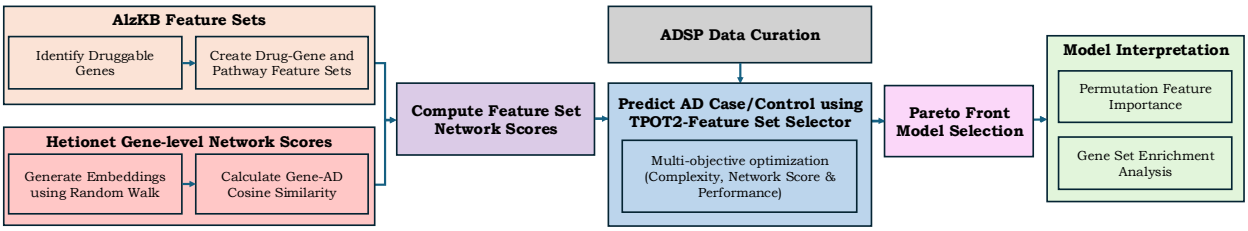

Fig. 1. Flowchart of overall study design

2.1. *Selection of druggable genes and construction of feature sets*

To identify actionable AD therapeutic targets, we restricted our analysis to druggable protein-coding genes found in AlzKB,[9] as detailed in prior work.[10] This yielded 3,612 druggable genes for downstream analysis. We constructed two biologically informed feature sets (drug–gene interaction and pathway-based) from these genes based on specific edge relationships in AlzKB.

Drug-gene sets, defined as groups of genes associated with a given drug, were obtained by extracting drug nodes from the AlzKB knowledge graph that are directly connected to druggable genes, denoting interactions. Each set consists of gene nodes that are linked to a specific drug node via defined relationships including general interactions (*chemicalbindsgene*) and specific mechanisms of drug action (*chemicaldecreasesexpression* and *chemicalincreasesexpression*). Likewise, pathway-based feature sets, defined as groups of genes associated with a given pathway, are generated by mapping druggable genes to biological pathways from AlzKB (*geneinpathway*). These pathway capture functional relationships relevant to clinical applications, particularly for AD pathology.

2.2. *Learning embeddings via random walk on Hetionet*

To learn the gene and disease embeddings from Hetionet, we applied two types of random-walk-based methods: node2vec[14] and edge2vec.[15] (Note that other types of random walk methods, such as DREAMwalk,[17] are not explored in this work as they require a diverse set of homogeneous network datasets, rather than a single heterogeneous knowledge graph.) Node2vec captures the sequence of nodes that a random walk traverses in the graph, while edge2vec includes the edge type information as well. The Hetionet network was downloaded as TSV files from the repository (https://github.com/hetio/hetionet), read into Python as a NetworkX object, and pruned to include only connected nodes. Node2vec was performed using using the $Node2Vec$ function from PyTorch Geometric while edge2vec was done based on scripts obtained from the edge2vec GitHub repository (https://github.com/RoyZhengGao/edge2vec). The extracted walk sequences were input into Word2vec to learn the continuous feature representations (embeddings). The hyperparameters used to learn the embeddings were optimized through grid search, guided by the prediction (XGBoost) performance on established gene–AD associations. The details of the optimized parameter sets are listed in the supplementary file [a] Finally, the similarity between each gene node and the derived AD embeddings was computed using the cosine similarity metric. These gene-level similarity scores ($S(G)$) were subsequently used to derive the feature set network scores.

2.3. *Computation of feature set network score*

The network scores for each feature set (per drug for the drug-gene sets while per pathway for the pathway sets) were computed as an aggregate of similarity-based scores for all genes within the set. There are four variations of network scores based on multiple levels of constraints on the raw similarity scores derived from the random walk step (see Section 2.2) from both individual gene and gene set levels. At the individual gene level, we imposed a constraint to penalize genes for proximity to known AD genes by discretizing $S(G)$ ($S_d(G)$) into five ordinal categories using quantile-defined thresholds (<50%, 50–75%, 75–85%, 85–95%, and >95%), corresponding to the scores -2, -1, 0, $+1$, and $+2$, respectively. An AD penalty score, $P(G)$, is mapped to each gene. $P(G)$ denotes the penalty for a gene (G) being a known AD gene (-2), a first-degree neighbor of AD gene (-1), or none of the above ($+1$). Thus $S*(G) = S_d(G) + P(G)$. At the feature set level, we imposed a constraint to exclude AD genes, i.e., all AD genes present in the feature set are excluded prior to computing the network score as an aggregate of the remaining genes. This yielded the following four setups for network scores. Let NS_i denote the network score for a feature gene set i (FS_i).

- Setup 1 (S1): NS_i is simply the average of all the raw similarity scores ($S(G)$), obtained from the random walk step, of the genes in set i. $NS_i^1 = avg(S(G))\ \forall G \in FS_i$. This served as the baseline experiment, as no constraints were imposed.
- Setup 2 (S2) adds a biological constraint by introducing penalties for proximity to known AD genes. $NS_i^2 = \sum_G S_d(G) + P(G)\ \forall G \in FS_i$.

[a]Supplementary information: `https://github.com/EpistasisLab/ADSP_Network_Score/`

- Setup 3 (S3) excludes AD genes from network score computation. $NS_i^3 = avg(S(G)\ \forall G \in FS_{i-\text{AD genes}}$, where $FS_{i-\text{AD genes}}$ denotes feature set i without the AD genes.
- Setup 4 (S4) assigns the strictest constraint of both AD penalty and excluding AD genes. $NS_i^4 = \sum_G S_d(G) + P(G)\ \forall G \in FS_{i-\text{AD genes}}$.

Note that the four types of aggregated network score are computed per feature set (for all drug-gene and pathway sets) per random walk type (node2vec vs. edge2vec).

2.4. *Multi-objective optimization with feature sets selector*

To assess the efficacy of using network scores with the gene feature sets, we construct AD case/control prediction models using TPOT2 with the feature selector set (FSS) module.[18,19] We configured the FSS using our predefined gene (drug-gene vs. pathway) feature sets (see Section 2.1). TPOT2 uses multi-objective optimization via the NSGA-II evolutionary algorithm[20] to balance performance (AUC) and model complexity (i.e., number of learned parameters). This generates a Pareto front, a set of solutions that are non-dominated by each other. We employed a custom objective function designed to jointly optimize three criteria: maximizing predictive performance, maximizing the feature set network score, and minimizing the complexity score [b]. This approach ensures that the selected solutions are simple, biologically relevant, and exhibit optimal model performance.

Optimal solutions were selected from the Pareto front set of solutions by applying median thresholds to each objective function component. Specifically, a solution was required to exceed the median AUC test set and median network score while remaining below the median model complexity. If no solution satisfied all three criteria, the first two thresholds (AUC and network score) were applied, and the solution with the lowest complexity among the remaining candidates was selected. Each selected solution was subsequently analyzed using permutation feature importance, knowledge graph-based network analysis, and functional gene set enrichment analysis.

2.5. *Model interpretation*

We examined the biological entities in the AlzKB that are associated with genes within a specific drug-gene or pathway set. For each gene in a given feature set, we retrieved the connected AlzKB entities, including body parts (anatomical structures) and biological pathways.

Enrichment analyses are also conducted on each drug or pathway set using hypergeometric tests to evaluate the over-representation of particular biological entities and context. For each biological entity (body parts or pathways), p-values from hypergeometric tests were corrected for multiple testing using the Benjamini-Hochberg method.

2.6. *AD data sample and curation*

This study utilized genetic data obtained from the Alzheimer's Disease Sequencing Project (ADSP), R4 v11 2023 release.[21] Data preprocessing and population stratification adjustments

[b]Supplementary information: `https://github.com/EpistasisLab/ADSP_Network_Score/`

followed the methodology in Orlenko et al.[10] Quality control was performed to exclude duplicate samples, singletons, rare variants, low-call-rate variants (missing at >1%), and poorly genotyped samples (missing at >5%). Only common variants (MAF >1%) were selected, resulting in 9,520,653 variants and 34,971 samples.

A novel propensity score matching (PSM) method was used to correct for population stratification in the ADSP dataset.[10] Principal component analysis (PCA) was performed on a subset of independent loci (MAF > 2%, Hardy-Weinberg equilibrium p > 1e-7, linkage disequilibrium $R^2 < 0.1$) to derive eight principal components. To balance Alzheimer's disease cases and controls, PSM was applied using logistic regression and k-nearest neighbor algorithms, resulting in a matched dataset of 22,560 samples. A quarter of the matched dataset was reserved for GWAS to generate gene-level risk scores (GRS). The remainder was evenly divided into training, validation, and test sets (5,640 samples each) using a multi-objective optimization method that preserved both case–control matching and the distribution of 30 significant SNPs identified from the Lancet 2023 review study[4] and additional filtering.

To compute GRS, GWAS was performed on the held-out subset using the SAIGE package,[22] which corrects for relatedness and imbalanced case-control ratios. Post-GWAS filtering involved clumping via PLINK2[23] with settings (`--clump p1`=1e-4, `p2`=1, `r2`=0.1), retaining only SNPs that met the threshold of $p \leq 0.05$. The GWAS variants were annotated using the Variant Effect Predictor),[24] and those located in the gene region or within 500 kilobases upstream were mapped to corresponding genes. Gene-level risk scores were computed using the PLINK2 `--score` function by multiplying individual genotype (0, 1, or 2) with GWAS-derived beta coefficients for each variant. These weighted values were summed per gene and normalized by the number of variants in the gene to account for gene size differences.

3. Results and Analysis

3.1. *Hetionet learned similarity scores*

The distributions of the cosine similarities between the AD disease node and the druggable gene nodes differed substantially between edge2vec and node2vec (Fig. 2). Node2vec produced a unimodal cosine similarity distribution centered around 0.08, with values ranging from –0.24 to 0.36. In contrast, edge2vec yielded a left-shifted distribution with a higher median value of 0.56 and a range from 0.10 to 0.81. These results suggest that the two embedding methods capture distinct aspects of the network structure relative to AD node proximity.

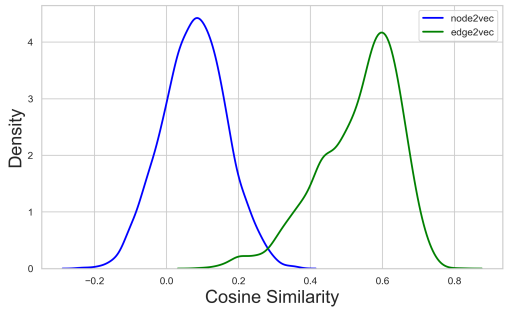

Fig. 2. Distribution of Hetionet gene similarity scores: edge2vec vs. node2vec.

3.2. *Multi-objective optimization with feature set selector identifies biologically informed AD predictive models*

The druggable gene space yielded 2,169 drug–gene feature sets and 4,233 pathway sets. The distribution of drug-gene set sizes was highly skewed, with a small number of drugs associated

with large gene sets and most drugs linked to fewer than 10 genes (Fig.3(a)) The largest set, corresponding to drug DB01254 (Dasatinib), comprised 243 genes, while the median set size was 7 genes. Pathway gene sets displayed a broader range with a median size of 9 genes and the largest set, Signal Transduction, containing 878 genes. The distribution was also skewed, indicating a prevalence of smaller pathways (Fig.3(b)).

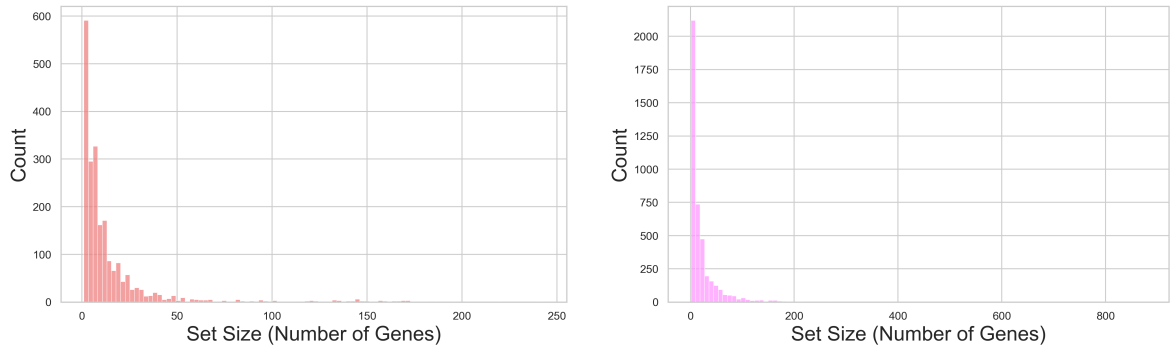

(a) Drug-gene set (b) Pathway sets

Fig. 3. Distribution of the gene feature sets' size

The distribution of the Pareto front solutions produced by TPOT2 with FSS varied greatly across all experiments (Fig.4, Table 1). The drug-gene feature set analysis based on node2vec yielded the largest number of Pareto front solutions. Its S2 experimental setup produced 98 models and 46 unique feature sets, while S3 had 97 with 54 distinct feature sets (Table 1). For edge2vec, the drug-gene feature set analysis produced fewer solutions and less unique feature sets: 55/30 (S1), 68/26 (S2), 56/39 (S3), and 43/26 (S4), but still substantially more solutions than pathway feature set analyses based on either walk methods, suggesting that biological constraints shaping drug-gene feature sets provide more flexibility in exploration of the tradeoffs among the three objectives. Drug-gene feature set analyses based on either node2vec or edge2vec prioritized feature sets containing a greater number of genes compared to pathway analyses. Notably, drug-gene feature set based on node2vec led to the best-performing models, specifically S1 (64.2%), S2 (63.9%), S3 (64.9%), and S4 (64.2%).

Pathway feature set analyses produced less complex models, likely due to smaller feature set sizes, while maintaining performance comparable to the more complex solutions. Specifically, in edge2vec S2 and node2vec S1 experiments, we observed the least complex median models. Network scores associated with Pareto front solutions from edge2vec-based pathway set analyses were notably higher than those from the corresponding drug-gene feature set setups (S2, S3, and S4); however, this trend was not observed in the node2vec experiments. Note that network scores are only directly comparable between S1 and S3, and between S2 and S4, due to differences in score computation methods across setups (see Section 2.3).

Table 1. Summary of Pareto front models for different walk methods (edge2vec and node2vec) on drug-gene and pathway feature sets across four experimental setups of network scores calculations.

Setup	# models	# unique feature sets [range size]	Complexity	Network score	Test ROC AUC (%)
Walk method: edge2vec - Drug-gene feature set analysis					
S1	55	30 [1, 221]	2.7 [1.1, 13.4]	0.6 [0.4, 0.7]	60.4 [49.7, 63.7]
S2	68	26 [1, 172]	2.7 [1.1, 13.6]	-0.3 [-2.5, 3.0]	60.8 [49.9, 64.0]
S3	56	39 [1, 198]	2.4 [1.1, 13.6]	0.6 [0.4, 0.7]	59.9 [49.9, 62.8]
S4	43	26 [1, 166]	2.6 [1.1, 12.5]	-0.1 [-2.7, 3.0]	60.5 [49.6, 63.7]
Walk method: node2vec - Drug-gene feature set analysis					
S1	95	43 [1, 180]	2.1 [1.1, 13.9]	0.2 [0.1, 0.4]	59.9 [48.7, 64.2]
S2	98	46 [1,174]	2.4 [1.1,13.6]	-0.4 [-1.7,3.0]	60.5 [50.9,63.9]
S3	97	54 [1, 217]	2.2 [1.1, 14.2]	0.1 [0.1, 0.4]	60.1 [50.8, 64.9]
S4	96	52 [1, 217]	2.2 [1.1, 14.3]	0.0 [-3.0, 3.0]	59.9 [50.5, 63.8]
Walk method: edge2vec - Pathway feature set analysis					
S1	40	22 [1, 21]	1.6 [1.1, 14.2]	0.6 [0.5, 0.7]	59.6 [50.9, 62.6]
S2	16	10 [2, 26]	1.4 [1.1, 5.2]	2.0 [-3.0, 3.0]	58.9 [51.2, 62.4]
S3	23	21 [1, 21]	1.4 [1.1, 13.2]	0.7 [0.6, 0.7]	57.9 [50.7, 62.0]
S4	20	12 [1, 10]	1.7 [1.1, 10.5]	1.6 [-2.7, 3.0]	60.5 [51.2, 62.3]
Walk method: node2vec - Pathway feature set analysis					
S1	28	14 [1, 14]	1.7 [1.1, 8.4]	0.2 [0.1, 0.4]	59.6 [50.9, 62.4]]
S2	35	15 [1, 21]	1.6 [1.1, 13.3]	-0.9 [-1.6, 2.0]	61.4 [50.7, 62.6]
S3	36	26 [1, 31]	1.9 [1.1, 13.2]	0.1 [0.1, 0.4]	60.0 [50.6, 62.0]
S4	43	25 [1, 28]	1.6 [1.1, 13.4]	0.0 [-1.3, 3.0]	59.2 [50.6, 61.8]

3.2.1. *Drug-gene and pathway feature sets optimal solutions*

For each experimental setup, no solutions satisfied all three criteria. Hence, we selected solutions that exceeded the median thresholds for both performance and network scores. The results of permutation feature importance (PFI) analysis on the selected solutions are presented in Fig.5. For the drug-gene feature sets results (Fig.5(a)), specifically for edge2vec, the optimal solution converged on the same drug–gene set for 3 of the 4 experimental setups: DB06637 (Dalfampridine). Dalfampridine is a potassium channel blocker consisting of 40 genes predominantly voltage-gated potassium channel genes (*KCN*) and one solute carrier transporter (*SLC22A2*) (Fig.5(a)). All three models reported an AUC of 61% but displayed variability in the PFI rankings as well as a small mean decrease in accuracy. This implies that, while no gene had a strong main effect, there could exist some interactions among the genes. For the S3 experiment, the optimal solution was the DB00128 (Aspartic acid) feature set. This drug is a non-essential amino acid commonly used in amino acid supplementation therapies. The feature set included 8 genes with diverse functional affiliations. The DB00128 model had an AUC of 61%, but its PFI analysis did not reveal any strong contributions from individual genes.

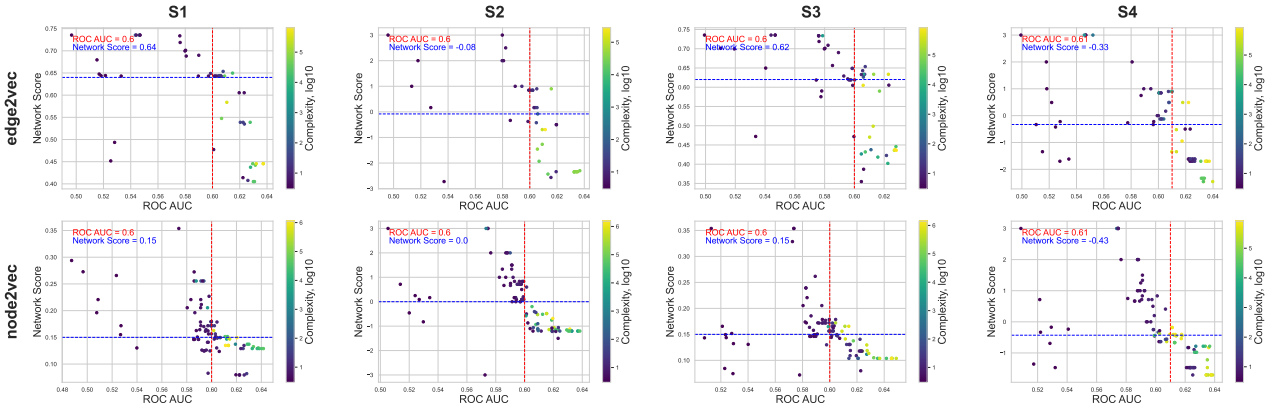

(a) Drug-gene feature set

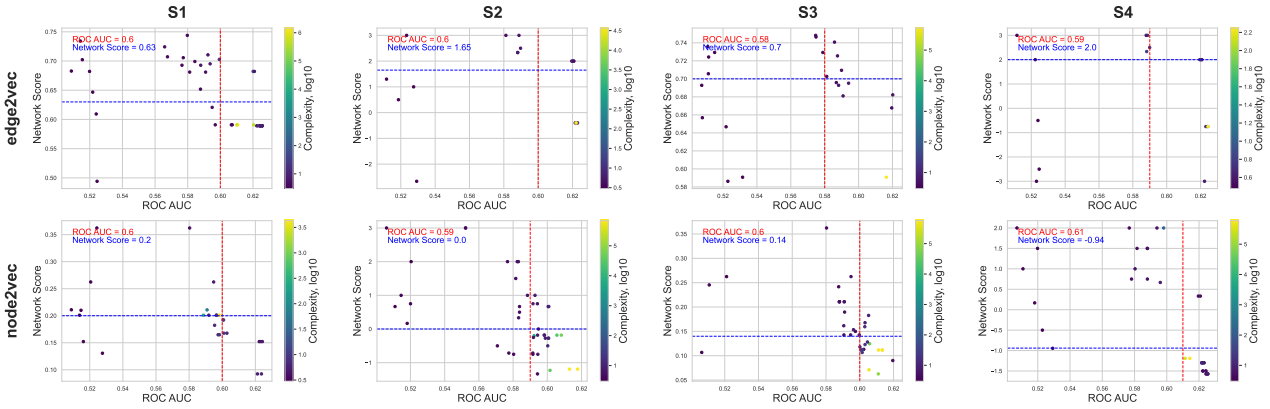

(b) Pathway feature set

Fig. 4. TPOT2 Pareto front solutions for drug-gene and pathway feature sets experiments

For node2vec, all four experimental setups identified an optimal solution. The best models were DB00832 (Phensuximide), DB00368 (Norepinephrine), DB00578 (Carbenicillin), and DB00964 (Apraclonidine) for S1, S2, S3, and S4, respectively. Their predictive performances were comparable. The drug-gene feature set sizes ranged from 6 to 22, with diverse functionality. The drugs also varied in their known functions. Phensuximide is an anticonvulsant medication used to treat absence seizures. Norepinephrine is a blood pressure medication, while Carbenicillin is an antibiotic drug. Apraclonidine is an adrenergic agonist used to treat raised intraocular pressure.

For edge2vec-based pathway feature sets (Fig. 5(b)), both S1 and S2 (top row) identified models with the Creatine Metabolism pathway as the optimal solution (AUC of 62%). This pathway consisted of three druggable genes: *CKM* (Creatine Kinase, Muscle), *GATM* (Glycine Amidinotransferase), and *SLC6A12* (Solute Carrier Family 6 Member). Notably, *CKM* exhibited a strong main effect in both models, with PFI coefficients of 0.09 and 0.12 mean decrease in AUC, respectively. In experiment S3, the Glycosaminoglycan Biosynthesis pathway was identified as the optimal solution (AUC=59%). This pathway has only one druggable gene, *XYLT2*. Best solution for S4 was Creatine-Phosphate Biosynthesis pathway (AUC=62%) and only included *CKM* gene (which was also key for S1 and S2 models).

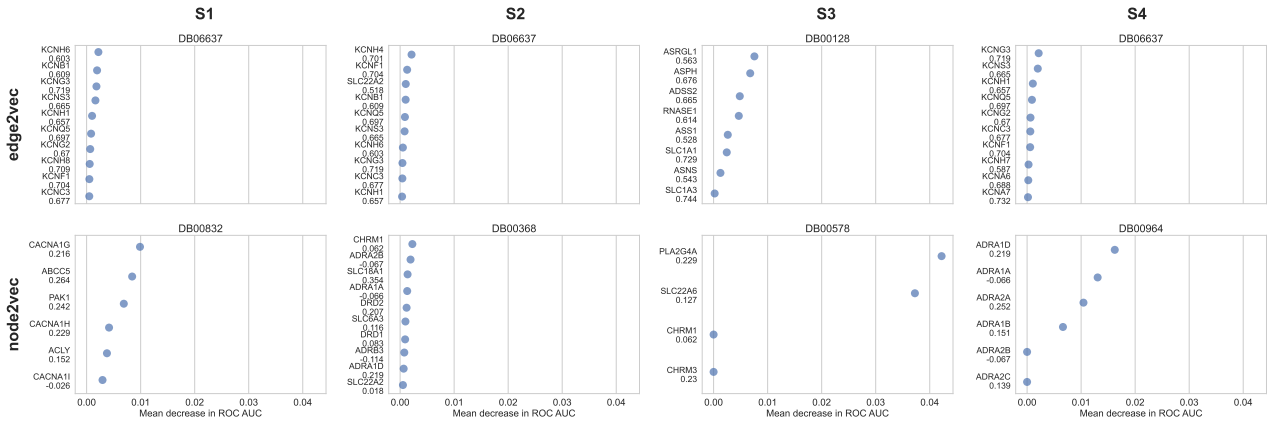

(a) Drug-gene feature set

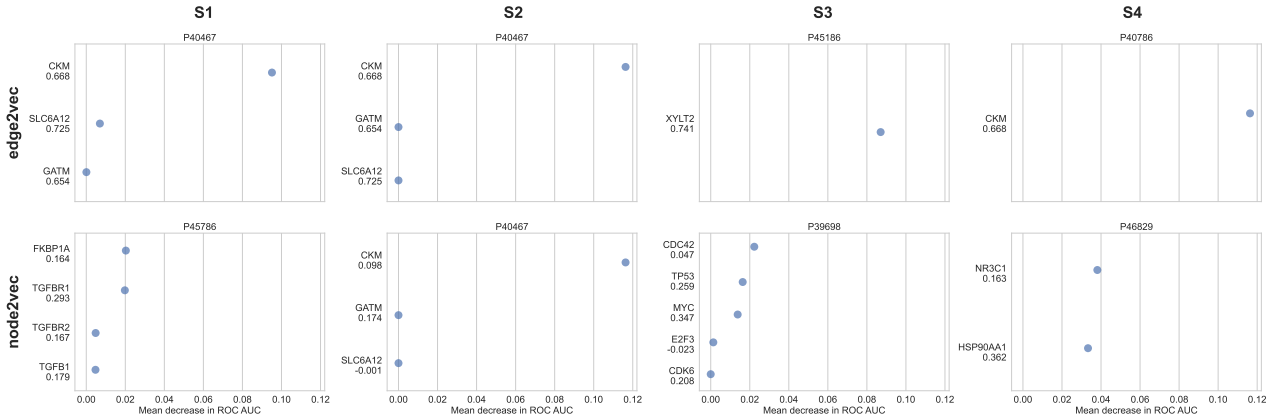

(b) Pathway feature set

Fig. 5. PFI for drug-gene and pathway feature sets optimal solution. Individual gene network scores are shown below each gene name.

For node2vec-based pathway set results, four distinct pathways were obtained per setup. Similar to edge2vec results, the Creatine Metabolism pathway was also identified as the optimal solution for S2 (AUC=62%). This model also indicates a strong individual contribution from *CKM* gene. For S1, the best solution was TGF-beta Receptor 1 (*TGFBR1*) Loss-of-Function pathway (AUC=60%). It includes 4 genes, primarily TGF-beta receptors. S3 best solution was the Metastatic Brain Tumor Process with a five-gene set: *E2F3*, *MYC*, *CDC42*, *CDK6*, and *TP53*, and AUC=60%. S4 yielded an optimal solution of Prednisolone Metabolism Pathway (AUC=60%) containing two genes, *HSP90AA1* and *NR3C1*.

3.3. *Functional analysis of drug-gene and pathway feature set models*

The gene set enrichment analysis results on the optimal set of solutions for the drug-gene feature sets are presented in Table 2. Multiple drug–gene sets were significantly enriched in genes associated with specific body parts and biological pathways. For edge2vec, the Dalfampridine gene set was enriched for brain-associated genes as well as pathways related to the neuronal system, voltage-gated and potassium channels (Table 2). The NADH-associated gene sets from S3 and S4 were enriched for blood- and heart-associated genes, along with key metabolic

Table 2. Enrichment analysis for drug-gene feature sets

Setup	Drug name	Size	AUC	Comp.	Body parts	Pathways
Enrichment analysis for edge2vec						
S1	Dalfampridine	40	60.8	1.63	Brain (27)*	Neuronal System (40), Voltage gated Potassium channels (39), Potassium Channels (39)*
S1	Amifampridine	42	61.5	4.24		Neuronal System (40), Voltage gated Potassium channels (39), Potassium Channels (39)*
S2	Guanidine	49	60.8	1.72		Neuronal System (43), Voltage gated Potassium channels (39), Potassium Channels (39)*
S2	Dalfampridine	40	61.0	1.46	Brain (27)*	Neuronal System (40), Voltage gated Potassium channels (39), Potassium Channels (39)*
S3	Pyridoxal phosphate	18	60.6	1.21		Metabolic pathways (17)*
S3	Aspartic acid	8	60.5	1.04		Alanine, aspartate and glutamate metabolism (4)*
S3	NADH	87	60.6	1.95	Blood (67), Heart (63)*	Metabolic pathways (81)*
S3	Guanidine	49	60.7	1.70		Neuronal System (43), Voltage gated Potassium channels (39), Potassium Channels (39)*
S3	Dalfampridine	40	60.7	1.43	Brain (27)*	Neuronal System (40), Voltage gated Potassium channels (39), Potassium Channels (39) *
S4	Pyridoxal phosphate	18	60.5	1.32		Metabolic pathways (17)*
S4	NADH	87	60.6	1.95	Blood (67), Heart (63)*	Metabolic pathways (81)*
S4	Dalfampridine	40	60.5	1.26	Brain (27)*	Neuronal System (40), Voltage gated Potassium channels (39), Potassium Channels (39)*
Enrichment analysis for node2vec						
S1	Vindesine	22	59.9	1.11		p53 signaling pathway (5)*
S1	Carbinoxamine	12	60.2	5.75		GnRH signaling pathway (4)*
S1	Phensuximide	6	60.0	0.95		Axon guidance (4)*
S1	Thioproperazine	7	60.4	1.00		
S1	Flubendazole	15	60.0	1.00	Endometrium (11)*	Imipramine Action Pathway (6)*
S2	Clotrimazole	67	61.2	4.67		Signal Transduction (35)*
S2	Clozapine	62	61.8	5.92	Brain (38)*	
S2	Norepinephrine	22	60.7	0.98		Monoamine GPCRs (12)*
S2	Haloprogin	33	61.1	5.77		Signal Transduction (16)*
S2	Dopamine	32	61.0	5.77		Signal Transduction (15)*
S3	Flunisolide	32	60.3	0.85	Adrenal cortex (19)*	Nuclear Receptors Meta-Pathway (8)*
S3	Vindesine	22	60.2	1.40		p53 signaling pathway (5)*
S3	Nitrofural	10	60.4	5.50		Neuroactive ligand-receptor interaction (38)*
S3	Carbenicillin	4	60.3	0.70		Signaling by GPCR (3)*
S3	Cefixime	18	60.9	5.75		Proton/oligonucleotide cotransporters (2)*
S3	Clobetasol propionate	35	60.5	1.19	Adrenal cortex (19)*	Nuclear Receptors Meta-Pathway (8)*
S3	Moclobemide	18	61.1	5.50		Integrated Pancreatic Cancer Pathway (4)*
S3	Thioproperazine	7	60.4	1.00		
S3	Flubendazole	15	60.2	0.78	Endometrium (11)*	Imipramine Action Pathway (6)*
S3	Brigatinib	14	60.2	1.20		Pathways in cancer (6)*
S4	Pseudoephedrine	11	59.9	1.04		Signal Transduction (7)*
S4	Apraclonidine	6	59.9	0.85		GPCR downstream signaling (6)*
S4	Lisdexamfetamine	5	59.9	0.90		SLC-mediated transmembrane transport (4)*
S4	Dextroamphetamine	10	60.1	1.11		Imipramine Action Pathway (5)*

* *FDR correction < 0.05 for body parts and pathways.*

pathways. Similarly, the Guanidine models (S2 and S3) and the Amifampridine model (S1) showed enrichment for neuronal system components and ion channel activity. For the node2vec results, the Clozapine model from S2 showed significant enrichment for brain-related genes. Several models, across all network score types, were enriched for signaling pathways. This included Vindesine (S1, S3), Carbinoxamine (S1), Clotrimazole, Haloprogin, and Dopamine (S2), Carbenicillin (S3), and both Pseudoephedrine and Apraclonidine (S4).

Pathway gene sets for both edge2ve and node2vec were not enriched for any body part-

associated genes. Most of the pathways feature sets were enriched with genes associated with the same pathway or a similar process (see supplementary file [c]). Creatinine metabolism and related pathways, which included the *CKM* gene, were presented across multiple setups in both edge2vec and node2vec results.

4. Discussion and Conclusion

This study presents a random-walk-based learning framework that identifies potential novel gene candidates for Alzheimer's disease therapeutics. Beginning with the heterogeneous knowledge graph Hetionet, we learned embeddings for druggable gene nodes and the AD node using two random walk methods, edge2vec and node2vec. The embeddings learned from edge2vec and node2vec captured different structural aspects of the network. Gene–AD similarities were quantified using the cosine similarity metric. The cosine similarity between the gene and AD embeddings provided a relative ranking of genes and served as the basis for computing the network scores to prioritize genes relevant to AD. We introduced four variants of the network score calculations that reflected varying levels of constraints (AD gene proximity penalty and/or exclusion of AD genes from sets). This resulted in four experimental setups (S1, S2, S3, and S4), with S1 being the least constrained one.

To validate the utility of these learned network scores in identifying novel drug targets, we constructed AD predictive models using ADSP genetic data. We employed TPOT2 with three objectives (predictive performance, complexity, and network scores) and FSS to explore the optimal solutions for both drug-gene interaction and pathway-gene feature sets.

TPOT2 identified multiple non-dominated (Pareto front) models for each experimental setup (Table1, Fig.4). Overall, experiments on drug-gene feature sets yielded more Pareto-optimal solutions and tended to produce more complex models, reflecting the use of larger gene sets. These experiments also included the higher-performing models (based on the AUC metric) across all setups. In contrast, experiments on pathway feature sets produced simpler models, likely as a result of smaller gene sets, yet achieved comparable predictive performance.

The optimal solutions across experiments demonstrated the diversity of feature sets enabled by network score gene differentiation (Fig.5). Optimal solution convergence was observed predominantly in drug-gene feature set edge2vec analyses for Dalfampridine, a potassium channel blocker. This feature set was primarily composed of voltage-gated potassium channel genes, which play critical roles in regulating diverse physiological and pathophysiological processes. These channels have been previously proposed as therapeutic targets for several conditions, including atrial fibrillation, epilepsy, neuropathic pain, and potentially neuropsychiatric disorders.[25] For node2vec-based drug-gene feature set analyses, the optimal solutions varied across setups. Notably, the S1 experiment identified the Phensuximide drug-gene feature set, consisting of six genes, including voltage-gated calcium channels. These channels play a critical role in nervous system function at both cellular and network levels and have been proposed as therapeutic targets for conditions such as Parkinson's disease, drug addiction, pain, anxiety, and epilepsy.[26] Pathway feature set analyses all found *CKM* (Creatine Kinase M-type) as the

[c]Supplementary information: `https://github.com/EpistasisLab/ADSP_Network_Score/`

most informative contributor to the optimal model for the creatine metabolism pathway. Notably, this gene alone was sufficient to predict AD with a 62% AUC, as reported in the Pareto front for the S4 edge2vec pathway feature set analyses. *CKM* isoenzymes are central to energy transduction in tissues with high and fluctuating energy demands, including skeletal muscle, heart, and brain. Although *CKM* has not been previously reported as a direct therapeutic target, it has been suggested as a biomarker of therapeutic effects in similar neurodegenerative Parkinson's disease.[27]

Gene set enrichment analysis revealed that several near-optimal solutions were significantly enriched for genes related to neurological functions. In the edge2vec drug-gene feature set analysis, the Dalfampridine gene set, selected across all experimental setups, was enriched for brain-associated genes and pathways related to the neuronal system and potassium channel activity (Table 2). Other edge2vec drug-gene feature sets (Amifampridine, Guanidine) and node2vec drug-gene feature sets (Clozapine and Lisdexamfetamine) were also linked to neuronal processes.

Both random-walk methods had comparable performance in terms of AUC (see Table 1), although node2vec[14] was computationally more efficient. However, edge2vec[15] retains edge types (relationships) between biomedical entities, such as drugs that upregulate versus downregulate gene expression levels, which provides an additional advantage in potentially capturing biologically meaningful results. This is reflected in the larger spectrum of results identified by node2vec compared to edge2vec which was fewer but more consistent (see Table 2). A limitation of this study is that we did not explore graph-based methods beyond node2vec and edge2vec due to computational and scalability constraints. Future work could examine other approaches capable of learning meaningful embeddings for nodes in a biomedical knowledge graph, such as GNNs[28,29] and representation learning models (e.g., RotateE,[30] TransE[31]). In addition, we did not examine alternative features commonly used in drug target discovery, such as molecular structure embeddings for drugs, which are more suitable for GNNs or representation learning methods.

Overall, the results demonstrate that the proposed random-walk-based learning method, integrated with an informed machine learning approach powered by TPOT, successfully identified functionally diverse gene sets. The achieved predictive performance is comparable to that of established AD risk factors,[10] underscoring its potential for the discovery of novel genetic candidates. This approach is generalizable to other diseases where structured knowledge graphs are available to guide drug repurposing efforts. Ultimately, we aim to develop a system that automatically learns meaningful semantic representations from heterogeneous knowledge graphs to profile AD patients and prioritize druggable gene candidates. Future work will explore alternative embedding methods and integrate additional biologically relevant features.

Acknowledgements

Data for this study were prepared, archived, and distributed by the National Institute on Aging Alzheimer's Disease Data Storage Site (NIAGADS) at the University of Pennsylvania (U24-AG041689), funded by the National Institute on Aging.

References

1. J. Cummings, T. Morstorf and K. Zhong, Alzheimer's disease drug-development pipeline: few candidates, frequent failures. alzheimers res ther. 2014; 6 (4): 37.
2. S. Mukhopadhyay and D. Banerjee, A primer on the evolution of aducanumab: the first antibody approved for treatment of alzheimer's disease, *Journal of Alzheimer's Disease* **83**, 1537 (2021).
3. C. H. Van Dyck, C. J. Swanson, P. Aisen, R. J. Bateman, C. Chen, M. Gee, M. Kanekiyo, D. Li, L. Reyderman, S. Cohen *et al.*, Lecanemab in early alzheimer's disease, *New England Journal of Medicine* **388**, 9 (2023).
4. S. J. Andrews, A. E. Renton, B. Fulton-Howard, A. Podlesny-Drabiniok, E. Marcora and A. M. Goate, The complex genetic architecture of alzheimer's disease: novel insights and future directions, *EBioMedicine* **90** (2023).
5. S. Pushpakom, F. Iorio, P. A. Eyers, K. J. Escott, S. Hopper, A. Wells, A. Doig, T. Guilliams, J. Latimer, C. McNamee *et al.*, Drug repurposing: progress, challenges and recommendations, *Nature reviews Drug discovery* **18**, 41 (2019).
6. R. Gupta, D. Srivastava, M. Sahu, S. Tiwari, R. K. Ambasta and P. Kumar, Artificial intelligence to deep learning: machine intelligence approach for drug discovery, *Molecular diversity* **25**, 1315 (2021).
7. D. S. Himmelstein, A. Lizee, C. Hessler, L. Brueggeman, S. L. Chen, D. Hadley, A. Green, P. Khankhanian and S. E. Baranzini, Systematic integration of biomedical knowledge prioritizes drugs for repurposing, *Elife* **6**, p. e26726 (2017).
8. P. Chandak, K. Huang and M. Zitnik, Building a knowledge graph to enable precision medicine, *Scientific Data* **10**, p. 67 (2023).
9. J. D. Romano, V. Truong, R. Kumar, M. Venkatesan, B. E. Graham, Y. Hao, N. Matsumoto, X. Li, Z. Wang, M. D. Ritchie *et al.*, The Alzheimer's Knowledge Base: A Knowledge Graph for Alzheimer Disease Research, *Journal of Medical Internet Research* **26**, p. e46777 (2024).
10. A. Orlenko, M. Venkatesan, L. Shen, M. D. Ritchie, Z. P. Wang, T. Obafemi-Ajayi and J. H. Moore, Biologically enhanced machine learning model to uncover novel gene-drug targets for alzheimer's disease, in *Biocomputing 2025: Proceedings of the Pacific Symposium*, 2024.
11. D. Bang, S. Lim, S. Lee and S. Kim, Biomedical knowledge graph learning for drug repurposing by extending guilt-by-association to multiple layers, *Nature Communications* **14**, p. 3570 (June 2023).
12. M. Cannon, J. Stevenson, K. Stahl, R. Basu, A. Coffman, S. Kiwala, J. F. McMichael, K. Kuzma, D. Morrissey, K. Cotto *et al.*, DGIdb 5.0: rebuilding the drug–gene interaction database for precision medicine and drug discovery platforms, *Nucleic acids research* **52**, D1227 (2024).
13. L. Wu, P. Cui, J. Pei, L. Zhao and X. Guo, Graph neural networks: foundation, frontiers and applications, in *Proceedings of the 28th ACM SIGKDD conference on knowledge discovery and data mining*, 2022.
14. A. Grover and J. Leskovec, node2vec: Scalable feature learning for networks, in *Proceedings of the 22nd ACM SIGKDD international conference on Knowledge discovery and data mining*, 2016.
15. Z. Gao, G. Fu, C. Ouyang, S. Tsutsui, X. Liu, J. Yang, C. Gessner, B. Foote, D. Wild, Y. Ding *et al.*, edge2vec: Representation learning using edge semantics for biomedical knowledge discovery, *BMC bioinformatics* **20**, p. 306 (2019).
16. Z. Sun, Z.-H. Deng, J.-Y. Nie and J. Tang, Rotate: Knowledge graph embedding by relational rotation in complex space, *arXiv preprint arXiv:1902.10197* (2019).
17. D. Bang, S. Lim, S. Lee and S. Kim, Biomedical knowledge graph learning for drug repurposing by extending guilt-by-association to multiple layers, *Nature Communications* **14**, p. 3570 (June 2023).
18. P. Ribeiro, A. Saini, J. Moran, N. Matsumoto, H. Choi, M. Hernandez and J. H. Moore, TPOT2:

A New Graph-Based Implementation of the Tree-Based Pipeline Optimization Tool for Automated Machine Learning, in *Genetic Programming Theory and Practice XX*, (Springer, 2024) pp. 1–17.
19. T. T. Le, W. Fu and J. H. Moore, Scaling tree-based automated machine learning to biomedical big data with a feature set selector, *Bioinformatics* **36**, 250 (2020).
20. K. Deb, A. Pratap, S. Agarwal and T. Meyarivan, A fast and elitist multiobjective genetic algorithm: Nsga-ii, *IEEE transactions on evolutionary computation* **6**, 182 (2002).
21. Y. Y. Leung, W.-P. Lee, A. B. Kuzma, P. Gangadharan, H. I. Nicaretta, L. Qu, Y. Ren, L. B. Cantwell, O. Valladares, Y. Zhao *et al.*, Adsp whole genome sequencing (wgs) release 4 data update from genome center for alzheimer's disease, *Alzheimer's & Dementia* **19**, p. e077351 (2023).
22. W. Zhou, J. B. Nielsen, L. G. Fritsche, R. Dey, M. E. Gabrielsen, B. N. Wolford, J. LeFaive, P. VandeHaar, S. A. Gagliano, A. Gifford *et al.*, Efficiently controlling for case-control imbalance and sample relatedness in large-scale genetic association studies, *Nature genetics* **50**, 1335 (2018).
23. C. C. Chang, C. C. Chow, L. C. Tellier, S. Vattikuti, S. M. Purcell and J. J. Lee, Second-generation plink: rising to the challenge of larger and richer datasets, *Gigascience* **4**, s13742 (2015).
24. W. McLaren, L. Gil, S. E. Hunt, H. S. Riat, G. R. Ritchie, A. Thormann, P. Flicek and F. Cunningham, The ensembl variant effect predictor, *Genome biology* **17**, p. 122 (2016).
25. H. Wulff, N. A. Castle and L. A. Pardo, Voltage-gated potassium channels as therapeutic targets, *Nature reviews Drug discovery* **8**, 982 (2009).
26. G. W. Zamponi, Targeting voltage-gated calcium channels in neurological and psychiatric diseases, *Nature reviews Drug discovery* **15**, 19 (2016).
27. Y. Gong, S. Qian, D. Chen, M. Ye, J. Wu and Y.-l. Wang, Serum blmh and ckm as potential biomarkers for predicting therapeutic effects of deep brain stimulation in parkinson's disease: a proteomics study, *Journal of Integrative Neuroscience* **22**, p. 163 (2023).
28. M. Schlichtkrull, T. N. Kipf, P. Bloem, R. van den Berg, I. Titov and M. Welling, Modeling Relational Data with Graph Convolutional Networks, in *The Semantic Web*, eds. A. Gangemi, R. Navigli, M.-E. Vidal, P. Hitzler, R. Troncy, L. Hollink, A. Tordai and M. Alam (Springer International Publishing, Cham, 2018).
29. Z. Hu, Y. Dong, K. Wang and Y. Sun, Heterogeneous Graph Transformer, in *Proceedings of The Web Conference 2020*, WWW '20 (Association for Computing Machinery, New York, NY, USA, April 2020).
30. Z. Sun, Z.-H. Deng, J.-Y. Nie and J. Tang, RotatE: Knowledge Graph Embedding by Relational Rotation in Complex Space, in *International Conference on Learning Representations*, September 2018.
31. A. Bordes, N. Usunier, A. Garcia-Duran, J. Weston and O. Yakhnenko, Translating embeddings for modeling multi-relational data, in *Advances in Neural Information Processing Systems*, eds. C. Burges, L. Bottou, M. Welling, Z. Ghahramani and K. Weinberger (Curran Associates, Inc., 2013).

DRIVE-KG: Enhancing variant-phenotype association discovery in understudied complex diseases using heterogeneous knowledge graphs

Ananya Rajagopalan[1], Tram Anh Nguyen[1], Lindsay A. Guare[1], Andre Luis Garao Rico[2], Rasika Venkatesh[1], Lannawill Caruth[3], Regeneron Genetics Center[8], Penn Medicine BioBank[4], Anurag Verma[5], Marylyn D. Ritchie[6,7], Molly A. Hall[2],

Joseph D. Romano[7†*], Shefali Setia-Verma[3‡*]

[1]*Genomics and Computational Biology Graduate Program,* [2]*Department of Genetics,* [3]*Department of Pathology and Laboratory Medicine,* [4]*Penn Medicine Biobank,* [5]*Department of Medicine,* [6]*Department of Genetics, Division of Informatics,* [7]*Department of Biostatistics, Epidemiology and Informatics, University of Pennsylvania, Philadelphia, PA, USA*

[8]*777 Old Saw Mill River Rd, Tarrytown, NY 10591, USA*

E-mails: †*joseph.romano@pennmedicine.upenn.edu,* ‡*shefali.setiaverma@pennmedicine.upenn.edu*

**co-corresponding authors*

Multi-omics data are instrumental in obtaining a comprehensive picture of complex biological systems. This is particularly useful for women's health conditions such as endometriosis, which has been historically understudied despite having a high prevalence (around 10% of women of reproductive age). Subsequently, endometriosis has limited genetic characterization: current genome-wide association studies explain only 11% of its 47% total estimated heritability, underscoring the need for integrative approaches. Graph representations provide an intuitive and meaningful way to harmonize biological data, using nodes to represent biological concepts (e.g., genes, single nucleotide polymorphisms, proteins, and phenotypes) and edges to represent their relationships. We present DRIVE-KG (Disease Risk Inference and Variant Exploration Knowledge Graph), which uses a heterogeneous graph representation to integrate data from diverse multi-omics datasets. We trained two distinct models using DRIVE-KG: a link prediction model to suggest associations between SNPs and two pilot phenotypes (endometriosis and obesity), and a graph convolutional network (GCN) for patient-level classification of endometriosis/adenomyosis as a combined phenotype. We conducted patient-level classification using data from 1,441 Penn Medicine BioBank participants with gold standard chart-reviewed endometriosis/adenomyosis status. The link prediction model uncovered 66 high-confidence (model score ≥ 0.95) candidate SNP-endometriosis associations, representing largely distinct genetic signals ($R^2 < 0.1$). These variants were enriched for obesity/body mass index traits (24.2%), lipid metabolism (6%), and depressive disorders (4.5%), showing agreement with emerging hypotheses about endometriosis etiology. In contrast, of the high-confidence, candidate SNP–obesity associations that could be evaluated using LDlink, 38.22% were in high linkage disequilibrium ($R^2 \geq 0.8$) with known obesity or comorbidity associations. The GCN to classify patient endometriosis/adenomyosis status had an F1 score of 0.752 compared to 0.698 for a genetic risk score. Despite this moderate improvement, we found that the GCN learned meaningful stratification of underlying adenomyosis signal and severe endometriosis grades. Together, these results demonstrate that heterogeneous integration of multi-omics data is valuable for diverse downstream tasks—including discovery and clinical prediction—particularly for understudied diseases where traditional genomic approaches are insufficient.

Keywords: Multi-Omics; Knowledge Graph; Women's Health; Endometriosis; Complex Diseases; Variant Discovery

© 2025 The Authors. Open Access chapter published by World Scientific Publishing Company and distributed under the terms of the Creative Commons Attribution Non-Commercial (CC BY-NC) 4.0 License.

1. Introduction

Multi-omics data integration involves combining diverse biological data types (including genomic, proteomic, epigenomic, and metabolomic data) to provide comprehensive insights into the mechanisms of diseases.[1] This approach is particularly useful for uncovering complex molecular interactions and biological pathways that remain hidden when analyzing individual data types in isolation, and leads to a more complete understanding of disease etiology and progression.[2] Despite this potential, significant computational challenges exist with multi-omics data integration. The high-dimensional, heterogeneous, and sparse nature of multi-omics data creates substantial barriers in developing analysis methods that are both biologically interpretable and computationally efficient.[3] These integration challenges highlight the need for analytical frameworks that can effectively represent the inherently complex relationships in multi-omics data.

Knowledge graphs have emerged as a promising solution to address these multi-omics integration challenges. By representing biological entities as nodes and the known relationships that exist between them as edges, knowledge graphs provide a framework that can capture the complex, interconnected nature of biological systems across data modalities.[3] Graph-based approaches are particularly well-suited for large-scale, multi-omics data because they can naturally accommodate heterogeneous data types while preserving their semantic relationships and biological context. For multi-omics integration, a heterogeneous knowledge graph representation offers particular advantages.[4] Unlike homogeneous graphs where all nodes and edges represent the same type of entity or relationship, heterogeneous knowledge graphs can simultaneously represent multiple entity types (e.g., genes, proteins, metabolites) and diverse relationship types (e.g., regulatory interactions, protein-protein interactions, metabolic pathways) within a single structure.[3] Another advantage of knowledge graph-based approaches for multi-omics integration is that they do not require data from the same individuals across different -omics layers. Instead, these methods can leverage population-level patterns and biological knowledge to create comprehensive representations that integrate information from disparate studies and cohorts. Existing biological knowledge encoded in the graph structure can then be leveraged via network analyses for a variety of purposes: making use of existing relationships in the graph to predict new connections, or for downstream tasks such as patient-level classification.

For many well-characterized complex diseases like obesity, extensive genetic studies have successfully explained a substantial proportion of disease heritability. Furthermore, polygenic risk scores (PRS) demonstrate strong predictive performance; for obesity, typical AUC values for PRS are around 0.8.[5] These genetic studies are enabled by large-scale biobanks (e.g., UK Biobank,[6] Penn Medicine BioBank,[7] and All of Us[8]) which are collections of de-identified genetic, lifestyle, clinical and biological data. In contrast, endometriosis—one of many complex gynecological conditions—affects approximately 10% of reproductive age women yet remains

severely understudied and underfunded.[9] Endometriosis is characterized by the presence of endometrial-like tissue outside the uterus and can cause chronic pain symptoms along with comorbidities including infertility.[10] Due to its underdiagnosis, traditional genomic approaches fall short as there is a much lower prevalence observed in biobanks. Despite a broad sense heritability estimation from a twin study of 47%,[11] variants identified through GWAS studies of endometriosis to-date ($N = 928,413$; $n_{cases} = 44,125$)[12] have only been able to explain roughly 11% of this heritability, and the predictive accuracy of genetic risk scores have been inconsistent as a result.[13] The ability of knowledge graph methods to integrate information across disparate studies and populations, without requiring matched individual-level data, makes them especially suited to address these gaps. While previous studies have applied graph representations to integrate multi-omics data for disease discovery[14] and prediction,[15] we are not aware of effective applications of these methods to complex and understudied conditions such as those in women's health. By leveraging existing multi-omics data from independent studies and incorporating established biological relationships contributing to disease, these approaches can potentially uncover disease mechanisms and improve predictive models for conditions where traditional large-scale genomic studies have been insufficient.

This study presents an innovative framework for integrating multi-omics data about disease associations through a heterogeneous knowledge graph representation. We hypothesize that by systematically incorporating knowledge from diverse -omics data sources within a unified graph structure, we can identify previously hidden candidate relationships that are both biologically meaningful and mechanistically relevant to disease pathogenesis. Combining large-scale biological data in this way will improve our ability to discover meaningful and interpretable insights about disease pathogenesis. This is particularly impactful for historically understudied women's health conditions where traditional genomic methods have not fully captured the complexity of disease etiology.

2. Methods

2.1. *Knowledge Graph Data Sources*

To construct a heterogeneous knowledge graph (KG), we integrated multiple biological data sources (node and edge types summarized in Table 1). The graph is comprised of four primary node types: single nucleotide polymorphisms (SNPs), genes, proteins, and phenotypes.

2.1.1. *Node Data Sources*

We derived SNP nodes from the Single Nucleotide Polymorphism Database (dbSNP).[16] To avoid node type imbalance caused by including tens of millions of variants, we included only SNPs with minor allele frequency (MAF) ≥ 0.01 in the Penn Medicine BioBank (PMBB). We obtained phenotype nodes from the Human Phenotype Ontology (HPO),[17] which contains standardized disease and trait terminology. We sourced gene information from the National Center for Biotechnology Information (NCBI) gene database,[18] and derived protein nodes from the Universal Protein Resource (UniProt).[19]

2.1.2. *Edge Data Sources*

We incorporated five distinct edge types connecting the four biological entities (SNP, gene, phenotype, and protein) into the KG. We established SNP-to-gene associations using expression quantitative trait loci (eQTL) data from version 8 of the Genotype-Tissue Expression (GTEx) project.[20] We derived SNP-to-phenotype relationships from Open Targets,[21] which aggregates evidence from genome-wide association studies (GWAS) and other sources. We obtained gene-to-phenotype associations from PheWAS (phenome-wide association study) summary statistics, published from OmicsPred.[22] We established SNP-to-protein connections through OmicsPred, and sourced gene-to-protein relationships from UniProt annotations.[19]

Table 1. Knowledge Graph Data Sources

Graph Concept	Data Source	Features
Node: SNP	dbSNP[16]	Bulk RefSNP JSON files
Node: Phenotype	Human Phenotype Ontology[17]	HP Ontology
Node: Gene	NCBI Gene[18]	Homo Sapiens, filtered to 9606 Taxa ID
Node: Protein	UniProtKB[19]	Swiss-Prot Entries (XML)
Edge: SNP to Gene	GTEx[20]	version 8, eQTL
Edge: SNP to Phenotype	Open Targets[21]	GWAS Summary Statistics
Edge: Gene to Phenotype	OmicsPred[22]	PheWAS Summary Statistics
Edge: SNP to Protein	OmicsPred[22]	Olink, Somalogic (Proteomics)
Edge: Gene to Protein	UniProtKB[19]	Swiss-Prot Entries (XML)

2.2. *Disease Risk Inference and Variant Exploration Knowledge Graph (DRIVE-KG) Construction*

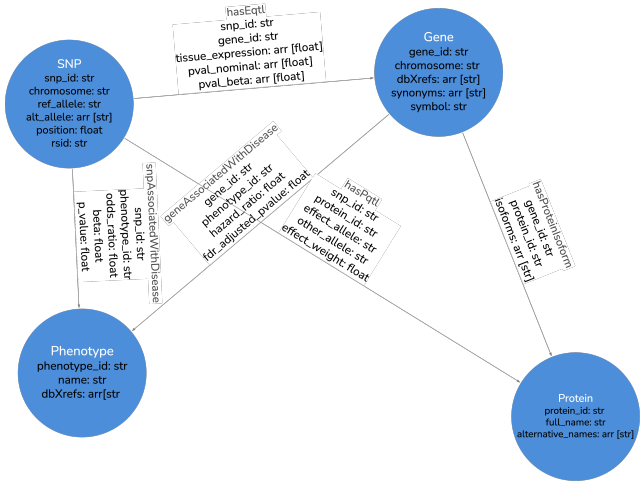

Figure 1. Knowledge Graph Schema.

When designing the DRIVE-KG schema (Figure 1), we prioritized having dense node properties and fewer edge types to avoid sparsity issues when performing machine learning analyses on the graph. We maintained cross references of node type identifiers across databases ('dbXrefs') as properties of the gene and phenotype node for possible future querying by other researchers. The 'tissue_expression' property of the 'hasEqtl' edge is an array of length 53 (number of tissues) that contains all tissue-specific beta values for eGenes in this dataset. Since eGenes (a gene whose expression is influenced by eQTLs) are

tissue-specific in the Omics Pred dataset, we aggregated all tissue-specific effects for a particular SNP–Gene pair into this list. If a particular SNP–Gene pair did not have a tissue-specific association, we set the beta value for that entry to 0.

Omics Pred pQTl data pertain to the same 53 tissue types as published by the GTEx consortium, with the exception of Bladder, Fallopian tube, and Cervix (Endocervix & Ectocervix), resulting in a total of 49 tissue types. We mapped the tissue expression array in the same alphabetical order as used by the GTEx consortium,[20] so the index of a given beta value in this array can be used to infer from which tissue it came from.

The DRIVE-KG construction process involved several key steps: first, we standardized identifiers across all data sources (e.g., harmonized to the same Entrez identifier for all gene-related data and ensured that hg38 was used to represent all SNP-related information). Finally, we ingested these files into Memgraph for subsequent visualization and analysis.

For the purposes of model training, we removed all unconnected nodes (node with degree = 0) in the graph (removing 94.2% of the original 13,806,079 nodes), yielding a total of 801,112 nodes and 1,390,440 edges in the graph. The removed nodes consisted mainly of highly specific genetic variants and phenotypes without documented associations in our data sources. This pre-processing step preserved the core connectivity structure necessary for effective graph-based learning and link prediction analyses.

2.3. *Link Prediction*

To identify previously unreported, biologically relevant relationships within DRIVE-KG, we employed link prediction methods that leverage its multi-modal data structure. The core premise of our link prediction framework is that missing edges can be inferred from graph connectivity patterns, because biologically meaningful associations often exhibit characteristic topologies. For instance, if a SNP is associated with multiple genes that are collectively linked to a specific phenotype, this suggests a potential direct SNP-phenotype relationship that may not be explicitly captured in current databases. Similarly, proteins sharing common genetic variants and phenotypic associations may indicate previously uncharacterized protein-protein interactions or shared functional pathways.

Given that DRIVE-KG is created with disease-agnostic biological data, it can be queried for links to any phenotype (using its HPO identifier). We were interested in predicting whether there should be a link between a given SNP node and two pilot phenotypes: endometriosis and obesity, both complex traits with contrasting levels of genetic characterization (67 versus 112 existing genome-wide significant variants, respectively).

We generated 64-dimension node embeddings using Memgraph's node2vec[23] module and then used these embeddings as input for a pairwise multilayer perceptron (MLP) model developed using the PyTorch Lightning[24] module. The three-layer feed-forward MLP used rectified linear unit (ReLU) activations and dropout, projecting 64-dim embeddings to 128, then sequentially reducing to 64 and finally 1 dimension. The output scalar represents the probability of a particular SNP-phenotype edge.

We trained the link prediction module on all *snpAssociatedWithDisease* (SNP-Phenotype) edges with Memgraph's native link prediction module, applying a 70-30 training-validation

split. To evaluate specific phenotypes, we queried the trained model with their HPO identifiers (HP_0030127 for endometriosis and HP_0001513 for obesity). The model outputs a score in the range [0,1] (from the final sigmoid activation), representing its confidence in a potential association. To assess the sensibility of these predictions, we focused on high-confidence edges (model score ≥ 0.95) and cross-referenced them with published GWAS results.[12] We also explored the neighborhood of these candidate associations within DRIVE-KG.

2.4. *Endometriosis Patient Classification*

In order to assess the utility of DRIVE-KG for disease risk stratification, we trained a graph convolutional network (separate from the link prediction procedure). In particular, we explored the potential of this graph to accurately stratify disease risk at the patient level when applied to endometriosis/adenomyosis. We obtained chart reviews for a cohort of 1,441 patients from the PMBB[7] with their status of endometriosis or adenomyosis (case or control) labeled, as these conditions are often grouped together during phenotyping despite likely differences in their underlying pathogenesis.[25] For endometriosis cases, the chart review also documented surgical disease stage according to established clinical classification systems, enabling both binary case-control analyses and stage-specific investigations. To calculate genetically inferred ancestry (GIA) for each participant, principal components were calculated from PMBB genotype data and then projected onto the reference HapMap3 dataset.[26] GIA for each participant was assigned by comparing their projected principal component scores to the HapMap3 reference populations and classifying them using a kernel density estimation approach.[27] Table 2 contains additional cohort demographics and GIA; a supplemental version with relevant co-morbidities is available in the project's Github repository.

Table 2. Demographics of PMBB Chart-Reviewed Cohort

Characteristic	Category	Overall (n=1441)	Control (n=732)	Case (n=709)
Sequenced gender	Female	1441 (100.0%)	732 (100.0%)	709 (100.0%)
GIA group	AFR	613 (42.5%)	256 (35.0%)	357 (50.4%)
	AMR	30 (2.1%)	20 (2.7%)	10 (1.4%)
	EAS	20 (1.4%)	13 (1.8%)	7 (1.0%)
	EUR	746 (51.8%)	422 (57.7%)	324 (45.7%)
	SAS	30 (2.1%)	19 (2.6%)	11 (1.6%)
	UNKNOWN	2 (0.1%)	2 (0.3%)	—

To curate the graph classification dataset, we generated per-patient copies of DRIVE-KG from the chart-reviewed cohort. We did this by first exporting the base KG (with existing network edges) and graph connectivity information from Memgraph into Python (PyTorch Geometric library[28]). Then, we assigned the value of each SNP node, for each patient's graph, as the imputed genotype dosage (where the value indicates the dosage of the alternate allele at a given locus) from imputed genotyping data in the 2024 PMBB data release 3.0, which was

processed using PLINK2.0.[29] Here, the prediction task is whether the entire graph represents endometriosis/adenomyosis (case) or not (control). For all non-SNP node types, we represented them with 8-dimension embeddings learned using the node2vec module. We also added per-patient covariates (age and the first 5 of overall ancestry principal components (PCs)) to the classifier.

We leveraged PyTorch Lightning to load the patient graph objects and train the graph classifier. The graph classifier architecture contains two convolutional layers for all edge types, with SAGEConv layers wrapping each of the edges. We chose SAGEConv due to its inductive capabilities, and ability to efficiently scale to large graphs. We used 64-dimension projections of the 8-dimension embeddings learned on all nodes as model input. We used ReLU activation functions for the two convolutional layers, and the 'sum' aggregation function (which generates 64-dimension tensors for each node type). We then generated pooled GNN embeddings over the SNP node type, which creates 64-dimension tensors for the entire graph. We pooled over the SNP node type alone since only the SNP node values differ across patient graphs; therefore, it is likely to contain biological signal that can be used to distinguish patients. We concatenated the pooled, 64-dimension tensors with the per-patient covariates data (6-dimension: age and 5 PCs) to get 70-dimension tensors. We fed these tensors into the first linear layer, which transformed them into 64-dimension tensors with the ReLU activation function. The second linear layer contained a sigmoid activation function that generated a binary classification value (single probability per graph/patient) from the 64-dimension tensors. For each epoch, we specified a batch size of 16, a learning rate of 0.001, and used the Adam optimization function.

We compared the performance of disease risk prediction using DRIVE-KG to a genetic risk score (GRS)[12] developed and evaluated on the same patient cohort (with the same training-validation split of patients between DRIVE-KG and the GRS). We calculate the GRS by linearly combining the patient's genetic information, age and 5 PCs (as covariates) to ensure a fair comparison.

3. Results

3.1. *Link Prediction*

We investigated link predictions for two phenotypes of interest: endometriosis (HP_0030127) and obesity (HP_0001513). For each phenotype, we obtained recommendations from the model of SNP-phenotype links, ranked by their binary classification score and annotated with whether they were existing or candidate associations.

3.1.1. *Endometriosis*

Our link prediction analysis identified 66 high confidence, candidate SNP-endometriosis associations. Notably, many of these predicted associations involved SNPs with well-established links to other complex traits and conditions yet had not been previously associated with endometriosis in the literature (except for rs10828249 located on *MLLT10*[30]). Specifically, 24.2% of the top-ranked predicted SNP-endometriosis links involved variants previously associated

with body mass index (BMI)/obesity-related traits, 6% with lipid metabolism (triglycerides and HDL), and 4.5% with depressive disorders. Additionally, these top-ranked predicted SNPs are enriched in previous endometriosis GWAS for p-values with an average magnitude of 0.473. The majority of these associations (60/66) are also not in LD with each other ($R^2 \leq 0.1$), with the exception of 3 variant pairs with R^2 values ranging from 0.4-0.65. We also estimated narrow sense heritability within the PMBB cohort, using previous GWAS associations versus these associations in addition to the 66 SNP-endometriosis candidates. The variant set from previous GWAS (136 SNPs)[12] explained an average variance of 16.73% (pseudo$-R^2$ 90% CI: 13.03–20.39%). Adding the 66 DRIVE-KG variants increased this to 24.64% (pseudo$-R^2$ 90% CI: 20.30–28.82%), an improvement of 7.91%. We observed a higher confidence for candidate associations compared to existing association scores. This could be because the model is undertrained on endometriosis associations compared to more well-studied diseases (i.e., those with a greater number of genome-wide significant associations) and biased towards positive predictions as a result. Candidate SNP-endometriosis associations had a mean confidence of 0.757 ± 0.179, whereas the 67 known SNP-endometriosis edges had a mean confidence of 0.634 ± 0.163. Figure 2 compares known versus candidate SNP$-$endometriosis associations in DRIVE-KG with $-log_2$ link prediction score on the y$-$axis. We also visualize the neighborhood of candidate signals, which are not explicitly connected to endometriosis as a phenotype, but rather relevant pathways and associated conditions.

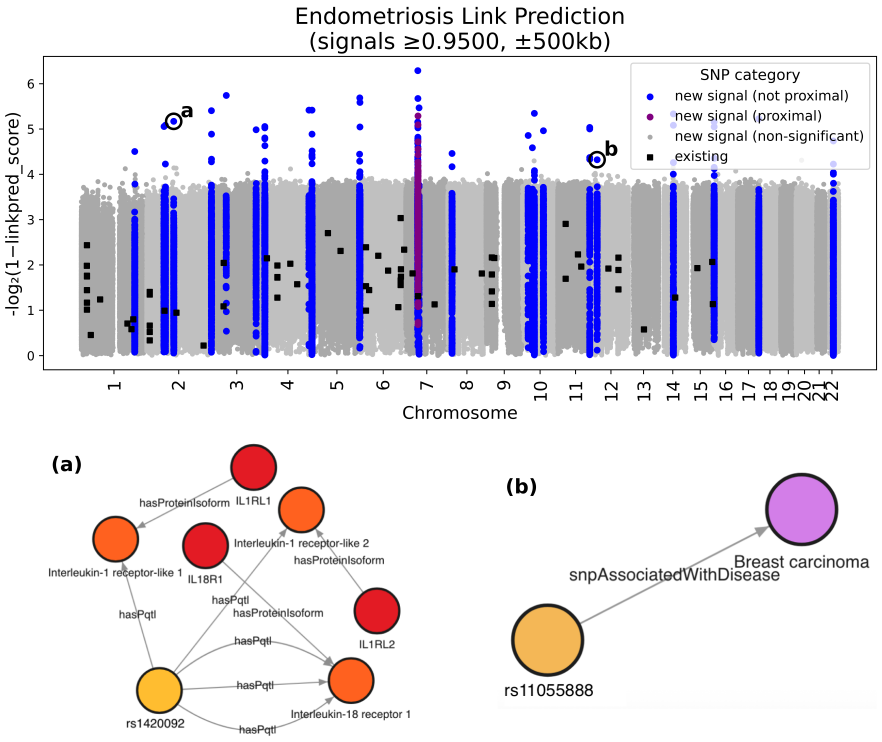

Figure 2. Endometriosis Link Prediction Results. (a) Subgraph view of rs1420092, with 100% of edges from pQTLs in the *IL−1* and *IL−8* family, which are key mediators of immune and inflammatory pathways. (b) Subgraph view of rs1105588 linked to breast cancer (GWAS), which is associated with endometriosis.

3.1.2. *Obesity*

In contrast to the endometriosis results, link prediction for obesity yielded markedly different patterns, reflecting extensive existing knowledge for these well-characterized phenotypes. The link prediction model ranked the 112 existing SNP-obesity associations with a mean confidence of 0.937 ± 0.111 (much higher than that of endometriosis), whereas the candidate SNP-obesity associations were ranked substantially lower with a mean confidence of 0.255 ± 0.178. Of the 1,575 high-confidence, candidate SNP–obesity associations, 348 could be evaluated using LDlink, as many variants lacked corresponding entries in the GWAS Catalog and thus could not be assessed. Among these, 38.22% were in high LD ($R^2 \geq 0.8$) with previously established loci (*NEGR1*[31] and *DNAJC27-AS1*[32]) for obesity or related comorbidities, rather than unreported associations. This suggests that the predicted associations largely recapitulated existing knowledge of metabolic pathways and obesity-related biological mechanisms already well-documented in the literature. The network visualizations for the high-confidence, candidate SNP-obesity associations in Figure 3 (rs74432706 and rs329642) demonstrate that these predictions are primarily driven by neighboring connections to obesity phenotypes, as opposed to distinct biological signals.

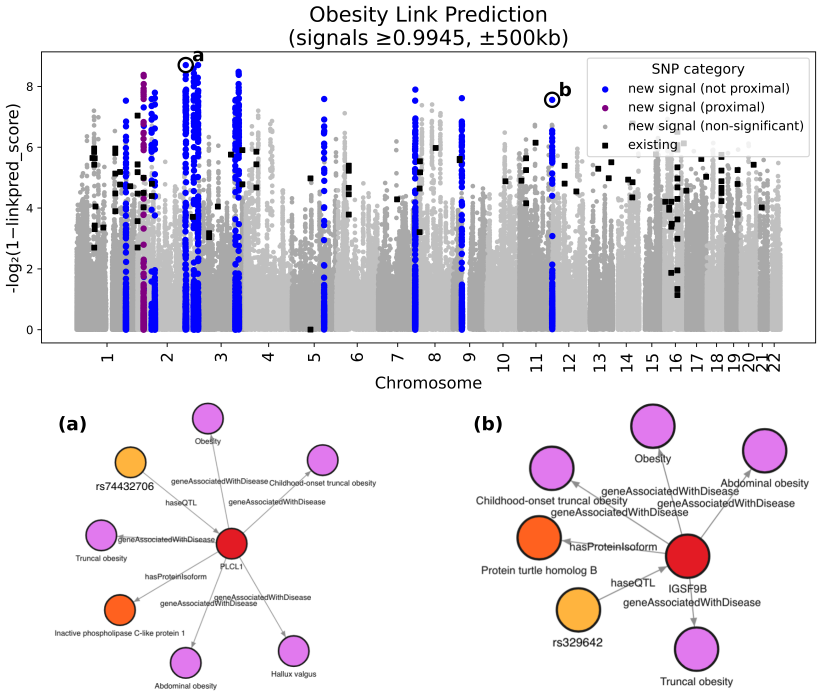

Figure 3. Obesity Link Prediction Results. (a) Subgraph view of rs74432706, with an eQTL edge (driven by the Brain Putamen basal ganglia tissue type) to *PLC1*, which modulates intracellular signaling pathways and has 4 PheWAS associations with obesity phenotypes. (b) Subgraph view of rs329642 with an eQTL edge (driven by Whole Blood and Sigmoid Colon tissue types) to *IGSF9B*, a cell adhesion molecule with 4 PheWAS associations with obesity phenotypes.

3.2. *Endometriosis Patient Classification*

Our cohort consisted of 1,411 PMBB participants assigned female at birth with imputed genotyping data and a chart reviewed label (0 or 1) for having endometriosis/adenomyosis or not. With a 70-30 training-validation split, the graph classifier had an F1 score of 0.752. We compared this to a GRS developed and evaluated on the same patient cohort, which had an F1 score of 0.698 (additional metrics displayed in Table 3). Since this is a binary classification task, the model provides a score (value between 0 and 1, inclusive) for its predicted likelihood of a given patient having either an endometriosis or adenomyosis diagnosis. Figure 4 provides model score distributions stratified both by disease subtypes from chart reviews (Figure 4a) and by surgically confirmed endometriosis stages (1-4) (Figure 4b).

Table 3. Patient Classification Evaluation (Mean ± Standard Deviation)

Model Type	AUC-ROC	AUPRC	F_1	Accuracy
DRIVE-KG	0.571 ± 0.032	0.739 ± 0.033	0.752 ± 0.0193	0.642 ± 0.0225
GRS	0.564 ± 0.032	0.738 ± 0.030	0.698 ± 0.022	0.598 ± 0.024

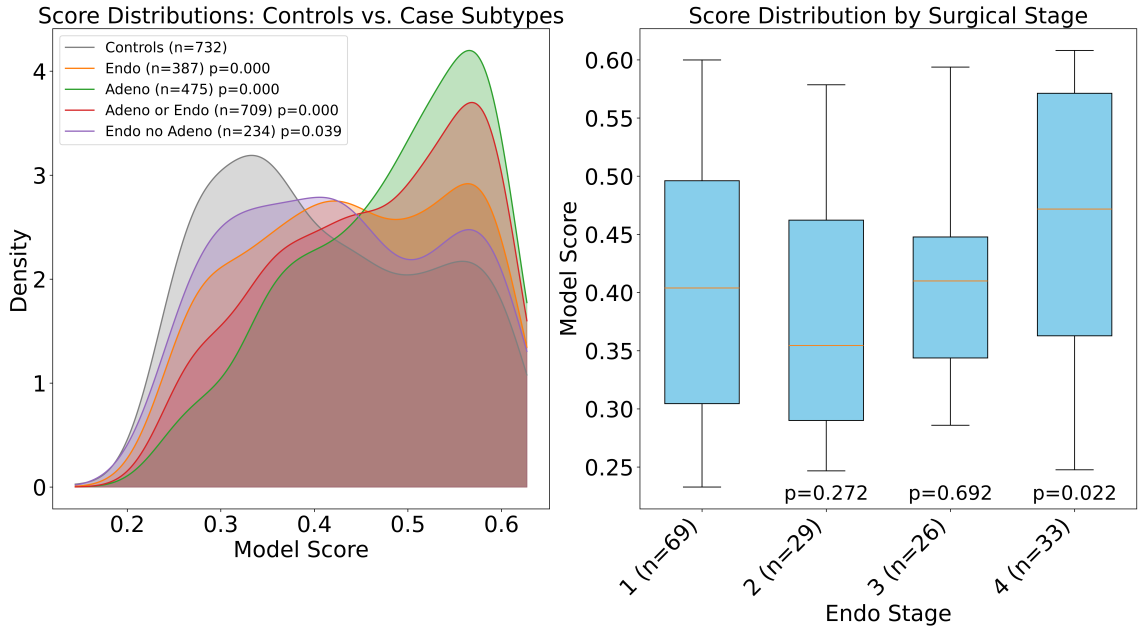

Figure 4. (a) Model score distribution for chart-reviewed disease subtypes. Density distribution indicates that high model scores for patient classification are primarily driven by adenomyosis signal. (b) Model score distribution by chart-reviewed, surgically confirmed endometriosis stages. Boxplots indicate that the model demonstrates particular strength in identifying the most severe endometriosis stage (stage 4).

4. Discussion

This study demonstrates the potential of heterogeneous KG approaches to advance our understanding of understudied diseases where traditional genomic methods have plateaued. Our findings provide several key insights into the utility of integrating multi-omics data through graph-based representations for both discovery and clinical prediction applications. Link prediction revealed a striking contrast between well-studied and understudied phenotypes, validating our central hypothesis. For endometriosis, we identified high-confidence candidate SNPs largely independent of one another ($R^2 < 0.1$) and enriched for variants linked to BMI, lipid metabolism, and depressive disorders—traits frequently co-morbid with endometriosis.[33–35] Network visualization further connected these variants to underlying inflammatory and cell proliferation pathways, providing additional insight into shared biological mechanisms. This pattern suggests shared biological pathways between endometriosis and these co-morbid conditions, which is consistent with emerging mechanistic hypotheses[12,30,36] and our PMBB chart reviewed cohort, which shows elevated risks of hyperlipidemia (RR 1.85), obesity (2.53), CVD (2.03), hypertension (1.79), and depression (1.95). These findings help address the "missing heritability" gap between traditional polygenic risk scores (explaining 11%) and the broad sense heritability estimate from a twin study (47%).[12] Conversely, link predictions for obesity—a trait with extensive genomic characterization—yielded lower confidence scores and predominantly identified variants in LD with known associations. This validates that DRIVE-KG appropriately finds fewer novel discoveries for well-mapped biological landscapes while successfully uncovering genuine candidates for understudied conditions.

Our patient classification for endometriosis demonstrates modest but meaningful improvements over traditional genetic approaches. The DRIVE-KG-based model achieved an F1 score of 0.752 compared to 0.698 for the GRS. These moderate effect sizes show potential clinical relevance for a condition where existing genomic tools perform poorly: the model showed enhanced prediction for adenomyosis and demonstrated particular strength in identifying patients with severe endometriosis (stage 4). The improved performance likely stems from DRIVE-KG's ability to capture complex multi-omics relationships that single-modality approaches miss, even when the only patient-specific input is genetic data. Rather than relying solely on individual genetic variants, our framework leverages broader biological knowledge encoded in protein associations, gene expression patterns, and phenotypic associations. This integrated approach may be particularly valuable for conditions like endometriosis where the genetic architecture is complex and poorly understood.

These findings have broader implications for addressing healthcare disparities in women's health research. Endometriosis exemplifies the challenges facing many gynecological conditions: high prevalence (affecting around 10% of women of reproductive-age[9]), significant clinical impact, yet persistent research neglect leading to limited therapeutic options. Our results suggest that graph-based approaches can help bridge these knowledge gaps by extracting additional insights from existing multi-omics data without requiring massive new cohort studies that may be infeasible for understudied populations. The identification of shared pathways with well-studied traits (obesity,[33] depression[35]) also suggests opportunities for re-purposing existing therapeutic targets and biomarkers. If endometriosis shares mechanistic pathways

with metabolic or psychiatric conditions, this could accelerate drug development and improve patient care through a better understanding of comorbidity patterns.

Our study has several limitations. First, the construction of DRIVE-KG relied on existing databases that may contain biases toward well-studied biological pathways, potentially limiting discovery of entirely new mechanisms. Second, while we harmonized variants across alleles when creating DRIVE-KG, we do not fully account for differences in the effect allele when processing the PMBB genotype data to make patient-specific graphs and simply drop variants that are in PMBB data but not in DRIVE-KG. Changing the SNP node representation to be per alternate allele would enable us to more completely utilize genotype data during patient classification. Third, we filtered the SNP nodes at a MAF ≥ 0.01 to accommodate memory constraints from Memgraph, but this restricted our analysis to common variants. Our future work will incorporate rare variants to explore associations with higher effect sizes. For patient classification, our modest AUC improvements will require further validation in independent cohorts, and generalizability across diverse, multi-institution populations remains to be established. Lastly, we cannot yet automatically incorporate data from source databases of DRIVE-KG. Ensuring the continual refreshment of its underlying data is critical for scalable biological discovery, and we plan to address this in subsequent development.

Our future work will focus on incorporating additional data modalities (e.g., transcriptomics, metabolomics, protein-protein interaction and existing genetic pathways) to further enhance the comprehensiveness of DRIVE-KG. Additionally, experimental validation of our predicted SNP-endometriosis associations will be crucial for translating these computational findings into biological insights.

In conclusion, our study demonstrates that DRIVE-KG offers a promising approach to advance precision medicine in understudied diseases. By integrating multi-omics data in a unified framework, we identified previously unreported biological candidates for endometriosis (that underscore emerging hypotheses about disease mechanisms) and improved patient classification beyond traditional genomic approaches. These findings highlight the value of graph-based methods for conditions where conventional genomic tools have reached their current limits, offering a path forward to address knowledge gaps in understudied populations.

5. Acknowledgments

We gratefully acknowledge the PMBB for providing data and thank the patient-participants of Penn Medicine who consented to participate in this research program. The PMBB is approved under IRB protocol #813913 and #852155 and supported by Perelman School of Medicine at University of Pennsylvania, a gift from the Smilow family, and the National Center for Advancing Translational Sciences of the National Institutes of Health under CTSA award number UL1TR001878. The research reported in this publication was supported by the Eunice Kennedy Shriver National Institute of Child Health and Human Development of the National Institutes of Health under award number R01HD110567-01A0, and by the US National Library of Medicine under award number R00LM013646.

Code Availability: `https://github.com/Setia-Verma-Lab/multi_omics_kg`.

References

1. Yehudit Hasin, Marcus Seldin, and Aldons Lusis. Multi-omics approaches to disease. *Genome Biol*, 18(1), December 2017. Publisher: Springer Science and Business Media LLC.
2. Srinivasan Mani, Seema R. Lalani, and Mohan Pammi. Genomics and multiomics in the age of precision medicine. *Pediatr Res*, 97(4):1399–1410, March 2025. Publisher: Springer Science and Business Media LLC.
3. Rachit Kumar, Joseph D. Romano, and Marylyn D. Ritchie. Network-based analyses of multi-omics data in biomedicine. *BioData Mining*, 18(1), May 2025. Publisher: Springer Science and Business Media LLC.
4. Aidan Hogan, Eva Blomqvist, Michael Cochez, Claudia D'amato, Gerard De Melo, Claudio Gutierrez, Sabrina Kirrane, José Emilio Labra Gayo, Roberto Navigli, Sebastian Neumaier, Axel-Cyrille Ngonga Ngomo, Axel Polleres, Sabbir M. Rashid, Anisa Rula, Lukas Schmelzeisen, Juan Sequeda, Steffen Staab, and Antoine Zimmermann. Knowledge Graphs. *ACM Comput. Surv.*, 54(4):1–37, May 2022. Publisher: Association for Computing Machinery (ACM).
5. Roelof A. J. Smit, Kaitlin H. Wade, Qin Hui, Joshua D. Arias, Xianyong Yin, Malene R. Christiansen, Loic Yengo, Michael H. Preuss, Mariam Nakabuye, Ghislain Rocheleau, Sarah E. Graham, Victoria L. Buchanan, Geetha Chittoor, Marielisa Graff, Marta Guindo-Martínez, Yingchang Lu, Eirini Marouli, Saori Sakaue, Cassandra N. Spracklen, Sailaja Vedantam, Emma P. Wilson, Shyh-Huei Chen, Teresa Ferreira, Yingjie Ji, Tugce Karaderi, Kreete Lüll, Moara Machado, Deborah E. Malden, Carolina Medina-Gomez, Amy Moore, Sina Rüeger, Masato Akiyama, Matthew A. Allison, Marcus Alvarez, Mette K. Andersen, Vivek Appadurai, Liubov Arbeeva, Eric Bartell, Seema Bhaskar, Lawrence F. Bielak, Joshua C. Bis, Sailalitha Bollepalli, Jette Bork-Jensen, Jonathan P. Bradfield, Yuki Bradford, Caroline Brandl, Peter S. Braund, Jennifer A. Brody, Ulrich Broeckel, Kristoffer S. Burgdorf, Brian E. Cade, Qiuyin Cai, Silvia Camarda, Archie Campbell, Marisa Cañadas-Garre, Jin-Fang Chai, Alessandra Chesi, Seung Hoan Choi, Paraskevi Christofidou, Christian Couture, Gabriel Cuellar-Partida, Rebecca Danning, Frauke Degenhardt, Graciela E. Delgado, Alessandro Delitala, Ayşe Demirkan, Xuan Deng, Alexander Dietl, Maria Dimitriou, Latchezar Dimitrov, Rajkumar Dorajoo, Fabian Eichelmann, Anders U. Eliasen, Jorgen E. Engmann, Michael R. Erdos, Zammy Fairhurst-Hunter, Aliki-Eleni Farmaki, Jessica D. Faul, Juan-Carlos Fernandez-Lopez, Lukas Forer, Mirjam Frank, Sandra Freitag-Wolf, Lars G. Fritsche, Christian Fuchsberger, Tessel E. Galesloot, Yan Gao, Frank Geller, Olga Giannakopoulou, Franco Giulianini, Anette P. Gjesing, Anuj Goel, Scott D. Gordon, Mathias Gorski, Jakob Grove, Xiuqing Guo, Stefan Gustafsson, Jeffrey Haessler, Thomas F. Hansen, Aki S. Havulinna, Simon J. Haworth, Nancy Heard-Costa, Daiane Hemerich, Heather M. Highland, George Hindy, Yuk-Lam Ho, Edith Hofer, Elizabeth Holliday, Katrin Horn, Whitney E. Hornsby, Jouke-Jan Hottenga, Hongyan Huang, Jie Huang, Alicia Huerta-Chagoya, Shaofeng Huo, Mi Yeong Hwang, Chii-Min Hwu, Hiroyuki Iha, Daisuke D. Ikeda, Masato Isono, Anne U. Jackson, Iris E. Jansen, Yunxuan Jiang, Ingegerd Johansson, Anna Jonsson, Torben Jørgensen, Ioanna P. Kalafati, Masahiro Kanai, Stavroula Kanoni, Line L. Kårhus, Anuradhani Kasturiratne, Tomohiro Katsuya, Takahisa Kawaguchi, Rachel L. Kember, Katherine A. Kentistou, Daeeun Kim, Han-Na Kim, Young Jin Kim, Marcus E. Kleber, Maria J. Knol, Azra Kurbasic, Marie Lauzon, Phuong Le, Rodney Lea, Jong-Young Lee, Wen-Jane Lee, Hampton L. Leonard, Hengtong Li, Shengchao A. Li, Xiaohui Li, Xiaoyin Li, Jingjing Liang, Honghuang Lin, Kuang Lin, Jun Liu, Xueping Liu, Ken Sin Lo, Jirong Long, Laura Lores-Motta, Jian'an Luan, Valeriya Lyssenko, Leo-Pekka Lyytikäinen, Anubha Mahajan, Md Zubbair Malik, Vasiliki Mamakou, Massimo Mangino, Ani Manichaikul, Jonathan Marten, Manuel Mattheisen, Aaron F. McDaid, Quanshun Mei, Heike Meiselbach, Tori L. Melendez, Yuri Milaneschi, Jason E. Miller, Iona Y. Millwood, Pashupati P. Mishra, Ruth E. Mitchell, Line T. Møllehave, Nina Mononen,

Sören Mucha, Matthias Munz, Juha Mykkänen, Masahiro Nakatochi, Giuseppe Giovanni Nardone, Christopher P. Nelson, Maria Nethander, Chu Won Nho, Aneta A. Nielsen, Ilja M. Nolte, Suraj S. Nongmaithem, Raymond Noordam, Ioanna Ntalla, Teresa Nutile, Anita Pandit, Marc Pauper, Eva R. B. Petersen, Liselotte V. Petersen, Francesco Piluso, Ozren Polašek, Alaitz Poveda, Saiju Pyarajan, Laura M. Raffield, Hiromi Rakugi, Julia Ramirez, Asif Rasheed, Dennis Raven, Nigel W. Rayner, Carlos Riveros, Rebecca Rohde, Daniela Ruggiero, Sanni E. Ruotsalainen, Kathleen A. Ryan, Maria Sabater-Lleal, Aurora Santin, Richa Saxena, Markus Scholz, Botong Shen, Jingchunzi Shi, Jae Hun Shin, Carlo Sidore, Julia Sidorenko, Xueling Sim, Roderick C. Slieker, Albert V. Smith, Jennifer A. Smith, Laura J. Smyth, Lorraine Southam, Valgerdur Steinthorsdottir, Liang Sun, Fumihiko Takeuchi, Kent D. Taylor, Bamidele O. Tayo, Catherine Tcheandjieu, Natalie Terzikhan, Paola Tesolin, Alexander Teumer, Elizabeth Theusch, Deborah J. Thompson, Gudmar Thorleifsson, Paul R. H. J. Timmers, Stella Trompet, Constance Turman, Simona Vaccargiu, Sander W. Van Der Laan, Peter J. Van Der Most, Jan B. Van Klinken, Jessica Van Setten, Shefali S. Verma, Niek Verweij, Yogasudha Veturi, Carol A. Wang, Chaolong Wang, Jun-Sing Wang, Lihua Wang, Ya Xing Wang, Zhe Wang, Helen R. Warren, Wen Bin Wei, Wanqing Wen, William A. Wheeler, Ananda R. Wickremasinghe, Matthias Wielscher, Bendik S. Winsvold, Andrew Wong, Matthias Wuttke, Rui Xia, Ken Yamamoto, Jingyun Yang, Jie Yao, Hannah Young, Noha A. Yousri, Lei Yu, Lingyao Zeng, Weihua Zhang, Xinyuan Zhang, Jing-Hua Zhao, Wei Zhao, Wei Zhou, Martina E. Zimmermann, Magdalena Zoledziewska, Leen M. 'T Hart, Linda S. Adair, Hieab H. H. Adams, Carlos A. Aguilar-Salinas, Fahd Al-Mulla, Donna K. Arnett, Folkert W. Asselbergs, Bjørn Olav Åsvold, John Attia, Bernhard Banas, Stefania Bandinelli, Lawrence J. Beilin, David A. Bennett, Tobias Bergler, Dwaipayan Bharadwaj, Ginevra Biino, Eric Boerwinkle, Carsten A. Böger, Judith B. Borja, Claude Bouchard, Donald W. Bowden, Ivan Brandslund, Ben Brumpton, Julie E. Buring, Mark J. Caulfield, John C. Chambers, Giriraj R. Chandak, Stephen J. Chanock, Nish Chaturvedi, Yii-Der Ida Chen, Zhengming Chen, Ching-Yu Cheng, Yoon Shin Cho, Kaare Christensen, Ingrid E. Christophersen, Marina Ciullo, John W. Cole, Francis S. Collins, Maria Pina Concas, Richard S. Cooper, Miguel Cruz, Francesco Cucca, Michael J. Cutler, Scott M. Damrauer, Thomas M. Dantoft, Gert J. De Borst, Eco J. C. De Geus, Lisette C. P. G. M. De Groot, Philip L. De Jager, Dominique P. V. De Kleijn, H. Janaka De Silva, George V. Dedoussis, Anneke I. Den Hollander, Shufa Du, Douglas F. Easton, Kai-Uwe Eckardt, Petra J. M. Elders, A. Heather Eliassen, Patrick T. Ellinor, Sölve Elmståhl, Jeanette Erdmann, Michele K. Evans, Diane Fatkin, Bjarke Feenstra, Mary F. Feitosa, Luigi Ferrucci, Jose C. Florez, Ian Ford, Myriam Fornage, Andre Franke, Paul W. Franks, Barry I. Freedman, Christian Gieger, Giorgia Girotto, Yvonne M. Golightly, Clicerio Gonzalez-Villalpando, Penny Gordon-Larsen, Harald Grallert, Struan F. A. Grant, Niels Grarup, Lyn Griffiths, Vilmundur Gudnason, Christopher Haiman, Hakon Hakonarson, Torben Hansen, Catharina A. Hartman, Andrew T. Hattersley, Caroline Hayward, Iris M. Heid, Chew-Kiat Heng, Christian Hengstenberg, Karl-Heinz Herzig, Alex W. Hewitt, Haretsugu Hishigaki, David M. Hougaard, Carel B. Hoyng, Paul L. Huang, Wei Huang, Wen-Yi Huang, Jennifer E. Huffman, Steven C. Hunt, Nina Hutri, Kristian Hveem, Elina Hyppönen, William G. Iacono, Sahoko Ichihara, M. Arfan Ikram, Carmen R. Isasi, Marjo-Riitta Jarvelin, Zi-Bing Jin, Karl-Heinz Jöckel, Jost B. Jonas, Peter K. Joshi, Pekka Jousilahti, J. Wouter Jukema, Mika Kähönen, Yoichiro Kamatani, Kui Dong Kang, Jaakko Kaprio, Sharon L. R. Kardia, Fredrik Karpe, Norihiro Kato, Maryam Kavousi, Frank Kee, Thorsten Kessler, Amit V. Khera, Chiea Chuen Khor, Lambertus A. L. M. Kiemeney, Bong-Jo Kim, Eung Kweon Kim, Hyung-Lae Kim, Paulus Kirchhof, Mika Kivimaki, Woon-Puay Koh, Heikki A. Koistinen, Alexander Kokkinos, Jaspal S. Kooner, Charles Kooperberg, Peter Kovacs, Adriaan Kraaijeveld, Peter Kraft, Ronald M. Krauss, Meena Kumari, Zoltan Kutalik, Markku Laakso, Leslie A. Lange, Claudia Langenberg, Lenore J. Launer, Hyejin Lee, Nanette R. Lee, Terho Lehtimäki, Rozenn N. Lemaitre, Huaixing Li, Liming Li, Wolfgang Lieb,

Xu Lin, Lars Lind, Allan Linneberg, Ching-Ti Liu, Jianjun Liu, Markus Loeffler, Barry London, Fan Lu, Steven A. Lubitz, David A. Mackey, Patrik K. E. Magnusson, JoAnn E. Manson, Gregory M. Marcus, Pedro Marques Vidal, Nicholas G. Martin, Winfried März, Fumihiko Matsuda, Mark I. McCarthy, Robert W. McGarrah, Matt McGue, Amy Jayne McKnight, Sarah E. Medland, Dan Mellström, Andres Metspalu, Braxton D. Mitchell, Paul Mitchell, Dennis O. Mook-Kanamori, Trevor A. Mori, Andrew D. Morris, Lorelei A. Mucci, Patricia B. Munroe, Mike A. Nalls, Saman Nazarian, Amanda E. Nelson, Matt J. Neville, Christopher Newton-Cheh, Christopher S. Nielsen, Harri Niinikoski, Kjell Nikus, Markus M. Nöthen, Adesola Ogunniyi, Claes Ohlsson, Albertine J. Oldehinkel, Lorena Orozco, Katja Pahkala, Päivi Pajukanta, Colin N. A. Palmer, Esteban J. Parra, Cristian Pattaro, Oluf Pedersen, Craig E. Pennell, Brenda W. J. H. Penninx, Louis Perusse, Annette Peters, Patricia A. Peyser, David J. Porteous, Danielle Posthuma, Chris Power, Peter P. Pramstaller, Michael A. Province, Bruce M. Psaty, Qibin Qi, Jia Qu, Daniel J. Rader, Olli T. Raitakari, Loukianos S. Rallidis, Dabeeru C. Rao, Susan Redline, Dermot F. Reilly, Alexander P. Reiner, Sang Youl Rhee, Paul M. Ridker, Michiel Rienstra, Samuli Ripatti, Marylyn D. Ritchie, Fernando Rivadeneira, Dan M. Roden, Frits R. Rosendaal, Jerome I. Rotter, Igor Rudan, Femke Rutters, Seungho Ryu, Charumathi Sabanayagam, Babatunde Salako, Danish Saleheen, Veikko Salomaa, Nilesh J. Samani, Dharambir K. Sanghera, Naveed Sattar, Börge Schmidt, Helena Schmidt, Reinhold Schmidt, Matthias B. Schulze, Heribert Schunkert, Laura J. Scott, Rodney J. Scott, Peter Sever, Wayne H. H. Sheu, M. Benjamin Shoemaker, Xiao-Ou Shu, Eleanor M. Simonsick, Mario Sims, Andrew B. Singleton, Moritz F. Sinner, J. Gustav Smith, Harold Snieder, Tim D. Spector, Beatrice Spedicati, Meir J. Stampfer, Klaus J. Stark, David P. Strachan, Yasuharu Tabara, E. Shyong Tai, Hua Tang, Jean-Claude Tardif, Thangavel A. Thanaraj, Anke Tönjes, Tiinamaija Tuomi, Jaakko Tuomilehto, Maria-Teresa Tusié-Luna, Rob M. Van Dam, Pim Van Der Harst, Nathalie Van Der Velde, Cornelia M. Van Duijn, Natasja M. Van Schoor, Veronique Vitart, Marie-Claude Vohl, Uwe Völker, Peter Vollenweider, Henry Völzke, Scott Vrieze, Niels H. Wacher-Rodarte, Mark Walker, Gurpreet S. Wander, Nicholas J. Wareham, Richard M. Watanabe, Hugh Watkins, David R. Weir, Thomas M. Werge, Elisabeth Widen, Gonneke Willemsen, Walter C. Willett, James F. Wilson, Peter W. F. Wilson, Tien Y. Wong, Jeong-Taek Woo, Alan F. Wright, Huichun Xu, Chittaranjan S. Yajnik, Jian Yang, Mitsuhiro Yokota, Jian-Min Yuan, Eleftheria Zeggini, Babette S. Zemel, Wei Zheng, Xiaofeng Zhu, M. Carola Zillikens, Alan B. Zonderman, John-Anker Zwart, 23andMe Research Team, DiscovEHR (DiscovEHR and MyCode Community Health Initiative), eMERGE (Electronic Medical Records and Genomics Network), GPC-UGR, The PRACTICAL Consortium, Understanding Society Scientific Group, VA Million Veteran Program, Goncalo R. Abecasis, Themistocles L. Assimes, Adam Auton, Michael Boehnke, Daniel I. Chasman, Tõnu Esko, Kari Stefansson, Guillaume Lettre, Cecilia M. Lindgren, Maggie C. Y. Ng, Christopher J. O'Donnell, Unnur Thorsteinsdottir, Peter M. Visscher, Robin G. Walters, Thomas W. Winkler, Andrew R. Wood, Panos Deloukas, Timothy M. Frayling, Anne E. Justice, Tuomas O. Kilpeläinen, Adam E. Locke, Karen L. Mohlke, Kari E. North, Yukinori Okada, Cristen J. Willer, Kristin L. Young, Segun Fatumo, Jeanne M. McCaffery, Nicholas J. Timpson, Joel N. Hirschhorn, Yan V. Sun, Sonja I. Berndt, and Ruth J. F. Loos. Polygenic prediction of body mass index and obesity through the life course and across ancestries. *Nat Med*, July 2025. Publisher: Springer Science and Business Media LLC.

6. Cathie Sudlow, John Gallacher, Naomi Allen, Valerie Beral, Paul Burton, John Danesh, Paul Downey, Paul Elliott, Jane Green, Martin Landray, Bette Liu, Paul Matthews, Giok Ong, Jill Pell, Alan Silman, Alan Young, Tim Sprosen, Tim Peakman, and Rory Collins. UK Biobank: An Open Access Resource for Identifying the Causes of a Wide Range of Complex Diseases of Middle and Old Age. *PLoS Med*, 12(3):e1001779, March 2015. Publisher: Public Library of Science (PLoS).

7. Anurag Verma, Scott M. Damrauer, Nawar Naseer, JoEllen Weaver, Colleen M. Kripke, Lindsay Guare, Giorgio Sirugo, Rachel L. Kember, Theodore G. Drivas, Scott M. Dudek, Yuki Bradford, Anastasia Lucas, Renae Judy, Shefali S. Verma, Emma Meagher, Katherine L. Nathanson, Michael Feldman, Marylyn D. Ritchie, Daniel J. Rader, and For The Penn Medicine BioBank. The Penn Medicine BioBank: Towards a Genomics-Enabled Learning Healthcare System to Accelerate Precision Medicine in a Diverse Population. *JPM*, 12(12):1974, November 2022. Publisher: MDPI AG.
8. The All of Us Research Program Investigators. The "All of Us" Research Program. *N Engl J Med*, 381(7):668–676, August 2019. Publisher: Massachusetts Medical Society.
9. Krina T. Zondervan, Christian M. Becker, Kaori Koga, Stacey A. Missmer, Robert N. Taylor, and Paola Viganò. Endometriosis. *Nat Rev Dis Primers*, 4(1), July 2018. Publisher: Springer Science and Business Media LLC.
10. J. Prescott, L.V. Farland, D.K. Tobias, A.J. Gaskins, D. Spiegelman, J.E. Chavarro, J.W. Rich-Edwards, R.L. Barbieri, and S.A. Missmer. A prospective cohort study of endometriosis and subsequent risk of infertility. *Hum. Reprod.*, 31(7):1475–1482, July 2016.
11. Rama Saha, Hans Järnbert Pettersson, Pia Svedberg, Matts Olovsson, Agneta Bergqvist, Lena Marions, Per Tornvall, and Ralf Kuja-Halkola. Heritability of endometriosis. *Fertility and Sterility*, 104(4):947–952, October 2015. Publisher: Elsevier BV.
12. Lindsay A Guare, Jagyashila Das, Lannawill Caruth, Ananya Rajagopalan, Alexis T. Akerele, Ben M Brumpton, Tzu-Ting Chen, Leah Kottyan, Yen-Feng Lin, Elisa Moreno, Ashley J Mulford, Vita Rovite, Alan R Sanders, Marija Simona Dombrovska, Noemie Elhadad, Andrew Hill, Gail Jarvik, James Jaworski, Yuan Luo, Shinichi Namba, Yukinori Okada, Yue Shi, Yuya Shirai, Jonathan Shortt, Wei-Qi Wei, Chunhua Weng, Yuji Yamamoto, Sinead Chapman, Wei Zhou, Digna R. Velez Edwards, and Shefali Setia-Verma. Expanding the genetic landscape of endometriosis: Integrative -omics analyses uncover key pathways from a multi-ancestry study of over 900,000 women, November 2024.
13. Kirstine Kloeve-Mogensen, Palle Duun Rohde, Simone Twisttmann, Marianne Nygaard, Kristina Magaard Koldby, Rudi Steffensen, Christian Møller Dahl, Dorte Rytter, Michael Toft Overgaard, Axel Forman, Lene Christiansen, and Mette Nyegaard. Polygenic Risk Score Prediction for Endometriosis. *Front. Reprod. Health*, 3, December 2021. Publisher: Frontiers Media SA.
14. Antoine Bodein, Marie-Pier Scott-Boyer, Olivier Perin, Kim-Anh Lê Cao, and Arnaud Droit. Interpretation of network-based integration from multi-omics longitudinal data. *Nucleic Acids Research*, 50(5):e27–e27, March 2022.
15. Tongxin Wang, Wei Shao, Zhi Huang, Haixu Tang, Jie Zhang, Zhengming Ding, and Kun Huang. MOGONET integrates multi-omics data using graph convolutional networks allowing patient classification and biomarker identification. *Nat Commun*, 12(1):3445, June 2021.
16. S. T. Sherry. dbSNP: the NCBI database of genetic variation. *Nucleic Acids Research*, 29(1):308–311, January 2001. Publisher: Oxford University Press (OUP).
17. Peter N. Robinson, Sebastian Köhler, Sebastian Bauer, Dominik Seelow, Denise Horn, and Stefan Mundlos. The Human Phenotype Ontology: A Tool for Annotating and Analyzing Human Hereditary Disease. *The American Journal of Human Genetics*, 83(5):610–615, November 2008. Publisher: Elsevier BV.
18. Garth R. Brown, Vichet Hem, Kenneth S. Katz, Michael Ovetsky, Craig Wallin, Olga Ermolaeva, Igor Tolstoy, Tatiana Tatusova, Kim D. Pruitt, Donna R. Maglott, and Terence D. Murphy. Gene: a gene-centered information resource at NCBI. *Nucleic Acids Research*, 43(D1):D36–D42, January 2015. Publisher: Oxford University Press (OUP).
19. A. Bairoch. The Universal Protein Resource (UniProt). *Nucleic Acids Research*, 33(Database issue):D154–D159, December 2004. Publisher: Oxford University Press (OUP).

20. John Lonsdale, Jeffrey Thomas, Mike Salvatore, Rebecca Phillips, Edmund Lo, Saboor Shad, Richard Hasz, Gary Walters, Fernando Garcia, Nancy Young, Barbara Foster, Mike Moser, Ellen Karasik, Bryan Gillard, Kimberley Ramsey, Susan Sullivan, Jason Bridge, Harold Magazine, John Syron, Johnelle Fleming, Laura Siminoff, Heather Traino, Maghboeba Mosavel, Laura Barker, Scott Jewell, Dan Rohrer, Dan Maxim, Dana Filkins, Philip Harbach, Eddie Cortadillo, Bree Berghuis, Lisa Turner, Eric Hudson, Kristin Feenstra, Leslie Sobin, James Robb, Phillip Branton, Greg Korzeniewski, Charles Shive, David Tabor, Liqun Qi, Kevin Groch, Sreenath Nampally, Steve Buia, Angela Zimmerman, Anna Smith, Robin Burges, Karna Robinson, Kim Valentino, Deborah Bradbury, Mark Cosentino, Norma Diaz-Mayoral, Mary Kennedy, Theresa Engel, Penelope Williams, Kenyon Erickson, Kristin Ardlie, Wendy Winckler, Gad Getz, David DeLuca, Daniel MacArthur, Manolis Kellis, Alexander Thomson, Taylor Young, Ellen Gelfand, Molly Donovan, Yan Meng, George Grant, Deborah Mash, Yvonne Marcus, Margaret Basile, Jun Liu, Jun Zhu, Zhidong Tu, Nancy J Cox, Dan L Nicolae, Eric R Gamazon, Hae Kyung Im, Anuar Konkashbaev, Jonathan Pritchard, Matthew Stevens, Timothèe Flutre, Xiaoquan Wen, Emmanouil T Dermitzakis, Tuuli Lappalainen, Roderic Guigo, Jean Monlong, Michael Sammeth, Daphne Koller, Alexis Battle, Sara Mostafavi, Mark McCarthy, Manual Rivas, Julian Maller, Ivan Rusyn, Andrew Nobel, Fred Wright, Andrey Shabalin, Mike Feolo, Nataliya Sharopova, Anne Sturcke, Justin Paschal, James M Anderson, Elizabeth L Wilder, Leslie K Derr, Eric D Green, Jeffery P Struewing, Gary Temple, Simona Volpi, Joy T Boyer, Elizabeth J Thomson, Mark S Guyer, Cathy Ng, Assya Abdallah, Deborah Colantuoni, Thomas R Insel, Susan E Koester, A Roger Little, Patrick K Bender, Thomas Lehner, Yin Yao, Carolyn C Compton, Jimmie B Vaught, Sherilyn Sawyer, Nicole C Lockhart, Joanne Demchok, and Helen F Moore. The Genotype-Tissue Expression (GTEx) project. *Nat Genet*, 45(6):580–585, June 2013. Publisher: Springer Science and Business Media LLC.
21. Gautier Koscielny, Peter An, Denise Carvalho-Silva, Jennifer A. Cham, Luca Fumis, Rippa Gasparyan, Samiul Hasan, Nikiforos Karamanis, Michael Maguire, Eliseo Papa, Andrea Pierleoni, Miguel Pignatelli, Theo Platt, Francis Rowland, Priyanka Wankar, A. Patrícia Bento, Tony Burdett, Antonio Fabregat, Simon Forbes, Anna Gaulton, Cristina Yenyxe Gonzalez, Henning Hermjakob, Anne Hersey, Steven Jupe, Şenay Kafkas, Maria Keays, Catherine Leroy, Francisco-Javier Lopez, Maria Paula Magarinos, James Malone, Johanna McEntyre, Alfonso Munoz-Pomer Fuentes, Claire O'Donovan, Irene Papatheodorou, Helen Parkinson, Barbara Palka, Justin Paschall, Robert Petryszak, Naruemon Pratanwanich, Sirarat Sarntivijal, Gary Saunders, Konstantinos Sidiropoulos, Thomas Smith, Zbyslaw Sondka, Oliver Stegle, Y. Amy Tang, Edward Turner, Brendan Vaughan, Olga Vrousgou, Xavier Watkins, Maria-Jesus Martin, Philippe Sanseau, Jessica Vamathevan, Ewan Birney, Jeffrey Barrett, and Ian Dunham. Open Targets: a platform for therapeutic target identification and validation. *Nucleic Acids Res*, 45(D1):D985–D994, January 2017. Publisher: Oxford University Press (OUP).
22. Yu Xu, Scott C. Ritchie, Yujian Liang, Paul R. H. J. Timmers, Maik Pietzner, Loïc Lannelongue, Samuel A. Lambert, Usman A. Tahir, Sebastian May-Wilson, Carles Foguet, Åsa Johansson, Praveen Surendran, Artika P. Nath, Elodie Persyn, James E. Peters, Clare Oliver-Williams, Shuliang Deng, Bram Prins, Jian'an Luan, Lorenzo Bomba, Nicole Soranzo, Emanuele Di Angelantonio, Nicola Pirastu, E. Shyong Tai, Rob M. Van Dam, Helen Parkinson, Emma E. Davenport, Dirk S. Paul, Christopher Yau, Robert E. Gerszten, Anders Mälarstig, John Danesh, Xueling Sim, Claudia Langenberg, James F. Wilson, Adam S. Butterworth, and Michael Inouye. An atlas of genetic scores to predict multi-omic traits. *Nature*, 616(7955):123–131, April 2023. Publisher: Springer Science and Business Media LLC.
23. Aditya Grover and Jure Leskovec. node2vec: Scalable Feature Learning for Networks, 2016. Version Number: 1.
24. William Falcon, Jirka Borovec, Adrian Wälchli, Nic Eggert, Justus Schock, Jeremy Jordan,

Nicki Skafte, Ir1dXD, Vadim Bereznyuk, Ethan Harris, Tullie Murrell, Peter Yu, Sebastian Præsius, Travis Addair, Jacob Zhong, Dmitry Lipin, So Uchida, Shreyas Bapat, Hendrik Schröter, Boris Dayma, Alexey Karnachev, Akshay Kulkarni, Shunta Komatsu, Martin.B, Jean-Baptiste SCHIRATTI, Hadrien Mary, Donal Byrne, Cristobal Eyzaguirre, Cinjon, and Anton Bakhtin. PyTorchLightning/pytorch-lightning: 0.7.6 release, May 2020.

25. Andrew W Horne and Stacey A Missmer. Pathophysiology, diagnosis, and management of endometriosis. *BMJ*, page e070750, November 2022.
26. The International HapMap 3 Consortium. Integrating common and rare genetic variation in diverse human populations. *Nature*, 467(7311):52–58, September 2010.
27. Yen-Chi Chen. A tutorial on kernel density estimation and recent advances. *Biostatistics & Epidemiology*, 1(1):161–187, January 2017.
28. Matthias Fey and Jan Eric Lenssen. Fast Graph Representation Learning with PyTorch Geometric, May 2019.
29. Christopher C Chang, Carson C Chow, Laurent Cam Tellier, Shashaank Vattikuti, Shaun M Purcell, and James J Lee. Second-generation PLINK: rising to the challenge of larger and richer datasets. *Gigascience*, 4(1), December 2015. Publisher: Oxford University Press (OUP).
30. Nilufer Rahmioglu, Sally Mortlock, Marzieh Ghiasi, Peter L. Møller, Lilja Stefansdottir, Geneviève Galarneau, Constance Turman, Rebecca Danning, Matthew H. Law, Yadav Sapkota, Paraskevi Christofidou, Sini Skarp, Ayush Giri, Karina Banasik, Michal Krassowski, Maarja Lepamets, Błażej Marciniak, Margit Nõukas, Danielle Perro, Eeva Sliz, Marta Sobalska-Kwapis, Gudmar Thorleifsson, Nura F. Topbas-Selcuki, Allison Vitonis, David Westergaard, Ragnheidur Arnadottir, Kristoffer S. Burgdorf, Archie Campbell, Cecilia S. K. Cheuk, Caterina Clementi, James Cook, Immaculata De Vivo, Amy DiVasta, O. Dorien, Jacqueline F. Donoghue, Todd Edwards, Pierre Fontanillas, Jenny N. Fung, Reynir T. Geirsson, Jane E. Girling, Paivi Harkki, Holly R. Harris, Martin Healey, Oskari Heikinheimo, Sarah Holdsworth-Carson, Isabel C. Hostettler, Henry Houlden, Sahar Houshdaran, Juan C. Irwin, Marjo-Riitta Jarvelin, Yoichiro Kamatani, Stephen H. Kennedy, Ewa Kepka, Johannes Kettunen, Michiaki Kubo, Bartosz Kulig, Venla Kurra, Hannele Laivuori, Marc R. Laufer, Cecilia M. Lindgren, Stuart MacGregor, Massimo Mangino, Nicholas G. Martin, Charoula Matalliotaki, Michail Matalliotakis, Alison D. Murray, Anne Ndungu, Camran Nezhat, Catherine M. Olsen, Jessica Opoku-Anane, Sandosh Padmanabhan, Manish Paranjpe, Maire Peters, Grzegorz Polak, David J. Porteous, Joseph Rabban, Kathyrn M. Rexrode, Hanna Romanowicz, Merli Saare, Liisu Saavalainen, Andrew J. Schork, Sushmita Sen, Amy L. Shafrir, Anna Siewierska-Górska, Marcin Słomka, Blair H. Smith, Beata Smolarz, Tomasz Szaflik, Krzysztof Szyłło, Atsushi Takahashi, Kathryn L. Terry, Carla Tomassetti, Susan A. Treloar, Arne Vanhie, Katy Vincent, Kim C. Vo, David J. Werring, Eleftheria Zeggini, Maria I. Zervou, DBDS Genomic Consortium, Kari Stefansson, Mette Nyegaard, FinnGen Study, Paivi Harkki, Oskari Heikinheimo, Johannes Kettunen, Venla Kurra, Hannele Laivuori, Outi Uimari, FinnGen Endometriosis Taskforce, The Celmatix Research Team, Geneviève Galarneau, Caterina Clementi, Piraye Yurttas-Beim, The 23andMe Research Team, Pierre Fontanillas, Joyce Y. Tung, Sosuke Adachi, Julie E. Buring, Paul M. Ridker, Thomas D'Hooghe, George N. Goulielmos, Dharani K. Hapangama, Caroline Hayward, Andrew W. Horne, Siew-Kee Low, Hannu Martikainen, Daniel I. Chasman, Peter A. W. Rogers, Philippa T. Saunders, Marina Sirota, Tim Spector, Dominik Strapagiel, Joyce Y. Tung, David C. Whiteman, Linda C. Giudice, Digna R. Velez-Edwards, Outi Uimari, Peter Kraft, Andres Salumets, Dale R. Nyholt, Reedik Mägi, Kari Stefansson, Christian M. Becker, Piraye Yurttas-Beim, Valgerdur Steinthorsdottir, Mette Nyegaard, Stacey A. Missmer, Grant W. Montgomery, Andrew P. Morris, and Krina T. Zondervan. The genetic basis of endometriosis and comorbidity with other pain and inflammatory conditions. *Nat Genet*, 55(3):423–436, March 2023.
31. Anonymous Reviewer and Stephen Cj Parker. eLife Assessment: 3D genomic features across >50

diverse cell types reveal insights into the genomic architecture of childhood obesity.
32. Arjen J. Boender, Margriet A. Van Gestel, Keith M. Garner, Mieneke C. M. Luijendijk, and Roger A. H. Adan. The obesity-associated gene *Negr1* regulates aspects of energy balance in rat hypothalamic areas. *Physiol Rep*, 2(7):e12083, July 2014.
33. Ingrid J. Rowlands, Richard Hockey, Jason A. Abbott, Grant W. Montgomery, and Gita D. Mishra. Body mass index and the diagnosis of endometriosis: Findings from a national data linkage cohort study. *Obesity Research & Clinical Practice*, 16(3):235–241, May 2022. Publisher: Elsevier BV.
34. Rong Zheng, Xin Du, and Yan Lei. Correlations between endometriosis, lipid profile, and estrogen levels. *Medicine*, 102(29):e34348, July 2023. Publisher: Ovid Technologies (Wolters Kluwer Health).
35. Dora Koller, Gita A. Pathak, Frank R. Wendt, Daniel S. Tylee, Daniel F. Levey, Cassie Overstreet, Joel Gelernter, Hugh S. Taylor, and Renato Polimanti. Epidemiologic and Genetic Associations of Endometriosis With Depression, Anxiety, and Eating Disorders. *JAMA Netw Open*, 6(1):e2251214, January 2023. Publisher: American Medical Association (AMA).
36. Nina Shigesi, Holly R. Harris, Hai Fang, Anne Ndungu, Matthew R. Lincoln, The International Endometriosis Genome Consortium, The 23andMe Research Team, Chris Cotsapas, Julian Knight, Stacey A. Missmer, Andrew P. Morris, Christian M. Becker, Nilufer Rahmioglu, and Krina T. Zondervan. The Association between Endometriosis and Immunological diseases, July 2024.

Workshop Introduction: Advances of AI Methods in Single Cell Spatial Omics

Lana Garmire
The University of Alabama at Birmingham
Birmingham, Alabama 35294, United States
Email: lgarmire@uab.edu

Xiuwei Zhang
Georgia Institute of Technology
Atlanta, Georgia, 30308, United States
Email: xzhang954@gatech.edu

Joshua Levy
Cedars Sinai Medical Center
Los Angeles, California, 90048, United States
Email: joshua.levy@cshs.org

The workshop "Advances of AI Methods in Single Cell Spatial Omics" will highlight recent developments in applying AI and machine learning to spatial transcriptomics, proteomics, and metabolomics. Featuring invited speakers and contributed talks, the program will cover methods for data integration, modeling cell–cell interactions, and translational applications to disease and precision medicine.

1. Background

Spatial omics technologies, including spatial transcriptomics, spatial proteomics, and spatial metabolomics, are rapidly redefining how we study biology at cellular resolution. By capturing both molecular information and spatial context, these technologies provide unprecedented opportunities to uncover the cellular architecture of tissues, the dynamics of cell–cell communication, and the molecular underpinnings of development and disease. In just a few years, spatial omics has expanded from pioneering proof-of-concept studies to large-scale applications across neuroscience, cancer biology, immunology, and precision medicine.

Despite this progress, the complexity of spatial omics data presents major challenges. Datasets are often high-dimensional, multimodal, and heterogeneous, with experimental protocols and spatial resolutions varying widely across platforms. Most technologies capture 2D tissue slices, leaving open the computational problem of reconstructing 3D tissue architecture. Moreover, extracting meaningful biological knowledge requires methods that can integrate spatial omics data with other modalities such as histology, imaging, and single-cell RNA-seq, while also ensuring reproducibility and interpretability. These challenges have created a unique opportunity for artificial intelligence

© 2025 The Authors. Open Access chapter published by World Scientific Publishing Company and distributed under the terms of the Creative Commons Attribution Non-Commercial (CC BY-NC) 4.0 License.

(AI) and machine learning (ML) methods, which are particularly well-suited for handling large-scale, complex, and noisy datasets.

2. Goal of workshop

The goal of this workshop is to bring together computational scientists, experimentalists, and biomedical researchers working at the intersection of AI and spatial omics. Through invited and contributed talks, the workshop will highlight recent methodological advances, explore open problems, and encourage discussion of future directions. Key themes include:

- AI-driven frameworks for integrating diverse spatial omics modalities and temporal data.
- Deep learning and generative modeling approaches for uncovering regulatory dynamics and reconstructing tissue-level organization.
- Methods to model and predict cell–cell interactions and signaling within tissue microenvironments.
- Development of scalable, generalizable, and interpretable foundation models for spatial omics.
- Translational applications, including biomarker discovery, drug repurposing, and the creation of clinically relevant tissue atlases.

3. Plan of workshop

This year's program features world-renowned invited speakers as well as eight contributed short talks**,** which together represent the breadth and depth of current innovation in this field.

The invited speakers are:

- Ben Raphael, Professor of Computer Science, Princeton University

  Ben Raphael is a leading researcher in computational genomics and cancer genomics, with a strong focus on spatial transcriptomics and tumor heterogeneity. His work has pioneered algorithmic methods for analyzing single-cell and spatial omics data, particularly in understanding cellular organization in cancer. His research has led to widely used computational tools for inferring spatial domains, tumor evolution, and network/pathway analysis of genetic variants.

- Theodore Alexandrov, Assistant Professor at the Department of Pharmacology, UCSD

  Theodore Alexandrov is a global expert in spatial metabolomics and computational mass spectrometry. He has developed machine learning methods to analyze spatial omics data, particularly for metabolite localization and tissue microenvironment profiling, with applications in drug discovery & therapy development.

- Xuegong Zhang, Professor, Tsinghua University

Xuegong Zhang is a pioneering researcher in computational biology and bioinformatics. His work focuses on developing AI-driven algorithms including foundation models to improve the analysis and interpretation of single cell multiomics data and spatially resolved gene expression data. His contributions have significantly advanced cell type identification, spatial domain detection, and embedding learning of cells. Xuegong currently serves as the vice-president of the International Society for Computational Biology (ISCB).

The selected contributed presentations address both core computational advances and real-world applications:

- *Learning mechanistic models of gene regulatory dynamics from spatial multi-omic datasets*
- *DeepCell at 10 years – AI for spatial biology*
- *STDrug: a computational method to use spatial transcriptomics to aid personalized drug-reposition recommendation*
- *A scalable human brain cell atlas foundation model dissects the cellular immune codes and cognitive resilience*
- *Mapping lineage-resolved scRNA-seq data with spatial transcriptomics using TemSOMap*
- *CELLestial: an end-to-end spatial proteomics framework for rapid cell type annotation and interactive visualization at scale for foundation model fine-tuning and large-scale clinical trial analyses*
- *Inferring cell migration, differentiation, and signaling from spatial transcriptomics*
- *STHD: probabilistic cell typing of single spots in whole transcriptome spatial data with high definition*

By combining technical innovation with biological applications, these talks reflect the transformative potential of AI in unlocking new insights from spatial omics. We expect lively discussions on how to tackle existing challenges, best practices for reproducibility, and the future of spatially resolved single-cell analysis.

4. Conclusions

In sum, this workshop is particularly timely given the rapid evolution of spatial omics technologies and the accelerating adoption of AI in biomedical research**.** It will provide a dedicated forum for advancing computational methodology, fostering interdisciplinary collaboration, and inspiring the next generation of scientific discoveries at the interface of spatial biology and AI.

AI for Health: Leveraging Artificial Intelligence to Revolutionize Healthcare

Ruowang Li
Department of Computational Biomedicine, Cedars-Sinai Medical Center, West Hollywood, California, USA
Email: ruowang.li@cshs.org

Brian D. Davison
Department of Computer Science and Engineering, Lehigh University, Bethlehem, Pennsylvania, USA
Email: davison@cse.lehigh.edu

Tiffani Bright
Department of Computational Biomedicine, Cedars-Sinai Medical Center, West Hollywood, California, USA
Email: Tiffani.Bright@cshs.org

Lifang He
Department of Computer Science and Engineering, Lehigh University, Bethlehem, Pennsylvania, USA
Email: lih319@lehigh.edu

1. Introduction to the Workshop

Artificial Intelligence (AI) is poised to transform healthcare, offering groundbreaking capabilities in disease diagnosis, treatment, drug discovery, and patient care. By improving access to health services, reducing costs, and addressing workforce shortages, AI can play a pivotal role in tackling global health challenges. However, successfully integrating AI into healthcare requires careful consideration of regulatory frameworks, governance structures, data equity, and privacy protections. As interest in applying AI to healthcare grows, close collaboration between academia, clinical practitioners, and the healthcare industry becomes increasingly crucial to ensure that AI technologies are inclusive, equitable, and ethical. This workshop will bring together AI researchers, clinicians, and industry experts to foster dialogues and insights that contribute to responsible AI development. Focus areas will include AI for medical data analysis, clinical decision support systems, drug discovery, personalized medicine, and digital health platforms, all of which promise to reshape the future of health services.

2. Session Scope

This workshop will address critical challenges and solutions for advancing AI in healthcare. Traditional AI models in healthcare often rely on limited, isolated datasets, facing challenges like

© 2025 The Authors. Open Access chapter published by World Scientific Publishing Company and distributed under the terms of the Creative Commons Attribution Non-Commercial (CC BY-NC) 4.0 License.

missing values, data imbalance, and insufficient representation of diverse patient populations. These issues can introduce algorithmic biases, impact generalizability, and reduce the accuracy of AI-driven predictions, especially in clinical settings. Ensuring access to large, high-quality datasets is key to addressing these limitations, yet privacy and security constraints often restrict data sharing and collaboration across institutions. By exploring both current and forward-looking perspectives, this workshop aims to inspire solutions that enhance AI's reliability, inclusivity, and ethical impact in healthcare. Furthermore, to encourage people to actively participate in sharing their health-related data, we need more accessible and user-friendly data management systems. Such systems should enable individuals of all backgrounds and income levels to contribute health-related data, including metrics from wearable technologies, supporting the development of comprehensive, personalized healthcare solutions. These systems should also provide intuitive interfaces for both patients and clinicians, allowing for easy interpretation of AI-generated insights with confidence. This workshop unites diverse stakeholders to drive scientific advances through cross- disciplinary collaboration, fostering people-centered, AI-enabled healthcare. Attendees will explore cutting-edge AI developments while emphasizing fairness, privacy, and transparency in global health. The workshop will feature experts from computer science, medicine, statistics, and AI to balance methodology presentations with interactive discussions, encouraging idea exchange and meaningful dialogue.

3. Organizing Team

Ruowang Li, Ph.D. is an Assistant Professor in the Department of Computational Biomedicine at Cedars Sinai Medical Center. His lab focuses on developing computational methods to extract knowledge from large-scale population-level data, such as biobank-linked electronic health record data. His area of research includes multi-omics data integration, federated learning of patients' data, genetic risk prediction, and genome- phenome associations.

Tiffani Bright, Ph.D. is an Assistant Professor of Computational Biomedicine at Cedars- Sinai and Co-Director of the Center for AI Research and Education. Her lab works to reduce bias in machine learning, ensuring clinical AI models treat all patients fairly. They enhance AutoML tools like TPOT to automate bias detection and mitigation, making fair model development more scalable. Instead of traditional proxies like race, they design predictive models based on fairer metrics to promote equitable healthcare outcomes.

Brian D. Davison, Ph.D. is a Professor and Chair of the Department of Computer Science and Engineering at Lehigh University. He is a co-founder of Lehigh's Center for Catastrophe Modeling, a founding co-director of the interdisciplinary Master's Program in Data Science and the founding director of Lehigh's undergraduate minor in data science. He serves as senior associate editor of the Association for Computing Machinery (ACM) journal Transactions on Intelligent Systems and Technology and associate editor for Frontiers in Big Data, Data Mining and Management Section. His research focuses on search, mining, recommendation, and classification problems in text and on the Web, as well as catastrophe modeling for natural disasters and health-related threats. Davison is an NSF Faculty Early CAREER award winner and his research has been supported by NSF, NIH, DARPA, Microsoft, Amazon, and Sun Microsystems.

Lifang He, Ph.D. is an Associate Professor in the Department of Computer Science and Engineering at Lehigh University, and the Chair of IEEE Computer Society Chapter at Lehigh Valley Section. She received her PhD degree in Computer Science and Postdoc training at UPenn and Cornell's medical schools. Dr. He has extensive expertise in developing advanced computational methods for biomedical research such as on understanding disease mechanisms, diagnosis, prognosis, disease biomarkers, and disease pathways. Her research span machine learning, computational medical imaging, AI for health, tensor computing, and multimodal analysis. She has published over 200 papers in peer-reviewed journals and conferences. Her work has been supported by NIH, NSF, ONR and DOE.

Applications of AI & ML in Biomanufacturing of Cell and Gene Therapies

Eric Neumann
IQUrium
52 Scholl St Duxbury MA 02332
Email: ekneumann@gmail.come

Karen Weisinger
CellX Technologies
12 Gill St. Suite 4000. Woburn, MA 01801
Email: kweisinger@cellxtechnologies.com

Tom Londo
TRL Enterprises, LLC
8 Walkup Lane Ashland, MA 01721
Email: tlondo@trlenterprise.com

This workshop highlights how AI/ML technologies are beginning to be applied to biomanufacturing and bioengineering of cell and gene therapies (CGT). AI/ML have demonstrated their utility in biocomputing and biomedical research applications, and are poised to become central to design, scaling, and optimization of bioengineering processes such as CAR-T cells, iPSC, and biomolecule production. Invited speakers from academia and industry will speak of their experience in leveraging these new intelligent technologies.

Keywords: Cell and Gene Therapeutics, Biomanufacturing, Knowledge Systems, Artificial Intelligence, Lab Automation

1. Introduction

Cell and gene therapies are transforming medicine, offering the possibility of cures rather than just treatments. Yet, despite their promise, the path from idea to market is long, costly, and fraught with failure. Nearly half of advanced therapy programs collapse before reaching manufacturing[3], often because their foundations are built on insufficient early characterization.

Process development in cell therapies is the critical phase in which every step —from induced pluripotent stem cells (iPSCs) reprogramming and expansion, to differentiation and scale-up—is systematically optimized and validated to ensure reproducibility and quality. Each parameter must be carefully tuned and statistically understood before the process is "locked down," because once it transitions into GMP manufacturing, no further changes can be made without resetting the entire regulatory pathway. The painstaking, iterative experimentation that defines process development is therefore not an academic exercise—it is the foundation that determines whether a cell therapy will function reliably, scale successfully, and ultimately reach patients safely.

To deliver a safe, effective product, developers must define Critical Quality Attributes (CQAs) (what "good" looks like) and Critical Process Parameters (CPPs) (which "levers" truly matter to

© 2025 The Authors. Open Access chapter published by World Scientific Publishing Company and distributed under the terms of the Creative Commons Attribution Non-Commercial (CC BY-NC) 4.0 License.

produce quality). This is the cornerstone of Quality by Design (QbD): ensuring quality is built in from the start, not inspected in at the end [3].

But today, the characterization process is slow, manual, and expensive. Biologists rely heavily on experience and intuition, while lacking the statistical frameworks needed for robust process design. As a result, companies often cut corners, locking down processes before they're truly understood—creating a fragile "house of cards" that collapses later in development.

1.1 Where automation fits in

Automation is not just about efficiency; it is about removing variability, ensuring consistency, and capturing every piece of data. In current practice, many of the most variability-prone steps—cell passaging, media changes, imaging, and offline assays—are performed manually by multiple operators. Each subtle difference adds noise and uncertainty to the process.

By automating these steps, we achieve:

1. Consistency: Robots perform the same actions identically every time, reducing operator-to-operator variability[4].
2. Throughput: Automated systems can run more experiments in parallel, compressing timelines.
3. Data integrity: Every action is logged, time-stamped, and linked to process metadata, ensuring traceability.
4. Contamination control: Automation reduces human handling, lowering risk in processes that often take months per dose.

Automation Systems (e.g. Celligent™ and BioPAT©) already integrate imaging, media handling, and culture interventions with automated, regulatory-compliant data capture. This ensures not only reproducibility, but also a digital record ready for regulatory review.

1.2 Automation combined with AI

AI is already being applied in therapeutic R&D to identify drug targets, design novel molecules, simulate drug effects, and optimize clinical trials[1]. However, this does not address the need to define and optimize the process development phase and quality assurance for therapies. Specifically, how can it address the needs of automation and quality management? While automation provides consistency and scale, AI unlocks the full value of the data generated. Together, they enable a new paradigm:

- Robust, multimodal data integration: AI combines imaging, omics, and metadata into holistic datasets, overcoming the "needle in a haystack" problem of finding meaningful quality metrics.
- Sentinel panels and predictive modeling: AI can detect early signals of drift, giving developers actionable insight long before failure becomes visible.
- Automated Design of Experiments (DoE): Instead of manual trial-and-error, AI can propose statistically rigorous experimental designs, test hypotheses, and iteratively refine CQAs and CPPs.

- Continuous learning: Each automated run feeds back into the knowledge base, improving predictive power over time—creating a "self-improving" ecosystem.
- Regulatory readiness: The combination of structured automation data and AI-driven analysis makes for powerful, evidence-rich submissions[5].

In short, automation creates reliable data at scale; AI transforms that data into knowledge and action. Together, they form the bedrock needed to de-risk advanced therapies, shorten timelines, and build confidence for investors and regulators alike.

2. Objectives

This workshop explores the different forms of applying AI to Process Development, and how this augments the larger picture. Specifically:

1. Have the ability to Recognize the core bottlenecks in advanced therapy development.
2. Have an understanding of the informatics needs that link operational data systems to deeper analytics and workflow optimizations.
3. Have an understanding why characterization is the foundation of therapeutic success and how CQAs/CPPs are defined.
4. See how automation reduces variability, increases throughput, and secures data integrity.
5. Learn how AI transforms automated data into actionable insights, accelerating discovery and regulatory readiness, and how this can be captured using Knowledge Graphs[2].
6. Envision a future where automation + AI enable Quality by Design in biology and aggregation of Therapeutic Process Knowledge , reducing cost and risk while increasing investor and patient confidence.

By embedding automation and AI into the earliest stages of development, we can create robust processes where quality is not an afterthought but a design principle. This will not only reduce wasted investment and accelerate speed to market but also build reusable knowledge frameworks that benefit the entire field[6].

This workshop will explore how to move from fragile, manual, corner-cutting practices to a future where automation and AI enable quality by design for biology—delivering therapies that are consistent, scalable, and accessible.

3. Workshop Program

- Introduction (Eric Neumann & Karen Weisinger)
- Presentations:
  - **Karen Weisinger** (Cell X Technologies) - Breaking the House of Cards: Characterization, QbD, and Automation for Reliable Innovative Advanced Therapies
  - **Timo Schmidberger** (Sartorius) - Digital Integration: Hardware's Key Role in AI/ML Advancement
  - **Eric Neumann** (IQUrium) - Cell Processing Combining Knowledge Models with AI
- Closing Remarks

4. References

1. Druedahl LC, Price WN, Minssen T, Sarpatwari A. Use of Artificial Intelligence in Drug Development. *JAMA Netw Open. 2024;7(5):e2414139*. doi: 10.1001/jamanetworkopen.2024.14139.
2. Chandak, P., Huang, K. & Zitnik, M. Building a knowledge graph to enable precision medicine. *Sci Data* 10, 67 (2023). https://doi.org/10.1038/s41597-023-01960-3**.**
3. Tobolowsky, Mark A. and Richard A. Lewis**.** "What Regenerative Medicine Manufacturers Have Been Waiting For." *Outsourced Pharma.* 9 Nov. 2023.
4. Alliance for Regenerative Medicine "Sector Snapshot: Building a Next-Gen Workforce)." . Aug. 2023.
5. Alliance for Regenerative Medicine. 2023. "Ongoing Clinical Trials by Phase and Therapeutic Approach."
6. Alliance for Regenerative Medicine "Investment Data – 2023 Q2." . Oct. 2023.

The Evolving Cyberinfrastructure at the National Institutes of Health to Support Data and AI in Biomedical Research*

Ojas A. Ramwala
Department of Biomedical Informatics and Medical Education, University of Washington, Seattle, Washington, 98195, USA
Email: ramwala@uw.edu

Nick Weber
Center for Information Technology, National Institutes of Health, Bethesda, Maryland, 20892, USA
Email: nick.weber@nih.gov

Sean D. Mooney†
Center for Information Technology, National Institutes of Health, Bethesda, Maryland, 20892, USA
Email: sean.mooney@nih.gov

Technological advancements have made biomedicine rich in data. With the generation of enormous volumes of biomedical and clinical data, it has become imperative to support biomedical computing investigators to utilize this wealth of biologically meaningful information. Moreover, advancements in Artificial Intelligence (AI) techniques, in conjunction with improved capabilities in implementing large-scale data processing pipelines, have led to the development of robust computational techniques and algorithms to solve complex biological problems. However, there are many challenges associated with providing researchers with secure systems for accessing biomedical data and computational resources that must be addressed. Establishing and maintaining an impactful data and AI ecosystem to support efforts in advancing biomedical research requires effective, scalable, and standardized information technology solutions, funding programs, and technical guidance that facilitate researchers in utilizing the state-of-the-art. The U.S. National Institutes of Health (NIH) has established novel initiatives to implement a cyberinfrastructure that democratizes secure access to large biomedical datasets and cloud-based computing resources, equipping biocomputing scientists to pursue pioneering research. This workshop will highlight the major issues restraining researchers' access to biomedical datasets and computing infrastructures and will cover the key components of the NIH's cyberinfrastructure aimed at advancing data science and AI research for biomedical applications.

Keywords: Artificial Intelligence; Biomedicine, Cloud Computing, Cyberinfrastructure, Data Science

* This work is supported by the Intramural Research Program of the National Human Genome Research Institute, National Institutes of Health, and the Office of Scientific Computing Services, Center for Information Technology (CIT), National Institutes of Health.
† Corresponding author.
© 2025 The Authors. Open Access chapter published by World Scientific Publishing Company and distributed under the terms of the Creative Commons Attribution Non-Commercial (CC BY-NC) 4.0 License.

1. Introduction

The rapidly evolving landscape of acquiring, sharing, and processing biological data has fueled the burgeoning volume of omics, clinical, imaging, and electronic health record (EHR) datasets available to biomedical researchers. While this has immense potential to enhance healthcare outcomes, intensive efforts are necessary to address challenges associated with big biomedical data. These challenges include, but are not limited to, data heterogeneity, patient data privacy and information security concerns, limited standardization and interoperability, and siloed data systems, which cause a lack of reproducibility in biomedical research. This is exacerbated by challenges in establishing secure and reliable high-performance computing infrastructures for analyzing large biomedical datasets.

A paradigm shift in the biomedical data-sharing and analysis workflow has emerged[1–3]. Traditional methods involve a resource-intensive process of curating de-identified data and sharing it with individual researchers, all under legal agreements aimed at safeguarding the privacy of biomedical data. Recently, improved data-sharing techniques involving centralized cloud-based infrastructures that host biomedical data have been developed to provide controlled access to data while addressing the limitations of traditional approaches. To operate effectively in this environment, researchers require efficient data access mechanisms that enable them to build computational workflows that facilitate the advancement of biological discoveries.

The growth of biomedical data implies a growing demand for computational resources to develop reusable interactive data science workflows and to build, validate, and deploy robust AI algorithms for diverse applications, including predicting diagnostic outcomes, proposing patient-specific treatment strategies, discovering novel therapeutics, and analyzing complex biological relationships, among many others. Cloud-based solutions have demonstrated the potential to aid researchers in rapidly acquiring scalable computational resources, often in a cost-effective fashion.

However, investigators and research institutions can leverage cloud technologies, but emergent tools in the cloud have been evolving somewhat slowly. Reasons for this often include structuring acquisition approaches, forecasting and budgeting for usage, negotiating costs, training and/or hiring staff, and implementing techniques to scale and secure prototype systems into robust infrastructures. Aligning with its Strategic Plan for Data Science and its Digital Strategy[4], the NIH has been developing a novel set of tools that provide secure biomedical data sharing mechanisms, affordable access to cloud services, and secure data analytics workspaces to enable the biomedical research community to achieve the potential of the emerging digital ecosystem. This workshop will be of interest to computational researchers who want to learn about and discuss cloud architecture, as well as explore successful approaches that leverage tools supporting the biodata community. Opportunities to leverage these platforms will be presented.

2. Workshop Goals and Organization

The workshop on **The Evolving Cyberinfrastructure at the National Institutes of Health to Support Data and AI in Biomedical Research** at the 2026 Pacific Symposium on Biocomputing is aimed at addressing the key technical factors enabling AI and Data Science research to advance biomedical and clinical medicine and healthcare. This workshop will highlight some of the major

challenges associated with storing and analyzing biomedical data, as well as developing robust algorithms. We will present impactful programs within the NIH digital ecosystem to tackle these challenges. Speakers will present a vision for reusable cyberinfrastructure "building blocks" and discuss how the biomedical research community can better understand, leverage, enhance, and extend NIH resources within an open ecosystem. The workshop will conclude with a moderated panel discussion designed to stimulate conversations and foster a deeper understanding of the technological needs of biomedical scientists, ultimately shaping AI research in biocomputing.

2.1. *Enhancing Access to Cloud Resources to Deploy Standardized and Scalable Infrastructures*

A multifaceted set of challenges acts as an obstacle to the adoption of cloud-based solutions in biomedical research workflows. The NIH STRIDES (Science and Technology Research Infrastructure for Discovery, Experimentation, and Sustainability)[5] program is designed to enhance biomedical discovery and improve efficiency through new digital data management strategies that contribute to NIH's efforts to develop and sustain a modern biomedical data ecosystem. Through partnerships with commercial cloud service providers (CSPs), STRIDES provides a cost-effective way for biomedical researchers at NIH and NIH-funded institutions to access advanced computational infrastructure, tools, and services provided by CSPs. The overall goal of the initiative is to accelerate biomedical advances by reducing economic and technological barriers to data and resources.

Today, STRIDES supports more than 2,500 research programs and, in aggregate, manages more than one-third of an exabyte of data (~370,000,000 gigabytes). Resources built within STRIDES include the All of Us Research Program; the Helping to End Addiction Long-term (HEAL) initiative; the Rapid Acceleration of Diagnostics (RADx) initiative for COVID research; the Accelerating Medicines Programs for Alzheimer's and Parkinson's Diseases (AMP AD / AMP PD); the Cancer Research Data Commons (CRDC) and Cancer Moonshot programs; the Gabriella Miller Kids First Pediatric Research Program; and the NIH INvestigation of Co-occurring conditions across the Lifespan to Understand Down syndromE (INCLUDE), to name a few. STRIDES aims to facilitate researchers' access to and use of high-value NIH research data that are currently stored in environments; to support researchers' transition to commercial cloud technologies through a cost-efficient framework; to provide NIH researchers access to and training on new and emerging cloud-based tools and services to enhance cutting-edge research; and ultimately to contribute to the formation of an interconnected ecosystem that breaks down silos that inhibit generating, analyzing, and sharing research data. STRIDES provides the following to the biomedical research community:

- **Discounts on Cloud CSP Services**: Favorable pricing on computing, storage, and related cloud services for NIH and NIH-funded institutions.
- **Professional Services**: Access to professional service consultations and technical support from CSP partners.
- **Training**: Access to training for researchers, data owners, and others to help ensure optimal use of available tools and technologies.
- **Potential Collaborative Engagements**: Opportunities to partner with CSPs to explore novel

methods and approaches to advance NIH's biomedical research objectives.

- **Access to Cloud Marketplaces**: Ability to find, purchase, and deploy cloud-based products and services from a wide variety of third-party CSP partners to jumpstart research and discovery.

2.2. *Effective Mechanisms for Secure Biomedical Data Sharing*

A modernized biomedical data ecosystem based on FAIR (i.e., Findable, Accessible, Interoperable, and Reusable) data principles is necessary to manage the plethora of health-related datasets generated for AI and data science research. However, risks associated with the privacy of patient or study participant information while sharing healthcare and other personal data can stymie the efforts to develop and deploy robust algorithms for applications in bioinformatics and clinical medicine. Thus, an advanced paradigm of data governance mechanisms is required to protect sensitive information in environments designed to enable greater access to and sharing of data.

NIH's Researcher Auth Service (RAS)[6] program has established a novel, cloud-based mechanism to authenticate and authorize researchers to controlled datasets. Based on Global Alliance for Genomics and Health (GA4GH)[7] standards, this initiative is designed to simplify and secure login processes — for example, by federating with trusted institutional identity providers — to allow researchers to safely access sensitive data using a model similar to "passports" (authentication) and "visas" (authorization) for international travel. This model serves to dynamically control access to biomedical data in a fine-grained fashion to align with consent agreements provided by patients/participants while implementing robust cybersecurity controls to minimize risk. Moreover, RAS features interoperable resources aimed at streamlining data sharing and analyses across biomedical data repositories and analytical platforms. With comprehensive auditing and a growing community of adopters, RAS and related approaches have the potential to greatly simplify and enhance computational research in healthcare by supporting secure mechanisms for sharing and accessing sensitive biomedical data.

2.3. *Secure Data Analytics Workspaces to Improve Collaboration and Advance AI*

Hundreds of domain-specific as well as generalist data repositories support the biomedical research enterprise. Significant challenges exist in bringing together data from multiple repositories; in meeting security and compliance requirements, especially with controlled-access data; and in providing common tools and interfaces to enable accessible, reproducible analysis to researchers regardless of local or institutional resources. The cyberinfrastructure ecosystem at the NIH is expanding to include secure, centralized, low-cost, cloud-based instances of workspace environments (i.e., "Secure Workspaces") that align with NIH expectations for interoperability within an open data ecosystem.

These workspaces are being designed to allow multiple researchers to study and interpret large-scale datasets from diverse data repositories and across cloud service providers to bring robust analysis tools and AI models to tackle complex biological questions. Common technical and data standards such as RAS, the Global Alliance for Genomics & Health (GA4GH) Data Repository Service (DRS)[8], the Health Level 7 (HL7) Fast Healthcare Interoperability Resources (FHIR)[9], and the Common Workflow Language[10] are being incorporated into these computational environments

to securely provide controlled data access to users and to enhance interoperability, data harmonization, and reproducibility of analyses. Moreover, within these environments, biomedical researchers can leverage popular informatics tools to perform interactive analyses and develop novel bioinformatics pipelines without having to download or manage large and complete datasets; set up, secure, manage, and support local IT infrastructure; or be an expert software developer.

Combined, NIH's STRIDES, RAS, and Secure Workspaces programs provide the biomedical research community with a stable foundation to build upon and modular, interoperable components to build with. By utilizing these cyberinfrastructure "building blocks", researchers can worry less about the technical aspects of authentication, authorization, computation, and data management and standardization, and instead, they can focus on the collaboration and innovation that drive biomedical discovery.

3. Workshop Topics and Speakers

3.1. *Building the tools to support the biomedical research digital ecosystem*

Sean D. Mooney, PhD (National Institutes of Health)

Dr. Sean Mooney, Ph.D., serves as the Director of the NIH Center for Information Technology and the NIH Associate Director for Information Technology, Cyberinfrastructure and Cybersecurity (AD ITCC). He oversees an approximately $400 million portfolio that includes a world-renowned supercomputer, a state-of-the-art network, cloud-based services, and the latest collaboration tools.

3.2. *From Infrastructure to Insight: Enabling the Next Generation of Biomedical Science*

Nick Weber, MBA (National Institutes of Health)

Nick Weber is the Acting Director of the Office of Scientific Computing Services at the NIH Center for Information Technology (CIT). He has been supporting cloud computing, high-performance computing, and other scientific infrastructure activities to enable research within the NIH for 17 years. For the past few years, he has been focused on the NIH Science and Technology Research Infrastructure for Discovery, Experimentation, and Sustainability (STRIDES) Initiative.

3.3. *Establishing Cyberinfrastructures for Trustworthy AI in Biomedicine*

Ojas A. Ramwala, B.Tech (University of Washington)

Ojas A. Ramwala is a final-year Ph.D. candidate at the University of Washington, Seattle, in the Department of Biomedical Informatics and Medical Education, School of Medicine. His research focuses on enhancing the clinical translation of deep learning algorithms for breast cancer screening.

3.4. *The Biomedical Data Sustainability Paradox*

Philip E. Bourne, PhD, FACMI (University of Virginia)

Philip E. Bourne, PhD, FACMI, is the Stephenson Founding Dean of the School of Data Science, Professor of Data Science and Biomedical Engineering at the University of Virginia, USA. Prior to that, he was the Associate Director for Data Science (ADDS) for the US National Institutes of Health (NIH) and a Senior Investigator at the National Center for Biotechnology Information (NCBI).

3.5. *Ten Tips for Effective AI Analysis of Biomedical Data*

Jason H. Moore, PhD, FACMI, FIAHSI, FASA (Cedars-Sinai Medical Center)

Dr. Moore completed a Ph.D. in Human Genetics and an M.A. in Statistics at the University of Michigan in 1999. He joined Cedars-Sinai Medical Center in 2021 as the founding Chair of the Department of Computational Biomedicine and Director of the Center for Artificial Intelligence Research and Education.

3.6. *Advancing Dementia Research with AI and Informatics: Mining Multidimensional Biobank Data*

Li Shen, PhD, FAIMBE, FACMI, FAMIA (University of Pennsylvania)

Li Shen, Ph.D., is Professor of Informatics and Radiology at the Perelman School of Medicine, University of Pennsylvania, where he serves as Associate Director for Bioinformatics at the Institute for Biomedical Informatics and Co-Director of the Penn Center for AI and Data Science for Integrated Diagnostics.

The workshop will also feature a talk from the ClinPGx team and conclude with a moderated panel discussion focusing on the following topics:

- Lessons learned from AI-driven biomedical discoveries
- Current challenges limiting access to high-quality biomedical datasets
- Community requirements for cost-effective and robust computing infrastructures
- Development of novel solutions to support the emerging AI and data ecosystem

References

1. Mooney, S. D. Technology Platforms and Approaches for Building and Evaluating Machine Learning Methods in Healthcare. *J. Appl. Lab. Med.* **8**, 194–202 (2023).
2. Ramwala, O. A. *et al.* ClinValAI: A framework for developing Cloud-based infrastructures for the External Clinical Validation of AI in Medical Imaging. *Pac. Symp. Biocomput. Pac. Symp. Biocomput.* **30**, 215–228 (2025).
3. Ramwala, O. A. *et al.* Establishing a Validation Infrastructure for Imaging-Based Artificial Intelligence Algorithms Before Clinical Implementation. *J. Am. Coll. Radiol.* **21**, 1569–1574 (2024).
4. Digital NIH: Innovation, Technology, and Computation for the Future of NIH FY2023 - FY2028.
5. About STRIDES. https://cloud.nih.gov/about-strides/.
6. Researcher Auth Service Initiative | Data Science at NIH. https://datascience.nih.gov/researcher-auth-service-initiative.
7. Rehm, H. L. *et al.* GA4GH: International policies and standards for data sharing across genomic research and healthcare. *Cell Genomics* **1**, 100029 (2021).
8. Data Repository Service (DRS). https://www.ga4gh.org/product/data-repository-service-drs/.
9. Index - FHIR v5.0.0. https://www.hl7.org/fhir/.
10. Language (CWL), C. W. Home. *Common Workflow Language (CWL)* https://www.commonwl.org/.

Trust, Reproducibility, and Progress: The Roles of Independent Blind Prediction and Assessment and Benchmarking in Computational Biology

Gaia Andreoletti, Serghei Mangul,
Sage Bionetworks
2901 3rd Ave, suite 330, Seattle (WA), United States of America
Email: gaia.andreoeltti@sagebase.org

Predrag Radivojac
Northeastern University
177 Huntington Avenue, Boston, MA 02115, United States of America
Email: *predrag@northeastern.edu*

Steven E. Brenner
University of California Berkeley
461A Koshland Hall #3102, CA 94720-3102, United States of America
Email: brenner@compbio.berkeley.edu

Abstract

When evaluations aren't trustworthy, entire research programs can chase mirages. Objective benchmarks and independent assessment have repeatedly catalyzed progress across computational biology, from protein structure prediction to variant interpretation and single-cell analysis. This workshop gathers leaders of community challenges and benchmarking infrastructures together with domain experts to provide a contemporary view of how to design trustworthy evaluations, why blind prediction matters, and where standards, infrastructure, and policy must evolve to meet the demands of AI-driven biology. We summarize the motivation and scope of the workshop; provide background on methodological and infrastructural advances that enable rigorous benchmarking; highlight invited speakers' contributions; and outline anticipated outcomes and community calls-to-action.

Keywords: benchmarking; blind prediction; reproducibility; evaluation; community challenges; standards; FAIR; open science; foundation models; genomics; proteomics; structural biology; biomedicine

© 2025 The Authors. Open Access chapter published by World Scientific Publishing Company and distributed under the terms of the Creative Commons Attribution Non-Commercial (CC BY-NC) 4.0 License.

1. Background and Motivation

Benchmarking, the systematic, reproducible evaluation of computational methods on well-characterized tasks, has been a primary engine of progress in computational biology. Community experiments built on blind prediction and independent assessment have delivered clear snapshots of the state-of-the-art while revealing gaps, biases, and practical limitations.

Structured challenges have established trust by separating training from evaluation via held-out or "model-to-data" test sets and by publishing transparent rules and metrics. In the "model-to-data" infrastructure, algorithms are sent to the data in a secure environment; test data never leave the enclave. These approaches have improved reproducibility through standardized data, well-defined tasks, and shared tooling such as containers, workflows, and leaderboards. They have accelerated translation by focusing evaluation on end-user-relevant criteria, including pathogenicity classification accuracy, clinical utility, and robustness across cohorts. Moreover, they have focused innovation by clarifying failure modes, encouraging ablation studies, and highlighting generalizable approaches.

The advent of large neural models and multi-omics assays makes rigorous, forward-compatible benchmarking both more urgent and more challenging. Data heterogeneity, potential leakage, shifting distributions, and compute-intensive models complicate fair comparisons. At the same time, funders, journals, and regulators increasingly look to community benchmarks to establish standards of evidence for methods intended for biomedical research and clinical use.

2. Principles of Trustworthy Benchmarking

1. Clear problem framing and intended use: precisely define the task and scope, with explicit target populations and contexts of use.

2. Data stewardship and curation: representative, consent-appropriate datasets; provenance; management of confounders; FAIR data practices; model-to-data evaluation when needed.

3. Separation of concerns: strict separation of training/validation/test; preregistered evaluation protocols where feasible.

4. Transparent, meaningful metrics: align with real-world utility; calibration and uncertainty; confidence intervals and significance tests.

5. Baselines, ablations, and error analysis: strong baselines; ablation studies; post-challenge error analyses.

6. Reproducible workflows: containerized submissions, version-controlled pipelines, archival of code/models, reference implementations and persistent identifiers.

7. Sustained infrastructure and governance: long-lived, community-maintained platforms and steering committees; open licenses; clear conflict-of-interest policies.

8. Equity and generalizability: evaluate across demographic, technical, and laboratory strata; robustness under dataset shift and rare-event conditions.

3. Landscape of Community Experiments and Benchmarking Infrastructures

The computational biology community has developed a rich ecosystem of benchmarking initiatives, each addressing distinct aspects of method evaluation and validation. Long-standing challenges such as CASP for protein structure prediction and CAFA for function annotation have demonstrated the power of iterative, multi-year assessments to drive algorithmic innovation and establish performance baselines. These initiatives have set precedents for blind prediction protocols, independent assessment frameworks, and community engagement that continue to influence new benchmarking efforts.

Recent years have witnessed a proliferation of domain-specific benchmarks spanning genomics, transcriptomics, proteomics, and integrative multi-omics analysis. Initiatives focused on variant interpretation, single-cell analysis, spatial transcriptomics, and clinical genomics have emerged to address the unique challenges of their respective domains. Simultaneously, infrastructure projects have developed platforms for secure model evaluation, including federated learning environments, containerized submission systems, and continuous benchmarking frameworks that enable ongoing assessment as new methods and data become available.

Despite this progress, significant gaps remain. Many benchmarks lack the infrastructure to prevent data leakage from large pre-trained models, struggle to evaluate generalization across diverse populations and experimental conditions or fail to capture clinically relevant performance metrics. The tension between open science principles and the need for truly held-out test data continues to challenge benchmark design. Furthermore, the computational resources required to evaluate modern deep learning models create barriers to participation and comprehensive comparison, while the rapid pace of methodological innovation often outstrips the capacity of static benchmarks to remain relevant.

4. Speakers

- Steven Brenner, University of California Berkeley, USA
- Predrag Radivojac, Northeastern University
- Brett Beaulieu-Jones, University of Chicago, USA
- Lana Garmire, University of Michigan, USA
- Panel Q&A

5. Workshop Format and Participation

This workshop begins with a framing introduction, followed by invited-talk blocks followed by a panel discussion with open Q&A and a live demo. Interactive polling will solicit audience views on priorities (e.g., preregistration, dataset access models, and required reporting) and capture community-endorsed recommendations.

5.1 Live Demo

Finding the right biomedical challenge or benchmark for your research can be frustratingly difficult. Information is scattered across different websites and platforms, making it hard to discover relevant datasets and tasks. OpenChallenges (OC) solves this problem by bringing together information about over 2,000 biomedical challenges from sources like Synapse and Kaggle into one searchable platform.

We will demonstrate how OC works with AI chatbots to make finding challenges as easy as having a conversation. Instead of manually searching through websites, you can simply ask questions like "show me genomics challenges with public baseline results" and get immediate, relevant answers. During the live demo, participants will see how to search for challenges, save useful queries, and export results in formats ready for analysis.

This session is designed for anyone interested in benchmarking—no technical expertise required. You'll leave with practical tools to discover challenges relevant to your work, whether you're looking for datasets to test new methods, teaching materials for courses, or opportunities to participate in community experiments.

6. Expected Outcomes

- A concise checklist for designing and reporting trustworthy benchmarks in computational biology.
- A community “wish list” for infrastructure and policy (e.g., preregistration; FAIR test sets; standardized container interfaces; uncertainty and error reporting).
- A shared bibliography of landmark challenges, infrastructure papers, and best-practice guidance to support new evaluations.

7. Acknowledgments

We thank the invited speakers for their contributions to community benchmarking and the organizers and sponsors of the Pacific Symposium on Biocomputing for supporting this workshop. We also acknowledge community contributors and maintainers of benchmarking platforms, dataset providers, and assessors for their essential roles in rigorous, open science.